Marek Procházka · Janina Kneipp ·
Bing Zhao · Yukihiro Ozaki *Editors*

# Surface- and Tip-Enhanced Raman Scattering Spectroscopy

## Bridging Theory and Applications

Springer

# Surface- and Tip-Enhanced Raman Scattering Spectroscopy

Marek Procházka · Janina Kneipp · Bing Zhao · Yukihiro Ozaki
Editors

# Surface- and Tip-Enhanced Raman Scattering Spectroscopy

## Bridging Theory and Applications

Springer

*Editors*
Marek Procházka
Charles University
Prague, Czech Republic

Janina Kneipp
Humboldt-Univeristät zu Berlin
Berlin, Germany

Bing Zhao
Jilin University
Changchun, China

Yukihiro Ozaki
Kwansei Gakuin University
Sanda, Japan

ISBN 978-981-97-5817-3 ISBN 978-981-97-5818-0 (eBook)
https://doi.org/10.1007/978-981-97-5818-0

© The Editor(s) (if applicable) and The Author(s), under exclusive license to Springer Nature Singapore Pte Ltd. 2024

This work is subject to copyright. All rights are solely and exclusively licensed by the Publisher, whether the whole or part of the material is concerned, specifically the rights of translation, reprinting, reuse of illustrations, recitation, broadcasting, reproduction on microfilms or in any other physical way, and transmission or information storage and retrieval, electronic adaptation, computer software, or by similar or dissimilar methodology now known or hereafter developed.
The use of general descriptive names, registered names, trademarks, service marks, etc. in this publication does not imply, even in the absence of a specific statement, that such names are exempt from the relevant protective laws and regulations and therefore free for general use.
The publisher, the authors and the editors are safe to assume that the advice and information in this book are believed to be true and accurate at the date of publication. Neither the publisher nor the authors or the editors give a warranty, expressed or implied, with respect to the material contained herein or for any errors or omissions that may have been made. The publisher remains neutral with regard to jurisdictional claims in published maps and institutional affiliations.

This Springer imprint is published by the registered company Springer Nature Singapore Pte Ltd.
The registered company address is: 152 Beach Road, #21-01/04 Gateway East, Singapore 189721, Singapore

If disposing of this product, please recycle the paper.

# Preface

It is our great pleasure to publish this book on the special occasion of the 50th anniversary of the discovery of surface-enhanced Raman signals. In the early 1970s, Fleischman, Hendra, and McQuillan observed extraordinarily strong Raman signals from pyridine adsorbed on a rough silver electrode. In 1977, two groups, Van Duyne and Jeanmaire, and Creighton and Albrecht, independently confirmed this observation and reached the conclusion that the strong Raman signals from pyridine are not due to a large number of molecules on the silver electrode but, more importantly, are caused by an enhancement of the Raman scattering efficiency for the molecules adsorbed on the rough nanostructured silver surface. Since its discovery, surface-enhanced Raman scattering (SERS) has opened new avenues in basic science and technology, and has stimulated both experiments and theories that concern both basic understanding of the effect, as well as its applications. The most remarkable examples are its enormous influence on the development of the fields of quantum optics and plasmonics. In the past decades, the advantages of SERS have been extended from basic studies to a huge number of advanced applications, ranging from work in photocatalysis to medical diagnostics.

Tip-enhanced Raman scattering (TERS) was developed by important contributions from several groups, with pioneering work by Kawata et al., Zenobi et al., and Anderson et al. at the end of last century. By exploiting a scanning probe, TERS has enabled vibrational spectroscopy at a lateral resolution in the nanometer to sub-nanometer region. It allows to explore the molecular structure on the order of Ångström, at the level of individual molecular bonds.

This book has been preceded by a large body of collections on the research field of SERS and TERS that are currently available. They include works that specifically review the history and development of SERS and TERS, along with explanations of their mechanisms, important aspects of the instrumentation, and their applications to a variety of research areas.

Nevertheless, we think there is a strong demand for a state-of-the-art review book on this faster and faster evolving field. Therefore, we have aimed at preparing a book which provides a continued documentation of the historical development of SERS and TERS, by including the most recent trends in the field.

This book consists of four parts. Part I, discussing "Basics of SERS and TERS", the recent progress on the electromagnetic enhancement mechanism of SERS, the chemical enhancement, and semiconductor-enhanced Raman scattering are described. Part I of the book also describes the application of machine learning for an analysis of SERS signals. In Part II, a variety of applications to material sciences and analytical chemistry are introduced, including monitoring of plasmon-assisted catalysis, the applications of semiconductor-enhanced Raman scattering, and electrochemical SERS. "Applications of SERS to biomedical sciences" are discussed in Part III. This part contains nine biomedical applications that include point-of-care applications, as well as medical applications of surface-enhanced spatially off-set Raman spectroscopy (SESORS). The last part of this collection is concerned with TERS studies. Ångström-resolved TERS, the nanoscale imaging of photocatalytic processes using TERS, and tip-enhanced Raman microscopy are outlined.

One of the attempts that we made when putting together this book was to put some emphasis on the different mechanisms of SERS enhancement, specifically by discussing the chemical mechanism, as well as the mechanism of semiconductor-enhanced Raman scattering, that is becoming of specific interest in the advent of a broad range of novel materials that can be exploited for an enhancement of Raman signals. Another emphasis of this book is to point out advanced analysis methods for SERS data such as machine learning and AI. As for the applications, this book covers almost all areas of applications to which SERS and TERS are currently applied. The selection, however, illustrates the importance of the methods in the biomedical science.

The contributors from the many different research fields and many countries are all front runners, and in addition to renowned senior colleagues include younger scientists who have been conducting their work as the "offspring generation" of those who discovered and explored the effects 50 years ago. We hope that this book will be useful for senior scientists, engineers, and graduate students in the range of fields where SERS and TERS are currently playing a role, such as chemistry and physics, as well as areas where their potential is about to develop at present, such as in the life science, pharmacology, and medicine. We encourage the readers of this book to become inspired and to open new directions of SERS and TERS research in their own basic studies and applications.

Last but not least we would like to thank Dr. Shinichi Koizumi of Springer/Nature for his continuous support and efforts in publishing this exciting book.

Prague, Czech Republic — Marek Procházka
Berlin, Germany — Janina Kneipp
Changchun, China — Bing Zhao
Sanda, Japan — Yukihiro Ozaki
July 2024

# Contents

**Part I Basics of SERS and TERS**

**1 Plasmon-Enhanced Spectroscopy and Photocatalysis** . . . . . 3
Sajal Kumar Giri and George C. Schatz

**2 Basics and Frontiers of Electromagnetic Mechanism of SERS Hotspots** . . . . . 19
Tamitake Itoh and Yuko S. Yamamoto

**3 Chemical Mechanism of SERS** . . . . . 49
Libin Yang, Xin Jiang, and Bing Zhao

**4 Semiconductor-Enhanced Raman Scattering: Enhancement Mechanism and Substrate Design** . . . . . 63
Junbo Li, Bo Jiang, and Wei Ji

**5 Towards Reliable and Practical SERS** . . . . . 87
Wafaa Aljuhani, Yingrui Zhang, Chunchun Li, Yikai Xu, and Steven E. J. Bell

**6 State-of-the-Art Tip-Enhanced Raman Scattering** . . . . . 117
Prompong Pienpinijtham and Yukihiro Ozaki

**7 Advances in Machine Learning for SERS Analysis** . . . . . 165
Clarice E. Froehlich, Cassandra L. Wouters, Mahmoud Matar Abed, Vivian E. Ferry, and Christy L. Haynes

**Part II Applications of SERS to Material Sciences and Analytical Chemistry**

**8 Wearable Surface-Enhanced Raman Spectroscopy** . . . . . 195
Yasutaka Kitahama and Keisuke Goda

**9 Non-plasmonic Metal Oxide Nanostructures for SERS Applications** ..... 219
Eva Kočišová, Ondřej Kylián, and Marek Procházka

**10 Principles, Characteristics, and Applications of Electrochemical Surface-Enhanced Raman Spectroscopy** ..... 249
Christa Brosseau

**11 Monitoring Plasmon-Assisted Catalysis by SERS** ..... 273
Zhiyang Zhang and Janina Kneipp

**12 Plasmonic Metal–Semiconductor Hybrids as Substrates for Photo-Induced Surface Raman Enhancement** ..... 315
Łukasz Pięta, Adrian Warzybok, and Kamilla Malek

**Part III Applications of SERS to Biomedical Sciences**

**13 SERS for Precision Medicine: A Promising Approach** ..... 337
Yibao Huang, Chenxiao Zhao, Linlu Zhao, and Ziyi Cheng

**14 SERS Bioanalysis Based on Tagging and Responsive Probes** ..... 371
Jun Cao, Wei Zhu, and Ai-Guo Shen

**15 Gap-Enhanced Raman Tags (GERTs): Synthesis, Optical Properties, and Applications** ..... 431
Yuqing Zhang and Jian Ye

**16 SERS for Diagnostics and Forensics: Selected Past, Present, and Future Highlights** ..... 453
Lawrence D. Ziegler

**17 Surface-Enhanced Raman Spectroscopy in Clinical Point-of-Care Testing** ..... 487
Tony Dib, Aradhana Dwivedi, Chen Liu, Edoardo Farnesi, Jürgen Popp, and Dana Cialla-May

**18 Advanced Medical SERS Applications** ..... 535
Chrysafis Andreou, Marios Stavrou, and Adrián Fernández-Lodeiro

**19 Analytical SERS for Liquid Biopsy Biomarkers Detection** ..... 567
Anastasiia Tukova, Wei Zhang, Alison Rodger, and Yuling Wang

**20 SORS and SESORS Biomedical Applications** ..... 609
Priyanka Dey

**21 Recent Advances in SERS-based Biomedical Diagnostics of Covid-19** ..... 635
Sungwoon Lee, Sang-Woo Joo, and Jaebum Choo

## Part IV TERS Studies

**22 Ångström-Resolved Tip-Enhanced Raman Spectroscopy** . . . . . 657
Yao Zhang and Zhen-Chao Dong

**23 Nanoscale Imaging of Photocatalytic Processes Using Tip-Enhanced Raman Spectroscopy** . . . . . 699
Dmitry Kurouski

**24 Tip-Enhanced Raman Microscopy: Theory, Practice, and Applications for Nanomaterials Visualization and Characterization** . . . . . 721
Atsushi Taguchi

# Contributors

**Wafaa Aljuhani** School of Chemistry and Chemical Engineering, Queen's University Belfast, Belfast, U.K.

**Chrysafis Andreou** Department of Electrical and Computer Engineering, University of Cyprus, Nicosia, Cyprus

**Steven E. J. Bell** School of Chemistry and Chemical Engineering, Queen's University Belfast, Belfast, U.K.

**Christa Brosseau** Saint Mary's University, Halifax, Canada

**Jun Cao** School of Bioengineering and Health, Wuhan Textile University, Wuhan, China

**Ziyi Cheng** Key Laboratory of Hainan Trauma and Disaster Rescue, The First Affiliated Hospital of Hainan Medical University, Hainan Medical University, Haikou, China

**Jaebum Choo** Department of Chemistry, Chung-Ang University, Seoul, South Korea

**Dana Cialla-May** Department Spectroscopy and Imaging, Leibniz Institute of Photonic Technology, Member of Leibniz Health Technologies, Member of the Leibniz Centre for Photonics in Infection Research (LPI), Jena, Germany; Institute of Physical Chemistry and Abbe Center of Photonics, Friedrich Schiller University Jena, Member of the Leibniz Centre for Photonics in Infection Research (LPI), Jena, Germany

**Priyanka Dey** School of Medicine, Pharmacy and Biomedical Sciences, University of Portsmouth, Portsmouth, UK

**Tony Dib** Department Spectroscopy and Imaging, Leibniz Institute of Photonic Technology, Member of Leibniz Health Technologies, Member of the Leibniz Centre for Photonics in Infection Research (LPI), Jena, Germany;
Institute of Physical Chemistry and Abbe Center of Photonics, Friedrich Schiller University Jena, Member of the Leibniz Centre for Photonics in Infection Research (LPI), Jena, Germany

**Zhen-Chao Dong** Hefei National Research Center for Physical Sciences at the Microscale, University of Science and Technology of China, Hefei, China;
Hefei National Laboratory, University of Science and Technology of China, Hefei, China

**Aradhana Dwivedi** Department Spectroscopy and Imaging, Leibniz Institute of Photonic Technology, Member of Leibniz Health Technologies, Member of the Leibniz Centre for Photonics in Infection Research (LPI), Jena, Germany;
Institute of Physical Chemistry and Abbe Center of Photonics, Friedrich Schiller University Jena, Member of the Leibniz Centre for Photonics in Infection Research (LPI), Jena, Germany

**Edoardo Farnesi** Department Spectroscopy and Imaging, Leibniz Institute of Photonic Technology, Member of Leibniz Health Technologies, Member of the Leibniz Centre for Photonics in Infection Research (LPI), Jena, Germany;
Institute of Physical Chemistry and Abbe Center of Photonics, Friedrich Schiller University Jena, Member of the Leibniz Centre for Photonics in Infection Research (LPI), Jena, Germany

**Adrián Fernández-Lodeiro** Department of Electrical and Computer Engineering, University of Cyprus, Nicosia, Cyprus

**Vivian E. Ferry** Department of Chemical Engineering and Materials Science, University of Minnesota, Minneapolis, MN, USA

**Clarice E. Froehlich** Department of Chemical Engineering and Materials Science, University of Minnesota, Minneapolis, MN, USA

**Sajal Kumar Giri** Department of Chemistry, Northwestern University, 2145 Sheridan Road, Evanston, IL, USA

**Keisuke Goda** Department of Chemistry, The University of Tokyo, Tokyo, Japan;
LucasLand, Co. Ltd., Tokyo, Japan;
Institute for Quantum Life Science, National Institute for Quantum and Radiological Science and Technology, Chiba, Japan;
Institute of Technological Sciences, Wuhan University, Hubei, China;
Department of Bioengineering, University of California, Los Angeles, CA, USA

**Christy L. Haynes** Department of Chemistry, University of Minnesota, Minneapolis, MN, USA

**Yibao Huang** Key Laboratory of Hainan Trauma and Disaster Rescue, The First Affiliated Hospital of Hainan Medical University, Hainan Medical University, Haikou, China

**Tamitake Itoh** Health and Medical Research Institute, National Institute of Advanced Industrial Science and Technology (AIST), Takamatsu, Kagawa, Japan

**Wei Ji** College of Chemistry, Chemical Engineering and Resource Utilization, Northeast Forestry University, Harbin, China

**Bo Jiang** College of Chemistry, Chemical Engineering and Resource Utilization, Northeast Forestry University, Harbin, China

**Xin Jiang** College of Chemistry and Chemical Engineering, Qiqihar University, Qiqihar, China

**Sang-Woo Joo** Department of Chemistry, Soongsil University, Seoul, South Korea

**Yasutaka Kitahama** Department of Chemistry, The University of Tokyo, Tokyo, Japan;
LucasLand, Co. Ltd., Tokyo, Japan

**Janina Kneipp** Department of Chemistry, Humboldt-Universität zu Berlin, Berlin, Germany

**Eva Kočišová** Faculty of Mathematics and Physics, Institute of Physics, Charles University, Prague, Czech Republic

**Dmitry Kurouski** Department of Biochemistry and Biophysics, Texas A&M University, College Station, Texas, USA;
Department of Biomedical Engineering, Texas A&M University, College Station, Texas, USA;
Institute for Advancing Health Through Agriculture, College Station, Texas, USA

**Ondřej Kylián** Faculty of Mathematics and Physics, Department of Macromolecular Physics, Charles University, Prague, Czech Republic

**Sungwoon Lee** Department of Chemistry, Chung-Ang University, Seoul, South Korea

**Chunchun Li** University of Shanghai for Science and Technology, Shanghai, China

**Junbo Li** College of Chemistry, Chemical Engineering and Resource Utilization, Northeast Forestry University, Harbin, China

**Chen Liu** Department Spectroscopy and Imaging, Leibniz Institute of Photonic Technology, Member of Leibniz Health Technologies, Member of the Leibniz Centre for Photonics in Infection Research (LPI), Jena, Germany;
Institute of Physical Chemistry and Abbe Center of Photonics, Friedrich Schiller University Jena, Member of the Leibniz Centre for Photonics in Infection Research (LPI), Jena, Germany

**Kamilla Malek** Department of Chemical Physics, Faculty of Chemistry, Jagiellonian University, Krakow, Poland

**Mahmoud Matar Abed** Department of Chemistry, University of Minnesota, Minneapolis, MN, USA

**Yukihiro Ozaki** School of Biological and Environmental Sciences, Kwansei Gakuin University, Sanda, Hyogo, Japan

**Prompong Pienpinijtham** Sensor Research Unit (SRU), Department of Chemistry, Faculty of Science, Chulalongkorn University, Pathumwan, Bangkok, Thailand;
Center of Excellence in Bioactive Resources for Innovative Clinical Applications, Chulalongkorn University, Pathumwan, Bangkok, Thailand

**Łukasz Pięta** Department of Chemical Physics, Faculty of Chemistry, Jagiellonian University, Krakow, Poland;
Doctoral School of Exact and Natural Sciences, Jagiellonian University, Krakow, Poland

**Jürgen Popp** Department Spectroscopy and Imaging, Leibniz Institute of Photonic Technology, Member of Leibniz Health Technologies, Member of the Leibniz Centre for Photonics in Infection Research (LPI), Jena, Germany;
Institute of Physical Chemistry and Abbe Center of Photonics, Friedrich Schiller University Jena, Member of the Leibniz Centre for Photonics in Infection Research (LPI), Jena, Germany

**Marek Procházka** Faculty of Mathematics and Physics, Institute of Physics, Charles University, Prague, Czech Republic

**Alison Rodger** School of Natural Sciences, Faculty of Science and Engineering, Macquarie University, Sydney, NSW, Australia;
Research School of Chemistry, Australian National University, Canberra, ACT, Australia

**George C. Schatz** Department of Chemistry, Northwestern University, 2145 Sheridan Road, Evanston, IL, USA

**Ai-Guo Shen** School of Bioengineering and Health, Wuhan Textile University, Wuhan, China

**Marios Stavrou** Department of Electrical and Computer Engineering, University of Cyprus, Nicosia, Cyprus

**Atsushi Taguchi** Research Institute for Electronic Science, Hokkaido University, Sapporo, Japan

**Anastasiia Tukova** School of Natural Sciences, Faculty of Science and Engineering, Macquarie University, Sydney, NSW, Australia

**Yuling Wang** School of Natural Sciences, Faculty of Science and Engineering, Macquarie University, Sydney, NSW, Australia

**Adrian Warzybok** Department of Chemical Physics, Faculty of Chemistry, Jagiellonian University, Krakow, Poland

**Cassandra L. Wouters** Department of Chemistry, University of Minnesota, Minneapolis, MN, USA

**Yikai Xu** East China University of Science And Technology Shanghai, Shanghai, China

**Yuko S. Yamamoto** School of Materials Science, Japan Advanced Institute of Science and Technology (JAIST), Nomi, Ishikawa, Japan

**Libin Yang** College of Chemistry and Chemical Engineering, Qiqihar University, Qiqihar, China

**Jian Ye** School of Biomedical Engineering, Shanghai Jiao Tong University, Shanghai, China

**Wei Zhang** School of Natural Sciences, Faculty of Science and Engineering, Macquarie University, Sydney, NSW, Australia

**Yao Zhang** Hefei National Research Center for Physical Sciences at the Microscale, University of Science and Technology of China, Hefei, China; Hefei National Laboratory, University of Science and Technology of China, Hefei, China

**Yingrui Zhang** School of Chemistry and Chemical Engineering, Queen's University Belfast, Belfast, U.K.

**Yuqing Zhang** School of Automation, Hangzhou Dianzi University, Hangzhou, China

**Zhiyang Zhang** CAS Key Laboratory of Coastal Environmental Processes and Ecological Remediation, Yantai Institute of Coastal Zone Research, Chinese Academy of Sciences, Yantai, China

**Bing Zhao** State Key Laboratory of Supramolecular Structure and Materials, Jilin University, Changchun, China

**Chenxiao Zhao** Key Laboratory of Hainan Trauma and Disaster Rescue, The First Affiliated Hospital of Hainan Medical University, Hainan Medical University, Haikou, China

**Linlu Zhao** Key Laboratory of Hainan Trauma and Disaster Rescue, The First Affiliated Hospital of Hainan Medical University, Hainan Medical University, Haikou, China

**Wei Zhu** School of Bioengineering and Health, Wuhan Textile University, Wuhan, China

**Lawrence D. Ziegler** Department of Chemistry and The Photonics Center, Boston University, Boston, MA, USA

# Part I
# Basics of SERS and TERS

# Chapter 1
# Plasmon-Enhanced Spectroscopy and Photocatalysis




**Sajal Kumar Giri and George C. Schatz**

**Abstract** This study examines the Raman scattering and charge transfer properties of molecules adsorbed on the surface of a tetrahedral $Au_{120}$ nanoparticle based on the time-dependent density functional tight-binding (TD-DFTB) method. We study Raman scattering (SERS) enhancements for pyridine where the molecule is adsorbed either on the tip (V-complex) or surface (S-complex) of the nanoparticle. The scattering intensity is enhanced by a factor of 3–15 due to chemical effects while significantly larger enhancements (in the order of $10^2-10^4$) are observed for plasmon resonance excitation at an energy of 2.5 eV depending on the adsorption site. Furthermore, we demonstrate charge transfer between the nanoparticle and a fullerene-based molecule after pulsed excitation of the plasmon resonance which shows how plasmon excitation can lead to negative molecular ion formation. All of these results are consistent with earlier studies using either TD-DFT theory or experimental measurements.

**Keywords** Plasmons · SERS · Photocatalysis · Charge transfer

## 1.1 Introduction

Surface-enhanced Raman scattering (SERS) is a widely used phenomenon among various research communities where the scattering intensity of molecules can be increased by several orders of magnitude when they are adsorbed on the surface of plasmonic nanoparticles [1–3]. The enhancement factors are as large as $10^{10}-10^{11}$, and therefore, SERS can be studied on the single-molecule level [4–8]. The unexpected enhancement in the Raman signal from pyridine adsorbed on an electrochemically roughened silver electrode was the first evidence of SERS [9], and this was attributed to the extensive surface coverage of molecules on the rough nanostruc-

S. K. Giri · G. C. Schatz (✉)
Department of Chemistry, Northwestern University,
2145 Sheridan Road, Evanston, IL 60208, USA
e-mail: g-schatz@northwestern.edu

© The Author(s), under exclusive license to Springer Nature Singapore Pte Ltd. 2024

M. Procházka et al. (eds.), *Surface- and Tip-Enhanced Raman Scattering Spectroscopy*,
https://doi.org/10.1007/978-981-97-5818-0_1

tured surface, but later it was identified as a plasmon-based phenomenon [1, 2]. SERS has been successfully applied to several fields including biosensing [10, 11], drug analysis [12], and electrochemistry [13, 14].

Raman scattering arises because the electric field of the incident electromagnetic radiation induces polarization in irradiated molecules and the component of the charge oscillation at the shifted Raman frequencies leads to emission of scattered light. The intensity of the scattered light depends on two components: incident light intensity and the polarizability of the molecule. In SERS, the weak Raman intensities for isolated molecules are increased in the presence of plasmonic nanoparticles due to amplification of the oscillating electric field at the molecule that arises from plasmon excitation. Thus, the treatment of SERS includes the interaction of light with both molecules and particles.

Broadly speaking, the two possible mechanisms that describe SERS involve electromagnetic and chemical effects. Localized surface plasmon resonance (LSPR) excitation of the conduction electrons in metal nanoparticles of Au, Ag, and Cu with dimensions of 5–200 nanometers generates an enhanced electromagnetic field at the interface of the particle [15]. This enhanced field can modulate several optical processes at the surface including photocurrent [16], luminescence [17], and Raman scattering [1–3]. Raman scattering scales with the local field as $|E_{\text{loc}}(\omega)|^4/|E_0(\omega)|^4$, where the numerator is the localized electromagnetic field and the denominator is the incident field [3]. SERS enhancement factors due to electromagnetic effects can reach values up to $10^9$ [6].

On the other hand, the chemical enhancement includes the effect of orbital overlap that occurs when molecules adsorb on the surface. Static charge transfer associated with adsorption modifies the Raman polarizability of the molecule, leading to a contribution to SERS. Charge transfer (CT) excitations at optical frequency can also contribute to enhancements through a resonance Raman mechanism [18]. Enhancements due to static chemical effects can be up to a factor of 3–20 as demonstrated theoretically for pyridine adsorbed on the surface of a small tetrahedral Au particle [19]. Resonance CT can lead to larger enhancements, but usually the Resonance CT and LSPR frequencies are sufficiently different, or the resonance CT transition is sufficiently broad, that one only has significant SERS enhancement from plasmon excitation and static CT.

Atomistic simulations based on quantum mechanics provide insight into the possible SERS mechanisms and enhancements, in addition to providing Raman shifts and adsorbate structures and reactions. Previous theoretical works have addressed SERS for pyridine adsorbed on the surface of Ag and Au particles with enhancement factors up to $10^2-10^4$ based on the time-dependent density functional theory (TD-DFT) [19]. However, the size of the nanoparticles that can be described with electronic structure theory has been limited to a small number of atoms ($\leq 20$) due to the large computational complexities associated with the calculations. It is therefore a subject of significant importance to explore SERS for larger nanoparticles. Typically this should involve hundreds or even thousands of atoms as quantum size effects lead to noticeable blue shifts of plasmon frequencies with decreasing particle size

for particles with less than 100 atoms. Semi-empirical methods based on INDO have been demonstrated successfully for the efficient simulation of SERS for Ag-pyridine complexes [20, 21]. As an alternative to the INDO calculations, the density functional tight-binding (DFTB) method may also provide efficient solutions for larger complexes [22]. We explore this possibility in this work.

Two recent papers provide details of the DFTB method [22, 23]. DFTB is a semi-empirical method which contains many features that are similar to the earlier INDO method, but it is developed from a DFT perspective, and with much greater functionality. As a consequence, this method provides results that are often comparable to DFT but with significantly lower computational costs, and therefore, the ground and excited state properties of larger complexes can be simulated efficiently. Previous works have demonstrated the success of the DFTB method in various applications including biomolecules [24], metals [25–27], semiconductors [28], plasmonic photocatalysis [29–31], etc. However, the accuracy of the prediction is limited by the quality of the parameters that describe the Hamiltonian ($H$) and overlap ($O$) matrices. To elevate accuracy and enable applications to a larger portion of the periodic table, new parameters need to be developed and further optimized.

The real-time time-dependent density functional tight-binding (RT-TD-DFTB) method allows us to study plasmon-driven charge and energy transfer processes at the metal-molecule interface by simulating laser-induced electron dynamics [23, 29, 30]. In these calculations, hot carriers generated through the decay of LSPR states can be transferred to the adsorbed molecules, initiating reaction dynamics on the surface of the metal nanoparticles. This includes several processes like molecular bond dissociation and formation [30, 31], charge transfer (CT) [32], energy transfer [29], spectral shift [33], etc. In the following, we study CT processes between $Au_{120}$ and a fullerene ($C_{60}$) after exciting plasmons at 2.5 eV with an external laser pulse. This work was inspired by a recent study from the Van Duyne group, where the fullerene-based molecule [6,6]-phenyl-$C_{61}$-butyric acid methyl ester (PCBM) was found to form negative ions in the presence of gold dimers when irradiated at 532 nm as revealed by SERS measurements. Given this, the present study addresses the ability of the DFTB method to study both SERS and plasmon-driven electron transfer processes at the metal-molecule interface.

The paper is divided into two parts, in the first part, we explore Raman scattering for $Au_{120}$-pyridine complexes and the second part contains plasmon-driven CT in a $Au_{120}$-$C_{60}$ complex. For Raman scattering, we discuss enhancements due to chemical and plasmon excitation at an energy of 2.5 eV. The molecular Raman spectrum obtained with the DFTB method is compared with the B3LYP/TZVP level of DFT theory. For the CT study, we demonstrate results with RT-TD-DFTB calculations. Thus, these two separate studies each addresses key benchmarks for using DFTB in future studies where the two calculations are combined.

## 1.2 Computational Details

All calculations in this work have been carried out with the DFTB+ and ORCA codes. To perform time-dependent density functional tight-binding (TD-DFTB) calculations, we use auorg/auorg-1-1 Slater-Koster parameters for gold-molecule complexes downloaded from the dftb.org site. To elucidate the accuracy of this method for predicting Raman spectra, we compare DFTB results with conventional results obtained with the B3LYP/TZVP level of DFT theory. The self-consistent-charge density functional tight-binding (SCC-DFTB) approach has been used to compute the ground state properties of all the complexes studied. To treat the dynamics induced by external driving fields, we use the time-dependent DFTB scheme that is an extension of SCC-DFTB to the time domain.

The Raman scattering activity $S_p$ for a vibrational mode $p$ is calculated from the polarizability derivatives as $S_p = 45\alpha_p'^2 + 7\gamma_p'^2$, where $\alpha_p'$ and $\gamma_p'$ are derivatives of the isotropic and anisotropic polarizabilities with respect to the normal mode $p$. The derivatives of the frequency-dependent polarizability are determined from single-point computations for small Cartesian coordinate displacements from the equilibrium geometry along the normal modes for both DFT and DFTB calculations. We compute polarizabilities in the frequency domain with a value of the damping parameter $\Gamma = 0.15$ eV. To obtain a smooth Raman spectrum as a function of Raman shifts, the scattering activity is broadened by a Lorentzian function with a 20 $cm^{-1}$ width.

In real-time TD-DFTB (RT-TD-DFTB), the one-body reduced density matrix is propagated according to the Liouville-von Neumann equation in a nonorthogonal basis [23]

$$\dot{\rho} = -i(O^{-1}H\rho - \rho H O^{-1}) \tag{1.1}$$

starting from an initial state defined by Hamiltonian ($H_0$), overlap ($O_0$), and density ($\rho_0$) matrices. Here, $O^{-1}$ represents the inverse of $O$. The Hamiltonian in the above equation includes a field-matter coupling term $V_A(t) = -\boldsymbol{\mu} \cdot \mathbf{E}(t)$, where $\mathbf{E}(t)$ is the external field and $\boldsymbol{\mu} = \sum_A \Delta q_A \mathbf{R}_A(t)$ is the dipole with atomic coordinate $\mathbf{R}_A$ and charge $\Delta q_A$ for atom A at time $t$. We consider a time-dependent pulse of the following form to drive the system

$$E(t) = E_0 \exp(-(t - t_c)^2/T_l^2)\sin(\omega_l t) \tag{1.2}$$

with field amplitude $E_0$, center of the pulse $t_c$, pulse duration $T_l$, and frequency $\omega_l$. For calculating spectra, the density matrix evolves in time due to purely electronic dynamics where the nuclei are "clamped" in space. This treatment has been extensively used to study optical processes of material and molecules induced by external time-dependent electric fields [23, 34, 35]. The Mulliken population is calculated as

$$q_A = \mathrm{Tr}_A[\rho O], \tag{1.3}$$

where $\mathrm{Tr}_A$ denotes trace over orbitals centered on atom A, and the $O$ matrix depends on the coordinates that are parameterized for each pair of orbitals.

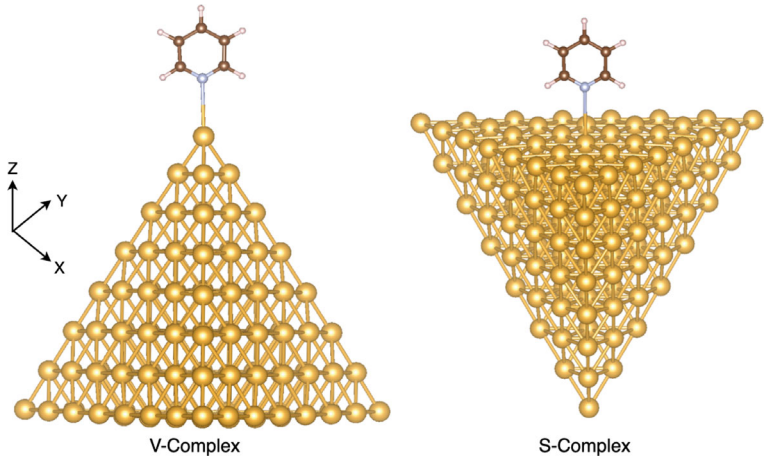



**Fig. 1.1** Optimized geometries of $Au_{120}$-pyridine complexes where pyridine is adsorbed on one of the tips (V-complex) and triangle surfaces (S-complex)

We compute all absorption spectra reported here in the time domain. The density matrix is propagated in time with an external Dirac $\delta$ perturbation of the form $E(t) = E_0\delta(t)\hat{e}$ with field amplitude $E_0$ and direction vector $\hat{e}$. The system evolves in time freely and the induced dipole contains information related to the transition energy and couplings between the ground and excited states. The absorption spectrum is obtained from the imaginary component of the Fourier-transformed dipole moment

$$\sigma_{\text{abs}}(\omega) = \frac{4\pi\omega}{3c}\text{Im}\{\text{Tr}[(\mu(\omega) - \mu_0)/E_0]\} \tag{1.4}$$

with an initial permanent dipole $\mu_0$. This method reproduces linear absorption spectra that are conventionally obtained in the frequency domain in the limit of a weak field intensity, $E_0 \to 0$, that induces linear photoabsorption. To broaden the absorption lines in energy, we damp the time-dependent dipoles with a damping function $\exp(-t/\tau)$ with a decay timescale of $\tau = 6$ fs.

## 1.3 Results and Discussion

### *Raman Scattering*

#### $Au_{120}$-Pyridine Complexes

We use a tetrahedral $Au_{120}$ nanoparticle for all of these studies, which is a similar structure (but larger) to what has been considered in earlier SERS studies [19]. This allows two distinct binding sites for an adsorbing pyridine molecule, either on one of the tips (V-complex) or in the middle of the triangle faces (S-complex). These two sites provide significantly different chemical environments for pyridine, affecting how the molecule interacts with the particle. It has been found that the S-complex better represents the experimental SERS spectra, however, the V-complex provides different SERS features due to a unique interaction between the particle and molecule.

We optimize all geometries with a maximum force tolerance of $10^{-5}$ a.u. for the movement of atoms. We attach pyridine on the tip (for V-complex) and surface (for S-complex) gold atoms of a previously optimized $Au_{120}$ and further optimize, freezing the atoms of the particle. Optimized geometries are shown in Fig. 1.1. For both the geometries pyridine binds through the N atom and the Au-N bond aligns with the Z-axis. The distance between N and the nearest Au is 2.21 Å for the V-complex and

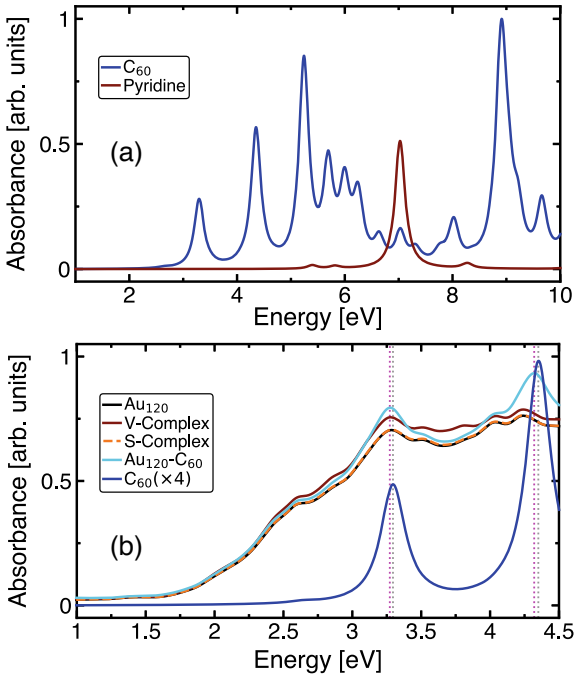



**Fig. 1.2** Absorption spectra of **a** isolated fullerene ($C_{60}$) and pyridine molecules and **b** $Au_{120}$ complexes. In **b**, peak positions for the first two lowest energy peaks (gray dotted lines) of the isolated $C_{60}$ are compared with the peaks that appear for the $Au_{120}$-$C_{60}$ complex (magenta dotted lines) near 3.3 and 4.4 eV. Absorption intensity for (**a**) and (**b**) is scaled differently

2.32 Å for the S-complex. A smaller distance between the particle and molecule was also observed in a $Au_{20}$-pyridine V-complex with TD-DFT calculations [19]. We find a small amount of electron transfer from pyridine to the particle in the ground state structures, 0.05e and 0.03e for the V- and S-complexes, respectively. Furthermore, we note that an electronic temperature of 300K is used throughout the study.

### Absorption Spectra

The absorption spectrum of pyridine is shown in Fig. 1.2a. Excited states between 5 and 6 eV are weakly absorbing while a strong absorption peak appears at an energy of 7 eV. The strong absorption peak involves $\pi \rightarrow \pi^*$ transition and is associated with a large oscillator strength. These spectral features are consistent with previous studies based on INDO/SCI and TD-DFT methods [21]. The absorption spectrum of fullerene (Fig. 1.2a) is discussed in the next section.

Absorption spectra for $Au_{120}$ and $Au_{120}$-pyridine complexes are shown in Fig. 1.2b. The spectrum for the gold particle shows multiple peaks that are comparable to the spectrum of a tetrahedral $Au_{20}$ investigated using the TD-DFT method [19]. It contains contributions from several intraband transitions at lower energies and interband transitions at relatively higher energies. However, the overall spectral intensity is increased with the particle size due to the large density of states available in $Au_{120}$. A weak LSPR peak appears at around 2.5 eV. We note that although a gold particle involving 120 atoms is large compared to the previous study with $Au_{20}$, it is still too small to sustain significant LSPR excitation. Nevertheless, excitation near 2.5 eV with dominant intraband transitions can generate results better resembling the LSPR characteristics that are usually observed experimentally for much larger particles. Note that the participation of $d$-electrons in photoexcitation causes decoherence of plasmon excitation, resulting in a broad plasmon peak that overlaps with interband transitions at higher energy. This makes it difficult to identify the LSPR peak for gold particles with a nearly spherical shape with less than about 300 atoms in the cluster, but for tetrahedral particles, the LSPR peak is apparent in our 120 atom results. The spectrum for the S-complex is very similar to the isolated gold particle spectrum, whereas for the V-complex the absorption intensity is slightly increased due to CT excitations as is consistent with previous TD-DFT results [19].

### Enhancement of Raman Scattering

We have used DFTB to compute the SERS enhancement for pyridine using low frequency (nominally static) calculations to determine the chemical enhancement factor, and with calculations at the plasmon energy of 2.5 eV for $Au_{120}$-pyridine complexes to determine the electromagnetic enhancement factor. We find that resonance CT excitations for the $Au_{120}$-pyridine complexes involve small transition strengths that overlap with the dominant $d$-band excitations and therefore can have negligible con-

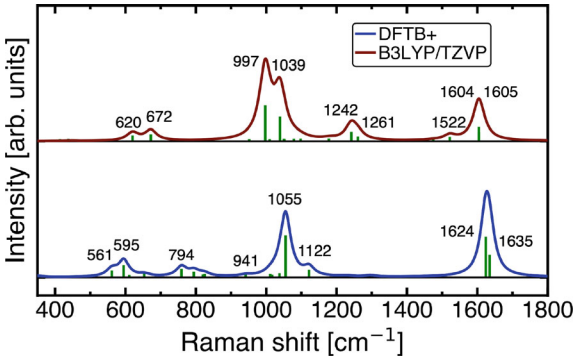



**Fig. 1.3** Raman spectra of pyridine using B3LYP/TZVP and TD-DFTB methods

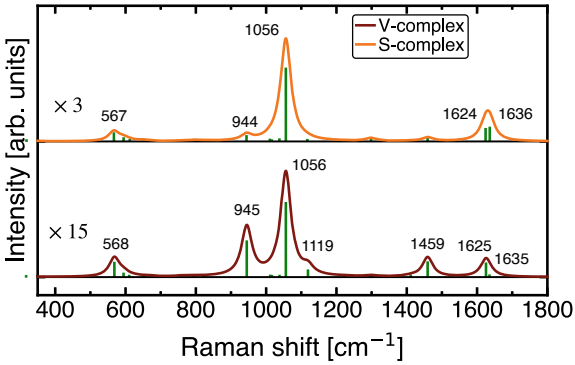



**Fig. 1.4** Surface-enhanced Raman scattering for $Au_{120}$-pyridine complexes using the static polarizability of the molecule. Throughout the scaling factors in the inset represent enhancements compared to the normal Raman intensities of an isolated pyridine

tributions to SERS. Thus in the following, we only consider enhancements due to static chemical and electromagnetic effects.

Normal Raman scattering spectra (obtained through computation of the static polarizability derivatives) for gas phase pyridine are shown in Fig. 1.3, with the TD-DFTB result compared with the spectrum obtained from an analogous B3LYP/TZVP DFT calculations. Here, we have scaled the normal mode frequencies from DFTB by a factor of 0.9 to correct for a systematic overestimation of the vibrational frequency obtained from this method. Overall the spectra agree reasonably well both for the mode frequencies and relative peak intensities. The Raman active modes from the TD-DFT calculation include a pair of ring deformation modes at 620 and 672 $cm^{-1}$, a pair of ring breathing modes at 997 and 1039 $cm^{-1}$, a symmetric C-H wag mode at 1242 $cm^{-1}$, and a pair of ring stretching modes at 1604 and 1605 $cm^{-1}$. The two noticeable discrepancies between spectra are (i) unphysical modes that appear in the TD-DFTB results near 794 $cm^{-1}$ and (ii) for the lower energy ring breathing mode (that appears at 941 $cm^{-1}$ in the TD-DFTB result) the intensity is significantly suppressed compared to the others. As will be discussed later the unphysical modes near 794 $cm^{-1}$ are not enhanced in SERS, however, the lower energy ring breathing mode can be significantly enhanced even though it is vanishingly small for the isolated gas phase molecule (TD-DFTB result).

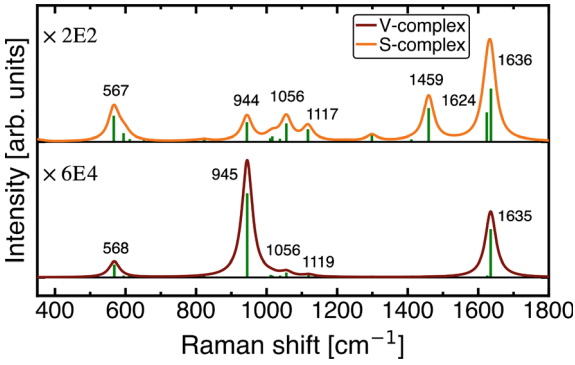



**Fig. 1.5** Surface-enhanced Raman scattering of $Au_{120}$-pyridine complexes for an incident laser energy of 2.5 eV

The normal Raman scattering spectra of pyridine adsorbed on the surface of $Au_{120}$ are shown in Fig. 1.4. These results show that the chemical enhancements are around a factor of 3 for the S-complex and 15 for the V-complex. These enhancement factors are comparable with the reported values (a factor 3 for the S-complex and 20 for the V-complex) for a $Au_{20}$-pyridine complex based on earlier TD-DFT calculations [19]. The larger enhancement and sensitivity for the V-complex is understandable as the chemical interaction between particle and molecule is larger for that complex compared to the other given that the pyridine interacts with a coordinately less saturated gold atom.

Interestingly the lower energy ring breathing mode (944 cm$^{-1}$) that has a small intensity for the isolated molecule (Fig. 1.3) is now enhanced by a factor of 15 for the V-complex, while the higher energy ring breathing mode (1056 cm$^{-1}$) shows a weak enhancement. Between these two ring breathing modes the higher energy mode is enhanced more than that for the lower energy mode for the S-complex. Again, this trend in enhancements is consistent with the TD-DFT calculation as observed for $Au_{20}$-pyridine complexes [19]. Further, the unphysical modes that appear in the isolated molecule near 794 cm$^{-1}$ have not been enhanced for either complex. Another mode with much higher enhancements is near 1459 cm$^{-1}$. This peak was also seen in the TD-DFT work, and it appears in experimental SERS measurements on gold but not silver [19].

The mode frequencies show blue shifts for both complexes as observed in the TD-DFT calculations, however, the shifts are relatively smaller compared to the TD-DFT results [19]. The V-complex shows higher blue shifts than the S-complex for most of the Raman active modes, as also observed in the TD-DFT calculations. The larger blue shifts in the V-complex can be associated with stronger bonding interaction in the V-complex as already mentioned.

The SERS scattering spectra of gold-pyridine for plasmon excitation at an energy of 2.5 eV are shown in Fig. 1.5 for both complexes. The resonant excitation of metal complexes leads to enhancements due to electromagnetic effects along with chemical enhancements. The overall enhancement factors are on the order of $10^1-10^2$ and

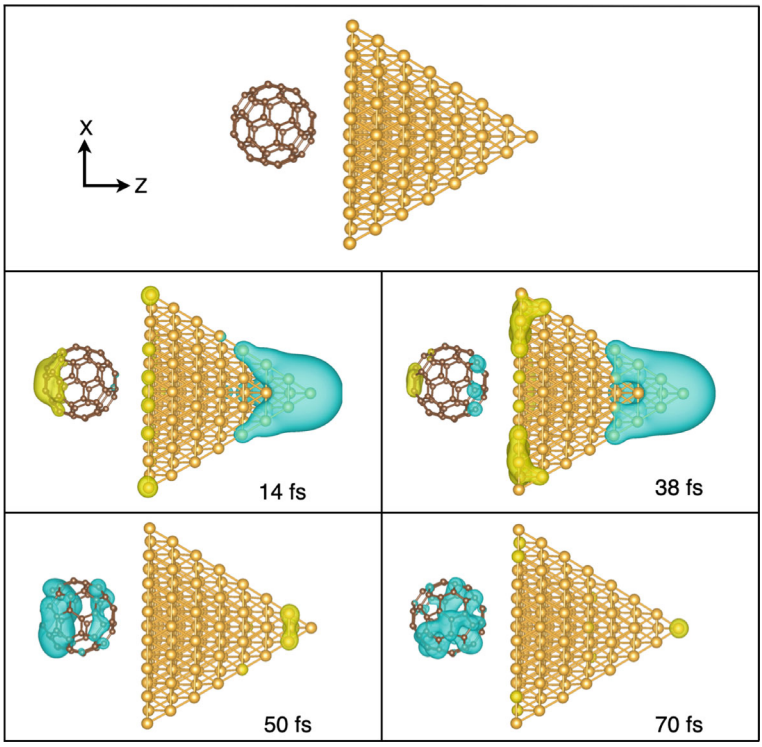



**Fig. 1.6** (Top) Optimized geometry of a $Au_{120}$-$C_{60}$ complex, and (Bottom) snapshots of charge density difference with respect to the initial charge at $t = 0$. The isosurface cutoff is set to $\pm 0.05$e. Yellow color represents positive and cyan color represents negative amplitudes

$10^3 - 10^4$ for the S- and V-complexes, respectively. Similar enhancement factors were also observed for $Au_{20}$-pyridine complexes with the TD-DFT method [19]. For the V-complex, the 941 and 1635 $cm^{-1}$ modes are enhanced significantly, by a factor of $8 \times 10^4$ and $4 \times 10^4$, respectively, while for the S-complex multiple modes are enhanced, with the maximum enhancement for 1636 $cm^{-1}$ mode. Further, a new Raman active mode appears in the S-complex at 1459 $cm^{-1}$. Interestingly this mode was strongly enhanced in the static Raman spectra and in the TD-DFT results noted above.

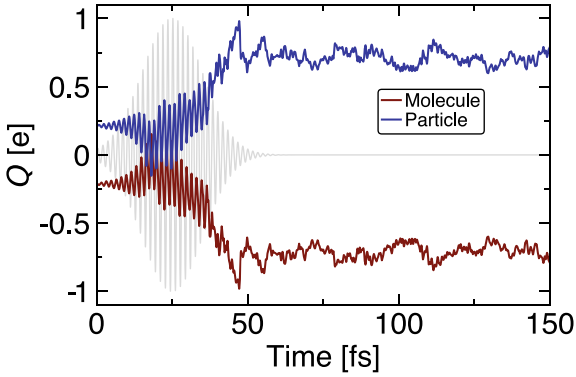



**Fig. 1.7** Time evolution of charges for particle and molecule for interaction with a Gaussian laser pulse shown by a light gray line in the background

## *Charge Transfer*

### $Au_{120}C_{60}$ Complex

To generate a suitable geometry to study plasmon-driven charge transfer, we place a fullerene ($C_{60}$) molecule on one of the triangular faces (as in the S-complex) of $Au_{120}$ (previously optimized) and then the geometry is optimized freezing atoms of the particle. The optimized geometry of $Au_{120}C_{60}$ is shown in Fig. 1.6. The minimum distance between C and Au atoms is around 3.5 Å. We observe a small electron transfer (around 0.2e) from the particle to the molecule for the optimized geometry in the ground state.

### Absorption Spectra

Absorption spectra for $C_{60}$ and $Au_{120}C_{60}$ are displayed in Fig. 1.2a, b, respectively. The molecular spectrum exhibits multiple peaks, with the first three peaks at 3.3, 4.35, and 5.2 eV. These calculated peaks well represent the experimental peaks found at 3.8, 4.9, and 6 eV, respectively, for the gas phase $C_{60}$ molecule [36]. The spectrum of the $Au_{120}C_{60}$ complex is dominated by the gold particle with two major peaks near 3.27 and 4.3 eV. These two peaks are slightly red-shifted compared to the first two lowest energy peaks of the isolated molecule. Previous studies demonstrated a shift in LSPR peaks due to the interaction between plasmon and molecular resonances [37, 38]. Moreover, a weak plasmon peak near 2.5 eV is also observed as in the other complexes in the figure.

**Laser-Induced Charge Transfer Dynamics**

A linearly polarized (polarized along the Z-axis) laser pulse of the form given in Eq. 1.2 is used to drive the system. Both molecule and particle couple with the external field. We use a driving field amplitude $E_0$, frequency $\omega_l$, and pulse duration $T_l$ of 0.7 V/Å, 2.5 eV and 14 fs, respectively. We note that for this value of the pulse duration, the field amplitude decays to zero at about 50 fs with a peak position at 25 fs. Figure 1.7 displays the time evolution of charges for the molecule and particle separately. We note that the total charge is preserved (here charge neutral complex) at all times, however, charge transfer can occur across the interface between the molecule and particle during the dynamics. As seen in Fig. 1.7, the initial charge (before interacting with a laser pulse) of the molecule is slightly negative, reflecting ground state charge transfer to the molecule. The charges of the two subsystems oscillate with the laser frequency during interaction with the laser pulse. There is an effective transfer of electrons from the molecule to the particle during the early time of the dynamics (Fig. 1.6), and the charge of the particle drops to about +0.15e at around 18 fs. After that the electron transfer changes direction and an effective transfer of electrons from the particle to the molecule is observed. At long times (after 50 fs), the charge on the molecule oscillates around a value of −0.75e. Figure 1.6 displays the negative charge on the molecule at long times (after 50 fs). The transfer of electrons and the formation of negative molecular ions for fullerene-based molecules have been experimentally demonstrated using SERS measurements, where the fullerene pentagonal pinch mode was found to change frequencies from that for the neutral fullerene to that for the fullerene anion after excitation of the gold/fullerene complex at 532 nm [33]. We note that since the fullerene is still in contact with the gold nanoparticle at the end of the calculation the amount of charge residing on the molecule is not necessarily a full electron.

## 1.4 Conclusions

In this study, we have presented two interrelated projects that test the ability of TD-DFTB to describe the influence of plasmon excitation on two physical phenomena: surface-enhanced Raman scattering (SERS) and plasmon-enhanced charge transfer. In the first, we calculated SERS spectra for $Au_{120}$-pyridine complexes, where we found enhancements due to both chemical and plasmon excitation effects that are consistent with earlier TD-DFT studies [19]. The enhancement factors for chemical effect are around 3–15 depending on the site of the adsorption. For the electromagnetic effect, the enhancement is on the order of $10^3 - 10^4$ for the V-complex (for adsorption on one of the tips) whereas $10^1 - 10^2$ for the S-complex (for adsorption on one of the triangle faces). In the second project, we studied plasmon-driven charge transfer across particle-molecule junctions after laser excitation of the particle near the plasmon energy at 2.5 eV. We found substantial electron transfer from particle to molecule for a $Au_{120}$-$C_{60}$ complex leading to the formation of a negative molecular

ion, $C_{60}^{-}$ on the particle. This observation is consistent with a previous experimental result that shows evidence of electron transfer from particle to molecule and the formation of negative molecular ions for a fullerene derivative [33]. Noteworthy in this result is that we did not see other photoprocesses in these simulations of laser pulses with intensities that are close to threshold, including C–C bond breakage, fragmentation of the particle, or desorption of the fullerene from the particle. The ability of the DFTB method to simulate SERS and charge transfer problems opens several new possibilities in the plasmonics field.

**Acknowledgements** This research was supported by the Office of Basic Energy Science, Department of Energy, through grant DE-SC0004752.

## References

1. Jeanmaire, D. L. & Van Duyne, R. P. Surface Raman Spectroelectrochemistry: Part I. Heterocyclic, Aromatic, and Aliphatic Amines Adsorbed on the Anodized Silver Electrode. J. Electroanal. Chem. Interfacial Electrochem. 84, 1–20 (1977).
2. Albrecht, M. G. & Creighton, J. A. Anomalously intense Raman Spectra of Pyridine at a Silver Electrode. J. Am. Chem. Soc. 99, 5215–5217 (1977).
3. Stiles, P. L., Dieringer, J. A., Shah, N. C. & Van Duyne, R. P. Surface-Enhanced Raman Spectroscopy. Annu. Rev. Anal. Chem. 1, 601–626 (2008).
4. Nie, S. & Emory, S. R. Probing Single Molecules and Single Nanoparticles by Surface-Enhanced Raman Scattering. Science 275, 1102–1106 (1997).
5. Kneipp, K., Wang, Y., Kneipp, H., Perelman, L. T., Itzkan, I., Dasari, R. R. & Feld, M. S. Single Molecule Detection Using Surface-Enhanced Raman Scattering (SERS). Phys. Rev. Lett. 78, 1667–1670 (1997).
6. Camden, J. P., Dieringer, J. A., Wang, Y., Masiello, D. J., Marks, L. D., Schatz, G. C. & Van Duyne, R. P. Probing the Structure of Single-Molecule Surface Enhanced Raman Scattering Hot Spots. J. Am. Chem. Soc. 130, 12616–12617 (2008).
7. Kneipp, J., Kneipp, H. & Kneipp, K. SERS-a Single-Molecule and Nanoscale Tool for Bioanalytics. Chem. Soc. Rev. 37, 1052–1060 (2008).
8. Zong, C., Premasiri, R., Lin, H., Huang, Y., Zhang, C., Yang, C., Ren, B., Ziegler, L. D. & Cheng, J.-X. Plasmon-Enhanced Stimulated Raman Scattering Microscopy with Single-Molecule Detection Sensitivity. Nat. Commun. 10, 5318 (2019).
9. Fleischmann, M., Hendra, P. & McQuillan, A. Raman Spectra of Pyridine Adsorbed at a Silver Electrode. Chem. Phys. Lett. 26, 163–166 (1974).
10. Shafer-Peltier, K. E., Haynes, C. L., Glucksberg, M. R. & Van Duyne, R. P. Toward a Glucose Biosensor Based on Surface-Enhanced Raman Scattering. J. Am. Chem. Soc. 125, 588–593 (2003).
11. Tripp, R. A., Dluhy, R. A. & Zhao, Y. Novel Nanostructures for SERS Biosensing. Nano Today 3, 31–37 (2008).
12. Das, A., Zhao, J., Schatz, G. C., Sligar, S. G. & Van Duyne, R. P. Screening of Type I and II Drug Binding to Human Cytochrome P450-3A4 in Nanodiscs by Localized Surface Plasmon Resonance Spectroscopy. Anal. Chem. 81, 3754–3759 (2009).
13. Zeng, Z.-C., Huang, S.-C., Wu, D.-Y., Meng, L.-Y., Li, M.-H., Huang, T.-X., Zhong, J.-H., Wang, X., Yang, Z.-L. & Ren, B. Electrochemical Tip-Enhanced Raman Spectroscopy. J. Am. Chem. Soc. 137, 11928–11931 (2015).
14. Kurouski, D., Mattei, M. & Van Duyne, R. P. Probing Redox Reactions at the Nanoscale with Electrochemical Tip-Enhanced Raman Spectroscopy. Nano Lett. 15, 7956–7962 (2015).

15. Willets, K. A. & Van Duyne, R. P. Localized Surface Plasmon Resonance Spectroscopy and Sensing. Annu. Rev. Phys. Chem. 58, 267–297 (2007).
16. Standridge, S. D., Schatz, G. C. & Hupp, J. T. Distance Dependence of Plasmon Enhanced Photocurrent in Dye-Sensitized Solar Cells. J. Am. Chem. Soc. 131, 8407–8409 (2009).
17. Achermann, M. Exciton-Plasmon Interactions in Metal-Semiconductor Nanostructures. J. Phys. Chem. Lett. 1, 2837–2843 (2010).
18. Jensen, L., Aikens, C. M. & Schatz, G. C. Electronic Structure Methods for Studying Surface-Enhanced Raman Scattering. Chem. Soc. Rev. 37, 1061–1073 (2008).
19. Aikens, C. M. & Schatz, G. C. TDDFT Studies of Absorption and SERS Spectra of Pyridine Interacting with Au20. J. Phys. Chem. A 110, 13317–13324 (2006).
20. Yang, W.-H. & Schatz, G. C. Ab-initio and Semiempirical Molecular Orbital Studies of Surface Enhanced and Bulk Hyper-Raman Scattering from Pyridine. J. Chem. Phys. 97, 3831–3845 (1992).
21. Gieseking, R. L., Ratner, M. A. & Schatz, G. C. Theoretical Modeling of Voltage Effects and the Chemical Mechanism in Surface-Enhanced Raman Scattering. Faraday Discuss. 205, 149–171 (2017).
22. Hourahine, B. et al. DFTB+, a Software Package for Efficient Approximate Density Functional Theory based Atomistic Simulations. J. Chem. Phys. 152, 124101 (2020).
23. Bonafé, F. P., Aradi, B., Hourahine, B., Medrano, C. R., Hernández, F. J.,Frauenheim, T. & Sanchez, C. G. A Real-Time Time-Dependent Density Functional Tight-Binding Implementation for Semiclassical Excited State Electron-Nuclear Dynamics and Pump-Probe Spectroscopy Simulations. J. Chem. Theory Comput. 16, 4454–4469 (2020).
24. Allec, S. I., Sun, Y., Sun, J., Chang, C.-e. A. & Wong, B. M. Heteroge neous CPU+GPU-Enabled Simulations for DFTB Molecular Dynamics of Large Chemical and Biological Systems. J. Chem. Theory Comput. 15, 2807–2815 (2019).
25. Van den Bossche, M. DFTB-Assisted Global Structure Optimization of 13- and 55-Atom Late Transition Metal Clusters. J. Phys. Chem. A 123, 3038–3045 (2019).
26. Asadi-Aghbolaghi, N., Rüger, R., Jamshidi, Z. & Visscher, L. TD-DFT+TB: An Efficient and Fast Approach for Quantum Plasmonic Excitations. J. Phys. Chem. C 124, 7946–7955 (2020).
27. D'Agostino, S., Rinaldi, R., Cuniberti, G. & Della Sala, F. Density Functional Tight Binding for Quantum Plasmonics. J. Phys. Chem. C 122, 19756–19766 (2018).
28. Jha, G. & Heine, T. DFTB Parameters for the Periodic Table: Part III, Spin Orbit Coupling. J. Chem. Theory Comput. 18, 4472–4481 (2022).
29. Sánchez, C. G. & Berdakin, M. Plasmon-Induced Hot Carriers: An Atomistic Perspective of the First Tens of Femtoseconds. J. Phys. Chem. C 126, 10015–10023 (2022).
30. Giri, S. K. & Schatz, G. C. Photodissociation of H2 on Ag and Au Nanoparticles: Effect of Size and Plasmon versus Interband Transitions on Threshold Intensities for Dissociation. J. Phys. Chem. C 127, 4115–4123 (2023).
31. Wu, X., van der Heide, T., Wen, S., Frauenheim, T., Tretiak, S., Yam, C. & Zhang, Y. Molecular Dynamics Study of Plasmon-Mediated Chemical Transformations. Chem. Sci. 14, 4714–4723 (2023).
32. Fojt, J., Rossi, T. P., Kuisma, M. & Erhart, P. Hot-Carrier Transfer across a Nanoparticle-Molecule Junction: The Importance of Orbital Hybridization and Level Alignment. Nano Lett. 22, 8786–8792 (2022).
33. Wu, Y., Yang, M., Ueltschi, T. W., Mosquera, M. A., Chen, Z., Schatz, G. C. & Van Duyne, R. P. SERS Study of the Mechanism of Plasmon-Driven Hot Electron Transfer between Gold Nanoparticles and PCBM. J. Phys. Chem C 123, 29908–29915 (2019).
34. Douglas-Gallardo, O. A., Berdakin, M. & Sánchez, C. G. Atomistic Insights into Chemical Interface Damping of Surface Plasmon Excitations in Silver Nanoclusters. J. Phys. Chem. C 120, 24389–24399 (2016).
35. Mansilla Wettstein, C., Bonafe, F. P., Oviedo, M. B. & Sánchez, C. G. Optical Properties of Graphene Nanoflakes: Shape Matters. J. Chem. Phys. 144, 224305 (2016).
36. Yasumatsu, H., Kondow, T., Kitagawa, H., Tabayashi, K. & Shobatake, K. Absorption Spectrum of C60 in the Gas Phase: Autoionization via Core-Excited Rydberg States. J. Chem. Phys. 104, 899–902 (1996).

37. Haes, A. J., Zou, S., Zhao, J., Schatz, G. C. & Van Duyne, R. P. Localized Surface Plasmon Resonance Spectroscopy near Molecular Resonances. J. Am. Chem. Soc. 128, 10905–10914 (2006).
38. Zhao, J., Jensen, L., Sung, J., Zou, S., Schatz, G. C. & Van Duyne, R. P. Interaction of Plasmon and Molecular Resonances for Rhodamine 6G Adsorbed on Silver Nanoparticles. J. Am. Chem. Soc. 129, 7647–7656 (2007).

# Chapter 2
# Basics and Frontiers of Electromagnetic Mechanism of SERS Hotspots




**Tamitake Itoh and Yuko S. Yamamoto**

**Abstract** Electromagnetic (EM) enhancement of Raman signals by plasmon resonance has been considered as the main mechanism of surface-enhanced Raman scattering (SERS). This mechanism is referred to EM mechanism. Recently, development in nanotechnology and calculation methods have realized the experimental and theoretical conditions beyond the conventional assumptions in EM mechanism and thus have brought the necessity to update the mechanism. In particular, hotspots (HSs), where single molecule SERS detections become possible, show various exotic phenomena related to both SERS and cavity quantum electrodynamic (QED). Thus, the scope of this chapter is to report new directions of EM mechanism, mainly from the viewpoint of HSs by QED. We here discusses four main topics: (1) cavity QED description of EM mechanism; (2) strong coupling between plasmon and molecular exciton resonances; (3) contribution of subradiant plasmon resonance to EM mechanism; and (4) EM mechanism of one-dimensionally extended SERS HSs.

**Keywords** Electromagnetic mechanism · Surface-enhanced Raman scattering · Plasmon resonance · Cavity quantum electrodynamics · Strong coupling · Subradiant plasmon resonance

## 2.1 Introduction

More than 45 years have passed since the discovery of surface-enhanced Raman scattering (SERS) [1–3]. SERS has been expected to open up a new era from the time of its naming because it enables more efficient analysis for analytes by enhancing Raman intensity, which reflects vibrational information of analytes. SERS is the phenomena

T. Itoh (✉)
Health and Medical Research Institute, National Institute of Advanced Industrial Science and Technology (AIST), 2217–14 Hayashi-Cho, Takamatsu 761–0395, Kagawa, Japan
e-mail: tamitake-itou@aist.go.jp

Y. S. Yamamoto
School of Materials Science, Japan Advanced Institute of Science and Technology (JAIST), Nomi 923–1292, Ishikawa, Japan

© The Author(s), under exclusive license to Springer Nature Singapore Pte Ltd. 2024

M. Procházka et al. (eds.), *Surface- and Tip-Enhanced Raman Scattering Spectroscopy*,
https://doi.org/10.1007/978-981-97-5818-0_2

that molecules on specific metal surfaces exhibit large enhancement in Raman scattering cross-sections. In 1997, the groups of Nie and Kneipp discovered that SERS exhibit single molecule (SM) sensitivity [4, 5]. This SM sensitivity was rigorously confirmed by bianalyte and isotopically differentiated analyte SERS detections [6, 7]. Thanks to the large efforts of the mechanistic studies by many researchers, the SERS has been understood now as the results of both electromagnetic (EM) and chemical enhancement mechanism [8].

The EM mechanism describes the SERS enhancement as being induced by a strong EM field generated by plasmon resonance. Jeanmaire and Van Duyne were the first to discuss the electric field enhancement as a SERS mechanism [3]. The EM mechanism by plasmon resonance was first developed by Moskovits et al. [9, 10] and then formulized by Kerker et al. [11]. Subsequently, the groups of Aravind, Inoue, and Xu demonstrated that this mechanism could successfully explain the large Raman enhancement factor ~ $10^{10}$ for a molecule located in the gaps of a plasmonic NP dimer, i.e., the SERS hotspots (HSs) [12–14]. There is not a rigorous definition of HS. If we assume that the definition is SM-SERS detection, according to fluorescence cross-section ~ $10^{-15}$ $cm^2$ and resonance Raman cross-section ~ $10^{-24}$ $cm^2$, the enhancement factor of SERS is needed to be $10^9$ to enable SM-SERS detection. This factor corresponds to the gap distance to be the range between 1 and 3 nm [12]. Therefore, the authors propose here to define the HS size of SM-SERS as 1–3 nm in terms of gap distance.

Thanks to development of the methods for both experiment (e.g., nanolithography) and calculation (e.g., time-dependent DFT), SERS HSs were recently found to exhibit various exotic phenomena related to cavity quantum electrodynamics (cavity QED) [15–18]. The origin of these phenomena is extremely small mode volumes of HSs which value is several to several tens $nm^3$. Indeed, the coupling energy, amplitude of vacuum fluctuation and light, and size of the electric field estimated from the mode volumes are beyond the assumptions in classical spectroscopies [15–18]. Thus, it is useful to understand these exotic phenomena including SERS in the framework of cavity QED. The development of various HSs also revealed the contribution of subradiant plasmons to SERS although superradiant plasmons have been used to improve SERS sensitivity. Based on these recent situations, we here discuss four main topics: (1) description of EM mechanism of SERS using cavity QED; (2) strong coupling between plasmon and molecular exciton at SERS HSs; (3) contribution of subradiant plasmon to EM mechanism at SERS HSs; and (4) EM mechanism of one-dimensional HSs, which volume is several tens of thousands times larger than the conventional HSs.

## 2.2 Electromagnetic Mechanism of SERS Based on Cavity Quantum Electrodynamics

We here explain the theoretical description and experimental examination of EM mechanism of SERS using cavity QED. In the explanation, plasmon resonance, which is the origin of EM enhancement, is treated as an optical cavity. The EM enhancement is expressed as a combination of excitation and emission enhancement by light and vacuum fluctuation, respectively. The experimental results are evaluated by electromagnetism calculations. The upper limit of EM enhancement is explained as the minimum mode volume of the optical cavity determined by surface tunneling electrons.

### *2.2.1 Theoretical Description of Electromagnetic Mechanism*

The enhancement of the molecular optical response requires "resonance" to enlarge the effective cross-section of interaction between a molecule and EM fields. In the case of EM mechanism, plasmon resonance is the origin of the enhancement. Plasmons are collective oscillation modes of conduction electrons. Plasmons of metal nanoparticle (NP) induce a depolarization to cancel the external electric fields [19]. When a phase difference between the external electric fields and dipole plasmon polarization of the NP reaches a value of $\pi/2$, the two components become resonant. This situation is called dipole plasmon resonance. This explanation is identical to that the negative real part of permittivity of metal can enlarge the polarizability of NP $\alpha \propto \frac{\varepsilon-\varepsilon_m}{\varepsilon+2\varepsilon_m}$ at $\mathrm{Re}[\varepsilon + 2\varepsilon_m] = 0$, where $\varepsilon$ and $\varepsilon_m$ are the permittivity of metal and surrounding medium, respectively. The value of $\alpha$ becomes large for metals having a small value of $\mathrm{Im}[\varepsilon]$, such as gold and silver [20]. If such metallic two NPs form a dimer, the light is further confined in the gap or junction of the dimer by the dipole–dipole (DD)-coupled plasmon, resulting in the largest enhancement factors of light intensity up to ~ $10^5$ [12–14]. By the way, a spontaneous Raman process is composed of excitation by light and de-excitation by vacuum fluctuation, which is corresponding to zero-point fluctuation of EM field in quantum optics [21]. The light and vacuum fluctuation intensity are enhanced by plasmon resonance. Thus, plasmon resonance contributes to the enhancement twice by increasing both the excitation and de-excitation rates [8].

The EM mechanism is here introduced using cavity QED, which can treat the interaction between light (or vacuum fluctuation) and a molecular dipole in an optical resonator which represents a HS [16]. Spontaneous Raman scattering includes a de-excitation process triggered by vacuum fluctuation, which does not appear in classical electromagnetism. Cavity QED explicitly includes the contribution of vacuum fluctuation to EM mechanism. In cavity QED, a HS of NP dimer is treated as an optical resonator which enhances transition rates of a molecule close to or inside the resonator. Excitation and de-excitation are enhanced by the coupling between a

molecular exciton and plasmon through exchanging photon inside a HS. Under dipole approximation, which assumes that the wavelength of the incident light is sufficiently larger than the size of the molecule, the coupling energy $\hbar\Omega$, where $\hbar$ and $\Omega$ are the Planck constant and coupling angular frequency, respectively, is determined by

$$\hbar\Omega = \langle f|\mathrm{ex}|\, i\rangle E, \tag{2.1}$$

where $\langle f|\mathrm{ex}|\, i\rangle$ is the dipole moment of the transition from the initial state $|i\rangle$ to the final state $|f\rangle$, $e$ is the elementary charge of an electron, $x$ is the position of center of gravity for the electron cloud, and $E$ is the amplitude of the electric field triggering the transition [21]. In the case of a spontaneous emission process, $E$ becomes the amplitude of the fluctuating vacuum electric field $E_{\mathrm{vac}}$. The zero-point energy $1/2(\hbar\omega)$ in the HS is equal to the EM field energy integrated through the mode volume of the HS $V_{\mathrm{HS}}$. Thus,

$$E_{\mathrm{vac}} = \sqrt{\frac{\hbar\omega}{2\varepsilon_{\mathrm{r}}\varepsilon_0 V_{\mathrm{HS}}}} \tag{2.2}$$

The $V_{\mathrm{HS}}$ is defined as $V_{\mathrm{HS}} = \int 2\varepsilon_r\varepsilon_0|E|^2/\max\left(\varepsilon_r\varepsilon_0|E|^2\right)d^3r$, where $E_{\mathrm{vac}}$ is the electric field amplitude inside the HS and $\varepsilon_r$ and $\varepsilon_0$ are the relative permittivity inside the HS and vacuum permittivity, respectively. The term $2\varepsilon_r\varepsilon_0 E_{\mathrm{vac}}^2$ includes the energies of both the electric and magnetic fields. The oscillator strength of a molecule is described by the equation $f = 2m\omega {l_{\mathrm{dip}}}^2/(e^2\hbar)$, where $l_{\mathrm{dip}}$ is the dipole length and $m$ is the free electron mass. Therefore, using Eq. (2.2), Eq. (2.1) can be rewritten as

$$\hbar\Omega = \hbar\sqrt{\frac{1}{4\pi\,\varepsilon_{\mathrm{r}}\varepsilon_0}\frac{\pi e^2 Nf}{mV_{\mathrm{HS}}}}, \tag{2.3}$$

where $N$ is the number of dye molecules inside a HS [22]. In Eq. (2.3), $\hbar\Omega$ is a function of $V_{\mathrm{HS}}$. The enhancement factor of the transition rate of a molecule inside a HS is expressed by the Purcell factor $F = W_{\mathrm{cav}}/W_{\mathrm{free}}$ at the resonant condition.

$$F\left(=\frac{W_{\mathrm{cav}}}{W_{\mathrm{free}}}\right) = \frac{Q(\lambda/n)^3}{4\pi^2 V_{\mathrm{HS}}}, \tag{2.4}$$

where $W_{\mathrm{free}}$ and $W_{\mathrm{cav}}$ are the transition rates of the molecule in free space and a HS, respectively; $\lambda$ is the resonant wavelength of the resonator; $n$ is the refractive index inside the HS, and $Q$ is the quality factor of the plasmon resonance (If the direction of the dipole in free space is random, $F = \frac{3Q(\lambda/n)^3}{4\pi^2 V_{\mathrm{SH}}}$) [16, 17]. The enhancement factor of a transition rate is a function of $V_{\mathrm{HS}}$. The term $F$ in Eq. (2.4) includes both a radiative and non-radiative rate. Note that the radiative and non-radiative rate are directly related to the linewidth of a plasmon resonance spectrum. If the rate, which is proportional to a linewidth $\Delta\omega$ of the plasmon resonance spectrum, is separated

into the radiative rate $\Delta\omega_{\mathrm{R}}$ and non-radiative rate $\Delta\omega_{\mathrm{NR}}$, then the radiative portion of $F$ is expressed as

$$F_R = \frac{F\Delta\omega_R}{\Delta\omega_R + \Delta\omega_{\mathrm{NR}}}, \tag{2.5}$$

where $F_R$ is the radiative portion of the Purcell factor, which is identical to the EM enhancement factor [16, 17]. Equation (2.5) indicates that the radiative portion of the plasmon resonance can contribute to the EM enhancement of Raman scattering. Note that the Raman process is composed of excitation and Raman scattering transitions. The EM enhancement contributes to both transitions. Thus, the EM enhancement factor of SERS is composed of twofold enhancements of excitation and Raman scattering as described in Eq. (2.6).

$$F_{\mathrm{R}}(\lambda_{\mathrm{ex}}, \mathbf{r})F_{\mathrm{R}}(\lambda_{\mathrm{em}}, \mathbf{r}) = \left|\frac{E_{\mathrm{loc}}(\lambda_{\mathrm{ex}}, \mathbf{r})}{E_{\mathrm{I}}(\lambda_{\mathrm{ex}})}\right|^2 \times \left|\frac{E_{\mathrm{loc}}(\lambda_{\mathrm{em}}, \mathbf{r})}{E_{\mathrm{I}}(\lambda_{\mathrm{em}})}\right|^2, \tag{2.6}$$

where $E_{\mathrm{I}}$ and $E_{\mathrm{loc}}$ indicate the amplitudes of the incident and enhanced local electric fields, respectively; $\lambda_{\mathrm{ex}}$ and $\lambda_{\mathrm{em}}$ denote the wavelengths of the incident and Raman-scattered light, respectively; and $\mathbf{r}$ is the position of a molecule in a HS. The large EM enhancement factor is due to the small $V_{\mathrm{HS}}$ value in Eq. (2.4). Notably, the values of $\Delta\omega_{\mathrm{R}}$ and $\Delta\omega_{\mathrm{NR}}$ in Eq. (2.5) are not constant but are functions of $V_{\mathrm{HS}}$ [16]. If $V_{\mathrm{HS}}$ decreases, the contribution of the non-radiative plasmons (i.e., higher-order plasmon, CT plasmon due to an unscreened electron gas of a metal surface) to $F_{\mathrm{R}}$ becomes dominant, resulting in the saturation or decrease in the EM enhancement [16].

### 2.2.2 *Experimental Examination of Electromagnetic Mechanism at SERS HSs*

The EM mechanism has been examined with the qualitative reproduction of SERS spectra by the mechanism using plasmonic NP dimers. In 2009, Yoshida et al. successfully carried out spectral variations in SERS of silver NP dimers by multiplying a Raman spectrum of a dye molecule with $F_{\mathrm{R}}(\lambda_{\mathrm{ex}}, \mathbf{r})F_{\mathrm{R}}(\lambda_{\mathrm{em}}, \mathbf{r})$ in Eq. (2.6), showing the existence of the EM mechanism in SERS [23]. Note that experimentally obtained coupled resonance between a plasmon and molecule exciton (molecule electronic transition dipole) is approximately treated as the plasmon resonance in the reproduction. Such treatment is called a "weak coupling approximation" [21]. Specifically, Eq. (2.1) indicates that the coupled resonance is different from the original plasmon resonance. The weak coupling assumes that $\Omega$ in Eq. (2.3) is sufficiently small compared to the dephasing rates of both the plasmon and molecular exciton resonances, so that it is unnecessary to distinguish between the plasmon and coupled resonances.

For the quantitative reproduction by Yoshida et al. in 2010, the plasmon resonance and SERS spectra are experimentally obtained under dark- and bright-field excitation conditions, respectively, using single silver NP dimers adsorbed by dye molecules at their HSs [24]. The point of reproduction is the selection of a superradiant (DD-coupled) plasmon resonance which Rayleigh scattering light shows an identical polarization dependence to the SERS light [25]. This point is crucial for identifying the DD-coupled plasmon inducing the $F_R$ in Eq. (2.5). Based on the shape of the dimer measured by scanning electron microscopy (SEM), the plasmon resonance spectra and $F_R$ are calculated by a finite-difference time-domain (FDTD) method. In the case of the DD-coupled plasmon mode, $F_R$ commonly contributes to both Raman excitation and emission as a result of optical reciprocity [24]. Thus, Eq. (2.6) indicates that the SERS cross-section $\sigma_{\mathrm{SERS}}(\lambda_{\mathrm{ex}}, \lambda_{\mathrm{em}})$ can be expressed as

$$\sigma_{\mathrm{SERS}}(\lambda_{\mathrm{ex}}, \lambda_{\mathrm{em}}, \mathbf{r}) = F_{\mathrm{R}}(\lambda_{\mathrm{ex}}, \mathbf{r}) F_{\mathrm{R}}(\lambda_{\mathrm{em}}, \mathbf{r}) \sigma_{\mathrm{RS}}(\lambda_{\mathrm{ex}}, \lambda_{\mathrm{em}}) \tag{2.7}$$

where $\sigma_{\mathrm{RS}}(\lambda_{\mathrm{ex}}, \lambda_{\mathrm{em}})$ is the experimentally obtained Raman scattering cross-section of a molecule in free space. Both experimental and calculated SERS cross-sections are quantitatively consistent to each other. The considerable spectral variations in SERS are also reproduced in the calculations [24]. This quantitative reproduction indicates that the EM mechanism is dominant for SERS.

### 2.2.3 *Upper Limitation of Electromagnetic Enhancement at SERS HSs*

The upper limit of $F_{\mathrm{R}}$ in Eq. (2.5) or the lower limit of $V_{\mathrm{HS}}$ in Eq. (2.4) has been studied by Zhu et al., who reported a problem called the plasmon quantum limit, which is a breakdown of the classical model for the plasmon oscillations of conduction electrons [26]. This limit indicates that the localized EM field volume cannot be smaller than the distribution volume of the unscreened metal surface electrons within the Debye radius. They experimentally confirmed that a quantum-based remodeling of the plasmons is necessary for a dimer gap smaller than 0.4 nm. The gap size gets sufficiently small so that electron tunneling can occur. The electron tunneling makes $F_{\mathrm{R}}$ stagnates and even decreases once the gap size falls below 1 nm. The EM mechanism using classical electromagnetism are unable to reproduce this result. However, once a quantum mechanical correction that accounts for electron tunneling is introduced, the calculated results agree much better with the experimental data. This limitation is summarized as (1) the lowest limitation of the EM field confinement and (2) appearance of plasmon oscillations by tunneling electrons. The tunneling-out of the conduction electrons, which loosens the field confinement, determines the lowest limit of the $V_{\mathrm{HS}}$, and thus, provides an estimation of the upper limitation of $F_{\mathrm{R}}$. Furthermore, with the decrease in $V_{\mathrm{HS}}$, the contribution of the higher-order plasmon resonances to $F_R$ increases, resulting in an increase in the non-radiative rate

$\Delta\omega_{NR}$ in Eq. (2.5). Thus, the value of ${F_R}^2$ exhibits a saturation tendency. The upper limitation of ${F_R}^2$ considerably depends on the quantum efficiency of the emission. In the case of the fluorescence and nonresonant Raman, the values are theoretically $10^2$ and $10^{14}$, respectively, excluding the effect of the plasmon quantum limit [27].

## 2.3 Strong Coupling Between a Plasmon and Molecular Exciton Resonances

If the coupling energy $\hbar\Omega$ in Eq. (2.3) between the plasmon and molecular exciton resonances becomes comparable to or larger than their dephasing energies, both resonances coherently exchange excitation energy, resulting in hybridization of both resonances [15–18]. This situation is called strong coupling. As the result of hybridization, two hybridized resonances appear as shown in Fig. 2.1a [28]. Strong coupling is closely related with EM mechanism at SERS HSs. The large value of $F_R \sim 10^5$ at HSs in Eq. (2.5) indicates $\hbar\Omega$ in Eq. (2.1), owing to the smallness of $V_{SH}$. In this section, firstly strong coupling is theoretically examined using HSs under near-SM conditions and secondly the examination is experimentally evaluated using silver NP dimers containing near-SM at HSs.

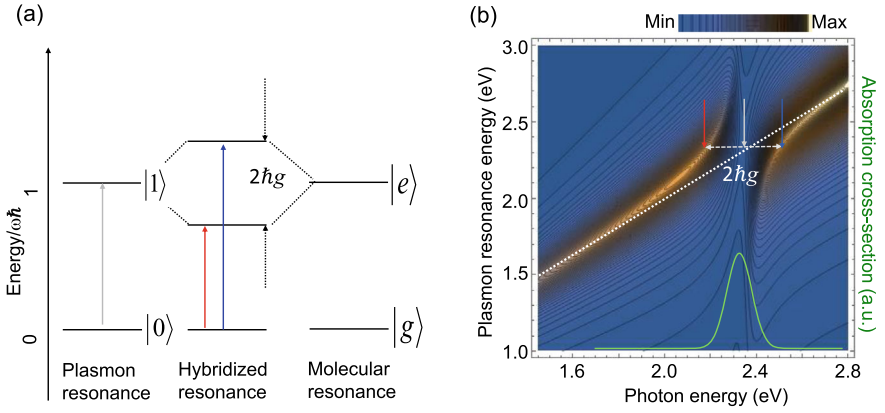



**Fig. 2.1** **a** Schematic image of strong coupling between plasmon and molecular resonances. Here, $|g\rangle$ and $|e\rangle$ are ground and excited states of two-level system, respectively; $|0\rangle$ and $|1\rangle$ are zero-photon and one-photon states of plasmon resonance; $2\hbar g$ indicates VRS. Red and blue arrows indicate two coupled resonance energies. **b** Calculated anti-crossing property of strong coupling between a plasmon and an exciton of a two-level system with a coupling energy of 400 meV. Inset: absorption spectrum of aqueous solution of R6G (green curve). Reprinted with permission from Ref. [28]: Copyright 2020 American Institute of Physics

### 2.3.1 *Strong Coupling Between a Plasmon and Molecular Exciton at the SERS HS*

This strong coupling is verified by observing the anti-crossing in coupled resonance by tuning DD-coupled plasmon resonance against exciton resonance [17, 28]. Anti-crossing is a phenomenon showing that two resonances cannot have an equal peak energy even after tuning as shown in Fig. 2.1b. The value of $\hbar\Omega$ is half of the anti-crossing energy gap under the rigorous resonance condition as shown in Fig. 2.1a and b. The gap in Fig. 2.1a and b is referred to the vacuum Rabi splitting (VRS).

A coupled oscillator model gives results essentially identical to those of a cavity QED model [29]. The model is useful for understanding strong coupling between DD-coupled plasmons and molecular excitons as the spectral properties of coupled resonance. We evaluated a SERS-active NP dimer under near-SM conditions to examine $\hbar\Omega$ in Eq. (2.3) by the coupled oscillator model [30]. Rayleigh scattering spectra are derived using the coupled oscillator composed of the plasmon and the molecular exciton oscillators. The molecular exciton represents the electronic resonance of a two-level system. The equations of motion for the two oscillators are

$$\frac{\partial^2 x_p(t)}{\partial t^2} + \gamma_p \frac{\partial x_p(t)}{\partial t} + \omega_{p^2} x_p(t) + \Omega \frac{\partial x_m(t)}{\partial t} = F_p(t), \tag{2.8}$$

$$\frac{\partial^2 x_m(t)}{\partial t^2} + \gamma_m \frac{\partial x_m(t)}{\partial t} + \omega_{m^2} x_m(t) - \Omega \frac{\partial x_p(t)}{\partial t} = F_m(t), \tag{2.9}$$

where the superscripts p and m refer to the DD-coupled plasmon and molecular electron resonances, respectively; $x_p$ and $x_m$ are their coordinates of position of center of gravity for the electron cloud; $\gamma_p$ and $\gamma_m$ are their line-widths; $\omega^p$ and $\omega_m$ are their resonance frequencies; and $F_p$ and $F_m$ are driving forces representing the incident light. If $\Omega > \gamma_p$ and $\gamma_m$ in Eqs. (8) and (9), both oscillators can coherently exchange their energy and form a strongly coupled resonances. The coupled oscillator can be assumed to be almost entirely driven by the excitation light energy obtained by the plasmonic oscillator; thus, we set $F_m(t) = 0$. By assuming $F_p(t) = F_p e^{-i\omega t}$, where $\omega$ is the incident light frequency, $x_p(t)$ and $x_m(t)$ can be derived from Eqs. (8) and (9). In the quasi-static limit, the Rayleigh scattering spectrum is $C_{\text{sca}} = (8\pi/3k)|\alpha|^2$ [19], where $k = \omega n/c$ is the wave vector of light and $\alpha$ is the polarizability of the dimer. We can obtain $C_{\text{sca}}$ as.

$$C_{\text{sca}}(\omega) = \frac{8\pi}{3} k|\alpha|^2 \propto \omega^4 \left| \frac{\omega_{m^2} - \omega^2 - i\gamma_m\omega}{(\omega^2 - \omega_{p^2} + i\gamma_p\omega)(\omega^2 - \omega_{m^2} + i\gamma_m\omega) - \omega^2\Omega^2} \right|^2 \tag{2.10}$$

The coupled resonance has been experimentally investigated as shifting or splitting in $C_{\text{sca}}$ spectra as shown in Fig. 2.2a1 to a3 [30]. The value of $\hbar\Omega$ to ~ 200 meV is estimated by comparing the typical spectral changes of coupled resonance with

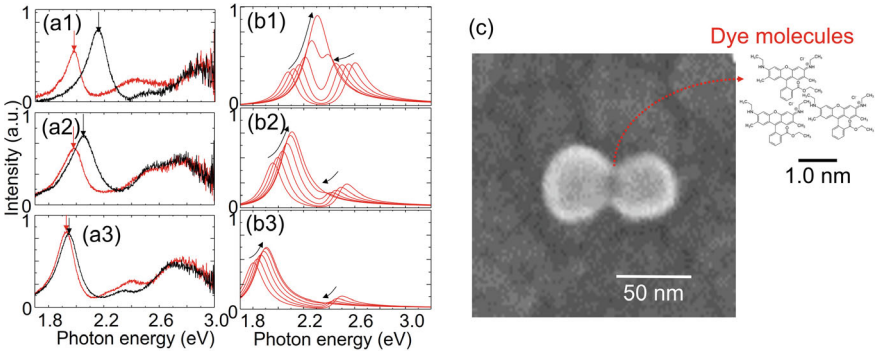



**Fig. 2.2** **a1–a3** Experimental $C_{sca}(\omega)$ spectra obtained before (red curve) and after (black curve) losing SERS activity. **b1–b3** Calculated $C_{sca}(\omega)$ spectra with $\hbar\Omega$ from 500 (red curve) to 0 meV (black curve) based on a coupled oscillator model as in Eq. (2.10). **c** SEM image of a typical silver NP dimer exhibiting SERS with a magnified image of R6G molecules. Reprinted with permission from Ref. [30]: Copyright 2014 American Physical Society

Eq. (2.10), as shown in Fig. 2.2b1 to b3. The value ~ 200 meV is larger than $\gamma_p$ and $\gamma_m$, which are both ~ 150 meV. Thus, strong coupling is likely realized at HSs. Note that $\hbar\Omega$ ~ 200 meV corresponds to ~ $2.0 \times 10^{-6}$ $(\lambda/n)^3$ at $\lambda = 600$ nm and $n = 1.33$ of $V_{HS}$ from $f$ of a R6G molecule using Eq. (2.3) by assuming a SM condition $N = 1$ in Eq. (2.3) [30]. This value ~ $2.0 \times 10^{-6}$ $(\lambda/n)^3$ is much larger than the experimentally confirmed minimum $V_{HS} = 1.7 \times 10^{-8}$ $(\lambda/n)^3$ [31], indicating that the spectral changes in Fig. 2.2a1 to a3 demonstrate a near-SM strong coupling effect. This calculation also suggests that the desorption of dye molecules from the HSs induces spectral changes in coupled resonance as shown in Fig. 2.2c.

The results of the coupled oscillator model should be examined by other methods accurately reflecting experimental conditions, because the coupled oscillator model intrinsically includes $\hbar\Omega$ as a fitting parameter for reproducing experimental spectra. It is difficult to experimentally demonstrate the anti-crossing using NP dimers by tuning the plasmon resonance as shown in Fig. 2.2b. This is because changing the parameters, such as NP size, shape, and gap distance, also changes both the original plasmon resonance energy and the coupling energy. Thus, it is important to theoretically evaluate the anti-crossing characteristics using realistic dielectric parameters of a silver NP dimer and dye molecules.

The first method for the evaluation is an analytical one based on classical electromagnetism. The effect of vacuum fluctuation is intrinsically included in the complex relative permittivity of the target materials and the structures of the dimer system [28]. Indeed, the imaginary parts of the dielectric responses of the system correspond to de-excitation by vacuum fluctuations. The polarizability of coated NP dimers was formulized by Ruppin [32]. Thus, the anti-crossing can be evaluated using the $C_{sca}(\omega)$ spectra of the coated dimers by changing parameters like the dye-film thicknesses and refractive index of their surrounding medium. From analyzing the spectra of the coupled resonance by changing these parameters, it was found that the anti-crossing

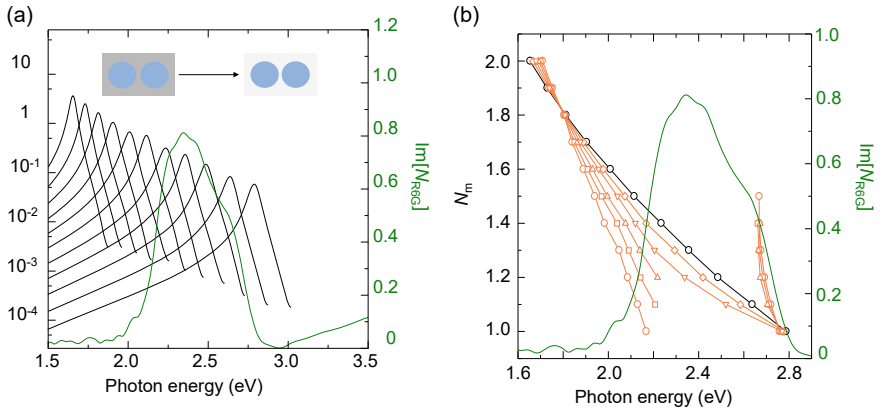



**Fig. 2.3** **a** $N_m$ dependences of $C_{sca}(\omega)$ obtained for dimers (black lines) with Im[$N_{R6G}$] (green curve), where $N_m$ and Im[$N_{R6G}$] are refractive index of surrounding medium of dimer and imaginary parts of refractive index of coated film, respectively. (b) $t_f$ dependences of peak energy of $C_{sca}(\omega)$ plotted against $N_m$ range from 2.0 to 1.0 with Im[$N_{R6G}$] (green curve), where $t_f$ is thickness of coated film. Orange symbols with lines ○, □, Δ, ∇, and ◊ correspond to $t_f$ values of 0.5, 0.4, 0.3, 0.2, and 0.1 nm, respectively. Black symbol with line ○ corresponds to $t_f = 0$ nm. Reprinted with permission from Ref. [28]: Copyright 2020 American Institute of Physics

characteristics of the dye-coated dimers are observed by changing the refractive index of the surrounding medium. Anti-crossing appears even when the coated film thickness is only 0.3 nm as shown in Fig. 2.3 [28]. Considering that the size of the dye molecule is approximately 0.5 nm and the surface area of the HS is several nm$^2$, this result indicates that anti-crossing is reasonably observed even under near-SM conditions.

The second method is numerical simulation like the FDTD method, which has been widely applied to calculate EM enhancement of various HSs [12, 24]. In the FDTD method, Maxwell's equation is discretized with a finite-difference method with Yee's mesh. The accuracy of the calculation depends on the mesh size because the EM fields are averaged within the mesh. To reproduce the spatial structures of the EM fields inside the HSs of NP dimers, the mesh size should be ~ 0.2 nm [24]. Chikkaraddy et al. calculated coupled resonance spectra under the condition that dye molecules are located inside a HS between gold NPs and a gold substrate [33]. They demonstrated a VRS of ~ 300 meV by placing approximately ten dye molecules inside HSs with $V_{HS}$ of less than 50 nm$^3$. The calculations reproduced the experimental results well, indicating that FDTD is a powerful tool for analyzing the strong coupling of HSs for any morphology.

The third method is quantum–mechanical calculation methods. In methods based on classical electromagnetism, bulk dielectric functions of metal are approximated as dielectric properties [24]. However, this approximation breaks down due to the electron tunneling effect when the gap distance of HS is below 0.5 nm [26.31]. In addition, classical electromagnetism method cannot include electronic interactions between

molecules and metal surfaces, such as charge transfer (CT) interactions, which is the origin of the chemical mechanism [15]. Time-dependent density-functional theory (TDDFT), which directly solves the time-dependent Schrödinger equation of a general quantum system, is a potential method of automatically including both the electron tunneling and CT effects in the calculation of strongly coupled systems. TDDFT also provides good forecasts for excited-state dynamics. Rossi et al. calculated coupled resonance spectra of a benzene molecule bonded to the surface of an aluminum cluster [34]. They demonstrated VRS ~ 200 meV with $V_{\mathrm{HS}}$ of 3.3 $\mathrm{nm}^3$. Such an approach can be applied to the HSs of NP dimers to reveal the modification of molecular electronic structures and their dynamics by strong coupling.

We propose that the calculated anti-crossing properties should be confirmed again by a coupled oscillator model. The confirmation is for checking the multi-level property of molecular excitons, which is not considered in the two-level system. Figure 2.4 shows that the multiple anti-crossing behaviors induced by the multi-level property of dye molecules pretend to exhibit single anti-crossing behavior, resulting in an overestimation of the coupling energy [17, 28]. For coupling energies ranging from 50 to 100 meV, the coupled resonance spectra clearly exhibit oscillatory structures corresponding to multiple anti-crossing properties. However, with increasing coupling energy, multiple anti-crossings appear similar to single anti-crossings with a huge energy gap of approximately 500 meV. This overestimation is induced by incorrectly assuming that a molecular multi-level system is a two-level system.

### 2.3.2 *Reproduction of SERS Spectra Under Strong Coupling Conditions at HSs*

Section 3.1 exhibits that the $\hbar\Omega$ between plasmon and molecular exciton resonances of NP dimer is in the strong coupling regime at SERS HSs. Thus, the coupled resonance is not identical to the original plasmon resonance. This fact indicates that the coupled resonance changes into the original plasmon resonance when SERS activity disappears due to $\hbar\Omega = 0$. Thus, one can estimate the value of $\hbar\Omega$ in Eq. (2.3) by analyzing the spectral changes in $C_{\mathrm{sca}}(\omega)$ using a coupled oscillator model [30]. Therefore, one can derive $F_R$ from $\hbar\Omega$ by assuming $\Delta\omega_R$ and $\Delta\omega_{\mathrm{NR}}$ in Eq. (2.6). The $F_R$ thus enables the reproduction of SERS spectra by using in Eq. (2.7). In this section, we explain this attempt of reproduction. Such attempt is worth carrying out to connect EM mechanism with strong coupling in the framework of cavity QED.

The Franck–Condon mechanism, which provides electron-vibration coupling, can reproduce multi-level properties using phonon replicas of the exciton line [27, 28]. Thus, the molecular exciton oscillator of Eq. (2.9) is modified into multiple oscillators representing a molecular exciton and its phonon replicas. Thus, the equations of motion become

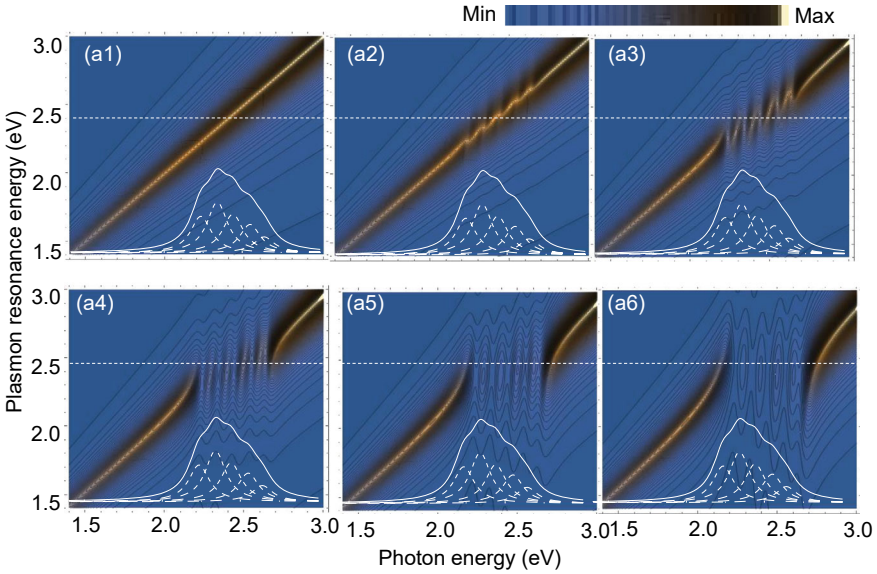



**Fig. 2.4** Anti-crossing properties present in coupled resonance $C_{\mathrm{sca}}(\omega)$ spectra calculated by five oscillators representing molecular multiple level. Value of $\hbar\Omega$ between largest oscillator and plasmon oscillator for **a1** 0 meV, **a2** 50 meV, **a3** 100 meV, **a4** 150 meV, **a5** 200 meV, and **a6** 250 meV. Molecular multi-level system is represented as five oscillators as indicated by white dashed lines. Reprinted with permission from Ref. [28]: Copyright 2020 American Institute of Physics

$$\frac{\partial^2 x_p(t)}{\partial t^2} + \gamma_{\mathrm{p}} \frac{\partial x_p(t)}{\partial t} + \omega_{p^2} x_p(t) + \sum_{\mathrm{n}=1}^{N} \Omega_n \frac{\partial x_{m,n}(t)}{\partial t} = F_p(t), \tag{2.11}$$

$$\frac{\partial^2 x_{m,n}(t)}{\partial t^2} + \gamma_{m,n} \frac{\partial x_{m,n}(t)}{\partial t} + \omega_{m,n^2} x_{m,n}(t) - \Omega_n \frac{\partial x_p(t)}{\partial t} = F_{m,n}(t) (n = 1, 2, 3 \ldots), \tag{2.12}$$

where $x_{m,n}$ indicates the coordinates of the $n$-th molecular exciton oscillation ($n = 1$ indicates an exciton and $n > 1$ indicates its phonon replicas), respectively; $\gamma_{m,n}$ is the corresponding linewidth; $\omega_{m,n}$ is the corresponding frequency; and $\hbar\Omega_n$ is the coupling rate between the plasmon and the $n$-th exciton [27]. The oscillator strengths, $\omega_{m,n}$, and $\gamma_{m,n}$ of the $n$-th exciton resonance can be derived from absorption spectra as shown in Fig. 2.5a. In the quasi-static limit, we can obtain $C_{\mathrm{sca}}$ as

$$C_{\mathrm{sca}}(\omega) \propto \omega^4 \left| \frac{\prod_{n=1}^{N} \left(\omega_{m,n^2} - \omega^2 - i\gamma_{m,n}\omega\right)}{\left(\omega^2 - \omega_{p^2} + i\gamma_p\omega\right)\prod_{n=1}^{N}\left(\omega^2 - \omega_{m,n^2} + i\gamma_{m,n}\omega\right)} - \sum_{n=1}^{N} \omega^2 \Omega_{\mathrm{n}}^2 \frac{\prod_{k=1}^{N}\left(\omega^2 - \omega_{m,k^2} + i\gamma_{m,k}\omega\right)}{\left(\omega^2 - \omega_{m,n^2} + i\gamma_{m,n}\omega\right)} \right|^2 \tag{2.13}$$

By decreasing $\hbar\Omega_n$, causing the disappearance of SERS activity, the coupled resonance is returned to the original plasmon resonance. The value of $\hbar\Omega_n$ can be obtained by comparing the experimental spectral changes with those from Eq. (2.13). Figure 2.5b shows the experimental spectra during the loss of SERS activity. A blue shift of the coupled resonance peak from 1.9 to 2.15 eV is observed, but the corresponding red shift of its counterpart shown in Fig. 2.2b2 is not. Figure 2.5c shows the calculated spectra obtained by decreasing $\hbar\Omega_1$ from 500 to 0 meV using Eq. (2.13). The calculated spectrum with four oscillators shows better consistency than that with a single oscillator, confirming that the unclearness in spectral splitting is caused by the multiple strong coupling between a plasmon and an exciton with

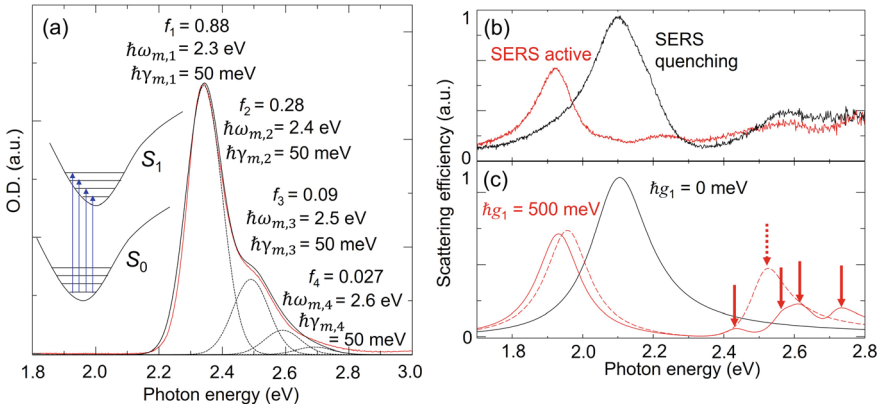



**Fig. 2.5** **a** Absorption spectrum of aqueous solution of R6G (red curves) fitted with four Lorentzian curves representing exciton and its three phonon replicas (dashed curves). Values of $\omega_{m,n}$ and $\gamma_{m,n}$ are indicated in panel. Black curve is sum of Lorentzian curves. Values of $f_n$ are indicated in panel. Inset: Photo-induced transitions from electronic excited state $S_1$ to electronic ground state $S_0$ including vibrational energy levels corresponding to four Lorentzian peaks. **b** Experimental $C_{\mathrm{sca}}(\omega)$ spectra before (red curve) and after (black curve) loss of SERS activity. **c** $C_{\mathrm{sca}}(\omega)$ spectra calculated by Eq. (2.13) with $\hbar g_1 = 500$ meV using a single exciton (dashed red curve) and an exciton with three phonon replicas (red curve), and not using an exciton coupled with the plasmon (black curve). The coupled resonances in the higher-energy region are indicated by a dashed arrow (strong coupling between the plasmon and a single exciton) and solid arrows (strong coupling between the plasmon and a single exciton with its phonon replicas), respectively. Reprinted with permission from Ref. [27]: Copyright 2018 American Institute of Physics

its phonon replicas [27]. The analysis considering the multi-level property is also important to avoid overestimation of coupling energy [28].

We here treat surface-enhanced fluorescence (SEF), which appears as a background spectrum of SERS, separately with SERS. For the reproduction of SERS and SEF spectra, $\hbar\Omega_n$ is converted to the EM enhancement and quenching factors of SERS and SEF. First, the value of $V_{\mathrm{HS}}$ is derived using $\hbar\Omega_n$ from Eq. (2.3). Note that it is the coupling energy of the first exciton $\hbar\Omega_1$ which mainly determines the value of $V_{\mathrm{HS}}$. Second, the Purcell factors of the dipole and higher-order plasmon modes are derived using this $V_{\mathrm{HS}}$. The Purcell factor of the dipole mode is converted to $F_R$ by Eq. (2.6), which involves multiplying it by $\frac{\Delta\omega_R}{\Delta\omega_R+\Delta\omega_{NR}}$, the coupling efficiency between external light and the HS. The efficiency is usually less than 10% in the visible light region [35]. The Purcell factors of higher modes are converted to quenching factors through multiplying them by the quantum efficiency of emission [16]. The quantum efficiencies of resonant Raman and fluorescence are approximately 0.001 and 0.9, respectively [27]. This large difference in quantum efficiencies is the reason that fluorescence is more severely quenched on metal surfaces than resonant Raman. The SERS and SEF spectra are then reproduced as the product of $F_R$, quenching factor, and original resonant Raman and fluorescence spectra. In the case of SEF reproduction, care must be taken in the transition from ultrafast to conventional SEF because the enhanced radiative rate at an SERS hotspot becomes larger than the vibrational relaxation rate [36]. Figure 2.6a–c shows the experimental coupled resonance, the experimental SERS with SEF spectra, and the SERS and SEF spectra reproduced via the above procedure. The spectral variations induced by the factor $F_R(\lambda_{\mathrm{em}})$ in Eq. (2.7) are well reproduced. Furthermore, the SEF is reproduced by increasing the quantum efficiency as the coupling energy decreases. This tendency indicates the transition from ultrafast to conventional SEF during the disappearance of SERS activity as shown in Fig. 2.6d. These analysis method will be useful for understanding various plasmon-enhanced spectroscopic results in the framework of cavity QED [18].

## 2.4 Contribution of Subradiant Plasmon Resonance to Electromagnetic Mechanism

In previous sections, DD-coupled plasmon resonance coupled with molecular exciton resonance has been focused for the reproduction of SERS with SEF spectra of NP dimers based on EM mechanism [27, 30]. However, when the sizes of the NPs of a dimer differ significantly, the largest $F_{\mathrm{R}}$ in Eq. (2.6) value is not mainly generated by the DD-coupled plasmon resonance but by dipole–quadrupole (DQ)-coupled plasmon resonance, which is a subradiant mode [37–39]. In such a situation, the DD-coupled plasmon resonance contributes to transfer the excitation light energy to the DQ-coupled plasmon resonance, and emits SERS with SEF by receiving energy from the DQ-coupled plasmon resonance through near-field interactions [40]. Briefly,

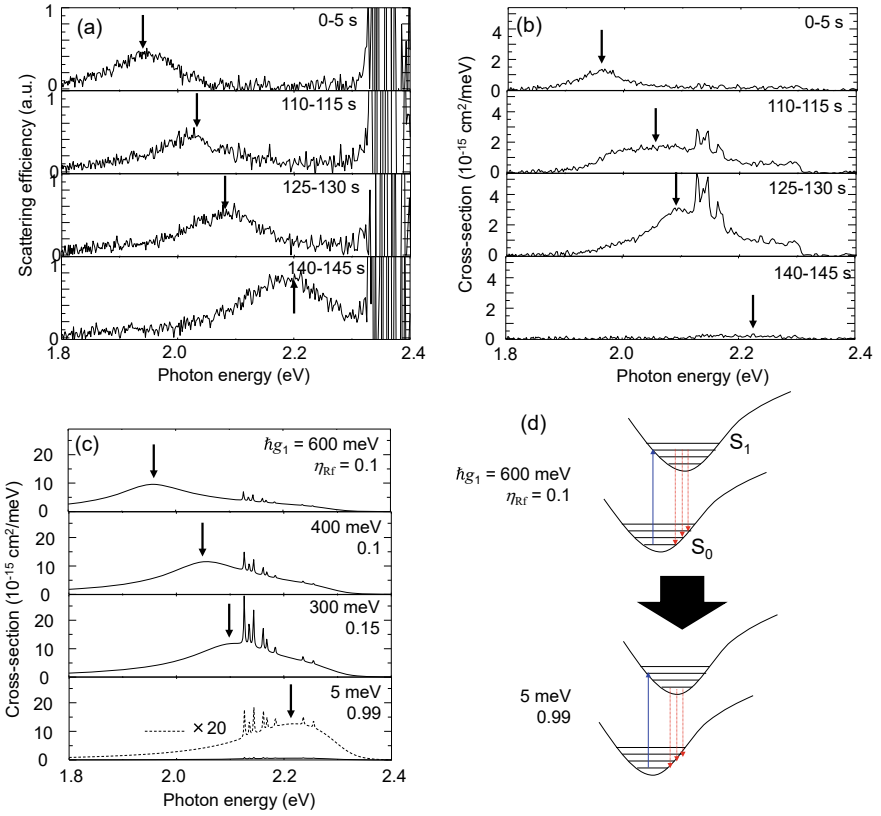



**Fig. 2.6** **a** and **b** Temporal changes in coupled resonance $C_{sca}(\omega)$ spectra and SERS with SEF spectra, respectively, at detection times indicated in panels. Maxima of envelopes are indicated by arrows. **c** Calculated combined spectra of SERS and SEF with product of enhancement (including quenching) factors extracted from $\hbar\Omega_1$ and Raman with fluorescence cross-sections. Values of coupling energy and quantum efficiency $\eta_{Rf}$ for SEF are indicated in panels. Value of quantum efficiency for SERS is fixed at 0.001. Maxima of envelopes are indicated by arrows. **d** Schematic image of changes from ultrafast to conventional SEF with decreasing $\hbar\Omega_1$. Reprinted with permission from Ref. [27]: Copyright 2018 American Institute of Physics

SERS light generated by DQ-coupled plasmon resonance emits through DD-coupled plasmon resonance. In this case, the plasmon resonance $C_{sca}(\omega)$ spectra obtained by dark-field spectroscopy are not identical to the $F_R$ spectra. This contribution of DQ-coupled plasmon resonance may look the breakdown of EM mechanism and thus is needed to be carefully examined.

In this section, the relationships between SERS with SEF spectra and DD-coupled plasmon resonance $C_{sca}(\omega)$ are systematically examined for single silver NP dimers to show the contribution of DQ-coupled plasmon resonance to SERS with SEF. The spectral envelopes of the SERS with SEF were mostly similar to those of the plasmon resonance spectra [23, 24]. However, some dimers showed their spectral

envelopes that shifted to higher-energy regions from the DD-coupled plasmon resonance maxima. There was also significant dimer-to-dimer variability in the degree of these shifts. The analysis of the relationships revealed that the SERS with SEF, which spectral envelope is similar to the plasmon resonance $C_{\mathrm{sca}}(\omega)$ spectra, is mainly caused by DD-coupled plasmon resonance in symmetric dimers. The SERS with SEF, which spectral envelopes shift to higher energies, is mainly caused by DQ-coupled plasmon resonance in asymmetric dimers. These results will be useful for application of subradiant plasmon to various plasmon-enhanced spectroscopies [18].

Figure 2.7a–c shows three different variations in the spectral relationships. The DD-coupled plasmon resonance appears as a maximum in the $C_{\mathrm{sca}}(\omega)$ spectra at photon energies in the range 1.6–2.0 eV. The peaks centered around 2.0 eV correspond to the plasmon resonance maxima along the long axis of the dimers. Figure 2.7a1–a4 shows that the maxima of the SERS with SEF spectra (red lines) are similar to the plasmon resonance maxima (blue lines). This spectral correlation is a dominant feature in the SERS-active dimers and is consistent with the EM mechanism [23, 24]. In the EM mechanism of SERS and SEF, the Raman and fluorescence processes are enhanced $F_R(\omega_{\mathrm{ex}})$ and $F_{\mathrm{R}}(\omega_{\mathrm{em}})$ in Eq. (2.6). However, some dimers do not exhibit that such clear spectral correlation. Figure 2.7b1–b4 does not show such clear spectral correlation, but show that the SERS with SEF spectra exhibit higher-energy shifts from the plasmon resonance maxima. Figure 2.7c1–c4 shows that the SERS with SEF spectra have maxima around the dips in the $C_{\mathrm{sca}}(\omega)$ spectra at around 2.2 eV.

The relationship between the plasmon resonance maxima in the $C_{\mathrm{sca}}(\omega)$ spectra and the spectral envelopes of the SERS with SEF was examined for 39 dimers. Two trends were observed in this relationship. The first trend is a proportional correlation

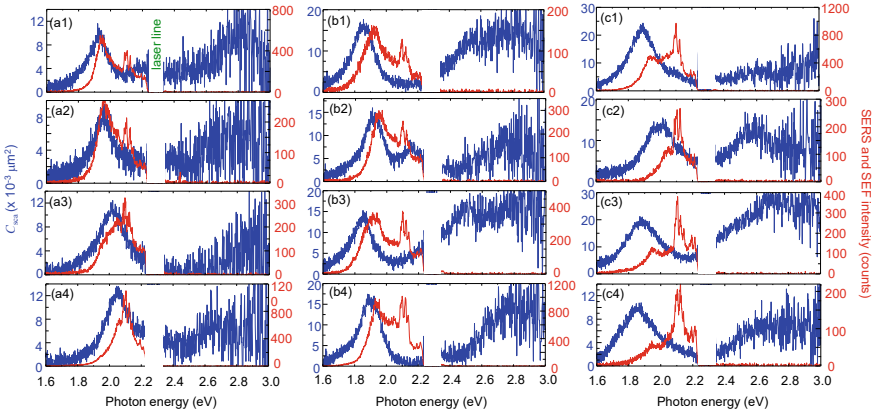



**Fig. 2.7** **a1–a4** $C_{\mathrm{sca}}(\omega)$ spectra (blue lines) and spectra of SERS and SEF (red lines) of single dimers exhibiting similar spectral shapes (Type I). **b1–b4** $C_{\mathrm{sca}}(\omega)$ spectra and spectra of SERS and SEF for single dimers exhibiting spectral deviation with respect to each other (intermediate type). **c1–c4** $C_{\mathrm{sca}}(\omega)$ spectra and spectra of SERS and SEF with maxima that are close to spectral dips in $C_{\mathrm{sca}}(\omega)$ (Type II). Reprinted with permission from Ref. [38]: Copyright 2023 American Chemical Society

between $\hbar\omega_P$ (plasmon resonance maximum energy) and $\hbar\omega_s$ (spectral maximum energy of SERS with SEF envelope). We refer to this correlation as "Type I" as shown in Fig. 2.7a1–a4. The second trend is that the values of $\hbar\omega_s$ remain around 2.1 eV; even as the values of $\hbar\omega_P$ vary widely from 1.85 to 2.2 eV. We refer to this lack of correlation as "Type II" as clearly shown in Fig. 2.7c1–c4. The fact that two types are commonly observed in the relationships between $\hbar\omega_P$ and $\hbar\omega_s$ suggests that there are two types of dimers emitting SERS and SEF light. The correlation and uncorrelation propose that the dimers responsible for Type I generate enhanced EM field directly through DD-coupled plasmon resonance; conversely, the dimers that cause Type II may generate EM enhancement through DQ-coupled plasmon resonance and emit SERS and SEF light through DD-coupled resonance that is coupled with DQ-coupled resonance [37, 38]. Note that there are the intermediate type between Types I and II as shown in Fig. 2.7b1–b4.

To explore the origin of Types I and II, the relationship between dimer shapes, SERS with SEF spectra, and plasmon resonance $C_{sca}(\omega)$ spectra was investigated. Figure 2.8a and b shows SEM images of dimers with their SERS with SEF spectra (red lines), and plasmon resonance $C_{sca}(\omega)$ spectra (blue lines). Figure 2.8a1–a4 and b1–b4 illustrates the spectral correlation and noncorrelation between SERS with SEF and plasmon resonance, respectively. The ratios of the two NP diameters, $D_1/D_2$, are approximately 1.0 to 1.3 and approximately 1.8 to 2.5 for Fig. 2.8a1–a4 and Fig. 2.8b1–b4, respectively. These results indicate that the morphological symmetry and asymmetry of the dimers resulted in Types I and II, respectively.

To further understand the properties of the spectral relationships between DD-coupled plasmon resonance and SERS with SEF, the experimental results were analyzed using the FDTD method. The key findings are summarized as follows:

(1) There are two spectral relationships between DD-coupled plasmon resonance $C_{sca}(\omega)$ and SERS with SEF. Type I exhibits an envelope maximum of SERS with a SEF at a position similar to the DD-coupled plasmon resonance maxima. Type II exhibits an envelope maxima of ~ 2.1 eV around the dips in the $C_{sca}(\omega)$ spectra, indicating the contribution of DQ-coupled plasmon resonance.
(2) The intermediate type between Types I and II is continuous as shown in Fig. 2.7b1–b4, with the envelope maxima of SERS with SEF existing continuously between the superradiant resonance maxima and dips in the $C_{sca}(\omega)$ spectra.
(3) Symmetric and asymmetric dimers are likely associated with Types I and II, respectively, as shown in Fig. 2.8a1–a4 and b1–b4.

The symmetric and asymmetric dimer shapes showing Type I and II in Fig. 2.8 indicate that DD- and DQ-coupled resonances of the symmetric and asymmetric dimers are the origins of Types I and II, respectively. The mechanism of DQ-coupled resonance of asymmetric dimer is here explained. Figure 2.9a1–a10 shows the diameter dependence of the $C_{sca}(\omega)$ spectra for spherical silver NPs. As the NP diameter increases, the dipole resonance in the $C_{sca}(\omega)$ spectra shifts to the lower energy region and quadrupole resonance begins to appear in the higher-energy region, as shown in Fig. 2.9a6. It then shifts to the lower energy region, as shown in Fig. 2.9a9.

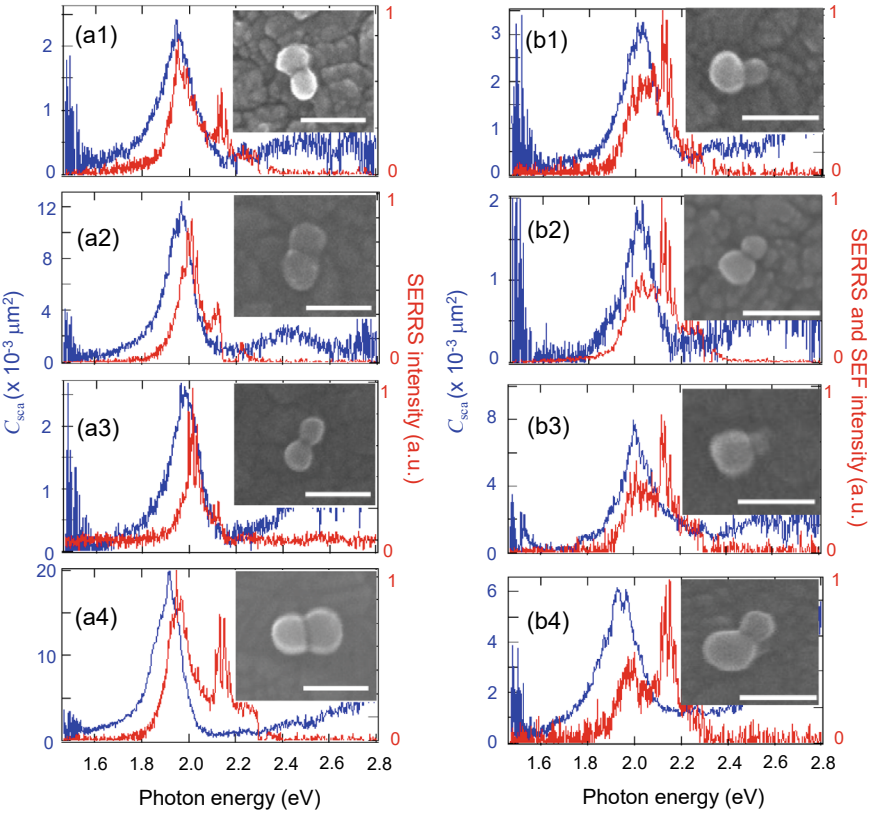



**Fig. 2.8** **a1**–**a4** SERS with SEF (red lines) and $C_{sca}(\omega)$ spectra (blue lines) of dimers exhibiting Type I spectral behavior. Insets are SEM images of dimers. **b1**–**b4** SERS with SEF (red lines) and $C_{sca}(\omega)$ spectra (blue lines) of dimers exhibiting Type II spectral behavior. Insets are SEM images of dimers. Scale bars are 100 nm. Reprinted with permission from Ref. [37]: Copyright 2023 American Chemical Society

Thus, the maximum energy of dipole resonance of smaller NP becomes overlapped with that of quadrupole resonance of larger NP, resulting in DQ-coupled resonance. Figure 2.9b1 and b2 illustrates the surface charge distributions of a dipole and a quadrupole, respectively. Figure 2.9c1 illustrates the surface charge distribution of a DQ-coupled plasmon of an asymmetric dimer by superposing the dipole plasmon of the smaller NP and quadrupole plasmon of the larger NP. Therefore, the combination of NPs in Fig. 2.9a2 and a8 can generate a DQ-coupled resonance [37].

To confirm these experimental results and theoretical considerations, FDTD calculation was carried out by changing the degree of asymmetry of dimers. The validation of the calculation conditions for reproducing the experimental conditions has been described elsewhere [24]. Figure 2.10a and b shows the calculated $C_{sca}(\omega)$ spectra

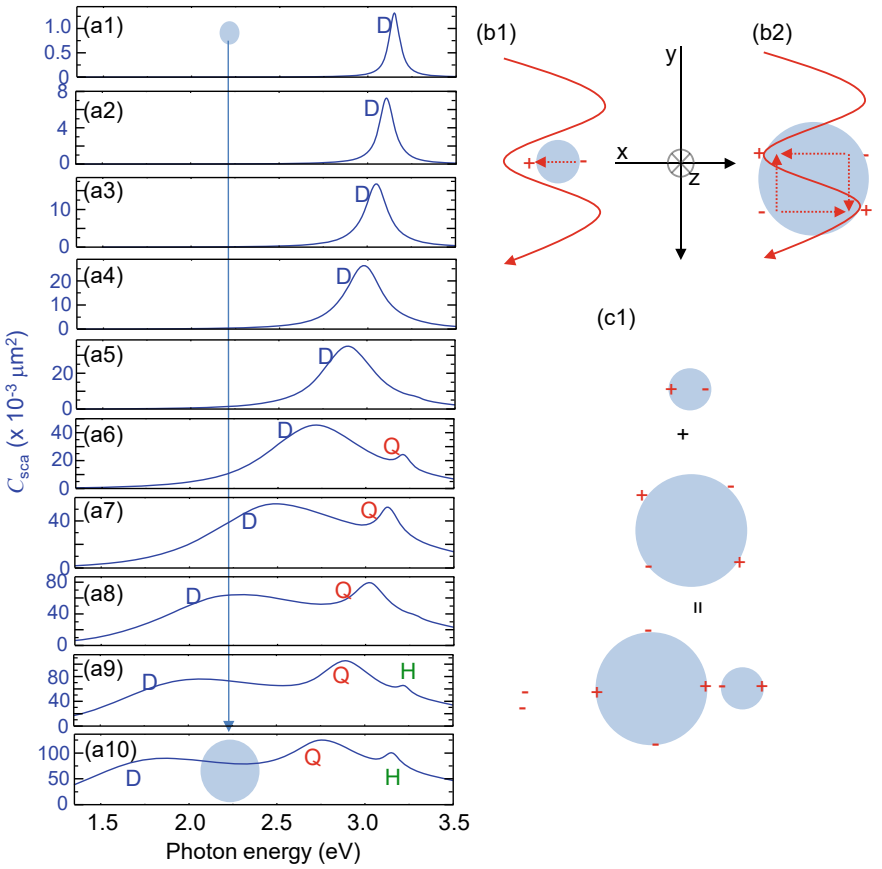



**Fig. 2.9** **a1–a10** $C_{sca}(\omega)$ spectra of single NPs with diameters of 30, 35, 40, 50, 60, 80, 100, 120, and 140 nm, respectively. D, Q, and H indicate dipole, quadrupole, and hexapole resonance, respectively. **b1** and **b2** Dipole and quadrupole on single NPs raised by light coming along y axis. **c1** and **c2** Dipole- and quadrupole-coupled resonance for symmetric and asymmetric dimers, respectively. Reprinted with permission from Ref. [37]: Copyright 2023 American Chemical Society

and the $F_R(\omega)$ spectra using the FDTD method with changing the degree of asymmetry. The excitation polarization is set to be parallel to the dimer long axis with a phase of $E_{loc}$ at the center gap set to 0. The phase of incident electric ($E_I$) set to 180°. The maximum energy in $F_R(\omega)$ spectrum is defined as $\hbar\omega_s$. The amount of phase retardation of $E_{loc}$ against the phase of $E_I$ is shown in Fig. 2.10. The $E_{loc}$ of the DD-coupled resonance induces a phase retardation of 90° as compared to $E_I$ [1]. The phase of $E_{loc}$ of the DQ-coupled resonance forces a further retardation of 90° from the DD-coupled resonance because the DQ-coupled resonance receives light energy by coupling with the DD-coupled resonance. Thus, the $E_{loc}$ of the DQ-coupled resonance exhibits a phase retardation of 180° from $E_I$. The destructive interference

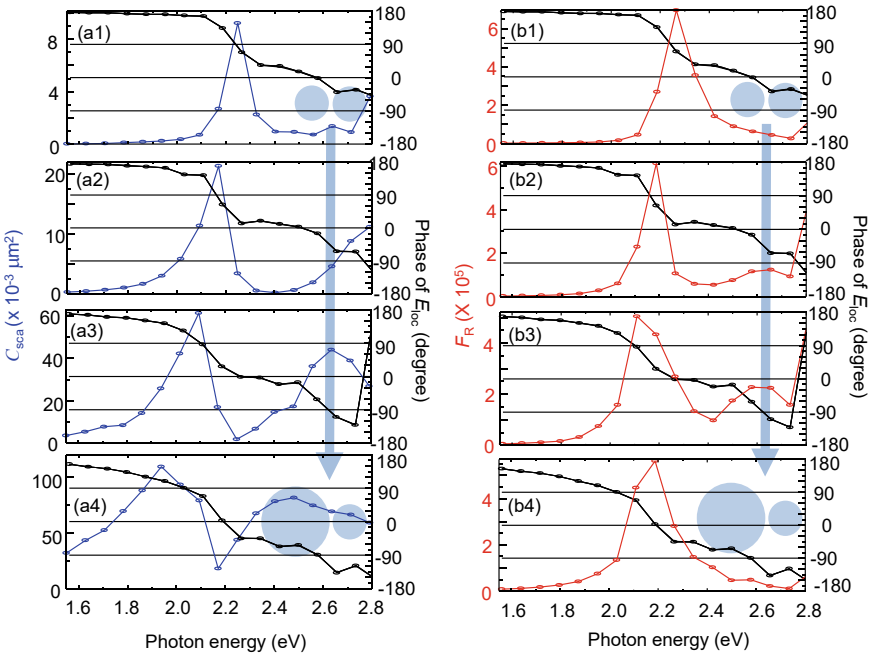



**Fig. 2.10** **a1–a4** $D_1$ dependence of $C_{sca}(\omega)$ spectra with phases of $E_{loc}$ with a $D_1$ of 30 nm and $D_2$ of 30, 50, 80, and 120 nm, respectively. Initial phase of $E_I$ and $D_2$ were set 180° and 30 nm, respectively. **b1–b4** $D_1$ dependence of $F_R(\omega)$ spectra and phases of $E_{loc}$ with a $D_1$ of 30 nm and $D_2$ of 30, 50, 80, and 120 nm, respectively. Initial phase of $E_I$ and $D_2$ were set 180° and 30 nm, respectively. Reprinted with permission from Ref. [37]: Copyright 2023 American Chemical Society

between the $E_{loc}$ of DD-coupled resonance and the $E_{loc}$ of DQ-coupled resonance appears as a dip structure in the $\sigma_{sca}(\omega)$ spectrum.

Figure 2.10a1–a4 illustrates the $D_1$ (diameter of larger NP) dependence of $C_{sca}(\omega)$ spectra on the phases of $E_{loc}$. The initial phase of $E_I$ was set to 180° and $D_2$ (diameter of smaller NP) was set to 30 nm. The $C_{sca}(\omega)$ spectra exhibit a phase retardation by 90° due to $E_{loc}$ at $\hbar\omega_p$, indicating that these spectral maxima correspond to the DD-coupled resonance. As the value of $D_1$ increases, the DD-coupled resonance spectra become broader due to the increasing effect of radiation damping. When $D_1$ is further increased, a dip structure appears in the $C_{sca}(\omega)$ spectrum at a phase retardation of 180°, indicating that the spectral dip is caused by destructive interference between the DD- and DQ-coupled resonance. Figure 2.10b1–b4 shows the $D_1$ dependence of the $F_R(\omega)$ spectra at an HS with the phase of $E_{loc}$. The $F_R(\omega)$ spectrum in Fig. 2.10b1 exhibits $\hbar\omega_s$ at a phase retardation of 90°, indicating that the maximum is the result of the EM enhancement by the DD-coupled resonance. As $D_1$ increases, $\hbar\omega_s$ exhibits a lower energy shift, as shown in Fig. 2.10b2. However, the lower energy shift in $\hbar\omega_s$ does not occur in Fig. 2.10b3 and $\hbar\omega_s$ remains at ~ 2.18 eV, as shown in Fig. 2.10b4, where the phase retardation is 180°. This position is the same as the dip in the

$C_{sca}(\omega)$ spectrum shown in Fig. 2.10a4, indicating that the $F_R(\omega)$ maximum at $\hbar\omega_s$ is the result of EM enhancement by the DQ-coupled resonance, which obtains light energy through DD-coupled resonance. This mechanism of EM enhancement by the DQ-coupled resonance reasonably explains the experimentally observed higher-energy shifts in the envelope maxima of SERS with SEF as shown in Fig. 2.7b. This mechanism also explains why the envelope maximum positions of SERS and SEF match the dip positions in the $C_{sca}(\omega)$ spectra shown in Fig. 2.7c. In short, the experimentally observed spectral deviation of the envelope of SERS with SEF from DD-coupled resonance is explained as the contribution of DQ-coupled resonance to the EM enhancement.

To further confirm the mechanism of spectral deviation in the envelopes of SERS with SEF caused by DQ-coupled plasmon resonance from $C_{sca}(\omega)$, we compared the experimental and calculated results. Figure 2.11 shows the calculated relationship between $\hbar\omega_p$ in the $C_{sca}(\omega)$ spectra and $\hbar\omega_s$ in the $F_R(\omega)$ spectra. This relationship is superimposed with the experimentally obtained relationship between $\hbar\omega_p$ and $\hbar\omega_s$. The calculated relationship well reproduces both Type I and II well using the symmetric and asymmetric dimers, respectively, indicating the validity of the mechanism in which Types I and II are raised by DD- and DQ-coupled resonance, respectively. The discussion in Fig. 2.11 shows that the experimentally obtained properties (1)–(3) are induced by the degree of asymmetry in the dimers.

In summary, the spectral relationships between SERS with SEF and DD-coupled plasmon resonance in $C_{sca}(\omega)$ were investigated using a single silver NP dimer. There are two types of relationships: Type I, in which the envelopes of the SERS with SEF are similar to the plasmon resonance maxima, and Type II, in which the envelopes

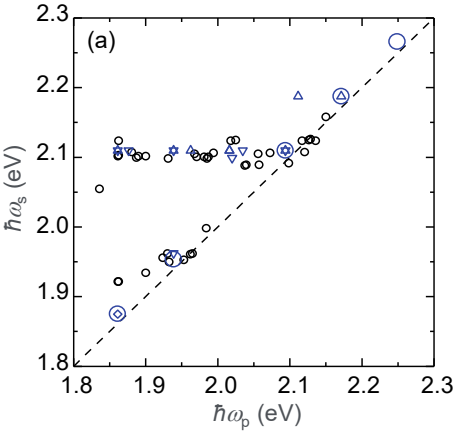



**Fig. 2.11** **a** Calculated relationship between $\hbar\omega_p$ and $\hbar\omega_s$ of single symmetric dimers (○) and asymmetric dimers with $D_2$ values of 35 (△), 40 (▽), 60 (◇) nm. Diameters of NP symmetric dimers are 30–140 nm. $D_1$ values for asymmetric dimers are 35–140 (△), 40–140 (▽), and 60–140 (◇) nm. Experimental relationship between $\hbar\omega_p$ and $\hbar\omega_s$ of single dimers (○). Reprinted with permission from Ref. [37]: Copyright 2023 American Chemical Society

shift to the higher-energy side from the maxima. Using FDTD calculations, the experimental spectra for both $C_{sca}(\omega)$ and SERS with SEF were successfully reproduced by changing the degree of morphological asymmetry in the dimers. This analysis of the calculation results revealed that Types I and II are caused by DD- and DQ-coupled resonance, respectively. The DQ-coupled resonance, which is subradiant, receives excitation light and emits SERS and SEF light through near-field interaction with DD-coupled resonance. The measurement of $F_R(\omega)$ by absorption spectroscopy can directly show the spectral correlation between $F_R(\omega)$ and plasmon resonance absorption, because both origins are common in QED, namely AP term [39]. The absorption spectroscopy of single dimers are described elsewhere [41].

## 2.5 Electromagnetic Mechanism of One-Dimensional SERS Hotspots

The development of effective plasmonic HSs is key to the SM-SERS spectroscopy [18]. Various types of HSs have been experimentally and theoretically developed by bottom-up and top-down methods to improve SM-SERS spectroscopy [18, 42]. One of the issue of HSs is their extremely small $V_{HS}$ in Eqs. (2)–(4). The $V_{HS}$ of HSs are restricted to only several cubic nanometers at the crevices or nanogaps of the NP dimers to obtain a SM-SERS sensitivity. Thus, SERS signals are usually unstable due to photo-induced thermal and chemical molecular fluctuations. For example, a SM-SERS observation is interrupted or terminated by desorption and carbonization of molecules at the HSs [43, 44]. Thus, it is important to increase the $V_{HS}$ to reduce the instability and improve the investigations of the phenomena. We introduce the SERS HS formed along the crevices or gaps between two parallel silver nanowires (NWs) [45, 46]. This HS is one-dimensionally extended by several micrometers to tens of micrometers, which $V_{HS}$ is tens of thousands times longer than that of the HSs of NP dimers. We call this type of HS as one-dimensional (1D) HS.

Figure 2.12a–c shows the dark-field, SERS, and SEM images of the NWs for an identical area of the sample ITO glass plate. By comparing these images, one can notice that the NWs with blue, yellow, and pink colors in Fig. 2.12a show the one-dimensionally extended SERS activity in Fig. 2.12b, and these NWs form aggregates as shown in Fig. 2.12c and d. The NWs with gray color in Fig. 2.12a do not show any SERS activity as in Fig. 2.12b, and these NWs are all monomers as shown in Fig. 2.12c. The plasmon resonance maxima along the length of the NWs are in the near infrared region [47]. Thus, the dark-field image may show the Rayleigh light scattering by the plasmon resonance along the NW diameter. Considering that this plasmon resonance of NW monomer is in the violet region [48], these relationships between the colors of the Rayleigh light scattering, SERS activity, and aggregation of NWs can be explained as that the aggregate formation by the NWs generates the coupled plasmon resonance of multiple NWs in the visible region and the aggregates

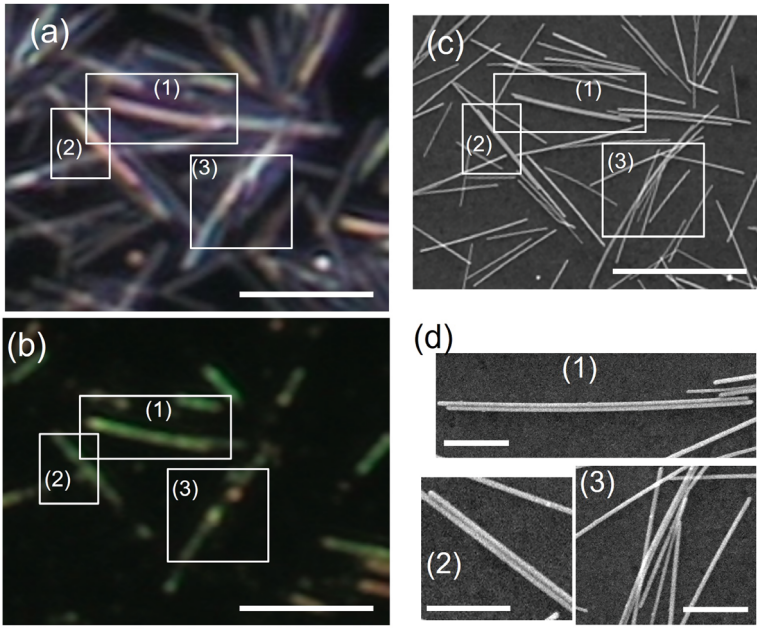



**Fig. 2.12** Images of **a** Rayleigh scattering, **b** SERS, and **c** SEM of NWs obtained from same area on sample glass plate covered with an ITO film. **d** Enlarged SEM images of NWs corresponding to white boxes (1)–(3) in **a**–**c**. Scale bars in **a**–**c** and **d** are 10 μm and 1.0 μm, respectively. Reprinted with permission from Ref. [45]: Copyright 2017 American Physical Society

exhibit the SERS activity. The results indicate coupled plasmon resonance along the crevices or gaps of the NW aggregates generates 1D HS.

To more precisely examine the above indication, an individual NW dimer was investigated using dark-field, SERS, and SEM images. Figure 2.13a–c shows the SEM, dark-field, and SERS images of the NW dimer. The dimer can be divided into two regions: one is a gap region and other is a monomer region as shown in Fig. 2.13a2 and a3. By superposing the dark-field image on the SEM image as in Fig. 2.13d, we determined that only the gap region shows blue color while the monomer region is gray, indicating that the plasmon resonances of two NWs are coupled and red-shifts to the blue region. By superposing the SERS image on the SEM image as in Fig. 2.13e, we found that only the gap region exhibits the SERS activity. These results indicate that a gap region in a NW dimer contains one-dimensionally extended HSs induced by the coupled plasmon resonance. There are two possibilities of coupled plasmon resonance, such as DD- or DQ-coupled plasmon resonances [49].

To analyze the coupled plasmon resonance that induces 1D HSs, the polarization dependence of the coupled plasmon resonance and SERS spectra were measured for a single NW dimer. Figure 2.14a and b shows the Rayleigh scattering and SERS spectra perpendicular and parallel to the length of the dimer, respectively. Both the coupled plasmon resonance around 520 nm and SERS reach the maximum for the polarization

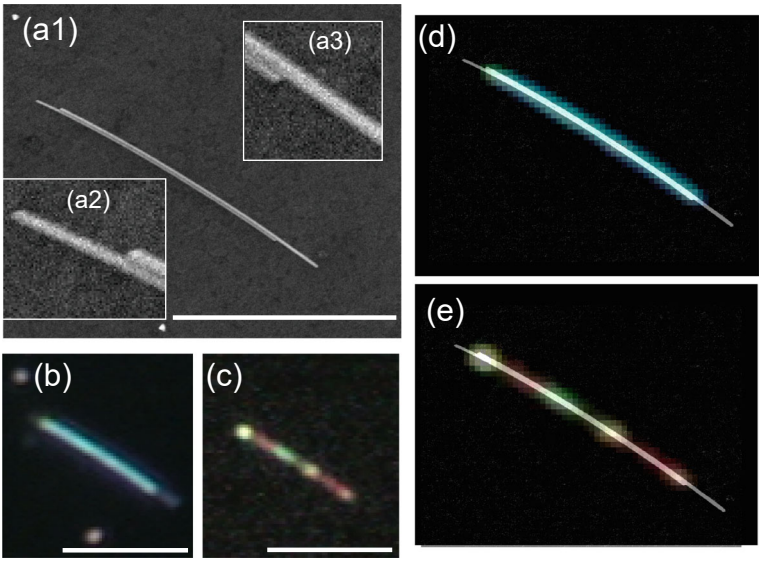



**Fig. 2.13** **a1** SEM image of NW dimer. Insets: **a2**–**a3** enlarged SEM images of edges of dimer crevice. **b**–**c** Dark-field and SERS images of dimer. **d** Superposition of SEM and dark-field image. **e** Superposition of SEM and SERS images. Scale bars in **a**–**c** are 5 μm. Reprinted with permission from Ref. [45]: Copyright 2017 American Physical Society

perpendicular to the dimer length. Both are minimized for the polarization along the dimer length. In contrast, a broad plasmon resonance around 750 nm, which is similar to the plasmon resonance of the monomer, reaches the maximum for the polarization parallel to the long axis. Figure 2.14c shows the polarization dependence of the plasmon resonance maxima at 520 and 750 nm, respectively. Figure 2.14d shows the polarization dependence of the SERS. The polarization dependence of the coupled plasmon resonance maxima at 520 nm is the same as that of the SERS, indicating that this coupled plasmon resonance perpendicular to the length of the dimer induces the EM enhancement generating the SERS along the dimer crevices.

To analyze the properties of $C_{\mathrm{sca}}(\omega)$ and SERS spectra of the NW dimers presented in Figs. 2.12, 2.13, and 2.14, FDTD calculation were carried out for the NW dimers. The experimental findings are summarized in Ref. [37] as indicated below.

(1) NWs forming dimers exhibit both the red-shifted plasmon resonance and SERS activity.
(2) The red-shifted plasmon resonance $C_{\mathrm{sca}}(\omega)$ and SERS light exhibit identical polarization dependence.
(3) The SERS intensities become the largest at edges of the 1D HSs.
(4) The HSs show the oscillating patterns along 1D HSs.
(5) The SERS intensities at the edges of 1D HSs do not disappear even when the incident light polarization is parallel to the dimer length.

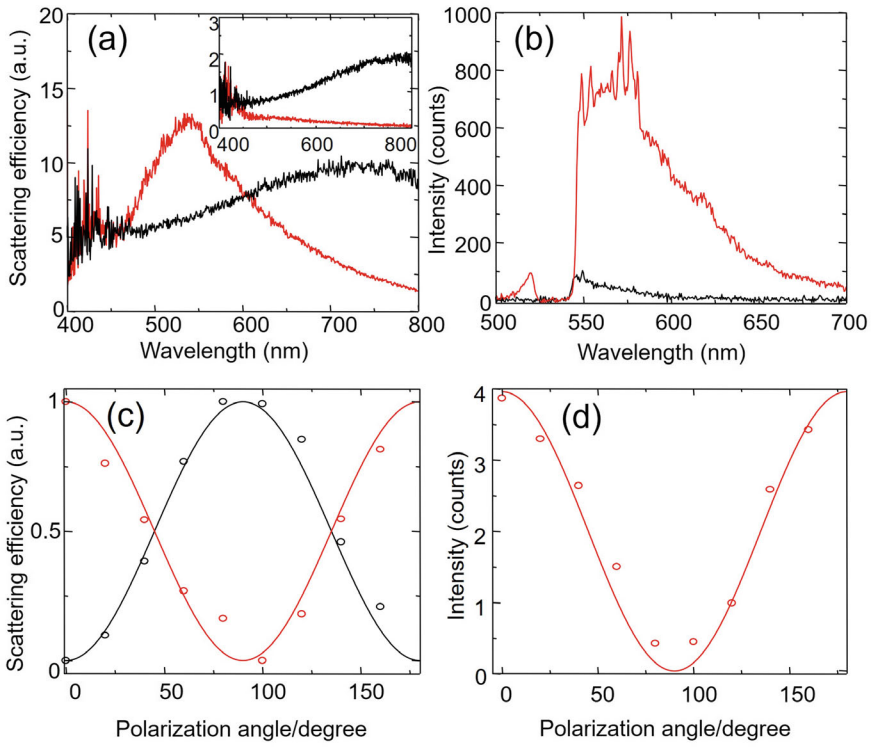



**Fig. 2.14** **a** Spectrum of $C_{sca}(\omega)$ for NW dimer and (inset) monomer perpendicular (red line) and parallel (black line) to dimer length. **b** Spectrum of SERS intensity perpendicular (red line) and parallel (black line) to dimer length. **c** Polarization dependence (circles and line) of plasmon resonance maxima at 520 nm (red) and 720 nm (black). **d** Polarization dependence of SERS intensity at 560 nm (red circles and red line). Reprinted with permission from Ref. [45]: Copyright 2017 American Physical Society

Figure 2.15a shows the structure of an NW dimer used for the FDTD calculations to understand the five abovementioned properties. The length and diameter of each NW in the dimer are 6.0 μm and 100 nm, respectively. The NWs are contacting each other. The length of the HS between the NWs is 5.0 μm. Figure 2.15b shows $C_{sca}(\omega)$ spectra perpendicular and parallel to the dimer length, and the inset shows those spectra for the monomer. When the polarization is perpendicular to the dimer length, DD-coupled plasmon resonance maximum appears around 620 nm, respectively. The maximum disappears when the polarization is along the dimer length. The plasmon resonance maximum does not appear in the monomer. These spectral properties support well the experimental results in Fig. 2.14, indicating that the calculations correctly reproduce the EM fields around the NW dimers. Figure 2.15c–e shows the EM field distributions in X, Y, and Z planes at the excitation wavelength of 532 nm, respectively. Figure 2.15c2 and c3 shows that an enhanced EM field appears at the crevice of the NW dimer when the polarization is oriented along the dimer width (Z

axis), and the EM field disappears when the polarization is parallel to the dimer length (X axis). Figure 2.15d2–d3 and e2–e3 shows Fabry–Pérot type oscillating patterns of the EM fields. The EM field intensity reaches the maximum at the edges of the crevices for the polarization oriented along the dimer width. Taking into account the incident light polarization and generation of 1D HSs, the surface plasmon involved in the oscillating patterns in the calculations should give rise to transverse antisymmetric surface plasmon waves propagating along the 1D HS [46]. Figure 2.15d3 and e3 shows the largest enhancement of the EM fields at the ends of the HSs even when the polarization is parallel to the dimer length. The calculation results can be explained as follows. A non-radiative longitudinal surface plasmon wave gives rise to the radiative local plasmon by contacting the edges of the 1D HSs. The local plasmon generates the enhanced EM field and supports the contribution of the Fabry–Pérot type resonance to the SERS. These calculation results well reproduce the experimental properties (1)–(5), indicating that the calculations correctly reproduce the EM fields generating the SERS hotspots. The phase analysis of EM fields revealed that DD- and DQ-coupled plasmon resonances contribute to SERS of NW dimers composed of thin (<80 nm) and large (>100 nm) NWs, respectively [49].

In the section, one-dimensionally extended HSs was examined using gaps of silver NW dimers. The comparison between experiments and FDTD calculations determined that a DD or DQ plasmon resonance in the direction along the dimer width generates the 1D HSs, and that oscillating patterns in SERS images are induced by a Fabry–Pérot type interference of the propagating surface plasmons. This 1D HS is useful for improving the stability in SERS measurement. Furthermore, the propagation of SERS light through 1D HSs have been observed [46]. Such propagation may be also useful for signal transfer inside extremely small optical circuits.

## 2.6 Conclusion

In the first half, the EM mechanism of SERS at HSs was explained using coupling energy between plasmon and molecular exciton resonances in the framework of cavity QED. The coupling energies were obtained by spectral changes in $C_{\mathrm{sca}}(\omega)$ during quenching processes of SERS and SEF. SERS with SEF spectra were reproduced by EM enhancement factor derived by the coupling energy. In the second half, the contribution of subradiant plasmon to SERS and 1D HSs along NW dimer junctions was explained based on the EM mechanism. The contribution of subradiant plasmon at HSs was evaluated by spectral inconsistency between SERS with SEF and $C_{\mathrm{sca}}(\omega)$. The inconsistency is reproduced by FDTD method using asymmetric dimers, indicating that the inconsistency is induced by contribution of DQ-coupled resonance, which is subradiant. The observed 1D HSs generated along NW dimer junctions were evaluated with EM mechanism. The evaluation revealed that both DD or DQ plasmon resonance and Fabry–Pérot type plasmon resonance generate SERS through 1D HSs. The EM mechanism will be applied to various HSs and phenomena in the framework of cavity QED.

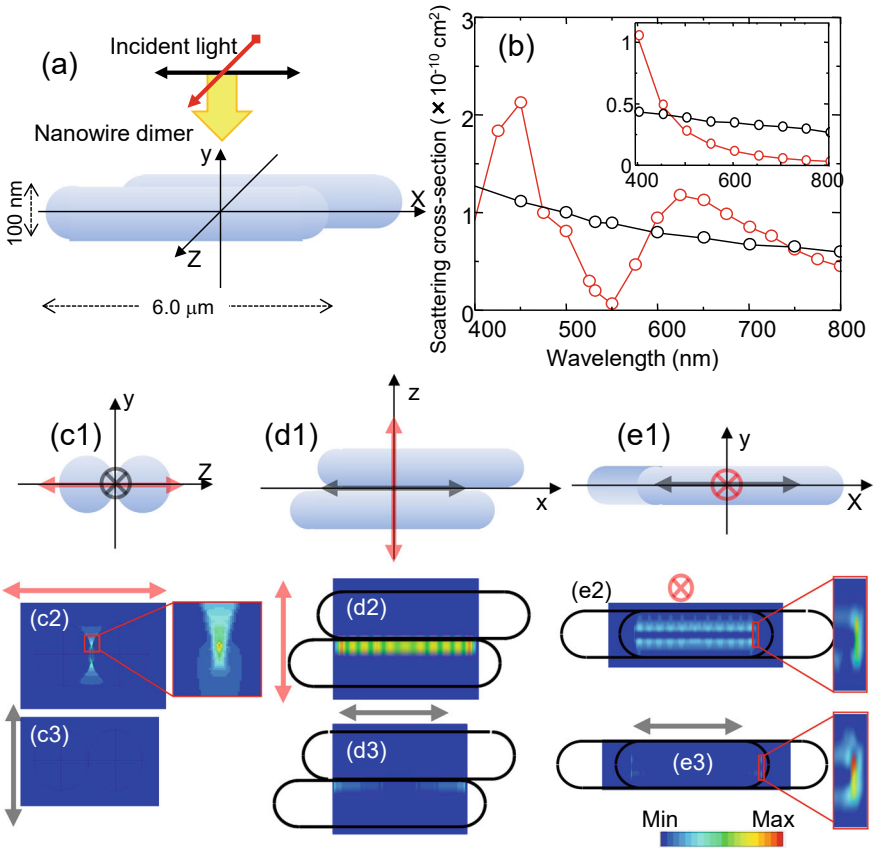



**Fig. 2.15** **a** Image of a NW dimer and direction of incident light (yellow arrow) with coordinate system used for FDTD calculations. Red and black arrows indicate direction of light polarization. **b** Calculated $C_{sca}(\omega)$ spectra for NW dimer and (inset) monomer perpendicular (red line) and parallel (black line) to dimer (monomer) length (X axis). **c1**–**e1** Images of dimer cross-section in X, Y, and Z planes, respectively. Red and black arrows indicate direction of polarization. **c2**–**e2** EM field distributions at 532 nm for incident light polarization along dimer width (Z axis). **c3**–**e3** EM field distributions at 532 nm for incident light polarization along X. Reprinted with permission from Ref. [45]: Copyright 2017 American Physical Society

## References

1. M. Fleischmann, P. J. Hendra, A. J. Mcquillan, Raman-spectra of pyridine adsorbed at a silver electrode. Chem. Phys. Lett. **26**, 163-166 (1974)
2. M. G. Albrecht, J. A. Creighton, Anomalously intense Raman-spectra of pyridine at a silver electrode. J. Am. Chem. Soc. **99**, 5215-5217 (1977)
3. D. L. Jeanmaire, R. P. Van Duyne, Surface Raman Spectroelectrochemistry: Part I. Heterocyclic, aromatic, and aliphatic amines adsorbed on the anodized silver electrode. J. Electroanal. Chem. **84**, 1–20 (1977)

4. S. Nie and S. Emory, Probing single molecules and single nanoparticles by surface-enhanced Raman scattering. Science **275**, 1102 (1997)
5. K. Kneipp, Y. Wang, H. Kneipp, L. Perelman, I. Itzkan, R. R. Dasari, and M. Feld, Single molecule detection using surface-enhanced Raman scattering (SERS). Phys. Rev. Lett. **78**, 1667 (1997)
6. E. C. Le Ru, M. Meyer, P. G. Etchegoin, Proof of Single-molecule sensitivity in surface enhanced Raman scattering (SERS) by means of a two-analyte technique. J. Phys. Chem. B, **110**, 1944-1948 (2006)
7. J. A. Dieringer, R. B., 2nd Lettan, K. A. Scheidt, R. P. Van Duyne, A frequency domain existence proof of single-molecule surface-enhanced Raman spectroscopy. J. Am. Chem. Soc. **129**, 16249–16256 (2007)
8. Y. S. Yamamoto, T. Itoh, Why and how do the shapes of surface-enhanced Raman scattering spectra change? recent progress from mechanistic studies. J. Raman Spectrosc. **47**, 78-88 (2016)
9. M. Moskovits, Surface-Enhanced Spectroscopy. Rev. Mod. Phys. **57**, 783-826 (1985)
10. M. Moskovits, Surface-roughness and enhanced intensity of Raman-scattering by molecules adsorbed on metals. J. Chem. Phys. **69**, 4159-4161 (1978)
11. D. S. Wang, M. Kerker, Enhanced Raman scattering by molecules adsorbed at the surface of colloidal spheroids. Phys. Rev. B **24**, 1777-1790 (1981)
12. H. Xu, H. J. Aizpurua, M. Kall, P. Apell, Electromagnetic contributions to single-molecule sensitivity in surface-enhanced Raman scattering. Phys. Rev. E **62**, 4318-4324 (2000)
13. P. K. Aravind, A. Nitzan, H. Metiu, The Interaction between electromagnetic resonances and its role in spectroscopic studies of molecules adsorbed on colloidal particles or metal spheres. Surf. Sci. **110**, 189-204 (1981).
14. M. Inoue, K. Ohtaka, Surface enhanced Raman-scattering by metal spheres. 1. Cluster effect. J. Phys. Soc. Japan. **52**, 3853–3864 (1983)
15. Y. S. Yamamoto, Y. Ozaki, T. Itoh, Recent progress and frontiers in the electromagnetic mechanism of surface-enhanced Raman scattering. J. Photochem. Photobio. C. **21**, 81 (2014)
16. T. Itoh, Y. S. Yamamoto, and Y. Ozaki, Plasmon-enhanced spectroscopy of absorption and spontaneous emissions explained using cavity quantum optics. Chem. Soc. Rev. **46**, 3904 (2017)
17. T. Itoh, Y. S. Yamamoto, Between plasmonics and surface-enhanced resonant Raman spectroscopy: Toward single-molecule strong coupling at a hotspot. Nanoscale. **13**, 1566 (2021)
18. T. Itoh, M. Procházka, Z. C. Dong, W. Ji, Y.S. Yamamoto, Y. Zhang, Y. Ozaki, Toward a New Era of SERS and TERS at the Nanometer Scale: From Fundamentals to Innovative Applications. Chem. Rev. **123**, 1552–1634 (2023).
19. C. F. Bohren, D. R. Huffman, *Absorption and Scattering of Light by Small Particles* (Wiley, 1983)
20. P. B. Johnson and R. W. Christy, Optical constants of the noble metals, Phys. Rev. B **6**, 4370–4379 (1972)
21. M. Fox, *Quantum Optics: An Introduction* (Oxford University Press, 2006)
22. L. C. Andreani, G. Panzarini, J. M. Gerard, Strong-coupling regime for quantum boxes in pillar microcavities: Theory. Phys. Rev. B, **60**, 13276 (1999)
23. K. Yoshida, T. Itoh, V. Biju, M. Ishikawa, Y. Ozaki, Experimental evaluation of the twofold electromagnetic enhancement theory of surface-enhanced resonance Raman scattering. Phys. Rev. B **79**, 085419 (2009).
24. K. Yoshida, T. Itoh, H. Tamaru, V. Biju, M. Ishikawa, Y. Ozaki, Quantitative evaluation of electromagnetic enhancement in surface-enhanced resonance Raman scattering from plasmonic properties and morphologies of individual Ag nanostructures. Phys. Rev. B **81**, 115406 (2010)
25. T. Itoh, V. Biju, M. Ishikawa, Y. Kikkawa, K. Hashimoto, A. Ikehata, and Y. Ozaki, Surface-enhanced resonance Raman scattering and background light emission coupled with plasmon of single Ag nanoaggregates. J. Chem. Phys. **124**, 134708 (2006)
26. W. Zhu, K. B. Crozier, Quantum mechanical limit to plasmonic enhancement as observed by surface-enhanced Raman scattering. Nat. Commun. **5**, 5228 (2014)

27. T. Itoh and Y. S. Yamamoto, Reproduction of surface-enhanced resonant Raman scattering, and fluorescence spectra of a strong coupling system composed of a single silver nanoparticle dimer and a few dye molecules. J. Chem. Phys. **149**, 244701 (2018)
28. T. Itoh, Y. S. Yamamoto, and T. Okamoto, Anti-crossing property of strong coupling system of silver nanoparticle dimers coated with thin dye molecular films analysed by electromagnetism. J. Chem. Phys. **152**, 054710 (2020)
29. M. Pelton, S. D. Storm, H. Leng, Strong coupling of emitters to single plasmonic nanoparticles: exciton-induced transparency and Rabi splitting. Nanoscale, **11**, 14540-14552 (2019)
30. T. Itoh, Y. S. Yamamoto, H. Tamaru, V. Biju, S. Wakida, and Y. Ozaki, Single-molecular surface-enhanced resonance Raman scattering as a quantitative probe of local electromagnetic field: The case of strong coupling between plasmonic and excitonic resonance. Phys. Rev. B **89**, 195436 (2014)
31. K. J. Savage, M. M. Hawkeye, R. Esteban, A. G. Borisov, J. Aizpurua, and J. J. Baumberg, Revealing the quantum regime in tunnelling plasmonics. Nature **491**, 574 (2012)
32. R. Ruppin, Optical absorption of a coated sphere above a substrate. Phys. A, **178**, 195 (1991)
33. R. Chikkaraddy, B. de Nijs, F. Benz, S. J. Barrow, O. A. Scherman, E. Rosta, A. Demetriadou, P. Fox, O. Hess, J. J. Baumberg, Single-molecule strong coupling at room temperature in plasmonic nanocavities. Nature **535**, 127-130 (2016)
34. T. P. Rossi, T. Shegai, P. Erhart, T. J. Antosiewicz, Strong plasmon-molecule coupling at the nanoscale revealed by first-principles modeling. Nat. Commun. **10**, 3336 (2019)
35. C. Sönnichsen, T. Franzl, T. Wilk, G. von Plessen, J. Feldmann, O. Wilson, and P. Mulvaney, Drastic reduction of plasmon damping in gold nanorods. Phys. Rev. Lett. **88**, 077402 (2002)
36. T. Itoh, Y. S. Yamamoto, H. Tamaru, V. Biju, N. Murase, and Y. Ozaki, Excitation laser energy dependence of surface-enhanced fluorescence showing plasmon-induced ultrafast electronic dynamics in dye molecules. Phys. Rev. B **87**, 235408 (2013)
37. T. Itoh, Y. S. Yamamoto, Contribution of subradiant plasmon resonance to electromagnetic enhancement in resonant Raman with fluorescence examined by single silver nanoparticle dimers. J. Phys. Chem. C **127**, 5886–5897 (2023)
38. 38 T. Itoh, Y. S. Yamamoto, Correlated polarization dependences between surface-enhanced resonant Raman scattering and plasmon resonance elastic scattering showing spectral uncorrelation to each other. J. Phys. Chem. B **127**, 4666–4675 (2023)
39. T. Itoh, Y. S. Yamamoto, Demonstration of electromagnetic enhancement correlated to optical absorption of single plasmonic system coupled with molecular excitons using ultrafast surface-enhanced fluorescence. J. Chem. Phys. **159**, 034709 (2023)
40. L. V. Brown, H. Sobhani, J. B. Lassiter, P. Nordlander, N. J. Halas, Heterodimers: plasmonic properties of mismatched nanoparticle pairs. ACS Nano 4, 819−832 (2010).
41. T. Itoh, Y. S. Yamamoto, and T. Okamoto, Absorption cross-section spectroscopy of a single strong-coupling system between plasmon and molecular exciton resonance using a single silver nanoparticle dimer generating surface-enhanced resonant Raman scattering. Phys. Rev. B, **99**, 235409 (2019)
42. S. Y. Ding, E. M. You, Z. Q. Tian, M. Moskovits, Electromagnetic theories of surface-enhanced Raman spectroscopy. Chem. Soc. Rev. **46**, 4042–4076 (2017)
43. T. Itoh, M. Iga, H. Tamaru, K. Yoshida, V. Biju, and M. Ishikawa, Quantitative evaluation of blinking in surface enhanced resonance Raman scattering and fluorescence by electromagnetic mechanism. J. Chem. Phys. **136**, 024703 (2012)
44. T. Itoh, Y. S Yamamoto, V. Biju, H. Tamaru, S. Wakida, Fluctuating single $sp^2$ carbon clusters at single hotspots of silver nanoparticle dimers investigated by surface-enhanced resonance Raman scattering. AIP Adv. **5**, 127113 (2015)
45. T. Itoh, T. Y. S. Yamamoto, Y. Kitahama, J. Balachandran, One-dimensional plasmonic hotspots located between silver nanowire dimers evaluated by surface-enhanced resonance Raman scattering. Phys. Rev. B **95**, 115441 (2017)
46. T. Itoh, Y. S. Yamamoto, and J. Balachandran, Propagation mechanism of surface plasmons coupled with surface-enhanced resonant Raman scattering light through a one-dimensional hotspot along a silver nanowire dimer junction. Phys. Rev. B **103**, 245425 (2021)

47. F. Neubrech, T. Kolb, R. Lovrincic, G. Fahsold, A. Puccia, J. Aizpurua, T.W. Cornelius, M. E. Toimil-Molares, R. Neumann, and S. Karim, Resonances of individual metal nanowires in the infrared. Appl. Phys. Lett. 89, 253104 (2006)
48. J. P. Kottmann, O. J. F. Martin, D. R. Smith, and S. Schultz, Plasmon resonances of silver nanowires with a nonregular cross section. Phys. Rev. B 64, 235402 (2001)
49. T. Itoh, T. Y. S. Yamamoto, Electromagnetic enhancement spectra of one-dimensional plasmonic hotspots along silver nanowire dimer derived via surface-enhanced fluorescence. J. Chem. Phys. **160**, 024703 (2024)

# Chapter 3
# Chemical Mechanism of SERS




**Libin Yang, Xin Jiang, and Bing Zhao**

**Abstract** This chapter focuses on the chemical mechanism of SERS. It includes five parts: 3.1 The Proposal of Chemical Mechanism; 3.2 The Description of Chemical Mechanism; 3.3 The Theory of Chemical Mechanism; 3.4 The Selection Rules of Chemical Mechanism; and 3.5 The Difference between Chemical Mechanism and Electromagnetic Mechanism.

**Keywords** Chemical mechanism · Charge transfer · Chemical adsorption · Theory

In addition to the electromagnetic mechanism (i.e., the physical enhancement mechanism), the chemical mechanism is also an important part of SERS-enhanced mechanism [1–7]. Both are involved to contribute the total SERS enhancement and to explain different SERS phenomena.

## 3.1 The Proposal of Chemical Mechanism

Although the electromagnetic mechanism can explain a lot of SERS phenomena and has been widely recognized by people, some experimental evidences also indicate that there must be other factors leading to the enhancement of Raman signal. Such as:

L. Yang (✉) · X. Jiang
College of Chemistry and Chemical Engineering, Qiqihar University, Qiqihar 161006, China
e-mail: yanglibin@qqhru.edu.cn

B. Zhao (✉)
State Key Laboratory of Supramolecular Structure and Materials, Jilin University, Changchun 130012, China
e-mail: zhaob@jlu.edu.cn

© The Author(s), under exclusive license to Springer Nature Singapore Pte Ltd. 2024

M. Procházka et al. (eds.), *Surface- and Tip-Enhanced Raman Scattering Spectroscopy*,
https://doi.org/10.1007/978-981-97-5818-0_3

(1) Influence of applied potential on Raman scattering enhancement in electrochemical testing. When the excitation wavelength is changed by fixing the potential or when the excitation wavelength is fixed by changing the potential, a wider resonance enhancement phenomenon can be observed [8, 9].
(2) The electromagnetic field mechanism should be non-selective for all molecules adsorbed onto a particular surface, that is, should have the same enhancement contribution for such molecules. However, under the same experimental conditions, the enhancement factors of $N_2$ and CO molecules with almost the same Raman scattering cross-section are 200 times different, which cannot be explained by the electromagnetic field enhancement mechanism [10]. Similarly, 4-mercaptobenzoic acid (4-MBA), 4-mercaptopyridine (4-MPy), and 4-aminothiophenol (4-ATP) three molecules with comparable Raman scattering cross-section also exhibit different SERS enhancements on semiconductors $TiO_2$ [11] and ZnO [12].
(3) In the absence of surface plasmon resonance effect, SERS enhancement can be observed on the surface of some semiconductors (such as $TiO_2$, ZnO, ZnS, CdS, InAs, and CdSe), and the enhancement factor can reach at least $10^3$ order of magnitude and above [13]. And, some non-totally symmetric vibration modes of molecules ($b_1$ and/or $b_2$) can be selectively enhanced when compared with those totally symmetric vibration modes ($a_1$), while they are very weak in the normal Raman spectrum.
(4) Not all molecules adsorbed on the substrate can generate SERS enhancement, and only those molecules adsorbed on some active sites of the substrate surface can exhibit strong SERS enhancement [14–16]. Many experiments have shown that SERS enhancement is closely related to chemisorption. For example, when the concentration of pyridine molecule is low, it is mainly physically adsorbed onto the substrate; when the coverage reaches to a certain degree, pyridine begins to be chemically adsorbed to the substrate through their lone pair electrons on the N atom, and then the SERS enhancement of molecules can be observed [17, 18].

The aforementioned phenomena and observations cannot be explained by the mechanism of electromagnetic field enhancement, which indicates that there are other enhancement mechanisms (namely, chemical enhancement mechanism) involving in SERS [1, 3, 19].

## 3.2 The Description of Chemical Mechanism

Chemical enhancement mainly includes three types of mechanisms, as shown in Fig. 3.1.

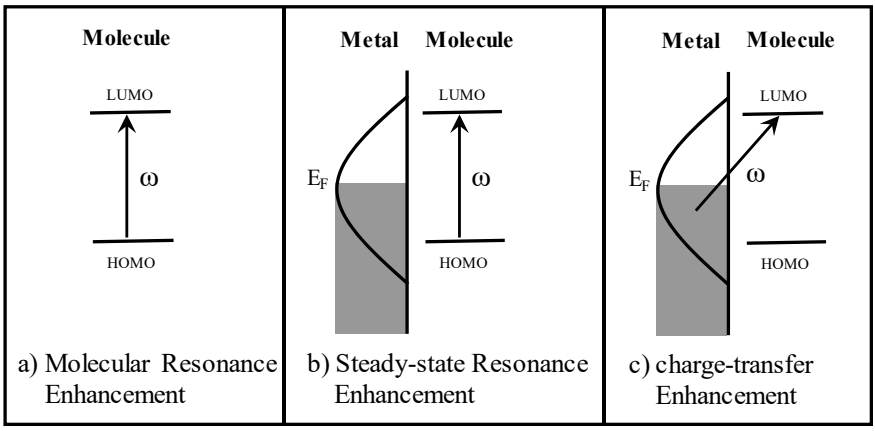



**Fig. 3.1** Illustration of the different types of chemical mechanism in SERS

(a) Enhancement derived from resonance of the molecule itself with the excitation wavelength (molecular resonance enhancement). It needs an energy matching of the excitation light with the energy level spacing between the highest occupied molecular orbital (HOMO) and the lowest unoccupied molecular orbital (LUMO) of the adsorbed molecule.

(b) Enhancement derived from resonance of the molecule adsorbed on the specific substrate with the excitation wavelength (steady-state resonance enhancement). In addition to the energy-matching requirement, the chemical interaction between the molecule and the substrate is another need that must be met. In this resonance enhancement, some researchers have also found that some adsorbed molecules can form a new surface complex with the substrate surface atoms [20]. As a new molecular system, the surface complexes have different HOMO and LUMO and can also achieve resonance under visible light excitation for SERS enhancement.

(c) Enhancement derived from charge-transfer resonance between the molecule and the substrate (charge-transfer enhancement, CT). The specific excitation light can achieve a substrate-to-molecule or molecule-to-substrate photo-induced charge transfer (PICT), which is similar to resonant Raman process.

Among them, the CT enhancement model between substrate and adsorbent is the most eye-catching, and therefore, it will be mainly discussed next. The formation of new chemical bond or the chemical interaction between the molecule and the substrate is the starting point and basis of CT mechanism. The chemical interaction (or bonding) has a direct effect on the electron density distribution of molecule, which can increase the polarizability of adsorbed molecule for SERS enhancement [21]. The CT process is slightly different for different substrates (metal substrate and semiconductor substrate). For metal–molecule system, the CT process (taking the metal-to-molecule CT as an example) is as follows:

(1) Electrons near the Fermi energy level ($E_F$) of metal are excited to a higher orbital than the $E_F$ level by absorbing the energy of the excited photon, and holes are produced in the orbital below the $E_F$ level, so that the electron–hole pair is formed on the metal side.
(2) Electrons that have absorbed the photon energy are transferred to the LUMO of the adsorbed molecule.
(3) Electrons transitioned to the LUMO of the adsorbed molecule transition back to the metal again. In this process, some vibrational energy levels of the molecule have changed, that is, the molecule is in a vibrationally excited state after the electron transition back to the metal.
(4) The returned electrons combine with the holes inside the metal, and at the same time, Raman scattering photons are released.

For semiconductor–molecule system, the CT process is slightly different from the metal–molecular system, which is mainly reflected in the first two processes. In semiconductor–molecule system (taking the semiconductor-to-molecule CT as an example), the electrons located at the valence band (VB) of semiconductor are initially excited to the defect/surface state energy level ($E_{SS}$) or conduction band (CB) energy level of semiconductor by the incident light with a certain energy, and the excited electrons can be trapped by defect states or CB. Then, the photoexcited electrons are transferred to the LUMO of the adsorbed molecule, followed by a back transition to the defect states and VB or CB and VB. In particular, for wide-bandgap semiconductors with abundant surface defects, electrons in VB tend to be excited to their surface state energy levels rather than their CBs for following semiconductor-to-molecule CT due to the energy-matching principle. Yang et al. [11] observed SERS effect of 4-MBA molecule adsorbed on anatase $TiO_2$ nanoparticles and proposed the $TiO_2$-to-molecule CT mechanism (as shown in Fig. 3.2), which has a certain universality to the wide-bandgap semiconductor-to-molecule CT mechanism.

In the above CT processes, the first two processes play a decisive role for SERS enhancement. First of all, it relates to whether the energy of the excited photon can match with the energy required for the electron transition. It can be seen that

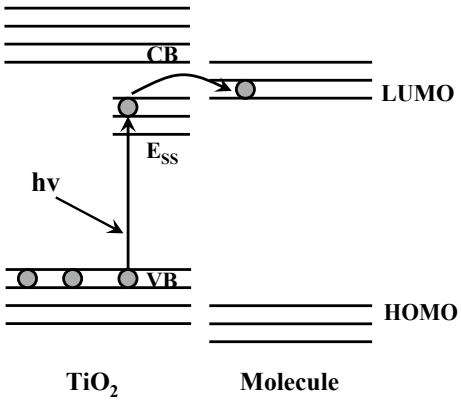



**Fig. 3.2** Mode of charge transfer between the adsorbed molecule and $TiO_2$ for SERS. From Ref. [11]

effective CT can be achieved by changing the wavelength of the excited light, which is often called as the excited light tuning effect. Secondly, the chemical interaction between the molecule and the substrate determines the probability of electron transfer to the LUMO orbital of the adsorbed molecule and the relaxation time (stability time) of the electron on the adsorbed molecule. This requires that the metal surface should have a certain degree of atomic roughness or the semiconductor surface should have a certain degree of surface defect (or active site), so that an effective surface interaction (bonding) can be formed between the molecule and the substrate. At the same time, whether the substrate surface has a suitable roughness (or surface defect) is also the main factor that determines whether the returned electrons can successfully recombine with the holes.

In the above description of the CT mechanism, the direction of CT is the substrate-to-molecule transition, but in fact, there is also the opposite direction, that is, the electron transition from the molecule to the substrate.

## 3.3 The Theory of Chemical Mechanism

The theory for chemical mechanism has been studied in several ways [1–3]. Adrian [1] investigated the metal-to-molecule CT by using a semiempirical Wolfsberg–Helmholtz method. Calculations for the system of ethylene adsorbed on silver, with CT excitation of an electron from the metal to the ethylene, showed that CT Raman enhancements of the order of 10 to 1000 are possible if the CT band is partially resonant with the exciting radiation. Symmetric vibrations usually will be enhanced substantially more than nonsymmetric ones by this mechanism because the vibrational coupling is primarily Franck–Condon rather than Herzberg–Teller. The presence of overtone and combination bands in charge-transfer-enhanced Raman spectra is also possible. The theory of Adrian is unsuccessful in explaining why overtones are observed only weakly and why totally symmetric mode and non-totally symmetric mode for some metal–molecule systems are equally enhanced.

Shortly thereafter, Lombardi et al. [3] presented a theory of CT Raman enhancement based on the Herzberg–Teller coupling mechanism following Albrecht [22]. The theory of Lombardi includes both molecule-to-metal and metal-to-molecule CTs, which is relatively comprehensive CT mechanism in SERS since it can explain correctly the dependence of the voltage maximum on the exciting wavelength, the absence of overtones, and the presence of non-totally symmetric modes. The intensity of a Raman transition can be obtained from the polarizability tensor by the expression:

$$I = \left[8\pi\left(\omega \pm \omega_{FI}\right)^4 I_L / 9c^4\right] \sum \left|\alpha_{\sigma\rho}\right|^2.$$

Lombardi et al. obtained an expression of polarizability tensor $\alpha_{\sigma\rho}$:

$$\alpha_{\sigma\rho} = A + B + C.$$

Term $A$ (includes terms $A_f$ and $A_k$) is the resonance Raman term in the normal Raman theory, which contributes solely to the totally symmetric modes and is negligible in contribution to SERS effect. Terms $B$ and $C$ can be expressed as:

$$B = -\left(2/\hbar^2\right) \sum_{K \neq I} \sum_{M<K} \frac{\left[\mu_{KI}^{\sigma} \mu_{MI}^{\rho} + \mu_{KI}^{\rho} \mu_{MI}^{\sigma}\right]\left(\omega_{KI}\omega_{MI} + \omega^2\right) h_{KM} \langle i|Q|f\rangle}{\left(\omega_{KI}^2 - \omega^2\right)\left(\omega_{MI}^2 - \omega^2\right)},$$

$$C = -\left(2/\hbar^2\right) \sum_{K \neq I} \sum_{M>I} \frac{\left[\mu_{KM}^{\sigma} \mu_{KI}^{\rho} + \mu_{KM}^{\rho} \mu_{KI}^{\sigma}\right]\left(\omega_{KI}\omega_{KM} + \omega^2\right) h_{IM} \langle i|Q|f\rangle}{\left(\omega_{KI}^2 - \omega^2\right)\left(\omega_{KM}^2 - \omega^2\right)}.$$

Term $B$ represents the molecule-to-metal (i.e., from the molecular ground state $I$ to one of the unfilled metal levels $M$) CT. The CT transition $\mu_{MI}$ can borrow intensity from the allowed molecular transition $\mu_{KI}$ through the Herzberg–Teller coupling term $h_{KM}$ (as shown in Fig. 3.3a). Term $h_{KM}$ represents coupling of the metal to excited molecular states through some vibrational modes. Term $C$ represents the metal-to-molecule (i.e., from one of the filled metal levels $M$ to the excited state $K$) CT. The CT transition $\mu_{KM}$ can borrow intensity from the allowed molecular transition $\mu_{KI}$ through the Herzberg–Teller coupling term $h_{IM}$ (as shown in Fig. 3.3b). Term $h_{IM}$ represents coupling of the metal to the ground molecular level through some vibrational modes.

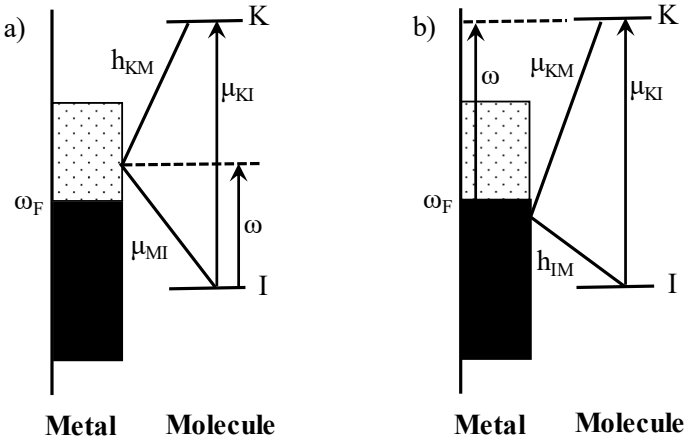



**Fig. 3.3** **a** Scheme for molecule-to-metal charge-transfer transition between the ground molecular state $I$ and the unfilled levels of the metal $M$. The transition borrows intensity from the allowed molecular transition by means of vibronic coupling between the metal levels and the excited molecular level through the matrix element $h_{KM}$. **b** The scheme for metal-to-molecule charge-transfer transition between the filled levels of the metal $M$ and the excited molecular state $K$. The transition borrows intensity from the allowed molecular transition by means of vibronic coupling between the metal levels and the ground molecular state through the matrix element $h_{IM}$. From Ref. [3]

For the semiconductor–molecule system, Lombardi et al. [13] also presented a theory of CT Raman enhancement based on the Herzberg–Teller coupling mechanism similar to the above metal–molecule system. Lombardi et al. employed a similar derivation, replacing the metal energy levels with those of the semiconductor. In those equations, the Fermi level is replaced by the conduction band edge in the molecule-to-semiconductor CT transition and the Fermi level is replaced by the valence band edge in the semiconductor-to-molecule CT transition, because the maximum SERS enhancement in semiconductors occurs at the edges of valence band (VB) or conduction band (CB) rather than at the Fermi level. Accordingly, an expression of polarizability tensor $\alpha_{\sigma\rho}$ similar to the metal–molecule system with the Albrecht *A*, *B*, and *C* terms was obtained for explaining CT enhancement in semiconductor. One small difference compared to the metal–molecular system is that the CT transitions in the semiconductor–molecule system can also borrow intensity from the exciton transition in semiconductor besides from the molecular transition. Similarly, term *B* in the $\alpha_{\sigma\rho}$ expression represents the molecule-to-semiconductor (i.e., from the molecule HOMO to the conduction band edge of semiconductor) CT. The CT transition $\mu_{\mathrm{CT}}$ can borrow intensity either from the exciton transition in semiconductor ($\mu_{\mathrm{ex}}$) or from the molecular transition ($\mu_{\mathrm{mol}}$) through the Herzberg–Teller coupling term $h_{VI}$ or $h_{CK}$ (as shown in Fig. 3.4). Terms $h_{VI}$ and $h_{CK}$ represent coupling of the semiconductor VB with the ground molecular level HOMO and coupling of the semiconductor CB with the excited molecular state LUMO through some vibrational modes, respectively. Term *C* represents the semiconductor-to-molecule (i.e., from the valence band edge of semiconductor to the molecule LUMO) CT. In this case, the CT transition $\mu_{\mathrm{CT}}$ can borrow intensity either from the molecular transition ($\mu_{\mathrm{mol}}$) or from the exciton transition in semiconductor ($\mu_{\mathrm{ex}}$) through the Herzberg–Teller coupling term $h_{VI}$ or $h_{CK}$ (as shown in Fig. 3.5). Terms $h_{VI}$ and $h_{CK}$ also represent coupling of the semiconductor VB with the ground molecular level HOMO and coupling of the semiconductor CB with the excited molecular state LUMO through some vibrational modes, respectively. Moreover, it should be mentioned that for the wide-bandgap semiconductor–molecule system, the electron transition between semiconductor and molecule tends to be the CT from the molecule HOMO to the surface state energy level of semiconductor or from the semiconductor VB via the surface state energy level to the molecule LUMO. The corresponding Herzberg–Teller coupling term *h* represents coupling of the surface state energy level or VB of semiconductor with the ground molecular level HOMO or coupling of the surface state energy level of semiconductor with the excited molecular state LUMO.

## 3.4 The Selection Rules of Chemical Mechanism

The expressions of Herzberg–Teller selection rules are as follows [7, 13]:

$$\Gamma(Q_k) = \Gamma(\mu_{\mathrm{CT}}) \times \Gamma(\mu_{\mathrm{mol}}),$$

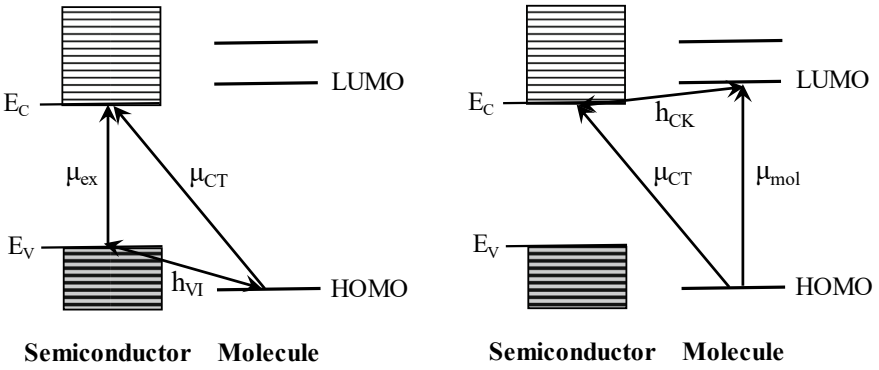



**Fig. 3.4** Coupling scheme for the B-term. Left: The charge-transfer resonance is coupled to the exciton resonance through the Herzberg–Teller constant ($h_{VI}$). Right: The charge-transfer resonance is coupled to the molecular resonance through the Herzberg–Teller constant ($h_{CK}$). From Ref. [13]

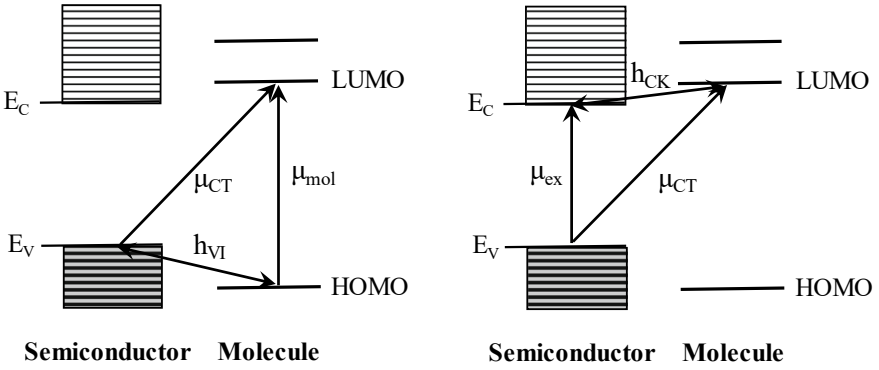



**Fig. 3.5** Coupling scheme for the C-term. Left: The charge-transfer resonance is coupled to the molecular resonance through the Herzberg–Teller constant ($h_{VI}$). Right: The charge-transfer resonance is coupled to the exciton resonance through the Herzberg–Teller constant ($h_{CK}$). From Ref. [13]

$$\Gamma(Q_k) = \Gamma(\mu_{\mathrm{CT}}) \times \Gamma(\mu_{\mathrm{ex}}).$$

Here, $\Gamma(Q_k)$ is the irreducible representation of the allowed vibrational mode ($Q_k$). $\Gamma(\mu_{\mathrm{CT}})$ is the irreducible representation of CT transition, while $\Gamma(\mu_{\mathrm{mol}})$ and $\Gamma(\mu_{\mathrm{ex}})$ are the irreducible representations of molecular and exciton transition from which intensity is borrowed. The first expression applies to both the metal–molecule system and the semiconductor–molecule system, while the second expression only applies to the semiconductor–molecule system.

The selection rules can be used to precisely predict the relative intensity of Raman bands in SERS spectrum. For example, the $b_1$ and $b_2$ vibrational modes of 4-MPy

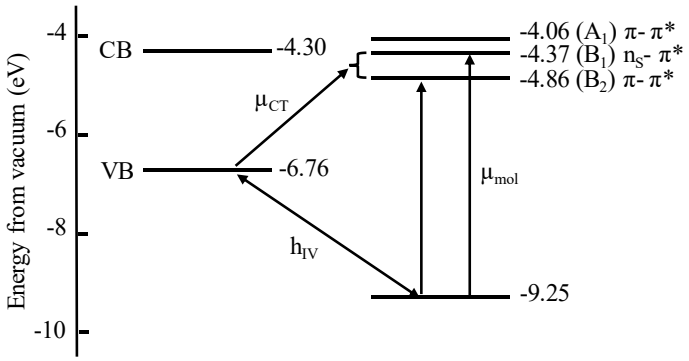



**Fig. 3.6** Energy level diagram for the 4-MPy-ZnSe system. From Ref. [13]

molecule adsorbed onto ZnSe nanoparticles can be obviously enhanced, while they are rather weak in the normal Raman spectrum [13, 23]. As shown in Fig. 3.6, in the 4-MPy-ZnSe system, the CT takes place between the VB edge of ZnSe and the unoccupied orbitals of 4-MPy. Due to the unoccupied $\pi^*$ orbitals of symmetry $B_1$, $B_2$, and $A_1$ in 4-MPy molecule, transitions from the occupied nonbonding orbital on sulfur ($n_S$) and the occupied $\pi$ orbitals in pyridine ring to these $\pi^*$ orbitals produce singlet excited states of $^1B_2$ ($\pi$–$\pi^*$), $^1B_1$($n_S$–$\pi^*$) and $^1A_1$ ($\pi$–$\pi^*$). Therefore, $\Gamma(\mu_{\text{mol}}) = B_1$ and $B_2$ for the two lowest lying states. $\Gamma(\mu_{\text{CT}}) = A_1$ because 4-MPy is vertically bonded to the surface of ZnSe. According to the selection rules, $\Gamma(\mu_{\text{mol}}) \times \Gamma(\mu_{\text{CT}}) = b_1$ and $b_2$. So, the $b_1$ and $b_2$ modes of 4-MPy adsorbed on ZnSe can be selectively enhanced in SERS spectrum via CT contribution.

The selective enhancement of Raman bands in SERS spectrum is highly dependent on the excitation frequency that modulates the CT process. For example, SERS spectra of 3,4,9,10-perylene tetracarboxylic acid (PTCA) adsorbed on Ag nanoparticle (NP) surface via weak Ag–O bonds show an obvious wavelength-dependent feature [24]. As shown in Fig. 3.7, when the laser energy is lowered to 785 nm, the $b_1$ and $b_2$ modes of PTCA on Ag NPs can be selectively enhanced. The PTCA molecule is attached to the surface of Ag through a weak Ag–O bond with several angles from the vertical direction of Ag surface, which leads to the conclusion that the $D_{2h}$ point group should be lowered to $C_{2v}$ with no inversion symmetry element. According to the energy level diagram (Fig. 3.7), the CT occurs from the Fermi level of Ag NPs to the LUMO level of PTCA. The CT dipole moment operator is associated with $A_1$ ($\theta = 0°$) and the vertical component $A_2$ ($\theta > 0°$). For the $C_{2v}$ point group, only one type of transition ($\pi$–$\pi^*$ transition) between the occupied and unoccupied molecular orbitals is allowed for PTCA. The lowest transition corresponds to the singlet state with $B_1$ symmetry. According to the Herzberg–Teller selection rules, the Raman bands belonging to $b_1$ ($A_1 \times B_1$) and $b_2$ ($A_2 \times B_1$) symmetry are expected to be selectively enhanced via the CT contribution. As expected, the $b_1$ and $b_2$ vibrational modes of PTCA initiate the dominance of the SERS spectrum, owing to the CT resonance (785 nm excitation).

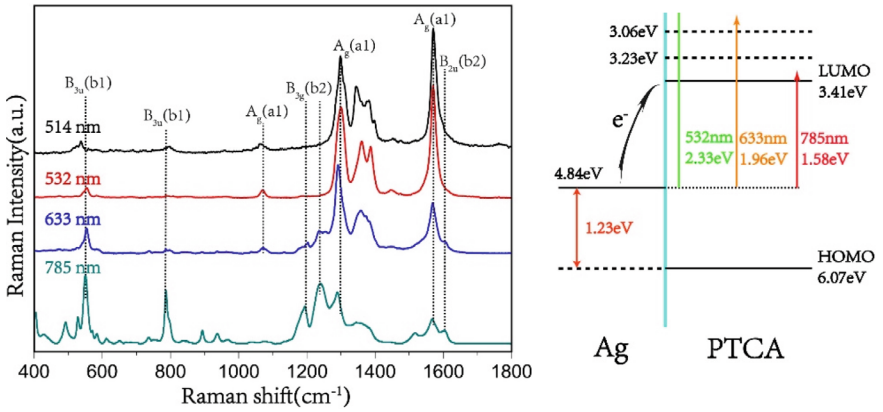



**Fig. 3.7** Wavelength-dependent SERS spectra of Ag/PTCA and the schematic illustration of CT mechanism in Ag/PTCA system. From Ref. [24]

## 3.5 The Difference Between Chemical Mechanism and Electromagnetic Mechanism

The chemical enhancement is based on the existence of chemical interaction (bonding) between molecule and substrate. CT is only generated between the first layer of adsorbed molecules and the substrate surface, so it does not enhance the adsorbed molecules in a long range like the electromagnetic field enhancement effect (the electromagnetic enhancement has a long-range effect), that is, the chemical enhancement has a short-range effect.

Compared with the electromagnetic enhancement, the chemical enhancement has the potentials of ultrasensitive detection not only in qualitative but also in quantitative terms. The differences between the two enhancement mechanisms have been reported by Jiang et al. [25]. In their work, the typical semiconductor $TiO_2$ nanoparticles and noble-metal Ag colloid were served as two representative substrates, and 4-MBA, a non-resonant molecule, was used as a SERS probe. Under this case, SERS enhancements of 4-MBA on $TiO_2$ mainly derive from the contribution of CT mechanism, while those on noble-metal Ag colloid derive from the contribution of electromagnetic mechanism. The 4-MBA molecules on two substrates exhibit the obvious different spectral behaviors. On $TiO_2$ substrate (Fig. 3.8), the peak intensity ratio of 4-MBA at 1592 and 1075 $cm^{-1}$ decreases gradually with the decrease in the concentration of probe molecule. However, the intensity ratio of two peaks assigned to aromatic ring characteristic vibrations (1584 and 1075 $cm^{-1}$) on the Ag substrate is almost invariable (Fig. 3.9). This obvious difference in the spectral behavior of 4-MBA on two substrates must be resulted from the difference of substrates (i.e., the difference of enhancement mechanisms in two substrates). It is known that the probe molecules are usually adsorbed on two substrates by a way of verticality under the high concentration, while they are more trend to be adsorbed onto the substrates

by a parallel way under the low concentration. That is, the change in the adsorption orientation of 4-MBA on $TiO_2$ can be effectively distinguished with the change in the concentration of the adsorbed molecule, compared with that on the noble-metal Ag substrate. This can be explained through the essential difference between CT mechanism and electromagnetic mechanism. The SERS enhancement on $TiO_2$ contributed by CT mechanism is derived from chemical adsorption (bonding) between molecule and substrate. The CT SERS enhancement not only depends on the behavior of the substrate but also depends on the behavior of the adsorbed molecule due to the chemical interaction and CT between substrate and molecule, which more tends to be selective for the adsorbed molecules and their SERS enhancements, and thus, it is more sensitive to the change in the adsorption orientation of probe molecule. However, the electromagnetic mechanism does not depend on the specific chemical adsorption (bonding) between molecule and substrate and is only derived from the contribution of electromagnetic field of substrate (i.e., the electromagnetic enhancement more depends on the behavior of the substrate, rather than the behavior of the adsorbed molecule), which consequently exerts a same influence on those molecules that lie in the electromagnetic field region. The electromagnetic mechanism is insensitive to the change in the adsorption orientation of the probe molecule (i.e., it more tends to be non-selective for the adsorbed molecules and their SERS enhancements).

In addition to accurately identifying spectral behavior, the CT mechanism also exhibits an ultrasensitive detection potential at low concentrations. It can be seen from Fig. 3.10a that the 4-MBA on the 3%Ni-doped $TiO_2$ (3%Ni–$TiO_2$) substrate shows a higher SERS enhancement, which is about three times greater than that on the pure $TiO_2$ substrate. However, the minimum detectable concentration of 4-MBA on 3%Ni–$TiO_2$ can reach to $1 \times 10^{-10}$ mol/L (Fig. 3.10b), which even decreases by four orders of magnitude compared to that ($1 \times 10^{-6}$ mol/L) on the pure $TiO_2$ substrate (Fig. 3.8a). But the results are quite different for the noble-metal substrate systems. As shown in Fig. 3.11, the 4-MBA on the KI modified Ag (KI/Ag) substrate

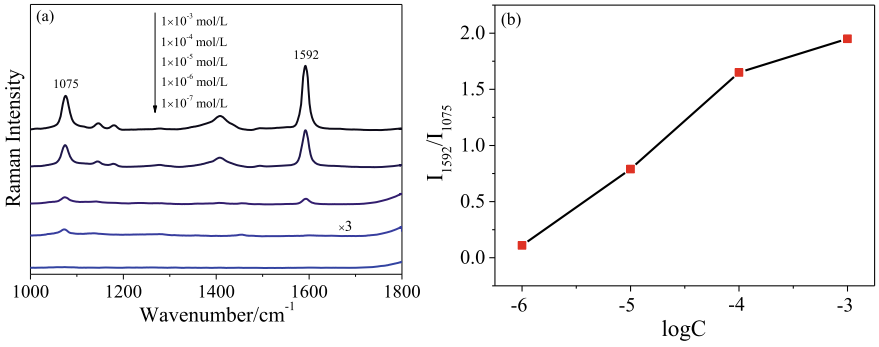



**Fig. 3.8** **a** SERS spectra of 4-MBA adsorbed on $TiO_2$ substrate from different concentrations of 4-MBA ethanol solution; **b** the plot of the intensity ratio of peaks at 1592 and 1075 $cm^{-1}$ versus the logarithm of 4-MBA concentration. From Ref. [25]

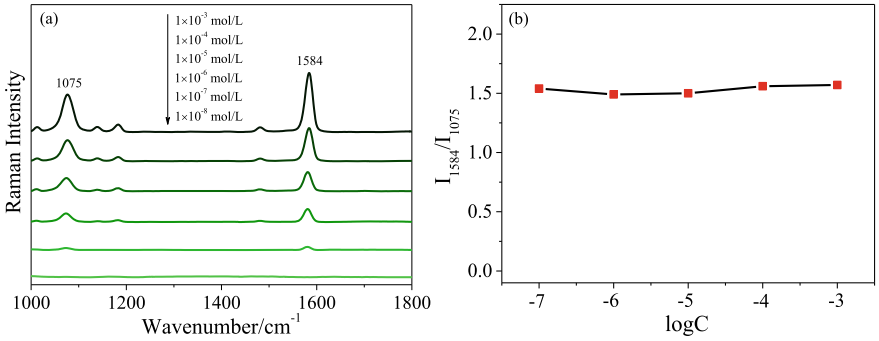



**Fig. 3.9** **a** SERS spectra of 4-MBA adsorbed on Ag NPs colloid substrate from different concentrations of 4-MBA ethanol solution; **b** the plot of the intensity ratio of peaks at 1584 and 1075 $cm^{-1}$ versus the logarithm of 4-MBA concentration. From Ref. [25]

shows the higher SERS enhancement, even ten times greater than that on the unmodified Ag substrate. However, the minimum detectable concentration of 4-MBA on KI/Ag ($1 \times 10^{-9}$ mol/L) only decreases by two orders of magnitude compared to that on the unmodified Ag substrate ($1 \times 10^{-7}$ mol/L, Fig. 3.9a). On two substrates, these distinct differences must also be derived from the difference between their enhancement mechanisms. For the SERS enhancement contributed by CT mechanism, as long as the molecules are bonded to the substrate and an effective CT is achieved, Raman signals of molecules can be enhanced by the CT. That is, SERS enhancement contributed by CT does not completely depend on the concentration of probe molecule. Even at the lower concentration, the probe molecule can also be effectively identified due to the high identifiability and the validity of the chemical adsorption and CT. So, the CT mechanism exhibits an ultrasensitive detection potential at low concentrations. This shows that the SERS enhancement by CT more depends on the efficiency of CT rather than the adsorption quantity of probe molecule because the physical adsorption may be invalid for CT enhancement, while the electromagnetic enhancement more depends on the number of molecules entering into the electromagnetic field region rather than the adsorption mode of probe molecule on substrate because the physical adsorption and the chemical adsorption are all valid for electromagnetic enhancement.

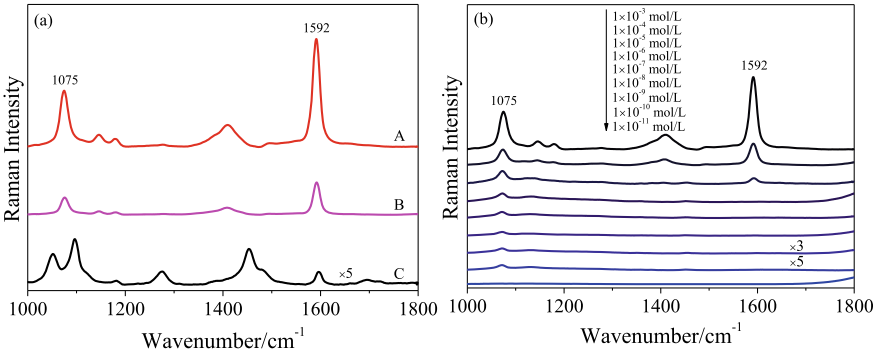



**Fig. 3.10** **a** SERS spectra of 4-MBA adsorbed on 3%Ni–$TiO_2$ substrate **A** and $TiO_2$ substrate **B** from $1 \times 10^{-3}$ mol/L ethanol solution and the normal Raman spectrum of 4-MBA in 0.1 mol/L ethanol solution **C**; **b** SERS spectra of 4-MBA adsorbed on 3%Ni–$TiO_2$ substrate from different concentrations of 4-MBA ethanol solution. From Ref. [25]

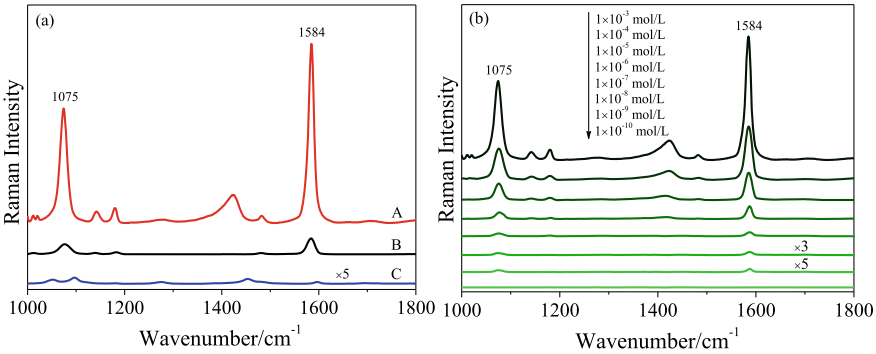



**Fig. 3.11** **a** SERS spectra of 4-MBA adsorbed on KI/Ag colloid substrate **A** and Ag colloid substrate **B** from $1 \times 10^{-3}$ mol/L ethanol solution and the normal Raman spectrum of 4-MBA in 0.1 mol/L ethanol solution **C**; **b** SERS spectra of 4-MBA adsorbed on KI/Ag colloid substrate from different concentrations of 4-MBA ethanol solution. From Ref. [25]

## References

1. F.J. Adrian, Charge transfer effects in surface-enhanced Raman scattering. J. Chern. Phys. **77**, 5302-5314 (1982)
2. A. Otto, The 'chemical' (electronic) contribution to surface-enhanced Raman scattering. J. Raman Spectrosc. **36**, 497-509 (2005)
3. J.R. Lombardi, R.L. Birke, T. Lu, J. Xu, Charge-transfer theory of surface enhanced Raman spectroscopy: Herzberg-Teller contributions. J. Chem. Phys. **84**, 4174-4180 (1986)
4. K. Kneipp, Surface-enhanced Raman scattering. Phys. Today **60**, 40-46 (2007)
5. Y.S. Yamamoto, T. Itoh, Why and How Do the Shapes of Surface-Enhanced Raman Scattering Spectra Change? Recent Progress from Mechanistic Studies. J. Raman Spectrosc. **47**, 78-88 (2016)

6. J.R. Lombardi, R.L. Birke, A Unified View of Surface-Enhanced Raman Scattering. Acc. Chem. Res. **42**, 734-742 (2009)
7. T. Itoh, M. Procházka, Z.C. Dong, W. Ji, Y.S. Yamamoto, Y. Zhang, Y. Ozaki, Toward a New Era of SERS and TERS at the Nanometer Scale: From Fundamentals to Innovative Applications. Chem. Rev. **123**, 1552-1634 (2023)
8. M.G. Albrecht, J.A. Creighton, Anomalously intense Raman spectra of pyridine at a silver electrode. J. Am. Chem. Soc. **99**, 5215-5217 (1977)
9. D.L. Jeanmaire, R.P. Van Duyne, Surface Raman spectroelectro-chemistry. 1. heterocyclic aromatic and aliphatic-amines adsorbed on anodized silver electrode. J. Electroanal. Chem. **84**, 1–20 (1977)
10. R.K. Chang, T.E. Furtak, eds., Surface-enhanced Raman scattering. (PlenumPress, 1982)
11. L.B. Yang, X. Jiang, W.D. Ruan, B. Zhao, W.Q. Xu, J.R. Lombardi, Observation of Enhanced Raman Scattering for Molecules Adsorbed on $TiO_2$ nanoparticles: Charge-Transfer Contribution. J. Phys. Chem. C **112**, 20095-20098 (2008)
12. X.T. Wang, W.X. Shi, Z. Jin, W.F. Huang, J. Lin, G.S. Ma, S.Z. Li, L. Guo, Remarkable SERS Activity Observed from Amorphous ZnO Nanocages. Angew. Chem. **129**, 9983-9987 (2017)
13. J.R. Lombardi, R.L. Birke, Theory of Surface-Enhanced Raman Scattering in Semiconductors. J. Phys. Chem. C **118**, 11120-11130 (2014)
14. H. Seki, M.R. Philpott, Surface enhanced Raman scattering by pyridine on silver island films in an ultrahigh vacuum. J. Chem. Phys. **73**, 5376-5379 (1980)
15. T.E. Furtak, D. Roy, Nature of the active site in surface-enhanced Raman scattering. Phys. Rev. Lett. **50**, 1301-1304 (1983)
16. C. Pettkofer, J. Eickmans, U. Erturk, et al., On the nature of “sers active sites”. Surf. Sci. **151**, 9-36 (1985)
17. E. Burstein, C.Y. Chen, S. Lundquist, In light scattering in solids. (Plenum, 1979)
18. J.E. Demuth, K. Christmann, P.N. Sanda, The vibrations and structure of pyridine chemisorbed on Ag (111): the occurrence of a compressional phase transformation. Chem. Phys. Lett. **76**, 201-206 (1980)
19. M. Moskovits, Surface-enhanced spectroscopy. Rev. Mod. Phys. **57**, 783-828 (1985)
20. S.Y. Ding, D.Y. Wu, Z.L. Yang, B. Ren, X. Xu, Z.Q. Tian, Some Progresses in Mechanistic Studies on Surface-Enhanced Raman Scattering. Chem. J. Chinese U. **29**, 2569-2581 (2008)
21. L. Jensen, C.M. Aikens, G.C. Schatzc, Electronic structure methods for studying surface-enhanced Raman scattering. Chem. Soc. Rev. **37**, 1061-1073 (2008)
22. A.C. Albrecht, On the Theory of Raman Intensities. J. Chem. Phys. **34**, 1476-1484 (1961)
23. S.K. Islam, M. Tamargo, R. Moug, J.R. Lombardi, Surface-Enhanced Raman Scattering on a Chemically Etched ZnSe Surface. J. Phys. Chem. C **117**, 23372-23377 (2013)
24. H. Ma, Y.F. Chen, H. Wang, X.L. Wang, X.L. Zhang, X.X. Han, C.Y. He, B. Zhao, Charge-Transfer Effect on Surface-Enhanced Raman Spectroscopy in Ag/PTCA: Herzberg-Teller Selection Rules. J. Phys. Chem. C **121**, 25788-25794 (2017)
25. X. Jiang, Y.L. Chen, J. Du, X.L. Li, Y. Shen, M. Yang, X.X. Han, L.B. Yang, B. Zhao, Comparative study of semiconductor $TiO_2$ and noble metal Ag substrates: The differences between chemical enhancement and electromagnetic enhancement in SERS. J. Raman Spectrosc. **49**, 1257-1264 (2018)

# Chapter 4
# Semiconductor-Enhanced Raman Scattering: Enhancement Mechanism and Substrate Design




**Junbo Li, Bo Jiang, and Wei Ji**

**Abstract** Semiconductor-enhanced Raman scattering, also known as semiconductor SERS, represents a new frontier in the field of SERS, which will be able to further broaden the possibilities for SERS applications. In the recent years, semiconductor SERS has achieved significant advancements in mechanism studies. Various charge transfer models for chemical mechanism have been elucidated, and new enhancement mechanism, such as exciton resonance, Mie resonance, plasmonic resonance, multiple scattering resonance, and their synergistic effect, is gradually being revealed. This chapter is devoted to the development history and unified theory in enhancement mechanism (see Chap. 3 for detailed introduction in enhancement mechanism), and specially focuses on the design principles of SERS-active semiconductors. Notably, we will introduce design principles with some examples, and the enhancement mechanism behind these principles also will be discussed in details.

**Keywords** Charge transfer · Mie resonance · Plasmon resonance · Synergistic effect · Semiconductor SERS

## 4.1 Brief Development History

SERS requires the use of a suitable substrate with nanoscale roughness to achieve the enhancement of Raman signal of surface adsorbed molecule. Since the discovery of the SERS in 1974, coinage metal materials (Au, Ag, and Cu) are the first choice to realize a substantial SERS effect because of their strong electromagnetic contribution due to the localized surface plasmon resonance [1]. Except the attenuated total-reflection (ATR) and interference-enhanced Raman scattering, the experimental observation of SERS on semiconducting materials can be traced back to the 1980s

J. Li · B. Jiang · W. Ji (✉)
College of Chemistry, Chemical Engineering and Resource Utilization, Northeast Forestry University, Harbin, China
e-mail: jiwei@nefu.edu.cn

© The Author(s), under exclusive license to Springer Nature Singapore Pte Ltd. 2024

M. Procházka et al. (eds.), *Surface- and Tip-Enhanced Raman Scattering Spectroscopy*,
https://doi.org/10.1007/978-981-97-5818-0_4

[2–5]. For instance, the first application of the charge transfer (CT) theory to semiconductor materials was in the study by Yamada et al. as early as 1983 [4]. They observed SERS from pyridine adsorbed on the surface of single crystal NiO (110). The enhancement was suggested to be from the CT transition from the crystal substrate to pyridine. However, the enhancement factor is just to be 10 orders of magnitude. Hayashi et al. first observed the enhanced Raman scattering originated from electromagnetic mechanism for copper phthalocyanine molecules on GaP NPs in 1988 [2]. The enhancement factor was estimated to be 700. The appearance of semiconductor SERS is extremely important for a better understanding of SERS phenomenon itself, but the relatively weak enhancement performance did not mean much to practical application. The development of semiconductor SERS has been stagnant for a long time in the 1990s.

Renewed interest in semiconductor SERS has been stimulated by the requirement of in situ characterization techniques in semiconductor materials involved fields [6]. Since 2000, growing semiconductor materials have been reported with SERS activity, further prompting the development of semiconductor-enhanced Raman scattering technique [7–20]. For example, Zhao cooperated with Lombardi et al. demonstrated a series of SERS-active semiconductor materials, including metal oxides, metal tellurides, metal sulfides, Wang et al. [7–12]. They found that the defect state in semiconductor materials introduced by self-doping and transition metal doping can significantly increase the sensitivity of semiconductor SERS [14–19]. Based on these works, they proposed a clear CT model to explain the enhanced Raman on semiconductor materials. Another representative work was reported by Zhang et al., in which Raman enhancement was observed on graphene surface [13]. Graphene is an ideal semiconductor substrate to further verify the semiconductor-enhanced Raman scattering effect and investigate the CT mechanism due to its flat surface and strong chemical interaction with organic molecules [21–27]. Following these works, researchers proposed more methods to prepare and optimize the semiconductor substrates.

In Table 4.1, we summarized the representative SERS-active semiconductor materials and possible mechanism reported in the last five years. Semiconductor-enhanced Raman scattering effect breaks the long limitation of SERS that only metals can exhibit huge Raman enhancement, and brings a new understanding of the intrinsic nature SERS. And more importantly, semiconductor SERS injects new vitality into traditional SERS and may lead to promising functions based on their unique optical, chemical, electrical, and catalytic properties.

## 4.2 Advantages of Semiconductor SERS

SERS-active semiconductor materials have been thoroughly reviewed elsewhere, and thus they are excluded from further discussion in this chapter [6, 46–48]. Instead, this chapter on the mechanism and applications of SERS-active semiconductor materials. Before starting, the main advantages of semiconductor SERS compared with metal-based SERS may be summarized as follows:

**Table 4.1** Summary of the representative SERS-active semiconductor materials in the last five years (2018–2023)

| Semiconductor materials | Adsorbate molecule | Enhancement factor | Possible mechanism | References |
|---|---|---|---|---|
| $Nb_2C$ and $Ta_2C$ MXenes | 4-MBA/MB/MV | $3 \times 10^6$ | CT/EM | [28] |
| $MnFeCuAgInPS_3$ | R6G and CV | $1.4 \times 10^6$ | CT | [29] |
| $WO_{3-x}/WO_3$ | R6G and MB | $1.36 \times 10^8$ | CT/EM | [30] |
| $WO_3$ | MB | $10^2$ | CT | [31] |
| $MnPS_{3-x}Se_x$ | R6G | $10^{14}$ | CT | [32] |
| $PtSe_2$ and $ReS_2$ | R6G | $1.95 \times 10^5$ | CT | [33] |
| $Cu_2Te$ | R6G | $1.8 \times 10^9$ | CT/EM | [34] |
| 1T'-W(Mo)$Te_2$ | R6G | $1.6 \times 10^8$ | EM | [35] |
| Mo-$Ta_2O_5$ | MV | $2.2 \times 10^7$ | CT/EM | [36] |
| ZnSe | R6G | $6.92 \times 10^7$ | CT | [37] |
| ZnO | 4-MPy | $10^5$ | CT/Mie resonances | [38] |
| ZnO | CV | $1.37 \times 10^6$ | CT/EM | [39] |
| $MoS_2$ | MB | $1.7 \times 10^6$ | CT | [40] |
| $SnS_2$ | MB | $3.0 \times 10^8$ | CT | [41] |
| $V_2O_5$ | MB | $10^6$ | CT/exciton | [42] |
| $TiO_2$ | 4-MBA | $4.5 \times 10^5$ | Mie resonance | [43] |
| $MoO_2$ | R6G | $4.3 \times 10^7$ | CT | [44] |
| ZnO@ZIF-8 | 4-NTP | 110 | Mie resonance | [45] |

*4-MBA* 4-mercaptobenzoic acid; *MB* methylene blue; *MV* methyl violet; *CV* crystal violet; *R6G* rhodamine 6G; *MB* methylene blue; *4-MPy* 4-mercaptopyridine; *4-NTP* 4-nitrobenzenethiol

(1) High chemical stability. Semiconductor materials have excellent thermodynamic stability compared to conventional metals, which can effectively avoid the problem of signal reproducibility caused by substrate oxidation. At the same time, semiconductor substrates widen the applicable media of SERS technology, such as strong oxidation medium, strong acid medium, high-pressure medium, and so on.

(2) Good biocompatibility. Semiconductor materials contain abundant hydroxyl groups on their surface, which can combine with proteins through amino groups and carboxyl groups. Such binding modes do not damage the spatial conformation and biological activity of proteins and solve the problem of biocompatibility of metal SERS technology.

(3) Surface modifiability. Metal materials can be only used for efficient adsorption of the analytes containing sulfhydryl group. In contrast, most of common functional groups can be directly adsorbed on semiconductor materials surface, and meanwhile, the modification strategies of semiconductor materials are more

flexible than that of metal materials. This advantage facilitates the deamination of analytes without the limitation of functional groups.

(4) Abundant species, low cost, and mature preparation process. The energy level structure of semiconductor materials can be regulated by size, shape, material, doping, and other methods. According to the test condition of the analyte, a suitable SERS-active semiconductor substrate can be selected to meet different SERS detection requirements. The synthesis of semiconductor substrates is cost effective and diverse synthetic techniques may be used; thus, making the application of the semiconductor substrates in SERS.

(5) Wide application range. Semiconducting materials are widely used as active components in practical devices related to electronics, optoelectronics, energy storage and conversion, catalysis, and biological sensor. The wide applications of semiconductor materials provide more possibilities for expanding the application range of SERS technology.

## 4.3 Enhancement Mechanism

Generally, CT between semiconductor and adsorbate is considered to be the major contribution to produce enhanced Raman scattering signal on semiconductor materials [49]. The CT models for semiconductor-enhanced Raman scattering is similar with metal-based SERS, which generally can be divided into three categories, namely ground-state CT, electronic resonant transition, and excited-state CT. The first two types correspond to the CT models proposed for metal-based SERS, but the excited-state CT for semiconductor SERS is more complex, which involves in the vibronic coupling of the molecular states to the valence band, conduction band, and defect states of semiconductor states. The detailed introduction has been described in the previous chapters. Besides, semiconductor micro/nanostructures also can produce electromagnetic field contributions to semiconductor SERS, but the physical models of the electric field are different from the metals, which originates from the Mie resonances excited in a nanoparticle with a high refractive index or collective oscillation of charge carrier at the nanoscale (defined as semiconductor SPR). We will give a detailed introduction of these theories in the substrate design section with specific examples. Here, we just use a unified theory to comprehensive discuss the enhancement mechanism in semiconductor-enhanced Raman scattering.

Using the "unified resonance" theory proposed by Lombardi et al., the polarizability tensor in the semiconductor-molecule system can be expressed as a sum over many resonances [49, 50]. With the development of semiconductor SERS in the recent years, we could reconsider this expression to further integrate the synergetic effect of multiple resonances:

$$R_{\text{mol - CT}}(\omega) = \frac{E^2 \cdot (\mu_{\text{mol}} \cdot \mu_{\text{CT}} \cdot h_{\text{mol - CT}})(\mu_{\text{ex}} \cdot \mu_{\text{CT}} \cdot h_{\text{ex - CT}}) i|Q_k|f}{\left(\left(\omega^2_{\text{Mie/SPR}} - \omega^2\right) + \gamma^2_{\text{Mie/SPR}}\right)\left(\left(\omega^2_{\text{CT}} - \omega^2\right) + \gamma^2_{\text{CT}}\right)} \\ \left(\left(\omega^2_{\text{mol}} - \omega^2\right) + \gamma^2_{\text{mol}}\right)\left(\left(\omega^2_{\text{ex}} - \omega^2\right) + \gamma^2_{\text{ex}}\right)$$

It can be seen that the denominator involves the product of four terms, each of which depicts a distinct resonance contribution to SERS. The first is due to the Mie resonance that may be complex refractive index and morphology-dependent. Alternatively, the first also can be considered as the surface plasmon resonance (SPR) in semiconductor that may be charge carriers concentration dependent. The second is the CT resonance either from the molecule occupied levels to the unoccupied electronic levels of semiconductor or from the occupied electronic levels of semiconductor to unoccupied molecular levels. The third is the molecular resonance that resides completely within the molecule. The fourth is the exciton resonance that is usually possible only for rather small particles sizes (typically around 1–10 nm). These resonances are coupled to each other through terms in the numerator. For example, the electric field ($E$) enhanced by Mie resonance at the surface of the semiconductor can be coupled with CT resonance ($\mu_{\mathrm{CT}}$), molecular resonance ($\mu_{\mathrm{mol}}$), and exciton resonance ($\mu_{\mathrm{ex}}$). Besides, the CT resonance and the molecular resonance can be coupled to each other through the Herzberg–Teller coupling constant ($h_{\mathrm{mol\text{-}CT}}$). Similarly, the CT resonance and resonance can be coupled to each other through the Herzberg–Teller coupling constant ($h_{\mathrm{ex\text{-}CT}}$). It should be noted that a particular CT resonance is approached by the laser, only on or at most very few of these terms make the largest contribution to the enhancement.

## 4.4 Substrate Design

According to the enhancement mechanism proposed above, several strategies for designing semiconductor substrates have been proposed as follows: (1) promoting CT interactions at the substrate-molecule interface; (2) producing electric field contribution near the substrate surface; (3) producing multiple scattering effect; (4) $\pi$-conjugated organic semiconductors; (5) synergistic effect. Next, we will introduce these strategies with some examples, and the enhancement mechanism behind these strategies also will be discussed in details.

### *4.4.1 Promoting CT Interactions at the Substrate-Molecule Interface*

(1) **Size Effect**

Enhanced Raman scattering is observed on semiconductors within a specific particle size range. As the particle size decreases, the specific surface area increases, resulting in a higher number of molecules being adsorbed on its surface. This increase in adsorption leads to an increase in SERS intensity with smaller particle sizes. However, when semiconductor nanopaticles approaching the size of the Bohr radius

of bulk excitons, the electron energy levels become discrete rather than continuous due to quantization effects, which may produce an abnormal enhancement.

Quagliano was reported the first observation of SERS from pyridine adsorbed on InAs/GaAs quantum dots synthesized by molecular beam epitaxy [51]. In the SERS spectrum, a new vibrational band was observed, which can be attributed to the strong interaction of pyridine with quantum dots via its nitrogen lone-pair electrons. Motivated by this work, Livingstone et al. demonstrated a sensitive SERS-active substrate of self-organized CdSe/CdZnSeMg quantum dots for the detection of bio-molecules with an enhancement factor of approximately $10^6$ [52]. They also observed the Raman enhancements for pyridine molecules adsorbed on CdSe/ZnBeSe quantum dots with the enhancement factor in the range of $10^4$–$10^5$ [53]. The excitation wavelength used in this work is in the vicinity of several interband and excitonic transitions located both in the quantum dots and the wetting layer, and it is likely that these resonances also contribute to the enhancement. Additionally, Lombardi et al. studied the nanoparticle size and excitation wavelength-dependent SERS of 4-MPy on PbS quantum dots [54].

It should be noted that the relationship between size-dependent SERS and the Bohr radius of bulk exciton is not always clear. For example, a particle size-dependent SERS phenomenon was observed on the surface of ZnO nanoparticles with the size in the range of 18–31 nm diameter [55]. The results indicated that the maximum enhancement was observed for 29 nm ZnO nanoparticles, which is inconsistent with the expected exciton Bohr radius of 2.4 nm for ZnO [55]. This can be attributed to changes in the Bohr radius of semiconductor excitons after the molecule adsorption on the semiconductor surface. The mechanism behind this is still unclear and further research is still needed.

(2) **Transition metal doping**

Doping transition metals into semiconductors introduces a large quantity of the doped element into the bandgap of semiconductors, and is an effective way to adjust surface defect states. A series of metal-doped $TiO_2$ materials (M-$TiO_2$, M = Fe, Co, Ni, Cu, Mn and Zn) was synthesized by Zhao et al. First, the SERS activity of small ($\leq$10 nm) anatase $TiO_2$ NPs was investigated using three common molecular probes, namely 4-MBA, 4-MPy, and 4-aminothipohenol (PATP) [56]. The three molecules have similar Raman scattering cross sections, whereas the enhanced abilities of their $TiO_2$ NPs are different (Fig. 4.1). The enhanced sequence was 4-MBA > 4-MPy > PATP, which is in accordance with the attractive electron ability of the functional groups in the three molecules. Considering the energy levels of $TiO_2$ and the molecules, the enhancement is considered to be due to the $TiO_2$-to-molecule CT contribution, or more precisely, the surface defect state-to-molecular LUMO CT transition.

After doping with different transition metals, they found that the SERS performance of M-doped $TiO_2$ NPs largely depended on the doping quantity and the intrinsic nature of the doping ions. The SERS enhancement capacity of the 3% Ni-doped $TiO_2$ NPs was four or more times higher than that of the undoped $TiO_2$ NPs. The increased enhancement capacity occurs because a suitable dopant prohibits the recombination of photoinduced carriers and promotes the $TiO_2$-to-molecule CT

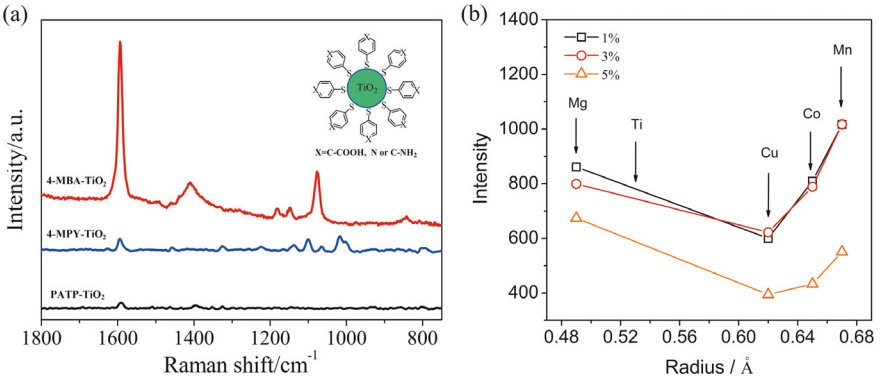



**Fig. 4.1** **a** SERS spectra of 4-MBA, 4-MPY, and PATP adsorbed on $TiO_2$ nanoparticles with the same Raman test condition. **b** SERS intensity of the 1594 $cm^{-1}$ mode of 4-MBA adsorbed on M-doped $TiO_2$ nanoparticles as function of ionic radius of dopant. Adapted with permission from [56]. Copyright 2008 American chemical society

transition. However, the excessive dopant becomes the recombination center of the photoinduced carriers, which prohibit the $TiO_2$-to-molecule CT transition. In addition, the SERS performance of $TiO_2$ NPs comprising different doping metals was found to be associated with the ionic radius of the transition metals, and the mechanism needs further investigation. A similar effect was observed for a sequence of transition metal-doped ZnO NPs. These studies clearly indicate that the appropriate introduction of surface defects by transition metal doping can improve the SERS performance of semiconductors.

(3) **Non-stoichiometry synthesis**

Non-stoichiometry is common among transition metal oxides, such as $TiO_x$ ($1.998 \leq \times \leq 2.000$), $VO_x$ ($0.79 \leq \times \leq 1.29$), $Ni_xO$ ($0.999 \leq \times \leq 1.000$), and $WO_x$ ($2.50 \leq \times \leq 3.00$). The stoichiometric composition of these semiconductors leads to the formation of intrinsic point defects (vacancies, ant sites, and interstitials). The correlation between the non-stoichiometry of the transition metal and the SERS performance is vital for the rational design of SERS-active semiconductors.

For example, the SERS behavior of R6G on non-stoichiometric $W_{18}O_{49}$ nanowires was revealed by Cong et al. [57]. The synthesized $W_{18}O_{49}$ sample contains a large number of oxygen vacancies, which can be modulated by simple annealing of the $W_{18}O_{49}$ sample in an $Ar/H_2$ atmosphere (Fig. 4.2). They found that the oxygen vacancies in $W_{18}O_{49}$ strengthened the vibronic coupling interaction of the substrate-R6G, and promoted the CT transition between the $W_{18}O_{49}$ nanowires and adsorbed R6G molecules. Thus, SERS sensitivity can be observed in non-stoichiometric $W_{18}O_{49}$ nanowires. Furthermore, the downsizing of $WO_{3-x}$ to ultrathin two-dimensional nanosheets could further improve the vibronic coupling effect, because the abundant surface defect states on the nanosheet surface promote CT activity at the substrate-molecular interface [58].

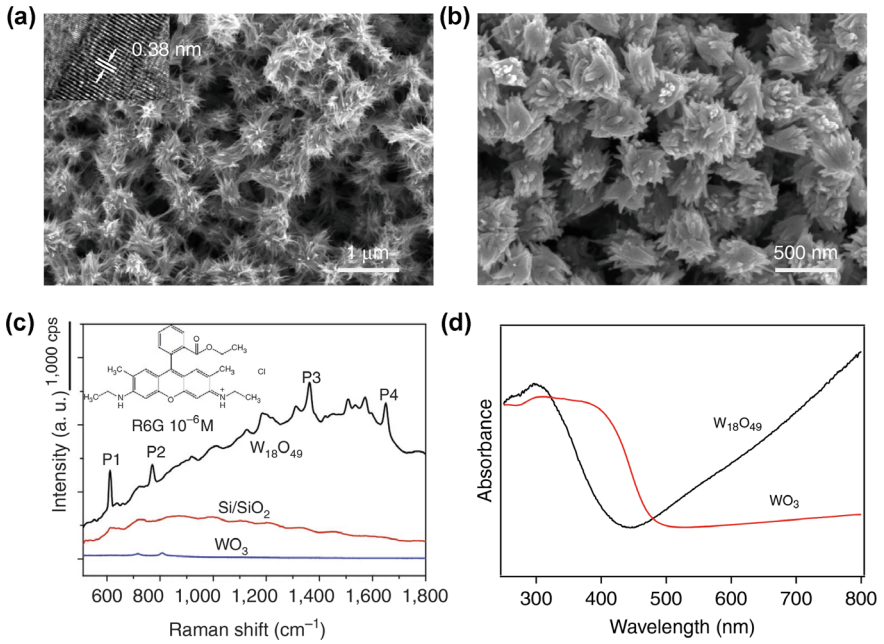



**Fig. 4.2** Scanning electron microscopy images for **a** $W_{18}O_{49}$ and **b** $WO_3$ samples, respectively. **c** Ultraviolet–visible profile comparison between $W_{18}O_{49}$ sample and annealed $WO_3$, showing a blue shift and an obvious absorption tail beyond the edge that may arise from the presence of oxygen vacancies. **d** Raman profile of R6G ($10^{-6}$ M) on substrates deposited with$W_{18}O_{49}$ sample compared with that for $WO_3$ and bare $SiO_2$/Si substrate. Inset: molecule structure of R6G. Adapted with permission from [57]. Copyright 2015 nature research

### (4) **Amorphous semiconductor materials**

Amorphous semiconductor materials exhibit two characteristic features: structural disorder and quasi-equilibrium. Thus, the electron energy band structure of amorphous semiconductors is essentially the same as that of crystalline semiconductors. However, the disordered structure of the amorphous semiconductors results in localized electronic states within the energy gap. The electronic density of states in amorphous semiconductor materials can improve vibronic coupling in substrate-molecule systems [59].

This was demonstrated by Guo et al. based on the study of the SERS activity of amorphous ZnO nanocages (Fig. 4.3) [60]. The first principle DFT simulation revealed that the CT process in amorphous ZnO nanocages was stronger than that in their crystalline structures, because of the weaker electron constraint of the metastable electronic states on the surface electrons in amorphous structures. This weak constraint on the surface electrons strengthens the coupling interaction of ZnO with surface adsorbates, and even with sulfhydryl adsorbates. An unusual π-interaction between Zn and S in amorphous ZnO nanocages was verified by X-ray absorption near-edge structure (XANES) characterization. The strong coupling effect

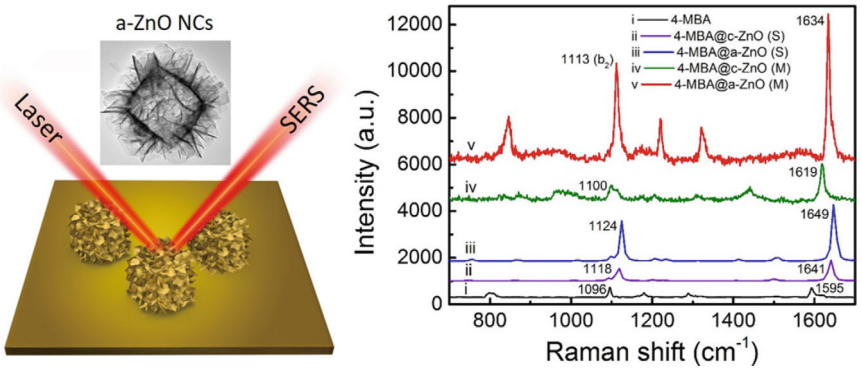



**Fig. 4.3** SERS activity observed for amorphous ZnO nanocages. (i–iii) simulated (*S*) and (iv–v) measured (*M*) SERS spectra of 4-mercaptobenzoic acid (4-MBA) molecules adsorbed on amorphous ZnO nanocages. Adapted with permission from [60]. Copyright 2017 John Wiley & Sons, Inc

efficiently improved the contribution of the CT to SERS enhancement. Based on this finding, two-dimensional amorphous $TiO_2$ nanosheets containing abundant oxygen defects were further designed by the same group [61]. In comparison with their crystalline counterparts, the higher electronic density of states of the amorphous $TiO_2$ nanosheets strongly affect the electron cloud distribution of the adsorbed molecules and endow a larger SERS contribution from the interfacial CT transitions.

### *4.4.2 Producing Electric Field Contribution Near the Substrate Surface*

(1) **Mie resonance**

High electromagnetic fields are also sustained by high refractive index dielectric nanostructures, referred to as Mie resonance modes. They are also known as whispering gallery modes (WGMs). Mie resonance, strictly speaking, is a special type of morphology-dependent optical resonance localized close to the external boundary of a dielectric spherical particle, which can be expected based on the Mie theory. In modern optics and photonics, Mie resonance is a generic term that refers to morphology-dependent optical resonances. The Mie resonance modes can be engineered by adjusting the particle size, wavelength, and refractive index. Mie resonance can confine free-space light into nanoscale volumes, exhibiting intriguing optical magnetic and electric resonance modes in the visible or near-IR spectral regions. If the Mie resonance modes match the incident laser, the enlarged local electromagnetic field significantly improves the SERS signal.

The electromagnetic field intensity at a spherical particle surface can be described by the near-field scattering efficiency ($Q_{NF}$) proposed by Messinger et al. [62]. $Q_{NF}$ is

a qualitatively similar to the scattering efficiency ($Q_{\text{scat}}$) and can be used to evaluate the ability of a spherical particle to convert an incident electric field intensity into an electric near-field intensity. In particular, for near dielectric sphere surfaces, the amplitude of the near-field scattering intensity can be much larger than that of the far-field scattering, leading to a local field enhancement. For a spherical particle, $Q_{\text{NF}}$ may be determined from the following Equation:

$$Q_{\text{NF}} = 2\sum_{n=1}^{\infty}\left\{|a_n|^2\left[(n+1)\left|h_{n-1}^{(2)}(x)\right|^2 + n\left|h_{n+1}^{(2)}(x)\right|^2\right]\right.$$
$$\left.+(2n+1)|b_n|^2\left|h_n^{(2)}(x)\right|^2\right\}$$

where $h_n^{(2)}$ is the Hankel function of the second type, $x = \pi d/\lambda$ is the size parameter, d is the diameter of the spherical particle, and $\lambda$ is the wavelength of the incident light. In addition, $a_n$ and $b_n$ are the Mie coefficients, which can be deduced using the complex Riccati–Bessel functions $\psi$ and $\zeta$:

$$a_n = \frac{\psi_n{}'(mx)\psi_n(x) - m\psi_n(mx)\psi_n{}'(x)}{\psi_n{}'(mx)\zeta_n(x) - m\psi_n(mx)\zeta_n{}'(x)}$$

$$b_n = \frac{m\psi_n{}'(mx)\psi_n(x) - \psi_n(mx)\psi_n{}'(x)}{m\psi_n{}'(mx)\zeta_n(x) - \psi_n(mx)\zeta_n{}'(x)}$$

where $m$ is the complex refractive index of the spherical particle. The complex refractive index is a fundamental physical parameter of a material, that changes with the wavelength of incident light. For a specific semiconductor material, the near-field scattering intensity depends mainly on the size of the spherical particles and the incident light wavelength. According to the classical electromagnetic field theory, the enhancement factor of SERS is approximately proportional to the second power of the amplitude enhancement of the near-field scattering intensity, $Q_{NF}^2$. To produce a high electric field contribution for SERS enhancement, the design of a SERS-active semiconductor substrate can proceed from the near-field scattering efficiency.

Semiconductor materials with high near-field scattering efficiency typically need to have a high refractive index, and small imaginary parts of their dielectric functions across a broad spectral range. The imaginary part is associated with dielectric losses, which represent the loss factor or energy-absorption capacity. For instance, Fig. 4.4a shows the near-field scattering efficiency of CdSe calculated by different imaginary part of the refractive index (0.356 and 0.010). The large imaginary part broadens the spectral lines and greatly weakens the scattering efficiency. This is because a semiconductor with a large imaginary part experiences the loss or absorption of the incident photon, and subsequently weakens the near-field Mie scattering of the incident photon.

For a selected semiconductor material, optimal dimensions are essential for highly efficient Mie resonances [64]. In contrast to plasmonic metal materials, a strong Mie resonance is usually observed in semiconductors having diameters in the submicron

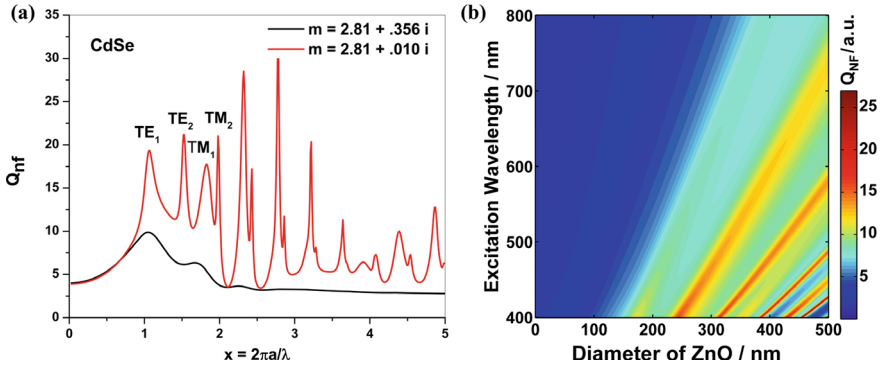



**Fig. 4.4** **a** Near-field scattering efficiency as a function of $x = 2\pi a/\lambda$ for CdSe calculated by different imaginary part of the refractive index (0.356 and 0.010). Adapted with permission from [49]. Copyright 2014 American chemical society. **b** Dependence on the incident wavelength and ZnO microsphere diameter for the near-field scattering efficiency. Adapted with permission from [63]. Copyright 2019 Wiley–VCH Verlag

range. For example, the map of the near-field scattering efficiency for spherical ZnO particles as a function of wavelength and particle diameter was calculated based on the Mie theory (Fig. 4.4b) [63]. The extrema shown in this map are related to the various transverse electric (TE) and transverse magnetic (TM) resonant modes [64]. This occurs because when the incident light resonates with the $TE_n$ (or $TM_n$) mode, the Mie coefficient $a_n$ (or $b_n$) appearing in the $Q_{NF}$ expression increases substantially, leading to a resonant peak in $Q_{NF}$. This allowed us to estimate the required particle size for the most effective exploitation of near-field scattering with a specific incident photon wavelength. It is clear that the TE and TM resonant modes become more pronounced for larger spherical ZnO particles with short-wavelength excitations, and particles with a diameter of > 100 nm appear to be suitable for producing high $Q_{NF}$. Accordingly, to achieve semiconductor-enhanced Raman scattering dominated by a high electric field contribution, the diameter of the ZnO particles should be larger than 100 nm.

The near-field Mie scattering theory was first applied to explain the enhanced Raman spectra of copper phthalocyanine adsorbed on GaP NPs [2]. They found that the enhancement factor increased as the increasing of the average particle size. The obtained dependence of enhancement factors on the particle diameter was in accordance with that calculated dependence of $Q_{NF}^2$. This size range of GaP NPs corresponded to the tail of the $TE_1$ resonance, in which $Q_{NF}$ monotonically increased along with the particle diameter increase. Another related work was reported by Rodriguez et al., they demonstrated that Si NPs exhibit a huge SERS effect owing to Mie resonances (Fig. 4.5) [65]. The simulation results demonstrated that the electric field induced by the Mie resonance for spherical Si exhibits the same or a larger intensity than that for Au plasmons at particular particle sizes. A high SERS of p-aminobenzoic acid on Si NPs was observed by the excitation of the different Mie resonance modes. Different methods including mechanical milling, pulsed laser

ablation in liquid, and gas phase synthesis have been developed for the fabrication of Si NPs. However, there is still no simple and suitable method for the large-scale preparation of high-quality Si NPs for practical applications. Other semiconductors, such as GaP, $TiO_2$, ZnO, and ZnS, also meet the requirements for producing strong Mie resonances in the visible region, more importantly, these semiconductors can be easily synthesized in the laboratory.

(2) **Surface plasmon resonance**

Recent advancements in theory and experimental technology evident that localized surface plasmon resonances (LSPR) are not limited to metal nanostructures, but can also be achieved in semiconductor nanoparticles with appreciable free carrier concentrations [66]. Unlike the SPR generated by the collective oscillation of free electrons in metals, the SPR of semiconductors involves three types of collective oscillations of carriers: valence band electrons, conduction band electrons, and valence band holes. According to the Drude model, the square of the SPR absorption frequency in semiconductor is proportional to the free carrier concentration. Thus, the SPR frequency of semiconductor nanomaterials can be precisely controlled by carrier concentration through creating intrinsic defects or introducing extrinsic impurities in semiconductor lattice.

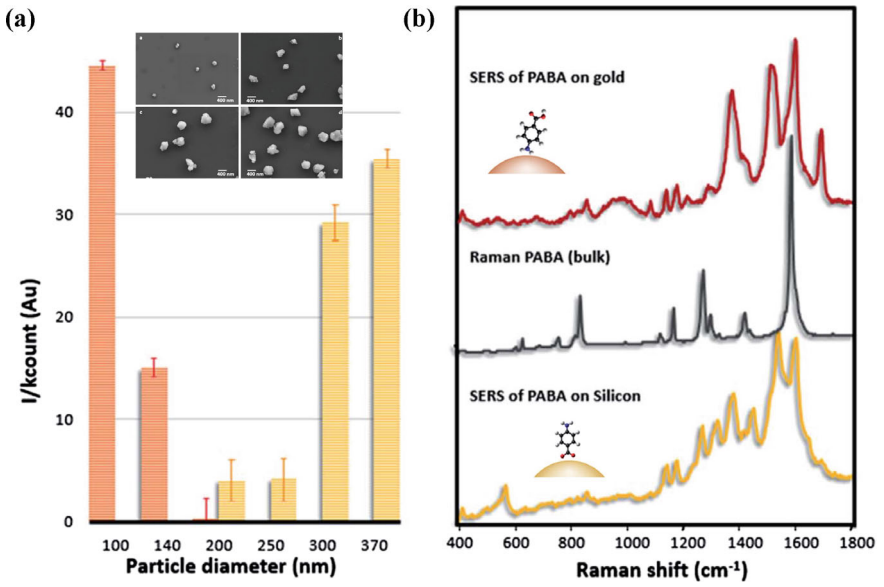



**Fig. 4.5** **a** Intensities and **b** SERS spectra of PABA excited at 785 nm on colloidal dispersions of gold (100–400 nm) and silicon (200–370 nm) particles. Gold (red) and silicon (yellow). Inset **a** shows the SEM image of Si NPs obtained through mechanical milling of silicon powder together with further particle separation through a colloidal sedimentation process: **a** 200, **b** 260, **c** 300 and **d** 370 nm. Adapted with permission from [65]. Copyright 2014 royal society of chemistry

In experiments, plasmonic semiconductors can be prepared by non-stoichiometric synthesis and heavy doping. The SPR frequencies of the synthesized semiconductors are significantly blue-shifted compared to that of intrinsic semiconductors, which are generally located in the visible, near-infrared, or mid-infrared region, such as copper sulfide ($Cu_{2-x}S$) [67], copper selenide ($Cu_{2-x}Se$) [68, 69], tungsten oxide ($WO_x$) [70], copper telluride ($Cu_{2-x}Te$) [71, 72], highly Al-doped ZnO [73–75], and indium tin oxide (Sn-doped $In_2O_3$, ITO) [76, 77].

Xi et al. presented a molybdenum nitride (MoN) porous structure with a well-defined hexagonal prism morphology (Fig. 4.6) [78]. This unique structure exhibits a notable visible-light SPR effect with a center at 534 nm. The observed SPR effect stems from the high density of *d*-orbital electron near the Fermi level of MoN. MoN hexagonalprisms exhibit a strong metallic behavior due to the absence of bandgap in MoN. Simultaneously, the densely packed porous architecture facilitates efficient plasmonic resonance coupling. Consequently, the LSPR effect achieved in MoN amplifies the Raman scattering signal to levels typically comparable to noble metals.

Besides, they also observed SERS effects on metallic few-layer nitrogen-doped titanium monoxide (N-$TiO_2$) nanosheets [79]. N-$TiO_2$ nanosheets exhibit a strong SPR in the visible region and improved oxidation resistance, which could improve the durability of SPR effect-based SERS substrates. Furthermore, plasmonic MoN and $Mo_2C$ hollow spheres were synthesized using a quasi-metal-based microwave method, and the synthesized MoN and $Mo_2C$ hollow spheres exhibit strong LSPR effect in visible region, which have been demonstrated to be ultrasensitive and stable SERS substrates [80].

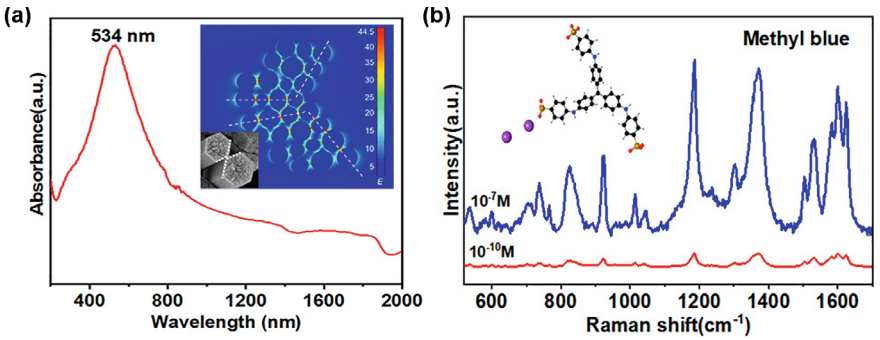



**Fig. 4.6** **a** UV − VIS-IR spectrum of the porous MoN hexagonalprisms. Inset shows the proposed enhanced mechanism of the porous MoN hexagonalprisms. **b** SERS spectra of methyl blue obtained in the porous MoN hexagonalprisms. Adapted with permission from [78]. Copyright 2022 American chemical society

### 4.4.3 Producing Multiple Scattering Effect

Multiple scattering effect can be interpreted as a succession of independent, single Mie-like scattering (morphology-dependent optical resonances) events, enhancing material-light interactions [81]. Alessandri et al. proposed the use of modulated multiple scattering effect for construction of plasmon-free semiconductor SERS substrates [82]. Core/shell resonators based on $SiO_2/TiO_2$ beads (T-rex) were fabricated by deposition of ultrathin (5 nm or less) anatase $TiO_2$ layer on $SiO_2$ NPs surface. The refractive index differences between $SiO_2$ core and $TiO_2$ shell layer resulted total internal reflection of light within the $TiO_2$ shell layer. Meanwhile, the electric field originated by the multiple light scattering effect was demonstrated to enhanced Raman scattering for the analytes adsorbed at the T-rex surface. Similarly, a $TiO_2$ inverse opal photonic microarray was reported by Zhang et al. for improved SERS sensitivity [83]. The highest SERS sensitivity can be achieved by appropriately utilizing slow light effect of photonic microarray. $TiO_2$ inverse opals with a cavity diameter of 225 nm exhibited the highest sensitivity, because the multiple lasers scattering in the cavity improved the light-matter interaction, which provides much more opportunities for the stimulation of Raman scattering. Furthermore, they also observed enhanced Raman scattering of methylene blue over the chiral carbonaceous nanotubes modified with titania nanocrystals [84]. The enhanced Raman scattering could be ascribed to the multiple light scattering effect induced by the birefringence in the unique helical structure.

### 4.4.4 Organic Semiconductors

$\pi$-Conjugated organic semiconductors with a high charge carrier mobility provided good alternative materials for SERS-active substrates. Compared with inorganic semiconductors, organic semiconductors have the following advantages: structural versatility, facile and highly controllable synthesis, and fine-tuning of optoelectronic properties.

For example, Yilmaz et al. reported a novel SERS platforms based on micro-/nanostructured 2,7-dioctyl[1]benzothieno[3,2-b][1]benzothiophene (C8-BTBT) thin films via an oblique-angle vapor deposition [85]. The results demonstrate the first example of an organic semiconductor-based SERS platform with excellent detection characteristics, indicating that $\pi$-conjugated organic semiconductors have a great potential for SERS applications.

Based on this work, they further studied the SERS response on n-type (electron-transporting) organic films [86]. A ivy-like nanostructured film of a molecular semiconductor was fabricated by vapor deposition of $\alpha,\omega$-diperfluorohexylquaterthiophene (DFH-4T) on Si(100) substrate (Fig. 4.7). The characteristic SERS peaks for methylene blue and rhodamine 6G have been observed on DFH-4T film, demonstrating that organic small-molecule based films can serve as

SERS platforms. Quantum mechanical computations revealed that the electronic structure of the DFH-4-methylene blue system allows for a narrow CT feature resonanting with the experimental SERS excitation energy, leading to a resonance CT enhancement for SERS. Besides, due to the superhydrophobic nature of the DFH-4T film surface, analyte droplets are confined to extremely small areas ($\sim$200 $\pm$ 30 $\mu$m in diameter) after solvent removal, increasing the local concentration for SERS measurement. DFH-4T films exhibited a Raman signal enhancement up to 3.4 $\times$ $10^3$ for the probe molecule methylene blue. By combining DFH-4T semiconductor films with a plasmonic Au layer (Au@DFH-4T), Raman signal enhancements up to $\sim 10^{10}$ and sub-zeptomole ($<10^{-21}$ mol) analyte detection can be achieved. Furthermore, they also demonstrated an Au-coated electrosprayed organic semiconductor film (Au@BDY-4T-BDY) on flexible regular aluminum foil for practical SERS and catalytic applications [87]. These works provide valuable insights for designing SERS-active organic semiconductors and easily fabricating SERS platforms for ultrasensitive trace analysis.

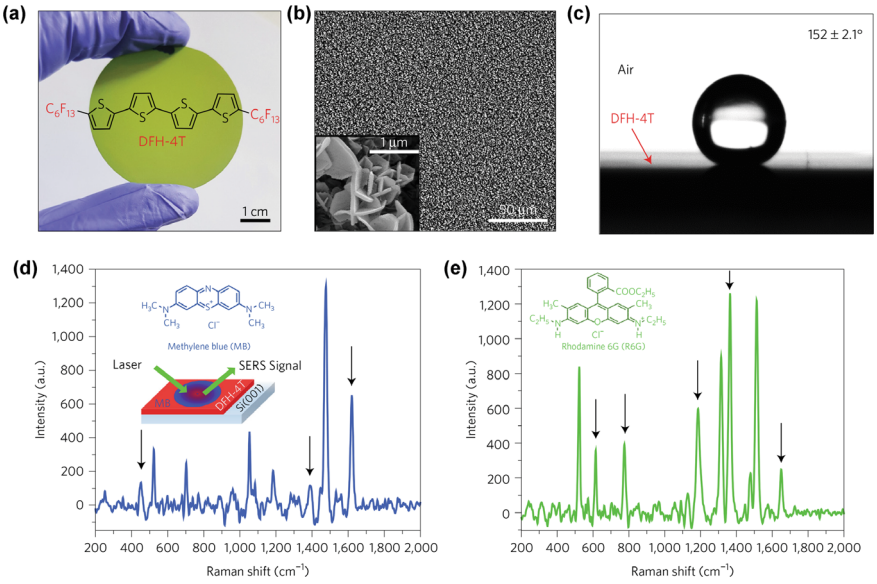



**Fig. 4.7** **a** Optical image of a vapor-deposited DFH-4T film (5 cm in diameter). **b** SEM images of nanostructured DFH-4T films. **c** Optical image of a water droplet on a nanostructured DFH-4T film used for contact-angle measurements. SERS spectra of methylene blue (MB) **d** and rhodamine 6G (R6G) **e** on nanostructured DFH-4T films (insets show the chemical structure of MB/R6G and for each analyte molecule, characteristic Raman peaks are highlighted). Adapted with permission from [86]. Copyright 2017 Copyright 2015 nature research

### 4.4.5 *Producing Synergistic Effect*

As we mentioned above, various mechanism, including CT resonance, Mie resonance, exciton resonance, and plasmon resonance, have been discovered to have enhancement contribution for semiconductor-enhanced Raman scattering, but most of current semiconductor substrates were designed based on a single enhancement mechanism. The coupling of multiple resonances to create synergistic effect is a new direction for further increase semiconductor SERS performance. The synergistic effect can be integrated and optimized from two perspectives: one is more focused on improvement of Mie resonance by engineering the morphology of semiconductor substrate, and the other focus on improvement of CT resonance by adjusting the energy band of semiconductor substrate [41, 63, 88–90].

For the first case, Ji et al. demonstrated that a synergistic effect between Mie resonance and CT resonance can be gained by ingenious design of spherical ZnO superstructures (Fig. 4.8a) [63]. In this work, the ZnO superstructure with a uniform diameter in the range of 200–500 nm, formed by aggregation of ~ 13 nm primary single crystallites, was designed for exploring Mie resonance scattered near-field enhancement effect for SERS enhancement and its synergistic effect with CT. The existence of the Mie scattering effect in these ZnO superstructures was confirmed by the extinction spectra, which was identical to that observed from Mie theory simulations. By engineering the superstructure size and excitation wavelength to induce Mie resonances, the Mie resonance contribution to the SERS enhancement was well studied. Results of SERS spectra and theoretical simulations, including near-field scattering efficiency simulations and Finite-element-method simulations, indicated that the Mie resonance induced by the secondary superstructure could enhance the electric near-field, leading to an electromagnetic contribution for SERS enhancement. Meanwhile, the primary nanocrystallites in these ZnO superstructures were able to yield a highly effective CT contribution for SERS enhancement, which was verified by the ultraviolet photoemission spectroscopy (UPS) and the degree of CT. The synergistic effect of CT and Mie resonances increases the enhancement factor by up to $10^5$. Even without the photo-induced CT contribution, the enhancement factor also can be up to $10^3$ due to the synergistic effect of Mie resonance and static chemical enhancement, implying that semiconductor superstructures may be used as a universal SERS-active substrate for different analytes. Based on this finding, Ji et al. further demonstrated a new type of multiple synergistic resonant strategy by utilization of a unique double-shelled hollow spherical $V_2O_5$ microstructure as a model [88]. In contrast to the lamellar structure, light is confined and guided inside the shell instead passing directly through the shell, indicating that reflections by multiple convex shells can provide an efficient resonance absorption for CT and exciton enhancements. Meanwhile, the coupling of Mie resonances from outer and inner shells strongly reinforces the magnitude of the electromagnetic near-field, leading to a high electromagnetic contribution for SERS enhancement. The synergy of all factors contributes to a significant increase of semiconductor SERS sensitivity.

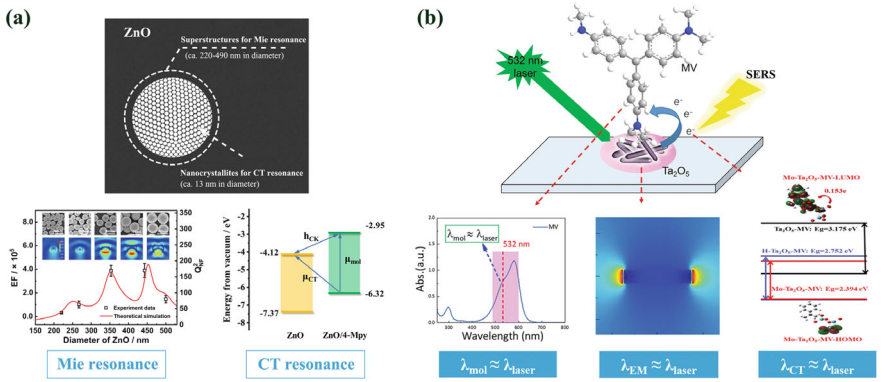



**Fig. 4.8** **a** Diagram that illustrates the microstructure of a ZnO superstructure comprised of closely packed nanocrystallites. The comparison of enhancement factor and near-field scattering efficiency observed on ZnO superstructures with different diameters under the 532 nm excitation. Inset shows the corresponding SEM and electric field distribution images of ZnO superstructures. Adapted with permission from [63]. Copyright 2019 Wiley–VCH Verlag. b Mechanism diagram of the synergistic resonance strategy on the Mo-doped $Ta_2O_5$ nanosheets. Adapted with permission from [89]. Copyright 2019 Wiley–VCH Verlag

For the second case, Mo-doped $Ta_2O_5$ nanosheets were synthesized by Yang et al. for optimization of the SERS performance of semiconductor (Fig. 4.8b) [89]. It should be noted that $Ta_2O_5$ is a typical dielectric material with high refractive index and low losses in the visible region, which also satisfies the requirement of Mie resonance. The Mie resonance-induced electric field distribution of $Ta_2O_5$ nanosheets was simulated by FDTD method. The maximum electric field enhancement factor was only 9 at the angular positions of the two $Ta_2O_5$ under irradiation with a 532 nm laser. This relative week electric field contribution is not surprising because the sheet structure cannot support strong Mie resonance. However, the CT contribution was significantly boosted by the energy band adjustment through Mo-doping. The DFT results indicated that doping of Mo atom could substantially lower the band gap of $Ta_2O_5$. The experimental results demonstrated that the $Ta_2O_5$ nanosheets with 15% Mo doping concentration showed the most suitable energy band structural match between methyl violet and the doped $Ta_2O_5$, leading to a best CT contribution for SERS. The lowest detection limit of methyl violet on Mo-doped $Ta_2O_5$ substrate was as low as $9 \times 10^{-9}$ M under the resonant excitation of the methyl violet with a 532 nm laser. The high enhancement performance can be attributed to the synergistic effect of Mie resonance, CT resonance, and molecular resonance. Similarly, they also reported other two types of two-dimensional materials, including nano-canyon liked $SnS_2$ structure and MXenes to couple the Mie resonance and CT resonance for SERS detection of coronavirus [41, 90].

Moreover, Xi et al. reported that metallic niobium nitride (NbN) hierarchical networks with open nanocavity structures exhibit a strong LSPR behavior in visible-light regions [91]. Besides, the DFT calculations reveal that NbN has continuous

energy levels from the −2 to 2 eV, and the rich energy level distribution could provide multiple charge transfer channels for SERS enhancement. Accordingly, the coupling effect of LSPR and charge transfer leads to a Raman enhancement factor $10^8$. Besides, a synergistic effect of SPR and CT was also observed on metallic $W_{18}O_{49}$ nanowires.

## 4.5 Conclusions and Perspectives

As described above, semiconductor-enhanced Raman scattering has achieved significant advancements in mechanism studies. The enhancement factor of semiconductor SERS was reported to be comparable to metal-based SERS in some works. The sensitivity of semiconductor SERS is no longer a major constraint for semiconductor SERS, and a critical challenge now is improving the universality of semiconductor substrates. Most current research has focused on vacancy defect-mediated methods based on CT mechanism, but the universality of such semiconductor substrates is difficult to achieve due to the requirement of energy level matching between substrate and analytes. Similar to metal SERS, creating an electric field contribution for semiconductor SERS can further broaden the universality of semiconductor SERS. Recent studies have demonstrated that Mie resonance can boost the electric near-field for semiconductor SERS, providing a new theoretical framework for designing versatile SERS-active semiconductor substrates. According to this theoretical framework, semiconductor materials with high refractive index are ideal for generating high electric contributions to semiconductor SERS. Additionally, coupling of multi-resonance effects, such as CT, Mie resonance, exciton resonance, and plasmon resonance, is a promising direction for designing SERS-active semiconductor substrates with synergistic effects. Moreover, the use of plasmonic and organic semiconductors opens up new possibilities for construction of SERS-active semiconductor substrates. With its rapid progress, we believe that semiconductor SERS will certainly play a significant role in the future development of SERS technique.

**Acknowledgements** This work was supported by the National Natural Science Foundation (22073014) of P. R. China. The authors also acknowledge the support from the Natural Science Foundation of Heilongjiang Province (GZ20220074).

## References

1. M. Fleischmann, P. J. Hendra and A. J. McQuillan, Raman spectra of pyridine adsorbed at a silver electrode. Chem. Phys. Lett. **26**, 163-166 (1974)
2. S. Hayashi, R. Koh, Y. Ichiyama and K. Yamamoto, Evidence for surface-enhanced Raman scattering on nonmetallic surfaces: Copper phthalocyanine molecules on GaP small particles. Phys. Rev. Lett. **60**, 1085-1088 (1988)

3. B. H. Loo, Observation of the surface enhanced raman scattering effect from the semiconductor—electrolyte interface. J. Electroanal. Chem. Inter. Electrochem. **136**, 209-213 (1982)
4. H. Yamada and Y. Yamamoto, Surface enhanced Raman scattering (SERS) of chemisorbed species on various kinds of metals and semiconductors. Surf. Sci. **134**, 71-90 (1983)
5. P. Zhang, Y. Wang, T. He, B. Zhang, X. Wang, H. Xin and F.-c. Liu, SERS of pyridine, 1,4-dioxane and 1-ethyl-3′-methyl-2-thiacyanine iodide adsorbed on α-$Fe_2O_3$ colloids. Chem. Phys. Lett. **153**, 215-222 (1988)
6. I. Alessandri and J. R. Lombardi, Enhanced Raman Scattering with Dielectrics. Chem. Rev. **116**, 14921-14981 (2016)
7. Y. Wang, Y. Wang, Y. Gao, Z. Sun, C. Zhao, H. Hu, W. Xu, Z. Wang and B. Zhao, Surface enhanced Raman spectroscopy of 4-mercaptopyridine molecules on $Pb_3O_4$ nanoparticles. Chem. Res. Chinese. U. **22**, 388-389 (2006)
8. Y. Wang, H. Hu, S. Jing, Y. Wang, Z. Sun, B. Zhao, C. Zhao and J. R. Lombardi, Enhanced Raman scattering as a probe for 4-mercaptopyridine surface-modified copper oxide nanocrystals. Anal. Sci. **23**, 787-791 (2007)
9. Y. Wang, Z. Sun, Y. Wang, H. Hu, B. Zhao, W. Xu and J. R. Lombardi, Surface-enhanced Raman scattering on mercaptopyridine-capped US microclusters. Spectrochim. Acta A **66**, 1199-1203 (2007)
10. Y. Wang, J. Zhang, H. Jia, M. Li, J. Zeng, B. Yang, B. Zhao, W. Xu and J. R. Lombardi, Mercaptopyridine surface-functionalized CdTe quantum dots with enhanced Raman scattering properties. J. Phys. Chem. C **112**, 996-1000 (2008)
11. Y. Wang, W. Ruan, J. Zhang, B. Yang, W. Xu, B. Zhao and J. R. Lombardi, Direct observation of surface-enhanced Raman scattering in ZnO nanocrystals. J. Raman Spectrosc. **40**, 1072-1077 (2009)
12. Y. F. Wang, Z. H. Sun, H. L. Hu, S. Y. Jing, B. Zhao, W. Q. Xu, C. Zhao and J. R. Lombardi, Raman scattering study of molecules adsorbed on ZnS nanocrystals. J. Raman Spectrosc. **38**, 34-38 (2007)
13. X. Ling, L. M. Xie, Y. Fang, H. Xu, H. L. Zhang, J. Kong, M. S. Dresselhaus, J. Zhang and Z. F. Liu, Can Graphene be used as a Substrate for Raman Enhancement? Nano Lett. **10**, 553-561 (2010)
14. X. Xue, W. Ji, Z. Mao, Z. Li, W. Ruan, B. Zhao and J. R. Lombardi, Effects of Mn doping on surface enhanced Raman scattering properties of $TiO_2$ nanoparticles. Spectrochim. Acta A **95**, 213-217 (2012)
15. X. Xue, W. Ji, Z. Mao, W. Ruan, B. Zhao, S. Ma and J. R. Lombardi, Study of enhanced Raman scattering for molecules adsorbed on Cu-doped $TiO_2$ nanoparticles. Sci. Sin. Chim. **41**, 398-402 (2011)
16. X. Xue, W. Ruan, L. Yang, W. Ji, Y. Xie, L. Chen, W. Song, B. Zhao and J. R. Lombardi, Surface-enhanced Raman scattering of molecules adsorbed on Co-doped ZnO nanoparticles. J. Raman Spectrosc. **43**, 61-64 (2012)
17. X. X. Xue, W. Ji, Z. Mao, Z. S. Li, Z. N. Guo, B. Zhao and C. Zhao, SERS study of Co-doped $TiO_2$ nanoparticles. Chem. Res. Chinese. U. **29**, 751-754 (2013)
18. L. L. Qu, Y. T. Li, D. W. Li, J. Q. Xue, J. S. Fossey and Y. T. Long, Humic acids-based one-step fabrication of SERS substrates for detection of polycyclic aromatic hydrocarbons. Analyst **138**, 1523-1528 (2013)
19. L. Yang, X. Jiang and M. Yang, Improvement of surface-enhanced Raman scattering performance for broad band gap semiconductor nanomaterial ($TiO_2$): Strategy of metal doping. Appl. Phys. Lett. **99**, 111114 (2011)
20. Y. Wang, Z. Sun, Y. Wang, H. Hu, B. Zhao, W. Xu and J. R. Lombardi, Surface-enhanced Raman scattering on mercaptopyridine-capped CdS microclusters. Spectrochim. Acta A **66**, 1199-1203 (2007)
21. X. Ling and J. Zhang, First-Layer Effect in Graphene-Enhanced Raman Scattering. Small **6**, 2020-2025 (2010)

22. X. Ling and J. Zhang, Interference Phenomenon in Graphene-Enhanced Raman Scattering. J. Phys. Chem. C **115**, 2835-2840 (2011)
23. X. Ling, L. G. Moura, M. A. Pimenta and J. Zhang, Charge-Transfer Mechanism in Graphene-Enhanced Raman Scattering. J. Phys. Chem. C **116**, 25112-25118 (2012)
24. X. Ling, J. Wu, W. Xu and J. Zhang, Probing the Effect of Molecular Orientation on the Intensity of Chemical Enhancement Using Graphene-Enhanced Raman Spectroscopy. Small **8**, 1365-1372 (2012)
25. X. Ling and J. Zhang, Investigation of the Adsorption Behavior of PbPc on Graphene by Raman Spectroscopy. Acta Phys-Chim. Sin. **28**, 2355-2362 (2012)
26. X. Ling, J. Wu, L. Xie and J. Zhang, Graphene-Thickness-Dependent Graphene-Enhanced Raman Scattering. J. Phys. Chem. C **117**, 2369-2376 (2013)
27. S. Huang, X. Ling, L. Liang, Y. Song, W. Fang, J. Zhang, J. Kong, V. Meunier and M. S. Dresselhaus, Molecular Selectivity of Graphene-Enhanced Raman Scattering. Nano Lett. **15**, 2892-2901 (2015)
28. Y. S. Peng, C. L. Lin, L. Long, T. Masaki, M. Tang, L. L. Yang, J. J. Liu, Z. R. Huang, Z. Y. Li, X. Y. Luo, J. R. Lombardi and Y. Yang, Charge-Transfer Resonance and Electromagnetic Enhancement Synergistically Enabling MXenes with Excellent SERS Sensitivity for SARS-CoV-2 S Protein Detection. Nano-Micro Lett. **13** (2021)
29. R. Wang, M. X. Chen, J. C. Han, X. H. Zhang, Z. H. Zhang, T. Yao, Y. Wang, L. L. Xu, X. J. Wang, P. Xu and B. Song, Entropy Engineering on 2D Metal Phosphorus Trichalcogenides for Surface-Enhanced Raman Scattering. Adv. Funct. Mater. (2023)
30. F. F. Li, X. Y. Mu, X. Q. Tang, G. Song, H. Z. Sun, X. L. Zha, P. Y. Sun, J. H. Fang, D. M. Hu, S. Cong and Z. G. Zhao, Semiconductor SERS on Colourful Substrates with Fabry-Perot Cavities. Angew. Chem. Int. Ed. (2023)
31. G. Song, W. B. Gong, S. Cong and Z. G. Zhao, Ultrathin Two-Dimensional Nanostructures: Surface Defects for Morphology-Driven Enhanced Semiconductor SERS. Angew. Chem. Int. Ed. **60**, 5505-5511 (2021)
32. X. Y. Hou, X. Y. Zhang, Q. W. Ma, X. Tang, Q. Hao, Y. C. Cheng and T. Qiu, Alloy Engineering in Few-Layer Manganese Phosphorus Trichalcogenides for Surface-Enhanced Raman Scattering. Adv. Funct. Mater. **30** (2020)
33. M. Z. Li, Y. M. Gao, X. C. Fan, Y. J. Wei, Q. Hao and T. Qiu, Origin of layer-dependent SERS tunability in 2D transition metal dichalcogenides. Nanoscale Horiz. **6**, 186-191 (2021)
34. Q. G. Li, H. Rao, X. Z. Ma, H. J. Mei, Z. T. Zhao, W. P. Gong, A. Camposeo, D. Pisignano and X. G. Yang, Unusual Red Light Emission from Nonmetallic $Cu_2Te$ Microdisk for Laser and SERS Applications. Adv. Opt. Mater. **10** (2022)
35. L. Tao, K. Chen, Z. F. Chen, C. X. Cong, C. Y. Qiu, J. J. Chen, X. M. Wang, H. J. Chen, T. Yu, W. G. Xie, S. Z. Deng and J. B. Xu, 1T′ Transition Metal Telluride Atomic Layers for Plasmon-Free SERS at Femtomolar Levels. J. Am. Chem. Soc. **140**, 8696-8704 (2018)
36. L. L. Yang, Y. S. Peng, Y. Yang, J. J. Liu, H. L. Huang, B. H. Yu, J. M. Zhao, Y. L. Lu, Z. R. Huang, Z. Y. Li and J. R. Lombardi, A Novel Ultra-Sensitive Semiconductor SERS Substrate Boosted by the Coupled Resonance Effect. Adv. Sci. **6** (2019)
37. M. Shafi, M. X. Zhou, P. Y. Duan, W. Y. Liu, W. J. Zhang, Z. P. Zha, J. J. Gao, S. Wali, S. Z. Jiang, B. Y. Man and M. Liu, Highly sensitive and recyclable surface-enhanced Raman scattering (SERS) substrates based on photocatalytic activity of ZnSe nanowires. Sensor Actuat. B-chem **356** (2022)
38. W. Ji, L. F. Li, W. Song, X. N. Wang, B. Zhao and Y. Ozaki, Enhanced Raman Scattering by ZnO Superstructures: Synergistic Effect of Charge Transfer and Mie Resonances. Angew. Chem. Int. Ed. **58**, 14452-14456 (2019)
39. R. Haldavnekar, K. Venkatakrishnan and B. Tan, Non plasmonic semiconductor quantum SERS probe as a pathway for in vitro cancer detection. Nat. Commun. **9** (2018)
40. Y. C. Zhang, T. R. Yang, J. Li, Q. Zhang, B. Z. Li and M. Gao, Construction of Ru, O Co-Doping $MoS_2$ for Hydrogen Evolution Reaction Electrocatalyst and Surface-Enhanced Raman Scattering Substrate: High-Performance, Recyclable, and Durability Improvement. Adv. Funct. Mater. **33** (2023)

41. Y. S. Peng, C. L. Lin, Y. Y. Li, Y. Gao, J. Wang, J. He, Z. R. Huang, J. J. Liu, X. Y. Luo and Y. Yang, Identifying infectiousness of SARS-CoV-2 by ultra-sensitive $SnS_2$ SERS biosensors with capillary effect. Matter **5**, 694-709 (2022)
42. W. Ji, L. F. Li, J. Guan, M. Mu, W. Song, L. Sun, B. Zhao and Y. Ozaki, Hollow Multi-Shelled $V_2O_5$ Microstructures Integrating Multiple Synergistic Resonances for Enhanced Semiconductor SERS. Adv. Opt. Mater. **9** (2021)
43. Y. M. Dong, Q. H. Xie, S. Wu, J. B. Li, L. Sun and W. Ji, Revealing Adsorption Mechanism of p-Mercaptobenzoic Acid with $TiO_2$ Surfaces Using Electric Field-Enhanced Semiconductor SERS. J. Phys. Chem. C **127**, 9418-9424 (2023)
44. W. Liu, W. T. Li, Y. H. Li, J. F. Li, H. Bai, M. Q. Zou and G. C. Xi, Determine the position of nanoparticles in cells by using surface-enhanced Raman three-dimensional imaging. Nano Res. **14**, 3402-3406 (2021)
45. X. Y. Liu, Z. W. Ye, Q. Xiang, Z. H. Xu, W. H. Yue, C. C. Li, Y. K. Xu, L. Z. Wang, X. M. Cao and J. L. Zhang, Boosting electromagnetic enhancement for detection of non-adsorbing analytes on semiconductor SERS substrates. Chem **9**, 1464-1476 (2023)
46. X. X. Han, W. Ji, B. Zhao and Y. Ozaki, Semiconductor-enhanced Raman scattering: active nanomaterials and applications. Nanoscale **9**, 4847-4861 (2017)
47. H. Sugimoto and M. Fujii, Broadband Dielectric–Metal Hybrid Nanoantenna: Silicon Nanoparticle on a Mirror. ACS Photonics **5**, 1986-1993 (2018)
48. B. Yang, S. Jin, S. Guo, Y. Park, L. Chen, B. Zhao and Y. M. Jung, Recent Development of SERS Technology: Semiconductor-Based Study. ACS Omega **4**, 20101-20108 (2019)
49. J. R. Lombardi and R. L. Birke, Theory of Surface-Enhanced Raman Scattering in Semiconductors. J. Phys. Chem. C **118**, 11120-11130 (2014)
50. J. R. Lombardi, The theory of surface-enhanced Raman scattering on semiconductor nanoparticles; toward the optimization of SERS sensors. Faraday. Discuss. **205**, 105-120 (2017)
51. L. G. Quagliano, Observation of Molecules Adsorbed on III-V Semiconductor Quantum Dots by Surface-Enhanced Raman Scattering. J. Am. Chem. Soc. **126**, 7393-7398 (2004)
52. R. Livingstone, L. Quagliano, N. Perez-Paz, M. Munoz, M. Tamargo, F. Jean-Mary and J. Lombardi, eds., *SERS as sensing method for bio-molecules on MBE-grown quantum dots*, (SPIE, 2005)
53. R. Livingstone, X. C. Zhou, M. C. Tamargo, J. R. Lombardi, L. C. Quagliano and F. Jean-Mary, Surface Enhanced Raman Spectroscopy of Pyridine on CdSe/ZnBeSe Quantum Dots Crown by Molecular Beam Epitaxy. J. Phys. Chem. C **114**, 17460-17464 (2010)
54. X. Fu, Y. Pan, X. Wang and J. R. Lombardi, Quantum confinement effects on charge-transfer between PbS quantum dots and 4-mercaptopyridine. J. Chem. Phys. **134** (2011)
55. Z. Sun, B. Zhao and J. R. Lombardi, ZnO nanoparticle size-dependent excitation of surface Raman signal from adsorbed molecules: Observation of a charge-transfer resonance. Appl. Phys. Lett. **91** (2007)
56. L. Yang, X. Jiang, W. Ruan, B. Zhao, W. Xu and J. R. Lombardi, Observation of Enhanced Raman Scattering for Molecules Adsorbed on $TiO_2$ Nanoparticles: Charge-Transfer Contribution. J. Phys. Chem. C **112**, 20095-20098 (2008)
57. S. Cong, Y. Yuan, Z. Chen, J. Hou, M. Yang, Y. Su, Y. Zhang, L. Li, Q. Li, F. Geng and Z. Zhao, Noble metal-comparable SERS enhancement from semiconducting metal oxides by making oxygen vacancies. Nat. Commun. **6**, 7800 (2015)
58. G. Song, W. Gong, S. Cong and Z. Zhao, Ultrathin Two-Dimensional Nanostructures: Surface Defects for Morphology-Driven Enhanced Semiconductor SERS. Angew. Chem. Int. Edit. **60**, 5505-5511 (2021)
59. X. Wang and L. Guo, SERS Activity of Semiconductors: Crystalline and Amorphous Nanomaterials. Angew. Chem. Int. Edit. **59**, 4231-4239 (2020)
60. X. Wang, W. Shi, Z. Jin, W. Huang, J. Lin, G. Ma, S. Li and L. Guo, Remarkable SERS Activity Observed from Amorphous ZnO Nanocages. Angew. Chem. Int. Edit. **56**, 9851-9855 (2017)
61. X. Wang, W. Shi, S. Wang, H. Zhao, J. Lin, Z. Yang, M. Chen and L. Guo, Two-dimensional Amorphous $TiO_2$ Nanosheets Enabling High-efficiency Photo-induced Charge Transfer for Excellent SERS Activity. J. Am. Chem. Soc. **141**, 5856−5862 (2019)

62. B. J. Messinger, K. U. von Raben, R. K. Chang and P. W. Barber, Local fields at the surface of noble-metal microspheres. Phys. Rev. B **24**, 649-657 (1981)
63. W. Ji, L. Li, W. Song, X. Wang, B. Zhao and Y. Ozaki, Enhanced Raman Scattering by ZnO Superstructures: Synergistic Effect of Charge Transfer and Mie Resonances. Angew. Chem. Int. Edit. **58**, 14452-14456 (2019)
64. Craig F. Bohren and D. R. Huffman, eds., *Absorption and Scattering of Light by Small Particles*, (WILEY-VCH Verlag GmbH & Co. KGaA, 2007)
65. I. Rodriguez, L. Shi, X. Lu, B. A. Korgel, R. A. Alvarez-Puebla and F. Meseguer, Silicon nanoparticles as Raman scattering enhancers. Nanoscale **6**, 5666-5670 (2014)
66. J. M. Luther, P. K. Jain, T. Ewers and A. P. Alivisatos, Localized surface plasmon resonances arising from free carriers in doped quantum dots. Nat. Mater. **10**, 361-366 (2011)
67. Y. Zhao, H. Pan, Y. Lou, X. Qiu, J. Zhu and C. Burda, Plasmonic $Cu_{2-x}S$ Nanocrystals: Optical and Structural Properties of Copper-Deficient Copper(I) Sulfides. J. Am. Chem. Soc. **131**, 4253-4261 (2009)
68. G. Della Valle, F. Scotognella, A. R. S. Kandada, M. Zavelani-Rossi, H. Li, M. Conforti, S. Longhi, L. Manna, G. Lanzani and F. Tassone, Ultrafast Optical Mapping of Nonlinear Plasmon Dynamics in $Cu_{2-x}Se$ Nanoparticles. J. Phys. Chem. Lett. **4**, 3337–3344 (2013)
69. D. Dorfs, T. Härtling, K. Miszta, N. C. Bigall, M. R. Kim, A. Genovese, A. Falqui, M. Povia and L. Manna, Reversible Tunability of the Near-Infrared Valence Band Plasmon Resonance in $Cu_{2-x}Se$ Nanocrystals. J. Am. Chem. Soc. **133**, 11175-11180 (2011)
70. K. Manthiram and A. P. Alivisatos, Tunable Localized Surface Plasmon Resonances in Tungsten Oxide Nanocrystals. J. Am. Chem. Soc. **134**, 3995-3998 (2012)
71. I. Kriegel, J. Rodríguez-Fernández, A. Wisnet, H. Zhang, C. Waurisch, A. Eychmüller, A. Dubavik, A. O. Govorov and J. Feldmann, Shedding Light on Vacancy-Doped Copper Chalcogenides: Shape-Controlled Synthesis, Optical Properties, and Modeling of Copper Telluride Nanocrystals with Near-Infrared Plasmon Resonances. ACS Nano **7**, 4367-4377 (2013)
72. H.-J. Yang, C.-Y. Chen, F.-W. Yuan and H.-Y. Tuan, Designed Synthesis of Solid and Hollow $Cu_{2-x}Te$ Nanocrystals with Tunable Near-Infrared Localized Surface Plasmon Resonance. J. Phys. Chem. C **117**, 21955-21964 (2013)
73. R. Buonsanti, A. Llordes, S. Aloni, B. A. Helms and D. J. Milliron, Tunable Infrared Absorption and Visible Transparency of Colloidal Aluminum-Doped Zinc Oxide Nanocrystals. Nano Lett. **11**, 4706-4710 (2011)
74. J. A. Faucheaux and P. K. Jain, Plasmons in Photocharged ZnO Nanocrystals Revealing the Nature of Charge Dynamics. J. Phys. Chem. Lett. **4**, 3024-3030 (2013)
75. A. M. Schimpf, N. Thakkar, C. E. Gunthardt, D. J. Masiello and D. R. Gamelin, Charge-Tunable Quantum Plasmons in Colloidal Semiconductor Nanocrystals. ACS Nano **8**, 1065-1072 (2014)
76. G. Garcia, R. Buonsanti, E. L. Runnerstrom, R. J. Mendelsberg, A. Llordes, A. Anders, T. J. Richardson and D. J. Milliron, Dynamically Modulating the Surface Plasmon Resonance of Doped Semiconductor Nanocrystals. Nano Lett. **11**, 4415-4420 (2011)
77. T. R. Gordon, T. Paik, D. R. Klein, G. V. Naik, H. Caglayan, A. Boltasseva and C. B. Murray, Shape-Dependent Plasmonic Response and Directed Self-Assembly in a New Semiconductor Building Block, Indium-Doped Cadmium Oxide (ICO). Nano Lett. **13**, 2857-2863 (2013)
78. X. Song, J. Li, Q. Kong, H. Bai and G. Xi, Molybdenum Nitride Porous Prisms with a Strong Plasmon Resonance Effect in the Visible Region for Surface-Enhanced Raman Spectroscopy. J. Phys. Chem. Lett. **13**, 6777-6782 (2022)
79. J. Li, W. Yi, Y. Li, W. Liu, H. Bai, Z. Jiao, Y. Zhang, X. Wang, M. Zou and G. Xi, Nitrogen-Doped Titanium Monoxide Flexible Membrane for a Low-Cost, Biocompatible, and Durable Raman Scattering Substrate. Anal. Chem. **93**, 12776-12785 (2021)
80. R. Du, W. Yi, W. Li, H. Yang, H. Bai, J. Li and G. Xi, Quasi-metal Microwave Route to MoN and $Mo_2C$ Ultrafine Nanocrystalline Hollow Spheres as Surface-Enhanced Raman Scattering Substrates. ACS Nano **14**, 13718-13726 (2020)
81. N. L. Swanson and D. B. Billard, Multiple scattering efficiency and optical extinction. Phys. Rev. E **61**, 4518-4522 (2000)

82. I. Alessandri, Enhancing Raman Scattering without Plasmons: Unprecedented Sensitivity Achieved by $TiO_2$ Shell-Based Resonators. J. Am. Chem. Soc. **135**, 5541-5544 (2013)
83. D. Qi, L. Lu, L. Wang and J. Zhang, Improved SERS Sensitivity on Plasmon-Free $TiO_2$ Photonic Microarray by Enhancing Light-Matter Coupling. J. Am. Chem. Soc. **136**, 9886-9889 (2014)
84. B. Qiu, M. Xing, Q. Yi and J. Zhang, Chiral Carbonaceous Nanotubes Modified with Titania Nanocrystals: Plasmon-Free and Recyclable SERS Sensitivity. Angew. Chem. Int. Edit. **54**, 10643-10647 (2015)
85. M. Yilmaz, M. Ozdemir, H. Erdogan, U. Tamer, U. Sen, A. Facchetti, H. Usta and G. Demirel, Micro-/Nanostructured Highly Crystalline Organic Semiconductor Films for Surface-Enhanced Raman Spectroscopy Applications. Adv. Funct. Mater. **25**, 5669-5676 (2015)
86. M. Yilmaz, E. Babur, M. Ozdemir, R. L. Gieseking, Y. Dede, U. Tamer, G. C. Schatz, A. Facchetti, H. Usta and G. Demirel, Nanostructured organic semiconductor films for molecular detection with surface-enhanced Raman spectroscopy. Nat. Mater. **16**, 918-924 (2017)
87. M. Yilmaz, M. Erkartal, M. Ozdemir, U. Sen, H. Usta and G. Demirel, Three-Dimensional Au-Coated Electrosprayed Nanostructured BODIPY Films on Aluminum Foil as Surface-Enhanced Raman Scattering Platforms and Their Catalytic Applications. ACS App. Mater. Inter. **9**, 18199-18206 (2017)
88. W. Ji, L. Li, J. Guan, M. Mu, W. Song, L. Sun, B. Zhao and Y. Ozaki, Hollow Multi-Shelled V2O5 Microstructures Integrating Multiple Synergistic Resonances for Enhanced Semiconductor SERS. Adv. Opt. Mater. **9**, 2101866 (2021)
89. L. Yang, Y. Peng, Y. Yang, J. Liu, H. Huang, B. Yu, J. Zhao, Y. Lu, Z. Huang, Z. Li and J. R. Lombardi, A Novel Ultra-Sensitive Semiconductor SERS Substrate Boosted by the Coupled Resonance Effect. Adv. Sci. **6**, 1900310 (2019)
90. Y. Peng, C. Lin, L. Long, T. Masaki, M. Tang, L. Yang, J. Liu, Z. Huang, Z. Li, X. Luo, J. R. Lombardi and Y. Yang, Charge-Transfer Resonance and Electromagnetic Enhancement Synergistically Enabling MXenes with Excellent SERS Sensitivity for SARS-CoV-2 S Protein Detection. Nano-Micro Lett. **13**, 52 (2021)
91. 92.J. Li, J. Li, W. Yi, M. Yin, Y. Fu and G. Xi, A Metallic Niobium Nitride with Open Nanocavities for Surface-Enhanced Raman Spectroscopy. Anal. Chem. **94**, 14635-14641 (2022)

# Chapter 5
# Towards Reliable and Practical SERS




**Wafaa Aljuhani, Yingrui Zhang, Chunchun Li, Yikai Xu, and Steven E. J. Bell**

**Abstract** The widespread availability of effective enhancing substrates means that the challenge for practical SERS studies has now moved to making the measurements reliable. Here, we first consider the factors which need to be controlled to minimise variability in SERS measurements. This is followed by discussion of methods, such as use of internal standards, which can further reduce uncertainty and increase the robustness of SERS measurements.

**Keywords** SERS · Reproducible · Internal standards

## 5.1 Introduction

SERS has now expanded from a technique for simple detection and characterisation of molecules at low concentration to a broad range of approaches which range from the development of particles carrying SERS labels which can be tracked in biological media [1] to methods for age-grading mosquitoes [2]. However, this chapter will concentrate on the challenge of making SERS a practical technique, which requires

W. Aljuhani · Y. Zhang · S. E. J. Bell (✉)
School of Chemistry and Chemical Engineering, Queen's University Belfast, Belfast, U.K.
e-mail: s.bell@qub.ac.uk

W. Aljuhani
e-mail: waljuhani01@qub.ac.uk

Y. Zhang
e-mail: yingrui.zhang@qub.ac.uk

C. Li
University of Shanghai for Science and Technology, 516 Jungong Road, Shanghai, China 200093
e-mail: chunchun_li@usst.edu.cn

Y. Xu
East China University of Science And Technology Shanghai, 130 Meilong Road, Shanghai, China 200237
e-mail: yikaixu@ecust.edu.cn

© The Author(s), under exclusive license to Springer Nature Singapore Pte Ltd. 2024

M. Procházka et al. (eds.), *Surface- and Tip-Enhanced Raman Scattering Spectroscopy*,
https://doi.org/10.1007/978-981-97-5818-0_5

development of methods where the same sample reliably gives the same SERS signal. Here, this is treated as a problem in analytical SERS, since this provides a useful framework for discussing the key issues. However, even if the goal is simply to observe the spectra of molecules in a sample, such as screening for drugs of abuse [3], it is still important that this can be done reliably, even if the degree of reproducibility can be more relaxed.

Routinely achieving reproducible results in SERS is a challenging problem because generating the signal depends on a sequence of processes and each of these must work consistently, since a failure or introduction of variance at any stage in the process will ultimately carry through to variation/uncertainty in the spectra which are obtained. This begins with creation of enhancing substrates with low batch-to-batch variation both in their plasmonic properties and surface chemistry. The properties of the surface are more difficult to characterise than the bulk plasmonic properties or physical structure but are crucial in determining the signal obtained with any given analyte. Even if the substrate is prepared with high reproducibility, there are still potential issues with degradation during storage and then numerous potential sources of variance in use. These can be due to changes in intensity which are observed with time during the measurements or point-to-point variation in the signal enhancement provided by solid substrates. In addition, matrix effects are significant and can dramatically reduce the signal. Methods to reduce all these potential sources of variance have been developed and are discussed below but although these can be effective, some of these problems are very challenging. For example, while reducing point-to-point variation on solid substrates below 10% is readily achievable, reducing below 1% is extremely difficult. Since the effects of variance in each individual part of the processes that lead to generation of the signal are cumulative, keeping the variance in the resulting absolute signal level low requires close control of multiple factors. This is difficult even in well-controlled environments but becomes even more challenging when practical measurements of real life samples in matrices of variable composition need to be made. The first section of this chapter discusses how variation in the absolute signal can be minimised using various control procedures.

Of course, even with very careful optimisation of experimental conditions, some residual variance in the absolute signal will remain or random events can give unexpected deviations in the spectra. If the residual variance is within the acceptable limits for a particular study, it may not pose an issue; but control of the variables may not give sufficiently high precision, for example in an analytical measurement. In addition, if a measurement leads to an important outcome or decision, it is essential that a high degree of confidence can be placed in it and that means that the methods need to be not only accurate and precise but also robust, i.e. not subject to variation caused by outside sources. The second part of this Chapter is centred on methods for making SERS practical by obtaining higher levels of reproducibility and robustness while working within the performance envelope which can be achieved by careful control of variables. This includes averaging signals in various ways, using standard addition and, crucially, using internal standards. The central argument is that adding these techniques to experimental approaches where variance has already been minimised as far as possible can gives SERS levels of reproducibility and robustness

that equal those of other forms of spectroscopy and indeed established analytical measurements.

## 5.2 Optimising Reproducibility of the Absolute Signal

### *5.2.1 Figures of Merit for Defining Performance and Reproducibility*

It is useful to begin by clarifying which figures of merit are most appropriate in this context. The most widely used measure of the enhancement given by a substrate is the EF which is widely defined as [4]:

$$\mathrm{EF} = \frac{I_{\mathrm{SERS}}}{N_{\mathrm{SERS}}} \cdot \frac{N_{\mathrm{RS}}}{I_{\mathrm{RS}}}.$$

Where $I_{\mathrm{SERS}}$ and $I_{\mathrm{RS}}$ are the intensities of the SERS and normal Raman signals being compared and the $N$ values are the respective numbers of molecules giving the signals. However, a high EF is not in itself an indicator that the substrate under test is the most suitable for a given measurement. Even setting aside the questions around how reliable any estimates of the EF for a given test molecule can actually be, there is a much larger issue that the measured enhancement is strongly sample dependent [5]. This is because, even though the use of the intensity ratio can correct for differences in the scattering probability between various test molecules, it does not correct for differences in their adsorption to the surface. In the most extreme case, no enhancement will be observed if the test molecule does not adsorb in the enhancing regions of the substrate, even if the substrate has excellent plasmonic properties. More commonly, it means that EFs are measured using strongly adsorbing molecules, to eliminate the possibility of poor adsorption. However, although this gives a measured EF that reflects the plasmonic properties of the substrate, it cannot be used to predict the EF which the same substrate will give for untested molecules whose adsorption properties are unknown and may be poor. More broadly, there is a natural tendency to assume that the best substrate is the one which provides the highest EF but it is also useful to consider if higher EFs are even necessary or relevant for the measurements which are being carried out. Materials with lower enhancement may be preferable if they can have other properties which make them desirable. For example, Fig. 5.1 shows calibration curves for detection of phenytoin obtained using substrates which contained Au aggregates held within dry hydroxyethylcellulose (HEC) films [6]. Even though the signals obtained from the films were 2 orders of magnitude lower than for the parent colloid, they were sufficiently high to provide data in the concentration range required for therapeutic monitoring. So in this case, the reduction in sensitivity on moving from simple aqueous colloids to films was

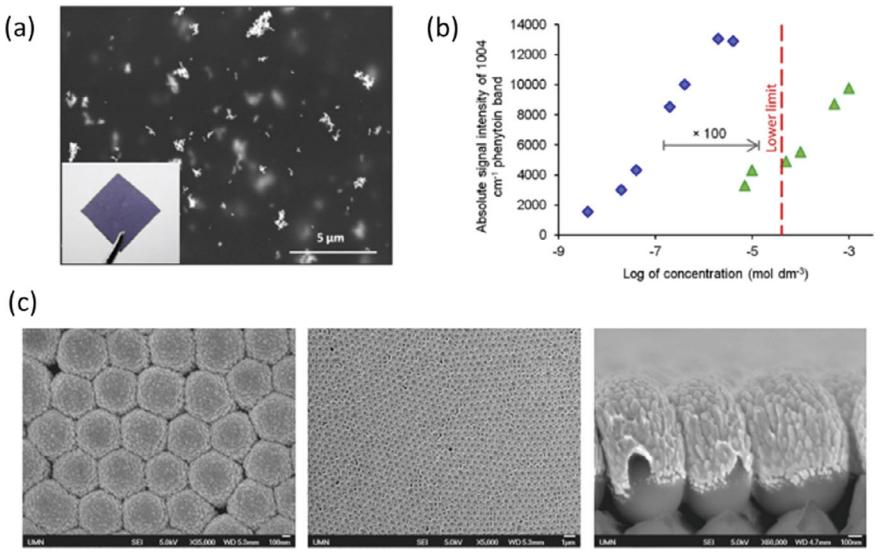



**Fig. 5.1** **a** SEM image of Au aggregates held within a dried hydroxyethylcellulose swellable polymer film, inset shows an optical image of the material. **b** Signal versus log (concentration) plots for detection of phenytoin comparing the parent Au colloid to the polymer films shown in **a**. Dotted line marks the lower limit of the target therapeutic range. **c** SEM images of a film-over-nanosphere substrate which contrasts with the substrate in **a** by showing order at the μm scale. Reproduced from **a**–**b** reference [6] and **c** [7] with permission

outweighed by the advantages which the films brought for practical applications, in particular their ease of use and long shelf life.

The other common performance metric used for SERS is the variance observed when the measurement is repeated with the same sample, commonly expressed at the RSD of the signal intensity. The most relevant measurement depends on the nature of the substrate. If it is uniform and stable, so that repeated measurements on the same sample give the same result, then the variation that occurs when fresh substrates are prepared and measured may be larger and therefore more important to characterise and control. Conversely, if the substrate is non-uniform, variance can be introduced by probing different points on the surface and, since there is typically no way of determining which regions give high or low readings, repeated measurements on even the same sample will give different readings, leading to an important source of variance which needs to be characterised. In either case, the variance can be characterised using the RSD of appropriate repeated measurements, an approach which can also be extended to batch-to batch variation in substrates. This means there are several RSD values that may be relevant for a single substrate, where the size of the absolute signal for a given concentration of target molecule may depend on point-to-point variation, differ between substrates from the same batch, and also show batch-to-batch variation.

Finally, the LOD of a given method (i.e. combination of substrate, instrument and target molecule) is often quoted to indicate the sensitivity achieved. Although this is not strictly correct, since sensitivity refers to the change in signal given by a change in concentration (i.e. the slope of a calibration line), the meaning of the term is widely understood in this context. More importantly, the LOD has very low reproducibility, in the sense of being a generally transferable numerical parameter than can characterise the performance of a substrate across a range of conditions. This is because it is normally defined as the concentration at which the signal is $> 3 \times$ the noise level. Therefore, changing to testing with a molecule with a high scattering cross section (e.g. a dye which is in resonance with the excitation laser) will increase the signal at a given concentration and therefore give lower LOD. Even if the test molecule is fixed, the noise level varies between instruments, so again the LOD obtained even with the same substrate and test molecules can be changed by switching instruments.

Overall, it is clear that the figures of merit used to describe the results of testing SERS methods are not ideal. However, this does not mean they have no value and provided they are treated with suitable caution they can provide some guidance on the success of the measurement. They are most useful when being used to compare cases which are broadly similar, i.e. using instruments with the same general levels of performance, molecular targets which have comparable scattering cross sections and adsorb to the surface in similar ways. It becomes increasingly difficult to make meaningful comparisons between results as the experimental conditions diverge. Fortunately, for the purposes of the current discussion, the reproducibility (as measured by the RSD of the signal) is probably the most transferable of all the parameters between experiments. It is easy to determine by carrying out repeated measurements (although which measurements need to be repeated is also important), and it is to some extent self-correcting because it is expressed as a percentage of the signal.

### *5.2.2 Plasmonic Enhancement*

The first step in carrying out a SERS measurements is to choose the enhancing substrate. However, the huge variety of enhancing substrates which have now been reported means that providing even a brief comment on the effectiveness of each would exceed the length of this chapter and would in any case rapidly become obsolete. Instead, aspects of the substrates which are important for generating reproducible SERS are discussed here and only illustrative examples of how these have been implemented through creation of particular substrates are included.

As a general observation, it is fair to say that preparation of nanomaterials has now developed into a mature technology and that problems with preparing enhancing substrates that provide acceptable levels of enhancement, which were common in early SERS work, have now been largely overcome. There is an ongoing search for increased enhancement, but as noted above, this may not be important in the context of many real life measurements. Figure 5.2 illustrates the extent to which

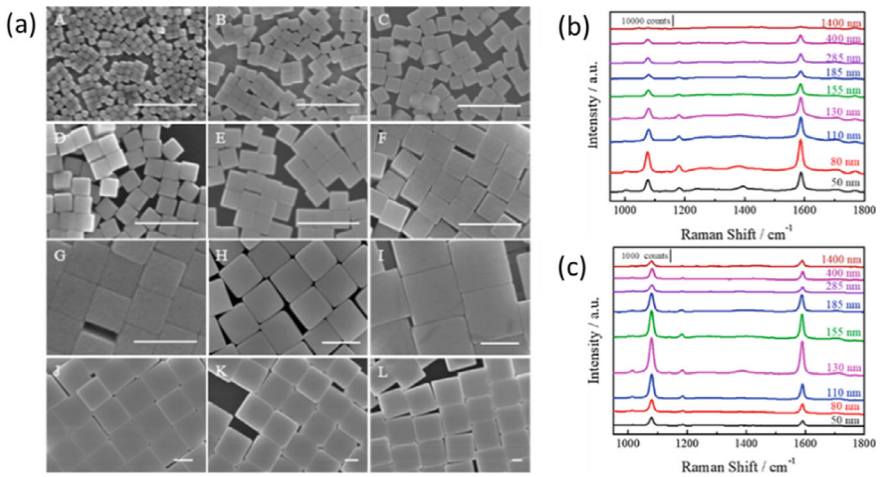



**Fig. 5.2** **a** SEM images of Au@Ag core–shell nanocubes with edge length ranging from 50 ± 3 nm to 1400 ± 83 nm. **b**, **c** SERS spectra of the nanocubes embedded with 4-methylthiobenzoic acid (MBA) internal standard assembled on a Au film. The data show the variation in SERS intensity obtained as the edge length was systematically altered from 50 to 1400 nm. Data were recorded using **b** 532 nm and **d** 785 nm excitation. Reproduced from reference [8] with permission

the area has matured by showing a single example, which is SEM and SERS data for a series of Au@Ag core–shell nanocubes spanning a very large range of edge lengths assembled on a Au film embedded with a 4-methylthiobenzoic acid (MBA) internal standard [8]. The data show the variation in SERS intensity obtained as the edge length was systematically altered from 50 to 1400 nm. Numerous other studies describing systematic preparation and optimisation of SERS substrates are available in the literature [9]. One notable trend is towards preparation of low-cost enhancing materials based on nanoparticles (NP) distributed on or in a porous support, most commonly paper, which can potentially give materials whose cost makes them suitable for routine applications [10]. In addition, NPs in various sizes, shapes, and materials suitable for SERS are commercially available, as are solid substrates [11, 12].

#### 5.2.2.1 Point-To-Point Variation in EF

Even a brief glance at different types of enhancing substrates under SEM reveals that some appear to be highly regular and uniform while others are extremely heterogeneous at the nm and um scales. Although it might appear obvious that randomly structured substrates would give very large variations in absolute signal while ordered materials would show high point-to-point reproducibility, this is only partly true. One reason is that since the EF is extremely sensitive to the changes in structure on the < nm scale, even materials which appear well ordered on the μm scale, as in the

images shown in Fig. 5.1, may have random variation at the < 10 nm length scales [7]. Conversely, with aggregated colloids, the inherent non-uniformity typically averages out over the course of a measurement as different aggregates move into and out of the probed volume.

It is difficult to provide a single typical RSD of point-to-point variation in solid substrates (particularly since the value depends on the measurement method used (see Sect. 5.3.1.1) but a recent survey of 49 substrates showed that the vast majority of solid substrates had point-to-point RSD of 5–15%, [13], which gives a reasonable indication of the levels of reproducibility that can be expected from solid substrates. Notably, there were very few values < 5% but this does not necessarily mean that absolute signal levels from ordered substrates cannot be obtained. Some systems, such as interfacial nanoparticle assemblies, have shown point-to-point variation of ca. 1% [14], and even for much less uniform substrates, averaging over numerous points can significantly reduce the variance in absolute signal height, as discussed in Sect. 2.1.1.

#### 5.2.2.2 Degradation in Storage

An important consideration for SERS substrates of all types is degradation during storage. The most obvious mechanism is oxidation of Ag substrates, which can happen surprisingly rapidly and can change the enhancement by altering the affinity of the target molecules for the surface or change any chemical contribution to the plasmonic enhancement. In an early study, Han et al. used ozone exposure to oxidise the surface of Ag NPs on a glass support [15]. Formation of $Ag_2O$ was detected by XPS while SERS was probed using the signal from trans-1,2-bis(4-pyridyl)ethylene (BPE) in ethanol as a model analyte. The EF of the 1200 $cm^{-1}$ BPE marker band was found to decrease by orders of magnitude as a thin oxide layer (<2 nm) was formed. See Fig. 5.3 Notably, even in this early study, it was found that the rate of decrease of the SERS signal was analyte dependent and that the signal from thiocyanide anions decreased markedly less than those of BPE during the first hour of ozone treatment. Subsequent studies by Matikienen et al. have shown that the signal from Ag surfaces can decrease rapidly even in laboratory air. In those experiments which used dry particles on a solid support, the signal from the R6G test molecule decreased by 60% in the first 5 h of exposure while the RSD of signals from different points on the surface rose from the initial 7% to 21% [16]. Of course, if oxygen exposure is reduced by the use of appropriate packaging, the lifetime can be significantly extended. Commercial Silmeco SERS substrates-based Ag tipped Si nanowires (which are packaged under inert gas) or Ag nanorod substrates stored in Ar-filled pouches have lifetimes of 1 year or longer [17]. Au surfaces are less prone to oxidation and so are favoured in applications where substrates with exposed dry surfaces need to be used for extended periods.

The extent of oxidation in metal colloids has not been as extensively studied as for dry substrates, partly because the fact that colloids are so extensively used demonstrates that oxidation does not appear to prevent detection of many different

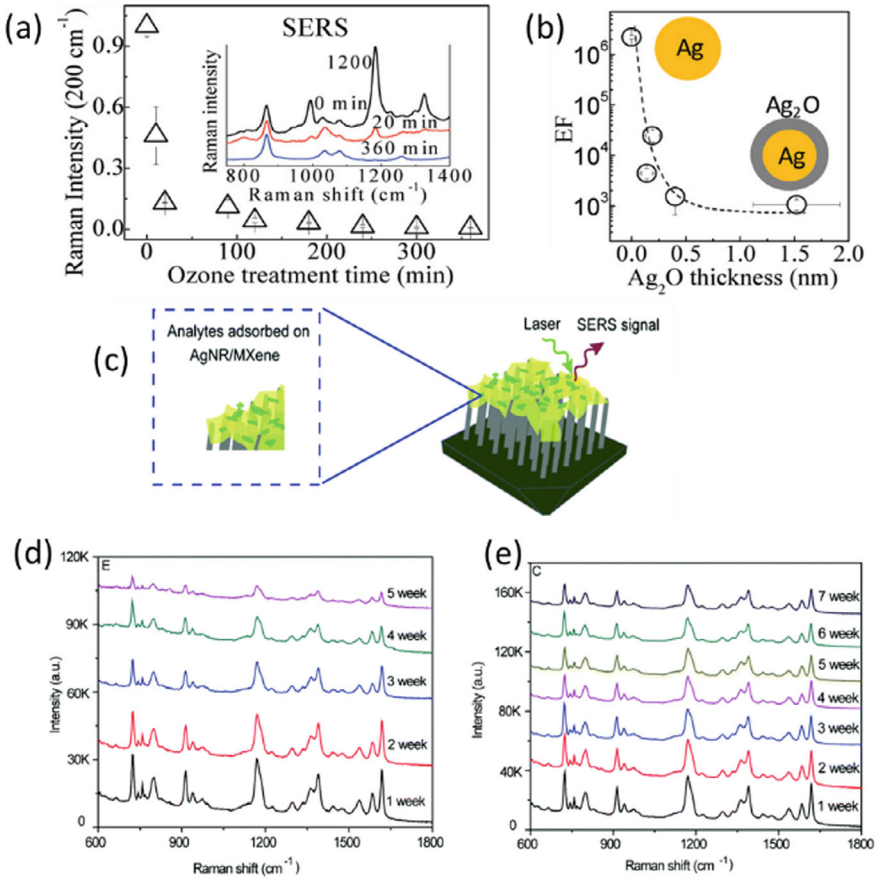



**Fig. 5.3** **a**, **b** Effect of oxidation on SERS signals from Ag particles, **a** Plot showing decrease in intensity of SERS signals from the BPE (2-bis(4-pyridyl)ethylene) test molecule with exposure to zone for different times. **b** Plot showing correlation between EFs calculated for BPE in ethanol and estimated thickness of the $Ag_2O$ layer formed. **c** Schematic diagram of SERS substrate composed of Ag nanorods covered with MXene nanosheet layer. **d**, **e** SERS spectra of crystal violet test molecule on Ag NR substrate at times shown after preparation **d** without or with **e** MXene layer. Reproduced from **a**–**b** reference [15], **c**–**e** reference [18] with permission

types of molecules. However, it has been shown that oxidation of Ag altered both the extent and type of bonding between nitrobenzene and Ag and that the sensitivity of the measurements could be increased by flushing with Ar to prevent oxidation [19]. More recently, in studies on polycyclic aromatic hydrocarbons (PAHs), it was found that while PAHs adsorb strongly to Au NPs sitting at liquid/liquid interfaces and naphthalene, for example, can be detected at concentrations $<10^{-5}$ M, they do not adsorb to Ag NPs, even though the binding energy would suggest that this would also be favourable [20]. In this case, it was found that the oxidation of the Ag surface which occurred even 20 min after preparation was sufficient to prevent the π-π interactions

which drive adsorption of the PAHs. However, PAHs could be detected with freshly prepared Ag NPs. Notably, the Ag particles could be used to detect other molecules, such as citrate ions even under conditions where oxidation prevented detection of PAHs.

SERS substrates may be protected from degradation by an external shell or coating. Scrabelli et al. have demonstrated polymer-encapsulated Au nanoclusters for use as tagged particles which resisted even immersion in aqua regia but for applications where the target molecules adsorb to the surface and are enhanced the shell needs to be thinner, so that the targets can sit in the enhanced electric field near the surface [21]. The best known example of materials using this approach is that particles are coated by a thin (1–2 nm) $SiO_2$ shell deposited to make SHINERS [22] but many other surface coverings are now reported. For example, Fang et al. have reported arrays covered with MXene which serves a dual purpose of enhancing adsorption and extending the lifetime; in this case, as shown in Fig. 5.3, the rate of loss was significantly reduced but still fell to 50% in 7 weeks [18]. Similarly, with arrays of Ag particles partly immersed in polyacrylamide supports, the decrease of the signal given by Ag and Au NPs over 21 days was 15–20% [23]. Longer shelf lives are possible if the particles are fully encapsulated, as in the example above but this raises the problem of how the analyte can approach the surface. This can be solved by preparing the NPs in a swellable polymer host, so that they are protected during storage but can be activated by adding aqueous analyte which causes the films to swell and allows contact between the surface and target molecules [6, 24]. Of course, it is essential that the polymers do not interact strongly with the NPs so that the surface is not blocked after rehydration. Both polycarbophil and HEC have been used for this application, and it was found that Ag NP aggregates in dried HEC films retained 70% of their SERS activity after being stored in air for 1 year [24].

### *5.2.3 Surface Chemistry of Substrate*

In development of new substrates for SERS, the plasmonic enhancement is often emphasised but the absolute signal that will be obtained in a SERS measurement is a function of both the probability that a molecule is found in the enhancing region and the enhancement which it experiences when it is located there. This means that the surface chemistry is critical in determining the reproducibility of the signal but it is often ignored in favour of parameters which are easier to measure, such as particle size. This is starting to change, particularly since it is recognised that SERS can itself be a superb in situ probe of the surface species present in exactly the most appropriate spot, the hot spots of the enhancing substrates [25].

#### 5.2.3.1 Mechanisms of Adsorption

In order to obtain reproducible SERS signals from enhancing substrates prepared in the same way, it is essential that not only is the nanostructure sufficiently consistent to give similar plasmonic enhancement but also that the binding of the target to the surface is similar each time. However, this is complicated by the fact that the surface binding of the target depends not only on the nature of the target but also on what surface species are already present. The established model is that analytes can typically be regarded as adsorbing by either displacing existing surface species or by co-adsorbing without ligand displacement [26]. In the case of the displacement mechanism, the target molecule can only be detected if it is more strongly binding than the exiting surface layer, so for relatively weakly binding species, it is important not to have strongly adsorbed ligands on the surface. This was first shown for halide ions and dipicolinic acid but is a general effect [26]. If the target molecule is strongly binding, such as an alkane thiol, it would be expected to successfully compete and the signals it generates would be expected to be more reproducible than those for weakly binding analytes, where more care needs to be taken to prevent interfering ions or molecules perturbing the adsorption. With co-adsorbing targets, similar considerations apply since the surface electrostatic interactions, for example, may be perturbed by changes in the zeta potential of the surface.

Of course, in many cases, the target may not adsorb strongly by either mechanism, so the surface may need to be modified in some way to increase the probability that the target will sit within the enhancing region of the substrate [28, 29].

This can be simply by altering the charge on the surface to convert metal nanoparticles, which typically have a negative zeta potential, to positively charged surfaces that can attract anions [30]. Figure 5.4 shows data for detection of scopolamine butyl bromide (SB, a tropane alkaloid) using colloids aggregated with different metal salts [27]. In this case, the addition of $I^-$ dramatically increased the signal due to a specific interaction with the SB but this example was included here as an example of a system where it was chemical effects rather than plasmonics which controlled the observed signal. The figure shows that with different salts, the extinction spectra of the aggregated colloids barely changed between samples but they gave spectra which differed in intensity by several orders of magnitude. Selective surface layers such as boronic acid [31], which binds glucose, molecularly imprinted polymers (MIPs) [32], or metal organic frameworks (MOFs) [33] have also been used to increase detection of specific molecular targets. The advantage of modified surfaces is that the surface chemistry is deliberately controlled, rather than being the result of whatever synthesis method was used, so in general they are expected to be less susceptible to random variation and to be better understood than those of as-prepared colloids.

#### 5.2.3.2 Matrix Effects

The discussion above suggests that, provided the enhancing substrate is prepared with the correct plasmonic properties and consistent surface chemistry, obtaining

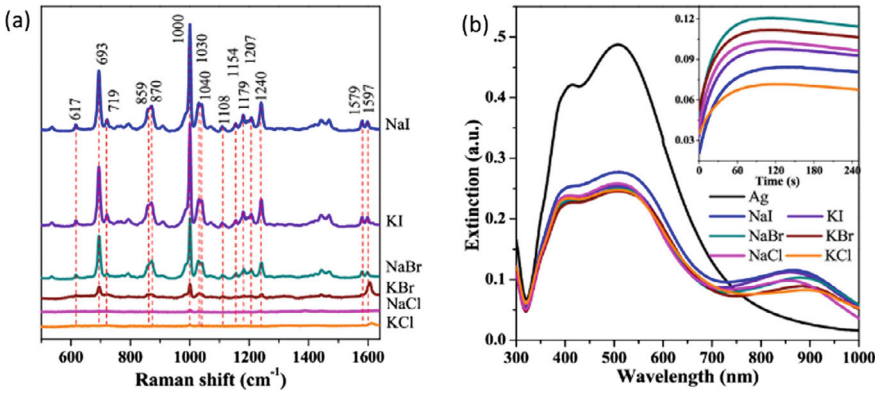



**Fig. 5.4** **a** SERS spectra of scopolamine butyl bromide (SB) obtained with Ag NPs and different aggregating salts, all at 1 M concentration. **b** Extinction spectra of Ag NPs aggregated with the same salts. Inset shows kinetics of aggregation monitored at 885 nm. Reproduced from reference [27] with permission

reproducible SERS signals from the same concentration of molecules in a sample should be readily achievable and in many cases this is true. There are now numerous examples of studies in the literature where a straightforward approach gives RSDs in signals of <20% without significant problems, provided simple precautions, such as using a standard sample to check that there is no significant change in EF between batches of substrate, are followed.

However, although this is possible for samples in a matrix which does not interfere or is at least consistent, as is the case for clean aqueous solution of the test molecule, it is not possible when matrix interference effects arise, which is often the case in real-world samples ranging from biofluids to foodstuffs [35]. Figure 5.5 shows the example of detection of benzotriazole in water using a substrate composed of PVA films containing Ag NPs and covered with MXene sheets where the absolute signal varied with pH, NaCl concentration and presence of other metal ions [34].

There are two separate but interconnected issues with matrix interference, the first is that the interference may be so extreme as to prevent detection, the second is if anything more problematical, which is that the extent of signal reduction may randomly vary between samples as the matrix changes composition. It may be possible to remove interfering species from samples using pre-treatment processes of various levels of sophistication and indeed this is very common across all types of chemical analysis. For example, Zhu et al. were able to obtain reproducible signals of creatine from urine samples using a simple liquid–liquid extraction process but often the main reason for choosing SERS is speed and convenience, so if more complex sample pre-treatment process is required, this may negate the advantages which SERS can provide [36]. This makes it attractive to suppress interference using convenient methods such as coating the substrate with a modifying layer that at least suppress the interference, for example, protein can interfere with measurements by

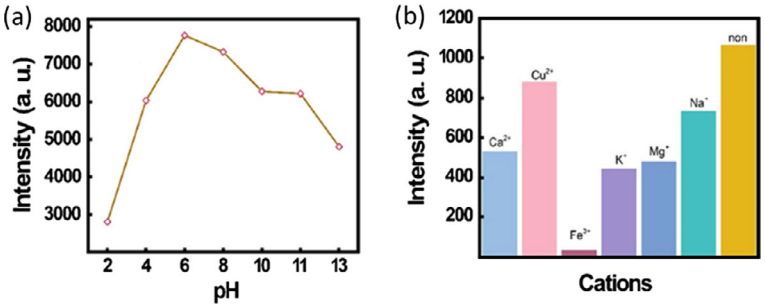



**Fig. 5.5** Effect of external perturbations on the intensity of BTA (benzotriazole) SERS signals obtained with nanocomposite Ag-PVA/Mxene substrates. **a** Intensity changes with pH. **b** Effect on the intensity of the BTA signal of adding $1 \times 10^{-4}$ M chloride salts of the cations shown. Reproduced from reference [34] with permission

adsorbing to the surface of and blocking access of target molecules but this can be minimised by adding a zwitterionic polymer brush layer to the surface [37].

Similarly, paper-based substrates, which are becoming popular due to their simplicity and low cost, [10] can also be used to filter samples if the SERS-active layer is applied to one side of the substrate and the analyte is applied from the other side. Figure 5.6 shows data for a paper-based substrate where the aggregated particles were sprayed onto the surface as a suspension in a dilute hydrogel which dried as a swellable film on the surface [38]. The figure shows the similarity between calibration plots of thiram concentration obtained using the paper substrate for samples in pure water and one which contained sufficient suspended solid matter to completely mask the normal SERS signal.

## *5.2.4 Sources of Variance in Experiments*

### 5.2.4.1 Aggregation

While solid substrates suffer from spatial non-uniformity, salt-aggregated colloids show significant temporal variations in the enhancement they provide. Initially, SERS signals will increase as the aggregates form and create plasmonically active "hot spots" but the aggregates will inevitably continue to grow over time because the added salt, and the associated charge screening effect, is still present. This leads to the eventual growth of the aggregates to the point where they sediment out of the suspension, so there is a finite time window within which measurements can be made. This means that it is normally necessary to find a salt concentration which is sufficiently high to give aggregation within an acceptable amount of time but not so high that the aggregates sediment out before the measurement is made. Figure 5.7

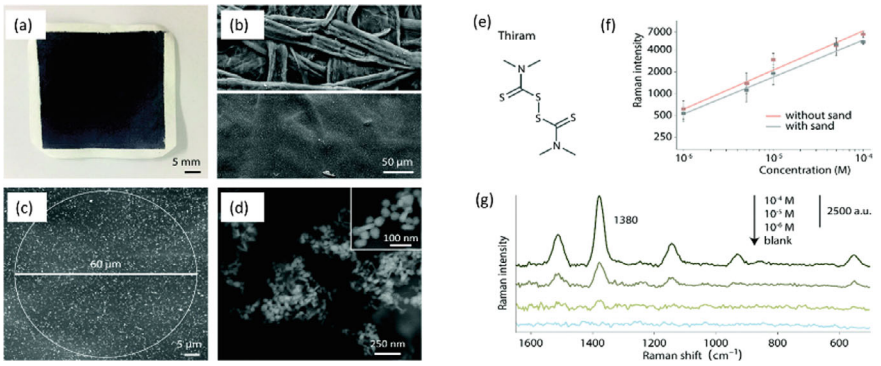



**Fig. 5.6** Illustration of heterogeneity on different length scales in a SERS substrate composed of Ag nanoparticle aggregates held within a hydroxy ethyl cellulose (HEC) polymer matrix sprayed onto a paper support. **a** Optical image of the substrate, which has an area is several $cm^2$. **b** SEM images of filter paper sprayed with aggregated NPs in 0.6 wt% (top) and 1% (bottom) HEC solution. **c** SEM image showing the distribution of nanoparticle aggregates in the substrate that fall within a 60 µm diameter laser spot. **d** SEM image showing the NP aggregates at high magnification. **e** Structure of thiram. **f** Semi-log plot of the SERS intensity of different concentrations of aqueous thiram solutions with (grey) and without (orange) sand contamination. Data points are an average over 5 measurements and error bars represent ±1 SD. **g** SERS spectra of several solutions contaminated with sand and containing different concentrations of thiram. Reproduced from reference [38] with permission

shows a plot of signal versus time for different concentrations of salt where this effect is clear.

To obtain reproducible SERS, it is necessary to record spectra at the same degree of aggregation each time. This would obviously require adding the same amount of salt and waiting a fixed time before making the measurement. Surprisingly, few literature reports state the time after aggregation when spectra were recorded or indeed if this was any consciously fixed value for the delay, although this may be set by the process where spectra are recorded since the mixing, sample transfer etc. may take similar amounts of time for every measurement. In the case where the time is monitored and the interparticle gaps are also controlled, the sample to sample repeatability can be excellent (<1%) [13]. Reproducibility will be improved if there is a long time window over which the signal is not simply visible but actually stays reasonably constant. The conditions where the plateau time is maximised can be found by varying the salt concentration as shown in Fig. 5.7. An alternative to allowing dynamic aggregation and fixing the observation point is to stop aggregation after a fixed time. This is not possible with simple salt addition but can be achieved if other physical methods are used. A recent study has used a "freeze–thaw-ultrasonication" method to obtain stable colloidal Ag nano-aggregates which gives a SERS detection window more than 25 min [40] but even greater stability can be achieved using assembly at liquid–liquid interfaces. In this case, the particles in an aqueous solution in contact with an immiscible solvent such as DCM will tend to move to the interface to reduce the interfacial energy. This process will normally stop

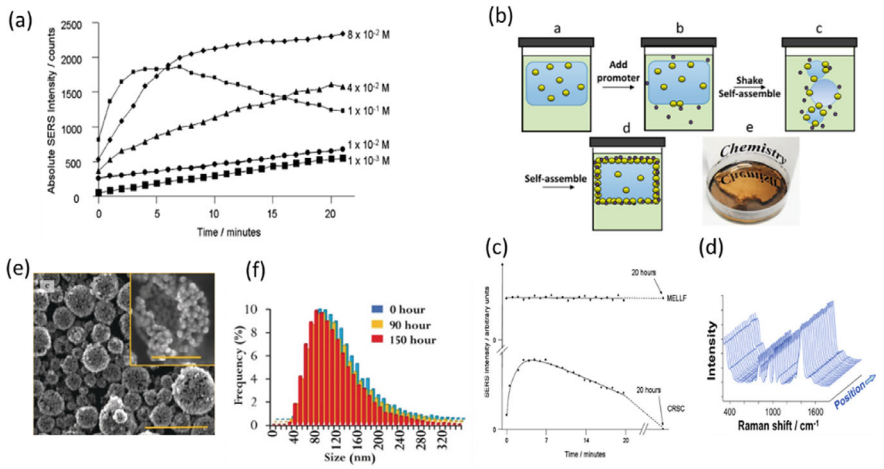



**Fig. 5.7** **a** Time dependence of the intensities of citrate SERS signals at 1393 $cm^{-1}$ obtained by aggregating citrate-reduced Ag colloid with the concentrations of $MgSO_4$ marked on the diagram. **b** Self-assembly of NP at liquid/liquid interfaces to form stable 2-dimensional arrays. **b** Schematic diagram of the formation of a metal-like liquid film (MeLLF) and photograph of the product prepared from the same colloid. **c** Plots of absolute SERS intensity versus time for the strongest citrate band (1393 $cm^{-1}$) in a Ag colloid after aggregation with $10^{-1}$ M $MgSO_4$ (bottom) and of a MeLLF. **d** SERS spectra recorded on a 5 × 5 grid of points with 0.25 mm spacing on the top surface of a Ag MeLLF. The spectra show citrate bands. The RSD of the absolute signal height is 1.1%. XU **e** SEM images of Au spherical particle aggregates (SPAs). Inset shows a single Au SPA with a cracked particle shell. Scale bars correspond to 500 nm and 250 nm in large image and inset, respectively. **f** Size distribution of the same batch of Au SPAs at different time points: immediately after formation (blue bar); after 90 h (yellow bar); after 150 h (red bar). Reproduced from **a**–**d** reference [14], **e**–**f** reference [39] with permission

at low interfacial particle density due to interparticle electrostatic repulsion but if this is reduced, either by modifying the surface of the particles or by adding a "promoter" compound to the solution to screen the charge repulsion in the organic phase, densely packed monolayer assemblies form at the interface [41]. These assemblies which are typically highly reflective and mobile were initially termed metal-like liquid films (MeLLFs). They were first used for SERS measurements in the 1980s [42] but they have recently become popular due to their high stability and uniformity [43, 44]. The time window for recording spectra of these aggregates is exceptionally long since the assembly stops when the interface is filled by particles. Figure 5.7 shows spectra obtained using a MeLLF and time-dependent data which contrasts the rise and fall of the signal from the parent aggregated colloid over minutes with the signal from these liquid aggregates which remained constant for > 20 h. If the particle layers are created as emulsions, evaporation of the internal solvent can leave either a spherical shell of aggregated particles [45] or a layer on a polymer core. Figure 5.7 shows the size distribution of the spherical aggregates which again barely changes over 150 h because aggregation was not initiated by addition of salt [39].

#### 5.2.4.2 Non-Uniform Sample Distribution

With solid SERS substrates, heterogeneous spatial distribution of the EF may be compounded by non-uniform distribution of the sample on the enhancing surface. If the substrate is dipped into the sample solution or immersed for long periods, it would be expected that uniform adsorption could occur. However, if the sample is dried onto the surface, physical forces can result in very large differences in the local concentration of the analyte at the surface. The first of these is the coffee-ring effect, which is the result of preferential deposition of material at the perimeter of a drying liquid droplet on a surface. While coffee-ring formation can be regarded as a useful method for pre-concentrating the sample, [46] the heterogeneous distribution of the material across the surface means that it is necessary to locate the appropriate area for analysis. If the signal is collected away from the concentrated ring, the intensity tends to be lower with a higher RSD [47]. Coffee-ring formation can be suppressed. For example, Fig. 5.8 shows optical images which illustrate coffee-ring formation using Rose Bengal preconcentrated onto a glass slide and the effect of depositing the droplet onto a swellable polymer (hydroxy ethyl cellulose) film doped with Ag NPs. The uniformity of the distribution shown in the optical image is also shown by the plot of SERS intensity versus position of a thiophenol droplet dried onto the enhancing polymer film [24].

In addition, some approaches extend the concept of pre-concentration by having drying droplet radially contract by reducing their tendency to pin at the circumference, by creating either superhydrophobic or liquid-infused "slippery" surfaces [48, 49]. Again, in this case, the deposit needs to be located if reproducible data are to

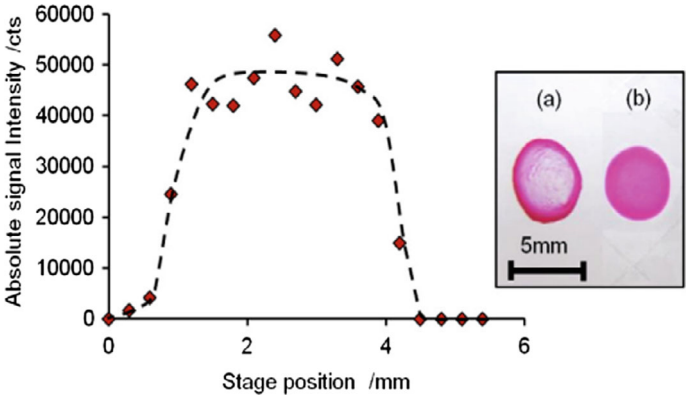



**Fig. 5.8** **a**, **b** Optical images comparing deposits created when 15 μL drops of $1 \times 10^{-3}$ M Rose Bengal were dried onto **a** a glass slide, creating a "coffee ring" and **b** a HEC film. **c** Intensities of thiophenol SERS signals obtained from nanocomposite Ag NP/HEC "poly-SERS" nanocomposite polymer film. Spectra were recorded at a line of points across the dried deposit in 0.3 mm increments. Reproduced from reference [24] with permission

be obtained but this can be aided by designing substrates where the droplets contract radially to a known point which can be on a surface or on top of a narrow pin [50].

#### 5.2.4.3 Time-Dependent Signals

In many cases, analytes spontaneously adsorb to the enhancing surface immediately on mixing but there are cases where the adsorption may require minutes or longer to reach maximum surface concentration. This is not an issue if an equilibration time is built into the procedure and the substrate remains active for the required time. For example, when adenine was being detected in excess albumin solutions using the spherical particle aggregates shown in Fig. 5.7, an equilibration time of >30 min was necessary to allow the adenine to diffuse through the blocking protein layer. However, this was not a problem because the aggregates were stable for 100's of hours [39].

A more extreme example of time-dependent changes comes in the D-SERS approach, where the signal from an evaporating droplet is monitored continuously. Since the signal will typically rise rapidly near the end of the drying process and then suddenly fall, it is difficult to obtain reproducible intensities, as shown in Fig. 5.9. However this problem may be addressed using signal normalisation, as described below in Sect. 5.3.2.

## 5.3 Techniques to Reduce Variance

Even with carefully controlled SERS experiments, very few studies show data where the signals are repeatable with RSD around 1%; typically absolute signal intensity using simple substrates have RSD $\geq$ 10% and can be considerably higher if matrix effects are present. However, these levels of variance can be reduced using approaches which are well-established in quantitative chemical analysis using methods such as high performance liquid chromatography (HPLC) and mass spectrometry.

### *5.3.1 Instrumental Approaches*

A surprisingly neglected area where SERS performance can be improved is in consideration of instrumental factors. In part, this may be because most SERS measurements are made on commercial systems of some type but this does not detract from the possibility that existing instruments can be used more effectively and that there is considerable scope for improving SERS measurements by developing more appropriate instruments, rather than developing yet more substrates.

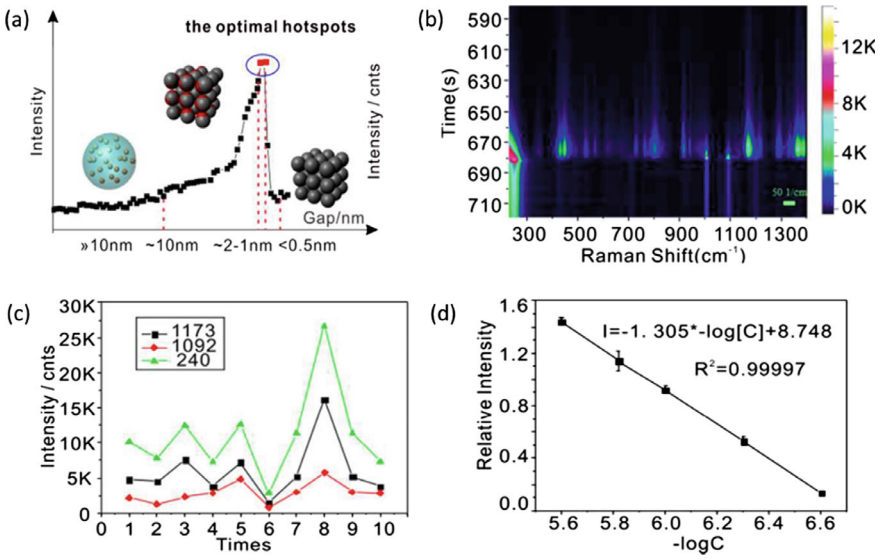



**Fig. 5.9** Use of an internal standard in D-SERS **a** Schematic diagram showing the formation of aggregates during drying of a suspension of NPs. **b** Time-dependent SERS mapping of 4-methylpyridine functionalised Au NPs mixed with $5 \times 10^{-7}$ M crystal violet (CV). **c** Variation of absolute intensity of SERS bands at 1173, 1092, and 240 $cm^{-1}$ from 10 independent measurements. **d** Calibration plot for detection of CV obtained from the relative intensities of the CV band at 1173 $cm^{-1}$ normalised to the 240 $cm^{-1}$ internal standard band. The standard deviation at each point was obtained from 10 independent measurements and shows that the relative intensity was highly reproducible even when the absolute signals varied dramatically between runs. Reproduced from reference [51] with permission

#### 5.3.1.1 Spatial Averaging

The issue of spatial variation in absolute signal intensity was discussed above, both for cases where the substrate gives different EF at different points on the surface and where the sample is unevenly distributed. For substrate-related variance, simple averaging over a larger number of points will increase the precision, since the standard deviation in the signal will decrease as the square root of the number of independent points sampled, assuming the EF is normally distributed. This is an extremely useful way of reducing the effect of point-to-point variation and will be most obvious in the case where the substrates are visibly heterogeneous, such as the dispersed aggregates shown in Fig. 5.6. This approach is common in conventional Raman studies of tableted pharmaceuticals, where the components are typically dispersed as microcrystals which are larger than the probe beam, so the statistics are well understood [52].

The important parameter is how many independent points are sampled, which is determined by the length scales of the heterogeneity and the measurement. If the laser spot size is larger than the heterogeneity, then the variation within the probed area

(or more accurately volume) will be averaged out. For example, in the SEM image of a polymer film containing dried aggregates shown in Fig. 5.6, the 60 μm circle which indicates the diameter of the laser spot includes hundreds of aggregates and the resulting signal will be an average of the contributions for all of these. Moving to an adjacent point will sample a new set of aggregates but the overall signal will be very similar. Conversely, if a < 1 μm spot was used to the probe the same film, the data from different points would be expected to change erratically as different aggregates (or regions with no particles) were randomly probed. In general terms, larger spot diameters will help to reduce point-to-point variation in solid substrates provided the diameter is larger than the length scale of the variation. Of course, it is not normally possible to change the instrument used to measure SERS spectra as desired but it is still useful to note that the RSD reported for a given substrate may vary significantly depending on the spot size used to record the measurements, which is important for comparing different substrates. Indeed, even the smaller differences in spot size given by switching between objectives with different numerical apertures in microscope-based systems have been shown to give significant difference in the point-to-point RSD of the absolute signals given by some commercial substrates, which are therefore clearly heterogeneous in the μm scale [11].

Even at a fixed spot size, point-to-point variation can be reduced by recording spectra at different points on the surface of the substrate. This can be achieved by driving the sample to different points using a mechanical stage which is straightforward with imaging systems where, to take an extreme example, data from an 80 × 80 grid of points was used to provide 6400 spectra for a single substrate [53]. Alternatively, the spatial averaging can be achieved by translating the sample mechanically under the beam [54] or moving the beam over the sample, as in Metrohm Inc's Orbital Raster Scan method. Again, the point is to average over distances larger than the extent of the heterogeneity. For example, as shown in Fig. 5.6, even though the large spot size averages of the aggregates, the physical structure of the support introduces variance at the μm scale (as shown by the RSD of 20% which is obtained with the 60 μm spot). Reduction in this variation would require additional averaging at the larger scale. This is a second reason why RSD values may be more difficult to compare than might appear since substrates often show smaller variation locally than they do over their entire surface, so a single value may not capture the whole picture. In one commercial substrate, the RSD is quoted as 2.5% over a mm scale but 7% over the entire surface, which gives a much clearer indication of the performance that can be expected [55].

#### 5.3.1.2 Temporal Averaging

A second instrumental factor which affects reproducibility is the S/N ratio, which is only significant at low signal levels but then becomes important since inclusion of random noise of comparable size to the signals means that the intensity recorded during a single measurement will fluctuate noticeably due to random statistical variation. The sources of the noise have been thoroughly explored, because for many years

reducing noise was critical in obtaining useable Raman spectra, but it is effectively a combination of statistical shot noise in the signal and instrument noise. With SERS, the scattering cross sections are often high and the modern commercial spectrometers (even compact or handheld systems) have reasonable performance, so noise sources are less frequently discussed. However, even with SERS, it is common to push to low signal levels by finding the limit of detection, which is commonly estimated in SERS as the concentration where the signal is 3 × the noise. This LOD is not determined simply by the combination of SERS substrate and sample because both the absolute size of the signal and the noise depends on the instrument used to make the measurement. Self-evidently, instruments with high collection efficiency and large aperture spectrometers fitted with low noise cooled detectors will give higher S/N ratios than more basic systems and this will change the LOD calculated for any substrate/target combination. Again, as with the spot size, it is useful to note that this may affect the apparent performance of a particular substrate reported in the literature. However, it is possible to improve reproducibility of spectra recorded on any system simply by increasing the accumulation time of the measurements, since the signal will increase linearly with the exposure time while random noise will increase as the square root. Therefore, the S/N will increase as the square root of the overall exposure, giving more reproducible values, even if all other factors are held constant. Of course, there is a limit to the exposure time which is acceptable but in most cases preparing the sample and inserting it into the instrument will take much longer than a few seconds, so increasing an exposure time from 1 to 30 s will have little effect on the overall analysis time but will increase the S/N (and decrease the LOD) by a factor of >5×.

### *5.3.2 Standard Addition*

The possible effects of matrix interference and methods to reduce them were discussed above. However, there may be situations where it is not possible to use sample pre-treatment to remove interfering materials or to prepare a model matrix which can be used to prepare a calibration curve. These samples can be treated using the standard addition method where a series of samples are prepared by adding additional amounts of the target analyte to the starting material and recording the resulting spectra. Since the matrix will affect both existing and added analyte in the same way, a plot of intensity versus added concentration can be extrapolated back to give the amount of target that would be need to be removed from the original sample to give a zero signal, which is the sample concentration. Figure 5.10 shows an example of a SERS calibration curve for added pyocyanin recorded in the complex environment of an ex situ biofilm. This environment would be extremely difficult to chemically reproduce and does have a significant effect on the SERS spectra, as shown in the figure where significant reductions in the signals from even a strongly binding thiophenol test sample were observed in the presence of the biofilm matrix. However, extrapolating back in the calibration plot for pyocyanin allowed the concentration in the original sample to be determined. The strength of the internal standard method is

that it is robust to changes in the matrix since a new calibration curve is effectively created by each set of measurements. This makes it extremely useful for making reproducible measurements on biofluids which have been obtained from different patients, for example, in detecting uric acid in urine [56]. One disadvantage of the standard addition method is that it does require several samples to be prepared and recorded to give a single measured concentration. However, this has been addressed by Hidi et al. who developed a lab-on-a-chip approach based on a microfluidic platform to carry out the measurements of nitroxoline in urine samples [57].

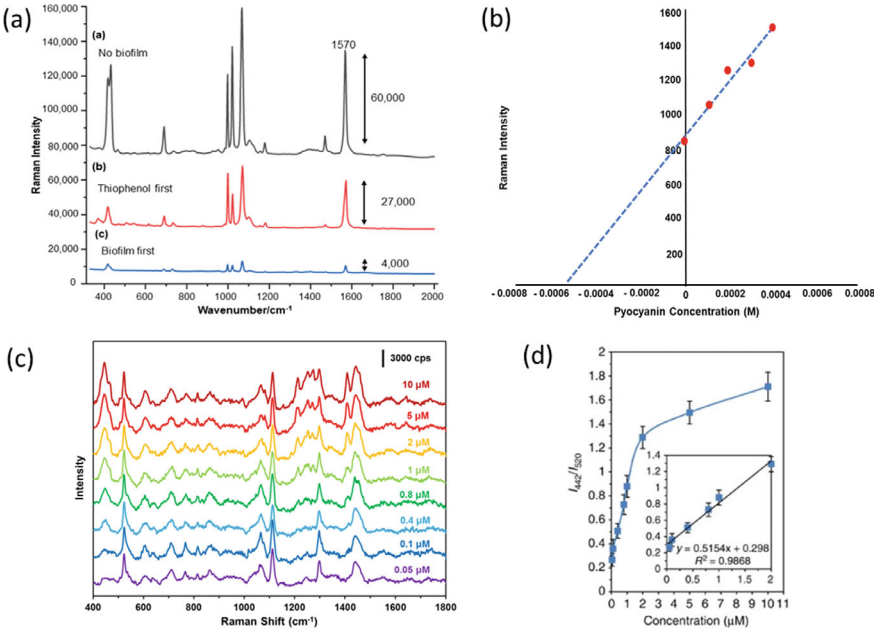



**Fig. 5.10** **a**, **b** Matrix interference due to ex situ biofilm. **a** Comparison of SERS spectra of thiophenol obtained with Ag NPs substrate in the absence of test analyte and when thiophenol was added before or after the ex situ biofilm. The effect if particularly large when the biofilm is added first and blocks access to the surface. **b** Standard addition data of SERS band intensity versus concentrations of added pyocyanin in a sample of ex situ *P. aeruginosa* biofilm. Extrapolation to zero intensity allows the pyocyanin concentration in the sample to be estimated as $6 \times 10^{-4}$ M. **c**, **d** Use of a non-SERS internal standard. **c** SERS spectra of Doxorubicin (DOX) in an optofluidic system at the concentrations marked. The 520 $cm^{-1}$ peak is due to Si in the substrate and can be used as an internal standard. **d** Calibration plots of the ratio of the intensities of the 442 $cm^{-1}$ drug band and the 520 $cm^{-1}$ standard against drug concentration. The reproducibility is shown by the small error bars. Reproduced from **a**–**b** reference [58] and **c**–**d** reference [37] with permission

### *5.3.3 Internal Standards*

The factors which determine the reproducibility of the absolute size of SERS signals were discussed in Sect. 7.1, and in many cases, control of these variables may be sufficient to obtain useable experimental results. To take a single example from many possible choices, Zhu et al. have shown quantitative detection of creatine using simple aggregated Au colloids [36]. By using liquid–liquid extraction to suppress matrix effects, selecting the appropriate aggregating agent, and using reproducible colloids (RSD for the creatine peak area measured for 20 different samples 5%), they obtained creatine concentrations in human urine which were within 6% of those measured by the much more complex and expensive standard analytical method. However, using this approach to give consistent signal intensities required considerable expertise in controlling all the variables, particularly the performance of the enhancing substrate, and was helped by the possibility of developing a simple and effective sample clean-up process. In many other cases, various factors associated with a particular measurement make achieving reproducible absolute intensities difficult, so it is helpful to include standard materials of various types and to measure relative, rather than absolute, intensities to reduce the effect of random variations in experimental conditions.

#### 5.3.3.1 Non-SERS Standards

The intensities or SERS signals are subject to the same instrument-related uncertainties that are found in normal Raman experiments, and these may be corrected by normalising the SERS signal to that of material that is always present at a fixed amount in the sample. If the intention is to correct for fluctuations in laser power or changes in focus, it may be sufficient to measure the ratio of the signal to the fixed standard, on the assumption that both signals will respond equally to changes in the conditions. For example, Fig. 5.10 shows SERS of different concentrations of Doxorubicin (DOX) in an optofluidic system where the 442 $cm^{-1}$ drug band could be measured against the 520 $cm^{-1}$ peak from Si in the substrate [37, 59]. Similarly, Yu et al. have used the signal from the acetone solvent as an internal standard for substrate based in Au nanoparticles at a cyclohexane/water interface. In this case, the introduction of the standard reduced the RSD in the substrate from 14.5% to 5.9% [59].

#### 5.3.3.2 Pre-adsorbed SERS Internal Standards

The examples above showed that using unenhanced standard materials can reduce random changes in intensity due to physical variations in the measurement but clearly they are unable to correct for important sources of variance in SERS experiments,

such as point-to-point variation in the EF caused by local changes in the physical or chemical structure of the enhancing substrate. For this, it is necessary use SERS-active internal standards. Ideally, the standard will be a substance which is present in all the samples but the nature of SERS means that often the experiment is designed so that the signal is dominated by the target species, so there are no other convenient standard bands available. There are some cases where intrinsic SERS-active internal standards are found, such as the oxidation of guanosine nucleotides illustrated in Fig. 5.11 but these are very much the exceptions [60]. This means that internal standards need to be added to the sample; a convenient and widely used approach is to pre-adsorb strongly scattering compounds to the substrate. In use, the intensities of bands due to the target can be normalised against those of the fixed standard. Different types of compounds have been used as the standards including NaSCN for which was used very effectively to correct for spatial variations in a coffee-ring-based SERS measurement of Clozapine and allowed a calibration plot with $R^2 = 0.9997$ to be obtained. Similarly, the strongly time-dependent signals in the droplet drying experiments shown in Fig. 5.9 could be normalised to the 240 $cm^{-1}$ band of the 4-mercaptopyridine internal standard to give ratiometric signal intensities which allowed accurate and precise quantification of MDMA (3,4-methylenedioxymethamphetamine) [51].

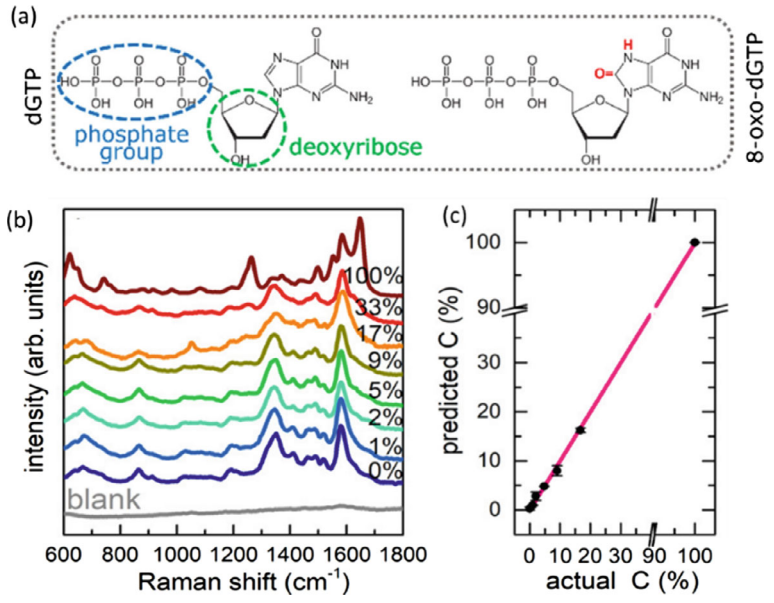



**Fig. 5.11** Oxidation of guanosine, a system with an intrinsic SERS-active standard. **a** Molecular structures of deoxyguanosine triphosphate and its 8-oxo product. **b** SERS spectra of nucleoside mixtures ($10^{-4}$ M) at varying 8-oxo contents, acquired as mircodroplets on superhydrophobic substrates. **c** PLS regression plot of predicted versus actual extent of oxidation. Error bars are PLS regression residuals. Reproduced from reference [60] with permission

One disadvantage of the pre-adsorbing internal standards is that they occupy some of the surface binding sites, reducing their availability for detecting the target molecules. This can be overcome by using core–shell particles where the internal standard either forms an outer shell or is part of a multilayer core–shell structure where a plasmonic core is covered with a layer of SERS-active standard before a final metallic outer shell is added [8, 61]. These systems will correct not only for physical variations between experiments but also uneven distribution of enhancing material within the bulk substrate.

#### 5.3.3.3 Co-adsorbed Chemically Matched Internal Standards and Isotopologues

The best internal standards are those which respond in exactly the same way as the target molecules to any perturbation of the measurement conditions. Isotopologues are excellent for this purpose since, if they are added along with the sample to the enhancing medium, they will respond in the same way to both physical and chemical perturbations. For example, while pre-added internal standards can correct for a batch of substrates giving low plasmonic enhancement, they will not be able to correct for a change in the surface chemistry which leads to a difference in adsorption of the target because the surface charge is changed or the surface blocked by adsorbed proteins. In contrast, since the target and its isotopologue will respond in the same way to such perturbations, their relative intensity of their signals will remain constant, even if the absolute signal intensity changes significantly. This approach therefore provides a very robust method of obtaining SERS signals whose intensity (or more accurately, relative intensity) can be reproduced even if control measures fail and the experimental conditions move significantly away from normal.

Figure 5.12 shows data obtained for quantification of nicotine in e-liquids [62]. This work used $d_4$-nicotine as the internal standard, and the spectra show the change in the relative intensities of the internal standard band at 974 $cm^{-1}$ against the nicotine target (1030 $cm^{-1}$) over a 0–40 μM concentration range. The calibration plot of normalised nicotine signal vs concentration gave $R^2 = 0.9991$ while the error bars (±1 SD) are included on the plot but are difficult to see since they are a similar size to the markers for the data points. A study describing the process for quantitative analysis of amines which has been developed into a commercial kit has shown the advantages of using $d_3$ and $d_4$-monoethanolamine (MEA-$d_4$) as internal standards measurement of MEA [64]. In this case, the spectra were scaled to the characteristic MEA-$d_4$ band 870 $cm^{-1}$ which gave excellent results for laboratory standards and refinery process water samples. The robustness which introduction of the internal provides was shown by the fact that the initial calibration was used over a period of seven years to analyse thousands of samples using hundreds of different nanoparticle batches without adjustment or recalibration.

While isotopologues are the best choice for internal standards, they may not be obtainable for a given target or be available only at an unacceptably high the cost. However, it is possible to obtain similar advantages to isotopologues by using

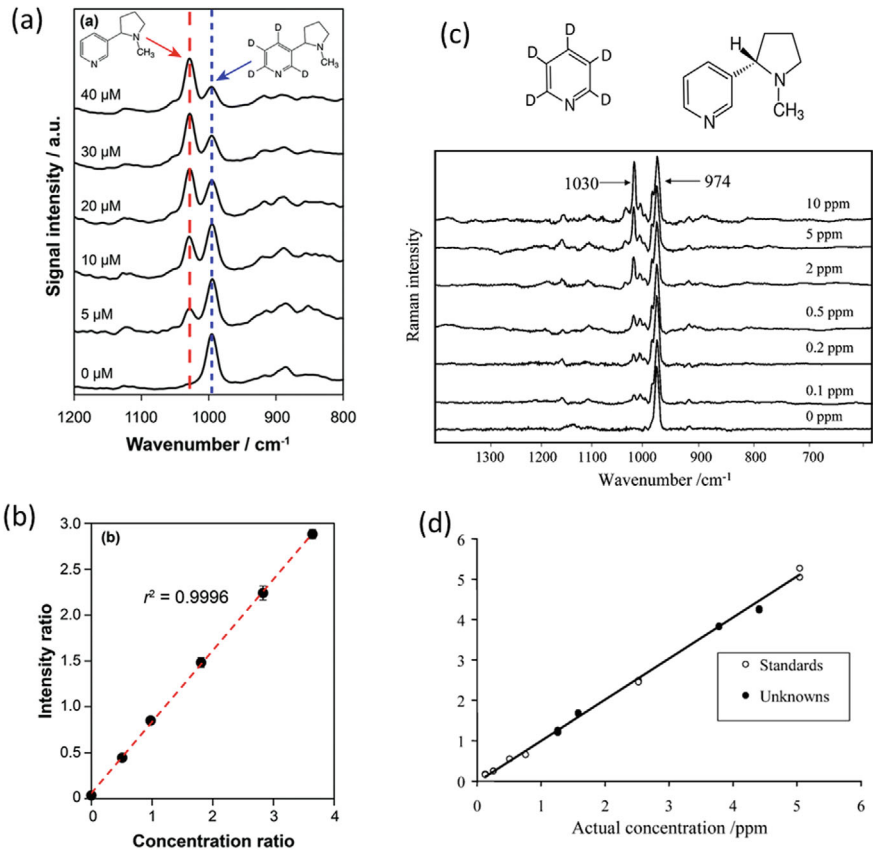



**Fig. 5.12** Quantitative measurement of nicotine by SERS using either an isotopologue of the analyte or a chemically matched compound as an internal standard. **a** SERS spectra of samples containing $d_4$-nicotine internal standard (974 $cm^{-1}$) and 0–40 μM nicotine (1030 $cm^{-1}$). **b** Calibration plot of nicotine signal normalised to the 1030 $cm^{-1}$ internal standard vs nicotine concentration. Error bars ± 1 SD are shown but are of similar size to the markers used for the data points. **c** SERS spectra of samples containing $d_5$-pyridine internal standard (974 $cm^{-1}$) and 0–10 ppm nicotine (1030 $cm^{-1}$). **b** Plot of predicted vs actual nicotine concentration obtained from spectra normalised to the internal standard band. Open circles show data used to build the PLS-1 calibration model and closed circles are blind unknowns. Reproduced from **a**–**b**) reference [62], **c**–**d** reference [63] with permission

compounds which are structurally similar to the target molecules as internal standards since they are also expected to respond to external perturbations in a similar way. Figure 5.12 shows data for a quantitative study of nicotine where $d_5$-pyridine was chosen as the chemically matched internal standard since it would expected to bind to the enhancing surface through its aromatic amine group in a similar way to nicotine. It was necessary to use $d_5$-pyridine because natural isotopic abundance pyridine has a band in a similar position to that of nicotine. As was the case for the isotopologue

experiments, altering the relative concentration of target and standard gave spectra where the ratio of the band intensities was highly reproducible, as shown by the plot of predicted versus actual concentration which has $R^2 = 0.998$ over the concentration range 1–10 ppm. Other examples of chemically matched internal standards include the use of 3,3'-methylenedianiline in a commercial system for determination of 4,4'-methylenedianiline in grease [65]. In that case, since the spectra of the internal standard and target were very different, natural isotopic abundance materials could be used, and again, the chemically matched standards allowed reproducible spectra to be obtained, even for industrial grease samples, allowing for quantitative analysis with performance comparable to GC–MS.

## 5.4 Conclusion

For many years following its discovery, it was widely believed that SERS measurements were very difficult to carry out reproducibly. However, the availability of nanoscale characterisation tools and deep understanding of the factors governing plasmonic enhancement mean that substrates which provide consistent levels of enhancement are now widely available. Simple clean aqueous solutions of target analytes which adsorb to the surface have been shown in numerous examples to give signals which vary by < 20% (sometimes as little as 5%) in repeat measurements, although some obvious precautions such as preventing substrate degradation are necessary. The main challenges arise when samples need to be measured in interfering matrices and/or when higher levels of precision are required. Matrix effects, which typically arise in real-world samples, can be reduced by sample pre-treatment but for critical applications, it is important to have confidence that the treatment has been successful. Similarly, even with careful control of the experimental variables some residual variance will remain. In these cases, further steps can be taken to improve the performance of the overall measurement process. This can be through instrumental approaches or use of internal standards. It has now been extensively demonstrated that when these additional controls are in place, SERS can be used as a remarkably rapid and sensitive method for obtaining reliable information on the structure and composition of both laboratory and real-world samples.

## References

1. S. Pal, S. Harmsen, A. Oseledchyk, H. T. Hsu and M. F. Kircher, MUC1 aptamer targeted SERS nanoprobes. Advanced Functional Materials **27**, 1606632 (2017)
2. D. Wang, J. Yang, J. Pandya, J. M. Clark, L. C. Harrington, C. C. Murdock and L. He, Quantitative age grading of mosquitoes using surface-enhanced Raman spectroscopy. Analytical Science Advances **3**, 47-53 (2022)

3. S. E. J. Bell, L. A. Fido, N. M. S. Sirimuthu, S. J. Speers, K. L. Peters and S. H. Cosbey, Screening tablets for DOB using surface-enhanced Raman spectroscopy. Journal of Forensic Sciences **52**, 1063-1067 (2007)
4. E. C. Le Ru, E. Blackie, M. Meyer and P. G. Etchegoint, Surface enhanced Raman scattering enhancement factors: A comprehensive study. Journal of Physical Chemistry C **111**, 13794-13803 (2007)
5. S. E. J. Bell, G. Charron, E. Cortés, J. Kneipp, M. L. de la Chapelle, J. Langer, M. Procházka, V. Tran and S. Schlücker, Towards reliable and quantitative surface-enhanced Raman scattering (SERS): From key parameters to good analytical practice. Angewandte Chemie - International Edition **59**, 5454-5462 (2020)
6. W. W. Y. Lee, C. P. McCoy, R. F. Donnelly and S. E. J. Bell, Swellable polymer films containing Au nanoparticles for point-of-care therapeutic drug monitoring using surface-enhanced Raman spectroscopy. Analytica Chimica Acta **912**, 111-116 (2016)
7. M. J. Styles, R. S. Rodriguez, V. M. Szlag, S. Bryson, Z. Gao, S. Jung, T. M. Reineke and C. L. Haynes, Optimization of film over nanosphere substrate fabrication for SERS sensing of the allergen soybean agglutinin. Journal of Raman Spectroscopy **52**, 482-490 (2021)
8. S. Lin, X. Lin, Y. Liu, H. Zhao, W. Hasi and L. Wang, Self-assembly of Au@Ag core-shell nanocubes embedded with an internal standard for reliable quantitative SERS measurements. Analytical Methods **10**, 4201-4208 (2018)
9. J. Langer, D. J. de Aberasturi, J. Aizpurua, R. A. Alvarez-Puebla, B. Auguié, J. J. Baumberg, G. C. Bazan, S. E. J. Bell, A. Boisen, A. G. Brolo, J. Choo, D. Cialla-May, V. Deckert, L. Fabris, K. Faulds, F. Javier García de Abajo, R. Goodacre, D. Graham, A. J. Haes, C. L. Haynes, C. Huck, T. Itoh, M. Käll, J. Kneipp, N. A. Kotov, H. Kuang, E. C. Le Ru, H. K. Lee, J. F. Li, X. Y. Ling, S. A. Maier, T. Mayerhöfer, M. Moskovits, K. Murakoshi, J. M. Nam, S. Nie, Y. Ozaki, I. Pastoriza-Santos, J. Perez-Juste, J. Popp, A. Pucci, S. Reich, B. Ren, G. C. Schatz, T. Shegai, S. Schlücker, L. L. Tay, K. George Thomas, Z. Q. Tian, R. P. van Duyne, T. Vo-Dinh, Y. Wang, K. A. Willets, C. Xu, H. Xu, Y. Xu, Y. S. Yamamoto, B. Zhao and L. M. Liz-Marzán, Present and future of surface-enhanced Raman scattering. ACS Nano **14**, 28–117 (2020)
10. Y. Cao, Y. Sun, R. J. Yu and Y. T. Long, Paper-based substrates for surface-enhanced Raman spectroscopy sensing. Microchimica Acta **191**, 8 (2024)
11. Y. Liu, Y. Zhang, M. Tardivel, M. Lequeux, X. Chen, W. Liu, J. Huang, H. Tian, Q. Liu, G. Huang, R. Gillibert, M. L. de la Chapelle and W. Fu, Evaluation of the reliability of six commercial SERS substrates. Plasmonics **15**, 743-752 (2020)
12. A. Azziz, W. Safar, Y. Xiang, M. Edely and M. Lamy de la Chapelle, Sensing performances of commercial SERS substrates. Journal of Molecular Structure **1248**, 131519 (2022)
13. D. B. Grys, R. Chikkaraddy, M. Kamp, O. A. Scherman, J. J. Baumberg and B. de Nijs, Eliminating irreproducibility in SERS substrates. Journal of Raman Spectroscopy **52**, 412-419 (2021)
14. M. P. Konrad, A. P. Doherty and S. E. J. Bell, Stable and uniform SERS signals from self-assembled two-dimensional interfacial arrays of optically coupled Ag nanoparticles. Analytical Chemistry **85**, 6783-6789 (2013)
15. Y. Han, R. Lupitskyy, T. M. Chou, C. M. Stafford, H. Du and S. Sukhishvili, Effect of oxidation on surface-enhanced Raman scattering activity of silver nanoparticles: A quantitative correlation. Analytical Chemistry **83**, 5873-5880 (2011)
16. A. Matikainen, T. Nuutinen, T. Itkonen, S. Heinilehto, J. Puustinen, J. Hiltunen, J. Lappalainen, P. Karioja and P. Vahimaa, Atmospheric oxidation and carbon contamination of silver and its effect on surface-enhanced Raman spectroscopy (SERS). Scientific Reports **6**, 37192 (2016)
17. Y. Zhao, A. Kumar and Y. Yang, Unveiling practical considerations for reliable and standardized SERS measurements: lessons from a comprehensive review of oblique angle deposition-fabricated silver nanorod array substrates. Chemical Society Reviews **53**, 1004-1057 (2023)
18. X. Fang, Y. Song, Y. Huang, G. Yang, C. Han, H. Li and L. Qu, Two-dimensional MXene modified AgNRs as a surface-enhanced Raman scattering substrate for sensitive determination of polychlorinated biphenyls. Analyst **145**, 7421-7428 (2020)

19. M. Erol, Y. Han, S. K. Stanley, C. M. Stafford, H. Du and S. Sukhishvili, SERS not to be taken for granted in the presence of oxygen. Journal of the American Chemical Society **131**, 7480-7481 (2009)
20. C. Li, Z. Chen, Y. Huang, Y. Zhang, X. Li, Z. Ye, X. Xu, S. E. J. Bell and Y. Xu, Uncovering strong π-metal interactions on Ag and Au nanosurfaces under ambient conditions via in-situ surface-enhanced Raman spectroscopy. Chem **8**, 2514-2528 (2022)
21. L. Scarabelli, M. Schumacher, D. Jimenez de Aberasturi, J. P. Merkl, M. Henriksen-Lacey, T. Milagres de Oliveira, M. Janschel, C. Schmidtke, S. Bals, H. Weller and L. M. Liz-Marzán, Encapsulation of noble metal nanoparticles through seeded emulsion polymerization as highly stable plasmonic systems. Advanced Functional Materials **29**, 1809071 (2019)
22. J. F. Li, Y. J. Zhang, S. Y. Ding, R. Panneerselvam and Z. Q. Tian, Core-shell nanoparticle-enhanced Raman spectroscopy. Chemical Reviews **117**, 5002-5069 (2017)
23. C. Huo, W. Han, W. Tang and X. Duan, Stable SERS substrate based on highly reflective metal liquid-like films wrapped hydrogels for direct determination of small molecules in a high protein matrix. Talanta **234**, 122678 (2021)
24. W. W. Y. Lee, V. A. D. Silverson, C. P. McCoy, R. F. Donnelly and S. E. J. Bell, Preaggregated Ag nanoparticles in dry swellable gel films for off-the-shelf surface-enhanced Raman spectroscopy. Analytical Chemistry **86**, 8106-8113 (2014)
25. C. Li, Y. Zhang, Z. Ye, S. E. J. Bell and Y. Xu, Combining surface-accessible Ag and Au colloidal nanomaterials with SERS for in situ analysis of molecule–metal interactions in complex solution environments. Nature Protocols **18**, 2717-2744 (2023)
26. S. E. J. Bell and N. M. S. Sirimuthu, Surface-enhanced Raman spectroscopy as a probe of competitive binding by anions to citrate-reduced silver colloids. Journal of Physical Chemistry A **109**, 7405-7410 (2005)
27. J. Lu, Z. Cai, Y. Zou, D. Wu, A. Wang, J. Chang, F. Wang, Z. Tian and G. Liu, Silver nanoparticle-based surface-enhanced Raman spectroscopy for the rapid and selective detection of trace tropane alkaloids in food. ACS Applied Nano Materials **2**, 6592-6601 (2019)
28. S. Wang, B. Sun, J. Feng, F. An, N. Li, H. Wang and M. Tian, Development of affinity between target analytes and substrates in surface enhanced Raman spectroscopy for environmental pollutant detection. Analytical Methods **12**, 5657-5670 (2020)
29. V. M. Szlag, R. S. Rodriguez, J. He, N. Hudson-Smith, H. Kang, N. Le, T. M. Reineke and C. L. Haynes, Molecular affinity agents for intrinsic surface-enhanced Raman scattering (SERS) sensors. ACS Applied Materials and Interfaces **10**, 31825-31844 (2018)
30. A. Stewart, S. Murray and S. E. J. Bell, Simple preparation of positively charged silver nanoparticles for detection of anions by surface-enhanced Raman spectroscopy. Analyst **140**, 2988-2994 (2015)
31. H. C. Schorr and Z. D. Schultz, Chemical conjugation to differentiate monosaccharides by Raman and surface enhanced Raman spectroscopy. Analyst **148**, 2035-2044 (2023)
32. Y. Yang, Y. Li, W. Zhai, X. Li, D. Li, H. Lin and S. Han, Electrokinetic preseparation and molecularly imprinted trapping for highly selective SERS detection of charged phthalate plasticizers. Analytical Chemistry **93**, 946-955 (2021)
33. Q. Ding, J. Wang, X. Chen, H. Liu, Q. Li, Y. Wang and S. Yang, Quantitative and sensitive SERS platform with analyte enrichment and filtration function. Nano Letters **20**, 7304-7312 (2020)
34. J. Liu, L. Xin, L. Qin, T. Zhang, X. Li and S. Z. Kang, Fabrication of a flexible SERS sensing platform with high sensitivity and its application in monitoring of trace benzotriazole in tap water. ACS ES and T Water **3**, 3141-3152 (2023)
35. A. Bonifacio, S. Dalla Marta, R. Spizzo, S. Cervo, A. Steffan, A. Colombatti and V. Sergo, Surface-enhanced Raman spectroscopy of blood plasma and serum using Ag and Au nanoparticles: A systematic study. Analytical and Bioanalytical Chemistry **406**, 2355–2365 (2014)
36. W. Zhu, B. Y. Wen, L. J. Jie, X. D. Tian, Z. L. Yang, P. M. Radjenovic, S. Y. Luo, Z. Q. Tian and J. F. Li, Rapid and low-cost quantitative detection of creatinine in human urine with a portable Raman spectrometer. Biosensors and Bioelectronics **154** (2020)

37. F. Sun, H. C. Hung, A. Sinclair, P. Zhang, T. Bai, D. D. Galvan, P. Jain, B. Li, S. Jiang and Q. Yu, Hierarchical zwitterionic modification of a SERS substrate enables real-time drug monitoring in blood plasma. Nature Communications **7** (2016)
38. H. S. Siebe, Q. Chen, X. Li, Y. Xu, W. R. Browne and S. E. J. Bell, Filter paper based SERS substrate for the direct detection of analytes in complex matrices. Analyst **146**, 1281-1288 (2021)
39. Z. Ye, C. Li, Q. Chen, Y. Xu and S. E. J. Bell, Ultra-Stable plasmonic colloidal aggregates for accurate and reproducible quantitative SE(R)RS in protein-rich biomedia. Angewandte Chemie - International Edition **58**, 19054-19059 (2019)
40. J. Cheng, Z. Zhang, L. Zhang, J. Miao, Y. Chen, R. Zhao, M. Liu, L. Chen and X. Wang, Size-controllable colloidal Ag nano-aggregates with long-time SERS detection window for on-line high-throughput detection. Talanta **257**, 124358 (2023)
41. Y. Xu, M. P. Konrad, W. W. Y. Lee, Z. Ye and S. E. J. Bell, A method for promoting assembly of metallic and nonmetallic nanoparticles into interfacial monolayer films. Nano Letters **16**, 5255-5260 (2016)
42. K. C. Gordon, J. J. McGarvey and K. P. Taylor, Enhanced Raman scattering from liquid metal films formed from silver sols. Journal of Physical Chemistry **93**, 6814-6817 (1989)
43. Y. Xu, M. P. Konrad, J. L. Trotter, C. P. McCoy and S. E. J. Bell, Rapid one-pot preparation of large freestanding nanoparticle-polymer films. Small **13**, 1602163 (2017)
44. Z. Ye, C. Li, Q. Chen, Y. Xu and S. E. J. Bell, Self-assembly of colloidal nanoparticles into 2D arrays at water-oil interfaces: Rational construction of stable SERS substrates with accessible enhancing surfaces and tailored plasmonic response. Nanoscale **13**, 5937-5953 (2021)
45. Z. Ye, C. Li, N. Skillen, Y. Xu, H. McCabe, J. Kelly, P. Robertson and S. E. J. Bell, A one-pot method for building colloidal nanoparticles into bulk dry powders with nanoscale magnetic, plasmonic and catalytic functionalities. Applied Materials Today **15**, 398-404 (2019)
46. M. Yang, D. Chen, J. Hu, X. Zheng, Z. J. Lin and H. Zhu, The application of coffee-ring effect in analytical chemistry. TrAC - Trends in Analytical Chemistry **157**, 116752 (2022)
47. D. Zhang, J. Fang and T. Li, Sensitive and uniform detection using Surface-Enhanced Raman Scattering: Influence of colloidal-droplets evaporation based on Au-Ag alloy nanourchins. Journal of Colloid and Interface Science **514**, 217-226 (2018)
48. F. De Angelis, F. Gentile, F. Mecarini, G. Das, M. Moretti, P. Candeloro, M. L. Coluccio, G. Cojoc, A. Accardo, C. Liberale, R. P. Zaccaria, G. Perozziello, L. Tirinato, A. Toma, G. Cuda, R. Cingolani and E. Di Fabrizio, Breaking the diffusion limit with super-hydrophobic delivery of molecules to plasmonic nanofocusing SERS structures. Nature Photonics **5**, 682-687 (2011)
49. S. Yang, X. Dai, B. B. Stogin and T. S. Wong, Ultrasensitive surface-enhanced Raman scattering detection in common fluids. Proceedings of the National Academy of Sciences of the United States of America **113**, 268-273 (2016)
50. C. Li, L. Chai, Q. Chen, Z. Ye, Y. Xu and S. E. J. Bell, Superhydrophobic needles tipped with 2-dimensional arrays of plasmonic colloidal nanoparticles for microdroplet SERS analysis. Journal of Raman Spectroscopy **52**, 386-393 (2021)
51. X. Yan, P. Li, B. Zhou, X. Tang, X. Li, S. Weng, L. Yang and J. Liu, Optimal hotspots of dynamic surfaced-enhanced Raman spectroscopy for drugs quantitative detection. Analytical Chemistry **89**, 4875-4881 (2017)
52. S. E. J. Bell, J. R. Beattie, J. J. McGarvey, K. L. Peters, N. M. S. Sirimu and S. J. Speers, Development of sampling methods for Raman analysis of solid dosage forms of therapeutic and illicit drugs. Journal of Raman Spectroscopy **35**, 409-417 (2004)
53. S. Mabbott, Y. Xu and R. Goodacre, Objective assessment of SERS thin films: Comparison of silver on copper: Via galvanic displacement with commercially available fabricated substrates. Analytical Methods **9**, 4783-4789 (2017)
54. M. A. De Jesús, K. S. Giesfeldt and M. J. Sepaniak, Use of a sample translation technique to minimize adverse effects of laser irradiation in surface-enhanced Raman spectrometry. Applied Spectroscopy **57**, 428-438 (2003)
55. K. Wu, T. Rindzevicius, M. S. Schmidt, A. H. Thilsted and A. Boisen, Optimizing silver-capped silicon nanopillars to simultaneously realize macroscopic, practical-level SERS signal

reproducibility and high enhancement at low costs. Journal of Raman Spectroscopy **48**, 1808-1818 (2017)
56. C. Westley, Y. Xu, B. Thilaganathan, A. J. Carnell, N. J. Turner and R. Goodacre, Absolute quantification of uric acid in human urine using surface enhanced Raman scattering with the standard addition method. Analytical Chemistry **89**, 2472-2477 (2017)
57. I. J. Hidi, M. Jahn, K. Weber, T. Bocklitz, M. W. Pletz, D. Cialla-May and J. Popp, Lab-on-a-chip-surface enhanced Raman scattering combined with the standard addition method: Toward the quantification of nitroxoline in spiked human urine samples. Analytical Chemistry **88**, 9173-9180 (2016)
58. W. Aljuhani, Y. Zhang, M. P. Wylie, Y. Xu, C. P. McCoy and S. E. J. Bell, Probing the interaction of ex situ biofilms with plasmonic metal nanoparticles using surface-enhanced Raman spectroscopy. Analyst (2023)
59. F. Yu, M. Su, L. Tian, H. Wang and H. Liu, Organic solvent as internal standards for quantitative and high-throughput liquid interfacial SERS analysis in complex media. Analytical Chemistry **90**, 5232-5238 (2018)
60. F. Ripanti, C. Fasolato, F. Mazzarda, S. Palleschi, M. Ceccarini, C. Li, M. Bignami, E. Bodo, S. E. J. Bell, F. Mazzei and P. Postorino, Advanced Raman spectroscopy detection of oxidative damage in nucleic acid bases: probing chemical changes and intermolecular interactions in guanosine at ultralow concentration. Analytical Chemistry **93**, 10825-10833 (2021)
61. W. Shen, X. Lin, C. Jiang, C. Li, H. Lin, J. Huang, S. Wang, G. Liu, X. Yan, Q. Zhong and B. Ren, Reliable quantitative SERS analysis facilitated by core-shell nanoparticles with embedded internal standards. Angewandte Chemie - International Edition **54**, 7308-7312 (2015)
62. N. Itoh and S. E. J. Bell, High dilution surface-enhanced Raman spectroscopy for rapid determination of nicotine in e-liquids for electronic cigarettes. Analyst **142**, 994-998 (2017)
63. S. E. J. Bell and N. M. S. Sirimuthu, Rapid, quantitative analysis of ppm/ppb nicotine using surface-enhanced Raman scattering from polymer-encapsulated Ag nanoparticles (gel-colls). Analyst **129**, 1032-1036 (2004)
64. M. Benhabib, S. L. Kleinman and M. C. Peterman, Quantification of amines in refinery process water via surface-enhanced Raman spectroscopy. Energy and Fuels **37**, 1881-1886 (2023)
65. S. L. Kleinman, M. C. Peterman, M. Benhabib, M. T. Cheng, J. D. Hudson and R. E. Mohler, Rapid quantification of 4,4′-methylenedianiline by surface-enhanced Raman spectroscopy. Analytical Chemistry **89**, 13190-13194 (2017)

# Chapter 6
# State-of-the-Art Tip-Enhanced Raman Scattering




**Prompong Pienpinijtham and Yukihiro Ozaki**

**Abstract** Tip-Enhanced Raman Scattering (TERS) has emerged as a revolutionary technique capable of probing matter at the nanoscale, offering unprecedented spatial resolution and sensitivity. This chapter provides a comprehensive overview of the recent advancements in TERS, highlighting its pivotal role in various scientific disciplines. We begin by tracing the historical development of TERS and discuss the significant breakthroughs that have propelled its progress. Subsequently, we delve into the unique capabilities of TERS in studying single molecules, unraveling the intricacies of nanostructures, and exploring the nanoscale properties of materials. The application of TERS in the realm of biomolecular research is also explored, shedding light on its potential to elucidate fundamental biological processes. Furthermore, the chapter addresses the ongoing development of TERS instrumentation, discussing innovative approaches to enhance sensitivity, spatial resolution, and versatility. We highlight the challenges and opportunities that lie ahead in the field of TERS, emphasizing its potential to drive future discoveries in nanoscience and related fields.

## 6.1 Introduction

Tip-enhanced Raman scattering (TERS) has recently received keen interest as a highly unique nano-spectroscopy [1–9]. It can yield site-specific information on a nano- to subnano-scale, with spatial resolution beyond the diffraction limit of light [1–9]. One can utilize TERS for any type of material surface, regardless of morphology. TERS can be performed in various environments, such as ambient air, ultrahigh

P. Pienpinijtham
Sensor Research Unit (SRU), Department of Chemistry, Faculty of Science, Chulalongkorn University, Pathumwan, Bangkok 10330, Thailand

Center of Excellence in Bioactive Resources for Innovative Clinical Applications, Chulalongkorn University, Pathumwan, Bangkok 10330, Thailand

Y. Ozaki (✉)
School of Biological and Environmental Sciences, Kwansei Gakuin University, Sanda 669–1330, Hyogo, Japan
e-mail: yukiz89016@gmail.com

© The Author(s), under exclusive license to Springer Nature Singapore Pte Ltd. 2024

M. Procházka et al. (eds.), *Surface- and Tip-Enhanced Raman Scattering Spectroscopy*,
https://doi.org/10.1007/978-981-97-5818-0_6

vacuum (UHV), solutions, and electrochemical environments. Therefore, TERS has been extensively employed as a highly sensitive analytical and structural technique for a wide area of nanomaterials, including biological nanomaterials.

This chapter aims to describe state-of-the-art TERS. Besides the introductory part, this chapter may be divided into three parts. The first part is concerned with studies of single molecules and single bonds. In this part, angstrom-scale resolution of TERS and its application are demonstrated. The second part reports on visualizing nanomaterials and unraveling nanostructures. TERS investigations of various carbon nanomaterials, metal nanomaterials, polymer nanocomposites, and so on are introduced. Biological nanomaterials are also involved in this part. The last part is involved in the progress of TERS instrumentation. Resolution improvement, tip fabrication, solution TERS, and electrochemical TERS are introduced.

### *6.1.1 Brief History and Recent Progress of TERS*

It has been generally known that TERS was proposed by three research groups, the Kawata [10], Zenobi [11], and Anderson [12] groups, independently around 2000 [10–13]. However, there is an important prehistory of TERS in the 1980s and 1990s [13]. We do not describe them in this chapter, but we point out that there are several important studies, for example, a study by Binnig et al. (1982) about the introduction of scanning tunneling microscopy (STM) [14], the one by Wessel (1985) on surface-enhanced optical microscopy by illuminating laser on a single metal nanoparticle [15], and one more by Inoue and Kawata (1994) on the detection of scattered light from the near field of a stainless-steel tip [16]. It is also worth noting that several methods of combining SPM with SERS were explored in the 1990s.

In 2000, the above three groups realized that TERS employed different kinds of methods. The Kawata group developed Ag-coated AFM tips and rough Ag films as substrates [10]. Using such SERS-active substrates, one can measure far-field spectra that can be detected easily even when a tip is retracted. The Zenobi group and the Anderson group utilized dielectric substrates, where the tip solely worked as a nanoantenna to support the surface plasmon. When the tip approached a sample on the substrate, strong TERS spectra were observed. Later in the same year, Pettinger et al. also carried out TERS using STM and sharp metallic Ag tips electrochemically etched from Ag wire [17]. In the experiments by Kawata et al. [10] and Pettinger et al. [17], there was a strong plasmonic coupling between the tip and substrate known as gap mode.

TERS has recently shown remarkable advances, particularly in experimental setups, such as angstrom TERS, ultrahigh vacuum (UHV)-TERS, electrochemical (EC)-TERS, and solution TERS. Angstrom TERS, which is described in Chap. 23, has opened a new era of TERS [1, 18–20]. It was born as a result of the combined power of enhanced Raman scattering and high-resolution scanning probe microscopy. Angstrom TERS enables one to delve deep into the details of molecular structure and dynamics at the sub-nanoscale level. It provides priceless

insights into atomic-level reaction mechanisms by enabling real-time observation of the amazing process of bond formation and breakdown. UHV-TERS has been developed by several groups [21–29]. UHV-TERS reduces the risk of contamination of the sample surface in open-air environments significantly. Moreover, the UHV-TERS experiments preserve TERS tips, especially silver ones, from oxidation. It is noted that UHV-TERS measurements are usually performed at a very low temperature. It was Pettinger et al. who reported the first UHV-TERS mapping of a single brilliant crystal blue (BCB) molecule [22].

According to recent studies, the TERS process was described as an analogue to broadband femtosecond stimulated Raman scattering, in which the laser serves as a Raman pump and the surface plasmon acts as a Raman probe [26–28]. UHV-TERS allows one to observe angstrom-resolved TERS, which will be described in some detail in this chapter. The Van Duyne group reported experiments to assess the feasibility of integrating pulsed laser excitation with TERS [30]. To acquire the TERS spectra of R6G and malachite green isothiocyanate, the researchers used an optical parametric oscillator (OPO) generating 1 ps pulses at a high repetition rate of 80 MHz.

In EC-TERS setups, control of the potential of a working electrode is very important [31]. Zeng et al. succeeded in controlling the potentials of the tip and substrate using a bipotentiostat relative to a Pt wire in their EC-STM-TERS setup. They carried out various applications of EC-TERS. For example, they investigated the redox reactions of a nonresonant molecule, thiolacetyl-terminated-phenylene ethynylene-substituted anthraquinone (2-AQ), on the Au(111) surface [32]. Van Duyne et al. reported EC-AFM-TERS based on bottom illumination to probe the nanoscale redox behavior of Nile Blue on a transparent indium tin oxide (ITO) electrode [33]. Moreover, a new side-illumination EC-TERS setup has recently been proposed [32–35]. A few recent studies of EC-TERS will be reported later.

Applications of TERS have been expanding remarkably. Of particular note is the progress in TERS studies of biological molecules and materials [7, 36–38]. TERS has been used not only for the studies of biomolecules, such as proteins, DNA [39], RNA [40], and amyloid [41], but also biological systems, such as biological membranes, biological monolayers with drugs or cytochrome *c* [42], and viruses [43].

Schmid et al. reported liquid TERS for the first time in 2009 [44]. Since that time, several new ideas have been born to overcome the difficulties of liquid TERS, and nowadays, liquid TERS has become a routine technique [45–50]. Pienpinijtham et al. designed chemically modified tips with various probe molecules to improve the sensitivity, selectivity, and stability of TERS tips during liquid phase measurements [45, 49]. They used them for nanoscale pH measurement in solutions and chirality discrimination using TERS.

Several innovative new techniques have been proposed to address the limitations of conventional TERS. For example, Lee et al. proposed adaptive tip-enhanced nanospectroscopy [51]. Chen et al. developed locally integrated Raman polarizability density (LIRPD) [52]. Umakoshi et al. explored the use of tapping-mode AFM for tip position control in TERS [53]. These studies and recent progress in tip fabrication will be discussed in this chapter. Taguchi et al. reported the first TERS measurement

using deep-ultraviolet (DUV) excitation [54, 55]. DUV-TERS is reported in Chap. 25 in detail.

In the last few years, there have been several reports on chemical imaging with a resolution of a few angstroms (chemical imaging of a single molecule or a single bond) [18–20, 51, 56]. It has become possible to utilize angstrom-resolved TERS microscopy, especially with the new scanning Raman picoscopy (SRP) methodology, for visually constructing the chemical structure in real space and the determination of structural and chemical heterogeneities of surface species at the single-bond limit. A "single molecule" can be chemically imaged under ambient conditions.

## 6.2 A Revolutionary Tool for Single-Molecule Studies (Angstrom-Scale Resolution)

TERS has ignited a revolution in our understanding of single molecules at the nanoscale, wielding the combined power of enhanced Raman scattering and high-resolution scanning probe microscopy [1, 7, 9, 52, 57–63]. This unprecedented resolution transcends mere morphological information, delving deep into the fascinating details of molecular structure and dynamics at the sub-nanoscale level. In this section, some recent TERS applications for single-molecule studies will be discussed. Recent advancements have pushed TERS even further, allowing us to witness the awe-inspiring process of bond breaking and formation in real time, offering invaluable insights into reaction mechanisms at the atomic level [18–20]. From deciphering subtle differences between isomers to unraveling the intricacies of molecule–substrate interactions [58, 60, 64], TERS serves as a transformative lens for observing and manipulating matter at the atomic and molecular level. This opens doors to a plethora of groundbreaking discoveries in diverse fields, ranging from materials science to quantum information technologies [61, 63], truly making TERS a revolutionary tool for the future of molecular science.

### *6.2.1 Distinguishing Two Adjacent Regioisomers with Angstrom Sensitivity*

Mahapatra et al. employed UHV-TERS mapping to achieve angstrom-scale chemical analysis of metal-supported *trans*- and *cis*-regioisomers of tetrakispentafluorophenyl-porphodilactone ($H_2F_{20}$TPPDL) [58]. These regioisomers play crucial roles in modulating the photophysical properties of porphyrins [65], making their differentiation crucial for understanding their functionalities. Both isomers were deposited onto a clean Ag(100) surface in submonolayer coverage under UHV conditions. TERS measurements were performed at liquid nitrogen temperature (∼77 K) using an electrochemically etched Ag tip and a 633-nm excitation laser within a scanning tunneling

microscope (STM) chamber. *Trans*-isomers exhibit a "pinwheel" conformation and form "AAA"-type packing in their self-assembly. *Cis*-isomers also display a "pinwheel" conformation, but their packing appears significantly different, with lactone moieties arranged in a "zigzag" pattern and molecular rows forming an "ABA" pattern. To investigate their behavior as a two-component organic heterostructure, both isomers were sequentially deposited on Ag(100). Two distinct self-assembled structures (Structures 1 and 2) were observed (Fig. 6.1a). While STM could not distinguish the identity of the molecules within these structures, TERS provided the key to unlocking their secrets. Mahapatra et al. performed sequential TERS measurements along a line spanning 8 nm across the boundary between the two structures (Fig. 6.1b). Their findings revealed that only modes parallel to the tip axis are significantly enhanced, following the SERS selection rules [66, 67], This characteristic allowed them to clearly identify the cis-isomers based on prominent peaks in the 500–900 $cm^{-1}$ region. Line profile analysis of the strongest peak (699 $cm^{-1}$) confirmed that Structure 1 consists solely of trans-isomers, while Structure 2 is composed only of *cis*-isomers (Fig. 6.1c). This demonstrates the remarkable capability of TERS to distinguish regioisomers with an impressive resolution of 8 Å, defined by the distance between the boundary points. Further investigations by the same group utilized TERS to analyze the orientation of these molecules on different substrates (Cu, Ag, and Au), showcasing the versatility of this technique [68].

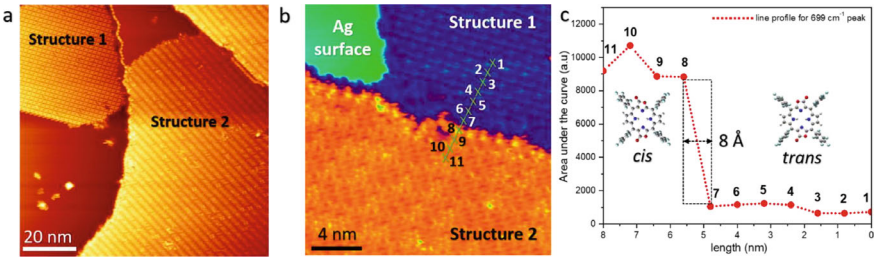



**Fig. 6.1** **a** A STM topographic image (100 nm × 100 nm) of co-deposited *trans*- and *cis*-isomers where structure 1 and structure 2 were identified. **b** A zoom-in STM image where TERS line profile measurements were performed. Eleven points are marked by green crosses. Structure 1 (blue), structure 2 (orange), and bare Ag surface (green) are highlighted. **c** TERS line profile measured with Ag tip for 699 $cm^{-1}$ peak (area under the curve) with spatial resolution 8 Å. This figure has been adapted/reproduced from ref. [58] with permission from American chemical society, copyright 2019

### 6.2.2 *Decoupling Molecules from Metal Substrates*

Jaculbia et al. utilized scanning tunneling microscope tip-enhanced Raman spectroscopy (STM-TERS) to probe the resonance Raman effect of a single copper naphthalocyanine molecule deposited on an ultrathin insulating film (Fig. 6.2) [60]. This innovative approach allowed them to observe the molecule's intrinsic vibrational and electronic properties without perturbation from a metal substrate. The authors demonstrate that the observed Raman enhancement arises directly from resonant excitation of the molecule's intrinsic absorption band, achieving this by precisely tuning the laser wavelength. Notably, TERS images revealed the symmetry of the vibrational modes by accounting for the lateral components of the electric field within the plasmonic nanocavity. This study highlights the effectiveness of STM-TERS in decoupling the molecule from the underlying metal surface, preserving its intrinsic properties, and revealing the direct link between resonance Raman scattering and the molecule's absorption band. Furthermore, the findings provide valuable insights into the optical processes occurring in molecular systems coupled to plasmonic nanocavities, paving the way for further exploration of light–matter interactions at the nanoscale.

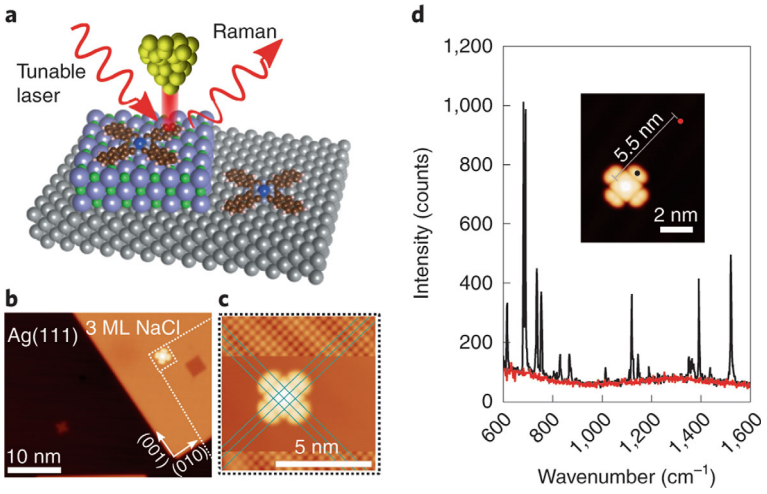



**Fig. 6.2** **a** Experimental setup for STM-TERS of CuNc molecule. **b** Single CuNc molecule adsorbed on a 3-monolayer NaCl/Ag(111) surface (wide-field view). **c** High-resolution STM image revealing structure of CuNc on NaCl. **d** STM-TERS data: black trace shows fingerprint near active "lobe", and red trace shows signal further away (>5.5 nm). Inset indicates tip positions during data collection. This figure has been adapted/reproduced from ref. [60] with permission from Springer Nature, copyright 2020

### 6.2.3 Unleashing the Power of Atomic-Scale Plasmonic Cavities for Ultrasensitive Analysis

Liu et al. have achieved ultrasensitive chemical analysis and imaging at the nanoscale by harnessing the power of atomic-scale plasmonic cavities [61]. Their study focuses on the evolution of TERS when a silver tip forms a stable atomic point contact (APC) with ultrathin zinc oxide or sodium chloride films on a silver surface at a cryogenic 10 K temperature. The key findings reveal dramatic changes in TERS intensity and spectra upon APC formation, with the degree of change depending on the film's chemical properties. When the film is zinc oxide, a significant increase in TERS intensity coupled with the emergence of a new vibrational mode indicates strong hybridization and charge transfer between the tip and the film. In stark contrast, the same experiment with sodium chloride shows no such enhancement or mode, suggesting negligible hybridization and charge transfer. To explain these intriguing observations, the authors employed a combination of density functional theory calculations and electrodynamic simulations. Their results support a charge transfer mechanism as the driving force behind the enhanced Raman scattering observed in the fused atomic-scale plasmonic junction. This work opens up exciting possibilities for utilizing charge transfer enhancement in atomic-scale plasmonic cavities to achieve unprecedented sensitivity in nanoscale chemical analysis and imaging. It also sheds light on the intricate nature of plasmonic fields and light–matter interactions within angstrom-scale gaps, paving the way for advancements in the fields of quantum plasmonics and optoelectronics. While the potential of this approach is undeniable, the research also highlights the importance of considering thermal instability and structural fluctuations in realistic applications. By addressing these challenges, researchers can unlock the full potential of TERS in atomic-scale cavities and further revolutionize our understanding and manipulation of matter at the nanoscale.

### 6.2.4 Witnessing Bond Breaking and Making at the Single-Bond Level

Wang et al. employed TERS to achieve a groundbreaking feat: observing bond breaking and formation in a single chemisorbed molecule at the single-bond level [18]. Using melamine as a model, they thermally evaporated melamine molecules onto a Cu(100) surface under UHV and precooled the sample to 6.2 K. Electrochemically etched silver tips coupled with a 532-nm laser enabled TERS measurements, revealing the spatial distribution of N–H bonds at $\sim$ 3453 $cm^{-1}$ and $\sim$ 3572 $cm^{-1}$ with sub-nanometer resolution. By tracking spectral evolution under laser illumination (Fig. 6.3), the researchers witnessed the photochemical reaction of the dehydrogenated molecule in real time. The disappearance of peaks corresponding to N–H stretching vibrations indicated bond breaking, while a red-shifted peak and the emergence of a new N–H peak confirmed the weakening of the remaining bond and the

formation of a new one in the cyanuric ring. This remarkable observation highlights the power of TERS in revealing intricate details of molecular adsorption and surface reactions, including bond dynamics at the single-bond level. It is noteworthy that TERS spectra of free or physically adsorbed melamine molecules are not observable due to the TERS selection rule [66, 67]. This emphasizes the unique capabilities of TERS in probing chemisorbed molecules and their transformations on surfaces, offering invaluable insights into the fundamental mechanisms of chemical processes at the nanoscale.

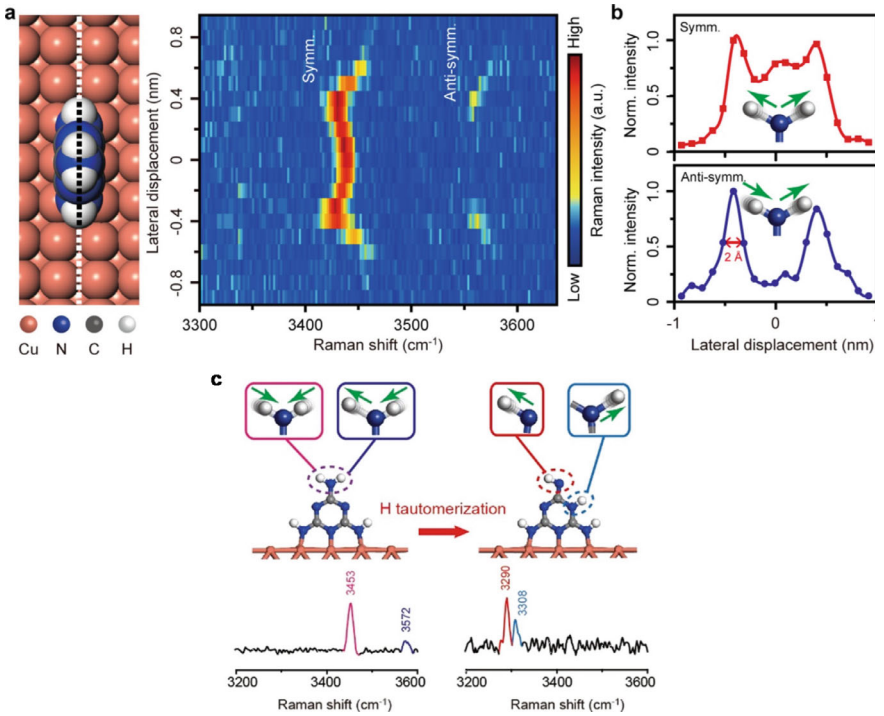



**Fig. 6.3** Line-trace TERS measurements over a single melamine molecule chemisorbed on Cu(100). **a** A waterfall plot of 19 consecutive TERS spectra corresponding to line-trace measurements indicated by dotted line in left panel. **b** Normalized Raman intensity profiles for the bands due to symmetric and antisymmetric stretching vibrations of N–H bonds at ~ 3434 and ~ 3560 $cm^{-1}$, respectively. Spatial resolution of ~ 2 Å is labeled for antisymmetric mode. **c** Schematic illustration of TERS spectral variations upon tautomerization of melamine. This figure has been adapted/reproduced from ref. [18] with permission from American chemical society, copyright 2021

### 6.2.5 *Visualizing Polymerization Reactions in Real Time*

Shao et al. employed *in situ* TERS imaging to shed light on the intriguing phenomenon of plasmon-induced two-dimensional [4 + 4]-cycloaddition polymerization on Au(111) [19]. This study utilized two types of anthracene-based monomers, prepared as monolayers in a Langmuir–Blodgett trough and transferred onto Au(111) substrates [69, 70]. TERS measurements were performed under ambient conditions, leveraging an integrated STM/Raman system with electrochemically etched silver probes [71, 72] and a 633-nm laser. Fig. 6.4a showcases the successful physisorption of both monomers and the resulting 2D polymers on the Au(111) surface. This weak interaction between the samples and the substrate makes these systems ideal models for investigating reaction mechanisms. The unique TERS configuration enabled real-time, spatially resolved monitoring of the photocatalytic reaction, providing valuable insights into both the hot carrier transfer excitation mechanism and the in-plane crosslinking growth mechanism at the nanoscale. Figure 6.4b–d depicts TERS images constructed using characteristic peaks of the polymer and monomer, revealing the polymerization process through changes in the intensity patterns. Analyzing the TERS spectra collected in Fig. 6.4b, a lateral resolution of approximately 3.7 nm was estimated based on the line profile analysis using a Gaussian fit (Fig. 6.4g). While not reaching the angstrom level, this resolution demonstrates the power of TERS imaging in providing direct evidence for covalent bond formation in complex systems under ambient conditions, a capability with vast potential applications. Furthermore, this work paves the way for utilizing modulated plasmon-induced [4 + 4]-cycloaddition reactions to explore the exciting field of 2D polymer monolayer nanolithography.

### 6.2.6 *Unveiling Borophene–DBP Interactions at the Angstrom Scale*

Li et al. employed ultrahigh-vacuum scanning tunneling microscopy-tip-enhanced Raman spectroscopy (UHV-STM-TERS) to probe the intricate interactions between two-dimensional boron monolayer (borophene) and adsorbed tetraphenyldibenzoperiflanthene (DBP) molecules at the angstrom scale, shedding light on their interfacial dynamics and strain-induced phenomena (Fig. 6.5) [64]. On an Ag(111) substrate, borophene can adopt two distinct structural polymorphs: $\nu_{1/6}$ or $\nu_{1/5}$. Analyzing the TERS spectra revealed characteristic peaks associated with the B23g or B2g vibrational modes (perpendicular to the plane) at 189 $cm^{-1}$ and 180 $cm^{-1}$ for the $\nu_{1/6}$ and $\nu_{1/5}$ phases, respectively. Interestingly, upon adsorption of DBP molecules on the borophene surface in either a herringbone or stripe arrangement, a substantial blue-shift and broadening of the $B^2{}_{3g}$ or B2g modes were observed. For the $\nu_{1/6}$ phase, the $B^2{}_{3g}$ mode shifted from 189 $cm^{-1}$ to 198 $cm^{-1}$, while for the $\nu_{1/5}$ phase, the $B^2{}_{g}$ mode shifted from 180 $cm^{-1}$ to 194 $cm^{-1}$. This phenomenon is

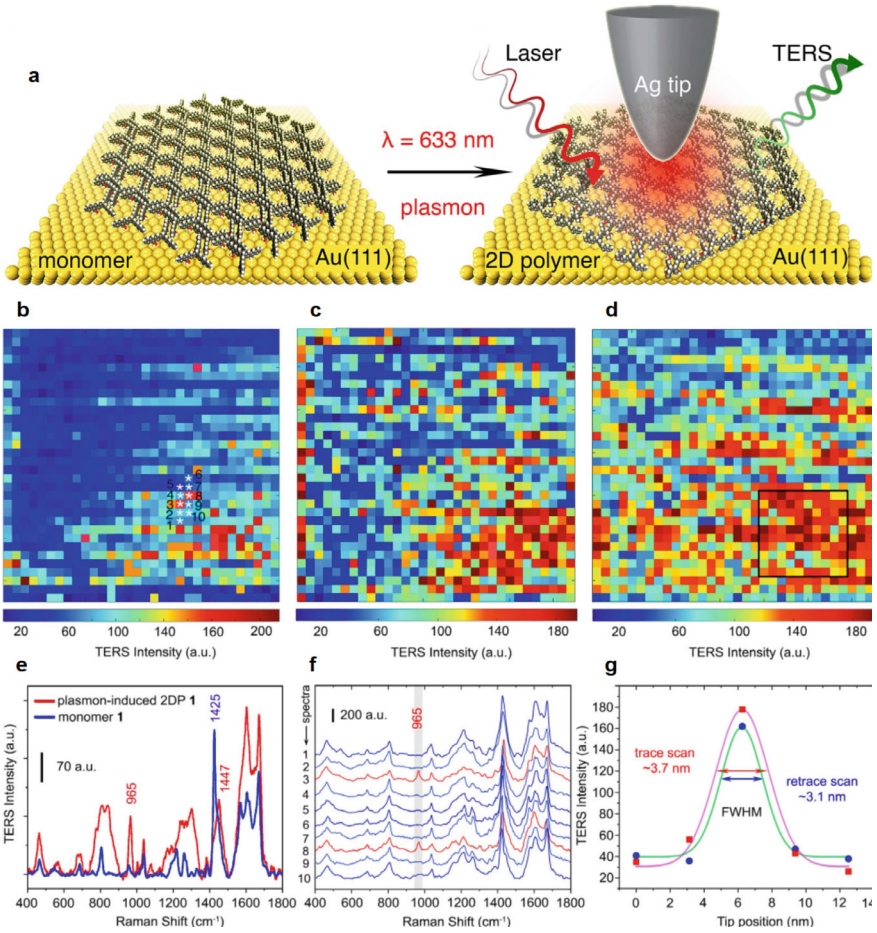



**Fig. 6.4** **a** Schematic illustrations of monomer ML on Au(111) and TERS imaging for plasmon-induced 2DP ML under visible laser irradiation (633 nm). Consecutive TERS imaging of plasmon-induced 2D polymerization within monomer **1** ML on Au(111). **b** The 1st, **c** 2nd, and **d** 3rd TERS intensity images of band at 965 $cm^{-1}$. The maps were repeatedly measured over a 100 × 100 $nm^2$ area with 3.125 × 3.125 $nm^2$ pixels resolution at same location under continuous laser irradiation. **e** Baseline corrected average TER spectra of monomer **1** and corresponding plasmon-induced 2DP **1**. **f** 10 sequential TERS measurements along line-trace and retrace scans marked in **b**. **g** Corresponding TERS intensity and Gaussian fitting of band at 965 $cm^{-1}$ in **f**. This figure has been adapted/reproduced from ref. [19] with permission from Springer Nature, copyright 2021

attributed to the localized interfacial strain induced by the adsorbed DBP molecules. Previous studies have shown that a 0.6% tensile strain can shift the $B^2{}_{3g}$ mode by − 6 $cm^{-1}$, further supporting this conclusion.

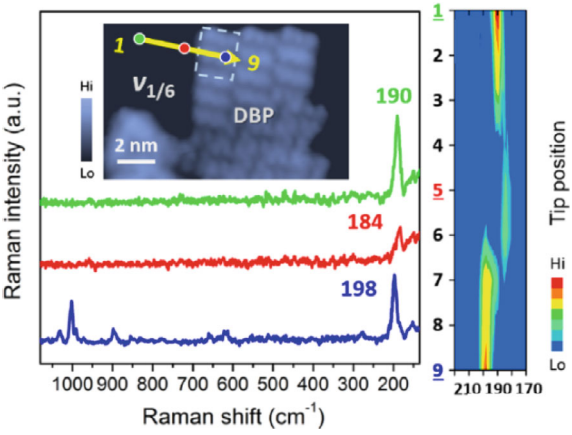



**Fig. 6.5** (Left) TERS spectra of borophene obtained at colored spots in inset STM image. (Right) TERS peak positions along yellow arrow in the inset. This figure has been adapted/reproduced from ref. [64] with permission from American Chemical Society, copyright 2021

### *6.2.7 Exploring Correlated Scattering and Quantum Information Applications*

Tschannen et al. employed tip-enhanced Raman scattering (TERS) to significantly amplify the Raman response of a single carbyne chain, a one-dimensional carbon allotrope confined within a double-walled carbon nanotube [63]. This study revealed a remarkable observation: a large anti-Stokes/Stokes ratio in the TERS spectrum, signifying a deviation from the expected thermal phonon statistics. This implies the intriguing possibility of correlated Stokes–anti-Stokes (SaS) scattering mediated by an excited phonon. The authors further explored the influence of resonance effects and laser-induced heating on the anti-Stokes/Stokes ratio, ultimately comparing TERS with surface-enhanced Raman scattering (SERS) as techniques for inducing SaS scattering. Their findings highlight the superior control and reproducibility offered by TERS in this context, solidifying its position as a powerful tool for studying SaS scattering. Furthermore, the study concludes that carbyne possesses immense potential as a material for generating entangled photon pairs, paving the way for exciting advancements in quantum information technologies.

## 6.3 Nanostructures Unraveled: The Power of TERS

The potential of nanostructures hinges on our ability to peer into their delicate atomic arrangements. TERS unlocks this hidden world, acting as a "molecular fingerprint reader" for molecules residing on their surfaces. This section delves into the remarkable power of TERS across diverse nanostructures, including carbon nanomaterials (e.g., carbon nanotubes [73, 74] and graphene [75–77]), metal compounds [78–80], metal nanostructures [81], and bimetallic nanostructures [82, 83]. Prepare to unravel their secrets, from deciphering strains and defects in carbon nanomaterials

to witnessing reaction pathways in bimetallic structures. Witness how TERS paves the way for the development of revolutionary materials and technologies, all by unraveling the hidden language of the nanoscale.

### *6.3.1 Carbon Nanomaterials*

Carbon nanomaterials, with their unique structures and remarkable properties, have revolutionized numerous fields, ranging from electronics and energy to medicine and environmental science. However, their complex nature necessitates advanced analytical tools to fully understand their properties and unlock their full potential. TERS has emerged as a powerful technique for probing these materials at the nanoscale, offering unparalleled spatial resolution and enhanced sensitivity.

Carbon materials exhibit prominent Raman peaks, including the D, G, and G' (2D) bands (Fig. 6.6) [9, 84, 85]. These peaks provide information about strain, doping, defects, stacking, and the number of layers in the material. Studies on single-walled carbon nanotubes (SWCNTs) using TERS have shown splitting of the D band and a higher wavenumber shift of the $G^+$ mode at bending positions [73]. Additionally, the bundling area exhibits both a higher wavenumber shift and increased G and G' (2D) band signals [86]. An asymmetric Fano peak appears in the G band at the crossover point [87]. The diameter of SWCNTs can be determined by the peak position of the radial breathing mode at low wavenumbers. However, it is more challenging to determine the diameter and the number of layers (walls) of multiwalled carbon nanotubes (MWCNTs). Using AFM-TERS, researchers have been able to measure the diameter and D band of MWCNTs [74]. As the diameter (number of walls) increases, the D band intensity strengthens due to the breakdown of symmetry in carbon rings by interwall interactions rather than an increase in defects. The observed intensities were plotted against the number of walls and fitted by calculating the enhanced electromagnetic field distribution on the Ag tip combined with the area of walls in the field.

For graphene, the G' (2D) and G bands are sensitive to both strain and doping. Compression and higher hole densities cause a redshift in these bands [89]. To determine their individual contributions, the peak positions of the G' (2D) and G bands are plotted against each other. A steep slope indicates strain, while a gentle slope indicates doping [89]. TERS measurements of graphene on Au(111) showed a slope that fell between those caused by pure strain and doping [75]. The ratio of the D to the G band intensity has been used to estimate the number of defects in graphene [84]. TERS measurements of this ratio were compared to those obtained by normal Raman scattering. The normalized ratios (TERS ratio divided by normal Raman scattering ratio) correlated with the normalized D band intensity [76]. Spatial variations in these ratios were observed by TERS on O- or N-functionalized graphene prepared using different methods [77]. Furthermore, TERS has been used to investigate the D-family bands in ultrathin amorphous carbon films coated on silica fibers and annealed via electrical bias or heating [90, 91]. The D band originates not only from defects but

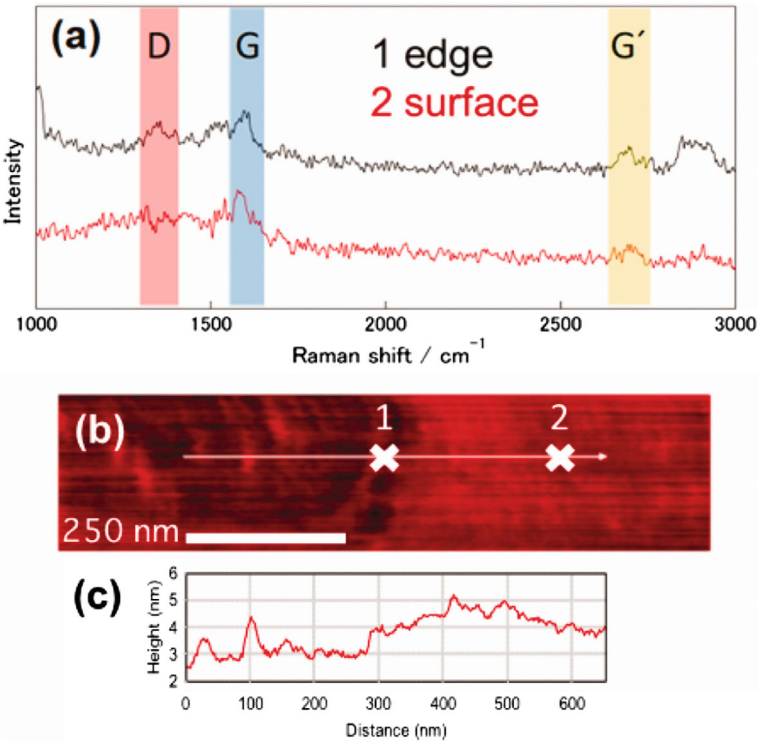



**Fig. 6.6** **a** TERS spectra at edge and inner part of epitaxial graphene ribbon without buffer layer on Si-face of 4H-SiC. The points are shown as 1 and 2 in **b** an AFM topography image. **c** Height trace analysis of **b**. This figure has been adapted/reproduced from ref. [88] with permission from SAGE Publications, copyright 2020

also from edges where carbon atoms are arranged in an armchair configuration [92]. Using non-contact AFM-TERS, the D band was observed at the edge of epitaxial graphene ribbons grown on the Si-face of a SiC substrate without a buffer layer (Fig. 6.6) [88, 93]. In contrast, the D band of graphene on the C-face disappeared at edges where armchair edges were expected. This absence of the D band is likely due to the binding of these edges to the C-face of 4H-SiC, which weakens the TERS signal compared to the edges on the Si-face without a buffer layer. The edge structure (armchair or zigzag) of graphene nanoribbons affects their band gap [94]. Graphene nanoribbons with a width of ~ 10 nm, fabricated using electron beam lithography, exhibited broadened D and G bands (38 to 86 cm$^{-1}$ and 28 to 66 cm$^{-1}$, respectively) and a missing G' (2D) band at the edges, unlike their exfoliated counterparts [95–97].

### 6.3.2 Two-Dimensional Transition Metal Compounds

Two-dimensional transition metal dichalcogenides (2D TMDs) like $MoS_2$ and $WSe_2$ have captivated researchers due to their potential in optoelectronics. TERS, offering sub-nanometer resolution, has emerged as a powerful tool for unraveling the intricate details of these materials at the nanoscale. Probing the edges of $MoS_2$, a prototypical 2D TMD, with TERS reveals a shift in the $A_{1g}$ vibrational mode peak (406 $cm^{-1}$) depending on their configuration. Armchair edges exhibit a higher peak, while zigzag edges show a lower peak, demonstrating TERS's ability to distinguish these structures (Fig. 6.7) [78]. Furthermore, combining TERS with photo-induced force microscopy (PiFM) and Kelvin probe force microscopy (KPFM) allows characterization of buried layers and work functions, providing valuable insights into phonon behavior and charge transfer [98, 99].

TERS has proven valuable for studying materials beyond dichalcogenides. AFM-TERS on GaS, a monochalcogenide, revealed layer-dependent peak redshift and sharpening in the $A^1{}_{1g}$ and $A^2{}_{1g}$ modes, indicating its sensitivity to layer number [79]. Similarly, combining TERS with scanning tunneling microscopy (STM) on ZnO grown on Ag(111) unveiled not only electromagnetic enhancement but also chemical enhancement, showcasing TERS's ability to detect chemical interactions and local strain [61, 100].

Kato et al. further explored the role of nanoscale inhomogeneities like defects and wrinkles in TMDCs using TERS [80]. Their work highlights the impact of these inhomogeneities on material properties, emphasizing the importance of nanoscale characterization. Another landmark achievement is the development of an ultra-stable TERS system by Kato et al. [101]. This system overcomes traditional limitations, enabling hyperspectral nanoimaging of large-scale 2D materials like $WS_2$ and revealing diverse nanoscale features. This opens doors for a wider range of applications and further exploration of the potential of 2D materials.

TERS has emerged as a game-changer for exploring the intricate world of 2D materials. From revealing edge structures and probing buried layers to uncovering

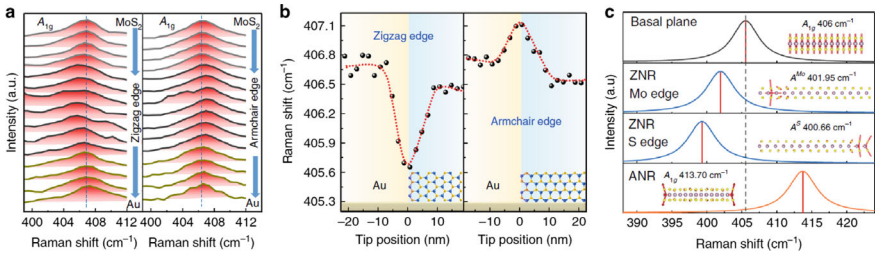



**Fig. 6.7** **a** TERS spectra of $MoS_2$ monolayer across zigzag (left panel) and armchair edge (right panel). **b** Peak positions plotted against tip positions. **c** Calculated Raman spectra and lattice vibration of basal plane, zigzag nanoribbon (ZNR) at Mo and S edges, and armchair nanoribbon (ANR). This figure has been adapted/reproduced from ref. [78] with permission from Springer Nature, copyright 2019

chemical interactions and local strain, TERS offers unprecedented insights, paving the way for advancements in optoelectronics and other fields.

### 6.3.3 Metal Nanostructures

In a significant advancement for plasmonic nanoimaging, Kato et al. introduce a novel TERS technique utilizing a chemically modified metallic tip. This method offers several advantages, including eliminating the need for sample functionalization with Raman markers that can alter plasmonic properties [81]. Additionally, the smooth, one-sided metal-coated pyramidal tip design reduces background signal and enhances measurement sensitivity and resolution. Demonstrating its efficacy, the authors successfully mapped the optical field distribution and resonance wavelength dependence of a gold nanostructure array with a remarkable 11 nm spatial resolution, achieving excellent agreement with numerical simulations. This breakthrough technique unlocks the potential for comprehensive investigation of intrinsic plasmonic properties in metallic nanostructures without sample modification, paving the way for further research and development in diverse applications, such as molecular sensing, energy transfer, and optical storage.

### 6.3.4 Bimetallic Nanostructures

Bimetallic nanostructures, combining catalytic and plasmonic metals, have been fabricated to exploit their unique catalytic activity and selectivity. Several studies have investigated these structures using TERS to gain insights into their properties. In the case of Pd sub-monolayers on Au(111), TERS revealed different adsorption configurations for phenyl isocyanide on terraces and step edges [82]. The observation of a weakened NC bond at the step edge suggests its instability for oxidation [82]. Similarly, TERS studies of chloronitrobenzenethiol (CNBT) hydrogenation to chloroaminobenzenethiol (CABT) provided evidence of site-selectivity, evident by the disappearance of the $NO_2$ peak in CNBT and the shift in the C = C stretching mode on Pd islands [83]. Interestingly, TERS images revealed a "low-hydrogenation" region on the Au surface, indicating spillover from the catalytic Pd sites [83]. TERS also sheds light on the catalytic properties of Pt or Pd nanostructures deposited on Au nanoplates (Au@PtNPs or Au@PdNPs) [102–105]. These structures facilitated the degradation of 4-mercaptophenylmethanol (MPM) and 4-mercaptobenzoic acid (MBA) to thiophenol, as observed by TERS spectra [102]. Furthermore, the plasmon-induced oxidation of MPM to MBA and the reduction of MBA to MPM were observed on Au@PtNPs and Au@PdNPs, evident by the decrease and increase in the peak intensity associated with the C = O stretching vibration, respectively [102]. The catalytic probability on Au@PtNPs was twice that of Au@PdNPs, and this correlated with the stronger rectified (DC) electric fields detected on the former

surface through Stark shift analysis [102, 103]. Finally, TERS studies revealed distinct reaction pathways for the photocatalysis of 4-aminothiophenol (4-ATP) to *p,p'*-dimercaptoazobisbenzene (DMAB) on AuNPs and Au@PtNPs [104, 105]. On the Au surface, 4-ATP molecules directly combine with each other. In contrast, on Au@PtNPs, a portion of 4-ATP was oxidized to 4-nitrobenzenethiol (4-NBT), while the remaining molecules reacted with 4-NBT. This study highlights the valuable insights gained from using TERS to probe the unique catalytic properties of bimetallic nanostructures. Understanding these interactions at the nanoscale provides a foundation for the further development of highly efficient and selective catalysts.

## 6.4 Nanoscale Secrets in Material Science

TERS revolutionizes material science by allowing researchers to map the vibrational signatures of materials with unprecedented detail, revealing how structure, composition, and properties interact at the nanoscale. This section explores TERS applications across diverse material systems, showcasing how it transforms our understanding and enables the design of advanced materials with superior properties. It unveils hidden information at the nanoscale, revealing how fillers affect polymer chains in composites and disentangling carbon nanotubes within them [106, 107]. TERS even deciphers the intricate world of graphene, detecting strain mechanisms and quantifying its content [108, 109]. Its power extends to deciphering how nanostructures in graphene influence its properties [110]. Finally, it reveals the hidden interactions between nanoparticles and graphene oxide, revealing fascinating structural changes [111]. This glimpse into TERS's diverse applications, spanning polymers to graphene, showcases its immense potential in unlocking the secrets of nanomaterials, paving the way for revolutionary discoveries and materials with superior properties.

### *6.4.1 Styrene–Butadiene Rubber/Carbon Nanotubes Nanocomposites*

Suzuki et al. employed TERS to study the interactions between styrene–butadiene rubber (SBR) and multiwalled carbon nanotubes (MWCNTs) in nanocomposites (Fig. 6.8) [106]. They found that TERS offered high spatial resolution and sensitivity, revealing the inhomogeneity and orientation changes of polymer chains caused by the filler. The authors presented Raman and TERS spectra of pure SBR, pure MWCNTs, and SBR/MWCNT nanocomposites, assigning Raman bands to corresponding vibrational modes. Notably, TERS spectra displayed marked variations depending on the measurement point, reflecting the distribution of MWCNTs in the polymer matrix. Additionally, changes in the relative intensities of vinyl and phenyl bands in TERS spectra suggested that $\pi$–$\pi$ interaction between MWCNTs and phenyl rings affected

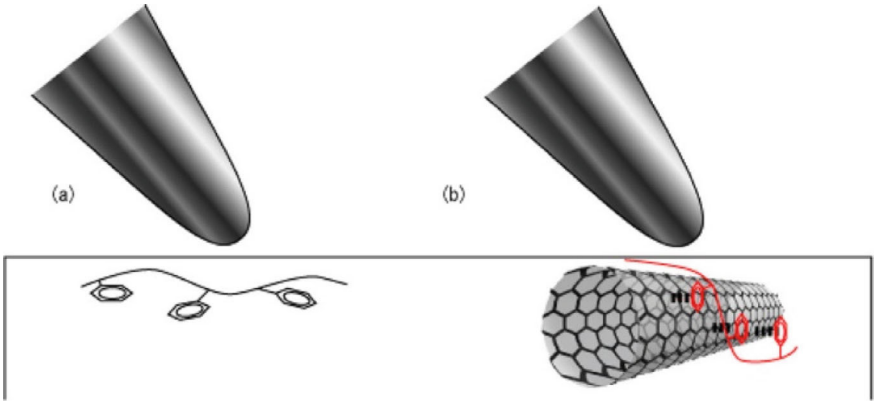



**Fig. 6.8** Schematic diagram of surface structure of SBR/MWCNT nanocomposites: **a** far from and **b** near CNT area. At interface between polymer and filler, phenyl ring should be oriented perpendicular to surface through a $\pi$–$\pi$ interaction between CNT and phenyl ring. This figure has been adapted/reproduced from ref. [106] with permission from American chemical society, copyright 2013

the orientation of polymer chains at the interface. The authors concluded that TERS provides valuable insights into local interactions and structure changes at the interface of polymer nanocomposites, potentially opening new avenues for future research.

### *6.4.2 Carbon Nanotube/Polystyrene (PS) Nanocomposites*

Yan et al. employed TERS to delve into the hidden world of single-walled carbon nanotubes (SWCNTs) and polystyrene (PS) nanocomposites, revealing their properties at the interface [107]. By comparing normal Raman and TERS spectra, the researchers observed significant differences. While normal Raman showed limited variation, TERS unveiled noticeable shifts and intensity changes in the vibrational bands of both SWCNTs and PS. These alterations reflected the mechanical compression from the PS matrix and the disentanglement of SWCNTs caused by polymer chain penetration. Additionally, the intensity ratio of specific bands provided insights into the distribution of SWCNTs within the PS matrix. This study concludes that TERS, with its superior sensitivity and spatial resolution, offers a powerful tool for investigating the local structure and interactions at the interface of CNT-based polymer nanocomposites, providing valuable information beyond the reach of traditional Raman spectroscopy.

### 6.4.3 *Epitaxial Graphene Grown on SiC*

Vantasin et al. investigated steps, ridges, and cracks on epitaxial graphene, revealing TERS's superior resolution and quantitative analysis capabilities (Fig. 6.9) [108]. Their findings highlight its ability to detect strain and graphene content in individual nanostructures. Notably, TERS observed relaxed compressive strain on ridges, confirming their formation as a stress relief mechanism. Additionally, the reduced graphene/SiC signal ratio in cracks suggested their potential absence of graphene, offering crucial information about their composition. This study concludes that TERS is transformative for characterizing nanostructures on epitaxial graphene.

Suzuki et al. developed a novel bulk silver tip for TERS, achieving high-quality spectra of epitaxial graphene on SiC [109]. This innovative tip enabled the observation of previously unseen G + G′ mode peaks, expanding our understanding of graphene's vibrational characteristics. The researchers observed intriguing position-dependent variations in the G band, attributed to local stresses induced by thermal expansion mismatches. Corresponding AFM images revealed ridge structures, further supporting the presence of local distortions in the graphene lattice. This study showcases TERS's power in selectively probing the local properties of graphene on SiC, offering insights beyond conventional techniques.

Vantasin et al. investigated single-layer graphene microislands synthesized on SiC using a novel laser engraving and annealing technique [110]. These islands displayed intriguing nanostructures like nanoridges, nanocracks, and nanosteps. By combining AFM, micro-Raman imaging, and TERS, the researchers delved into the nanoscale details of these structures. They discovered that nanoridges induce nanoscale variations in strain across the graphene sheet, leading to strain relaxation. Additionally, the absence of the D band in the Raman spectra suggests that the edges of the islands are likely of the armchair type. TERS further revealed the significant impact

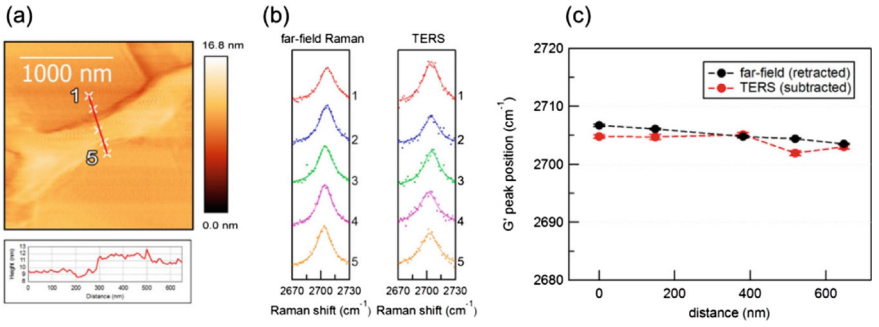



**Fig. 6.9** TERS measurement on step structure. **a** AFM topology image and line height profile. **b** G′ band in far-field Raman and TERS spectra from five measurement points shown in **a**. **c** Peak position of each G′ band in **b**, plotted against distances from point 1 along line profile in **a**. This figure has been adapted/reproduced from ref. [108] with permission from American chemical society, copyright 2013

of nanoridges on the Raman spectra of graphene, indicating differences in strain compared to flat areas. This finding effectively ruled out alternative mechanisms for nanoridge formation. The study also explored the properties and growth mechanisms of these graphene microislands, proposing the exciting possibility of manipulating nanostructures to create graphene with adjustable band gaps, potentially paving the way for novel electronic devices.

Collectively, these studies demonstrate the transformative power of TERS in advancing our understanding of diverse graphene nanostructures. By offering unparalleled spatial resolution and quantitative analysis, TERS opens doors to exciting possibilities in the field of graphene research and paves the way for the development of next-generation devices with superior properties.

### *6.4.4 Silver Nanoparticles/Graphene Oxide (AGO) Nanocomposites*

Pienpinijtham et al. employed the powerful technique of TERS to unravel the properties of silver nanoparticles/graphene oxide (AGO) nanocomposites [111]. This technique merges the strengths of surface-enhanced Raman scattering and scanning probe microscopy, enabling the acquisition of detailed molecular information at the nanoscale. Notably, TERS allows researchers to distinguish local spectra from the average spectra obtained by conventional Raman scattering, revealing hidden intricacies within the composite material. Using TERS, the researchers investigated AGO nanocomposites synthesized via chemical reduction of $AgNO_3$ in a GO dispersion. The resulting Ag nanoparticles (AgNPs) averaged 42.2 nm in size and were deposited on the GO surface. By meticulously collecting TERS spectra at different positions around AgNPs of varying sizes, the authors observed significant changes in the peak positions and areas of four key component bands associated with the C–C bonds within the GO layers. Based on these observations, the research team proposed an interaction model suggesting the presence of strong attraction forces between AgNPs and GO layers (Fig. 6.10). These forces cause the GO layers to flatten and bend, accompanied by charge transfer and a shortening of C–C bonds directly beneath the AgNPs. Remarkably, these structural changes extend for 200–250 nm away from the center of the AgNPs, propagated through the network of C–C bonds within the material. This study highlights the exceptional capabilities of TERS in uncovering the intricate interactions and structural changes occurring within AGO nanocomposites. By revealing this hidden information, the research paves the way for a deeper understanding of the properties of these materials and opens doors for their optimization in various technological applications.

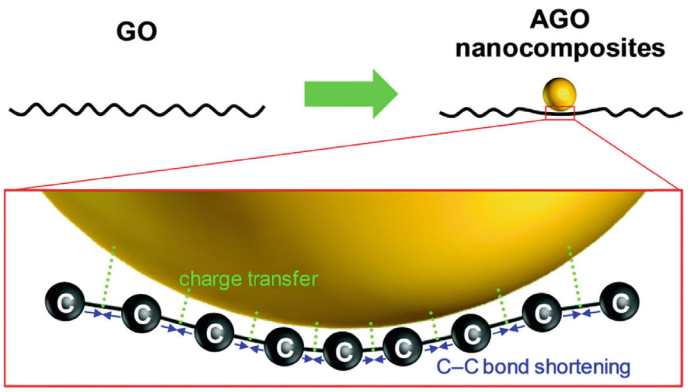



**Fig. 6.10** Structural changes of a GO layer in AGO nanocomposites at the molecular level. This figure has been adapted/reproduced from ref. [111] with permission from Royal society of chemistry, copyright 2018

### *6.4.5 Secondary Batteries*

In secondary batteries, particularly lithium-ion batteries, a critical layer called the solid electrolyte interphase (SEI) forms at the interface between the solid anode and the liquid electrolyte. This SEI plays a crucial role in battery performance and safety. However, traditionally, studying the SEI formation on an amorphous Si anode during charge–discharge cycles has been a challenge. To address this limitation, a specialized technique called "electrochemical tip-enhanced Raman spectroscopy (EC-TERS)" in an Ar-filled chamber was employed. This innovative approach allowed them to observe the SEI formation *in situ*, revealing its intricate nano-mosaic structure. Notably, the study found that the SEI structure varied significantly with the number of charge–discharge cycles, highlighting its dynamic nature [112]. This research provides valuable insights into the complex formation and evolution of the SEI on amorphous Si anodes in lithium-ion batteries.

## 6.5 Delving into Biomolecular Secrets with TERS

From proteins to viruses and DNA, TERS is transforming our understanding of biomolecules at the nanoscale, offering exquisite detail without harming these delicate structures [36–38, 113]. In this section, TERS unveils how light interacts with heme proteins, revealing their native states crucial for various biological processes [113]. It further unravels how peptides bind to surfaces, like the intriguing pH-dependent interaction of bradykinin with silver [37]. Beyond individual interactions,

TERS maps the organization of lung surfactant components on surfaces, uncovering structural variations at an impressive 20-nm resolution [42]. This versatile technique even sheds light on the mysteries of Alzheimer's disease by tracking protein aggregation [41]. It can also differentiate viruses based on their unique protein and RNA signatures [43]. Remarkably, TERS pushes the boundaries by resolving individual DNA and RNA strands, reconstructing their sequences with over 90% accuracy [39, 40]. This glimpse into TERS's diverse capabilities across biomolecules highlights its immense potential to unlock the hidden origin of life at the nanoscale, paving the way for groundbreaking discoveries in medicine, bioengineering, and beyond.

### *6.5.1 Biomolecules*

One of the major challenges faced in studying heme proteins, crucial for various biological processes, is photooxidation. Traditional techniques, such as surface-enhanced resonance Raman scattering (SERRS), can inadvertently alter the oxidation state of these proteins, leading to inaccurate results. Tanabe et al. addressed this issue by employing TERS [113]. Their study demonstrated that TERS, due to its non-invasive nature and superior spatial resolution, successfully preserved the native oxidation states of both deoxymyoglobin and reduced cytochrome c, two key heme proteins (Fig. 6.11). This breakthrough paves the way for accurate and reliable characterization of heme proteins, furthering our understanding of their function and role in various diseases.

Swiech et al. employed TERS to delve into the intricate interactions of bradykinin (BK), a biologically active peptide, with silver surfaces [37]. Their study revealed that BK primarily binds to silver through specific amino acids, $Phe^{5/8}$ and $Arg^{9}$. Interestingly, the orientation and conformation of these residues were found to be influenced by both pH and excitation wavelength, highlighting the dynamic nature of biomolecule interactions. Additionally, the carboxylate group of $Arg^{9}$ displayed a pH-dependent interaction with silver, suggesting a complex binding mode. This detailed analysis provided valuable insights into the structure–function relationship of BK and its interactions with metallic surfaces.

Moreover, Swiech et al. employed TERS to investigate the binding modes of BK antagonists on silver nanowires [38]. Their research revealed that the binding of BK and its antagonist [D-$Arg^{0}$,$Hyp^{3}$,$Thi^{5,8}$,L-$Pip^{7}$]BK involved C-terminal Phe and Arg residues, known for their role in receptor recognition. This observation further confirms the importance of these residues in BK-mediated biological activity. However, the other antagonist, [D-$Arg^{0}$,$Hyp^{3}$,$Thi^{5}$,D-$Phe^{7}$,L-$Pip^{8}$]BK, displayed a distinct binding mode, involving residues located further from the C-terminus. This finding suggests that different antagonists may interact with BK receptors through different mechanisms, offering valuable information for drug discovery and development.

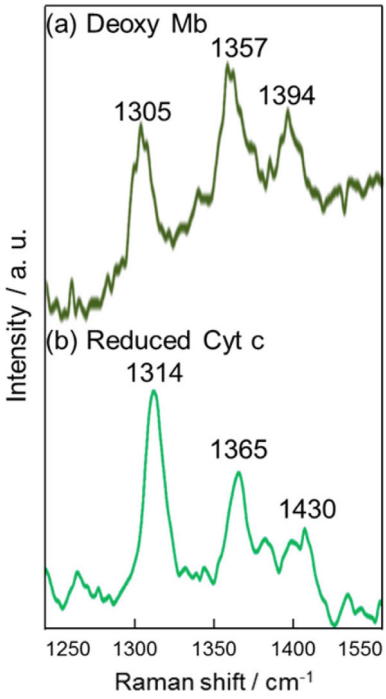



**Fig. 6.11** Normalized TERS spectra of **a** deoxymyoglobin and **b** reduced cytochrome c. This figure has been adapted/reproduced from ref. [113] with permission from American chemical society, copyright 2013

These studies by Tanabe et al. and Swiech et al. demonstrate the immense potential of TERS in unlocking the mysteries of biomolecules. By overcoming photooxidation challenges and providing detailed insights into biomolecule interactions, TERS promises to revolutionize our understanding of life at the nanoscale. This knowledge holds immense potential for advancements in various fields, including medicine, bioengineering, and drug discovery. As technology continues to evolve, TERS is poised to become an indispensable tool for unraveling the secrets of the biomolecular world.

### *6.5.2 Biological Monolayers and Those with Drug or Cytochrome C*

TERS has emerged as a powerful tool for investigating biomolecules at the nanoscale, offering unique insights into their organization, interactions, and intrinsic properties. In one study, STM-TERS imaging revealed the molecular order of dipalmitoylphosphatidylcholine (DPPC), a key component of lung surfactants, on a gold surface [42]. By analyzing the C–H stretching vibrations, researchers identified regions with varying degrees of order, with higher ratios of peak intensity at 2930 $cm^{-1}$ (associated with Fermi resonance) to intensity at 2850 $cm^{-1}$ (methylene stretch) indicating

higher disorder [114, 115]. This approach enabled clear differentiation of ordered and disordered regions with 20 nm spatial resolution.

Non-contact AFM-TERS was also employed to probe the binding between proteins and drugs in a mixture [93]. This technique prevented contamination, allowing for the analysis of drug concentration dependence on specific positions within the sample. Additionally, tapping-mode AFM-TERS combined with total internal reflection was used to characterize the oxidation, spin, and ligation states of cytochrome c deposited on a gold substrate [116]. This system provided minimal excitation laser power, minimizing biomolecule degradation. The TERS spectra revealed marker bands indicating the ferric ($Fe^{3+}$) 6-coordinated low spin state of the heme group, confirming the preservation of the protein's native state.

### 6.5.3 *Amyloid Linked to Alzheimer's Disease*

AFM-TERS was employed to investigate the various phases of amyloid-β aggregation in liquid environments, a process closely linked to Alzheimer's disease [41]. Using hierarchical cluster analysis (HCA), the acquired spectra were classified into three distinct groups, representing oligomers, protofibrils, and fibrils. Interestingly, the analysis revealed a shift in the secondary structure of amyloid-β, transitioning from antiparallel β-sheets in oligomers to parallel β-sheets in fibrils, observed at the nanoscale. Furthermore, a hyperspectral map, constructed using the Pearson correlation coefficient between the derivatives of peaks representing unstructured coils and turns, antiparallel β-sheets, and parallel β-sheets (located at 1650, ~ 1684, and 1626 $cm^{-1}$, respectively), revealed the presence of antiparallel β-sheets in the vicinity of protofibrils and fibrils (Fig. 6.12). This observation suggests that the transition from the antiparallel to the parallel secondary structure might occur during the conversion of protofibrils to fibrils. These findings shed light on the dynamics of amyloid-β aggregation, providing valuable insights into the early stages of Alzheimer's disease development. By unraveling the structural changes associated with different phases of aggregation, AFM-TERS holds promise for identifying potential targets for therapeutic interventions and disease prevention.

### 6.5.4 *Virus*

Amidst the COVID-19 pandemic, viral detection has become a global priority. TERS emerges as a powerful tool in this battle, offering unparalleled capabilities for analyzing single virus particles. By probing the surface of viruses, TERS provides detailed information about their morphology and protein composition, crucial factors in understanding their behavior and developing effective countermeasures. TERS was employed to study two distinct viruses: an enveloped influenza A virus H1N1 and a non-enveloped coxsackie virus B3 (CVB3) (Fig. 6.13) [43]. The TERS spectra

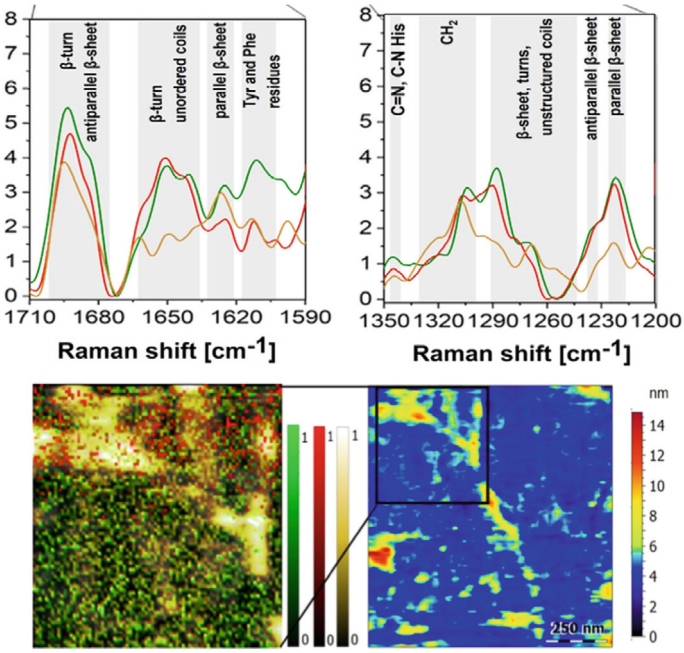



**Fig. 6.12** (Upper) Averaged TERS spectra attributed to oligomers (green), protofibrils (red), and fibrils (yellow) of amyloid-β. (Lower left) TERS image of unstructured coils/turns (green), antiparallel (red), and parallel β-sheet (yellow), which is superimposed on AFM topography image (lower right). This figure has been adapted/reproduced from ref. [41] with permission from John Wiley and Sons, copyright 2021

revealed the characteristic peaks of the spike proteins and the underlying lipid bilayer in H1N1, which appeared as spherical or rod-like structures with sizes ranging from 150 to 400 nm. In contrast, CVB3, with its icosahedral structure and size range of 20 to 30 nm, exhibited peaks associated with the protein lattice and RNA strands within its capsid. To gain deeper insights beyond surface proteins and explore the internal contents of viruses, TERS was combined with atomic force microscopy-infrared (AFM-IR) [117]. This powerful combination leverages the ability of AFM-IR to measure thermal expansions triggered by pulsed infrared light, allowing researchers to differentiate between herpes simplex virus type 1 (HSV-1) and MS2 phage based on the vibrational spectra of their nucleic acids and proteins through partial least-squares discriminant analysis (PLA-DA). Notably, TERS further contributed by revealing the protein secondary structure of the MS2 phage, providing a more comprehensive understanding of the virus's composition. These studies showcase the immense potential of TERS in the fight against viral diseases. By unveiling the intricate details of viral structures and compositions, TERS paves the way for advancements in viral diagnostics, therapeutics, and vaccine development. As the technology continues to evolve, TERS promises to be a vital weapon in our arsenal against future pandemics.

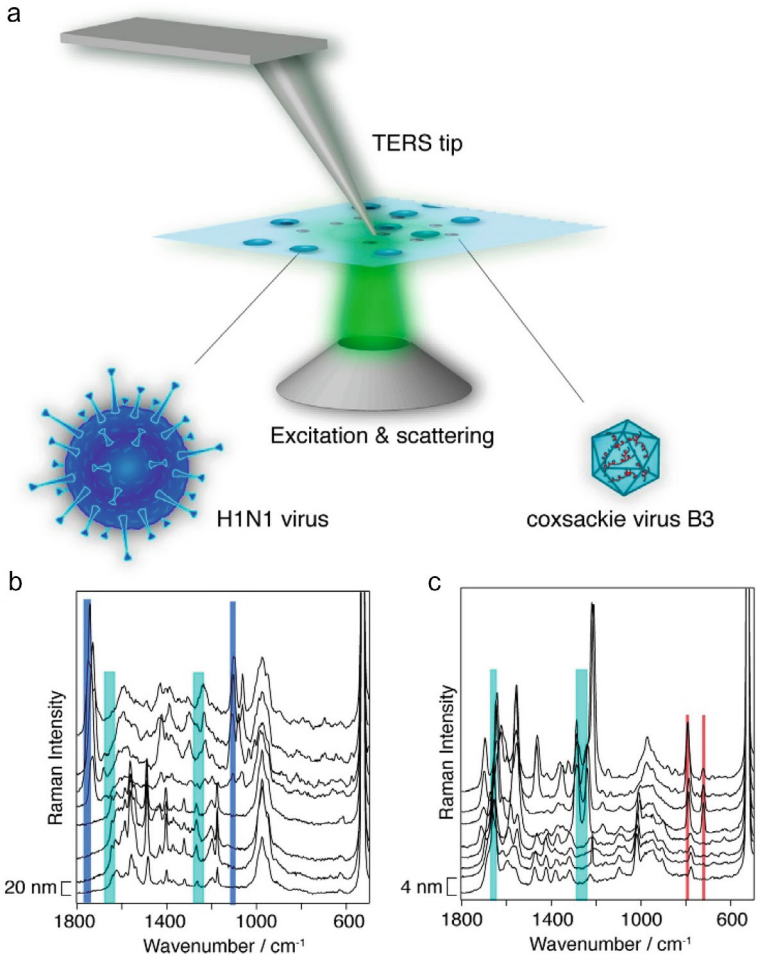



**Fig. 6.13** **a** Transmission TERS setup for viruses on a slide. TERS spectra from single **b** H1N1 virus and **c** coxsackievirus B3. This figure has been adapted/reproduced from ref. [43] with permission from National Academy of Sciences of the United States of America, copyright 2020

### *6.5.5 DNA and RNA Sequencing*

By employing gap-mode TERS, remarkable spatial resolution can be achieved, allowing for the resolution of individual strands of DNA and RNA [39, 40]. This technique utilizes a noble metal tip and substrate to enhance the Raman signal, enabling detailed analysis of single molecules. The DNA and RNA samples were first aligned in a buffer on a gold surface and then dried using nitrogen gas. Interestingly, for DNA molecules, the width of the TERS line profile was found to be narrower compared to that obtained by traditional tapping-mode Atomic Force Microscopy

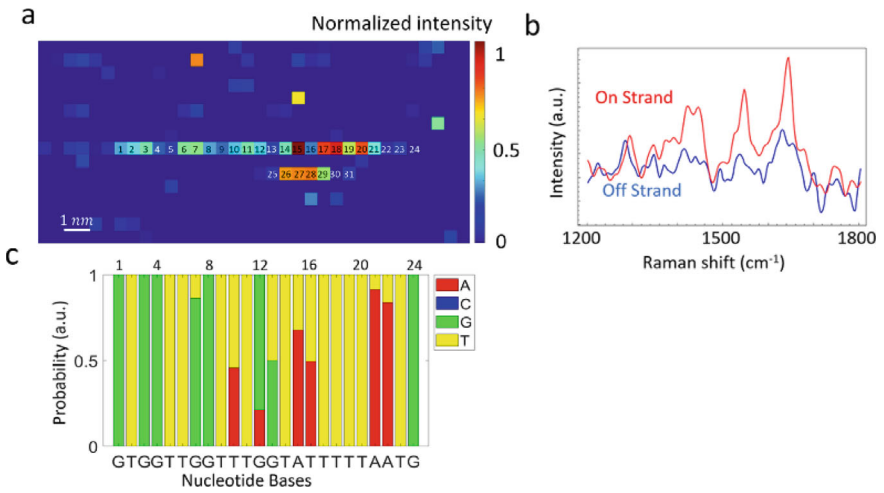



**Fig. 6.14** **a** TERS intensity image at 1630–1650 $cm^{-1}$ on single strand DNA. **b** TERS spectra from pixel 7 and one step above "7" (on and off strand). **c** A bar chart of probabilities at positions in **a**. Real DNA sequence is GTGGTTCGTTCGGTATTTTTAATG. Errors took place at pixel 7 and 11; C were misidentified as G and T, respectively. This figure has been adapted/reproduced from ref. [39] with permission from American chemical society, copyright 2019

(AFM) [39]. This observation highlights the superior spatial resolution achieved by TERS. Additionally, characteristic peaks in the TERS spectra allowed researchers to distinguish between the four DNA/RNA bases: adenine (A), cytosine (C), guanine (G), and thymine (T)/uracil (U). Utilizing the Pearson correlation function, a statistical measure of the linear relationship between two variables, researchers were able to evaluate the correlation between the intensities of the sample and reference spectra [40]. This analysis enabled them to assign probabilities to each base at specific positions along the aligned strand, ultimately leading to the reconstruction of the DNA and RNA sequences (Fig. 6.14). Remarkably, the accuracy of the reconstructed sequences achieved by TERS surpassed 90% [39, 40].

## 6.6 Development of TERS Instruments

The development of TERS has been a collaborative effort, driven by advances in both near-field optics and scanning probe technologies. This section will provide a comprehensive overview of the historical development of TERS, highlighting key milestones and contributions from various researchers. We will delve into the fundamental principles underlying this technique, explore different TERS configurations and their specific advantages, and discuss the challenges and limitations that remain to be addressed.

### 6.6.1 Resolution Improvement

Recent advancements in TERS have revolutionized the field of chemical imaging, pushing the boundaries of spatial resolution and enabling the study of materials at the molecular and even atomic levels. Demonstrating the power of TERS for single-molecule imaging, Cai et al. employed STM-TERS to create chemical maps of individual cobalt(II) tetraphenyl-porphyrin coordination complexes with approximately 2 nm resolution [56]. This study highlights the potential of TERS for studying individual molecules and their properties with unprecedented detail.

Zhang et al. utilized TERS to investigate the coupling of terminal alkynes on Ag(111), revealing the formation of hybrid sp-sp$^2$-carbon skeletons and their *in situ* dehydrogenation [20]. This study demonstrates the potential of TERS for studying complex chemical reactions and visualizing the generated structures at the "single-chemical-bond" level.

Significant progress has been made in achieving sub-nanometer and even angstrom-scale resolution with TERS. Mahapatra et al. achieved angstrom-scale chemical analysis of metal-supported *trans*- and *cis*-regioisomers using UHV-TERS mapping, showcasing the remarkable capabilities of this technique [58]. Wang et al. demonstrated Raman detection of bond breaking and making in a single molecule with single-bond resolution, pushing the boundaries of chemical analysis to the single-molecule level [18]. Shao et al. employed *in situ* nano-spectroscopy with TERS to visualize plasmon-induced two-dimensional [4 + 4]-cycloaddition polymerization on Au(111), highlighting the potential of TERS for studying complex chemical processes at the nanoscale [19].

These remarkable developments demonstrate the transformative power of TERS in revolutionizing chemical imaging. By achieving unprecedented resolutions and enabling the study of chemical processes and structures at the molecular and atomic levels, TERS promises to open new horizons in materials science, nanotechnology, and beyond.

### 6.6.2 Variation of Development

The boundaries of TERS have been continuously pushed with the development of innovative techniques and methods. Here are some recent advancements in TERS development.

To address the limitations of conventional TERS, Lee et al. developed "adaptive tip-enhanced nano-spectroscopy" (Fig. 6.15) [51]. This innovative technique utilizes dynamic wavefront shaping to achieve precise control over light coupling to the tip, leading to enhanced sensitivity and polarization-controlled TERS. This approach offers a remarkable 1.3–2.5-fold increase in signal intensity compared to conventional TERS, paving the way for more sensitive and versatile chemical imaging.

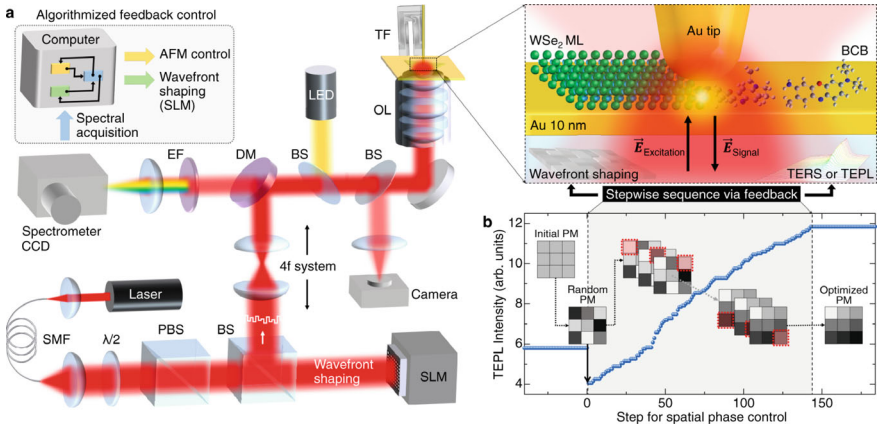



**Fig. 6.15** Adaptive nano-scope for vector-field controlled tip-enhanced nano-spectroscopy based on dynamic wavefront shaping. This figure has been adapted/reproduced from ref. [51] with permission from Springer Nature, copyright 2021

Chen et al. proposed Locally Integrated Raman Polarizability Density (LIRPD), a powerful method for measuring molecular properties with sub-nanometer resolution. This technique sheds light on the physical mechanism behind TERS by probing molecules within a confined sub-nanometer junction [52]. LIRPD offers a simple and intuitive way to understand the complexities of TERS signals and opens doors for its use in the microscopic characterization of molecular structure and dynamics.

Umakoshi et al. investigated the use of tapping-mode AFM for tip position control in TERS. Their research demonstrates that minimizing the tapping amplitude optimizes signal intensity while reducing sample damage, making it a potentially gentler and more effective approach for TERS measurements [53].

These advancements showcase the continuous evolution of TERS and its growing potential for a diverse range of applications in nanoscale research. By addressing limitations and exploring new approaches, researchers are opening doors for exciting discoveries and further pushing the boundaries of TERS capabilities.

### *6.6.3 Progress in Tip Fabrication*

#### Fabrication of tips with high reproducibility and high enhancement

The tip is a critical component of TERS, responsible for amplifying the Raman signals of minute samples [2, 3, 8, 9, 57, 118–121]. A high electric field enhancement at the tip empowers TERS to probe samples with smaller sizes or weaker Raman scattering coefficients. As a result, theoretical calculations optimizing tip geometry for achieving high electric field enhancement have received significant attention [122–124]. Researchers have explored various strategies to fabricate TERS tips with

high enhancement, including focused ion beam (FIB) milling [125], silver nanowire attachment [126–130], electrodeposition [131, 132], and automated electrochemical etching [133]. Table 6.1 summarizes different types of tips fabricated using these diverse methods and their characteristics. However, achieving high enhancement is not the sole objective of tip fabrication. Reproducibility of the tip poses a significant challenge, as fluctuations in the enhanced signal can lead to misinterpretations of spectra, especially when multiple tips are used throughout an experiment. Additionally, many fabricated tips lack TERS activity and are unusable. Therefore, the fabrication process must ensure reproducibility in both the tip's shape and its enhancement. Consequently, the ideal tip geometry should not only offer high electric field enhancement but also be simple and easy to fabricate and reproduce consistently using straightforward techniques. This section delves into the latest techniques for fabricating metallic tips and explores recent strategies for designing plasmonic tips for nanofocusing.

Itoh et al. propose a novel evaluation method for TERS probes using darkfield microspectroscopy [138]. By manipulating the illumination, the method reveals the spatial distribution of surface nanostructures and tip shapes through colorful spots. These spots exhibit spectral variations reflecting the tip curvatures, enabling *in situ* assessment of the probe's plasmonic properties. Additionally, temporal color changes within the spots indicate surface degradation due to oxidation.

Kitahama et al. address the challenge of low reproducibility in TERS due to variable tip properties [139]. Their work compares polarized scattering spectra from localized surface plasmon resonance (LSPR) at the tip apex with corresponding TERS spectra obtained using various excitation polarizations. They demonstrate a consistent correlation between the polarization dependence of LSPR and TERS signals. This finding suggests that optimizing the tip's optical properties prior to TERS measurement by choosing the excitation polarization that induces the strongest LSPR signal can significantly improve the technique's reproducibility.

Huang et al. introduced the concept of shell-isolated TERS to address the issue of tip contamination and the rapid decline in plasmonic activity experienced by conventional tips [135]. Tip contamination presents a significant challenge, generating artifacts and interfering with the Raman information of analytes, particularly when working with solutions. Additionally, analyte molecules can adsorb onto the tip, hindering its reusability. To address these limitations, Huang et al. developed a method using atomic layer deposition (ALD) to fabricate shell-isolated Au or Ag tips coated with a variety of shell materials, including silica, aluminum oxide, and titanium oxide. The thickness of the shell is precisely controlled within the range of 1–20 nm. These innovative tips exhibit strong electromagnetic enhancement while offering significant advantages for TERS in solution. The key benefit of shell-isolated tips is their ability to exclude interference from other molecules present in the solution, allowing them to detect only the enhanced Raman signal of the analyte. This is demonstrated in Fig. 6.16b, where the authors compare the TERS spectra of 4-PBT assembled on Au(111) obtained using both bare and 2-nm silica shell-isolated Au tips. The spectrum acquired using the bare tip exhibits signals from both 4-PBT and pyridine present in the solution (Fig. 6.16a, black curve). In contrast, only the

**Table 6.1** TERS tips fabricated by several strategic methods and their characteristics

| Fabrication technique | Tip morphology | Materials | Enhancement factor | Year | Authors |
|---|---|---|---|---|---|
| FIB | Tip with a plasmonic grating | Au | 20 | 2012 | Berweger et al. [122] |
| FIB and thermal deposition | Mushroom-shaped apex | $SiO_2$/Ag | 1436 | 2015 | Maouli et al. [125] |
| Sputtering and FIB | Tip with a thin-film waveguide | Si/Au | $10^6$–$10^7$ | 2021 | Zhang et al. [134] |
| Silver nanowire attachment | Tip with a silver nanowire | Ag | N.A | 2016 | Ma et al. [126] |
| Silver nanowire attachment | Tip with a silver nanowire | Ag | $10^6$ | 2018 | Walke et al. [127] |
| Silver nanowire attachment | Tip with a silver nanowire | Ag | 47 | 2019 | Ma et al. [128] |
| Silver nanowire attachment | Tip with a silver nanowire | Ag | N.A | 2019 | Kim et al. [129] |
| Silver nanowire attachment | Tip with a silver nanowire | Ag | $1.1 \times 10^6$ | 2019 | Liu et al. [130] |
| Pulse electrodeposition | Au-coated tip | Si/Au | $10^4$ | 2015 | Yang et al. [131] |
| Electrodeposition | Ag-coated tip | Si/Ag | $10^5$ | 2018 | Huang et al. [132] |
| Automated electrochemical etching | Cone-shaped tip with a smooth surface | Au | 22,253 | 2020 | Kim et al. [133] |
| Vacuum vapor deposition | Tip with metal grains | $SiO_2$/Ag | $5.5 \times 10^3$ | 2015 | Taguchi et al. [123] |
| Atomic layer deposition | Shell-isolated tip | Ag/$SiO_2$ or Au/$SiO_2$ | $1.7 \times 10^3$ | 2018 | Huang et al. [135] |
| Physical vapor deposition | One-side metal-coated pyramidal cantilever tips | Si/Ag | $1.0 \times 10^5$ | 2020 | Kato et al. [136] |
| Spinodal dewetting and RF plasma treatment | Coral-like tip | Ag/Si | $4.3 \times 10^7$ | 2020 | Capaccio et al. [137] |

* N.A. Not Available

Raman signals of 4-PBT are observed when the 2-nm silica shell-coated tip is used (Fig. 6.16a, red curve). The concept of shell-isolated tips has gained widespread recognition and has been adopted in various tip fabrication works [34, 140, 141]. This innovative approach represents a significant advancement in TERS, paving the way for more reliable and accurate analysis of samples in solution.

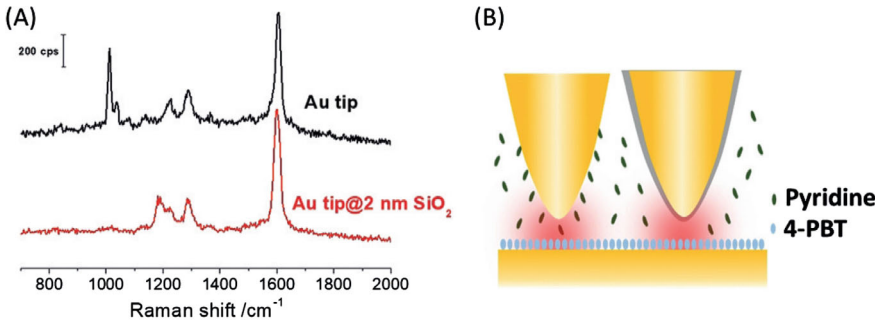



**Fig. 6.16** **a** TERS spectra of 4-PBT assembled on Au(111) acquired by a bare Au tip (black line) and a Au tip coated with 2-nm $SiO_2$ (red line) in an aqueous solution containing 5 mM pyridine and 10 mM $NaClO_4$. **b** Schematic of TERS in a solution using a bare or shell-isolated tip. This figure has been adapted/reproduced from ref. [135] with permission from John Wiley and Sons, copyright 2018

Kato et al. proposed a simple and cost-effective method to fabricate one-side metal-coated pyramidal cantilever tips for highly reproducible TERS measurements [136]. This method utilizes physical vapor deposition to coat a smooth silver layer on only one side of the pyramidal tip, significantly improving reliability compared to conventional techniques (Fig. 6.17). All fabricated tips displayed a high EF of more than $10^4$, indicating excellent performance in enhancing Raman signals. Remarkably, all fabricated tips were TERS-active, eliminating the issue of unusable tips encountered in other methods. The physical vapor deposition technique ensures a smooth and uniform silver coating, unlike the granular structures obtained from traditional methods. The coating process does not affect the resonance frequency of the AFM cantilevers, ensuring optimal imaging capabilities. This method demonstrates consistent results with a 100% success rate in producing TERS-active tips, addressing the crucial challenge of reproducibility in TERS tip fabrication. The fabricated tips were able to image isolated single-walled carbon nanotubes (SWCNTs) with a step height around 1.0 nm, demonstrating their high resolution for nanoscale characterization. The tips were successfully used for TERS measurements on various samples, achieving EFs ranging from $10^4$ to $10^5$, showcasing their effectiveness in enhancing Raman signals. Overall, the one-side metal-coated pyramidal cantilever tips offer a promising solution for reliable and reproducible TERS measurements, paving the way for further advancements in nanoscale Raman spectroscopy.

Zhang et al. proposed a novel design for low-background TERS employing a plasmon thin-film waveguide [134]. Traditional TERS setups suffer from strong background fluorescence and far-field Raman signals originating from the illuminated areas, significantly reducing the near-field to far-field signal contrast in TERS spectra. To address this issue, Zhang et al. developed an indirect-illumination TERS approach that utilizes surface plasmon polaritons (SPPs) excited on a flat Si/Au

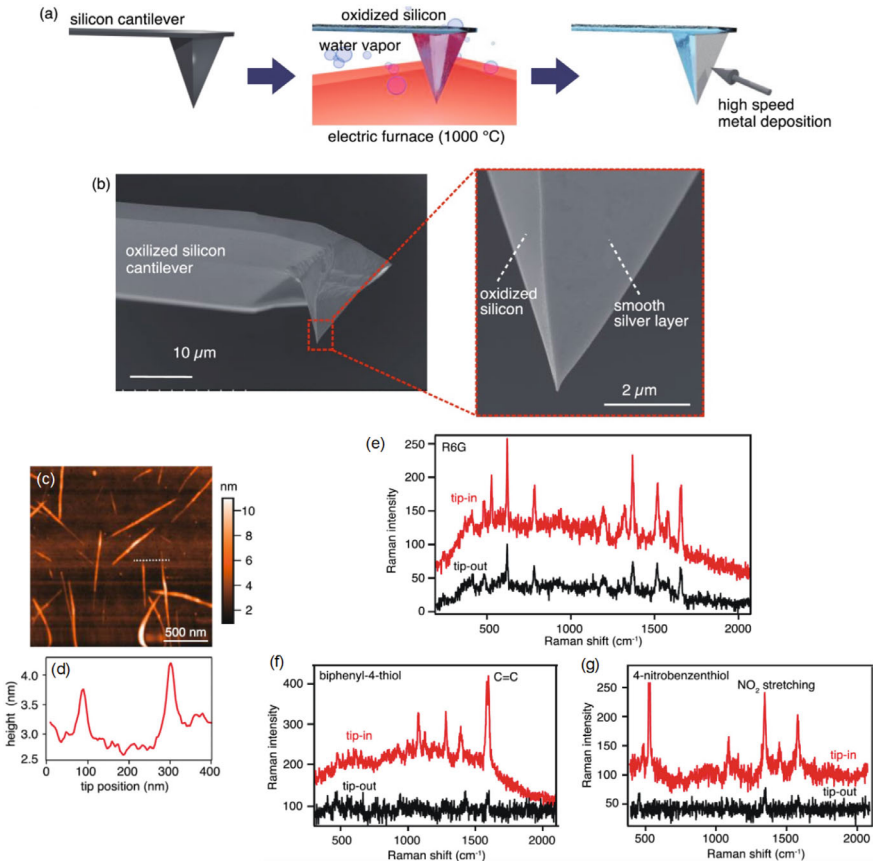



**Fig. 6.17** **a** Fabrication process for one-side coated pyramidal tips. **b** SEM images of the silver-coated oxidized Si tip. **c** An AFM image of SWCNTs measured by the one-side coated tip operated by the tapping-mode, and **d** topographic line profile along the white dotted line in the AFM image. **e** Typical TERS (tip-in) and far-field (tip-out) Raman spectra of a monolayer of R6G, **f** biphenyl-4-thiol, and **g** 4-nitrobenzenthiol. This figure has been adapted/reproduced from ref. [136] with permission from IOP Publishing, copyright 2020

Kretschmann configuration at the tip apex, acting as a triangular thin-film waveguide (Fig. 6.18). By avoiding direct illumination of the tip apex, the background signal from fluorescence and far-field Raman scattering is significantly reduced, leading to a cleaner and more accurate TERS spectrum. The confined near-field spot generated by SPPs at the tip apex enables stable and high-resolution TERS measurements with a spatial resolution of less than 10 nm. This indirect-illumination setup offers several advantages, including increased user-friendliness, potentially reduced measurement times, and simplified instrument development due to the reduced need for precise nanofocusing on the tip apex. The authors successfully demonstrated the effectiveness of their approach by achieving non-gap TERS measurement on a diamond

plate, a challenging sample for direct-illumination TERS due to its transparency and large Raman cross-section. The fabricated tips also achieved high-resolution TERS mapping with a spatial resolution of less than 10 nm on a 4-PBT thin-film sample. Overall, the plasmon thin-film waveguide design offers a promising solution for low-background TERS with significant improvements in performance and user-friendliness, paving the way for further advancements in nanoscale Raman spectroscopy.

Taguchi et al. demonstrate a novel approach for creating a nanoscale light source using plasmon nanofocusing [142]. This technique generates light spanning the entire visible to near-infrared region, significantly surpassing traditional plasmon resonance methods limited to a 100 nm bandwidth. This breakthrough opens doors for utilizing multiple wavelengths at the nanoscale for diverse applications. The authors explored the broadband properties of aluminum, silver, and gold, finding aluminum to exhibit the best performance across the entire spectrum. Silver and gold, however, proved more suitable for longer wavelengths. They also analyzed the trade-offs between

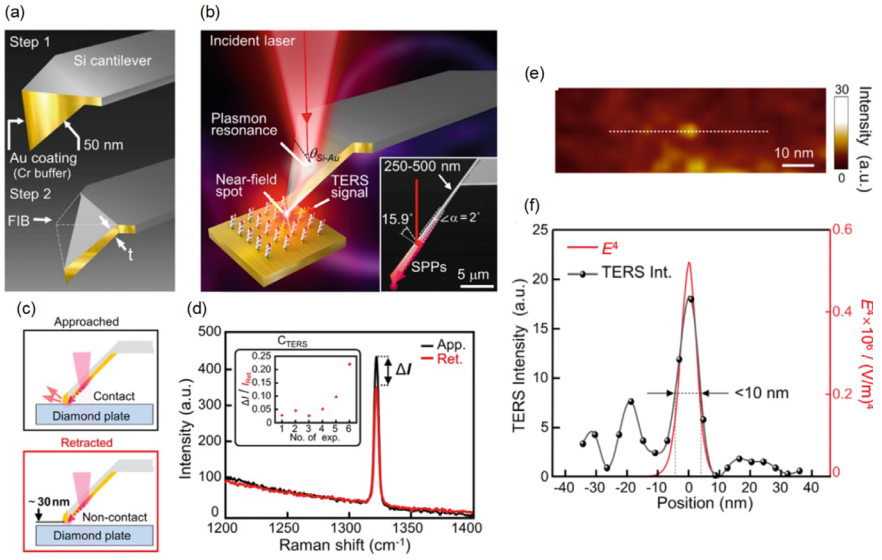



**Fig. 6.18** Schematic illustrations of the fabrication and the working principle of low-background TERS using a plasmon thin-film waveguide. **a** Two-step fabrication of a thin-film waveguide structure on a Si cantilever tip. **b** Working principle of the thin-film waveguide probe. The laser illuminates the waveguide at the plasmon resonance angle. Inset: A SEM image showing the laser-excitation processes (red region). **c** Schematic illustration of the TERS experiment on a diamond plate. **d** Raman spectra obtained from a diamond plate surface with the tip in the contact or non-contact mode. Inset: $\Delta I/I_{\text{retracted}}$ and TERS contrast ($C_{\text{TERS}}$) results of six experiments with two different probes in different areas. **e** A 2D TERS mapping of the 4-PBT sample at the characteristic peak (~1600 $\text{cm}^{-1}$). **f** Line profile (black line) corresponding to the white line in **e** and $E^4$ line profile (red line) for the gap between the tip apex and Au substrate. This figure has been adapted/reproduced from ref. [134] with permission from American chemical society, copyright 2021

key properties like electric field strength, propagation length, and chemical stability for each material. Furthermore, they investigated the influence of various geometrical parameters, such as thickness, taper angle, and slit width, on the broadband property. Their findings revealed that the thickness of the metallic layer plays the most significant role in shaping the localized near-field light at the apex, while the other two parameters have less impact. Experimental validation was achieved by fabricating two-dimensional tapered metallic structures and measuring the scattering spectra of the resulting bright spots. These results confirmed the broadband property for all materials and showcased good agreement with simulations. Additionally, the polarization-dependent characteristics of the bright spot validated its generation through plasmon nanofocusing.

Inconsistent plasmonic enhancement due to non-standardized manufacturing techniques necessitates the need for effective strategies to maintain tip performance. Recycling TERS-active tips have emerged as a promising solution, offering significant potential for extending their lifespan. Demonstrations of successful recycling in both ambient [143] and UHV [144, 145] conditions further strengthen its case as a viable approach. Zhang et al. proposed a simple and effective solution to a major challenge in TERS: probe contamination [145]. Traditional TERS probes are expensive and susceptible to contamination, leading to unreliable measurements. To address this, Zhang et al. introduce UV light cleaning as a novel approach. UV light breaks down organic molecules and oxidizes them with reactive oxygen species, effectively removing contaminants. The authors demonstrate this method using a thin-film waveguide TERS probe and a 4-PBT molecule layer, achieving significant results. Within 15–20 min of UV irradiation, most organic molecules and amorphous carbon are removed from the tip apex. The cleaned probe not only produces stable and strong TERS signals on a 4-PBT monolayer substrate but even surpasses its pre-cleaning performance. This innovative method offers several advantages: simplicity, rapidity, and cost-effectiveness. UV cleaning can regenerate TERS probes, extending their lifespan, reducing the cost, and improving the reproducibility of TERS measurements.

### *6.6.4 Exploring Nanoscale Phenomena in Solution*

In this section, we delve into the world of nanoscale phenomena in solution using TERS. Pienpinijtham et al. demonstrate a novel TERS technique for nanoscale pH measurements in solution [45]. By employing *p*-mercaptobenzoic acid (*p*MBA) and *p*-aminothiophenol (*p*ATP) molecules attached to the tip, they measure the pH profile near an amino-group-modified surface (Fig. 6.19), revealing a local increase in pH due to water dissociation and an exponential decay with distance. This technique opens doors for studying pH in biological samples and other solution-based properties by utilizing various tip-modifying molecules.

Sukmanee et al. introduce a TERS method for enantiomeric discrimination using a *para*-mercaptopyridine (*p*MPY)-coated silver tip [49]. The asymmetric electric field

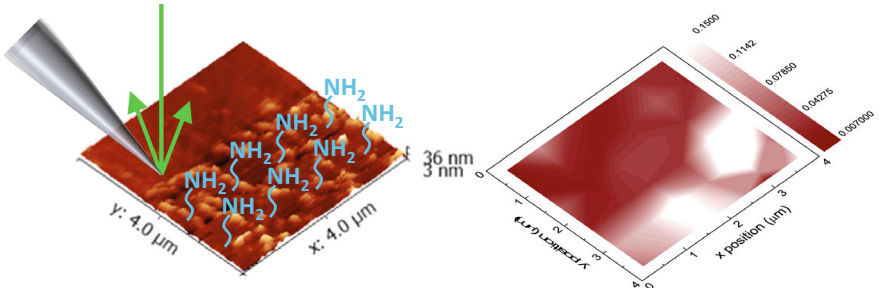



**Fig. 6.19** TERS setup for nanoscale pH measurements in solution and the pH profile near an amino-group-modified surface. This figure has been adapted/reproduced from ref. [45] with permission from American chemical society, copyright 2016

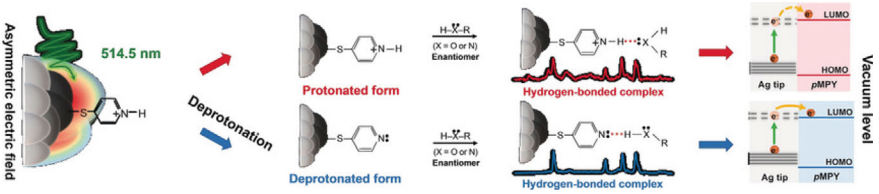



**Fig. 6.20** The mechanism for enantiomer discrimination using TERS tips modified with an achiral probe molecule. This figure has been adapted/reproduced from ref. [49] with permission from John Wiley and Sons, copyright 2020

at the tip apex, arising from the arrangement of silver atoms, interacts differently with enantiomers, leading to distinct changes in *p*MPY's Raman spectra (Fig. 6.20). For this reason, even if *p*MPY is an achiral molecule, different spectra from different enantiomers can be obtained, and then enantiomeric discrimination can be achieved. The authors utilize the intensity ratio of specific Raman bands as a parameter for differentiation, demonstrating success with alcohols and amines. Compared to SERS, their TERS approach offers advantages, such as higher spatial resolution, reduced interference from aggregation, and a stronger near-field effect.

Both studies showcase the versatility of TERS in exploring nanoscale phenomena in solution. From pH measurements to enantiomer discrimination, TERS provides valuable insights into local properties and interactions.

### *6.6.5 Unveiling the Nanoscale Secrets of Electrochemistry with Electrochemical TERS*

While SERS' discovery stemmed from a roughened silver electrode bathed in pyridine, TERS initially focused on air–solid interfaces through combinations of Raman microscopes with STM or AFM. For liquid environments, researchers ingeniously

coated STM tips with insulators, preserving tunneling effects while preventing unwanted currents [35, 50, 146]. Additionally, AFM cantilevers adapted for liquid TERS boasted lower resonance frequencies, and protective layers enhanced tip stability and signal strength [34].

Enter Electrochemical TERS (EC-TERS), where the magic truly unfolds. The noble metal tip and single-crystal substrate become working electrodes, playing host to analyte molecules. Alongside a silver reference electrode and a platinum counter electrode, all seamlessly connected to a bipotentiostat, this setup grants exquisite control over electrode potentials at both tip and sample. Think of it as a nanoscale version of cyclic voltammetry, probing redox and photoelectrochemical reactions with unparalleled detail. Figure 6.21 beautifully illustrates this setup [32].

The advancements have never stopped there. Shell-isolated EC-AFM-TERS (pictured in Fig. 6.22) has opened doors to exciting research in electrophotocatalysis and energy-related systems [34, 35]. Huang et al. even devised a water-immersion EC-TERS setup with superior sensitivity, paving the way for deeper dives into aqueous electrochemical reactions [32]. Kang et al. leveraged EC-AFM-TERS for unprecedented *in situ* nanoscale redox mapping on electrode surfaces, showcasing its potential for deciphering local electrochemical processes at the atomic level [147]. Pfisterer et al. further emphasized the transformative power of this technique by simultaneously mapping topography and reactivity on electro-active surfaces under real-time reaction conditions [148].

These are just a few glimpses into the immense potential of EC-TERS. From unlocking the secrets of electrophotocatalysis to revolutionizing our understanding of nanoscale electrochemical processes, this powerful technique stands poised to transform numerous fields, from energy research to materials science and beyond. Its ability to bridge the gap between electrochemistry and nanoscale characterization promises a future laden with groundbreaking discoveries and advancements.

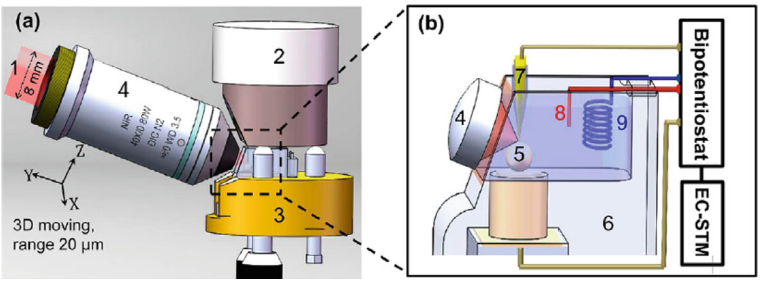



**Fig. 6.21** **a** 3D drawing and **b** schematic illustration of EC-TERS. 1: laser beam, 2: STM scanner head, 3: sample holder, 4: water-immersion objective lens, 5: Au single crystal (working electrode), 6: cell body, 7: insulated tip, 8: Ag quasi reference electrode, 9: Pt counter electrode. This figure has been adapted/reproduced from ref. [32] with permission from American Chemical Society, copyright 2019

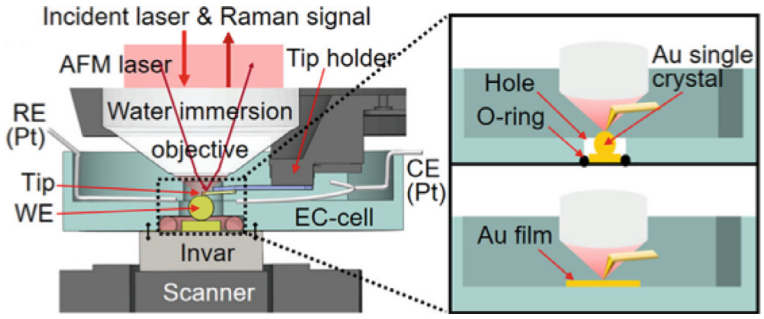



**Fig. 6.22** Schematic illustration of the top-illumination shell-isolated EC-AFM-TERS setup. This figure has been adapted/reproduced from ref. [34] with permission from American chemical society, copyright 2020

## 6.7 Perspectives

About a quarter century has passed since TERS was born in 2000. Its recent development is remarkable. Therefore, it is high time to discuss the perspectives of TERS. One can consider a variety of possibilities as the perspectives of TERS.

(i) ***Unlocking new realms of light–matter interaction***: TERS may open a completely new world in the investigations of various phenomena related to light–molecule interaction in cavity quantum electrodynamics (cavity QED). Using TERS, one can control the space size of light, which becomes similar to that of molecules. Thus, one can probe the photoreaction of the molecules on an angstrom scale. In a place where the electric field of light is smaller than a molecule, totally new electronic and vibrational transitions were observed. For example, J. J. Baumberg observed IR modes in a SERS spectrum [149].

(ii) ***Exploring the realm of strong coupling***: Studies of strong coupling began with SERS [150–152], but similar studies can also be possible with TERS. The advantageous point of TERS is the control of the coupling energy degree between plasmons and molecular excitons in a place where strong coupling occurs. Thus, one can continuously control from a weak to a strong coupling regime and monitor a photoreaction while changing the size of the electronic field. Various theoretical considerations, including a unified quantum–mechanical theory of TERS and SERS, are required to understand angstrom TERS.

(iii) ***Pushing the boundaries of spatial resolution***: To achieve higher spatial resolution, the refinement of near-field control and the optimization of light–tip interactions through advanced nanofabrication and plasmonic engineering may be essentially important. Combining nanofabrication with high-resolution microscopy is also essential. Exploration of alternative excitation sources may be considered, as may investigation of the use of non-classical light sources, X-rays, and terahertz waves for novel information and deeper

penetration. Angstrom TERS should bring various exciting applications that are commonly important for chemical science. The TERS technique is limited in temporal resolution because of the slow collection of Raman spectra. Therefore, one clear trend in this field is to move from static to dynamic studies. Combination with ultrafast spectroscopic techniques, including ps- and fs-lasers, may enable the TERS technique to have simultaneous ultra-high spatial–temporal resolution. TERS imaging with a resolution of a few angstroms provides information about a single molecule or a single bond, providing a strong impact on a wide area of nanoscience and technology.

(iv) ***Pioneering of new photochemical reactions***: Due to the development of angstrom TERS, TERS may open new research fields in photochemistry. The nanoscale characterization of plasmon-enhanced reactions should be deepened. Of note is that even if one does not use angstrom TERS, plasmon chemistry brings many possibilities for new research in the field of photochemistry.

(v) ***The quest for robust and tailored tips***: TERS technology is still stuck in tip dependency. Therefore, the development of ultrasensitive and robust tips is crucial for the advances in TERS. Tailor tips for specific applications and tips with improved biocompatibility and stability are highly desired.

(vi) ***TERS imaging revolutionizes nanoscience***: TERS imaging with a resolution of a few angstroms provides information about a single molecule or a single bond, providing a strong impact on a wide area of nanoscience and technology. Nanoscale imaging of plasmon-driven processes is also an interesting field. The hybrid FDTD-density functional theory simulations can be used to simulate both ultrasensitive and ensemble-averaged TERS spectral images.

(vii) ***Chemically modified tips and expanding into liquid environments***: We proposed chemically modified tips and applied them to the studies of nanoscale pH profiles and enantiomer discrimination. For exploring various nanoscale phenomena and nanoscale monitoring of the solid–liquid interface in solution, one must develop a variety of more robust probes with enhanced chemical and electrochemical resistance. *In situ* characterizations of biological systems by chemically modified tips may be possible in the near future. It is also noted to explore advanced fluidic setups, design microfluidic chambers and flow cells for controlled sample environments, and conduct dynamic studies. The integration of TERS with electrochemistry, photocatalysis, and other liquid-based processes for real-time analysis is promising.

(viii) ***Leveraging advanced signal processing and data analysis***: For all kinds of spectroscopies, the development of advanced signal processing and data analysis is important. On one hand, quantum chemical calculations are very important to interpret the TERS data, but on the other hand, chemometric treatment is often useful for spectroscopic data analysis. For the analysis of imaging data, chemometrics, such as principal component analysis (PCA), multivariate curve resolution (MCR), or classical least squares (CLS), play an important role. Machine learning has already started to be used for Raman

spectroscopy, and the development of robust AI-powered algorithms is now expected.

(ix) ***Exploring new frontiers of application***: TERS holds various kinds of novel applications. As pointed out above, TERS applications to photochemical and photocatalytic reactions are an exciting area. Kurouski discusses nanoscale imaging of photocatalytic processes using TERS (Chap. 24). Applications to biological molecules and systems are particularly promising. UV excitation with high spatial resolution in TERS may bring novel frontiers in biological applications, including applications to cells. As described above, liquid TERS and chemically modified tips may play important roles in the novel application of TERS, *e.g.*, nanoscale monitoring of the solid–liquid interface and chiral discrimination using TERS. Applications of TERS imaging to 2D and 3D nanomaterials are also promising. One of the directions to go for the application of this technique is to extend from simple planar molecules to more complex molecules, such as those with three-dimensional structures and even twisted biomolecules, including DNA/RNA chains and proteins. The detection of these complex molecular systems may need further efforts to improve the vertical resolving ability of TERS as well as data processing methods.

(x) ***Bridging the gap with multimodal techniques***: For comprehensive nanoscale characterization, integrating TERS data with other analytical techniques like AFM and SEM is attractive. Correlative approach is a combination of TERS with AFM, force microscopy, and other techniques for complementary topographical and mechanical insights. Combining TERS data with other spectroscopic data, such as those of Raman and infrared, is important to collect comprehensive structural and chemical information. The development of hybrid nanotools and the design of multifunctional probes that combine TERS with other functionalities like sensing, manipulation, and delivery are expected.

## References

1. T. Itoh, M. Procházka, Z.-C. Dong, W. Ji, Y.S. Yamamoto, Y. Zhang, and Y. Ozaki, *Toward a New Era of SERS and TERS at the Nanometer Scale: From Fundamentals to Innovative Applications.* Chemical Reviews **123**, 1552-1634 (2023)
2. S. Kawata, T. Ichimura, A. Taguchi, and Y. Kumamoto, *Nano-Raman Scattering Microscopy: Resolution and Enhancement.* Chemical Reviews **117**, 4983-5001 (2017)
3. M. Richard-Lacroix, Y. Zhang, Z. Dong, and V. Deckert, *Mastering high resolution tip-enhanced Raman spectroscopy: towards a shift of perception.* Chemical Society Reviews **46**, 3922-3944 (2017)
4. Y. Cao and M. Sun, *Tip-enhanced Raman spectroscopy.* Reviews in Physics **8**, 100067 (2022)
5. F. Shao and R. Zenobi, *Tip-enhanced Raman spectroscopy: principles, practice, and applications to nanospectroscopic imaging of 2D materials.* Analytical and Bioanalytical Chemistry **411**, 37-61 (2019)

6. P. Pienpinijtham and Y. Ozaki, *Tip-Enhanced Raman Scattering in Liquid/Solution*, in *Recent Developments in Plasmon-Supported Raman Spectroscopy*, edited by K. Kneipp, Y. Ozaki, and Z.-Q. Tian (2017, WORLD SCIENTIFIC (EUROPE)), pp. 299–321
7. P. Pienpinijtham, Y. Kitahama, and Y. Ozaki, *Progress of tip-enhanced Raman scattering for the last two decades and its challenges in very recent years.* Nanoscale **14**, 5265-5288 (2022)
8. M.M. Sartin, H.-S. Su, X. Wang, and B. Ren, *Tip-enhanced Raman spectroscopy for nanoscale probing of dynamic chemical systems.* The Journal of Chemical Physics **153**, 170901 (2020)
9. P. Pienpinijtham, Y. Kitahama, and Y. Ozaki, *Electric field analysis, polarization, excitation wavelength dependence, and novel applications of tip-enhanced Raman scattering.* Journal of Raman Spectroscopy **52**, 1997-2017 (2021)
10. N. Hayazawa, Y. Inouye, Z. Sekkat, and S. Kawata, *Metallized tip amplification of near-field Raman scattering.* Optics Communications **183**, 333-336 (2000)
11. R.M. Stöckle, Y.D. Suh, V. Deckert, and R. Zenobi, *Nanoscale chemical analysis by tip-enhanced Raman spectroscopy.* Chemical Physics Letters **318**, 131-136 (2000)
12. M.S. Anderson, *Locally enhanced Raman spectroscopy with an atomic force microscope.* Applied Physics Letters **76**, 3130-3132 (2000)
13. J.-H. Zhong, X. Wang, T.-X. Huang, S.-C. Huang, and B. Ren, *Tip-Enhanced Raman Spectroscopy for Surface and Interface Analysis*, in *Recent Developments in Plasmon-Supported Raman Spectroscopy*, edited by K. Kneipp, Y. Ozaki, and Z.-Q. Tian (2017, WORLD SCIENTIFIC (EUROPE)), pp. 255–298
14. G. Binnig, H. Rohrer, C. Gerber, and E. Weibel, *Surface Studies by Scanning Tunneling Microscopy.* Physical Review Letters **49**, 57-61 (1982)
15. J. Wessel, *Surface-enhanced optical microscopy.* J. Opt. Soc. Am. B **2**, 1538-1541 (1985)
16. Y. Inouye and S. Kawata, *Near-field scanning optical microscope with a metallic probe tip.* Opt. Lett. **19**, 159-161 (1994)
17. B. Pettinger, G. Picardi, R. Schuster, and G. Ertl, *Surface Enhanced Raman Spectroscopy: Towards Single Molecule Spectroscopy.* Electrochemistry **68**, 942-949 (2000)
18. R.-P. Wang, B. Yang, Q. Fu, Y. Zhang, R. Zhu, X.-R. Dong, Y. Zhang, B. Wang, J.-L. Yang, Y. Luo, Z.-C. Dong, and J.G. Hou, *Raman Detection of Bond Breaking and Making of a Chemisorbed Up-Standing Single Molecule at Single-Bond Level.* The Journal of Physical Chemistry Letters **12**, 1961-1968 (2021)
19. F. Shao, W. Wang, W. Yang, Z. Yang, Y. Zhang, J. Lan, A. Dieter Schlüter, and R. Zenobi, *In-situ nanospectroscopic imaging of plasmon-induced two-dimensional [4+4]-cycloaddition polymerization on Au(111).* Nature Communications **12**, 4557 (2021)
20. C. Zhang, R.B. Jaculbia, Y. Tanaka, E. Kazuma, H. Imada, N. Hayazawa, A. Muranaka, M. Uchiyama, and Y. Kim, *Chemical Identification and Bond Control of $\pi$-Skeletons in a Coupling Reaction.* Journal of the American Chemical Society **143**, 9461-9467 (2021)
21. J. Steidtner and B. Pettinger, *High-resolution microscope for tip-enhanced optical processes in ultrahigh vacuum.* Review of Scientific Instruments **78**, 103104 (2007)
22. J. Steidtner and B. Pettinger, *Tip-Enhanced Raman Spectroscopy and Microscopy on Single Dye Molecules with 15 nm Resolution.* Physical Review Letters **100**, 236101 (2008)
23. N. Peica, S. Röhrig, A. Rüdiger, K. Brose, C. Thomsen, and J. Maultzsch, *Characterization of dye molecules and carbon nanostructures by tip-enhanced Raman spectroscopy.* Physica status solidi (b) **246**, 2708–2712 (2009)
24. N. Jiang, E.T. Foley, J.M. Klingsporn, M.D. Sonntag, N.A. Valley, J.A. Dieringer, T. Seideman, G.C. Schatz, M.C. Hersam, and R.P. Van Duyne, *Observation of Multiple Vibrational Modes in Ultrahigh Vacuum Tip-Enhanced Raman Spectroscopy Combined with Molecular-Resolution Scanning Tunneling Microscopy.* Nano Letters **12**, 5061-5067 (2012)
25. N. Chiang, G. Goubert, E.A. Pozzi, M.O. McAnally, C. Chapman, N. Jiang, G.C. Schatz, and R.P. Van Duyne, *Ultra-High Vacuum Tip-Enhanced Raman Spectroscopy*, in *Recent Developments in Plasmon-Supported Raman Spectroscopy*, edited by K. Kneipp, Y. Ozaki, and Z.-Q. Tian (2017, WORLD SCIENTIFIC (EUROPE)), pp. 231–253
26. S. Duan, G. Tian, and Y. Luo, *Visualization of Vibrational Modes in Real Space by Tip-Enhanced Non-Resonant Raman Spectroscopy.* Angewandte Chemie International Edition **55**, 1041-1045 (2016)

27. S. Duan, G. Tian, Y. Ji, J. Shao, Z. Dong, and Y. Luo, *Theoretical Modeling of Plasmon-Enhanced Raman Images of a Single Molecule with Subnanometer Resolution.* Journal of the American Chemical Society **137**, 9515-9518 (2015)
28. L. Meng, Z. Yang, J. Chen, and M. Sun, *Effect of Electric Field Gradient on Sub-nanometer Spatial Resolution of Tip-enhanced Raman Spectroscopy.* Scientific Reports **5**, 9240 (2015)
29. R. Zhang, Y. Zhang, Z.C. Dong, S. Jiang, C. Zhang, L.G. Chen, L. Zhang, Y. Liao, J. Aizpurua, Y. Luo, J.L. Yang, and J.G. Hou, *Chemical mapping of a single molecule by plasmon-enhanced Raman scattering.* Nature **498**, 82-86 (2013)
30. J.M. Klingsporn, M.D. Sonntag, T. Seideman, and R.P. Van Duyne, *Tip-Enhanced Raman Spectroscopy with Picosecond Pulses.* The Journal of Physical Chemistry Letters **5**, 106-110 (2014)
31. Z.-C. Zeng, S.-C. Huang, D.-Y. Wu, L.-Y. Meng, M.-H. Li, T.-X. Huang, J.-H. Zhong, X. Wang, Z.-L. Yang, and B. Ren, *Electrochemical Tip-Enhanced Raman Spectroscopy.* Journal of the American Chemical Society **137**, 11928-11931 (2015)
32. S.-C. Huang, J.-Z. Ye, X.-R. Shen, Q.-Q. Zhao, Z.-C. Zeng, M.-H. Li, D.-Y. Wu, X. Wang, and B. Ren, *Electrochemical Tip-Enhanced Raman Spectroscopy with Improved Sensitivity Enabled by a Water Immersion Objective.* Analytical Chemistry **91**, 11092-11097 (2019)
33. D. Kurouski, M. Mattei, and R.P. Van Duyne, *Probing Redox Reactions at the Nanoscale with Electrochemical Tip-Enhanced Raman Spectroscopy.* Nano Letters **15**, 7956-7962 (2015)
34. Y.-F. Bao, M.-F. Cao, S.-S. Wu, T.-X. Huang, Z.-C. Zeng, M.-H. Li, X. Wang, and B. Ren, *Atomic Force Microscopy Based Top-Illumination Electrochemical Tip-Enhanced Raman Spectroscopy.* Analytical Chemistry **92**, 12548-12555 (2020)
35. S.-C. Huang, Y.-F. Bao, S.-S. Wu, T.-X. Huang, M.M. Sartin, X. Wang, and B. Ren, *Electrochemical Tip-Enhanced Raman Spectroscopy: An In Situ Nanospectroscopy for Electrochemistry.* Annual Review of Physical Chemistry **72**, 213-234 (2021)
36. Y. Kitahama and Y. Ozaki, *Surface-enhanced resonance Raman scattering of hemoproteins and those in complicated biological systems.* Analyst **141**, 5020-5036 (2016)
37. D. Swiech, Y. Ozaki, Y. Kim, and E. Proniewicz, *Surface- and tip-enhanced Raman scattering of bradykinin onto the colloidal suspended Ag surface.* Physical Chemistry Chemical Physics **17**, 17140-17149 (2015)
38. D. Święch, I. Tanabe, S. Vantasin, D. Sobolewski, Y. Ozaki, A. Prahl, S. Maćkowski, and E. Proniewicz, *Tip-enhanced Raman spectroscopy of bradykinin and its B2 receptor antagonists adsorbed onto colloidal suspended Ag nanowires.* Physical Chemistry Chemical Physics **17**, 22882-22892 (2015)
39. Z. He, Z. Han, M. Kizer, R.J. Linhardt, X. Wang, A.M. Sinyukov, J. Wang, V. Deckert, A.V. Sokolov, J. Hu, and M.O. Scully, *Tip-Enhanced Raman Imaging of Single-Stranded DNA with Single Base Resolution.* Journal of the American Chemical Society **141**, 753-757 (2019)
40. Z. He, W. Qiu, M.E. Kizer, J. Wang, W. Chen, A.V. Sokolov, X. Wang, J. Hu, and M.O. Scully, *Resolving the Sequence of RNA Strands by Tip-Enhanced Raman Spectroscopy.* ACS Photonics **8**, 424-430 (2021)
41. E. Lipiec, J. Kaderli, J. Kobierski, R. Riek, K. Skirlińska-Nosek, K. Sofińska, M. Szymoński, and R. Zenobi, *Nanoscale Hyperspectral Imaging of Amyloid Secondary Structures in Liquid.* Angewandte Chemie International Edition **60**, 4545-4550 (2021)
42. Y. Pandey, N. Kumar, G. Goubert, and R. Zenobi, *Nanoscale Chemical Imaging of Supported Lipid Monolayers using Tip-Enhanced Raman Spectroscopy.* Angewandte Chemie International Edition **60**, 19041-19046 (2021)
43. V. Deckert, T. Deckert-Gaudig, D. Cialla-May, J. Popp, R. Zell, S. Deinhard-Emmer, A.V. Sokolov, Z. Yi, and M.O. Scully, *Laser spectroscopic technique for direct identification of a single virus I: FASTER CARS.* Proceedings of the National Academy of Sciences **117**, 27820 (2020)
44. T. Schmid, B.-S. Yeo, G. Leong, J. Stadler, and R. Zenobi, *Performing tip-enhanced Raman spectroscopy in liquids.* Journal of Raman Spectroscopy **40**, 1392-1399 (2009)
45. P. Pienpinijtham, S. Vantasin, Y. Kitahama, S. Ekgasit, and Y. Ozaki, *Nanoscale pH Profile at a Solution/Solid Interface by Chemically Modified Tip-Enhanced Raman Scattering.* The Journal of Physical Chemistry C **120**, 14663-14668 (2016)

46. R. Meyer, X. Yao, and V. Deckert, *Latest instrumental developments and bioanalytical applications in tip-enhanced Raman spectroscopy.* TrAC Trends in Analytical Chemistry **102**, 250-258 (2018)
47. N. Kumar, W. Su, M. Veselý, B.M. Weckhuysen, A.J. Pollard, and A.J. Wain, *Nanoscale chemical imaging of solid–liquid interfaces using tip-enhanced Raman spectroscopy.* Nanoscale **10**, 1815-1824 (2018)
48. A. Bhattarai and P.Z. El-Khoury, *Nanoscale Chemical Reaction Imaging at the Solid–Liquid Interface via TERS.* The Journal of Physical Chemistry Letters **10**, 2817-2822 (2019)
49. T. Sukmanee, K. Wongravee, Y. Kitahama, S. Ekgasit, T. Itoh, P. Pienpinijtham, and Y. Ozaki, *Distinguishing Enantiomers by Tip-Enhanced Raman Scattering: Chemically Modified Silver Tip with an Asymmetric Atomic Arrangement.* Angewandte Chemie International Edition **59**, 14564-14569 (2020)
50. A.B. Britz-Grell, M. Saumer, and A. Tarasov, *Challenges and Opportunities of Tip-Enhanced Raman Spectroscopy in Liquids.* The Journal of Physical Chemistry C **125**, 21321-21340 (2021)
51. D.Y. Lee, C. Park, J. Choi, Y. Koo, M. Kang, M.S. Jeong, M.B. Raschke, and K.-D. Park, *Adaptive tip-enhanced nano-spectroscopy.* Nature Communications **12**, 3465 (2021)
52. X. Chen, P. Liu, Z. Hu, and L. Jensen, *High-resolution tip-enhanced Raman scattering probes sub-molecular density changes.* Nature Communications **10**, 2567 (2019)
53. T. Umakoshi, K. Kawashima, T. Moriyama, R. Kato, and P. Verma, *Tip-enhanced Raman spectroscopy with amplitude-controlled tapping-mode AFM.* Scientific Reports **12**, 12776 (2022)
54. A. Taguchi, N. Hayazawa, K. Furusawa, H. Ishitobi, and S. Kawata, *Deep-UV tip-enhanced Raman scattering.* Journal of Raman Spectroscopy **40**, 1324-1330 (2009)
55. A. Taguchi, *Deep-Ultraviolet Surface- and Tip-Enhanced Raman Spectroscopy*, in *Recent Developments in Plasmon-Supported Raman Spectroscopy*, edited by K. Kneipp, Y. Ozaki, and Z.-Q. Tian (2017, WORLD SCIENTIFIC (EUROPE)), pp. 117–135
56. Z.-F. Cai, L.-Q. Zheng, Y. Zhang, and R. Zenobi, *Molecular-Scale Chemical Imaging of the Orientation of an On-Surface Coordination Complex by Tip-Enhanced Raman Spectroscopy.* Journal of the American Chemical Society **143**, 12380-12386 (2021)
57. A.B. Zrimsek, N. Chiang, M. Mattei, S. Zaleski, M.O. McAnally, C.T. Chapman, A.-I. Henry, G.C. Schatz, and R.P. Van Duyne, *Single-Molecule Chemistry with Surface- and Tip-Enhanced Raman Spectroscopy.* Chemical Reviews **117**, 7583-7613 (2017)
58. S. Mahapatra, Y. Ning, J.F. Schultz, L. Li, J.-L. Zhang, and N. Jiang, *Angstrom Scale Chemical Analysis of Metal Supported Trans- and Cis-Regioisomers by Ultrahigh Vacuum Tip-Enhanced Raman Mapping.* Nano Letters **19**, 3267-3272 (2019)
59. Y. Zhang, R. Zhang, S. Jiang, Y. Zhang, and Z.-C. Dong, *Probing Adsorption Configurations of Small Molecules on Surfaces by Single-Molecule Tip-Enhanced Raman Spectroscopy.* ChemPhysChem **20**, 37-41 (2019)
60. R.B. Jaculbia, H. Imada, K. Miwa, T. Iwasa, M. Takenaka, B. Yang, E. Kazuma, N. Hayazawa, T. Taketsugu, and Y. Kim, *Single-molecule resonance Raman effect in a plasmonic nanocavity.* Nature Nanotechnology **15**, 105-110 (2020)
61. S. Liu, B. Cirera, Y. Sun, I. Hamada, M. Müller, A. Hammud, M. Wolf, and T. Kumagai, *Dramatic Enhancement of Tip-Enhanced Raman Scattering Mediated by Atomic Point Contact Formation.* Nano Letters **20**, 5879-5884 (2020)
62. J. Xu, X. Zhu, S. Tan, Y. Zhang, B. Li, Y. Tian, H. Shan, X. Cui, A. Zhao, Z. Dong, J. Yang, Y. Luo, B. Wang, and J.G. Hou, *Determining structural and chemical heterogeneities of surface species at the single-bond limit.* Science **371**, 818-822 (2021)
63. C.D. Tschannen, M. Frimmer, T.L. Vasconcelos, L. Shi, T. Pichler, and L. Novotny, *Tip-Enhanced Stokes–Anti-Stokes Scattering from Carbyne.* Nano Letters **22**, 3260-3265 (2022)
64. L. Li, J.F. Schultz, S. Mahapatra, X. Liu, C. Shaw, X. Zhang, M.C. Hersam, and N. Jiang, *Angstrom-Scale Spectroscopic Visualization of Interfacial Interactions in an Organic/Borophene Vertical Heterostructure.* Journal of the American Chemical Society **143**, 15624-15634 (2021)

65. X.-S. Ke, Y. Chang, J.-Z. Chen, J. Tian, J. Mack, X. Cheng, Z. Shen, and J.-L. Zhang, *Porphodilactones as Synthetic Chlorophylls: Relative Orientation of β-Substituents on a Pyrrolic Ring Tunes NIR Absorption.* Journal of the American Chemical Society **136**, 9598-9607 (2014)
66. N. Jiang, N. Chiang, L.R. Madison, E.A. Pozzi, M.R. Wasielewski, T. Seideman, M.A. Ratner, M.C. Hersam, G.C. Schatz, and R.P. Van Duyne, *Nanoscale Chemical Imaging of a Dynamic Molecular Phase Boundary with Ultrahigh Vacuum Tip-Enhanced Raman Spectroscopy.* Nano Letters **16**, 3898-3904 (2016)
67. J.F. Schultz, L. Li, S. Mahapatra, C. Shaw, X. Zhang, and N. Jiang, *Defining Multiple Configurations of Rubrene on a Ag(100) Surface with 5 Å Spatial Resolution via Ultrahigh Vacuum Tip-Enhanced Raman Spectroscopy.* The Journal of Physical Chemistry C **124**, 2420-2426 (2020)
68. S. Mahapatra, J.F. Schultz, Y. Ning, J.-L. Zhang, and N. Jiang, *Probing surface mediated configurations of nonplanar regioisomeric adsorbates using ultrahigh vacuum tip-enhanced Raman spectroscopy.* Nanoscale **11**, 19877-19883 (2019)
69. W. Wang, F. Shao, M. Kröger, R. Zenobi, and A.D. Schlüter, *Structure Elucidation of 2D Polymer Monolayers Based on Crystallization Estimates Derived from Tip-Enhanced Raman Spectroscopy (TERS) Polymerization Conversion Data.* Journal of the American Chemical Society **141**, 9867-9871 (2019)
70. V. Müller, F. Shao, M. Baljozovic, M. Moradi, Y. Zhang, T. Jung, W.B. Thompson, B.T. King, R. Zenobi, and A.D. Schlüter, *Structural Characterization of a Covalent Monolayer Sheet Obtained by Two-Dimensional Polymerization at an Air/Water Interface.* Angewandte Chemie International Edition **56**, 15262-15266 (2017)
71. F. Shao, V. Müller, Y. Zhang, A.D. Schlüter, and R. Zenobi, *Nanoscale Chemical Imaging of Interfacial Monolayers by Tip-Enhanced Raman Spectroscopy.* Angewandte Chemie International Edition **56**, 9361-9366 (2017)
72. F. Shao, W. Dai, Y. Zhang, W. Zhang, A.D. Schlüter, and R. Zenobi, *Chemical Mapping of Nanodefects within 2D Covalent Monolayers by Tip-Enhanced Raman Spectroscopy.* ACS Nano **12**, 5021-5029 (2018)
73. T.-a. Yano, T. Ichimura, S. Kuwahara, F. H'Dhili, K. Uetsuki, Y. Okuno, P. Verma, and S. Kawata, *Tip-enhanced nano-Raman analytical imaging of locally induced strain distribution in carbon nanotubes.* Nature Communications **4**, 2592 (2013)
74. R. Kato, S. Igarashi, T. Umakoshi, and P. Verma, *Tip-Enhanced Raman Spectroscopy of Multiwalled Carbon Nanotubes through D-Band Imaging: Implications for Nanoscale Analysis of Interwall Interactions.* ACS Applied Nano Materials **3**, 6001-6008 (2020)
75. M.V. Balois, N. Hayazawa, S. Yasuda, K. Ikeda, B. Yang, E. Kazuma, Y. Yokota, Y. Kim, and T. Tanaka, *Visualization of subnanometric phonon modes in a plasmonic nano-cavity via ambient tip-enhanced Raman spectroscopy.* NPJ 2D Materials and Applications **3**, 38 (2019)
76. C. Rabelo, T.L. Vasconcelos, B.C. Publio, H. Miranda, L.G. Cançado, and A. Jorio, *Linkage Between Micro- and Nano-Raman Spectroscopy of Defects in Graphene.* Physical Review Applied **14**, 024056 (2020)
77. E.J. Legge, K.R. Paton, M. Wywijas, G. McMahon, R. Pemberton, N. Kumar, A.P. Aranga Raju, C.P. Dawson, A.J. Strudwick, J.W. Bradley, V. Stolojan, S.R.P. Silva, S.A. Hodge, B. Brennan, and A.J. Pollard, *Determining the Level and Location of Functional Groups on Few-Layer Graphene and Their Effect on the Mechanical Properties of Nanocomposites.* ACS Applied Materials & Interfaces **12**, 13481–13493 (2020)
78. T.-X. Huang, X. Cong, S.-S. Wu, K.-Q. Lin, X. Yao, Y.-H. He, J.-B. Wu, Y.-F. Bao, S.-C. Huang, X. Wang, P.-H. Tan, and B. Ren, *Probing the edge-related properties of atomically thin MoS2 at nanoscale.* Nature Communications **10**, 5544 (2019)
79. R.S. Alencar, C. Rabelo, H.L.S. Miranda, T.L. Vasconcelos, B.S. Oliveira, A. Ribeiro, B.C. Públio, J. Ribeiro-Soares, A.G.S. Filho, L.G. Cançado, and A. Jorio, *Probing Spatial Phonon Correlation Length in Post-Transition Metal Monochalcogenide GaS Using Tip-Enhanced Raman Spectroscopy.* Nano Letters **19**, 7357-7364 (2019)
80. R. Kato, T. Umakoshi, R.T. Sam, and P. Verma, *Probing nanoscale defects and wrinkles in MoS2 by tip-enhanced Raman spectroscopic imaging.* Applied Physics Letters **114**, 073105 (2019)

81. R. Kato, T. Umakoshi, and P. Verma, *Raman Spectroscopic Nanoimaging of Optical Fields of Metal Nanostructures with a Chemically Modified Metallic Tip.* The Journal of Physical Chemistry C **125**, 20397-20404 (2021)
82. J.-H. Zhong, X. Jin, L. Meng, X. Wang, H.-S. Su, Z.-L. Yang, C.T. Williams, and B. Ren, *Probing the electronic and catalytic properties of a bimetallic surface with 3 nm resolution.* Nature Nanotechnology **12**, 132-136 (2017)
83. H. Yin, L.-Q. Zheng, W. Fang, Y.-H. Lai, N. Porenta, G. Goubert, H. Zhang, H.-S. Su, B. Ren, J.O. Richardson, J.-F. Li, and R. Zenobi, *Nanometre-scale spectroscopic visualization of catalytic sites during a hydrogenation reaction on a Pd/Au bimetallic catalyst.* Nature Catalysis **3**, 834-842 (2020)
84. L.M. Malard, L. Lafeta, R.S. Cunha, R. Nadas, A. Gadelha, L.G. Cançado, and A. Jorio, *Studying 2D materials with advanced Raman spectroscopy: CARS, SRS and TERS.* Physical Chemistry Chemical Physics **23**, 23428-23444 (2021)
85. M.S. Dresselhaus, A. Jorio, and R. Saito, *Characterizing Graphene, Graphite, and Carbon Nanotubes by Raman Spectroscopy.* Annual Review of Condensed Matter Physics **1**, 89-108 (2010)
86. Y. Okuno, Y. Saito, S. Kawata, and P. Verma, *Tip-Enhanced Raman Investigation of Extremely Localized Semiconductor-to-Metal Transition of a Carbon Nanotube.* Physical Review Letters **111**, 216101 (2013)
87. C. Chen, N. Hayazawa, and S. Kawata, *A* 1.7 nm *resolution chemical analysis of carbon nanotubes by tip-enhanced Raman imaging in the ambient.* Nature Communications **5**, 3312 (2014)
88. S. Uemura, S. Vantasin, Y. Kitahama, Y.Y. Tanaka, T. Suzuki, D. Doujima, T. Kaneko, and Y. Ozaki, *Interactions Between Epitaxial Graphene Grown on the Si- and C-Faces of 4H-SiC Investigated Using Raman Imaging and Tip-Enhanced Raman Scattering.* Applied Spectroscopy **74**, 1384-1390 (2020)
89. J.E. Lee, G. Ahn, J. Shim, Y.S. Lee, and S. Ryu, *Optical separation of mechanical strain from charge doping in graphene.* Nature Communications **3**, 1024 (2012)
90. S.S. Kharintsev, S.V. Saparina, A.I. Fishman, A.A. Stolov, and J. Li, *Spectrally Resolving Coherent TERS Spectroscopy of Electrically Biased Carbon-Coated Fibers.* The Journal of Physical Chemistry C **124**, 14752-14758 (2020)
91. S.S. Kharintsev, S.V. Saparina, A.I. Fishman, A.A. Stolov, and J. Li, *Water-Anchored Edge Defects in Amorphous Carbon Probed with Thermal- and Electroassisted Raman Spectroscopy and Nanoscopy.* The Journal of Physical Chemistry C **124**, 15886-15894 (2020)
92. L.G. Cançado, M.A. Pimenta, B.R.A. Neves, M.S.S. Dantas, and A. Jorio, *Influence of the Atomic Structure on the Raman Spectra of Graphite Edges.* Physical Review Letters **93**, 247401 (2004)
93. D.N. Voylov, V. Bocharova, N.V. Lavrik, I. Vlassiouk, G. Polizos, A. Volodin, Y.M. Shulga, A. Kisliuk, T. Thiyagarajan, D.D. Miller, R. Narayanan, B.G. Sumpter, and A.P. Sokolov, *Noncontact tip-enhanced Raman spectroscopy for nanomaterials and biomedical applications.* Nanoscale Advances **1**, 3392-3399 (2019)
94. K.A. Ritter and J.W. Lyding, *The influence of edge structure on the electronic properties of graphene quantum dots and nanoribbons.* Nature Materials **8**, 235-242 (2009)
95. W. Su, A. Esfandiar, O. Lancry, J. Shao, N. Kumar, and M. Chaigneau, *Visualising structural modification of patterned graphene nanoribbons using tip-enhanced Raman spectroscopy.* Chemical Communications **57**, 6895-6898 (2021)
96. W. Su and D. Roy, *Visualizing graphene edges using tip-enhanced Raman spectroscopy.* Journal of Vacuum Science & Technology B **31**, 041808 (2013)
97. W. Su, N. Kumar, N. Dai, and D. Roy, *Nanoscale mapping of intrinsic defects in single-layer graphene using tip-enhanced Raman spectroscopy.* Chemical Communications **52**, 8227-8230 (2016)
98. R. Meyer, S. Trautmann, K. Rezaei, A. George, A. Turchanin, and V. Deckert, *Synergy of Photoinduced Force Microscopy and Tip-Enhanced Raman Spectroscopy—A Correlative Study on MoS2.* ACS Photonics **6**, 1191-1198 (2019)

99. A. Krayev, C.S. Bailey, K. Jo, S. Wang, A. Singh, T. Darlington, G.-Y. Liu, S. Gradecak, P.J. Schuck, E. Pop, and D. Jariwala, *Dry Transfer of van der Waals Crystals to Noble Metal Surfaces To Enable Characterization of Buried Interfaces.* ACS Applied Materials & Interfaces **11**, 38218-38225 (2019)
100. S. Liu, M. Müller, Y. Sun, I. Hamada, A. Hammud, M. Wolf, and T. Kumagai, *Resolving the Correlation between Tip-Enhanced Resonance Raman Scattering and Local Electronic States with 1 nm Resolution.* Nano Letters **19**, 5725-5731 (2019)
101. R. Kato, T. Moriyama, T. Umakoshi, T.-a. Yano, and P. Verma, *Ultrastable tip-enhanced hyperspectral optical nanoimaging for defect analysis of large-sized WS2 layers.* Science Advances **8**, eabo4021)
102. Z. Li and D. Kurouski, *Probing the Redox Selectivity on Au@Pd and Au@Pt Bimetallic Nanoplates by Tip-Enhanced Raman Spectroscopy.* ACS Photonics **8**, 2112-2119 (2021)
103. Z. Li, J. Rigor, N. Large, P.Z. El-Khoury, and D. Kurouski, *Underlying Mechanisms of Hot Carrier-Driven Reactivity on Bimetallic Nanostructures.* The Journal of Physical Chemistry C **125**, 2492-2501 (2021)
104. Z. Li and D. Kurouski, *Elucidation of Photocatalytic Properties of Gold–Platinum Bimetallic Nanoplates Using Tip-Enhanced Raman Spectroscopy.* The Journal of Physical Chemistry C **124**, 12850-12854 (2020)
105. Z. Li, R. Wang, and D. Kurouski, *Nanoscale Photocatalytic Activity of Gold and Gold–Palladium Nanostructures Revealed by Tip-Enhanced Raman Spectroscopy.* The Journal of Physical Chemistry Letters **11**, 5531-5537 (2020)
106. T. Suzuki, X. Yan, Y. Kitahama, H. Sato, T. Itoh, T. Miura, and Y. Ozaki, *Tip-Enhanced Raman Spectroscopy Study of Local Interactions at the Interface of Styrene–Butadiene Rubber/ Multiwalled Carbon Nanotube Nanocomposites.* The Journal of Physical Chemistry C **117**, 1436-1440 (2013)
107. X. Yan, T. Suzuki, Y. Kitahama, H. Sato, T. Itoh, and Y. Ozaki, *A study on the interaction of single-walled carbon nanotubes (SWCNTs) and polystyrene (PS) at the interface in SWCNT–PS nanocomposites using tip-enhanced Raman spectroscopy.* Physical Chemistry Chemical Physics **15**, 20618-20624 (2013)
108. S. Vantasin, I. Tanabe, Y. Tanaka, T. Itoh, T. Suzuki, Y. Kutsuma, K. Ashida, T. Kaneko, and Y. Ozaki, *Tip-Enhanced Raman Scattering of the Local Nanostructure of Epitaxial Graphene Grown on 4H-SiC (000$\bar{1}$).* The Journal of Physical Chemistry C **118**, 25809-25815 (2014)
109. T. Suzuki, T. Itoh, S. Vantasin, S. Minami, Y. Kutsuma, K. Ashida, T.-a. Kaneko, Y. Morisawa, T. Miura, and Y. Ozaki, *Tip-enhanced Raman spectroscopic measurement of stress change in the local domain of epitaxial graphene on the carbon face of 4H-SiC(000–1).* Physical Chemistry Chemical Physics **16**, 20236-20240 (2014)
110. S. Vantasin, Y. Tanaka, S. Uemura, T. Suzuki, Y. Kutsuma, D. Doujima, T. Kaneko, and Y. Ozaki, *Characterization of SiC-grown epitaxial graphene microislands using tip-enhanced Raman spectroscopy.* Physical Chemistry Chemical Physics **17**, 28993-28999 (2015)
111. P. Pienpinijtham, S. Vantasin, O. Wong-u-ra, Y. Kitahama, S. Ekgasit, and Y. Ozaki, *Local structural changes in graphene oxide layers induced by silver nanoparticles.* Physical Chemistry Chemical Physics **20**, 21498-21505 (2018)
112. J. Nanda, G. Yang, T. Hou, D.N. Voylov, X. Li, R.E. Ruther, M. Naguib, K. Persson, G.M. Veith, and A.P. Sokolov, *Unraveling the Nanoscale Heterogeneity of Solid Electrolyte Interphase Using Tip-Enhanced Raman Spectroscopy.* Joule **3**, 2001-2019 (2019)
113. I. Tanabe, M. Egashira, T. Suzuki, T. Goto, and Y. Ozaki, *Prevention of Photooxidation of Deoxymyoglobin and Reduced Cytochrome c during Enhanced Raman Measurements: SERRS with Thiol-Protected Ag Nanoparticles and a TERS Technique.* The Journal of Physical Chemistry C **118**, 10329-10334 (2014)
114. C. Lee and C.D. Bain, *Raman spectra of planar supported lipid bilayers.* Biochimica et Biophysica Acta (BBA)—Biomembranes **1711**, 59–71 (2005)
115. R.G. Snyder, H.L. Strauss, and C.A. Elliger, *Carbon-hydrogen stretching modes and the structure of n-alkyl chains. 1. Long, disordered chains.* The Journal of Physical Chemistry **86**, 5145–5150 (1982)

116. D. Talaga, A. Bremner, T. Buffeteau, R.A.L. Vallée, S. Lecomte, and S. Bonhommeau, *Total Internal Reflection Tip-Enhanced Raman Spectroscopy of Cytochrome c.* The Journal of Physical Chemistry Letters **11**, 3835-3840 (2020)
117. T. Dou, Z. Li, J. Zhang, A. Evilevitch, and D. Kurouski, *Nanoscale Structural Characterization of Individual Viral Particles Using Atomic Force Microscopy Infrared Spectroscopy (AFM-IR) and Tip-Enhanced Raman Spectroscopy (TERS).* Analytical Chemistry **92**, 11297-11304 (2020)
118. T. Deckert-Gaudig, A. Taguchi, S. Kawata, and V. Deckert, *Tip-enhanced Raman spectroscopy – from early developments to recent advances.* Chemical Society Reviews **46**, 4077-4110 (2017)
119. P. Verma, *Tip-Enhanced Raman Spectroscopy: Technique and Recent Advances.* Chemical Reviews **117**, 6447-6466 (2017)
120. G. Kolhatkar, J. Plathier, and A. Ruediger, *Nanoscale investigation of materials, chemical reactions, and biological systems by tip enhanced Raman spectroscopy – a review.* Journal of Materials Chemistry C **6**, 1307-1319 (2018)
121. S. Mahapatra, L. Li, J.F. Schultz, and N. Jiang, *Tip-enhanced Raman spectroscopy: Chemical analysis with nanoscale to angstrom scale resolution.* The Journal of Chemical Physics **153**, 010902 (2020)
122. S. Berweger, J.M. Atkin, R.L. Olmon, and M.B. Raschke, *Light on the Tip of a Needle: Plasmonic Nanofocusing for Spectroscopy on the Nanoscale.* The Journal of Physical Chemistry Letters **3**, 945-952 (2012)
123. A. Taguchi, J. Yu, P. Verma, and S. Kawata, *Optical antennas with multiple plasmonic nanoparticles for tip-enhanced Raman microscopy.* Nanoscale **7**, 17424-17433 (2015)
124. A.A. Sifat and E.O. Potma, *Optimizing the near-field and far-field properties of tips in tip-enhanced Raman scattering.* Journal of Raman Spectroscopy **52**, 2018-2028 (2021)
125. I. Maouli, A. Taguchi, Y. Saito, S. Kawata, and P. Verma, *Optical antennas for tunable enhancement in tip-enhanced Raman spectroscopy imaging.* Applied Physics Express **8**, 032401 (2015)
126. X. Ma, Y. Zhu, S. Kim, Q. Liu, P. Byrley, Y. Wei, J. Zhang, K. Jiang, S. Fan, R. Yan, and M. Liu, *Sharp-Tip Silver Nanowires Mounted on Cantilevers for High-Aspect-Ratio High-Resolution Imaging.* Nano Letters **16**, 6896-6902 (2016)
127. P. Walke, Y. Fujita, W. Peeters, S. Toyouchi, W. Frederickx, S. De Feyter, and H. Uji-i, *Silver nanowires for highly reproducible cantilever based AFM-TERS microscopy: towards a universal TERS probe.* Nanoscale **10**, 7556-7565 (2018)
128. X. Ma, Y. Zhu, N. Yu, S. Kim, Q. Liu, L. Apontti, D. Xu, R. Yan, and M. Liu, *Toward High-Contrast Atomic Force Microscopy-Tip-Enhanced Raman Spectroscopy Imaging: Nanoantenna-Mediated Remote-Excitation on Sharp-Tip Silver Nanowire Probes.* Nano Letters **19**, 100-107 (2019)
129. S. Kim, N. Yu, X. Ma, Y. Zhu, Q. Liu, M. Liu, and R. Yan, *High external-efficiency nanofocusing for lens-free near-field optical nanoscopy.* Nature Photonics **13**, 636-643 (2019)
130. Q. Liu, S. Kim, X. Ma, N. Yu, Y. Zhu, S. Deng, R. Yan, H. Zhao, and M. Liu, *Ultra-sharp and surfactant-free silver nanowire for scanning tunneling microscopy and tip-enhanced Raman spectroscopy.* Nanoscale **11**, 7790-7797 (2019)
131. L.-K. Yang, T.-X. Huang, Z.-C. Zeng, M.-H. Li, X. Wang, F.-Z. Yang, and B. Ren, *Rational fabrication of a gold-coated AFM TERS tip by pulsed electrodeposition.* Nanoscale **7**, 18225-18231 (2015)
132. T.-X. Huang, C.-W. Li, L.-K. Yang, J.-F. Zhu, X. Yao, C. Liu, K.-Q. Lin, Z.-C. Zeng, S.-S. Wu, X. Wang, F.-Z. Yang, and B. Ren, *Rational fabrication of silver-coated AFM TERS tips with a high enhancement and long lifetime.* Nanoscale **10**, 4398-4405 (2018)
133. D.H. Kim, C. Lee, B.G. Jeong, S.H. Kim, and M.S. Jeong, *Fabrication of highly uniform nanoprobe via the automated process for tip-enhanced Raman spectroscopy.* Nanophotonics **9**, 2989-2996 (2020)
134. K. Zhang, Y. Bao, M. Cao, S.-i. Taniguchi, M. Watanabe, T. Kambayashi, T. Okamoto, M. Haraguchi, X. Wang, K. Kobayashi, H. Yamada, B. Ren, and T. Tachizaki, *Low-Background*

*Tip-Enhanced Raman Spectroscopy Enabled by a Plasmon Thin-Film Waveguide Probe.* Analytical Chemistry **93**, 7699-7706 (2021)
135. Y.-P. Huang, S.-C. Huang, X.-J. Wang, N. Bodappa, C.-Y. Li, H. Yin, H.-S. Su, M. Meng, H. Zhang, B. Ren, Z.-L. Yang, R. Zenobi, Z.-Q. Tian, and J.-F. Li, *Shell-Isolated Tip-Enhanced Raman and Fluorescence Spectroscopy.* Angewandte Chemie International Edition **57**, 7523-7527 (2018)
136. R. Kato, K. Taguchi, R. Yadav, T. Umakoshi, and P. Verma, *One-side metal-coated pyramidal cantilever tips for highly reproducible tip-enhanced Raman spectroscopy.* Nanotechnology **31**, 335207 (2020)
137. A. Capaccio, A. Sasso, O. Tarallo, and G. Rusciano, *Coral-like plasmonic probes for tip-enhanced Raman spectroscopy.* Nanoscale **12**, 24376-24384 (2020)
138. T. Itoh, Y.S. Yamamoto, T. Suzuki, Y. Kitahama, and Y. Ozaki, *Darkfield microspectroscopy of nanostructures on silver tip-enhanced Raman scattering probes.* Applied Physics Letters **108**, 021604 (2016)
139. Y. Kitahama, S. Uemura, R. Katayama, T. Suzuki, T. Itoh, and Y. Ozaki, *Polarization dependence of tip-enhanced Raman and plasmon-resonance Rayleigh scattering spectra.* Applied Physics Letters **110**, 233104 (2017)
140. C.-Y. Li, M. Meng, S.-C. Huang, L. Li, S.-R. Huang, S. Chen, L.-Y. Meng, R. Panneerselvam, S.-J. Zhang, B. Ren, Z.-L. Yang, J.-F. Li, and Z.-Q. Tian, *"Smart" Ag Nanostructures for Plasmon-Enhanced Spectroscopies.* Journal of the American Chemical Society **137**, 13784-13787 (2015)
141. L. Opilik, Ü. Dogan, C.-Y. Li, B. Stephanidis, J.-F. Li, and R. Zenobi, *Chemical Production of Thin Protective Coatings on Optical Nanotips for Tip-Enhanced Raman Spectroscopy.* The Journal of Physical Chemistry C **120**, 20828-20832 (2016)
142. K. Taguchi, T. Umakoshi, S. Inoue, and P. Verma, *Broadband Plasmon Nanofocusing: Comprehensive Study of Broadband Nanoscale Light Source.* The Journal of Physical Chemistry C **125**, 6378-6386 (2021)
143. G.L. Bartolomeo, G. Goubert, and R. Zenobi, *Tip Recycling for Atomic Force Microscopy-Based Tip-Enhanced Raman Spectroscopy.* Applied Spectroscopy **74**, 1358-1364 (2020)
144. S. Mahapatra, L. Li, J.F. Schultz, and N. Jiang, *Methods to fabricate and recycle plasmonic probes for ultrahigh vacuum scanning tunneling microscopy-based tip-enhanced Raman spectroscopy.* Journal of Raman Spectroscopy **52**, 573-580 (2021)
145. K. Zhang, S.-i. Taniguchi, T. Saeki, Y. Bao, M. Cao, M. Watanabe, X. Wang, K. Kobayashi, B. Ren, and H. Yamada, *Simple cleaning and regeneration of tip-enhanced Raman spectroscopy probe with UV sources.* Journal of Raman Spectroscopy **53**, 2023-2030 (2022)
146. Y. Yokota, N. Hayazawa, B. Yang, E. Kazuma, F.C.I. Catalan, and Y. Kim, *Systematic Assessment of Benzenethiol Self-Assembled Monolayers on Au(111) as a Standard Sample for Electrochemical Tip-Enhanced Raman Spectroscopy.* The Journal of Physical Chemistry C **123**, 2953-2963 (2019)
147. G. Kang, M. Yang, M.S. Mattei, G.C. Schatz, and R.P. Van Duyne, *In Situ Nanoscale Redox Mapping Using Tip-Enhanced Raman Spectroscopy.* Nano Letters **19**, 2106-2113 (2019)
148. J.H.K. Pfisterer, M. Baghernejad, G. Giuzio, and K.F. Domke, *Reactivity mapping of nanoscale defect chemistry under electrochemical reaction conditions.* Nature Communications **10**, 5702 (2019)
149. F. Benz, M.K. Schmidt, A. Dreismann, R. Chikkaraddy, Y. Zhang, A. Demetriadou, C. Carnegie, H. Ohadi, B. de Nijs, R. Esteban, J. Aizpurua, and J.J. Baumberg, *Single-molecule optomechanics in "picocavities".* Science **354**, 726-729 (2016)
150. T. Itoh, K. Hashimoto, A. Ikehata, and Y. Ozaki, *Direct demonstration for changes in surface plasmon resonance induced by surface-enhanced Raman scattering quenching of dye molecules adsorbed on single Ag nanoparticles.* Applied Physics Letters **83**, 5557-5559 (2003)

151. T. Itoh, Y.S. Yamamoto, H. Tamaru, V. Biju, S.-i. Wakida, and Y. Ozaki, *Single-molecular surface-enhanced resonance Raman scattering as a quantitative probe of local electromagnetic field: The case of strong coupling between plasmonic and excitonic resonance.* Physical Review B **89**, 195436 (2014)
152. K.J. Savage, M.M. Hawkeye, R. Esteban, A.G. Borisov, J. Aizpurua, and J.J. Baumberg, *Revealing the quantum regime in tunnelling plasmonics.* Nature **491**, 574-577 (2012)

# Chapter 7
# Advances in Machine Learning for SERS Analysis




**Clarice E. Froehlich, Cassandra L. Wouters, Mahmoud Matar Abed, Vivian E. Ferry, and Christy L. Haynes**

**Abstract** Surface-enhanced Raman scattering (SERS) has advanced significantly since the initial report in 1974. With the current substrates, characterization methods, and measurement systems, SERS has great potential as an analytical tool, and this potential is amplified with machine learning-based analysis of the measured spectra. This chapter will review the basics of machine learning relevant for SERS analysis, including underlying principles, the commonly used methods, and consideration of validation and figures of merit. For context, the chapter will review a range of specific examples where various ML techniques have been used for SERS analysis, finishing with an in-depth consideration of ML-enabled SERS detection of bacteria. Thoughtful ML application is an excellent way to maximize the utility of this sensitive and selective spectroscopic tool.

**Keywords** SERS · Machine learning · Chemometrics · Bacteria identification

## 7.1 Introduction

In the early days of surface-enhanced Raman scattering research, in the 1970s and 1980s, scientists were focused on two major areas: (1) working out the mechanisms responsible for the unexpectedly large enhancement factors (EFs) and (2) developing nanofabrication methods that allowed tuning of plasmonic properties. In a time when researchers were focused on achieving consistent EFs and measuring only from a small collection of analytes considered relevant for SERS, linear algebra-based chemometric methods were considered by many to be a way to overinterpret spectral

C. E. Froehlich · V. E. Ferry
Department of Chemical Engineering and Materials Science, University of Minnesota, Minneapolis, MN, USA

C. L. Wouters · M. Matar Abed · C. L. Haynes (✉)
Department of Chemistry, University of Minnesota, Minneapolis, MN, USA
e-mail: chaynes@umn.edu

© The Author(s), under exclusive license to Springer Nature Singapore Pte Ltd. 2024

M. Procházka et al. (eds.), *Surface- and Tip-Enhanced Raman Scattering Spectroscopy*,
https://doi.org/10.1007/978-981-97-5818-0_7

data. This can be traced to the fact that, in some of the early applications of chemometrics in SERS, there are examples where too many loading vectors were used and where the analyzed features were not necessarily correlated with vibrational features of the molecules of interest. Of course, this was not due to malintent of researchers but simply a naivete that speaks to insufficient communication between spectroscopists and data scientists.

As substrates became more repeatable and best practices emerged around sampling and data analysis, many scientists began to think of SERS as an analytical tool (rather than just a physical chemistry or physics phenomenon). At this point, chemometrics-based data analysis became more common—several examples from this study type are shared in Sect. 7.4.

In the last few years, as big data and machine learning have become ubiquitous throughout science, it is no surprise that the techniques being developed and deployed in other areas have also been used to analyze SERS data. Of course, the particular model or analysis method must suit the data that has been collected. Different machine learning models will be useful in gaining different insights into SERS studies, but in general they are able to tease out complex patterns in data linked to multiple analytes or complex media, allow for quicker and more in-depth analysis of large datasets of tens of thousands of spectra, and more. This chapter will explore the various options currently available, making it easy for SERS spectroscopists to choose one that will work well for their data, whether that be applied studies of contaminants in complex matrices or fundamental studies of plasmon-driven reactions.

## 7.2 Machine Learning Methods

### *7.2.1 General Principles of Machine Learning*

Simply put, machine learning (ML) is a method of using an algorithm to extract knowledge from data and apply it to problems to make predictions and gain insights. An ML model is trained on data, also called features, from many samples and is generally used to make target property predictions about new samples based on the knowledge gained from training (Fig. 7.1). The model can also be used to obtain a lower-dimensional representation of the data or to find underlying structures in the data such as clusters. The main goals of ML include making predictions, gaining insights about data, and making predictions more quickly than other methods, such as by training a model on density functional theory (DFT) data to predict Raman spectra for new molecules [1].

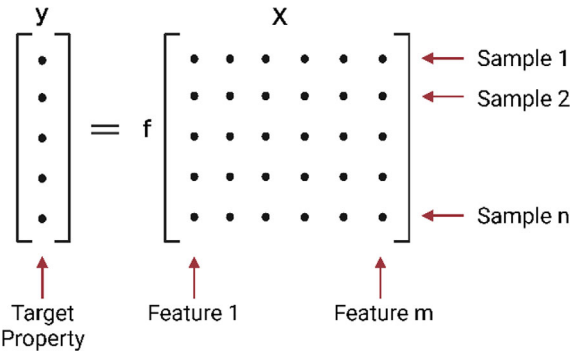



**Fig. 7.1** General data format for machine learning, where **f** is a function representing the ML model. Figure created with bioren der.com

#### 7.2.1.1 Types of Machine Learning

Two broad subsets of ML exist: supervised learning and unsupervised learning. The main differentiator between these two types of ML is whether the model is trained on data where it knows a target property, or label, that it is trying to predict. In supervised learning, the model is given labeled data to train on, whereas in unsupervised learning, the model is given unlabeled or raw data. For example, in SERS, unlabeled data would be a Raman spectrum for each sample, but labeled data would contain both the Raman spectrum and the concentration or identity for each sample. Generally, supervised learning is used for making predictions, whereas unsupervised learning is used for performing dimensionality reduction or finding underlying data structures. Some machine learning models exist outside of supervised or unsupervised learning, such as reinforcement-type models, but these are much less frequently used in chemistry, and there are few examples in the field of Raman spectroscopy [2, 3].

#### 7.2.1.2 Feature Processing

The features and training data used in an ML model determine how effective the model can be. The model can only be as good as the data it is trained on, so poor training data can only yield a poor model. A good training dataset will have a lot of data; hundreds, thousands, or even millions of samples can be needed depending on the type of model and the features used. Additionally, the training data needs to be representative and unbiased, meaning that the range of possible values for the target property is well-sampled. Having a good understanding of the underlying fundamental principles of the system being modeled is helpful for determining which features are most important to include, but ML is still a useful method when those principles are not well-understood. Feature importance testing can be used to find which features are most important for maintaining accuracy of the model, and this in turn can give insight into the fundamental characteristics of the system.

To improve model efficacy, features are often processed prior to training the model. This can include scaling so that features are of the same magnitude, baselining of

spectra, or removing features with no or low correlation with the target property. If other assay conditions such as substrate type or fabrication conditions are different between spectra, those variables can also be included as features along with each spectrum. Further, if any features have non-numerical values, such as categorical features, then one-hot-encoding is typically used to create a new feature for each category, where the feature value is 1 or 0 to indicate belonging, or not belonging, to that category. In cases where there is missing data, such as a sample not having a measured value for one of the features, then a decision must be made to either remove that feature entirely from the model, or to impute the value. Imputing data can be done by replacing missing values with the average, minimum, maximum, or another value from the rest of the samples. Whether to pick the average or another value depends on the feature, so careful consideration of the effect of imputing data is needed, and all feature processing including imputing should be thoroughly described in the methods section of any ML article so that the reader knows what assumptions are being made. For SERS data, feature processing should always include baselining of spectra and oftentimes include normalization or scaling. Open-source software packages are available for baselining of Raman data, such as the Bubblefill algorithm within the open Raman processing library (ORPL) for Python [4]. Other common baselining algorithms include asymmetric least squares and improved modified polynomial (iModPoly) fits [4, 5].

The popular and highly useful open-source Python package scikit-learn contains many algorithms for data processing as well as a large library of algorithms for unsupervised and supervised learning, validation and model analysis, and data visualization, including many of the techniques described here [6].

## *7.2.2 Unsupervised Learning*

### 7.2.2.1 Dimensionality Reduction

Depending on the origin of the data used in machine learning, there can be anywhere from a few features to thousands or millions. In the case of many features, this can require very high computational power and memory as well as a large amount of time to train and use the model. Additionally, much of the information within these features may not actually correlate with the target property. Therefore, dimensionality reduction is a popular technique that condenses many features down to a smaller number of new features. Dimensionality reduction can be done using either a linear or nonlinear algorithm; linear algorithms have the advantage of being simpler and more inherently interpretable, but they are not able to deal with nonlinear trends in the data.

The most common type of dimensionality reduction is principal component analysis (PCA). It is a linear method that changes the coordinate system of the data to put most of the variation in the data in the first few transformed dimensions, which reduces the number of data dimensions needed to preserve most of the information

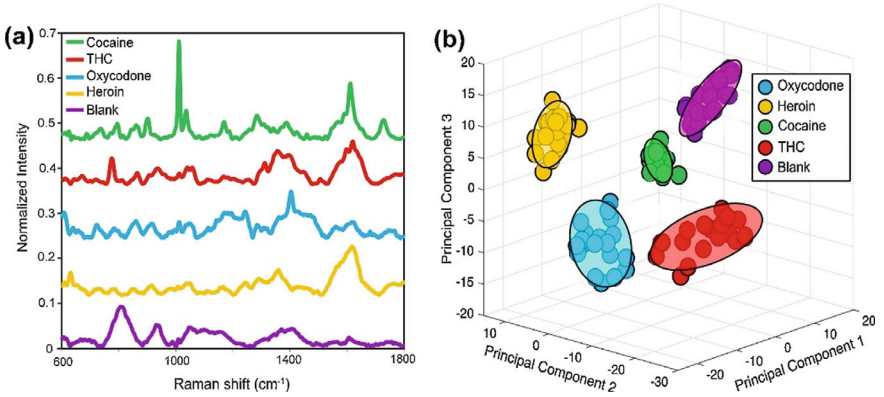



**Fig. 7.2** **a** SERS spectra of various illicit drugs, **b** results of PCA analysis on SERS spectra with ovals used to represent clusters of spectra into different drug types. Reproduced from Dies et al. [3]

contained within the data. To perform the change in basis, principal components (PCs) are calculated, where the first PC is a direction or basis vector along which the largest amount of data variance occurs, and the second PC is an orthogonal basis vector along which the second largest amount of data variance occurs, and so on. The output of PCA is then the projection of the data along each of the PCs. Often for SERS, some PCs resemble spectral features that are different between samples and can give an idea of which peaks are important for distinguishing samples [7]. Typically, the percentage of variance explained by each of the PCs is calculated to determine how many PCs are needed and which will be discarded in the dimensionality reduction. Oftentimes, a dataset comprised of SERS spectra with over a thousand points can be reduced to only two or three dimensions. The reduced data could then be used in a supervised learning model, or the samples could be plotted as points along the first few principal components to observe clustering, as in Fig. 7.2. It is also important to not keep too many of these PCs as features, as the ones that explain relatively less variance in the dataset often represent noise, and keeping them as features would lead to overfitting of the data.

#### 7.2.2.2 Clustering

Clustering algorithms split up the datapoints of a dataset into clusters, which can reveal trends within the data and help classify new datapoints. These algorithms consider distances between points within the feature space to make decisions about which datapoints to cluster together, though they differ in what criteria they use to make these decisions. KMeans is a common algorithm where a number ($K$) of clusters are preselected, and then the algorithm optimizes the location of $K$ cluster centers, or

mean points, to minimize the sum of squared distances to datapoints in the associated cluster [8]. This algorithm works well when the clusters are radially symmetric and around the same size, but functions poorly in cases where certain clusters are more spread out or are stretched or curved shapes. Other algorithms such as hierarchical clustering methods (see below) consider pairwise distances instead of distances to a mean point in a cluster and work better in these other cases. Additionally, methods exist for optimizing the number of clusters, such as the elbow method for KMeans clustering, where the number of clusters is chosen to be that with the greatest decrease in sum of squared distances to the center within a cluster as compared to one fewer cluster [9].

Hierarchical cluster analysis (HCA) methods, which are popular for SERS data, work differently in that they either consider all datapoints as one cluster at first and then successively split it into smaller clusters (called divisive clustering), or consider all datapoints as having their own single-datapoint cluster then successively merge clusters (called agglomerative clustering). This cluster division or agglomeration is typically visualized in a dendrogram which shows the order in which clusters are split or merged. Decisions for how to split or merge clusters can be made based on the linkage type used, typically Ward, complete, average, or single linkage. Each of these linkage types, except Ward, can be used with different distance metrics such as Euclidean or cosine distance to determine closeness of points and clusters [10].

### *7.2.3 Supervised Learning*

The goal of supervised learning is generally to learn from training data to make predictions about new datapoints. Two main types of supervised learning exist: classification and regression. Classification methods predict which discrete class or category a datapoint belongs to, whereas regression methods predict a value on a continuous scale. For example, from a SERS spectrum, a classification algorithm might predict the presence of a bacterial species, whereas a regression algorithm might predict the concentration of an analyte. Many algorithms exist for supervised learning, many more than can be covered here, but the following methods are common and useful for SERS analyses. It is also worthwhile to note that most algorithms can be used either for classification or regression, such as by acting as a regressor but assigning certain ranges of predicted values to certain classes.

#### 7.2.3.1 Polynomial Regression

The simplest form of supervised learning is polynomial regression, where the prediction is the sum of the features to various integer exponents, multiplied by weights. The main hyperparameter, a parameter that the user sets to control how the model

learns, is the maximum degree of the polynomial functions. For linear regression, this maximum degree is one. Learning occurs by selecting weights according to a selection criterion. Commonly, ordinary least squares (OLS) is used as the selection criterion, where weights are chosen to minimize the sum of squared error between the actual and predicted value of the target property at each training datapoint. Two other prominent selection criteria exist: least absolute shrinkage and selection operator (LASSO) and ridge. Both criteria combine OLS with functions that serve to lower the number of nonzero weights and to prefer lower-magnitude weights, which help to prevent overfitting to the training data [11].

#### 7.2.3.2 Linear Discriminant Analysis (LDA)

LDA is a commonly used method in SERS for supervised dimensionality reduction in classification problems. This means that in contrast to PCA, LDA uses labeled data (including both the spectra and the true class labels). LDA works by projecting the data into a lower-dimensional linear space using the directions in the data that maximize class separation, unlike PCA which similarly projects data into a linear space but maximizes variation in the data without considering classes. LDA also fits a decision boundary, like the linear support vector machine method, which uses a straight line in the lower-dimensional space that best separates the classes and can be used for classification of new samples.

#### 7.2.3.3 Decision Trees

Decision tree algorithms function by asking questions of the data to split it into groups at various nodes, with the nodes and questions optimized for the greatest impurity loss at each node. While impurity can be measured in different ways, this generally means that at each node, the decision tree aims to split the data into homogeneous groups with the same label. Each node functions by splitting data into groups based on a rule or question, such as splitting samples with mass as a feature into groups based on whether they are more or less than one kilogram. To prevent overfitting, hyperparameters are usually set to give a maximum depth of the tree, which is the highest number of consecutive nodes in the tree, and to give a minimum number of samples required to split a node. Together, these hyperparameters keep the model from making decisions based on features of single training samples rather than based on trends within the training data. While commonly used as classifiers, decision trees can also be used as regressors [12, 13]. This is frequently done by finding which leaf node (point at which the data is no longer split) a new sample belongs to, then calculating the average target property of the training samples at that node, which is used as the prediction for the new sample.

#### 7.2.3.4 Support Vector Machines (SVMs)

In SVMs, datapoints are viewed as $m$-dimensional vectors where $m$ is the number of features, and the algorithm finds one or multiple $(m - 1)$-dimensional hyperplanes that separate the training datapoints between classes. Hyperplanes are chosen to have the maximum margin between the plane and the nearest datapoints to the plane. This basic type of SVM is considered linear SVM since it can only linearly separate classes. Nonlinear separation via SVM becomes possible by using a nonlinear kernel function such as a polynomial or sigmoid function to transform the feature space into a higher-dimensional one where a linear SVM can be used. In this case, a hyperplane in the transformed feature space corresponds to a nonlinear separation in the original feature space which can classify nonlinear data. Similar to decision trees, support vector machines (SVMs) are commonly used as classifiers but can also function as regressors [14, 15]. Support vector regression works by finding a function that takes the numerical features and outputs a predicted target property with an error less than a specified value, so that as many points as possible are located within this margin of the function. This function acts as the hyperplane in this case, and it is used to make predictions.

#### 7.2.3.5 Artificial Neural Networks (ANNs)

While the aforementioned types of supervised learning are shallow methods, ANNs are a form of deep learning that are much less interpretable but can learn complex trends within data [16, 17]. ANNs are formed by linking layers of computational nodes together. Each node functions by combining the data input to that node through a linear function, then by transforming the result of the linear function using a nonlinear activation function (Fig. 7.3a). This new result is then sent to other nodes in the next layer as an input. When training data is sent to an ANN, it first goes to the input layer which can have multiple nodes. The nodes of the input layer output data to nodes in the first hidden layer, which output data to the second hidden layer, and so on until the last hidden layer outputs to the output layer (Fig. 7.3b). This output layer serves to convert the resulting data into a prediction, which can be either for classification or regression. While developing an ANN, the number of hidden layers, number of nodes in each of the layers, and the activation function can be adjusted to optimize performance. Using too many nodes and layers can lead to overfitting and requires much more computational power, but using too few may lead to an underfit model. Popular activation functions include ReLU, leaky ReLU, SoftMax, Sigmoid, and Tanh [18].

For the ANN to learn from training data, back-propagation and gradient descent are commonly used. Back-propagation involves the calculation of derivatives propagating from the output back to the inputs. The purpose is to find how the overall prediction error changes with the weights of the linear functions in each of the nodes so that they can be adjusted to reduce error between the actual and predicted output for each of the training datapoints. Gradient descent is used to determine how these

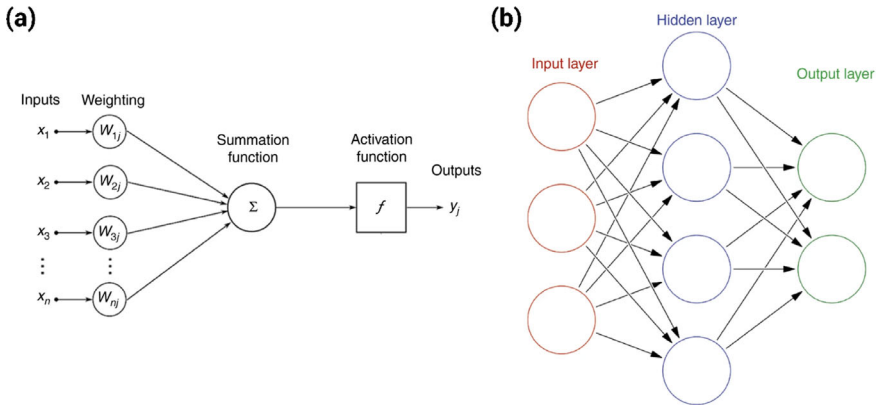



**Fig. 7.3** **a** Schematic of an ANN node, **b** ANN structure with one hidden layer. Reproduced from Zhang et al. [17] under a Creative Commons version 4.0 license

weights should be adjusted, since it is used to gradually decrease the total error or loss from the predictions on the training data by following the loss gradients. There are many algorithms available for this optimization process, including vanilla, stochastic, or minibatch gradient descent, as well as momentum, Adam, and others.

#### 7.2.3.6 Ensembling Methods

There are often cases where a single model is not able to achieve a high level of accuracy on its own. These cases can benefit from the use of an ensembling method, which combines weaker learning models into an ensemble to get a stronger learning model. These methods are usually either averaging or boosting methods.

Averaging methods work by taking an average of predictions across multiple models of either the same or different types. Different models have different strengths and weaknesses, so using an average can reduce the effects of the weaknesses. Common examples of averaging methods include random forests, which are an ensemble of decision trees, and voting classifiers, which use different model types to vote on the prediction [19].

Boosting models involve sequential training of weaker models, where the results of the first model are passed to the second model for training, the results from the second model are passed to the third, and so forth. This type of method can be beneficial for learning what types of samples tend to have less accurate predictions. For example, AdaBoost is a popular boosting model which functions by giving incorrectly predicted samples a higher weight in the next model in the sequence [20]. This means that the models put the focus of their training on samples that previous models have had trouble predicting accurately.

### *7.2.4 Validation and Model Analysis*

#### 7.2.4.1 Performance Metrics and Loss Functions

To optimize a supervised model, we need to have a metric for how well a model makes predictions. Different metrics exist for classification and regression models due to the difference in data type, and there is no one metric that is best for all classification models or for all regression models. Additionally, during model optimization, loss functions are generally used to gauge whether the model is improving (lower or more negative loss function) or worsening (larger or more positive loss function).

For classification models, it is common to use accuracy, which describes the fraction of correctly predicted samples, as a simple performance metric. However, accuracy gives no indication of what types of samples are being incorrectly predicted, unlike the false positive rate (FPR) for binary classification. Other common metrics for binary classification are precision and recall, which describe the fraction of correct positive predictions and the fraction of correctly predicted positive samples, respectively. Precision and recall can also be combined into the $F_1$ score [21]. For model optimization, log loss or cross-entropy loss is frequently used as the loss function for binary classification. While these metrics and loss functions are most often defined for binary classification, there also exist versions for multiclass classification.

For regression models, typical metrics and loss functions include mean squared error (MSE) and mean average error (MAE), which are the average of the squared error and of the error, respectively, for all predictions. An additional performance metric for regression is the $R^2$ value. While a higher MSE or MAE means worse prediction capability, the $R^2$ value ranges from 0 to 1 with values closer to 1 indicating better predictions.

#### 7.2.4.2 Validation

It is critical to perform model validation to optimize a supervised ML model before putting the model to use predicting new samples. The process of validation is when the optimization of hyperparameters occurs. Models with varied hyperparameters are trained and validated to find which set of hyperparameters leads to the best validation performance. When developing a supervised ML model, the dataset should always be split into two sections (training and testing) as the first step. While the fraction of data to assign as test data can be varied, it is common to use stratified random sampling to select twenty percent of the data, representative of the entire dataset, for testing. This test set should then be set aside until the model is trained, optimized, and completed so that no decisions for model development are made based on the test data. This means that at the end of model development, the model can be tested on the reserved test set, and the aforementioned performance metrics determine how well the model will perform on new data.

Since the test data cannot be used during model development, validation is used during development to interrogate the model. However, the model should not only be tested on the data which it was trained on, since that gives no indication of how generalizable the model is to data other than the training data. There are many ways to perform validation, but in general cross-validation (CV) is used, which involves taking a subset of the training dataset to be the validation set, training the model on the remaining training data, then evaluating model predictions on the validation set. Multiple types of CV exist, including K-fold CV where the training set is split into $K$ subsets and validation is performed $K$ times where each time a different subset is used as the validation set, stratified K-fold CV which is the same as K-fold CV but the training set is split so each subset is roughly representative of the overall training set, and leave-one-out CV where CV is performed with only one sample as the validation set many times until all samples have been used [22].

## 7.3 Using Machine Learning for SERS Analysis

### *7.3.1 History of ML Applications in the SERS Field*

Machine learning has been used to interpret SERS data since at least 1989, when an early example used PCA to identify significant differences between protonation states of 1,4-diazabicyclo[2.2.2]octane to better understand the mechanism of enhancement [23]. Now, machine learning methods like artificial neural networks are commonly used at the cutting edge of the field. These methods allow for spectra which are too complex to understand by eye to be interpreted and classified. Among machine learning techniques lies the field of chemometrics, rooted primarily in principle component analysis (PCA) and multivariate regression methods [24]. Though chemometric analysis is a powerful tool, supervised machine learning techniques can be used to model complex data with small differences more accurately and are generally better for quantification than unsupervised methods. These innovations in data handling and extracting information can push the SERS field forward alongside novel substrate designs and other experimental improvements.

### *7.3.2 Selecting the Machine*

Unsupervised learning methods are an especially useful place to start when considering ML to interpret data. Most commonly, PCA is used to understand sources of variance in data and reduce the dimensionality. In the SERS analysis of a mycotoxin, Szlag et al. used PCA to investigate the binding strength of different linear polymer affinity agents with the contaminant [25]. Often, the simplified data set yielded from PCA can then be fed into a supervised learning method as the input data. Another

useful unsupervised learning mode is hierarchical clustering analysis (HCA), used by Vikesland and Zhou to analyze differences in time-points for biofilms infected with bacteriophages within a concentration class [26]. PCA was applied to the different concentration classes in the same paper. In this case, using multiple methods allowed for the analysis of spatiotemporal data. Had more complex ML methods been used (e.g., SVM), a single method would likely have been sufficient to understand data in both domains.

Among the most common supervised machine learning techniques exploited for SERS analysis are SVMs, RFs, and ANNs. They all follow an overall similar structure of utilizing a training data set, adjusting parameters to optimize the model, and testing an additional known data set to verify the accuracy of the model. RFs and SVMs require less computational power than deep learning (like ANNs) and are designed for pattern analysis, which can be an advantage if developing and running an algorithm on a computer not designed for heavy computational loads. Additionally, all these methods can consider peak position, height, and width in spectra. Another supervised learning method which is generally simpler to use is linear discriminant analysis (LDA), which works similarly to PCA with the exception that it requires labeled input data. Diao et al. used LDA after initially reducing the dimensionality of their breast and cervical cancer biomarker exosome spectra with PCA to create a diagnostic model with 93.3% accuracy [27]. The logic of LDA as maximizing class separation and minimizing variance within a class is easy to understand and makes it a compelling algorithm in many cases. LDA is an advantageous algorithm as it requires less data than more complex ML methods because it has less variables requiring optimization, especially as compared to deep learning. However, LDA is limited to functioning within a linear space.

SVM is one of the most versatile ML methods used in SERS and is commonly used both as a classifier and as a regressor. SVMs can be modified by implementing different kernel functions, though it should be noted that only linear kernels are able to extract spectral features which contribute most to the variance. In the literature, SVM is often leveraged to develop classifiers for bacteria on a strain level with high accuracy [28–30]. Choi and colleagues used ssDNA-functionalized gold substrates to differentiate highly virulent influenza strains, including H1N1, by pre-selecting spectral features with statistical tests which were then fed into the algorithms [31]. SVM discriminant analysis ultimately yielded high sensitivity and specificity for the different infectious flu strains studied. SVM is highly effective as a classifier because projection of the data into higher-dimensional space and drawing a hyper-plane boundary can resolve more complex data than simpler machines may be able to cluster. On the other hand, SVM is also used for regression problems. When working in complex sample matrices, use of SVM is often necessitated; a common example is in food contamination analyses. For instance, Bao and colleagues detected Flibanserin (a drug which can be dangerous when consumed with alcohol and is sometimes abused) in several drinking alcohol matrices [32]. The beverage matrix used substantially affected the presence of the drug's spectral fingerprint, such that the characteristic peaks were not visible in the beer or wine matrices. For the simpler hard liquor matrix, partial least squares analysis was enough to yield a calibration

curve with high prediction accuracy. Because the beer and wine spectra did not visually match the standard fingerprint of the Flibanserin, SVM was used to quantify the amount of drug in the drinks with about 92% accuracy. Similarly, Leong et al. used SVM to identify and quantify chemicals responsible for different flavor profiles in wine [33].

Random forests offer several advantages which make them useful for SERS: they are robust to outliers and have built-in functions allowing for the analysis of feature importance. This method has less complexity in tuning parameters than SVM and can be trained quickly. For example, Weng et al. compared RF and SVM in the detection of pesticides and found high and nearly equal accuracies between the two algorithms while the RF was much faster and more reliable when trained with different data sets [34]. A study which sought to differentiate the receptor-binding-domains of SARS-CoV-2 and MERS-CoV using a variety of ML methods including RF was able to achieve high accuracy and precision, as well as determine the feature importance [35]. This showed promise for differentiation of different strains of COVID-19 based on the spike protein genetic information. Achieving this level of viral differentiation through a quick and simple-to-perform method is a major step in the field of virus sensing and further demonstrates the advantages of SERS in bioanalytical sensing. One interesting use of RF in the literature was to predict Raman modes of *trans*-1,2-bis (4-pyridyl) ethylene (BPE), which resulted in good agreement with the more traditional method of predicting Raman modes through DFT modeling [1]. First, molecular dynamics were applied to find the most stable conformation. DFT was then used with the information yielded from molecular dynamics for geometric information. The 4000 conformations determined by molecular dynamics and their associated calculations were split into testing and training data for the RF. For the RF, the spatial position of the BPE with regard to the gold, the intramolecular bonds, and bond angles were used as descriptors for the Raman-active vibrational frequencies and intensities to output spectra. This was certainly not a typical use of RF (such as to create a classifier or regressor) but represents another frontier of the utility of ML in the SERS field. Clearly, random forests can be applied to a wide variety of problems, though they remain less popular in SERS than SVM to date.

Deep learning algorithms are the most complex ML algorithm type, require the most data, and can resolve otherwise inseparable input classes or inaccurate regressions in many cases. There are many versions of artificial intelligence platforms that can be exploited for SERS analysis, but two of the most common are artificial neural networks and convolutional neural networks (CNNs). For complex matrices and elusive analytes where accurate classification or quantification is of the utmost importance, neural networks can be leveraged. For example, when developing a non-invasive diagnostic for oral cancer, Xie, Yu, and colleagues used an ANN to determine the presence of oral cancer biomarkers in breath with an accuracy of 99%, significantly exceeding the accuracy of the traditional ML methods they tested [36]. This type of diagnostic is at the forefront of the SERS field and further shows the advantages of using SERS for label-free, non-invasive disease detection. Multiplexed quantification is another situation wherein ANNs may be useful. For example, Alharbi et al. found poor prediction ability for traditional PLS regression

of mixtures of nicotine and its metabolites and thus progressed to ANN development, for which they attained highly accurate quantification [37]. Similarly, a drug analysis in urine utilizing a CNN slightly outperformed traditional ML methods [38]. There are many other examples in the literature of CNNs which are beyond the scope of this chapter. Overall, deep learning algorithms can yield exquisite accuracy and will generally perform better than traditional ML methods, making them extremely useful if inherent interpretability and computational power are not issues.

Table 7.1 outlines the primary uses for several of the most commonly used machines to aid the user in their selection, alongside a sampling of the literature for (a non-exhaustive list of) examples. Figure 7.4 shows a flowchart of a suggested guide for selecting an appropriate ML technique to use for a classification problem. A metric to consider for successful classification is data clustering after dimensionality reduction, as this is the simplest and most interpretable stage. If there is adequate separation between the analyte classes, it is not suggested to proceed to a more complex machine unless improvement to the figures of merit is necessary. For regressions (Fig. 7.5), data clustering after dimensionality reduction is not a primary consideration. Instead, PCA serves to primarily simplify the data as a pre-processing step before it is fed to a supervised ML algorithm. As depicted in both the classifier and regressor flowcharts, it is important to consider whether analysis of the spectral features as variance sources is desired. It is helpful to understand the statistical importance of Raman modes to yield chemical information about the system being studied. Additionally, computational power should be considered before selecting a deep learning model, as these may require use of a supercomputer.

### *7.3.3 How Much Data Is Enough?*

A key factor in selecting a machine and subsequently using it is ensuring that there is enough experimental data to yield a robust ML model. When the number of dimensions (i.e., wavenumbers) is greater than the number of samples, SVM can be used, but overfitting is a concern. Statistical calculations may be performed to determine if there is adequate sampling (such as using the Kaiser–Meyer–Olkin test for PCA), but generally, a more complex machine calls for more data [45]. It should be noted that there is no accepted standard for an exact number of samples required for machine learning. In fact, the amount of SERS spectra varies widely among the literature examples cited in this chapter. Conventional supervised machines such as RF and SVM need hundreds to a few thousands of spectra [35, 44], whereas deep learning methods require much more data, perhaps in the tens of thousands of spectra (Zarei et al. used over 12,000 spectra [46]). Consideration should be given to the amount of time required to obtain this many spectra by a particular Raman system when determining the appropriateness of different ML algorithms. While some spectral databases exist [47, 48], caution must be used when combining spectra from different sources to use in a model since differences in experimental conditions such as laser power can affect the model predictions, leading models to train on

**Table 7.1** Common ML methods used in SERS analyses and their main functions

| Algorithm | Unsupervised or supervised? | Primary utility | Literature examples |
|---|---|---|---|
| PCA | Unsupervised | Reducing dimensionality, clustering, simple classification, easy to do (does not require hundreds of samples), easy to determine real feature/variable leading to variance | [26, 27, 33, 35, 39, 40] |
| LDA | Supervised | Reducing dimensionality, classification (accounts for input classes), often coupled with PCA | [26, 27, 41, 42] |
| SVM | Supervised | High dimensional linear-based classification and regression. Customizable through kernel functions, but only a linear kernel can show feature importance | [28–33, 35, 41, 43, 44] |
| RF | Supervised | High dimensional nonlinear classification and regression. Hyperparameters can be adjusted. Bootstrapping and bagging of samples minimize outlier impact. Built-in determination of feature importance | [1, 34, 35, 44] |
| ANN | Supervised | Best for highly complex datasets but requires a large number of spectra and high computational power. Customizable through activation functions and layers | [36, 37] |

differences between experimental conditions instead of analytes or concentrations. These effects can be reduced by including experimental conditions as features for each sample.

## *7.3.4 Understanding and Presenting the Data*

### 7.3.4.1 Figures of Merit for Classification

A confusion matrix is a helpful visualization for classification algorithms, such as the example in Fig. 7.6. The diagonal shows the number of correctly identified samples,

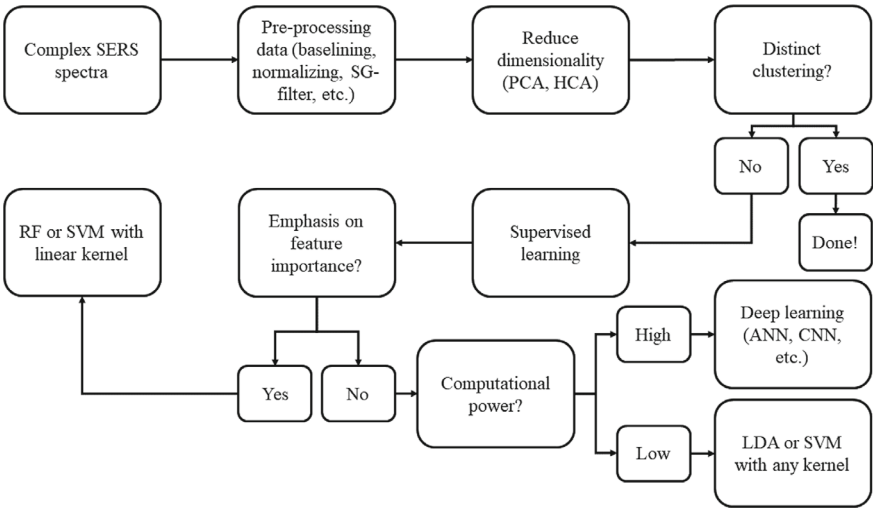



**Fig. 7.4** Flowchart outlining a suggested process for selecting an appropriate ML algorithm for classification

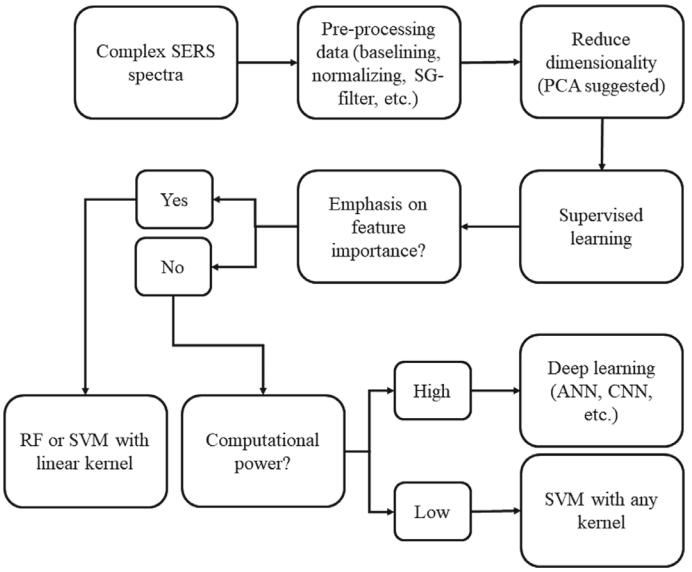



**Fig. 7.5** Flowchart outlining a suggested process for selecting an appropriate ML algorithm for regression

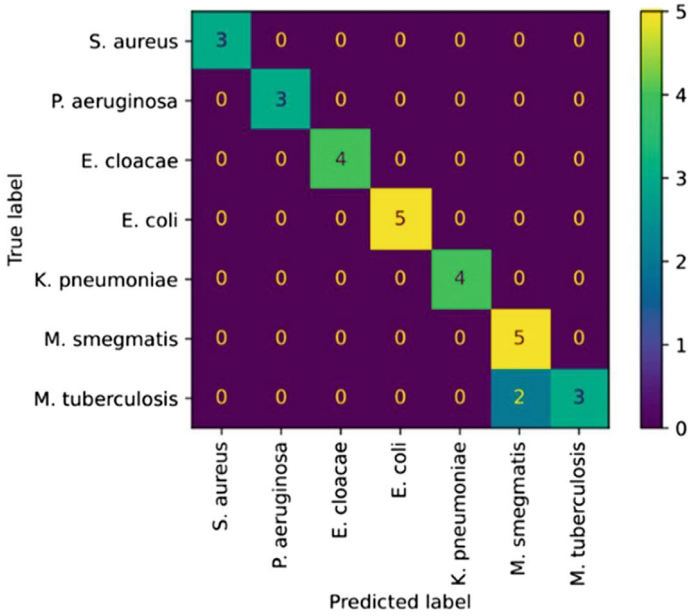



**Fig. 7.6** Confusion matrix visualizing the frequencies with which every bacteria strain studied was correctly or incorrectly classified by species. Adapted from Das et al. [49]. Copyright 2023 American Chemical Society

while those off-diagonal are misclassifications with the columns as predicted class and the rows as true class. In this example, the matrix can be read to see what bacterial strain each misclassification was and how frequently this misidentification occurred. A pattern among misclassifications may be revealed through a confusion matrix. For example, different bacteria may be mistaken for each other due to bacterial similarity, as is suggested for the *Mycobacterium smegmatis* and *Mycobacterium tuberculosis* confusion [49]. Other figures of merit for binary classifiers are accuracy, sensitivity, and specificity, where sensitivity can be understood as the percentage of true positives and specificity as the percentage of true negatives correctly identified and can be easily extrapolated from the confusion matrix. Another common representation of sensitivity and specificity is the receiver operating characteristic curve in which a perfect classifier would have a true positive rate of one and a false positive rate of zero.

#### 7.3.4.2 Figures of Merit for Quantification

Traditional calibration curves and the associated linear regression metrics are the most common way to present quantification data extracted from ML. For example, when analyzing wine flavor compounds, Ling et al. first developed a classifier for

multiplex identification of these molecules and then used SVM discriminant analysis to quantify the concentrations of the individual compounds in the mixture [33]. They also present the percent differences between the predicted and actual concentrations as a metric. In other quantification methods in which the concentration of the analyte is determined via classification into numerical categories (such as concentration ranges), the same metrics and data representations as for other qualitative classifiers are used [26].

### *7.3.5 Interpreting ML Results Back into Real Variables*

Depending on the ML method used, interpretability varies. Largely, unsupervised methods are easier to connect back to real features or variables. Data points cluster because of real spectral variance rather than looking for similarities within a class like LDA. For example, Vikesland and Zhou were able to determine which Raman wavenumbers were contributing to variance between classes by considering the loading scores (i.e., weights) when analyzing *Pseudomonas syringae* biofilms infected with varying concentrations of bacteriophage [26]. Interpretability is generally sacrificed as complexity of the ML method increases, leaving most supervised ML techniques difficult to relate back to the spectra. Nonlinear methods especially lack interpretability, including SVM with nonlinear kernels, with neural networks being the most difficult to interpret. Thus, finding the balance between the desired figures of merit and the interpretability affects which ML methods are most appropriate for analyzing the data.

## 7.4 ML in SERS Detection of Bacteria

### *7.4.1 Background on Bacteria and SERS Analysis with ML*

As an exemplar case of implementing machine learning (ML) in SERS technologies, the integration of machine learning with bacterial detection using SERS will be explored. Research has been dedicated to the development of SERS sensors that meet the demand for rapid detection and classification of pathogenic bacterial species in clinical and food safety environments for effective outbreak controls [47, 48, 50]. Machine learning presents solutions for challenges frequently encountered in conventional SERS sensing schemes, including the time-intensive processing of extensive datasets and the precise classification of multiple analytes.

Biological analytes like bacterial cells are inherently complex due to their diverse array of molecular components such as lipids, nucleic acids, carbohydrates, and proteins. Bacteria can be classified through defining features within their cell wall structure, mainly separated into two groups: Gram-positive or gram-negative

bacteria. Gram-positive bacteria are characterized by a distinctive, thick peptidoglycan layer. On the other hand, gram-negative bacteria have a lipid membrane with lipopolysaccharides in the outermost part of the cell. These differences in bacterial cell wall chemical structures are evident in their vibrational bands. The combination of Raman vibrational bands stemming from all these biomolecules produces a molecular fingerprint unique to each bacterial species.

Bacterial cell structures have similarities in their cell wall components, especially when strains belong to the same gram type. These commonalities in chemical composition within the cell wall pose a challenge in the context of SERS bacterial detection due to similar Raman bands. The ability to accurately classify spectra with only slight variations is crucial for the successful distinction of various bacterial analytes. This is exactly where the capabilities of machine learning are most useful. By integrating machine learning algorithms into SERS spectral analysis, an additional layer of insight is introduced to effectively decipher and differentiate bacterial SERS spectra. Biosensors can benefit from ML by facilitating the classification of vast datasets within complex sample matrices and the interpretation of results that exhibit significant spectral overlap [51].

To enhance the analysis of complicated SERS datasets and gain deeper insights into the underlying data correlations, the integration of machine learning techniques has been strategically implemented within this research field, with more advanced and computationally intensive techniques like ANNs becoming more common as access to more powerful computers improves. The most common machine learning techniques that have been combined with SERS bacterial detection platforms are PCA, HCA, and SVM [52]. Additionally, the use of machine learning for detection of bacteria with SERS is fairly new, with most publications coming within the past five years (Fig. 7.7). This application of ML has been growing rapidly as machine learning algorithms improve, becoming more widely accessible, and will have lasting impacts on the field by enabling rapid analysis of highly complex spectra.

### *7.4.2 Example 1: PCA and HCA*

In a study by Wei et al., SERS detection of three different food-borne pathogens was performed with silver colloidal nanoparticles synthesized using microwave technology [53]. The bacteria *Escherichia coli* O157:H7, *Staphylococcus aureus*, and *Salmonella enterica*, in the concentration range of $10^7$–$10^8$ colony forming units (CFU) per mL, were characterized with a combination of PCA and HCA. This combination facilitated the precise differentiation of these pathogens despite similar SERS spectra. In this work, the SERS spectral data were preprocessed by baseline correction, smoothing, and second-derivative transformation to eliminate background noise and separate overlapping bands. PCA was then applied to the second-derivative transformed data which showed the three species clustered in different regions of the plot. They constructed HCA dendrograms via the Ward-linkage algorithm and squared distances to quantify dissimilarities and further categorize the samples. The

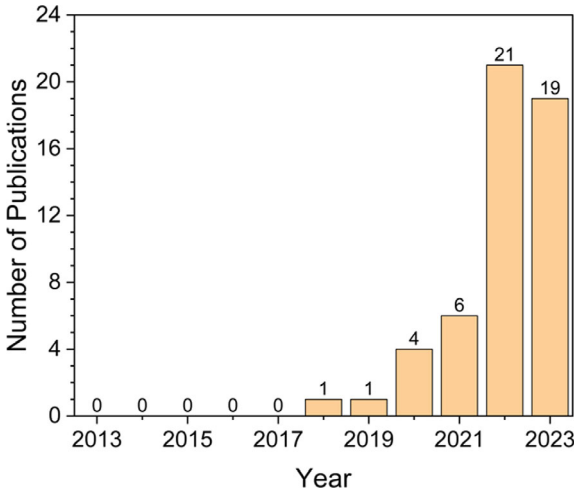



**Fig. 7.7** Number of SERS bacteria sensing articles involving machine learning published each year from 2013 to December 5, 2023. *Source* Scopus search for articles with "bacteria" and "SERS" in the title, abstract, or keywords, and "machine learning" within the document

resulting dendrogram showed that the three pathogens could be clearly distinguished from one another. Importantly, these dendrogram statistics aligned with the obtained PCA outcomes, offering further corroboration. Additionally, this study was able to demonstrate a high degree of reproducibility in their silver nanoparticles, which is critical when using ML analysis because any changes to variables other than the analyte and its concentration can lead to the algorithm learning to distinguish differences in those confounding variables instead of in the analyte. If there are issues with the reproducibility of substrates, randomization of the substrates across analyte type and concentration is critical to preventing the algorithm from learning based on the substrates. For example, this would mean that with three substrate batches and three analyte concentrations, each substrate batch should be split across the three analyte concentrations. Combining PCA and HCA in this study resulted in the successful analysis of SERS spectra from bacterial species with similar vibrational spectra, as they were able to identify patterns that are not obvious to the naked eye.

### *7.4.3 Example 2: RamanNet CNN*

The development of neural networks has led to significant advances in the classification of bacterial SERS spectra. The progression in methodologies extends further to neural networks such as RamanNet [54]. This is a convolutional neural network developed with the goal of improving the classification accuracy of CNNs tailored to bacterial Raman spectra. While previous CNNs used on Raman spectra, such as ResNet, were intended for multidimensional data like images, RamanNet is designed to work more efficiently for one-dimensional data like spectra. This means that a much lower number of convolutional layers and filters is used, which greatly reduces

training time and still leads to accurate spectral classification. Additionally, due to this simplification, RamanNet can be trained using only central processing units (CPU) instead of requiring graphics processing units (GPU) which allows for a wider range of computers to perform the analysis.

RamanNet has 296.9 times fewer parameters than the ResNet CNN, which is used to classify Raman spectra and was used for comparison in the study. The authors stated that one filter (which applies different weights to each input feature) per convolutional layer and two or three convolutional layers are enough for the accurate identification of bacterial Raman spectra, since it yields similar classification accuracies to other CNNs with far more layers and filters. The model was formulated for the identification of bacteria based on single-cell Raman spectroscopy and was trained and validated on the Bacteria-ID dataset [47], which contains a total of 66,000 spectra from 30 different bacterial isolates, and separately on the PKU-bacterial dataset [48], which contains 7200 spectra from 15 bacteria species. RamanNet achieved an average 96.04% accuracy identifying 15 different species of bacteria in the PKU-bacterial dataset, more accurate than the 94.53% accuracy of ResNet. Though this accuracy improvement is relatively small, the simplified model has the added advantage of being far less computationally intensive [54]. Additionally, this work shows how machine learning, particularly neural network models requiring thousands of datapoints, is able to leverage extensive SERS datasets gathered from literature. With the capabilities gained from machine learning, it is now much easier to analyze such large datasets and gain new insights not possible with smaller datasets and other analysis methods intended to make the most of a small amount of data. Further, spectra from literature sources using different experimental conditions, such as laser wavelength and power or substrate type, can be used in the same model if the experimental conditions are included as features in the model along with the spectra.

### *7.4.4 Example 3: SVM*

It is challenging to discriminate among diverse bacterial strains when doing label-free bacterial SERS due to the spectral similarities of the molecular components of bacterial cell walls. Support vector machines have been adapted to classify strains within large bacterial spectral datasets. Rahman et al. demonstrated the effectiveness of SVMs for classifying 19 bacterial strains using label-free bacterial SERS data [28]. In this work (Fig. 7.8), a total of 400 spectra per bacterial species were collected and preprocessed to develop the SVM classifier. Each spectrum collected was preprocessed by cosmic ray removal, Savitzky–Golay smoothing, and baseline correction. Different SVM kernel functions were compared to find that the medium Gaussian kernel achieved the highest overall accuracy. The model performance was validated with a tenfold cross-validation where 6667 out of the 7000 total spectra were correctly predicted. The overall accuracy of the model was reported to be 87.7% with a high specificity of $\geq$ 98.4% for all species.

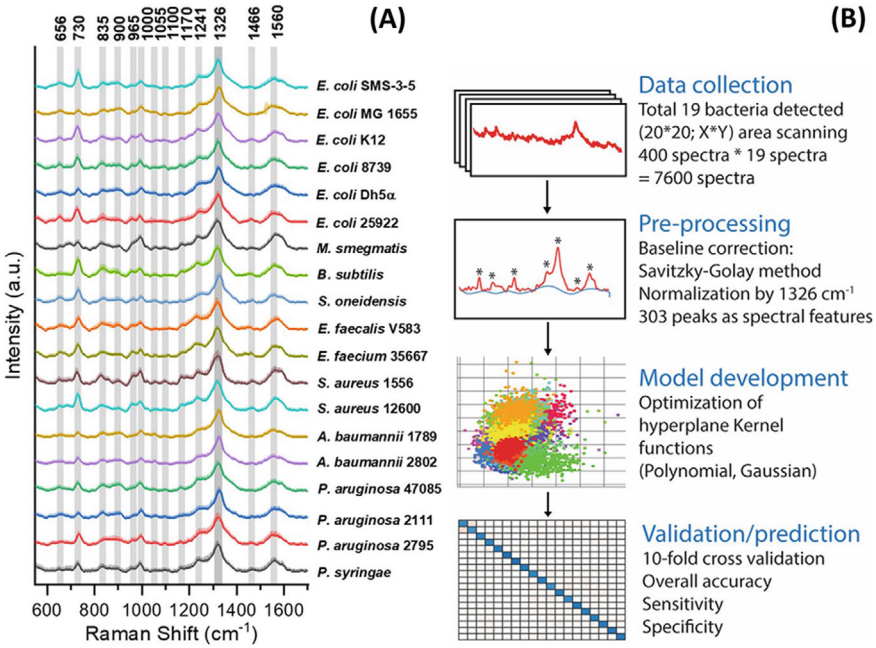



**Fig. 7.8** **a** SERS spectra for 19 different bacterial strains. **b** Schematic describing the major steps involved in creating a SVM model. Reprinted with permission from Rahman et al. [28]. Copyright 2022 American Chemical Society

### *7.4.5 Complex Matrices and Biomarker Detection*

In biosensing, challenges arise when detecting multiple pathogens within complex matrices like food, blood, or wastewater. A promising approach to overcome these hurdles emerges by combining SERS and machine learning, which collectively foster the distinction of pathogens in complex mixtures. For instance, SERS detection and differentiation of food-borne pathogenic bacteria in mung bean sprouts has been made possible by harnessing PCA to overcome challenges of signal interference from the surrounding matrix [50]. Moreover, they were able to precisely distinguish different notorious food-borne pathogens and even discriminate different serotypes of the same species. Pathogens found responsible for previous sprout outbreaks were analyzed. These bacteria include *Salmonella enterica serotype Anatum*, *Salmonella enterica serotype Cubana*, *Salmonella enterica serotype Stanley*, *Salmonella enteritidis*, *E. coli* O157:H7, and *Staphylococcus epidermidis*. Bacteria were inoculated on mung bean sprout samples followed by a two-step filtration process with final bacteria concentrations of $10^2$ CFU/mL. PCA results showed a successful discrimination through principal components forming different clusters based on bacterial

species. While the four *Salmonella* species were clustered together, both *E. coli* O157:H7 and *S. epidermidis* formed individual and separated clusters. A separate PCA plot of the four Salmonella serotypes clearly demonstrates the components separating into four different clusters.

Efforts to develop faster bacterial detection methods are increasing as the need to prevent the spread of bacterial infections becomes more pressing. Separation-free bacterial SERS, a method that removes the need for prior separation from the surrounding matrix, offers a promising approach for achieving rapid bacterial detection. Rho et al. proposed a novel deep learning model named dual-branch wide-kernel neural network (DualWKNet) to facilitate the detection of bacteria in complex media without the need for bacteria separation [55]. This work addresses challenges encountered in SERS signal interference from complex matrices by implementing the proposed model capable of extracting and learning patterns in spectral data. The DualWKNet model is built with two separate network branches, each branch having three residual blocks and an average pooling layer followed by a self-attention block. The residual blocks are convolutional layers used as trainable filters to extract spectral patterns, with large kernel sizes (> 15) to prevent overfitting, and the task of the pooling layer is to reduce spectral features and learn parameters, while the self-attention block extracts crucial information by finding correlations between spectral features. This allows for the calculation of the probabilities of a spectrum belonging to each class, where the class with the highest probability is the one predicted for the classification. To evaluate the proposed deep learning model, SERS detection of *E. coli* and *S. epidermidis* in complex media including artificial urine, ground beef solution, milk, and nutrient broth was conducted. For each sample analyzed, 500 SERS measurements were acquired then processed through baseline correction by using iterative polynomial fitting. The model's classification accuracy of the two bacterial targets in the five media was tested by fivefold cross-validation. Classification accuracy in identifying the two bacterial targets was 98.0% in water, 96.6% in artificial urine, 88.3% in ground beef, 86.4% in milk and 84.3% in nutrient broth. These accuracies could likely have been improved by using a greater number of training spectra for each media type. Additional assessment of classification accuracy was performed by constructing confusion matrices to examine accuracy represented in true positive rates. The results showed more than 90% true positives for bacterial discrimination in water and artificial urine. For the other three media, there was an 83% true positive rate. Hence, this work successfully identified both *E. coli* and *S. epidermidis* in multiple media, circumventing the need of bacteria separation for detection. This achievement was primarily attributed to the employment of the deep learning model. This approach offers a solution to signal interference in complex mixtures for bacteria detection.

Alternatively, SERS sensing can be achieved by detecting bacterial biomarkers, such as genomic DNA. A study by Shvalya et al. showcases the potential use of this approach. They successfully extracted DNA fragments from four distinct bacterial species and characterized their vibrational fingerprints by SERS [56]. Following this, the spectral data, including spectra from 10 samples per bacterial species, underwent

a PCA analysis for analyte classification. It is often the case that the first two principal components (PC1 vs. PC2) are enough to distinguish and categorize bacterial analytes based on their SERS spectra. However, in this case, PC1 and PC2 both mainly served to distinguish *S. aureus* from the other three bacteria, and PC3 was needed to distinguish the other three bacteria from each other. So, PC2 and PC3 were chosen to perform classification since PC2 provided more separation of *S. aureus* than PC1. Additionally, the principal components themselves were plotted to see which wavenumbers had a larger effect on each PC. This revealed the spectral features contributing to each PC, which is important to interpreting how the classification is being performed and can help ensure that the algorithm is learning from actual spectral differences between analytes instead of learning based on differences in sample matrices or other confounding factors. For example, PC1 scores are raised by the presence of both guanine and thymine ring-breathing vibrations in a spectrum, and PC2 scores are raised by more intense thymine ring-breathing vibrations without regard to the presence of guanine. If these PCs did not correspond to peaks expected in the analytes, then the trustworthiness of the PC analysis would be suspect. Ultimately, this use of SERS and PCA facilitated successful discrimination of bacteria based on their base-pair molecular vibrations and achieved this discrimination with lower sample amounts, fewer preparation steps, lower cost, and lower analysis time than traditional DNA sequencing.

### *7.4.6 Conclusions on ML for SERS Detection of Bacteria*

Integrating machine learning into SERS technologies offers a promising solution to the complications encountered in bacterial detection. SERS and ML synergistically improve the rapid detection of bacteria within complex matrices. By taking advantage of powerful machine learning algorithms, researchers in the field of SERS biosensing are developing a deeper understanding of complex datasets related to bacterial detection. This development is aiding SERS sensors in meeting demands in clinical and food safety applications, where rapid identification and classification of bacterial pathogens is critical for outbreak control. The integration of machine learning methods with SERS on-site detection technologies holds significant potential for enhancing real-time detection capabilities. The FirstDefender RM handheld Raman spectrometer has been successfully employed to detect *E. coli* O157:H7 in mung bean sprouts, with the entire detection process, including sample preparation, being completed within less than four hours [55]. PCA analysis in this study yielded clear classification of different bacterial concentrations and control (matrix) measurements. The field of SERS detection of bacteria is an example where the implementation of machine learning techniques such as PCA, HCA, and CNN results in remarkable progress toward achieving accurate discrimination of analytes, demonstrating the potential combination of SERS with machine learning algorithms as an innovative approach to addressing challenges in the field of biosensing.

**Acknowledgments** CEF acknowledges an NSF graduate research fellowship (2237827). CEF, VEF, and CLH acknowledge support from the International Institute for Biosensing. CLW acknowledges support from an NSF graduate research fellowship (1839286). MMA acknowledges support from a GEM fellowship sponsored by NASA.

## References

1. W. Hu, S. Ye, Y. Zhang, T. Li, G. Zhang, Y. Luo, S. Mukamel, and J. Jiang, Machine Learning Protocol for Surface-Enhanced Raman Spectroscopy. J. Phys. Chem. Lett. **10**, 6026 (2019).
2. T. Komatsuzaki, On-the-fly Raman microscopy guaranteeing the accuracy of diagnosis by reinforcement learning. In *High-Speed Biomed. Imaging Spectrosc. VIII*, edited by K. Goda and K. K. Tsia (SPIE, 2023), p. 5.
3. H. Dies, J. Raveendran, C. Escobedo, and A. Docoslis, Rapid identification and quantification of illicit drugs on nanodendritic surface-enhanced Raman scattering substrates. Sensors Actuators B Chem. **257**, 382 (2018).
4. G. Sheehy, F. Picot, F. Dallaire, K. Ember, T. Nguyen, K. Petrecca, D. Trudel, and F. Leblond, Open-sourced Raman spectroscopy data processing package implementing a baseline removal algorithm validated from multiple datasets acquired in human tissue and biofluids. J. Biomed. Opt. **28** (2023).
5. V. I. Korepanov, Asymmetric least-squares baseline algorithm with peak screening for automatic processing of the Raman spectra. J. Raman Spectrosc. **51**, 2061 (2020).
6. F. Pedregosa, G. Varoquaux, A. Gramfort, V. Michel, B. Thiron, O. Grisel, M. Blondel, P. Prettenhofer, R. Weiss, V. Dubourg, J. Vanderplas, A. Passos, D. Cournapeau, M. Brucher, M. Perrot, and E. Duchesnay, Scikit-learn: Machine Learning in Python. J. Mach. Learn. Res. **12**, 2825 (2011).
7. H. Shin, H. Jeong, J. Park, S. Hong, and Y. Choi, Correlation between Cancerous Exosomes and Protein Markers Based on Surface-Enhanced Raman Spectroscopy (SERS) and Principal Component Analysis (PCA). ACS Sensors **3**, 2637 (2018).
8. X. Wu, Z. Liu, Y. Liu, M. Qiu, and D. Xu, Construct high performance SERS sensing platform assisted by machine learning. Alexandria Eng. J. **81**, 284 (2023).
9. E. Umargono, J. E. Suseno, and S. Vincensius Gunawan, K-Means Clustering Optimization Using the Elbow Method and Early Centroid Determination Based on Mean and Median Formula. In *Proc. 2nd Int. Semin. Sci. Technol. (ISSTEC 2019)* (Atlantis Press, Paris, France, 2020).
10. P. Contreras and F. Murtagh, Hierarchical Clustering. In *Handb. Clust. Anal.*, 1st ed. (Chapman and Hall, New York, NY, 2015), pp. 103–120.
11. E. A. Slipchenko, I. A. Boginskaya, R. R. Safiullin, I. A. Ryzhikov, M. V. Sedova, K. N. Afanasev, N. L. Nechaeva, I. N. Kurochkin, A. M. Merzlikin, and A. N. Lagarkov, SERS Sensor for Human Glycated Albumin Direct Assay Based on Machine Learning Methods. Chemosensors **10**, 520 (2022).
12. S. Peng, D. Lu, B. Zhang, R. You, J. Chen, H. Xu, and Y. Lu, Correction to: Machine learning–assisted internal standard calibration label-free SERS strategy for colon cancer detection. Anal. Bioanal. Chem. **415**, 2865 (2023).
13. N. Banaei, J. Moshfegh, A. Mohseni-Kabir, J. M. Houghton, Y. Sun, and B. Kim, Machine learning algorithms enhance the specificity of cancer biomarker detection using SERS-based immunoassays in microfluidic chips. RSC Adv. **9**, 1859 (2019).
14. R. Dong, S. Weng, L. Yang, and J. Liu, Detection and Direct Readout of Drugs in Human Urine Using Dynamic Surface-Enhanced Raman Spectroscopy and Support Vector Machines. Anal. Chem. **87**, 2937 (2015).

15. A. Tan, Y. Zhao, K. Sivashanmugan, K. Squire, and A. X. Wang, Quantitative TLC-SERS detection of histamine in seafood with support vector machine analysis. Food Control **103**, 111 (2019).
16. W. Nam, H. Chen, X. Ren, M. Agah, I. Kim, and W. Zhou, Nanolaminate Plasmonic Substrates for High-Throughput Living Cell SERS Measurements and Artificial Neural Network Classification of Cellular Drug Responses. ACS Appl. Nano Mater. **5**, 10358 (2022).
17. Q. Zhang, H. Yu, M. Barbiero, B. Wang, and M. Gu, Artificial neural networks enabled by nanophotonics. Light Sci. Appl. **8**, 42 (2019).
18. S. Sharma, S. Sharma, and A. Athaiya, Activation Functions in Neural Networks. Int. J. Eng. Appl. Sci. Technol. **4**, 310 (2020).
19. L. Shen, Y. Du, N. Wei, Q. Li, S. Li, T. Sun, S. Xu, H. Wang, X. Man, and B. Han, SERS studies on normal epithelial and cancer cells derived from clinical breast cancer specimens. Spectrochim. Acta Part A Mol. Biomol. Spectrosc. **237**, 118364 (2020).
20. H. Li, S. Liu, M. M. Hassan, S. Ali, Q. Ouyang, Q. Chen, X. Wu, and Z. Xu, Rapid quantitative analysis of $Hg^{2+}$ residue in dairy products using SERS coupled with ACO-BP-AdaBoost algorithm. Spectrochim. Acta Part A Mol. Biomol. Spectrosc. **223**, 117281 (2019).
21. C. Goutte and E. Gaussier, A Probabilistic Interpretation of Precision, Recall and F-Score, with Implication for Evaluation. In (2005), pp. 345–359.
22. X. Lin, X. Jia, J. Y. Lin, P. H. Wu, Y. Weng, and S. Feng, A comparative study based on serum SERS spectra in and on the coffee ring for high precision breast cancer detection. J. Raman Spectrosc. **53**, 1371 (2022).
23. D. A. Guzonas, D. E. Irish, and G. F. Atkinson, Surface-enhanced Raman scattering of the protonated forms of 1,4-diazabicyclo[2.2.2]octane at a silver electrode. Langmuir **5**, 787 (1989).
24. Ondalys, Chemometrics and Machine Learning Methods (2019).
25. V. M. Szlag, S. Jung, R. S. Rodriguez, M. Bourgeois, S. Bryson, G. C. Schatz, T. M. Reineke, and C. L. Haynes, Isothermal Titration Calorimetry for the Screening of Aflatoxin B1 Surface-Enhanced Raman Scattering Sensor Affinity Agents. Anal. Chem. **90**, 13409 (2018).
26. A. Garg, W. Nam, W. Wang, P. Vikesland, and W. Zhou, In Situ Spatiotemporal SERS Measurements and Multivariate Analysis of Virally Infected Bacterial Biofilms Using Nanolaminated Plasmonic Crystals. ACS Sensors **8**, 1132 (2023).
27. X. Diao, X. Li, S. Hou, H. Li, G. Qi, and Y. Jin, Machine Learning-Based Label-Free SERS Profiling of Exosomes for Accurate Fuzzy Diagnosis of Cancer and Dynamic Monitoring of Drug Therapeutic Processes. Anal. Chem. **95**, 7552 (2023).
28. A. Rahman, S. Kang, W. Wang, Q. Huang, I. Kim, and P. J. Vikesland, Lectin-Modified Bacterial Cellulose Nanocrystals Decorated with Au Nanoparticles for Selective Detection of Bacteria Using Surface-Enhanced Raman Scattering Coupled with Machine Learning. ACS Appl. Nano Mater. **5**, 259 (2022).
29. F. Uysal Ciloglu, A. M. Saridag, I. H. Kilic, M. Tokmakci, M. Kahraman, and O. Aydin, Identification of methicillin-resistant *Staphylococcus aureus* bacteria using surface-enhanced Raman spectroscopy and machine learning techniques. Analyst **145**, 7559 (2020).
30. A. Walter, A. März, W. Schumacher, P. Rösch, and J. Popp, Towards a fast, high specific and reliable discrimination of bacteria on strain level by means of SERS in a microfluidic device. Lab Chip **11**, 1013 (2011).
31. J. Choi, S. J. H. Martin, R. A. Tripp, S. M. Tompkins, and R. A. Dluhy, Detection of neuraminidase stalk motifs associated with enhanced N1 subtype influenza A virulence via Raman spectroscopy. Analyst **140**, 7748 (2015).
32. Q. Bao, H. Zhao, S. Han, C. Zhang, and W. Hasi, Surface-enhanced Raman spectroscopy for rapid identification and quantification of Flibanserin in different kinds of wine. Anal. Methods **12**, 3025 (2020).
33. Y. X. Leong, Y. H. Lee, C. S. L. Koh, G. C. Phan-Quang, X. Han, I. Y. Phang, and X. Y. Ling, Surface-Enhanced Raman Scattering (SERS) Taster: A Machine-Learning-Driven Multireceptor Platform for Multiplex Profiling of Wine Flavors. Nano Lett. **21**, 2642 (2021).
34. S. Weng, M. Li, C. Chen, X. Gao, S. Zheng, and X. Zeng, Fast and accurate determination of organophosphate pesticides using surface-enhanced Raman scattering and chemometrics. Anal. Methods **7**, 2563 (2015).

35. K. Zhang, Z. Wang, H. Liu, N. Perea-López, J. C. Ranasinghe, G. Bepete, A. M. Minns, R. M. Rossi, S. E. Lindner, S. X. Huang, M. Terrones, and S. Huang, Understanding the Excitation Wavelength Dependence and Thermal Stability of the SARS-CoV-2 Receptor-Binding Domain Using Surface-Enhanced Raman Scattering and Machine Learning. ACS Photonics **9**, 2963 (2022).
36. X. Xie, W. Yu, Z. Chen, L. Wang, J. Yang, S. Liu, L. Li, Y. Li, and Y. Huang, Early-stage oral cancer diagnosis by artificial intelligence-based SERS using Ag NWs@ZIF core–shell nanochains. Nanoscale **15**, 13466 (2023).
37. O. Alharbi, Y. Xu, and R. Goodacre, Simultaneous multiplexed quantification of nicotine and its metabolites using surface enhanced Raman scattering. Analyst **139**, 4820 (2014).
38. S. Weng, H. Yuan, X. Zhang, P. Li, L. Zheng, J. Zhao, and L. Huang, Deep learning networks for the recognition and quantitation of surface-enhanced Raman spectroscopy. Analyst **145**, 4827 (2020).
39. S. Lee, J. Oh, K. Lee, M. Cho, B. Paulson, and J. K. Kim, Diagnosis of Ischemic Renal Failure Using Surface-Enhanced Raman Spectroscopy and a Machine Learning Algorithm. Anal. Chem. **94**, 17477 (2022).
40. K. Gao, H. Zhu, B. Charron, T. Mochizuki, C. Dong, H. Ding, Y. Cui, M. Lu, W. Peng, S. Zhu, L. Hong, and J.-F. Masson, Combining Dense Au Nanoparticle Layers and 2D Surface-Enhanced Raman Scattering Arrays for the Identification of Mutant Cyanobacteria Using Machine Learning. J. Phys. Chem. C **126**, 9446 (2022).
41. Z. Liu, T. Li, Z. Wang, J. Liu, S. Huang, B. H. Min, J. Y. An, K. M. Kim, S. Kim, Y. Chen, H. Liu, Y. Kim, D. T. W. Wong, T. J. Huang, and Y.-H. Xie, Gold Nanopyramid Arrays for Non-Invasive Surface-Enhanced Raman Spectroscopy-Based Gastric Cancer Detection via sEVs. ACS Appl. Nano Mater. **5**, 12506 (2022).
42. Y. Xie, Y. Wen, X. Su, C. Zheng, and M. Li, Label-Free Plasmon-Enhanced Spectroscopic HER2 Detection for Dynamic Therapeutic Surveillance of Breast Cancer. Anal. Chem. (2022).
43. S. Kang, I. Kim, and P. J. Vikesland, Discriminatory Detection of ssDNA by Surface-Enhanced Raman Spectroscopy (SERS) and Tree-Based Support Vector Machine (Tr-SVM). Anal. Chem. **93**, 9319 (2021).
44. Y. Yang, H. Li, L. Jones, J. Murray, J. Haverstick, H. K. Naikare, Y.-Y. C. Mosley, R. A. Tripp, B. Ai, and Y. Zhao, Rapid Detection of SARS-CoV-2 RNA in Human Nasopharyngeal Specimens Using Surface-Enhanced Raman Spectroscopy and Deep Learning Algorithms. ACS Sensors **8**, 297 (2023).
45. Principal Components Analysis (PCA) Using SPSS Statistics. Laerd Stat. (n.d.).
46. M. Zarei, N. V. Solomatova, H. Aghaei, A. Rothwell, J. Wiens, L. Melo, T. G. Good, S. Shokatian, and E. Grant, Machine Learning Analysis of Raman Spectra to Quantify the Organic Constituents in Complex Organic–Mineral Mixtures. Anal. Chem. **95**, 15908 (2023).
47. C.-S. Ho, N. Jean, C. A. Hogan, L. Blackmon, S. S. Jeffrey, M. Holodniy, N. Banaei, A. A. E. Saleh, S. Ermon, and J. Dionne, Rapid identification of pathogenic bacteria using Raman spectroscopy and deep learning. Nat. Commun. **10**, 4927 (2019).
48. B. Zhou, L. Sun, T. Fang, H. Li, R. Zhang, and A. Ye, Rapid and accurate identification of pathogenic bacteria at the single-cell level using laser tweezers Raman spectroscopy and deep learning. J. Biophotonics **15** (2022).
49. S. Das, K. Saxena, J.-C. Tinguely, A. Pal, N. L. Wickramasinghe, A. Khezri, V. Dubey, A. Ahmad, V. Perumal, R. Ahmad, D. N. Wadduwage, B. S. Ahluwalia, and D. S. Mehta, SERS Nanowire Chip and Machine Learning-Enabled Classification of Wild-Type and Antibiotic-Resistant Bacteria at Species and Strain Levels. ACS Appl. Mater. Interfaces **15**, 24047 (2023).
50. X. Wu, C. Xu, R. A. Tripp, Y. Huang, and Y. Zhao, Detection and differentiation of foodborne pathogenic bacteria in mung bean sprouts using field deployable label-free SERS devices. Analyst **138**, 3005 (2013).
51. F. Cui, Y. Yue, Y. Zhang, Z. Zhang, and H. S. Zhou, Advancing Biosensors with Machine Learning. ACS Sensors **5**, 3346 (2020).
52. X. Wu, Y.-W. Huang, B. Park, R. A. Tripp, and Y. Zhao, Differentiation and classification of bacteria using vancomycin functionalized silver nanorods array based surface-enhanced Raman spectroscopy and chemometric analysis. Talanta **139**, 96 (2015).

53. C. Wei, M. Li, and X. Zhao, Surface-Enhanced Raman Scattering (SERS) With Silver Nano Substrates Synthesized by Microwave for Rapid Detection of Foodborne Pathogens. Front. Microbiol. **9** (2018).
54. B. Zhou, Y.-K. Tong, R. Zhang, and A. Ye, RamanNet: a lightweight convolutional neural network for bacterial identification based on Raman spectra. RSC Adv. **12**, 26463 (2022).
55. E. Rho, M. Kim, S. H. Cho, B. Choi, H. Park, H. Jang, Y. S. Jung, and S. Jo, Separation-free bacterial identification in arbitrary media via deep neural network-based SERS analysis. Biosens. Bioelectron. **202**, 113991 (2022).
56. V. Shvalya, A. Vasudevan, M. Modic, M. Abutoama, C. Skubic, N. Nadižar, J. Zavašnik, D. Vengust, A. Zidanšek, I. Abdulhalim, D. Rozman, and U. Cvelbar, Bacterial DNA Recognition by SERS Active Plasma-Coupled Nanogold. Nano Lett. **22**, 9757 (2022).

# Part II
# Applications of SERS to Material Sciences and Analytical Chemistry

# Chapter 8
# Wearable Surface-Enhanced Raman Spectroscopy




**Yasutaka Kitahama and Keisuke Goda**

**Abstract** Wearable sensors have been developed to facilitate in situ chemical analysis of the wearer's biofluids in a non-invasive manner. However, traditional wearable chemical sensors exhibit sensitivity exclusively to one chemical type within an analyte at a time. In contrast, wearable chemical sensors employing surface-enhanced Raman spectroscopy (SERS) provide a sophisticated means for the highly sensitive simultaneous measurement of multiple biomolecules in biofluids. The recent implementation of a highly scalable wearable SERS sensor was based on noble metal-coated mesh, specifically biocompatible polyvinyl alcohol (PVA) nanomesh. The usability of noble metal/PVA nanomesh was verified in terms of sensitivity, flexibility, stretchability, durability, reproducibility, uniformity, and wearability. Finally, the noble metal/PVA nanomesh, which is a sampling-free substrate, demonstrated its versatility and practicality in food safety testing and health monitoring.

**Keywords** Flexible sensor · In situ detection · Multiplexed detection · Electrospinning · Sampling-free substrate · Place and Play SERS · Food safety testing · Health monitoring

Y. Kitahama · K. Goda (✉)
Department of Chemistry, The University of Tokyo, Tokyo 113-0033, Japan
e-mail: goda@chem.s.u-tokyo.ac.jp

LucasLand, Co. Ltd., Tokyo 113-0023, Japan

K. Goda
Institute for Quantum Life Science, National Institute for Quantum and Radiological Science and Technology, Chiba 263-8555, Japan

Institute of Technological Sciences, Wuhan University, Hubei 430072, China

Department of Bioengineering, University of California, Los Angeles, CA 90095, USA

© The Author(s), under exclusive license to Springer Nature Singapore Pte Ltd. 2024

M. Procházka et al. (eds.), *Surface- and Tip-Enhanced Raman Scattering Spectroscopy*,
https://doi.org/10.1007/978-981-97-5818-0_8

## 8.1 Wearable Sensors

Over the past two decades, wearable sensor technology has expanded, developing flexible, stretchable sensors that attach to the skin and provide detailed information about the user's environment and health [1]. Traditional wearable sensors track the user's activities and vital signs, monitoring metrics such as steps taken, respiration rate, heart rate, blood pressure, and blood oxygen saturation [1]. For example, smartwatches have been used to collect data on physical metrics such as steps taken, heart rate, blood pressure, and sleep duration, serving as tools for health monitoring. Athletes also use global positioning system (GPS) tracking vests to record metrics such as distance, speed, acceleration, deceleration, and changes in direction to facilitate game analysis and injury prevention [2]. Despite recent advances, measuring chemical information from biomolecules in biofluids such as sweat, tears, urine, and bacteria has proven elusive.

Wearable chemical sensors have been developed to perform in situ chemical sensing of biofluids non-invasively [3–7]. Of particular note are pulse oximeters, which are among the established methods for non-invasive collecting chemical data. These have been extensively used during the COVID-19 pandemic for spectroscopically evaluating the absorption of oxygen-bound hemoglobin in the near-infrared range to measure oxygen saturation in arterial blood [3]. Recent developments have made it possible for wearable chemical sensors to perform on-site detection of various biofluids, such as sweat, saliva, tears, and urine, in a non-invasive manner [4–7]. Multiplexed chemical analysis of biomarkers in these biofluids plays a critical role in accurately and comprehensively understanding wearers' complex physiological and pathological conditions [7]. Unfortunately, conventional wearable chemical sensors detect only one chemical type within an analyte at a time, requiring customization for the target analyte due to their limited, primarily electronic sensing mechanism [4–7]. As a result, these sensors cannot simultaneously detect multiple chemicals in a single measurement. Alternatively, designs enabling the measurement of multiple chemical species are often larger, more expensive to fabricate, require more synthetic steps, and require prior knowledge of the target analyte [4–7].

## 8.2 Wearable SERS Sensors

### *8.2.1 Surface-Enhanced Raman Spectroscopy (SERS)*

Surface-enhanced Raman spectroscopy (SERS) is a spectroscopic technique that can simultaneously detect multiple chemical species [8, 9]. This phenomenon relies on an extremely high enhancement of the Raman peaks of molecules adsorbed on the substrate via localized surface plasmon resonance [8, 9] or the resonance Raman effect of the charge transfer complex [8–11], enabling highly sensitive and label-free detection. The sharp peaks resulting from the vibrational modes of individual

molecules are measured without overlap, allowing the simultaneous identification of various target molecules. In addition, SERS is insensitive to water molecules, which make up most living organisms, due to the Raman spectroscopic nature of SERS. The insensitivity to water provides advantages for applications in biological systems, particularly in the detection of trace amounts of biomolecules in biofluids. Wearable chemical sensors using SERS technology provide a sophisticated method for highly sensitive simultaneous measurement of different biomolecules in biofluids [12–15].

### *8.2.2 Various Types of Wearable SERS Sensors*

For wearable SERS sensors, plasmonic (gold and silver) nanostructures are integrated with flexible substrates [12–15]. These nanostructures consist of either silver or gold. Silver, which is characterized by high SERS efficiency through the electromagnetic mechanism via plasmon resonance, has the disadvantage of susceptibility to oxidation and inherent sterilization power. Conversely, gold, which has chemical stability and biocompatibility, exhibits lower SERS efficiency compared to silver-based substrates. Combining these plasmonic nanostructures with three different flexible substrates—microfluidic channel, film, and mesh—is achieved through various techniques such as nanostructure adsorption, chemical synthesis, and metal deposition on the nanostructures, resulting in fabricating wearable SERS sensors [12–15]. The microfluidic SERS sensor is an advanced technology tailored for the sampling and detecting of biofluids on the skin, while the wearable SERS film and mesh offer fabrication ease and scalability. In particular, a mesh, which can be used as a sampling-free substrate, has been mainly chosen as the flexible substrate and integrated silver or gold [12–15].

## 8.3 Noble Metal Nanomesh

Recently, a highly scalable wearable SERS sensor with a combination of mesh and noble metal has been presented [16–18]. This innovative sensor is based on an effortlessly fabricated, low-cost, ultra-thin, flexible, stretchable, adhesive, and biointegratable noble metal (gold or silver) nanomesh, as shown in Fig. 8.1a, b. The inspiration for this sensor came from a recently developed inflammation-free, gas-permeable, lightweight, stretchable electronic sensor made of gold-coated biointegratable polyvinyl alcohol (PVA) nanofibers. This electronic sensor can be attached to human skin or non-flat, non-rigid surfaces for extended periods [19]. The optical properties of this sensor have also been investigated and optimized [16–18]. Its dimensions provide SERS capabilities while maintaining its exceptional properties: ease of fabrication, low cost, ultra-thin, flexible, stretchable, adherent, and biointegratable. This flexible two-dimensional sensor can be conformed to various shapes

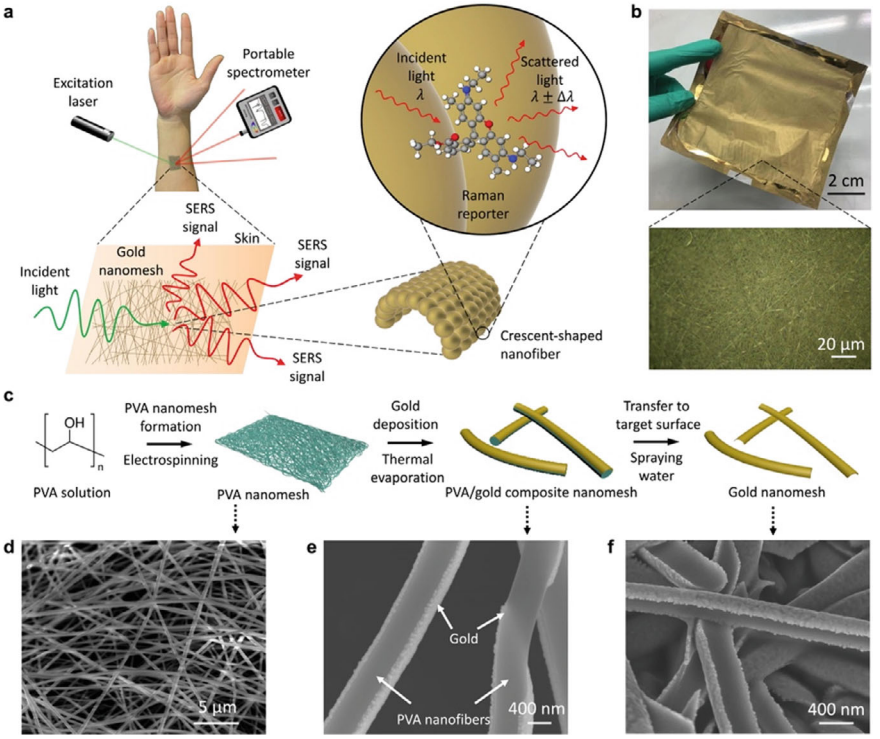



**Fig. 8.1** Gold/PVA nanomesh as a wearable SERS sensor. **a** Schematic illustration of the wearable SERS sensor on the skin. **b** Photograph and optical microscope image of gold/PVA nanomesh. **c** Fabrication process of gold/PVA nanomesh. SEM images of **d** electrospun PVA fiber nanomesh, **e** gold-coated PVA nanomesh, and **f** gold nanomesh after removal of PVA by spraying water. This figure has been adapted from Ref. [16]. Copyright © 2022 Liu et al., Advanced Optical Materials, Wiley–VCH GmbH. Distributed under the Creative Commons Attribution License 4.0 (CC BY)

and adapted for placement on virtually any surface. It enables label-free, large-scale, in situ sensing of diverse analytes ranging from low to high concentrations. To demonstrate the practical utility of this wearable SERS sensor, biomarkers have been detected in sweat and urine.

### *8.3.1 Fabrication of Noble Metal Nanomesh*

The noble metal/PVA nanomesh fabrication process required a thermal deposition of gold or silver onto electrospun PVA nanomesh acting as a template as depicted in Fig. 8.1c [16–18]. Initially, a low-cost and scalable electrospinning technique was used to fabricate PVA nanomesh using an 8 wt% PVA solution. The PVA nanomesh

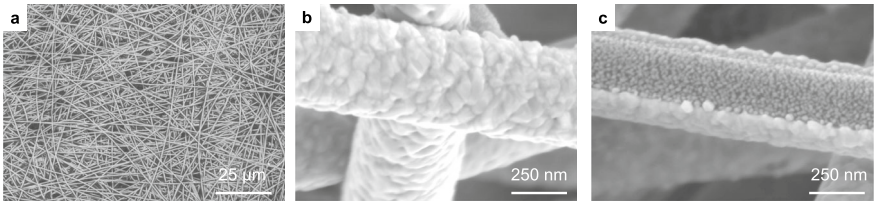



**Fig. 8.2** SEM images of the top surface of silver/PVA nanomesh at **a** low and **b** high magnification. **c** SEM image of the bottom surface of silver/PVA nanomesh after removing the PVA by spraying water, showing the crescent structure of the silver fiber with nanostructures. This figure has been adapted from Ref. [18]. Copyright © 2023 Kesava Rao et al., Advanced Photonics Research, Wiley–VCH GmbH. Distributed under the Creative Commons Attribution License 4.0 (CC BY)

was subsequently coated with a 150 or 300-nm-thick layer of gold or silver, respectively, via thermal evaporation conducted in high vacuum conditions ($< 2 \times 10^{-4}$ Pa) at a deposition rate of 0.1 nm/s. The PVA nanomesh was thermally deposited on one side to produce a noble metal nanofiber, which has a concave cross-sectional profile. In the final stage, the PVA nanomesh templates were dissolved with sprayed water, resulting in the formation of a gold or silver nanomesh. The gold or silver nanomesh was further analyzed by scanning electron microscope (SEM, Regulus 8230, Hitachi). Figure 8.1d, e portrays an evident gold network comprised of interlinked gold fibers, each measuring more than 100 μm in length and approximately 400 nm in width. As shown in Fig. 8.1f, the bottom-view SEM image revealed a concave cross-sectional profile of the gold nanofiber, indicating complete removal of the PVA fiber template. In the case of silver nanomesh, a similar structure is observed, except that silver nanoparticles with diameters close to 30 nm can be seen within these concave silver nanofibers, as shown in Fig. 8.2.

## *8.3.2 SERS Performance of Noble Metal Nanomesh*

### 8.3.2.1 Sensitivity

To illustrate the outstanding sensitivity of the silver/PVA nanomesh for molecular detection, the Raman spectra of R6G solutions (Fig. 8.3a) were measured [18]. First, the Raman spectrum of bulk R6G on a silicon substrate was acquired using an excitation wavelength of 532 nm, yielding a relatively weak spectrum, as shown in Fig. 8.3a. In contrast, Raman spectrum of a 100 μM solution of R6G on the silver/PVA nanomesh adhered to a glass plate displayed distinct R6G peaks at 613, 775, 1187, 1309, 1360, 1506, 1569, and 1648 $cm^{-1}$, consistent with previous research [16, 17]. An enhancement factor (EF) using the silver/PVA nanomesh was derived to be approximately $1.25 \times 10^6$ [18]. On the other hand, similar SERS experiments were performed with R6G solutions using an excitation wavelength of 785 nm to

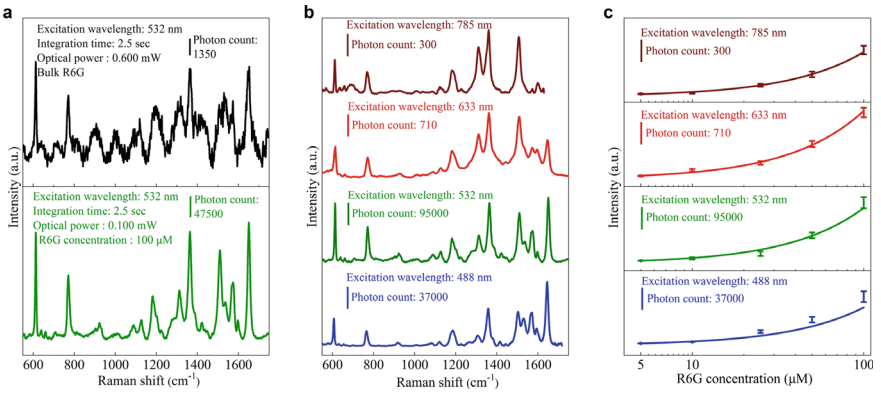



**Fig. 8.3** **a** Raman spectra for bulk R6G on a silicon substrate and an aqueous solution of R6G at 100 μM on the silver/PVA nanomesh, after baseline collection. **b** SERS spectra of an aqueous solution of R6G at 100 μM on the silver/PVA nanomesh, obtained by excitation at 785, 633, 532, and 488 nm (integration time: 2.5 s; optical power: 0.1 mW), after baseline collection. **c** Intensities of the SERS peak at 1361 $cm^{-1}$ over different R6G concentrations obtained by excitation at 785, 633, 532, and 488 nm. This figure has been adapted from Ref. [18]. Copyright © 2023 Kesava Rao et al., Advanced Photonics Research, Wiley–VCH GmbH. Distributed under the Creative Commons Attribution License 4.0 (CC BY)

evaluate the sensitivity of the gold/PVA nanomesh for molecular detection. A remarkable EF using the gold/PVA nanomesh was derived to be approximately $10^8$ [16]. These results underscore the ability of the nanomesh to enhance the Raman signal, highlighting its superior sensitivity for molecular detection.

#### 8.3.2.2 Broadband Response

To demonstrate the broadband response of the silver/PVA nanomesh, SERS measurements were performed over a range of excitation wavelengths. Figure 8.3b shows that Raman spectra were acquired using excitation laser wavelengths of 488, 532, 633, and 785 nm [18]. Across this range of wavelengths, the silver/PVA nanomesh consistently enhanced the Raman spectrum, highlighting its adaptability to different laser sources. To further explore its broadband sensitivity as a SERS sensor, measurements were performed on the silver/PVA nanomesh over a spectrum of R6G solution concentrations ranging from 5 to 100 μM, using different excitation wavelengths (Fig. 8.3c). With decreasing solution concentrations, the SERS spectra retained distinguishable signatures that were detectable at a minimum concentration of 10 μM. Notably, regardless of the selected excitation wavelength, the limits of detection remained remarkably consistent. For quantitative analysis, the 1361 $cm^{-1}$ Raman peak of R6G was selected. Figure 8.3c illustrates the relationship between peak intensities and R6G concentrations at different excitation wavelengths. The semi-log plot shows a linear correlation between the Raman intensity at 1361 $cm^{-1}$ and the concentration.

The coefficient of determination ($R^2 = 0.987$) underlines its potential for quantitative SERS analysis. These results strongly validate the broadband capability of the silver/PVA nanomesh and suggest a wearable SERS sensor that can be integrated with various portable Raman spectrometers.

To confirm the origin of this broadband response, the transmission spectrum of the silver nanomesh was measured using a JASCO V-770 UV–visible/NIR spectrophotometer. Figure 8.4a shows a broad absorption band, most likely due to plasmon resonance, manifesting in the range of 400–800 nm [18]. This indicates the broadband character of the SERS response, corresponding with excitations between 488 and 785 nm. The observed absorption band is similar to those observed in the plasmon resonance scattering spectra from the apex of the silver tip measured by darkfield illumination [20–23], suggesting a common plasmonic response in one-dimensional silver nanostructures. In contrast, the gold nanomesh failed to exhibit broadband response under excitation at 532 nm (data not shown). This discrepancy is likely due to the presence and absence of nanoparticles within the silver and gold nanofibers, respectively, as shown in Figs. 8.1f and 8.2c. To substantiate the broad performance of the silver nanomesh, numerical simulations of the plasmon resonance scattering spectra were performed using COMSOL Multiphysics based on the finite element method (Fig. 8.4b) [18]. A silver nanomesh model, as shown in Fig. 8.4c, which mimics the structure shown in Fig. 8.2c, was used in the simulation. The model comprises a concave silver nanofiber with a diameter of 400 nm and a thickness of 80 nm, inclusive of a periodic array of 100 silver nanoparticles having a diameter of 15 nm within the concave area. The simulation takes into account the incident broadband plane-wave light, with polarization parallel to the nanofiber, in the *Z*-direction. The simulation was performed assuming air as the surrounding medium. To implement periodic boundary conditions, the Bloch method was used in the *XY* plane, and the frequency-dependent refractive index according to Johnson et al. [24] was used to account for the properties of the silver material. The periodicity along the *X*- and *Y*-direction was set to 800 and 900 nm, respectively. These results as shown in Fig. 8.4a, b solidify the concept that surface plasmons on the silver nanomesh can resonate with different excitation sources in both the visible and near-infrared regions, resulting in a broadband response.

#### 8.3.2.3 Flexibility, Stretchability, Durability, Reproducibility, and Uniformity

For use in wearable SERS applications, the substrate must demonstrate flexibility, stretchability, durability, reproducibility, and uniformity. To demonstrate the flexibility of the gold/PVA nanomesh as a wearable SERS sensor, a crumpling test was conducted by adhering it to a glove and repeatedly opening and closing the hand. Even after 1000 crumpling cycles, the peak intensities of R6G showed no noticeable change (Fig. 8.5a) [16]. Similarly, a stretchability test was performed by adhering it to a 50% pre-stretched polydimethylsiloxane (PDMS) substrate and conducting multiple stretching and release cycles. Even after 1000 stretching cycles,

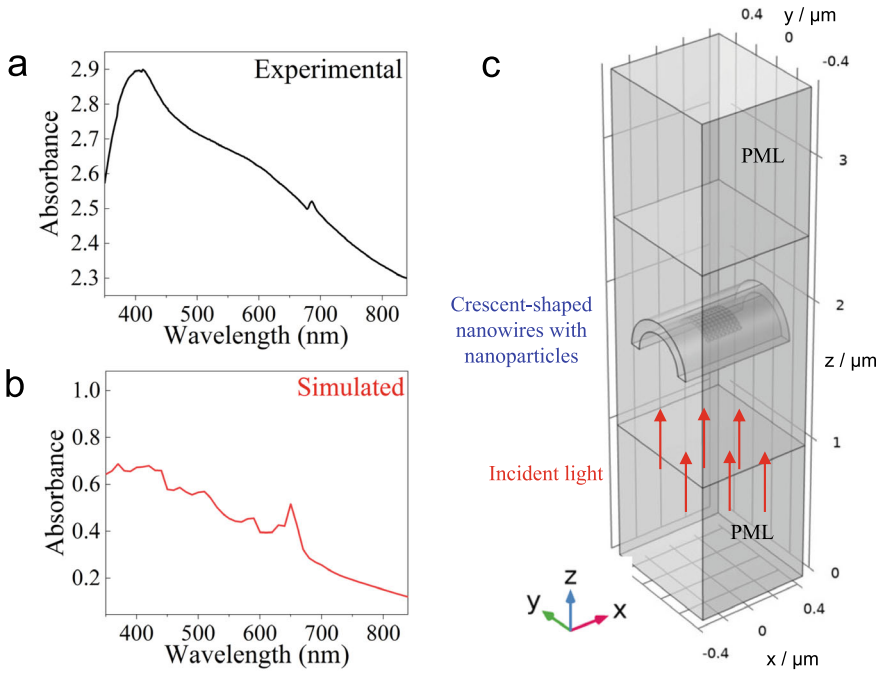



**Fig. 8.4** **a** Experimental UV–vis absorption spectrum of the silver nanomesh. **b** Simulated UV–vis absorption spectra of the silver nanomesh model composed of 100 silver nanoparticles inside a concave silver nanofiber. **c** Geometrical configuration of the silver nanomesh model composed of 100 silver nanoparticles inside a concave silver nanofiber for numerical simulations of the silver nanomesh using COMSOL Multiphysics based on the finite element method. This figure has been adapted from Ref. [18]. Copyright © 2023 Kesava Rao et al., Advanced Photonics Research, Wiley–VCH GmbH. Distributed under Creative Commons Attribution License 4.0 (CC BY)

the peak intensities of R6G showed no noticeable change (Fig. 8.5b) [16]. The silver/PVA nanomesh also showed similar flexibility and stretchability [18]. These findings clearly underscore the user-friendly nature and practical applicability of the wearable SERS sensor.

To evaluate its durability, SERS measurements of R6G on the silver/PVA nanomesh were conducted over various time intervals ranging from several hours (0, 1, 2, 3, 4 h) to days (1, 2, 3, 4 days), and then weeks (1, 2, 3, 4 weeks). Figure 8.5c exhibits that the peak intensities of R6G showed no noticeable change during the 30-day period [18]. This durability is due to the multifunctionality of the PVA fiber, which serves as both a template for fabricating the silver/PVA nanomesh and a protector against surface oxidation of the silver, ensuring the stability of the silver/PVA nanomesh [25, 26]. To assess the reproducibility of the silver/PVA nanomesh, SERS measurements of R6G were conducted on five nanomesh substrates from

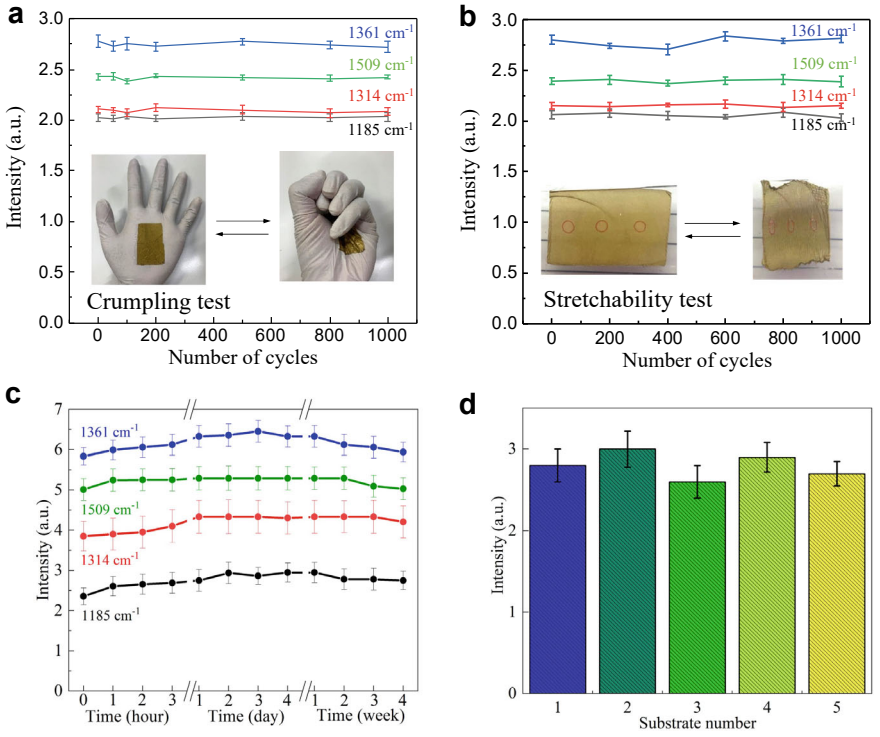



**Fig. 8.5** Flexibility, stretchability, durability, and reproducibility of SERS measurements on the noble metal/PVA nanomesh. **a** Peak intensity variations in the Raman spectra of R6G on the gold/PVA nanomesh attached to a glove during a 1000-cycle crumpling test. The inset images show the gold/PVA nanomesh on the glove during the crumpling test. **b** Peak intensity variations in the Raman spectra of R6G on the gold/PVA nanomesh attached to a pre-stretched PDMS substrate through a 1000-cycle stretchability test. The inset images show the gold/PVA nanomesh on the PDMS substrate during the stretch test. **c** Peak intensity variations in the Raman spectra of R6G on the surface-attached silver/PVA nanomesh at different times after fabrication. **d** Intensity variations of the peak at 1361 $cm^{-1}$ in the Raman spectra of R6G over several silver/PVA nanomesh substrates. The error bars in **a**, **b**, **c**, and **d** show the standard deviations derived from the spectra obtained at five, five, six, and six different locations, respectively. This figure has been adapted from Refs. [16, 18]. Copyright © 2022 Liu et al., Advanced Optical Materials, Wiley–VCH GmbH; 2023 Kesava Rao et al., Advanced Photonics Research, Wiley–VCH GmbH. Distributed under the Creative Commons Attribution License 4.0 (CC BY)

different batches. The intensities of the Raman peak at 1361 $cm^{-1}$ exhibit similar variations across the substrates (Fig. 8.5d) [18]. These findings highlight the durability and reproducibility of the nanomesh substrate.

To characterize the surface uniformity of the silver/PVA nanomesh, Raman mapping of R6G on the nanomesh was obtained, targeting the prominent Raman peak at 1361 $cm^{-1}$. The measurements used a step size of 1.0 and 0.25 μm for each point, coupled with an exposure time of 1 s, using 785 nm excitation lasers, as shown

in Fig. 8.6a [18]. Statistical analysis was performed based on the intensities of the 1361 $cm^{-1}$ peak, as shown in Fig. 8.6b. The distribution of SERS intensities from the silver/PVA nanomesh deviates from a normal distribution, similar to that of the carbon-based SERS substrate [27], and aligns with the Poisson distribution, similar to that of single molecules on a single silver nanoaggregate [28], suggesting a stochastic process of entering a confined electric field in a gap of the noble metal nanostructures (hot spot). Notably, Fig. 8.6b revealed that the nanomesh has an average coefficient of variation (CV) of less than 20%.

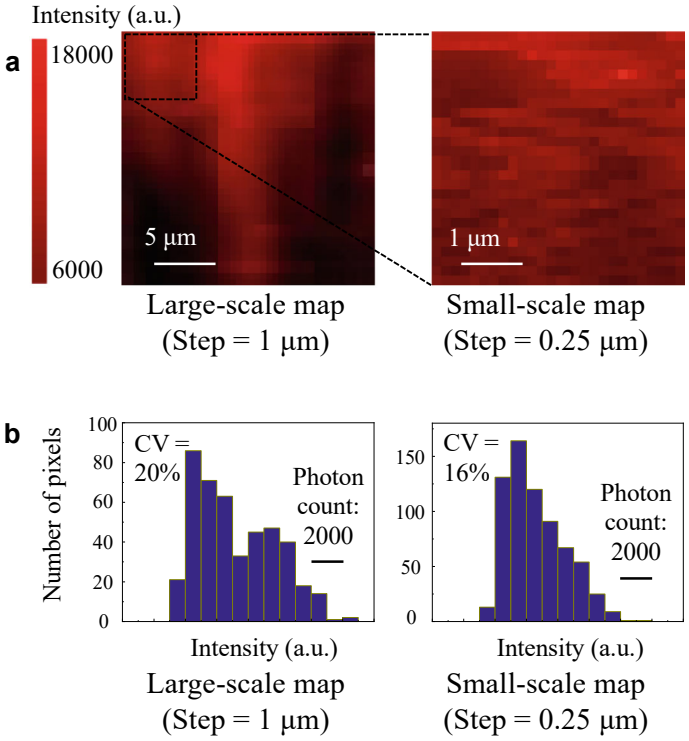



**Fig. 8.6** Uniformity of SERS measurements on the silver/PVA nanomesh. **a** Raman intensity map of the peak at 1361 $cm^{-1}$ of R6G on the silver/PVA nanomesh. These maps were obtained using step sizes of 1 and 0.25 μm. **b** Histograms of the peak intensities on the large- and small-scale maps. This figure has been adapted from Ref. [18]. Copyright © 2023 Kesava Rao et al., Advanced Photonics Research, Wiley–VCH GmbH. Distributed under the Creative Commons Attribution License 4.0 (CC BY)

#### 8.3.2.4 Wearability

To showcase the wide-ranging potential of the wearable SERS sensor in various SERS scenarios, its inherent adhesiveness, which eliminates the need for any adhesives, was demonstrated. This was confirmed by attaching the sensor to surfaces made from various materials, such as metals, plastics, fabrics, and organic substrates [16]. As displayed in Fig. 8.7a–c, the wearable SERS sensor was fastened to an individual's wrist to identify sweat biomarkers. The sensor's visual documentation depicts its outstanding properties of being highly flexible, stretchable, adhesive, and biointegrable. The nanomesh adheres firmly to the skin and withstands typical flexion and extension conditions. The lack of noticeable side effects on human skin is due to gold nanomesh's non-inflammatory and gas-permeable properties [19]. Figure 8.7d, e displays the wearable SERS sensor linked to a human cheek and contact lens, which detects tear biomarkers [29, 30]. Additionally, Fig. 8.7f portrays the wearable SERS sensor affixed to a face mask's surface, intended for detecting biomarkers in breath and saliva, which are relevant to respiratory, oral, and COVID-19-related diseases [31, 32]. Figure 8.7g–j displays the utilization of the wearable SERS sensor on various metallic and plastic surfaces such as an elevator control panel, a door handle, a doorknob, and a computer keyboard. The images emphasize the potential of the sensor as a tool for monitoring environmental conditions and detecting infections in smart cities [33]. Additionally, Fig. 8.7k, l exhibits the wearable SERS sensor attached to an apple and a leaf, showcasing its ability to be used in food safety testing [17, 18].

#### 8.3.2.5 Sampling-Free SERS

For practical use of wearable SERS sensors, biofluids adsorbed on the bottom surface of the substrate need to be detected by excitation directed to the top surface of the substrate (epi-excitation). Unfortunately, conventional SERS measurements typically require sample collection and preparation, namely, collecting a sample from a target object and dropping it on a SERS substrate for the measurements. Therefore, the need for sampling-free SERS substrates tailored for wearable SERS sensors remains.

To illustrate the concept of "Place and Play SERS" using the noble metal nanomesh substrate, which allows placing the substrate on an object of interest and performing SERS measurements by epi-excitation, three different methods were employed to acquire the SERS spectra of analytes using the gold/PVA nanomesh substrate with a portable Raman spectrometer (WSERS-785, BaySpec) [17].

1. The gold/PVA nanomesh substrate was placed on the wet target surface to generate pure gold nanomesh by dissolving PVA. An analyte solution (3 μL) was then dropped onto the deposited side (top surface) of the substrate on the target surface (conventional SERS).

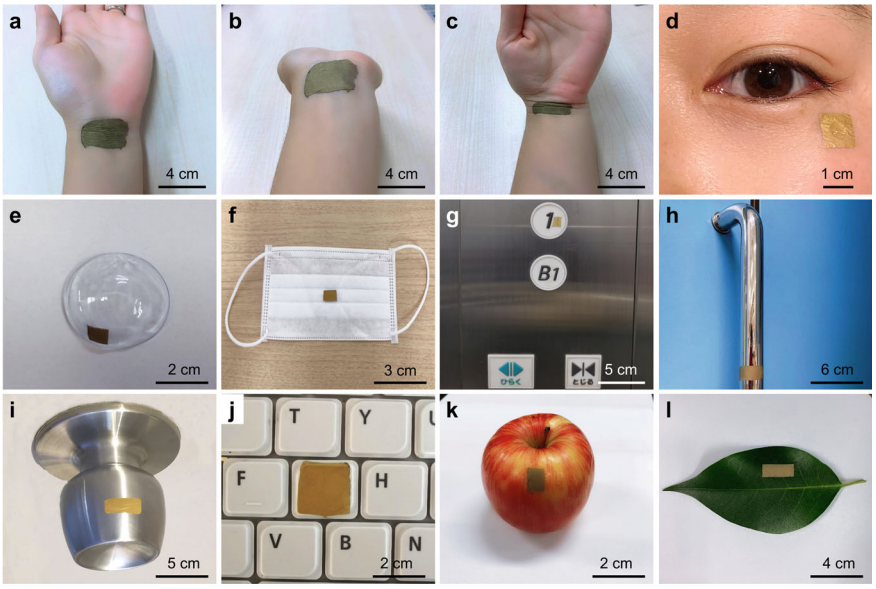



**Fig. 8.7** Pictures of the gold/PVA nanomesh attached to various surfaces to demonstrate its wearability. **a**–**c** Gold/PVA nanomesh adhered to a human wrist, flexed wrist, and extended wrist to detect biomarkers in sweat. **d**, **e** Gold/PVA nanomesh adhered to a human cheek and contact lens to detect biomarkers in tears. **f**–**j** Gold/PVA nanomesh adhered to a face mask, elevator control panel, door handle, doorknob, and computer keyboard for infection surveillance. **k**, **l** Gold/PVA nanomesh adhered to an apple and a leaf for food safety testing. This figure has been adapted from Ref. [16]. Copyright © 2022 Liu et al., Advanced Optical Materials, Wiley–VCH GmbH. Distributed under the Creative Commons Attribution License 4.0 (CC BY)

2. The gold/PVA nanomesh substrate was placed on an analyte solution (3 μL) on the target surface (Place and Play SERS). The analyte was adsorbed on the non-deposited side (bottom surface) of the gold/PVA nanomesh substrate.
3. An analyte solution (3 μL) was dried on the target surface and then sprayed with water. The re-wetted analyte was covered with the gold/PVA nanomesh substrate (Place and Play SERS) and adsorbed on the non-deposited side (bottom surface) of the gold/PVA nanomesh substrate.

The gold/PVA nanomesh substrate was placed on various surfaces, and the SERS spectra of R6G (1 mM) were measured on these surfaces using a wearable Raman spectrometer (Fig. 8.8a–f). In the first set of demonstrations showing Place and Play SERS on water-repellent surfaces, SERS measurements of R6G were performed on a polystyrene dish (Fig. 8.8a) and a nitrile butadiene rubber (NBR) glove (Fig. 8.8b). The figures clearly show that the SERS spectrum of R6G from the bottom surface of the substrate in the Place and Play SERS measurement is very similar, both spectrally and in intensity, to that obtained from the top surface of the substrate in the conventional SERS measurement, thus validating Place and Play SERS. In addition, Fig. 8.8a, b shows that even a trace of R6G after drying can be detected by spraying

the dried R6G with water and placing the substrate on top of it. In the second set of demonstrations highlighting Place and Play SERS on water-absorbent surfaces, SERS measurements of R6G were performed on a polyester cloth (Fig. 8.8c), a concrete brick (Fig. 8.8d), a face mask (Fig. 8.8e), and a paper towel (Fig. 8.8f). Similar to the results in Fig. 8.8a, b, the figures show a close resemblance between the SERS spectrum of R6G from the bottom surface of the substrate in the Place and Play SERS measurement and that obtained from the top surface of the substrate in the conventional SERS measurement, providing further validation of Place and Play SERS. Contrary to the previous results, the detection of a trace of R6G after drying was difficult despite spraying the dried R6G with water. These outcomes effectively illustrate the practical applicability of Place and Play SERS under real-time, in situ conditions.

To compare the sensitivity of conventional SERS to Place and Play SERS measurement schemes, SERS measurements of R6G on a glass plate were performed using both the top and bottom surfaces of the gold/PVA nanomesh substrate under identical conditions [17]. Figure 8.9a, b shows the SERS peak intensity values of R6G aqueous solutions at different concentrations at 775 $cm^{-1}$, an isolated peak of R6G minimally affected by its neighboring peaks and background, obtained from the top and bottom surfaces of the gold/PVA nanomesh, respectively. The observations show that while the sensitivities of the conventional SERS and Place and Play SERS measurement schemes were similar at higher concentrations of R6G, distinct differences emerged at lower concentrations. The reduced sensitivity at lower concentrations in the Place and Play SERS measurement scheme cannot be attributed to optical excitation from the top surface (epi-excitation), as the SERS intensity values at lower concentrations showed minimal dependence on substrate thickness. Instead, it is postulated that a substantial concentration of dissolved PVA competes with R6G at lower concentrations, resulting in decreased sensitivity at the bottom surface [34]. Meanwhile, sensitivity remains intact on the top surface, which is free of PVA. These results illustrate that the sensitivity of Place and Play SERS is similar to that of conventional SERS, except at very low concentrations.

To investigate the sensitivity dependence of Place and Play SERS on the thickness of the gold/PVA nanomesh substrate, a series of SERS measurements on both the top and bottom surfaces of the substrate, each of which has different thickness values, were performed [17]. Analogous to the results shown in Fig. 8.9a, b, the SERS peak intensity values of R6G at 775 $cm^{-1}$ were used for the evaluation. As shown in Fig. 8.10a (top surface), thicker substrates tend to exhibit stronger SERS intensity values at 100 μM and 1 mM. This is due to the increase in the hotspots adsorbs R6G molecules, which increases proportionally with substrate thickness. In contrast, as shown in Fig. 8.10b (bottom surface), thinner substrates produce an inverse trend because they facilitate the easy penetration of the analyte through the substrate, resulting in stronger SERS intensity values. It is noteworthy that the error bars in Fig. 8.10b are smaller than those in Fig. 8.10a, indicating that the uniformity of the Place and Play SERS measurements exceeds that of the conventional SERS measurement, as shown in Fig. 8.6. Thus, the ultra-thin noble metal nanomesh demonstrates the capability of wearable SERS sensors.

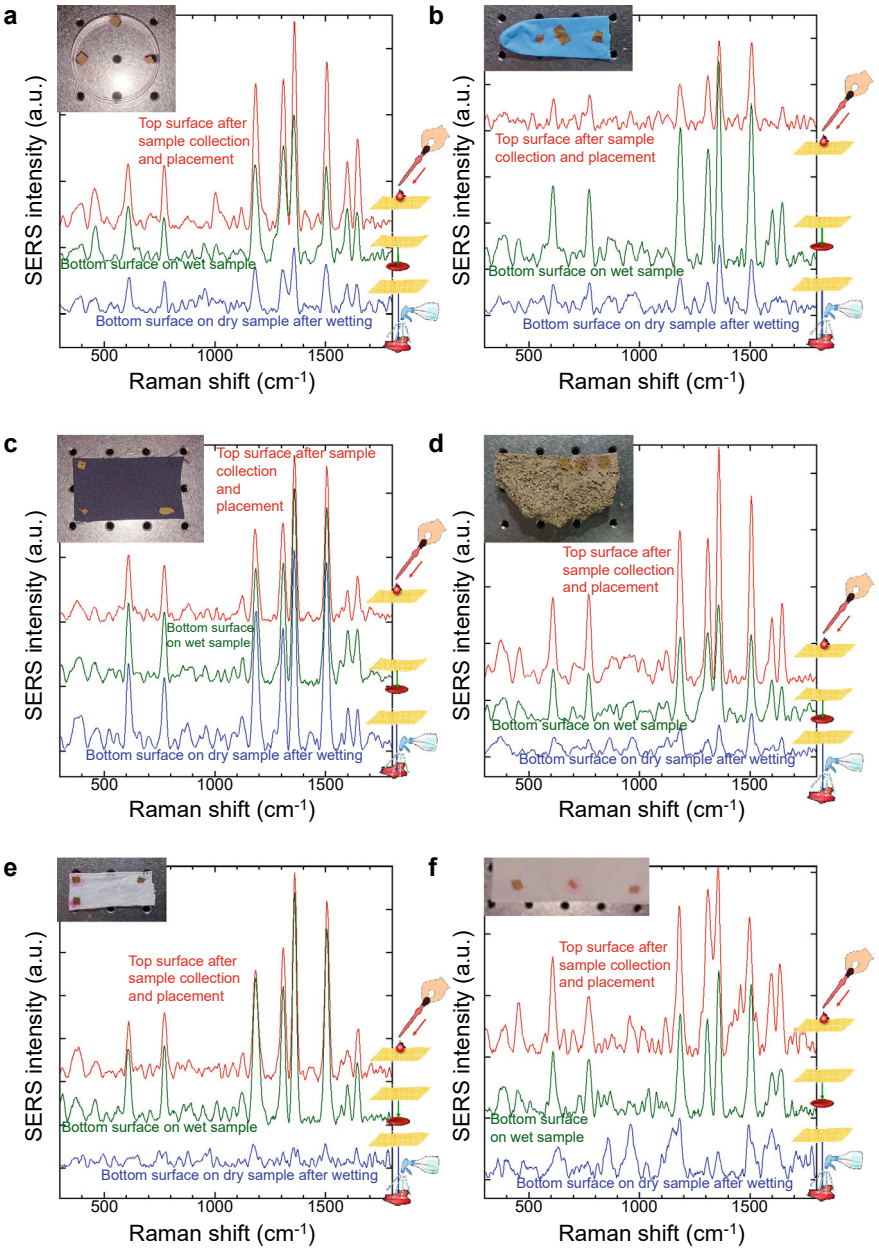



**Fig. 8.8** SERS spectra of an aqueous solution of R6G at 1 mM on the top and bottom surfaces of the gold/PVA nanomesh positioned on various surfaces: **a** polystyrene dish, **b** nitrile butadiene rubber (NBR) glove, **c** polyester cloth, **d** concrete brick, **e** face mask, and **f** paper towel. The insets show images of the different surfaces with the gold/PVA nanomesh. SERS signals were obtained by epi-excitation using a wearable Raman spectrometer (BaySpec; excitation wavelength: 785 nm, optical power: 20 mW, integration time: 2.5 s). Reproduced from Ref. [17] with permission. Copyright © 2023, The Royal Society of Chemistry

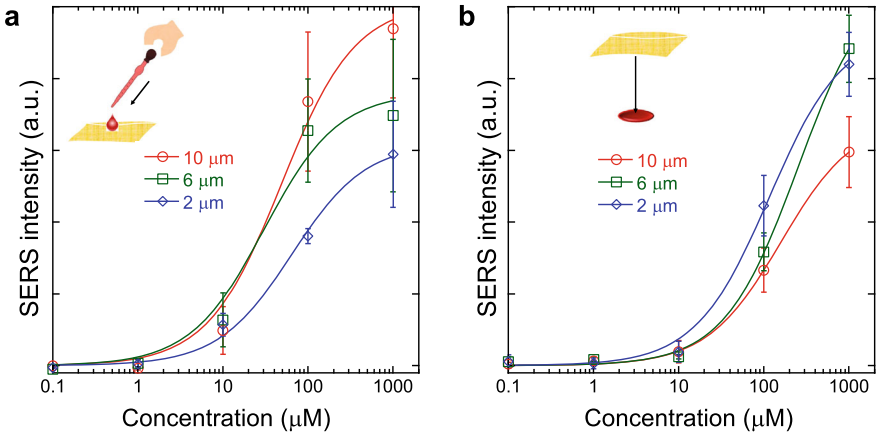



**Fig. 8.9** Concentration dependence of the SERS peak intensity at 775 $cm^{-1}$ of an aqueous solution of R6G on **a** the top surface and **b** the bottom surface of the gold/PVA nanomesh with thickness values of 10, 6, and 2 μm. Error bars show the standard deviations derived from the spectra obtained at three different locations. Polynomial curves show the concentration dependence. Panels **a** and **b** have the same intensity scale. SERS signals were obtained by epi-excitation using a table-top Raman spectrometer (Renishaw; excitation wavelength: 785 nm, optical power: 10 mW, integration time: 1 s with 20 accumulations). Reproduced from Ref. [17] with permission. Copyright © 2023, Royal Society of Chemistry

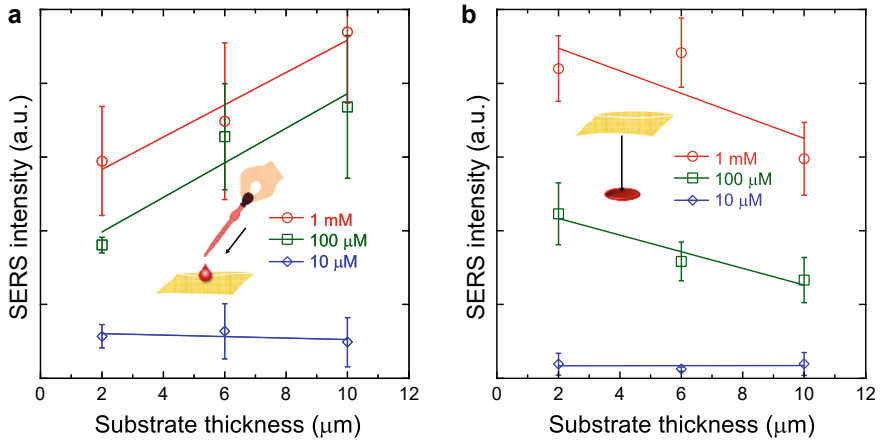



**Fig. 8.10** Substrate thickness dependence of the SERS peak intensity at 775 $cm^{-1}$ of an aqueous solution of R6G at concentrations of 1000, 100, and 10 μM on **a** the top and **b** the bottom surface of the gold/PVA nanomesh. Error bars show the standard deviations derived from the spectra obtained at three different locations. The substrate thickness dependence is shown by lines. Panels **a** and **b** have the same intensity scale. SERS signals were obtained by epi-excitation using a table-top Raman spectrometer (Renishaw; excitation wavelength: 785 nm, optical power: 10 mW, integration time: 1 s with 20 accumulations). Reproduced from Ref. [17] with permission. Copyright © 2023, Royal Society of Chemistry

## 8.3.3 Applications of Wearable SERS Sensors

### 8.3.3.1 Detection of Biocides

To illustrate the practical applicability of the Place and Play wearable SERS sensor, food safety testing was performed using the silver/PVA nanomesh. Specifically, thiabendazole (TBZ), a fungicide typically used to preserve and package oranges [18], was utilized in our experiment. The European Union has set a maximum residue limit (MRL) of 6 mg/kg for TBZ in citrus produce [35]. Within the experimental setup, five different concentrations of TBZ ranging from 1 mM to 100 nM in ethanol were applied to orange peels. The Raman spectra, displayed in Fig. 8.11, were obtained through the use of a wearable Raman spectrometer. In the presence of the silver/PVA nanomesh, the TBZ signals were clearly exhibited. These distinguishable TBZ vibrational patterns were discernible even at minimal concentrations, up to 100 μM (or 20 ppm) using the wearable Raman spectrometer. Our control experiment utilizing Raman spectra of orange bound to the silver/PVA nanomesh indicated an absence of outstanding peaks corresponding to orange peel. These results strongly support the suitability of the nanomesh as a simple Place and Play wearable sensor for food safety testing via non-destructive, real-time, and in situ Raman-based detection of fungicides.

To further elucidate the practical efficacy of the Place and Play SERS wearable sensor, SERS measurements of a biocide, 5-chloro-2-methyl-4-isothiazolin-3-one (CMIT), on the surface of an orange peel were performed using the gold/PVA

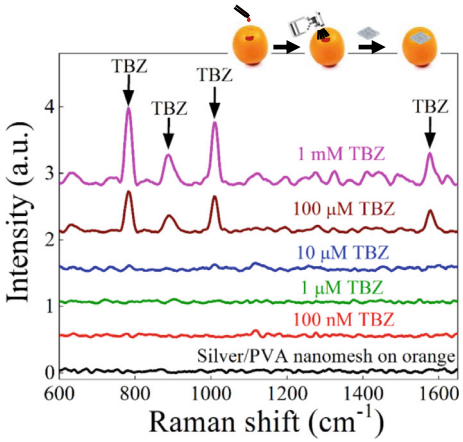



**Fig. 8.11** SERS spectra of an aqueous solution of TBZ (10 μL) at concentrations ranging from 1 mM to 100 nM, acquired from the bottom surface of the silver/PVA nanomesh attached to an orange peel using a wearable Raman spectrometer (BaySpec; excitation wavelength: 785 nm, optical power: 20 mW, integration time: 25 s). This figure has been adapted from Ref. [18]. Copyright © 2023 Kesava Rao et al., Advanced Photonics Research, Wiley–VCH GmbH. Distributed under Creative Commons Attribution License 4.0 (CC BY)

nanomesh [17]. In this context, biocides are chemical compounds designed to control yeasts, bacteria, and fungi and are commonly used as postharvest preservatives for plants and fruits [36–38]. Several household products, including cosmetics and antiseptics, contain CMIT, a group of heterocycles used as biocides. At high concentrations, it causes chemical burns, whereas rinse-off and leave-on cosmetic products have acceptable concentrations of 15 and 7.5 ppm, respectively [39]. Figure 8.12 shows the SERS spectra obtained from aqueous solutions of CMIT at different concentrations (14, 1.4, and 0.14%) applied to an orange peel using a wearable Raman spectrometer coupled to the gold/PVA nanomesh. The SERS peaks observed at 720, 940, and 1340 $cm^{-1}$ have been tentatively attributed to N–$CH_3$ stretching, C–C skeletal stretching, and C–H deformation vibrational modes, respectively [40, 41]. These vibrational modes were detectable at concentrations as low as 1400 ppm (0.14%) by using the wearable Raman spectrometer. In contrast, the spontaneous Raman spectrum of 14% CMIT on the orange peel was identical to the spectrum of the orange peel itself (Fig. 8.12). The spontaneous Raman peaks at 1525, 1150, and 1000 $cm^{-1}$ were caused by the carotenoids in the fruit [42–46]. The peak at 1525 $cm^{-1}$ corresponds to the in-phase $\upsilon$(C=C) vibration of the polyene chain, while the peak at 1150 $cm^{-1}$ is assignable to $\upsilon$(C–C) stretching vibrations of the polyene chain [46, 47]. The peaks at 1000 $cm^{-1}$ correspond to the in-phase rocking modes of the $CH_3$ groups attached to the polyene chain [46, 47]. These results underscore the exceptional performance of Place and Play SERS and suggest the potential of Place and Play wearable SERS sensors for not only food safety testing but also health monitoring via non-destructive, real-time, and in situ Raman-based detection of biofluids on the skin, rather than the skin itself.

#### 8.3.3.2 Analysis of Biofluids

To illustrate the versatility and practical utility of the silver/PVA nanomesh in health monitoring, its efficacy in the analysis of human sweat was investigated, focusing on the following specific biomarkers: urea, lactic acid, and ascorbic acid [48, 49]. Using the silver/PVA nanomesh, Raman spectra from a 2 μL sweat sample collected from a volunteer during routine activity and exercise were acquired (Fig. 8.13a). The peak at 1000 $cm^{-1}$ indicates the presence of urea. The Raman peaks at 776, 852, and 1441 $cm^{-1}$ correspond to lactic acid. The peaks at 1196 and 1625 $cm^{-1}$ are attributed to ascorbic acid, while those at 671 and 1490 $cm^{-1}$ are associated with proteins [18, 49]. Conversely, no distinguishable Raman peaks were obtained from the same sweat sample on a silicon substrate. This result underscores the ability of the nanomesh to detect minute amounts of urea, lactic acid, ascorbic acid, and proteins. Moreover, these results corroborate the evidence of an increase in ascorbic acid and protein levels in sweat after exercise compared to normal activity. Ascorbic acid, commonly known as vitamin C, is a water-soluble vitamin that plays a key role in several biological processes for the synthesis of collagen, which is essential for wound healing, skin elasticity, and overall tissue structure and is primarily excreted in the urine [50]. On the other hand, lactic acid, a primary metabolic byproduct of

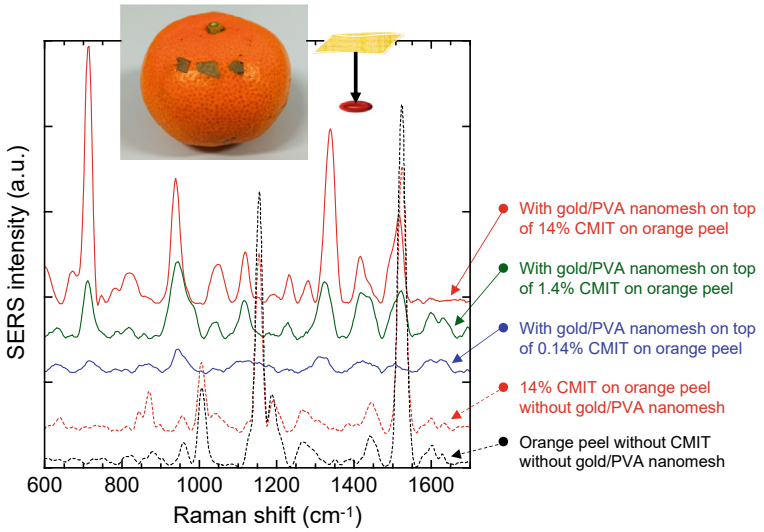



**Fig. 8.12** SERS spectra (solid curves) of an aqueous solution of CMIT (3 μL) at concentrations ranging from 14 to 0.14%, acquired from the bottom surface of the gold/PVA nanomesh attached to an orange peel and spontaneous Raman spectrum of a 14% CMIT aqueous solution on the orange peel and the orange peel itself (dashed curves) using a wearable Raman spectrometer (BaySpec; excitation wavelength: 785 nm, optical power: 20 mW, integration time: 25 s). Reproduced from Ref. [17] with permission. Copyright © 2023, Royal Society of Chemistry

anaerobic glycolysis, is produced in response to the body's need for rapid energy production, especially during periods of high-intensity physical activity or limited oxygen availability. Its concentrations directly correlate with physiological conditions, and during periods of intense physical exertion, this pathway may contribute to muscle fatigue by simultaneously lowering pH [51]. However, an increase in lactic acid after jogging could not be confirmed as shown in Fig. 8.13a. In addition to being a technical achievement, it highlights the real-world applicability of the substrate to study sweat directly on human skin, especially given the typical concentration range of these biomarkers after sweat evaporation.

To further demonstrate the practical utility of the silver/PVA nanomesh in health monitoring, human urine was analyzed [18]. Three key biomarkers—urea, uric acid, and hypoxanthine—were focused on [48, 49]. Raman spectra were obtained from 2 μL of human urine samples collected from a volunteer under two different conditions: before and 3 h after a regular meal (Fig. 8.13b). The Raman peak at 1000 $cm^{-1}$ indicates the presence of urea. The peaks at 810, 889, 1134, and 1467 $cm^{-1}$ are indicative of uric acid, while those at 641, 723, and 1374 $cm^{-1}$ correspond to hypoxanthine [18, 49]. Conversely, no peaks associated with the biomarkers were obtained from the urine sample on a silicon wafer. These results underscore the exceptional ability of the nanomesh to detect minute concentrations of urea, uric acid, and hypoxanthine. The results also shed light on an increase in the amount of uric acid and

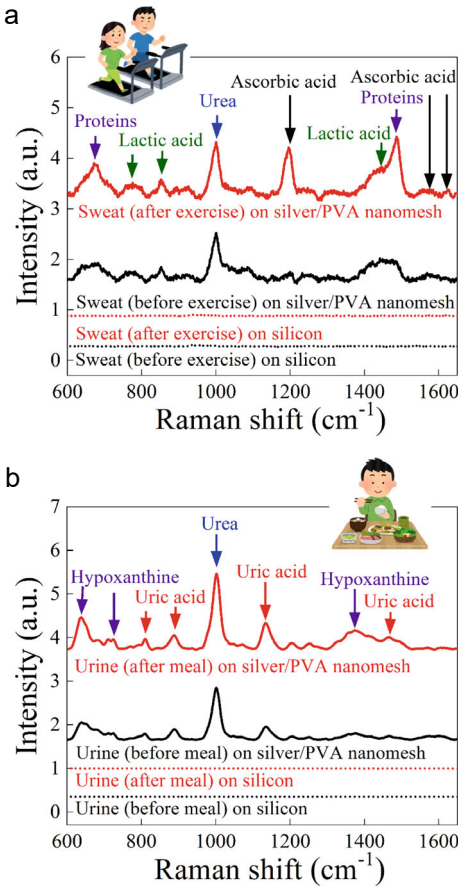



**Fig. 8.13** Healthcare applications of the silver/PVA nanomesh. SERS spectra of **a** human sweat before and after jogging and **b** human urine before and after a regular meal on a silver/PVA nanomesh. These spectra were obtained using a table-top Raman spectrometer (Renishaw; excitation wavelength: 785 nm, optical power: 8 mW, integration time: 20 s). This figure has been adapted from Ref. [18]. Copyright © 2023 Kesava Rao et al., Advanced Photonics Research, Wiley–VCH GmbH. Distributed under the Creative Commons Attribution License 4.0 (CC BY)

hypoxanthine in human urine after a regular meal compared to before the meal, a phenomenon attributed to the metabolic effects of food intake. Uric acid, a metabolic byproduct of purine catabolism, is excreted from the body via the bloodstream to the kidneys. The accumulation of uric acid in the bloodstream is associated with hyperuricemia, a condition that can lead to the formation of uric acid crystals, which contribute to painful gout. The concentration of uric acid in urine is an indicator of kidney function [52]. Hypoxanthine, a naturally occurring purine derivative and a component of DNA, RNA, adenosine triphosphate (ATP), and other nucleotides,

results from the metabolism of adenine and guanine, which are also purine derivatives. It can be converted to xanthine and ultimately to uric acid in the body [53]. The result as shown in Fig. 8.13b is consistent with previous reports [54]. Given the ease of urine collection, it holds promise for the diagnosis of various diseases through the application of the SERS technique [49].

## 8.4 Concluding Remarks

In summary, a highly scalable, low-cost, ultra-thin, flexible, stretchable, adhesive, and biointegratable nanomesh composed of noble metal-coated PVA nanofibers was developed via electrospinning and metal deposition. The efficacy of both the gold/PVA and silver/PVA nanomesh in the field of wearable SERS sensors was demonstrated by investigating aspects such as sensitivity, flexibility, stretchability, durability, reproducibility, and uniformity. The wearable SERS sensors demonstrated exceptional practical utility in various applications, including food safety testing through biocide analysis and health monitoring through biomarker detection in biofluids. Specifically, the detection of biocides on fruit was conducted by placing the nanomesh on the peel and performing SERS measurements without sample collection using a wearable Raman spectrometer. While the initial biomarker detection involved sampling from volunteers using a table-top Raman spectrometer, the wearable SERS sensor is poised to emerge as a key component of wearable sensing technology for health monitoring.

**Acknowledgements** This research was supported by MEXT Quantum Leap Flagship Program (JPMXS0120330644), JSPS Core-to-Core Program (JPJSCCA20190007), JSPS Bilateral Program (JPJSBP120227703), White Rock Foundation, Mitsubishi UFJ Technology Development Foundation, UTokyo IPC, KISTEC, Murata Science Foundation, University of Tokyo GAP Fund, Kawasaki Deep Tech Accelerator Program, Plug and Play Japan Accelerator Program, MEXT Advanced Research Infrastructure for Materials and Nanotechnology in Japan (ARIM), JSPS KAKENHI (JP18K13798, JP20K14785), the Grant-in-Aid for JSPS Fellows (P20789). The JSPS Grant-in-Aid for Young Scientists (20K15227), and the Grant-in-Aid for JSPS Fellows (19F19805). We are grateful to all members of Goda Lab.

**Competing Interests** KG is a shareholder of LucasLand and holds a pending patent for the noble metal nanomesh sensor.

**Ethics Approval** The SERS test of human sweat and urine was sanctioned by the Research Ethics Committee at the Graduate School of Science, University of Tokyo (approval numbers: 20-352 and 23-30). The human subject expressed informed consent prior to the sample collection.

## References


1. Y. Khan, A. E. Ostfeld, C. M. Lochner, A. Pierre, A. C. Arias, Monitoring of vital signs with flexible and wearable medical devices. Adv. Mater. **28**, 4373–4395 (2016)
2. M. Cardinale, M. C. Varley, Wearable training-monitoring technology: applications, challenges, and opportunities. Int. J. Sports Phys. Ther. **12**, 55–62 (2017)
3. K. Tekin, M. Karadogan, S. Gunaydin, K. Kismet, Everything about pulse oximetry—part 2: clinical applications, portable/wearable pulse oximeters, remote patient monitoring, and recent advances. J. Intensive Care Med. **38**, 887–896 (2023)
4. J. R. Sempionatto, J. A. Lasalde-Ramírez, K. Mahato, J. Wang, W. Gao, Wearable chemical sensors for biomarker discovery in the omics era. Nat. Rev. Chem. **6**, 899–915 (2022)
5. M. Wang, Y. Yang, J. Min, Y. Song, J. Tu, D. Mukasa, C. Ye, C. Xu, N. Heflin, J. S. McCune, T. K. Hsiai, Z. Li, W. Gao, A wearable electrochemical biosensor for the monitoring of metabolites and nutrients. Nat. Biomed. Eng. **6**, 1225–1235 (2022)
6. D. R. Seshadri, R. T. Li, J. E. Voos, J. R. Rowbottom, C. M. Alfes, C. A. Zorman, C. K. Drummond, Wearable sensors for monitoring the physiological and biochemical profile of the athlete. npj Digit. Med. **2**, 72 (2019)
7. J. Kim, A. S. Campbell, B. E.-F. de Ávila, J. Wang, Wearable biosensors for healthcare monitoring. Nat. Biotechnol. **37**, 389–406 (2019)
8. X. X. Han, R. S. Rodriguez, C. L. Haynes, Y. Ozaki, B. Zhao, Surface-enhanced Raman spectroscopy. Nat. Rev. Methods Primers **1**, 87 (2021)
9. T. Itoh, M. Procházka, Z.-C. Dong, W. Ji, Y. S. Yamamoto, Y. Zhang, Y. Ozaki, Toward a new era of SERS and TERS at the nanometer scale: from fundamentals to innovative applications. Chem. Rev. **123**, 1552–1634 (2023)
10. P. M. Pancorbo, H. Zhang, X. Yu, T.-H. Xiao, K. Goda, Metal-free SERS: where we are now, where we are heading. EPL, **136**, 34001 (2021)
11. X. Tang, N. Kishimoto, Y. Kitahama, T.-T. You, M. Adachi, Y. Shigeta, S. Tanaka, T.-H. Xiao, K. Goda, Deciphering the potential of multidimensional carbon materials for surface-enhanced Raman spectroscopy through density functional theory. J. Phys. Chem. Lett. **14**, 10208–10218 (2023)
12. K. Xu, R. Zhou, K. Takei, M. Hong, Toward flexible surface-enhanced Raman scattering (SERS) sensors for point-of-care diagnostics. Adv. Sci. **6**, 1900925 (2019)
13. V. T. N. Linh, M. S. Al Ja'farawy, E. H. Koh, M. Y. Lee, S. G. Park, D. H. Kim, H. S. Jung, Flexible surface-enhanced Raman scattering substrates toward sampling approaches for on-site sensing and diagnosis applications. Appl. Spectrosc. Rev. **59**, 90–123 (2024)
14. E. S. Prikhozhdenko, D. N. Bratashov, D. A. Gorin, A. M. Yashchenok, Flexible surface-enhanced Raman scattering-active substrates based on nanofibrous membranes. Nano Res. **11**, 4468–4488 (2018)
15. Y. Kitahama, M. Egawa, P. K. Dwivedi, W. Yang, K. Goda, An emerging tool in healthcare: wearable surface-enhanced Raman spectroscopy. J. Phys. Photonics **6**, 021001 (2024)
16. L. Liu, P. M. Pancorbo, T.-H. Xiao, S. Noguchi, M. Marumi, H. Segawa, S. Karhadkar, J. Gala de Pablo, K. Hiramatsu, Y. Kitahama, T. Itoh, J. Qu, K. Takei, K. Goda, Highly scalable, wearable surface-enhanced Raman spectroscopy. Adv. Optical Mater. **10**, 2200054 (2022)
17. Y. Kitahama, P. M. Pancorbo, H. Segawa, M. Marumi, T. H. Xiao, K. Hiramatsu, W. Yang, K. Goda, Place & play SERS: sample collection and preparation-free surface-enhanced Raman spectroscopy. Anal. Methods **15** 1028–1036 (2023)
18. V. Kesava Rao, X. Tang, Y. Sekine, M. Egawa, P. K. Dwivedi, Y. Kitahama, W. Yang, K. Goda, An ultralow-cost, durable, flexible substrate for ultrabroadband surface-enhanced Raman spectroscopy. Adv. Photonics Res. **5**, 2300291 (2024)
19. A. Miyamoto, S. Lee, N. F. Cooray, S. Lee, M. Mori, N. Matsuhisa, H. Jin, L. Yoda, T. Yokota, A. Itoh, M. Sekino, H. Kawasaki, T. Ebihara, M. Amagai, T. Someya, Inflammation-free, gas-permeable, lightweight, stretchable on-skin electronics with nanomeshes. Nat. Nanotechnol. **12**, 907–913 (2017)

20. P. Pienpinijtham, Y. Kitahama, Y. Ozaki, Electric field analysis, polarization, excitation wavelength dependence, and novel applications of tip-enhanced Raman scattering (TERS). J. Raman Spectrosc. **52**, 1997–2017 (2021)
21. T. Itoh, Y. S. Yamamoto, T. Suzuki, Y. Kitahama, Y. Ozaki, Darkfield microspectroscopy of nanostructures on silver tip-enhanced Raman scattering probes. Appl. Phys. Lett. **108**, 021604 (2016)
22. Y. Kitahama, S. Uemura, R. Katayama, T. Suzuki, T. Itoh, Y. Ozaki, Polarization dependence of tip-enhanced Raman and plasmon-resonance Rayleigh scattering spectra. Appl. Phys. Lett. **110**, 233104 (2017)
23. Y. Kitahama, T. Itoh, T. Suzuki, Calculated shape dependence of electromagnetic field in tip-enhanced Raman scattering by using a monopole antenna model. Spectrochimica Acta A **197**, 142–147 (2018)
24. P. B. Johnson, R. W. Christy, Optical constants of the noble metals. Phys. Rev. B **6**, 4370–4379 (1972)
25. D. He, B. Hu, Q. F. Yao, K. Wang, S. H. Yu, Large-scale synthesis of flexible free-standing SERS substrates with high sensitivity: electrospun PVA nanofibers embedded with controlled alignment of silver nanoparticles. ACS Nano **3**, 3993–4002 (2009)
26. Y. Chen, J. Cao, H. Wei, Z. Wu, X. Wang, Y. Pei, Synthesis of polyvinyl alcohol/Ag electrospun nanofibers as highly efficient flexible SERS substrates. Vib. Spectrosc. **114**, 103246 (2021)
27. N. Chen, T. H. Xiao, Z. Y. Luo, Y. Kitahama, K. Hiramatsu, N. Kishimoto, T. Itoh, Z. Z. Cheng, K. Goda, Porous carbon nanowire array for surface-enhanced Raman spectroscopy. Nat. Commun. **11**, 4772 (2020)
28. Y. Kitahama, M. Funaoka, Y. Ozaki, Plasmon-enhanced optical tweezers for single molecules on and near a colloidal silver nanoaggregate. J. Phys. Chem. C **123**, 18001–18006 (2019)
29. S. Hagan, E. Martin, A. Enríquez-de-Salamanca, Tear fluid biomarkers in ocular and systemic disease: potential use for predictive, preventive and personalised medicine. EPMA J. **7**, 15 (2016)
30. M. Tamhane, S. Cabrera-Ghayouri, G. Abelian, V. Viswanath, Review of biomarkers in ocular matrices: challenges and opportunities. Pharm. Res. **36**, 40 (2019)
31. G. Ponti, M. Maccaferri, C. Ruini, A. Tomasi, T. Ozben, Biomarkers associated with COVID-19 disease progression. Critical Reviews. Clin. Lab. Sci. **57**, 389–399 (2020)
32. M. Samprathi, M. Jayashree, Biomarkers in COVID-19: an up-to-date review. Front. Pediatr. **8**, 607647 (2021)
33. G. P. Hancke, B. de C. E. Silva, G. P. Hancke Jr, The role of advanced sensing in smart cities. Sensors **13**, 393–425 (2012)
34. J.-H. Fu, Z. Zhong, D. Xie, Y.-J. Guo, D.-X. Kong, Z.-X. Zhao, Z.-X. Zhao, M. Li, SERS-active MIL-100(Fe) sensory array for ultrasensitive and multiplex detection of VOCs. Angew. Chem. Int. Ed. **59**, 20489–20498 (2020)
35. C. M. Wang, P. K. Roy, B. K. Juluri, S. Chattopadhyay, A SERS tattoo for in situ, ex situ, and multiplexed detection of toxic food additives. Sens. Actuators B Chem. **261**, 218–225 (2018)
36. T. Yang, Z. Zhang, B. Zhao, R. Hou, A. Kinchla, J. M. Clark, L. He, Real-time and in situ monitoring of pesticide penetration in edible leaves by surface-enhanced Raman scattering mapping. Anal. Chem. **88**, 5243–5250 (2016)
37. A. Kim, S. J. Barcelo, Z. Li, SERS-based pesticide detection by using nanofinger sensors. Nanotechnology **26**, 015502 (2015)
38. K. Walton, R. Walker, J. J. van de Sandt, J. V. Castell, A. G. Knapp, G. Kozianowski, M. Roberfroid, B. Schilter, The application of *in vitro* data in the derivation of the acceptable daily intake of food additives. Food Chem. Toxicol. **37**, 1175–1197 (1999)
39. R. L. Elder, Final report on the safety assessment of methylisothiazolinone and methylchloroisothiazolinone. J. Am. Coll. Toxicol. **11**, 75–128 (1992)
40. T. H. Kang, C. M. Jin, S. Lee, I. Choi, Dual mode rapid plasmonic detections of chemical disinfectants (CMIT/MIT) using target-mediated selective aggregation of gold nanoparticles. Anal. Chem. **92**, 4201–4208 (2020)

41. S. Jaitpal, S. R. Chavva, S. Mabbott, 3D printed SERS-active thin-film substrates used to quantify levels of the genotoxic isothiazolinone. ACS Omega **7**, 2850–2860 (2022)
42. T. Dhanani, T. Dou, K. Biradar, J. Jifon, D. Kurouski, B. S. Patil, Raman spectroscopy detects changes in carotenoids on the surface of watermelon fruits during maturation. Front. Plant Sci. **13**, 832522 (2022)
43. R. Hara, M. Ishigaki, Y. Kitahama, Y. Ozaki, T. Genkawa, Excitation wavelength selection for quantitative analysis of carotenoids in tomatoes using Raman spectroscopy. Food Chem. **258**, 308–313 (2018)
44. M. Ishigaki, P. Meksiarun, Y. Kitahama, L. Zhang, H. Hashimoto, T. Genkawa, Y. Ozaki, Unveiling the aggregation of lycopene in vitro and in vivo: UV–vis, resonance Raman, and Raman imaging studies. J. Phys. Chem. B **121**, 8046–8057 (2017)
45. J. Qin, K. Chao, M. S. Kim, Investigation of Raman chemical imaging for detection of lycopene changes in tomatoes during postharvest ripening. J. Food Eng. **107**, 277–288 (2011)
46. H. Schulz, M. Baranska, R. Baranski, Potential of NIR-FT-Raman spectroscopy in natural carotenoid analysis. Biopolymers **77**, 212–221 (2005)
47. J. Jehliča, H. G. Edwards, A. Oren, Raman spectroscopy of microbial pigments. Appl. Environ. Microbiol. **80**, 3286–3295 (2014)
48. M. R. C. Marques, R. Loebenberg, M. Almukainzi, Simulated biological fluids with possible application in dissolution testing. Dissolution Technol. **18**, 15–28 (2011)
49. F. Tian, L. F. d. C. e. S. d. Carvalho, A. Casey, M. S. Nogueira, H. J. Byrne, Surface-enhanced Raman analysis of uric acid and hypoxanthine analysis in fractionated bodily fluids. Nanomaterials **13**, 1216 (2023)
50. S. A. Bingham, C. Gill, A. Welch, A. Cassidy, S. A. Runswick, S. Oakes, R. Lubin, D. I. Thurnham, T. J. Key, L. Roe, K. T. Khaw, N. E. Day, Validation of dietary assessment methods in the UK arm of EPIC using weighed records, and 24-hour urinary nitrogen and potassium and serum vitamin C and carotenoids as biomarkers. Int. J. Epidemiol. **26**, S137–S151 (1997)
51. Y. Y. Broza, X. Zhou, M. Yuan, D. Qu, Y. Zheng, R. Vishinkin, M. Khatib, W. Wu, H. Haick, Disease detection with molecular biomarkers: from chemistry of body fluids to nature-inspired chemical sensors. Chem. Rev. **119**, 11761–11817 (2019)
52. T. Jiang, Y. Li, A. T. Layton, W. Wang, Y. Sun, M. Li, H. Zhou, B. Yang, Generation and phenotypic analysis of mice lacking all urea transporters. Kidney Int. **91**, 338–351 (2017)
53. M. Furuhashi, New insights into purine metabolism in metabolic diseases: role of xanthine oxidoreductase activity. Am. J. Physiol.—Endocrinol. Metab. **319**, E827–E834 (2020)
54. D. Brulé, G. Sarwar, L. Savoie, Changes in serum and urinary uric acid levels in normal human subjects fed purine-rich foods containing different amounts of adenine and hypoxanthine. J. Am. Coll. Nutr. **11**, 353–358 (1992)

# Chapter 9
# Non-plasmonic Metal Oxide Nanostructures for SERS Applications




**Eva Kočišová, Ondřej Kylián, and Marek Procházka**

**Abstract** Non-plasmonic metal oxide (MeO) nanomaterials have become very promising surface-enhanced Raman scattering (SERS) substrates due to their unique physicochemical properties. Although significantly fewer SERS applications of MeO substrates have been reported so far compared to plasmonic noble metals-based ones, SERS-active MeO platforms have some important advantages. Most importantly, MeO-based nanomaterials provide good biocompatibility, low biotoxicity, good spectral stability, as well as some of them also have strong photocatalytic activity. On the other hand, the main limiting factor for their applications is the low SERS sensitivity. However, as shown in recent studies, this can be substantially improved through rationally tuning resonance conditions for the target analyte and MeO substrate. Moreover, it may be promising to profit from a synergy of both the chemical and electromagnetic enhancement in the case of a combination of MeO materials with plasmonic noble metals. The recent SERS applications of MeO materials include the detection of anions, pesticides, pollutants, biomarkers, and employment in cancer diagnosis. This chapter provides background information on non-plasmonic MeO nanostructures and their SERS-related applications.

**Keywords** Raman scattering · Surface-enhanced Raman spectroscopy · Metal oxide · Semiconductors · Plasmonics · Charge transfer

E. Kočišová · M. Procházka (✉)
Faculty of Mathematics and Physics, Institute of Physics, Charles University, Ke Karlovu 5, 12116 Prague, Czech Republic
e-mail: marek.prochazka@matfyz.cuni.cz

O. Kylián
Faculty of Mathematics and Physics, Department of Macromolecular Physics, Charles University, V Holešovičkách 2, 18000 Prague, Czech Republic

© The Author(s), under exclusive license to Springer Nature Singapore Pte Ltd. 2024

M. Procházka et al. (eds.), *Surface- and Tip-Enhanced Raman Scattering Spectroscopy*,
https://doi.org/10.1007/978-981-97-5818-0_9

## 9.1 Introduction

In the last decades, surface-enhanced Raman scattering (SERS) spectroscopy has become a common spectroscopic technique with a rapidly growing number of applications in the chemical, material, and life sciences [1, 2]. Traditionally, various nanostructures primarily based on noble plasmonic metals (mainly silver and gold) are employed as SERS-active substrates, profiting from prominent localized surface plasmon resonance (LSPR), generating huge enhancement of the Raman signal of the target molecule. This electromagnetic (EM) enhancement can achieve $10^{10}$ orders of magnitude and allow ultrahigh SERS sensitivity. Recently, non-plasmonic nanostructures have been introduced as a promising alternative to conventionally used plasmonic metallic substrates [2–5]. Among various SERS-active non-plasmonic materials, e.g., graphene [6, 7], organic semiconductors [8, 9], chalcogenides [10, 11], MXenes [12, 13], the high attention is received nowadays by various metal oxides (MeO) and MeO-based nanomaterials.

MeO belongs to the most studied materials. They possess unique physicochemical and bio-related properties including physicochemical stability, high uniformity, high refractive index, and tunable band gap [14]. Thanks to these functional properties, MeO found applications in modern technological areas such as gas-, bio-, and chemical sensors, biomedical applications, catalysis and photocatalysis, energy harvesting, water cleaning or production of smart windows, etc. (e.g., [15–18]). The use of MeO for SERS thus further widens the impressive range of their possible applications.

The first reports revealing the SERS activity of MeO appeared in the 80's of the last century [19, 20]. Since then, numerous studies indicated that various MeO including ZnO, $Fe_3O_4$, $Cu_2O$, $MoO_2$, $WO_3$, $Ta_2O_5$, $Ti_3O_5$, $TiO_2$, and $V_2O_5$ may also be employed as platforms for SERS [21–23]. In the case of MeO, unlike plasmonic materials, the way in which the Raman signal is enhanced is markedly different. Although some EM mechanism (Mie resonance, exciton resonance, or even plasmon resonance) was proposed to potentially contribute to the SERS activity of MeO, it seems that the enhancing mechanism is in this case predominately connected with a chemical mechanism (CM) such as charge transfer (CT) process which increases the molecular polarizability tensor. CT occurs when the excitation wavelength is in resonance with the molecule-nanostructure CT transitions. This means that the highest occupied molecular orbital (HOMO) and the lowest unoccupied molecular orbital (LUMO) of the molecule that is adsorbed onto the nanostructure surface have to energetically match the valence and the conduction bands of the nanostructure. Two basic photoinduced CT mechanisms were proposed for the defect-free MeO as schematically depicted in Fig. 9.1.

In addition to purely CT process, Lombardi [24] proposed that the Mie resonances also could couple with the CT dipoles and the molecular or exciton dipoles, which may further optimize the enhancement factor (EF). Their studies showed that the Mie resonances occur in particle sizes around 100–300 nm, while the highly efficient CT resonances take place in particle sizes much smaller than 50 nm [25].

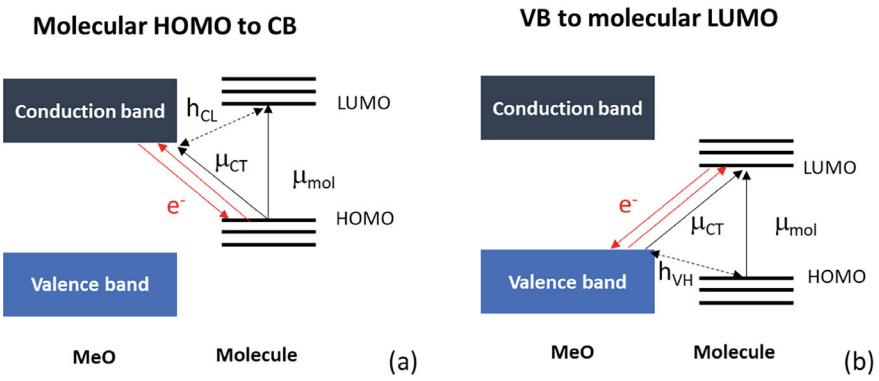



**Fig. 9.1** Basic mechanisms of photoinduced CT process (red lines) and coupling scheme (black lines). **a** The electrons are directly photoexcited from the molecular HOMO to the conduction band of a MeO. The electrons subsequently transit back to the vibrational ground energy level of a molecule which is accompanied by the emission of a Raman photon. The SERS intensity is "borrowed" from the molecular transition ($\mu_{mol}$) by the molecule-to-MeO transition ($\mu_{CT}$) through the Herzberg−Teller coupling term $h_{CL}$. **b** The electrons are photoexcited from the valence band of the MeO to the LUMO of the molecule. The electron quickly transits back to the valence band of a MeO releasing a Raman photon. In this case, the SERS intensity is "borrowed" from the molecular transition ($\mu_{mol}$) by the MeO-to-molecule transition ($\mu_{CT}$) through the Herzberg−Teller coupling term $h_{VH}$. More details as well as other possible mechanisms of the photoinduced CT process may be found in [2] or in chapter by W. Ji et al. in this book

Therefore, designing submicrometer superstructures, which are feasible for providing good Mie resonances and maintaining a highly efficient CT, is necessary to profit from the synergy of both effects.

Since non-plasmonic SERS nanostructures do not require well-designed hot-spots (strongly enhancing sites due to the EM mechanism) and the SERS enhancement is primarily connected with the CT mechanism, they provide better spectral reproducibility and reduced local heating upon laser irradiation in comparison with plasmonic materials [22, 23]. More importantly, the preparation of non-plasmonic substrates is in general cheaper than noble metals, especially if compared with gold, and they possess superior biocompatibility and chemical stability as compared to metallic SERS-active nanomaterials.

Furthermore, the non-plasmonic MeO nanostructures may be combined with plasmonic metals (Ag, Cu, and Au) to produce hybrid multicomponent metal/metal oxide (Me/MeO) nanostructures profiting from the advantages of both components. If the properties of such Me/MeO nanostructure are precisely tuned, it offers multifunctionality and/or enhanced functionality due to the mutual interactions of different MeO and Me constituent materials and analyte. In the case of SERS detection, hybrid Me/MeO nanomaterials produced utilizing chemical methods were already reported as efficient platforms to enhance the Raman signal. This is primarily due to the synergy of the EM enhancement coming from plasmonic metal and the CT process between Me/MeO nanostructures and analyte [26, 27]. In addition, the Me/MeO

heterostructures may pave the way for novel approaches for Raman scattering spectroscopy (e.g., photoinduced enhanced Raman spectroscopy (PIERS), see Chapter by K. Malek et al. in this book) as well as to produce recyclable SERS platforms, reducing thus further the costs associated with SERS. The main aim of this chapter is to summarize the state-of-the-art of MeO-based materials for SERS (Sect. 9.2) and to list their potential applications (Sect. 9.3).

## 9.2 Testing of MeO Substrates for SERS

### *9.2.1 Transition Metals*

An important class of SERS-active MeO is oxides of transition metals from groups IV, V, and VI of a periodic table of elements.

Concerning the oxides of transition metals from group IV, the prominent MeO in SERS is titania ($TiO_2$). $TiO_2$ was, together with NiO [20], the first reported SERS-active MeO material. In his pioneering study [19], Loo demonstrated in 1982 the possibility of obtaining SERS spectra of electrogenerated $I_2$ adsorbed onto a polycrystalline $TiO_2$ electrode. The possibility of employing $TiO_2$ nanoparticles (NPs) for SERS detection of pyridine was one year later also confirmed by Yamada and Yamamoto [28]. Since then, $TiO_2$ has become probably the most investigated MeO for SERS (e.g., [29–33]). As shown by numerous authors, the SERS performance of $TiO_2$ may be dramatically enhanced by the introduction of surface defects on $TiO_2$ nanomaterials induced by its doping (e.g., [34–37]). Such produced surface defects promote $TiO_2$-to-molecule CT that in turn leads to the higher SERS signal of 4-mercaptobenzoic acid (4-MBA) (Fig. 9.2).

In addition to its ability to enhance the Raman scattering, $TiO_2$ provides UV-induced self-cleaning performance through photoinduced degradation of adsorbed analytes, achieving the recyclability of the substrate [38]. It was first reported for rhodamine 6G (R6G) adsorbed on Ag-decorated $TiO_2$ nanotubes [39, 40]. Chong et al. [40] obtained a limit of detection (LOD) of R6G $10^{-8}$ M and observed that once the Ag/$TiO_2$ nanotube array is cleaned upon UV irradiation (140 min), it is possible to reach reproducible signals on further SERS measurements, as performed on R6G molecules, demonstrating the reusability three times. Kumar et al. [41] observed the same effect on $TiO_2$ nanorod (NR) arrays fabricated by glancing angle deposition. Yang et al. [42] reported a $TiO_2$ flower-like nanomaterial synthesized via a hydrothermal method that was subsequently Ag-decorated through electron beam evaporation. Such nanostructures exhibited high sensitivity for malachite green (MG) (LOD of $4.47 \times 10^{-16}$ M), high reproducibility with relative standard deviation (RSD) less than 13%, and three times recyclability after cleaning with UV radiation for 1 h. Zhu et al. [43] obtained LOD $10^{-7}$ M of formaldehyde on Ag-coated $TiO_2$ nanotube arrays and proved reusability three times after 20 min-cleaning with UV radiation. Wei et al. [44] reported $MoS_2$@$TiO_2$@Au platform which could rapidly

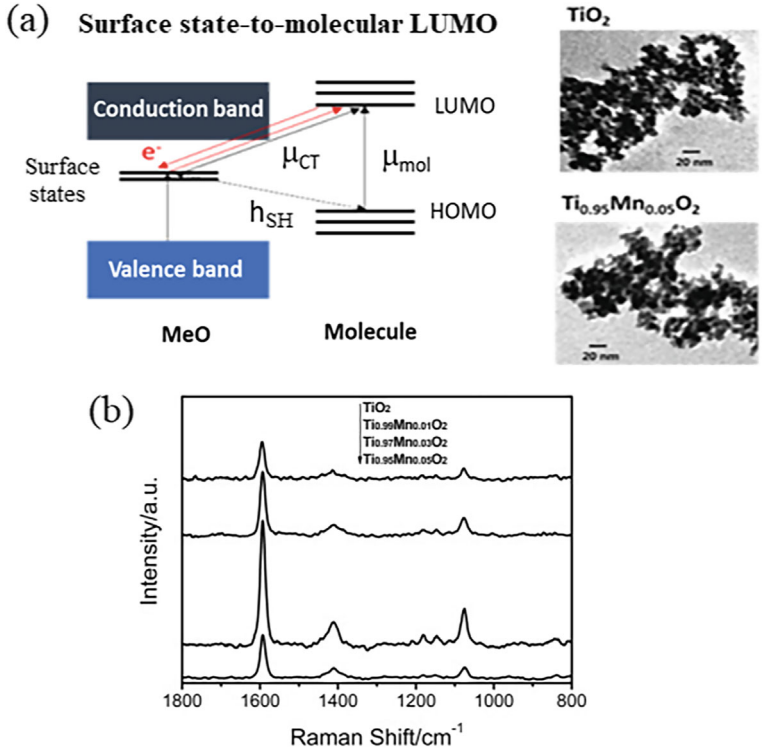



**Fig. 9.2** **a** Surface state-to-molecular LUMO (left). In this case, an electron is first excited from the valence band of a MeO to surface defects. Subsequently, the electron is excited to the LUMO of a molecule. Finally, the electron is transiting back to the surface defects in MeO, which is accompanied by the release of Raman photon. The SERS intensity is "borrowed" from the molecular transition ($\mu_{\mathrm{mol}}$) by the surface state-to-molecule transition ($\mu_{\mathrm{CT}}$) through the Herzberg−Teller coupling term $h_{\mathrm{SH}}$. TEM images of $TiO_2$ and $Ti_{0.95}Mn_{0.05}O_2$ NPs (right). **b** Recorded SERS spectra of 4-MBA molecules adsorbed on the $TiO_2$ and Mn–$TiO_2$ NPs. Adapted with permission from Xue et al. [34]. Copyright 2012 Elsevier

degrade 90.7% of crystal violet (CV) in 120 min under solar light irradiation. The platform could also be reused five times due to the unique integrated merits of the $MoS_2$@$TiO_2$@Au heterojunction.

In our recent study [45], we compared the SERS performance of Ag/$TiO_2$ coatings with three different architectures of $TiO_2$ base layer—planar, tubular, and NPs-based—prepared by means of plasma-assisted techniques. Our results showed that the highest SERS signal of methylene blue (MB) was observed for planar $TiO_2$ film decorated with Ag, followed by a $TiO_2$ NPs array coated with Ag nanoislands and anodized sputter deposited $TiO_2$ nanotubes capped with Ag nanoislands. This was explained by the differences in the surface coverage by Ag nanoislands. On the other hand, only the nanostructured substrates (nanotubular and NP-based) provide recyclability after cleaning with UV irradiation. The effect of photocatalytic self-cleaning

is attributed to $TiO_2$ crystallinity and enhanced effective surface area of nanostructured substrates. The $TiO_2$ NP films decorated with Ag nanoislands offered the best trade-off between SERS enhancement (LOD $5 \times 10^{-9}$ M MB) comparable with the commonly used Ag nanostructures and the possibility of multiple uses (three times). These highly porous Ag/$TiO_2$ coatings are composed of $TiO_2$ spherical NPs (diameter ~ 50 nm) homogenously seeded from the top by the nanometer-sized and well-separated individual Ag nanoislands (Fig. 9.3a). According to XRD, the $TiO_2$ NPs are characterized by the presence of mixed phases—rutile, brookite, and anatase. The Raman signal of $1 \times 10^{-6}$ M MB (Fig. 9.3b, top) disappeared after UV irradiation (Fig. 9.3b, middle), and such cleaned surface may be reused for new measurement providing again the SERS spectra comparable to the spectra acquired using as-deposited NP Ag/$TiO_2$ surfaces (Fig. 9.3b, bottom). Moreover, the 2D maps (40 μm × 30 μm, 2 μm step) of the intensity of MB peak at 1624 $cm^{-1}$ showed good reproducibility of the measurements performed both on the freshly deposited MB droplet and measurements on the UV-cleaned surfaces.

$TiO_2$-based nanomaterials combined with plasmonic metals may also be used for a relatively recently developed PIERS technique [46], in which the $TiO_2$ is activated via UV irradiation. Oxygen vacancies formed in $TiO_2$ upon its exposure to UV light cause a substantial improvement of the Raman signal by facilitating the CT between the photoirradiated oxide semiconductor film and analyte molecules via metallic nanostructures deposited on the surface. As shown by Shondo et al. [47] the proper design of $TiO_2$/Ag substrate may lead not only to approximately 50-fold enhancement of SERS signal after UV pre-irradiation but also provide a high photocatalytic degradation of analytes, allowing its reuse without any loss of PIERS activity. More details concerning the PIERS are presented in chapter by K. Malek et al. in this book.

Besides $TiO_2$, SERS activity was also obtained on $Ti_3O_5$ [48]. This novel quasi-metallic material is fabricated by reducing the semiconducting $TiO_2$ microspheres (Fig. 9.4). We mention that it is a MeO nanostructure, but it provides a strong LSPR effect. The results showed that such produced γ-$Ti_3O_5$ offers a 10,000-times increase in SERS sensitivity compared to $TiO_2$ microspheres, and the lowest detectable limit is up to $10^{-10}$ M for R6G. This new type of non-noble metal SERS substrate can withstand high-temperature oxidation at 200 °C and strong acid–base corrosion without performance degradation. Benefiting from its excellent ability of visible-light photocatalytic degradation of organic molecules, the substrate can be reused as well.

Another perspective transition MeO semiconductor substrates for SERS spectroscopy from group V are vanadium oxides ($VO_2$, $V_2O_5$). Miao et al. [49] performed a study of the phase transition-induced Raman enhancement on $VO_2$ nanosheets of different crystal symmetry. They found that an increase in the crystal symmetry from $VO_2$(B) to $VO_2$(M) and $VO_2$(R) results in a dramatic decline in the enhancement ability of the probe dye molecules. On defect-rich $VO_2$(B) nanosheets, a detection limit as low as $10^{-7}$ M can be reached for various dye molecules. This study strongly indicates that a synergetic strategy of low-dimension and low-symmetry may be a new path for the design of highly efficient MeO-based semiconductor SERS substrates.

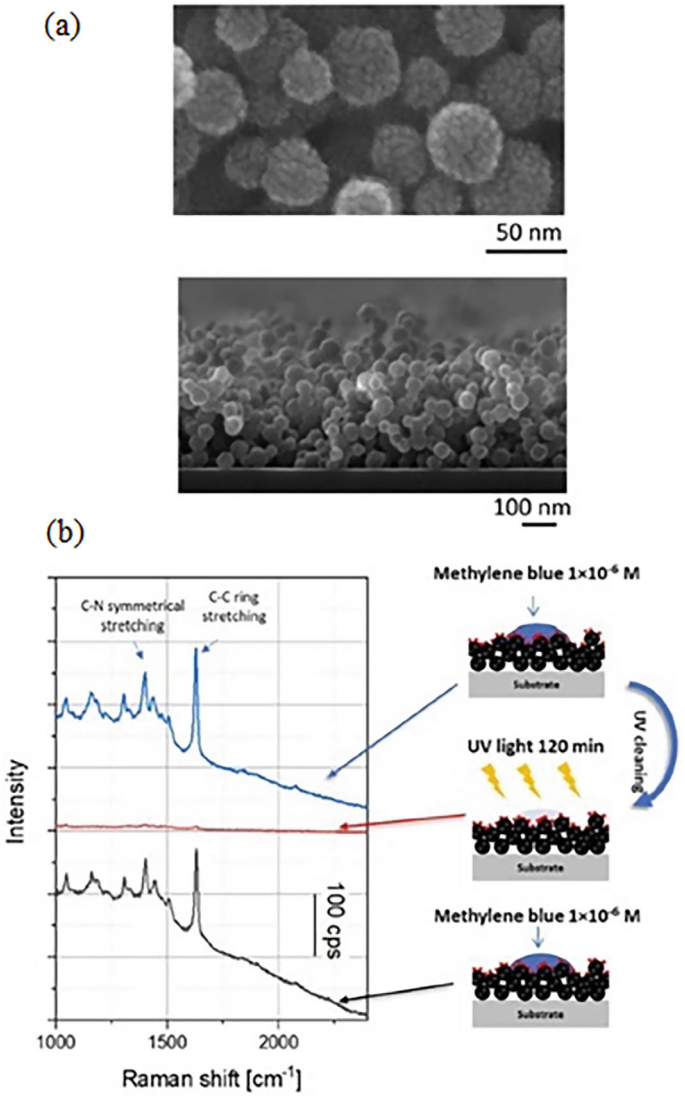



**Fig. 9.3** **a** SEM images of top-view and cross-section of Ag/$TiO_2$ substrates based on $TiO_2$ NPs decorated with Ag nanoislands. **b** SERS spectra of $1 \times 10^{-6}$ M MB on the as-deposited substrate (top), SERS spectra recorded after 2 h irradiation by UV light (middle) and SERS spectra acquired after spotting and drying fresh MB containing droplet on UV-cleaned substrate (bottom). Reprinted with permission from [45]. Copyright 2022 Elsevier

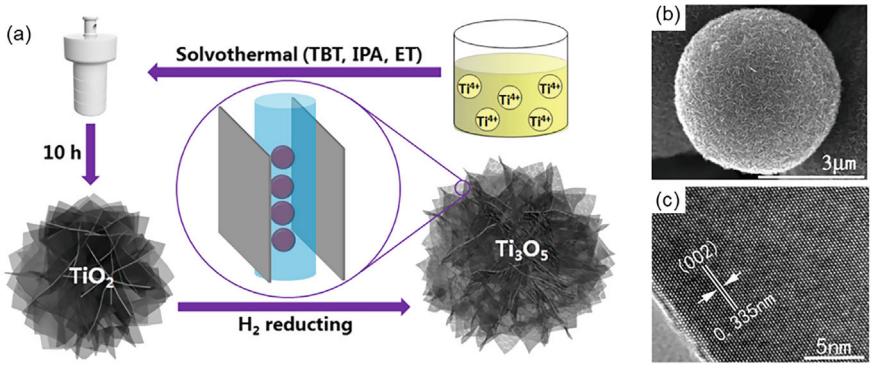



**Fig. 9.4** **a** Synthetic route of the γ-$Ti_3O_5$ hierarchical microspheres. **b** SEM image of the as-synthesized γ-$Ti_3O_5$ hierarchical microspheres. **c** HRTEM image of the highly crystalline γ-$Ti_3O_5$ nanosheets. Adapted with permission from [48]. Copyright 2019 American Chemical Society

Guan et al. [50] synthesized $VO_2$ (D) nanostars and nanospheres with highly dense and rough surfaces. They exhibited high SERS activity for R6G (the detection limit as low as $10^{-9}$ M).

Concerning $V_2O_5$, it is readily available and the most stable form of the vanadium oxides family with a huge application potential including energy storage and harvesting, catalysis, and sensing. The applicability of $V_2O_5$ NPs as SERS-active material was first reported in 2015 by Pan et al. [51]. These authors employed a microwave-assisted hydrothermal reduction combined with subsequent annealing treatment to produce $V_2O_5$ NPs of different sizes (from 42 to 87 nm) and found that such prepared NPs are suitable for SERS detection. It was found that the smaller the $V_2O_5$ NPs led to the higher SERS activity. The $V_2O_5$ NPs with the size of 42 nm demonstrated the lowest detection limit of R6G ($10^{-8}$ M). The SERS activity in detecting R6G was also excitation wavelength-dependent, and the 532 nm laser represented optimal conditions. The SERS activity was explained by the CT process between $V_2O_5$ NPs and R6G molecules.

The applicability of $V_2O_5$ for highly sensitive SERS detection was recently improved by Ji et al. [52], where an EF of $1.18 \times 10^6$ was reported for MB adsorbed on $V_2O_5$ hollow-shelled spherical microstructures due to multiple synergistic enhancement. Three types of $V_2O_5$ microstructures double-shelled hollow spherical (DS-V), single-shelled hollow spherical (SP-V), and lamellar one (S-V), were fabricated and compared. The excellent SERS activity was attributed to the unique DS-V structures, possessing a light-trapping effect on EM waves that can provide efficient exciton absorption and photoinduced CT. The coupling of inner and outer shells generated a much higher electric field contribution for SERS enhancement compared to SP-V and S-V microstructure (see theoretical simulation in Fig. 9.5a for 532 nm excitation). Besides, a high-order resonant mode was excited for the 532 nm excitation, indicating that the light-trapping efficiency with the 532 nm excitation is higher than that with the 785 nm excitation. The EF obtained from experiments and that

calculated from the electric field (Mie contribution) exhibit the same variation trends (Fig. 9.5b, c). Compared with S-V, the EF of Mie resonance of DS-V increases by a factor of 50 with the excitation of 532 nm. In the experiment, the value of EF for DS–V was approximately 30 times larger than that on S-V, which is similar to the enhancement amount of EF of Mie resonance. Therefore, the synergy of all factors contributed to a significant increase in SERS sensitivity. Both experiments and simulations showed that the double-shelled $V_2O_5$ spherical microstructure exhibits the best SERS performance with the detection limit of MB $5 \times 10^{-9}$ M and EF value of $1.18 \times 10^6$.

In both above-mentioned studies on $V_2O_5$ NPs, the SERS-active system was prepared by disperging $V_2O_5$ NPs in a liquid solution containing analyte molecules, followed by washing and drying steps, which is challenging for routine testing. In our recent study [53], we demonstrated the feasibility of $V_2O_5$ NP films prepared using

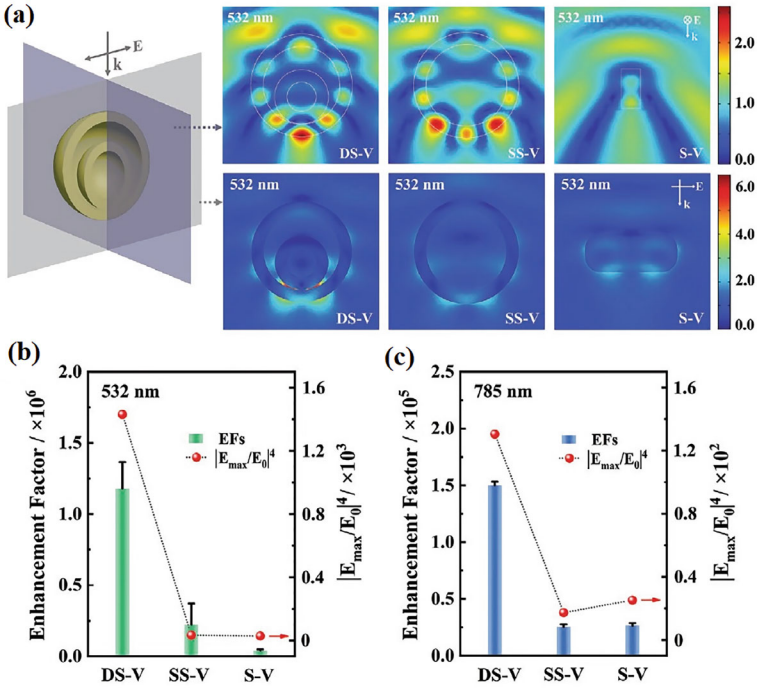



**Fig. 9.5** **a** Spatial maps of EM near-field distribution around single double-shelled hollow spherical (DS-V), single-shelled hollow spherical (SP-V), and lamellar one (S-V) microstructure with the 532 nm excitation simulated through finite element analysis. The incident direction and the polarization are shown in the corresponding images. EF of MB adsorbed on the three kinds of $V_2O_5$ microstructures with the **b** 532 and **c** 785 nm excitations. Cylinders represent the EF obtained from the experimental data, while spheres represent the calculated estimate of EF from the electric field. Reprinted with permission from [52]. Copyright 2021 Wiley

a facile and time-effective, solvent- and linker-free deposition procedure to fabricate a reliable and sensitive solid-state SERS-active platform. It was produced by the gas-phase synthesis of vanadium NPs followed by their thermal annealing [54]. The SERS performance of $V_2O_5$ NP films was found to be strongly linked with porosity and the appropriate crystalline structure adjusted by annealing. A Raman spectroscopy and X-ray diffraction revealed that $V_2O_5$ crystalline NPs are formed only after the annealing at temperatures equal to or higher than 300 ˚C. Such produced $V_2O_5$ NP films allow for sensitive and reproducible detection of organic dyes: MB (detection limit of $5 \times 10^{-8}$ M), R6G, and CV. To compare the SERS activity of $V_2O_5$ films and $V_2O_5$ NPs, the vanadium NPs were deposited through a Si mask onto a smooth magnetron-sputtered vanadium film. Such patterned surface with spots of vanadium NPs (25 μm in diameter, center-to-center distance of 60 μm) was subsequently annealed at 450 ˚C to obtain the $V_2O_5$ phase. This preparation resulted in a homogeneous crystal structure over the sample but in two different morphologies: relatively smooth zones that correspond to sputtered films and highly porous zones composed of $V_2O_5$ NPs (Fig. 9.6a). Using mapping of the SERS signal, the patterned surface allowed a direct comparison of the SERS performance of smooth and porous $V_2O_5$ without possible uncertainties connected with the preparation of MB solution or acquisition of SERS spectra per se. The result of this experiment, which is depicted in Fig. 9.6b for $1 \times 10^{-6}$ M MB, fully highlights the importance of nanostructuring of $V_2O_5$ for SERS enhancement: although the weak SERS bands of MB were detectable also in the NPs-free zones, the SERS signal is significantly higher when acquired from the positions on the sample that contained $V_2O_5$ NPs. Although the produced $V_2O_5$ NP films do not reach the SERS activity comparable to commonly used plasmonic platforms containing hot-spots or DS-V structures developed by Ji et al. [52], their stability and spectral reproducibility (RSD about 11%) are considerable advantages and thus represent an interesting alternative to plasmon-based materials. Furthermore, another aspect that is worth stressing is the fully solvent- and linker-free character of the investigated procedure for fabricating $V_2O_5$ SERS-active coatings, making it environmentally benign.

Similarly to $TiO_2$, an intriguing approach could be the combination of non-plasmonic $V_2O_5$ and plasmonic materials. A Cu/$V_2O_5$ composite was obtained via a simple and time-saving microwave-assisted reduction method from a single-source precursor, copper vanadate [55]. This composite exhibited excellent SERS sensitivity and reproducibility for both R6G ($1.0 \times 10^{-7}$ M) and 4-MBA ($1.0 \times 10^{-5}$ M) probe molecules, with an EF of $1.9 \times 10^6$ for R6G. Our preliminary results show that the $V_2O_5$ NPs decorated with plasmonic Au nanoislands significantly enhanced the SERS signal of MB as compared to Au nanoislands or $V_2O_5$ NPs alone. Such an enhancement is believed to benefit from the mutual interaction of plasmonic metals with semiconducting MeO and their nanostructured character.

The notable examples of transition metals from group VI, whose oxides exhibit SERS activity, are tungsten and molybdenum. Concerning the tungsten oxides, mainly the sub-stoichiometric $WO_{3-x}$ oxides seem to be promising for SERS applications as the tungsten trioxide, $WO_3$, only gave extremely weak Raman signals of R6G [56]. In contrast, $W_{18}O_{49}$ produced by the artificial creation of oxygen vacancy

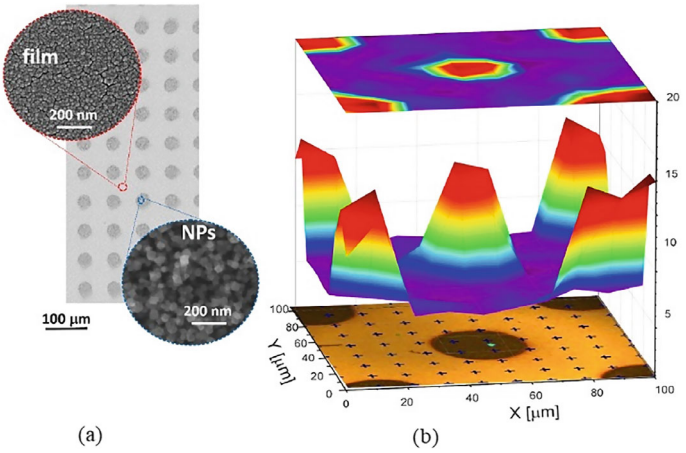



**Fig. 9.6** **a** SEM image of magnetron-sputtered vanadium film regions decorated with vanadium NPs alongside magnified NPs-free and NPs-containing zones. **b** Spatial map of SERS signal corresponding to 1624 $cm^{-1}$ of MB measured on patterned NPs-free/NPs-containing surface. For better clarity, the optical image of the surface is presented at the bottom of the graph. Reprinted with permission from [53]. Copyright 2024 Elsevier

by annealing (at 300 °C temperature) in an inert or reducing atmosphere ($Ar/H_2$) showed a large EF ($3.4 \times 10^5$) and low detection limit of $10^{-7}$ M for R6G [56], which is due to the strong CT between $W_{18}O_{49}$ and R6G molecule. In another study, Zhou et al. [57] demonstrated an electrical control of SERS enhancement based on a $WO_{3-x}$ surface deposited on a $SiO_2/Si$ substrate. This SERS improvement is realized by better CT between the oxide surface and the studied molecules rhodamine B (RhB) due to an electric field that introduced oxygen vacancies in a tungsten oxide surface. A programmed current of leakage equal to 1 mA was found to be optimal for enhancing the SERS signal. A LOD of 0.1 µM RhB and an EF of $1.2 \times 10^6$ were obtained. Wei et al. [58] reported the SERS performances of Ag nanowires (NW) decorated with $WO_{3-x}$ quantum dots ($WO_{3-x}$ QD/AgNW). The SERS activity was investigated by using MB molecules and LOD 1 µM was reached.

In the case of $MeO_3$, He et al. [59] investigated the SERS substrates based on large-size, few-layered $MoO_3$ nanosheets deposited on a $SiO_2/Si$ substrate. Authors demonstrated that the decrease of $MoO_3$ layer number converted the intrinsic $MoO_3$ from non-SERS active to sensitive SERS substrate, with LOD of $2 \times 10^{-8}$ M for R6G. SERS enhancement was due to a CT when the thickness of these nanosheets was reduced and was further enhanced *via* atomic intercalation in the van der Walls gap. Moreover, the SERS of $MoO_3$ showed high homogeneity with RSD as small as 2.95%, The Raman intensity of R6G on the SERS substrate remained higher than 90% after storage in the atmosphere for 160 days, demonstrating excellent air stability.

In addition to the above-mentioned examples of transition MeO from groups IV, V, and IV, the SERS activity was observed also for $ZrO_2$ [60–62], $Nb_2O_5$ [63, 64],

and $Ta_2O_5$ [65]. The only MeO from groups IV, V, and VI for which SERS activity was, to our best knowledge, so far not observed is thus chromium and hafnium oxide. However, $HfO_2$ is due to its strong chemical resistance, high melting point, high thermal conductivity, and optical transparency, a valuable material used as a protective shell for plasmonic SERS-active metals [66].

### *9.2.2 Oxides of Heavy Metals and Lanthanides*

Although high attention is nowadays devoted to SERS of transition metal oxides, also oxides of heavy metals were successfully employed for SERS applications. For instance, zinc oxide (ZnO) nanocrystals (20 nm size) displayed an EF of $10^3$ with a 4-mercaptopyridine (4-MPy) [67]. These authors conclude that only the CT is most responsible for the observed enhancement while plasmon resonances were excluded. Wei et al. remarkably improved EF for ZnO substrates by designing submicrometer-sized spherical ZnO superstructures due to the synergy of CT and Mie resonance [68]. The secondary superstructures of ZnO particles with a uniform diameter in the range of 220–490 nm were formed by aggregating primary single crystallites with size of approximately 13 nm (Fig. 9.7). A highly efficient CT contribution derived from the primary structure of the ZnO nanocrystallites enhanced the SERS signal. The threshold energy for the charge injection from the ZnO/4-MPy complex into the ZnO was estimated to be 2.20 eV. It was found that the degree of CT ($p_{CT}$) values (defined in [69]) obtained with the 532 nm (2.33 eV) excitation are significantly larger than those with the 633 and 785 nm ones (Fig. 9.7g).

The 532 nm excitation wavelength has sufficient energy to excite the CT, and thus, the non-totally symmetric modes are selectively enhanced by the CT mechanism through the Herzberg–Teller coupling term. Furthermore, at a specific excitation wavelength, the $p_{CT}$ values for all ZnO superstructures were approximately constant, indicating that the CT contribution mainly originates from these primary single crystallites and that the particle size dependence of the SERS enhancement cannot be derived from the CT contribution. Moreover, with 532 nm excitation, both CT and Mie resonance have significant contributions to the SERS enhancement of 4-MPy. The maximum field enhancement was about 13 for the 353 nm diameter ZnO, and thus, the Mie resonance EF was estimated to be $10^2$. Therefore, the synergistic effect of Mie resonances and CT resonances provides a total Raman EF of $10^5$. This EF is one of the highest among these reported for semiconductor substrates and non-resonant molecules.

Highly interesting for SERS applications are iron oxides. As shown, $\alpha$-$Fe_2O_3$ nanocrystals enhance the Raman signal of 4-Mpy with an EF of $10^4$ because of CT between the $\alpha$-$Fe_2O_3$ nanocrystals and the 4-Mpy molecule [70]. Fu et al. [71] reported the possibility of detecting sub-micromolar and nanomolar concentrations of 4-Mpy on adsorbed on $\alpha$-$Fe_2O_3$ NPs. However, the popularity of iron oxides is

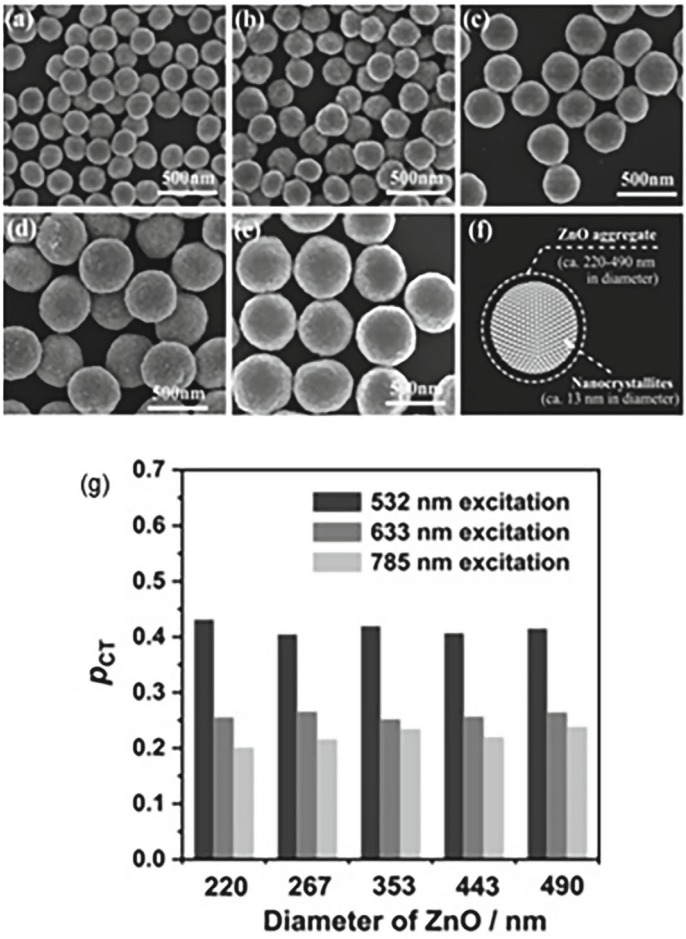



**Fig. 9.7** SEM images of ZnO superstructures. The average diameters of the superstructures are **a** 220, **b** 267, **c** 353, **d** 443, and **e** 490 nm. **f** A diagram that illustrates the microstructure of a ZnO particle comprised of closely packed nanocrystallites. **g** Degree of charge transfer ($p_{CT}$) as functions of ZnO particle size and excitation wavelength. Adapted with permission from [68]. Copyright 2019 Wiley

predominately connected with their magnetic properties. Because of this, $Fe_2O_3$/ plasmonic metal nanostructures may combine a high SERS performance with the possibility to capture the target analyte, concentrating it, and generate unique hot-spots for superior enhancement without centrifugation and/or filtering [72–76]. Kang et al. [73] used a hybrid nanocomposite that consists of plasmonic Au NPs and super-paramagnetic iron oxide ($Fe_3O_4$) NPs supported on bacterial cellulose nanocrystals (BCNCs) for rapid and sensitive detection of MG isothiocyanate (MGITC) at concentrations as low as $10^{-10}$ M. Berganza et al. [76] developed Au/ $Fe_2O_3$ core–shell NR-like nanomaterial applicable as colloidal SERS sensing substrates with magnetic




**Fig. 9.8** Schematic representation of the measurement procedure, by adding the NR@Au to an analyte-containing solution, magnetic separation and accumulation, and Raman measurement at the pellet spot. Reprinted with permission form [76]. Copyright 2022 American Chemical Society

capture and accumulation of 4-MBA (LOD ~50 nM) and of antibiotic ciprofloxacin (LOD ~ 100 nM) (Fig. 9.8).

While metallic copper is a well-known plasmonic material, its rapid oxidation in air was often considered a limiting factor for its use in SERS applications. However, copper oxides ($Cu_2O$ and CuO) were found to be SERS-active. For example, SERS spectra of 4-MBA were obtained from $Cu_2O$ nanospheres and EF was estimated to be as high as $10^5$ [77]. In addition, in the case of $Cu_2O$/Cu core–shell NPs, the SERS enhancement besides CT benefits also from the contribution of EM plasmonic mechanisms of the Cu metallic core [78].

An example of SERS-active lanthanoid oxide is ceria ($CeO_2$). In this case, it was demonstrated that the SERS enhancement is highly facet-dependent [79]. $CeO_2$ is a broadband gap semiconductor that is not conducive to CT. However, if facet junctions are formed, charge separation is facilitated which in turn promotes CT between the $CeO_2$ and adsorbed molecule. As shown, the presence of homojunction between {100} and {111} facets allows EF for MB in the order of $10^6$ and the detection of adenosine triphosphate in nanomolar concentrations.

## 9.3 Selected SERS Applications on MeO Substrates

### *9.3.1 Electrochemistry Studies*

MeO materials are in general biocompatible and have frequently been proposed as ideal surfaces for the immobilization of biomolecules for instance in redox electrochemistry studies of proteins.

A nanostructured $TiO_2$ electrode was used to probe the electron-transfer process of Cyt $b_5$ [80]. The electrode surface comprised half-ellipsoidal $TiO_2$, which was fabricated by the simple anodization of Ti foils. $TiO_2$ electrodes can be used directly for the biocompatible immobilization of proteins without further modifications, compared with metal electrodes. According to the SERS spectra measured at different electrode potentials, the protein oxidation marker band located at 1374 $cm^{-1}$ (oxidized state) shifted to 1360 $cm^{-1}$ (reduced state), indicating a redox protein process has occurred. Later, these authors extended their studies with a new type of $TiO_2$ electrode with nanotubular geometry where the high electric field contribution to SERS was

attributed to the multiple scattering and interference effects within the nanotubes [81]. The SERS signal of Cyt $b_5$ was approximately 10 times higher than that observed on the $TiO_2$ electrodes with half-ellipsoidal geometries.

Alessandri et al. [82] demonstrated that $SiO_2$-$TiO_2$ core–shell colloidal crystals can be used as a SERS sensor to monitor the glutathione (L-γ-glutamyl-cysteinyl-glycine, GSH) redox cycle at physiological concentration in an aqueous environment. When GSH is oxidized to its disulfide derivative, the signal of SH stretching disappears in the SERS spectrum. Thus, the GSH oxidation process can be monitored. Chen et al. [83] found that $K_2Ti_6O_{13}$ NWs were ideal biocompatible substrates for protein immobilization. The SERS signal corresponding to the reduced form of Cyt c was clearly observed when Cyt c was attached to the surface of the $K_2Ti_6O_{13}$ NWs. Molecular dynamics simulations proved the CT from $K_2Ti_6O_{13}$ to the Fe center of heme.

### *9.3.2 Detection of Ions and Small Molecules*

MeO substrates were used to detect various ions in aqueous solution.

Ji et al. [83] designed a simple SERS sensor based on the $TiO_2$ surface for the detection of phosphate anions. Pyrocatechol was adsorbed on a $TiO_2$ surface *via* a bidentate chelation mode, resulting in the formation of a new ligand-to-metal CT transition. The chelation between pyrocatechol and colloidal $TiO_2$ NPs was inhibited when phosphate anions preadsorbed on the colloidal $TiO_2$ NP surface under acidic pH conditions, resulting in a gradual decrease in the SERS intensity of the pyrocatechol molecule. In this way, a quantitative analysis of phosphate anions was achieved. As an extended study [84], they employed the $TiO_2$ NPs to detect Cr(VI) in water. In this case, they profited from the SERS mechanism of alizarin red (AR)–$TiO_2$ complexes and found that the strong electronic coupling between AR and colloidal $TiO_2$ NPs gives rise to the formation of a ligand-to-metal CT transition. Colloidal $TiO_2$ NPs were used as active catalyzers to induce the self-degradation of the adsorbed Raman probes in the presence of Cr(VI). The sensitivity and linearity of this sensing system were evaluated with different concentrations of Cr(VI) (Fig. 9.9a). The spectral intensities were normalized to that of the signal from 2-propanol at 816 $cm^{-1}$. The normalized Raman intensity at 1260 $cm^{-1}$ *versus* the Cr(VI) concentration is shown in Fig. 9.9b. The inset plots the relative Raman intensity $[(I_{R0} - I_R)/I_{R0}]$ in the low concentration range. A good inverse proportionality was observed between the SERS intensity and the amount of Cr(VI) in the concentration range of 0.6–10 μM. The lowest concentration at which Cr(VI) could be detected was 0.6 μM. This concentration is lower than the maximum level of Cr(VI) in drinking water allowed by the WHO. In addition, the water samples spiked with different concentrations of Cr(VI) were also measured by employing our sensing system. The measurements, which accurately reported the concentrations of the added standard Cr(VI) with good recoveries, confirmed that the sensing system proposed in this work has great potential for the quantitative analysis of Cr(VI) in environmental samples.

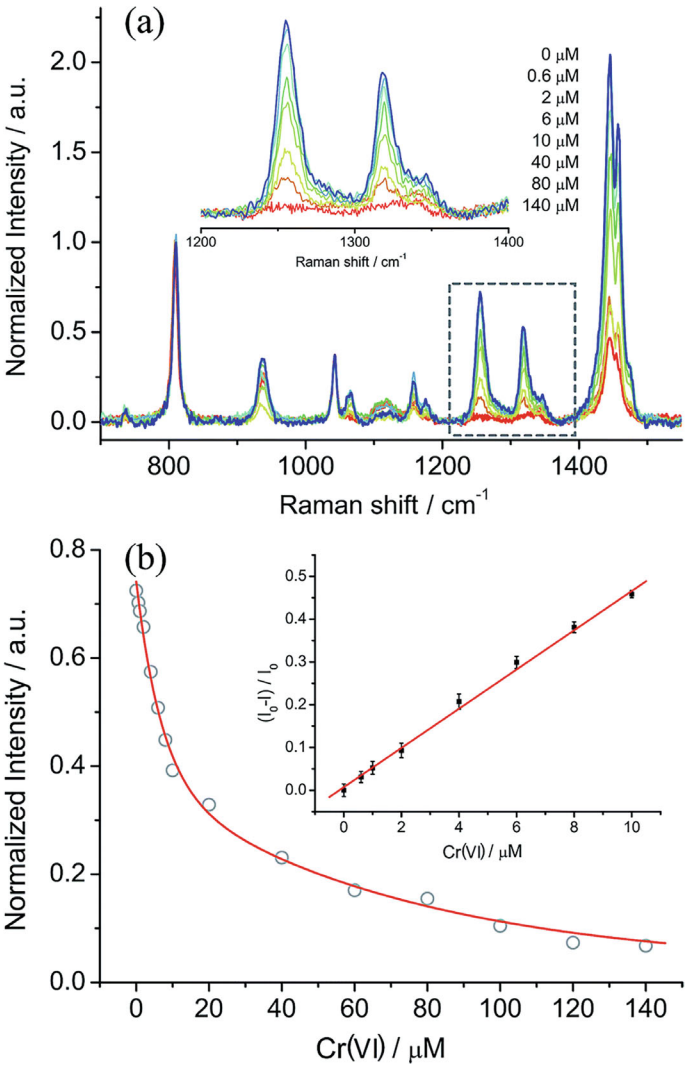



**Fig. 9.9** **a** SERS spectra of AR–$TiO_2$ complexes (50 μM AR) in the absence and presence of Cr(VI) with different concentrations. **b** The normalized Raman intensity at 1260 $cm^{-1}$ *versus* the Cr(VI) concentration. The inset shows the relative Raman intensity $[(I_{R0} - I_R)/I_{R0}]$ in the low concentration range. Reprinted with permission from [84]. Copyright 2015 The Royal Society of Chemistry

Concerning other small molecules, the $SiO_2$@$TiO_2$ NPs allowed the detection of $CO_2$ [85]. Typical Raman peaks of $CO_2$ were observed at 1388 and 1286 $cm^{-1}$. In addition, the Raman intensity of the $CO_2$ peaks was inversely related to the temperature, which is in accordance with previous findings on the adsorption and thermal desorption of $CO_2$ bound to the $TiO_2$ surfaces. The high sensitivity indicates that these $SiO_2$@$TiO_2$ NPs beads have immense potential for the development of SERS-based sensing systems for monitoring environmental $CO_2$ over a wide temperature range. The catalytic activity of some of the MeO substrates was used not only to detect but also to degrade toxic analytes. Mesoporous $TiO_2$ NPs, functionalized by p-aminothiophenol, were used to capture toxic anilines and phenols by azo coupling [86]. Loading these nanodevice with Ag NPs offers the possibility for a sensitive quantitative determination of target compounds by SERS spectroscopy. Sensitivity and selectivity can be further enhanced by concentrating the hybrid particles with an external magnet and compound-specific binding (anilines *vs.* phenols).

The bound toxic compounds can be degraded by $TiO_2$-assisted photocatalysis after the removal of the loaded hybrid particles from the sample solution with an external magnet. Furthermore, the degradation process was found to be enhanced in the presence of plasmonic Ag nanostructures.

In another MeO (ZnO)-Ag nanostructure, ZnO nanofibers deposited on silver foil were fabricated [87]. The strong interactions between ZnO nanofibers and silver foil afford continuous delocalized surface plasmons, generating a large EM field enhancement at the gap between the ZnO nanofibers and silver foil. This ZnO-Ag nanostructure exhibited enhanced photocatalytic activity toward the degradation of organic pollutants due to the charge separation effect and an increase in the lifetime of the photogenerated excitons under UV light irradiation.

### *9.3.3 Detection of Pollutants*

The pollutants (such as pesticides) and other air- or water-contaminants are a group of molecules often studied by SERS. The use of MeO and hybrid Ag/MeO substrates not only provides sensitive SERS detection but can also be used for in situ detection of photodegradation of pollutants.

For example, Zhang et al. [88] prepared a plasmonic $MoO_2$ nanosphere as a highly sensitive SERS substrate for the detection of various pesticides: clenbuterol hydrochloride (known as lean meat powder in China) and methyl parathion (a common pesticide). This new non-noble metal substrate material shows a high detection limit of $10^{-8}$ M and exhibits great near-field enhancement with one of the highest EF of $4.8 \times 10^6$. More importantly, the oxide with intermediate valence displays unexpected ultrahigh stability, which can withstand the corrosion of strong acid and strong alkali as well as high-temperature oxidation in air at 150 °C. Moreover, the authors have attempted to successfully test a series of multicomponent samples (R6G, MB, methyl orange) by using the $MoO_2$ nanospheres. Liang et al. [89]

detected paraquat with a LOD of 275 μg/L on a CuO substrate of special shape (so-called balsam pear) ensuring dense NP protuberance and consequently, higher SERS enhancement. Moreover, Quan et al. [90] successfully prepared $MoS_2/TiO_2$ substrate to detect trace amounts of harmful substances including MG, bisphenol A, and endosulfan (LOD $10^{-8}$ M).

Thirumalairajan and Girija [91] used Ag-assembled $CeO_2$ microspheres constituting nanospheres and nanospindles of the average size of approximately 56 and 32 nm. First, the adhesive tape was made immobile on the glass substrate. Then, 10 μl of the $5 \times 10^{-3}$ M concentration of the shape different $Ag/CeO_2$ nanostructure solutions were tumbled uniformly onto the sticky side of the tape. The prepared substrate was dried at 30 °C for 2 h and used for additional analysis. The detection of thiram on the surface of an apple using such nanosphere and nanospindle SERS-active substrate achieved a wide detection range from $10^{-2}$ to $10^{-9}$ M (Fig. 9.10). The correlation coefficient of 0.9929 as well as LOD 27 nM were better for the $Ag/CeO_2$ nanospindles, when compared to 0.9907 and 30 nM for the nanospheres. In addition, the CT mechanism between the $Ag/CeO_2$ nanostructures and thiram molecules has also been proposed.

Shi et al. [92] used a robust SERS sensor based on $ZrO_2@TiO_2/Ag$ substrate profiting from the synergetic effects of MeO-derived porous heterostructure-induced CT enhancement and the EM enhancement from the plasmonic Ag NPs. They were able to detect pesticides triazophos and fonofos at low concentrations ($10^{-8}$ M). The SERS substrate exhibited long-term stability and signal homogeneity for SERS quantitative analysis. They simulated the quantitative detection of pesticide residues on real objects by spraying pesticides on plant leaves, followed by transferring them

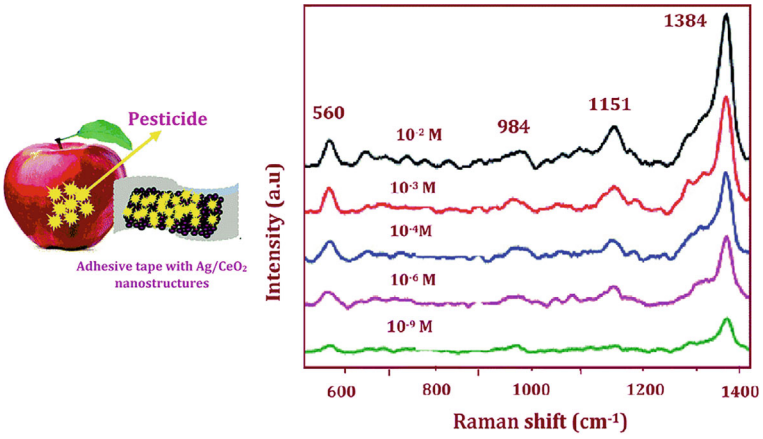



**Fig. 9.10** Schematic illustration of detection of the pesticide residues and SERS spectra of thiram on apple peel with different concentrations ($10^{-2}$ to $10^{-9}$ M) using $Ag/CeO_2$ nanospheres. Adapted with permission from [91]. Copyright 2020 The Royal Society of Chemistry

to the SERS platform to perform analysis. A nearly linear fitting curve was obtained over a wide concentration range. Remarkably, two components and three components of the pesticides were readily and rapidly identified.

### 9.3.4 Detection of Antibiotics

Antibiotics are an important source of water pollution, so their sensitive detection is highly desirable.

Magro et al. [93] demonstrated that ZnO- and $TiO_2$-based sensors produced by DC magnetron sputtering either with 50% or 100% $O_2$ in the sputtering chamber were able to detect the three antibiotics azithromycin, clarithromycin, and erythromycin in water matrices (mineral and river water) in concentrations between $10^{-15}$ M and $10^{-5}$ M. In river water, the principal component analysis (PCA) discrimination presented patterns and trends, between non-doped and doped, and sorting the different concentrations of all three antibiotics. Jiao et al. [94] used aligned $TiO_2$ NR arrays decorated with closely interconnected Au/Ag NPs for near-infrared SERS-active sensors for the detection of antibiotics ciprofloxacin and chloramphenicol in environmental water samples with detection limits of $10^{-9}$ M and $10^{-8}$ M, respectively.

Berganza et al. [76] used Au/$Fe_2O_3$ core–shell NR-like nanomaterial applicable as colloidal SERS sensing substrates with magnetic capture and accumulation (Fig. 9.8). A portable Raman instrument was used to detect antibiotic ciprofloxacin from water reservoirs at concentration as low as 100 nM within minutes, making it highly relevant in practical point-of-care devices and in situ use.

### 9.3.5 Detection of Biomarkers

MeO surfaces served also as platforms for the detection of biomarkers. In this way, tumor markers, including protein, and nucleic acid can be monitored by MeO SERS substrates to achieve early screening of cancers.

For example, an EF up to $\sim 10^3$ was obtained in the solutions containing $TiO_2$ NPs and biomarkers, including the important class of neurotransmitters such as dopamine and DOPAC (3,4-dihydroxy-phenylacetic acid) [31]. $\gamma$-$Fe_2O_3$ NPs with an average size of $77 \pm 10$ nm were shown to be suitable for SERS detection of neurotransmitters [95]. Wang et al. [96] in their study recently reported the possibility to enhance the SERS performance of $\alpha$-$Fe_2O_3$ by facet engineering.

Liu et al. [97] designed MB-modified aptamer (serving as a SERS signal source) attached to the tungsten trioxide ($WO_3$) film for the SERS detection of glioblastoma biomarkers, vascular endothelial growth factor (VEGF), in human serum samples. After the aptamer specifically linked to VEGF, it folded into a restricted stem-loop structure, forcing the MB molecule to contact the substrate, leading to a significant

enhancement of SERS signals, thereby achieving sensitive detection of VEGF. The proposed aptasensor could detect VEGF with high selectivity, while the detection limit was down to 8.7 pg/mL.

Keshavarz et al. [98] reported a highly sensitive detection of tumor biomarkers, such as epidermal growth factor receptors (EGFR), to diagnose breast cancer. Due to the incorporation of oxygen vacancies as a strategy to significantly increase the SERS enhancement of Q-structured $TiO_2$, they obtained the detection limit was as low as 1 nM and the maximum EF was $3.4 \times 10^7$. The results with breast and cervical cancer cell lines were used to demonstrate the clinical application of the proposed SERS platform.

Jiang et al. [99] developed a 3D $WO_3$ hollow microsphere as a SERS-active substrate for miRNA 155 detection. The 3D $WO_3$ hollow microsphere with a small band gap and rich surface defects promoted an increase in CT, resulting in a large SERS enhancement. Then, using a catalytic hairpin assembly (CHA) strategy, a SERS biosensor based on a 3D $WO_3$ hollow microsphere was constructed for the sensitive detection of miRNA 155 with a LOD of 0.18 fM. In order to verify the feasibility of this biosensor, miRNA 155 from HeLa (cervical cancer cells) and MDA-MB-231 (human breast cancer cells) were chosen as models. Experimental data proved that this biosensor could achieve the detection of miRNA 155 in actual samples.

### *9.3.6 Detection of Cancer Cells*

MeO surfaces have also served as platforms for the detection of cancer cells and even circulating tumor cells (CTCs) for screening early stages of various cancers.

Lin et al. [100] designed black $TiO_2$ NPs (B-$TiO_2$ NPs) with crystal-amorphous core–shell structures for the accurate diagnosis and treatment of cancer. The feasibility of applying the high sensitive SERS bioprobe based on B-$TiO_2$ NPs modified with AR signal molecule, polydopamine (PD) layer, and an antibody (AB) was verified by the detection of MCF-7 drug-resistant (MCF-7/ADR) breast cancer cells.

Xu et al. [101] used a $TiO_2$-based nontoxicity for CTCs detection. The bioprobe consisted of AR, reduced bovine serum protein (rBSA), and folic acid (FA) to functionalize $TiO_2$ NPs and 4-MBA adsorbed on the surface of $TiO_2$ NPs as a signal molecule (Fig. 9.11a). The $TiO_2$ NPs showed remarkable SERS sensitivity for 4-MBA and AR molecules, both of which provided a LOD at $5 \times 10^{-7}$ M. Benefiting from the high targeting ability of FA toward folate receptor (FR) overexpressed in cancer cells, the proposed SERS bioprobe was able to identify different kinds of cancer cells in rabbit blood. There was an obvious Raman signal of a single cancer cell after incubation with the SERS bioprobe for 1 h, suggesting that this approach has great potential to effectively detect a single CTC. The results are summarized in Fig. 9.11 where the red cycle represents the $TiO_2$-AR-rBSA-FA bioprobe captured by SY5Y (Fig. 9.11b), H226 (Fig. 9.11c), KYSE-150 (Fig. 9.11d), and HeLa (Fig. 9.11e) cells. The SERS spectra were uniform, stable, and significant. Furthermore, AR also

owns a fluorescence imaging function, which carefully verifies that the $TiO_2$-AR-rBSA-FA were precisely targeted to CTCs based on immunofluorescence staining experiments. This research reports that the pure $TiO_2$-based SERS substrate was successfully used in CTCs measurement for the first time.

FA-specific recognition and ultrahigh SERS activity of $TiO_2$ NPs, a novel strategy that combines microfilter isolation and SERS detection of CTCs from peripheral blood at single-cell resolution was proposed by Xu et al. [102]. The bioprobe was composed of Raman reporting molecule AR and FA-functionalized $TiO_2$ NPs. Due to the rapid separation of microfilters and the high sensitivity of SERS spectroscopy, the SERS bioprobe of $TiO_2$-AR-PEG-FA could distinguish FR-positive CTCs from peripheral blood cells efficiently within 1.5 h, and the LOD of CTCs in rabbit blood reached 2 cells/mL. Furthermore, this strategy has also been successfully employed in blood samples from cancer patients. In addition, Feng et al. [103] fabricated ternary heterostructure $Fe_3O_4$@graphite-oxide (GO)@$TiO_2$ (denoted as MGT) with a significant EF of $8.08 \times 10^6$. They found the remarkably enhanced effect of the

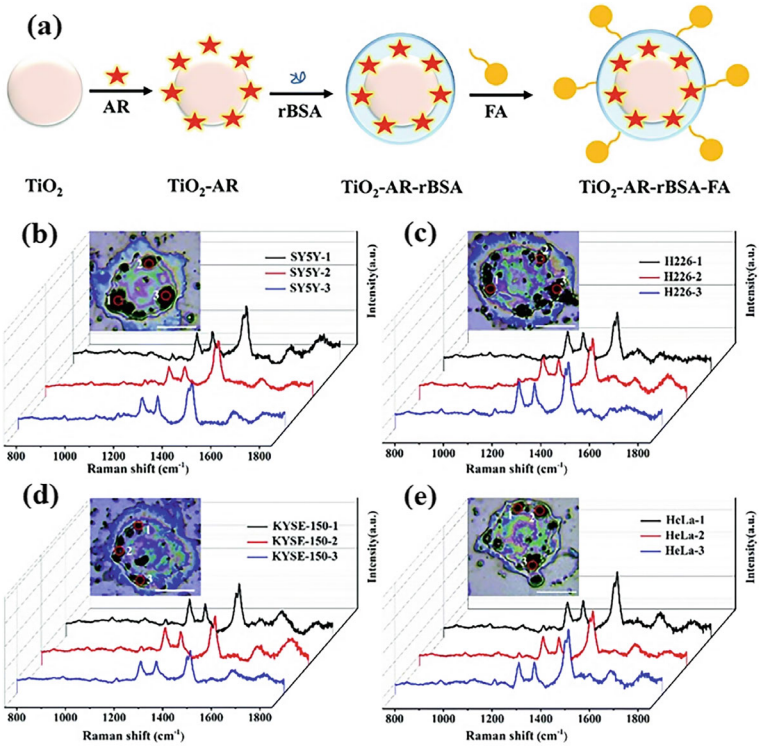



**Fig. 9.11** **a** Simplified design drawing for the preparation of the $TiO_2$-AR-rBSA-FA SERS bioprobe. Single-cell detection of the $TiO_2$-based SERS bioprobe for **b** SY5Y, **c** H226, **d** KYSE-150 and **e** HeLa cells in rabbit blood. Adapted with permission from [101]. Copyright 2022 The Royal Society of Chemistry

SERS signal to be attributed to the resonance effect of copper phthalocyanine (CuPc) probe molecule, CT between GO and $TiO_2$, and enrichment from a porous $TiO_2$ shell. This robust SERS biosensor was successfully used for the sensitive and selective detection of triple-negative breast cancer cells (TNBCs). In this detection strategy, the AB can adsorb on the surface of MGT, and the cancer cells can be specifically captured by MGT-AB. The detection of TNBCs models such as HCC38, MDA-MB-231, and MCF-7 was monitored by the bioprobe. The LOD was calculated to be ~ 3 HCC38 cells. Moreover, the SERS bioprobe proved good recyclability under visible-light illumination. They also applied this probe for in situ quantification and imaging of programmed cell death receptor ligand 1 (PD-L1) on triple-negative breast cancer cell surface at the single-cell level and for monitoring the expression variation of PD-L1 during drug treatment.

In contrast to the aforementioned studies on $TiO_2$-based CTCs SERS detection, Haldavnekar et al. [104] introduced a quantum-size 3D ZnO SERS bioprobe for the first time in the study of label-free in vitro diagnosis of cancer. Due to the significant reduction of the probe size, the surface defects, such as oxygen vacancies and stacking faults, resulted in a unique exponential increase in SERS signal. The in vitro sensing of the 3D ZnO SERS bioprobe was demonstrated by successful distinguishing between cancer and non-cancer cells based on the ratio of peak intensities of lipids and proteins. Owing to the surface oxygen vacancies and stacking faults, the bioprobe could achieve the EF ~ $10^6$ with LOD down to $10^{-9}$ M. The ratio of peak intensities of lipids and proteins was used to distinguish between cancer and non-cancer. In this way, the probe achieved label-free, in vitro SERS diagnosis of cancer with single-cell-level detection. Lin et al. [100] fabricated $TiO_2$ NPs that could enhance Raman scattering with the EF $4.3 \times 10^5$. On the one hand, the B-$TiO_2$ NPs could be applied to SERS mapping imaging technology, which has been employed to accurately diagnose the MCF-7 drug-resistant breast cancer cells. On the other hand, with excellent photothermal conversion efficiency, the B-$TiO_2$ NPs could also act as a promising heat mediator for efficient photothermal ablation of cancer cells.

## 9.4 Conclusions and Perspectives

Non-plasmonic MeO nanomaterials have become very promising SERS substrates due to their unique physicochemical properties. The enhancing mechanism is in this case predominately connected with a CM such as the CT process between the surface and the analyte molecule. Therefore, non-plasmonic SERS nanostructures do not require well-designed hot-spots (strongly enhancing sites by EM mechanism), and consequently, they provide better spectral reproducibility and reduced local heating upon laser irradiation in comparison with plasmonic noble nanomaterials. On the other hand, if only CT is taking place, EF and, consequently, the detection sensitivity of MeO substrates are lower than for the optimized noble metal SERS substrates (Au and Ag). Although the main limiting factor of MeO substrates for their routine applications is a low sensitivity, it can be improved by rationally tuning the resonance

conditions for the target analyte and MeO substrate, e.g., by the design of novel superstructures or by defect and facet engineering. Moreover, it may be promising to profit from a synergy of both the CM and EM enhancement in the case of the combination of MeO materials with plasmonic noble metals.

Although significantly fewer SERS applications of MeO substrates have been reported compared to noble metals-based ones, MeO substrates have some advantages over conventional plasmonic SERS substrates. Most importantly, they provide good biocompatibility, low biotoxicity, and good spectral stability as well as some of them also have strong photocatalytic activity. The recent applications of MeO materials based on SERS technology include the detection of anions, pesticides, pollutants, biomarkers, and employment in cancer diagnosis (such as the detection of CTCs). Although there is still a certain gap between the analytical detection using MeO SERS substrates in the laboratory and practical in situ applications, the adequate development of MeO SERS substrates is meaningful to enrich their high-performance and to expand their practical SERS application range. SERS on MeO substrates can also be integrated into other optical spectroscopy techniques or atomic force microscopy which can achieve multiplexed analysis. One can expect that due to the rapid development in the field of preparation and testing of non-plasmonic MeO materials, they can become the new generation of multifunctional SERS substrates for overcoming various challenges in practical applications.

**Acknowledgements** Financial support by the Czech Science Foundation in the frame of the grant GAČR 22-16667S is acknowledged.

## References

1. M. Procházka, *Surface-Enhanced Raman Spectroscopy - Bioanalytical, Biomolecular and Medical Applications*, (Springer International Publishing, 2016)
2. T. Itoh, M. Procházka, Z. C. Dong, W. Ji, Y. S. Yamamoto, Y. Zhang and Y. Ozaki, Toward a New Era of SERS and TERS at the Nanometer Scale: From Fundamentals to Innovative Applications. Chem. Rev. **123**, 1552–1634 (2023)
3. Y. Chen, Y. Hu and G. Li, A Review on Non-Noble Metal Substrates for Surface-Enhanced Raman Scattering Detection. Chemosensors **11**, 427 (2023)
4. X. X. Han, W. Ji, B. Zhao and Y. Ozaki, Semiconductor-enhanced Raman scattering: active nanomaterials and applications. Nanoscale **9**, 4847–4861 (2017)
5. B. Yang, S. Jin, S. Guo, Y. Park, L. Chen, B. Zhao and Y. M. Jung, Recent Development of SERS Technology: Semiconductor-Based Study. ACS Omega **4**, 20101–20108 (2019)
6. X. Ling, L. Xie, Y. Fang, H. Xu, H. Zhang, J. Kong, M. S. Dresselhaus, J. Zhang and Z. Liu, Can graphene be used as a substrate for Raman enhancement? Nano Lett. **10**, 553–561 (2010)
7. H. Xu, L. Xie, H. Zhang and J. Zhang, Effect of graphene Fermi level on the Raman scattering intensity of molecules on graphene. ACS Nano **5**, 5338–5344 (2011)
8. M. Yilmaz, E. Babur, M. Ozdemir, R. L. Gieseking, Y. Dede, U. Tamer, G. C. Schatz, A. Facchetti, H. Usta and G. Demirel, Nanostructured organic semiconductor films for molecular detection with surface-enhanced Raman spectroscopy. Nat. Mater. **16**, 918–924 (2017)
9. G. Demirel, R. L. M. Gieseking, R. Ozdemir, S. Kahmann, M. A. Loi, G. C. Schatz, A. Facchetti and H. Usta, Molecular engineering of organic semiconductors enables noble metal-comparable SERS enhancement and sensitivity. Nat. Commun. **10**, 5502 (2019)

10. W. Li, R. Zamani, P. Rivera Gil, B. Pelaz, M. Ibanez, D. Cadavid, A. Shavel, R. A. Alvarez-Puebla, W. J. Parak, J. Arbiol and A. Cabot, CuTe nanocrystals: shape and size control, plasmonic properties, and use as SERS probes and photothermal agents. J. Am. Chem. Soc. **135**, 7098–7101 (2013)
11. Y. Wang, Z. Sun, Y. Wang, H. Hu, B. Zhao, W. Xu and J. R. Lombardi, Surface-enhanced Raman scattering on mercaptopyridine-capped CdS microclusters. Spectrochim. Acta A: Mol. Biomol. Spectrosc. **66**, 1199–1203 (2007)
12. A. Sarycheva, T. Makaryan, K. Maleski, E. Satheeshkumar, A. Melikyan, H. Minassian, M. Yoshimura and Y. Gogotsi, Two-Dimensional Titanium Carbide (MXene) as Surface-Enhanced Raman Scattering Substrate. J. Phys. Chem. C **121**, 19983–19988 (2017)
13. B. Soundiraraju and B. K. George, Two-Dimensional Titanium Nitride ($Ti_2N$) MXene: Synthesis, Characterization, and Potential Application as Surface-Enhanced Raman Scattering Substrate. ACS Nano **11**, 8892–8900 (2017)
14. Samriti, V. Rajput, R. K. Gupta and J. Prakash, Engineering Metal Oxide Semiconductor Nanostructures for Enhanced Charge Transfer: Fundamentals and Emerging SERS Applications. J. Mat. Chem. C **10**, 73–95 (2022)
15. A. Raghunath and E. Perumal, Metal oxide nanoparticles as antimicrobial agents: a promise for the future. Int. J. Antimicrob. Agents **49**, 137–152 (2017)
16. Y. F. Sun, S. B. Liu, F. L. Meng, J. Y. Liu, Z. Jin, L. T. Kong and J. H. Liu, Metal oxide nanostructures and their gas sensing properties: a review. Sensors (Basel) **12**, 2610–2631 (2012)
17. A. Dey, Semiconductor metal oxide gas sensors: A review. Mater. Sci. Eng. B **229**, 206–217 (2018)
18. Y. Wu, eds., *Metal Oxides in Energy Technologies*, (Elsevier, 2019)
19. B. H. Loo, Observation of the surface enhanced Raman scattering effect from the semiconductor—electrolyte interface. J. Electroanal. Chem. Interf. Electrochem. **136**, 209–213 (1982)
20. H. Yamada, Y. Yamamoto and N. Tan, Surface-Enhanced Raman Scattering (SERS) of Adsorbed Molecules on Smooth Surfaces of Metals and a Metal Oxide. Chem. Phys. Lett. **86**, 397–400 (1982)
21. Z. Tian, H. Bai, C. Chen, Y. Ye, Q. Kong, Y. Li, W. Fan, W. Yi and G. Xi, Quasi-Metal for Highly Sensitive and Stable Surface-Enhanced Raman Scattering. iScience **19**, 836–849 (2019)
22. G. Barbillon, Application of Novel Plasmonic Nanomaterials on SERS. Nanomaterials (Basel) **10**, 1200 (2020)
23. J. Krajczewski, R. Ambroziak and A. Kudelski, Substrates for Surface-Enhanced Raman Scattering Formed on Nanostructured Non-Metallic Materials: Preparation and Characterization. Nanomaterials (Basel) **11**, 75 (2020)
24. J. R. Lombardi, The theory of surface-enhanced Raman scattering on semiconductor nanoparticles; toward the optimization of SERS sensors. Faraday Discuss. **205**, 105–120 (2017)
25. Z. Sun, B. Zhao and J. R. Lombardi, ZnO nanoparticle size-dependent excitation of surface Raman signal from adsorbed molecules: Observation of a charge-transfer resonance. Appl. Phys. Lett. **91**, 221106 (2007)
26. V. Sharma, R. Balaji, N. Kumari and V. Krishnan, SERS Application of Noble Metal–Metal Oxide Hybrid Nanoparticles, in *Noble Metal-Metal Oxide Hybrid Nanoparticles*, Edited by S. Mohapatra, T. A. Nguyen and P. Nguyen-Tri, (Woodhead Publishing 2019), pp. 457–486.
27. Z. Q. Tian, B. Ren, J. F. Li and Z. L. Yang, Expanding generality of surface-enhanced Raman spectroscopy with borrowing SERS activity strategy. Chem. Commun. (Camb), 3514–3534 (2007)
28. H. Yamada and Y. Yamamoto, Surface enhanced Raman scattering (SERS) of chemisorbed species on various kinds of metals and semiconductors. Surf. Sci. **134**, 71–90 (1983)
29. D. Qi, L. Lu, L. Wang and J. Zhang, Improved SERS sensitivity on plasmon-free $TiO_2$ photonic microarray by enhancing light-matter coupling. J. Am. Chem. Soc. **136**, 9886–9889 (2014)

30. L. Yang, X. Jiang, W. Ruan, B. Zhao, W. Xu and J. R. Lombardi, Observation of Enhanced Raman Scattering for Molecules Adsorbed on $TiO_2$ Nanoparticles: Charge-Transfer Contribution. J. Phys. Chem. C **112**, 20095–20098 (2008)
31. A. Musumeci, D. Gosztola, T. Schiller, N. M. Dimitrijevic, V. Mujica, D. Martin and T. Rajh, SERS of semiconducting nanoparticles ($TiO_2$) hybrid composites. J. Am. Chem. Soc. **131**, 6040–6041 (2009)
32. S. J. Hurst, H. C. Fry, D. J. Gosztola and T. Rajh, Utilizing Chemical Raman Enhancement: A Route for Metal Oxide Support-Based Biodetection. J. Phys. Chem. C **115**, 620–630 (2011)
33. P. Tarakeshwar, D. Finkelstein-Shapiro, T. Rajh and V. Mujica, Quantum confinement effects on the surface enhanced Raman spectra of hybrid systems molecule-$TiO_2$ nanoparticles. Int. J. Quantum Chem. **111**, 1659–1670 (2010)
34. X. Xue, W. Ji, Z. Mao, Z. Li, W. Ruan, B. Zhao and J. R. Lombardi, Effects of Mn doping on surface enhanced Raman scattering properties of $TiO_2$ nanoparticles. Spectrochim. Acta A: Mol. Biomol. Spectrosc. **95**, 213–217 (2012)
35. L. Yang, Y. Zhang, W. Ruan, B. Zhao, W. Xu and J. R. Lombardi, Improved sur-face-enhanced Raman scattering properties of $TiO_2$ nanoparticles by Zn dopant. J. Raman Spectrosc. **41**, 721–726 (2009)
36. L. Yang, X. Jiang and M. Yang, Improvement of surface-enhanced Raman scattering performance for broad band gap semiconductor nanomaterial ($TiO_2$): Strategy of metal doping Appl. Phys. Lett. **99**, 111114 (2011)
37. J. Li, Y. Tang, X. Wang, W. Kan, L. Yang, X. Jiang, Y. Ozaki, X. X. Han and B. Zhao, Sr-Doped $TiO_2$ with Positive Double Defects for a Highly Sensitive and Stable Surface-Enhanced Raman Substrate. J. Phys. Chem. C **128**, 296–303 (2024)
38. J. Jimenez-Cisneros, J. P. Galindo-Lazo, M. A. Mendez-Rojas, J. R. Campos-Delgado and M. Cerro-Lopez, Plasmonic Spherical Nanoparticles Coupled with Titania Nanotube Arrays Prepared by Anodization as Substrates for Surface-Enhanced Raman Spectroscopy Applications: A Review. Molecules **26**, 7443 (2021)
39. J. Chen and L. Yang, Synthesis and SERS performance of a recyclable SERS substrate based on Ag NPs coated $TiO_2$ nanotube arrays. Integr. Ferroelectr. **147**, 17–23 (2013)
40. X. Chong, B. Zhao, R. Li, W. Ruan and W. Yang, Photocatalytic degradation of R6G on Ag modified $TiO_2$ nanotubes: Surface-enhanced Raman scattering study on catalytic kinetics and substrate recyclability. Colloids Surf. A: Physicochem. Eng. Asp. **481**, 7–12 (2015)
41. S. Kumar, D. K. Lodhi and J. P. Singh, Highly sensitive multifunctional recyclable Ag–$TiO_2$ nanorod SERS substrates for photocatalytic degradation and detection of dye molecules. RSC Adv. **6**, 45120–45126 (2016)
42. W. Yang, J. Tang, Q. Ou, X. Yan, L. Liu and Y. Liu, Recyclable Ag-Deposited $TiO_2$ SERS Substrate for Ultrasensitive Malachite Green Detection. ACS Omega **6**, 27271–27278 (2021)
43. T. Zhu, H. Wang, L. Zang, S. Jin, S. Guo, E. Park, Z. Mao and Y. M. Jung, Flexible and Reusable Ag Coated $TiO_2$ Nanotube Arrays for Highly Sensitive SERS Detection of Formaldehyde. Molecules **25**, 1199 (2020)
44. Q. Wei, Q. Dong, D. W. Sun and H. Pu, Synthesis of recyclable SERS platform based on $MoS_2$@$TiO_2$@Au heterojunction for photodegradation and identification of fungicides. Spectrochim. Acta A: Mol. Biomol. Spectrosc. **285**, 121895 (2023)
45. A. Hanková, A. Kuzminova, J. Hanuš, P. Sezemsky, R. Simerova, V. Stranak, K. Grochowska, D. S. Kouao, K. Siuzdak, M. Procházka, Y. Košutová and O. Kylián, $TiO_2$/Ag nanostructured coatings as recyclable platforms for surface-enhanced Raman scattering detection. Surf. Interfaces **35**, 102441 (2022)
46. S. Ben-Jaber, W. J. Peveler, R. Quesada-Cabrera, E. Cortes, C. Sotelo-Vazquez, N. Abdul-Karim, S. A. Maier and I. P. Parkin, Photo-induced enhanced Raman spectroscopy for universal ultra-trace detection of explosives, pollutants and biomolecules. Nat. Commun. **7**, 12189 (2016)
47. J. Shondo, S. Veziroglu, T. Tjardts, T. B. Sarwar, Y. K. Mishra, F. Faupel and O. C. Aktas, Nanoscale Synergetic Effects on Ag-$TiO_2$ Hybrid Substrate for Photoinduced Enhanced Raman Spectroscopy (PIERS) with Ultra-Sensitivity and Reusability. Small **18**, e2203861 (2022)

48. Y. Li, H. Bai, J. Zhai, W. Yi, J. Li, H. Yang and G. Xi, Alternative to Noble Metal Substrates: Metallic and Plasmonic $Ti_3O_5$ Hierarchical Microspheres for Surface Enhanced Raman Spectroscopy. Anal. Chem. **91**, 4496–4503 (2019)
49. P. Miao, J. Wu, Y. Du, Y. Sun and P. Xu, Phase transition induced Raman enhancement on vanadium dioxide ($VO_2$) nanosheets. J. Mat. Chem. C **6**, 10855–10860 (2018)
50. H. Guan, Z. Tian, Q. Kong and G. Xi, Vanadium dioxide nanostructures with remarkable surface-enhanced Raman scattering activity. Chem. Commun. (Camb) **57**, 4815–4818 (2021)
51. J. Pan, M. Li, Y. Y. Luo, H. Wu, L. Zhong, Q. Wang and G. H. Li, Synthesis and SERS activity of $V_2O_5$ nanoparticles. Appl. Surf. Sci. **333**, 34–38 (2015)
52. W. Ji, L. Li, J. Guan, M. Mu, W. Song, L. Sun, B. Zhao and Y. Ozaki, Hollow Multi-Shelled $V_2O_5$ Microstructures Integrating Multiple Synergistic Resonances for Enhanced Semiconductor SERS. Adv. Opt. Mater. **17**, 2101866 (2021)
53. E. Kočišová, A. Kuzminova, A. Kuižová, A. Hanková, T. Košutová, M. Procházka and O. Kylián, $V_2O_5$ nanoparticle films as a platform for plasmon-free surface-enhanced Raman spectroscopy. Ceram. Int. **50**, 10026–10033 (2024)
54. A. Hanková, T. Košutová, J. Hanuš, A. Kuzminova, P. Pleskunov, M. Červená, P. Zeman, N. Khomiakova, F. Hájek and O. Kylián, Morphological and structural evolution of gas-phase synthesized vanadium nanoparticle films induced by thermal treatment. Mat. Chem. Phys. **301**, 127587 (2023)
55. Q. Cai, F. Liao, F. Hu, Y. Li, T. Wang and M. Shao, A single-source precursor route to a Cu/$V_2O_5$ composites as surface-enhanced Raman scattering substrates and catalysts for cross coupling. RSC Adv. **4**, 6424–6429 (2014)
56. S. Cong, Y. Yuan, Z. Chen, J. Hou, M. Yang, Y. Su, Y. Zhang, L. Li, Q. Li, F. Geng and Z. Zhao, Noble metal-comparable SERS enhancement from semiconducting metal oxides by making oxygen vacancies. Nat. Commun. **6**, 7800 (2015)
57. C. Zhou, L. Sun, F. Zhang, C. Gu, S. Zeng, T. Jiang, X. Shen, D. S. Ang and J. Zhou, Electrical Tuning of the SERS Enhancement by Precise Defect Density Control. ACS Appl. Mater. Interfaces **11**, 34091–34099 (2019)
58. W. Wei, Y. Yao, Q. Zhao, Z. Xu, Q. Wang, Z. Zhang and Y. Gao, Oxygen defect-induced localized surface plasmon resonance at the $WO_{3-x}$ quantum dot/silver nanowire interface: SERS and photocatalysis. Nanoscale **11**, 5535–5547 (2019)
59. R. He, H. Lai, S. Wang, T. Chen, F. Xie, Q. Chen, P. Liu, J. Chen and W. Xie, Few-layered vdW $MoO_3$ for sensitive, uniform and stable SERS applications. Appl. Surf. Sci. **507**, 145116 (2020)
60. P. Ji, Z. Wang, X. Shang, Y. Zhang, Y. Liu, Z. Mao and X. Shi, Direct Observation of Enhanced Raman Scattering on Nano-Sized $ZrO_2$ Substrate: Charge-Transfer Contribution. Front. Chem. **7**, 245 (2019)
61. P. Ji, Z. Mao, Z. Wang, X. Xue, Y. Zhang, J. Lv and X. Shi, Improved Surface-Enhanced Raman Scattering Properties of $ZrO_2$ Nanoparticles by Zn Doping. Nanomaterials (Basel) **9**, 983 (2019)
62. M. Yi, Y. Zhang, J. Xu, D. Deng, Z. Mao, X. Meng, X. Shi and B. Zhao, Surface-Enhanced Raman Scattering Activity of $ZrO_2$ Nanoparticles: Effect of Tetragonal and Monoclinic Phases. Nanomaterials (Basel) **11**, 2162 (2021)
63. Y. Shan, Z. Zheng, J. Liu, Y. Yang, Z. Li, Z. Huang and D. Jiang, Niobium pentoxide: a promising surface-enhanced Raman scattering active semiconductor substrate. Npj Comput. Mater. **3**, 11 (2017)
64. S. Ghosal, A. Bora and P. K. Giri, Evidence of oxygen vacancy-mediated ultrahigh SERS sensitivity of Niobium pentoxide nanoparticles through defect engineering: theoretical and experimental studies. Nanoscale **16**, 309–321 (2023)
65. L. Mingjin, S. Cheng, X. Du, J. Li, Q. Peng, C. Zhao, Y. Wang and X. Xiu, Preparation and SERS applications of $Ta_2O_5$ composite nanostructures. Opt. Express **31**, 38699–38714 (2023)
66. L. Ma, H. Wu, Y. Huang, S. Zou, J. Li and Z. Zhang, High-Performance Real-Time SERS Detection with Recyclable Ag Nanorods@$HfO_2$ Substrates. ACS Appl. Mater. Interfaces **8**, 27162–27168 (2016)

67. Y. Wang, W. Ruan, J. Zhang, B. Yang, W. Xu, B. Zhao and J. R. Lombardi, Direct observation of surface-enhanced Raman scattering in ZnO nanocrystals. J. Raman Spectrosc. **40**, 1072–1077 (2009)
68. W. Ji, L. Li, W. Song, X. Wang, B. Zhao and Y. Ozaki, Enhanced Raman Scattering by ZnO Superstructures: Synergistic Effect of Charge Transfer and Mie Resonances. Angew. Chem. Int. Ed. Engl. **58**, 14452–14456 (2019)
69. A. P. Richter, J. R. Lombardi and B. Zhao, Size and Wavelength Dependence of the Charge-Transfer Contributions to Surface-Enhanced Raman Spectroscopy in Ag/PATP/ZnO Junctions. J. Phys. Chem. C **114**, 1610–1614 (2010)
70. X. Q. Fu, F. L. Bei, X. Wang, X. J. Yang and L. D. Lu, Surface-enhanced Raman scattering of 4-mercaptopyridine on sub-monolayers of α-$Fe_2O_3$ nanocrystals (sphere, spindle, cube). J. Raman Spectrosc. **40**, 1290–1295 (2009)
71. X. Fu, S. Wang, Q. Zhao, T. Jiang and H. Yin, Thin films of α-$Fe_2O_3$ nanoparticles using as nonmetallic SERS-active nanosensors for submicromolar detection. Front. Chem. China **6**, 206–212 (2011)
72. M. Gühlke, S. Selve and J. Kneipp, Magnetic separation and SERS observation of analyte molecules on bifunctional silver/iron oxide composite nanostructures. J. Raman Spectrosc. **43**, 1204–1207 (2012)
73. S. Kang, A. Rahman, E. Boeding and P. J. Vikesland, Synthesis and SERS application of gold and iron oxide functionalized bacterial cellulose nanocrystals (Au@$Fe_3O_4$@BCNCs). Analyst **145**, 4358–4368 (2020)
74. K. Kim, H. J. Jang and K. S. Shin, Ag nanostructures assembled on magnetic particles for ready SERS-based detection of dissolved chemical species. Analyst **134**, 308–313 (2009)
75. F. Bao, J. L. Yao and R. A. Gu, Synthesis of magnetic $Fe_2O_3$/Au core/shell nanoparticles for bioseparation and immunoassay based on surface-enhanced Raman spectroscopy. Langmuir **25**, 10782–10787 (2009)
76. L. B. Berganza, L. Litti, M. Meneghetti, S. Lanceros-Mendez and J. Reguera, Enhancement of Magnetic Surface-Enhanced Raman Scattering Detection by Tailoring $Fe_3O_4$@Au Nanorod Shell Thickness and Its Application in the On-site Detection of Antibiotics in Water. ACS Omega **7**, 45493–45503 (2022)
77. L. Jiang, T. You, P. Yin, Y. Shang, D. Zhang, L. Guo and S. Yang, Surface-enhanced Raman scattering spectra of adsorbates on $Cu_2O$ nanospheres: charge-transfer and electromagnetic enhancement. Nanoscale **5**, 2784–2789 (2013)
78. H. Dizajghorbani Aghdam, S. Moemen Bellah and R. Malekfar, Surface-enhanced Raman scattering studies of Cu/$Cu_2O$ Core-shell NPs obtained by laser ablation. Spectrochim. Acta: A Mol. Biomol. Spectrosc. **223**, 117379 (2019).
79. C. He, L. Jiang, R. Yuan and Y. X., Facet junction of $CeO_2$ with high SERS activity for sensitive detection of ATP. Sens. Actuators B: Chem. **374**, 132777 (2023)
80. X. X. Han, C. Kohler, J. Kozuch, U. Kuhlmann, L. Paasche, A. Sivanesan, I. M. Weidinger and P. Hildebrandt, Potential-dependent surface-enhanced resonance Raman spectroscopy at nanostructured $TiO_2$ : a case study on cytochrome $b_5$. Small **9**, 4175–4181 (2013)
81. I. H. Oner, C. J. Querebillo, C. David, U. Gernert, C. Walter, M. Driess, S. Leimkuhler, K. H. Ly and I. M. Weidinger, High Electromagnetic Field Enhancement of $TiO_2$ Nanotube Electrodes. Angew. Chem. Int. Ed. Engl. **57**, 7225–7229 (2018)
82. I. Alessandri and L. E. Depero, All-oxide Raman-active traps for light and matter: probing redox homeostasis model reactions in aqueous environment. Small **10**, 1294–1298 (2014)
83. L. Chen, J. Tang, H. Ma, S. Jin, X. Xue, X. X. Han and Y. M. Jung, High-efficiency charge transfer on SERS-active semiconducting $K_2Ti_6O_{13}$ nanowires enables direct transition of photoinduced electrons to protein redox centers. Biosens. Bioelectron. **191**, 113452 (2021)
84. W. Ji, Y. Wang, I. Tanabe, X. Han, B. Zhao and Y. Ozaki, Semiconductor-driven "turn-off" surface-enhanced Raman scattering spectroscopy: application in selective determination of chromium(vi) in water. Chem. Sci. **6**, 342–348 (2015)
85. N. Bontempi, L. Carletti, C. De Angelis and I. Alessandri, Plasmon-free SERS detection of environmental $CO_2$ on $TiO_2$ surfaces. Nanoscale **8**, 3226–3231 (2016)

86. X. X. Han, L. Chen, U. Kuhlmann, C. Schulz, I. M. Weidinger and P. Hildebrandt, Magnetic titanium dioxide nanocomposites for surface-enhanced resonance Raman spectroscopic determination and degradation of toxic anilines and phenols. Angew. Chem. Int. Ed. Engl. **53**, 2481–2484 (2014)
87. W. Song, W. Ji, S. Vantasin, I. Tanabe, B. Zhao and Y. Ozaki, Fabrication of a highly sensitive surface-enhanced Raman scattering substrate for monitoring the catalytic degradation of organic pollutants. J. Mat. Chem. A **3**, 13556–13562 (2015)
88. Q. Zhang, X. Li, W. Yi, W. Li, H. Bai, J. Liu and G. Xi, Plasmonic $MoO_2$ Nanospheres as a Highly Sensitive and Stable Non-Noble Metal Substrate for Multicomponent Surface-Enhanced Raman Analysis. Anal. Chem. **89**, 11765–11771 (2017)
89. P. Liang, Y. Cao, Q. Dong, D. Wang, D. Zhang, S. Jin, Z. Yu, J. Ye and M. Zou, A balsam pear-shaped CuO SERS substrate with highly chemical enhancement for pesticide residue detection. Microchim. Acta. **187**, 335 (2020)
90. Y. Quan, R. Su, S. Yang, L. Chen, M. Wei, H. Liu, J. Yang, M. Gao and B. Li, In-situ surface-enhanced Raman scattering based on $MTi_{20}$ nanoflowers: Monitoring and degradation of contaminants. J. Hazard Mater. **412**, 125209 (2021)
91. S. Thirumalairajan and K. Girija, Efficient and tunable shape selective synthesis of $Ag/CeO_2$ nanostructures modified highly stable SERS substrate for ultrasensitive detection of pesticides on the surface of an apple. Nanoscale Adv. **2**, 3570–3581 (2020)
92. X. Shi, G. Y., Z. Li, M. He, Z. D. Zhu, X. Sun, H. Sun, M. F. Zhang, J. Li and Y. Huang, The synergetic enhancement of the porous $ZrO_2@TiO_2$ heterostructure and the plasmonic silver nanoparticles for efficient surface-enhanced Raman scattering. Appl. Organomet. Chem. **37**, e7133 (2023)
93. C. Magro, T. Moura, J. Dionisio, P. A. Ribeiro, M. Raposo and S. Serio, Nanostructured Metal Oxide Sensors for Antibiotic Monitoring in Mineral and River Water. Nanomaterials (Basel) **12**, 1858 (2022)
94. A. Jiao, Q. Q. Cui, S. Li, H. S. Li, L. Xu, Y. Tian, H. Ma, M. Zhang, X. D. Liu and M. Chen, Aligned $TiO_2$ nanorod arrays decorated with closely interconnected Au/Ag nanoparticles: Near-infrared SERS active sensor for monitoring of antibiotic molecules in water. Sens. Actuators B: Chem. **350**, 130848 (2022)
95. E. Proniewicz, A. Tąta, A. Szkudlarek, J. Świder, M. Molenda, M. Starowicz and Y. Ozaki, Electrochemically synthesized γ-Fe2O3 nanoparticles as peptide carriers and sensitive and reproducible SERS biosensors. Comparison of adsorption on $\gamma$-$Fe_2O_3$ versus Fe. Appl. Surf. Sci. **495**, 143578 (2019)
96. Y. Wang, P. Wen, L. Niu, Y. Chen, Y. Luo, Y. Gong, C. Li and S. Xu, Experimental and theoretical study on the facet-dependent SERS activity of $\alpha$-$Fe_2O_3$ films. J. Raman Spectrosc. **55**, 667-677 (2024)
97. X. Liu, Y. Zhou, T. Zheng and Y. Tian, Surface-enhanced Raman Scattering Technology Based on $WO_3$ Film for Detection of VEGF. Chem. Res. Chin. Univ. **37**, 900–905 (2021)
98. M. Keshavarz, P. Kassanos, B. Tan and K. Venkatakrishnan, Metal-oxide surface-enhanced Raman biosensor template towards point-of-care EGFR detection and cancer diagnostics. Nanoscale Horiz. **5**, 294–307 (2020)
99. L. Jiang, Y. Hu, H. Zhang, X. Luo, R. Yuan and X. Yang, Charge-Transfer Resonance and Surface Defect-Dominated $WO_3$ Hollow Microspheres as SERS Substrates for the miRNA 155 Assay. Anal Chem **94**, 6967–6975 (2022)
100. J. Lin, W. Ren, A. Li, C. Yao, T. Chen, X. Ma, X. Wang and A. Wu, Crystal-Amorphous Core-Shell Structure Synergistically Enabling $TiO_2$ Nanoparticles' Remarkable SERS Sensitivity for Cancer Cell Imaging. ACS Appl. Mater. Interfaces **12**, 4204–4211 (2020)
101. Y. Xu, J. Lin, X. Wu, X. Xu, D. Zhang, Y. Xie, T. Pan, Y. He, A. Wu and G. Shao, A $TiO_2$-based bioprobe enabling excellent SERS activity in the detection of diverse circulating tumor cells. J. Mater. Chem. B **10**, 3808–3816 (2022)
102. X. Xu, J. Lin, Y. Guo, X. Wu, Y. Xu, D. Zhang, X. Zhang, X. Yujiao, J. Wang, C. Yao, J. Yao, J. Xing, Y. Cao, Y. Li, W. Ren, T. Chen, Y. Ren and A. Wu, $TiO_2$-based Surface-Enhanced Raman Scattering bio-probe for efficient circulating tumor cell detection on microfilter. Biosens. Bioelectron. **210**, 114305 (2022)

103. E. Feng, T. Zheng, X. He, J. Chen and Y. Tian, A novel ternary heterostructure with dramatic SERS activity for evaluation of PD-L1 expression at the single-cell level. Sci. Adv. **4**, eaau3494 (2018)
104. R. Haldavnekar, K. Venkatakrishnan and B. Tan, Non plasmonic semiconductor quantum SERS probe as a pathway for in vitro cancer detection. Nat. Commun. **9**, 3065 (2018)

# Chapter 10
# Principles, Characteristics, and Applications of Electrochemical Surface-Enhanced Raman Spectroscopy




**Christa Brosseau**

**Abstract** This chapter describes the principles and characteristics of electrochemical surface-enhanced Raman spectroscopy (EC-SERS), a spectroelectrochemical technique that combines the advantages of SERS and electrochemistry for routine analysis at the electrified interface. This chapter seeks to introduce the technique while highlighting the multitude of applications that have been explored to date. A theoretical basis of the technique is provided along with important limitations. Nanostructured electrodes for EC-SERS applications are also described.

**Keywords** Electrochemistry · Raman spectroscopy · Interfacial · Nanostructured · Spectroelectrochemistry

## 10.1 Introduction

Electrochemistry and surface-enhanced Raman spectroscopy (SERS) have been entangled since the first observation [1] and subsequent discovery [2, 3] of SERS in the mid-1970s. Enhanced Raman signals for pyridine adsorbed on a roughened silver electrode marked the beginning of a now 50-year old odyssey into a deeper understanding of this vibrational spectroscopic technique. Various applications of SERS have been explored since the initial discovery, many of which are highlighted in this book. However, EC-SERS has a been a constant in the field and has re-emerged over the last 10–15 years as a powerful technique for enhanced SERS-based sensing, largely due to the development of novel nanostructured electrodes. This chapter is focused on EC-SERS specifically, and the next section will highlight the characteristics of this technique that make it a truly unique spectroscopic tool. In addition, the advantages that are inherent when electrochemistry and SERS are combined are outlined.

C. Brosseau (✉)
Saint Mary's University, Halifax, Canada
e-mail: christa.brosseau@smu.ca

© The Author(s), under exclusive license to Springer Nature Singapore Pte Ltd. 2024

M. Procházka et al. (eds.), *Surface- and Tip-Enhanced Raman Scattering Spectroscopy*,
https://doi.org/10.1007/978-981-97-5818-0_10

## 10.2 Characteristics and Advantages of EC-SERS

### *10.2.1 Characteristics of EC-SERS*

EC-SERS is a traditional spectroelectrochemical technique in the sense that spectroscopic data is collected during electrochemical perturbations in an effort to better understand various processes, including surface redox phenomena [4], interfacial dynamics [5] and adsorption/desorption behavior [6], to name a few. Fundamentally, EC-SERS has two components, the electrochemical cell and potentiostat to control the electrochemical reaction, and a Raman spectrometer to provide efficient Raman scattering from the electrode surface. An electrochemical cell consisting of a nanostructured working electrode (WE) that is SERS-active is combined with both a reference electrode (RE) as well as an inert counter electrode (CE). The reaction of interest takes place at the WE, which is typically constructed of a coinage metal (Ag, Au, Cu), as these materials provide an efficient plasmonic response in the visible region of the electromagnetic spectrum [7]. Common supporting electrolytes include phosphate buffer, sodium and potassium salts, and dilute acids and bases. SERS measurements are collected through the electrochemical cell which is designed to accommodate the optics of the Raman spectrometer, which for confocal Raman microscope systems often means a thin-layer cell configuration and/or long working distance objectives. As with non-EC-SERS, EC-SERS signals arise due to a combination of complex electromagnetic and chemical enhancement mechanisms, detailed in earlier chapters in this book. However, for EC-SERS measurements, two electric fields co-exist: the oscillating electromagnetic field and a static electrochemical field. This electrochemical field influences adsorption/desorption, surface orientation, surface redox processes, and in turn contributes to the observed SERS signal [8]. To overcome some of the limitations encountered with EC-SERS, such as a restriction to coinage metals with nanoscale roughness and a limited spatial resolution, variations on EC-SERS have come online. One example is electrochemical shell-isolated nanoparticle-enhanced Raman spectroscopy (EC-SHINERS), in which a very thin (< 3 nm) "shell" of a material (semiconductor, transition metal) is deposited onto a plasmonic core, making use of the near field enhancement effect in SERS to interrogate non-plasmonic surfaces [9, 10]. Another more recent example is electrochemical tip-enhanced Raman spectroscopy (EC-TERS), where a plasmonic tip from scanning probe microscopy (AFM, STM) is brought very close to a surface and illuminated with a laser [11].

### *10.2.2 Advantages of EC-SERS*

EC-SERS is a powerful spectroscopic technique that, like infrared spectroscopy, provides a rich vibrational fingerprint of the sample being probed. While infrared spectroscopy is based on absorption of infrared radiation, Raman scattering relies on

an inelastic scattering process, and this difference gives rise to some of the advantages (and limitations) of Raman scattering when compared to infrared spectroscopy. Primary advantages of EC-SERS compared to surface infrared spectroelectrochemical techniques (i.e., surface-enhanced infrared reflection absorption spectroscopy (SEIRAS), polarization modulation infrared reflection absorption spectroscopy (PM-IRRAS), subtractively normalized interfacial FTIR spectroscopy (SNIFTIRS), etc.) are noted below.

1. *Weak scattering of water*: Since most electrochemical measurements are done in aqueous supporting electrolytes, the weak inelastic scattering of water in Raman spectroscopy is an enormous advantage over infrared spectroscopy, where water is a strong absorber of infrared radiation. In infrared measurements, this strong absorption of water in an electrochemical measurement requires long collection times, complex spectral subtraction algorithms, and thin-layer cells which minimize the thickness of the electrolyte layer [12, 13]. Typical EC-SERS acquisition times are between 1 and 30 s, which allows for the collection of a complete set of spectroelectrochemical data at a multitude of applied potentials within a 30–60 min time frame. Comparative measurements using surface infrared spectroscopy typically take several hours.
2. *Weak scattering of glass*: Electrochemical measurements are conducted in electrochemical cells which are typically made of glass. In infrared spectroelectrochemistry, glass must be avoided for cell components which interact with the infrared beam as glass is a strong absorber of infrared radiation. As such, infrared spectroelectrochemical cells require infrared-transparent windows such as $CaF_2$ or ZnSe. On the contrary, glass is a weak scatterer of light and poses little interference in EC-SERS measurements, especially when the focal point is far from the glass interface.
3. *Wider spectral range*: A commonly stated advantage of Raman spectroscopy over infrared spectroscopy more generally is the ability to access low frequency (low wavenumber) modes below the typical spectral cutoff for infrared spectroscopy at ~ 500 $cm^{-1}$. Modern Raman spectrometers can routinely reach a wavenumber limit of 50 $cm^{-1}$, which provides useful information on vibrational modes that involve heavy atoms, of particular interest in materials science and inorganic chemistry. As electrochemical methods, especially voltammetry, are routinely used to characterize inorganic compounds, this wider spectral range is an asset for accurate characterization.
4. *Instrumentation simplicity*: In general, interfacing an electrochemical cell with a Raman spectrometer is more straightforward than in infrared spectroscopy, largely due to the reasons highlighted in points 1 and 2 above. For confocal Raman spectrometers, an added challenge can be the short focal length, although this can be remedied by using a long working distance objective. For benchtop Raman spectrometers, the laser beam is often more readily accessed and is especially useful for EC-SERS measurements if the focal length is on the order of at least 5 mm or more. In addition, the advent of portable USB potentiostats has opened

up the field of electrochemistry enormously and has reduced the cost associated with spectroelectrochemical measurements.

*In addition to the advantages listed above, EC-SERS has advantages over SERS more generally, and these are important to note.*

5. *Enhancement of SERS signal*: A defining feature of SERS is the near-field dependence of the surface enhancement which decays sharply away from the surface such that only molecules that are within or in very close proximity (ideally < 3 nm) to the surface are detected [14]. The presence of the static electrochemical field in EC-SERS can thus function to bring analytes, both neutral and charged, closer to the surface and thus within the near-field electromagnetic enhancement region. In particular, the most enhanced signals in EC-SERS are often observed close to the potential of zero charge (PZC) for the metal being used, where there is surface charge neutrality [8]. This is particularly true for neutral molecules, which may be electrostatically repelled by an electrode surface which has a resting potential far from PZC.
6. *Electrified interface characterization*: A significant advantage of EC-SERS is the ability to obtain a vibrational fingerprint of the electrified interface in situ, thus providing important information not readily obtained through other techniques. As a result, EC-SERS has become a useful tool for studying a variety of electrochemical interfaces, including understanding the solid electrolyte interphase (SEI) for lithium-ion batteries [15], exploring fundamentals of surface charge-transfer processes [16], and *operando* nanoparticle reactions [17].
7. *Removal of surface contaminants*: Many SERS substrates are prepared using metal nanoparticles which have been synthesized using chemical reduction methods, which often leaves material behind on the surface, such as residual reducing agent, oxidation products, and capping and/or stabilizing agents. These surface contaminants can be problematic, as they produce spectral interferences and in addition block access to surface sites which are key to a strong SERS enhancement [18]. EC-SERS has been shown to be an effective route for the electrochemical desorption of interfering contaminants, such as citrate [19] and chloride [20].

## 10.3 Principles of EC-SERS

### *10.3.1 Theory of EC-SERS*

As noted above, EC-SERS involves a coupling of electrochemistry and SERS. Inherently, the SERS signal is still due to a combination of both electromagnetic and chemical enhancement mechanisms, but both of these are influenced by the presence of an applied electrochemical field [8, 21]. This makes EC-SERS signals amongst the most complicated spectroelectrochemical signals to interpret, and computational research

in this field is still in its infancy [22]. The spectral changes observed during EC-SERS measurements can be due to one, or a combination, of the following effects:

(i) *Electrochemical charge transfer*—This occurs as part of an oxidation or reduction reaction that takes place at the surface. When there is an overlap of the excitation energy and the charge-transfer energy, such as can happen when the Fermi level of the metal is manipulated through application of a voltage, a resonance condition can occur which enhances the SERS signal further. The resulting resonant-like Raman scattering effect increases the SERS enhancement by typically 1–2 orders of magnitude [8, 21].

(ii) *Surface charge effects*—As the potential is adjusted, the surface charge changes, which in turn allows for the selective adsorption/desorption of species at the metal interface. This can facilitate desorption of interfering contaminants and allow for the adsorption of molecular targets. By changing the applied potential, the potential of zero charge (PZC) for a particular metal can be approached, which is the potential at which the surface charge is neutral. Many neutral adsorbates will prefer to adsorb at potentials close to the PZC where electrostatic interference is reduced. For polycrystalline silver (Ag(poly)), for example, the PZC is approximately − 0.95 V versus Ag/AgCl [23], which is much more negative than the open circuit potential for Ag(poly), which is approximately − 0.1 V. This means that under non-electrochemical conditions (i.e. regular SERS), the surface charge of a Ag(poly) surface is highly positively charged. This makes SERS much less selective than EC-SERS, since the ability to quickly and easily alter the surface charge is not possible.

(iii) *Surface orientation changes*—In SERS, the surface selection rules are active, which means that polarizability tensors oriented along the surface normal will be enhanced, while those parallel to the surface are attenuated [24]. Since changes in applied potential are well-known to change the adsorption orientation of molecules at metal electrodes [25], these orientational changes can be monitored in situ using EC-SERS, providing valuable insight into molecular organization at the electrified interface [26, 27].

(iv) *Electrochemical Stark tuning*—During an EC-SERS measurement, it is possible that the vibrational frequency of an adsorbate may change with applied potential, a phenomenon known as electrochemical Stark tuning [8]. Two mechanisms are at play here; the first is related to potential-dependent metal-adsorbate interactions, while the second originates from the coupling of highly polarizable electrons in molecules with the strong electrostatic field. The electrochemical Stark effect is most pronounced for very large electric fields ($> 10^8$ V m$^{-1}$) [28] and for small molecular ions [29].

(v) *Distance dependence*—As noted earlier, the surface enhancement in SERS decays exponentially away from the surface, following a $r^{-10}$ dependence, where $r$ is the distance between adsorbate and surface [30]. Due to this sharp distance dependence, the strongest SERS signals are observed closest to the surface (ideally < 3 nm), and for this reason, the functional groups closest to the

electrode surface, such as those involved in adsorption, will be preferentially enhanced especially for large macromolecules.

(vi) *Plasmon-mediated reactions*—Surface plasmons which are at play in SERS generate hot carriers (electrons and holes) which can mediate chemical reactions at surfaces, in what is termed *plasmon-mediated* chemistry. These surface reactions can further complicate the EC-SERS signals, since many of these processes are redox reactions [31]. One of the first reported examples of a plasmon-mediated redox reaction was the plasmon-catalyzed oxidation of *para*-aminothiophenol (p-ATP) to dimercaptoazobenzene (DMAB), which was observed using SERS [32, 33] and EC-SERS [19, 34] measurements. Since plasmon-mediated reactions can chemically alter the species expected to be present at the electrified interface, such processes must be carefully considered when interpreting EC-SERS signals.

### *10.3.2 Experimental Details*

EC-SERS experiments require the typical instrumentation that accompanies both electrochemical and SERS measurements and this is briefly commented on below.

(i) *Laser source*—The laser selection in EC-SERS is similar to regular SERS, in that a careful choice must be made which balances the attributes of the laser with the plasmonic properties of the metal substrate. 532, 633, and 785 nm are the most widely used excitation sources, with the latter two working for all commonly used coinage metals (Au, Ag, and Cu). Additionally, the 785 nm laser is preferred for samples that exhibit intrinsic fluorescence, which is reduced when the less energetic wavelength is used. Laser wavelengths longer than 785 nm are rarely used for EC-SERS measurements [8]. Since EC-SERS measurements are typically conducted in aqueous electrolyte solutions, much of the heat generated by the incident laser is dissipated in comparison to non-EC-SERS, such that higher laser powers can be exploited.

(ii) *Spectrometer*—The spectrometer has three primary components: the monochromator entrance slit, the grating, and the detector. Larger entrance slits are preferred for improved sensitivity but reduce spectral resolution. Gratings and detectors are selected based on the excitation wavelength, and high- and low-resolution gratings are both available. Detectors are normally cooled CCDs which offer advantages of fast response times and high sensitivity. EC-SERS measurements generally do not require any additional features for the spectrometer.

(iii) *Optical path configurations*—For SERS measurements, bottom, top, and side illumination are the optical path configurations most commonly employed. EC-SERS measurements use both bottom and top illumination, while side illumination is less common [8]. Bottom illumination offers high optical efficiency but requires a transparent sample, while top illumination offers good optical efficiency while being applicable to most commonly used electrode materials.

Side illumination offers reduced collection efficiency but can be useful for some applications such as electrochemical tip-enhanced Raman spectroscopy (EC-TERS). Confocal Raman microscope systems can be used for EC-SERS measurements provided a long working distance objective and/or thin-layer electrochemical cell is used.

(iv) *Spectroelectrochemical cell*—The spectroelectrochemical cell is central to the EC-SERS measurement. Most EC-SERS cells have a typical three-electrode configuration, consisting of a counter electrode (CE), a reference electrode (RE), and a working electrode (WE). As with most other spectroelectrochemical cells, the counter electrode is usually an inert conductive material (Pt, Au, C) and the reference electrode is typically a saturated calomel electrode (SCE) or a silver/silver chloride electrode (Ag/AgCl). The working electrode is the heart of the EC-SERS measurement and as a result will be described in more detail in the next section. The electrochemical cell is typically made of glass, since as noted above, glass is a weak scatterer of light. Teflon or polyether ether ketone (PEEK) components are incorporated into the cell as well, all of which are easily machined and cleaned for repeated use.

(v) *Nanostructured working electrodes*—The working electrode is the heart of the EC-SERS measurement and must satisfy the requirements for both the SERS measurement (nanoscale roughness, plasmonic response in the visible/NIR, uniform distribution of SERS-active "hot spots," etc.) and the electrochemical measurement (electrochemical stability, fast electron transfer kinetics, etc.) [35]. By far, the most common electrode materials for EC-SERS investigations are Au and Ag, due to their excellent stability and plasmonic response, with Cu being used less frequently due to oxide formation and a lack of stable reported nanostructures. Some examples of typical working electrodes that find use in EC-SERS are outlined below.

***Electrochemically Roughened Electrodes***: The first SERS observation was conducted using a silver electrode that had been electrochemically roughened. One of the simplest ways to produce a SERS-active electrode, this method involves the application of multiple oxidation–reduction cycles (ORC). A positive potential is applied initially to form ions or surface complexes, after which a negative potential is applied to reduce these species at the surface [35]. Established methods for electrochemical roughening of Au, Ag, and Pt have been described in detail elsewhere [21] and typically involve fast cycling of the potential between a cathodic and anodic limit in high ionic strength solutions, such as 0.1 M KCl. The electrochemically roughened electrode is typically noted by a darkening of the working electrode surface. An example of an electrochemically roughened surface is shown in Fig. 10.1a.

Despite their ease of fabrication and widespread early adoption, modern EC-SERS investigations have typically moved away from electrochemically roughened electrodes due to their physical instability, relatively low SERS enhancement factors, and their irreproducible, heterogeneous structure. Some recent studies have highlighted the use of in situ electrochemical roughening to fabricate SERS-active screen-printed

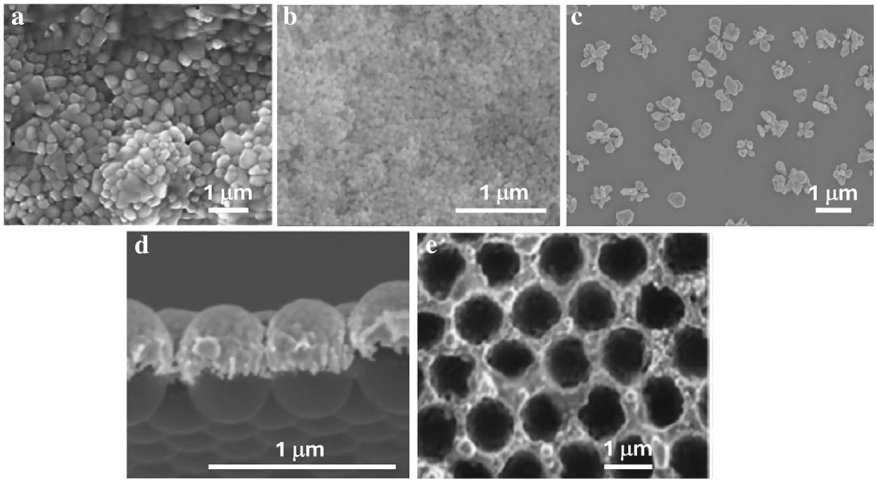



**Fig. 10.1** Scanning electron microscope (SEM) images of various nanostructured electrodes used for EC-SERS. **a** Electrochemically roughened electrode, **b** colloidal nanoparticle electrode, **c** electrodeposited electrode, **d** metal film-over-nanoparticle (MFON) electrode, **e** sphere segment void (SSV) electrode. Part **a** adapted from [36] with permission. Copyright Elsevier, 2018. Part **b** adapted from [37] with permission. Copyright Elsevier, 2018. Part **c** adapted from [38] with permission. Copyright Elsevier, 2015. Part **d** adapted from [39] with permission. Copyright American Chemical Society, 2017. Part **e** adapted from [40] with permission. Copyright American Chemical Society 2019

electrodes [36, 41]; however, electrochemical roughening has largely fallen out of favor compared to other methods of electrode fabrication.

***Colloidal Nanoparticle Electrodes***: Since the early days of SERS, metal nanoparticles produced using wet chemical methods, such as chemical reduction strategies, have been popular due to their ease of synthesis, low cost of manufacture, and the wide variety of shapes and sizes of nanoparticles available with good control over polydispersity. For gold nanoparticles, the common synthetic approaches include the Turkevich–Frens [42, 43] method for gold nanospheres and the seeded-growth approach for gold nanorods [44]. For silver nanoparticles, the most common synthetic methods for silver nanospheres include variations on the traditional Lee and Meisel citrate reduction [45] as well as the Leopold and Lendl hydroxylamine reduction [46]. Once synthesized, these nanoparticles can be characterized and then deposited onto a traditional electrode material as a rigid conductive support (gold, glassy carbon, ITO, etc.). Often, several layers of a concentrated colloidal sol are required to have a functional SERS-active electrode (Fig. 10.1b). SERS-active electrodes produced using colloidal particles generally exhibit good SERS signal uniformity and have been used in a variety of EC-SERS-based sensing applications, ranging from biomarker analysis [47, 48] to bacterial screening [49] to environmental monitoring [27, 50]. Spherical nanoparticles have advantages such as ease of synthesis, fast synthetic times, and

relatively few additives; however, they generally give rise to only moderate enhancement factors, owing to a lack of sharp structural features which produce more efficient electromagnetic enhancements. To date, such anisotropic structures have not been explored in EC-SERS investigations; however, given the tunable plasmonic response of these structures and the potential to electrochemically remove surface contaminants, these materials should be explored going forward [35]. A limitation of drop-casted colloidal particles is that as a result of the deposition process, the nanoparticles lack large-scale uniformity and organization, which can result in a lack of signal uniformity due to a non-uniform distribution of plasmonic hot spots. Some researchers have tried to address this issue by employing modified nanoparticles [51] as well as 2D particle arrays [52, 53].

***Electrodeposited Electrodes***: Nanostructured electrodes can also be produced through electrodeposition, wherein a metal cation ($Ag^{+}$, $Au^{3+}$) is electrochemically reduced onto a conductive solid support (Fig. 10.1c). This is a potentially attractive method for making SERS-active electrodes, as it requires little additional equipment and is relatively fast. By varying the electrochemical parameters as well as the electrolyte composition, the nucleation and growth of metal nanoparticles can be controlled [35]. Electrodeposition also allows for the creation of novel nanostructures including bimetallic nanoparticles [54]. Some limitations with electrodeposition methods also are apparent however, such as challenges in careful control of nanoparticle growth, which can cause the metal particles to become too large in size (and thus no longer SERS-active), as well as non-uniform coverage of the underlying conductive material, which can lead to background signals and residual fluorescence.

***Template-Based Electrodes***: While nanoparticle-based electrodes are easy and economical to fabricate, they suffer from drawbacks, the largest of which is the non-uniform deposition of the nanoscale features. This leads to a non-uniform distribution of hot spots for SERS and can make quantitative analysis challenging. Template-based methods of electrode fabrication are a good solution to this problem. Two methods of templating have shown the most promise over the past several decades: nanosphere lithography (NSL) and anodic aluminum oxide (AAO) templating.

Nanosphere lithography (NSL) was first developed by Van Duyne and Hulteen in 1995 [55] and extended to EC-SERS by Van Duyne [56] and Bartlett [57]. In NSL, a solid conductive material (ITO, Au, Ag) is used as the support and a thin layer of monodispersed polystyrene or silica nanospheres of a desired diameter are dispersed onto the surface using either drop casting or spin coating and are allowed to self-assemble into a close-packed array. This colloidal crystal array acts as a template for the next step, where a thin layer of metal is deposited over top of the array to a desired thickness. The thickness of the metal film is chosen carefully and results in one of three types of structures: (a) for thick metal films, the spheres are completely coated and form what is termed a metal film-over-nanosphere (MFON) substrate (Fig. 10.1d), (b) for thin metal films, the polystyrene spheres are dissolved away using an organic solvent, leaving behind a periodic particle array (PPA), and (c) if the metal is deposited electrochemically, and the spheres are then removed, the resulting structure is a hexagonal array of segment sphere voids (SSV) (Fig. 10.1e). Of these

three structural possibilities, the MFON substrate has found the most widespread use for EC-SERS measurements due to the ease of preparation, electrochemical stability, and excellent reproducibility.

Anodic aluminum oxide (AAO) templates, known more generally as porous alumina templates, have also found use in EC-SERS measurements. These templates are formed when electrochemically polished aluminum foil is oxidized and very ordered two-dimensional arrays of cylindrical nanopores can be obtained. The diameter of the pores is easily tuned between 15 and 150 nm by adjusting the anodic voltage, solution pH and composition, and temperature [21]. The AAO film is then immersed in a metal salt solution of interest, and application of an AC current and DC voltage allows the formation of thin metal nanowires within the porous alumina template. These nanowires can then either be maintained within the template or are more often released by etching away the aluminum template [58]. In either case, fashioning the nanowires into an effective SERS-active electrode that maintains electrical conductivity can be challenging [21].

Another technique used to create nanostructured SERS-active electrodes is electron beam lithography (EBL). This technique offers the advantage of creating nanoscale features with precise size, shape, and interparticle spacing. In EBL, a substrate is coated with a polymer film (resist) and a focused electron beam draws custom shapes in the film. The electron beam alters the polymer solubility and results in a patterned mask. A metal film is then deposited on top of the mask and the polymer is washed away, leaving behind the nanopatterned surface [59]. Despite the advantages of EBL, numerous disadvantages include the requirement for expensive and complicated instrumentation, long fabrication times, and limited ability to scale. These disadvantages make EBL for SERS-active electrode fabrication challenging beyond use for fundamental studies where nanoscale precision is required [35].

***Screen-Printed Electrodes***: Starting in the mid-1990s, screen-printing technology adapted from the microelectronics industry was explored for routine production of disposable low-cost electrodes for electroanalytical measurements [60]. Screen-printing technology offers advantages of high-volume production, low cost, high reproducibility, and reliability. In the early 2010s, screen-printed electrodes (SPEs) began to be explored for EC-SERS [19, 61], and since this time, SPEs have become a favored SERS-active electrode platform, since the SPE greatly simplifies EC-SERS in general and reduces cost since the carbon electrodes are disposable, eliminating time-consuming electrode cleaning and polishing. To render the SPE SERS-active, a variety of methods have been explored, as highlighted in Fig. 10.2. The most straight forward way to make a metal (i.e., gold) SPE electrode SERS-active is to apply ORC as outlined above [36]. Simple electrodeposition of metal onto a carbon SPE works well [54] but can result in poor coverage of the working electrode surface. Drop casting of metal nanoparticles is cost effective and easy to do and has been demonstrated to provide quantitative results for EC-SERS investigations [48]. More recently, other techniques have been explored to provide nanoscale roughness to carbon SPEs, including vacuum deposition of metal on top of the carbon paint surface, where the carbon black particles function as an ideal template for creating nanoscale

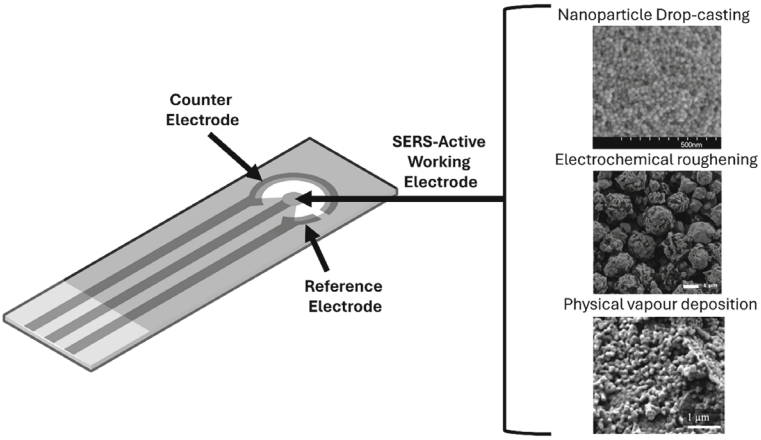



**Fig. 10.2** Screen-printed electrodes contain the three electrodes required for voltammetric studies incorporated into a single chip. The working electrode can be rendered SERS-active through a variety of methods, including drop casting of colloidal nanoparticles (top right), electrochemical roughening (middle right), and physical vapor deposition (bottom right). Top right image is adapted from [48] with permission. Copyright American Chemical Society, 2015. Middle right image is adapted from [63] with permission. Copyright Elsevier, 2020. Bottom right image is adapted from [62]

metal features [62]. To a large extent, the explosion of interest in EC-SERS over the past decade has largely been a result of the use of SPEs for EC-SERS, which greatly simplifies the technique more generally, making it more accessible to a larger community of researchers.

(vi) *Supporting electrolytes and solvents*—For EC-SERS measurements, the same supporting electrolytes are used as for typical electrochemical studies, with the added caveat that one should avoid species that have strong SERS signals on their own or use species that have vibrational modes that are distinct from the analyte of interest. Additionally, anions that exhibit a strong specific adsorption on gold and silver ($Cl^-$, $Br^-$, $I^-$) can be problematic. Very acidic and basic supporting electrolytes can undergo reactions with the plasmonic surface and should be avoided [8]. Common supporting electrolytes include NaF, $Na_2SO_4$, $NaClO_4$, and phosphate buffer. Since most EC-SERS measurements are done in aqueous electrolyte, the use of water as the solvent is never an issue due to the weak Raman scattering of water. Use of organic solvents, however, such as in non-aqueous electrochemistry can be challenging due to the typically strong Raman signal of organic solvents.

## 10.4 Applications of EC-SERS

Since EC-SERS provides surface-specific vibrational spectra under controlled electrode polarization in an electrochemical cell, a multitude of applications arise. Adsorption/desorption processes can be studied, redox reactions can be monitored, and corrosion inhibition can be elucidated, to name a few. A strength of EC-SERS is the ability to explore a multitude of experimental systems, ranging from biosensor development to environmental monitoring to fundamental studies of catalysis. In the sections below, some noteworthy applications of EC-SERS are highlighted. Some selected applications of EC-SERS are highlighted in Fig. 10.3.

***Analytical Sensing***: One of the largest applications of EC-SERS is electroanalytical sensing. Due to the enhanced Raman signal often achievable when a potential is applied, EC-SERS can often provide more sensitive analysis with lower limits of detection when compared to non-EC-SERS. Recent excellent reviews have provided an overview of EC-SERS for analytical sensing [68, 69]. Various analytes have been the spectroelectrochemical targets, ranging from small molecules such as dopamine [70], uric acid [47, 48], and adenine [37], to large biomolecules such as polyphenolic compounds [71] and penicillin [72].

Despite numerous examples of EC-SERS applied for analytical sensing, many of these reports are qualitative in nature and lack robust figures of merit, such as limits of detection and dynamic linear range determinations. A comparison of reported figures

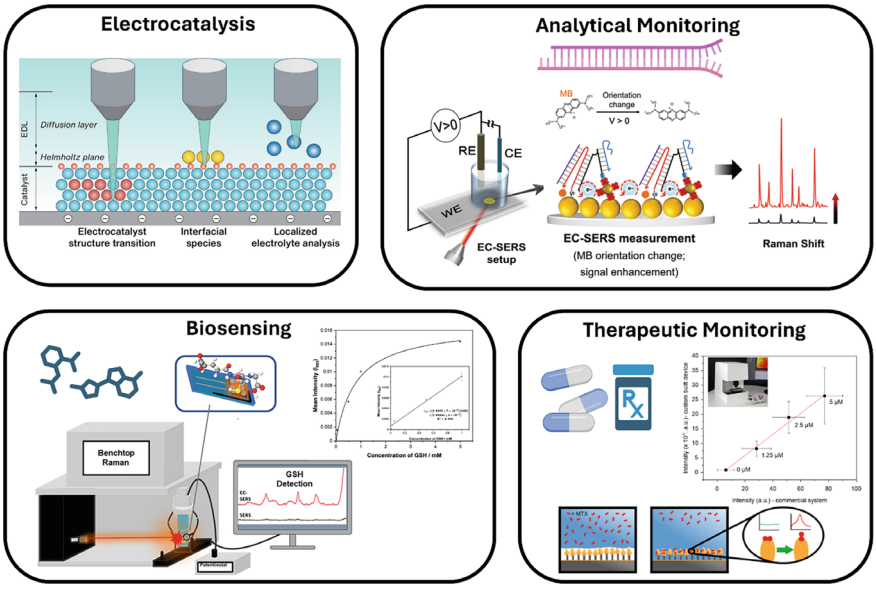



**Fig. 10.3** Some selected examples of applications of electrochemical surface-enhanced Raman spectroscopy (EC-SERS). Adapted with permission from [64–67]

of merit from a survey of publications highlighted that these values are comparable to non-EC-SERS in general, with no significant improvement in signal RSD values [69]. Linear dynamic ranges reported generally spanned 1–2 orders of magnitude for most cases and 4–6 orders of magnitude for select cases [69]. Direct analysis using EC-SERS is generally not overly selective, since matrix species can pose an interference at the electrified interface. To improve selectivity, various approaches have been explored including standard addition calibration [63], careful pH control [73], and chemical modification of the surface with capture agents such as aptamers [74]. Chemometric methods of analysis have been applied to analytical EC-SERS measurements to improve precision and sensitivity [75]; however, these studies have not been evaluated in real samples. At this point, EC-SERS for electroanalytical analysis is still a field in its infancy which would benefit from more rigorous analytical treatment and evaluation of the technique's potential in real sample matrices [69].

***Biosensor Development***: Since the early days of SERS, biosensor development as an application has been an attraction. SERS, as a vibrational characterization tool, naturally lends itself well to the analysis of biologically relevant molecules, including metabolites, proteins, and nucleic acids. Early reviews on SERS as a developing technique noted that biosensor development was likely to be a primary application [76, 77]. Since many biomolecules are also electroactive, it is natural to extend EC-SERS to biosensor development as well. Karaballi et al. reported on the first EC-SERS aptasensor—an EC-SERS sensor that uses an aptamer as the recognition agent [74]. In this work, a DNA sequence likely to be present in the urine of a tuberculosis patient was detected using an aptamer-modified silver nanoparticle (AgNP) SPE. The aptamer was devoid of adenine, while the target DNA contained adenine, and hence, detection of the vibrational modes of adenine confirmed the presence of the target DNA strand, which would result in a positive TB diagnosis. Lynk et al. explored EC-SERS as a method to spectrally characterize bacteria [49]. In this work, various bacterial species were explored, with the result that only small molecule metabolites from the bacteria were observed, as has been noted in SERS studies of bacteria more generally [78]. However, it was still possible to differentiate the bacteria based on the relative intensities of the various metabolites in the sample. Ibañez et al. have demonstrated that SERS-based spectroelectrochemistry can be used to study redox mechanisms of important biomolecules, such as adenine and guanine [79].

Lee et al. have reported on a functionalized gold nanoparticle electrodeposited onto indium tin oxide for detecting microRNA using EC-SERS [64]. By holding the electrode potential at + 0.2 V vs Ag/AgCl, a significant enhancement in the SERS signal was observed such that highly sensitive ($60 \times 10^{-18}$ M) detection of microRNA in serum was achieved. Uric acid has been a popular biological target for EC-SERS investigations due to its importance in monitoring pregnancy-induced hypertension. Uric acid is readily detected using EC-SERS, compared to the lengthy and complicated enzymatic assays currently used in clinical work [47, 80, 81]. In a recent work by Chotoye et al., EC-SERS was used to directly detect glutathione in saliva [65]. Glutathione is an important free radical scavenger in biological systems,

aiding in reducing oxidative stress. Quantitative determination of glutathione in artificial saliva was achieved with a limit of detection of 5 μM with a good reported linear dynamic range of 0.005–1.0 mM.

***Environmental Monitoring***: Owing to the relative simplicity of EC-SERS, especially when screen-printed electrodes and portable instrumentation are used, there has been interest in applying this technique for environmental monitoring. For example, Ibañez et al. reported on the use of EC-SERS for the detection of three classes of common pesticides; dithiocarbamate, chloronicotinyl, and organophosphate. In this work, EC-SERS was coupled with a preconcentration step which helped to overcome the lack of sensitivity of normal Raman and SERS. Cyclic voltammetry was completed after the preconcentration step, which provided enhanced sensitivity due to the in situ generation of new nanostructures on the surface [50]. EC-SERS has also been used to detect atrazine [27], a common herbicide, and azithromycin [82] in wastewater, a commonly prescribed antibiotic.

A challenge in developing analytical methods for environmental monitoring is the very low concentration at which the target analytes are typically found. Additionally, the locations where sampling would be of interest can often be isolated, such that even with portable instrumentation, analysis is complicated and often not possible. One solution to this problem is to combine solid-phase extraction with SERS. While this has been increasingly popular in the SERS field [83], combining solid-phase extraction and EC-SERS is not something that has been explored to date.

***Electrocatalysis***: One of the largest and most widespread applications of EC-SERS is electrocatalysis. Since electrocatalytic processes take place at the electrified surface, using EC-SERS to monitor and characterize electrocatalytic reactions is well established. Many electrochemical storage and conversion systems involve electrocatalytic reactions [8]. Such reactions involve a variety of processes including adsorption, desorption, diffusion, and electron/charge transfer, among others. Probing the interfacial structure and intermediate species formed during electrocatalytic reactions is important to both understand and improve electrocatalytic reactions. Early work in this area focused on combining normal Raman analysis of the surface during electrocatalysis; however, these investigations were often limited in their sensitivity and scope. EC-SERS, on the other hand, has the sensitivity and rapid response time needed to follow electrocatalytic reactions on surfaces in situ and under operando conditions [84]. Several studies have used EC-SERS to study formic acid electrooxidation, important for direct formic acid fuel cell technology [85, 86]. In these works, the ability to monitor the electrocatalytic reaction at the Pt surface using EC-SERS was beneficial not only for a deeper understanding of the system but also provided insight into how to improve the catalytic activity. Recent excellent reviews have discussed the usefulness of Raman spectroelectrochemistry for electrocatalytic applications [66, 87].

***Forensics***: The field of forensic chemistry relies heavily on confirmatory testing, especially with respect to illicit drug identification. This is often done using LC-MS or GC-MS; however, infrared and Raman spectroscopy are also heavily utilized. For

illicit drug identification using normal Raman spectroscopy, intrinsic fluorescence from the sample itself can lead to large spectral backgrounds, obscuring the much weaker Raman signal. Additionally, if the analyte of interest is present in lower concentration (a drug metabolite in urine, for example), normal Raman will lack the sensitivity needed to provide an accurate identification. Recent reviews on SERS for forensic applications have focused on advancements in this field and the advantages that SERS can offer [88–90]. In particular, enhanced sensitivity and selectivity over normal Raman are highlighted, allowing for smaller sample sizes and lower detection limits, which is useful for forensic applications. These reviews highlight the screening potential of SERS for forensic applications, which has numerous advantages over the typical screening tests in use today, many of which are simple chemical spot tests which only detect the presence of certain functional groups, and as a result lack selectivity and are prone to false positives.

The extension of EC-SERS as a tool in the field of forensics is more recent. In 2020, Bindesri et al. reported on the use of EC-SERS to detect tetrahydrocannabinol (THC), the primary psychoactive cannabinoid in *Cannabis sativa*, and carboxy-tetrahydrocannabinol (THC-COOH), the main secondary metabolite of THC, in synthetic saliva and urine, respectively [91]. Monitoring of molecular markers of recent or sustained cannabis use is important to prevent drugged driving and for regular screening of employees who are prohibited from using cannabis. This work combined EC-SERS studies with ab initio calculations and demonstrated that applied potential was essential for efficient detection of THC and THC-COOH at low concentrations and in complex matrices. A recent study explored the use of simultaneous cyclic voltammetry and in situ SERS for determination of two synthetic designer drugs, mephedrone (4-MMC), and 4-methylethcathinone (4-MEC), in an effort to quantify these drugs in seized drug samples and spiked synthetic urine [92]. More recent works have focused on detection of fentanyl and fentanyl analogs which are extremely potent and a large contributor to the global opioid crisis. These works focused on the development of a fentanyl screening method based on EC-SERS [93], which showed very good accuracy, rapid result time, and a lack of false positives, when compared to the current fentanyl screening methods in use [94].

***Food Safety***: Another application of EC-SERS is food security. An early EC-SERS paper using screen-printed electrodes focused on the determination of melamine in skim milk as a way to monitor this food product adulterant [19]. Melamine can be intentionally added to food products (infant formula, powdered milk, etc.) to boost the apparent nitrogen content. A more recent study explored a multiamperometric-SERS detection of melamine on gold screen-printed electrodes which provided appropriate figures of merit and a notable measurement time of only 25 s [95]. In a related work, electrodeposited metal nanopillar SERS-active electrodes were used to detect plasticizers such as phthalate esters and bisphenol A [96]. Such substances can migrate out of food storage materials, leading to low-dose, long-term exposure in humans. The accumulation of these substances over time can trigger disruptions in fertility, reproduction, and metabolism. In this work, EC-SERS provided a limit of detection

of 0.002 ppb and a percent relative standard deviation of < 10%, showcasing this technique for quantitative analysis of plasticizers.

Related to food safety is the monitoring of pesticides and fungicides on the surfaces of fruit and vegetables as well as their respective juices. Moldovan et al. reported on the use of EC-SERS to monitor thiabendazole, a fungicide used for post-harvest treatment, in apple juice [41]. In this work, a good limit of detection (0.061 ppm), a reasonable linear range (0.5–10 μM), and a good intermediate precision (%RSD < 10%) were reported for thiabendazole and paves the way for integrated, portable analytical systems based on EC-SERS. Emerging concern over neonicotinoid pesticides inspired Tang et al. to use EC-SERS to study acetamiprid (AAP), a common neonicotinoid pesticide, using a "mix and detect" method wherein a screen-printed electrode was modified by dropping silver nanoparticles onto the SPE surface [97]. This work highlighted a wide linear range (0.1–1000 μM) and a low limit of detection (0.04 μM) for acetamiprid and was used to successfully detect this pesticide in bok choy.

***Therapeutic Monitoring***: Owing to the redox activity of many drugs and their respective metabolites, the use of EC-SERS for therapeutic monitoring has recently been highlighted. Greene et al. used EC-SERS for monitoring 6-thiouric acid, a metabolite of Azathioprine™, a drug used to treat acute lymphoblastic leukemia (ALL), the most common childhood leukemia [20]. This study highlighted that EC-SERS could reliably provide a signal for 6-thiouric acid down to μM concentrations in synthetic urine. Zaleski et al. noted that errors in intravenous drug therapies can cause harm and in some cases can lead to death, and in their work, they highlighted a case where EC-SERS was used to quantitate an IV therapy analyte within a clinically relevant concentration range [39]. Specifically, EC-SERS was used to evaluate dobutamine, a drug commonly administered after heart surgery. Dobutamine detection with EC-SERS was found to have a limit of detection that was four orders of magnitude below the clinical range. Additionally, this work highlighted hand-held Raman instrumentation for EC-SERS studies, showcasing the technique for clinical setting application. Göksel et al. used electrochemically assisted SERS to detect and monitor methotrexate (MTX) in human serum at clinically relevant concentrations using a portable, benchtop Raman system [67]. The authors noted that by optimizing the pH and the electrochemical parameters, enhanced sensitivity for MTX detection was demonstrated using a benchtop Raman system that provided fast SERS chip mapping at a relatively low cost.

***Fundamental Electrochemistry***: It goes without saying that one of the most important applications of EC-SERS is for the study of fundamental electrochemical and surface processes. Early spectroelectrochemical investigations involving Raman spectroscopy highlight a diverse array of applications, ranging from catalysis [98, 99], to thin films [100, 101] to corrosion [102]. More recently, EC-SERS has found use for exploring the fundamental electrochemistry of emerging systems. For example, Dominique et al. used SERS under potential control to investigate the electrochemical stability of N-heterocyclic carbene (NHC) monolayers on gold [103]. Recently, NHC monolayers have been transforming electrocatalysis and biosensor design via

their increased performance and stability when compared to traditional thiols [104]. However, the electrochemical stability of these films remains underexplored. In the work by Dominique and others, NHC monolayers on gold exhibited electrochemical stability over a wide voltage range but were found to degrade at strongly reducing or oxidizing potentials [103]. Under continuous voltammetric interrogation via cyclic voltammetry, NHC monolayers were stable for up to ~ 40 h and this stability was highly influenced by NHC modification.

In work by Karaballi and co-authors, EC-SERS was used to probe the interaction between protein aggregates and a biomimetic membrane [105]. Specifically, a model biological lipid membrane was deposited onto a AgNP modified SPE using Langmuir–Blodgett/Langmuir–Schaefer (LB/LS) deposition, and this membrane was then allowed to interact with protein aggregates at various stages of aggregation to better understand the amyloid pore hypothesis of Alzheimer's disease. Resulting deterioration of the model membrane due to interaction with the protein aggregates could be monitored directly and indirectly using SERS, and the addition of an applied potential was important to mimic electric field conditions experienced by real cell membranes. In this study, it was found that oligomers and protofibrils caused the most significant membrane deterioration while native protein appeared to play a protective role, preventing pore formation [105].

## 10.5 Future Outlook and Opportunities

Electrochemical SERS has a long and established history, particularly within the electrochemical community, but due to recent advances which include screen-printed electrodes, portable instrumentation, and enhanced computational power, EC-SERS is increasingly entering the mainstream of electroanalytical techniques. Numerous advantages include increased sensitivity and enhanced selectivity compared to non-EC-SERS, reduced spectral interference from bulk species, and a wide range of potential analytes that can be monitored. EC-SERS also has its limitations that require further investigation, which includes a need for a better understanding of the analytical performance of EC-SERS and issues related to the requirement that the species of interest be present on the surface of the electrode, which can lead to both memory effects and a reduced selectivity [69]. Additionally, more studies are needed which demonstrate the potential of EC-SERS using real samples, such as bodily fluids and natural waters.

There are number of emerging areas where EC-SERS is likely to have a valuable impact in the future, and these are briefly outlined below.

**2D Semiconductor Materials**: Two-dimensional (2D) semiconductor materials are an emerging area in materials science and plasmonics. These materials are attractive because they possess unique properties that make them useful for nanotechnology applications. Such materials include graphene, hexagonal boron nitride, and the 2D dichalcogenides such as $MoS_2$. $MoS_2$ nanosheets exhibit unique physical, optical,

and electrical properties and have potential application in nanoelectronics, optoelectronics, and energy harvesting. Some early studies have explored both the electrochemical and SERS activity of these materials, including $MoS_2$ [106]; however, explorations using the combined technique of EC-SERS are rare. Additionally, some 2D semiconductor materials have reported plasmonic properties, making them useful in their own right for the development of new plasmonic substrates for SERS [107] as well as EC-SERS [108] investigations.

**Operando Measurements**: Operando spectroscopy involves the simultaneous collection and characterization of time-resolved spectroscopic data coupled with online product analysis. Such measurements allow for a deeper understanding of a material's performance under operational conditions, and the material of interest can include catalysts, batteries, and fuel cell components, to name a few. Operando measurements require tools that provide detailed information on the materials of interest, have fast response times, and can be readily adapted for a variety of measurement conditions, and therefore, time resolved EC-SERS is likely to be a useful future addition to the operando measurement toolkit.

**High-Temperature, High-Pressure Measurements**: Most EC-SERS measurements are done under conditions of ambient temperature and pressure. Many relevant processes, however, take place under conditions of high temperature and pressure. Since these same processes often involve chemical reactions taking place on surfaces, spectroelectrochemical studies under relevant temperature and pressure conditions should be explored.

**Single Molecule EC-SERS**: The development of single molecule SERS (SM-SERS) over the past several decades has paved the way for single molecule EC-SERS (SM-EC-SERS), which exploits the numerous advantages of SM-SERS for studying nanoscale electrochemistry. Recent investigations using SM-EC-SERS have highlighted a number of applications including fundamental studies of redox probes [109] and a coupling of electrochemistry and tip-enhanced Raman spectroscopy (EC-TERS) to study redox reactions at the single or few molecule level [11]. While still a technique in its infancy, SM-EC-SERS holds significant potential for single molecule electrochemistry, cellular biochemistry, and electrocatalysis.

**Computational Studies**: A challenge with EC-SERS is the complexity of the measured signal, which can result in inconclusive interpretations of what is happening at the electrified interface. Computational methods which can help unravel the complexity of the contributions from the co-existing alternating electromagnetic field and the static electrical potential are in development but have not been routinely applied for EC-SERS studies. More work in this area is needed, especially as computational techniques advance.

**Dual EC-SERS Analysis**: Most EC-SERS studies make use of the applied potential during the measurement to improve the Raman signal and enhance selectivity. However, electrochemical measurements are powerful for characterization in their

own right. Hence, moving forward, more effort should be used to conduct electrochemical measurements in parallel to the SERS measurements to learn more about the system under study. Simple cyclic voltammetry, for example, can prove valuable information which is key to understanding the electron transfer process being monitored spectroscopically.

## References


1. Fleischmann, M., Hendra, P. J. & McQuillan, A. J. Raman spectra of pyridine adsorbed at a silver electrode. Chem. Phys. Lett. **26**, 163–166 (1974).
2. Jeanmaire, D. L. & Duyne, R. P. V. Surface raman spectroelectrochemistry: Part I. Heterocyclic, aromatic, and aliphatic amines adsorbed on the anodized silver electrode. J. Electroanal. Chem. **84**, 1–20 (1977).
3. Albrecht, M. G. & Creighton, J. A. Anomalously intense Raman spectra of pyridine at a silver electrode. J. Am. Chem. Soc. **99**, 5215–5217 (1977).
4. Tsai, M.-H., Lin, Y.-K. & Luo, S.-C. Electrochemical SERS for in Situ Monitoring the Redox States of PEDOT and Its Potential Application in Oxidant Detection. ACS Appl. Mater. Interfaces **11**, 1402–1410 (2019).
5. Willets, K. A. Probing nanoscale interfaces with electrochemical surface-enhanced Raman scattering. Curr. Opin. Electrochem. **13**, 18–24 (2019).
6. Dai, K. *et al*. Adsorption and reduction reactions of anthraquinone derivatives on gold electrodes studied with electrochemical surface-enhanced Raman spectroscopy. J. Raman Spectrosc. **43**, 1367–1373 (2012).
7. Rycenga, M. *et al*. Controlling the Synthesis and Assembly of Silver Nanostructures for Plasmonic Applications. Chem. Rev. **111**, 3669–3712 (2011).
8. Brosseau, C. L. *et al*. Electrochemical surface-enhanced Raman spectroscopy. Nat Rev Methods Primers **3**, 79 (2023).
9. Li, J.-F., Rudnev, A., Fu, Y., Bodappa, N. & Wandlowski, T. In situ SHINERS at electrochemical single-crystal electrode/electrolyte interfaces: Tuning preparation strategies and selected applications. ACS Nano **7**, 8940–8952 (2013).
10. Wang, J. *et al*. In situ SERS and SHINERS study of electrochemical hydrogenation of p-ethynylaniline in nonaqueous solvents. Electrochem. Commun. **78**, 16–20 (2017).
11. Kurouski, D., Mattei, M. & Van Duyne, R. P. Probing Redox Reactions at the Nanoscale with Electrochemical Tip-Enhanced Raman Spectroscopy. Nano Lett. **15**, 7956–7962 (2015).
12. Osawa, M. Dynamic Processes in Electrochemical Reactions Studied by Surface-Enhanced Infrared Absorption Spectroscopy (SEIRAS). Bulletin of the Chemical Society of Japan **70**, 2861–2880 (1997).
13. Zawisza, I., Bin, X. & Lipkowski, J. Potential-Driven Structural Changes in Langmuir–Blodgett DMPC Bilayers Determined by in situ Spectroelectrochemical PM IRRAS. Langmuir **23**, 5180–5194 (2007).
14. Masango, S. S. *et al*. High-Resolution Distance Dependence Study of Surface-Enhanced Raman Scattering Enabled by Atomic Layer Deposition. Nano Lett. **16**, 4251–4259 (2016).
15. Hy, S. *et al*. In situ surface enhanced Raman spectroscopic studies of solid electrolyte interphase formation in lithium ion battery electrodes. J. Power. Sources **256**, 324–328 (2014).
16. Li, R. *et al*. SERS Detection of Charge Transfer at Electrochemical Interfaces Using Surface-Bound Ferrocene. J. Phys. Chem. C **127**, 14263–14269 (2023).
17. Wonner, K. *et al*. Operando electrochemical SERS monitors nanoparticle reactions by capping agent fingerprints. Nano Res. **15**, 4517–4524 (2022).
18. Morder, C. J., Schorr, H. C., Balss, K. M. & Schultz, Z. D. Bleach Cleaning of Commercially Available Gold Nanopillar Arrays for Surface-Enhanced Raman Spectroscopy (SERS). Appl Spectrosc **78**, 268–276 (2024).

19. Robinson, A. M., Harroun, S. G., Bergman, J. & Brosseau, C. L. Portable Electrochemical Surface-Enhanced Raman Spectroscopy System for Routine Spectroelectrochemical Analysis. Anal. Chem. **84**, 1760–1764 (2012).
20. Greene, B. H. C., Alhatab, D. S., Pye, C. C. & Brosseau, C. L. Electrochemical-Surface Enhanced Raman Spectroscopic (EC-SERS) Study of 6-Thiouric Acid: A Metabolite of the Chemotherapy Drug Azathioprine. J. Phys Chem. C **121**, 8084–8090 (2017).
21. Wu, D.-Y., Li, J.-F., Ren, B. & Tian, Z.-Q. Electrochemical surface-enhanced Raman spectroscopy of nanostructures. Chem. Soc. Rev. **37**, 1025–1041 (2008).
22. Aranda, D. *et al*. Computational Model for Electrochemical Surface-Enhanced Raman Scattering: Key Role of the Surface Charges and Synergy between Electromagnetic and Charge-Transfer Enhancement Mechanisms. J. Chem. Theory Comput. **18**, 6802–6815 (2022).
23. Larkin, D., Guyer, K. L., Hupp, J. T. & Weaver, M. J. Determination of specific adsorption of some simple anions at a polycrystalline silver-aqueous interface using differential capacitance and kinetic probe techniques. Journal of Electroanalytical Chemistry and Interfacial Electrochemistry **138**, 401–423 (1982).
24. Moskovits, M. Surface selection rules. J. Chem. Phys. **77**, 4408–4416 (1982).
25. *Adsorption of Molecules at Metal Electrodes.* (VCH, New York, NY, 1992).
26. Dendisova, M., Nemeckova, Z., Clupek, M. & Prokopec, V. EC-SERS study of phenolic acids sorption behavior on Au, Ag and Cu substrates - Effect of applied potential and metal used. Appl. Surf. Sci. **470**, 716–723 (2019).
27. Albarghouthi, N., Eisnor, M. M., Pye, C. C. & Brosseau, C. L. Electrochemical Surface-Enhanced Raman Spectroscopy (EC-SERS) and Computational Study of Atrazine: Toward Point-of-Need Detection of Prevalent Herbicides. J. Phys. Chem. C. **126**, 9836–9842 (2022).
28. Oklejas, V., Sjostrom, C. & Harris, J. M. SERS Detection of the Vibrational Stark Effect from Nitrile-Terminated SAMs to Probe Electric Fields in the Diffuse Double-Layer. J. Am. Chem. Soc. **124**, 2408–2409 (2002).
29. Zhang, N. *et al*. Probing double layer structure at Au/[BMIm]$BF_4$ interface by molecular length-dependent SERS Stark effect. J. Electroanal. Chem. **751**, 137–143 (2015).
30. Sharma, B., Frontiera, R. R., Henry, A.-I., Ringe, E. & Van Duyne, R. P. SERS: Materials, applications, and the future. Materials Today **15**, 16–25 (2012).
31. Cui, L. *et al*. Plasmon-driven catalysis in aqueous solutions probed by SERS spectroscopy. J Raman Spectrosc. **47**, 877–883 (2016).
32. Huang, Y.-F. *et al*. When the Signal Is Not from the Original Molecule To Be Detected: Chemical Transformation of *para* -Aminothiophenol on Ag during the SERS Measurement. J. Am. Chem. Soc. **132**, 9244–9246 (2010).
33. Huang, Y.-F. *et al*. Surface-enhanced Raman spectroscopic study of p-aminothiophenol. Phys. Chem. Chem. Phys. **14**, 8485 (2012).
34. Devasenathipathy, R., Rani, K. K., Liu, J., Wu, D.-Y. & Tian, Z.-Q. Plasmon mediated photoelectrochemical transformations: The example of para-aminothiophenol. Electrochim. Acta **367** (2021).
35. Jones, T. Fabrication of nanostructured electrodes for electrochemical surface-enhanced Raman spectroscopy (E-SERS): a review. Materials Science and Technology **39**, 2287–2301 (2023).
36. Martín-Yerga, D. *et al*. Quantitative Raman spectroelectrochemistry using silver screen-printed electrodes. Electrochim. Acta **264**, 183–190 (2018).
37. Lynk, T. P., Clarke, O. J. R., Kesavan, N. & Brosseau, C. L. Development of a sustainable plasmon-enhanced spectroelectrochemical sensor using avocado pit (*Persea americana*) extract. Sensors and Actuators B Chemical **257**, 270–277 (2018).
38. Bian, J. *et al*. Reproducible and recyclable SERS substrates: Flower-like Ag structures with concave surfaces formed by electrodeposition. Appl. Surf. Sci. **333**, 126–133 (2015).
39. Zaleski, S. *et al*. Identification and Quantification of Intravenous Therapy Drugs Using Normal Raman Spectroscopy and Electrochemical Surface Enhanced Raman Spectroscopy. Anal. Chem. **89**, 2497–2504 (2017).

40. Dong, X. *et al*. Cu/Ag Sphere Segment Void Array as Efficient Surface Enhanced Raman Spectroscopy Substrate for Detecting Individual Atmospheric Aerosol. Anal. Chem. **91**, 13647–13657 (2019).
41. Moldovan, R. *et al*. EC-SERS detection of thiabendazole in apple juice using activated screen-printed electrodes. Food Chemistry **405**, 134713 (2023).
42. Turkevich, J., Stevenson, P. C. & Hillier, J. A study of the nucleation and growth processes in the synthesis of colloidal gold. Discuss. Faraday Soc. **11**, 55 (1951).
43. Frens, G. Controlled Nucleation for the Regulation of the Particle Size in Monodisperse Gold Suspensions. Nature Physical Science **241**, 20–22 (1973).
44. Lohse, S. E. & Murphy, C. J. The Quest for Shape Control: A History of Gold Nanorod Synthesis. Chem. Mater. **25**, 1250–1261 (2013).
45. Lee, P. C. & Meisel, D. Adsorption and surface-enhanced Raman of dyes on silver and gold sols. J. Phys. Chem. **86**, 3391–3395 (1982).
46. Leopold, N. & Lendl, B. A New Method for Fast Preparation of Highly Surface-Enhanced Raman Scattering (SERS) Active Silver Colloids at Room Temperature by Reduction of Silver Nitrate with Hydroxylamine Hydrochloride. J. Phys. Chem. B **107**, 5723–5727 (2003).
47. Goodall, B. L., Robinson, A. M. & Brosseau, C. L. Electrochemical-surface enhanced Raman spectroscopy (E-SERS) of uric acid: a potential rapid diagnostic method for early preeclampsia detection. Phys. Chem. Chem. Phys. **15**, 1382–1388 (2013).
48. Zhao, L., Blackburn, J. & Brosseau, C. L. Quantitative Detection of Uric Acid by Electrochemical-Surface Enhanced Raman Spectroscopy Using a Multilayered Au/Ag Substrate. Anal. Chem. **87**, 441–447 (2015).
49. Lynk, T. P., Sit, C. S. & Brosseau, C. L. Electrochemical Surface-Enhanced Raman Spectroscopy as a Platform for Bacterial Detection and Identification. Anal. Chem. **90**, 12639–12646 (2018).
50. Ibanez, D., Begona Gonzalez-Garcia, M., Hernandez-Santos, D. & Fanjul-Bolado, P. Detection of dithiocarbamate, chloronicotinyl and organophosphate pesticides by electrochemical activation of SERS features of screen-printed electrodes. Spectrochimica Acta Part A-Molecular and Biomolecular Spectroscopy **248** (2021).
51. Wang, H., Levin, C. S. & Halas, N. J. Nanosphere Arrays with Controlled Sub-10-nm Gaps as Surface-Enhanced Raman Spectroscopy Substrates. J. Am. Chem. Soc. **127**, 14992–14993 (2005).
52. Albarghouthi, N., MacMillan, P. & Brosseau, C. L. Optimization of gold nanorod arrays for surface enhanced Raman spectroscopy (SERS) detection of atrazine. Analyst **146**, 2037–2047 (2021).
53. Smith, S. R. & Lipkowski, J. Guided Assembly of Two-Dimensional Arrays of Gold Nanoparticles on a Polycrystalline Gold Electrode for Electrochemical Surface-Enhanced Raman Spectroscopy. J. Phys. Chem. C **122**, 7303–7311 (2018).
54. Clarke, O. J. R., St Marie, G. J. H. & Brosseau, C. L. Evaluation of an Electrodeposited Bimetallic Cu/Ag Nanostructured Screen-Printed Electrode for Electrochemical Surface-Enhanced Raman Spectroscopy (EC-SERS) Investigations. J. Electrochem. Soc. **164**, B3091–B3095 (2017).
55. Hulteen, J. C. & Van Duyne, R. P. Nanosphere lithography: A materials general fabrication process for periodic particle array surfaces. Journal of Vacuum Science & Technology A: Vacuum, Surfaces, and Films **13**, 1553–1558 (1995).
56. Dick, L. A., McFarland, A. D., Haynes, C. L. & Van Duyne, R. P. Metal Film over Nanosphere (MFON) Electrodes for Surface-Enhanced Raman Spectroscopy (SERS): Improvements in Surface Nanostructure Stability and Suppression of Irreversible Loss. J. Phys. Chem. B **106**, 853–860 (2002).
57. Abdelsalam, M. E. *et al*. Electrochemical SERS at a structured gold surface. Electrochem. Commun. **7**, 740–744 (2005).
58. Bang, D. *et al*. One-step electrochemical fabrication of vertically self-organized silver nanograss. J. Mater. Chem. A **1**, 4851 (2013).

59. Abu Hatab, N. A., Oran, J. M. & Sepaniak, M. J. Surface-Enhanced Raman Spectroscopy Substrates Created *via* Electron Beam Lithography and Nanotransfer Printing. ACS Nano **2**, 377–385 (2008).
60. Renedo, O. D., Alonso-Lomillo, M. A. & Martínez, M. J. A. Recent developments in the field of screen-printed electrodes and their related applications. Talanta **73**, 202–219 (2007).
61. Li, D., Li, D.-W., Fossey, J. S. & Long, Y.-T. Portable Surface-Enhanced Raman Scattering Sensor for Rapid Detection of Aniline and Phenol Derivatives by On-Site Electrostatic Preconcentration. Anal. Chem. **82**, 9299–9305 (2010).
62. Farling, C. G., Stackaruk, M. C., Pye, C. C. & Brosseau, C. L. Fabrication of high quality electrochemical SERS (EC-SERS) substrates using physical vapour deposition. Phys. Chem. Chem. Phys. **23**, 20065–20072 (2021).
63. Hernandez, S. *et al*. Determination of nicotinamide in a multivitamin complex by electrochemical-surface enhanced Raman spectroscopy. J. Electroanal. Chem. **879** (2020).
64. Lee, T. *et al*. Single Functionalized pRNA/Gold Nanoparticle for Ultrasensitive MicroRNA Detection Using Electrochemical Surface-Enhanced Raman Spectroscopy. Advanced Science **7** (2020).
65. Chotoye, S. A. B., Eisnor, M. M., Ball, R. B. E. & Brosseau, C. L. Development of an electrochemical surface-enhanced Raman spectroscopic biosensor for the direct detection of glutathione. J Raman Spectrosc. **54**, 587–595 (2023).
66. Zheng, W. Beginner's Guide to Raman Spectroelectrochemistry for Electrocatalysis Study. Chemistry Methods **3**, e202200042 (2023).
67. Goksel, Y. *et al*. Methotrexate Detection in Serum at Clinically Relevant Levels with Electrochemically Assisted SERS on a Benchtop, Custom Built Raman Spectrometer. ACS Sensors **7**, 2358–2369 (2022).
68. Moldovan, R. *et al*. Review on combining surface-enhanced Raman spectroscopy and electrochemistry for analytical applications. Analytica Chimica Acta **1209**, 339250 (2022).
69. Markin, A. V., Arzhanukhina, A. I., Markina, N. E. & Goryacheva, I. Y. Analytical performance of electrochemical surface-enhanced Raman spectroscopy: A critical review. TrAC Trends in Analytical Chemistry **157**, 116776 (2022).
70. Lee, N. Soo, Hsieh, Y. Zung, Paisley, R. F. & Morris, M. D. Surface-enhanced Raman spectroscopy of the catecholamine neurotransmitters and related compounds. Anal. Chem. **60**, 442–446 (1988).
71. Eisnor, M. M. *et al*. Electrochemical surface-enhanced Raman spectroscopy (EC-SERS): a tool for the identification of polyphenolic components in natural lake pigments. Phys. Chem. Chem. Phys. **24**, 347–356 (2021).
72. Li, Y.-T. *et al*. Rapid and sensitive in-situ detection of polar antibiotics in water using a disposable Ag–graphene sensor based on electrophoretic preconcentration and surface-enhanced Raman spectroscopy. Biosensors and Bioelectronics **43**, 94–100 (2013).
73. Wicaksono, W. P., Dang, H., Lee, S. & Choo, J. Electrochemical surface-enhanced Raman spectroscopy analysis of malachite green on gold substrates. Appl. Surf. Sci. **649**, 159163 (2024).
74. Karaballi, R. A., Nel, A., Krishnan, S., Blackburn, J. & Brosseau, C. L. Development of an electrochemical surface-enhanced Raman spectroscopy (EC-SERS) aptasensor for direct detection of DNA hybridization. Phys. Chem. Chem. Phys. **17**, 21356–21363 (2015).
75. Hernandez, S., Perales-Rondon, J. V., Heras, A. & Colina, A. Electrochemical SERS and SOERS in a single experiment: A new methodology for quantitative analysis. Electrochim. Acta **334**, 135561 (2020).
76. Cotton, T. M., Kim, J. & Chumanov, G. D. Application of surface-enhanced Raman spectroscopy to biological systems. J Raman Spectrosc. **22**, 729–742 (1991).
77. Tripp, R. A., Dluhy, R. A. & Zhao, Y. Novel nanostructures for SERS biosensing. Nano Today **3**, 31–37 (2008).
78. Premasiri, W. R. *et al*. The biochemical origins of the surface-enhanced Raman spectra of bacteria: a metabolomics profiling by SERS. Anal. Bioanal. Chem. **408**, 4631–4647 (2016).

79. Ibañez, D., Santidrian, A., Heras, A., Kalbáč, M. & Colina, A. Study of Adenine and Guanine Oxidation Mechanism by Surface-Enhanced Raman Spectroelectrochemistry. J. Phys. Chem. C **119**, 8191–8198 (2015).
80. Zhao, L., Blackburn, J. & Brosseau, C. L. Quantitative Detection of Uric Acid by Electrochemical-Surface Enhanced Raman Spectroscopy Using a Multi Layered Au/Ag Substrate. Anal. Chem. **87**, 441–447 (2015).
81. Huang, C.-Y. & Hsiao, H.-C. Integrated EC-SERS Chip with Uniform Nanostructured EC-SERS Active Working Electrode for Rapid Detection of Uric Acid. Sensors **20** (2020).
82. Ball, R. & Brosseau, C. Targeting Antibiotic Pollution: An Investigation of Azithromycin in Wastewater by Electrochemical Surface-Enhanced Raman Spectroscopy. Can. J. Chem. **102**, cjc-2023-0120 (2024).
83. Jin, M., Shan, J., Wang, X., Ren, T. & Li, X. Determination of Florfenicol in Antibiotic Mixtures by Solid-Phase Extraction (SPE) and Surface-Enhanced Raman Scattering (SERS). Anal. Lett. **55**, 517–528 (2022).
84. Zaleski, S. *et al*. Investigating Nanoscale Electrochemistry with Surface- and Tip-Enhanced Raman Spectroscopy. Accounts of Chemical Research **49**, 2023–2030 (2016).
85. Chang Xie, W. *et al*. In-situ electrochemical surface-enhanced Raman spectroscopy study of formic acid electrooxidation at variable temperatures by high-frequency heating technology. Electrochim. Acta **281**, 323–328 (2018).
86. Solla-Gullón, J., Gómez, R., Aldaz, A. & Pérez, J. M. A combination of SERS and electrochemistry in Pt nanoparticle electrocatalysis: Promotion of formic acid oxidation by ethylidyne. Electrochem. Commun. **10**, 319–322 (2008).
87. Chen, M. *et al*. In-situ/operando Raman techniques for in-depth understanding on electrocatalysis. Chemical Engineering Journal **461**, 141939 (2023).
88. Fikiet, M. A. *et al*. Surface enhanced Raman spectroscopy: A review of recent applications in forensic science. Spectrochimica Acta Part A: Molecular and Biomolecular Spectroscopy **197**, 255–260 (2018).
89. Ott, C. E. & Arroyo, L. E. Transitioning surface-enhanced Raman spectroscopy (SERS) into the forensic drug chemistry and toxicology laboratory: Current and future perspectives. WIREs Forensic Science **5**, e1483 (2023).
90. Akçan, R. & Yıldırım, M. Ş. Raman Spectroscopy as a Novel Technology in Forensic Toxicological Analyses. *CAC* **17**, 1082–1096 (2021).
91. Bindesri, S. D., Jebailey, R., Albarghouthi, N., Pye, C. C. & Brosseau, C. L. Spectroelectrochemical and computational studies of tetrahydrocannabinol (THC) and carboxy-tetrahydrocannabinol (THC-COOH). Analyst **145**, 1849–1857 (2020).
92. Gonzalez-Hernandez, J. *et al*. Rapid Determination of the 'Legal Highs' 4-MMC and 4-MEC by Spectroelectrochemistry: Simultaneous Cyclic Voltammetry and In Situ Surface-Enhanced Raman Spectroscopy. Sensors **22** (2022).
93. Cooman, T., Ott, C. E. & Arroyo, L. E. Evaluation and classification of fentanyl-related compounds using EC-SERS and machine learning. Journal of Forensic Sciences **68**, 1520–1526 (2023).
94. Ott, C. E., Burns, A., Sisco, E. & Arroyo, L. E. Targeted fentanyl screening utilizing electrochemical surface-enhanced Raman spectroscopy (EC-SERS) applied to authentic seized drug casework samples. Forensic Chemistry **34**, 100492 (2023).
95. Hernandez, S. *et al*. Multiamperometric-SERS detection of melamine on gold screen-printed electrodes. J. Electroanal. Chem. **918** (2022).
96. Lee, S. H. *et al*. 3D plasmonic hotspot engineering toward ultrasensitive and rapid EC-SERS recognition of plasticizers. Microchemical Journal **196**, 109599 (2024).
97. Tang, X. *et al*. An applied potential powered screen-printed electrode for sensitive EC-SERS detection of acetamiprid. Sensors and Actuators B: Chemical **404**, 135279 (2024).
98. Holze, R. Surface Raman spectroelectrochemical studies of oxygen reduction catalysts: Co—tetramethoxyphenylporphyrin. Electrochim. Acta **36**, 999–1007 (1991).
99. Joya, K. S. & Sala, X. In situ Raman and surface-enhanced Raman spectroscopy on working electrodes: spectroelectrochemical characterization of water oxidation electrocatalysts. Phys. Chem. Chem. Phys. **17**, 21094–21103 (2015).

100. Desilvestro, J., Corrigan, D. A. & Weaver, M. J. Spectroelectrochemistry of thin nickel hydroxide films on gold using surface-enhanced Raman spectroscopy. J. Phys. Chem. **90**, 6408–6411 (1986).
101. Munce, C. G., Parker, G. K., Holt, S. A. & Hope, G. A. A Raman spectroelectrochemical investigation of chemical bath deposited $Cu_xS$ thin films and their modification. Colloids and Surfaces A: Physicochemical and Engineering Aspects **295**, 152–158 (2007).
102. Melendres, C. A., Pankuch, M., Li, Y. S. & Knight, R. L. Surface enhanced Raman spectroelectrochemical studies of the corrosion films on iron and chromium in aqueous solution environments. Electrochim. Acta **37**, 2747–2754 (1992).
103. Dominique, N. L., Chandran, A., Jensen, I. M., Jenkins, D. M. & Camden, J. P. Unmasking the Electrochemical Stability of N-Heterocyclic Carbene Monolayers on Gold. Chemistry A European J **30**, e202303681 (2024).
104. Crudden, C. M. *et al*. Ultra stable self-assembled monolayers of N-heterocyclic carbenes on gold. Nature Chem. **6**, 409–414 (2014).
105. Karaballi, R. A., Merchant, S., Power, S. R. & Brosseau, C. L. Electrochemical surface-enhanced Raman spectroscopy (EC-SERS) study of the interaction between protein aggregates and biomimetic membranes. Phys. Chem. Chem. Phys. **20**, 4513–4526 (2018).
106. Zhao, J., Zhang, Z., Yang, S., Zheng, H. & Li, Y. Facile synthesis of $MoS_2$ nanosheet-silver nanoparticles composite for surface enhanced Raman scattering and electrochemical activity. Journal of Alloys and Compounds **559**, 87–91 (2013).
107. Ling, X. *et al*. Raman Enhancement Effect on Two-Dimensional Layered Materials: Graphene, h-BN and $MoS_2$. Nano Lett. **14**, 3033–3040 (2014).
108. Qu, S. *et al*. An Electrochromic Ag-Decorated $WO_{3-x}$ Film with Adjustable Defect States for Electrochemical Surface-Enhanced Raman Spectroscopy. Nanomaterials **12**, 1637 (2022).
109. Cortés, E. *et al*. Monitoring the electrochemistry of single molecules by surface-enhanced Raman spectroscopy. J. Am. Chem. Soc. **132**, 18034–18037 (2010).

# Chapter 11
# Monitoring Plasmon-Assisted Catalysis by SERS




**Zhiyang Zhang and Janina Kneipp**

**Abstract** Due to its high efficiency and selectivity, plasmonic catalysis has attracted a lot of attention in heterogeneous catalysis. This chapter discusses plasmon-assisted reactions in the context of surface-enhanced Raman spectroscopic probing, which, as plasmon-enhanced spectroscopic tool, has been providing one of the main means to obtain an understanding of important steps in reaction mechanisms that involve the excitation of localized surface plasmon resonances as primary event. Important model reactions will be introduced, and aspects of their mechanisms will be discussed, together with methodological approaches that led to their observation, as well as their potential applications.

## 11.1 Introduction

The conversion and storage of solar energy in the form of chemical bonds through catalysis is attractive and promising. Plasmonic catalysis is a way to convert light energy to chemical energy based on plasmon-induced heterogeneous catalytic reactions [1]. The use of localized surface plasmon resonances (LSPR) in the improvement of semiconductor photocatalysis can be found in early work since 2000 [2–4]. The term "plasmonic photocatalysis" was used on of the first times by Awazu et al. in 2008 [5], and this work illustrated the enhancement of photocatalysis by LSPR. Plasmonic catalysis is achieved, either (i) by inducing photocatalysis on plasmonic nanostructures themselves or (ii) by enhancing the photocatalytic activity on composite photocatalysts containing a solid catalyst (e.g., semiconductor or other metal catalysts) and plasmonic nanostructures [1].

Z. Zhang
CAS Key Laboratory of Coastal Environmental Processes and Ecological Remediation, Yantai Institute of Coastal Zone Research, Chinese Academy of Sciences, Yantai 264003, China

J. Kneipp (✉)
Department of Chemistry, Humboldt-Universität zu Berlin, Brook-Taylor-Str. 2, 12489 Berlin, Germany
e-mail: janina.kneipp@chemie.hu-berlin.de

© The Author(s), under exclusive license to Springer Nature Singapore Pte Ltd. 2024

M. Procházka et al. (eds.), *Surface- and Tip-Enhanced Raman Scattering Spectroscopy*,
https://doi.org/10.1007/978-981-97-5818-0_11

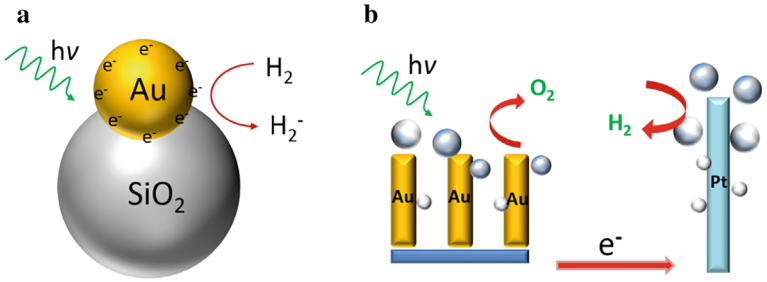



**Fig. 11.1** Application examples of plasmonic catalysis. **a** Schematics of hot-electron-induced $H_2$ dissociation on gold nanoparticles supported on $SiO_2$, redrawn after Ref. [8]. **b** Schematics of plasmon-induced water splitting with visible light, redrawn using the concept from Ref. [13]. Adapted from Ref. [8] with permission from American Chemical Society, Copyright 2013 and from Ref. [13] with permission from American Chemical Society, Copyright 2012

Due to its high efficiency and selectivity, plasmonic catalysis has attracted a lot of attention in heterogeneous catalysis [6–19]. A few examples: The hot-electron-induced photodissociation of $H_2$ on gold nanoparticles supported on $SiO_2$ (Fig. 11.1a) [8] depended linearly on laser intensity, with a wavelength dependence. The group of Moskovits reported a plasmonic water splitting cell using a dense array of aligned gold nanorods capped with $TiO_2$ (Fig. 11.1b) [13]. The results showed that the fuel production efficiencies were 20-fold higher at visible wavelengths, as compared to UV light. Apart from these, many other applications of plasmonic catalysis have been reported, such as CO oxidation [6], $H_2$ dissociation [7–9], $N_2$ dissociation [10], water splitting [11–13], pollutant decomposition [14–18], and $CO_2$ reduction [19].

Screening is one of the most important steps to identify suitable materials for the plasmonic catalysis of specific reactions. Usually, optimization of the materials depends on numerous trial-and-error experiments. However, mechanistic studies at the microscopic scale down to the molecular level can provide a better understanding of structure–activity relationships, increasing the efficiency of screening for catalysts. For nanoparticle-catalyzed heterogeneous reactions, it is challenging to monitor the molecular transformation at interfaces by conventional analytical techniques, such as gas chromatography (GC) and high-performance liquid chromatography (HPLC) [20]. Monitoring becomes even more difficult when the intermediates are unstable.

In this chapter, we discuss examples from recent research that illustrate the diversity of applications, as well as the omnipresence of plasmonic chemistry in the vicinity of plasmonic nanostructures, using well-known chemical transformations. Since the excitation of LSPR can greatly enhance optical fields, probing by spectroscopy, in particular by using surface-enhanced Raman scattering (SERS), plasmon-enhanced vibrational spectroscopies can serve as extremely sensitive analytical tool to detect

intermediates and reaction products and to study the mechanisms of plasmon-catalyzed reactions. Providing high local sensitivity, as well as the fingerprint information of molecular vibrational spectra, SERS has become the most popular tool for studies of nanoparticle-catalyzed reactions [21–30].

## 11.2 The Role of Localized Surface Plasmons in Plasmon-Supported Catalysis

### *11.2.1 The Beginning: Decay of Localized Surface Plasmon Resonances*

Localized surface plasmon resonances (LSPR) are one of the most important properties of noble metal nanoparticles. Noble metal nanoparticles have been widely used in energy harvesting, environmental monitoring, food safety, chemical catalysis, and medical diagnostics because they exhibit LSPR in the frequency range of visible light, such as Au, Ag, and Cu. When the frequency of the incident light matches the intrinsic frequency of the surface conduction electrons in a metal nanoparticle, the incident light will excite the LSPR, leading to strong light–matter interaction. For a small metal nanoparticle, the extinction can be described by Mie theory [31]. For a single metal nanoparticle, many parameters influence the resonance frequency, including metal species, size, shape, and the refractive index of the surrounding medium [32–34]. Moreover, the distance between nanoparticles will influence the LSPR, and the frequency will shift with the distance decrease of two nanoparticles due to their coupling [32, 35].

Figure 11.2 describes the different physical processes of the excitation and decay of LSPR [36–38]. Generally, after the excitation of LSPR by incident light, the plasmon decay has two channels, a radiative channel and a non-radiative channel. In radiative decay, the confined plasmon energy is transformed into photons in the form of far-field scattering or luminescence [37]. The scattering event, as a result of the radiative decay process of the plasmon, competes with the non-radiative decay, and the ratio of their respective contributions is dependent on nanoparticle structure, size, and shape [39–41]. The luminescence of the metal is another possibility of radiative decay, albeit was shown to be very inefficient [42–44]. In non-radiative decay, the plasmon energy is damped rapidly through the creation of hot electron–hole pairs, or through the generation of heat via electron–electron and electron–phonon interactions [36–38]. The non-radiative decay channel is a multi-step process following Landau damping [37, 45]. The first step of the non-radiative decay is dephasing of the coherent plasmon into individual electrons and holes. Since the energies of these charge carriers are significantly higher than that in a thermal distribution at the experimental temperature, they are commonly referred to as “hot” electrons and holes. The non-thermal distribution of electron–hole pairs decays either through the emission of photons or through carrier multiplication—the absorption of a single photon leads

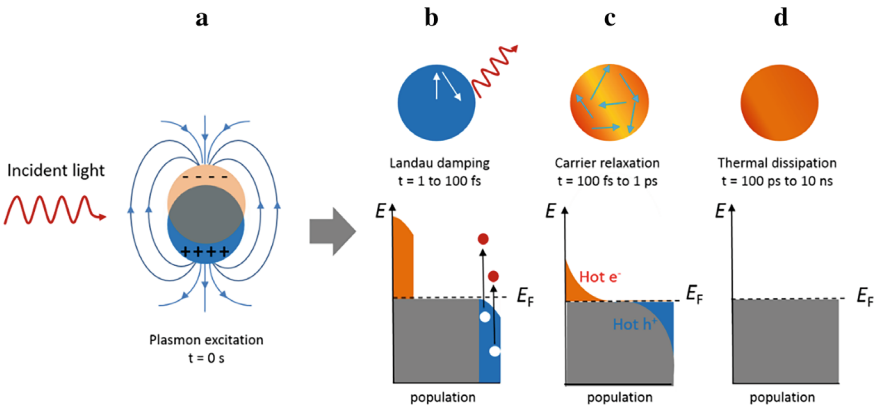



**Fig. 11.2** Scheme for plasmon excitation and decay on metal nanoparticles. **a** the excitation of LSPR with light. **b–d** Schematics for the decay of the plasmon and the population of the electronic states (gray) following plasmon excitation. Hot electrons are represented by the red areas above the Fermi energy $E_F$ and the blue area below $E_F$ represents hot hole distributions). Reproduced/ Adapted from Ref. [36] with permission from Nature Publishing, Copyright 2015

to the excitation of multiple electrons—via electron–electron interactions in the first 1–100 fs (Fig. 11.2b) [45]. Although the relaxation processes of the hot carriers have been extensively studied for extended surfaces, this process is more difficult to explore in nanoparticle systems. The studies based on extended metal surfaces suggest that the hot carriers redistribute their energy to form a Fermi–Dirac-like distribution by electron–electron scattering processes on a timescale ranging from 100 fs to 1 ps (Fig. 11.2c) [46, 47]. The electron–phonon interaction increases when lower-energy electrons decrease their velocity and the subsequent equilibration with the lattice of nanoparticles finishes over several ps (Fig. 11.2c). In a final step, heat is transferred to the surroundings of the metal nanoparticles via thermal conduction within a time of ~ 100 ps to 10 ns (Fig. 11.2d). When adsorbates are present on the plasmonic surface, the non-radiative decay may happen via so-called chemical interface damping (CID) [48, 49], where the excited localized surface plasmon interacts with unpopulated adsorbate acceptor states.

### *11.2.2 Effects of the Decay*

Based on their properties and decay, LSPR can lead to different effects in plasmonic catalysis [1, 50] (Fig. 11.3)

(i) *Redox reactions induced by the hot carriers (electrons and holes).* For the non-radiative plasmon decay, the generated hot carriers can be transferred to an adsorbate or a nearby semiconductor [1, 50]. In the case of adsorbed molecules, they can transiently transfer between the plasmonic nanostructure surface and

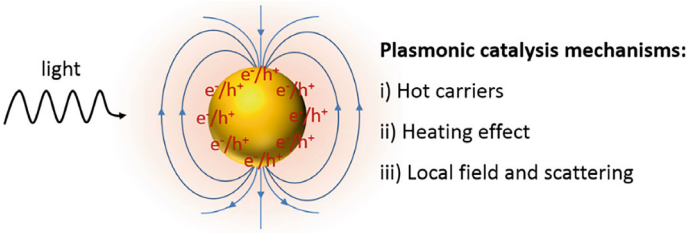



**Fig. 11.3** Effects of localized surface plasmon resonances of metal nanoparticles in plasmonic catalysis. The hot carriers at the surface are denoted as $e^-/h^+$. Color highlights the local heating

unpopulated or populated orbitals of the adsorbate. As a well-known example, hot holes can induce the oxidation of adsorbed citrate on metal nanoparticles, leading to the growth of silver nanoparticles due to the reduction of silver ions contained in the solution [51, 52]. In the charge transfer process, the adsorbed molecules can be oxidized by transferring electrons to the nanostructure, or they can be reduced by accepting hot electrons from the metal nanoparticle. In the case of a semiconductor, the hot carriers can be directly injected from excited plasmonic nanostructures into the conduction band of the semiconductor [53]. The plasmonic nanoparticles act similarly to a sensitizer dye, absorbing resonant photons and transferring the energetic electron to the nearby semiconductor. As a result, hot carriers become abundant in the semiconductor and further induce redox reactions at the semiconductor surface. As example, the rate of oxygen evolution is significantly enhanced by using silver/N-doped $TiO_2$ composites under broadband visible illumination [53].

(ii) *Heating effect*. As described above, as a consequence of the Landau damping, the local temperature on the plasmonic structure can dramatically increase as a result of the hot carriers relaxation through electron–electron and electron–surface scattering [1, 50]. The heating effect can become beneficial for a chemical reaction by changing the reaction kinetics and promoting the mass transport in the surrounding environment. For example, both plasmonic photocatalysis and photothermal conversion were reported to contribute to the enhancement of a Suzuki reaction using Au–Pd nanostructures [54].

(iii) *Near-field electromagnetic and scattering effects.* The local field enhancement caused by LSPR has a contribution to the increase of the photocatalytic activity, as was shown for semiconductors [1, 50] in a system where the semiconductor and plasmonic nanoparticles were separated to prevent any direct charge exchange between them. Besides the local field enhancement, the scattering process, as a radiative channel of plasmon decay, can also support the plasmonic photocatalysis. Essentially, the plasmonic nanostructure can act as a nano-mirror, increasing the probability for a photon to interact with a photocatalyst. In other words, the near-field electromagnetic and scattering effects will play roles when the reaction itself is a photoreaction.

## 11.3 Elucidating Mechanisms of Important Model Reactions

### *11.3.1 The Formation of 4,4′-Dimercaptoazobenzene (DMAB)*

The important role of LSPR in catalysis has been discussed for many different types of chemical transformations. Nevertheless, mechanistic studies… This section gives an overview of them, and where they will be used in the following to discuss important aspects regarding investigation of their mechanism.

Due to the plasmonic origin of the electromagnetic enhancement in SERS, it is surely the method-of-choice to study plasmonic catalysis. As two typical probes, p-aminothiophenol (PATP) and p-nitrothiophenol (PNTP) have been broadly used in such SERS investigations of plasmonic catalysis (Fig. 11.4). The two probes provide stable SERS signals due to the strong chemical bond between their thiol group and metal nanoparticles. In a plasmon-catalyzed oxidation, the photo-induced dimerization of PATP to 4,4′-dimercaptoazobenzene (DMAB) has been extensiveld characterized on gold and silver nanoparticles [55–59]. As a counterpart, the photo-induced dimerization of PNTP to DMAB is often discussed as a typical plasmon-catalyzed reduction reaction [60–71]. Both reactions have been discussed under variation of many different factors, including pH, laser intensity, and laser wavelength. Due to the complexity and the multitude of parameters that influence the mechanism, several aspects of the two reactions are still under discussion [72–76]. Studies of the plasmon-catalyzed formation of DMAB, moreover, can provide an understanding of the photochemical synthesis of azobenzene using solar energy. Aromatic azo compounds are high-value chemicals widely used as dyes, pigments, drugs, and food additives [77–79]. However, the yields and selectivity of their production have been limited by the high energy cost and environmental effects in heterogeneous catalysis.

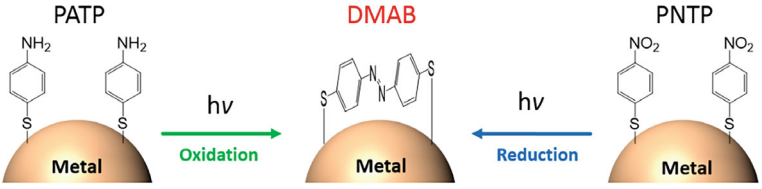



**Fig. 11.4** Scheme for two important plasmon-catalyzed model reactions, the oxidation of PATP and the plasmon-catalyzed reduction of PNTP

### 11.3.2 Photo-Oxidation of PATP and Important Aspects of its Mechanism

PATP is one of the molecules most frequently studied by SERS. Most interestingly, this molecule has long been considered as a textbook model of the photon-driven charge transfer mechanism in SERS chemical enhancement, since Osawa et al. have proposed this in 1994 [80]. In comparison with the normal Raman spectrum of PATP, in the SERS spectra of PATP, there appear three new peaks at around 1143, 1390, and 1436 $cm^{-1}$. According to the proposed photon-driven charge transfer mechanism, the newly appearing peaks were assigned to the so-called $b_2$ modes of PATP [80, 81]. This assignment has been accepted widely until now.

In 2009, Wu and co-workers initiated a discussion regarding the assignment of the three bands in the SERS spectrum of PATP [82]. On the basis of theoretical calculations combined with other reports, the authors pointed out that the previously identified $b_2$-modes could be produced by DMAB, a photoreaction product formed in the photo-induced dimerization of PATP on metal nanoparticles. The interpretation rapidly attracted a lot of attention in the SERS community and caused a vigorous debate about the charge transfer mechanism *vs.* the observation of the plasmon-catalyzed reaction product [72]. In the last years, more evidence from experiments and theoretical calculations suggested that DMAB produces the SERS bands at 1143, 1390, and 1436 $cm^{-1}$. Sun and coworkers provided the first experimental evidence of the formation of DMAB on silver nanostructures in 2010 [83]. In the same year, the group of Tian provided the direct evidence of the photoreaction product by measuring the mass spectra of DMAB and comparing the Raman spectra of lab-synthesized DMAB molecules (Fig. 11.5a) [21]. The mass spectra were recorded on a silver electrode with adsorbed PATP after illumination with a high-intensity laser [21]. The molecular ion peak at an *m*/*z* of 245.5 is assigned to the H + S–Ph–N = N–Ph–S fragment (Fig. 11.5a), while a peak at an *m*/*z* of 164 is assigned to K + S–Ph–$NH_2$. Therefore, the mass spectra convincingly demonstrated the formation of DMAB from PATP under the laser illumination. More persuasively, lab-synthesized DMAB showed identical SERS spectra with the illuminated PATP sample (Fig. 11.5a). Then, Kim et al. presented detailed spectroscopic and mass spectrometric evidence for the photogeneration of DMAB from PATP on a silver surface Fig. 11.5b) [84]. Furthermore, they also certified that the amount of DMAB is sufficient to explain the new SERS bands at 1143, 1390, and 1436 $cm^{-1}$.

Although it is widely accepted that the so-called $b_2$ bands in the SERS spectra of PATP can be attributed to the formation of DMAB, there are still some debates that are only currently being resolved. The pH dependence of the bands in the SERS spectrum has been one of these subjects [85–88]. It was reported that the decrease of pH values would reversibly lead to a decrease of the intensities of the $b_2$ bands in the SERS spectrum of PATP on metal nanoparticles [86, 87]. Specifically, it was interpreted that the reversibility of the typical bands at low pH is that the protonation of the amine group of PATP hinders the degree of photo-induced charge transfer due to the increase of the molecular orbital level [86, 87]. As we will discuss in a later

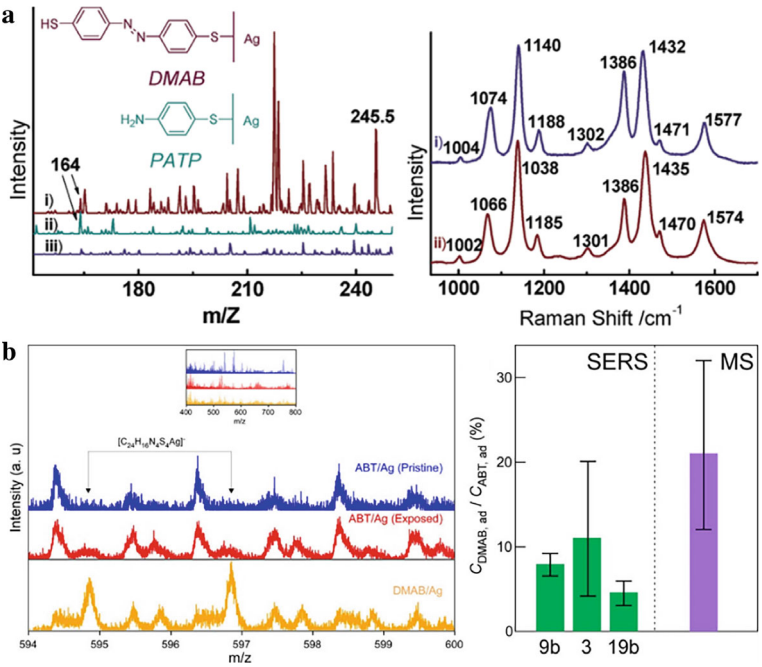



**Fig. 11.5** Confirmation of DMAB formation from the photo-induced dimerization of PATP. **a** Mass spectra of PATP adsorbed roughened Ag electrodes illuminated with a laser (i) and without any irradiation (ii) and a roughened Ag free of PATP (iii). The Raman spectrum of PATP (i) and DMAB (ii) on the roughened Ag electrode. **b** Mass spectra of PATP/Ag, PATP/Ag, and DMAB/Ag (the inset shows the same set of MS displaying wider mass range). The two peaks corresponding to $m/z = 594.84$ and 596.84 (two major isotopes of $[DMAB]_2Ag^-$). The estimated relative concentration of DMAB derived from the $b_2$ peaks (9b, 3, or 19b) of the SERS spectra and that from the mass spectra. Reproduced from Ref. [21] and [84] with permission from American Chemical Society, Copyright 2010 and 2013, respectively

section of this chapter (Sect. 11.4.2), the disappearance of the bands when pH is lowered can be brought in good agreement with their assignment to DMAB [73].

The photo-induced dimerization of PATP has been explored under the variation of many different parameters, including varied pH values, laser intensity, laser wavelength, electrode potential, temperature, molecule coverage, and nanoparticle species [21, 58, 84, 85, 89–92]. Although all these parameters affect the reaction, it is not entirely clear how exactly they exert their influence in the mechanism. An important landmark of the mechanistic studies were the findings on the role of molecular $O_2$. Xu and coworkers found that the presence of $O_2$ molecules, which is easily neglected, is a crucial element in the plasmon-catalyzed oxidation process (Fig. 11.6a) [90]. Interestingly, DMAB can be reversibly reduced to PATP under laser illumination in the presence of $H_2$ or $H_2O$-saturated $N_2$, but not in pure $N_2$ (Fig. 11.6a) [90]. The reduction of DMAB is proposed to be caused by the hot electrons generated from plasmon decay and a proton source provided by $H_2$ or $H_2O$ [90]. Huang and

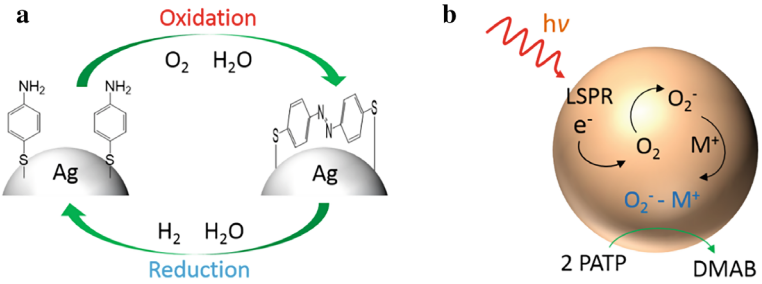



**Fig. 11.6** The role of oxygen in the plasmon-catalyzed oxidation of PATP. **a** Scheme for the reversible reactions of PATP in oxidative $O_2$ and reductive $H_2$ environments. **b** LSPR-assisted selective oxidation of PATP to DMAB on the surfaces of Au or Ag nanoparticles. Adapted from Refs. [90] and [59] with permission from the authors and from Wiley, Copyright 2013 and 2014, respectively

coworkers provided a clear image about the role of $O_2$ in the plasmon-catalyzed oxidation of PATP [59]. They found that the activation of $O_2$ by LSPR excitation is the key step in the selective reaction of PATP to DMAB, which is supported by the different reactivity under excitation by different laser wavelengths (Fig. 11.6b) [59]. Furthermore, theoretical calculations by density functional theory reveal that the formation of metal oxides or hydroxides on the nanoparticle surface can be a key active intermediate for the plasmon-catalyzed oxidation [59]. The theoretical calculation was supported by a set of control experiments in which acid was used to remove the oxidized species at the surface, and no DMAB was observed [59].

The important role played by metal oxides or hydroxides and their formation from activated oxygen was underpinned by experimental results from our work, in experiments conducted on gold nanoparticles under the addition of metal ions [93]. Based on our results, we concluded that the selective oxidation of PATP to DMAB takes place via formation of a metal oxide from the ionic species in a plasmon-catalyzed process. There, no formation of DMAB was observed, when no metal ions were added, or when the metal oxide cannot be stabilized, namely at low pH. In contrast, when $Ag^+$, $Au^{3+}$, $Pt^{4+}$, and $Hg^{2+}$ ions are added, when the conditions for the LSPR are optimized, as well as when the formation of metal oxides is favored (at high pH values), the dimer product forms, and XPS data allowed to infer on small amounts of $Ag_2O$ in the samples containing $Ag^+$. Assuming an activation of oxygen on the gold nanoparticles' surface according to ref. [59], this would imply that activated $^2O_2^-$, adsorbed to the gold nanoparticle surface, reacts directly with the added metal ions, forming the respective metal oxide at the surface of the gold nanoparticles. Based on our results and using the description for generation of the metal oxide from Refs. [21, 59, 94], dimerization of PATP can then take place according to the following steps:

$$Ag^+ + OH^- \rightarrow AgOH \tag{11.1}$$

$$2\mathrm{AgOH} \rightarrow \mathrm{Ag_2O} + \mathrm{H_2O} \tag{11.2}$$

$$2\mathrm{PATP} + 2\mathrm{Ag_2O} \rightarrow \mathrm{DMAB} + 4\mathrm{Ag} + 2\mathrm{H_2O} \tag{11.3}$$

$$4\mathrm{Ag} + \mathrm{O_2} \rightarrow 2\mathrm{Ag_2O} \tag{11.4}$$

### *11.3.3 Photo-Reduction of PNTP*

Birke and Lombardi reported that *p*-nitrobenzoic acid could be photo-reduced into either *p*-aminobenzoic acid or azodibenzoate on the surface of nanostructured silver electrodes in 1988 [95]. Kim and coworkers reported the first SERS study on the photo-reduction of PNTP on silver nanostructures in 2003 [96]. As reduction product, PATP was suggested, due to the appearance of the so-called $b_2$-mode peaks in the SERS spectrum, discussed in the previous section. In 2011, the group of Sun demonstrated that the real product could in fact be DMAB, based on the assignment of the DMAB bands in the SERS spectrum [60]. Up to now, the plasmon-catalyzed reduction of PNTP has frequently been studied by SERS and TERS [60–71].

*Photo-reduction of PNTP to DMAB in a four-electron reduction process.* Normally, the plasmon-catalyzed reduction of PNTP is found to be a four-electron reduction process, with the product DMAB. The dimerization of PNTP has been observed on different metal nanoparticles, such as silver and gold nanoparticles [72]. The PNTP dimerization reaction is influenced by many parameters, including laser wavelength, and laser intensity. For the mechanism of the reaction process, Kim and coworkers suggested that an intermediate of the first step must be involved in the photocatalytic reduction of PNTP on metal nanoparticles (Fig. 11.7) [70]. The formation of the intermediate is identified by a fast red shift of the symmetric stretching band of $NO_2$ in the SERS spectra of PNTP. They concluded that the intermediate was the anion radical of PNTP brought about in a single-electron transfer process. The conclusion is based on the results from electrochemical SERS and quantum chemical calculations (Fig. 2.12) [70]. Interestingly, the observation of such an anion radical intermediate is not limited to the photo-reduction of PNTP. As we observed in the SERS-based characterization of the gold-catalyzed reduction of PNTP by $NaBH_4$, it can also be observed in a single-electron reduction process [97].

*Photo-reduction of PNTP to PATP in a six-electron reduction process.* Although molecules adsorbed on metal nanoparticles can be reduced by hot electrons, the charge-carrier recombination normally limits the reduction reaction. As mentioned above, the photo-reduction of PNTP on metal nanoparticles is usually a four-electron

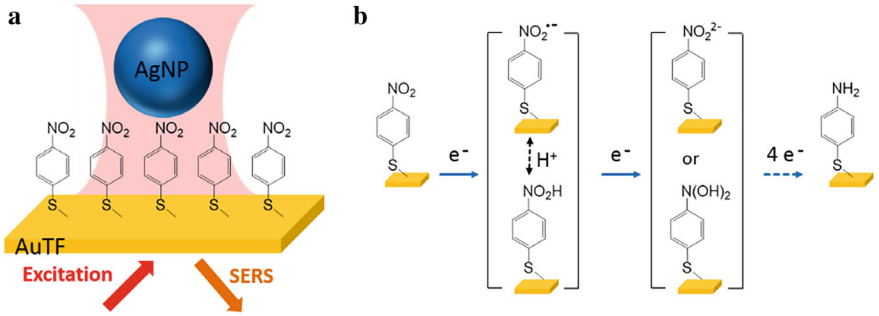



**Fig. 11.7** Identification of the first step of the plasmon-catalyzed reduction of PNTP. **a** Schematic diagram of the silver nanoparticles (AgNP)/PNTP/Au thin-film (AuTF) junction and **b** reaction steps and possible intermediates for the photocatalytic reduction of PNTP, according to the concept of Choi et al. [70]

reduction process. In fact, also a six-electron reduction of PNTP on metal nanoparticles can happen in the presence of strong reducing agents, such as sodium borohydride, with PATP as the product [22–25, 27–29]. The four-electron reduction process of the dimerization of PNTP can be attributed to the low efficiency of the generation of hot electrons. As was reported first by Xie and Schlücker [26], and later also others [98, 99], a six-electron reduction of PNTP can be achieved by plasmon-catalyzed reduction on silver nanoparticles, without the addition of any sodium borohydride or molecular hydrogen (Fig. 11.8). This observation provides a way to improve the efficiency of light-to-energy conversion processes and to control the reaction selectivity during plasmonic catalysis. First, the six-electron reduction process was only observed on silver nanoparticles, and not on gold nanoparticles (Fig. 11.8a) [26, 98]. Xie and Schlücker attributed the preferential reaction on silver to the photo-induced recycling of silver atoms from photosensitive silver halides (Fig. 11.8b) [26]. As will be explained in more detail in Sect. 11.4, newer results suggest a different mechanism for the six-electron reduction of PNTP [99] and specifically indicate its occurrence on other metal nanoparticles, i.e., gold and copper, as well, which greatly expands the concept of hot electron reduction and its possible applications in practical catalysis.

### *11.3.4 Other Chemical Transformations that Benefit from Plasmon-Supported Catalysis*

Plasmon-supported catalysis has proven to be an efficient way to convert light energy in $CO_2$ reduction [19], water splitting [11], dissociation of $H_2$ [9], or the decomposition of organic pollutants [17]. There is an extreme wealth of reactions in organic chemistry that can benefit from plasmonic excitations [100]. As an important example, catalysts help to achieve oxidations without harsh oxidants and byproducts, namely with oxygen gas, that can be activated on silver and gold nanostructures

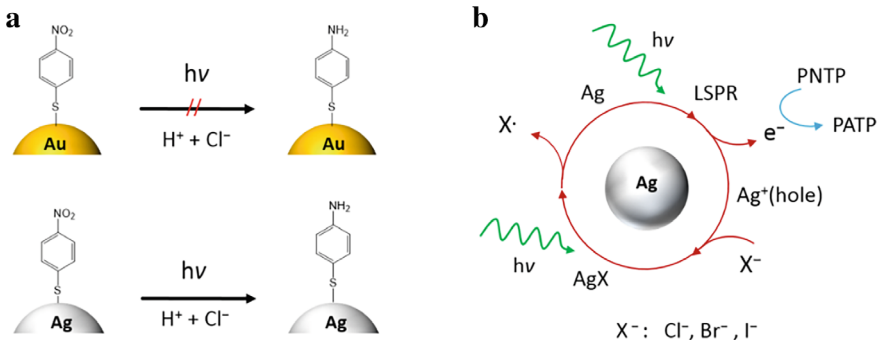



**Fig. 11.8** Six-electron photocatalytic reduction from PNTP to PATP on silver nanoparticles, as proposed by Xie and Schlücker [26]. **a** Hot-electron-induced reduction from PNTP to PATP on Ag versus on Au surfaces. **b** Six-electron photocatalytic reduction from PNTP to PATP and the corresponding hot electron/hole photo-recycling mechanism. Adapted from Ref. [26] with permission from Nature Publishing, Copyright 2015

assisted by the LSPR [59]. Since the first plasmon-supported photocatalytic oxidation of methyl and ethyl alcohol [101], plasmonic catalysis has been employed for many different oxidation reactions, often using combined gold-$TiO_2$ nanostructures [100, 102]. The activation of $H_2$ is an important step in different transfer hydrogenation reactions that were shown to benefit from the field enhancement and thermal effects caused by LSPR of plasmonic nanostructures or hybrid nanostructures containing gold or silver.

Apart from the described transformations of nitro to amino compounds observed in the examples of PATP and PNTP or the formation of azobenzene in the above sections, LSPR can be employed in a broad range of coupling reactions, helping to form C–C and C–N bonds in many different mechanisms [100]. Many publications report on the use of plasmonic support in polymerization reactions [103–107], where new functional materials can be generated from the polymer and the plasmonic structure. The use of light of specific polarization, together with adjustment of the reactant composition enables precise patterning of polymer-functionalized plasmonic structures [108] and a directed growth of polymer materials [109].

## 11.4 Hot Electrons and Enhanced Light Harvesting

### *11.4.1 Ligand-Enhanced Light Harvesting*

As pointed out in Sect. 11.3.3, the six-electron reduction of PNTP was initially found only on silver nanoparticles, and the photo-induced recycling of silver atoms from photosensitive silver halides was proposed as a crucial step in the reaction mechanism [26]. Different from these first reports, as we observed in experiments

with nanoparticles from gold and copper, it is in fact possible to achieve the six-electron reduction of PNTP in the absence of photosensitive halide species as well, when conditions are optimized [99]. Specifically, the reaction can take place on gold, silver, and copper nanoparticles in the presence of protons and appropriate ligands, including $Cl^-$, $Br^-$, $I^-$, $SCN^-$, and $SC(NH_2)_2$. The six-electron reduction can also happen, albeit with lower efficiency, on silver and copper nanoparticles in the absence of any ligands. This indicated that the ligands should be considered promoters instead of mandatory elements in the reaction. Based on comparison with standard redox potentials, we found that that the reaction happens preferably at lower redox potential and that this is regulated by the ligands. This finding broadens the concept of the hot-electron-induced reduction on metal nanoparticles.

It is well-known that nucleophile and electrophile ligands have the ability to tune the electronic properties of metal nanoparticles [110–113]. Two effects contribute to the shift of the Fermi level of metal nanoparticles: (i) the charging effect, e.g., upon the adsorption of a negatively charged nucleophile that raises the Fermi level and (ii) the chemisorption of neutral dipoles that modify the surface potential and alters the Fermi level [111, 112]. In the discussion here, we argue that the adsorption of the ligands to the metal nanoparticles alter the Fermi level, thereby influencing hot electron generation [99].

The results were obtained in experiments with immobilized Au, Ag, and Cu nanoparticles on glass (Fig. 11.9a–c) [23, 114]. In the copper substrates, the formation of $Cu@Cu_2O$ nanostructures was avoided since the reaction was conducted in an acidic environment in all experiments, so that metallic copper was reconstituted. Using the different immobilized metal nanostructures functionalized with PNTP, we obtained SERS spectra in the presence of HCl and $H_2SO_4$, respectively, that indicated the reduction of PNTP and the formation of PATP. PATP signals obtained with copper nanoparticles, as well as the one with the gold nanoparticles at higher HCl concentration, indicate that the reaction also takes place on copper and gold nanoparticles. It occurred also in the absence of $Cl^-$, namely in experiments with $H_2SO_4$, showing that no photosensitive halide species is necessary [99].

We found that the relative PATP intensity follows the trend Cu > Ag > Au in the presence of both HCl and $H_2SO_4$. This is inversely related to the standard redox potential of the respective metal. The position of the Fermi levels with respect to the vacuum level relates to the redox potential [112, 115]. Therefore, a more negative redox potential, corresponding to a higher Fermi level, will indicate a decreased confinement of electrons. Although the experiments in this work were not conducted under standard conditions, the comparison of the standard redox potentials appears to provide a rationale for the discussion of the reaction activity, due to their relation with the Fermi level. Nevertheless, other effects, such as nanoparticle size, shape, and aggregate formation, cannot be excluded. In agreement with this discussion, in situ Raman experiments that we conducted in an electrochemical cell revealed a more efficient photo-reduction of PNTP under more negative potential (higher Fermi level) on silver nanoparticles, also consistent with the potential-dependent photoreaction of nitrobenzene derivatives reported early on by Sun et al. [95]. The inverse relation between the reaction efficiency and electrode potential dominates over other effects

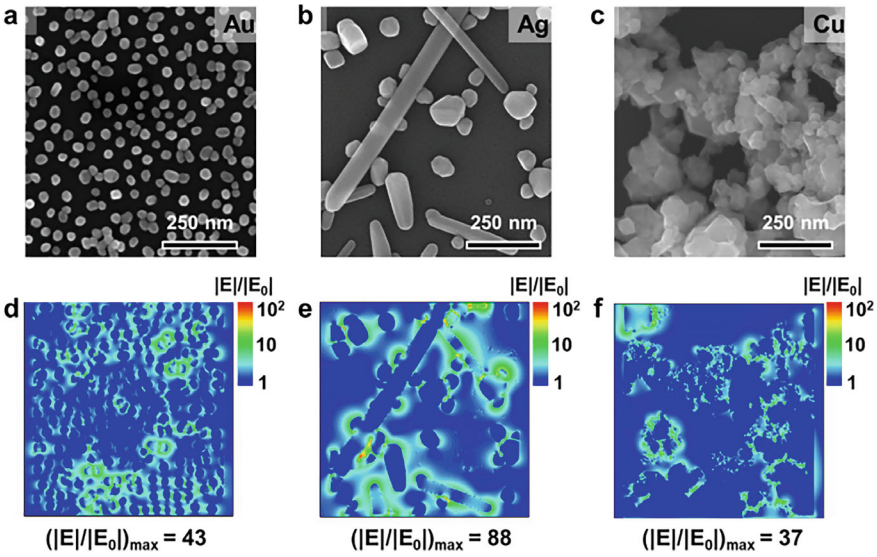



**Fig. 11.9** Scanning electron micrographs of **a** gold, **b** silver, and **c** copper nanoparticles immobilized on glass slides and field enhancement distribution obtained by finite-difference time-domain (3D-FDTD) simulation in the xy-plane over the imaged areas of 723 × 782 $nm^2$.on **d** gold, **e** silver, and **f** copper nanoparticles. The field distribution in (**d**–**f**) was calculated for an excitation wavelength of 633 nm, corresponding to the wavelength used in the experiments. Adapted from Ref. [99] with permission from Elsevier, Copyright 2020

that could relate to catalytic activity as well. These include, e.g., the highest local field enhancement in nanoparticle aggregates (compare Fig. 11.9d–e), which would positively influence the generation of hot electrons [116] specifically on silver, or the affinity of each respective metal for $Cl^-$ ions, which is higher in gold compared to silver and copper [117] that could inhibit electron–hole recombination [26] and yield higher PATP signals for the gold nanoparticles. Neither of these effects were observed though when comparing product formation.

Moreover, experiments at different wavelengths and intensities demonstrated that a high laser intensity of a specific wavelength promotes the six-electron reduction of PNTP to PATP, which confirms its nature as a photocatalytic reaction that is influenced by the LSPR. The generated hot electrons are in a dynamic equilibrium, and recombine with holes [118]. An increase in laser intensity can improve the number of hot carriers, but will also increase the local temperature on the nanoparticle surfaces, which could enhance the reaction rate even further. A higher catalytic activity at higher intensity is also found in the reduction of other nitrobenzene derivatives. On copper nanoparticles, *4*-nitrobenzyl thiol is reduced by hot electrons to form *4*-aminobenzyl thiol as reaction product [99].

*Role of the ligands.* Several aspects in the results indicate that the $Cl^-$ ions enhance the hot electron reduction on both gold and copper nanoparticles. Since photosensitive halide species are not formed on gold and copper, we infer that this must take place without the formation of a photosensitive species that has been suggested for silver nanoparticles [26]. In accordance with the work by Xie and Schlücker [26], the spectra obtained with silver nanoparticles in the presence of $Cl^-$, $Br^-$, and $I^-$ ions showed an increase in the relative PATP signal. Interestingly, this occurred also with the addition of the pseudo-halide ligands $SCN^-$ and $SC(NH_2)_2$. The onset of the increase in the relative PATP signal is at very low ligand concentrations for $I^-$ and at highest concentrations for $Cl^-$, and has a good correlation with the electrode potentials of the corresponding metal–ligand systems [117], including the non-halide ligands. The observation of lower potentials for the $I^-$ species and also for $SC(NH_2)_2$ and their positive influence on activity are in accordance with the conclusion drawn above that the ligands must increase the Fermi level and hence decrease the confinement of the electrons.

Also at neutral pH, where a four-electron reduction process with the product DMAB takes place due to the deficiency of protons [29, 60, 63, 68, 72], the $Cl^-$ and $Br^-$ ions enhance the photo-induced reduction of PNTP on the gold and silver nanoparticles [99]. This demonstrates that the ligands enhance both the six-electron and the four-electron reduction by hot carriers under both acidic and neutral condition, respectively.

In summary, the hot-electron-induced reduction of PNTP to PATP is influenced by the metal species, the ligands, and the intensity of the light that excites the LSPR. Using the description for the generation of hot electrons from refs. [36, 38, 118, 119] shown in picture (i) of Fig. 11.10, we infer from our data that the six-electron reduction of PNTP on metal nanoparticles can take place as follows: In the absence of the ligand, the required energy Ø for the generation of hot electrons is high (Fig. 11.10, picture (i)), only very few electrons have enough energy to participate in the reduction reaction at the nanoparticle surface, and the reaction is slow. When the ligand adsorbs on the nanoparticle surface (picture (ii) in Fig. 11.10), the Fermi level with respect to vacuum level on the nanoparticle surface increases (and modifies the surface potential) [110–113], and the required energy Ø will decrease. As a result, more energetic hot electrons are generated. This description is different from a model that involves a surface field mediated excitation of hybridized (interfacial) metal–molecule states formed upon chemisorption [38]. Specifically, under acidic conditions in the absence of ligands, the photo-induced reduction of PNTP is slow due to the smaller number of hot electrons. In contrast, in the presence of the ligand, the decay of the LSPR produces more hot electrons, leading to the fast reduction of PNTP to PATP. The proposed mechanism is supported by the observation of a higher reaction efficiency at more negative potentials shown in in-situ Raman/electrochemical experiments [99]. In addition, XPS data clearly showed the presence of $Cl^-$ after the treatment of the PNTP decorated Ag particles with HCl and a possible correlation to the formation of PATP [99].

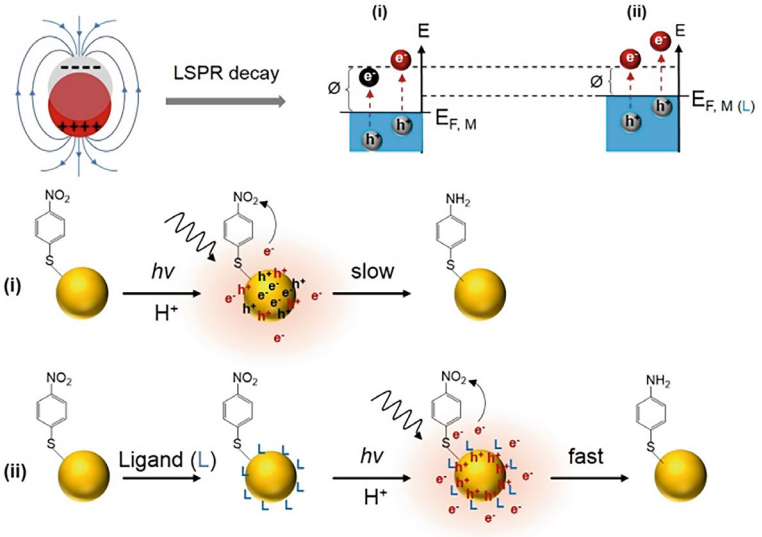



**Fig. 11.10** Schematic illustration of the ligand-enhanced hot electron reduction on metal nanoparticles. Generation of hot electron–hole pairs within the metal from the decay of the localized surface plasmon resonance (LSPR) in (i) the absence and (ii) the presence of a ligand and the proposed mechanism for the six-electron reduction of PNTP to PATP on the metal nanoparticles under acidic condition for both situations as proposed by Zhang and Kneipp. Reproduced from Ref. [99] with permission from Elsevier, Copyright 2020

The ligands may also have further roles, including the impairment of charge-carrier recombination [26, 120], directly serving as electron donor [101], the change of LSPR band width that is related to the chemical induced damping (CID) process [116], and formation of a photosensitive metal–ligand complex as has been discussed in the case of silver nanoparticles [26]. The data discussed here support a mechanism of the six-electron reduction as follows:

$$\mathrm{M} + \mathrm{L} \rightarrow \mathrm{M(L)} \tag{11.5}$$

$$\mathrm{M(L)} + \mathrm{h}\nu \rightarrow \mathrm{M^{+}(L)} + \mathrm{e^{-}} \tag{11.6}$$

$$\mathrm{PNTP} + 6\mathrm{e^{-}} + 6\mathrm{H^{+}} \rightarrow \mathrm{PATP} + 2\mathrm{H_2O} \tag{11.7}$$

M and L in the above reaction equations stand for the metal and the ligand, respectively. The adsorption of ligands on the nanoparticles (1) is followed by the generation of the hot electrons when the LSPR decays (2) and by the reduction of PNTP by these energetic electrons (3). While the concentration of protons will influence whether a four-electron process or the six-electron process takes place as step (3), the metal species, laser intensity, and ligands determine the hot electron density

in step (2) and hence the overall reaction rate. In this step, the role of the ligands is to decrease the energy threshold and to limit the electron–hole recombination, both of which increases the hot electron density on the nanoparticle surface.

The counterpart half reactions can happen as discussed previously [69, 101]. As described in Eqs. (11.8) [13], (9) [121], and (10) [101], water and ligands (e.g., $Cl^-$, $Br^-$, $I^-$) can act as electron donors in the counterpart half reactions.

$$4M^+ + 2H_2O \rightarrow 4M + O_2 + 4H^+ \tag{11.8}$$

$$M^+ + H_2O \rightarrow M + OH \cdot + H^+ \tag{11.9}$$

$$M^+ + L^- \rightarrow L \cdot + M \tag{11.10}$$

The observation of the hot electron reduction of 4-nitrobenzyl thiol on copper nanoparticles, where charge transfer may be hampered by the additional carbon in the chain, suggests that in step (3), there possibly occurs a direct transfer of hot electrons from the metal to the $NO_2$ group of PNTP. However, as suggested in previous work, hot electrons could also be injected into water via the plasmon excitation [122]. Therefore, a direct contact of $NO_2$ to the metal surface would not be mandatory to achieve the electron transfer process.

### *11.4.2 Applications of Ligand-Enhanced Light Harvesting: Re-interpreting the 'pH Reversibility' of the PATP Spectrum*

As mentioned in Sect. 11.3.2, three bands at 1145, 1392, and 1436 $cm^{-1}$ appear and disappear in the SERS spectrum of PATP when pH values change from basic to acidic condition, respectively, in SERS experiments with PATP on silver nanoparticles [86, 87]. This reversible pH response has even been applied for pH sensing by SERS in living cells [123–125]. In agreement with the interpretation of the bands as originating from photo-induced charge transfer [80], the disappearance of the three bands under acidic conditions was discussed as result of the protonation of the amino group of the molecule, which would increase the molecular orbital level and thus hinder the degree of CT [86, 87]. However, the pH-related reversibility of the SERS spectrum is not observed on gold nanoparticles [88, 93], suggesting that protonation of the amino group of PATP may not fully explain it. Interestingly, in previous reports on the pH-related reversibility of the PATP SERS spectrum, HCl solution was used to decrease the pH value [86, 87]. Therefore, we have studied the role of $Cl^-$ ions in the context of PATP dimerization and the decomposition of DMAB at acidic pH [73]. Similar to the discussion on the enhancement of PNTP reduction by hot carriers in the previous section, we will see here that the presence of $Cl^-$ ions, as well as of other

ligands plays a central role in the hot electron reduction of DMAB when occurring on silver nanoparticles, while a decrease in pH alone is not sufficient to promote the reaction.

The effect of acidification on the SERS spectrum obtained from PATP was studied using silver nanoparticles and PATP in water that had been incubated at room temperature for 30 min before SERS spectra were acquired using an excitation wavelength of 532 nm. The typical bands at 1147, 1392, and 1436 $cm^{-1}$ indicated the formation of DMAB from PATP. With addition of HCl, the bands assigned to DMAB disappeared completely. In contrast, the DMAB bands decreased only slightly when $HNO_3$, $H_2SO_4$, and $H_3PO_4$ were used. This renders an explanation in agreement with impaired charge transfer due to protonation [80, 86, 87] not plausible any longer. When HCl is added to gold nanoparticles incubated with PATP, the bands around 1145, 1392, 1436 $cm^{-1}$ indicate DMAB formation, but no effect of HCl on the DMAB signal is found [73]. The possibility that DMAB is detected that formed newly during the SERS experiment when $HNO_3$, $H_2SO_4$, and $H_3PO_4$ are present could be ruled out in control experiments where the incubation sequence was reversed, and where PATP was added to the silver nanoparticles after adjustment of the pH by the different acids.

The high efficiency of HCl to promote the photo-reduction of existing DMAB molecules that have formed on the silver nanoparticles, as opposed to the other acids, also indicates the effect of the $Cl^-$ ions and possibly of other ligands on hot electron generation, in line with the discussion in Sect. 11.4.1. Figure 11.11 shows the SERS spectra of silver nanoparticles pre-incubated with PATP and with 0.1 M $H_2SO_4$, as well as with the further addition of a series of halide and non-halide ligands constituting $Cl^-$, $Br^-$, $I^-$, $SCN^-$, $SC(NH_2)_2$, $S_2O_3{}^{2-}$, and $S^{2-}$, respectively. A control spectrum was acquired from a sample containing neither of the ligands and confirms the strong DMAB signal at 1147, 1392, and 1436 $cm^{-1}$ in $H_2SO_4$ discussed above (Fig. 11.11a, black spectrum). With the presence of $Cl^-$, the DMAB bands almost disappear (Fig. 11.11a, gray spectrum). Similarly, the other ligands also lead to a dramatic decrease of DMAB signals in the SERS spectra (Fig. 11.11a) and of the relative DMAB band intensity $I_{1147}/I_{1080}$ (Fig. 11.11b). While the efficiency of $Br^-$ and $I^-$ could potentially point to a contribution by a silver halide species, as has been discussed above [26], the effect of all the non-halide ligands (Fig. 11.11a, top four spectra) rules out a mechanism based on such a photosensitive species.

We can conclude that also here the decrease of the DMAB signal indicates the hot electron reduction of DMAB to PATP at low pH in the presence of ligands. The addition of ligands alone, including $Cl^-$, $Br^-$, $I^-$, without the acidification by $H_2SO_4$, has little effect on the DMAB bands in the spectra, indicating that both $H^+$ ions and ligands are essential for the hot electron reduction of DMAB. We can infer on the mechanism of the reduction of DMAB on silver nanoparticles as follows:

$$Ag + L \rightarrow Ag(L) \tag{11.11}$$

$$Ag(L) + h\nu \rightarrow Ag^+(L) + e^- \tag{11.12}$$

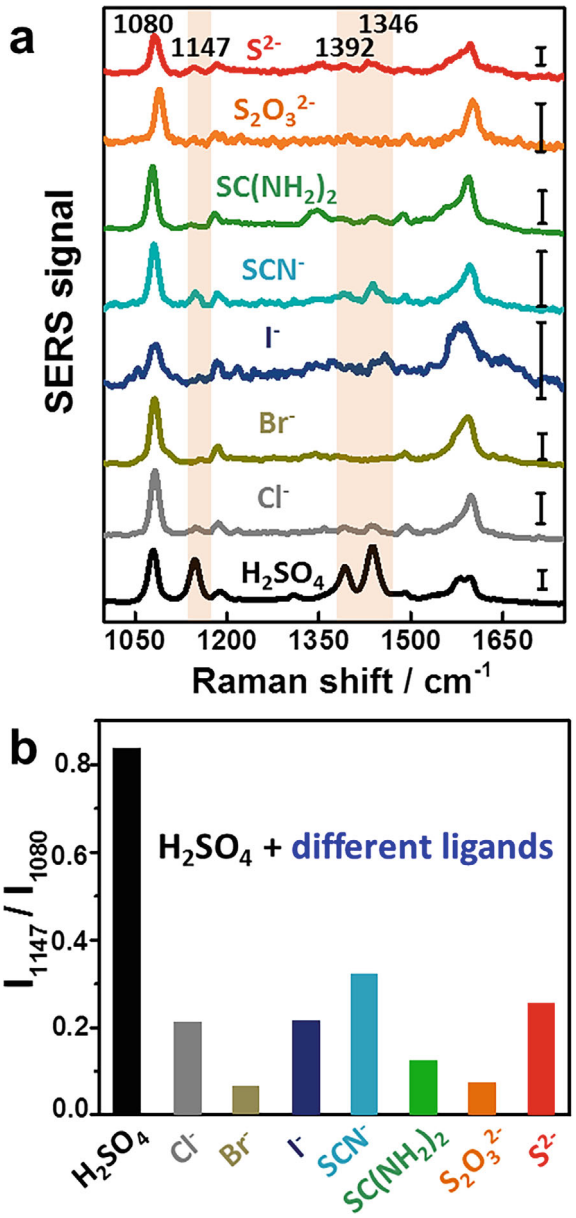



**Fig. 11.11** SERS spectra of silver nanoparticles pre-incubated with PATP in water for 30 min, measured after addition of $H_2SO_4$ at pH 1 in the presence of different ligands as indicated (excitation wavelength 532 nm; laser intensity 19 kW/cm$^2$; acquisition time 1 s, scale bars from top to bottom: 100, 50, 200, 100, 50, 100, 200, 200 cps). **a** Ratio of the signal intensity at 1147 cm$^{-1}$ assigned to DMAB and at 1080 cm$^{-1}$ assigned to both PATP and DMAB ($I_{1147}/I_{1080}$) of the SERS spectra in **a**. Reproduced from Ref. [73] with permission from American Chemical Society, Copyright 2021

$$\mathrm{DMAB} + 8\mathrm{e}^- + 8\mathrm{H}^+ \rightarrow 2\mathrm{PATP} + 4\mathrm{H_2O} \tag{11.13}$$

$$\mathrm{h}^+ + \mathrm{H_2O} \rightarrow \mathrm{OH}\cdot + \mathrm{H}^+ \tag{11.14}$$

$$\mathrm{h}^+ + \mathrm{L}^- \rightarrow \mathrm{L}\cdot \tag{11.15}$$

Different from the effect of ligands on the reduction of PNTP discussed in Sect. 11.4.1, the reduction of DMAB here does not occur at all in the absence of the ligands on silver. The absence of the reduction of DMAB on gold nanoparticles even in the presence of the $Cl^-$ ligand confirms the lower catalytic activity of gold compared to silver nanoparticles that was found for the $Cl^-$ enhanced reduction of PNTP recently with such gold nanoparticles as well [99]. The counterpart half reactions can happen as discussed previously [101, 121, 126]. Water and ligands (e.g., $Cl^-$) can act as electron donors, as shown in Eqs. (11.14) [121] and (11.15) [101].

Apart from these central findings, as was also observed in the experiments, the plasmon-catalyzed oxidation of PATP on silver nanoparticles is extremely efficient, so that all the PATP molecules can be oxidized into DMAB in very short time during the 1 s laser irradiation in the Raman measurement. As discussed in Sect. 11.3.2 [93], we attribute the efficient catalytic reaction on the silver to the existence of silver oxidized species that we detected on the silver nanoparticle surface by XPS. In those samples where $H_2SO_4$ was added after the incubation of silver nanoparticles and PATP, the DMAB signal intensities at 1147, 1392, and 1436 $cm^{-1}$ were found to increase gradually with increasing incubation time, confirming that DMAB forms during the incubation. Resembling the previous observation of a non-photochemical dimerization of PATP on gold nanoparticles [127], there is no difference in the relative DMAB intensity when comparing the incubation process in room light and in the dark. These results indicate that the DMAB formation during the incubation process occurs mainly in a non-photocatalytic reaction on the silver nanoparticles here.

Figure 11.12 summarizes the central conclusions that can be made based on the results. (i) When PATP is incubated with silver nanoparticles at neutral pH, DMAB forms in a non-photocatalytic reaction or (ii) a plasmon-catalyzed reaction. The non-photocatalytic formation of DMAB on the silver nanoparticles resembles the dimer formation observed on gold nanoparticles previously described [127] and is suggested to occur in a similar mechanism [128] (iii) The formed DMAB on the silver nanoparticles is reduced to PATP via a hot-electron-induced reduction reaction that requires the presence of ligands, such as $Cl^-$ ions, in order to produce sufficiently energetic hot carriers, as well as low pH.

Our findings indicate that the "pH-reversible" response of the PATP SERS spectrum on silver nanoparticles is the result of detecting DMAB at high pH and PATP obtained in the plasmon-catalyzed reduction of DMAB at low pH, when $Cl^-$ or others of the ligands reported here are present. Apart from providing another example of improved hot electron harvesting for catalysis in the presence of different ligands that enhance hot carrier generation by elevating the Fermi level [99], the results

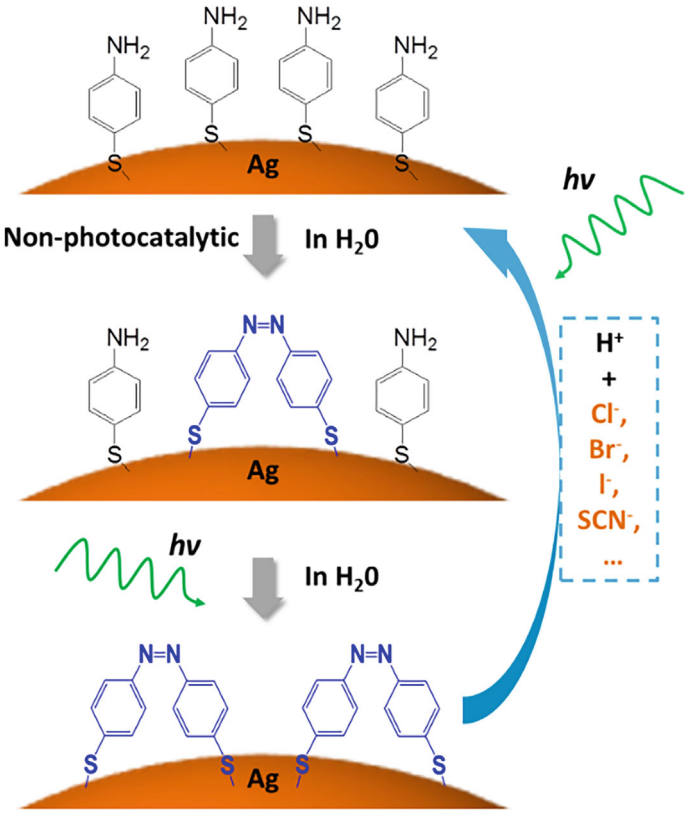



**Fig. 11.12** Summary of the reversible formation of DMAB as observed on the silver nanoparticles. Top to bottom: DMAB forms in a non-photocatalytic process during incubation of PATP with the silver nanoparticles. Furthermore, it forms in a photocatalytic process when irradiated at neutral pH. At low pH, and in the presence of a series of halide and non-halide ligands, ligand-enhanced hot electron reduction of DMAB takes place. Reproduced from Ref. [73] with permission from American Chemical Society, Copyright 2021

clearly point out the requirements of SERS-based pH sensing with PATP: the presence of appropriate ligands, including those shown here, and a SERS substrate that can provide the sufficient catalytic activity.

### *11.4.3 Surface Molecular Patterning with Hot Electrons*

Surface patterning by laser-induced photoreactions is an important technology. With knowledge about the mechanisms of plasmon-supported reactions and the possibility to influence them by controlling reaction conditions, the concept of laser direct writing can be extended to plasmon-supported chemistry, and new, versatile ways

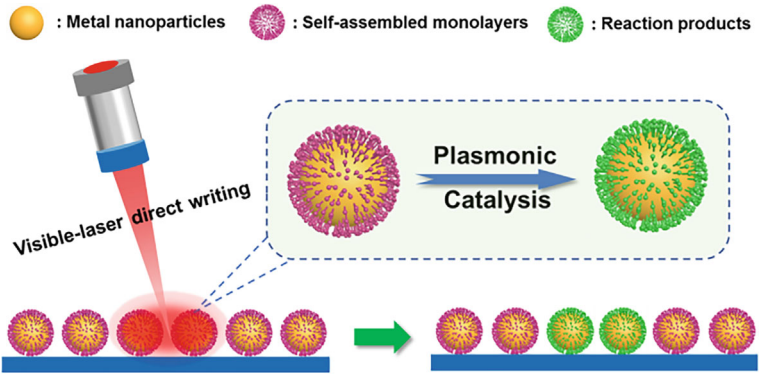



**Fig. 11.13** Schematic illustration of surface molecular patterning of self-assembled monolayers on a plasmonic substrate based on visible-laser direct writing. Reproduced from Ref. [129] with permission from American Chemical Society, Copyright 2021

for modular surface functionalization can be developed. We have shown recently that using the oxidation of PATP to DMAB, as well as the two hot-electron-based reduction reactions discussed above in Sect. 11.3.3, namely the four-electron reduction of PNTP to DMAB at neutral pH and the six-electron reduction of PNTP to PATP at acidic pH, microscopic patterns with different structures and functionalities can be fabricated in a conventional microscope (Fig. 11.13) [129]. The information encoded by the structures can be directly read out by Raman imaging, suggesting the utilization for information storage, e.g., in SERS-based security labels. By altering the reaction conditions appropriately, the obtained molecular patterns can be erased and re-written, enabling their reparation, modification, and re-use in a wide range of applications.

Since the plasmon-catalyzed oxidation of PATP to form DMAB on immobilized gold nanoparticles depends on excitation intensity, separation of the writing and read-out process can be attained, as shown in the schematic of Fig. 11.14a. Using a laser operating at 633 nm, DMAB molecules are formed on the gold nanoparticles (Fig. 11.14b) during the irradiation with a laser intensity of 500 kW/cm$^2$, while the written DMAB patterns are read out by SERS mapping with a laser operating at significantly lower intensity of 5 kW/cm$^2$. Figure 11.14c, d show the SERS spectra of immobilized gold nanoparticles modified with PATP obtained after different durations of irradiation at these two intensities. After irradiation with 500 kW/cm$^2$, the bands at 1143, 1392, and 1436 cm$^{-1}$ indicate the formation of DMAB from PATP in the plasmon-catalyzed oxidation reaction (Fig. 11.14c). In contrast, when the substrate is irradiated at an intensity of 5 kW/cm$^2$, the characteristic bands assigned to DMAB are not observed (Fig. 11.14d). The ratio of the signal intensities of the band at 1143 cm$^{-1}$ assigned to DMAB and the band at 1080 cm$^{-1}$ that is found both in PATP and DMAB, termed $I_{1143}/I_{1080}$ here, can be used as a measure of the formation of DMAB. Figure 11.14e (red trace) shows that the relative amount of

DMAB increases with irradiation time in the first few seconds and then remains at high level, apart from smaller fluctuations that are typical of a SERS experiment.

The map of the $I_{1143}/I_{1080}$ SERS intensity ratio of a spot of DMAB that was obtained before by illumination of a single focal volume with a nominal spot size of ~ 1.5 μm for 3 min (Fig. 11.14f) shows a gradual decrease of the DMAB contribution from the center of the spot, example spectra are displayed in Fig. 11.14g. The DMAB signal decays completely across a distance of 5–6 μm from the center of the spot, yielding a spot diameter of ~ 11 μm as obtained from the mapping profiles. The observation of DMAB formation in an area that is larger than the laser spot size is in agreement with the scattering of the light by the glass surface and the gold nanoaggregates, yielding excitation of the surface plasmon and formation of the

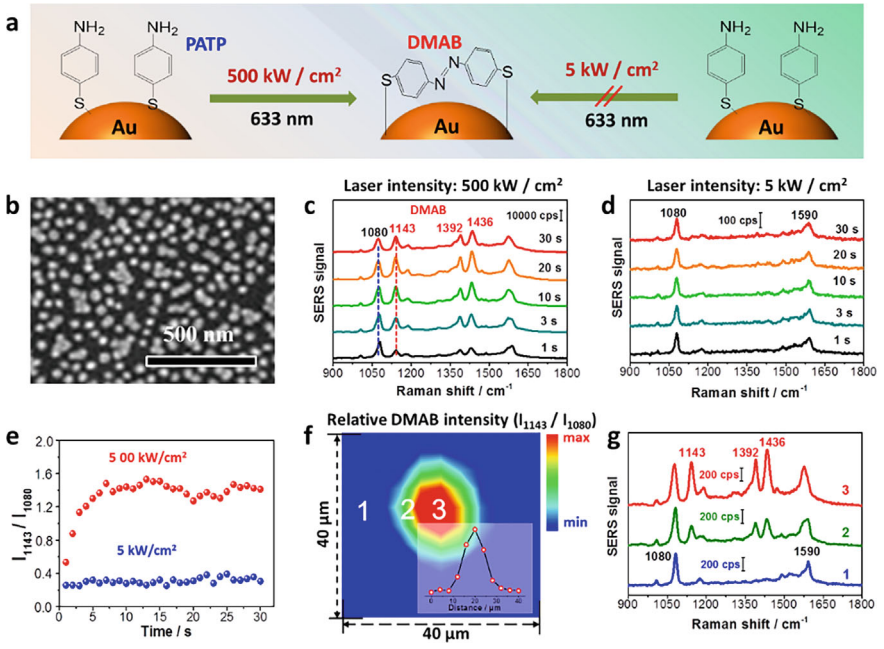



**Fig. 11.14** **a** Schematic illustration of the plasmon-catalyzed oxidation of PATP on immobilized gold nanoparticles that can be used to generate a surface molecular pattern of DMAB. **b** Scanning electron micrograph of a substrate with the silane immobilized gold nanoparticles. The small aggregates of some of the gold nanoparticles result in the formation of an extended plasmon band around 650 nm in the absorbance spectrum (Fig. 11.14e). **c**–**d** SERS spectra of immobilized gold nanoparticles modified with PATP using the two indicated laser intensities and an acquisition time of 1 s. **e** Relative DMAB intensity ($I_{1143}/I_{1080}$) of a series of spectra as shown in panels (**c**) and (**d**). **f** SERS map of a spot of DMAB using the band ratio $I_{1143}/I_{1080}$ in an area of 40 × 40 μm$^2$ ($\lambda_{excitation}$ 633 nm; excitation intensity 5 kW/cm$^2$; mapping step size in x and y direction: 4 μm). The region of high DMAB signal is formed by plasmon-catalyzed oxidation. The inset shows the profile of the band ratio in *x*-direction across the center of the spot. **g** SERS spectra from the marked points in panel **f**. Reproduced from Ref. [129] with permission from American Chemical Society, Copyright 2021

reaction product at lower efficiency in the proximity of the focus. Using the described illumination conditions, different patterns of DMAB in PATP can be generated, e.g., spot-wise or line shaped, etc.

DMAB patterns were also generated from PNTP in the four-electron reduction, which is equipped by hot electrons generated upon the decay of the localized surface plasmon of the gold nanoparticles as described in Sect. 12.3.3. As was discussed above, the efficiency of the generation of hot carriers can be improved significantly in the presence of halide ions and other ligands [99], so that such a fabrication of DMAB pattern could also be achieved at lower intensity than the one chosen here.

Moreover, we were able to demonstrate the possibility to introduce positions that are selectively functionalized by an amino group before a background of nitro groups by using the six-electron reduction of PNTP to PATP that is induced at acidic pH by hot electrons [129]. This was achieved both on gold and silver nanoparticles. Here, the spot diameters found on the silver nanoparticles were slightly larger than on the gold nanoparticles under the same excitation conditions, supporting our previous observations of a higher efficiency of the reaction on silver nanostructures [99].

Erasing and rewriting of the active molecules in a molecular pattern is extremely attractive, since it enables re-use, deletion of stored information, or reparation. Also, sensor arrays for immobilization or functionalization with multiple targets can be generated. The DMAB formed on gold nanoparticles in a plasmon-catalyzed oxidation can be (non-photochemically) reduced to PATP in the presence of $NaBH_4$, which makes it possible to delete DMAB patterns produced by plasmon-assisted laser direct writing. After erasing by the reduction reaction, a new DMAB pattern can be generated again by irradiation. Of course, also other possibilities can be used reverse the reaction, e.g., the hot-electron-based reduction carried out at low pH and in the presence of chloride ions or of a range of other ligands that promote hot electron harvesting as discussed in the previous section. The reuse of the functionalized plasmonic substrate by erasing molecular patterns using chemical (or photochemical) reactions adds further flexibility to the plasmon-catalyzed derivatization approach. The approach of photochemically modifying the molecular derivatization of a fixed plasmonic substrate will further improve fingerprinting for increased security levels, as well as functionalization and registration of SERS-based microarrays.

## 11.5 Monitoring Plasmon-Catalyzed Reactions

### *11.5.1 Catalytic Mapping and the Heterogeneity of Plasmonic Substrates*

Many reports demonstrate that the active catalytic sites of nanoparticle catalysts are not homogeneously distributed [130], since the catalytic activity is influenced by many parameters of the nanostructured surfaces. Nevertheless, often the characterization of a catalyst material is based on the macroscopic monitoring of a reaction,

implying an averaging of many different catalytic sites. In contrast, if information on the reaction kinetics is obtained at the micrometer to nanometer scale [63, 131–133], averaging effects are avoided. Although the detailed characterization of catalytic sites requires nanoscale resolution [132–137], for fast optical monitoring of reactions, probing the surface of a catalyst at the micrometer scale is of particular interest, e.g., in microfluidic systems [97, 138, 139]. As we found, in spite of their very homogeneous plasmon-based enhancement of optical signals that has been exploited for probing by surface-enhanced Raman scattering (SERS) mapping [23, 114], collections of gold nanoparticles, e.g., when immobilized on a glass surface, exhibit a high heterogeneity in catalytic activity [127].

We conducted experiments, where we mapped the formation of the reaction product DMAB as an indicator of catalytic activity for several experimental conditions at the microscopic scale [127]. We obtained spectroscopic data during incubation processes of typical samples of PATP-covered nanostructured surfaces as they are used for example, for PATP serving as a reporter molecule in sensing of pH [125], explosives [140–142], and nitrite [78]. Also in the formation of DMAB by reduction of PNTP [61], the inhomogeneity of the catalytic activity became visible in SERS micromapping [127]. We observed changes in catalytic activity between micron-sized areas, in each sampled spot averaging over many individual nanoparticles. As the distribution of the gold nanoparticles on the surface under study was very homogeneous and very similar in each spot, the observed variation suggests that only very few out of tens or hundreds of nanostructures may be responsible for the high activity in some of the spots.

The heterogeneity in catalytic activity becomes very evident at lower molecular concentrations. In an experiment, where the molecular coverage of PATP on gold nanoparticles was controlled by immersing the immobilized gold nanoparticles in PATP solutions of varying concentration, the intensity of DMAB bands in the average spectra and also in the maps increased gradually with the increase of PATP molecular coverage (Fig. 11.15). The minimum concentration of PATP required to result in the full coverage of the gold nanoparticles, estimated according to Refs. [143, 144], in the conditions chosen here is ~ 1.0 μM. The data suggest that at lower coverage of PATP molecules, their reaction is more difficult, and therefore DMAB production is lower. On the contrary, a PATP concentration one or two orders of magnitude higher, i.e., 10 μM or 100 μM, may compensate for spots of low catalytic activity and leads to a relatively homogenous signal of the reaction product (Fig. 11.15).

By the SERS mapping experiments, we were also able to demonstrate some properties of the PATP oxidation reaction and PATP stability that are relevant for the application of PATP. Specifically, we found that dimer formation not only happens within seconds under the intense laser illumination, but also in low intensity room light during typical incubation times of the samples [127]. Moreover, our data obtained after incubation in the dark demonstrated that DMAB forms on the gold nanoparticles also without light in the presence of oxygen. Under illumination, the plasmon-catalyzed reaction takes place in addition. During the incubation process, PATP on gold nanoparticles was oxidized to DMAB by $O_2$ with the help of room light in a plasmon-catalyzed reaction. It was possible to reversibly transform the generated

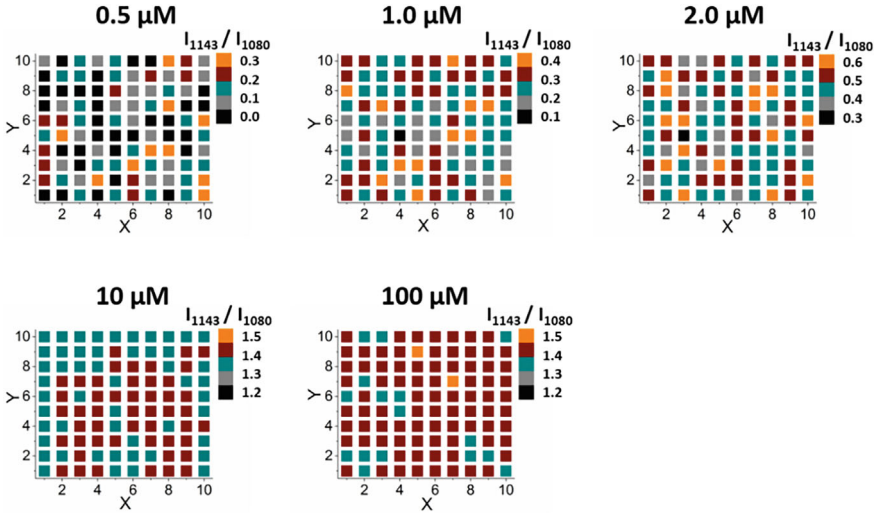



**Fig. 11.15** SERS maps of the intensity at 1143 $cm^{-1}$ ($I_{1143}$) and the intensity at 1080 $cm^{-1}$ ($I_{1080}$), indicating the formation of DMAB formed from PATP on immobilized gold nanoparticles after incubation in air under room light for 3 h with different coverage by PATP molecules (average spectra are shown in Fig. 11.4c of the main text.) The PATP coverage is controlled by incubation of the immobilized gold nanoparticles in the indicated concentrations of PATP solution ($\lambda_{excitation}$ 633 nm; laser intensity 50 kW/$cm^2$; exposure time 1 s). The *X* and *Y* coordinates indicate the position in the grid with a step size of 10 µm in both directions, spots with a diameter of 1.5 µm were used, the sizes of the individual squares are not to scale. Reproduced from Ref. [127] with permission from American Chemical Society, Copyright 2018

DMAB to PATP with the addition of $NaBH_4$. Some of the observed effects only became evident in the mapping experiments, yet disappear in bulk experiments due to averaging effects. Therefore, our results strongly suggest that SERS mapping can be a more precise way for the characterization of nanostructured catalysts at a microscale resolution, and have implications for the future characterization of catalytic reactions. In particular, the observation of some events only at the microscopic level will have effects on the conclusions that are drawn on the kinetics of a particular reaction.

### *11.5.2 Optofluidic Devices to Monitor Plasmon-Supported Reactions*

Microfluidic technology provides an efficient enabling technology that can integrate the mixture, the reaction, and the detection in the same platform. The combination of SERS and microfluidics has shown excellent merits due to the high sensitivity and miniaturization [145]. In general, two ways are applied for the integration of SERS

into microfluidics, namely (i) the simple mixing of colloidal metal nanoparticles and target molecules in the channel and (ii) on pumping of the target molecules through nanoparticle-functionalized channels [146]. While in (i), the SERS substrates in solution on-chip are always fresh, and timescales and homogeneity of mixing enable fast probing, the monitoring of a reaction faces several difficulties, such as in reactions that involve molecules in the gas phase or fast reactions in the timescale of seconds. Moreover, a so-called "memory effect" can occur due to the adsorption of nanoparticles on the channel. In contrast, the immobilization method (ii) provides reproducible SERS signals. Nevertheless, re-utilization of immobilized SERS active nanostructures on-chip is restricted to some specific cases [147].

The application of SERS microfluidics for reaction monitoring has demonstrated great potential due to the excellent possibilities of both control and monitoring. For example, Xie and Schlücker successfully used a microfluidic chip for SERS monitoring of the reduction of PNTP by sodium borohydride ($NaBH_4$) on Au-Pt-Au nanoparticles [28]. This chip could avoid the photoreaction to DMAB (Sect. 11.3.2) that was considered a side reaction in their particular experiment due to short and discontinuous illumination time on the nanoparticles [28]. By precise control of the reaction parameters, a great influence of the pH values on the reduction of PNTP due to the hydrolysis of $NaBH_4$ was found, and different reaction kinetics when the pH was varied [28].

Another possibility is the use of a "plug-in" reusable SERS optofluidic platform that we developed to adapt SERS for studies of heterogeneous catalysis. There, monitoring of catalytic reactions in both liquid and gaseous condition is enabled [97]. The optofluidic platform contains multifunctional gold nanostructures and was used first to further demonstrate the important role of oxygen in the plasmon-catalyzed dimerization of PATP discussed above in Sect. 11.3.2. Specifically, supporting theoretical suggestions [59] and our experimental findings [93] that metal oxide species are crucial for DMAB formation, we could conclude that the important role of $^3O_2$ must lie in the formation of such a species. By integrating a "plug-in" SERS probe as optical component, we enhance the sensing performance and simplify the design of the microfluidic system. As shown in Fig. 11.16, a "plug-in" SERS probe is generated from a glass rod, onto which gold nanoparticles of ~ 30 nm in diameter were immobilized using aminopropyltriethoxysilane (APTES) using a procedure reported previously [114, 148]. Alternatively, gold nanoparticles can also be immobilized on a slab of polydimethylsiloxane (PDMS) using silane chemistry, and many "plug-in" SERS probes can be obtained by punching out the slab (Fig. 11.16b). The optical probes are inserted into a PDMS-glass microfluidic chip with appropriate pre-punched holes on the PDMS side (Fig. 11.16c). For the assembly of the chip, the PDMS-glass chip was firstly fabricated, and the holes were punched before sealing the chip. In the case of the PDMS probes, these can also be inserted through a pipette tip. On both, the glass rod (Fig. 11.16a) and the PDMS (Fig. 11.16b), the gold nanoparticles are uniformly distributed, with slight aggregation as studied by electron microscopy and absorbance spectra. The electromagnetic enhancement in SERS is determined

by both the excitation and the Raman field enhancement factor, each contributing quadratically to the SERS signal [149]. Therefore, at high field enhancement factors, a high SERS signal can be obtained even at relatively low excitation fields. Low excitation laser intensities keep local field-dependent plasmonic catalysis, leading to wanted or unwanted reactions, at a low level.

Using the plug-in SERS platform, we investigated the photo-induced dimerization of PATP under stable and controllable gas atmosphere [97]. With a flow of air, containing $O_2$, in the channel, the characteristic bands of DMAB gradually increased in intensity with increasing irradiation time when the air flow passed the plug-in SERS probe. As a control, under $N_2$ flow, the SERS spectra were almost unchanged during the monitoring time, and no significant amount of DMAB was formed. This result supported the necessity of oxygen in photo-induced dimerization of PATP, through the mechanism of $^3O_2$ activation [59, 90]. As discussed in Sect. 11.3.2, it was proposed that metal oxides are important in the dimerization reaction and that they are generated through the plasmon-catalyzed activation of oxygen on the surface of the gold nanoparticles [59]. The absence of the reaction product in the absence of oxygen suggested that no metal oxide or hydroxide species could be formed and that the reaction did not take place.

### *11.5.3 Multiphoton-Excited Microscopy to Detect Reaction Products in Plasmonic Catalysis*

In order to create greater versatility with respect to both the excitation conditions for the plasmonic reaction and an efficient probing, it is of great interest to explore new approaches in vibrational microspectroscopy. SERS is an optimal tool to study the interaction of a reacting species with the surface of the catalyst, yet for a comprehensive characterization complementary methods may be desirable. At the same time, as discussed in Sect. 11.5.1, achievement of a high lateral confinement may be attractive as well, considering the heterogeneity of a catalytic surface at the microscopic level.

Due to several advantages that the two-photon excited process of hyper Raman scattering (HRS) offers, the non-linear analog of SERS, surface-enhanced hyper Raman scattering (SEHRS) [150], has gained increasing importance for studying organic structures and materials [151–154]. In particular, HRS follows different selection rules than those acting in Raman scattering, and therefore SEHRS can provide complementary vibrational information, specifically from infrared-active and silent modes [152, 153, 155].

SEHRS spectra of the three isomers of PATP, 4-aminothiophenol (4-ATP), i.e., PATP itself, 2-aminothiophenol (2-ATP), and 3-aminothiophenol (3-ATP) at 1064 nm were obtained with citrate stabilized gold nanostructures at different pH values. SERS spectra from the identical samples were excited at a wavelength of 633 nm for comparison. The spectra indicated a different interaction of the different isomers with the gold [156]. When pH in the local environment was varied, structural changes,

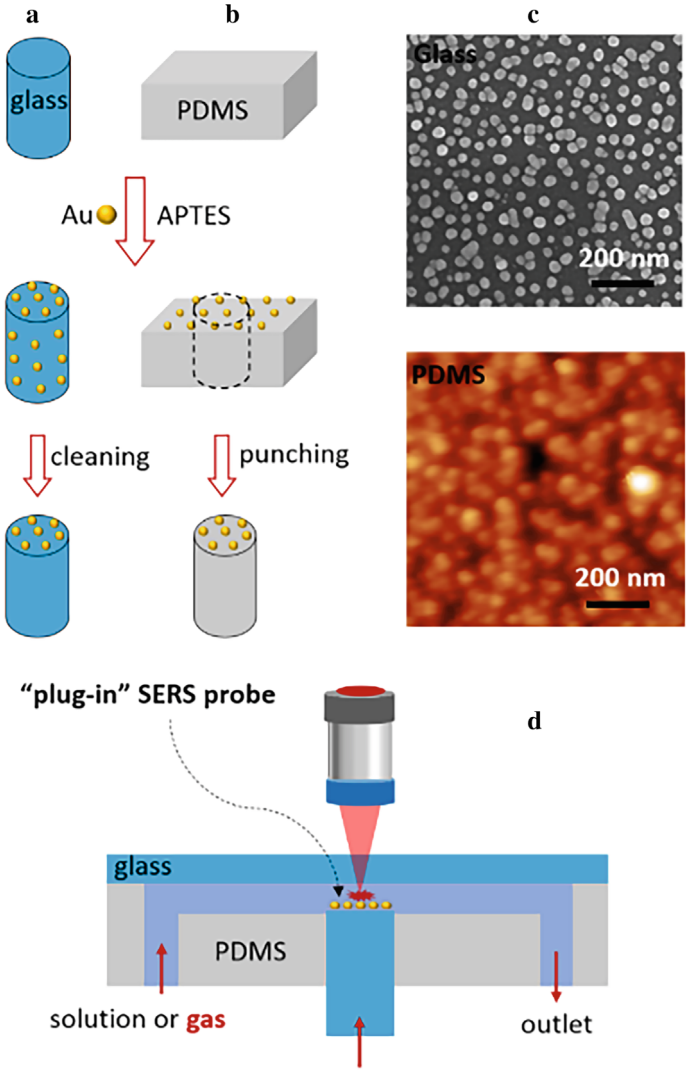



**Fig. 11.16** Procedure for the fabrication of plug-in multifunctional SERS probes based on **a** glass and **b** PDMS. **c** Corresponding SEM and AFM image, revealing the 3-aminopropyltriethoxysilane (APTES) immobilized gold nanostructures. **d** Schematic of the whole plug-in optofluidic platform for monitoring nanoparticle-catalyzed reactions in a microfluidic platform. Reproduced from Ref. [97] with permission from American Chemical Society, Copyright 2018

that included both the direct de-/protonation of the amino group, but also the emergence of new molecular species, could be monitored. As observed in the spectrum of PATP (cf. discussion in Sect. 11.3.2), also the SERS spectrum of 2-ATP at high pH shows contributions from DMAB modes. This indicates that also 2-ATP undergoes a dimerization reaction at the given excitation conditions. Interestingly, a strong signal from the N=N stretching mode is observed also in the SEHRS spectrum of 2-ATP. The latter indicates that the dimerization of 2-ATP must have occurred also when using 1064 nm laser excitation in the hyper Raman experiment. We have shown that, in order for SEHRS on gold nanoaggregates to be efficient, plasmon resonances at the near-infrared (NIR) excitation wavelength play a major role [157, 158]. These plasmon resonances in the NIR are suggested to assist the plasmon-catalyzed oxidation reaction of 2-ATP here [156]. Especially the high peak intensities coming from the ps laser pulses used for excitation of the SEHRS could facilitate this activation. In the SEHRS spectrum of PATP at high pH, none of the bands associated with DMAB vibrations are present. Although this could indicate that the dimerization does not take place under excitation with 1064 nm despite their presence in the 633 nm excited SERS spectrum, it is possible that the (few) characteristic modes of the reaction product are not enhanced in the SEHRS spectrum of PATP. The much stronger contributions of DMAB in the SERS spectra of 2-ATP and the presence of the N = N stretching band of DMAB in the SEHRS spectrum of 2-ATP point to a more efficient generation of the dimer, possibly due to the different interaction of 2-ATP with the surface that could result in a different efficiency of the plasmon-assisted reaction steps and/or an orientation of the 2-ATP monomers that favor dimer formation.

Although the dependence of product formation on laser intensity, presence of other metal species, and the influence of other ligand molecules, as well as a comparison with the mechanisms discussed for this reaction at visible wavelengths will have to be the subject of future studies, the observation of the plasmon-catalyzed reaction by SEHRS suggests that the combination of SEHRS and SERS could be very beneficial for the further elucidation of plasmon-assisted reaction mechanisms, especially in the NIR frequency range.

## 11.6 Beyond Gold and Silver

### *11.6.1 Why Study Different Plasmonic Catalysts?*

Gold and silver nanoparticles have been used widely in photocatalysis because of their excellent plasmonic properties. Besides, easy preparation and their high chemical stability make it easy to reproduce related studies in many different lab environments. Owing to these advantages, gold and silver nanomaterials have been the most frequently used in basic studies on plasmon-assisted catalysis, including both mechanisms and applications. Despite the wide use of gold and silver, however, it is still

necessary to explore plasmonic catalysis with other materials. Firstly, to have a better understanding of plasmonic catalysis mechanisms, we need to compare the catalytic activities/efficiencies of nanomaterials with different compositions and structures. Secondly, there may be the possibility to control reaction selectivity (namely reaction product) by applying different catalytic materials. Thirdly, considering practical applications, developing cheaper materials that can be used in large scale at lower cost is desired. The extensive body of literature, including excellent recent reviews cited below, underpins the enormous importance of this research field but cannot nearly be covered within the scope of this chapter, so we are listing some very promising types of materials in the following.

### *11.6.2 Other Metal and Composite Nanostructures*

*Other pure metal nanoparticles.* Many other metals are also used for the preparation of plasmonic nanomaterials, such as Cu, Al, and Pd [159, 160]. Since these metals have different electronic structures, they display different catalytic activities and even reaction selectivity, and therefore, they can be used for different catalytic reactions. For example, Cu nanomaterials have attracted tremendous attention in plasmonic catalysis owing to the low cost, high natural abundance, and obvious LSPR effect in the wavelength range of visible light [161]. An example of the much better catalytic performance of Cu nanoparticles compared to gold and silver nanoparticles was in the hot-electron-induced reduction of PNTP, discussed in Sect. 11.4.1. It has been attributed to the higher Fermi level of the Cu nanoparticles [99].

*Metal nanocomposites.* By combining plasmon active metals with "traditional" catalysts, metal nanocomposites with different structures improve both light conversion and reaction selectivity simultaneously, expanding the library of plasmonic catalysts [162]. The main nanostructures of the metal composite includes: metal/semiconductor, antenna–reactor, core–shell, and alloyed nanoparticle systems. Each nanostructure hosts its own unique interactions that affect the photocatalytic response [162]. As important examples, metal/semiconductor systems have been proposed since the very early days of plasmonic catalysis, and the active metal mainly plays the role of light absorber and hot electron source [163]. So-called antenna–reactor systems rely exclusively on optical coupling between a plasmonic antenna and a catalytic reactor to enhance reaction activity [164]. Core–shell and alloy architectures adjust the optical properties by introducing strong electronic interactions between different metals. [162]. As a result, these electronic interactions strongly influence the plasmonic response and offer the potential to enhance the reactivity and product selectivity.

*Plasmonic semiconductors.* Plasmonic semiconductors are a kind of degenerately doped semiconductors that can exhibit metal-like plasmon behavior [165, 166]. Since the carriers (holes and electrons) concentration in semiconductors are much lower

than in noble metals, semiconductors normally do not exhibit an LSPR effect. To realize the LSPR effect, a high concentration of carriers can be introduced into the semiconductor by controlled doping. The degenerately doped plasmonic semiconductors can be divided into *n*-type (doping electrons) and *p*-type (doping holes) semiconductors [166]. Generally, degenerately doped semiconductors still have much lower free carrier concentration than noble metals, and their LSPR responses can cover the visible, near-infrared (NIR), and mid-infrared regime, providing these systems with great versatility [165, 166]. Similar to noble metal nanomaterials, a variety of degenerately doped semiconductors has been used as plasmonic catalysts toward a whole range catalytic reactions, including Suzuki coupling reaction, hydrogen evolution reaction, $CO_2$ reduction, and several more [167]. Moreover, compared to metal nanoparticles, these plasmonic semiconductors mainly contain earth-abundant elements, such as Cu, Mo. The lower price of these materials will benefit their wide industrial applications for plasmonic catalysis.

**Acknowledgements** The authors wish to thank all their co-authors of their original papers that have been discussed in this chapter. The work reporting own results was conducted at Humboldt-Universität zu Berlin, Germany, in the framework funding provided by the German Excellence Initiative to DFG GSC 1013 SALSA. Moreover, funding by DFG grant Kn 557/12-1 and DFG-CRC1636 Project ID 510943930—Project No. B02 is gratefully acknowledged.

## References

1. S. Linic, P. Christopher and D. B. Ingram, Plasmonic-metal nanostructures for efficient conversion of solar to chemical energy. Nature materials **10**, 911 (2011)
2. N. Chandrasekharan and P. V. Kamat, Improving the photoelectrochemical performance of nanostructured TiO2 films by adsorption of gold nanoparticles. The Journal of Physical Chemistry B **104**, 10851–10857 (2000)
3. P. V. Kamat, ACS Publications, 2002.
4. T. Hirakawa and P. V. Kamat, Charge separation and catalytic activity of Ag@ TiO2 core− shell composite clusters under UV− irradiation. Journal of the American Chemical Society **127**, 3928–3934 (2005)
5. K. Awazu, M. Fujimaki, C. Rockstuhl, J. Tominaga, H. Murakami, Y. Ohki, N. Yoshida and T. Watanabe, A plasmonic photocatalyst consisting of silver nanoparticles embedded in titanium dioxide. Journal of the American Chemical Society **130**, 1676–1680 (2008)
6. P. Christopher, H. Xin and S. Linic, Visible-light-enhanced catalytic oxidation reactions on plasmonic silver nanostructures. Nature chemistry **3**, 467–472 (2011)
7. S. Mukherjee, F. Libisch, N. Large, O. Neumann, L. V. Brown, J. Cheng, J. B. Lassiter, E. A. Carter, P. Nordlander and N. J. Halas, Hot electrons do the impossible: plasmon-induced dissociation of H2 on Au. Nano Lett **13**, 240–247 (2013)
8. S. Mukherjee, L. Zhou, A. M. Goodman, N. Large, C. Ayala-Orozco, Y. Zhang, P. Nordlander and N. J. Halas, Hot-electron-induced dissociation of H2 on gold nanoparticles supported on SiO2. Journal of the American Chemical Society **136**, 64–67 (2013)
9. L. Zhou, C. Zhang, M. J. McClain, A. Manjavacas, C. M. Krauter, S. Tian, F. Berg, H. O. Everitt, E. A. Carter and P. Nordlander, Aluminum nanocrystals as a plasmonic photocatalyst for hydrogen dissociation. Nano letters **16**, 1478–1484 (2016)
10. J. M. P. Martirez and E. A. Carter, Excited-State N2 Dissociation Pathway on Fe-Functionalized Au. Journal of the American Chemical Society **139**, 4390–4398 (2017)

11. Z. Liu, W. Hou, P. Pavaskar, M. Aykol and S. B. Cronin, Plasmon resonant enhancement of photocatalytic water splitting under visible illumination. Nano letters **11**, 1111–1116 (2011)
12. S. C. Warren and E. Thimsen, Plasmonic solar water splitting. Energy & Environmental Science **5**, 5133–5146 (2012)
13. J. Lee, S. Mubeen, X. Ji, G. D. Stucky and M. Moskovits, Plasmonic photoanodes for solar water splitting with visible light. Nano letters **12**, 5014–5019 (2012)
14. W. Hou, Z. Liu, P. Pavaskar, W. H. Hung and S. B. Cronin, Plasmonic enhancement of photocatalytic decomposition of methyl orange under visible light. Journal of catalysis **277**, 149–153 (2011)
15. C. Hu, T. Peng, X. Hu, Y. Nie, X. Zhou, J. Qu and H. He, Plasmon-induced photodegradation of toxic pollutants with Ag− AgI/Al2O3 under visible-light irradiation. Journal of the American Chemical Society **132**, 857–862 (2009)
16. S. Song, B. Cheng, N. Wu, A. Meng, S. Cao and J. Yu, Structure effect of graphene on the photocatalytic performance of plasmonic Ag/Ag 2 CO 3-rGO for photocatalytic elimination of pollutants. Applied Catalysis B: Environmental **181**, 71–78 (2016)
17. J. Chen, H. Che, K. Huang, C. Liu and W. Shi, Fabrication of a ternary plasmonic photocatalyst CQDs/Ag/Ag 2 O to harness charge flow for photocatalytic elimination of pollutants. Appl. Catal. B- Environ. **192**, 134–144 (2016)
18. X. Chen, H. Y. Zhu, J. C. Zhao, Z. F. Zheng and X. P. Gao, Visible-Light-Driven Oxidation of Organic Contaminants in Air with Gold Nanoparticle Catalysts on Oxide Supports. Angewandte Chemie **120**, 5433–5436 (2008)
19. H. Zhang, T. Wang, J. Wang, H. Liu, T. D. Dao, M. Li, G. Liu, X. Meng, K. Chang and L. Shi, Surface-plasmon-enhanced photodriven CO2 reduction catalyzed by metal–organic-framework-derived iron nanoparticles encapsulated by ultrathin carbon layers. Advanced Materials **28**, 3703–3710 (2016)
20. W. Xie and S. Schlücker, Surface-enhanced Raman spectroscopic detection of molecular chemo-and plasmo-catalysis on noble metal nanoparticles. Chemical Communications **54**, 2326–2336 (2018)
21. Y.-F. Huang, H.-P. Zhu, G.-K. Liu, D.-Y. Wu, B. Ren and Z.-Q. Tian, When the signal is not from the original molecule to be detected: chemical transformation of para-aminothiophenol on Ag during the SERS measurement. J. Am. Chem. Soc. **132**, 9244–9246 (2010)
22. W. Xie, C. Herrmann, K. Kömpe, M. Haase and S. Schlücker, Synthesis of bifunctional Au/Pt/Au core/shell nanoraspberries for in situ SERS monitoring of platinum-catalyzed reactions. Journal of the American Chemical Society **133**, 19302–19305 (2011)
23. V. Joseph, C. Engelbrekt, J. Zhang, U. Gernert, J. Ulstrup and J. Kneipp, Characterizing the Kinetics of Nanoparticle-Catalyzed Reactions by Surface-Enhanced Raman Scattering. Angewandte Chemie International Edition **51**, 7592–7596 (2012)
24. W. Xie, B. Walkenfort and S. Schlücker, Label-free SERS monitoring of chemical reactions catalyzed by small gold nanoparticles using 3D plasmonic superstructures. Journal of the American Chemical Society **135**, 1657–1660 (2012)
25. J. Huang, Y. Zhu, M. Lin, Q. Wang, L. Zhao, Y. Yang, K. X. Yao and Y. Han, Site-specific growth of Au–Pd alloy horns on Au nanorods: a platform for highly sensitive monitoring of catalytic reactions by surface enhancement Raman spectroscopy. Journal of the American Chemical Society **135**, 8552–8561 (2013)
26. W. Xie and S. Schlücker, Hot electron-induced reduction of small molecules on photorecycling metal surfaces. Nature communications **6**, 7570 (2015)
27. J. Li, J. Liu, Y. Yang and D. Qin, Bifunctional Ag@ Pd-Ag nanocubes for highly sensitive monitoring of catalytic reactions by surface-enhanced Raman spectroscopy. Journal of the American Chemical Society **137**, 7039–7042 (2015)
28. W. Xie, R. Grzeschik and S. Schlücker, Metal Nanoparticle-Catalyzed Reduction Using Borohydride in Aqueous Media: A Kinetic Analysis of the Surface Reaction by Microfluidic SERS. Angewandte Chemie International Edition **55**, 13729–13733 (2016)
29. H.-K. Choi, W.-H. Park, C.-G. Park, H.-H. Shin, K. S. Lee and Z. H. Kim, Metal-Catalyzed Chemical Reaction of Single Molecules Directly Probed by Vibrational Spectroscopy. J. Am. Chem. Soc **138**, 4673–4684 (2016)

30. H. Zhang, X.-G. Zhang, J. Wei, C. Wang, S. Chen, H.-L. Sun, Y.-H. Wang, B.-H. Chen, Z.-L. Yang and D.-Y. Wu, Revealing the Role of Interfacial Properties on Catalytic Behaviors by in Situ Surface-Enhanced Raman Spectroscopy. Journal of the American Chemical Society **139**, 10339–10346 (2017)
31. G. Mie, Contributions to the optics of turbid media, particularly of colloidal metal solutions. Contributions to the optics of turbid media, particularly of colloidal metal solutions Transl. into ENGLISH from Ann. Phys.(Leipzig), v. 25, no. 3, 1908 p 377–445 (1976)
32. S. K. Ghosh and T. Pal, Interparticle coupling effect on the surface plasmon resonance of gold nanoparticles: from theory to applications. Chemical reviews **107**, 4797–4862 (2007)
33. P. K. Jain, K. S. Lee, I. H. El-Sayed and M. A. El-Sayed, Calculated absorption and scattering properties of gold nanoparticles of different size, shape, and composition: applications in biological imaging and biomedicine. The journal of physical chemistry B **110**, 7238–7248 (2006)
34. H. Chen, X. Kou, Z. Yang, W. Ni and J. Wang, Shape-and size-dependent refractive index sensitivity of gold nanoparticles. Langmuir **24**, 5233–5237 (2008)
35. R. Elghanian, J. J. Storhoff, R. C. Mucic, R. L. Letsinger and C. A. Mirkin, Selective colorimetric detection of polynucleotides based on the distance-dependent optical properties of gold nanoparticles. Science **277**, 1078–1081 (1997)
36. M. L. Brongersma, N. J. Halas and P. Nordlander, Plasmon-induced hot carrier science and technology. Nature nanotechnology **10**, 25 (2015)
37. R. L. Gieseking, M. A. Ratner and G. C. Schatz, Review of plasmon-induced hot-electron dynamics and related SERS chemical effects, in *Frontiers of Plasmon Enhanced Spectroscopy Volume 1*, Edited by, (ACS Publications, 2016), pp. 1–22
38. C. Boerigter, U. Aslam and S. Linic, Mechanism of charge transfer from plasmonic nanostructures to chemically attached materials. ACS nano **10**, 6108–6115 (2016)
39. M. Van Dijk, A. Tchebotareva, M. Orrit, M. Lippitz, S. Berciaud, D. Lasne, L. Cognet and B. Lounis, Absorption and scattering microscopy of single metal nanoparticles. Physical Chemistry Chemical Physics **8**, 3486–3495 (2006)
40. D. D. Evanoff and G. Chumanov, Size-controlled synthesis of nanoparticles. 2. Measurement of extinction, scattering, and absorption cross sections. The Journal of Physical Chemistry B **108**, 13957–13962 (2004)
41. C. Langhammer, Z. Yuan, I. Zorić and B. Kasemo, Plasmonic properties of supported Pt and Pd nanostructures. Nano letters **6**, 833–838 (2006)
42. A. Mooradian, Photoluminescence of metals. Physical Review Letters **22**, 185 (1969)
43. E. Dulkeith, T. Niedereichholz, T. Klar, J. Feldmann, G. Von Plessen, D. Gittins, K. Mayya and F. Caruso, Plasmon emission in photoexcited gold nanoparticles. Physical Review B **70**, 205424 (2004)
44. M. B. Mohamed, V. Volkov, S. Link and M. A. El-Sayed, Thelightning'gold nanorods: fluorescence enhancement of over a million compared to the gold metal. Chemical Physics Letters **317**, 517–523 (2000)
45. X. Li, D. Xiao and Z. Zhang, Landau damping of quantum plasmons in metal nanostructures. New Journal of Physics **15**, 023011 (2013)
46. M. Lisowski, P. Loukakos, U. Bovensiepen, J. Stähler, C. Gahl and M. Wolf, Ultra-fast dynamics of electron thermalization, cooling and transport effects in Ru (001). Applied Physics A **78**, 165–176 (2004)
47. H. Inouye, K. Tanaka, I. Tanahashi and K. Hirao, Ultrafast dynamics of nonequilibrium electrons in a gold nanoparticle system. Physical Review B **57**, 11334 (1998)
48. J. Bosbach, C. Hendrich, F. Stietz, T. Vartanyan and F. Träger, Ultrafast dephasing of surface plasmon excitation in silver nanoparticles: Influence of particle size, shape, and chemical surrounding. Physical review letters **89**, 257404 (2002)
49. C. Hendrich, J. Bosbach, F. Stietz, F. Hubenthal, T. Vartanyan and F. Träger, Chemical interface damping of surface plasmon excitation in metal nanoparticles: a study by persistent spectral hole burning. Applied Physics B **76**, 869–875 (2003)

50. X.-J. Chen, G. Cabello, D.-Y. Wu and Z.-Q. Tian, Surface-enhanced Raman spectroscopy toward application in plasmonic photocatalysis on metal nanostructures. Journal of Photochemistry and Photobiology C: Photochemistry Reviews **21**, 54–80 (2014)
51. P. L. Redmond, X. Wu and L. Brus, Photovoltage and photocatalyzed growth in citrate-stabilized colloidal silver nanocrystals. The Journal of Physical Chemistry C **111**, 8942–8947 (2007)
52. E. Kazuma, N. Sakai and T. Tatsuma, Nanoimaging of localized plasmon-induced charge separation. Chemical Communications **47**, 5777–5779 (2011)
53. D. B. Ingram and S. Linic, Water splitting on composite plasmonic-metal/semiconductor photoelectrodes: evidence for selective plasmon-induced formation of charge carriers near the semiconductor surface. Journal of the American Chemical Society **133**, 5202–5205 (2011)
54. F. Wang, C. Li, H. Chen, R. Jiang, L.-D. Sun, Q. Li, J. Wang, J. C. Yu and C.-H. Yan, Plasmonic harvesting of light energy for Suzuki coupling reactions. Journal of the American Chemical Society **135**, 5588–5601 (2013)
55. A. G. Da Silva, T. S. Rodrigues, V. G. Correia, T. V. Alves, R. S. Alves, R. A. Ando, F. R. Ornellas, J. Wang, L. H. Andrade and P. H. Camargo, Plasmonic Nanorattles as Next-Generation Catalysts for Surface Plasmon Resonance-Mediated Oxidations Promoted by Activated Oxygen. Angewandte Chemie International Edition **55**, 7111–7115 (2016)
56. J. Wang, R. A. Ando and P. H. Camargo, Controlling the Selectivity of the Surface Plasmon Resonance Mediated Oxidation of p-Aminothiophenol on Au Nanoparticles by Charge Transfer from UV-excited TiO2. Angewandte Chemie **127**, 7013–7016 (2015)
57. H. Yang, L. Q. He, Y. W. Hu, X. Lu, G. R. Li, B. Liu, B. Ren, Y. Tong and P. P. Fang, Quantitative detection of photothermal and photoelectrocatalytic effects induced by SPR from Au@ Pt nanoparticles. Angewandte Chemie **127**, 11624–11628 (2015)
58. J. Wang, R. A. Ando and P. H. Camargo, Investigating the Plasmon-Mediated Catalytic Activity of AgAu Nanoparticles as a Function of Composition: Are Two Metals Better than One? ACS Catalysis **4**, 3815–3819 (2014)
59. Y. F. Huang, M. Zhang, L. B. Zhao, J. M. Feng, D. Y. Wu, B. Ren and Z. Q. Tian, Activation of oxygen on gold and silver nanoparticles assisted by surface plasmon resonances. Angewandte Chemie International Edition **53**, 2353–2357 (2014)
60. B. Dong, Y. Fang, L. Xia, H. Xu and M. Sun, Is 4-nitrobenzenethiol converted to p, p′-dimercaptoazobenzene or 4-aminothiophenol by surface photochemistry reaction? Journal of Raman Spectroscopy **42**, 1205–1206 (2011)
61. M. Sun, Z. Zhang, H. Zheng and H. Xu, In-situ plasmon-driven chemical reactions revealed by high vacuum tip-enhanced Raman spectroscopy. Sci. Rep. **2**, 647 (2012)
62. M. Sun and H. Xu, A novel application of plasmonics: plasmon-driven surface-catalyzed reactions. Small **8**, 2777–2786 (2012)
63. E. M. Van Schrojenstein Lantman, T. Deckert-Gaudig, A. J. Mank, V. Deckert and B. M. Weckhuysen, Catalytic processes monitored at the nanoscale with tip-enhanced Raman spectroscopy. Nature nanotechnology **7**, 583–586 (2012)
64. Z. Zhang, M. Sun, P. Ruan, H. Zheng and H. Xu, Electric field gradient quadrupole Raman modes observed in plasmon-driven catalytic reactions revealed by HV-TERS. Nanoscale **5**, 4151–4155 (2013)
65. L. Kang, P. Xu, B. Zhang, H. Tsai, X. Han and H.-L. Wang, Laser wavelength-and power-dependent plasmon-driven chemical reactions monitored using single particle surface enhanced Raman spectroscopy. Chemical Communications **49**, 3389–3391 (2013)
66. X. Zhang, P. Wang, Z. Zhang, Y. Fang and M. Sun, Plasmon-driven sequential chemical reactions in an aqueous environment. Scientific reports **4** (2014)
67. L.-B. Zhao, J.-L. Chen, M. Zhang, D.-Y. Wu and Z.-Q. Tian, Theoretical study on electroreduction of p-nitrothiophenol on silver and gold electrode surfaces. The Journal of Physical Chemistry C **119**, 4949–4958 (2015)
68. K. Kim, J.-Y. Choi and K. S. Shin, Photoreduction of 4-nitrobenzenethiol on Au by hot electrons plasmonically generated from Ag nanoparticles: gap-mode surface-enhanced raman scattering observation. The Journal of Physical Chemistry C **119**, 5187–5194 (2015)

69. X. Shi, H.-W. Li, Y.-L. Ying, C. Liu, L. Zhang and Y.-T. Long, In situ monitoring of catalytic process variations in a single nanowire by dark-field-assisted surface-enhanced Raman spectroscopy. Chemical Communications **52**, 1044–1047 (2016)
70. H.-K. Choi, K. S. Lee, H.-H. Shin and Z. H. Kim, Identification of the First Elementary Step in the Photocatalytic Reduction of Nitrobenzenethiols on a Metallic Surface. J. Phys. Chem. Lett. **7**, 4099–4104 (2016)
71. W. Lin, Y. Shi, X. Yang, J. Li, E. Cao, X. Xu, T. Pullerits, W. Liang and M. Sun, Physical mechanism on exciton-plasmon coupling revealed by femtosecond pump-probe transient absorption spectroscopy. Materials Today Physics **3**, 33–40 (2017)
72. L.-B. Zhao, M. Zhang, Y.-F. Huang, C. T. Williams, D.-Y. Wu, B. Ren and Z.-Q. Tian, Theoretical study of plasmon-enhanced surface catalytic coupling reactions of aromatic amines and nitro compounds. The journal of physical chemistry letters **5**, 1259–1266 (2014)
73. Z. Zhang and J. Kneipp, Ligand-Supported Hot Electron Harvesting: Revisiting the pH-Responsive Surface-Enhanced Raman Scattering Spectrum of p-Aminothiophenol. The journal of physical chemistry letters **12**, 1542–1547 (2021)
74. W. Lin, X. Ren, L. Cui, H. Zong and M. Sun, Electro-optical tuning of plasmon-driven double reduction interface catalysis. Applied Materials Today **11**, 189–192 (2018)
75. H. Li, M. Si, L. Liu, X. Chu, S. Wang, L. Wan, R. Yan, M. Sun and Y. Fang, Ag nanoparticle-induced oxidative dimerization of thiophenols: efficiency and mechanism. Langmuir **34**, 11347–11353 (2018)
76. Y. Zhao, Q. Zhang, L. Ma, P. Song and L. Xia, AP/N type silicon semiconductor loaded with silver nanoparticles used as a SERS substrate to selectively drive the coupling reaction induced by surface plasmons. Nanoscale Advances **2**, 3460–3466 (2020)
77. A. Grirrane, A. Corma and H. García, Gold-catalyzed synthesis of aromatic azo compounds from anilines and nitroaromatics. Science **322**, 1661–1664 (2008)
78. X. Liu, H. Q. Li, S. Ye, Y. M. Liu, H. Y. He and Y. Cao, Gold-Catalyzed Direct Hydrogenative Coupling of Nitroarenes To Synthesize Aromatic Azo Compounds. Angewandte Chemie International Edition **53**, 7624–7628 (2014)
79. K. Venkataraman, eds., *The chemistry of synthetic dyes*, (Elsevier, 2012)
80. M. Osawa, N. Matsuda, K. Yoshii and I. Uchida, Charge transfer resonance Raman process in surface-enhanced Raman scattering from p-aminothiophenol adsorbed on silver: Herzberg-Teller contribution. The Journal of Physical Chemistry **98**, 12702–12707 (1994)
81. W.-H. Park and Z. H. Kim, Charge transfer enhancement in the SERS of a single molecule. Nano letters **10**, 4040–4048 (2010)
82. D.-Y. Wu, X.-M. Liu, Y.-F. Huang, B. Ren, X. Xu and Z.-Q. Tian, Surface catalytic coupling reaction of p-mercaptoaniline linking to silver nanostructures responsible for abnormal SERS enhancement: a DFT study. The Journal of Physical Chemistry C **113**, 18212–18222 (2009)
83. Y. Huang, Y. Fang, Z. Yang and M. Sun, Can p, p′-Dimercaptoazobisbenzene Be Produced from p-Aminothiophenol by Surface Photochemistry Reaction in the Junctions of a Ag Nanoparticle− Molecule− Ag (or Au) Film? The Journal of Physical Chemistry C **114**, 18263–18269 (2010)
84. H.-K. Choi, H. K. Shon, H. Yu, T. G. Lee and Z. H. Kim, $b_2$ peaks in SERS spectra of 4-aminobenzenethiol: a photochemical artifact or a real chemical enhancement? The journal of physical chemistry letters **4**, 1079–1086 (2013)
85. M. Sun, Y. Huang, L. Xia, X. Chen and H. Xu, The pH-controlled plasmon-assisted surface photocatalysis reaction of 4-aminothiophenol to p, p′-dimercaptoazobenzene on Au, Ag, and Cu colloids. The Journal of Physical Chemistry C **115**, 9629–9636 (2011)
86. K. Kim, K. L. Kim, D. Shin, J.-Y. Choi and K. S. Shin, Surface-enhanced Raman scattering of 4-aminobenzenethiol on Ag and Au: pH dependence of b 2-type bands. The Journal of Physical Chemistry C **116**, 4774–4779 (2012)
87. W. Ji, N. Spegazzini, Y. Kitahama, Y. Chen, B. Zhao and Y. Ozaki, pH-response mechanism of p-aminobenzenethiol on ag nanoparticles revealed by two-dimensional correlation surface-enhanced raman scattering spectroscopy. The journal of physical chemistry letters **3**, 3204–3209 (2012)

88. E. Tan, P. Yin, T. You and L. Guo, Direct evidence for conversion of p-aminothiophenol to p, p'-dimercaptoazobenzene by in situ reduplicative surface-enhanced Raman scattering measurements. Journal of Raman Spectroscopy **44**, 1200–1203 (2013)
89. J.-F. Xu, S.-Y. Luo and G.-K. Liu, Different behaviors in the transformation of PATP adsorbed on Ag or Au nanoparticles investigated by surface-enhanced Raman spectroscopy–A study of the effects from laser energy and annealing. Spectrochimica Acta Part A: Molecular and Biomolecular Spectroscopy **143**, 35–39 (2015)
90. P. Xu, L. Kang, N. H. Mack, K. S. Schanze, X. Han and H.-L. Wang, Mechanistic understanding of surface plasmon assisted catalysis on a single particle: cyclic redox of 4-aminothiophenol. Sci. Rep. **3**, 2997 (2013)
91. V. Canpean and S. Astilean, Temperature effect on the SERS signature of p-aminothiophenol: A new evidence for the production of p, p'-dimercaptoazobenzene on metallic nanostructures. Spectrochimica Acta Part A: Molecular and Biomolecular Spectroscopy **96**, 862–867 (2012)
92. J.-F. Xu and G.-K. Liu, Laser-induced chemical transformation of PATP adsorbed on Ag nanoparticles by surface-enhanced Raman spectroscopy—A study of the effects from surface morphology of substrate and surface coverage of PATP. Spectrochimica Acta Part A: Molecular and Biomolecular Spectroscopy **138**, 873–877 (2015)
93. Z. Zhang, V. Merk, A. Hermanns, W. E. Unger and J. Kneipp, The role of metal cations in plasmon-catalyzed oxidation: a case study of p-aminothiophenol dimerization. ACS Catalysis **7**, 7803–7809 (2017)
94. A. Gannoruwa, B. Ariyasinghe and J. Bandara, The mechanism and material aspects of a novel $Ag_2O/TiO_2$ photocatalyst active in infrared radiation for water splitting. Catalysis Science & Technology **6**, 479–487 (2016)
95. S. Sun, R. L. Birke, J. R. Lombardi, K. P. Leung and A. Z. Genack, Photolysis of p-nitrobenzoic acid on roughened silver surfaces. The Journal of Physical Chemistry **92**, 5965–5972 (1988)
96. K. Kim, I. Lee and S. J. Lee, Photolytic reduction of 4-nitrobenzenethiol on Au mediated via Ag nanoparticles. Chemical physics letters **377**, 201–204 (2003)
97. Z. Zhang, U. Gernert, R. Gerhardt, E.-M. Höhn, D. Belder and J. Kneipp, Catalysis by Metal Nanoparticles in a Plug-in Optofluidic Platform: Redox Reactions of p-Nitrobenzenethiol and p-Aminothiophenol. ACS Catalysis **8**, 2443−2449 (2018)
98. E. Cortés, W. Xie, J. Cambiasso, A. S. Jermyn, R. Sundararaman, P. Narang, S. Schlücker and S. A. Maier, Plasmonic hot electron transport drives nano-localized chemistry. Nature Communications **8** (2017)
99. Z. Zhang, Y. Li, J. Frisch, M. Bär, J. Rappich and J. Kneipp, In situ surface-enhanced Raman scattering shows ligand-enhanced hot electron harvesting on silver, gold, and copper nanoparticles. Journal of Catalysis **383**, 153–159 (2020)
100. A. Gellé, T. Jin, L. de la Garza, G. D. Price, L. V. Besteiro and A. Moores, Applications of Plasmon-Enhanced Nanocatalysis to Organic Transformations. Chemical Reviews **120**, 986–1041 (2020)
101. Y. Tian and T. Tatsuma, Mechanisms and applications of plasmon-induced charge separation at TiO2 films loaded with gold nanoparticles. Journal of the American Chemical Society **127**, 7632–7637 (2005)
102. E. Kowalska, R. Abe and B. Ohtani, Visible light-induced photocatalytic reaction of gold-modified titanium(iv) oxide particles: action spectrum analysis. Chemical Communications, 241–243 (2009)
103. J. Gargiulo, R. Berté, Y. Li, S. A. Maier and E. Cortés, From Optical to Chemical Hot Spots in Plasmonics. Accounts of Chemical Research **52**, 2525–2535 (2019)
104. I. Kherbouche, Y. Luo, N. Félidj and C. Mangeney, Plasmon-Mediated Surface Functionalization: New Horizons for the Control of Surface Chemistry on the Nanoscale. Chemistry of Materials **32**, 5442–5454 (2020)
105. K. Ueno, S. Juodkazis, T. Shibuya, Y. Yokota, V. Mizeikis, K. Sasaki and H. Misawa, Nanoparticle plasmon-assisted two-photon polymerization induced by incoherent excitation source. Journal of the American Chemical Society **130**, 6928–6929 (2008)

106. M. Erzina, O. Guselnikova, P. Postnikov, R. Elashnikov, Z. Kolska, E. Miliutina, V. Švorčík and O. Lyutakov, Plasmon-Polariton Induced, "from Surface" RAFT Polymerization, as a Way toward Creation of Grafted Polymer Films with Thickness Precisely Controlled by Self-Limiting Mechanism. Advanced Materials Interfaces **5** (2018)
107. O. Guselnikova, S. R. A. Marque, E. V. Tretyakov, D. Mares, V. Jerabek, G. Audran, J. P. Joly, M. Trusova, V. Svorcik, O. Lyutakov and P. Postnikov, Unprecedented plasmon-induced nitroxide-mediated polymerization (PI-NMP): A method for preparation of functional surfaces. Journal of Materials Chemistry A **7**, 12414–12419 (2019)
108. I. Tijunelyte, I. Kherbouche, S. Gam-Derouich, M. Nguyen, N. Lidgi-Guigui, M. L. de la Chapelle, A. Lamouri, G. Lévi, J. Aubard, A. Chevillot-Biraud, C. Mangeney and N. Felidj, Multi-functionalization of lithographically designed gold nanodisks by plasmon-mediated reduction of aryl diazonium salts. Nanoscale Horizons **3**, 53–57 (2018)
109. M. Fedoruk, M. Meixner, S. Carretero-Palacios, T. Lohmüller and J. Feldmann, Nanolithography by Plasmonic Heating and Optical Manipulation of Gold Nanoparticles. ACS Nano **7**, 7648–7653 (2013)
110. A. Henglein, Physicochemical properties of small metal particles in solution: "microelectrode" reactions, chemisorption, composite metal particles, and the atom-to-metal transition. The Journal of Physical Chemistry **97**, 5457–5471 (1993)
111. P. Mulvaney, T. Linnert and A. Henglein, Surface chemistry of colloidal silver in aqueous solution: observations on chemisorption and reactivity. The Journal of Physical Chemistry **95**, 7843–7846 (1991)
112. M. D. Scanlon, P. Peljo, M. A. Méndez, E. Smirnov and H. H. Girault, Charging and discharging at the nanoscale: Fermi level equilibration of metallic nanoparticles. Chemical Science **6**, 2705–2720 (2015)
113. E. Smirnov, M. D. Scanlon, D. Momotenko, H. Vrubel, M. A. Méndez, P.-F. Brevet and H. H. Girault, Gold Metal Liquid-Like Droplets. ACS Nano **8**, 9471–9481 (2014)
114. V. Joseph, M. Gensler, S. Seifert, U. Gernert, J. r. P. Rabe and J. Kneipp, Nanoscopic properties and application of mix-and-match plasmonic surfaces for microscopic SERS. The Journal of Physical Chemistry C **116**, 6859–6865 (2012)
115. H. Reiss, The Fermi level and the redox potential. The Journal of Physical Chemistry **89**, 3783–3791 (1985)
116. G. V. Hartland, L. V. Besteiro, P. Johns and A. O. Govorov, What's so Hot about Electrons in Metal Nanoparticles? ACS Energy Letters **2**, 1641–1653 (2017)
117. J. G. Speight, eds., *Lange's handbook of chemistry*, (McGraw-Hill New York, 2005)
118. C. Clavero, Plasmon-induced hot-electron generation at nanoparticle/metal-oxide interfaces for photovoltaic and photocatalytic devices. Nature Photonics **8**, 95–103 (2014)
119. J. B. Khurgin, How to deal with the loss in plasmonics and metamaterials. Nature nanotechnology **10**, 2–6 (2015)
120. B. Kafle, M. Poveda and T. G. Habteyes, Surface Ligand-Mediated Plasmon-Driven Photochemical Reactions. The Journal of Physical Chemistry Letters **8**, 890–894 (2017)
121. Y. Kim, J. G. Smith and P. K. Jain, Harvesting multiple electron–hole pairs generated through plasmonic excitation of Au nanoparticles. Nature chemistry, 1 (2018)
122. P. Zilio, M. Dipalo, F. Tantussi, G. C. Messina and F. De Angelis, Hot electrons in water: injection and ponderomotive acceleration by means of plasmonic nanoelectrodes. Light: Science & Applications **6**, e17002 (2017)
123. P. Chen, Z. Wang, S. Zong, H. Chen, D. Zhu, Y. Zhong and Y. Cui, A wide range optical pH sensor for living cells using Au@ Ag nanoparticles functionalized carbon nanotubes based on SERS signals. Analytical and bioanalytical chemistry **406**, 6337–6346 (2014)
124. M. Liu, Z. Wang, S. Zong, R. Zhang, J. Yang and Y. Cui, Intracellular surface-enhanced Raman scattering probe based on gold nanorods functionalized with mercaptohexadecanoic acid with reduced cytotoxicity. Biotechnology and applied biochemistry **59**, 381–387 (2012)
125. S. Zong, Z. Wang, J. Yang and Y. Cui, Intracellular pH sensing using p-aminothiophenol functionalized gold nanorods with low cytotoxicity. Analytical chemistry **83**, 4178–4183 (2011)

126. H. Shi, G. Li, H. Sun, T. An, H. Zhao and P.-K. Wong, Visible-light-driven photocatalytic inactivation of E. coli by Ag/AgX-CNTs (X= Cl, Br, I) plasmonic photocatalysts: Bacterial performance and deactivation mechanism. Applied Catalysis B: Environmental **158**, 301–307 (2014)
127. Z. Zhang and J. Kneipp, Mapping the Inhomogeneity in Plasmonic Catalysis on Supported Gold Nanoparticles Using Surface-Enhanced Raman Scattering Microspectroscopy. Analytical Chemistry **90**, 9199–9205 (2018)
128. S. Cai, H. Rong, X. Yu, X. Liu, D. Wang, W. He and Y. Li, Room temperature activation of oxygen by monodispersed metal nanoparticles: Oxidative dehydrogenative coupling of anilines for azobenzene syntheses. ACS Catalysis **3**, 478–486 (2013)
129. Z. Zhang and J. Kneipp, Surface Molecular Patterning by Plasmon-Catalyzed Reactions. ACS Applied Materials & Interfaces (2021)
130. I. L. Buurmans and B. M. Weckhuysen, Heterogeneities of individual catalyst particles in space and time as monitored by spectroscopy. Nature chemistry **4**, 873 (2012)
131. X. Zhou, N. M. Andoy, G. Liu, E. Choudhary, K.-S. Han, H. Shen and P. Chen, Quantitative super-resolution imaging uncovers reactivity patterns on single nanocatalysts. Nature nanotechnology **7**, 237 (2012)
132. N. Kumar, B. Stephanidis, R. Zenobi, A. J. Wain and D. Roy, Nanoscale mapping of catalytic activity using tip-enhanced Raman spectroscopy. Nanoscale **7**, 7133–7137 (2015)
133. J.-H. Zhong, X. Jin, L. Meng, X. Wang, H.-S. Su, Z.-L. Yang, C. T. Williams and B. Ren, Probing the electronic and catalytic properties of a bimetallic surface with 3 nm resolution. Nature nanotechnology **12**, 132 (2017)
134. T. W. Hansen, J. B. Wagner, P. L. Hansen, S. Dahl, H. Topsøe and C. J. Jacobsen, Atomic-resolution in situ transmission electron microscopy of a promoter of a heterogeneous catalyst. Science **294**, 1508–1510 (2001)
135. G. Ertl, Heterogeneous catalysis on atomic scale. Journal of Molecular Catalysis A: Chemical **182**, 5–16 (2002)
136. E. de Smit, I. Swart, J. F. Creemer, G. H. Hoveling, M. K. Gilles, T. Tyliszczak, P. J. Kooyman, H. W. Zandbergen, C. Morin and B. M. Weckhuysen, Nanoscale chemical imaging of a working catalyst by scanning transmission X-ray microscopy. Nature **456**, 222 (2008)
137. M. Behrens, F. Studt, I. Kasatkin, S. Kühl, M. Hävecker, F. Abild-Pedersen, S. Zander, F. Girgsdies, P. Kurr and B.-L. Kniep, The active site of methanol synthesis over Cu/ZnO/Al2O3 industrial catalysts. Science, 1219831 (2012)
138. E. Cao, X. Guo, L. Zhang, Y. Shi, W. Lin, X. Liu, Y. Fang, L. Zhou, Y. Sun, Y. Song, W. Liang and M. Sun, Electrooptical Synergy on Plasmon–Exciton-Codriven Surface Reduction Reactions. Advanced Materials Interfaces **4**, 1700869 (2017)
139. H. Zhang, C. Wang, H.-L. Sun, G. Fu, S. Chen, Y.-J. Zhang, B.-H. Chen, J. R. Anema, Z.-L. Yang and J.-F. Li, In situ dynamic tracking of heterogeneous nanocatalytic processes by shell-isolated nanoparticle-enhanced Raman spectroscopy. Nature communications **8**, 15447 (2017)
140. N. Chen, P. Ding, Y. Shi, T. Jin, Y. Su, H. Wang and Y. He, Portable and Reliable Surface-Enhanced Raman Scattering Silicon Chip for Signal-On Detection of Trace Trinitrotoluene Explosive in Real Systems. Anal. Chem. **89**, 5072–5078 (2017)
141. J. Wang, L. Yang, B. Liu, H. Jiang, R. Liu, J. Yang, G. Han, Q. Mei and Z. Zhang, Inkjet-printed silver nanoparticle paper detects airborne species from crystalline explosives and their ultratrace residues in open environment. Analytical chemistry **86**, 3338–3345 (2014)
142. H. Zhou, Z. Zhang, C. Jiang, G. Guan, K. Zhang, Q. Mei, R. Liu and S. Wang, Trinitrotoluene explosive lights up ultrahigh Raman scattering of nonresonant molecule on a top-closed silver nanotube array. Analytical chemistry **83**, 6913–6917 (2011)
143. A. Gole, S. Sainkar and M. Sastry, Electrostatically controlled organization of carboxylic acid derivatized colloidal silver particles on amine-terminated self-assembled monolayers. Chemistry of materials **12**, 1234–1239 (2000)
144. Y. T. Kim, R. L. McCarley and A. J. Bard, Scanning tunneling microscopy studies of gold (111) derivatized with organothiols. The Journal of Physical Chemistry **96**, 7416–7421 (1992)

145. D. Mark, S. Haeberle, G. Roth, F. Von Stetten and R. Zengerle, Microfluidic lab-on-a-chip platforms: requirements, characteristics and applications, in *Microfluidics Based Microsystems*, Edited by, (Springer, 2010), pp. 305–376
146. I. M. White, S. H. Yazdi and W. Y. Wei, Optofluidic SERS: synergizing photonics and microfluidics for chemical and biological analysis. Microfluidics and nanofluidics **13**, 205–216 (2012)
147. T.-A. Meier, E. Poehler, F. Kemper, O. Pabst, H.-G. Jahnke, E. Beckert, A. Robitzki and D. Belder, Fast electrically assisted regeneration of on-chip SERS substrates. Lab on a Chip **15**, 2923–2927 (2015)
148. K. C. Grabar, R. G. Freeman, M. B. Hommer and M. J. Natan, Preparation and characterization of Au colloid monolayers. Analytical chemistry **67**, 735–743 (1995)
149. K. Kneipp, H. Kneipp and J. Kneipp, Surface-enhanced Raman scattering in local optical fields of silver and gold nanoaggregates from single-molecule Raman spectroscopy to ultrasensitive probing in live cells. Accounts of chemical research **39**, 443–450 (2006)
150. F. Madzharova, Z. Heiner and J. Kneipp, Surface enhanced hyper Raman scattering (SEHRS) and its applications. Chemical Society Reviews **46**, 3980–3999 (2017)
151. M. Gühlke, Z. Heiner and J. Kneipp, Surface-Enhanced Raman and Surface-Enhanced Hyper-Raman Scattering of Thiol-Functionalized Carotene. The Journal of Physical Chemistry C **120**, 20702–20709 (2016)
152. J. C. Hulteen, M. A. Young and R. P. Van Duyne, Surface-Enhanced Hyper-Raman Scattering (SEHRS) on Ag Film over Nanosphere (FON) Electrodes: Surface Symmetry of Centrosymmetric Adsorbates. Langmuir **22**, 10354–10364 (2006)
153. J. Kneipp, H. Kneipp and K. Kneipp, Two-photon vibrational spectroscopy for biosciences based on surface-enhanced hyper-Raman scattering. Proceedings of the National Academy of Sciences **103**, 17149–17153 (2006)
154. M. J. Trujillo and J. P. Camden, Utilizing Molecular Hyperpolarizability for Trace Analysis: A Surface-Enhanced Hyper-Raman Scattering Study of Uranyl Ion. ACS Omega **3**, 6660–6664 (2018)
155. J. T. Golab, J. R. Sprague, K. T. Carron, G. C. Schatz and R. P. V. Duyne, A surface enhanced hyper-Raman scattering study of pyridine adsorbed onto silver: Experiment and theory. The Journal of Chemical Physics **88**, 7942–7951 (1988)
156. F. Madzharova, Z. Heiner and J. Kneipp, Surface-Enhanced Hyper Raman Spectra of Aromatic Thiols on Gold and Silver Nanoparticles. The Journal of Physical Chemistry C **124**, 6233–6241 (2020)
157. F. Madzharova, Z. Heiner, J. Simke, S. Selve and J. Kneipp, Gold Nanostructures for Plasmonic Enhancement of Hyper-Raman Scattering. The Journal of Physical Chemistry C **122**, 2931–2940 (2018)
158. A. Dusa, F. Madzharova and J. Kneipp, Excitation Conditions for Surface-Enhanced Hyper Raman Scattering With Biocompatible Gold Nanosubstrates. Frontiers in Chemistry **9** (2021)
159. S. Kim, J. M. Kim, J. E. Park and J. M. Nam, Nonnoble-Metal-Based Plasmonic Nanomaterials: Recent Advances and Future Perspectives. Advanced Materials **30**, 1704528 (2018)
160. V. A. Spata and E. A. Carter, Mechanistic Insights into Photocatalyzed Hydrogen Desorption from Palladium Surfaces Assisted by Localized Surface Plasmon Resonances. ACS Nano **12**, 3512–3522 (2018)
161. Y. Xin, K. Yu, L. Zhang, Y. Yang, H. Yuan, H. Li, L. Wang and J. Zeng, Copper-Based Plasmonic Catalysis: Recent Advances and Future Perspectives. Advanced Materials, 2008145 (2021)
162. K. Sytwu, M. Vadai and J. A. Dionne, Bimetallic nanostructures: combining plasmonic and catalytic metals for photocatalysis. Advances in Physics: X **4**, 1619480 (2019)
163. Y.-C. Pu, G. Wang, K.-D. Chang, Y. Ling, Y.-K. Lin, B. C. Fitzmorris, C.-M. Liu, X. Lu, Y. Tong and J. Z. Zhang, Au nanostructure-decorated TiO2 nanowires exhibiting photoactivity across entire UV-visible region for photoelectrochemical water splitting. Nano letters **13**, 3817–3823 (2013)

164. D. F. Swearer, H. Zhao, L. Zhou, C. Zhang, H. Robatjazi, J. M. P. Martirez, C. M. Krauter, S. Yazdi, M. J. McClain and E. Ringe, Heterometallic antenna− reactor complexes for photocatalysis. Proceedings of the National Academy of Sciences **113**, 8916–8920 (2016)
165. Y. Zhao, H. Pan, Y. Lou, X. Qiu, J. Zhu and C. Burda, Plasmonic Cu2− x S nanocrystals: optical and structural properties of copper-deficient copper (I) sulfides. Journal of the American Chemical Society **131**, 4253–4261 (2009)
166. X. Liu and M. T. Swihart, Heavily-doped colloidal semiconductor and metal oxide nanocrystals: an emerging new class of plasmonic nanomaterials. Chemical Society Reviews **43**, 3908–3920 (2014)
167. A. Agrawal, S. H. Cho, O. Zandi, S. Ghosh, R. W. Johns and D. J. Milliron, Localized surface plasmon resonance in semiconductor nanocrystals. Chemical reviews **118**, 3121–3207 (2018)

# Chapter 12
# Plasmonic Metal–Semiconductor Hybrids as Substrates for Photo-Induced Surface Raman Enhancement




**Łukasz Pięta, Adrian Warzybok, and Kamilla Malek**

**Abstract** This chapter provides background information on Photo-Induced Enhanced Raman Spectroscopy (PIERS) and the characteristics of the metal–semiconductor hybrids used in this technique. It is divided into three subsections. Section 12.1 describes the basics of the PIERS technique and proposed signal amplification mechanism. Section 12.2 contains a comprehensive overview of the metal–semiconductor hybrids employed in the PIERS technique, outlining the correlation between the substrate structure, signal enhancement, phenomena associated with charge migration at the interface and other related mechanisms. The final Sect. 12.3 summarizes PIERS applications, perspectives related to future developments, and limitations.

**Keywords** Raman spectroscopy · Photo-induced enhanced Raman spectroscopy · Metal nanoparticles · Semiconductors · Plasmonics · Charge transfer

## Abbreviations

| | |
|---|---|
| CB | Conduction band |
| CE | Chemical enhancement |
| CT | Charge transfer |
| HEI | Hot electron injection |
| EF | Enhancement factor |
| $E_F$ | Fermi energy |
| EM | Electromagnetic enhancement |
| LSPR | Localized surface plasmon resonance |
| MNPs | Metal nanoparticles |

Ł. Pięta (✉) · A. Warzybok · K. Malek
Department of Chemical Physics, Faculty of Chemistry, Jagiellonian University, Krakow, Poland
e-mail: l.pieta@uj.edu.pl

Ł. Pięta
Doctoral School of Exact and Natural Sciences, Jagiellonian University, Krakow, Poland

© The Author(s), under exclusive license to Springer Nature Singapore Pte Ltd. 2024

M. Procházka et al. (eds.), *Surface- and Tip-Enhanced Raman Scattering Spectroscopy*,
https://doi.org/10.1007/978-981-97-5818-0_12

| | |
|---|---|
| PIERS | Photo-Induced Enhanced Raman Spectroscopy |
| PIRET | Photo-Induced Resonant Energy Transfer |
| SERS | Surface Enhanced Raman Spectroscopy |
| SC | Semiconductor |
| $t_{rel}$ | Relaxation time |
| VB | Valence band |
| $V_O$ | Oxygen vacancy |
| $\Phi_B$ | Schottky barrier |

## 12.1 Photo-Induced Enhanced Raman Spectroscopy (PIERS)

### *12.1.1 PIERS Phenomenon—Introduction*

In the realm of nanotechnology, the strategic assembly of materials endowed with semiconducting, photosensitive, and plasmonic properties has unlocked unprecedented possibilities. A recent breakthrough in this domain is the emergence of **Photo-Induced Enhanced Raman Spectroscopy (PIERS)**, leveraging photo-activated semiconductor substrates adorned with metallic nanostructures. This novel technique surpasses Surface Enhanced Raman Spectroscopy (SERS) by providing additional chemical (CE) and electromagnetic (EM) enhancements to the Raman signal. While SERS currently dominates applications in medical diagnostics and environmental chemistry, the PIERS technique exhibits the potential to redefine sensitivity in analytical methodologies, boasting enhancements of at least an order of magnitude over its predecessor.

The genesis of photo-induced enhanced Raman spectroscopy dates back to 2016 when Parkin's group reported its inception [1]. Through the integration of plasmonic metal nanoparticles (MNPs) employed in SERS, with a UV light pre-irradiated photoactive semiconductor (SC), enhancement factors exceeding those of traditional SERS signals by an order of magnitude have been achieved. This augmentation is notable even in the case of analytes characterized by low Raman cross sections. To date, research has concentrated on the interaction of Ag or Au nanoparticles with semiconductors such as $TiO_2$, $WO_3$, ZnO [2], or transition metal dichalcogenides such as $WS_2$ [3] and metal niobates $LiNbO_3$ [4]. It is noteworthy that the PIERS effect has been also observed on $TiO_2$ even in the absence of metal nanoparticles [5]. PIERS enhancements consistently manifest magnitudes ranging from 2 to 10 times [2] greater than those observed in SERS, occasionally reaching remarkable enhancements up to 50 times [6], which underscores the substantial potential of PIERS in amplifying Raman signal.

Recent reports showcase the versatility of the PIERS technique, detecting compounds such as explosives (DNT, PETN), organic dyes (rhodamine 6G, malachite green), as well as biomolecules like thrombin and adenosine triphosphate (ATP) with a limit of detection of 0.1 nM [2]. The high sensitivity, even in substrates with non-optimized structures, underscores the analytical prowess of PIERS.

A typical PIERS measurement does not significantly differ from that conducted for solid substrates utilized in SERS techniques, except for the so-called pre-irradiation step. In that, the PIERS substrate, comprising nanoparticles and a semiconductor, is exposed to UV light for a specified duration. In most cases, the substrate is illuminated first, followed by the deposition of analyte molecules, which is referred to as substrate irradiation. The enhancement obtained in PIERS is typically quantified relative to the signal obtained without prior illumination of the substrate, i.e., in comparison to classical SERS measurements. It has been demonstrated that the photon energy of UV light should exceed the semiconductor's bandgap to induce the PIERS effect. The optimal pre-irradiation time depends on the structure and electronic properties of the substrate and may vary from a few minutes to several hours. However, in most reports, the maximum PIERS signal was obtained after 15–30 min of illumination [2].

The temporal characteristics of the PIERS phenomenon, particularly the duration of signal enhancement called relaxation time ($t_{rel}$), play a pivotal role in its analytical applications and is crucial for evaluating the reproducibility of analytical readouts. Upon termination of UV light irradiation, the recombination of electrons and holes initiates a relaxation process, resulting in a decay of PIERS signal intensity. The literature indicates that $t_{rel}$ for most tested substrates does not exceed 60 min [2], except for specific cases like Ag@$LiNbO_3$ [4], AuNPs co-deposited with porous $TiO_2$ [7] and AgNPs grown on a nanometer-thick $TiO_2$ film [8] for that it can last from a few hours to even several days.

It is also worth noting that the combination of semiconducting materials, particularly those with photocatalytic properties such as $TiO_2$, with noble metal nanoparticles provides numerous benefits. Beyond the analytical realm, these hybrid nanomaterials possess a remarkable self-cleaning capability when exposed to UV light [1, 9], thus facilitating the reusability of the substrate for SERS/PIERS measurements and concurrently reducing production expenses. Moreover, the presence of photocatalytic semiconductors facilitates the direct synthesis of MNPs through the reduction of metal ions under UV illumination of the $TiO_2$ film. This method proves to be relatively rapid, straightforward, and reproducible, representing a greener alternative to more intricate technological processes for nanoparticle fabrication.

However, due to the recent invention of this technique and its continuous development, the literature currently lacks detailed insights into the origins of PIERS enhancement and its lifetime, the optimal substrate structure, semiconducting layer thickness, and the correlation between plasmonic properties generated by metal nanostructures and optimal PIERS enhancement. Furthermore, systematic studies elucidating the relationship between UV light characteristics, PIERS enhancement levels, and decay times are conspicuously absent.

### 12.1.2 PIERS Enhancement and Relaxation Mechanism

The enhancement mechanisms of PIERS and its relaxation remain subjects of debate, with various models proposed based on specific systems under investigation.

For instance, Parkin's group [1, 10, 11] has emphasized that the pivotal contributor to the enhancement phenomenon is the generation of oxygen vacancies ($V_O$) within the metal–metal oxide semiconductor structure like $TiO_2$, ZnO and $WO_3$, facilitated by the interaction of UV light with adsorbed oxygen and water. This process initiates the creation of additional electron states beneath the conduction band (CB) of the semiconductor (Fig. 12.1). During Raman measurement, visible laser light prompts the transfer of electrons from these vacancies to CB states and, subsequently, to the metal nanoparticles. This injection induces a shift in the Fermi energy ($E_F$) of the nanoparticles, intensifying their electromagnetic field and augmenting the likelihood of charge transfer (CT) between the PIERS-active substrates and the molecules adsorbed onto their surfaces, and consequently enhancing the Raman scattering process. The elucidation of the PIERS phenomenon, grounded in the generation of oxygen vacancies, is prevalent in the scientific literature concerning this phenomenon in metal–metal oxide semiconductors. However, it is not exclusive and cannot be universally applied to all PIERS systems investigated so far. It is important to note that in the case of PIERS mechanisms relying on the $V_O$ generation, the relaxation time does not exceed one hour. During this period, the PIERS signal gradually declines until reaching a level comparable to the signal observed before the excitation of the substrate with UV light, ultimately attaining a signal like that of SERS. This is correlated with the lifetime of these oxygen vacancies in such materials which is no longer than one hour.

Alternative models have emerged, particularly in systems such as organic semiconductors—diphenylalanine peptide [12] and lithium niobate [4] for that the expulsion of oxygen atoms by UV photons proves challenging (Fig. 12.2). In these scenarios, PIERS is posited to result from charge separation and migration within the semiconductors facilitated by UV-pre-irradiation of the substrate. Exposure of the semiconductor to UV light with energy equal to or surpassing its intrinsic band gap results in the transfer of electrons from the valence to the conduction band, facilitating their subsequent migration to neighboring nanoparticles. As a result, the Raman signal of molecules adsorbed to MNPs is amplified, like in the model proposed by Parkin and co-workers.

Based on PIERS studies on hybrid Au/$WS_2$ nanosheets, Maalej et al. [3] postulated that this effect is related to charge transfer from AuNPs to $WS_2$ nanosheets, contrary to the previous models. At the pre-irradiation step, UVC radiation excites localized surface plasmon resonance (LSPR), generating hotspots that significantly contribute to signal enhancement. The excitation energy of LSPR is close to the Fermi energy of AuNPs, which facilitates charge transfer between the AuNPs and the semiconductor. As a result, this translates into an enhancement of the Raman signal of the molecule being in contact with the $WS_2$ surface.

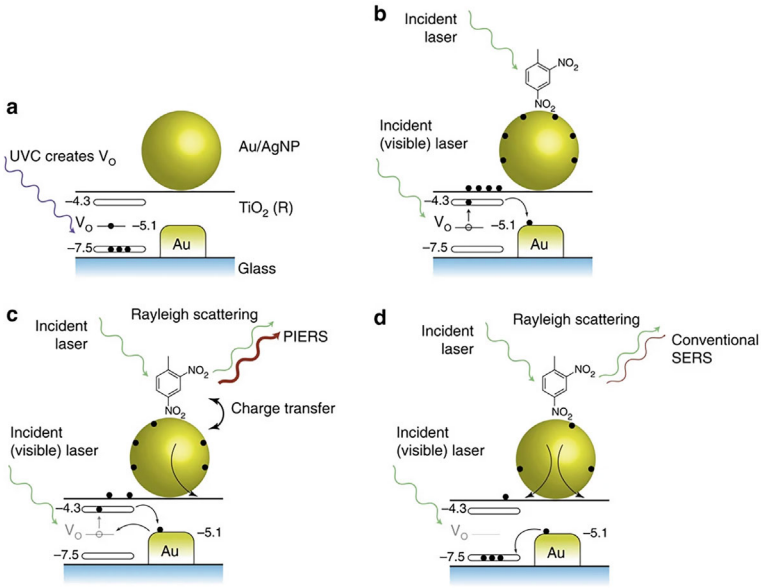



**Fig. 12.1** **a** Ultraviolet C light (UVC) pre-irradiation creates oxygen vacancies ($V_O$) below the $TiO_2$ CB. **b** The molecule (here dinitrotoluene) is deposited and irradiation with the Raman laser photoexcites $TiO_2$, leading to an increase in charge on the nanoparticles. **c** The charged nanoparticles lead to the PIERS enhancement. As the $V_O$ are replenished, upon exposure to air, fewer electrons can be photoexcited into the CB of $TiO_2$. **d** The PIERS effect gradually disappears as the $V_O$ states are completely replenished over time. Reproduced from Ref. [1]

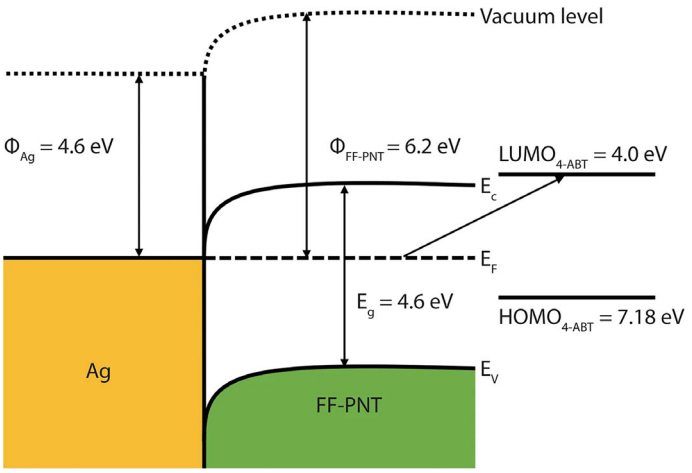



**Fig. 12.2** Proposed band structure of the Ag-FF-PNT (diphenylalanine peptide nanotubes) junction where Φ is the work function, $E_F$ is the Fermi energy, $E_c$ is the conduction band, and $E_v$ is the valance band. Reproduced from Ref. [12]

Recent research on PIERS directs their focus toward the conventional examination of oxygen vacancy generation and direct electron flow under UV light. Works of Lidgi-Guigui [7], Malek [8] and Aktas [6] groups have unveiled additional crucial mechanisms within metal–semiconductor systems for PIERS purposes. These mechanisms encompass the formation of the Schottky barrier at the metal–semiconductor interface, Photo-Induced Resonant Energy Transfer (PIRET), and Hot Electrons Injection (HEI) sometimes referred to as Photo-Induced Charge Separation (PICS).

The studies of Lidgi-Guigui indicated a different mechanism of PIERS enhancement depending on the method of depositing gold nanoparticles on the $TiO_2$ film [7]. For AuNPs drop-casted onto the semiconductor surface, the PIERS enhancement after UV pre-irradiation is based on the injection of charges from oxygen vacancy states in $TiO_2$ into AuNPs. In the case of co-deposition of Au and $TiO_2$, AuNPs are partially buried in $TiO_2$ and partially available for analyte molecules grafting which imposes another mechanism. The defects induced by UV irradiation play a significant role in modifying the width of the depletion zone on the $TiO_2$ surface and facilitating the back-transfer of charges to AuNPs based on the PIRET phenomenon. The excess of electrons on AuNPs is crucial for the enhancement of Raman scattered intensity, contributing to the overall effectiveness of the system. In the case of the substrates with co-deposited Au and $TiO_2$, the PIERS effect lasted up to eight days, in contrast to the drop-casting of MNPs on the SC surface.

Two other groups investigated the PIERS effect on titanium dioxide films with silver nanoparticles produced through the direct photo-reduction of silver ions on the semiconductor surface under UV light [6, 8]. In both cases, a significant PIERS enhancement (ca. 50-fold and 20, respectively) was observed and it lasted for at least several hours regardless of differences in the thickness of SC. The prolonged relaxation time was attributed to the presence of the Schottky barrier at the interface between Ag and $TiO_2$ (Fig. 12.3). This barrier effectively traps electrons in MNPs that are next injected into them from $TiO_2$ upon UV pre-irradiation. As a result, the increased electron density on the metal can remain stable for a long time, directly contributing to the extended lifetime of the PIERS effect. They additionally proposed that the reduction of electron density on MNPs over time is the HEI effect induced by the laser light during Raman measurements. Indeed, if the substrate is illuminated with a laser of a wavelength close to the LSPR of the metal, so-called hot electrons are generated. Their energy can be greater than the Schottky barrier energy. This results in a partial outflow of electrons from MNPs and thereby the reduction of the PIERS enhancement.

The study by Ye et al. [13] aimed to elucidate the chemical mechanism behind PIERS, leveraging a range of techniques including X-ray and time-resolved optical spectroscopies, electron microscopy, cyclic voltammetry, and density functional theory simulations to understand the atomic-scale mechanism behind PIERS. The research reveals that the enhancement mechanism involves an increase in the intrinsic polarizability of the adsorbed molecule upon charge transfer rather than the previously proposed charge transfer resonance Raman enhancement model (Fig. 12.4). The study also explores various hypotheses for the final step of the enhancement process, concluding that strong adsorption of the probe molecule to AgNPs increases

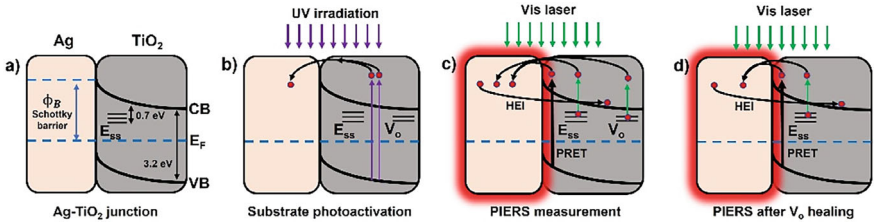



**Fig. 12.3** A schematic of the proposed mechanisms of PIERS. **a** Formation of a Schottky barrier at Ag–$TiO_2$ junction. **b** Photoactivation of hot electrons due to irradiation with UVA or UVC light and the simultaneous formation of oxygen vacancies. **c** Induction of the electron flow due to irradiation with laser Vis light during PIERS measurement, shortly after the photoactivation process. **d** Electron flow during PIERS measurement with laser Vis light after more than an hour after the photoactivation process. $E_{ss}$—the energy of electron trapping sites and surface states. Reproduced from Ref. [8]

its intrinsic Raman polarizability, further enhanced by photo-induced charge transfer from $TiO_2$ to Ag. A key element to induce PIERS effect is that the probe molecule should be capable of undergoing charge transfer and its Raman polarizability must be enhanced and not suppressed upon charge transfer. In addition, charge transfer from the metal nanoparticle to the probe molecule is possible when its reduction potential lies below the Fermi level of the metal.

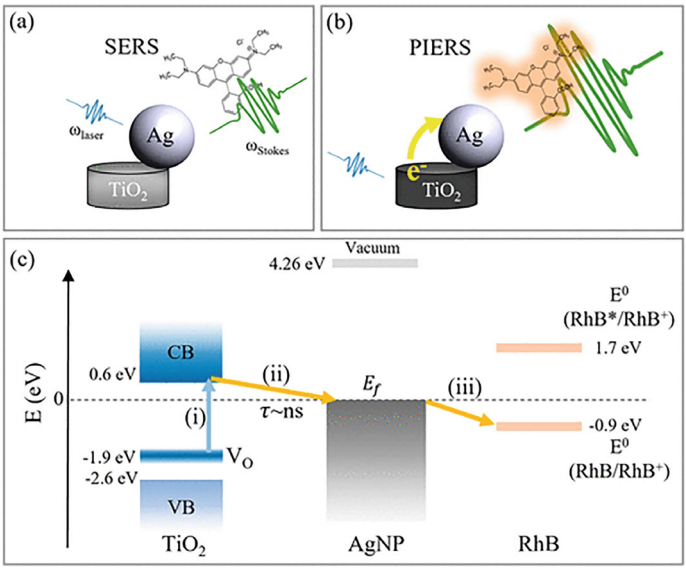



**Fig. 12.4** SERS versus PIERS. **a** Plasmonic field enhancement mechanism for SERS. **b** Charge transfer enhancement for PIERS. **c** PIERS mechanism: (i) excitation of electrons from defect states to the CB level, (ii) electron transfer from $TiO_2$ to AgNPs Fermi level with a ns decay time ($\tau$), and (iii) electromagnetic enhancement and charge transfer interaction of AgNPs with the rhodamine B molecule (RhB). Reproduced from Ref. [13]

Interestingly, the PIERS effect was recently achieved on defected noble-metal-free $TiO_{2-x}$ films [5]. Various post-treatment methods were employed to induce the formation of oxygen vacancies in the semiconductor structure. The post-treatment techniques encompassed UV-light irradiation analogous to UV pre-irradiation during PIERS experiments, vacuum annealing, and argon etching. In each case, Raman band enhancement was observed, compared to the non-treated $TiO_2$. The observed enhancement decayed over time and was closely correlated with the lifetime of oxygen vacancies; however, in no case, it persisted beyond 40 min. Raman band enhancement is here primarily attributed to the CE mechanism induced by oxygen vacancies. As mentioned above, the $V_O$ defects introduce band states below the conduction band of $TiO_{2-x}$, enabling viable charge-transfer pathways between the valence band, $V_O$ level, and LUMO of the adsorbed molecule (Fig. 12.5). This charge-transfer resonance enhances the Raman cross-section of the molecule, as certain Raman bands were enhanced selectively.

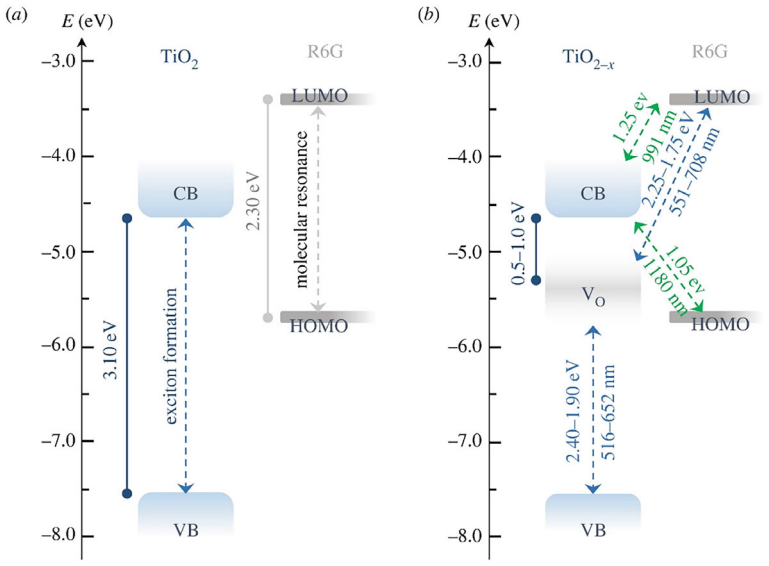



**Fig. 12.5** Proposed charge transfer pathways in defected $TiO_{2-x}$. **a** Energy level diagram showing the band structure of $TiO_2$ and the HOMO/LUMO of rhodamine 6G (R6G). **b** Oxygen-vacancy defects introduce band states at 0.5–1.0 eV below CB of $TiO_{2-x}$. Viable resonant CT pathways open between transient vacancy, VB, and LUMO levels. Reproduced from Ref. [5]

## 12.2 Overview of Plasmonic Metal-Dielectric Materials for PIERS Applications

### *12.2.1 Tested Substrates for PIERS Applications*

The selection of an appropriate substrate is paramount for PIERS in terms of the enhancement factor and its relaxation time. A wide range of substrates has been systematically elucidated for PIERS applications, with significant differences in EF and $t_{rel}$ parameters. Currently, investigations have predominantly focused on combinations of silver and gold nanoparticles with various semiconductors such as $TiO_2$, ZnO, and $WO_3$. Notably, metal oxide semiconductors are only a subset of the semiconductor types studied so far; combinations with $WS_2$, diphenylalanine peptide nanotubes (an organic semiconductor), $LiNbO_3$, and even insulators such as $SiO_2$ have been investigated. As mentioned above, studies are delving into the PIERS effect where semiconductors were pre-irradiated in the absence of nanoparticles. Table 12.1 summarizes selected scientific reports that tested substrates utilized for PIERS to date. The table compiles key information regarding the type of the metal and the semiconductor, a brief description of their morphology, the enhancement of the PIERS signal in comparison to SERS, and the duration of signal enhancement. Readers also find parameters of the UV pre-irradiation process such as the wavelength of the applied light and the irradiation time. It is important to note that in the showcased publications, this step was employed at various stages of the preparation of the substrate for PIERS measurements. In most cases, UV irradiation of the substrate occurred after depositing metal nanoparticles on the semiconductor, immediately before the analyte application and subsequent Raman measurement. This sequence is referred to as "substrate irradiation." For clarity in the table, if the column "UV pre-irradiation" includes only wavelength and irradiation time without additional information, researchers followed the described sequence. "Sample irradiation" refers to a method in which the substrate with adsorbed analyte molecules undergoes irradiation followed by Raman measurements. This methodology is not universal, and if the UV pre-irradiation process deviated from the previously described approach, additional information about this step is included in the table. The penultimate column also provides a concise description of the PIERS enhancement mechanism proposed by the study authors. It is important to note that these descriptions are very concise and contain only the key aspects of the proposed mechanism.

Numerous substrates for PIERS applications were tested, often featuring distinct structures and employing different methodologies of data collection as well as the sequences of UV irradiation and analyte deposition. The achieved amplification of PIERS compared to SERS ranges from several to even several dozen times. It strongly depends on the experimental parameters of the PIERS induction. Therefore, finding specific relationships between the substrate composition and morphology, the Raman probes and the PIERS enhancement and its mechanisms is not straightforward.

**Table 12.1** A list of selected PIERS substrates, with a brief description of their properties, employed methodology and proposed enhancement mechanisms

| Substrate | Substrate characterization | EF PIERS versus SERS | $t_{rel}$ | UV pre-irradiation wavelength and time | Proposed enhancement mechanism | References |
|---|---|---|---|---|---|---|
| Au/AgNPs on $TiO_2$ | Flat rutile $TiO_2$ (thickness: 500 nm)—APCVD[a]<br>Au/Ag nanospheres (*d*: 27 and 58 nm, respectively)—drop casting | 35 (AuNPs)<br>3 (AgNPs) | 30–60 min | 254 nm, 4 h | (1) UV-induced $V_O$ formation<br>(2) Laser-induced CT from $V_O$ to MNPs | [1] |
| AgNPs on lithium niobate (LN) | Waveguide structured LN (thickness: 130–300 nm)<br>AgNPs—photoreduction | 7 | 10 h | 254 nm, 150 min (substrate irradiation) | UV-induced CT from LN to AgNPs | [4] |
| | | 3 | 40 min | 254 nm, 27 min (sample irradiation) | | |
| Ag/AuNPs on diphenylalanine peptide nanotubes (PNTs) | Self-assembled PNTs (*d*: ca. 3.2 μm)<br>Ag/Au nanospheres (*d*: 40 nm)—mixing of the sol with PNTs | 7 (AgNPs) | 60 min | 254 nm, 45 min | UV-induced CT from FF-PNTs to MNPs | [12] |
| | | 4 (AuNPs) | – | | | |
| | | 0 (AgNPs) | – | 365 nm, 45 min | | |
| AuNPs on $TiO_2$, $WO_3$, ZnO | Thin films<br>Au nanospheres—drop-casting of functionalized AuNPs with 4MBA[b] | 3 ($TiO_2$) | ~ 30 min | 254 nm, 1 h | (1) UV-induced $V_O$ formation<br>(2) Vis laser-induced CT from $V_O$ states to AuNPs | [10] |
| | | 5 ($WO_3$) | | | | |
| | | 3 (ZnO) | | | | |
| AuNPs on $TiO_2$ and $WO_3$ | Thin semiconductor films, rutile $TiO_2$<br>Au nanospheres (*d*: 5, 50, 100, 150 nm)—drop casting | Max. 2 ($TiO_2$/50 nm AuNPs) | 30 min | 254 nm, 30 min | (1) UV-induced $V_O$ formation<br>(2) Vis laser-induced CT from $V_O$ states to AuNPs | [14] |
| | | Max. 9 ($WO_3$/50 nm AuNPs) | | | | |

(continued)

**Table 12.1** (continued)

| Substrate | Substrate characterization | EF PIERS versus SERS | $t_{rel}$ | UV pre-irradiation wavelength and time | Proposed enhancement mechanism | References |
|---|---|---|---|---|---|---|
| AgNPs on $TiO_2$ | $TiO_2$ heterostructure—rutile nanorods (*d*: ca. 250 nm) on an anatase film (thickness: 230 nm)<br>AgNPs—silver mirror reaction | 28 | 40 min | UPV mercury lamp | (1) UV-induced charge separation in the $TiO_2$ heterostructure<br>(2) CT from $TiO_2$ to AgNPs | [9] |
| AuNPs on $WS_2$ | $WS_2$ nanosheets (flake size: ca. 100 nm)<br>Ag nanospheres—mixing the $WS_2$ solution with the AuNP sol | 4 | – | 254 nm (sample irradiation) | CT from AuNPs to $WS_2$ | [3] |
| AgNPs on $TiO_2$ | Nanostructured $TiO_2$ grown on a Ti foil<br>AgNPs—magnetron sputtering; a sandwich complex with ssDNA@AuNPs | 3 | 60 min | 365 nm (sample irradiation) | (1) UV-induced $V_O$ formation<br>(2) Vis laser-induced CT from $V_O$ states to AgNPs | [15] |
| AuNPs embedded in $TiO_2$ | Porous $TiO_2$ co-deposited with AuNPs by laser ablation | 9 | 8 days | 254 nm, 3 h | (1) UV-induced $V_O$ formation<br>(2) PICS | [7] |
| AgNPs on $TiO_2$ | Nanocolumnar $TiO_2$ structure with rutile and anatase phases<br>AgNPs—photoreduction | 50 | 300 min | 365 nm, 8 min | (1) UV-induced $V_O$ formation<br>(2) Vis laser-induced CT from $V_O$ states to AgNPs | [6] |

(continued)

**Table 12.1** (continued)

| Substrate | Substrate characterization | EF PIERS versus SERS | $t_{rel}$ | UV pre-irradiation wavelength and time | Proposed enhancement mechanism | References |
|---|---|---|---|---|---|---|
| AuNPs on ZnO | ZnO nanorods ($d$: ~ 300 nm) AuNPs—DC sputtering | 30 | – | 365 nm, simultaneously with Raman measurement | UV-induced CT from ZnO to AuNPs | [16] |
| Au nanotriangles (NTs) with $SnO_2$NPs | Colloidal NTs (size: ~ 50 nm) coated with a layer of $SnO_2$ via condensation of sodium stannate | 22 | – | 365 nm, simultaneously with Raman measurement | Vis laser-induced CT from $V_O$ states to AuNPs | [17] |
| AgNPs on $TiO_2$ | Nanometer-thick (20 nm) $TiO_2$ anatase film AgNPs ($\lambda_{LSPR}$: 370 and 415 nm)—photoreduction | 12–17[c] | 4 h | 254 nm, 15 min | (1) UV-induced $V_O$ formation<br>(2) Vis laser-induced CT from $V_O$ states to AgNPs<br>(3) PIRET | [8] |
| | | 8–19[c] | | 254 nm, 30 min | | |
| | | 5–13[c] | | 365 nm, 15 min | | |
| | | 6–10[c] | | 365 nm, 30 min | | |

[a] Atmospheric pressure chemical vapor deposition
[b] 4-mercaptobenzoic acid
[c] EF depends on the LSPR positions

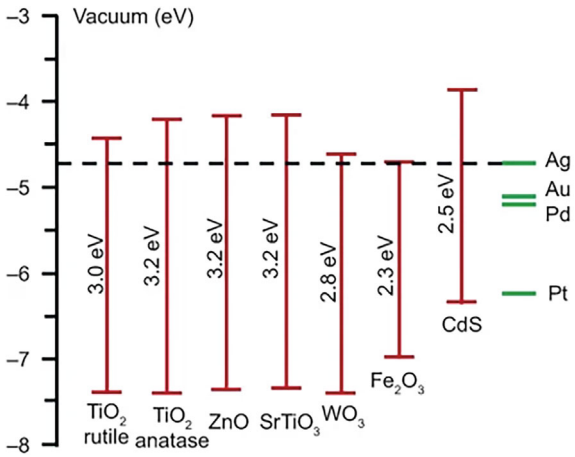



**Fig. 12.6** Energy band positions of some common semiconductor photocatalysts and plasmonic metals. The energies are given on a potential scale versus vacuum. Reproduced from Ref. [18]

### *12.2.2 Properties of the Substrates and PIERS Parameters*

The predominant semiconductor type employed in the PIERS substrates is metal oxides, although organic semiconductors, dichalcogenides, and even insulators have also been investigated. These materials differ in various aspects, including bandgap width and their ability and efficiency to generate oxygen vacancies. Furthermore, the mutual overlap of the conduction and valence bands concerning the Fermi energy of the metal also affects the direction of electron flow between these materials (Fig. 12.6).

Metals like Ag and Au exhibit lower Fermi energies than most semiconductors (e.g., $TiO_2$). In tight SC-metal heterojunctions, charges flow from the semiconductor to the metal. This is continued until equilibrium is attained between the Fermi energy of both entities, resulting in a constant $E_F$ value. In consequence, a potential barrier occurs and alters band structure at the semiconductor–metal interface (Fig. 12.7). This Schottky barrier ($\Phi_B$) is described by the following equation:

$$\Phi_B = \Phi_M - X_{SM} \tag{12.1}$$

where $X_{SM}$ is the electron affinity, and $\Phi_M$ is the working function of the metal.

This process causes an electron accumulation onto the metal and the formation of the depletion zone to preserve an electrically neutral surface of the semiconductor. The Schottky barrier acts as an efficient electron trap preventing electron–hole recombination and extending charge lifespan in the system. A high $\Phi_B$ value caused by large disparities between the metal work function and semiconductor allows for efficient photogenerated electron transfer blocking also electron flow back to the semiconductor. So the Schottky barrier at the metal–semiconductor interface plays an important role in retaining electrons in MNPs. The successful preservation of augmented electron density on the metal after UV irradiation enhances the PIERS signal. This

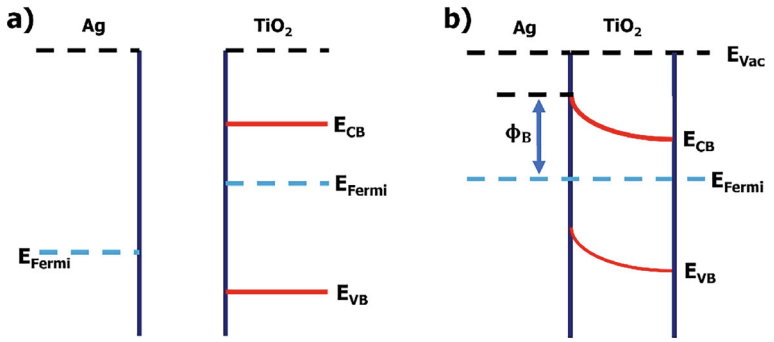



**Fig. 12.7** Formation of the Schottky barrier between $TiO_2$ and Ag **a** before contact and **b** after contact

phenomenon is attributed to the intensified electromagnetic field surrounding the nanoparticles and the amplified rate of CT events occurring between the MNPs and the analyte molecules. For this reason, it is important to select hybrid materials in that the CB level of the semiconductor is higher than the Fermi level of the plasmonic nanoparticles.

In addition, the Schottky barrier is formed only in the case of direct contact between the metal and the semiconductor, so a method of depositing nanoparticles onto SC is a key step. In over twenty PIERS studies published so far, drop-casting and magnetron sputtering of ready-made colloidal solutions of MNPs were employed and the PIERS effect was observed for up to 1 h. While the direct photoreduction of metal ions on the semiconductor surface under UV light or simultaneous co-deposition of SC and MNPs through laser ablation were utilized, the photo-induced Raman signal lasted for several hours or days [4, 6–8]. These methods of the MNP deposition yield close contact between substrate components facilitating and significantly enhancing the transport of excited electrons. Simply, the weak SC-MNP junctions do not prevent the absorption of chemical species like water, oxygen, surface –OH groups or stabilizers used in the MNP synthesis. This fact highlights that the lifetime of the PIERS effect is influenced not only by the intrinsic features of the substrate components but also by the result of their integration.

In addition to the relative position of the semiconductor bandgap and the Fermi level of the metal, the width of the bandgap and the selection of an appropriate wavelength of UV-light irradiation are important factors. First, efficient photoexcitation of the semiconductor must occur due to pre-irradiation, involving the excitation of electrons from the valence band to the conduction band. The generated free electrons can flow to the metal nanoparticles deposited on the semiconductor surface and subsequently to the analyte. Currently, it is not evident whether the PIERS effect is solely induced by the increased CT between the metal nanoparticles and the molecules, or if the molecules absorbed on the surface of the excited SC also generate the enhanced Raman signal. Both scenarios are possible, but due to the relatively short lifetime of excited electrons in semiconductors, this pathway of signal enhancement could be

difficult to register. In both cases, it is necessary to match the energy of the UV light used for the pre-irradiation to the bandgap energy of the semiconductor. This was demonstrated in studies on PIERS using silver nanoparticles deposited on $LiNbO_3$ [4] and diphenylalanine peptide nanotubes (PNTs) [12] for that bandgap energies were 3.78 and 4.6 eV, respectively, and UV light with wavelengths of 365 nm (~ 3.4 eV) and 254 nm (~ 4.9 eV) were employed. In both cases, the PIERS effect appeared only for the 254 nm pre-irradiation of photon energy exceeding the SC bandgap. This emphasizes that in such systems, effective excitation of the semiconductor during pre-irradiation leads to the occurrence of the PIERS effect.

Excitation of the semiconductor by UV light, leading to the generation of electron–hole pairs, also plays a crucial role in PIERS. This effect is necessary but not sufficient to achieve the Raman signal enhancement. Excited electrons within the semiconductor must reach the surface of the nanoparticle before recombining with holes. Commonly used crystalline forms of $TiO_2$ (rutile or anatase) are considered suitable semiconductors for PIERS purposes. However, studies [6, 9] indicated that hybrid materials composed of both forms exhibit higher Raman enhancement than the individual ones. Such interfacial junctions enable efficient spatial separation of electrons and holes, reducing their recombination rate. Rutile has a smaller bandgap value (3.0 eV) than anatase (3.2 eV), so its conduction band lies slightly lower than that of anatase. Therefore, upon UV light excitation of the hybrids, rutile effectively collects electrons from the conduction band of anatase, leading to efficient spatial charge separation. Consequently, a significantly increased electron density is formed on the surface of the rutile, contributing effectively to the enhancement of the PIERS signal in such systems.

As mentioned above, PIERS substrates with metal oxides ($TiO_2$, ZnO, and $WO_3$) amplify the Raman signal due to simultaneous excitation of the semiconductor and generation of oxygen vacancies (Table 12.1). The presence of $V_O$ results in the formation of additional energy levels within the oxide bandgap, increasing the number of CT processes. In $TiO_2$, $V_O$ energy levels are located approximately 0.7 eV below the conduction band. Electrons from the $V_O$ levels are excited by the Raman laser light to the CB level, and from that, they migrate to MNPs and ultimately to the molecules (Fig. 12.8). After switching off the UV light source causing additional the VB → CB excitation, the Vis laser light is an alternative source of increasing the electron density on the nanoparticles contributing to the Raman enhancement. The presence of MNPs on the semiconductor surface stabilizes and supports the $V_O$ generation, although the lifetime of such defects in metal oxides under oxygen conditions typically does not exceed one hour.

In the case of the substrate composed of the semiconductor only, the $V_O$ also allows for the PIERS enhancement because electrons trapped in the vacancies can be transferred directly to the molecules upon the laser excitation. In such systems, the optimal UV pre-irradiation time depends on the rate of oxygen vacancy generation and healing as well as the energy required for their formation. The excitation of the semiconductor is less relevant due to the very short lifetime of free charge carriers that are not trapped in defects. The current studies on the PIERS effect also emphasized the beneficial role of additional energy states within the semiconductor bandgap.

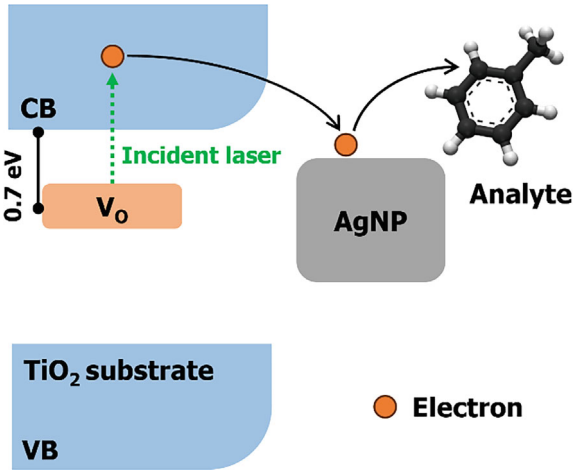



**Fig. 12.8** A schematic representation of the electrons excitation from $V_O$ to CB levels by Raman laser light. The excited electrons migrate to the metallic nanoparticles and later to the analyte molecules

For example, doping of such materials generates energy levels below the conduction band and their lifetime is longer than $V_O$. Furthermore, the facile tunability of semiconductor electronic properties and the ability to synthesize nanostructures with tailored architectures enable the generation of additional effects, such as Mie resonances, which further contribute to enhanced Raman signals [19, 20]. Perhaps this direction of the substrate designs will enable the development of the robust, long-lasting PIERS phenomenon.

It is also worth considering the properties of the plasmonic nanoparticles. The quantity of the metal deposited on the semiconductor constitutes another key factor that impacts PIERS. An increased number of MNPs on the SC surface does not necessarily correlate with a proportional augmentation of the Schottky barrier within the system. The effect of the metal loading lies in its capacity to enhance the number of charge-trapping sites while simultaneously diminishing the surface area of the semiconductor exposed to the pre-irradiation. This effect was investigated in [6], and this study showed that the optimal coverage of the $TiO_2$ surface by AgNPs is ca. 50%. In SERS, a high MNP coverage creating hot spots induces high electromagnetic enhancement. In PIERS, an excessive number of nanoparticles on the semiconductor limits the access of photons to the semiconductor surface and reduces the generation of free charge carriers.

Among possible CT processes, the transference of energy from the plasmon nanoparticle to an adjacent absorber, such as a semiconductor, is denoted as plasmon resonance energy transfer (PIRET). PIRET in the metal–semiconductor system is a near-field effect that significantly enhances the absorption of the semiconducting materials (Fig. 12.9a). The MNPs with large absorption cross-sections interact with light and efficiently confine the light energy in their vicinity. This concentrated energy is then transferred to the neighboring semiconductor, locally generating electron–hole pairs within the semiconductor material. PIRET improves the absorption ability of the semiconductor at energies below its optical band gap edge and occurs in the

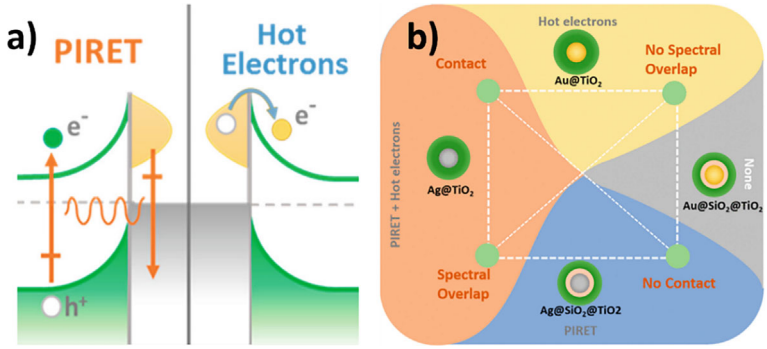



**Fig. 12.9** **a** After excitation of the plasmon by the pump laser, the plasmon can enhance carrier creation in the $TiO_2$ by hot electron injection or PIRET. **b** Variables that control the possible plasmonic enhancement mechanisms for extending photoconversion. Connecting the line between the properties of the given core@shell nanoparticle gives the corresponding enhancement mechanisms present. Reproduced from Ref. [21]

spectral overlap between the semiconductor and MNPs. It is observed even in the presence of an isolating layer between the SC and MNPs because the near field of the metal can penetrate the isolating layer. The rate at which a semiconductor absorbs optical energy is directly proportional to the intensity of the electric field. The impact of PIRET lies in its ability to amplify the electric field intensity within a confined and precisely defined area of the semiconductor, consequently augmenting the absorbed power in this specific region. This implicates a design of the PIERS substrates because the SC absorption band must align as closely as possible with the LSPR of MNPs. In such cases, the Raman laser light excites LSPR and stimulates electromagnetic enhancement, and simultaneously excites the semiconductor generating free charge carriers due to the PIRET effect. These carriers then flow to the metal nanoparticles and ultimately to the molecules contributing to the PIERS effect.

The Raman laser light also negatively affects the PIERS signal because of the decrease in the electron density on the MNPs due to Hot Electron Injection (HEI) (Fig. 12.9b). HEI is a phenomenon in which hot electrons, generated through non-radiative damping in light-absorbing nanoparticles, are transferred to the SC conduction band. Its efficiency depends on several factors such as the size of plasmonic MNPs, the energy of the Schottky barrier, and the electron-acceptor and electron-donor abilities of the semiconductor. MNPs smaller than 20 nm generate hot electrons with energies ($E_H$) in the range of $E_F < E_H < E_F \pm h\omega$ (where $\omega$ represents the incident photon energy), whereas the larger MNPs produce hot electrons with energies close to the Fermi energy. If the energy of these electrons surpasses the Schottky barrier energy, they migrate to the conduction band of the semiconductor. Conversely, electrons with energies below the Schottky barrier typically experience relaxation through electron–electron and electron–photon collisions, leading to the generation of heat.

Consequently, metal–semiconductor composites with larger Schottky barrier energies exhibit a less efficient HEI process. Nevertheless, possessing energies exceeding the Schottky barrier is not the sole condition for the injection of hot electrons into the conduction band. It is equally imperative for the hot electron to effectively reach the surface of the nanoparticle before undergoing subsequent relaxation processes. The type of MNPs is a crucial factor in the context of HEI efficiency. The hot electrons are generated through either intraband or interband transitions. A recent theoretical study revealed that interband transitions induced by visible light (from the d-band) lead to high-energy hot holes but relatively low-energy hot electrons (ca. $E_F$) [22]. In contrast, hot electrons generated by the intraband transitions possess energies up to $E_F + \hbar\omega$. The silver, for instance, exhibits an interband energy of ca. 3.7 eV. Hence, only intraband transitions are expected upon the Vis-light illumination. The gold has an interband energy of ca. 2.3 eV, potentially limiting HEI-related processes due to interband excitations induced by the violet, blue, and green light.

So far, no systematic studies related to the contributions of PIRET and HEI in PIERS have been conducted. Both phenomena occur very likely simultaneously, and there is also the probability of an equilibrium between the accumulation and outflow of electrons from the metal nanoparticles. These mechanisms are not only important for understanding of the PIERS as well as photocatalytic reactions in the metal–semiconductor hybrids. A study of Guan et al. [23] demonstrated that charge transfer at the interface between semiconductors and metals plays a crucial role in generating hot electrons from plasmonic nanostructures, paving the way for optimizing photocatalysts. Further research is required to explore these phenomena in detail.

## 12.3 Perspectives and Critical Comments

Photo-induced enhanced Raman spectroscopy expands the current techniques of enhanced spectroscopy since it improves the Raman scattering intensity by the use of a variety of new hybrid nanomaterials of multiple functionalities. So far, dielectrics have been widely investigated in terms of conventional SERS, but they show the weak ability of Raman enhancement compared to nanostructured noble metals. The current development of enhanced spectroscopies is mainly focused on the design and fabrication of nanomaterials that provide ultra-sensitive sensing of molecules in vast applications for environmental chemistry, clinical diagnostics, and other analytical purposes. Thus, one can expect improvements in these approaches by the use of the PIERS technique. The first proof-of-principles were already shown for the detection of the low- and high-Raman scatters and even the immunoSERS assays. However, one should consider the rationale of additional steps required to develop the PIERS analytical method.

The unique advantage of the PIERS phenomenon is its generation through charge transfer processes initiated in the non-metallic component of the substrate. If we consider that the hybrid nanomaterials are the target in photocatalysis, optical and

electronic nanotechnology, the PIERS technique is an excellent tool for sensing their features and functionalities, including the presence and stability of defects, the direction of charge migration in the material systems as well as plasmon-assisted catalytic reactions. Undoubtedly, extensive studies should be undertaken to give an insight into mechanisms of charge migration and their correlation with the observed PIERS enhancement and relaxation time. The multifaceted nature of the PIERS effect influenced by the substrate composition and morphology, and electromagnetic and chemical mechanisms, underscores the complexity of this spectroscopic technique. It is urgent to comprehend how the features of the nanostructured material, along with its interaction with light pre-irradiation and illumination by the Raman laser affect the overall enhancement mechanism. Understanding these distinct mechanisms will empower the design of PIERS substrates and open up opportunities for simple and in situ investigations of functional materials.

## References

1. S. Ben-Jaber, W. J. Peveler, R. Quesada-Cabrera, E. Cortés, C. Sotelo-Vazquez, N. Abdul-Karim, S. A. Maier, I. P. Parkin, Photo-induced enhanced Raman spectroscopy for universal ultra-trace detection of explosives, pollutants and biomolecules. Nat. Commun. **7**, 1 (2016)
2. J. Zhao, Z. Wang, J. Lan, I. Khan, X. Ye, J. Wan, Y. Fei, S. Huang, S. Li, J. Kang, Recent advances and perspectives in photo-induced enhanced Raman spectroscopy. Nanoscale **13**, 8707 (2021)
3. K. Abid, N. H. Belkhir, S. B. Jaber, R. Zribi, M. G. Donato, G. Di Marco, P. G. Gucciardi, G. Neri, R. Maâlej, Photoinduced Enhanced Raman Spectroscopy with Hybrid Au@$WS_2$ Nanosheets. J. Phys. Chem. C **124**, 20350 (2020)
4. R. M. Al-Shammari, M. A. Baghban, N. Al-attar, A. Gowen, K. Gallo, J. H. Rice, B. J. Rodriguez, Photoinduced Enhanced Raman from Lithium Niobate on Insulator Template. ACS Appl. Mater. Interfaces **10**, 30871 (2018)
5. S. Ben-Jaber, D. Glass, T. Brick, S. A. Maier, I. P. Parkin, E. Cortés, W. J. Peveler, R. Quesada-Cabrera, Photo-induced enhanced Raman spectroscopy as a probe for photocatalytic surfaces. Philos. Trans. R. Soc. Math. Phys. Eng. Sci. **381**, 20220343 (2023)
6. J. Shondo, S. Veziroglu, T. Tjardts, T. B. Sarwar, Y. K. Mishra, F. Faupel, O. C. Aktas, Nanoscale Synergetic Effects on Ag–$TiO_2$ Hybrid Substrate for Photoinduced Enhanced Raman Spectroscopy (PIERS) with Ultra-Sensitivity and Reusability. Small **18**, 2203861 (2022)
7. A. Brognara, B. R. Bricchi, L. William, O. Brinza, M. Konstantakopoulou, A. L. Bassi, M. Ghidelli, N. Lidgi-Guigui, New Mechanism for Long Photo-Induced Enhanced Raman Spectroscopy in Au Nanoparticles Embedded in $TiO_2$. Small **18**, 2201088 (2022)
8. Ł. Pięta, A. Kisielewska, I. Piwoński, K. Malek, Modulation of photo-induced Raman enhancement in Ag nanoparticles deposited on nanometer-thick $TiO_2$ films. An interplay between plasmonic properties and irradiation energy. Spectrochim. Acta. A. Mol. Biomol. Spectrosc. **305**, 123537 (2024)
9. M. Zhang, H. Sun, X. Chen, J. Yang, L. Shi, T. Chen, Z. Bao, J. Liu, Y. Wu, Highly Efficient Photoinduced Enhanced Raman Spectroscopy (PIERS) from Plasmonic Nanoparticles Decorated 3D Semiconductor Arrays for Ultrasensitive, Portable, and Recyclable Detection of Organic Pollutants. ACS Sens. **4**, 1670 (2019)

10. D. Glass, E. Cortés, S. Ben-Jaber, T. Brick, W. J. Peveler, C. S. Blackman, C. R. Howle, R. Quesada-Cabrera, I. P. Parkin, S. A. Maier, Dynamics of Photo-Induced Surface Oxygen Vacancies in Metal-Oxide Semiconductors Studied Under Ambient Conditions. Adv. Sci. **6**, (2019)
11. D. Glass, R. Quesada-Cabrera, S. Bardey, P. Promdet, R. Sapienza, V. Keller, S. A. Maier, V. Caps, I. P. Parkin, E. Cortés, Probing the Role of Atomic Defects in Photocatalytic Systems through Photoinduced Enhanced Raman Scattering. ACS Energy Lett. **6**, 4273 (2021)
12. S. Almohammed, F. Zhang, B. J. Rodriguez, J. H. Rice, Photo-induced surface-enhanced Raman spectroscopy from a diphenylalanine peptide nanotube-metal nanoparticle template. Sci. Rep. **8**, 41 (2018)
13. J. Ye, R. Arul, M. K. Nieuwoudt, J. Dong, T. Zhang, L. Dai, N. C. Greenham, A. Rao, R. L. Z. Hoye, W. Gao, M. C. Simpson, Understanding the Chemical Mechanism behind Photoinduced Enhanced Raman Spectroscopy. J. Phys. Chem. Lett. **14**, 4607 (2023)
14. D. Glass, E. Cortés, S. Ben-Jaber, T. Brick, R. Quesada-Cabrera, W. J. Peveler, Y. Zhu, C. S. Blackman, C. R. Howle, I. P. Parkin, S. A. Maier, Photo-induced enhanced Raman spectroscopy (PIERS): sensing atomic-defects, explosives and biomolecules, in *Chem. Biol. Radiol. Nucl. Explos. CBRNE Sens. XX*, edited by J. A. Guicheteau and C. R. Howle (SPIE, Baltimore, United States, 2019), p. 13
15. T. Man, W. Lai, M. Xiao, X. Wang, A. R. Chandrasekaran, H. Pei, L. Li, A versatile biomolecular detection platform based on photo-induced enhanced Raman spectroscopy. Biosens. Bioelectron. **147**, 111742 (2020)
16. V. T. Tran, T. H. Tran, M. P. Le, N. H. Pham, V. T. Nguyen, D. B. Do, X. T. Nguyen, B. N. Q. Trinh, T. T. V. Nguyen, V. T. Pham, M. Q. Luu, A. B. Ngac, Highly efficient photo-induced surface enhanced Raman spectroscopy from ZnO/Au nanorods. Opt. Mater. **134**, 113069 (2022)
17. G. Davison, Y. Yin, T. Jones, I. P. Parkin, W. J. Peveler, T.-C. Lee, Multi-mode enhanced Raman scattering spectroscopy using aggregation-free hybrid metal/metal-oxide nanoparticles with intrinsic oxygen vacancies. J. Mater. Chem. C **11**, 3334 (2023)
18. X.-C. Ma, Y. Dai, L. Yu, B.-B. Huang, Energy transfer in plasmonic photocatalytic composites. Light Sci. Appl. **5**, e16017 (2016)
19. W. Ji, L. Li, W. Song, X. Wang, B. Zhao, Y. Ozaki, Enhanced Raman Scattering by ZnO Superstructures: Synergistic Effect of Charge Transfer and Mie Resonances. Angew. Chem. Int. Ed. **58**, 14452 (2019)
20. W. Ji, L. Li, J. Guan, M. Mu, W. Song, L. Sun, B. Zhao, Y. Ozaki, Hollow Multi-Shelled $V_2O_5$ Microstructures Integrating Multiple Synergistic Resonances for Enhanced Semiconductor SERS. Adv. Opt. Mater. **9**, 2101866 (2021)
21. S. K. Cushing, J. Li, J. Bright, B. T. Yost, P. Zheng, A. D. Bristow, N. Wu, Controlling Plasmon-Induced Resonance Energy Transfer and Hot Electron Injection Processes in Metal@$TiO_2$ Core–Shell Nanoparticles. J. Phys. Chem. C **119**, 16239 (2015)
22. M. Valenti, M. P. Jonsson, G. Biskos, A. Schmidt-Ott, W. A. Smith, Plasmonic nanoparticle-semiconductor composites for efficient solar water splitting. J. Mater. Chem. A **4**, 17891 (2016)
23. J. Guan, S. Wu, L. Li, X. Wang, W. Ji, Y. Ozaki, New Insights of Charge Transfer at Metal/Semiconductor Interfaces for Hot-Electron Generation Studied by Surface-Enhanced Raman Spectroscopy. J. Phys. Chem. Lett. **13**, 3571 (2022)

# Part III
# Applications of SERS to Biomedical Sciences

# Chapter 13
# SERS for Precision Medicine: A Promising Approach




**Yibao Huang, Chenxiao Zhao, Linlu Zhao, and Ziyi Cheng**

**Abstract** In the field of precision medicine, the integration of Surface-Enhanced Raman Scattering (SERS) technology is a crucial breakthrough, particularly in the early diagnosis and treatment of complex diseases. This chapter explores the combination of SERS with nanotechnology, emphasizing its role in enhancing diagnostic accuracy and treatment efficacy. We focus on the design and optimization of nanomaterials and SERS substrates to improve detection sensitivity and specificity. Delving into the principles of SERS in biomedicine, challenges in standardization and reproducibility are discussed, along with the synthesis and stability of nanostructures essential for effective application. The use of SERS in various biomedical analysis applications, including biomarker detection, pathogen identification, and advanced imaging techniques, is highlighted. The chapter underscores the enrichment of fields like phototherapy and targeted drug delivery guided by SERS, showcasing its transformative impact on disease diagnosis and treatment in precision medicine.

**Keywords** SERS · Precision medicine · Diagnostic accuracy · Therapeutic efficacy · Biomarker detection · Pathogen identification · Biomedical imaging

## 13.1 Introduction

Biomedical science, an interdisciplinary domain, is dedicated to tackling the intricate issues surrounding human health and diseases [1]. This field synthesizes knowledge from biology, medicine, and engineering, striving to develop effective strategies for prevention, diagnosis, and treatment. Over recent decades, advancements in biomedical science have significantly enhanced the quality of life and life expectancy. Yet, it confronts unprecedented challenges due to global population growth, aging societies, and the emergence of novel diseases. Against this backdrop, the prevention and treatment of diseases become the focal points in biomedical research. Precise and timely

Y. Huang · C. Zhao · L. Zhao · Z. Cheng (✉)
Key Laboratory of Hainan Trauma and Disaster Rescue, The First Affiliated Hospital of Hainan Medical University, Hainan Medical University, Haikou 571199, China
e-mail: chengziyi@hainmc.edu.cn

© The Author(s), under exclusive license to Springer Nature Singapore Pte Ltd. 2024

M. Procházka et al. (eds.), *Surface- and Tip-Enhanced Raman Scattering Spectroscopy*,
https://doi.org/10.1007/978-981-97-5818-0_13

diagnosis is particularly crucial for intractable diseases such as cancer, neurodegenerative disorders, and autoimmune diseases. This underscores why genetic medicine has emerged as a pivotal research avenue, investigating genetic factors to unravel the etiology and progression of diseases. However, translating these research findings into clinical applications remains fraught with challenges. Concurrently, the unequal distribution of global medical resources leads to significant health disparities, rendering the realization of health equity through technological advancements a matter of great importance.

In response to these multifaceted challenges, the field of biomedical science is continually innovating and developing new technologies, among which Surface-Enhanced Raman Scattering (SERS) and the application of nanomaterials have shown immense potential [2]. SERS is an analytical technique that dramatically amplifies Raman signals by exploiting the properties of nanomaterials. It boasts exceptional sensitivity and resolution, enabling detection at the single-molecule level. SERS operates by measuring Raman scattering induced by molecular vibrational modes, providing intricate details about molecular structure and environment. The mechanisms of SERS are generally categorized into two types: the electromagnetic mechanism, primarily reliant on noble metal nanomaterials such as gold (Au) and silver (Ag). These materials can generate powerful Local Surface Plasmon Resonances (LSPR), significantly enhancing Raman signals. The chemical mechanism, on the other hand, often relates to charge transfer processes and may involve various materials, including metallic and non-metallic nanomaterials, as well as their surface modifications. For instance, introducing specific functional groups on the surface of nanomaterials can facilitate chemical interactions with target molecules, thereby augmenting the Raman signal. Additionally, the surface of nanomaterials can be functionalized in multiple ways to achieve specific biomolecular recognition and signal transduction.

In the realm of biomedical science, SERS technology, by providing rapid, sensitive, and precise detection methods, plays a crucial role in the early diagnosis and treatment of diseases. It enables the identification and quantification of specific molecules within biological samples, including pathogens and biomarkers, thus aiding physicians in making accurate diagnoses and formulating personalized treatment plans. Furthermore, in conjunction with nanomaterials, SERS technology can also be applied in drug delivery and therapeutic monitoring, offering patients safer and more effective treatment options. In the diagnosis and treatment of oncology, infectious diseases, and genetic disorders, SERS technology has demonstrated tremendous potential, heralding transformative possibilities in the field of biomedical science [3].

This chapter delves deeply into various strategies to overcome these limitations and challenges, along with existing solutions and progress. Special emphasis will be placed on the synthesis and modification of nanomaterials, the design and optimization of SERS substrates, as well as the latest advancements and future directions of SERS technology in biomedical applications. Concurrently, the exploration

will extend to how multidisciplinary collaboration can accelerate the adoption and widespread application of SERS technology and nanomaterials in biomedical science [4].

## 13.2 Principles of SERS Technology Applications in Biomedicine

SERS technology and nanomaterials have demonstrated remarkable potential and widespread impact in the biomedical field. These advanced technologies provide not only new and effective tools for biomedical research and practical applications but also guide future scientific and medical explorations. To maximize their potential, this section focuses on further optimizing SERS technology in terms of quantitative analysis, biocompatibility of nanomaterials, and detection sensitivity. Additionally, it explores cost reduction and expansion of application scope through standardization and large-scale production [5].

### *13.2.1 Accuracy in Quantitative Analysis*

SERS technology faces significant challenges in quantitative analysis, primarily because SERS signals often originate from tiny "hotspot" regions with extremely high local electric fields. This localized nature makes SERS performance unpredictable and may lead to inconsistent results among different research groups using similar substrates or colloids. To improve accuracy in quantitative analysis, internal standard (IS) labels are typically introduced. However, relying solely on IS labels is insufficient. Therefore, in addition to calibration procedures, validation steps, including recovery rate and predicted root-mean-square error (RMSE), are strongly recommended to ensure SERS technology accurately predicts not only calibrated datasets but also other unknown samples. This comprehensive approach ensures accurate and reliable results in practical applications [6].

### *13.2.2 Detection Sensitivity*

The inherent sensitivity limitations of Raman spectroscopy in biomedical applications present a challenge. Factors such as the distribution and stability of hotspots, quality, and consistency of nanomaterials, and potential hotspot saturation effects can all impact the sensitivity and reliability of SERS technology. Additionally, interactions between nanomaterials and biomolecules in complex biological systems or detection environments, along with sensitivity to biological molecules amidst

complex matrices, are influential factors. Optical absorption and scattering properties of biological tissues and autofluorescence can obscure SERS signals, while a lack of selectivity may further affect sensitivity and accuracy. These factors need to be adequately considered in practical applications [7].

### *13.2.3 Standardization and Reproducibility*

Standardization of SERS technology in actual clinical applications is a key step but can be relatively lengthy. Like other biomedical testing methods, strict protocols and quality control standards are needed to ensure accuracy, reliability, and repeatability of tests. This includes standardization of SERS substrate preparation, choice of labeling molecules, and data processing and interpretation. Achieving standardization of detection methods, including the establishment of internal and external quality control procedures, and conducting inter-laboratory comparison studies, is key to ensuring consistency of measurements across different laboratories and over time. Ongoing standardization activities and quality monitoring, along with the establishment and acceptance of international and national standards, are also crucial for the widespread clinical application of SERS technology. The standardization process requires substantial time and resources, including multicenter clinical trials, development of standards and quality control procedures, and integration with existing clinical diagnostic methods and standardization procedures, to ensure effective clinical implementation of SERS technology and lay the foundation for its widespread application in the fields of biomedicine and clinical diagnostics [8].

### *13.2.4 Synthesis and Stability of Nanostructures*

Precise control over the size, shape, and surface chemistry of nanomaterials is crucial for effective SERS applications. The synthesis process can affect the final properties of nanomaterials, and their size and shape, especially in liquid or biological environments, may influence their behavior. Larger or irregularly shaped nanomaterials may be more prone to aggregation or degradation, potentially hindering the practical application of SERS technology in biomedicine. The characteristics of nanomaterials are influenced by factors such as chemical stability, surface chemical properties, synthesis process, size and shape, environmental conditions, and surface modifications. Surface chemical properties are particularly important for SERS applications. Environmental conditions like temperature, pH, and ionic strength can affect nanomaterials. Surface modifications, such as coating with protective layers or altering surface functional groups, can improve the characteristics of nanomaterials, reducing their reactivity with the environment [9].

### *13.2.5 Biocompatibility and Toxicity*

The biocompatibility of nanomaterials is crucial for biomedical applications. Different nanomaterials behave differently in biological systems and may pose certain toxicity risks, limiting their in vivo applications or necessitating additional steps to modify or coat the nanomaterials to ensure safety. For instance, common nanomaterials used in SERS technology, such as silver nanoparticles (AgNPs), gold nanoparticles (AuNPs), and carbon-based SERS probes, may have varying toxicity and biocompatibility depending on factors like size, shape, concentration, surface chemistry, and exposure conditions [10].

## 13.3 Applications of SERS in Biomedical Analysis

### *13.3.1 Detection of Biomarkers*

Biomarkers play a pivotal role in modern medical research and clinical practice, crucial for disease prediction, monitoring, and treatment. These measurable indicators reveal the health status or presence of disease and can be molecular, genetic, protein-based, cellular changes, or physiological or behavioral variations. Advancements in biotechnology have expanded the types and applications of biomarkers, including prognostic, safety, monitoring, and pharmacodynamic/response biomarkers. A shared understanding of their definition and application is vital in patient care, clinical research, and therapeutic development. They are significant in predicting toxicology and system pharmacology and indispensable in monitoring treatment effects and direct patient outcomes. With technological advancements and deeper understanding, significant progress in disease management and personalized medicine is anticipated [11].

In modern medical diagnostics, high-precision and accurate biosensor technologies are crucial. These technologies, including mass spectrometry (MS), nuclear magnetic resonance (NMR), high-performance liquid chromatography (HPLC), immunoassay techniques (such as ELISA), flow cytometry, fluorescence microscopy, and chip-based microarray technologies, typically rely on advanced laboratory equipment and complex analytical instruments [12]. They play a key role in hospital laboratories and research labs for precise identification and quantification of molecules in biological samples, analysis of protein and other biomacromolecules' structure, monitoring drug concentrations, and detecting and quantifying biomarkers. Their combined application is vital in early disease diagnosis, treatment monitoring, new drug development, and in driving personalized and precision medicine. These high-precision technologies are integral to ensuring the accuracy and reliability of biomarker detection, indispensable in modern medical research and clinical diagnostics. With technological progress, these techniques are continuously optimized,

providing more in-depth and comprehensive analysis for medical diagnostics. Meanwhile, low-cost, real-time, on-site sensing devices (such as POCT) are emerging, aimed at providing rapid, portable detection methods, enabling effective biomarker detection in non-laboratory environments. These devices include paper-based diagnostic strips, portable optical devices (such as fluorescence detectors and Raman spectrometers), microfluidic chips, ion mobility spectrometry (IMS), and portable mass spectrometers. Designed for simplicity and ease of operation, they are suitable for rapid diagnostics and field testing, such as pregnancy tests, viral infection detection, blood glucose monitoring, and environmental monitoring. While they may not match the performance of laboratory-grade devices, they show great potential for rapid on-site detection of specific compounds, especially in applications requiring rapid response and portability [13].

The detection and analysis of biomarkers play a crucial role in disease diagnosis, monitoring, and prognostic assessment. These markers, including diagnostic, monitoring, and prognostic markers, play key roles in early disease identification, tracking the course of treatment, and long-term disease management. In this field, optical detection technologies, particularly Raman spectroscopy and SERS, are especially important due to their ability to provide detailed information on molecular vibrations. SERS technology, by using nanostructures to enhance Raman scattering signals, significantly improves detection sensitivity, enabling single-molecule detection. This technology's high sensitivity and rapid response characteristics show tremendous application potential in rapid diagnosis, pathogen detection, and drug monitoring. The use of SERS in biomedicine is increasingly widespread, especially in the detection of diagnostic markers, disease monitoring, and prognostic assessment, providing new perspectives and tools for early disease diagnosis, personalized treatment planning, and disease management.

#### 13.3.1.1 Diagnostic Biomarkers

Diagnostic biomarkers play a crucial role in modern medicine, serving as biomolecules used for diagnosing diseases or monitoring changes in health status [14]. Typically found in bodily fluids, these biomarkers, including proteins, nucleic acids, or other small molecules, undergo changes such as variations in concentration or molecular structure during disease onset. For instance, certain proteins may exhibit abnormal expression in cancer, while specific nucleic acid sequences could be linked to genetic disorders. Monitoring these biomarkers allows physicians to identify and diagnose diseases at early stages, facilitating timely intervention and treatment. SERS technology, with its high sensitivity, can detect biomarkers at extremely low concentrations, pivotal for early disease diagnosis. Compared to other biometric detection techniques, SERS offers faster detection speeds and requires smaller sample volumes, providing significant advantages in clinical applications. Therefore, SERS plays an important role in enhancing the accuracy and efficiency of disease diagnostics, especially in early cancer detection, infectious disease diagnosis, and genetic disorder screening [15].

Regarding the detection of diagnostic biomarkers, researchers have developed an immunosorbent assay based on SERS, specifically for assessing the free-to-total Prostate-Specific Antigen (PSA) ratio (f/t PSA ratio) [16] (Fig. 13.1a). This ratio is crucial in enhancing the diagnostic performance for prostate cancer. The technique employs magnetic beads and SERS nanotags, enabling simultaneous detection of two PSA markers: free PSA (f-PSA) and complexed PSA (c-PSA), with a particular focus on the clinical gray zone where total PSA (t-PSA) levels range between 4.0 and 10.0 ng/mL. For concurrent detection of f-PSA and c-PSA, researchers prepared two distinct types of SERS nanotags, each targeting f-PSA and c-PSA, subsequently forming magnetic sandwich immunocomplexes. The study's objective was to assess the feasibility of this analytical technique as a clinical tool for prostate cancer diagnosis. SERS-based analysis was compared with electrochemiluminescence (ECL) analysis, focusing on 13 clinical samples in the diagnostic gray zone of t-PSA levels. The detection limits (LOD) were 0.012 ng/mL for f-PSA and 0.15 ng/mL for c-PSA. Moreover, each analysis required a minimal volume of clinical serum (less than 10 μL) and a relatively short duration (less than 1 h). The SERS-based analysis indicated that the f/t PSA ratio measured by the simultaneous detection method provided superior precision, as evidenced by a considerably narrower distribution of standard deviations compared to parallel detection methods. Thus, this SERS-based analysis for dual PSA marker detection holds potent potential as an innovative tool for accurate diagnosis of prostate cancer. Additionally, Gao et al. developed a novel SERS technique for a no-wash magnetic immunoassay of PSA (Fig. 13.1b) [17], utilizing a droplet-based SERS sensor to detect PSA by separating free and bound SERS tags. This method's advantage lies in its ability to rapidly and sensitively detect PSA cancer biomarkers in serum without any washing steps, significantly simplifying the detection process. The SERS signal's measurement frequency was 174 droplets per minute for PSA quantitative assessment. The LOD of this SERS-based droplet sensor was estimated to be below 0.1 ng/mL, far lower than the clinical diagnostic threshold for prostate cancer. This discovery offers an efficient, precise new tool for early prostate cancer diagnosis, showcasing the vast potential of SERS technology in biomedical fields [18].

#### 13.3.1.2 Monitoring Biomarkers

Monitoring biomarkers play a crucial role in modern medicine, with applications ranging from disease diagnosis to treatment evaluation, infectious disease detection, and drug monitoring. These biomarkers, such as small molecular metabolites in blood, specific proteins, hormone levels, cell counts, surface characteristics, and viral or bacterial particles themselves, are key biological molecules reflecting disease activity, treatment effectiveness, or pathogen presence. They provide continuous information on disease states and treatment responses, crucial for physicians to timely adjust treatment plans. However, whether monitoring specific tumor markers during chemotherapy or detecting trace viral particles in infectious monitoring, traditional

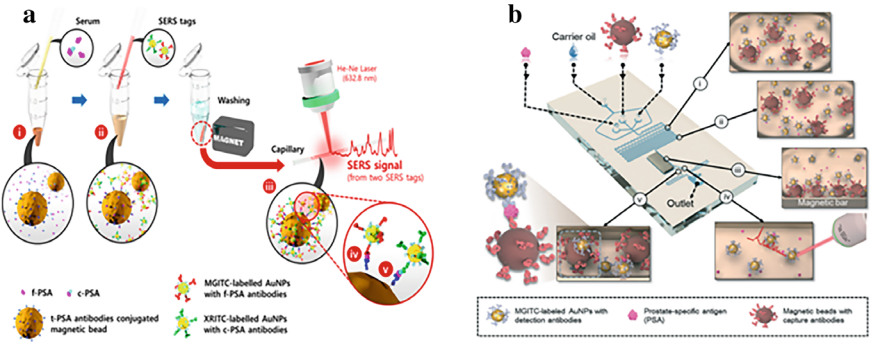



**Fig. 13.1** **a** Sequential SERS-based assay process for the simultaneous detection of f-PSA and c-PSA. Adapted from Ref. [16] with permission from the American Chemical Society. **b** Schematic illustration of the SERS-based microdroplet sensor for wash-free magnetic immunoassay. Adapted from Ref. [17] with permission from the Royal Society of Chemistry

detection methods often face limitations in sensitivity and specificity. SERS technology, with its high sensitivity and specificity, stands out, providing accuracy and timeliness in disease monitoring. Moreover, SERS platforms integrated with machine learning further enhance the detection capabilities for complex biomarkers, offering new tools for drug efficacy assessment and personalized medicine [19].

Recently, Yang et al. (Fig. 13.2) [20] developed a novel nanostructure capable of accurately capturing SARS-CoV-2 and detecting single viruses using SERS technology. The team utilized human ACE2 protein-functionalized gold nanostructures as "virus traps" to enhance the capture efficiency of SARS-CoV-2. The crux lies in the specific binding of ACE2 protein to the viral spike protein, effectively capturing the virus. Concurrently, the captured virus is detected using SERS, offering high sensitivity and specificity. The study also noted that these novel nanostructures could detect simulated contaminated water samples with SARS-CoV-2 virus down to a detection limit of 80 virus copies/mL in complex environments, with a detection time as short as 5 min. This finding is significant for real-time monitoring and early warning of coronaviruses. Additionally, this method can establish recognition standards for future unknown coronaviruses, enabling highly sensitive and rapid detection of novel viruses.

In another study [21], a research team focused on developing a fabric-based Electrochemical Surface-Enhanced Raman Spectroscopy (EC-SERS) sensor for clinical diagnostics. The core of this work involved creating a conductive plasmonic electrochemical sensor by blending silver nanoparticles and conductive ink-modified cotton fabrics. The team initially used p-aminothiophenol (pATP) as a probe molecule to assess the fabric-based electrode's performance in EC-SERS measurements. They further explored its capability to detect commonly used antibiotic levofloxacin under conditions of 0.1 M NaF and synthetic urine as supporting electrolytes. The study found that this fabric-based electrode provided excellent EC-SERS signals comparable to commercial screen-printed electrodes, enabling rapid detection of clinically

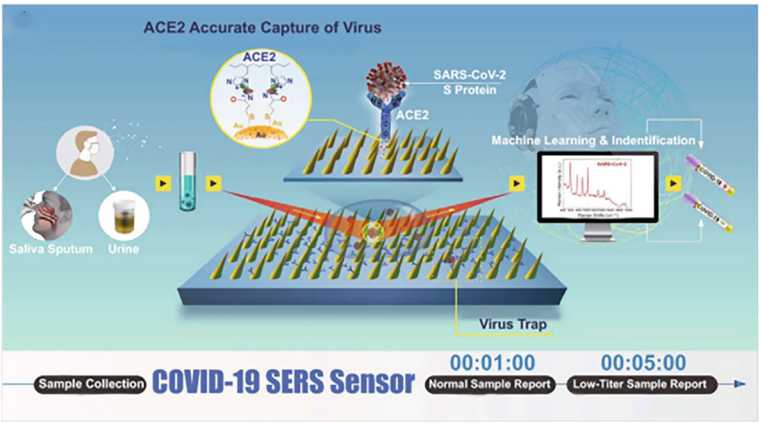



**Fig. 13.2** Schematic diagram of COVID-19 SERS sensor design and operation procedure. Adapted from Ref. [20] with permission from the Springer

relevant concentrations of levofloxacin. To the authors' knowledge, this is the first report of using fabric-based electrodes for EC-SERS research, highlighting the platform's tremendous potential in wearable clinical diagnostic sensors. The significance of this study lies not only in showcasing a novel wearable sensor technology but also in offering new possibilities for rapid, accurate medical testing. Integrating such sensors into everyday clothing could enable continuous monitoring of chemical and biological markers, crucial for early disease diagnosis and health monitoring [22].

#### 13.3.1.3 Prognostic Biomarkers

In contemporary medical practice, the identification and analysis of prognostic biomarkers are crucial for disease management and therapeutic decision-making. Prognostic biomarkers are those used to determine the likelihood of clinical events, disease recurrence, or progression in patients with relevant diseases or medical conditions. These biomarkers indicate an increased (or decreased) likelihood of future clinical events, disease recurrence, or progression in a defined population. Such biomarkers, including specific proteins, nucleic acids, and small molecular metabolites, provide critical information about disease progression, patient response to treatment, and long-term prognosis. Particularly in the management of cancer, cardiovascular diseases, and chronic conditions, accurate detection of prognostic biomarkers is vital for formulating personalized treatment plans and improving patient outcomes. SERS technology, in prognostic assessment of cancers and cardiovascular diseases, not only enhances diagnostic accuracy but also augments real-time monitoring of disease progression [23].

miRNA-21, closely associated with liver cancer development, also serves as a crucial prognostic indicator. This technique employs specific probe molecules that bind with miRNA, generating enhanced Raman signals for high sensitivity and specificity detection of miRNA-21. Another example, in nasopharyngeal and pancreatic cancer studies, involves SERS technology for simultaneous detection of multiple protein biomarkers using gold-silver alloy nanoboxes and nanoyeast single-chain variable fragments. Detecting these biomarkers is crucial for assessing cancer prognosis, with the technology's principle based on the LSPR effect of SERS-active nanostructures and the selective binding of specific antibody fragments. Finally, in sepsis research, SERS technology has been utilized for rapid, sensitive detection of key biomarkers in human whole blood and plasma, vital for assessing the prognosis of septic patients. This technique involves using specific nanoprobe molecules that generate distinct Raman scattering signals upon binding with the target biomarkers. These studies demonstrate the vast potential of SERS technology in detecting prognostic biomarkers, providing new perspectives for prognostic assessment in cancer and other serious diseases [24].

### *13.3.2 Pathogen Detection*

Pathogens, including bacteria, viruses, fungi, and parasites, are microorganisms capable of causing diseases and hold immense significance across medical, environmental monitoring, and food safety domains. Traditional pathogen detection methods, such as microbial culturing, Polymerase Chain Reaction (PCR), and Enzyme-Linked Immunosorbent Assay (ELISA), are effective yet typically require lengthy durations and complex sample preparation steps. SERS technology demonstrates significant advantages in pathogen detection, offering high sensitivity and resolution, making it an ideal tool for rapid and accurate identification of various pathogens. Importantly, SERS allows for label-free detection, greatly simplifying the sample preparation process and enabling multiplexed detection in complex biological samples [25].

In the following sections, we will delve into SERS's capabilities in detecting four primary types of pathogens—fungi, bacteria, viruses, and parasites. These pathogens play a crucial role not only in medical diagnostics but are increasingly significant in environmental and food safety monitoring. A comprehensive understanding of SERS's applications in these areas will offer a broader perspective on its potential and value in pathogen detection and biomedical research.

#### 13.3.2.1 Viruses

Viruses, as microbes that replicate dependently on host cells, have impacts far exceeding their minute size. The importance of virus detection has garnered global attention, especially with the outbreak of the 2019 novel coronavirus (SARS-CoV-2)

pandemic. Accurate and rapid virus detection is critical for controlling the spread of outbreaks and ensuring public health and safety [26]. Viruses can be classified based on various factors, including nucleic acid type, morphology, and host range. For instance, RNA viruses include coronaviruses and influenza viruses, while DNA viruses include adenoviruses and hepatitis B virus [27]. This classification is crucial for understanding viruses' biological characteristics and transmission pathways. Traditional virus detection primarily involves molecular detection and antigen/antibody testing. Molecular detection typically uses Polymerase Chain Reaction (PCR) or Reverse Transcription Polymerase Chain Reaction (RT-PCR) to amplify specific DNA or RNA segments of the virus. Although accurate, these methods usually require specialized laboratory equipment and highly trained technicians [28]. Antigen/antibody testing diagnoses viral infections by detecting virus-specific antigens or antibodies and is generally quicker but may not be as accurate as molecular detection [29]. SERS technology shows significant advantages in virus detection, with its high sensitivity and multiplexing capability, making it an ideal virus detection platform. SERS can not only rapidly and accurately identify viruses but also be used to study their structure and function, contributing to more effective prevention and treatment of virus-related diseases.

In the current global health crisis, rapid and accurate detection of respiratory viruses, especially SARS-CoV-2, is crucial. To meet this need, Yang et al. [30] primarily explored a label-free diagnostic platform combining SERS and machine learning algorithms. This platform used highly sensitive $SiO_2$-coated silver nanorod arrays to rapidly and accurately detect and quantify 13 different respiratory viruses, including SARS-CoV-2 and other common human coronaviruses. Experimentally, the study used oblique angle deposition (OAD) to prepare silver nanorod (AgNR) arrays and uniformly coated a thin, dense silica layer on AgNRs through hydrolysis of TEOS to prevent chemical degradation of AgNRs in buffer solutions. With appropriate spectral processing procedures and various machine learning algorithms, such as Support Vector Machine (SVM), k-Nearest Neighbors (KNN), and Random Forest (RF), the platform achieved distinction and classification of virus species, strains, and variants. Impressively, the method attained over 99% classification accuracy. Furthermore, the study also employed an SVM-based regression approach to construct quantitative calibration curves, accurately estimating the concentration of unknown viruses in buffer solutions and saliva. These achievements not only demonstrate the immense potential of SERS and machine learning methods in rapid virus detection but could also provide robust technical support for future point-of-care diagnostic platforms.

To enhance the accuracy of label-free SERS detection in virus detection, researchers have developed a rapid virus detection platform employing SERS with internal standards, utilizing silver nanoparticles modified with bromine ions and acetonitrile [31]. Acetonitrile serves dual purposes in this setup: as an internal standard for assessing viral content and as a stabilizer for the silver nanoparticle substrate. This method can achieve rapid virus diagnosis within 1–2 min, with an exceptionally low detection limit of only 100 PFU/test. It has been employed for the detection

of SARS-CoV-2, human adenovirus, and H1N1 influenza virus. Utilizing machine-learning techniques, the platform can qualitatively distinguish these three different viral molecules. The method's high sensitivity and specificity largely derive from the combined effects of acetonitrile and calcium ions, creating "hotspots" ideal for virus detection. Thus, this approach holds broad application prospects in clinical diagnostics, emergency management of viral infectious diseases, and research into the interactions between viruses and host cells.

Moreover, differing from label-free SERS detection, labeled methods demonstrate high specificity and sensitivity in biomedical applications. In response to the urgent need for high sensitivity and portable detection of SARS-CoV-2 amid the COVID-19 pandemic, Ma et al. proposed a novel nanobiological assay named OVER-SARS-CoV-2 (One-Vessel Enhanced RNA test on SARS-CoV-2) [32]. This method combines SERS with CRISPR/Cas12a technology, enabling reverse transcription of RNA, cross-cutting activity of Cas12a, and cross-linking of SERS nanoprobes within a single tube. The assay utilizes gold nanoparticles (AuNPs), Raman reporter molecules, and single-stranded DNA (ssDNA) probes to construct the SERS nanoprobes. The aggregation-to-dispersion transition of these nanoprobes, finely controlled by target-activated Cas12a cross-cutting activity, cleverly transforms, and amplifies nucleic acid signals into SERS signals. This method can detect SARS-CoV-2 at concentrations as low as 200 copies/mL within about 45 min, without any need for pre-amplification. The researchers also designed a special "tube-in-tube" reaction vessel to simplify the detection process and prevent cross-contamination. This innovation not only enhances the sensitivity and specificity of CRISPR/Cas12a and SERS but also leverages the simplicity, portability, and quantitative capabilities of SERS detection [33].

#### 13.3.2.2 Bacteria

Bacteria, as single-celled microorganisms, are ubiquitously distributed across the globe, from soil and water bodies to extreme environments and within human and other living organisms. Being among the earliest forms of life, bacteria have billions of years of evolutionary history. Their diversity and adaptability are remarkable, with some species thriving in anaerobic or high-salt environments, demonstrating exceptional ecological adaptability. Bacteria play various key roles in ecosystems, including decomposing organic matter, fixing nitrogen, and forming symbiotic relationships with plants and animals. In the medical field, bacteria's dual nature is particularly striking: on one hand, gut microbiota aid in digestion and nutrient absorption; on the other, they can cause diseases like pneumonia, food poisoning, and more severe infectious diseases. Additionally, bacteria have extensive applications in bioengineering and industrial production, such as in fermentation processes for producing antibiotics, enzymes, or other useful biochemicals. However, bacteria also pose challenges, especially in human health and environmental safety, including increased antibiotic resistance, the emergence of novel pathogens, and environmental pollution [34].

Conventional bacterial detection methods, including colony counting, Polymerase Chain Reaction (PCR), and Enzyme-Linked Immunosorbent Assay (ELISA), are relatively mature but often suffer from issues like insufficient sensitivity, time consumption, and high costs [35]. Therefore, finding an accurate, fast, and economical method for bacterial detection is a pressing need. In recent years, SERS technology has increasingly gained prominence in the biomedical field due to its exceptional sensitivity and specificity. The main advantages of this technology are multifaceted:

- **High Sensitivity and Specificity**: SERS provides highly sensitive and specific spectral information for rapid and accurate identification of bacteria and related biomarkers [36].
- **No Culturing Needed**: Compared to traditional methods, SERS enables direct, culture-free detection, significantly reducing analysis time [37].
- **Diverse Substrate Choices**: SERS allows the use of various substrates (such as gold and silver nanoparticles) to adapt to different application scenarios [38].
- **Environmental Factor Studies**: SERS can be used for real-time monitoring of physiological and metabolic changes in bacteria under different environmental factors like temperature, salinity, and pH [39].
- **Multifunctionality and Real-Time Monitoring**: SERS is not only useful for differentiating between types of bacteria but also for real-time monitoring of bacterial infections and treatment effectiveness, providing timely guidance for clinical treatment [40].
- **Cost-Effectiveness**: SERS is simple to use and relatively low in cost, making it an economically viable tool for microbial diagnostics [41].

The combination of these attributes significantly expands the scope of SERS in biomedical applications, making it a promising technology for future developments in medical diagnostics, therapeutic monitoring, and environmental health studies:

- **Identification and Differentiation**: SERS can accurately identify and differentiate between various types or strains of bacteria. Rho et al. used SERS technology, supplemented by the deep learning model DualWKNet, to achieve separation-free bacterial identification in arbitrary media (Fig. 13.3a) [42]. This method achieved up to 98% accuracy in classifying common bacteria such as *Escherichia coli* and *Staphylococcus epidermidis* and their growth media, breaking through the limitations of traditional bacterial detection that requires culturing and separation, significantly shortening analysis time. This study not only demonstrates the strong potential of SERS in bacterial identification but also shows how machine learning can effectively enhance its accuracy and range of applications, especially in food safety and clinical diagnostics.
- **Antibiotic Sensitivity Testing**: SERS can quickly assess the sensitivity of bacteria to different antibiotics, aiding in personalized treatment. Bi et al. developed SERS-active Au@Ag core–shell nanorod (Au@AgNR) tags for ultra-sensitive bacterial detection and antibiotic-susceptibility testing (Fig. 13.3b) [43]. The study used SERS technology and Principal Component Analysis (PCA) for rapid assessment

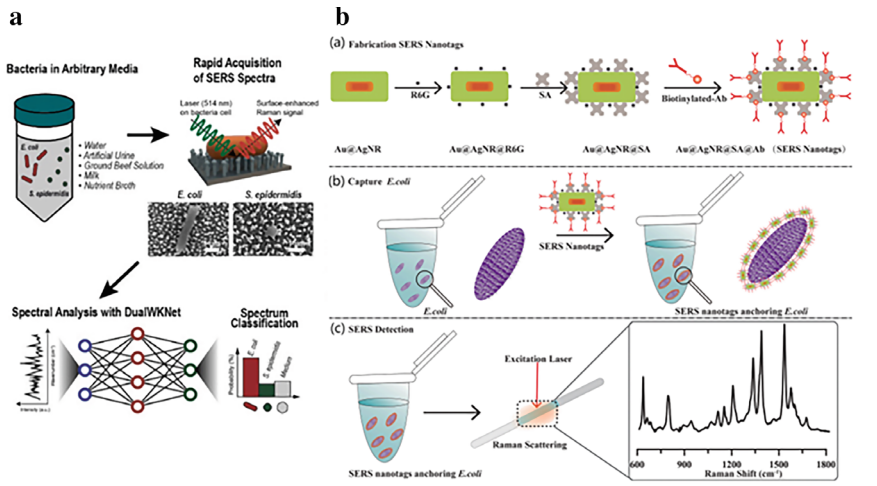



**Fig. 13.3** **a** General experimental procedure with analyte images and measured Raman spectra. Adapted from Ref. [42] with permission from the Elsevier. **b** Diagram of the preparation process of functionalized Au@AgNR as SERS nanotag and their attachment to *E. coli*. Adapted from Ref. [43] with permission from the Elsevier

of Minimum Inhibitory Concentrations (MIC), accurately determining bacterial antibiotic sensitivity. This technique not only offers a highly sensitive and specific detection method but also has potential clinical applications, particularly in quickly determining the most effective treatment plans.

- **Public Health Impact Monitoring**: SERS can be used to assess how environmental changes affect the physiological state of bacteria, which is significant for environmental science research. For example, Wang et al. developed a SERS-based integrated device for bacterial detection [44]. This technology uses Plasmonic Microneedle (P-MN) arrays for sample extraction. These microneedles can penetrate meat samples for related bacterial SERS detection. Using this method, the entire preprocessing and detection process can be completed in just 10 min, with high specificity and reliability. This integrated detection device is expected to be used in field applications, especially in rapid response to food safety and public health events, providing a rapid, accurate, and convenient method for bacterial detection, helping to protect public health and prevent disease transmission.

#### 13.3.2.3 Fungi

Fungi, a diverse group of eukaryotic microorganisms, play both symbiotic and pathogenic roles in human health. Ubiquitous in nature, fungi are a significant part of the human microbiome. They primarily fall into categories like yeasts, molds, and larger fungi, with over 10,000 genera and more than 100,000 species known. Their cell structures are complex, comprising organelles like mitochondria, ribosomes, and

lysosomes, with cell walls primarily made of chitin and cellulose. Some species are pathogenic to humans, causing various infections from superficial to systemic. Over a billion people globally are affected by fungal diseases, with more than 1.5 million deaths annually. For instance, Candida species, especially *Candida auris*, account for a significant portion of hospital infections, with mortality rates nearing 40%. These infections also complicate chronic conditions like asthma, COPD, diabetes, and viral diseases like COVID-19, leading to increased mortality rates. Traditional fungal detection methods, such as culturing and microscopy, are time-consuming and prone to errors. Molecular biology techniques, although specific and sensitive, are costly and require specialized training. Hence, there is an urgent need for rapid, efficient, and economical methods for fungal detection and identification [45].

Traditionally, fungi are identified through phenotypic analysis, involving the identification of morphological and metabolic characteristics. Common methods are culture-based, where pathogenic fungi thrive at temperatures between 25 and 30 °C. SERS can analyze various organelles in fungal cells, aiding in understanding cell dynamics and studying cells under different environmental stresses. The characteristic vibrational Raman spectra obtained through SERS are attributed to the variability of fungal cell wall and subcellular components like chitin, hemicellulose, β-1,3-glucan, α-1,3-glucan, amide I, mannose, β-1,4-N-acetylglucosamine, and ergosterol. However, the application of SERS in fungal detection is still in its nascent stages, facing challenges like low detection sensitivity, poor signal stability, and difficulty in signal recognition. Despite these limitations, SERS holds tremendous potential for rapid and efficient fungal detection, with ongoing research aimed at overcoming these challenges through improved detection modes and the development of more efficient SERS substrates and nanostructures [46].

- **Diagnosis and Monitoring**: Researchers have used SERS and magnetic nanoparticles ($Fe_3O_4$@PEI) for rapid detection of three common pathogenic fungi: *Candida albicans*, *Candida tropicalis*, and *Candida krusei* [47]. The method's advantage lies in not needing to destroy the fungal cell wall, and the detection process can be completed within 40 min.
- **Fungal Resistance Mechanisms**: SERS technology's ability to quickly detect fungi and analyze their interactions with drugs is vital for identifying resistance and assessing antifungal drug efficacy. For instance, a study used triangular silver nanoplates as stable SERS substrates and prepared $Fe_3O_4$@PEI nanoparticles to capture non-*C. albicans* [48]. By mixing clinical samples with $Fe_3O_4$@PEI and applying silver nanoplates, researchers could directly use SERS for detection, identifying resistance directly from samples within 90 min without needing cultivation. The stable triangular nanoplates and uniform $Fe_3O_4$@PEI improved the method's repeatability. SERS enabled rapid diagnosis of fungi without destroying the cell wall, while Orthogonal Partial Least Squares Discriminant Analysis (OPLS-DA) differentiated various resistance mechanisms through spectral differences [49].
- **Drug Discovery**: Therapeutic Drug Monitoring (TDM) is a clinical practice that optimizes drug therapy by measuring drug concentrations in patient samples. It

helps physicians adjust drug dosages to maximize efficacy while minimizing side effects. SERS-based TDM offers a new method for measuring drug concentrations, especially in the field of fungal treatment. Considering this, researchers developed a novel vertical flow membrane system with an inkjet-printed SERS sensor for quantitative detection of flucytosine levels in undiluted human serum. Flucytosine is an antifungal drug, and its TDM is crucial for effective patient care [50]. The system aims to provide a low-cost, easy-to-use device for TDM of flucytosine. The paper-based SERS sensor detected flucytosine in undiluted serum as low as 10 μg/mL. The detection process was shortened to about 15 min, much faster than current standard methods. The study suggests the system's potential for near-patient TDM, which could lead to safer and more effective use of life-saving drugs. The paper-based SERS sensor was integrated into a passive vertical flow system for serum separation and could quantitatively detect flucytosine across its entire therapeutic range [51].

#### 13.3.2.4 Parasites

Parasitic diseases pose a significant challenge to global public health, especially in impoverished areas of developing countries. These diseases not only cause high mortality rates, particularly in children, but also lead to severe health issues such as anemia, malnutrition, and organ damage, impacting patients' quality of life and community economic development. Beyond traditional blood sample testing, Raman imaging technology at the tissue level offers a new perspective for malaria diagnosis. Using label-free Raman imaging, researchers have developed a method to distinguish between tissues infected with malaria parasites and uninfected tissues. This technology can differentiate between tissues infected with malaria parasites and uninfected ones. During the red blood cell stage of Plasmodium infection, the parasite digests hemoglobin and produces the toxic byproduct hemozoin. Parasites detoxify by converting hemozoin into an insoluble crystalline substance. When infected red blood cells rupture, hemozoin and parasites are released into the bloodstream. Hemozoin circulates in the blood before being digested by macrophages in organs like the spleen, aiding in clearing parasitized red blood cells and hemozoin. However, proteins on infected red blood cells allow them to bind to receptors on tissue blood vessels, a process known as sequestration, which reduces clearance from the blood and contributes to the severity of malaria symptoms.

In methods for malaria diagnosis, the integration of microfluidic technology offers a unique detection platform. A simple polystyrene microfluidic device combines immunoassay and SERS for detecting malaria infections [52]. The device uses a two-chamber design, one for detecting Plasmodium biomarkers and the other for a control SERS marker. The chambers are coated with TO-RCH, covalently linking capture antibodies for efficient immobilization of the antibodies. The microfluidic device also includes two sets of vertical channels, one set for sensor preparation and the other for sample analysis. The sensor preparation channels consist of two independent parallel channels, each leading to a chamber. This design allows parallel

preparation while maintaining spatial separation of the detection chambers for clear differentiation. By immobilizing the corresponding antibodies in parallel channels in each detection chamber, cross-contamination is avoided. With this design, the microfluidic device can sensitively detect malaria infections and provide accurate results.

In pursuing ultra-sensitive SERS diagnostic methods for parasites, nanoparticles are synthesized in situ to achieve closer contact between nanoparticles and hemozoin [53]. This significantly enhances the Raman signal and lowers the detection limit to an extremely low 0.00005% parasite density, comparable to the most sensitive existing technologies. However, due to the dispersed and uneven distribution of parasites containing nanoparticles, there is considerable variability in spectral intensity. This method surpasses almost all existing methods, including laser desorption mass spectrometry, PCR, and attenuated total reflection infrared spectroscopy. Compared to existing technologies, the SERS method has advantages of being simple, fast, and low-cost. With further development of reasonably priced Raman spectrometers and microfluidic sample preparation technologies, they show great potential for malaria diagnosis in resource-limited settings. With optimization, SERS has the potential to replace microscopy as the gold standard diagnostic tool. In summary, SERS has been proven to be a highly sensitive and promising method for malaria diagnosis, especially for detecting very low parasite density levels critical to disease control and eradication efforts [54].

## 13.4 SERS Imaging in Biomedical Applications

SERS has become indispensable to the field of biomedical imaging, offering unprecedented sensitivity and specificity for molecular detection. Its distinctive enhancement of Raman signals provides a detailed spectral analysis that is essential for identifying molecular structures and dynamics. As a non-destructive analytical technique, SERS enables the examination of biological specimens with minimal alteration, facilitating a deeper understanding of cellular processes and tissue composition. The key strength of SERS lies in its multiplexing capability, which allows for the simultaneous detection of multiple biomolecules. This feature is particularly valuable for elucidating the complex biochemical states of cells and tissues, which is critical for detecting early-stage pathophysiological changes. The application of SERS for early disease detection is promising, given its ability to identify minute molecular alterations that precede broader disease manifestations [55, 56].

Nowadays, SERS technology has been successfully applied in both cellular and tissue imaging, proving to be a powerful tool in the clinical setting. It enhances the accuracy of diagnostics, particularly in oncology, by clearly demarcating cancerous tissues from healthy ones in real-time during surgery. Although in vivo imaging presents certain challenges, the development of biocompatible probes and the refinement of imaging techniques continue to advance the potential of SERS for real-time monitoring within living organisms. Throughout this section, we will detail the use

of SERS across three distinct biological scales: beginning with cellular imaging, we will discuss its role in identifying intracellular biomarkers and contributing to our understanding of cellular disease mechanisms. The focus will then shift to tissue imaging, where SERS contributes to precision medicine, particularly in the delineation of tumor margins for surgical guidance. Lastly, we will consider the emergent applications of SERS in in vivo imaging, assessing its current capabilities and future prospects for live biological system analysis. The exploration of these areas will underscore the ongoing progress and future potential of SERS in advancing the frontiers of biomedical imaging and its pivotal role in the development of personalized medical interventions [57].

### *13.4.1 Cellular Imaging*

The advent of SERS in the realm of cellular imaging has provided a powerful spectroscopic tool that probes the complex inner workings of cells with remarkable precision. By harnessing the enhanced Raman signals facilitated by metal nanostructures, SERS enables the mapping of molecular constituents within cells, offering insights into cellular biochemistry that are critical for understanding the occurrence and progression of diseases at the most fundamental level. The cellular environment presents a complex landscape of biological molecules, where the ability to discern specific biomarkers is essential for identifying disease states and monitoring cellular responses to therapeutic interventions. The application of SERS in cellular imaging is boosted by the development of sophisticated SERS tags and probes, which can be tailored to target distinct biomolecules or cellular compartments, allowing for targeted imaging and analysis [58].

In the exploration of SERS applications in cellular imaging, a particularly noteworthy advancement is its capability for in situ activation imaging within cells. The Pinaud team demonstrated an innovative approach for cellular imaging by directly assembling metal NPs into photonic clusters within living cells (Fig. 13.4a) [59]. Utilizing split-fluorescent protein (FP) segments as molecular "glue", the self-assembly of gold or silver NPs on cancer cell surface markers can be achieved through the reconstruction of full-length FP. These NP-formed SERS nanoclusters, uniformly distributed in hotspot areas, achieved selective and sensitive SERS imaging of target cells through the self-catalytic activation of FP pigments and the near-field amplification of their Raman fingerprints. This FP-driven assembly of metal colloids also enhanced photoacoustic (PA) signals, enabling these hybrid FP/NP nanoclusters to serve as contrast agents for multimodal SERS and PA microscopy with single-cell sensitivity. In experiments, researchers induced the activation of nanoclusters by targeting cell surface biomarkers, such as folate receptors (FR) or exogenous biomarkers like biotinylated avidin, achieving highly specific imaging of cells via SERS and PA microscopy. This strategy can also be applied to target other endogenous surface markers overexpressed on cancer cells, for instance, by using complementary NPs functionalized with antibodies. Compared to pre-activated

SERS probes, this dual NP assembly and in situ SERS activation offer highly selective detection of pathological cells versus normal cells, especially when complementary NPs target two different overexpressed biomarkers. This technique propels the application of SERS imaging in the biomedical field, particularly demonstrating its unique value in the selective detection of cancer cells.

Utilizing SERS to visualize intracellular pH values plays a pivotal role in understanding cellular processes, including their interactions with nanoparticles. Three-dimensional (3D) SERS imaging technology offers a new perspective in observing changes in intracellular pH in living cells, effectively addressing the limitations of traditional two-dimensional SERS that fails to account for changes occurring throughout the entire cell volume. Liz-Marzán and colleagues developed a biocompatible and stable SERS pH probe, which was composed of gold nanostars functionalized with a pH-sensitive Raman reporter (4-mercaptobenzoic acid) and encapsulated

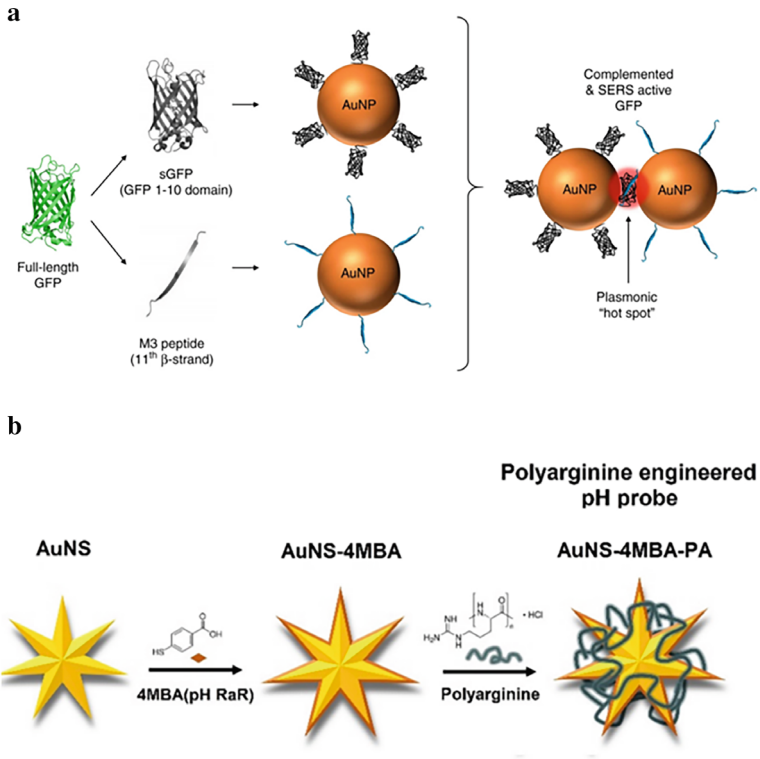



**Fig. 13.4** **a** Schematic illustration of surface modification on AuNPs by sGFP and M3 peptide fragments and formation of SERS active hot spot through self-assembly and GFP complementation. Adapted from Ref. [59] with permission from the Nature. **b** Schematic illustration of the stepwise synthesis of PA-engineered pH probes (AuNS-4MBA-PA): AuNSs are functionalized with 4MBA (pH-RaR) and then wrapped with PA. Adapted from Ref. [60] with permission from the American Chemical Society

in a cationic biocompatible polymer, poly-L-arginine hydrochloride (PA) (Fig. 13.4b) [60]. The positive charge of the PA coating not only enhanced cellular uptake of the probe but also provided chemical and colloidal stability within the cellular environment. This SERS-active pH probe precisely visualized local changes in intracellular pH, such as acidification during nanoparticle uptake. In terms of cellular imaging performance, the probe demonstrated exceptional capability, providing a comprehensive intracellular pH profile within a single cell and visualizing dynamic changes in intracellular pH distribution. This study not only proves the effectiveness of 3D SERS imaging in monitoring intracellular pH in living cells but also offers a novel tool for understanding the internal cellular environment.

### *13.4.2 Tissue Imaging*

In the context of tissue imaging, SERS provides not only a topographical map of tissue sections but also a biochemical snapshot of the diverse molecular entities present. This dual function is invaluable in differentiating between healthy and diseased tissue regions, facilitating the detection of pathological changes at early stages. The application of SERS in tissue imaging extends to oncology, where it can be instrumental in the identification and delineation of tumor margins. By enabling the real-time visualization of tissue biochemistry, SERS guides surgeons during excision procedures, ensuring the complete removal of malignant tissues while preserving as much healthy tissue as possible. Algorithms capable of analyzing complex SERS spectra can identify specific patterns associated with pathological states, leading to more accurate diagnoses. This analytical power, coupled with the ability to perform rapid, non-destructive imaging, positions SERS as a promising approach for intraoperative assessment, potentially reducing the rates of re-operation and improving patient outcomes [61, 62].

For brain diseases, tissue-level specific imaging is critical for accurate diagnosis. In view of this, Tian and colleagues developed an innovative label-free, ratio-based SERS platform for real-time monitoring and imaging of the entire Aβ aggregation process, including in live cells and brain tissues (Fig. 13.5) [63]. This platform utilizes distinct gold nanoparticles generated as templates with Aβ monomers and fibrils, serving as efficient SERS substrates, achieving high sensitivity detection with detection limits of $70 \pm 4$ pM for Aβ40 monomers and $3.0 \pm 0.5$ pM for fibrils. Moreover, by introducing a ratio metric measurement ($I_{1244}/I_{1268}$) of Aβ monomers and fibrils, the platform enables real-time tracking of the entire Aβ monomer aggregation process with high precision and selectivity, distinguishing it from other proteins and amino acids. The notable analytical performance of this platform, combined with its excellent biocompatibility, long-term stability, and superior spatial resolution, allows the SERS platform to be effectively utilized in imaging and biosensing applications. In the study, APP/PS1 transgenic mice were used, treated with a control

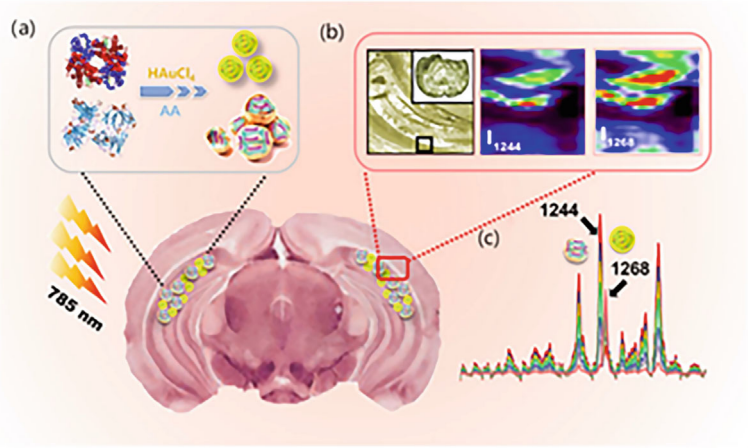



**Fig. 13.5** Design and application of Aβ-templated AuNPs for SERS imaging in mice brain. Adapted from Ref. [63] with permission from the American Chemical Society

diet and metal ions for three weeks, respectively. Brain tissue slices obtained were incubated under specific conditions, and SERS imaging revealed a decrease in the SERS signal of Aβ40 at 1268 $cm^{-1}$ and an increase at 1244 $cm^{-1}$ in the hippocampal region compared to the control group, indicating the influence of metal ions on Aβ40 aggregation.

In addressing a key challenge in SERS tissue imaging, which involves the precise detection of microenvironmental changes in deep tissue layers, Li and colleagues developed a novel pH ratio-responsive SERRS probe. This marks a significant breakthrough in tissue imaging technology [64]. Utilizing a spatially oriented induced energy transfer (SOIET) mechanism, this probe could accurately detect subtle pH variations deep within tissues. The synthesis of the probe involved the creation of gold nanostars (AuS), modified on their surface to carry pH-sensitive Raman molecular markers IR7p. Triggering a substantial SERRS signal enhancement in acidic environments, the probe demonstrated high sensitivity and specificity in tissue imaging. In vitro experiments revealed the probe's exceptionally low detection limits and superior imaging capabilities, allowing for precise visualization of pH changes at the cellular level. In vivo pH mapping generated by chemical exchange saturation transfer (CEST)-MRI highlighted significant acidosis in tumor tissues, a phenomenon not observed in normal brain tissue. Overall, this study introduces a novel SERRS probe for tissue imaging, particularly in mapping the microenvironment of tumor tissues, showcasing the further application potential of SERS technology in biomedical imaging.

### *13.4.3 In Vivo Imaging*

In vivo SERS imaging has shown significant promise in preclinical and clinical settings, especially in oncology for the detection and monitoring of tumors. The ability to track the distribution and changes of specific biomarkers in real time offers a potent tool for understanding disease progression and the body's response to treatments. This capability is critical for advancing personalized medicine, where interventions can be tailored and adjusted based on the direct observation of therapeutic effects within the body of a patient. Challenges remain in optimizing the delivery and stability of SERS probes within the complex in vivo environment, as well as in ensuring that signal acquisition is efficient and reliable. Nevertheless, continuous advancements in nanoprobe technology and imaging systems are overcoming these hurdles. For example, the integration of SERS with endoscopic techniques has opened up new possibilities for internal imaging, providing a minimally invasive route to observe and diagnose internal pathologies. The promise of SERS in vivo imaging is vast, with potential applications ranging from guided surgery to the monitoring of drug delivery and therapeutic response. As we refine the technology and expand our understanding of its capabilities, SERS is set to become a cornerstone technique in future of in vivo biomedical imaging, offering a window into the living body with unprecedented clarity and detail [65–67].

In the field of multiplexed imaging, SERS imaging has outstanding advantages. For example, Jun et al. successfully prepared an NIR SERS nanoprobe with high sensitivity, which has uniformly synthesized multiple hotspots and a narrow nanogap structure. This nanoprobe could absorb long-wavelength light and highly enhance the Raman signal, resulting in a strong SERS signal in the NIR region. The researchers also achieved multiple SERS imaging by combining 14 different Raman-labeled compounds with $SiO_2$@Au@Au nanoparticles. After subcutaneous injection of these nanoparticles in mice, each compound demonstrated a unique SERS signal. In addition, the researchers demonstrated that $SiO_2$@Au@Au nanoparticles could still detect observable SERS signals at a depth of 7 mm in animal tissues. Thus, this work opens up the potential for multiple molecular imaging and applications of SERS in in vivo imaging [68, 69].

Development of new materials has greatly advanced the use of SERS in in vivo imaging. Li's group have developed a new class of porous nanostructures consisted of a cubic AuAg alloy nanoshell and numerous nanopores for in vivo imaging, specifically for the visualization of tumors. These nanostructures showed excellent NIR-II plasmonic properties, which can be tuned by varying the pore features. The researchers demonstrated the exceptional performance of these nanostructures in NIR-II SERS. They also created NIR-II SERS probes using these porous cubic AuAg nanoshells, which showed remarkable capability for in vivo visualization of sub-millimeter microtumors in a living mouse model. The study suggests that these NIR-II SERS probes could be very useful for precisely marking the boundaries of tumors and identifying microscopic tumors [70, 71].

## 13.5 Application of SERS-Based Theranostic

The emergence of theranostic nanomedicine has initiated a new phase in personalized health care, combining diagnostic procedures with targeted treatments for improved clinical results. Among various analytical methods, SERS has gained prominence due to its high sensitivity, quick detection, and minimal sample preparation needs. SERS provides unique biochemical fingerprinting capabilities, offering real-time insights into cellular and molecular changes. This is especially useful for evaluating the effectiveness of various disease treatments, such as chemotherapy, photothermal therapy (PTT), and radiation therapy, etc. By monitoring specific, time-dependent biochemical changes, SERS contributes valuable data for understanding treatment responses, making it a crucial tool in theranostic applications [72, 73].

The use of near-infrared active probes in SERS further extends its applications. These probes offer the advantage of deeper tissue penetration and reduced background noise, which are vital for real-time monitoring and therapy guidance. The incorporation of nanoparticles made of materials like gold, silver, and copper improves the photothermal effects, facilitating more effective targeted therapies. Multifunctional SERS probes, which can perform both imaging and therapeutic functions, have received significant attention. These can be integrated into theranostic nanoplatforms for various applications, ranging from early cancer diagnosis to real-time treatment efficacy monitoring. Combining these capabilities into a single platform presents both challenges and opportunities in current medical research, particularly in cancer therapeutics. In this section, we will explore the growing field of SERS-based theranostic applications, focusing on three key areas: SERS-based delivery systems, photothermal therapy monitored by SERS, and SERS imaging-guided surgery, aiming to provide a comprehensive overview of how SERS is influencing the development of precision medicine [74, 75].

### *13.5.1 SERS-Based Delivery System: An Integrated Approach to Theranostics*

The integration of SERS into drug delivery systems offers a transformative approach in the realm of theranostics. SERS not only serves as a highly sensitive detection modality but also offers the potential for real-time monitoring of therapeutic agents. This dual functionality makes SERS-based delivery systems an invaluable asset in personalized medicine, particularly in the management of cancer therapies. Traditional chemotherapeutic regimens have relied on a range of natural and synthetic agents to combat cancer, yet the evaluation of their effectiveness has often been challenging. SERS has revolutionized this aspect by facilitating the precise identification and monitoring of chemotherapeutic agents like doxorubicin, 5-fluorouracil,

and paclitaxel within cellular environments. By elucidating the mechanisms of drug action and their metabolic pathways, SERS contributes to a more targeted and efficient treatment strategy [76–78].

In the realm of Raman imaging-guided therapy, the most straightforward approach is to directly utilize the Raman spectral variations of chemotherapeutic agents. Cui and colleagues innovatively coupled gold nanostars with the anticancer drug mitoxantrone (MTX), leveraging the surface plasmon resonance of the nanostars to amplify the Raman signal of MTX for real-time SERS detection and drug delivery (Fig. 13.6a) [79]. Intriguingly, the study revealed a marked disparity in the Raman signals of this nanoprobes between intracellular and extracellular environments; virtually no signal was detected extracellularly, while strong characteristic Raman peaks were observed intracellularly. This feature offered the potential for real-time monitoring of drug delivery. Further investigations in healthy mouse models and lung cancer mouse models successfully demonstrated drug accumulation in cardiac tissues and pulmonary tumors, respectively. Hence, this methodology exhibits high efficacy in detecting drug accumulation in both healthy and cancerous tissues and uniquely enables the precise identification of individual tumor cell clusters in the lungs. Consequently, this work not only showcases the immense potential of SERS technology in accurately tracking drug delivery and release but also pioneeringly applies this technology in imaging-guided cancer therapy, offering a novel perspective and toolset for future cancer diagnosis and treatment.

It is well known that Au–Ag coexisting multilayered core–shell nanomaterials have stronger Raman signals than single Au or Ag shell, which is more advantageous for tracing chemotherapeutic drug delivery. Recently, Sun and colleagues reported the construction of a nanoplatform known as GO-$Fe_3O_4$@Au@Ag-MPBA-DOX, which

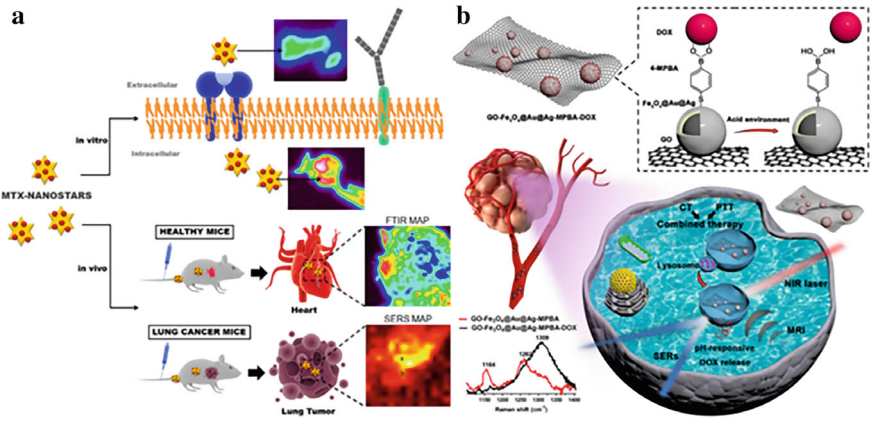



**Fig. 13.6** **a** Gold nanostars for theranostics: intracellular and in vivo SERS detection combined with real-time drug delivery using plasmonic-tunable Raman/FTIR imaging. Adapted from Ref. [80] with permission from the Elsevier. **b** Real-time monitoring of pH-responsive DOX release for SERS/MR imaging-guided chemo-phototherapy. Adapted from Ref. [81] with permission from the Elsevier

can serve as a dual-functional SERS-based delivery system, enabling real-time, pH-sensitive monitoring of drug release (Fig. 13.6b) [80]. $Fe_3O_4$ NPs was selected as the core motif due to their excellent MR imaging ability, followed by the sequential introduction of Au and Ag shells onto the surface of $Fe_3O_4$ core to achieve strong SERS signal with 4-mercaptophenylboronic acid (4-MPBA) as a stable Raman reporter after connection onto graphene oxide (GO) sheets. The chemotherapy drug doxorubicin (DOX) is linked via pH-sensitive borate esters. Upon entering acidic tumor environments, the ester linkage breaks, triggering DOX release and a corresponding change in 4-MPBA's SERS signal. Additionally, the nanocomposite showcases high photothermal conversion efficiency, facilitating more effective targeted therapies. This is further enhanced by the active tumor targeting capabilities of the free PBA moieties, which bind to sialic acid residues overexpressed on the surface of tumor cells. Tests on MCF-7 human breast cancer cells confirm its efficacy and biocompatibility, showing the capability in integrating SERS monitoring, MR imaging, and pH-sensitive drug release for highly efficient chemo-phototherapy [80–82].

### *13.5.2 Photothermal Therapy (PTT) Monitored by SERS*

PTT has gained prominence as a targeted cancer treatment strategy, capitalizing on the conversion of near-infrared light into localized heat to induce cellular damage and eliminate tumors. Noble metal nanostructures, known for their unique optical properties such as surface plasmon resonance, serve as efficient photothermal agents, enhancing the effectiveness of PTT. The groundbreaking integration of SERS with PTT has ushered in a new era in nanomedicine, offering a theranostic platform that unifies diagnostic imaging with therapeutic action. This is exemplified by the pioneering work in 2009, which employed gold nanorods (AuNRs) for both SERS-based multiplexed detection and PTT. The study utilized three different NIR Raman reporters tagged to PEGylated AuNRs for in vivo multiplexed detection in a mouse model bearing bilateral MDA-MB-435 tumors. This dual functionality is particularly advantageous, as many metal nanostructures that are efficient photothermal converters are also excellent substrates for SERS. The unification of SERS and PTT offers a multifaceted platform that not only enables targeted treatment but also allows for real-time monitoring of therapeutic progress. This synergistic approach enhances the precision and efficacy of cancer therapy, providing a robust toolset for future advancements in cancer diagnosis and treatment [83, 84].

Recently, a novel GOx-synergistic PTT system (SGA) was designed and fabricated for bacterial elimination, which was consisted of glucose oxidase (GOx) embedded in a silk film with arrayed plasmonic silver graphitic nanocapsules (Ag@G) (Fig. 13.7) [85]. The unique structure of the SGA system allowed for the stabilization of the embedded antibacterial GOx even during the hyperthermal conditions of PTT, enabling continuous GOx-synergistic PTT. The Ag@G component, with silver nanoparticles encapsulated in a thin graphitic shell, provided excellent

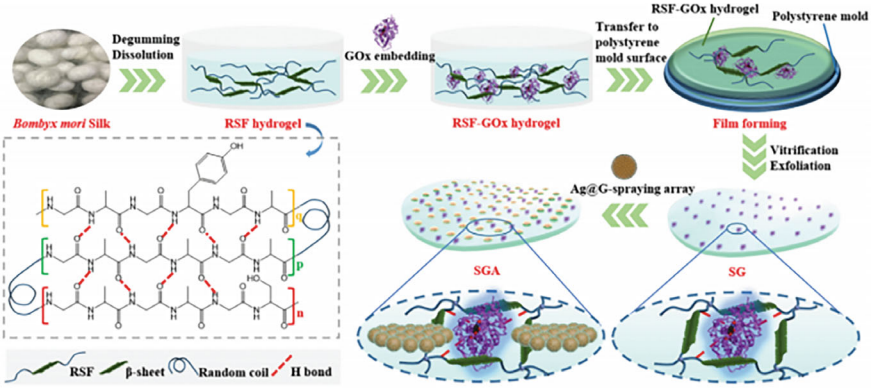



**Fig. 13.7** Construction and characterization of SGA. Schematic diagram illustrating brief construction process of SGA. Adapted from Ref. [86] with permission from the Wiley

chemical stability and a stable plasmonic effect for PTT in a hydrogen peroxide environment. Additionally, the Ag@G demonstrated a significant SERS effect, while the SGA system remained optically transparent due to the vitrification of silk fibroin. This system was demonstrated to be effective against *E. coli*, *Staphylococcus aureus*, and methicillin-resistant *S. aureus* (MRSA) in vivo, guided by in situ bacterial SERS identification. The integration of SERS allows for the precise identification of bacterial infections, which is crucial for targeted therapy. The rational design in this system ensures the stability of therapeutic proteins in a hyperthermal environment, offering a new avenue for treating bacterial infections, particularly those that are resistant to conventional antibiotics.

In addition to its applications in antimicrobial therapy, SERS-based imaging for PTT is also pivotal in the treatment of tumors. Notably, the recently developed NIR-II fluorescence imaging, with its deep tissue penetration capabilities, when combined with SERS, offers significant advantages for multimodal imaging that can greatly enhance the guidance of PTT. Zhou and coworkers designed a SERS/NIR-II optical nanoprobe, $AuDAg_2S$, adept at enhancing tumor-targeted photothermal therapy (PTT) [86]. This probe, a composite of gold nanostars, Raman tags, and NIR-II fluorescent quantum dots linked via a silica matrix, was tailored for precise, multi-scale oncological applications. The $AuDAg_2S$ nanoprobe exceled in photothermal efficiency, achieving a notable 67.1% under NIR-II laser exposure, and was demonstrated exceptional SERS sensitivity for tumor imaging. Its dual imaging capability allowed for picomolar-level detection and up to 1 cm tissue penetration, facilitating accurate tumor delineation and treatment guidance. In vivo studies revealed the probe's efficacy in illuminating and thermally eradicating CT26 colon cancer cells. Post-administration, the $AuDAg_2S$ nanoprobe provided high-resolution, specific imaging from organismal to cellular levels, significantly enhancing tumor detection. The

probe's integration of SERS imaging and NIR-II PTT culminated in a potent therapeutic impact on colorectal tumors, showcasing its potential for clinical translation and setting a new benchmark for cancer theranostics [83, 86].

### *13.5.3 SERS Imaging-Guided Surgery*

It is well known that many malignant tumors possess high invasiveness and metastatic potential, infiltrating into surrounding tissues and critical organs, making it challenging to clearly distinguish the tumor margins [87]. This complicates the surgical process for oncologists and also directly affects the postoperative prognosis. With the advancement of precision medicine and molecular imaging, minimizing damage and protecting surrounding organs during tumor surgery have become the focused efforts and goals of surgeons. Accurate identification of tumor boundaries can improve the rate of surgical resection and enhance postoperative relapse and survival rates. To precisely determine the tumor boundaries, molecular imaging techniques must be utilized. Clinically used techniques such as magnetic resonance imaging (MRI) can localize the macroscopic contours of the tumor. However, the limited spatial resolution of MRI and tissue displacement during surgery can make the MRI-delineated boundaries inconsistent with the actual intraoperative tumor boundaries, affecting the accuracy and success rate of the surgery. SERS imaging technology has high sensitivity and specificity and can detect multiple substances with long tumor retention, allowing for preoperative and intraoperative imaging with a single injection. Therefore, SERS imaging holds great potential for precise determination of tumor margins and guide the surgical removal of the tumor [65].

SERS technology was first applied to in vivo tumor detection by Nie and colleagues in 2008 [88], marking a pivotal moment for biomedical research. Since then, an increasing number of scholars have explored and implemented SERS imaging in various biomedical applications. For instance, Kircher et al. [89] utilized SERS imaging to delineate the margins of glioblastomas. They developed a triple-modality imaging probe with MRI/PA/SERS capabilities, harnessing the high sensitivity and superior resolution of SERS imaging to assist in the surgical resection process, thereby compensating for the limitations of MRI and PA imaging. Furthermore, the same team investigated the application of SERS imaging in the detection of other infiltrative tumors [90]. Their findings revealed that SERS imaging could distinctly identify the invasive margins of tumors, providing critical guidance for the formulation of precise therapeutic strategies such as surgery.

In recent years, the sophistication of multimodal imaging for surgical guidance has significantly advanced, providing substantial benefits in accurately pinpointing tumor locations and discerning their boundaries. For example, Li et al. developed a "three-in-one" theranostic nanoprobe, termed the starPART probe, which was composed of an Au nanostar core, a Raman molecule layer, and a silica outer layer [91]. This probe harnessed the capabilities of photoacoustic (PA) imaging, SERS detection, and photothermal tumor ablation. The design of starPART probe allowed

for preoperative PA imaging to guide the surgical resection of tumors and intraoperative SERS-guided thermosurgery to completely eliminate any residual microtumors. Notably, this approach integrated the precision of SERS with the efficacy of thermosurgery to address the challenge of residual microtumors post-surgical resection, which are a significant cause of lethal cancer recurrence. In the in vivo experiments, the team demonstrated that this integrated strategy could successfully eradicate microtumors without local recurrence, achieving a 100% tumor-free survivability rate. The starPART probe enabled the accurate delineation of tumor margins and the real-time intraoperative detection and subsequent thermosurgical removal of microscopic tumors. This resulted in a significant improvement in surgical outcomes, offering a robust platform for real-time intraoperative eradication of residual microtumors and potentially improving the prognosis for patients undergoing cancer surgery [92].

## 13.6 Conclusion and Perspective

With the rapid development of the biomedical field, especially breakthroughs in frontier areas such as gene therapy, RNA therapy, mRNA vaccine technology, synthetic biology, drug conjugate technology, therapeutic gene editing, cell therapy, novel drug delivery technologies, immune checkpoint inhibitors, and brain–computer interface technologies, SERS as a highly sensitive and specific analytical technique, holds vast potential in biomedical applications. SERS technology demonstrates unique advantages in biomolecule detection, disease diagnosis, drug monitoring, and therapeutic efficacy evaluation. For instance:

- **In Gene Therapy and Therapeutic Gene Editing**: SERS can be utilized to monitor molecular changes and off-target effects during the gene editing process. Its ability to detect specific molecular signatures makes it valuable for ensuring the accuracy and safety of these therapies.
- **In mRNA Vaccine and Drug Conjugate Development**: SERS can provide crucial information about the molecular structure and dynamic distribution of drug molecules, enhancing our understanding of how these treatments interact at the cellular level.
- **In Cell Therapy**: SERS aids in tracking and analyzing the behavior and state of therapeutic cells, offering insights into how these cells respond to different conditions and their mechanisms of action.

Moreover, with advances in nanotechnology and synthetic biology, the design and functionalization of SERS probes are becoming more precise and diverse, further broadening its application scope in biomedicine. For example:

- **Targeted SERS Nanotags**: By designing specific SERS nanotags, efficient identification and imaging of certain cell types or biomarkers can be achieved. This is crucial for early disease diagnosis and real-time therapeutic monitoring.

- **Non-invasive and High-Throughput Analysis**: The non-invasive nature and high-throughput capabilities of SERS technology make it a powerful tool in personalized and precision medicine, enabling tailored treatments based on individual patient profiles.

In summary, the application of SERS technology in future of biomedicine will not only provide powerful tools for early diagnosis and treatment of diseases but will also play an increasingly important role in new drug development and biomedical research. As the technology continues to advance and innovate, SERS is expected to become one of the key forces driving forward developments in the field of biomedicine.

## References

1. Y. Jun, J. Seo, J. Cheon: Nanoscaling laws of magnetic nanoparticles and their applicabilities in biomedical sciences. Acc. Chem. Res. **41**, 179–189 (2008)
2. B. Sharma, R.R. Frontiera, A.-I. Henry, E. Ringe, R.P.V. Duyne: SERS: Materials, applications, and the future. Mater. Today **15**, 16–25 (2012)
3. M. Blanco-Formoso, R.A. Alvarez-Puebla: Cancer diagnosis through SERS and other related techniques. Int. J. Mol. Sci. **21**, 2253 (2020)
4. M.F. Cardinal, E.V. Ende, R.A. Hackler, M.O. McAnally, P.C. Stair, G.C. Schatz, R.P.V. Duyne: Expanding applications of SERS through versatile nanomaterials engineering. Chem. Soc. Rev. **46**, 3886–3903 (2017)
5. J. Perumal, Y. Wang, A.B.E. Attia, U. Dinish, M. Olivo: Towards a point-of-care SERS sensor for biomedical and agri-food analysis applications: A review of recent advancements. Nanoscale **13**, 553–580 (2021)
6. H. Zhou, X. Li, L. Wang, Y. Liang, A. Jialading, Z. Wang, J. Zhang: Application of SERS quantitative analysis method in food safety detection. Rev. Anal. Chem. **40**, 173–186 (2021)
7. K.L. Norrod, L.M. Sudnik, D. Rousell, K.L. Rowlen: Quantitative comparison of five SERS substrates: sensitivity and limit of detection. Appl. Spectrosc. **51**, 994–1001 (1997)
8. J.J. Santos, S.H. Toma, P. Corio, K. Araki: Key role of surface concentration on reproducibility and optimization of SERS sensitivity. J. Raman Spectrosc. **48**, 1190–1195 (2017)
9. S.M. Ansar, M. Gadogbe, K. Siriwardana, J.Y. Howe, S. Dogel, H. Hosseinkhannazer, W.E. Collier, J. Rodriguez, S. Zou, D. Zhang: Dispersion stability, ligand structure and conformation, and SERS activities of 1-alkanethiol functionalized gold and silver nanoparticles. J. Phys. Chem. C **118**, 24925–24934 (2014)
10. S. Sasidharan, D. Bahadur, R. Srivastava: Albumin stabilized gold nanostars: a biocompatible nanoplatform for SERS, CT imaging and photothermal therapy of cancer. RSC Adv. **6**, 84025–84034 (2016)
11. A. Issatayeva, E. Farnesi, D. Cialla-May, M. Schmitt, F.M.A. Rizzi, D. Milanese, S. Selleri, A. Cucinotta: SERS-based methods for the detection of genomic biomarkers of cancer. Talanta 125198 (2023)
12. S. Vigneshvar, C. Sudhakumari, B. Senthilkumaran, H. Prakash: Recent advances in biosensor technology for potential applications—an overview. Front. Bioeng. Biotechnol. **4**, 11 (2016)
13. X. Liu, J. Guo, Y. Li, B. Wang, S. Yang, W. Chen, X. Wu, J. Guo, X. Ma: SERS substrate fabrication for biochemical sensing: Towards point-of-care diagnostics. J. Mater. Chem. B **9**, 8378–8388 (2021)
14. K. Wang, I. Lee, G. Carlson, L. Hood, D. Galas: Systems biology and the discovery of diagnostic biomarkers. Dis. Markers **28**, 199–207 (2010)

15. L. Lu, S. Guan, Y. Guan, M. Hong: Dual-Modal Fluorescence-SERS Detection of Blood Glucose Engineered by Hierarchical Laser-Induced Micro/Nano Structures for Diabetes Screening. Adv. Mater. Interfaces **9**, 2102532 (2022)
16. Z. Cheng, N. Choi, R. Wang, S. Lee, K.C. Moon, S.-Y. Yoon, L. Chen, J. Choo: Simultaneous detection of dual prostate specific antigens using surface-enhanced Raman scattering-based immunoassay for accurate diagnosis of prostate cancer. ACS Nano **11**, 4926–4933 (2017)
17. R. Gao, Z. Cheng, A.J. deMello, J. Choo: Wash-free magnetic immunoassay of the PSA cancer marker using SERS and droplet microfluidics. Lab Chip **16**, 1022–1029 (2016)
18. M. Haroon, M. Tahir, H. Nawaz, M.I. Majeed, A.A. Al-Saadi: Surface-enhanced Raman scattering (SERS) spectroscopy for prostate cancer diagnosis: A review. Photodiagn. Photodyn. Ther. **37**, 102690 (2022)
19. C. Qiu, W. Zhang, Y. Zhou, H. Cui, Y. Xing, F. Yu, R. Wang: Highly sensitive surface-enhanced Raman scattering (SERS) imaging for phenotypic diagnosis and therapeutic evaluation of breast cancer. Chem. Eng. J. **459**, 141502 (2023)
20. Y. Yang, Y. Peng, C. Lin, L. Long, J. Hu, J. He, H. Zeng, Z. Huang, Z.-Y. Li, M. Tanemura: Human ACE2-functionalized gold "virus-trap" nanostructures for accurate capture of SARS-CoV-2 and single-virus SERS detection. Nano Micro Lett. **13**, 1–13 (2021)
21. S.D. Bindesri, D.S. Alhatab, C.L. Brosseau: Development of an electrochemical surface-enhanced Raman spectroscopy (EC-SERS) fabric-based plasmonic sensor for point-of-care diagnostics. Analyst **143**, 4128–4135 (2018)
22. L. Liu, P.M. Pancorbo, T. Xiao, S. Noguchi, M. Marumi, H. Segawa, S. Karhadkar, J.G. de Pablo, K. Hiramatsu, Y. Kitahama: Highly scalable, wearable surface-enhanced Raman spectroscopy. Adv. Opt. Mater. **10**, 2200054 (2022)
23. J. Li, J. Wang, Y.S. Grewal, C.B. Howard, L.J. Raftery, S. Mahler, Y. Wang, M. Trau: Multiplexed SERS detection of soluble cancer protein biomarkers with gold–silver alloy nanoboxes and nanoyeast single-chain variable fragments. Anal. Chem. **90**, 10377–10384 (2018)
24. A. Kundu, R. Rani, A. Ahmad, A. Kumar, M. Raturi, T. Gupta, R. Khan, K.S. Hazra: Ultrasensitive and label-free detection of prognostic and diagnostic biomarkers of sepsis on a AgNP-laden black phosphorous-based SERS platform. Sens. Diagn. **1**, 449–459 (2022)
25. H. Kearns, R. Goodacre, L.E. Jamieson, D. Graham, K. Faulds: SERS detection of multiple antimicrobial-resistant pathogens using nanosensors. Anal. Chem. **89**, 12666–12673 (2017)
26. F.B. Schuch, R.A. Bulzing, J. Meyer, D. Vancampfort, J. Firth, B. Stubbs, I. Grabovac, P. Willeit, V.D.O. Tavares, V.C. Calegaro: Associations of moderate to vigorous physical activity and sedentary behavior with depressive and anxiety symptoms in self-isolating people during the COVID-19 pandemic: A cross-sectional survey in Brazil. Psychiatry Res. **292**, 113339 (2020)
27. E. Volz, V. Hill, J.T. McCrone, A. Price, D. Jorgensen, Á. O'Toole, J. Southgate, R. Johnson, B. Jackson, F.F. Nascimento: Evaluating the effects of SARS-CoV-2 spike mutation D614G on transmissibility and pathogenicity. Cell **184**, 64–75. e11 (2021)
28. J.M. Ferdinands, S. Rao, B.E. Dixon, P.K. Mitchell, M.B. DeSilva, S.A. Irving, N. Lewis, K. Natarajan, E. Stenehjem, S.J. Grannis: Waning 2-dose and 3-dose effectiveness of mRNA vaccines against COVID-19–associated emergency department and urgent care encounters and hospitalizations among adults during periods of Delta and Omicron variant predominance—VISION Network, 10 states, August 2021–January 2022. Morb. Mortal. Wkly. Rep. **71**, 255 (2022)
29. A. Newman, D. Smith, R.R. Ghai, R.M. Wallace, M.K. Torchetti, C. Loiacono, L.S. Murrell, A. Carpenter, S. Moroff, J.A. Rooney: First reported cases of SARS-CoV-2 infection in companion animals—New York, March–April 2020. Morb. Mortal. Wkly. Rep. **69**, 710 (2020)
30. Y. Yang, B. Xu, J. Murray, J. Haverstick, X. Chen, R.A. Tripp, Y. Zhao: Rapid and quantitative detection of respiratory viruses using surface-enhanced Raman spectroscopy and machine learning. Biosens. Bioelectron. **217**, 114721 (2022)
31. Z. Zhang, D. Li, X. Wang, Y. Wang, J. Lin, S. Jiang, Z. Wu, Y. He, X. Gao, Z. Zhu: Rapid detection of viruses: Based on silver nanoparticles modified with bromine ions and acetonitrile. Chem. Eng. J. **438**, 135589 (2022)

32. L. Ma, W. Zhang, L. Yin, Y. Li, J. Zhuang, L. Shen, S. Man: A SERS-signalled, CRISPR/Cas-powered bioassay for amplification-free and anti-interference detection of SARS-CoV-2 in foods and environmental samples using a single tube-in-tube vessel. J. Hazard. Mater. **452**, 131195 (2023)
33. B. Yin, Q. Zhang, X. Xia, C. Li, W.K.H. Ho, J. Yan, Y. Huang, H. Wu, P. Wang, C. Yi: A CRISPR-Cas12a integrated SERS nanoplatform with chimeric DNA/RNA hairpin guide for ultrasensitive nucleic acid detection. Theranostics **12**, 5914 (2022)
34. H. Georjon, A. Bernheim: The highly diverse antiphage defence systems of bacteria. Nat. Rev. Microbiol. **21**, 686–700 (2023)
35. S. Hameed, L. Xie, Y. Ying: Conventional and emerging detection techniques for pathogenic bacteria in food science: A review. Trends Food Sci. Technol. **81**, 61–73 (2018)
36. J. Xia, W. Li, M. Sun, H. Wang: Application of SERS in the Detection of Fungi, Bacteria and Viruses. Nanomaterials **12**, 3572 (2022)
37. X. Ren, W. Nam, P. Ghassemi, J.S. Strobl, I. Kim, W. Zhou, M. Agah: Scalable nanolaminated SERS multiwell cell culture assay. Microsyst. Nanoeng. **6**, 47 (2020)
38. C. Li, Y. Huang, X. Li, Y. Zhang, Q. Chen, Z. Ye, Z. Alqarni, S.E. Bell, Y. Xu: Towards practical and sustainable SERS: A review of recent developments in the construction of multifunctional enhancing substrates. J. Mater. Chem. C **9**, 11517–11552 (2021)
39. H. Wei, S.M.H. Abtahi, P.J. Vikesland: Plasmonic colorimetric and SERS sensors for environmental analysis. Environ. Sci.: Nano **2**, 120–135 (2015)
40. H. Chen, Z. Liu, S. Li, C. Su, X. Qiu, H. Zhong, Z. Guo: Fabrication of graphene and AuNP core polyaniline shell nanocomposites as multifunctional theranostic platforms for SERS real-time monitoring and chemo-photothermal therapy. Theranostics **6**, 1096 (2016)
41. S. Sarkar: Is 3D surface structuring always a prerequisite for effective SERS? Surf. Interfaces **33**, 102223 (2022)
42. E. Rho, M. Kim, S.H. Cho, B. Choi, H. Park, H. Jang, Y.S. Jung, S. Jo: Separation-free bacterial identification in arbitrary media via deep neural network-based SERS analysis. Biosens. Bioelectron. **202**, 113991 (2022)
43. L. Bi, X. Wang, X. Cao, L. Liu, C. Bai, Q. Zheng, J. Choo, L. Chen: SERS-active Au@Ag core-shell nanorod (Au@ AgNR) tags for ultrasensitive bacteria detection and antibiotic-susceptibility testing. Talanta **220**, 121397 (2020)
44. Y. Wang, H. Ni, H. Li, J. Chen, D. Zhang, L. Fu: Plasmonic microneedle arrays for rapid extraction, SERS detection, and inactivation of bacteria. Chem. Eng. J. **442**, 136140 (2022)
45. M. Bahram, T. Netherway: Fungi as mediators linking organisms and ecosystems. FEMS Microbiol. Rev. **46**, fuab058 (2022)
46. Y. Xu, F. Gu, S. Hu, Y. Wu, C. Wu, Y. Deng, B. Gu, Z. Chen, Y. Yang: A cell wall-targeted organic-inorganic hybrid nano-catcher for ultrafast capture and SERS detection of invasive fungi. Biosens. Bioelectron. **228**, 115173 (2023)
47. S. Hu, H. Kang, F. Gu, C. Wang, S. Cheng, W. Gong, L. Wang, B. Gu, Y. Yang: Rapid detection method for pathogenic Candida captured by magnetic nanoparticles and identified using SERS via AgNPs+. Int. J. Nanomed. 941–950 (2021)
48. F. Gu, S. Hu, Y. Wu, C. Wu, Y. Yang, B. Gu, H. Du: A SERS Platform for Rapid Detection of Drug Resistance of Non-*Candida albicans* Using $Fe_3O_4$@ PEI and Triangular Silver Nanoplates. Int. J. Nanomed. 3531–3541 (2022)
49. N. Gao, Q. Wang, J. Tang, S. Yao, H. Li, X. Yue, J. Fu, F. Zhong, T. Wang, J. Wang: Non-invasive SERS serum detection technology combined with multivariate statistical algorithm for simultaneous screening of cervical cancer and breast cancer. Anal. Bioanal. Chem. **413**, 4775–4784 (2021)
50. A.G. Berger, S.M. Restaino, I.M. White: Vertical-flow paper SERS system for therapeutic drug monitoring of flucytosine in serum. Anal. Chim. Acta **949**, 59–66 (2017)
51. A. Jaworska, S. Fornasaro, V. Sergo, A. Bonifacio: Potential of surface enhanced Raman spectroscopy (SERS) in therapeutic drug monitoring (TDM). A critical review. Biosensors **6**, 47 (2016)

52. M.J. Oliveira, S. Caetano, A. Dalot, F. Sabino, T.R. Calmeiro, E. Fortunato, R. Martins, E. Pereira, M. Prudêncio, H.J. Byrne: A simple polystyrene microfluidic device for sensitive and accurate SERS-based detection of infection by malaria parasites. Analyst **148**, 4053–4063 (2023)
53. K. Chen, C. Yuen, Y. Aniweh, P. Preiser, Q. Liu: Towards ultrasensitive malaria diagnosis using surface enhanced Raman spectroscopy. Sci. Rep. **6**, 20177 (2016)
54. P. DeBach, H.S. Smith: Effects of parasite population density on rate of change of host and parasite populations. Ecology **28**, 290–298 (1947)
55. C. Qiu, Z. Cheng, C. Lv, R. Wang, F. Yu: Development of bioorthogonal SERS imaging probe in biological and biomedical applications. Chin. Chem. Lett. **32**, 2369–2379 (2021)
56. L. Fabris: Gold-based SERS tags for biomedical imaging. J. Opt. **17**, 114002 (2015)
57. Q. Li, H. Huo, Y. Wu, L. Chen, L. Su, X. Zhang, J. Song, H. Yang: Design and Synthesis of SERS Materials for In Vivo Molecular Imaging and Biosensing. Adv. Sci. **10**, 2202051 (2023)
58. R.H. Lahr, P.J. Vikesland: Surface-enhanced Raman spectroscopy (SERS) cellular imaging of intracellulary biosynthesized gold nanoparticles. ACS Sustainable Chem. Eng. **2**, 1599–1608 (2014)
59. T. Köker, N. Tang, C. Tian, W. Zhang, X. Wang, R. Martel, F. Pinaud: Cellular imaging by targeted assembly of hot-spot SERS and photoacoustic nanoprobes using split-fluorescent protein scaffolds. Nat. Commun. **9**, 607 (2018)
60. Y. Zhang, D.J. de Aberasturi, M. Henriksen-Lacey, J. Langer, L.M. Liz-Marzán: Live-cell surface-enhanced Raman spectroscopy imaging of intracellular pH: From two dimensions to three dimensions. ACS Sens. **5**, 3194–3206 (2020)
61. M. Schütz, C.I. Müller, M. Salehi, C. Lambert, S. Schlücker: Design and synthesis of Raman reporter molecules for tissue imaging by immuno-SERS microscopy. J. Biophotonics **4**, 453–463 (2011)
62. M. Salehi, D. Steinigeweg, P. Ströbel, A. Marx, J. Packeisen, S. Schlücker: Rapid immuno-SERS microscopy for tissue imaging with single-nanoparticle sensitivity. J. Biophotonics **6**, 785–792 (2013)
63. Y. Zhou, J. Liu, T. Zheng, Y. Tian: Label-free SERS strategy for in situ monitoring and real-time imaging of Aβ aggregation process in live neurons and brain tissues. Anal. Chem. **92**, 5910–5920 (2020)
64. W. Duan, Q. Yue, Y. Liu, Y. Zhang, Q. Guo, C. Wang, S. Yin, D. Fan, W. Xu, J. Zhuang: A pH ratiometrically responsive surface enhanced resonance Raman scattering probe for tumor acidic margin delineation and image-guided surgery. Chem. Sci. **11**, 4397–4402 (2020)
65. Z. Du, Y. Qi, J. He, D. Zhong, M. Zhou: Recent advances in applications of nanoparticles in SERS in vivo imaging. Wiley Interdiscip. Rev. Nanomed. Nanobiotechnol. **13**, e1672 (2021)
66. X. Niu, H. Chen, Y. Wang, W. Wang, X. Sun, L. Chen: Upconversion fluorescence-SERS dual-mode tags for cellular and in vivo imaging. ACS Appl. Mater. Interfaces **6**, 5152–5160 (2014)
67. S. Bock, Y.-S. Choi, M. Kim, Y. Yun, X.-H. Pham, J. Kim, B. Seong, W. Kim, A. Jo, K.-M. Ham: Highly sensitive near-infrared SERS nanoprobes for in vivo imaging using gold-assembled silica nanoparticles with controllable nanogaps. J. Nanobiotechnol. **20**, 130 (2022)
68. X.-H. Pham, E. Hahm, T.H. Kim, H.-M. Kim, S.H. Lee, S.C. Lee, H. Kang, H.-Y. Lee, D.H. Jeong, H.S. Choi: Enzyme-amplified SERS immunoassay with Ag-Au bimetallic SERS hot spots. Nano Res. **13**, 3338–3346 (2020)
69. X.-H. Pham, V.-K. Tran, E. Hahm, Y.-H. Kim, J. Kim, W. Kim, B.-H. Jun: Synthesis of Gold-Platinum Core-Shell Nanoparticles Assembled on a Silica Template and Their Peroxidase Nanozyme Properties. Int. J. Mol. Sci. **23**, 6424 (2022)
70. L. Li, R. Jiang, B. Shan, Y. Lu, C. Zheng, M. Li: Near-infrared II plasmonic porous cubic nanoshells for in vivo noninvasive SERS visualization of sub-millimeter microtumors. Nat. Commun. **13**, 5249 (2022)
71. L.A. Lane, R. Xue, S. Nie: Emergence of two near-infrared windows for in vivo and intraoperative SERS. Curr. Opin. Chem. Biol. **45**, 95–103 (2018)

72. M.M. Joseph, N. Narayanan, J.B. Nair, V. Karunakaran, A.N. Ramya, P.T. Sujai, G. Saranya, J.S. Arya, V.M. Vijayan, K.K. Maiti: Exploring the margins of SERS in practical domain: An emerging diagnostic modality for modern biomedical applications. Biomaterials **181**, 140–181 (2018)
73. J. Wang, D. Liang, Q. Jin, J. Feng, X. Tang: Bioorthogonal SERS nanotags as a precision theranostic platform for in vivo SERS imaging and cancer photothermal therapy. Bioconjugate Chem. **31**, 182–193 (2020)
74. S. Wen, X. Miao, G.-C. Fan, T. Xu, L.-P. Jiang, P. Wu, C. Cai, J.-J. Zhu: Aptamer-conjugated au Nanocage/$SiO_2$ core–shell bifunctional nanoprobes with high stability and biocompatibility for cellular SERS imaging and near-infrared photothermal therapy. ACS Sens. **4**, 301–308 (2019)
75. A. Sarkar, S. Roy, P. Sanpui, A. Jaiswal: Plasmonic gold nanorattle impregnated chitosan nanocarrier for stimulus responsive theranostics. ACS Appl. Bio Mater. **2**, 4812–4825 (2019)
76. M.S. Strozyk, D.J. de Aberasturi, L.M. Liz-Marzan: Composite polymer colloids for SERS-based applications. Colloidal Synth. Plasmonic Nanomet. 821–844 (2020)
77. P. Dey, W. Olds, I. Blakey, K.J. Thurecht, E.L. Izake, P.M. Fredericks: SERS-based detection of barcoded gold nanoparticle assemblies from within animal tissue. J. Raman Spectrosc. **44**, 1659–1665 (2013)
78. A.H. Mo, P.B. Landon, K.S. Gomez, H. Kang, J. Lee, C. Zhang, W. Janetanakit, V. Sant, T. Lu, D.A. Colburn: Magnetically-responsive silica–gold nanobowls for targeted delivery and SERS-based sensing. Nanoscale **8**, 11840–11850 (2016)
79. F. Tian, J. Conde, C. Bao, Y. Chen, J. Curtin, D. Cui: Gold nanostars for efficient in vitro and in vivo real-time SERS detection and drug delivery via plasmonic-tunable Raman/FTIR imaging. Biomaterials **106**, 87–97 (2016)
80. X. Huang, B. Sheng, H. Tian, Q. Chen, Y. Yang, B. Bui, J. Pi, H. Cai, S. Chen, J. Zhang: Real-time SERS monitoring anticancer drug release along with SERS/MR imaging for pH-sensitive chemo-phototherapy. Acta Pharm. Sin. B **13**, 1303–1317 (2023)
81. C. Song, Y. Dou, L. Yuwen, Y. Sun, C. Dong, F. Li, Y. Yang, L. Wang: A gold nanoflower-based traceable drug delivery system for intracellular SERS imaging-guided targeted chemo-phototherapy. J. Mater. Chem. B **6**, 3030–3039 (2018)
82. M.-M. Chen, H.-L. Hao, W. Zhao, X. Zhao, H.-Y. Chen, J.-J. Xu: A plasmon-enhanced theranostic nanoplatform for synergistic chemo-phototherapy of hypoxic tumors in the NIR-II window. Chem. Sci. **12**, 10848–10854 (2021)
83. C. Song, F. Li, X. Guo, W. Chen, C. Dong, J. Zhang, J. Zhang, L. Wang: Gold nanostars for cancer cell-targeted SERS-imaging and NIR light-triggered plasmonic photothermal therapy (PPTT) in the first and second biological windows. J. Mater. Chem. B **7**, 2001–2008 (2019)
84. J. Feng, L. Chen, Y. Xia, J. Xing, Z. Li, Q. Qian, Y. Wang, A. Wu, L. Zeng, Y. Zhou: Bioconjugation of gold nanobipyramids for SERS detection and targeted photothermal therapy in breast cancer. ACS Biomater. Sci. Eng. **3**, 608–618 (2017)
85. Z. Liu, S. Li, Z. Yin, Z. Zhu, L. Chen, W. Tan, Z. Chen: Stabilizing enzymes in plasmonic silk film for synergistic therapy of in situ SERS identified bacteria. Adv. Sci. **9**, 2104576 (2022)
86. J. He, S. Hua, D. Zhang, K. Wang, X. Chen, M. Zhou: SERS/NIR-II optical nanoprobes for multidimensional tumor imaging from living subjects, pathology, and single cells and guided NIR-II photothermal therapy. Adv. Funct. Mater. **32**, 2208028 (2022)
87. J. Fares, M.Y. Fares, H.H. Khachfe, H.A. Salhab, Y. Fares: Molecular principles of metastasis: a hallmark of cancer revisited. Signal Transduction Targeted Ther. **5**, 28 (2020)
88. X. Qian, S. Nie, P.M. Champion, L.D. Ziegler: Surface-Enhanced Raman Nanoparticles for in-vivo Tumor Targeting and Spectroscopic Detection. AIP Conf. Proc. **1267**, 81–81 (2010)
89. M.F. Kircher, A.D.L. Zerda, J.V. Jokerst, C.L. Zavaleta, P.J. Kempen, E. Mittra, K. Pitter, R. Huang, C. Campos, F. Habte: A brain tumor molecular imaging strategy using a new triple-modality MRI-photoacoustic-Raman nanoparticle. Nat. Med. **18**, 829–834 (2012)
90. S. Harmsen, R. Huang, M.A. Wall, H. Karabeber, J.M. Samii, M. Spaliviero, J.R. White, S. Monette, R. O'Connor, K.L. Pitter: Surface-enhanced resonance Raman scattering nanostars for high-precision cancer imaging. Sci. Transl. Med. **7**, 271ra7 (2015)

91. Y. Wen, V.X. Truong, M. Li: Real-time intraoperative surface-enhanced Raman spectroscopy-guided thermosurgical eradication of residual microtumors in orthotopic breast cancer. Nano Lett. **21**, 3066–3074 (2021)
92. H. Liu, X. Gao, C. Xu, D. Liu: SERS tags for biomedical detection and bioimaging. Theranostics **12**, 1870 (2022)

# Chapter 14
# SERS Bioanalysis Based on Tagging and Responsive Probes




**Jun Cao, Wei Zhu, and Ai-Guo Shen**

**Abstract** This chapter describes the recent progress of SERS bioanalysis based on tagging and responsive probes. It is mainly divided into four sections, Sect. 14.1, overview of the advantages of SERS bioanalysis. Some examples of SERS bioanalysis based on tagging and responsive probes are explained in Sects. 14.2 and 14.3, which detailed explanation about the principle of tagging and responsive SERS probes and their application. Finally, challenges and prospects of this theme are given in Sect. 14.4.

**Keywords** SERS bioanalysis · Tagging · Responsive · Prospects

## 14.1 Overview of the Advantages of SERS Bioanalysis

Since Fleischmann et al. firstly observed surface enhanced Raman scattering (SERS) phenomenon, SERS gradually shined in bioanalysis because of their unbeatable advantages [1–3]. **First of all**, SERS technique has the advantages of high sensitivity that opened up the research boom for detecting ultra-low concentration biomolecules, even achieved the detection of single molecule using SERS technology [4]. **Second**, SERS technique exhibits high specificity for discriminating biomolecules because of "molecular fingerprint" with characteristic peaks, and Raman signals are increased by several orders of magnitude since molecules are usually adsorbed on the noble metal surface, thus SERS has been applied for detecting proteins, cytochrome, liposomes, and other varied biocomponents directly [3, 5]. **Third**, SERS is suitable for long-term imaging thanks to its negligible photobleaching, and it has been widely applied to imaging of cell, tissue, and in vivo living body, aiming for real time

J. Cao · W. Zhu (✉) · A.-G. Shen (✉)
School of Bioengineering and Health, Wuhan Textile University, Wuhan 430200, China
e-mail: weiz@wtu.edu.cn

A.-G. Shen
e-mail: agshen@whu.edu.cn

© The Author(s), under exclusive license to Springer Nature Singapore Pte Ltd. 2024

M. Procházka et al. (eds.), *Surface- and Tip-Enhanced Raman Scattering Spectroscopy*,
https://doi.org/10.1007/978-981-97-5818-0_14

monitoring dynamic biological processes [6]. **Fourth**, SERS-based probes are inherently suitable for advanced multiplex bioanalysis, owing to their quite narrow band's widths (~ 1 nm), while abroad used fluorescent bands can be as wide as 50 nm [7, 8]. Moreover, Raman scattering is excited by single laser, thereby being more suitable for simultaneous multiplex bioanalysis when compared to fluorescent tags with different wavelength exciting light. Quite specially, Raman spectroscopy exhibits great advantage in bioanalysis as relatively low Raman signal toward water [9].

In this chapter, we aimed to summarize the development of SERS in bioanalysis based on two strategies, tagging and responsive mechanism. With the help of specific binding, such as antigen–antibody, aptamer, etc., SERS based on tagging strategy has emerged as a spectacular tool for qualitative bioanalysis, and it has been widely studied to label multiscale biotargets from biomolecules, organelles, cells, and living organism [10–12]. And, SERS tagging bioanalysis has achieved serial progress in disease detection, and intraoperative guidance for in vivo tumor resection [13]. Furthermore, this strategy based on SERS nanotags developed with multiplex labeled capabilities for the selective tagging of a wide range of biomedically important targets, achieved wildly multiplex detection and multiplex imaging of biomarkers, cancer cells, etc. [14]. To extend the applicability of SERS spectroscopy and improve detection accuracy in bioanalysis, SERS based on responsive probes provide significant advantages for simultaneous and qualitative/quantitative analysis of multiple targets in complex biological systems, especially in unnecessarily of pretreatment for separation. Responsive SERS probes exhibit concentration-dependent changes in signal intensity or Raman shift that modulated by the chemical activity of the target (redox, catalysis, reactivity, etc.), thereby possessing great advantages for monitoring some pathological indicators, such as reactive oxygen species (ROS), pH and other pathological microenvironmental parameters, and they are also wildly applied for biosensing detection or bioimaging [15–17].

## 14.2 SERS Bioanalysis Based on Tagging Probes

In the past dozen years, SERS has emerged as a spectacular tool for qualitative bioanalysis with the development of tagging strategy. This strategy is paving the way for SERS bioanalysis from SERS enhanced substrate to bio-specific exogenous nanotags, accompanied by great improvements in sensitivity and selectivity and thus accuracy as well. Nanotags have been developed with multiplex capabilities for the selective tagging of a wide range of biomedically important targets, such as bacteria, cancer cells, and individual biomolecules.

Generally, SERS bioanalysis based on tagging is common served as the signal output, which is similar to the traditional fluorescent tags, with the help of SERS nanotags and relying on the high-resolution property of Raman signal to realize simultaneous detection of multiple species. Such strategy is commonly seen in surface/interface label detection, or in label imaging studies of cells, biological tissues, etc.

### *14.2.1 The Principle of Tagging SERS Probes*

High quality of tagging system is dependent on SERS probes with strong enhanced ability, characteristic signal output, and specific targeting. A typical SERS tag is composed of four parts: a metal nano-substrate, an organic Raman reporter molecule, a protection shell, and targeting molecules [12, 14]. The following will introduce the research progress based on the principle of tagging SERS probes from four aspects of the substrates, reporters, shell materials, and targeting ligand (Fig. 14.1).

#### 14.2.1.1 SERS Substrate Building for Strongly Raman Activity

Notal metal materials (Au, Ag, Cu, etc.), semiconductor materials (ZnO, CuO, $TiO_2$, etc.), and series of 2D materials (graphene, g-$C_3N_4$, etc.) have been demonstrated to enhance Raman signal of molecules adsorbed on these materials by electromagnetic enhancement or chemical enhancement [12, 18]. Generally, the principle of the strong SERS activity mainly confirms the electromagnetic enhancement mechanism by producing local electric field enhancement on the NPs surface from the localized surface plasmon resonance (LSPR). Therefore, the size, geometry and type of nanomaterials have been also proved to affect the Raman enhancement due to different distribution of LSPR, thereby greatly expanding the development of SERS substrate as well as providing convenience for the analysis of various biological samples [19, 20].

In addition, SERS substrate for the practical application depends on the suitable SPR absorption, one factor is that Raman intensity relates with surface plasmon resonance of the metal substrate and the frequency of incident laser, another is to avoid the interference of spontaneous fluorescence of biological endogenous substances, thus near-infrared laser will widely use as excitation laser for biological samples. In the following section, several typical noble metal nanoparticles will serve as example of SERS substrate, and the effects of size, morphology, and composition on their SPR will be detailed discussed.

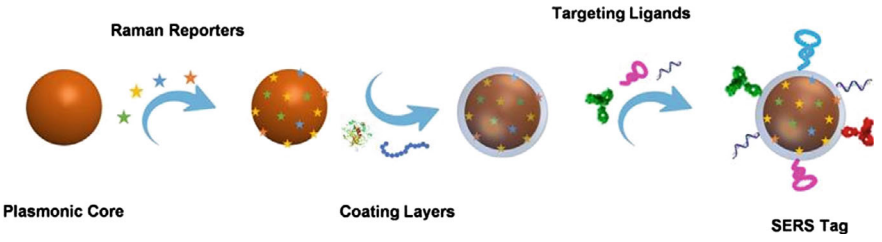



**Fig. 14.1** Design of traditional tagging SERS probes, consisting of a plasmonic core, adsorbed Raman reporters on the plasmonic surface, a biocompatible layer, and targeting ligands. Reproduced from Ref. [14] with the permission

**SERS Substrate Based on Single Metal Nanoparticles**. According to long time verification, Au and Ag NPs are the most widely used as SERS substrates for simple and primary research on biological samples because their simple preparation methods, easy control of particle size, uniformity, good stability and so on. Among them, Frens, Lee-Meisel, and Leopold method have been verified as the admitted preparation methods of spherical Au and Ag NPs by reducing $HAuCl_4$ with trisodium citrate at high temperature, reducing silver nitrate with trisodium citrate at high temperature, reducing silver nitrate with hydroxylamine hydrochloride at room temperature, respectively.

SERS signal enhancement will promote with the regulation of the electromagnetic field of notal metal particle to match the exciting laser, including by increasing particle's size, altering particle's morphology, and adjusting particle's constitutes. As shown in Fig. 14.2a, the surface plasmon vibration frequency of gold and silver NPs occurs red shift with the increase of particle size, and Raman intensity have been also augmented by increasing particle size [21]. Nevertheless, the increase of particle size will lead to greater radiation damping effect, thus reducing the enhancement factor. Of note, the SERS signal generated by silver NPs is 10–100 times stronger than that of gold NPs, whereas Au NPs are extensive selected for SERS substrate in biological application because of better structural stability, lower toxicity than Ag NPs. Moreover, gold/silver composites (gold core silver shell NPs, silver core gold shell NPs, and gold silver alloy NPs) exhibit stronger SERS enhancement effect than individual silver or gold NPs. As shown in Fig. 14.2b, researchers evaluated the SERS enhancing properties of Au@Ag core–shell NP colloids with three different laser lines (532, 633, and 785 nm). Importantly, such core–shell NPs also exhibit a higher SERS efficiency than Ag NPs of similar size under near-infrared excitation. In addition, SERS enhanced property relates with particle's morphology, and Au nanorods exhibit superior SERS activity than Au nanospheres because of one order of magnitude of the absorption coefficient higher than that of gold nanospheres [22]. As shown in Fig. 14.2c, the aspect ratio of gold nanorods can be adjusted from 2.4 to 5.6 by changing the amount of silver nitrate in the synthesis, and the SPR peak corresponding to the aspect ratio direction will move from the visible region to the near-infrared region [23], and their excitation wavelengths of SERS substrate might be more suitable for bioanalytical and bioimaging applications with deeper optical penetration. Besides, Au nanostars, Au nanoflower, or Au nanocubes have also been developed to produce highly sensitive substrates for SERS tags. Taking the anisotropic flower as an example, the anisotropic flower like nanomaterials have stronger and more stable SERS signals than spherical NPs. One reason is that the radius of curvature at the ends of their branches shrinks sharply, and the resulting super local electromagnetic field has a very large enhancement factor, which is usually called "tip effect". And the other is that the ends of their branches have a very large specific surface area, which can connect more molecules and cause local signal enhancement.

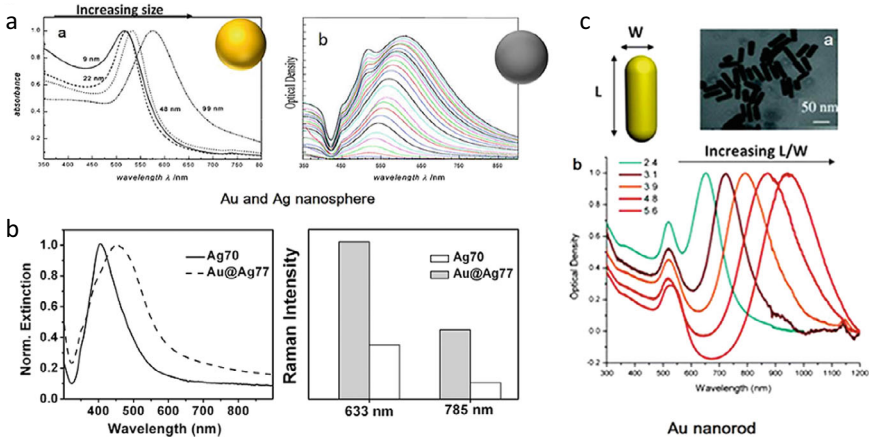



**Fig. 14.2** Influence factors of Raman intensity by adjusting surface plasmon resonance absorption wavelengths. **a** Increasing size of Au and Ag NPs. Reproduced from Ref. [21] with the permission. **b** Coupling plasmonic property by gold/silver composites. Reproduced from Ref. [22] with the permission. **c** Adjusting the aspect ratio of gold nanorods. Reproduced from Ref. [23] with the permission

**SERS Substrate Based on "Hot Spots": Metal Nanoparticles Rich in Nanogaps**. Nanogaps originated from metallic nanoparticles between plasmonic core and plasmonic shell, and the Raman signal efficiently can be greatly enhanced when Raman reporters placed in the gap. Lim et al. synthesized a structure with ultra-small (less than 1 nm), gold NPs acted as the core, and DNA were modified to act as a bridge, the gold shell growed into the outside through reduction of $HAuCl_4$ by hydroxylamine hydrochloride [24]. In order to enhance the Raman signal effectively, three different lengths of DNA were modified to regulate the size of the nanogaps. This study showed the stronger the Raman signal with the smaller of the gap (Fig. 14.3a). Based on this discovery, Ye et al., have designed and synthesized a series of nanogap enhanced Raman tags (GERTs), which consisted of multi-shell nanostructure [25]. First, the uniform gold cores were coated with a layer of Raman reporters as seeds to grow the first layer of gold shell. Next, the obtained particles were coated with a Raman reporter layer again, and then underwent a second gold shell growth to form a double shell nanostructure. By repeating this process, these particles become nanostructures with three or more shells. In this ingenious design, 1, 4-phenyldithiol (BDT), as a Raman reporter, can contribute more Raman signals than general SERS nanotags in terms of the content. At the same time, BDT, as an insulating layer, provides conditions for generating more shells (Fig. 14.3b). Furthermore, Ye's group have reported another kind of ultra-bright nanogap enhanced Raman tags (p-GERTs), which exhibited strong electromagnetic hot spots from the inner sub-nanogap and the outer petal like shell structure, large surface area, and Raman scattering cross section of reporter molecules [26]. TEM images confirmed that by there was a uniform internal gap between gold core and rough shell structure (shown by the red arrow in Fig. 14.3c)

in a single p-GERTs, which was determined by the thickness of the monolayer of embedded 4-NBT molecules. Different from s-GERTs 2 with a complete and smooth outer gold shell, a large number of 1–3 nm nanogaps (shown by the yellow arrow in Fig. 14.3c) were formed in the rough petal-like structure within the gold shell of p-GERTs, which were defined as external nanogaps. The Raman enhancement factor of these GERTs is more than $5 \times 10^9$, and the detection sensitivity is as low as that of single NPs. Only 370 μW laser was used to achieve high-resolution cell imaging within 6 s, and sentinel lymph node imaging with high contrast (SNR 80) and wide area ($3.2 \times 2.8$ cm$^2$) within 52 s.

**SERS Substrate Based on "Hot Spots": Dimer and Multimer**. When metallic NPs occur the mild aggregation to form nanoparticle dimers and small clusters, which are commonly called "hot spots". And, the enhancement factor at hot spots can be greater than $10^{10}$, upon to obtain single-molecule detection [4]. Therefore, metal NP aggregates have also been developed to produce highly sensitive substrates for SERS tags. Moreover, the aggregated NPs have new absorption bands toward the long-wavelength region for Ag clusters around 500–600 nm and Au clusters around 700–900 nm, and the latter is coincident with the longer laser wavelengths used for in vivo investigations. Precise control of the shape and size of the aggregated NPs is essential to fabricate homogeneous, nanosized probes with reproducible signals. Therefore, the moderate aggregation strategy has been widely investigated.

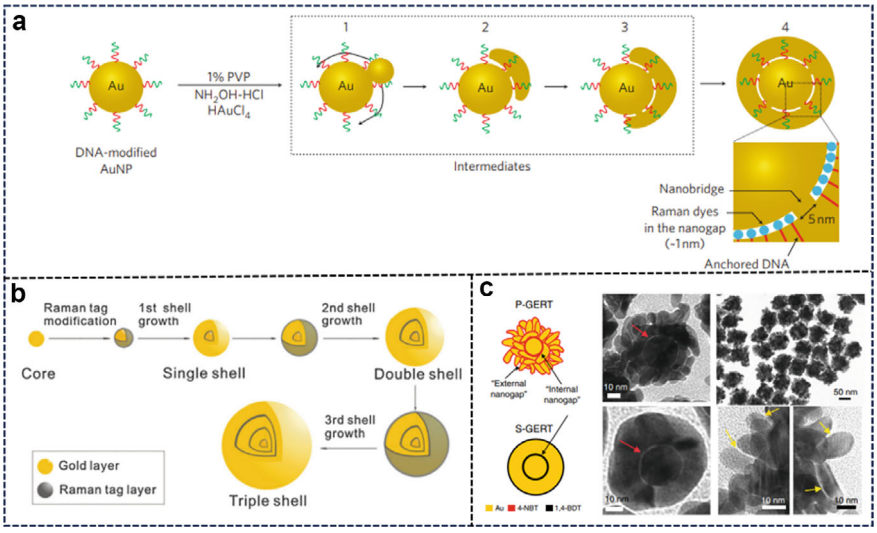



**Fig. 14.3** **a** Surface DNA-mediated synthesis and characterization of DNA-anchored nanobridged nanogap particles. Reproduced from Ref. [24] with the permission. **b** Schematic illustration of the synthesis of nanomatryoshkas (NMs) with single, double and triple Au shell layers. Reproduced from Ref. [25] with the permission. **c** Schematic diagrams and representative TEM images of GERTs with a petal-like shell (P-GERTs), and GERTs with a smooth-surface shell (S-GERTs). Reproduced from Ref. [26] with the permission

Salt-induced aggregation is the most common aggregation method by destroying the electrostatic repulsion between NPs [27]. As shown in Fig. 14.4a, Ren et al. proposed a simple SERS detection protocol using iodide-modified Ag nanoparticles (Ag IMNPs), and $MgSO_4$ was served to enhance the interaction of DNA with the Ag IMNPs, so that strong and reproducible SERS signals could be detected by aggregation of SERS tags [27]. Tan et al. used NaCl solution to induce the aggregation of Ag nanoparticles, and the SERS intensity was greatly enhanced. In their study, they further used polyvinylpyrrolidone (PVP) to control the aggregation and improve the tags' chemical stability (Fig. 14.4b) [28].

As shown in Fig. 14.4c, it is a more controllable method to load the smaller noble metal NPs on the large-size materials to form the aggregation coating layer. In this method, silica, polystyrene and polymer spheres were often used as carriers for gold

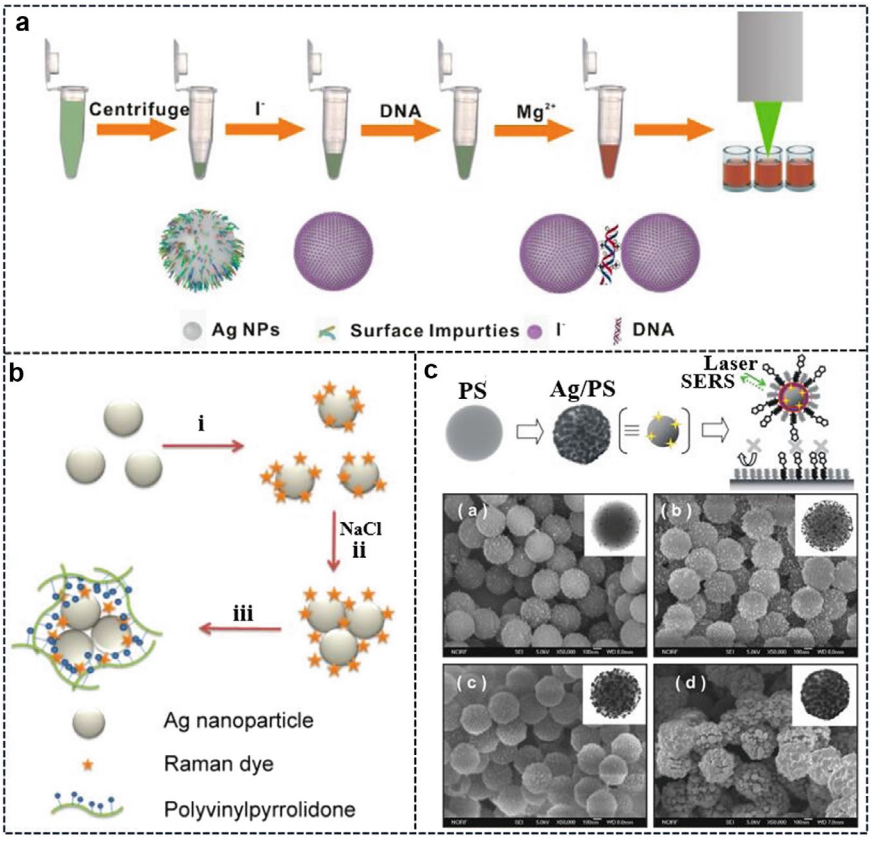



**Fig. 14.4** Influence factors of Raman intensity by constructing SERS "hotspots". **a** $MgSO_4$-induced aggregation. Reproduced from Ref. [27] with the permission. **b** NaCl-induced aggregation. Reproduced from Ref. [28] with the permission. **c** Polymer acted as carrier for loading Ag NPs. Reproduced from Ref. [29] with the permission

NPs aggregation [29, 30]. When the surface of polymer support was treated with 3-mercaptopropyltrimethoxysilicon (MPTMS) or other methods to produce a large number of –SH groups, a layer of noble metal NPs could be directly grown on the surface by in situ synthesis, and the number and size of the aggregates could also be adjusted by adding the amount of $HAuCl_4$ or $AgNO_3$ [31]. The SERS nanotags prepared by this method usually have strong SERS response and good signal stability. With the increase of the number of particles in the aggregate, the SERS intensity of a single SERS nanotags increases greatly.

#### 14.2.1.2 The Optimization of Raman Reporters for Fingerprint Recognition

As known, Raman spectrometer served as a characterization tool to identify different molecular structures by fingerprint spectrum. Thereout, unique Raman signal can be obvious discovered and read, thereby series of molecules with Raman characteristic signals have been studied as Raman reporters. More important, typical SERS nanotags have also acted as a kind of signal output technology for tagging bioanalysis, especially with sensitive, specific and stable (3S) optical signals. How to select Raman reporters with a characteristic Raman spectral signature, it has attracted many researchers interesting. Several principles apply to the selection of Raman reporters and the deposition method used to prepare SERS tags with strong, stable multiplex signals: (1) Generally, optical enhancement requires that Raman reporter molecules be attached on or near the surface of SERS substrates because chemical enhancement requires chemical bonding and electromagnetic enhancement is strongly distance-dependent. Meanwhile, the interaction between the reporters and metals should be strong enough to prevent desorption during further modification or use. Therefore, nitrogen- or sulfur-containing molecules are often used because of their high affinity to silver and gold [32]. (2) The reporter molecules must have a relatively large Raman scattering cross section, which helps produce strong SERS signals [33]. (3) When the excitation-laser's wavelength matches the optical absorption of Raman reporters, then surface-enhanced resonant Raman scattering (SERRS) occurs, and the enhancement factor may be further enhanced 100 times. So, in some circumstances, the absorption wavelength should also be taken into consideration when choosing an ideal reporter [34]. (4) The signal level is also influenced by the number of reporters encapsulated in the tag. Good coating methods that can form a dense, uniform reporter layer on the substrates will result in a higher signal [12]. (5) Ideal Raman reporters prefer with relatively characteristic peaks to avoid signal overlap of the tags and endogenous molecules [3, 8, 15]. Currently, a large number of Raman reporter molecules for SERS have been selected, which are usually divided into three categories: nitrogen-containing cationic molecules, sulfur-containing molecules and sulfhydryl small molecules. Their advantages and disadvantages are shown in Table 14.1.

Specially, tiny triple bond, including alkynes (C≡C), cyano bond (C≡N), and metal carbonyl bond (metal-C≡O), are preferred as excellent Raman reporters

**Table 14.1** Classification and characteristics of typical Raman reporter molecules for SERS

| Category | Connection mode | Advantages | Disadvantages | Examples |
|---|---|---|---|---|
| Nitrogen containing cationic molecule | Electrostatic adsorption and N–Au (Ag) bonding | Low cost, large Raman cross section and easy to implement SERRS | Weak affinity, poor signal stability and difficulty in subsequent modification | Crystal violet (CV), rhodamine 6G (R6G), Nile blue (NB) |
| Sulfur molecule | S–Au (Ag) bonding | Strong affinity, easy to implement SERRS and simple subsequent modification | High price, few species, difficult to realize self-assembly monolayer | Malachite green (mg) and 3.3′ diethylthioaldehyde tricarbocyanine iodide |
| Sulfhydryl molecule | S–Au (Ag) bonding | Low price, strong affinity and simple Raman characteristic peak | Small scattering cross section, no SERRS potential | *p*-mercaptobenzoic acid, *p*-mercaptoaniline |

because of their characteristic Raman shifts in the region of 1800–2800 $cm^{-1}$, which is nearly non-existent inside cells or tissues, thereby avoiding the spectral overlapping from biological endogenous molecules effectively [35, 36]. Even more excitedly, the triple bonds exhibit narrow peak widths (< 2 nm), thus providing super-capacity with spectral barcoding technology for multiplexed detection in complex bio-system [36]. Inspired by these advantages, numerous novel triple bond-based Raman reporters are progressively emerging as powerful optical labels, playing a vital role in monitoring some bio-molecular activities. In the following section, we will summarize the classification of triple bond and the evolutive history of each other as Raman reporters, especially in novel SERS reporters.

**Metal Carbonyl Bond (Metal-C≡O)**. Metal carbonyl bond belongs to triple bond due to the unique electron distribution, which lone pair electrons of C atom enter the empty d orbital of metal atom, thereby forming a feedback $\pi$ bond to the CO ligand by the d electron of the metal central atom entering the $\pi$ anti-bonding orbital of CO ligand. Olivo et al. first explored metal carbonyl-gold NPs conjugates for enhancing the metal carbonyl Raman intensity with the help of SERS property [37]. They reported that an organometallic osmium carbonyl cluster, $Os_3(CO)_{10}(m\text{-}H)_2$, onto the surface of gold NPs (henceforth designated as "OM-NP"), which could significantly enhance the inherently weak Raman signal of the metal carbonyl CO stretching vibrations (Fig. 14.5a), and the CO intensity was increased by over four orders of magnitude (a factor of $\approx$ 15,000).

**Cyano Bond (C≡N)**. Interestingly, C≡N bond is the most polar of the above triple bonds, and novel organic molecules containing cyano group have been wildly applied

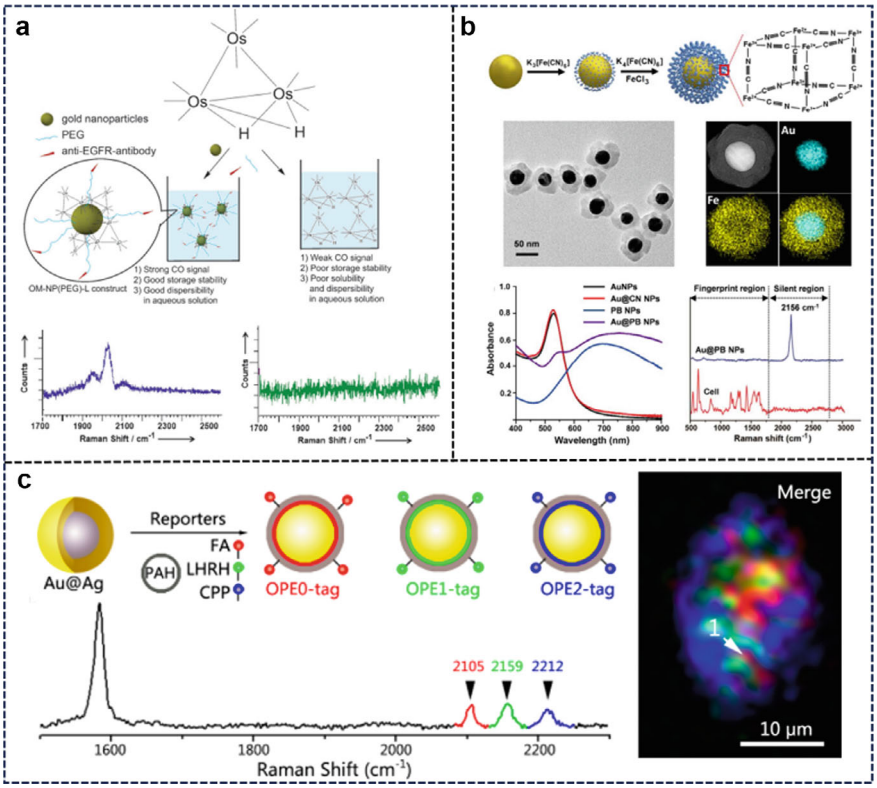



**Fig. 14.5** Novel SERS tags based on triple bond. **a** Organometallic osmium carbonyl cluster, $Os_3(CO)_{10}(m\text{-}H)_2$, onto the surface of gold NPs OM-NP as novel SERS tag. Reproduced from Ref. [37] with the permission. **b** Prussian blue (PB) containing with C≡N bond for novel SERS tag. Reproduced from Ref. [35] with the permission. **c** 4-ethynylphenylmercaptan derivatives with alkynes (C≡C) for novel SERS tags. Reproduced from Ref. [8] with the permission

as Raman reporters. 4-cyano-benzenethiol (MBN) has been well known because of owning cyano group and thiol group, as well as MBN performs Raman emission at 2200 $cm^{-1}$ that falls in a spectroscopically silent region of the Raman spectrum of a cell and exhibits strong chemisorption capability with plasmonic metal substrate to guarantee strong Raman signal output [38]. Liu et al. reported Prussian blue (PB) with abundant cyano-bonds can be employed as a highly sensitive and background-free resonant Raman reporter (Fig. 14.5b) [35].

**Alkynes (C≡C).** Encouragingly, alkynes were gradually served as attractive triple bonded Raman reporters since researchers discovered that nearly all mammalian cells exist a Raman silent region. Alkyne-tag Raman imaging (ATRI) has been reported for simultaneous multicolor imaging of biotargets in live cells by Raman microscopy, giving a great example for potential Raman label labeled with small molecules in biological research [39]. Our group constructed the SERS palette

modulated by alkyne based on the reasonably designed 4-ethynylphenylmercaptan derivatives (Fig. 14.5c) [8]. Among them, Au@Ag NPs were used as the core of optical reinforcement, polyacrylamine is used as the shell for protecting and bonding. Even for pigment rich plant cells (such as pollen), alkyne encoded SERS nanotags can be highly recognized in two-dimensional distribution without strong organic interference caused by resonance-enhanced Raman scattering or autofluorescence. In addition, when the alkynyl group is located in the para position of mercaptobenzene ring, the alkynyl containing Raman reporter has narrow emission, tunable (2100–2300 $cm^{-1}$) and greatly enhanced Raman signal. This research induce researchers more attention to design and synthesis some ideal Raman reporter molecules, bringing new opportunities for the development and application of SERS nanotags and other Raman scattering tags.

#### 14.2.1.3 Protective Layer for Stability and Biocompatibility

Core–shell SERS tags have attracted increasing research attention due to their outstanding properties as follows: (1) Versatility: A core–shell nanoparticle consists of an inner core and an outer shell made of different material; therefore, the combination of different properties of different materials leads to several novel properties of core–shell materials, for example the shell could act as signal source. (2) Tunability: The properties of core–shell nanoparticles can be easily and dramatically tuned by changing the size, shape, morphology, and components of core, as well as thickness, shape, and components of shell materials. (3) Stability and dispersibility: The coated shell can protect the nanoparticles from aggregation, sintering, or the effect of other reagents. (4) Biocompatibility: the biocompatibility is one of the important issues from the perspective of practical bioapplication, and the biocompatibility of core–shell nanoparticles can be improved by coating with silica ($SiO_2$), polymer, etc.

On the basis of the coating materials, core–shell nanoparticles in SERS can be broadly categorized into two following types: metal shell and nonmetal shell. The metal shells have been discussed in the above gap SERS tags. Many efforts have been made to modify biocompatible molecules onto SERS notal core, the types of protective shells reported include biomolecular shell, polymer shell, silica shell, carbon shell and so on.

**Biomolecule**. The shell of biomacromolecule usually improves the biocompatibility of SERS nanotags and is beneficial to the subsequent modification of biological functional molecules. Bovine serum albumin (BSA) is the most frequently used biomacromolecule coating material, which can bind to gold nanoparticles through electrostatic interaction. If glutaraldehyde was added, the amino groups in BSA would be crosslinked, which could further enhance the stability of the nanolabel. Xie et al. ever used d-BSA as the coating shell of gold nanoflower substrate, and also encapsulated a large number of Rhodamine B as Raman reporter molecules in the pores of three-dimensional structure protein to prepare SERS nanotags with strong stability and excellent biocompatibility, as shown in Fig. 14.6a [40]. Liposome is a

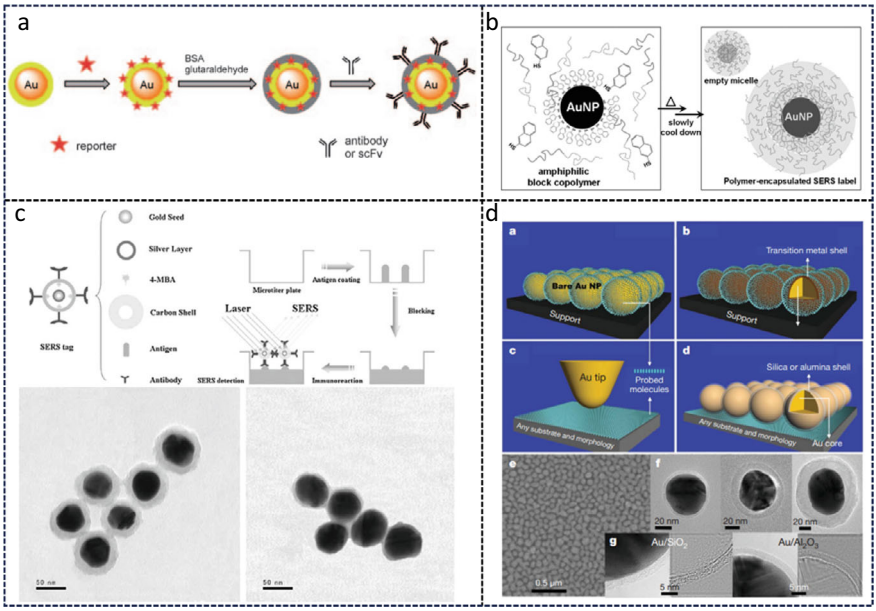



**Fig. 14.6** **a** Biomolecules used as protective shell to construct SERS tag. Reproduced from Ref. [40] with the permission. **b** SERS tag based on polymer-encapsulation. Reproduced from Ref. [41] with the permission. **c** SERS tag based on triplex Au@Ag@C core–shell NPs. Reproduced from Ref. [42] with the permission. **d** SHINERS tag based on transition metal shell coated Au NPs. Reproduced from Ref. [43] with the permission

kind of synthetic phospholipid bilayer similar to biomass membrane, which has good biocompatibility. In recent years, there are many studies trying to use liposomes as the protective shell of SERS nanotags.

**Polymer**. HS-PEG polymer with good biocompatibility has been modified into SERS nanotags to make protective shell. In addition to HS-PEG, polymer molecules such as PVP and chitosan are often used as the protective shell of SERS nanotags due to their good biocompatibility and biodegradability. In 2009, Yang et al. used a novel amphiphilic block polymer (PS-PAA60, PS154-b-PAA60) as the coating materials of SERS nanotags [41]. The self-assembly process of this polymer is very simple, and a protective shell with uniform thickness can be formed by simple operation of heating and cooling in a reaction vessel (as shown in Fig. 14.6b). Our group developed monodisperse, easily grafted and biocompatible SERS nanotagging materials, which were composed of reinforced bimetallic substrates Au@Ag NPs, three kinds of self-assembly organic monolayers and the outermost carbon shell (Fig. 14.6c) [42]. Furthermore, Prussian blue shell used as layer to protect the SERS tags, of which Prussian blue is composed of a large number of cyanogen groups, using as SERS signal of the triple bond. In the study, the metal-cyanide coordination bond

could be formed between CN from the precursors of Prussian blue and Au nanoparticles, and then the Prussian blue shell layer could be in situ grown on the surface of Au nanoparticles, and the prepared Au@PB nanoparticles could be used as stable SERS tags containing triple bond [35].

**Shell-Isolated Nanoparticle-Enhanced Raman Spectroscopy (SHINERS) Based on Silica Shell**. Tian's group developed a new generation of Raman technique in 2010, known as "shell-isolated nanoparticle-enhanced Raman spectroscopy" (SHINERS) to overcome the limitations of materials and morphology generalities in SERS [43]. In general, gold or silver nanoparticles are employed with a layer of ultrathin and pinhole-free inert silica shell. Each Au core-inert shell nanoparticle can be considered as a TERS tip. Under a laser spot, the shell-isolated nanoparticles monolayer is equal to thousands of tips, thus the obtained Raman signal is very strong (Fig. 14.6d). Besides, the ultrathin and pinhole-free shell is used to avoid the direct contact of molecules with gold or silver NPs, thus the obtained signal is just from the interested species adsorbed on the substrate. In principle, this method can be used for the surface with any material and morphology, thus high quality of Raman spectrum can be obtained from single-crystals of platinum, gold, or silicon. Furthermore, yeast cells, pesticide residues on fruits, and even biological tissues can also be studied or detected. These applications attest that SHINERS has very wide applicability. Simultaneously, SHINERS is also becoming a promising and powerful tool in various fields, such as surface science, material science, biological analysis, pharmaceutical analysis, food safety, and environmental protection. Furthermore, based on the shell-isolated mode, researchers have also developed a variety of shells such as alumina ($Al_2O_3$), manganese oxide, titanium oxide ($TiO_2$), carbon, and graphene for SHINERS, which further broadens the scope of its applications [43].

#### 14.2.1.4 Modification of Targeting Moieties for Specific Tagging

Based on the physical mechanism of SERS, one can design nanostructures for bioanalytical SERS for improved performance while keeping the physical and chemical parameters constant. However, the biological system is very complex and dynamic. When such fabricated nanostructures are exposed to biological environments such as cells, biological fluids, tissues, or animals, the performance of the nanomaterials is typically compromised due to the unforeseen physical–chemical phenomena in physiological environments (e.g., corrosion, aggregation, unspecific absorption of biomolecules). In this case, modification of targeting moiety can make SERS tags become a practical and reliable tagging bioanalysis technique for cells, biological fluids, tissues, or animals. Above all, targeting moieties on the NP surface are key to specific biomarker detection, multiplexing, and to reduce non-specific binding.

**Antibodies**. Antibodies are the most conventional choice for receptor targeting due to their ease of availability and high selectivity for a given molecular target. Wang et al. also showed the application of bioorthogonal SERS in the multiplexed detection of three biomarkers using gold nanoflowers with heterogeneous targeting moieties,

including anti-CD44 antibodies for CD44 receptors [44]. Moreover, some disease-related biomarkers have been labeled by SERS tags grafted with the corresponding antibodies.

**Peptides**. Cell-penetrating peptides (CPPs) are widely utilized to overcome the cell membrane barrier to deliver therapeutic molecules into cells due to a strong electrostatic interaction with the negatively charged components of the membrane. CPPs have been widely used to modify the SERS active nanoparticles to improve the delivering efficiency of these nanoparticles into cells for intracellular SERS analysis [45]. In order to label nucleus using SERS tag, nuclear-localization signal (NLS) peptides have been modified to help nanoparticles pass through the barrier on the membrane via a signal and energy dependent process. The most frequently used NLS are PKKKRKV, CGGGPKKKRKVGG, etc. Besides, other peptide sequences have been also reported for SERS targeting modification, for example, mitochondrial-targeting peptide sequences (MLALLGWWWFFSRKKC) can be used for preparing probes for the mitochondrial SERS imaging [46].

**Aptamer**. Recently, aptamers are being investigated as a viable alternative to more traditional antibody targeting due to their low immunogenicity and low cost of production. A strategy is developed to functionalize SERS NPs with DNA aptamers, which target Mucin1 (MUC1) in human breast cancer (BC) [47]. Gold nanoflowers with heterogeneous targeting moieties of AS1411 aptamer for SERS imaging of nucleolin (Fig. 14.7a). An ultrasensitive method for surface enhanced Raman scattering (SERS) detection of prostate-specific antigens (PSAs) was established based on the aptamer directed core–satellite nanostructures [48].

**Small Molecules**. Receptor agonists such as folate, hyaluronic acid, etc. are also useful targeting moieties albeit with less selectivity than antibodies. Our group reported on the time-dependent changes of cell nuclei as well as membrane receptor proteins during apoptosis by a stereoscopic description of the intrinsic chemical nature of nuclei and the precise localization of folate (FA) and luteinizing hormone-releasing hormone (LHRH) on the membrane under highly confocal conditions (Fig. 14.7b) [49]. Targeting organelles have also attracted more researchers' attention, and series of targeting molecules have been discovered. For example, 4-(2-hydroxyethyl) morpholine and N, N-dimethylethylenediamine are two commonly used lysosomal targeting groups, and both of them have been used for the surface decoration of notal metal nanoparticles. Triphenylphosphine (TPP) as the ligand for mitochondria targeting, and Lim et al. successfully achieved SERS detecting of the mitochondria using triphenylphosphine-modified gold nanoparticles (Fig. 14.7c) [50].

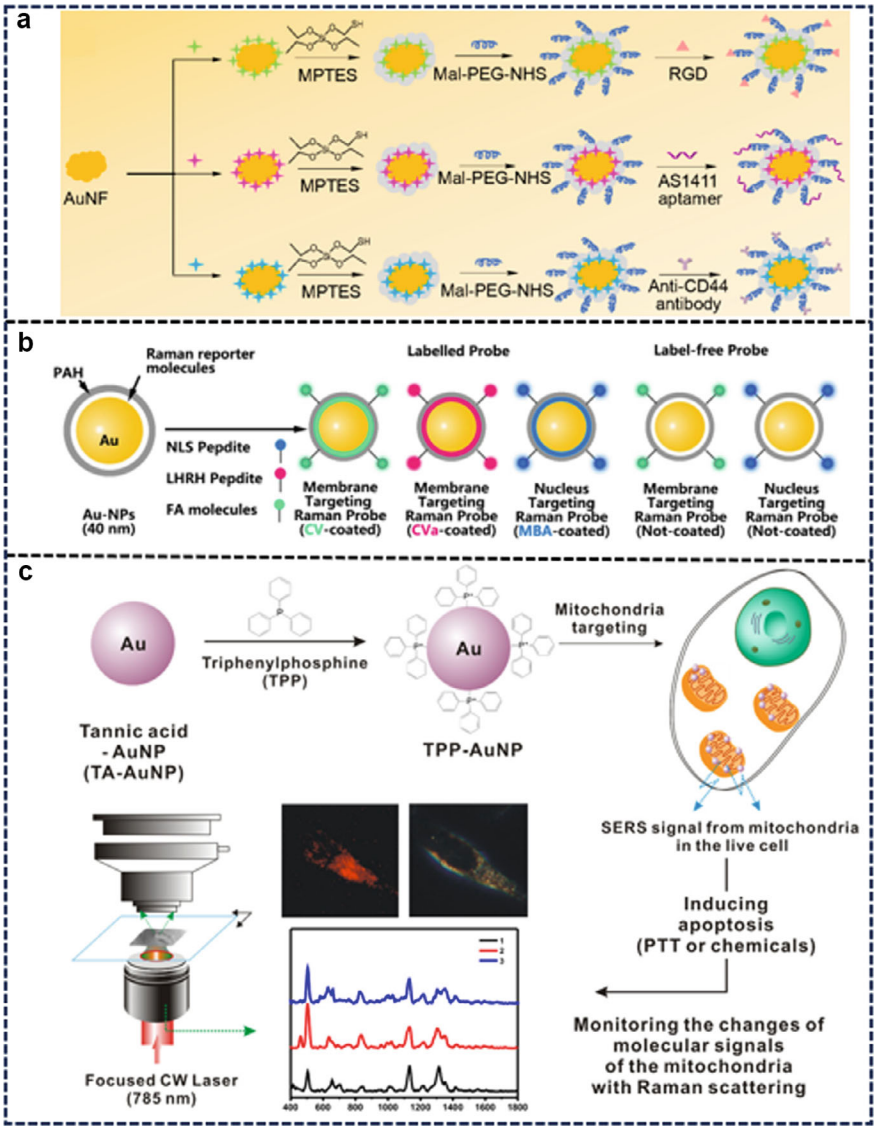



**Fig. 14.7** **a** Anti-CD44 antibody, AS1411 aptamer, RGD used as targeting moieties, respectively. Reproduced from Ref. [47] with the permission. **b** SERS tag with peptides for targeting label. Reproduced from Ref. [49] with the permission. **c** Small molecules of TPP acted as mitochondria targeting moiety. Reproduced from Ref. [50] with the permission

### *14.2.2 SERS Nanotags for Bio-detection*

Developing a sensitive and specific method for analyzing biomolecules has been still hot research, aiming for a comprehensive understanding of biological processes and early diagnosis of disease. Significantly, the life processes involve the dynamic changes in the conformation, distribution, and interaction of various biomolecules, such as proteins, nucleic acids, and metabolites, in both time and space. SERS tags has been successfully used to determine the biomolecular structure, the conformation, and the interaction between molecules. The advances in detecting biomolecules using SERS tags will be discussed in this part.

#### 14.2.2.1 Detection of Biomarkers with SERS Tags

Biomarkers such as DNAs, miRNAs, proteins, and other biomolecules have been investigated for early cancer diagnosis and prognosis. The specificity and sensitivity of the SERS tag make it possible for accurate detection of the physiologically relevant analytes in complex biological environment. As discussed in above section, the SERS tags are labeled with corresponding recognition molecules (such as antibodies, aptamers, and molecules) to allow specific detection of some important biomolecules with tagging strategy using Raman signals. With this concept, tagging detection platforms based on the SERS tags have also been developed with superior multiplexing capability and high sensitivity. The following part will introduce the detection of biomarkers with SERS tags detailly.

**DNA**. Rapid and accurate detection of DNA has become a powerful tool for early cancer diagnosis. The Bell group obtained the first SERS spectra for all the DNA/RNA mononucleotides with Ag colloids using $MgSO_4$ as aggregating reagent [51]. Mirkin et al. first achieved detection of DNA using SERS tags, and they proposed the sandwich assay for multiplexed detection of oligonucleotide targets with gold nanoparticle probes labeled with oligonucleotides and Raman-active dyes [52]. Wang et al. developed a new class SERS-based lateral flow assay (LFA) to simultaneously detect dual DNA markers as illustrated in Fig. 14.8a [53]. They obtained quantitatively evaluation of the dual DNA markers using DNA probes to label SERS nanotags. They also employed target DNA, associated with Kaposi's sarcoma-associated herpesvirus (KSHV) and bacillary angiomatosis (BA) to validate the detection capability of this SERS-based LFA strip. The LOD for KSHV and BA, determined by method, were estimated to be 0.043 and 0.074 pM, respectively. To accurately detect the specific DNA in biological fluids using SERS tags, a magnetic bead (MB) for magnetic separation is an effective strategy. Sandwich-like structures are formed to capture DNA in the homogeneous solution, of which probe-immobilized MB, the reporter probe-tied SERS tags, and the specific DNA targets. As a result, the detectable Raman signals can be used for DNA analysis [54]. To improve the detection sensitivity of DNA, researchers have also proposed some novel platforms to combine amplification strategies with SERS tags. Polymerase chain reaction (PCR)

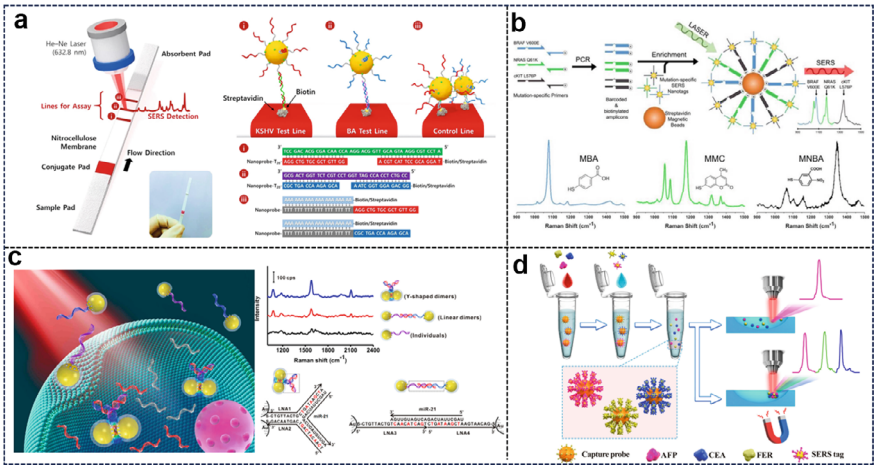



**Fig. 14.8** **a** SERS tags for the detection of nucleic acid biomarkers. Reproduced from Ref. [53] with the permission. **b** PCR/SERS assay for multiplex specific detection of tumor DNA. Reproduced from Ref. [55] with the permission. **c** Construction of SERS hotpot for the detection of mRNA. Reproduced from Ref. [56] with the permission. **d** Multiplex SERS assay based on SERS tags with magnetic force for multi-target protein biomarkers detection. Reproduced from Ref. [57] with the permission

is a traditional technology for nucleic acid detection. As shown in Fig. 14.8b, Matt et al. successfully employed to specifically detect three important melanoma mutations in multiplex, genotype cell lines and ctDNA from serum samples by SERS tags with the simplicity of standard PCR [55].

**miRNA**. Recently, miRNAs have emerged as a novel kind of biomarker since their aberrant expressions are associated with a variety of diseases, such as cancers, genetic disorders, and neurological issues. Numerous efforts have been made for multiple miRNAs detections with SERS tags. Examining micro-RNA sequences by deconvoluting SERS spectra by the characteristic bands of the four nucleotide bases has been performed by Abell et al. Highly sensitive miRNA assays would be built by combining the amplification strategy with SERS tags, in which Raman intensities of SERS tags were used for miRNA quantification. Koo et al. was described for simultaneously detecting promising next-generation RNA biomarkers in real-time polymerase chain reaction with SERS tags within 80 min [58]. This assay involved the use of multiplexed isothermal RT-RPA to amplify RNA targets in the sample before labeling the amplicons with different synthesized SERS nanotags for rapid one-pot SERS detection. The test of clinical urine and tissue specimens demonstrated this method was capable of highly sensitive (200 zmol). Building hot spots in the SERS platform is an effective strategy to improve sensing sensitivity. SERS tagging strategy for further building hotspot are employed to detect miRNA. Liu et al. designed a Y-shape duplex by LNA sequences hybridizing with the target miRNA (Fig. 14.8c), of which the LNA modified SERS tags turned to be dimer in the presence of target miRNA [56].

**Proteins**. Many proteins serve as a characteristic biomarker for a specific disease. Measurement of biomarkers in blood such as protein biomarkers is commonly considered as a simple way to screen patients and also enable routine monitoring. Porter and co-workers developed SERS-based sandwich immunoassay platform for protein biomarkers, providing a sound basis for the development SERS-based immunoassay. Proteins such as prostate-specific antigen (PSA), hepatitis B surface antigen (HBsAg), and carcinoma embryonic antigen (CEA) have been used as cancer biomarkers. By incorporating high sensitivity SERS tags and specific immunoassays, Liu et al. proposed a SERS-based immunoassay for the HBsAg [57], the antibodies on the SERS tags could bind HBsAg with high specificity. Our group reported simultaneous m-SERS detection of AFP, CEA or FER markers to improve the accuracy of liver cancer diagnosis (Fig. 14.8d). Typically, three triple bonds (C≡N and C≡C) coded SERS tags with well separated Raman shifts were synthesized, and the corresponding antibodies (antiAFP1, antiCEA1, and antiFER1) were further modified into SERS tags. Moreover, antibodies (antiAFP2, antiCEA2, and antiFER2) were bitched conjugated on the surface of magnetic beads (MBs). This assay based on the 3D packing of SERS tags absorbed MBs with the reaction of specific antigens, and the limit of detection (LOD) of AFP, CEA, and FER was counted at 0.15, 20, and 4 pg/mL, respectively [59].

#### 14.2.2.2 Detection of Cells with SERS Tags

SERS is an ultrasensitive vibrational spectroscopic technique to detect molecules on or near the surface of plasmonic nanostructures. Therefore, SERS tags have been proved to detect biomolecules in targeting position. The key questions of all life activities are found in the cell for answers, so cells play vital role in life. SERS-active nanoparticles have been widely studied for cell identification and classification, as well as for analyzing cellular living processes, cellular stress responses, and nanoparticle and cell interactions, and SERS tagging strategy plays a vital role in the fundamental studies for supplying abundant detailed information of cells.

**Organelles**. Our group firstly presented a novel nuclear targeting SERS tag based on nuclear localization signal (NLS) peptide functionalized gold nanoparticles. The gold nanoparticles successfully entered the cell nucleus and achieved real-time SERS detection of chemical information of the nucleus (Fig. 14.9a) [60]. Lim et al. monitored changes in intracellular molecular signatures during mitochondrially mediated apoptosis in real time using triphenylphosphine-modified gold nanoparticles, which were localized successfully to the mitochondria and greatly enhanced to obtain the intrinsic Raman scattering spectrum of mitochondria and cytochrome c in the live cell [50].

**Cancer Cell**. SERS possesses the capacity to distinguish cancer cells from healthy ones when coupled with multivariate data analysis. SERS spectra of cultured cancer cells or blood plasma of cancer patients served to distinguish cancer and health cells. The vibrational signatures have been associated with diagnostic capabilities due to

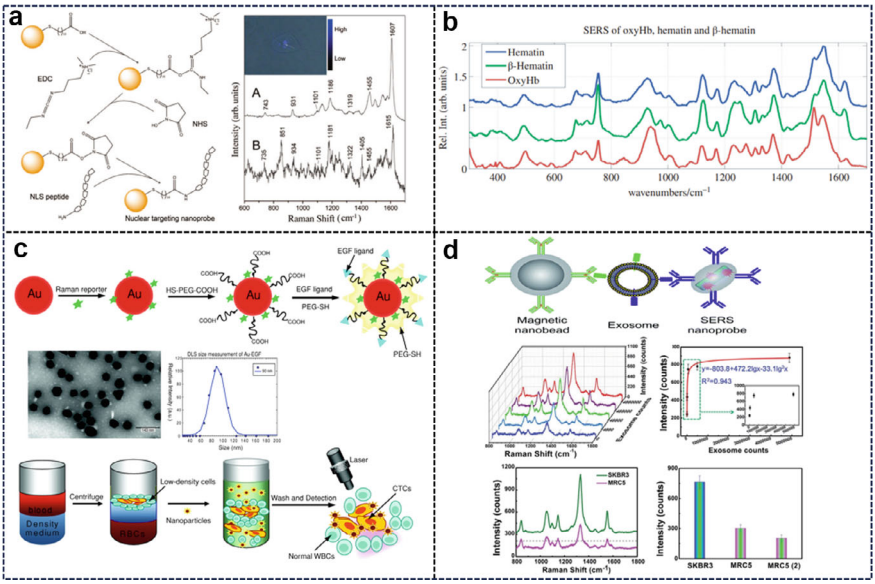



**Fig. 14.9** **a** SERS spectral detection of targeting cell nucleus. Reproduced from Ref. [60] with the permission. **b** SERS spectra of cancer cell. Reproduced from Ref. [61] with the permission. **c** CTCs detection using SERS tagging probe. Reproduced from Ref. [62] with the permission. **d** Sandwich assay for detecting exosome based on SERS tags with magnetic force. Reproduced from Ref. [63] with the permission

altered levels of nucleic acids, proteins, saccharides, or lipids in circulating body fluids. Interestingly, adenine or to the C–N bond of quaternary ammonium groups showed the Raman peak at ~ 725 $cm^{-1}$, attributed to lipid bilayer components. Other anomalous band at 655 or 638 $cm^{-1}$, assigning to the C–S stretch in cysteine or a tyrosine mode, respectively (Fig. 14.9b). Ziegler et al. demonstrated that the SERS spectra of renal cancer cells changed continuously over the 2 h duration, and the species that contributed to the time-dependent SERS spectra are dominantly adenine, hypoxanthine, and adenosine. Most of the SERS-based approaches for the identification of cancer cells have centered on the use of antibody-labeled metal nanoparticles that exhibit selective binding for cancer cell surface biomarkers [61].

**Circulating Tumor Cell**. Detection of the circulating tumor cells (CTCs) has been used as a diagnostic of the disease progression or prognostic of the tumor response to treatment, owing to CTC related well with the aggressiveness and increased metastatic ability of the disease. Natan and co-workers firstly obtained CTC detection in blood samples using SERS nanotags with magnetic beads, and a limit of detection around 50 spiked tumor cells per milliliter with a confidence of 99.7% [64]. Qian et al., further demonstrated CTC detection on real clinical samples of human patients of head and neck cancer in addition to healthy controls [65]. The authors found a strong correlation between the number of SERS tags and disease progression. Recent

improvements in the SERS tag-based assay have allowed detection of one tumor cell out of approximately 10 million normal cells, which is equivalent to the detection sensitivity of reverse transcription-polymerase chain reaction (RT-PCR).

**Exosomes**. Exosomes with nanoscale size, originate from different type of cells, are recommended as novel disease markers because of carrying molecular information from proteins, lipids, and nucleic acids within cells. Meanwhile they served as intercellular communication vectors in physiological and pathological processes. Various works based on SERS tags have been reported for detecting exosomes. Cui's group firstly reported to detect tumor-derived exosomes using the designed SERS tags, of which a sandwich-type immunocomplex formed by the SERS tag, exosome, and MB after conjugating with anti-CD63 and anti-HER2 antibodies in presence of a target exosome [7]. Similarly, Zhang's group achieved the detection of exosomes using a cholesterol-modified SERS probe combined with epithelial cell adhesion molecule (EpCAM) aptamer-modified MBs, and a LOD of MCF-7 cells-derived exosomes was $1.1 \times 10^2$ particles/μL (Fig. 14.9c) [62].

To identify different types of exosomes for obtaining accurate cancer detection, Wang et al. reported a simultaneous detecting method of multiple kinds of exosomes by three kinds of SERS probes [63]. In detail, MBs functionalized with aptamer CD63 captured most kinds of exosomes, and SERS probes were modified with specific aptamers for targeting exosomes. A sandwich assay formed by the target exosome, MB, and the corresponding kind of SERS probes, while the other non-specific probes remain in the suspension. Consequently, a decreased SERS signal will be recorded in the supernatant, indicating the presence of the target exosomes (Fig. 14.9d).

#### 14.2.2.3 Detection of Pathogens with SERS Tags

The identification and timely detection of pathogenic bacteria is very important because many diseases are caused by bacterial infection or contamination. Wang et al. used the synthesized SERS substrate for bacteria detection at a low concentration of 10 CFU/mL with great signal reproducibility. They also accomplished differentiation of three key pathogens (*E. coli* O157, *S. typhimurium*, and *Staphylococcus aureus*) including live and dead cells, using canonical variate analysis (CVA) in conjunction with Raman spectra. Then, an immunomagnetic SERS assay based on silica-coated magnetic probes and SERS nanotags was developed to detect two key pathogens, *Salmonella enterica* serovar Typhimurium and *S. aureus* [66]. They could detect the pathogen at cell concentration of $10^3$ CFU/mL, demonstrating high sensitivity and specificity of the SERS nanotag for pathogen detection. Rapid detection of pathogens has also achieved by the advanced SERS tags, such as, the targeted detection of a single bacterial pathogen *S. aureus* was achieved by combining the high sensitivity of SERS tags with the high specificity of single-domain antibodies (sdAbs). Significantly, silica-encapsulated SERS tags combined with three successful surface conjugation strategies to achieve the detection of a single bacterium using SERS with the Salmonella-specific tail spike protein.

### *14.2.3 SERS Nanotags for Bioimaging*

Bioimaging has gained constant attention for its application in bioanalysis for describing biological structure, real-time tracing various biologically relevant species, monitoring dynamic bio-behavior, and so on. SERS-active nanotags exhibit superior bioimaging function than other bioimaging technologies due to their ultra-sensitivity, specificity, multiplexing, biocompatibility, and photostability. For bioimaging, SERS tags have been used as competitive imaging agents for both in vitro and in vivo bioimaging. In the following part, we will focus on discussing the recent progress of in vitro and in vivo bioimaging using SERS nanotags.

#### 14.2.3.1 In Vitro Imaging with SERS Tags

In vitro imaging of biomarkers in cell, bacteria, and tissue samples using SERS nanotags is wildly studied by many researchers.

**Cell Imaging**. Cell bioimaging plays a vital role in the fundamental studies for bioanalysis that can supply abundant detailed information on the cellular surface biomarkers, interactions, dynamics, organelles, and microenvironments. Firstly, SERS tags were used for accurate imaging of the cellular biomarkers, so that for better understanding the related biological events. Wen et al. fabricated SERS nanotags based on AuNC/$SiO_2$/Apt for targeted SERS imaging and PTT of nucleolin-overexpressing cancer cells, of which Au nanocage as SERS-active substrate, 4-MBA as Raman reporter, $SiO_2$ as a protective shell, and aptamer AS1411 as recognition unit [67]. High-intensitive SERS tags can potentially use to image of living cell with bright imaging quality, Duan's group reported a new strategy to synthesize core–shell metal nanoparticles with an interior, Raman tag-encoded nanogap to generate a high SERS enhancement, nanoparticle templated self-assembly of amphiphilic block copolymers as well as the localized metal precursor reduction via redox-active polymer brushes to perform SERS imaging of living cells (Fig. 14.10a) [68]. Besides, ultrabright gap-enhanced SERS tags have been developed by Nam's and Ye's groups for cell imaging [14]. To avoid signal overlapping between Raman reporters and endogenous molecules, triple bond, including alkyne, nitrile, and metal carbonyl have been developed as Raman tags possessing characteristic peaks in the Raman silent region (2000–2700 $cm^{-1}$ range). Olivo et al. designed a metal carbonyl based SERS tag by combining osmium carbonyl clusters with Au nanoparticles and used the enhanced CO signal at 2030 $cm^{-1}$ to perform high-contrast live-cell imaging [37].

Compared with fluorescence microscopy, single component imaging by SERS is not advantageous, SERS tags possess the capacity of multiplex imaging with single wavelength excitation, and simultaneously with much narrower bandwidth of SERS peaks than that of fluorescence. For an efficient SERS-based multiplex imaging, our group carefully designed three 4-ethynylbenzenethiol derivatives (OPE molecules) with different Raman peak position of the alkyne group. Then, we achieved three color interference-free SERS multiplex cellular imaging by modifying the three

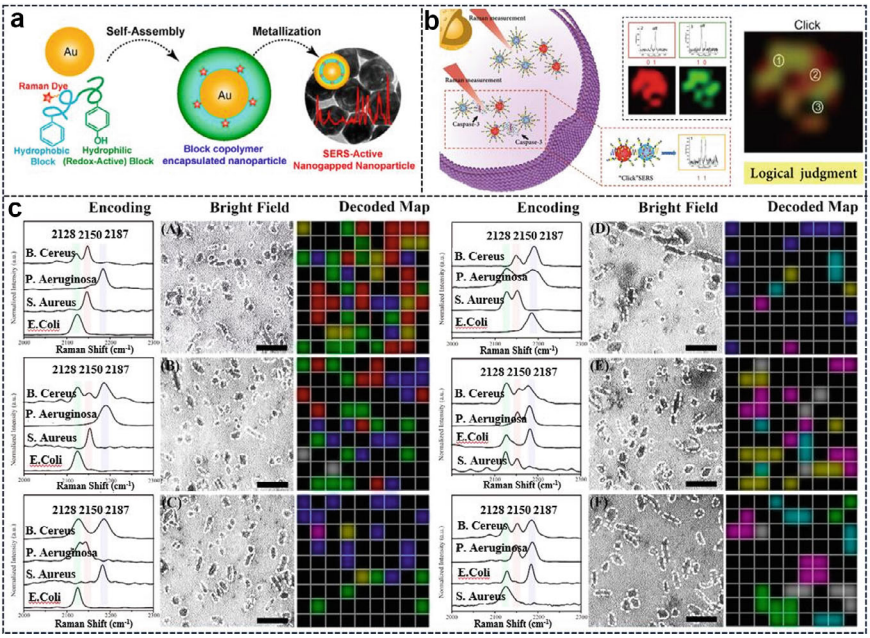



**Fig. 14.10** **a** SERS imaging of living cells by Raman tag with high SERS enhancement. Reproduced from Ref. [68] with the permission. **b** Precise imaging of caspase-3 in cell based on "promoted Click" SERS tagging method. Reproduced from Ref. [69] with the permission. **c** Super-multiplex bacteria imaging using SERS tagging probe. Reproduced from Ref. [70] with the permission

SERS tags with different receptors to anchor to different positions of the cell [8]. Subsequently, our group developed novel readout techniques for precise cell imaging. "Click" SERS, based on triple bond-containing reporters-encoded SERS-active NPs, achieved accurate cellular imaging under double exposure that different with "sole code related to sole target" [71]. Moreover, we proposed "Promoted Click" SERS based on mutually confirmed logical judgment with two spliced SERS emissions and their relative intensity, and then we successfully achieved more precise imaging of caspase-3 in cell (Fig. 14.10b) [69].

**Bacteria Imaging**. SERS-based bacterial imaging is mainly developed with the help of identification unit-conjugated SERS nanotags. Choo et al. reported a fast Raman spectral mapping technique for fast detection of bacterial pathogens. They prepared a poly (L-lysine)-coated plasmonic substrate for bacteria capture, and antibody-conjugated SERS nanotags used to label bacterial pathogens with reliable SERS imaging [72]. Our group have achieved the simultaneously multiplex imaging of micrometer-sized bacteria by the as-prepared three distinct SERS tags the bacteria-specific aptamers. Moreover, we adjusted SERS emissions of Au@PB by simply replacing the original $Fe^{2+}/Fe^{3+}$ with other metal ions (i.e., $Pb^{2+}$, $Co^{2+}$, $Cu^{2+}$), and then we developed a super-multiplex bacteria barcoding model to an encoding

capacity of $2^n - 1$, $n$ represented the number of SERS emission (Fig. 14.10c) [70]. Recently, smart SERS tags with multifunction for bacteria imaging, and elimination triggered many researchers' interesting, Liu's group reported the Au@PB NPs were not only served as a SERS tag but also as an antibacterial agent due to their photothermal effect. Liu et al. illustrated an integrated theranostic system for imaging, and precision killing of drug resistant bacteria based on photoactive silver nanoagents [73]. In order to improve synchronous anti-bacterial activity of drug-resistant bacteria, our group developed highly effective antibacterial agents to destroy biofilms and eradicate bacteria based on poly(4-cyanostyrene)@silver@polylysine nanocomposites, which polylysine (PLL) could rapidly capture the biofilms and exhibit excellent antibacterial efficacy together with decorated silver (Ag) nanoparticles (NPs) through the charge effect and $Ag^+$ release, and poly(4-cyanostyrene) with biological silent Raman imaging capacity is able to illustrate the relationship between antibacterial efficiency and biofilm breakage [74].

**Tissue Imaging**. The biological tissue is closely related to the physiological function of the organism, especially the pathological changes of the tissue will directly lead to the physiological function abnormality of the organism, and it precedes the morphological pathological changes. Therefore, providing imaging strategy about the tissue structure of organisms is of great significance. Schlücker et al. demonstrated the first realization of SERS tags for in situ antigen imaging in tissue samples [75]. By incubating the PSA antibody-modified SERS tags with the tissue samples, the localization of PSA in epithelial tissue was monitored based on the characteristic Raman signals of SERS labels. And then, Schlücker's group further realized the two-color imaging of p63 and PSA on prostate tissue based on two different SERS labels comprising silica-coated gold nanoparticle clusters and Raman reporters [76].

In clinical, immunological analysis of tissue exhibited great practical value in pathology, which could provide comprehensive information about cellular structure, micro-environmental condition, differences of bio-molecular components, and it was tractable for carrying out retrospective study within long preserved tissue. Among them, immunological proteins within tissue slices have become significant tool for clinical analysis, meanwhile, Raman immunological analysis based on SERS tags has also obtained great development in this filed. By coupling Raman probes with specific antibodies, triple bonded Raman reporters have achieved EpCAM or EGFR imaging within tumor slice. For practical biomedical diagnosis, it is often necessary to detect multiple components simultaneously to improve diagnostic sensitivity and specificity. Therefore, it is vital to develop probes with excellent multi-color properties for clinical diagnosis. Liu et al. proposed simultaneously pathological imaging method for HER2, ER, PR and EGFR in breast cancer tumor tissues, using high-resolution triple bonded SERS probes, after conjugating with specific antibodies [77]. Recently, Ye's group reported a rational strategy for predicting combined drugs of combined immune checkpoint (ICP) inhibitors based on supermultiplexed SERS imaging and correlation network analysis. In their report, they demonstrated one-shot ten-color imaging of ICPs with high spectral resolution in clinical biopsies of

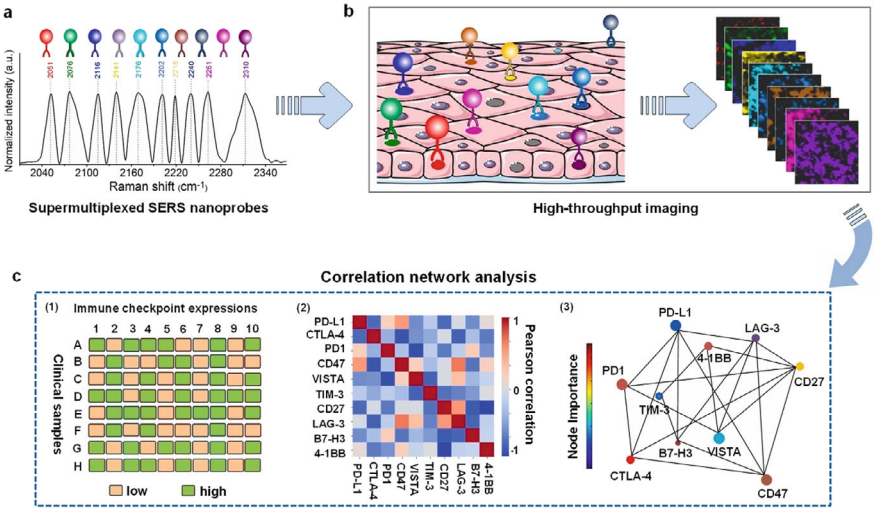



**Fig. 14.11** Schematic illustration of multiplexed SERS nanoprobes for high-throughput tissue imaging

breast cancer tissues based on antibodies tagging silent SERS tags, suggesting highly heterogeneous expression patterns of ICPs across tumor subtypes (Fig. 14.11) [78].

### 14.2.3.2 In Vivo Imaging with SERS Tags

Since Nie et al. pioneered the development of biocompatible SERS nanoparticles for in vivo tumor targeting, various researches have further reported SERS nanoparticles could be used in tumor targeting, medical imaging, and guided surgical applications in living animals.

**Targeting SERS Imaging of Specific Disease**. SERS tags can be able to accumulate in tumors by receptor targeting and/or the EPR effect. Gambhir et al. firstly reported whole-body deep-tissue imaging after tail-vein injection of tumor targeting SERS biotag [79]. Kircher and his co-workers have also been successfully imaged premalignant lesions of pancreatic and prostatic neoplasia by their as-designed SERRS probe with the high sensitivity, in which the SERRS nanostars contain a star-shaped gold core, a resonant Raman reporter, and a silica layer [80]. Classically, Gambhir et al. demonstrate the ability of Raman spectroscopy to separate the spectral fingerprints of up to 10 different types of surface enhanced Raman scattering (SERS) nanoparticles in a living mouse after s.c. injection. Significantly, they simultaneously injected the five most intense and spectrally unique SERS nanoparticles i.v. to image their natural accumulation in the liver. All five types of SERS nanoparticles were successfully identified and spectrally separated using our optimized noninvasive Raman imaging system (Fig. 14.12a). As the result, this work performed the potential for

multiplexed imaging in living subjects in cases in which several targeted SERS tags could offer better detection of multiple biomarkers associated with a specific disease [81]. Kircher et al. has attempted high precision visualization of the true extent of malignant brain tumors using RGD-peptide-conjugated surface-enhanced resonance Raman spectroscopy (SERRS) nanoparticles, and the RGD-SERRS nanoparticles afforded a major improvement in visualization of the true extent and the diffuse margins of the main tumor [82].

**Intraoperative SERS Imaging of Cancer**. Surgery is the first line of treatment for numerous cancer patients, and it also provides the strongest advantage among many cancers where surgical resection of the tumor leads to 45% survival. For a successful surgery to be achieved, precise confirming of tumor tissue region and clearing tumor margin is of great significant for the surgeon to remove the entire tumor. SERS imaging offers opportunities to achieve intraoperative tumor margin and residual tumor detection for surgical guidance with a higher specificity, sensitivity and spatial resolution. Significantly, recent studies demonstrated that intraoperative SERS imaging could accurately identify tumor margins to guide surgery.

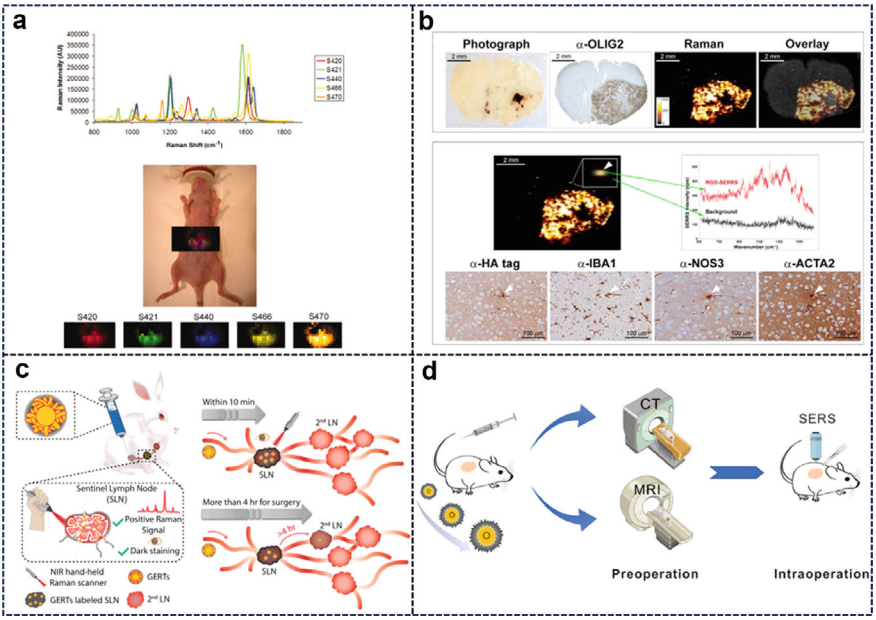



**Fig. 14.12** **a** Multiplexed imaging in living subjects by the targeted SERS tags. Reproduced from Ref. [81] with the permission. **b** SERS imaging for guiding brain tumor resections based on the targeted SERS tag. Reproduced from Ref. [83] with the permission. **c** Accurate detection of sentinel lymph node (SLN) by gap-enhanced Raman tags (GERTs) Reproduced from Ref. [84] with the permission. **d** Accurate preoperative CT/MRI diagnosis and intraoperative Raman imaging-guide resection of cancers by gadolinium-loaded gap-enhanced Raman tags (Gd-GERTs). Reproduced from Ref. [85] with the permission

Kircher's group developed a hand-held Raman scanner for the guidance of brain tumor resections (Fig. 14.12b) [83]. They used mice with implanted glioblastomas for the demonstration as this particular cancer has 80–90% of recurrence in the same area, so incomplete resections are a major problem for this disease. Recently, Ye et al. obtained the accurate positioning of sentinel lymph node (SLN) by their synthesized gap-enhanced Raman tags (GERTs), and the ultra-high sensitivity of GERTs (detection limit is $0.5 \times 10^{-12}$ M) allows detection of labeled SLNs before surgery, thereby providing preoperative positioning information for minimally invasive surgery (Fig. 14.12c) [84]. Recently, SERS-guided theranostic platforms based on multi-modality have reported to accurately help delineate the margins of tumors intraoperatively. For example, Ye et al. designed mesoporous silica gadolinium-loaded gap-enhanced Raman tags (Gd-GERTs) accurate preoperative CT/MRI diagnosis and intraoperative Raman imaging-guide resection of cancers (Fig. 14.12d) [85]. Additionally, novel SERRS probe has also been designed as a dual-modality contrast agent for combined SERS and PA imaging to delineate brain tumor margin.

**Theranostics Based on SERS Imaging Guided Multimodal Therapy**. Theranostic systems include accurate diagnosis and timely effective therapeutics in a single platform, and there were various works reported to improve the survival rates and life quality of patients. SERS-guided multimodal theranostic systems have obtained new possibilities for the development of theranostics, this part will be detailed reviewed.

Owing to the plasmonic property of SERS substrate with high photothermal conversion efficiency, SERS tags have been designed as theranostic agents by coupling SERS bioimaging with phototherapy. Ye's group developed GERTs for Raman detection and photothermal ablation of residual microtumors. SERS signals of GERTs for imaging the residual tumor lesions with a 785 nm laser excitation, then the residual tumors were eradicated via photothermal therapy upon switching an 808 nm laser [86]. Similarly, Ye's group have further developed a cisplatin-loaded GERTs (C-GERTs) nanoprobe for intraoperative Raman detection and elimination of unresectable disseminated advanced ovarian tumors via chemo-photothermal synergistic therapy (Fig. 14.13a) [87]. In order to meet the need of imaging spatial resolution and depth of cancer therapeutics in vivo, our group have synthesized a kind of monodispersed Prussian blue encapsulated gold nanoparticles (Au@PB NPs) for zero-background SERS and magnetic resonance imaging (MRI) guided phototherapy (Fig. 14.13b) [88]. To avoid cancer recurrence from the residual microtumors after surgical resection, Li et al. designed "three-in-one" theranostic nanoprobe for image-guided surgical resection of tumors and intraoperative SERS-guided thermosurgical elimination of residual microtumors (Fig. 14.13c). In vivo experiments confirmed complete eradication of microtumors without local recurrence and with a 100% tumor-free survivability [89].

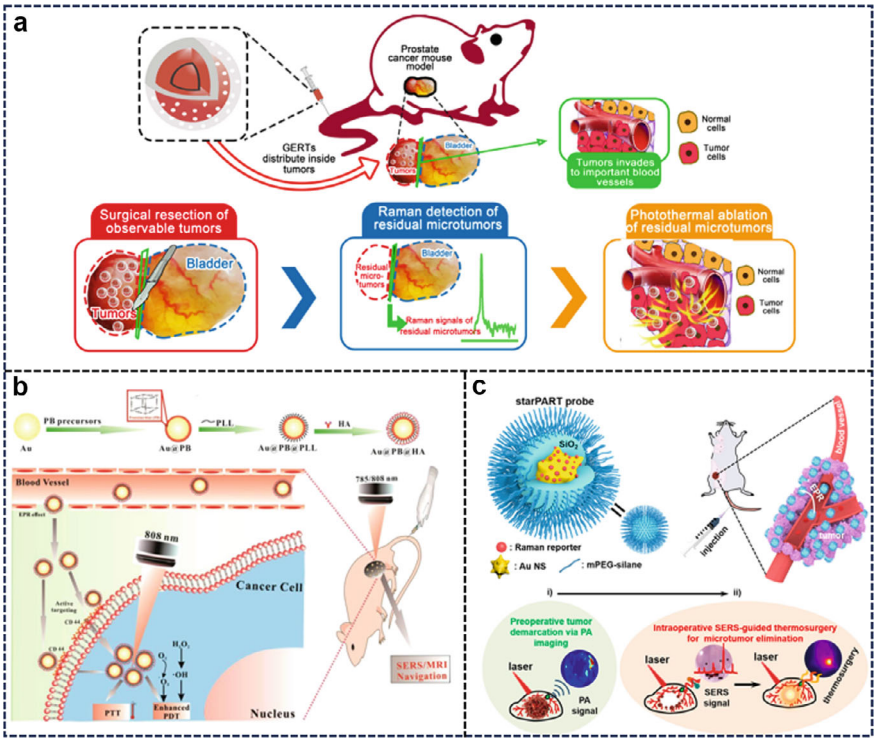



**Fig. 14.13** **a** Intraoperative Raman detection and elimination of unresectable disseminated advanced ovarian tumors. Reproduced from Ref. [87] with the permission. **b** Zero-background SERS and magnetic resonance imaging (MRI) guided phototherapy. Reproduced from Ref. [88] with the permission. **c** Intraoperative SERS guided thermosurgical elimination of residual microtumors. Reproduced from Ref. [89] with the permission

## 14.3 SERS Bioanalysis Based on Responsive Probes

### *14.3.1 Advantages of Responsive SERS Probes*

Extraction of target signals from complex biological systems is essential for biomedical analysis and clinical diagnosis. Thanks to the high sensitivity and "molecular fingerprinting" properties of SERS, label-based "artificial fingerprinting" can confer distinct SERS signals to targets [90], but this strategy generally requires tedious and time-consuming separation processes. In addition, some pathological indicators, such as reactive oxygen species (ROS), pH and other pathological microenvironmental parameters, are difficult to be labeled. Therefore, the labeled SERS probes for bioanalytical applications are limited. In order to achieve highly sensitive and specific detection of the above targets and to improve the applicability of Raman spectroscopy in bioassay, responsive SERS probes have been developed. Modulated by

the chemical activity of the target (redox, catalysis, reactivity, etc.), responsive SERS probes exhibit concentration-dependent changes in signal intensity or Raman shift, and thus possess powerful biosensing detection or bioimaging capabilities [91]. As a bioanalytical spectroscopic sensing platform, responsive SERS probes have shown various advantages in biomedical research. (1) High specificity. The inherent selectivity of the probe in response to the chemical activity of the target, coupled with the unique "molecule fingerprinting" capability of SERS, allows the target to be distinguished from other components. (2) Separation-free. Unlike labeled SERS analysis, which requires separation of unlabeled SERS probes from the biological system, the molecular structures of the Raman reporters in responsive probe would change upon contacting with the target, generating new Raman peaks that can be used for qualitative or quantitative analysis of the target, thus avoiding false-positive signals. (3) Wide applicability. Labeled SERS probes specifically recognize and capture targets mainly by antibodies or nucleic acid aptamers, while responsive SERS probes are designed based on the chemical activity of the target, and thus enabling the detection of a wider range of targets. (4) Multievent analysis with a single probe. Different from the "one-to-one" detection mode of labeled SERS probes, responsive SERS probes can integrate different response modes to achieve simultaneous analysis of multiple targets, thus avoiding mutual interference between different SERS probes. Overall, the high specificity, high sensitivity, multiplexing potential and separation-free feature of responsive SERS probes provide significant advantages for simultaneous and quantitative analysis of multiple targets in complex biological systems, and thus have great application prospects in the early diagnosis of diseases and real-time pathophysiological monitoring.

### *14.3.2 Characteristics of Responsive SERS Probes*

A responsive SERS probe usually comprises three major components: metal substrate, responsive Raman reporter, and protective layer. The substrate materials are typically noble metals (gold [92], silver [93], copper [94], etc.) and inorganic nanomaterials (graphene [95], boron nitride [96], semiconductors [97], etc.). In addition, the morphology of the metal substrate can be shaped into spheres [98], rods [99], and stars [100]. Different substrate materials or metal substrates with different geometries can produce different SERS effects [101], and therefore, permutation and combination of the above two terms can be used to optimize the enhancement of the substrate. The Raman reporter is responsible for giving the SERS probes high specificity as well as a unique signature spectrum [102]. Several requests need to be met to detect multiple targets simultaneously: (1) The chemical structures of the reporter molecules should be designed differently to produce symbolic Raman peaks, accurately identifying the target in the complex Raman spectra of samples. In addition, these reporter molecules should have nonoverlapping fingerprint peaks for the convenience to distinguish from each other. (2) The selected reporter molecules also should

have a large Raman scattering cross section, which can avoid the Raman characteristics peaks of some molecules to be overwhelmed. (3) These reporter molecules need to be modified easily into nanoparticles or polymer scaffolds. However, the structure of metal substrate decorated with Raman reporter usually lacks stability, and the surrounding environment easily disturb the Raman signal. Well-designed protective layers and targeting molecules are important to improve the stability of SERS probes and reduce the non-specific binding. So far, a variety of protective coating materials including bovine serum albumin [103], polyethylene glycol [104], liposomes [105], and silicon dioxide [106] have been widely used. Among them, polyethylene glycol and silicon dioxide are most commonly used. To sum up, the structure of the responsive SERS probes is relatively complex, so researchers need to conduct a reasonable and comprehensive design.

### *14.3.3 Mechanisms of Responsive SERS Probes*

The strategy for designing responsive SERS probes involves the specific interaction of targets and the reporter molecules to produce different SERS signals before and after response. Currently, responsive SERS strategies can be classified into two types: signal intensity-based response and Raman shift-based response (Fig. 14.14).

#### 14.3.3.1 Signal Intensity-Based Responsive Mechanism

Responsive SERS probes can be designed using a fundamental approach based on the formation or destruction of hot spot structure by particular targets, which will result in notable variations in SERS intensity. Current responsive proposals are categorized into four primary types based on signal intensity: aggregation, distance mediator, competitive combination, and intensity ratio.

*Aggregation-Induced Signal Enhancement*: Aggregation of gold or silver nanoparticles creates a large number of "hot spots" in the nanoscale gaps between them, which enhances the SERS signal of the probe. Therefore, designing SERS probes for target-induced aggregation can achieve its sensitive and specific detection. Currently, strategies for triggering SERS probe aggregation include electrostatic affinity [107], hydrophobic interactions [108], and crosslinker-mediated assembly [57]. For example, Jung and colleagues reported pH-sensitive gold nanoparticles with positive and negative charges on their surface when under mildly acidic conditions [107]. The oppositely charged gold nanoparticles then rapidly aggregated due to electrostatic attraction, forming "hot spots" that significantly enhanced the SERS signal. Li et al. altered the surface polymer charge of gold nanoparticles by modulating pH and induced self-assembly of gold nanoparticles based on hydrophobic interactions [108]. Although the above strategies are capable of inducing SERS

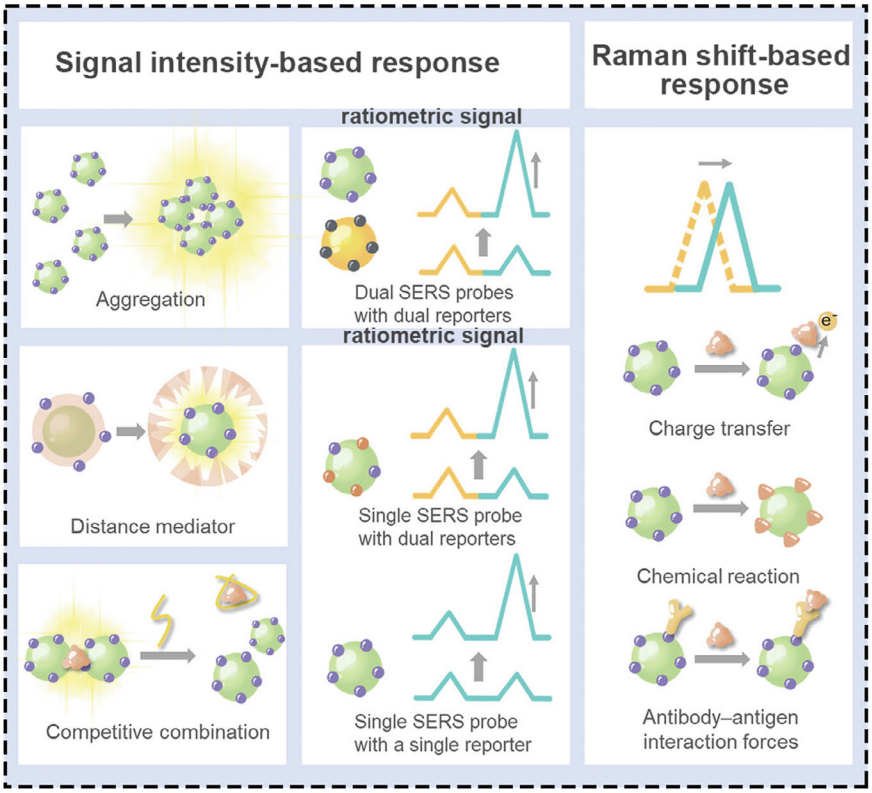



**Fig. 14.14** Schematic diagram of mechanisms leading to the responsive SERS signal. The responsive SERS mechanisms are cataloged into three types: intensity-dependent SERS signal and shift-dependent SERS signal. Reproduced from Ref. [91] with the permission

probe aggregation, the physiological instability and irreproducible nature of amorphous aggregates structures make these probes difficult to be applied in biomedical analysis. In contrast, crosslinkers enable controlled aggregation of the SERS probes, thus generating SERS signals with good stability and reproducibility. For example, Shen et al. reported a gold nanoparticle modified with polyA-DNA and Asp-Glu-Val-Asp peptide sequences, in which the peptide sequences were removed in response to caspase-3, and polyA-DNA hybridization induced controlled aggregation of the nanoparticles to produce a stable SERS signal [70].

*Distance-Induced Signal Changes*: The responsive mechanism of this strategy is to modulate the distance between the reporter molecules and the SERS substrate to induce changes in signal intensity. A shielding layer is usually modified onto the probe to isolate the reporter molecules from the gold nanoparticle core. When the probe encounter the target, the shielding layer structure is disrupted due to the chemical reaction, and the distance between the Raman tag and the gold nanoparticle

core decreases to turn on the SERS signal. For example, Liu et al. used manganese dioxide ($MnO_2$) shells as a distance regulator between gold nanoparticles and outside Raman reporters. When the $MnO_2$ shells were decomposed in response to hydrogen peroxide ($H_2O_2$), the distance between the gold nanoparticles core and the Raman reporters reduced to trigger the SERS signal [109]. On the other hand, separating the Raman tags on the probe from the SERS substrate to reduce the SERS signal can also be used for sensing detection of the target. Si et al. employed the DNA cleavage reaction to monitor the activity of endonuclease under in vitro and living cells [110]. Upon exposure to endonuclease, the single stranded DNA (ssDNA), a linker between alloyed Ag/Au nanospheres and Raman reporters, underwent cleavage, reducing the SERS signal of the probe.

*Competitive Combination-Induced Signal Attenuation*: This tactic primarily relies on the "hot spot" geometry breaking due to the competitive combination between analytes and probe linkers. When the probe dimers or polymers are dispersed into monomers, the SERS signals are significantly weakened. For example, Shen et al. reported a SERS "switch off" strategy based on the competitive binding of biothiols and 4-mercaptobenzonitrile reporters to $Hg^{2+}$ [111]. Since the affinity of biothiols for $Hg^{2+}$ is higher than that of the SERS tags, $Hg^{2+}$ linkers in the nano-aggregates were competitively bound by the analyte biothiols, leading to the disruption of the "hot spot" geometries and dispersion of the SERS probes, which significantly reduces the SERS signals.

Due to the great sensitivity, quick response time, low background signal, and multiplexed analysis, SERS has drawn more and more interest. However, the majority of conventional SERS sensing and imaging methods rely on the detection of absolute signal intensity, which is influenced by a variety of target-independent factors such as the focal length, substrate condition, probe concentration, and others. In order to avoid the above factors tampering with the quantification process and resulting in inaccurate results. The researchers developed the ratio signal measurement technique to replace the absolute signal intensity measurement. Ratio SERS probes use one of their unchanged Raman signals as an internal reference, and the ratio between the responsive signal and the internal reference is used as the signal output. Currently, two general SERS-based ratiometric strategies have been reported: the dual SERS probe ratiometric signal strategy and the single SERS probe ratiometric signal strategy.

*Dual SERS Probes Ratiometric Signals*: Typically, two probes with different SERS signatures are added simultaneously to the system, with one probe responding to a specific stimulus or analyte and the other acting as an internal reference, and the SERS intensity ratios of the two probes can be reliably quantified for a specific target. For example, Wang et al. developed a series of SERS probes responsive to breast cancer cell surface biomarkers [112]. Cellular imaging based on the SERS signal intensity ratios of the responsive to non-responsive probes allows for rapid visualization of 4 biomarkers separately, thus facilitating an accurate and multiplexed detection of tumor markers.

*Single SERS Probe Ratiometric Signals*: The ratiometric sensing approach based on two independent SERS probes is straightforward but needs complicated multi-step synthesis. The second feasible strategy can avoid the shortcoming, which can be further subdivided according to the types of Raman reporters. (a) Dual Raman reporters signal ratiometric output. Two different Raman tags are modified onto one nanoparticle, where one Raman reporter can respond specifically to the analyte and the other acts as an internal standard for ratiometric output of the SERS signal. For example, Tian et al. modified three different types of Raman reporter molecules onto a probe, one of which was served as an internal standard, and successfully achieved the detection of $CO_3^{2-}$ and pH values in the living brain through the ratiometric signal [113]. (b) Single Raman reporter signal ratiometric readout. Although the SERS probes with dual Raman reporters can achieve ratiometric signal output well, the complex synthesis procedures of the probes and the high cost need to be considered. On the contrary, the strategy of single Raman reporter signal ratio only requires one target-responsive Raman reporter onto the surface of SERS substrate, where the responsive reporter act as both analyte sensing units (responsive moieties) and as internal standard (non-responsive moieties). For example, Duan et al. developed a pH ratiometrically responsive SERS probe [104]. The SERS intensity of the responsive group in the reporter molecule gradually increases upon acidification, while the Raman intensity of the internal standard group remains essentially constant. There was a linear relationship between the SERS intensity ratio and a certain range of pH values.

#### 14.3.3.2 Raman Shift-Based Responsive Mechanism

Raman shift-based SERS has recently demonstrated significant promise in biomedical applications. The difference of fingerprint information before and after SERS reporters react with target analytes is reflected in the Raman shift. It is possible to accurately determine the concentration of the target by establishing the functional correlation between the peak shift and analyte level. For example, Ma et al. systematically explored the mechanism of Raman band shift of reporter molecules interacting with their surroundings [114]. They found that both the effective electric field generated by solvent polarization and the linked protein with different molecular weights can induce the shift of spectral bands in Raman tags. Zhao et al. developed a frequency-shifted SERS microarray sensor [115]. The Raman reporter molecules on the SERS substrate are specifically bound to biomarkers and their characteristic Raman bands are shifted, thus enabling simultaneous detection of multiple microRNA in serum.

In summary, both of these responsive mechanisms have their own characteristics and shortcomings. Absolute signal intensity-based responsive SERS probes are highly sensitive and signal intensity changes are intuitive. However, this strategy is less accurate because it is susceptible to interference from instrumental factors, laser intensity, focal length, substrate structure and environmental factors. Ratiometric signal intensity-based responsive SERS probes can eliminate these interferences and

obtain accurate and highly reproducible quantitative results. However, the lack of regularity in the ratiometric signals of some responsive reporter molecules makes the design of Raman tags complicated. In addition, it is necessary to consider the signal intensity matching between the internal standard and the responsive molecule or responsive group to avoid the ratio of the two being too large or too small. For the Raman shift-based responsive SERS probes, although the design of the reporter molecules is relatively easy, there still exist some shortcomings: small Raman wavenumber shifts (2–10 $cm^{-1}$) require Raman instruments with higher spectral resolution to be visible; however, high-resolution gratings inevitably reduce the Raman signal intensity, which may explain why this strategy is not as widely used as the other.

### *14.3.4 Biomedical Applications of Responsive SERS Probes*

As previously described, responsive SERS probes mainly adopt the chemical activity of the target to achieve its specific detection, which not only provides the probe with good specificity, but also allows the SERS probe to further extend its detection to some "unlabeled" physiological indicators. In addition, based on the target-induced changes in SERS signal (signal intensity or Raman shift), false-positive signals of the probe itself can be avoided, facilitating accurate quantitative results. These advantages of responsive SERS probes make them particularly suitable for quantitative detection or imaging of specific targets in complex biological systems. Currently, various responsive SERS probes have been developed to measure physiological and pathological conditions or as a supplementary method for liquid biopsy, guiding cancer surgery, or treatment monitoring. In this section, we will summarize the applications of responsive SERS Probes in biomedical research.

#### 14.3.4.1 Responsive SERS Probe for In Situ Monitoring of Pathological Indicators

*pH Sensing*: The local pH in biological systems varies in response to cellular events and phenotypes, which is important for monitoring metabolism, growth, development and disease progression in organisms. Extracellular pH ($pH_e$) is one of the most important regulators and plays a crucial role in biological functions such as cell proliferation, metastasis, apoptosis, and drug resistance. The activity of many proteases is affected by even subtle changes in $pH_e$, which in turn affects the remodeling of the extracellular matrix, suppresses the immune response and plays a crucial role in tumor cell invasion. It has been shown that acidification of tumor extracellular fluid is a biomarker of solid tumors, mainly due to faster metabolic rate activating cellular glycolytic activity (i.e., the Warburg effect), which upregulates proton production [116]. In addition, intracellular pH ($pH_i$) is also an important regulator of cellular

function, and even small changes in $pH_i$ may significantly affect cellular activity and even cause disease. Therefore, $pH_i$ or $pH_e$ detection is one of the channels to confirm the normal function of different organelles, and is also one of the methods to understand the pathology of diseases such as cancer.

A common approach to pH response is to attach pH-sensitive Raman reporter molecules to nanoparticles. As the ambient pH changes, the reporter molecule undergoes a protonation/deprotonation structural change and its vibrational modes change, thus displaying different Raman signals. The most commonly used pH-sensitive Raman reporter molecules are 4-mercaptobenzoic acid (4-MBA), 2-aminothiophenol or 4-mercaptopyridine (4-MPy). For pH measurement of extracellular fluids, the closer the pH is to the cell membrane, the more accurate quantification and the more valuable and meaningful the monitoring. Marunaka et al. used gold nanoparticles to create a high spatial resolution SERS sensor for measuring extracellular pH in proximity of the cell membrane [117]. As shown in Fig. 14.15a, the gold nanoparticles with the surface functionalized with 4-MBA were linked to the cell's membrane proteins by pyridyldithiol-biotin compound (HPDP-B), streptavidin (SA) and sulfo-NHS-ester-biotin compound (NHS-B) successively, thus the ratiometric SERS signal intensity between $COO^-$ and C–H (internal standard) vibration could be used to quantify the local pH. The nanometer size of the cell membrane anchored sensor and the use of SERS enable us to visualize highly localized variation of pH induced by $H^+$ extrusion, which is particularly upregulated in cancer cells.

The detection of intracellular pH is also crucial. However, due to the complexity of substances in biological systems, a number of other relevant biomolecules in the same microenvironment, or even $pH_e$, may interfere with the detection of $pH_i$. To address the issue, Fang et al. developed a silver nanowire-based SERS platform for simultaneous sensing of $pH_i$ and $pH_e$ [118]. As shown in Fig. 14.15b, a surface-roughened silver nanowire (Ag NW) modified by 4-MBA was used as a pH sensing probe. The 4-MBA@AgNW probe can be inserted into cells with minimal invasive damage and the 4-MBA exhibits distinct Raman peaks at different pH conditions. Further investigation proves that the AgNW can also be used in monitoring the dynamic variation of $pH_i$ and $pH_e$ of cancer cells upon stimulation with anticancer drugs or under a hypoxic environment.

Besides the protonation and deprotonation reactions of organic small molecules, pH-responsive assembly of DNA nanostructures can also be used for the pH sensing. Recently, Xi et al. proposed a clever assembly method to exploit a novel pH sensing platform that inherits the excellent properties of AuNPs and the reversible pH responding performance of i-motif [119]. Specifically, the i-motif nanostructures formed from cytosine-rich ssDNA sequences in response to the intracellular pH can cause the aggregation of gold nanoparticles to generate hotspots and significantly enhance Raman signals (Fig. 14.15c). In addition, 4-mercaptobenzonitrile terminated with nitrile (CN) was chosen as a Raman reporter molecule, which exhibited a strong and distinct peak in the Raman-silenced region of the cell (1800–2800 $cm^{-1}$) to eliminate the background interference of endogenous biomolecules.

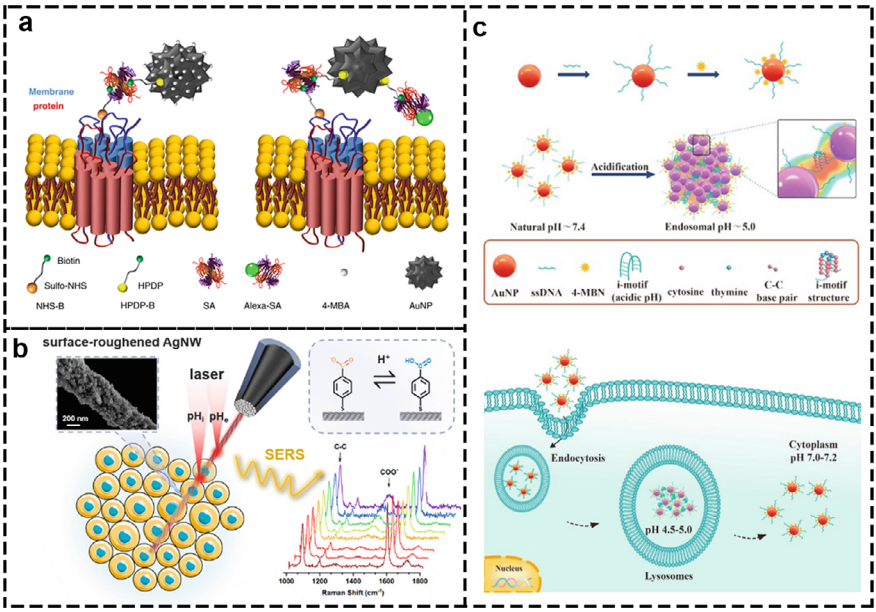



**Fig. 14.15** Responsive SERS probe for in situ monitoring of pH. **a** Explanatory sketch illustrating the structure of the pH nanosensor: the surface of AuNP is functionalized with 4-MBA and HPDP-B. Conjugated AuNP labeled with Alexa-SA: the attachment of the nanoparticles to the cell membrane was confirmed using AuNP functionalized with HPDP-B, some biotins of which reacted with Alexa-SA to enable visualization by SERS. Reproduced from Ref. [117] with the permission. **b** Schematic illustration of the fabrication procedure of a 4-MBA@AgNW with a rough surface and its application for simultaneous detection of $pH_i$ and $pH_e$ in multiple tumor cells. Reproduced from Ref. [118] with the permission. **c** Schematic illustration of the procedure for preparation of the Au-i-motif based SERS probe and pH-responsive aggregation behavior of the Au-i-motif based SERS probe for intracellular pH dynamic monitoring. Reproduced from Ref. [119] with the permission

*Reactive Species Sensing*: Reactive species including reactive oxygen species (ROS), reactive sulfur species (RSS), and reactive nitrogen species (RNS) are related to many important bio-events such as signal transduction, immune regulation, and cellular metabolic processes [120]. As a typical feature of the tumor microenvironment, high levels of ROS promote the cancer cell invasion through activation of epidermal growth factor receptor. In addition, ROS motivates the cancer progression and multidrug resistance. Therefore, monitoring these reactive species is essential for diagnosis and treatment of disease, especially the tumor.

The inherent redox properties of reactive species provide inspiration for the development of responsive Raman probes. Currently, Most ROS-responsive SERS sensing strategies assemble reporter molecules on the surface of plasma Nanoparticles that chemically react with ROS, such as 4-mercaptophenyl ester usually for $H_2O_2$ detection [121], 2-mercapto-4-methoxyphenol for HOCl detection [122], and 4-mercaptophenylboronic acid ester for peroxynitrate detection [123]. Concretely Speaking, the structure changes of these reporter molecules responded to specific

ROS will give rise to the frequency shift of Raman characteristic peaks, achieving the accurate detection and dynamic monitoring of ROS. Li et al. developed a reversible SERS nanosensor based on covalent organic frameworks (COFs) to dynamically monitor the redox processes in living cells (Fig. 14.16a) [124]. The nanosensor was prepared by modifying the redox-responsive Raman reporter molecule 2-mercaptobenzoquinone (2-MBQ) on the surface of gold nanoparticles, which were then coated in situ by COFs shells. When ascorbic acid (AA) and hypochlorite ($ClO^-$) were used as models for reductive and oxidative substances, respectively, the 2-MBQ molecule could repeatedly and rapidly undergo reduction and oxidation, which led to reciprocal changes in the SERS spectra at 900 $cm^{-1}$. The structure of the COFs shells enabled the nanosensors to have good stability and immunity to interference, thus reliably visualizing the dynamics of intracellular redox species such as AA and $ClO^-$. Yanmei et al. constructed a ratiometric SERS probe capable of detecting intra/extracellular $H_2O_2$ content by attaching a reporter molecule, 4-mercaptophenylacetylene (MPAE), to the probe as an internal standard for the responsive reporter molecule [4-mercaptophenylboronic acid]-dopamine-[3-(4-(phenylethynyl) benzylthio) propanoic acid] (4-MPBA-DA-PEB) [125]. In the presence of $H_2O_2$, the alkyne groups (2214 $cm^{-1}$) on the PEB were released from the surface of the Au–Ag alloy nanoparticles due to the boric acid to phenol conversion, which significantly reduced the Raman signal at 2214 $cm^{-1}$. Since the Raman signal of MPAE at 1986 $cm^{-1}$ remains unchanged, the $H_2O_2$ concentration can be quantitatively analyzed based on the ratiometric value of $I_{1986}/I_{2214}$.

RSS in biosystems typically include glutathione (GSH), cysteine (Cys), homocysteine (Hcy), and hydrogen sulfide ($H_2S$). They are most commonly reductive and play an excellent role in anti-oxidative effects. The azide group is a widely used bioorthogonal functional group that has been used for the specific detection of $H_2S$ in chemoselective reduction processes [126]. Liu et al. synthesized a bioorthogonal Raman probe, 4-azidobenzenethiol (4-ABT), for endogenous $H_2S$ imaging in single live cells. 4-ABT bears a thiol group and an azido group in the benzene ring, thus affording a bifunction to firmly bind to the gold nanoparticle surface and specifically respond to $H_2S$ [127]. The 4-ABT-based responsive SERS nanoprobes showed dose-dependent spectral changes in the Raman-silenced region of the cell upon reaction with $H_2S$, allowing proportional quantitative detection and visualization of the intracellular $H_2S$ without biological interference. As for biothiols with similar structure (GSH, Cys, Hcy), competing thiol reactivity and their low content make them difficult to quantify in a complex intracellular environment. To address this challenge, Chen and coworkers exploited the thiol-based click reaction with cyanides to discriminate these three biothiols (Fig. 14.16b) [128]. The reaction kinetics were monitored using the responsive Raman probes and three products were identified using quantitative principal component analysis, which allowed for the simultaneous quantification of the above three biothiols in cell lyses and single living cells.

RNS are a series of molecules with oxidative nitrogen atoms, such as nitric oxide (NO), peroxynitrite ($ONOO^-$), and nitroxyl (HNO). Due to their high pathophysiological biofunctional characteristics and short lifetime, the detection of RNS is difficult but crucial. Li et al. developed a novel responsive SERS nanoprobe by

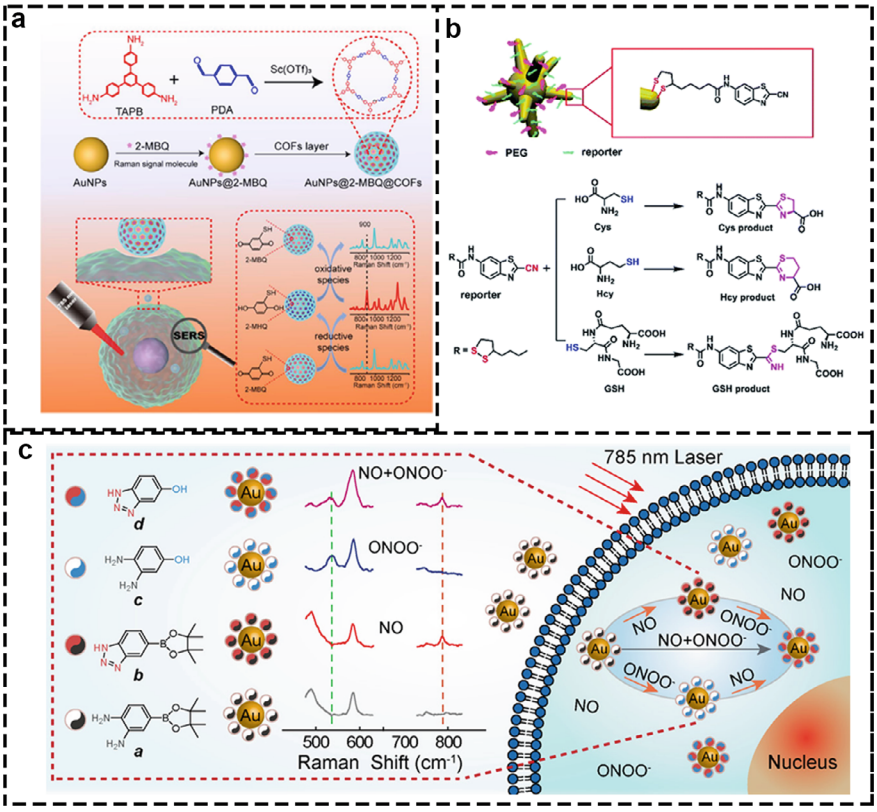



**Fig. 14.16** Responsive SERS probe for in situ monitoring of reactive species. **a** Illustration of monitoring redox process in living cells by AuNPs@2-MBQ@COFs nanosensor. Reproduced from Ref. [124] with the permission. **b** An illustration of the AuNS conjugated to PEG and the Raman reporter denoted as plasmonic Raman probes (PRPs); the reaction mechanism of PRPs with Cys, Hcy and GSH. Reproduced from Ref. [128] with the permission. **c** Schematic diagram of detecting endogenous NO and $ONOO^-$ in live macrophages by using the SERS nanosensor. Reproduced from Ref. [130] with the permission

assembling 3,4-diaminobenzene-thiols on the surface of porous $SiO_2$-coated Au–Ag alloy nanoparticles and successfully applied it to ratiometric imaging analysis of NO in living cells [129]. Furthermore, Li et al. fabricated a responsive SERS nanosensor for simultaneous in situ detection of endogenous NO and $ONOO^-$ by assembling the 3,4-diaminophenylboronic acid pinacol ester (DAPBAP) molecules onto gold nanoparticles (Fig. 14.16c) [130]. Specifically, the DAPBAP molecule includes o-phenylenediamino moiety and boronic pinacol ester groups that responded selectively to NO and $ONOO^-$, respectively, enabling the simultaneous monitoring of above two in the Raw264.7 cells because of the SERS spectral changes of the nanosensor.

*Metal Ions Sensing*: Metal ions play a unique role in life activities, such as involving in many biological processes and assume various functions in living organisms, such as electron transfer, oxygen carrying, and enzyme activity center. Dysregulation of metal homeostasis in the body can lead to disruption of normal physiological functions and cause various diseases. Therefore, clarifying the spatial and temporal dynamics of metal ions in life activities is of pivotal significance in understanding disease pathology.

In terms of metal ion sensors, a number of molecular recognition reactions have been reported, such as electrophilic substitution reactions between $Hg^{2+}$ and boric acid [131] and coordination reactions between metal ions and ligands. For example, Wang's group developed a powerful SERS nanopipettes modified with 4-mercaptobenzonitrile (MBN) to accurately detect trivalent iron ($Fe^{3+}$) in single cells in real time via Fe-CN coordination (Fig. 14.17a) [132]. The nanoprobes were prepared by coating a glass capillary tip (100 nm) with a thin gold film, enabling highly localized studies in living cell systems. Due to the versatile interaction pattern of MBN to the gold surface, two characteristic peaks of –C≡N (at 2126 and 2225 $cm^{-1}$) within the bio-silent region were observed and the intensity ratio of these two peaks was likely to be sensitive for the formation of Fe–C≡N complex on iron exposure, which enables the quantification of iron content in living cell. Joo et al. synthesized coumarin-lipoic acid (Cou-LA)-based fluorescent and Raman dual-mode probes to monitor intracellular Cu(II) [133]. The Cou-LA conjugate-functionalized silver nanoparticles decorated on nanopipettes (CSNs) were fabricated and the SERS intensity enhancement and fluorescence quenching of CSNs were observed upon selectively responding to Cu(II). In a single HeLa cell, Cu(II) was determined on the basis of the change in the ratio of the Raman intensity at 500 and 597 $cm^{-1}$ and the fluorescence intensity at 469 nm due to the trapping of Cu(II) by CSNs. It is widely recognized that metabolic disorders of Cu(II) are thought to be highly associated with Wilson's disease (WD). In order to understand WD pathology and to assist an early, non-invasive and accurate diagnosis of WD, Song's group developed a type of $Cu^{2+}$-activated nanoprobe based on nanogapped gold nanoparticles (AuNNP) and poly(N-isopropylacrylamide) (PNIPAM) for simultaneous quantification of liver and urinary $Cu^{2+}$ content in WD by photoacoustic (PA) imaging and ratiometric SERS, respectively (Fig. 14.17b) [134]. Specifically, the 2-naphthylthiol (NAT) was placed in the nanogap of AuNNP, while PNIPAM and MBN were modified on the AuNNP surface. The $Cu^{2+}$ could effectively coordinate with the chelator PNIPAM and led to the aggregation of the nanoprobe, resulting in the absorption red shift and improved PA performance of the nanoprobe. Meanwhile, the SERS signal of MBN at 2223 $cm^{-1}$ was amplified, while the SERS signal at 1378 $cm^{-1}$ remained stable. Because $PA_{1250\,nm}$ and SERS $I_{2223}/I_{1378}$ signals of the nanoprobes were linearly related to $Cu^{2+}$ concentration, the nanoprobe was successfully applied for in vivo quantitative detection of liver $Cu^{2+}$ of WD mice through NIR-II PA imaging and accurate quantification of urinary $Cu^{2+}$ of WD patients by ratiometric SERS.

Besides the detection of one type of metal ion, responsive SERS probe has the potential to analyze multiple metallic ions simultaneously in living systems. For instance, the imbalance of $Cu^{+}$ and $Cu^{2+}$ in the brain is strongly

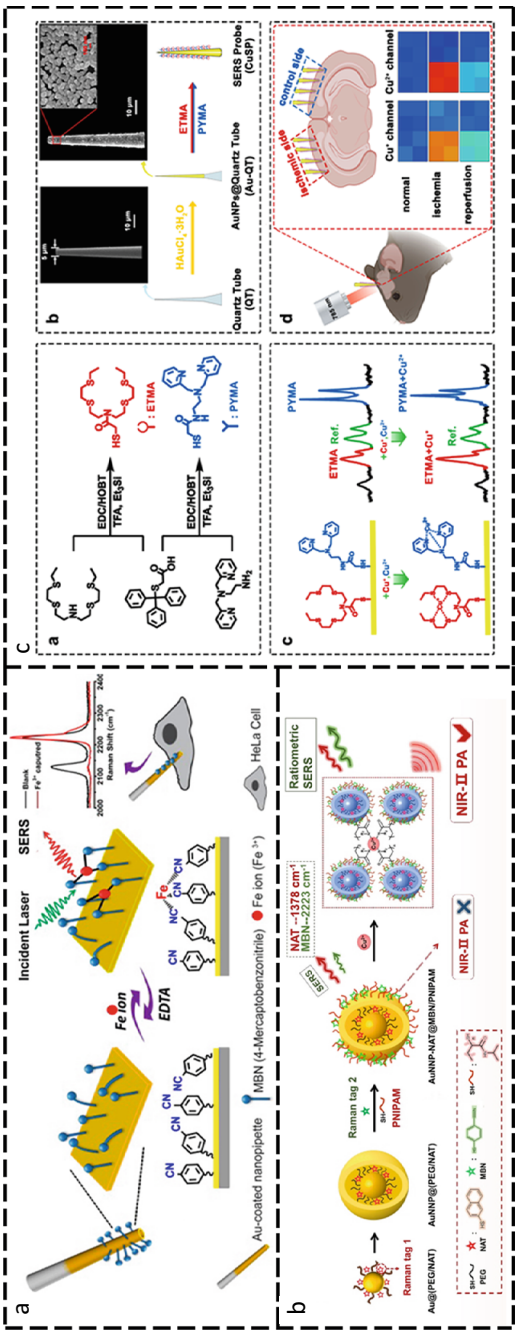



**Fig. 14.17** Responsive SERS probe for in situ monitoring of metal ions. **a** Schematic of nanoprobe surface-modified with MBN and its interaction with $Fe^{3+}$ for detection; suggested mechanism for $Fe^{3+}$ detection process by Au-MBN nanoprobe. Reproduced from Ref. [132] with the permission. **b** Illustration of the structure of AuNNP-NAT@MBN/PNIPAM and $Cu^{2+}$-induced aggregation of AuNNP-NAT@MBN/PNIPAM to "turn on" the NIR-II PA signal and ratiometric SERS signal (i.e., $I_{2223}/I_{1378}$). Reproduced from Ref. [134] with the permission. **c** (**a**) Synthetic route for the designed ETMA and PYMA molecules; (**b**) SEM images of QT with a tip size of 5 μm (top, left), Au-QT (top, right), and gold nanoparticles deposited on the surface of QT (top, right, inset). Assembled processes for constructing CuSP probe (bottom); (**c**) the principle of dual-recognition mode of the developed CuSP probe for simultaneous recognition of $Cu^{+}$ and $Cu^{2+}$; (**d**) biosensing of $Cu^{+}$ and $Cu^{2+}$ in the cerebral cortex of live mouse upon MCAO. Reproduced from Ref. [135] with the permission

associated with neurodegenerative diseases. Thus, the real-time monitoring of the interconversion of $Cu^{2+}$ and $Cu^{+}$ helps understand the mechanism of ischemia. Tian et al. developed a responsive SERS probe for real-time monitoring and accurate quantification of $Cu^{+}$ and $Cu^{2+}$ concentrations in the brain of living mice (Fig. 14.17c) [135]. Firstly, two molecules, N, N-bis(2-((2-(ethylthio)ethyl)thio)ethyl)-2-mercaptoacetamide (ETMA) and N-(2-(bis(pyridin-2-ylmethyl)amino)ethyl)-2-mercaptoacetamide (PYMA), were synthesized for the specific recognition of $Cu^{+}$ and $Cu^{2+}$, respectively. And then gold nanoparticles were deposited onto quartz tubes (QTs) with tip sizes of 100 nm ~ 5 μm, named Au-QTs. Finally, the above two responsive Raman molecules were decorated onto Au-QTs (denoted as CuSP) and the CuSP probe enabled specific detection of $Cu^{+}$ and $Cu^{2+}$ simultaneously, further discovering the mechanisms of the increased concentrations of $Cu^{+}$ and $Cu^{2+}$ in the cortex of live mammalian brain.

*Enzyme Sensing*: Human growth, metabolism, and the onset and progression of disease involve numerous biochemical reactions, among which enzyme catalysis is indispensable. Most enzymatic reactions are characterized by rapidity, efficiency, and specificity. Enzyme, as an endogenous substance, plays a significant role in managing disease and regulating the specific metabolic process. Moreover, high expression levels of some enzymes, such as phosphatases and proteases, have been identified as biomarkers for the diagnosis of inflammation and cancer. Therefore, the sensing investigation of enzyme activity facilitate a profound insight of their functions in many pathophysiological processes.

Typically, enzyme-responsive SERS probes are designed by linking the Raman reporter molecules with enzyme-recognized groups to the noble metal nanoparticles. When the enzyme specifically touched the substrate, the SERS signal of probe would change (signal intensity or Raman shift) due to the specific enzymatic reactions. Tang et al. established a new kind of responsive SERS nanoprobe based on covalent Au–Se bonding between the gold nanoparticle and the TAMRA reporter molecules grafted with responsive peptide chain for matrixmetalloproteinase-2 (MMP-2) bioimaging and quantification (Fig. 14.18a) [136]. In the absence of MMP-2, the probe exhibited a strong SERS signal of TAMRA. Once the probe was exposed to MMP-2, the peptide chains would be recognized and cut by the activated MMP-2, causing TAMRA to separate from gold nanoparticle and the Raman signal to diminish. To further improve the reproducibility of detection, a ratiometric SERS nanoprobe was created by incorporating 1,4-benzenedithiol (1,4-BDT) as a constant internal standard, allowing to quantify MMP-2 in live cells with high accuracy.

ROS-induced intracellular oxidation reactions are initiated by the peroxidase myeloperoxidase (MPO). Through the redox reaction with tyrosine, MPO breaks down proteins in cells, resulting in dimerization between tyrosine (Tyr) units. Kong et al. developed a background-free photoinduced enhanced Raman (PIER) probe for tracing MPO-mediated oxidation process in inflammatory cells [137]. The PIER probe composed of $TiO_2$–Au–C≡C–Tyr could selectively detect the oxidation activity of MPO because the Tyr is one of the major target of MPO and could be induced to dimerize. As shown in Fig. 14.18b, a large cluster of probes were

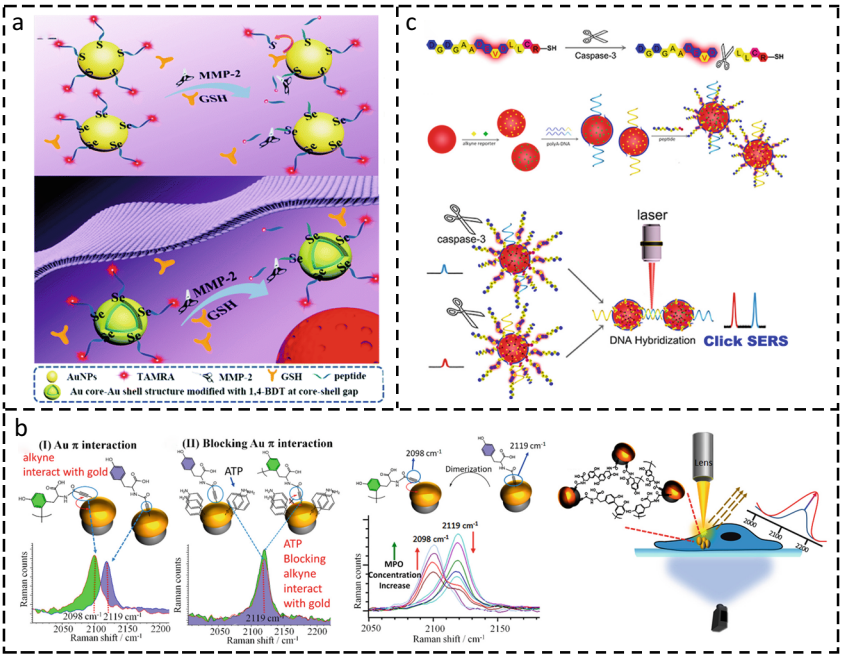



**Fig. 14.18** Responsive SERS probe for in situ monitoring of enzyme. **a** Au–Se SERS nanoprobes for high-fidelity MMP-2 detection in living cells; the Au–Se SERS nanoprobes respond specifically to MMP-2, while the traditional Au–S SERS nanoprobes are destroyed by intracellular GSH, producing signal distortion; Au–Se–CS SERS nanoprobes for high fidelity quantitative analysis of MMP-2 in living cells. Reproduced from Ref. [136] with the permission. **b** Band red shift from 2119 to 2098 $cm^{-1}$; inhibition of C≡C–Au $\pi$ interaction; band red shift from 2119 to 2098 $cm^{-1}$ with various concentrations of MPO; illustration of photoinduced enhanced Raman probe for use in highly specific and sensitive imaging for tyrosine dimerization in inflammatory cells. Reproduced from Ref. [137] with the permission. **c** Schematic illustration of "Click" SERS detection for caspase-3; principle of reaction between caspase-3 and the peptides; synthesized process of the probes; detected strategy of caspase-3 by "Click" SERS. Reproduced from Ref. [70] with the permission

observed when $TiO_2$–Au–C≡C–Tyr came into contact with MPO. Due to the direction change of C≡C, the Raman peak at 2119 $cm^{-1}$ vanished and a new peak at 2098 $cm^{-1}$ emerged. However, when the 2-(aminothio)phenol layer was employed to impede the $\pi$ interaction between Au and alkyne, the Raman peak at 2119 $cm^{-1}$ remained unaltered. The primary cause of the Raman peak's red shift (from 2119 to 2098 $cm^{-1}$) was demonstrated to be the alteration in the $\pi$ bonding mode brought about by the Au–$\pi$ interaction. Furthermore, the intensity of Raman Peak varied with MPO concentration, which enabled the monitoring of MPO in living cells.

The SERS-based nanoprobes have been widely used to achieve accurate in situ imaging of biomolecules. Yet, non-specific adsorption between probes and biomolecules, especially the proteins, is still problems to be solved. Shen et al.

develop a promoted "Click" SERS strategy for realizing highly selective detection of protease in cells through simultaneous dual-enhanced SERS emissions and the logical judgements from mutual confirmation (Fig. 14.18c) [70]. In detail, polyA-DNA and the Asp-Glu-Val-Asp (DEVD)-containing peptide sequence were modified into alkyne and nitrile-coded gold nanoparticles. During the cell apoptosis process, the production of caspase-3 would lead to the breakage of the tetrapeptide sequence DEVD, which removes the negative protective layer of peptide from the Au NPs. Subsequently, two different triple bond-labeled gold nanoparticles can be linked together by DNA hybridization to form a SERS "hotspot", resulting in simultaneous amplification of two triple-bond Raman signal. Moreover, the SERS intensity was found to be positively related with caspase-3 concentration. Thus, the simultaneously enlarged signals by "Click" SERS could be used for in situ and precise imaging of caspase-3 and have wide potential applications in the diagnosis of protease associated diseases.

*Gaseous Messenger Sensing*: Gaseous molecules generated in human physiological and pathological processes, such as NO, carbon monoxide (CO), and $H_2S$, are important physiological messenger molecules in biological systems that indicate the progress and prognosis of cancer. There is proof that CO plays a vital role in a mass of pathophysiological processes such as neurotransmission, proliferation, metabolism, and inflammatory response [138]. In addition, CO has drawn extend attention as a promising therapeutic reagent for various human diseases. However, although researchers have demonstrated that CO possesses diverse effects in biological processes, many and specific functions are still indistinct. To understand the biological roles of CO, some analytical techniques have been used for the detection of gaseous molecules, including electrochemical tests, mass spectrometry, colorimetry, and infrared absorption [91]. Nevertheless, most of these methods are not suitable for the direct and noninvasive detection of gases because of the low concentration of these tiny molecule gases and their short existence time in living cells. While in situ analysis based on fluorescence in biological systems is possible, photobleaching and phototoxicity can still affect fluorescence sensing capabilities.

SERS technology has advanced significantly in gas detection in living cells in recent years, due to its exceptional sensitivity, high selectivity, and remarkable resistance to photobleaching and autofluorescence. These factors suggest that SERS will likely be used extensively for probing small molecule gases in biological systems. A compound that interacts with gas molecules is generally assembled onto the surface of the SERS probe, and the gaseous molecule-responsive process results in notable alterations to the SERS peaks. Long et al. developed a SERS nanosensor on the basis of palladacycle carbonylation for the highly selective detection of intracellular CO (Fig. 14.19a) [139]. By assembling palladacycles (PC) on the surface of gold nanoparticles, the carbonylation of the PC was initiated when the nanosensors were incubated with a CO-containing system, and the corresponding SERS spectra of the probe changed significantly, which allowed the carbonylation reaction to be directly

observed in situ. On the basis of this, the SERS nanosensor was utilized for the physiological CO detection following the SERS observation of CO-dependent carbonylation. In addition, Kong et al. designed a SERS-based CO-releasing nanoparticles (CORN) to investigate the chemical reaction of CO delivery in live cells (Fig. 14.19b) [140]. A half-sandwich tungsten tricarbonyl complex ($CpW(CO)_3H$) which serves as a CO-release moiety was constructed and anchored to the nano-tip of Ag nanoparticles, and thus, the inherently weak Raman signal of the CO stretching vibrations can be envisioned. By using the SERS CORNs, the decarbonylation process to CORNs followed by an irreversible oxidative degradation was present clearly, which provide unambiguous evidence for the step transition of the CO-release process in cells. More interesting, a alkyne/ruthenium(II) (alkyne/Ru(II)) complex-based ratiometric SERS nanoprobe for in vitro and ex vivo tracking of CO [141]. The nanoprobe was composed of gold–silver alloy nanoparticle as a highly active SERS substrate, an alkyne/Ru(II) complex as a CO-sensing element fixed on the surface (Fig. 14.19c), and a porous silicon shell to improve the stability and biocompatibility of the particles. Replacing the alkyne ligand with CO can reduce the vibration of the alkyne and increase the signal of the metal carbonyl complex, so as to realize the real-time and effective ratiometric detection of CO. The assay in clean buffered environments, live cells and tissue sections demonstrated the great potential for the detection of CO.

*Multiple Targets Sensing*: A common feature shared by the majority of probes is that they are limited to responding to one kind of target. But for some mixed diseases or tumors, it is not precise enough to employ one as a biomarker because of the intricacy of human physiological and pathological processes. Simultaneous detection of multiple targets relevant to disease has the following significance: (1) It can reduce the false-negative or false-positive defect caused by the interference of tumor heterogeneity in single metabolite detection. (2) Intraoperative quantitative detection of various metabolites helps to establish new strategies for tumor classification based on metabolic profiling. (3) It can make up for the lack of timeliness and other aspects of the widespread use of genotyping and pathotyping. Therefore, it has become a trend to develop probes that respond to multiple analytes at the same time to more accurately localize disease sites and monitor disease processes. To date, electrochemical, fluorescence, and other methods have been used for the independent response to specific target in situ. However, these methods still suffer from a number of shortcomings. For example, electrochemical methods are challenging to detect multiple metabolites in living cells simultaneously without damaging the cells. Although fluorescence methods have been widely used in biological systems, it is difficult to monitor multiple analysts simultaneously because of their broad peak width and their associated peaks tend to overlap. In contrast, SERS has the advantages of high sensitivity, multiplexing, and rich vibrational fingerprint information, which makes it a promising analytical method. As mentioned previously, a number of responsive sensing strategies between analytes and SERS probes have been developed to accurately monitor tumor-associated metabolites. In addition, SERS can provide narrow peak and characteristic fingerprint spectra for multiplex analysis, making the SERS method well suited for the simultaneous detection of multiple metabolites in biosystems.

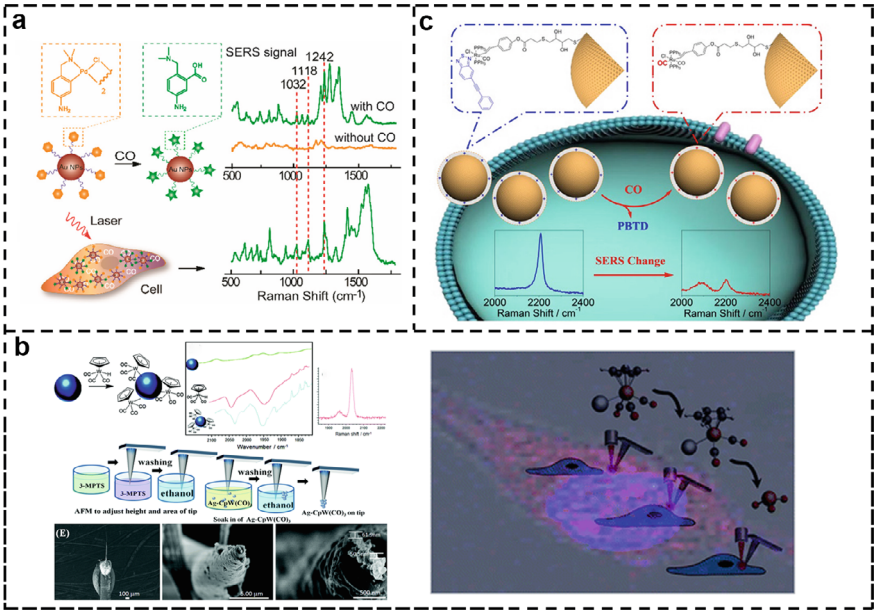



**Fig. 14.19** Responsive SERS probe for in situ monitoring of gaseous messenger. **a** SERS response and sensing mechanism of palladacycle carbonylation on AuNP/PC nanosensors for CO; SERS detection of CO in living cells using AuNP/PC nanosensors. Reproduced from Ref. [139] with the permission. **b** Preparation of CORN-Ag-CpW$(CO)_3$ as detected by IR and SERS; schematic and SEM images for fabrication of CORN-Ag-CpW$(CO)_3$ anchored nano-tip. Reproduced from Ref. [140] with the permission. **c** Schematic illustration of the preparation of the SERS nanoprobe and its sensing mechanism. Reproduced from Ref. [141] with the permission

Tian et al. created a micrometer- to nanometer-sized SERS optophysiological probe to determine both the $CO_3^{2-}$ concentration and the pH in live brains and neurons because both species play important roles in regulating the acid–base balance in the brain (Fig. 14.20a) [113]. They pulled different tip sizes of quartz tapers (QTs) from 50 nm to 5 μm by using a P-2000 laser puller with the correct programs. Then, the quartz taper was coated with a layer of rough gold film by magnetron sputtering (denoted as Au-QT), and the 1-(4-aminophenyl)-2,2,2-trifluoroethanone (AT) and 4-mercaptobenzoic acid (MBA) as the specific recognition elements for $CO_3^{2-}$ and pH, respectively, were co-modified onto the Au-QTs. In addition, MBN with a C≡N group was used as an internal reference in a SERS-silent region of the cell to provide in-built correction. The ratiometric SERS probe showed a good linear response for $CO_3^{2-}$ concentrations in the range of 1.00 ~ 35.0 μM with a limit of detection of 0.16 μM. Meanwhile, the developed probe was able to determine pH values from 5.53 to 8.52. Overall, this work achieved the real-time mapping and simultaneous quantification of $CO_3^{2-}$ and pH in a live brain. Tang et al. designed a dual-signal switchable (DSS) nanoprobe using the fluorescence-Raman signal switch for simultaneous direct imaging with absolute quantification of multiple intracellular

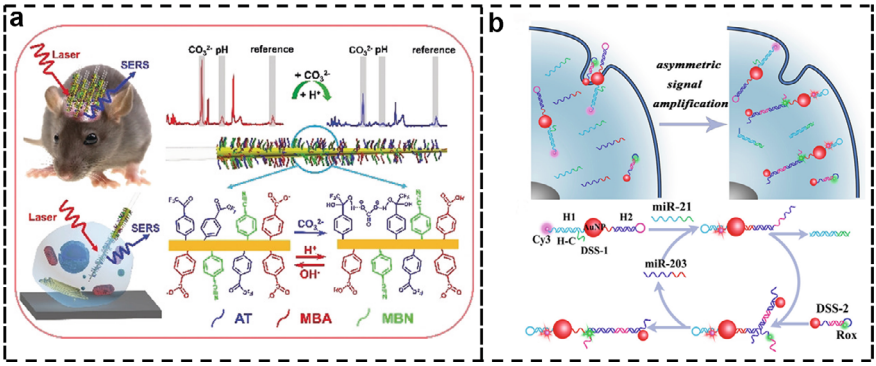



**Fig. 14.20** Responsive SERS probe for in situ monitoring of multiple targets. **a** The principle of the developed SERS probe for the simultaneous biosensing of $CO_3^{2-}$ concentration and pH value in live brains and single neurons. Reproduced from Ref. [113] with the permission. **b** Detection of miR-21 and miR-203 in living cells using DSS probes; mechanism for sensing the asymmetric signal amplification of the DSS probes for miR-21 and miR-203. Reproduced from Ref. [142] with the permission

microRNAs (miRNAs) (Fig. 14.20b) [142]. The fluorescence signal of the probe monitors the intracellular uptake and dynamic behavior of the probe. At the same time, the DSS probe made the real-time quantitative detection of multiple miRNAs possible by measuring the SERS signal ratios. In addition, the in vitro results from the same batch of cell lysates indicated that the low-abundance miR-21 and miR-203 were sensitively and accurately quantified in living MCF-7 cells.

#### 14.3.4.2 Responsive SERS Probe for Liquid Biopsy

It is well known that early screening is essential for effective control, prevention and treatment of disease, especially cancer. Current screening methods for early clinical detection include radiology, histology, endoscopy and liquid biopsy, among which liquid biopsy has distinct advantages. Firstly, liquid biopsy can measure biomarkers in body fluids such as blood or urine with minimal impact on the individual being screened. Secondly, automated analyzer can be used to process a large number of samples for many biomarkers in a relatively short period of time. Thirdly, biomarker testing based on liquid biopsy is relatively inexpensive. Therefore, the development of novel liquid biopsy techniques for tumor biomarker measurement is a mainstream for early cancer screening.

Since some cancer biomarkers are already present in the early stages of the disease process, liquid biopsy can facilitate early prevention and timely treatment for better outcomes. Although many techniques are used in liquid biopsy, SERS still stands out for its strong advantages. Notably, the SERS probes responding to tumor microenvironmental biomarkers for liquid biopsy will provide a tool with higher sensitivity and specificity for liquid biopsy. In addition, the responsive SERS probes will make

simultaneous detection of various biomarkers possible and make liquid biopsy more efficient.

Hepatocellular carcinoma (HCC) is one of the most common and highly lethal malignancies. To provide a rapid, convenient and reliable liquid biopsy method for HCC-associated miRNA (miRNA-224) detection, Zhou et al. proposed a SERS and fluorescence dual-mode biosensor for clinical staging of HCC patients based on serum samples (Fig. 14.21a) [143]. In this work, a well-arranged gold nanoarray (Au NAs) substrates were prepared by etching an ordered polystyrene (PS) cylinder monolayer on the surface of the silicon (Si) substrate as a sacrificial template followed by subsequent gold ion sputtering. Then, the hairpin DNA (Cy3-$H_1$) was attached to the SERS array and provided strong Raman signals. With the addition of miRNA-224, the catalytic hairpin assembly (CHA) caused Cy3-$H_1$ to hybridize with Rhodamine X-labeled hairpin DNA (Rox-$H_2$) through competitive binding to form $H_1$-$H_2$ duplex strands. As a result, the Cy3 molecules left and the Rox molecules got closer to the surface of gold nanoparticles, resulting in enhanced Raman signals for Rox and weakness for Cy3. Based on the sensing strategy, HCC cancer patients and normal ones can be differentiated and miRNA-224 in 6 patients before and after hepatectomy and 16 HCC patients with different Barcelona clinic liver cancer stages can further be detected.

In addition, distinguishing tumor subtypes is essential for developing personalized diagnostic and therapeutic protocols. Simultaneous quantitative analysis of multiple exosomal proteins can facilitate the subtyping of tumors but remains challenging. To address the unmet need, Li et al. developed a paper-based SERS-vertical flow biosensor, named iREX (integrated Raman spectroscopic exosomes) biosensor, for multiplexed quantitative profiling of exosomal proteins in clinical serum samples of patients (Fig. 14.21b) [144]. Utilizing the corresponding aptamer to specifically capture and bind to the exosome to form sandwich complexes, three exosomal proteins (MUC1, HER2 and CEA) in different cell subtypes (luminal A, $HER2^+$, triple negative, and luminal B) can be simultaneously quantified on the basis of the SERS signal brightness associated with the concentration of different exosomes, allowing for accurate diagnosis and molecular subtyping of breast cancer.

Besides the serum, saliva, a pivotal constituent of biofluids, exhibits dynamic fluctuations across diverse pathophysiological states. The identification of salivary biomarkers is also conducive to disease diagnosis [145]. Kong et al. report a versatile SERS platform for the quantitative detection of monosaccharides (glucose, fructose, and galactose) in clinical human saliva samples using a displace-and-trap mechanism (Fig. 14.21c) [146]. This assay relies on the abilities of glucose and galactose to form bidentate glucose and galactose boronic complexes and fructose to form boronic monodentate complexes. The primary probe 3,4-dihydroxybenzonitrile (DBN-CN; a displacement probe with a nitrile group signal at 2226 $cm^{-1}$) can detect the total concentration of the above three monosaccharides by weakly bound to the 4-mercaptophenylboronic acid (MPBA) capture receptor. Then, all the three monosaccharides are first captured by MPBA through the displacement of DBN-CN, followed by subsequent strong binding of the MPBA-triosmium carbonyl cluster

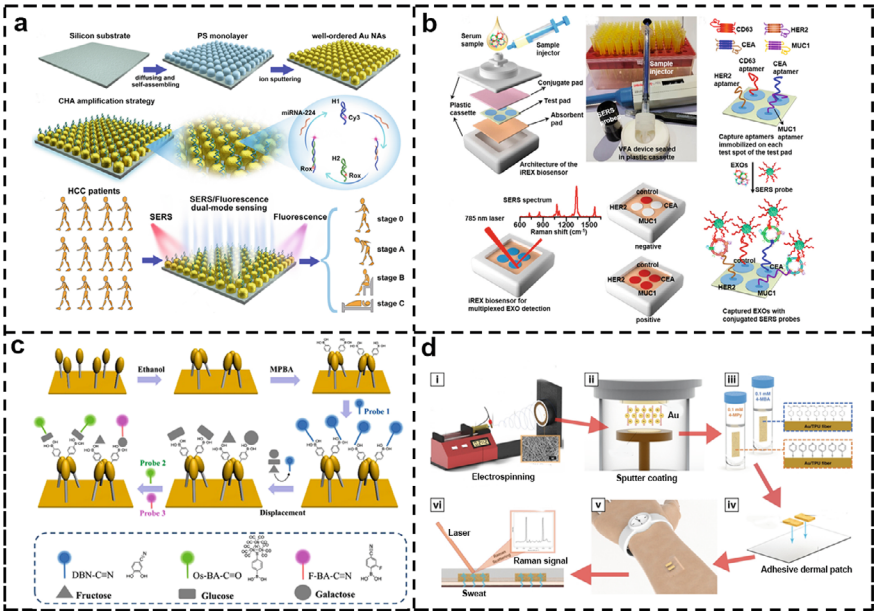



**Fig. 14.21** Responsive SERS probe for liquid biopsy. **a** Schematic illustration of self-assembly process of the Au NA substrate; principle of the Au NA substrate coupled with the CHA amplification strategy for miR-224 detection; procedures of the Au NA substrate-based SERS/FL dual-modal sensing and application for clinical staging. Reproduced from Ref. [143] with the permission. **b** The VFA device is stacked with a conjugate pad, a test pad of four spatially separated test spots and an absorbent pad orderly from the top to the bottom; illustration of multiplexed detection of exosomal proteins in serum samples; schematic of the iREX biosensor based multiplexed detection of exosomal proteins in the presence of no EXOs (negative test) and multiple EXOs (positive test). Reproduced from Ref. [144] with the permission. **c** Schematic representation of the detection mechanism of glucose, fructose, and galactose via multiple optical interference-free SERS probes. Reproduced from Ref. [146] with the permission. **d** Concept outline of SERS-active Au/TPU electrospun wearable sweat pH sensor fabrication and application with (i) electrospinning of TPU nanofibers; (ii) gold sputter coating of TPU electrospun fibers; (iii) pH-responsive SAM assembly on Au/TPU fibers; (iv) attachment of SERS-active Au/TPU electrospun fibers to a transparent adhesive dermal patch; (v) attachment of wearable pH sensor to the subject's arm; (vi) Raman spectroscopy performed. Reproduced from Ref. [147] with the permission

(Os-BA-CO, at 2111 $cm^{-1}$) to glucose and 4-cyano-3-fluorophenyl-boronic acid (F-BA-CN, at 2235 $cm^{-1}$) to galactose. The concentrations of glucose and galactose can be selectively quantified via the CO and CN stretching vibrations of Os-BA-CO and F-BA-CN, respectively. Overall, the facile tandem reaction of the three carbohydrates with boronic acid probes exhibits high response rate and the levels of them in saliva samples are essentially detected and quantified.

In recent years, sweat has also received much attention as a health assessment and biological diagnostic tool. Sweat can convey quite rich physiological information,

such as the rate and amount of sweat secreted by the skin can reflect health information, and sweat is also rich in chemicals and metabolites, which is an even more valuable dataset for research. Radacsi's group fabricated a flexible sweat pH sensor based on SERS-active gold/thermoplastic polyurethane (Au/TPU) electrospun nanofibers for monitoring sweat pH (Fig. 14.21d) [147]. In this work, a nanofibrous SERS-active substrate was prepared by a combination of electrospinning of TPU and Au sputter coating. This substrate was then functionalized with two commonly used pH-responsive molecules, 4-mercaptobenzoic acid (4-MBA), and 4-mercaptopyridine (4-MPy). The SERS spectra at varying pH values indicated that the pH-responsive vibrational modes of both the MBA ($\nu$C=O) and MPy (vC=C). It was found that the 4-MBA/Au/TPU nanofibers could provide accurate pH sensing within the range of pH 5.5–7.0 while 4-MPy/Au/TPU nanofibers can serve as a good supplement to extend the sensitive range of the pH sensor to the full sweat pH range (pH 4.0–7.0).

#### 14.3.4.3 Responsive SERS Probe for Surgery Guiding

Surgical resection is an essential treatment for solid tumors, and the degree of surgical resection is positively correlated with the survival benefit for patients. However, the infiltrating cancer tissue is difficult to resect accurately and completely due to the similarity in color and texture with the normal tissue. How to completely remove the tumor tissue while maximally preserving normal neural tissue poses a great challenge to clinicians. Therefore, the development of intraoperative tumor navigation probes with accurate tracing and rapid response is an urgent clinical need to improve the surgical prognosis of tumor and reduce the damage to functional regions.

With the rapid development of brain tumor surgical navigation, advanced techniques such as neuronavigation, magnetic resonance imaging (MRI), and intraoperative fluorescence imaging have been introduced to help neurosurgeons distinguish between tumor tissues and adjacent normal brain tissues. However, due to the inevitable brain shift during craniotomy, the tumor margins depicted by the preoperative MRI strategy often do not coincide with the actual boundaries. In addition, false positives due to strong autofluorescence excited by blue light and false negatives due to low density of cancer cells at the infiltration boundary of glioma affect its accuracy. Therefore, the analytical method with high sensitivity, high spatial resolution and high signal to background ($S/B$) ratio is extremely demanded.

Responsive SERS probe has unique advantages such as inherent specificity, high sensitivity, multi-channel detection (narrow half peak width) and the localization ability of cells and even molecules, and therefore has broad application prospects in describing tumor boundaries and guiding surgical resection during surgery. Since almost all solid tumors have a common feature in acidic microenvironment, Li et al. created a pair of self-assembled surface-enhanced resonance Raman spectroscopy (SERRS) probes for guiding the surgical removal of gliomas, which was realized by forming their specific assembly in acidic tumor extracellular fluid to activate the SERRS signals (Fig. 14.22a) [148]. Two different kinds of nanoprobes (Au–AZ

and Au–AK) were synthesized and exhibited monodisperse status in neutral environment. While in the acidic tumor environment, the acid-labile exterior shielding layer of these nanoprobes was destroyed, exposing the azide and alkyne functional groups thus then triggered a "Click" cycloaddition reactions. Heptamethine cyanine derivative IR783B was chosen as the Raman reporter because its absorption maxima could resonate with near-infrared (NIR) excitation light. Consequently, the creation of "hot spots" during probes assembly allows for the dual amplification of the SERRS signal, facilitating the response of the probes to the acidic environment of the tumor. With the assistance of a hand-held Raman scanner, the glioma margin in the mouse can be precisely demarcated by the assembled nanoprobes. Furthermore, Li group proposed a pH-responsive ratiometric SERRS probe that determined physiological pHs via an innovative mechanism named spatial orientation induced intramolecular energy transfer (SOIET) (Fig. 14.22b) [100]. The unprotonated IR7p shows parallel conformation relative to the substrate surface but titled or even perpendicular conformation under acidic conditions due to the intermolecular electrostatic repulsion triggered by the protonation of Raman reporter molecule IR7p, producing pH ratiometrically responsive SERRS signals. With assistance of this probe, the intraoperative assessment of tissue malignancies was conducted in live animal models via real-time determination of pH values and further used for navigation the tumor resection surgery.

Although this approach shows valid promise for reducing systemic toxicity and improving surgical prognosis, clinical translation of exogenous probes is still heavily regulated, as they require approval from drug regulatory authorities. Therefore, the development of in vitro imaging probes for surgical navigation is more advantageous in terms of clinical translation. Li et al. further exploited an intelligent SERS navigation system delineating glioma acidic margins without administration of exogenous probes (Fig. 14.22c) [149]. With the help of this system, metabolites from the tumor margins can be transferred non-destructively within a water droplet onto a pH-sensitive SERS chip. A home-made deep learning model automatically processes the Raman spectra acquired by the SERS chip and maps the pH of the tumor resection bed at a faster rate. The overall survival in animal models after SERS system-guided surgery was significantly improved compared to conventional strategies used in clinical practice, implying the promise in accelerating clinical transition of acidic margin-guided surgery for solid tumors.

## 14.4 Conclusion and Prospects

This chapter summarizes the recent progress of SERS-based tagging and responsive probes for biomedical applications. We elaborated the advantages of SERS bioanalysis, including high specificity, outstanding sensitivity and especially the unparalleled multiplex capabilities. The key points lie in the principles of the construction of SERS nanotags, mechanisms of responsive SERS probes and their significant contributions to bioanalysis. The past decades have witnessed the rapid development of

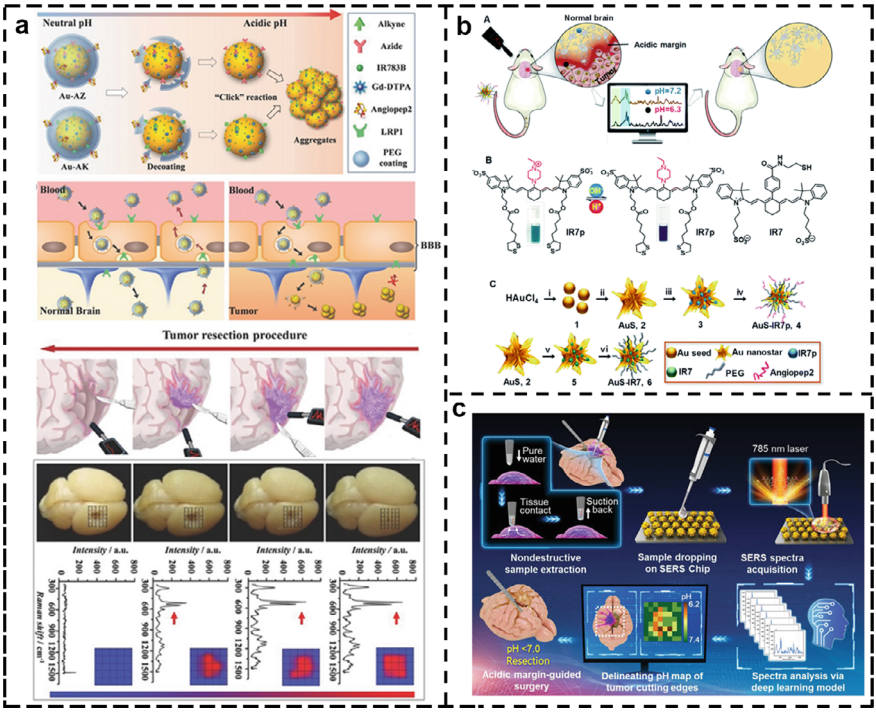



**Fig. 14.22** Responsive SERS probe for surgery guiding. **a** The cleavage of the PEG coating in physiological acidity triggers aggregation between Au–AZ and Au–AK via "Click" cycloaddition reactions; due to the LPR1-mediated, bidirectional, BBB-traversing strategy, while the bulky AuNS aggregates are continuously trapped in tumor acidic interstitium, the intact nanoprobes in the normal brain tissue can be transported back into the blood stream, which increases the sensitivity for the brain tumor margins; Au–AZ/Au–AK mixture intraoperatively guiding glioma resection using a handheld Raman detector. Reproduced from Ref. [148] with the permission. **b** Illustration presenting the acidic margin-guided brain tumor surgery by intraoperatively determining tissue pH values/malignancies in tumor cutting edges; chemical structure of the pH-responsive reporter molecule IR7p and the control reporter IR7 without pH sensitivity; synthesis of pH-responsive SERRS probe AuS-IR7p and the control probe AuS-IR7. Reproduced from Ref. [100] with the permission. **c** Schematic diagram of the SERS navigation system intraoperatively delineating acidic margin of glioma. Reproduced from Ref. [149] with the permission

labeled and responsive SERS probes and the combination of both makes SERS shine in bioanalysis. Recent advancements have seen the applications of above two types of SERS probes for in situ biomolecules detection and bioimaging, liquid biopsy and surgical navigation. However, there are still stepping stones that need to reach when employing these SERS probes for clinical translation.

Looking into the future, the applications of the tagging and responsive SERS probes in the biomedical field still face challenges. **Firstly**, the identification of the analytes primarily relies on signal changes in the fingerprint region of the SERS probe. However, in complex biosystems or during multi-targets analysis, effectively

addressing signal overlap within the fingerprint region has proved to be challenging. Currently, the triple bond-based SERS probes are predominantly utilized as undisturbed interreference signals in the bio-silent region and are not actively involved in the response process to analytes. Consequently, the development of responsive and labeled SERS probes based on triple bond sensing can effectively circumvent the problem of signal overlap, allowing for the simultaneous analysis of multiple analytes within complex systems. **Secondly**, the current lack of Raman scanners with wide fields of view and fast image acquisition speeds has been a barrier to the clinical application of SERS probes. Although many efforts have been made to improve the imaging speed, mainly in the development of ultra-high brightness SERS probes and the adoption of advanced imaging methods, the current SERS imaging speed is still slower than fluorescence imaging. Recently, the machine learning technologies have been reported to transform the low-resolution image obtained at a rapid acquisition speed into a high-resolution one [150], which may provide a new avenue to speed up the SERS imaging application in future. In addition, Using the large amount of spectral data collected previously to train deep learning models, multiple targets can be identified and quantified simultaneously from complex Raman spectra in a more accurate and timely manner. **Thirdly**, the clinical translation is the biggest challenge faced by SERS probes. The critical issues that need to be addressed in the clinical application of SERS probes are quality standardization, in vivo biocompatibility, uncertainty about long-term toxicity. The materials used in the preparation of gold or silver SERS substrate, such as biocompatible silica and polyethylene glycol protective coatings, should be carefully considered to minimize systemic cytotoxicity and optimize pharmacokinetic behavior. Last but not least, developing instruments with advanced performance is also an aspect of applying the SERS probes in bioanalysis. In brief, with the development of technology, we anticipate that the above strategies will facilitate the clinical application of SERS probes for in situ monitoring of pathological indicators, depicting the margins of tumor infiltration, and quantitatively detecting the tumor-associated metabolites.

## References

1. M. Fleischmann, P. J. Hendra, A. J. McQuillan, Raman spectra of pyridine adsorbed at a silver electrode. Chem. Phys. Lett., **26**, 163–166 (1974)
2. D. Graham, M. Moskovits, Z. Q. Tian, SERS-facts, figures and the future. Chem. Soc. Rev. **46**, 3864–3865 (2017)
3. C. Zong, M. Xu, L. J. Xu, T. Wei, X. Ma, X. S. Zheng, R. Hu, B. Ren, Surface-Enhanced Raman Spectroscopy for Bioanalysis: Reliability and Challenges. Chem. Rev., **118**, 4946–4980 (2018)
4. S. Nie, S. R. Emory, Probing single molecules and single nanoparticles by surface-enhanced Raman scattering. Science, **275**, 1102–1106 (1997)
5. H. Ma, S. Yan, X. Y. Lu, Y. F. Bao, J. Liu, L.X. Liao, K. Dai, M. F. Cao, X. J. Zhao, H. Yan, H. L. Wang, X. H. Peng, N. Y. Chen, H. S. Feng, L. L. Zhu, G. B. Yao, C. H. Fan, B. J. Wang, X. Wang, B. Ren, Rapidly determining the 3D structure of proteins by surface-enhanced Raman spectroscopy. Sci. Adv. **9**, 8362–8373 (2023)

6. Q. Li, H. Huo, Y. Wu, L. Chen, L. Su, X. Zhang, J. Song, H. Yang, Design and Synthesis of SERS Materials for In Vivo Molecular Imaging and Biosensing. Adv. Sci. **10**, 2202051 (2023)
7. Z. Wang, S. Zong, L. Wu, D. Zhu, Y. Cui, SERS-Activated Platforms for Immunoassay: Probes, Encoding Methods, and Applications. Chem. Rev. **117**, 7910–7963 (2017)
8. Y. Chen, J. Q. Ren, X. G. Zhang, D. Y. Wu, A. G. Shen, J. M. Hu, Alkyne-Modulated Surface-Enhanced Raman Scattering-Palette for Optical Interference-Free and Multiplex Cellular Imaging. Anal. Chem. **88**, 12, 6115–6119 (2016)
9. G. Cutshaw, S. Uthaman, N. Hassan, S. Kothadiya, X. Wen, R. Bardhan, The Emerging Role of Raman Spectroscopy as an Omics Approach for Metabolic Profiling and Biomarker Detection toward Precision Medicine. Chem. Rev. **123**, 8297–8346 (2023)
10. T. Gong, C. M. Das, M. J. Yin, T. R. Lv, N. M. Singh, A. M. Soehartono, G. Singh, Q. F. An, K. T. Yong, Development of SERS tags for human diseases screening and detection. Coordin. Chem. Rev. **470**, 214711 (2022)
11. J. Wang, K. M. Koo, Y. Wang, Matt Trau, Engineering State-of-the-Art Plasmonic Nanomaterials for SERS-Based Clinical Liquid Biopsy Applications. Adv. Sci. 6, 1900730 (2019)
12. Y. Wang, B. Yan, L. Chen, SERS tags: novel optical nanoprobes for bioanalysis. Chem. Rev. **113**, 1391 (2013)
13. B. Deng, Y. Wang, Y. Wu, W. Yin, J. Lu, J. Ye, Raman nanotags-guided intraoperative sentinel lymph nodes precise location with minimal invasion. Adv. Sci. **9**, 2102405 (2022)
14. H. Liu, X. Gao, C. Xu, D. Liu, SERS Tags for Biomedical Detection and Bioimaging. Theranostics, **12**, 4, 1870–1903 (2022)
15. X. Liu, X. Liu, P. Rong, D. Liu, Recent advances in background-free Raman scattering for bioanalysis. Trac-Trend. Anal. Chem. **123**, 115765 (2020)
16. X. Liang, N. Li, R. Zhang, P. Yin, C. Zhang, N. Yang, K. Liang, B. Kong, Carbon-based SERS biosensor: from substrate design to sensing and bioapplication. NPG Asia Materials, **13**, 8 (2021)
17. R. Zhang, T. D. James, Responsive Probes and Molecular Bioimaging. Chem. Asian J. **18**, e202300058 (2023)
18. M. J. Banholzer, J. E. Millstone, L. Qin, C. A. Mirkin, Rationally Designed Nanostructures for Surface-Enhanced Raman Spectroscopy. Chem. Soc. Rev. **37**, 885–897 (2008)
19. S. Schlücker, SERS Microscopy: Nanoparticle Probes and Biomedical Applications. Chem. Phys. Chem. **10**, 1344–1354 (2009)
20. W. Xie, P. Qiu, C. Mao, Bio-imaging, Detection and Analysis by Using Nanostructures as SERS Substrates. J. Mater. Chem. **21**, 5190–5202 (2011)
21. S. Link, M. A. El-Sayed, Size and Temperature Dependence of the Plasmon Absorption of Colloidal Gold Nanoparticles. J. Phys. Chem. B, **103**, 4212–4217 (1999)
22. A. K. Samal, L. Polavarapu, S. R. Cedeira, L. M. L. Marzán, J. P. Juste, I. P. Santos, Size Tunable Au@Ag Core–Shell Nanoparticles: Synthesis and Surface-Enhanced Raman Scattering Properties. Langmuir, **29**, 48, 15076–15082 (2013)
23. X. Huang, I. H. El-Sayed, W. Qian, M. El-Sayed, Cancer Cells Assemble and Align Gold Nanorods Conjugated to Antibodies to Produce Highly Enhanced, Sharp, and Polarized Surface Raman Spectra: a Potential Cancer Diagnostic Marker. Nano Lett. **7**, 1591–1597 (2007)
24. D. K. Lim, K. S. Jeon, J. H. Hwang, H. Kim, S. Kwon, Y. D. Suh, J. M. Nam, Highly uniform and reproducible surface-enhanced Raman scattering from DNA-tailorable nanoparticles with 1-nm interior gap. Nat. Nanotech. **6**, 452–460 (2011)
25. L. Lin, H. C. Gu, J. Ye, Plasmonic multi-shell nanomatryoshka particles as highly tunable SERS tags with built-in reporters. Chem. Comm. **51**, 17740–17743 (2015)
26. Y. Q. Zhang, Y. Q. Gu, J. He, B. D. Thackray, J. Ye. Ultrabright gap-enhanced Raman tags for high-speed bioimaging. Nat. Comm. **10**, 3905–3916 (2019)
27. L. J. Xu, Z. C. Lei, J. Li, C. Zong, C. J. Yang, Bin Ren, Label-Free Surface-Enhanced Raman Spectroscopy Detection of DNA with Single-Base Sensitivity. J. Am. Chem. Soc. **137**, 15, 5149–5154 (2015)

28. X. Tan, Z. Wang, J. Yang, Polyvinylpyrrolidone-(PVP-) coated silver aggregates for high performance surface-enhanced Raman scattering in living cells. Nanotechnology, **20**, 445102 (2009)
29. K. Kim, H.B. Lee, H.K. Park, K.S. Shin, Easy deposition of Ag onto polystyrene beads for developing surface-enhanced-Raman-scattering-based molecular sensors. J. Colloid Inter. Sci. **318**, 195–201 (2008)
30. J. M. Li, W. F. Ma, C. Wei, J. Guo, C. C. Wang, Poly (styrene-co-acrylic acid) core and silver nanoparticle/silica shell composite microspheres as high performance surface-enhanced Raman spectroscopy (SERS) substrate and molecular barcode label. J. Mater. Chem. **21**, 5992–5998 (2011)
31. J. H. Kim, J. S. Kim, H. Choi, S. M. Lee, B. H. Jun, K. N. Yu, E. Kuk, Y. K. Kim, D. H. Jeong, M. H. Cho, Y. S. Lee, Nanoparticle probes with surface enhanced Raman spectroscopic tags for cellular cancer targeting. Anal. Chem. **78**, 6967–6973 (2006)
32. L. C. Martin, I. A. Larmour, K. Faulds, Turning up the lights-fabrication of brighter SERRS nanotags. Chem. Comm. **46**, 5247–5249 (2010)
33. K. Kneipp, H. Kneipp, I. Itzkan, R. R. Dasari, M. S. Feld, Ultrasensitive chemical analysis by Raman spectroscopy. Chem. Rev. **99**, 2957–2976 (1999)
34. G. McNay, D. Eustace, W. E. Smith, Surface-enhanced Raman scattering (SERS) and surface-enhanced resonance Raman scattering (SERRS): a review of applications. Appl. Spectro. **65**, 825–837 (2011)
35. Y. Yin, Q. Li, S. Ma, H. Liu, B. Dong, J. Yang, D. Liu, Prussian Blue as a Highly Sensitive and Background-Free Resonant Raman Reporter. Anal. Chem. **89**, 1551–1557 (2017)
36. L. Wei, Z. Chen, L. Shi, R. Long, A. V. Anzalone, L. Zhang, F. Hu, R. Yuste, V. W. Cornish, W. Min, Super-multiplex vibrational imaging. Nature, **544**, 465–470 (2017)
37. K. V. Kong, Z. Lam, W. D. Goh, W. K. Leong, M. Olivo, Metal Carbonyl–Gold Nanoparticle Conjugates for Live-Cell SERS Imaging. Angew. Chem. Int. Ed. **51**, 9796–9799 (2012)
38. D. C. Kennedy, L. L. Tay, R. K. Lyn, Y. Rouleau, J. Hulse, J. P. Pezacki, Nanoscale Aggregation of Cellular $\beta_2$-Adrenergic Receptors Measured by Plasmonic Interactions of Functionalized Nanoparticles. ACS Nano, **3**, 8, 2329–2339 (2009)
39. H. Yamakoshi, K. Dodo, A. Palonpon, J. Ando, K. Fujita, S. Kawata, M. Sodeoka, Alkyne-Tag Raman Imaging for Visualization of Mobile Small Molecules in Live Cells. J. Am. Chem. Soc. **134**, 20681–20689 (2012)
40. J. Xie, Q. Zhang, J. Y. Lee, D. I. Wang, The Synthesis of SERS-Active Gold Nanoflower Tags for In Vivo Applications. ACS Nano **2**, 2473–2480 (2008)
41. M. Yang, T. Chen, W. S. Lau, Y. Wang, Q. H. Tang, Y. H. Yang, H. Y. Chen, Development of polymer-encapsulated metal nanoparticles as surface-enhanced Raman scattering probes. Small **5**, 198–202 (2009)
42. A. G. Shen, L. F. Chen, W. Xie, J. C. Hu, A. Zeng, R. Richards, J. M. Hu, Triplex Au-Ag-C Core-Shell Nanoparticles as a Novel Raman Label. Adv. Funct. Mater. **20**, 969–975 (2010)
43. J. F. Li, Y. J. Zhang, S. Y. Ding, R. Panneerselvam, Z. Q. Tian, Core-Shell Nanoparticle-Enhanced Raman Spectroscopy. Chem. Rev. **117**, 5002–5069 (2017)
44. J. Wang, D. Liang, J. Feng, X. Tang, Multicolor Cocktail for Breast Cancer Multiplex Phenotype Targeting and Diagnosis Using Bioorthogonal Surface-Enhanced Raman Scattering Nanoprobes. Anal. Chem. **91**, 11045–11054 (2019)
45. A. M. Fales, H. Yuan, T. Vo-Dinh, Cell-Penetrating Peptide Enhanced Intracellular Raman Imaging and Photodynamic Therapy. Mol. Pharmaceutics **10**, 2291–2298 (2013)
46. J. W. Kang, P. T. So, R. R. Dasari, D. K. Lim, High Resolution Live Cell Raman Imaging Using Subcellular Organelle-Targeting SERS-Sensitive Gold Nanoparticles with Highly Narrow Intra-Nanogap. Nano Lett. **15**, 1766–1772 (2015)
47. S. Pal, S. Harmsen, A. Oseledchyk, H. T. Hsu, M. F. Kircher, MUC1 Aptamer Targeted SERS Nanoprobes. Adv. Funct. Mater. **27**, 1606632 (2017)
48. W. Ma, H. Yin, L. Xu, X. Wu, H. Kuang, L. Wang, C. Xu, Ultrasensitive aptamer-based SERS detection of PSAs by heterogeneous satellite nanoassemblies. Chem. Commun. **50**, 9737–9740 (2014)

49. Y. Chen, X. Bai, L. Su, Z. Du, A. Shen, A. Materny, J. Hu, Combined Labelled and Label-free SERS Probes for Triplex Three-dimensional Cellular Imaging. Sci. Rep. **6**, 19173 (2016)
50. H. J. Shin, J. H. Lee, Y. D. Kim, I. Shin, T. Sim, D. K. Lim, Raman-Based in Situ Monitoring of Changes in Molecular Signatures during Mitochondrially Mediated Apoptosis. ACS Omega **4**, 5, 8188–8195 (2019)
51. S. E. J. Bell, N. M. S. Sirimuthu, Surface-enhanced Raman spectroscopy (SERS) for sub-micromolar detection of DNA/RNA mononucleotides. J. Am. Chem. Soc. **128**, 15580–15581 (2006)
52. Y. C. Cao, R. Jin, C. A. Mirkin, Nanoparticles with Raman spectroscopic fingerprints for DNA and RNA detection. Science, **297**, 1536 (2002)
53. X. Wang, N. Choi, Z. Cheng, J. Ko, L. Chen, J. Choo, Simultaneous detection of dual nucleic acids using a SERS-based lateral fow assay biosensor. Anal. Chem. **89**, 2, 1163–1169 (2017)
54. H. T. Ngo, N. Gandra, A. M. Fales, S. M. Taylor, T. Vo-Dinh, Sensitive DNA detection and SNP discrimination using ultrabright SERS nanorattles and magnetic beads for malaria diagnostics. Biosens. Bioelectron. **81**, 8–14 (2016)
55. E. J. Wee, Y. Wang, S. C. Tsao, M. Trau, Simple, sensitive and accurate multiplex detection of clinically important melanoma DNA mutations in circulating tumour DNA with SERS nanotags. Theranostics, **6**, 1506–1513 (2016)
56. W. Zhou, Q. Li, H. Liu, J. Yang, D. Liu, Building electromagnetic hot spots in living cells via target-triggered nanoparticle dimerization. ACS Nano **11**, 3532–3541 (2017)
57. M. H. Liu, C. H. Zheng, M. L. Cui, X. Y. Zhang, D. P. Yang, X. S. Wang, Graphene oxide wrapped with gold nanorods as a tag in a SERS based immunoassay for the hepatitis B surface antigen. Microchim. Acta. **185**, 458 (2018)
58. S. J. Ye, X. X. Li, M. L. Wang, B. Tang, Fluorescence and SERS imaging for the simultaneous absolute quantification of multiple miRNAs in living cells. Anal Chem. **89**, 5124–5130 (2017)
59. X. R. Bai, L. H. Wang, J. Q. Ren, X. W. Bai, L. W. Zeng, A. G. Shen, J. M. Hu, Accurate Clinical Diagnosis of Liver Cancer Based on Simultaneous Detection of Ternary Specific Antigens by Magnetic Induced Mixing Surface-Enhanced Raman Scattering Emissions. Anal. Chem. **91**, 2955–2963 (2019)
60. W. Xie, L. Wang, Y. Zhang, L. Su, A. Shen, Ji. Tan, J. Hu, Nuclear Targeted Nanoprobe for Single Living Cell Detection by Surface-Enhanced Raman Scattering. Bioconjugate Chem. **20**, 768–773 (2009)
61. W. R. Premasiri, P. Lemler, Y. Chen, Y. Gebregziabher, L. D. Ziegler, SERS Analysis of Bacteria, Human Blood, and Cancer Cells: a Metabolomic and Diagnostic Tool. **12**, 257–283 (2014)
62. X. Zhang, C. Li, Y. Pei, W. Song, S. Zhang, Preparation of a Novel Raman Probe and Its Application in the Detection of Circulating Tumor Cells and Exosomes. ACS Appl. Mater. Interfaces **11**, 32, 28671–28680 (2019)
63. Z. Wang, S. Zong, Y. Wang, N. Li, L. Li, J. Lu et al., Screening and multiple detection of cancer exosomes using an SERS-based method. Nanoscale, **10**, 9053–9062 (2018)
64. M. Y. Sha, H. Xu, M. J. Natan, R. Cromer, Surface-Enhanced Raman Scattering Tags for Rapid and Homogeneous Detection of Circulating Tumor Cells in the Presence of Human Whole Blood. J. Am. Chem. Soc. **130**, 17214–17215 (2008)
65. X. Wang, X. Qian, J. J. Beitler, Z. G. Chen, F. R. Khuri, M. M. Lewis, H. J. C. Shin, S. Nie, D. M. Shin, Detection of Circulating Tumor Cells in Human Peripheral Blood Using Surface-Enhanced Raman Scattering Nanoparticles. Cancer Res. 71, 1526–1532 (2011)
66. Y. Wang, S. Ravindranath, J. Irudayaraj, Separation and detection of multiple pathogens in a food matrix by magnetic SERS nanoprobes. Anal. Bioanal. Chem. **399**, 3, 1271–1278 (2011)
67. S. Wen, X. Miao, G. C. Fan, T, Xu, L. P. Jiang, P. Wu, Aptamer-conjugated Au nanocage/$SiO_2$ core-shell bifunctional nanoprobes with high stability and biocompatibility for cellular SERS imaging and near-infrared photothermal therapy. ACS Sens. **4**, 301–308 (2019)
68. J. Song, B. Duan, C. Wang, J. Zhou, L. Pu, Z. Fang, P. Wang, T. T. Lim, H. Duan, SERS-Encoded Nanogapped Plasmonic Nanoparticles: Growth of Metallic Nanoshell by Templating Redox Active Polymer Brushes. J. Am. Chem. Soc. **136**, 6838–6841 (2014)

69. W. Zhu, C. Y. Wang, J. M. Hu, A. G. Shen, Promoted "Click" SERS Detection for Precise Intracellular Imaging of Caspase-3. Anal. Chem. **93**, 4876–4883 (2021)
70. M. Y. Gao, Q. Chen, W. Li, A. G. Shen, J. M. Hu, Combined surface-enhanced Raman scattering emissions for high-throughput optical labels on micrometer-scale objects. Anal Chem. **91**, 13866–13873 (2019)
71. Y. Zeng, J. Q. Ren, A. G. Shen, J. M. Hu, Splicing Nanoparticles-Based "Click" SERS Could Aid Multiplex Liquid Biopsy and Accurate Cellular Imaging. J. Am. Chem. Soc. **140**, 34, 10649–10652 (2018)
72. J. Ko, S. G. Park, S. Lee, X. Wang, C. Mun, S. Kim, Culture-free detection of bacterial pathogens on plasmonic nanopillar arrays using rapid Raman mapping. ACS Appl. Mater. Interfaces. **10**, 6831–6840 (2018)
73. Z. Xu, C. Zhang, Y. Yu, W. Li, Z. Ma, J. Wang, Photoactive silver nanoagents for background-less monitoring and precision killing of multidrug-resistant bacteria. Nanotheranostics, **5**, 472–487 (2021)
74. W. Zhu, J. Y. Tang, D. Yu, A. G. Shen, Silent Raman imaging of highly effective anti-bacterial activity synchronous with biofilm breakage using poly(4-cyanostyrene)@silver@polylysine nanocomposites. Analyst, **148**, 628–635 (2023)
75. S. Schlücker, B. Küstner, A. Punge, R. Bonfig, A. Marx, P. Ströbel, Immuno-Raman microspectroscopy: In situ detection of antigens in tissue specimens by surface-enhanced Raman scattering. J. Raman. Spectrosc. **37**, 719–721 (2006)
76. M. Salehi, L. Schneider, P. Ströbel, A. Marx, J. Packeisen, S. Schlücker, Two-color SERS microscopy for protein co-localization in prostate tissue with primary antibody-protein A/G-gold nanocluster conjugates. Nanoscale **6**, 2361–2367 (2014)
77. J. Li, H. Liu, P. Rong, W. Zhou, X. Gao, D. Liu, A Universal Strategy for One-pot Synthesis of SERS Tags. Nanoscale, **10**, 8292–8297 (2018)
78. J. Li, F. Liu, X. Bi, J. Ye, Imaging immune checkpoint networks in cancer tissues with supermultiplexed SERS nanoprobes. Biomaterials, **302**, 122327 (2023)
79. S. Keren, C. Zavaleta, Z. Cheng, A. de la Zerda, O. Gheysens, S. S. Gambhir, Noninvasive molecular imaging of small living subjects using Raman spectroscopy. PNAS, **105**, 5844–5849 (2008)
80. S. Harmsen, R. Huang, M. A. Wall, H. Karabeber, J. M. Samii, M. Spaliviero, et al., Surface-enhanced resonance Raman scattering nanostars for high-precision cancer imaging. Sci Transl Med. 7, 271ra7 (2015)
81. Cristina L. Zavaleta, Bryan R. Smith, Ian Walton, William Doering, Glenn Davis, Borzoyeh Shojaei, Michael J. Natan, and Sanjiv S. Gambhir, Multiplexed imaging of surface enhanced Raman scattering nanotags in living mice using noninvasive Raman spectroscopy. PNAS, **106**, 13511–13516 (2009)
82. R. Huang, S. Harmsen, J. M. Samii, H. Karabeber, K. L. Pitter, E. C. Holland, M. F. Kircher, High Precision Imaging of Microscopic Spread of Glioblastoma with a Targeted Ultrasensitive SERRS Molecular Imaging Probe. Theranostics, **6**, 1075–1084 (2016)
83. H. Karabeber, R. Huang, P. Iacono, J. M. Samii, K. Pitter, E. C. Holland, M. F. Kircher, Guiding Brain Tumor Resection Using Surface-Enhanced Raman Scattering Nanoparticles and a Hand-Held Raman Scanner. ACS Nano **8**, 9755–9766 (2014)
84. B. Deng, Y. Wang, Y. Wu, W. Yin, J. Lu, J. Ye, Raman Nanotags-Guided Intraoperative Sentinel Lymph Nodes Precise Location with Minimal Invasion. Adv. Sci. **9**, 2102405 (2022)
85. B. Shi, B. Zhang, Y. Zhang, Y. Gu, C. Zheng, J. Yan, W. Chen, F. Yan, J. Ye, H. Zhang, Multifunctional gap-enhanced Raman tags for preoperative and intraoperative cancer imaging. Acta Biomater, **1**, 210–220 (2020)
86. Y. Qiu, Y. Zhang, M. Li, G. Chen, C. Fan, K. Cui, J. Wan, A. Han, J. Ye, Z. Xiao, Intraoperative Detection and Eradication of Residual Microtumors with Gap-Enhanced Raman Tags. ACS Nano, **12**, 7974–7985 (2018)
87. Zhang Y, Liu Z, Thackray BD, Bao Z, Yin X, Shi F, et al. Intraoperative Raman-guided chemo-photothermal synergistic therapy of advanced disseminated ovarian cancers. Small **14**, 1801022 (2018)

88. W. Zhu, M. Y. Gao, Q. Zhu, B. Chi, L. W. Zeng, J. M. Hu, A. G. Shen, Monodispersed plasmonic Prussian blue nanoparticles for zero-background SERS/MRI-guided phototherapy. Nanoscale, **12**, 3292–3301 (2020)
89. Y. Wen, V. X. Truong, M. Li, Real-Time Intraoperative Surface-Enhanced Raman Spectroscopy-Guided Thermosurgical Eradication of Residual Microtumors in Orthotopic Breast Cancer. Nano Lett. **21**, 3066–3074 (2021)
90. P. D. Howes, S. Rana, M. M. Stevens, Plasmonic nanomaterials for biodiagnostics. Chem. Soc. Rev. **43**, 3835–3853 (2014)
91. H. Yin, Z. Jin, W. Duan, B. Han, L. Han, C. Li, Emergence of responsive surface-enhanced Raman scattering probes for imaging tumor-associated metabolites. Adv. Healthc. Mater. **11**, 2200030 (2022)
92. W. Nam, X. Ren, S.A.S. Tali, P. Ghassemi, I. Kim, M. Agah, W. Zhou, Refractive-index-insensitive nanolaminated SERS substrates for label-free Raman profiling and classification of living cancer cells. Nano Lett. **19**, 7273–7281 (2019)
93. S. Vantasin, W. Ji, Y. Tanaka, Y. Kitahama, M. Wang, K. Wongravee, H. Gatemala, S. Ekgasit, Y. Ozaki, 3D SERS imaging using chemically synthesized highly symmetric nanoporous silver microparticles. Angew. Chem. Int. Ed. **55**, 8391–8395 (2016)
94. J. Lin, Y. Shang, X. Li, J. Yu, X. Wang, L. Guo, Ultrasensitive SERS detection by defect engineering on single $Cu_2O$ superstructure particle. Adv. Mater. **29**, 1604797 (2017)
95. D. Liu, X. Chen, Y. Hu, T. Sun, Z. Song, Y. Zheng, Y. Cao, Z. Cai, M. Cao, L. Peng, Y. Huang, L. Du, W. Yang, G. Chen, D. Wei, A.T.S. Wee, D. Wei, Raman enhancement on ultra-clean graphene quantum dots produced by quasi-equilibrium plasma-enhanced chemical vapor deposition. Nat. Commun. **9**, 193 (2018)
96. J. Liu, T. Zheng, Y. Tian, Functionalized h-BN nanosheets as a theranostic platform for SERS real-time monitoring of Microrna and photodynamic therapy. Angew. Chem. Int. Ed. **58**, 7757–7761 (2019)
97. X. Wang, L. Guo, SERS activity of semiconductors: crystalline and amorphous nanomaterials. Angew. Chem. Int. Ed. **59**, 4231–4239 (2020)
98. L. Litti, M. Meneghetti, Predictions on the SERS enhancement factor of gold nanosphere aggregate samples. Phys. Chem. Chem. Phys. **21**, 15515–15522 (2019)
99. L. Jiang, J. Qian, F. Cai, S. He, Raman reporter-coated gold nanorods and their applications in multimodal optical imaging of cancer cells. Anal. Bioanal. Chem. **400**, 2793–2800 (2011)
100. W. Duan, Q. Yue, Y. Liu, Y. Zhang, Q. Guo, C. Wang, S. Yin, D. Fan, W. Xu, J. Zhuang, J. Gong, X. Li, R. Huang, L. Chen, S. Aime, Z. Wang, J. Feng, Y. Mao, X. Zhang, C. Li, A pH ratiometrically responsive surface enhanced resonance Raman scattering probe for tumor acidic margin delineation and image-guided surgery. Chem. Sci. **11**, 4397–4402 (2020)
101. H. Chen, Z. Cheng, X. Zhou, R. Wang, F. Yu, Emergence of surface-enhanced Raman scattering probes in near-infrared windows for biosensing and bioimaging. Anal. Chem. **94**, 143–164 (2022)
102. S. Laing, L.E. Jamieson, K. Faulds, D. Graham, Surface-enhanced Raman spectroscopy for in vivo biosensing. Nat. Rev. Chem. **1**, 0060 (2017)
103. P. Pinkhasova, L. Yang, Y. Zhang, S. Sukhishvili, H. Du, Differential SERS activity of gold and silver nanostructures enabled by adsorbed poly(vinylpyrrolidone). Langmuir **28**, 2529–2535 (2012)
104. Q. Yue, X. Gao, Y. Yu, Y. Li, W. Hua, K. Fan, R. Zhang, J. Qian, L. Chen, C. Li, Y. Mao, An EGFRVIII targeted dual-modal gold nanoprobe for imaging-guided brain tumor surgery. Nanoscale **9**, 7930–7940 (2017)
105. W. T. Al-Jamal, K. T. Al-Jamal, B. Tian, A. Cakebread, J. M. Halket, K. Kostarelos, Tumor targeting of functionalized quantum dot-liposome hybrids by intravenous administration. Mol. Pharm. **6**, 520–530 (2009)
106. W. E. Doering, S. Nie, Spectroscopic tags using dye-embedded nanoparticles and surface-enhanced Raman scattering. Anal. Chem. **75**, 6171–6176 (2003)
107. S. Jung, J. Nam, S. Hwang, J. Park, J. Hur, K. Im, N. Park, S. Kim, Theragnostic pH-sensitive gold nanoparticles for the selective surface enhanced Raman scattering and photothermal cancer therapy. Anal. Chem. **85**, 7674–7681 (2013)

108. W. Li, I. Kanyo, C. Kuo, S. Thanneeru, J. He, pH-programmable self-assembly of plasmonic nanoparticles: hydrophobic interaction versus electrostatic repulsion. Nanoscale **7**, 956–964 (2015)
109. C. Zhang, X. Liu, Z. Xu, D. Liu, Multichannel stimulus-responsive nanoprobes for $H_2O_2$ sensing in diverse biological milieus. Anal. Chem. **92**, 12639–12646 (2020)
110. Y. Si, Y. Bai, X. Qin, J. Li, W. Zhong, Z. Xiao, J. Li, Y. Yin, Alkyne-DNA-functionalized alloyed Au/Ag nanospheres for ratiometric surface-enhanced Raman scattering imaging assay of endonuclease activity in live cells. Anal. Chem. **90**, 3898–3905 (2018)
111. Y. Shen, J. Yue, W. Shi, W. Xu, S. Xu, Target-triggered hot spot dispersion for cellular biothiol detection via background-free surface-enhanced Raman scattering tags. Biosens. Bioelectron. **151**, 111957 (2020)
112. Y.W. Wang, J.D. Doerksen, S. Kang, D. Walsh, Q. Yang, D. Hong, J.T.C. Liu, Multiplexed molecular imaging of fresh tissue surfaces enabled by convection-enhanced topical staining with SERS-coded nanoparticles. Small **12**, 5612–5621 (2016)
113. W. Wang, F. Zhao, M. Li, C. Zhang, Y. Shao, Y. Tian, A SERS optophysiological probe for the real-time mapping and simultaneous determination of the carbonate concentration and pH value in a live mouse brain. Angew. Chem. Int. Ed. **58**, 5256–5260 (2019)
114. H. Ma, S. Liu, N. Zheng, Y. Liu, X.X. Han, C. He, H. Lu, B. Zhao, Frequency shifts in surface-enhanced Raman spectroscopy-based immunoassays: mechanistic insights and application in protein carbonylation detection. Anal. Chem. **91**, 9376–9381 (2019)
115. W. Zhu, L. Cheng, M. Li, D. Zuo, N. Zhang, H. Zhuang, D. Xie, Q. Zeng, J.A. Hutchison, Y. Zhao, Frequency shift Raman-based sensing of serum MicroRNAs for early diagnosis and discrimination of primary liver cancers. Anal. Chem. **90**, 10144–10151 (2018)
116. M. G. Vander Heiden, L.C. Cantley, C.B. Thompson, Understanding the Warburg effect: the metabolic requirements of cell proliferation. Science **324**, 1029–1033 (2009)
117. L. Puppulin, S. Hosogi, H. Sun, K. Matsuo, T. Inui, Y. Kumamoto, T. Suzaki, H. Tanaka, Y. Marunaka, Bioconjugation strategy for cell surface labelling with gold nanostructures designed for highly localized pH measurement. Nat. Commun. **9**, 5278 (2018)
118. L. Fang, X. Pan, K. Liu, D. Jiang, D. Ye, L. Ji, K. Wang, X. Xia, Surface-roughened SERS-active single silver nanowire for simultaneous detection of intracellular and extracellular pHs. ACS Appl. Mater. Interfaces **15**, 20677–20685 (2023)
119. Y. Zhang, Q. Liu, M. Liu, X. Zhang, X. Li, L. Dai, M. Meng, D. Liu, Y. Yin, R. Xi, Dual functional molecule aided background-free SERS sensor for intracellular pH dynamic monitoring based on foldable DNA transition. Sens. Actuators B Chem. **353**, 131162 (2022)
120. V.S. Lin, W. Chen, M. Xian, C.J. Chang, Chemical probes for molecular imaging and detection of hydrogen sulfide and reactive sulfur species in biological systems. Chem. Soc. Rev. **44**, 4596–4618 (2015)
121. L. Bai, X. Wang, K. Zhang, X. Tan, Y. Zhang, W. Xie, Etchable SERS nanosensor for accurate pH and hydrogen peroxide sensing in living cells. Chem. Commun. **55**, 12996–12999 (2019)
122. D. Li, J. Sun, Z. Gan, H. Chen, D. Guo, Reaction-based SERS nanosensor for monitoring and imaging the endogenous hypochlorous acid in living cells. Anal. Chim. Acta **1018**, 104–110 (2018)
123. I. J. Jahn, A. Mühlig, D. Cialla-May, Application of molecular SERS nanosensors: where we stand and where we are headed towards? Anal. Bioanal. Chem. **412**, 5999–6007 (2020)
124. Z. Chen, H. Xu, H. Chen, S. Zhu, W. Huang, Y. He, M.E. Hafez, R. Qian, D. Li, AuNPs-COFs core-shell reversible SERS nanosensor for monitoring intracellular redox dynamics. Anal. Chem. **94**, 14280–14289 (2022)
125. Y. Si, L. Li, X. Qin, Y. Bai, J. Li, Y. Yin, Porous $SiO_2$-coated Au-Ag alloy nanoparticles for the alkyne-mediated ratiometric Raman imaging analysis of hydrogen peroxide in live cells. Anal. Chim. Acta **1057**, 1–10 (2019)
126. C. Zeng, F. Hu, R. Long, W. Min, A ratiometric Raman probe for live-cell imaging of hydrogen sulfide in mitochondria by stimulated Raman scattering. Analyst **143**, 4844–4848 (2018)
127. Q. Zhong, R. Zhang, B. Yang, T. Tian, K. Zhang, B. Liu, A rational designed bioorthogonal surface-enhanced Raman scattering nanoprobe for quantitatively visualizing endogenous hydrogen sulfide in single living cells. ACS Sens. **7**, 893–899 (2022)

128. S. S. Li, Q.Y. Guan, M. Zheng, Y.Q. Wang, D. Ye, B. Kang, J.J. Xu, H.Y. Chen, Simultaneous quantification of multiple endogenous biothiols in single living cells by plasmonic Raman probes. Chem. Sci. **8**, 7582–7587 (2017)
129. L. Li, Y. Si, B. He, J. Li, Au-Ag alloy/porous-$SiO_2$ core/shell nanoparticle-based surface-enhanced Raman scattering nanoprobe for ratiometric imaging analysis of nitric oxide in living cells. Talanta **205**, 120116 (2019)
130. H. Chen, E. Kouadio Fodjo, L. Jiang, S. Chang, J. Li, D. Zhan, H. Gu, D. Li, Simultaneous detection of intracellular nitric oxide and peroxynitrite by a surface-enhanced Raman scattering nanosensor with dual reactivity. ACS Sens. **4**, 3234–3239 (2019)
131. J. Yao, Z. Jin, Y. Zhao, Electroactive and SERS-active Ag@$Cu_2O$ NP-programed aptasensor for dual-mode detection of tetrodotoxin. ACS Appl. Mater. Interfaces **15**, 10240–10249 (2023)
132. S. Hanif, H. Liu, M. Chen, P. Muhammad, Y. Zhou, J. Cao, S.A. Ahmed, J. Xu, X. Xia, H. Chen, K. Wang, Organic cyanide decorated SERS active nanopipettes for quantitative detection of hemeproteins and $Fe^{3+}$ in single cells. Anal. Chem. **89**, 2522–2530 (2017)
133. V.T.T.X. Ho, H. Park, S. An, G. Kim, N.H. Ly, S.Y. Lee, J. Choo, H.S. Jung, S. Joo, Coumarin-lipoic acid conjugates on silver nanoparticle-supported nanopipettes for in situ dual-mode monitoring of intracellular Cu(II) and potential chemodynamic therapy applications. Sens. Actuators B Chem. **344**, 130271 (2021)
134. H. Feng, Q. Fu, W. Du, R. Zhu, X. Ge, C. Wang, Q. Li, L. Su, H. Yang, J. Song, Quantitative assessment of copper(II) in Wilson's disease based on photoacoustic imaging and ratiometric surface-enhanced Raman scattering. ACS Nano **15**, 3402–3414 (2021)
135. J. Liu, Z. Liu, W. Wang, Y. Tian, Real-time tracking and sensing of $Cu^+$ and $Cu^{2+}$ with a single SERS probe in the live brain: toward understanding why copper ions were increased upon ischemia. Angew. Chem. Int. Ed. **60**, 21351–21359 (2021)
136. X. Li, X. Duan, L. Li, S. Ye, B. Tang, An accurate and ultrasensitive SERS sensor with Au-Se interface for bioimaging and in situ quantitation. Chem. Commun. **56**, 9320–9323 (2020)
137. Z. Ke, C. Tsai, P. Liao, K.V. Kong, Photoinduced enhanced Raman probe for use in highly specific and sensitive imaging for tyrosine dimerization in inflammatory cells. J. Phys. Chem. Lett. **11**, 7443–7448 (2020)
138. C. Di Pietro, H.H. Öz, T.S. Murray, E.M. Bruscia, Targeting the heme oxygenase 1/carbon monoxide pathway to resolve lung hyper-inflammation and restore a regulated immune response in cystic fibrosis. Front. Pharmacol. **11**, 1059 (2020)
139. Y. Cao, D.W. Li, L.J. Zhao, X.Y. Liu, X.M. Cao, Y.T. Long, Highly selective detection of carbon monoxide in living cells by palladacycle carbonylation-based surface enhanced Raman spectroscopy nanosensors. Anal. Chem. **87**, 9696–9701 (2015)
140. P.H. Liao, C.Y. Tseng, Z.Y. Ke, C.L. Hsieh, K.V. Kong, Operando characterization of chemical reactions in single living cells using SERS. Chem. Commun. **56**, 4852–4855 (2020)
141. X. Qin, Y. Si, Z. Wu, K. Zhang, J. Li, Y. Yin, Alkyne/ruthenium(II) complex-based ratiometric surface-enhanced Raman scattering nanoprobe for in vitro and ex vivo tracking of carbon monoxide. Anal. Chem. **92**, 924–931 (2020)
142. S. Ye, X. Li, M. Wang, B. Tang, Fluorescence and SERS imaging for the simultaneous absolute quantification of multiple miRNAs in living cells. Anal. Chem. **89**, 5124–5130 (2017)
143. X. Huang, H. Tian, L. Huang, Q. Chen, Y. Yang, R. Zeng, J. Xu, S. Chen, X. Zhou, G. Liu, H. Li, Y. Zhang, J. Zhang, J. Zheng, H. Cai, H. Zhou, Well-ordered Au nanoarray for sensitive and reproducible detection of hepatocellular carcinoma-associated miRNA via CHA-assisted SERS/fluorescence dual-mode sensing. Anal. Chem. **95**, 5955–5966 (2023)
144. X. Su, X. Liu, Y. Xie, M. Chen, C. Zheng, H. Zhong, M. Li, Integrated SERS-vertical flow biosensor enabling multiplexed quantitative profiling of serological exosomal proteins in patients for accurate breast cancer subtyping. ACS Nano **17**, 4077–4088 (2023)
145. I.T. Gug, M. Tertis, O. Hosu, C. Cristea, Salivary biomarkers detection: analytical and immunological methods overview. Trac Trend. Anal. Chem. **113**, 301–316 (2019)
146. D. Lin, S. Yang, C. Hsieh, K. Hsu, T. Gong, Q. Wu, S. Qiu, S. Feng, K.V. Kong, Tandem quantification of multiple carbohydrates in saliva using surface-enhanced Raman spectroscopy. ACS Sens. **6**, 1240–1247 (2021)

147. M. Chung, W.H. Skinner, C. Robert, C.J. Campbell, R.M. Rossi, V. Koutsos, N. Radacsi, Fabrication of a wearable flexible sweat pH sensor based on SERS-active Au/TPU electrospun nanofibers. ACS Appl. Mater. Interfaces **13**, 51504–51518 (2021)
148. X. Gao, Q. Yue, Z. Liu, M. Ke, X. Zhou, S. Li, J. Zhang, R. Zhang, L. Chen, Y. Mao, C. Li, Guiding brain-tumor surgery via blood-brain-barrier-permeable gold nanoprobes with acid-triggered MRI/SERRS signals. Adv. Mater. **29**, 1603917 (2017)
149. Z. Jin, Q. Yue, W. Duan, A. Sui, B. Zhao, Y. Deng, Y. Zhai, Y. Zhang, T. Sun, G.P. Zhang, L. Han, Y. Mao, J. Yu, X.Y. Zhang, C. Li, Intelligent SERS navigation system guiding brain tumor surgery by intraoperatively delineating the metabolic acidosis. Adv. Sci. **9**, e2104935 (2022)
150. H. He, M. Xu, C. Zong, P. Zheng, L. Luo, L. Wang, B. Ren, Speeding up the line-scan Raman imaging of living cells by deep convolutional neural network. Anal. Chem. **91**, 7070–7077 (2019)

# Chapter 15
# Gap-Enhanced Raman Tags (GERTs): Synthesis, Optical Properties, and Applications

**Yuqing Zhang and Jian Ye**

**Abstract** Gap-enhanced Raman tags (GERTs) represent innovative optical nanotags designed based on the surface-enhanced Raman scattering (SERS) effect. SERS is a highly sensitive spectroscopic technique used to detect molecular vibrational and transitional information. In the context of SERS, the interaction between molecules and metallic nanostructures, such as Au or Ag nanoparticles, leads to a significant enhancement of Raman scattering signals—a phenomenon capable of amplifying molecular Raman scattering signals by over 10 orders of magnitude. By embedding Raman reporter molecules inside the internal plasmonic metallic nanojunction, GERTs exhibit extraordinary detection sensitivity down to the single-particle detection level; coupled with their ability to provide high-resolution molecular features, GERTs have found extensive applications across a multitude of fields. This article comprehensively introduces the preparation and optical properties of GERTs, aiming to realize practical applications. In this article, we provide a comprehensive introduction to the preparation and optical properties of GERTs, with the goal of realizing their use in practical applications. At the same time, we provide a comprehensive review of the pioneering use of GERTs as physically unclonable tags, along with their recent advances in biomedical imaging and integrated diagnostics. Finally, we provide a comprehensive assessment of the challenges GERTs face in real-world application scenarios, providing critical reference points for advancing the clinical translation of GERTs technology. Looking ahead, with further research and development, the novel, stable, and super-bright GERTs probes are poised to become a central analytical tool, offering even richer opportunities for practical applications and scientific research.

**Keywords** Surface-enhanced Raman spectroscopy · Nanoprobes · Gap-enhanced Raman tags · Bio-detection · Medical imaging

Y. Zhang
School of Automation, Hangzhou Dianzi University, Hangzhou, China

J. Ye (✉)
School of Biomedical Engineering, Shanghai Jiao Tong University, Shanghai, China
e-mail: yejian78@sjtu.edu.cn

© The Author(s), under exclusive license to Springer Nature Singapore Pte Ltd. 2024

M. Procházka et al. (eds.), *Surface- and Tip-Enhanced Raman Scattering Spectroscopy*,
https://doi.org/10.1007/978-981-97-5818-0_15

## 15.1 Introduction of Surface-Enhanced Raman Spectroscopy and Gap-Enhanced Raman Tags

### *15.1.1 Basic Principles of Surface-Enhanced Raman Spectroscopy*

Raman spectrum (also known as Raman scattering) is the inelastic scattering effect generated when light interacts with molecules, which is closely related to the rotation and vibration mode of molecules, with high specificity, known as the fingerprint spectrum of molecules, which can be used for the analysis and identification of molecular structures. However, the general Raman scattering signal is very weak, and in order to obtain enough signal, enhancement has become an essential means. Surface-enhanced Raman spectroscopy refers to the significant enhancement of Raman scattering from molecules adsorbed on the surface of noble metal nanostructures due to the excitation of surface plasmons and surface chemical effects. Its maximum enhancement factor can reach $10^{10}$-$10^{11}$ [1–3]. In addition, the unique fingerprint spectrum of Raman spectroscopy offers it ultra-high specificity, and the ultra-narrow half-width peak is conducive to multi-index detection and imaging [1, 2, 4].

### *15.1.2 Structures of Traditional Surface-Enhanced Raman Tags and Gap-Enhanced Raman Tags*

At present, the application of SERS technology is mainly realized through labeled and unlabeled methods. The unlabeled method refers to the direct enhancement of the Raman spectrum of the target molecule using the noble metal nanostructure, while the labeled method refers to the amplification of the target molecular signal through SERS probes. SERS probes usually consist of four parts, including noble metal nanoparticles, Raman reporter molecules, protective layer, and modification layer (see Fig. 15.1) [1]. The noble metal nanoparticles are mainly used as the reinforcement substrate to enhance Raman reporter molecules by electromagnetic field enhancement or (and) chemical enhancement. Raman reporter molecules are the source of Raman signals, usually with large Raman cross sections, and adsorbed to the surface of nanoparticles by self-assembly or electrostatic interaction. The protective layer can improve the stability and biocompatibility of the nanoprobes and is often composed of polymers or silica. The modification layer mainly utilizes functional ligands (such as nucleic acids, antibodies, and aptamers) to enable the nanoprobes to bind to targets (such as overexpressed markers on the surface of tumor cells) with high specificity and affinity.

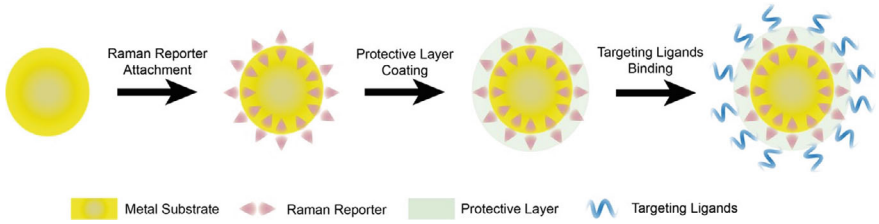



**Fig. 15.1** SERS nanotag fabrication [1]

In traditional SERS probes, reporter molecules are mainly adsorbed on the surface of noble metal substrate, but there may be defects such as insufficient enhancement factor, easy desorption of molecules, and influence of the solution environment. Different from the structure of traditional SERS probes, gap-enhanced Raman tags (GERTs) are core–shell SERS probes with embedded Raman reporter molecules in the internal nanogaps between metal core and shell (as shown in Fig. 15.2) [5, 6]. GERTs show great flexibility in structural design and synthesis, choice of Raman reporters, surface modification and functionalization, and exhibit a number of unique optical properties, including great electromagnetic field and Raman enhancement, ultra-high photo- and chemical-stability. In recent years, GERTs, as nanoprobes with excellent performance, have been widely used in information security [7–10], in vitro detection [8, 11–16], in vivo detection and imaging [5, 17–23], multifunctional theranostics [24–28], and other fields. This chapter mainly introduces the recent progress of GERTs in terms of their preparation [16, 17], optical properties [29, 30], and applications in many fields.

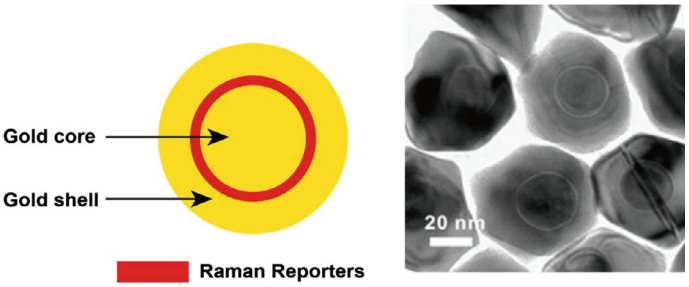



**Fig. 15.2** Schematic structure (left) and the corresponding representative transmission electron microscopic image (right) of GERTs; the red part indicates Raman reporters in the internal nanogaps [5]

## 15.2 Preparation of Gap-Enhanced Raman Tags (GERTs)

### *15.2.1 Design and Tunability of Structure*

Embedded Raman reporters and electromagnetic "hotspots" within GERTs can greatly enhance the SERS intensity, reproducibility, and stability of nanoparticles, making them a reliable SERS nanotags. In order to prepare GERTs with high sensitivity, specificity, and stability, it is necessary to design the internal gap size and structure, select appropriate Raman reporter molecules and substrate materials, and control the morphology of nanotags [1, 2].

#### 15.2.1.1 Highly Controllable Gap Size

The size of the "gap" within GERTs determines the degree of plasmon coupling between the metal core and shell and the near-field enhancement within the gap structure. Various methods for preparing internal ultra-small gap structures have been reported, which can be divided into two approaches [31, 32]. (1) Hollow gap structures. This one is through the displacement reaction between gold and silver to create gaps by etching the silver core while generating the gold shell. However, this method suffers from poor reaction controllability and low uniformity of the gap structure, hindering stable shrinking to sub-nanometers [31]. (2) Raman-active separation layer. The second approach is more prevalent and starts with the formation of a metal core, followed by the wrapping of a specific Raman-active layer around it and further growth of gold shell. This process leads to a creation of a thin intermediate layer to form a gap structure between the core and shell. Reported Raman-active layers include silica matrix with embedded Raman reporters, specialized nucleic acid chains modified with fluorescent molecules, aromatic ring polymer chains, organic aromatic small molecules, etc. [32]. These intermediate layers insulate metallic core and shell, and simultaneously possess Raman signals, acting as the source of Raman signals for the particle.

Among these materials, using a thin silica layer as the intermediate layer material necessitates additional modification of Raman signal molecules and involves a complex preparation process, with limited control over the thickness at sub-nanometer levels. On the other hand, intermediate layer materials such as specially designed nucleic acid chains and aromatic ring polymer chains modified with fluorescent molecules face constraints related to cost and availability, hindering large-scale preparation. In contrast, organic aromatic molecules offer wide availability and lower material costs. Moreover, organic small molecules with thiol, amino, or carboxyl groups exhibit strong metal affinity and can be directly anchored on metal surface, simplifying the synthesis process. Consequently, our research group have extensively explored the structure of GERTs based on organic aromatic molecules.

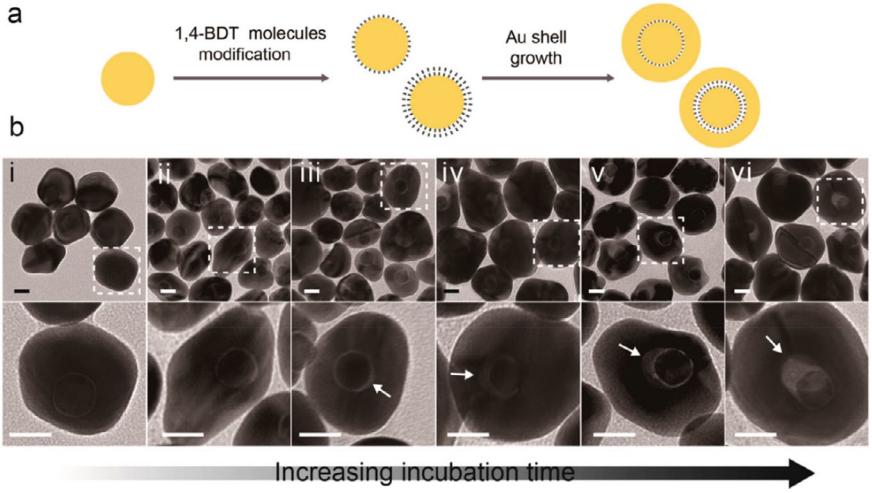



**Fig. 15.3** Highly tunable gap size of GERTs [32]. **a** Schematic synthesis procedures of Au GERTs with varied interior gap size. **b** TEM images of GERTs with different gap sizes prepared by incubation Au cores and 50 μM 1,4-BDT for 0.5–96 h. All scale bars are 20 nm

Here, GERTs embedded with 1,4-benzenedithiol (1,4-BDT) were used as an example to exhibit the internal gap structure by high-resolution transmission electron microscopy. Our investigation revealed that the embedded Raman report molecular layer plays a pivotal role in gap structure formation, with the gap width directly governed by the thickness of the molecular layer. This discovery lays the foundation for regulating and preparing gap structures of different sizes [29]. Precise control of gap size poses a challenge due to limitations in chemical synthesis methods. However, we take advantage of the fact that 1,4-BDT possesses two sulfhydryl groups, enabling the formation of disulfide bonds between 1,4-BDT molecules. By prolonging the mixing time of 1,4-BDT and gold cores, molecules can be self-assembled into multilayer structures on the gold core surface. Consequently, various surface molecular layer thicknesses can be achieved by controlling the mixing time of 1,4-BDT molecules and gold core. Following the regrowth of the gold shell, GERTs with different gap sizes can be obtained (as shown in Fig. 15.3). In short, optimizing the synthetic parameters for gap size offers a strategy for preparing GERTs with superior Raman performance [32].

#### 15.2.1.2 Raman Reporters Embedded

Raman reporters adsorbed in the metal core–shell structures serve as the signal source of GERTs. Typically, Raman reporters possess a large scattering cross section to ensure a strong Raman signal. Simultaneously, they exhibit simple and identifiable

characteristic peaks, minimizing overlap with other Raman reporter bands. The interaction between Raman reporters and metal fall into two categories: covalent and electrostatic bonding. Molecules covalently adsorbed typically have thiol groups [10, 23], forming robust gold-sulfur bonds and firmly adhering to metal surface. In contrast, electrostatically adsorbed molecules (e.g., amino, carboxyl, and other groups) typically exhibit opposite charges with metal core or stabilizers [22]. When the absorption wavelength of the Raman reporters is close to the excitation laser wavelength, the signal of the reporters can be further enhanced, resulting in resonance Raman spectroscopy. Such Raman reporters, capable of resonating with the laser, are termed resonance Raman reporters [22]. However, while introduction of resonant Raman reporters can improve the sensitivity of GERTs, they often generate strong fluorescent backgrounds during laser resonance, which can hinder applications in biological detection and imaging. To address this challenge, we have recently introduced a new type of non-fluorescent resonance Raman reporter in NIR-II region. This molecule maximizes the resonant Raman signal while avoiding the interference from fluorescent background, enhancing its suitability for biomedical imaging [33].

The Raman signals of biomolecules are intricate and predominantly distributed in the fingerprint region (200–1800 $cm^{-1}$). If using SERS nanotags with signals located in the fingerprint region, their Raman peaks may overlap with those of biomolecules, compromising accurate quantitative detection and imaging. Therefore, the selection of reporters in the fingerprint region is limited. Conversely, in the 1800–2800 $cm^{-1}$ region, biological tissue usually lacks characteristic Raman signals, earning it the designation of the "bio-silent region". To tackle these challenges, as illustrated in Fig. 15.4a, we have introduced Raman reporters with signal in the bio-silent region to construct orthogonal gap-enhanced Raman probes (O-GERTs). Compared to conventional SERS probes (C-SERS), O-GERTs typically feature vibrational modes of functional groups, such as alkynes, cyanides, and azides, exhibiting characteristic Raman peaks in the range of 1800–2800 $cm^{-1}$. During tumor imaging, more precise detection can be achieved by utilizing the characteristic Raman signals of molecules in the silent region, without interference from tissue background signals [19] (Fig. 15.4b–d).

#### 15.2.1.3 Substrate Materials

The remarkable SERS enhancement effect hinges upon the provision of electromagnetic "hot spots" by the SERS active substrate, thereby exponentially amplifying signals of reporter molecules adsorbed on the surface. The enhancement ability of the substrate is mainly tied to its material and optical properties. Common SERS active substrates typically include noble metals, semiconductor nanomaterials, and their combination. Owing to the strong plasmon resonance effect of noble metals in the visible to NIR region and the high compatibility of lasers in this range, they have emerged as the predominant choice for both fundamental research and practical applications. For example, gold stands out due to its exceptional chemical stability, biocompatibility, and controllable plasmon resonance optical properties, rendering

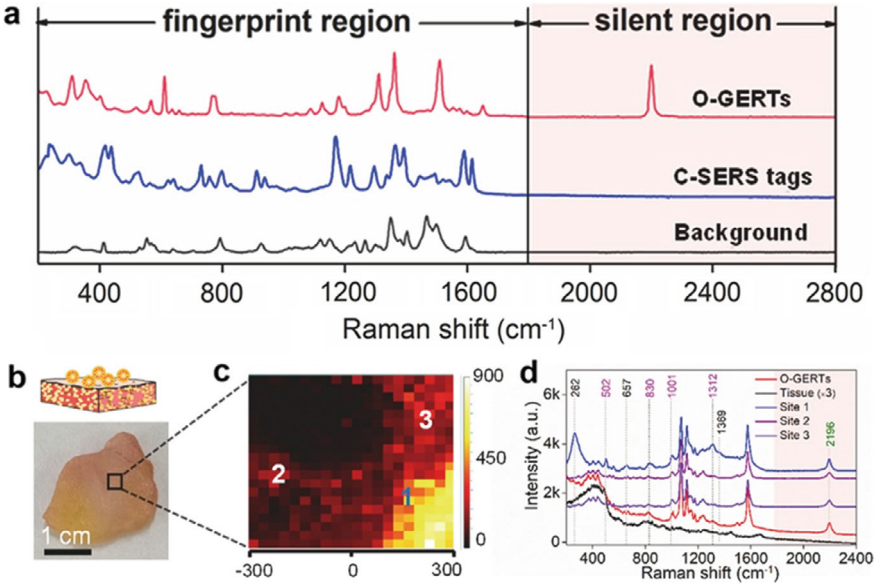



**Fig. 15.4** Orthogonal GERTs and its application in tumor imaging. **a** Schematic diagram of Raman spectra of O-GERTs, conventional SERS (C-SERS) tags, and tumor tissue. **b** Schematic illustration of O-GERTs for tumor imaging. **c** Raman imaging based on the characteristic peak (2196 $cm^{-1}$) in the silent region of O-GERTs. **d** Representative Raman spectra of the corresponding positions in panel (**c**)

it the preferred SERS-active substrate for biomedical detection and imaging. Meanwhile, silver offers superior SERS enhancement capability and cost-effectiveness, further solidifying its status as an excellent candidate material in the SERS field.

As research on plasmon metal materials advances, an increasing number of research groups are devoted to fine-tuning the composition and structure of multimetal nanostructures. This pursuit aims to maximize the synergistic coupling between different metals and optimize the SERS enhancement performance. The most prevalent active substrate in this regard is the composite nano-enhanced substrate comprising both gold and silver components. This unique combination capitalizes on the exceptional stability of gold and the superior SERS activity of silver. In this context, we have reported innovative gold–silver composite GERTs (Au-Ag GERTs). These GERTs use petal-like gold nanoparticles as the core to provide a plethora of "hot spots" for Raman reporters, and use the silver shell to further improve the SERS performance of the nanotags. Notably, Au-Ag GERTs exhibit a remarkable brightness enhancement of 1–2 orders of magnitude compared to Au-Au counterparts, with detection limits of down to 10 fM, even reaching the level of single-particle detection [18–22].

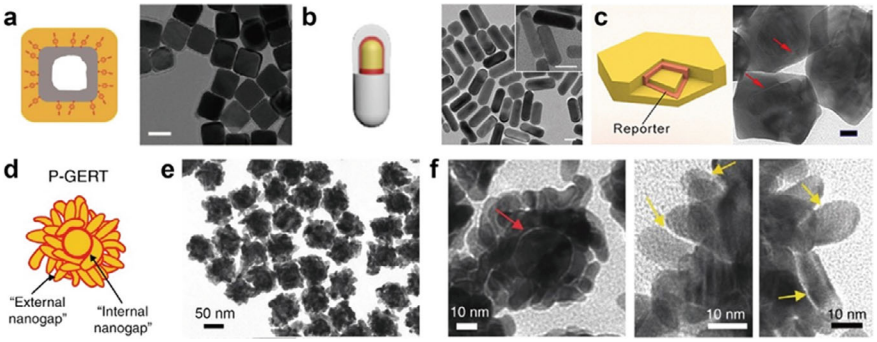



**Fig. 15.5** GERTs synthesized from metallic cores with different shapes [5]: **a** nanocage (scale bar is 50 nm). **b** nanorods (scale bars are 50 nm), and **c** nanotriangular sheets (scale bar is 20 nm). **d** Schematic diagrams of GERTs with a petal-like shell (P-GERTs). **e** Representative low-resolution TEM image of P-GERTs. **f** The high-resolution TEM images of P-GERTs

#### 15.2.1.4 Tunability of GERTs Morphology

The SERS enhancement capability of noble metals nanostructures varies significantly with their distinct morphologies. A judicious design of noble metals morphology can effectively fine-tune optimize their SERS properties. Beyond the conventional nanospheres and nanorods [34], researchers are increasingly focused on developing SERS substrates with diverse morphologies to improve SERS enhancement properties. These novel shapes include nanostars, nanocages, nanoflowers, and nanowires [35, 36]. By deliberately engineering sharp angles and protrusions on the nanoparticle surface or internal gaps, a greater number of "hot spots" can be generated, resulting in an order of magnitude increase in Raman signals. Consequently, the precise control and design of the morphology of noble metal nanostructure bear immense significance in obtaining highly active SERS substrates. As shown in Fig. 15.5a–c, we have dedicated many efforts to develop ultra-high performance GERTs with diverse core morphologies over the years. These include GERTs based on nanocages, nanorods, and nanotriangles. Compared with conventional GERTs, the petal-like multibranched GERTs (Fig. 15.5d and e) provide a greater abundance of electromagnetic "hot spots" for Raman reporters. The gap structure between the petals (Fig. 15.5f) creates a larger and more stable electromagnetic field enhancement effect. Both simulated calculations and Raman spectroscopic measurements have confirmed that petal-like GERTs exhibit superior sensitivity [5].

### *15.2.2 Modification and Functionalization of GERTs*

Surface modification is a crucial step in enhancing the stability and biocompatibility of SERS nanotags. Furthermore, surface coating can mitigate the issue of

protein corona formation, which occurs when SERS nanotags become encased in proteins in biological environments rich in proteins. At present, common protective layers of SERS nanotags include silica and polymers. In biomedical applications, achieving specific recognition between SERS nanotags and the target being tested often necessitates the selection of specific antibodies and short peptides based on the expression level of surface receptors or proteins. These molecules are then used to functionalize SERS nanotags, thus enabling precise targeting. As depicted in Fig. 15.6, we initially modified GERTs with the mesoporous silica layer to improve their stability and biocompatibility. Subsequently, through amination and gadolinium (Gd) loading, we introduce folic acid (FA) small molecules and Ibrutinib to realize tumor cell targeting and therapy, respectively. This innovative approach allowed us to achieve multi-modal CT/MR/SERS imaging, thereby facilitating tumor theranostics based on functionalized GERTs. Importantly, *in vivo* biological distribution studies and long-term toxicity assessments have demonstrated that Gd-GERTs exhibit good biocompatibility. Therefore, Gd-GERTs, serving as a multifunctional nanoplatform, has great potential for precise preoperative CT/MRI diagnosis and intraoperative Raman imaging guidance during cancer resection [24].

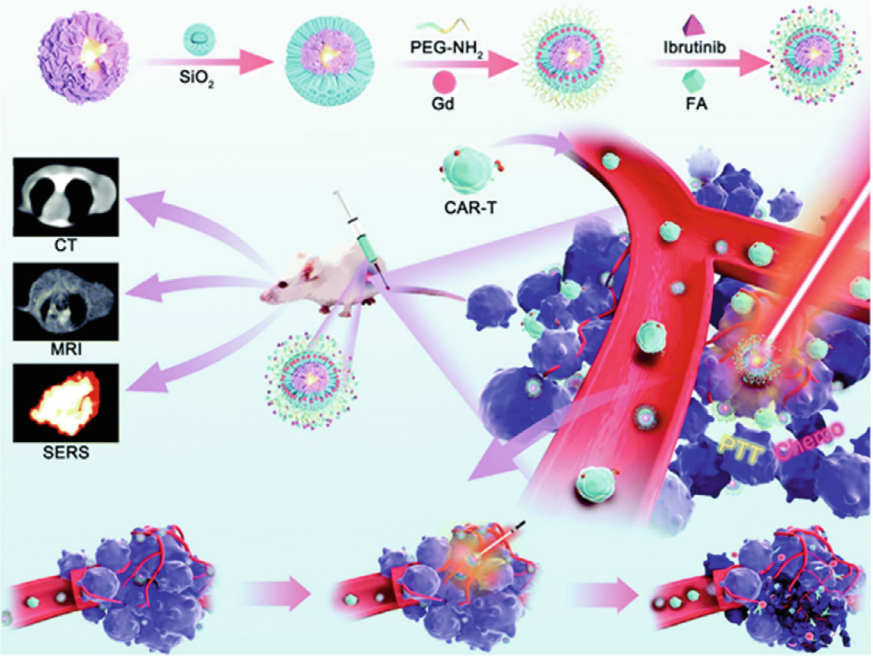



**Fig. 15.6** Synthesis process of FA-Gd-GERTs@Ibrutinib and the corresponding schematic illustrations of their multi-modal imaging and the chemo/photothermal therapy for destruction of physical tumor barriers and the reconstruction of the microenvironment to achieve enhanced CAR-T infiltration in tumors [24]

## 15.3 Optical Properties of GERTs

### *15.3.1 Far-Field and Near-Field Optical Properties*

According to classical electromagnetic theory, the creation of extremely narrow gap structures can induce strong plasmon coupling between the metal core and the metal shell produce, resulting in a highly effective electromagnetic field enhancement within the gap. However, it is essential to acknowledge that the gap cannot be indefinitely narrowed. When the gap size reaches the sub-nanometer level, some quantum effects, such as electron tunneling, become notably influential. These quantum effects can alter the optical properties of the metallic nanogap structure in a manner different from classical theory, affecting both the far-field and near-field optical response of the structure. The electric field enhancement may diminish, but new chemical enhancement effects may arise. Time-dependent density functional theory (TDDFT) has demonstrated that when the gap size is less than 0.4 nm in core–shell metal particles, a plasmon tunneling effect occurs, significantly changing the absorption cross section of core–shell particles and enhancing their local electric field [32].

Consequently, we conducted an in-depth investigation into the relationship between the size of the internal gap structure of GERTs and their optical properties. Through quantum-corrected model (QCM) simulations, we obtained extinction spectrum that closely aligned with experimentally measured one. In contrast, traditional electromagnetic theory model calculations did not yield results consistent with experimental observations, suggesting the presence of electron tunneling effects within GERTs. To delve deeper into the far-field and near-field optical properties of GERTs, we precisely modulated the gap size of GERTs by controlling the adsorption of Raman reporter 1,4-BDT on gold cores. The broadening of resonance peaks in both the far-field spectrum and the SERS spectrum provided the evidence of electron transfer phenomena within the gap of GERTs, which in turn affected the near-field optical response of particles. Our research unveiled that the gap size value at which the strongest SERS signal was achieved was approximately 1.4 nm (785 nm excitation) or 1.8 nm (633 nm excitation). These findings to some extent challenged the conventional belief that maximizing the adsorption of Raman molecules on the surface of metal particles or narrowing gaps in plasmon structures invariably enhances SERS performance. Simultaneously, our study affirmed that GERTs could be employed to investigate charge transfer resulting from molecular gaps and its influence on enhanced Raman signals. This offers scientists a valuable avenue for employing SERS testing to explore changes in the near-field optical properties of GERTs and confirms that the maximum Raman enhancement is constrained by the electron transfer effect within the gap structure.

### 15.3.2 Sensitivity of Single-Particle Detection

GERTs exhibit significant potential in ultra-sensitive biomedical detection and imaging. Building upon prior adjustments and optimizations of the internal gap size of GERTs, along with careful consideration of parameters such as Raman reporters, substrate materials, and particle morphology, SERS performance can be maximized, achieving the present capability for single-particle detection. The SERS properties of individual GERT particles in the solid state were further investigated using confocal Raman microscopy combined with atomic force microscopy or scanning electron microscopy. As illustrated in Fig. 15.7, after identifying individual GERT particles via atomic force microscopy (Fig. 15.7a and b) or scanning electron microscopy (Fig. 15.7d and e), characteristic Raman spectra with excellent signal-to-noise ratios were successfully acquired (Fig. 15.7c and f). These findings underscore the single-particle detection capability of GERTs [5–22].

### 15.3.3 Stability

The stability of SERS nanotags encompasses both material stability in various environments and optical stability under continuous excitation. GERTs, with their Raman reporters located within metal particles and protected by the metal shell, effectively shield these reporters from external factors such as water, air, and other environmental impacts. This strategy avoids potential photochemical reactions, greatly enhancing the material stability of the nanotags. Consequently, GERTs prove particularly suitable for detection and imaging applications in various biological environments [6].

Furthermore, GERTs typically exhibit a plasmon resonance in the visible region, but we deliberately applied NIR light for non-resonant excitation. This approach effectively mitigates the photothermal effects associated with plasmon resonance, thereby improving the photostability of the nanotags. At the same time, it safeguards biological samples from the thermal effects that may arise during SERS detection or imaging. Moreover, NIR light can effectively excite the gap mode and chemical enhancement of GERTs, delivering excellent Raman enhancement capabilities. This non-resonant excitation strategy endows GERTs with exceptional SERS performance while maintaining ultra-high photostability. As demonstrated in Fig. 15.8, when dry GERTs particles were continuously irradiated with 785 nm wavelength laser at a power density of $4.71 \times 10^5$ W/cm$^2$ for 30 min under a 100 × objective lens, the characteristic Raman peak intensity remained remarkably stable, affirming their superior photostability.

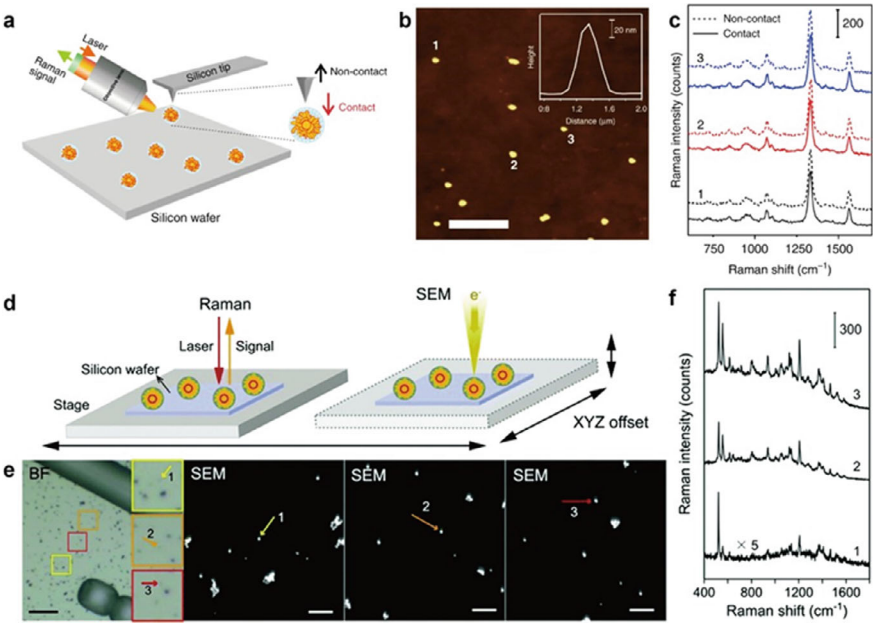



**Fig. 15.7** Single-particle Raman analysis of GERTs. **a** Schematic illustration of AFM-correlated nano-Raman spectroscopy [5–22]. **b** A representative AFM image of GERTs on silicon wafer. The scale bar is 5 μm. The inset shows a typical cross-sectional profile of a single GERT. **c** SERS spectra of three single GERTs (particle 1, 2, and 3) indicated in panel b measured in contact and noncontact modes. All measurements were performed with a 633 nm laser, 110 μW power, 10 s acquisition time, and × 100 objective lens. **d** Schematic illustration of the Raman imaging and scanning electron microscopy (RISE) system. **e** A representative bright-field (BF) image of GERTs on a silicon wafer and the corresponding scanning electron microscopy (SEM) images of three selected single GERTs (indicated by arrows). Scale bars are 20 μm for the BF image and 1 μm for SEM images. **f** SERS spectra of three single GERTs (particle 1, 2 and 3) indicated in panel **e**. Raman measurements were performed using a 785 nm laser, 1 mW power, 20 s acquisition time, and × 100 objective lens

## 15.4 Application of GERTs

### *15.4.1 Optical Information Security*

Anti-counterfeiting labels represent one of the most economical and effective solutions to combat counterfeit goods. Their efficacy depends on the technical barriers during the production process and the limited control over access to processed materials, which, strictly speaking, lack foolproof security. In the realm of security, physical unclonable functions (PUFs) have emerged as a promising avenue due to their inherent properties of randomness, ease of generation, and resistance to replication. GERTs is particularly suitable for PUF tags with their ultra-strong Raman signals, expansive coding capability facilitated by narrow Raman linewidth, and outstanding

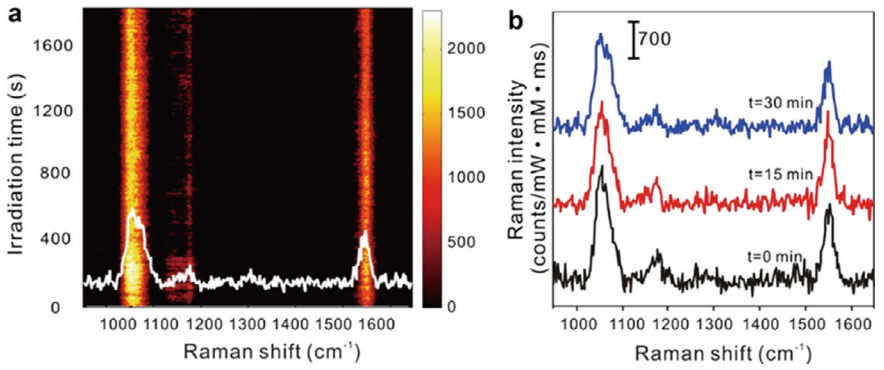



**Fig. 15.8** Photostability of GERTs [6]. **a** Photostability measurement of time-resolved SERS spectra of solid GERTs on a silicon wafer during continuous irradiation for 30 min at a power density of $4.71 \times 10^5$ W/cm$^2$. **b** Three representative SERS spectra at selected irradiation times in panel (**a**)

stability. We recently prepared a PUF label based on GERTs (Fig. 15.9a). It was constructed simply by directly applying a GERT solution to the substrate. Due to the random distribution of nanoparticles on the substrate, along with the generation of unpredictable patterns, rendered it impervious to counterfeiting attempts. A confocal Raman system was employed for rapid Raman signal reading, enabling the digitization of the Raman signal at each pixel. The coding capacity of PUF labels is based on the spatial position, the tag type, and the Raman intensity of the nanotags. For a PUF label composed of ten types of GERTs, Raman intensity level at each pixel is encoded in a quaternary mode with a scanning resolution of 2500 pixels. This leads to an extraordinary three-dimensional coding capacity over $3 \times 10^{15051}$ (Fig. 15.9b). Verification experiments ensure the robustness and security of the PUF system, validating its practical viability [10]. Very recently, we introduce orthogonal reporter molecules with characteristic Raman signals in 1800-2800 cm$^{-1}$ to construct orthogonal GERTs (O-GERT). By randomly dispersing O-GERT within a polymer matrix, a PUF label with a remarkably large encoding capacity (~ $10^{5852}$) and ultra-high information density (~ $10^{5844}$ Tbit cm$^{-3}$) can be formed, based on the probe frequency, intensity, and three-dimensional spatial information. In addition, the polymer matrix provides mechanical protection for the tags without interfering with Raman coding in its silent range. We further leveraged microfluidic sliding chip technology to enable rapid mass production of these labels (approximately 10 minutes) with high throughput (tens of thousands of labels per production run). To enhance security, we incorporated micro-patterning and integrated two-dimensional QR codes to deliver multi-layered information anti-counterfeiting [7, 8].

Steganography serves as a method for securing information during transmission by concealing it within another medium, such as video, audio, images, or text. This approach ensures that the existence of hidden information remains discreet,

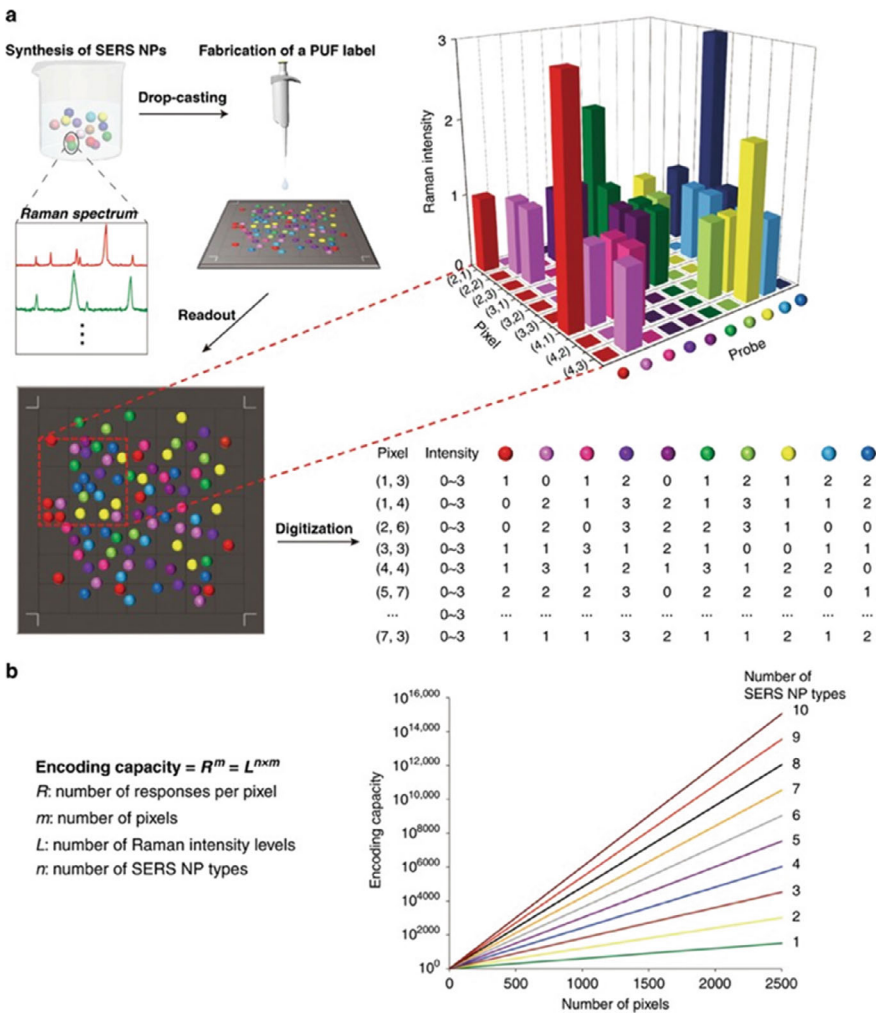



**Fig. 15.9** Physical unclonable functions (PUF) anti-counterfeiting labels based on GERTs [10]. **a** The preparation process of PUF labels based on Raman signals includes: synthesis of GERTs probes containing different Raman reporters, random formation of two-dimensional (2D) patterns by different kinds of GERTs, and readout of PUF tags. **b** Calculation of the encoding capacity of a Raman PUF label. The encoding capacity of 10 different GERTs will be $4^{10\times2500}$ ($3.2 \times 10^{15051}$)

avoiding suspicion and safeguarding the data. We have reported a Raman ink-based steganography using GERTs. By incorporating two different kinds of GERTs into conventional inks, we generated two kinds of Raman inks featuring different

Raman signals for multi-color steganography [6]. Under 785 nm non-resonant excitation, GERTs ink can produce prominent characteristic Raman signals while maintaining minimal background interference, establishing its suitability for information encoding. Different Raman inks can be simultaneously excited with a single laser, effectively reducing imaging time. Moreover, GERTs ink exhibits excellent photostability and long-term material stability, ensuring the enduring legibility of written text. In our experiments, two kinds of GERTs inks, along with regular inks, were employed for multi-color steganography, yielding seven distinct combinations of extractable information. The exceptional multiplexed encoding capacity of Raman ink enhances the security and reliability of steganography system, presenting promising applications in the field of information security.

### *15.4.2 In Vitro Detection*

Cholesterol plays a pivotal role in numerous physiological processes within the human body. Monitoring intracellular cholesterol levels can facilitate the early detection of various diseases, including hypertension, coronary heart disease, atherosclerosis, and lipid metabolism dysfunction. To address this, we designed gold–silver core–shell GERTs incorporated with the Raman reporter 1,4-BDT as the internal standard for nondestructive detection of $H_2O_2$ and cholesterol (Fig. 15.10a) [11]. Employing the classic least square (CLS) spectral fitting method, we were able to accurately isolate the Raman signals of the internal standard (1,4-BDT) and the target molecules, namely 4-mercophenylboric acid (4-MPBA) and 4-hydroxyphenylthiophenol (4-HBT), from the complex spectra. The inclusion of internal standard molecules allows for the calibration of obtained Raman signals, mitigating fluctuations arising from varying measurement conditions and local nanoparticle states, such as aggregation. Consequently, the reproducibility of SERS signals markedly improved, yielding a more robust linear relationship of the detection working curve. By utilizing these GERTs, we successfully achieved quantitative detection of $H_2O_2$ and cholesterol, both in solution and within living cells at the single-cell level.

Thanks to the characteristics of the GERTs core–shell structure, the internal Raman reporters show exceptional photostability and signal reproducibility. Even in the agglomeration state, GERTs maintain a linear signal response, making them highly suitable for quantitative and highly sensitive *in vitro* detection. Consequently, GERTs were further modified with antibodies and employed for lateral flow immunoassay (LFIA) (see Fig. 15.10b). Notably, the detection limit for human chorionic gonadotropin reached as low as 0.7 mIU/mL (0.077 ng/mL) [37], much higher than the detection limit of traditional visual detection and non-quantitative LFIA (typically exceeding 10 mIU/mL).

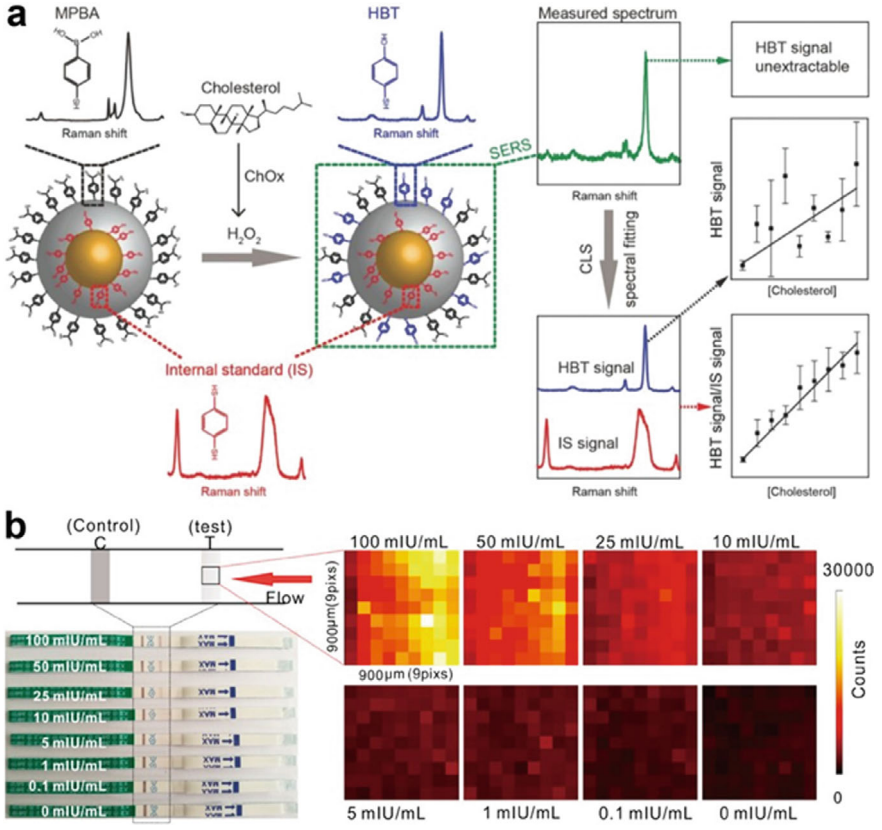



**Fig. 15.10** In vitro detection based on GERTs. **a** Schematic illustration of SERS nanoprobes with the embedded internal standard for quantitative detection of cholesterol via the Raman spectral fitting method [11]. **b** Quantitative detection of human chorionic gonadotropin combined with lateral flow immunoassay [37]

### *15.4.3 In Vivo Detection and Imaging*

Sentinel lymph node (SLN) biopsy is widely employed technique in clinic for studying lymphatic metastasis in malignant tumors. The intraoperative localization of SLNs is an important prerequisite for SLN biopsy, so the selection of suitable SLN tracers is particularly of importance. Currently, clinical practice relies on SLN tracers like blue dyes (e.g., methylene blue), radioisotopes, and NIR fluorescent dyes (e.g., indocyanine green). However, a notable limitation with small molecule dyes, including blue dyes and fluorescent dyes, is their rapid diffusion through lymphatic vessels, resulting in swift migration from the SLN to the secondary lymph nodes ($2^{nd}$ LNs). This limited surgical window can lead to excessive excision.

We have introduced GERTs as a novel tracer for intraoperative SLN localization and imaging. Thanks to the appropriate particle size of GERTs, they can remain

within the SLN for an extended period (several hours), providing surgeons with an adequate time window for surgery. The experimental results in the mouse model demonstrated that GERTs could persist in SLNs for over 24 h [23]. A more comprehensive study in a New Zealand rabbit model (Fig. 15.11) revealed that GERTs reached the SLN within 10 min, and GERTs signals were not detected in the second lymph nodes using multiple methods (Raman imaging and atomic absorption spectrometry) within four hours. This extended duration allowed surgeons a generous window to differentiate between SLNs and the second lymph nodes. *Furthermore, the ultra-sensitive nature of GERTs (detection limit of 0.5 pM) permits the identification of labeled SLNs before surgery, offering precise location information for minimally invasive procedures. Rigorous biosafety assessments of GERTs were carried out in compliance with the biosafety requirements for nanomaterials. The results of these evaluations indicated that GERTs exhibited no significant toxicity, providing a promising future for clinical applications in accurately identifying SLNs in the axillary region of breast cancer patients [20–23].

Building upon the accuracy of SLN localization, we have introduced the "ratiometric Raman dual-nanotag strategy". This method utilizes two types of GERTs: non-functionalized (naked) GERTs and targeted GERTs equipped with folic acid. Upon reaching the SLNs, the latter selectively targets tumor cells within the lymph

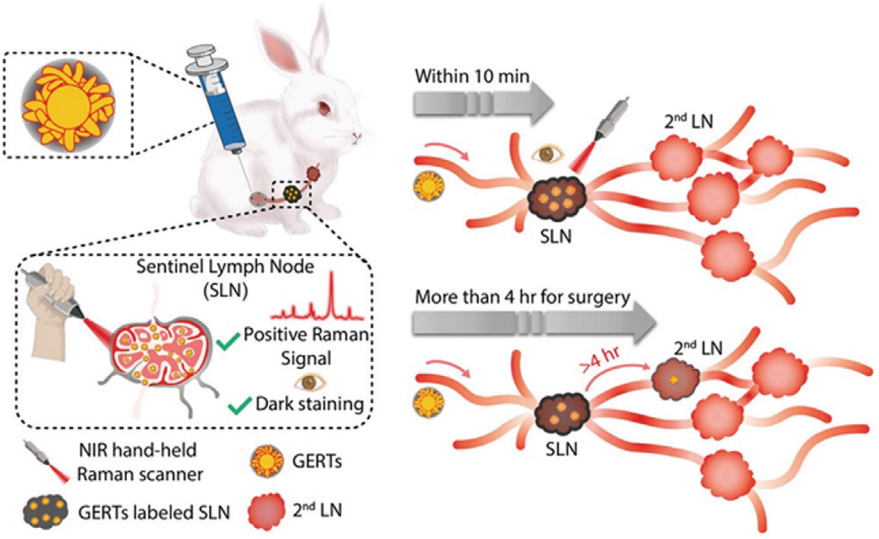



**Fig. 15.11** Schematic illustration of SLNs detection using Raman nanotags of GERTs [20]. GERTs are injected subcutaneously before the surgery and migrate to SLNs after a gentle massage. SLNs can be in vivo identified from the unique Raman signal of GERTs within 10 min by a hand-held Raman probe. GERTs only reach the second LNs after 4 h, which provides a suitable time window for surgery and avoids excessive resection of the LNs

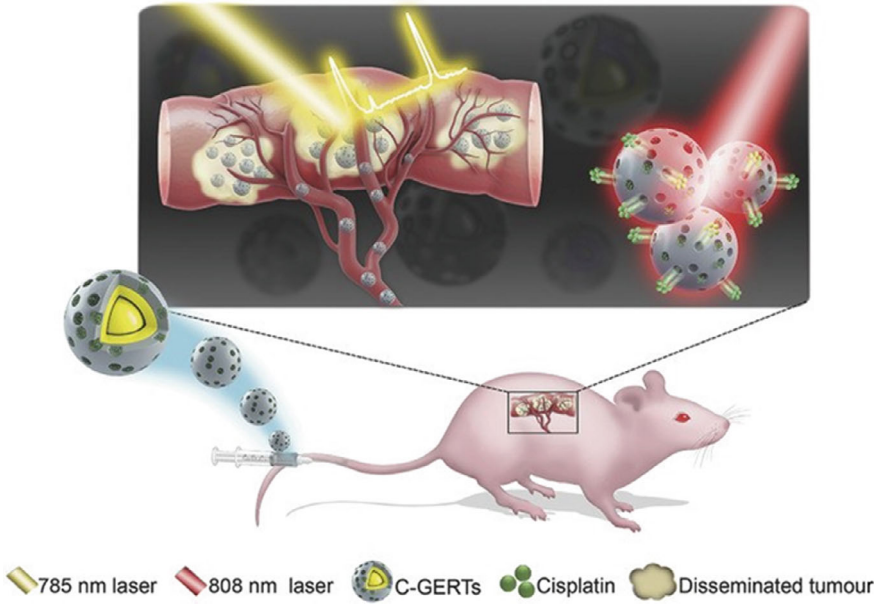



**Fig. 15.12** Raman-guided detection and chemo-photothermal synergistic therapy of abdominal disseminated microtumors with cisplatin-loaded gap-enhanced Raman tags (C-GERTs). The tumors on the intestine represent advanced disseminated ovarian microtumors [28]

nodes, while the former remains passively within the lymph nodes or is engulfed by resident macrophages. This leads to varying concentrations of the two GERTs within the lymph nodes. By injecting both GERTs into animal models, performing Raman imaging of SLNs, and employing classical least squares data processing techniques, we have achieved intraoperative diagnosis of SLN metastasis. This approach holds the potential to outperform current histopathological assessment methods for SLN metastasis diagnosis and may play a pivotal role in guiding surgical decision-making in the future (Fig. 15.12) [25].

### *15.4.4 Multifunctional Imaging and Therapy*

Patients with advanced ovarian cancer often experience widespread peritoneal dissemination and abdominal metastasis. The current standard treatment for advanced ovarian cancer involves cytoreductive surgery (CRS) combined with hyperthermic intraperitoneal chemotherapy (HIPEC). However, due to the challenge of completely removing small tumors during surgery, the outcomes of CRS are often suboptimal. Although HIPEC can improve prognosis, its therapeutic effects lack precision, leading to potential damage to healthy organs and complications. Therefore, there is an urgent need for innovative multifunctional strategies that can

accurately detect and eliminate disseminated microtumors while minimizing side effects. We have recently introduced cisplatin-loaded GERTs specifically designed for intraoperative detection and eradication of unresectable disseminated advanced ovarian tumors [28]. With unique and strong Raman signals, good biocompatibility, decent plasmonic photothermal conversion, and good drug loading capacity, cisplatin-loaded GERTs enable detection and specific elimination of microtumors with a minimum diameter of 1 mm via chemo-photothermal synergistic therapy, causing minimal side effects and significantly prolonging survival in mice. These results demonstrate that cisplatin-loaded-GERT-based chemo-photothermal synergistic therapy can effectively control the spread of disseminated tumors in mice and has potential as a safe and powerful method for treatment of advanced ovarian cancers, to improve survival and life quality of patients [28]. Furthermore, based on the same strategy, GERTs have also achieved the detection and elimination of residual microtumors in prostate cancer [27]. Therefore, GERT-guided surgery not only effectively prevents local cancer recurrence but also enables the precise detection and removal of residual microtumors, expanding the application potential of GERTs probes in the field of therapeutic precision medicine.

## 15.5 Summary and Outlook

This chapter has provided a comprehensive overview of our recent research progress in the preparation of GERTs and their latest advancements in the fields of information security and biomedicine. GERTs, as a highly sensitive nanomaterial with vast application prospects, have garnered extensive research interest in recent years. Its outstanding performance is attributed not only to its exceptional Raman enhancement effect but also to its superior physicochemical stability, laying a robust foundation for its versatile applications. In terms of GERTs preparation, we have developed a range of synthesis methods to produce high-quality GERTs, allowing effective control over their morphology and structure and enabling large-scale industrial production. This not only provides practical feasibility but also offers a platform for further research and optimization.

Despite the remarkable progress achieved with GERTs in various fields, several challenges remain that necessitate further in-depth research and exploration: (1) Biocompatibility and Toxicity. GERTs hold immense potential in the biomedical arena, but their biocompatibility and toxicity must be thoroughly assessed for practical applications. Collecting more data and conducting systematic studies to evaluate the long-term effects and safety of GERTs in living organisms is essential. Furthermore, in-depth investigations at the molecular level are needed to unravel the probe's interactions with biological systems and understand its behavior and effects in a biological environment. (2) Optical penetration in tissue. As an optical technique, the limited penetration ability in biological tissues poses a significant challenge to its clinical application. The absorption and scattering of light within biological tissues reduce signal strength, limiting imaging depth and resolution. Researchers

must explore novel imaging methods and techniques to overcome this limitation, such as combining GERTs with deep Raman spectroscopy to achieve deeper detection and imaging. (3) NIR-II biomedical applications. The weakened absorption and scattering effects of tissues on photons in the NIR-II region offer an opportunity to extend the application of GERTs to this spectral range. Doing so would improve the safety of imaging, reduce damage to organisms, enhance imaging resolution, and strengthen signal intensity, thereby better meeting the demands of clinical and research applications.

With continued in-depth research and technological advancements, the new generation of stable and high-brightness GERTs holds the potential to become a pivotal nanomaterial, opening up broader possibilities for practical applications and scientific research. Through ongoing innovation and collaboration, we firmly believe that GERTs will conquer these challenges in the future, further advancing related fields and contributing to scientific progress and development.

## References

1. N. G. Khlebtsov, L. Lin, B. N. Khlebtsov and J. Ye, Gap-enhanced Raman tags: fabrication, optical properties, and theranostic applications. Theranostics **10(5)**, 2067 (2020)
2. L. Lin, X. Bi, Y. Gu, F. Wang and J. Ye, Surface-enhanced Raman scattering nanotags for bioimaging. Journal of Applied Physics **129**, 191101 (2021)
3. A. Campion and P. Kambhampati, Surface-enhanced Raman scattering. Chemical society reviews **27**, 241-250 (1998)
4. J. Langer, D. Jimenez de Aberasturi, J. Aizpurua, R. A. Alvarez-Puebla, B. Auguié, J. J. Baumberg, G. C. Bazan, S. E. Bell, A. Boisen and A. G. Brolo, Present and future of surface-enhanced Raman scattering. ACS Nano **14**, 28-117 (2019)
5. Y. Zhang, Y. Gu, J. He, B. D. Thackray and J. Ye, Ultrabright gap-enhanced Raman tags for high-speed bioimaging. Nature Communications **10**, 3905 (2019)
6. Y. Zhang, Y. Qiu, L. Lin, H. Gu, Z. Xiao and J. Ye, Ultraphotostable mesoporous silica-coated gap-enhanced Raman tags (GERTs) for high-speed bioimaging. ACS Applied Materials & Interfaces **9**, 3995-4005 (2017)
7. J. Li, C. He, H. Qu, F. Shen and J. Ye, Five-dimensional unclonable anticounterfeiting orthogonal Raman labels. Journal of Materials Chemistry C **10**, 7273-7282 (2022)
8. J. Li, F. Liu, C. He, F. Shen and J. Ye, Orthogonal gap-enhanced Raman tags for interference-free and ultrastable surface-enhanced Raman scattering. Nanophotonics **11**, 1549-1560 (2022)
9. Y. Gu, C. He, F. Liu and J. Ye, Raman ink for steganography. Advanced Optical Materials **9**, 2002038 (2021)
10. Y. Gu, C. He, Y. Zhang, L. Lin, B. D. Thackray and J. Ye, Gap-enhanced Raman tags for physically unclonable anticounterfeiting labels. Nature Communications **11**, 516 (2020)
11. X. Jiang, Z. Tan, L. Lin, J. He, C. He, B. D. Thackray, Y. Zhang and J. Ye, Surface-Enhanced Raman Nanoprobes with Embedded Standards for Quantitative Cholesterol Detection. Small Methods **2**, 1800182 (2018)
12. C. He, X. Wu, J. Zhou, Y. Chen and J. Ye, Raman optical identification of renal cell carcinoma via machine learning. Spectrochimica Acta Part A: Molecular and Biomolecular Spectroscopy **252**, 119520 (2021)
13. Y. Lu, L. Lin and J. Ye, Human metabolite detection by surface-enhanced Raman spectroscopy. Materials Today Bio **13**, 100205 (2022)

14. C. He, S. Zhu, X. Wu, J. Zhou, Y. Chen, X. Qian and J. Ye, Accurate Tumor Subtype Detection with Raman Spectroscopy via Variational Autoencoder and Machine Learning. ACS Omega **7**, 10458-10468 (2022)
15. W. Wang, B. Shi, C. He, S. Wu, L. Zhu, J. Jiang, L. Wang, L. Lin, J. Ye and H. Zhang, Euclidean distance-based Raman spectroscopy (EDRS) for the prognosis analysis of gastric cancer: A solution to tumor heterogeneity. Spectrochimica Acta Part A: Molecular and Biomolecular Spectroscopy **288**, 122163 (2023)
16. X. Jin, B. N. Khlebtsov, V. A. Khanadeev, N. G. Khlebtsov and J. Ye, Rational design of ultrabright SERS probes with embedded reporters for bioimaging and photothermal therapy. ACS Applied Materials & Interfaces **9**, 30387-30397 (2017)
17. Y. Zhang, L. Lin and J. Ye, A rapid and universal method for depth estimation of lesions in heterogeneous tissues via photosafe ratiometric transmission Raman spectroscopy. View **4**, 20230022 (2023).
18. Y. Zhang, R. Chen, F. Liu, P. Miao, L. Lin and J. Ye, In Vivo Surface-Enhanced Transmission Raman Spectroscopy under Maximum Permissible Exposure: Toward Photosafe Detection of Deep-Seated Tumors. Small Methods **7**, 2201334 (2023)
19. S. Zhu, B. Deng, F. Liu, J. Li, L. Lin and J. Ye, Surface-enhanced Raman scattering bioimaging with an ultrahigh signal-to-background ratio under ambient light. ACS Applied Materials & Interfaces **14**, 8876-8887 (2022)
20. B. Deng, Y. Wang, Y. Wu, W. Yin, J. Lu and J. Ye, Raman Nanotags-Guided Intraoperative Sentinel Lymph Nodes Precise Location with Minimal Invasion. Advanced Science **9**, 2102405 (2022)
21. Y. Zhang, L. Lin, J. He and J. Ye, Optical penetration of surface-enhanced micro-scale spatial offset Raman spectroscopy in turbid gel and biological tissue. Journal of Innovative Optical Health Sciences **14**, 2141001 (2021)
22. Y. Gu, X. Bi and J. Ye, Gap-enhanced resonance Raman tags for live-cell imaging. Journal of Materials Chemistry B **8**, 6944-6955 (2020)
23. Z. Bao, Y. Zhang, Z. Tan, X. Yin, W. Di and J. Ye, Gap-enhanced Raman tags for high-contrast sentinel lymph node imaging. Biomaterials **163**, 105-115 (2018)
24. B. Shi, D. Li, W. Yao, W. Wang, J. Jiang, R. Wang, F. Yan, H. Liu, H. Zhang and J. Ye, Multi-functional theranostic nanoparticles for multi-modal imaging-guided CAR-T immunotherapy and chemo-photothermal combinational therapy of non-Hodgkin's lymphoma. Biomaterials Science **10**, 2577-2589 (2022)
25. Z. Bao, B. Deng, Y. Zhang, X. Li, Z. Tan, Z. Gu, B. Gu, Z. Shao, W. Di and J. Ye, Ratiometric Raman nanotags enable intraoperative detection of metastatic sentinel lymph node. Biomaterials **276**, 121070 (2021)
26. B. Shi, B. Zhang, Y. Zhang, Y. Gu, C. Zheng, J. Yan, W. Chen, F. Yan, J. Ye and H. Zhang, Multifunctional gap-enhanced Raman tags for preoperative and intraoperative cancer imaging. Acta Biomaterialia **104**, 210-220 (2020)
27. Y. Qiu, Y. Zhang, M. Li, G. Chen, C. Fan, K. Cui, J.-B. Wan, A. Han, J. Ye and Z. Xiao, Intraoperative detection and eradication of residual microtumors with gap-enhanced Raman tags. ACS Nano **12**, 7974-7985 (2018)
28. Y. Zhang, Z. Liu, B. D. Thackray, Z. Bao, X. Yin, F. Shi, J. Wu, J. Ye and W. Di, Intraoperative Raman-guided chemo-photothermal synergistic therapy of advanced disseminated ovarian cancers. Small **14**, 1801022 (2018)
29. L. Lin, M. Zapata, M. Xiong, Z. Liu, S. Wang, H. Xu, A. G. Borisov, H. Gu, P. Nordlander and J. Aizpurua, Nanooptics of plasmonic nanomatryoshkas: shrinking the size of a core–shell junction to subnanometer. Nano letters **15**, 6419-6428 (2015)
30. L. Lin, H. Gu and J. Ye, Plasmonic multi-shell nanomatryoshka particles as highly tunable SERS tags with built-in reporters. Chemical Communications **51**, 17740-17743 (2015)
31. M. Kim, S. M. Ko, J.-M. Kim, J. Son, C. Lee, W.-K. Rhim and J.-M. Nam, Dealloyed intra-nanogap particles with highly robust, quantifiable surface-enhanced Raman scattering signals for biosensing and bioimaging applications. ACS Central Science **4**, 277-287 (2018)

32. L. Lin, Q. Zhang, X. Li, M. Qiu, X. Jiang, W. Jin, H. Gu, D. Y. Lei and J. Ye, Electron transport across plasmonic molecular nanogaps interrogated with surface-enhanced Raman scattering. ACS Nano **12**, 6492-6503 (2018)
33. J. Li, B. Deng and J. Ye, Fluorescence-free bis (dithiolene) nickel dyes for surface-enhanced resonance Raman imaging in the second near-infrared window. Biomaterials **300**, 122211 (2023)
34. S. Wang, Z. Liu, C. Bartic, H. Xu and J. Ye, Improving SERS uniformity by isolating hot spots in gold rod-in-shell nanoparticles. Journal of Nanoparticle Research **18**, 1-11 (2016)
35. X. Jin, J. He and J. Ye, Nanotriangle-based gap-enhanced Raman tags for bioimaging and photothermal therapy. Journal of Applied Physics **125**, 073102 (2019)
36. D. D. Gurav, Y. A. Jia, J. Ye and K. Qian, Design of plasmonic nanomaterials for diagnostic spectrometry. Nanoscale Advances **1**, 459-469 (2019)
37. Z. Ye, L. Lin, Z. Tan, Y.-J. Zeng, S. Ruan and J. Ye, Sub-100 nm multi-shell bimetallic gap-enhanced Raman tags. Applied Surface Science **487**, 1058-1067 (2019)

# Chapter 16
# SERS for Diagnostics and Forensics: Selected Past, Present, and Future Highlights




**Lawrence D. Ziegler**

**Abstract** The use of SERS for bacterial diagnostics, and for detection and identification of trace amounts of human body fluids has the potential for making transformative impacts in the fields of infectious disease management and forensic science respectively. 785 nm excited SERS spectra of vegetative bacterial cells, fungi, and spores are described. While bacterial species and strain identification via SERS and multivariate data analysis approaches is possible within limited reference data sets, the promise of SERS ultra-rapid antibiotic susceptibility testing that can provide best treatment options for combatting infectious disease and mitigate the growing concerns about multidrug resistant bacteria is seen as the most promising SERS application in the area of bacterial diagnostics. In addition, a SERS-based methodology may provide forensic scientists with a single platform for the rapid identification of trace amounts of blood, semen, vaginal fluid, and saliva at crime scenes or laboratories, and would be a new capability in forensic science. A key value underlying our efforts in these areas is to provide a molecular and biochemical understanding of all the features and interactions that give rise to the observed spectroscopic signatures and is fully illustrated in this chapter.

**Keywords** SERS · Bacteria · Fungi · Spores · Antibiotic susceptibility testing · Forensics · Protoporphyrin IX · Hemoglobin · Vibronic coupling

L. D. Ziegler (✉)
Department of Chemistry and The Photonics Center, Boston University, Boston, MA 02215, USA
e-mail: lziegler@bu.edu

© The Author(s), under exclusive license to Springer Nature Singapore Pte Ltd. 2024

M. Procházka et al. (eds.), *Surface- and Tip-Enhanced Raman Scattering Spectroscopy*,
https://doi.org/10.1007/978-981-97-5818-0_16

## 16.1 Introduction

Following its initial discovery and accurate characterization [1–4], worldwide research efforts have sought to exploit the sensitivity provided by surface-enhanced Raman spectroscopy to find impactful applications for this potentially transformative discovery [5–11]. Combining the standard advantages of Raman spectroscopy: molecularly specific vibrational signatures, label-free identification, multiplexing capabilities due to narrow bandwidths, small sample size, portability, non-destructive probing, and convenient integration into multivariate data analysis platforms including machine learning approaches, with the effective $10^5$–$10^9$ enhancement of Raman cross sections resulting from SERS, offers the possibilities for unprecedented analytical developments. While well-recognized challenges still remain regarding the realization of the full potential of SERS [12–14], work in our laboratory has focused on biomedical and forensic applications that especially exploit these attributes of SERS and will be briefly summarized in this review. Aside from sensitivity, the most widely recognized attribute of SERS, the results described here also serve to illustrate lesser recognized qualities that can be appreciated and used to maximize the analytical impact of SERS. Firstly, this includes SERS ability to provide simple spectra of complex samples due to selective and competitive metal surface-molecule interactions. From a chemical point of view, one may view this as a special solvation effect. Secondly, although the use of different metals, almost exclusively due to the inherent dielectric properties, a choice between Au and Ag, SERS sensing outcomes can be decisively different for these two plasmonic metals. Finally, for biomedical sensing where samples of interest may be complex mixtures, the selection of an optimal solvent, can be central to the success of a given SERS application. The selection of analytical results described in this chapter was made with the goals of highlighted less-appreciated attributes of SERS that can be exploited for successful SERS applications especially in the realm of biomedical sensing as described below.

## 16.2 SERS of Vegetative Bacteria

### *16.2.1 Phenomenological Characterization of Bacterial SERS Spectra*

With the goal of whole organism fingerprinting, many research groups worldwide have reported on the SERS spectra of vegetative bacterial cells over the past twenty years with applications in clinical human health diagnostics, food and environmental safety, and biothreat assessment in mind [15–33]. Most efforts have been focused on acquisition of these vibrational signatures for rapid, phenomenological species or even strain-specific detection and identification via chemometric analyses. All the SERS spectra shown here were obtained with samples on Au or Ag SERS

substrates produced in our laboratory by an in situ metal ion doped sol–gel procedure. The recipe and performance characteristics of these SERS chips have been described previously [34, 35]. Bacterial samples are enriched from growth media or presenting body fluids, washed in pH 7 water, and centrifuged three times, before re-suspension in ~ 10 μL of water. 1 μL of this solution is then pipetted onto Au or Ag chips. Bacterial spectra are excited with < 1 mW of 785 nm radiation and result from about 5–10 10 s accumulations after drying on the SERS substrates for ~ 5–10 min. Examples of typical 785 nm SERS spectra of six strains of different bacterial species on Au substrates are shown in Fig. 16.1a. Both gram-negative; *P. mirabalis, E. coli, P. aeruginosa*, and gram-positive: *M. luteus, K. rhizophila, B. cereus,* species enriched from growth media are displayed in this figure. As seen, several bands of the same vibrational frequencies are evident in these representative bacterial SERS spectra.

As regards, the widely desired goal of using SERS for bacterial identification purposes, the results of a PLS-DA treatment are shown in Fig. 16.1b for this set of species. Spectra in the training set readily classify with 100% specificity and sensitivity, and 18 "unknown" spectra not used to make the classification model are correctly classified via this procedure. For this purpose, and for all the classification efforts pursued in our laboratory, we use a barcode reduction of spectral data as inputs to relatively standard data analysis approaches such as PCA or PLS-DA. For this barcode procedure, the curvature, i.e., second derivative, of the spectrum at each wavenumber is assigned a "0" or a "1" depending on the sign of this quantity. This technique serves to minimize errors due to background corrections and effects of inhomogeneities that might contribute to relative intensity changes in complex, multicomponent samples and results in enhanced classification analytical sensitivity and specificity [36].

Other examples of bacterial SERS spectra excited at 785 nm on Au substrates are shown in Fig. 16.2. With the potential goal of demonstrating the value of SERS for rapid UTI diagnostics, these 12 spectra were obtained from bacteria enriched from urine samples initially spiked at the UTI clinically relevant $10^5$ cfu/mL concentration [37]. Furthermore, the spectra of several strains of the four most common UTI causative bacterial species, again including both gram-positive (*S. saprophyticus, K. pneumoniae* and *E. faecalis*) and gram-negative species (*E. coli*), are shown in Fig. 16.2a. Similar vibrational features also appear common to these representative strain-specific SERS signatures. As demonstrated for Fig. 16.1 spectra, within this relatively small pathogen set, these dozen SERS bacterial spectra set can be successfully classified via the barcode PLS-DA procedure with 100% sensitivity and specificity. This data set, however, includes different strains of different bacterial species. As a demonstration of the use of SERS for bacterial identification, 20 spectra of an unknown strain were all correctly identified as *E. coli* 6594 (Fig. 16.2 lower panel) when classified with a prior set of these 12 reference strains [37]. The generality of this result, and its prospects for practical adoption for rapid bacterial detection and identification, is addressed further below.

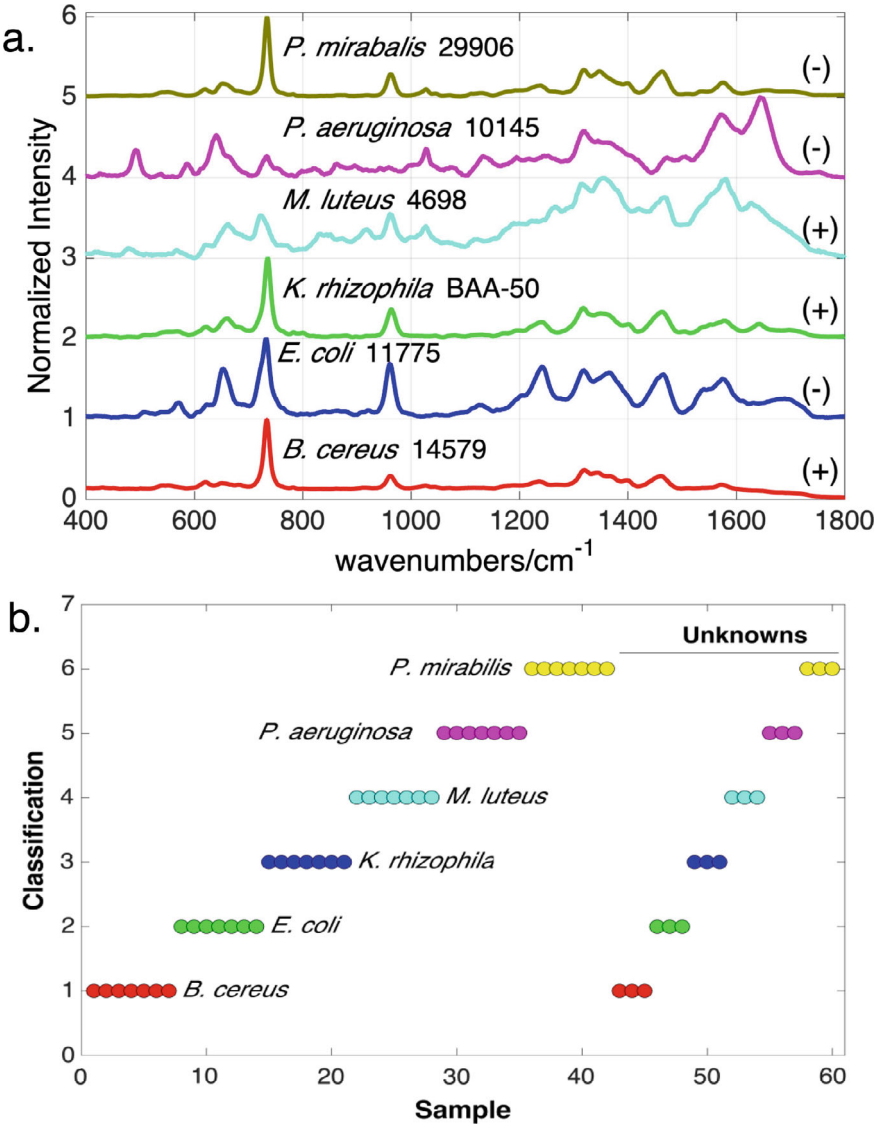



**Fig. 16.1** Representative SERS spectra of six bacterial strains belonging to different species excited at 785 nm are displayed in the upper panel. As noted by the ± sign both gram-positive and gram-negative species are shown here. Intensities are normalized to the maximum in each spectrum. A PLS-DA classification result shows that within this limited data set of ~ 80 spectra belonging to these six classes, a training set provides 100% sensitivity and specificity. All "unknowns", not used to create this training are shown to be correctly identified by this procedure

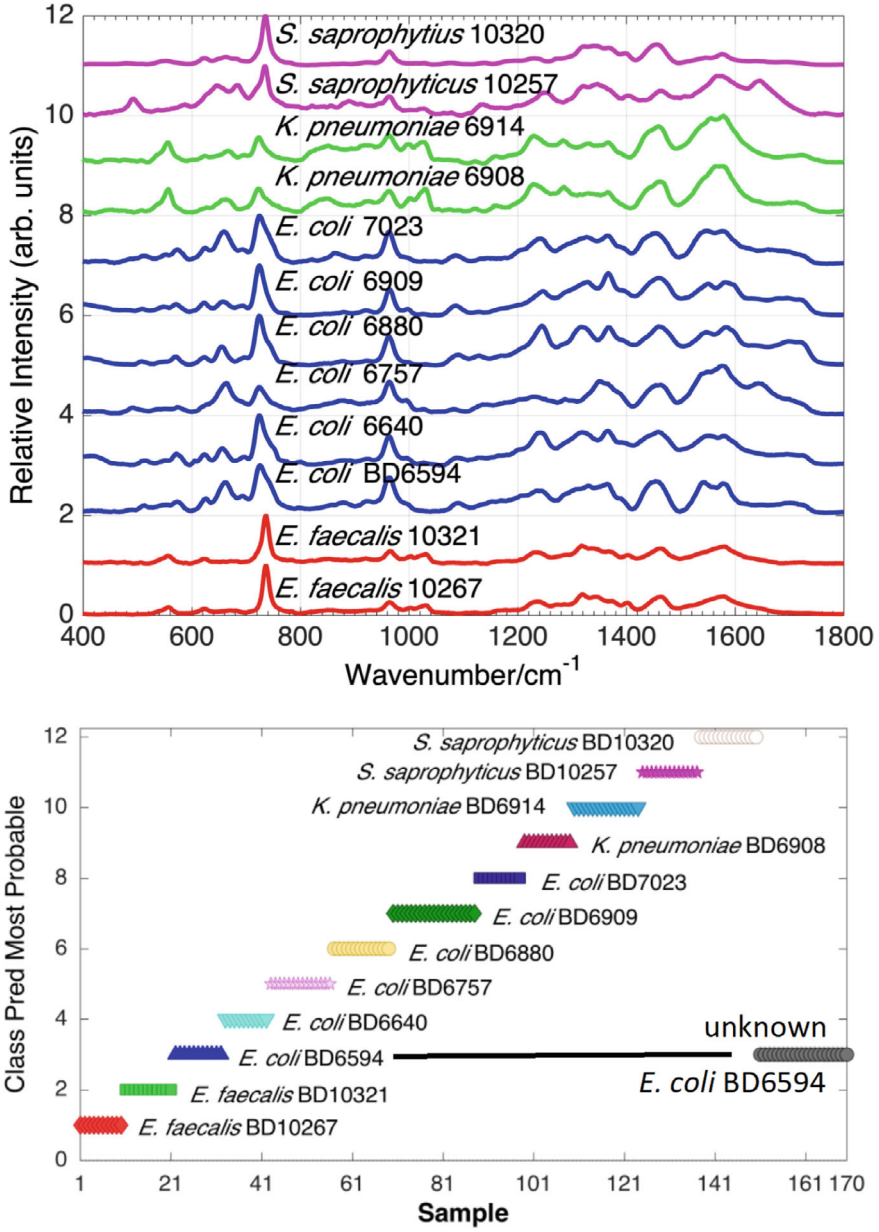



**Fig. 16.2** Normalized 785 nm excited SERS spectra of 12 UTI causative bacterial clinical isolates grown in processed human urine are displayed in the upper panel. The color-coded strains of *S. saprophyticus* (2), *K. pneumoniae* (2), *E. coli* (6) and *E. faecalis* (2) SERS spectra are displayed here. Each spectrum shown is an average of ~ 10 spectra. Results of a cross-validated PLS-DA classification treatment of the SERS spectra of the twelve bacterial strains grown and enriched from processed urine show 100% sensitivity and specificity. The use of this data set for bacterial identification of an "unknown" set of spectra (not used in the training set) is illustrated in this lower panel. All "unknowns" correctly identify as *E. coli* BD6594

### 16.2.2 Molecular Components of 785 nm Excited Bacterial SERS Spectra

In order to fully exploit the analytical value and impact of the ability to rapidly acquire bacterial SERS spectra, we believe that understanding the chemical and biochemical origins of these signals is essential. These vibrational features were originally attributed to bacterial cell wall components, and still continue to be assigned these molecular origins in some bacterial SERS reports. The fact that both gram-positive and gram-negative bacteria can have very similar SERS spectra, e.g., compare *P. mirabalis* (–) versus. *K. rhizophilia* (+) in Fig. 16.1, should have been recognized as being a contradiction for this hypothesis. However, as shown previously [37–39], nearly each band in the SERS spectra of water washed bacterial cells excited at 785 nm is due to the purine metabolic degradation products of nucleic acids, most probably, RNA, as a result of the well-known stringent or starvation response of bacteria [40–42].

More specific evidence of how each band in the SERS spectra of vegetative bacterial cells can be assigned to RNA purine degradation products has been provided by best-fits to observed bacterial SERS spectra of contributing purines [37–39]. In Fig. 16.3, the "best-fit" spectra (in red) resulting from the linear combination of indicated purine component 785 nm SERS spectra are shown in comparison with the corresponding observed spectra (in black) for four representative bacterial strains. The color-coded component spectra are scaled in proportion to their relative contribution to the best-fit spectra determined by inspection. As shown, these SERS spectra result from different combinations of adenine, guanine, hypoxanthine, xanthine, uric acid, and adenosine. Additional purine contributors, guanosine and AMP, and occasionally the pyrimidine cytosine, are also found in these 785 nm excited SERS spectra. The best-fit determined relative purine components to the dozen spectra shown in Fig. 16.2 are summarized in the bar graph in Fig. 16.4 [37]. The uniqueness of each spectrum is due to different amounts of these RNA degradation products appearing in the extracellular region of bacterial cells close to the cell wall region. Other evidence consistent with this origin of the 785 nm excited bacterial SERS spectra includes the equivalence of the SERS spectra of enriched cell-free bacterial supernatant and those of the bacterial cells, gene knockout experiments where deletions of specific nucleic acid degradation enzymes results in very different SERS spectra [38], and the lack of a similar SERS signature in the SERS spectrum of *Clamydia trachomatis*, a parasitic bacterium that lacks the RNA degradation enzymes [39]. Bacteria rapidly react to environmental changes by re-wiring metabolic activity that will enhance their survival in response to detected threats [43]. The rapid starvation response is initiated when bacteria are removed from growth media during the sample preparation step and placed in the low nutrient environment of water. The secretion of purine degradation products from enzymes located in the pericellular regions of bacterial cells is a known component of this starvation response [44–47]. Hence, when bacterial cells are brought into contact with a SERS substrate, these small molecules are already near the substrate surface giving rise to these SERS signatures predominately

dominated by the degradation products of RNA nucleotides [38]. Different bacterial species and strains have different combinations of the purine degradation enzymes and hence different SERS spectra result. Furthermore, turnover rates, i.e., metabolic kinetics and control of the same degradation enzymes, may be specific to different bacterial strains, thus also contributing to the observed species/strain-specific SERS signatures. An attribute sometimes neglected by SERS researchers in this area is that Raman excitation at bluer frequencies, say 532 or 514 nm, results in SERS spectra with features dominated by FAD due to the proximity of electronic resonance enhancement effects. Thus, the analytical specificity afforded by the range of purine degradation components (Fig. 16.3) is greatly reduced at bluer wavelengths [19, 38, 48].

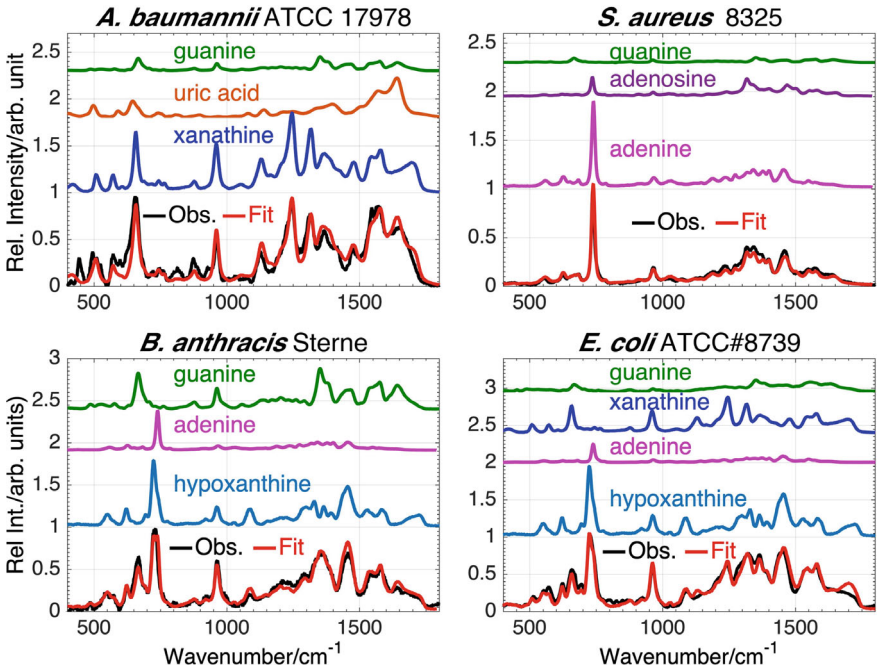



**Fig. 16.3** Empirically determined best-fits (red) of four representative normalized observed bacterial spectra (black) to a linear combinations of purine (adenine, hypoxanthine, xanthine, guanine, uric acid, and adenosine) SERS spectra. Fits identify the molecular origins of nearly every peak in this set of spectra. The amplitudes of the relative contributions of the purine components are shown above each bacterial SERS spectrum

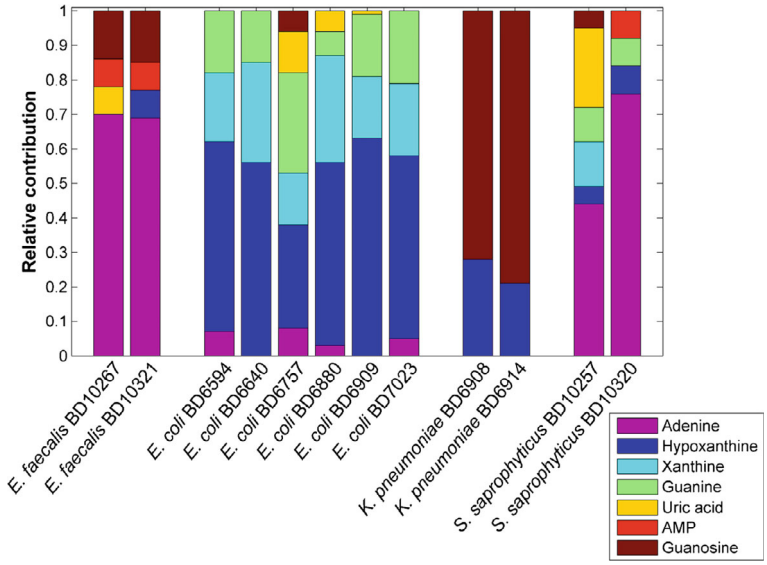



**Fig. 16.4** Relative contribution of each of the seven color-coded purines found to contribute to the bacterial SERS spectra are summarized in this bar graph. The success of the PLS-DA classification model (Fig. 16.2) is due to the reproducible differences in these relative contributions of purines to the strain-specific SERS signatures. Although strain-specific differences are evident, the pattern of contributing purines is more different between the four species than between strains of a given species

### *16.2.3 Evaluation of Bacterial Identification via SERS*

Although Figs. 16.1 and 16.2 indicate that within limited data sets and well-controlled reproducible experimental preparation conditions highly accurate bacterial classification is possible, SERS use for this purpose is probably relatively limited. We have previously been able to identify bacteria with > 95% sensitivity and specificity for data sets of ~ 20–25 different species/stains [49]. However, the important result illustrated by the spectra in Fig. 16.2 is that 785 nm excited SERS spectra are not only species but strain-specific, thus complicating the ability to use SERS spectra for many medically relevant purposes given the vast numbers of unique strains for each bacterial species, an already large number. The palette of bands based on the finite number of purine components may not provide a sufficiently broad range of vibrational features for unequivocal identification of the large numbers of potential bacterial infectious agents for most disease presentations. Furthermore, successful classification procedures need examples of the identified organism in a reference library, and thus, emerging pathogens, an increasingly recognized major health problem given the rapid evolution of multidrug resistant strains (MDR), will evade detection and identification by such SERS procedures. Finally, given the role of the degradation kinetics that can result in SERS signatures that are dependent on starvation time,

strict control of experimental procedures is required to maximize the use of SERS for bacterial ID [50]. However, in some medical cases where limited pathogen ID libraries are required, SERS may prove useful for bacterial identification purposes as demonstrated (Figs. 16.1 and 16.2).

### *16.2.4 SERS-Antibiotic Susceptibility Testing (AST)*

The greatest impact of bacterial SERS may be in the rapid, quantitative determinations of antibiotic susceptibility testing (AST) profiles. An example of how SERS can be exploited for this ultra-rapid drug susceptibility purpose is summarized in Fig. 16.5 for the *E. coli* ATCC#2452 strain, which is known to be susceptible and resistant to the antibiotics tetracycline and ampicillin, respectively. The 785 nm SERS spectra following a 30 min, 37 °C incubation period with growth media and different doses of antibiotics, and washing before being pipetted onto Au substrates are shown in Fig. 16.5. These spectra, normalized to the peak intensity of the *E. coli* 2452 spectrum incubated in the absence of the antibiotic (Fig. 16.5b, red), display a monotonically decreasing intensity as a function of tetracycline concentration. The same trend is observed if the peak height at ~ 730 $cm^{-1}$ where adenine has its maximum or the total (400–1800 $cm^{-1}$) spectral area is used as the SERS intensity figure of merit (Fig. 16.5c). Furthermore, the minimal inhibitory concentration (MIC) determined by gold standard CLSI 24 h growth results is 2 mg/L for this strain/drug pair. The MIC is the lowest concentration that can be seen to halt bacterial cell growth. OD measurements for the *E. coli* sample incubated with tetracycline indicates the turbidity loss at 2 mg/L determining the MIC via the 24-h procedure (Fig. 16.5a). If we take the doubling concentration where the SERS intensity (peak maximum or spectral area) falls to under 20% of the maximum intensity as the SERS figure of merit for determining MIC, then we have demonstrated how SERS provides the fastest quantitative MIC measure of any method we are aware of. While SERS acquisition determination for a single antibiotic concentration can take ~ 1 h in total including the 30 min incubation period, when these results can be parallelized, an MIC can be accurately determined in this same ~ 1 h timeframe.

As a phenomenological contrast, when the same procedure is repeated for the same *E. coli* 2452 incubated with doses of ampicillin, the intensity of the SERS spectra is effectively antibiotic concentration independent as shown in Fig. 16.5e and f. The ampicillin independence of the SERS intensity of this strain is consistent with its observed resistance to this antibiotic via the 24-h growth results (Fig. 16.5d). The only significant difference between the growth and SERS-AST result is that the SERS-AST is generated in a one-hour time frame, not 24 h. For medical treatments where delayed administration of the best antibiotic treatment can result in higher morbidities and mortalities, such as blood infections, the SERS-AST approach has the potential to be transformative. In Fig. 16.6, four additional examples of SERS-AST are displayed. The bars represent the integrated SERS spectral area as a function of antibiotic concentration during 30-min incubation period. Again, the resistance

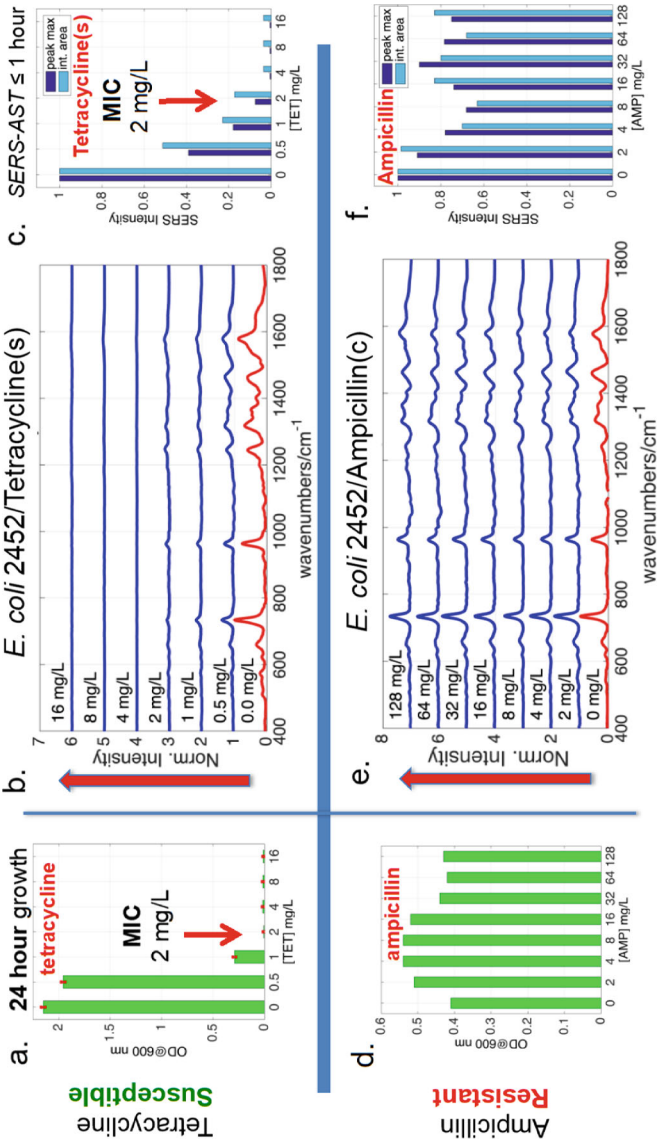



**Fig. 16.5** **a** OD measures of turbidity determine that the MIC for the *E. coli* 2452 strain is 2 mg/L after incubation with the antibiotic tetracycline and growth media for 24 h. **b** SERS spectra of *E. coli* 2452 30 min incubation with tetracycline and growth media as a function of doubling antibiotic concentration. Red spectrum corresponds to *E. coli* 2452 grown without any antibiotic. **c** The *E. coli* 2452 SERS intensity measure by the spectral peak maximum and integrated entire spectral area as a function of tetracycline concentration. SERS measurements take ~ one hour including incubation time. The SERS-AST value of the MIC results when the intensity is just below 20% of the maximum. **d–f** are the corresponding growth determined MIC, SERS spectra and representations of the SERS intensity for the *E. coli* 2452 strain incubated with ampicillin. The ampicillin concentration independence indicates this strain is resistant to ampicillin as found both by the 24 h growth and 1- hour SERS-AST approach

of the *K. pneumoniae* 6908 strain for ampicillin is clearly evident, as is the different MICs determined for the other strains shown. The red and green arrows refer to the rapid SERS and 24-h growth MIC value, respectively, and show that quantitative agreement is found between the SERS and growth results. The only significant difference is the time to result. To date we have obtained ~ 90 bacterial strain/drug combinations where SERS MICs are in agreement with 24 h growth results within ± 1 doubling concentration which is the antibiotic concentration range that is taken as essential agreement. Similar SERS-AST results have been reported by another group although the time to result is significantly slower than resulting from the methodology described here [51, 52].

This rapid, consequential SERS-AST methodology relies on two ubiquitous and fast bacterial responses. One is the detection step which is the stringent or starvation response that provides the purine metabolic degradation signaling species, the other is the upstream rapid bacterial response to antibiotics. At concentrations below the MIC, SERS intensities can either monotonically decrease or increase before they fall below the ~ 20% value at the MIC as shown in these representative examples (Figs. 16.5 and 16.6). Increasing or decreasing SERS bacterial intensities at sub-MIC drug-dose concentrations appears correlated with the bacteriostatic or bactericidal activity of the specific antibiotic, i.e., antibiotics either kill cells (bactericidals) or stop their growth (bacteriostatics) to achieve their desired medical outcomes, and these two outcomes have been correlated with either enhanced or decreased bacterial cellular respiration rates [53]. These metabolic rate changes for bactericidal or bacteriostatic drugs appear to be reflected in the SERS intensity trends at sub-MIC dosages.

As a further example of how knowledge of the molecular components contributing to these SERS signals may be used to learn about bacterial responses to antibiotics, the relative contributions of the different purines contributing to the SERS spectra of *E. coli* 2452 as a function of the bacteriostatic tetracycline are shown in Fig. 16.7. The relative purine component concentrations are determined by the best-fit procedure demonstrated in Fig. 16.3, and then scaled to the normalizing peak intensity feature. For this pathogen/drug combination, the SERS spectrum only significantly changes in relative molecular composition at the tetracycline concentration of 2 mg/L which is the MIC for this strain/drug pair (Fig. 16.5a–c). Molecular composition of the SERS spectrum at higher tetracycline concentrations is not possible given the weakness of these spectra for this strain/drug pair. This is not a general trend for bacteriostatic or for bactericidal drug-dose-dependent responses. Some strain/drug pairs exhibit consistent changes in the relative concentration of nucleic acid degradation products with drug dose as determined by this molecularly specific SERS analysis, and for others, the change is more abrupt with antibiotic concentration. These effects will be detailed in a subsequent report. However, this example is, however, meant to illustrate that knowledge of the chemical components of these 785 nm excited SERS spectra allows studies of the inherent bacterial metabolic degradation responses with enzymatic pathway specificity. The use of SERS for ultra-rapid AST is not just an opportunity for a potentially transformative diagnostic platform but also opens new possibilities for learning about mechanisms of antibiotic responses in bacteria. Work in our laboratory is pursuing these possibilities along with the development

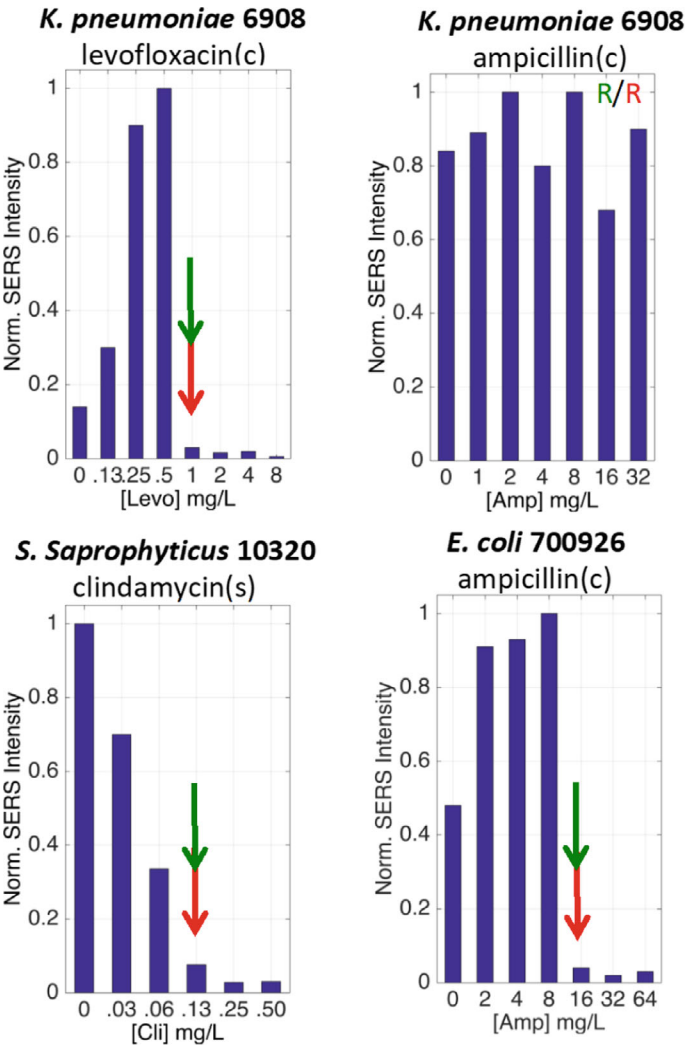



**Fig. 16.6** Bar graphs represent the integrated area of SERS spectra of four bacterial species incubated with the indicated antibiotic concentration for 30 min. The green arrow is the 24 h growth determined MIC, and the red arrow is the corresponding SERS determined MIC. *K. pneumonia* 6908 is found to be ampicillin resistant by both methods. The (*c*) and (s) designations indicate if the antibiotic is bactericidal or bacteriostatic

of instrumentation in order to exploit this discovery of rapid purine-based SERS detection for AST.

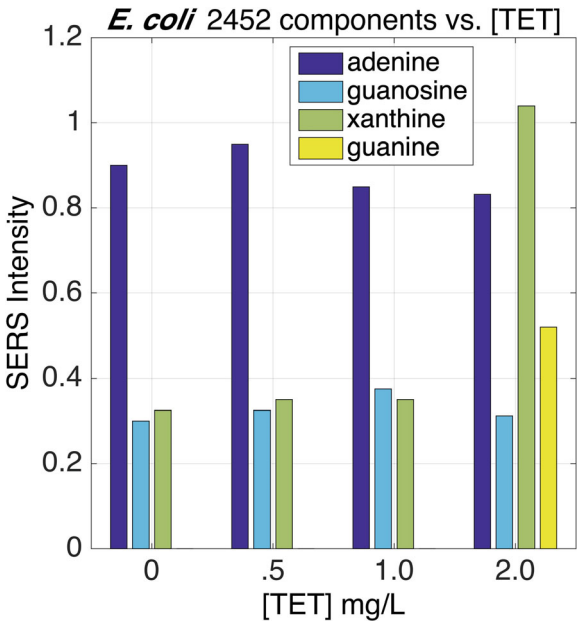



**Fig. 16.7** Relative purine contributions to the *E. coli* 2452 SERS spectra shown in Fig. 16.5 normalized to their peak height maxima as a function of tetracycline concentration. For this strain-drug combination, the composition of the SERS spectrum changes at the MIC (2 mg/l)

## 16.3 SERS of Fungi

The consequences of fungal infections to human health are increasingly recognized as a growing threat especially as the exploding threat of multidrug resistant strains continue to expand, the number of immune compromised patients increase and as a consequence of global warming [54–56]. Approximately 2 million deaths a year worldwide result from fungal infections. One component of the strategies needed to minimize the impact of emerging fungal pathogens on human public health is the development of quicker diagnostic tests that can allow for the selection of effective drug treatments earlier and indicate other required responses, including isolation, to reduce transmission threats. Hence, the development of an analogous SERS-based antifungal susceptibility testing platform would be a valuable addition to the arsenal of tools for combatting human infections.

We and others have previously demonstrated the ability to acquire SERS spectra of fungi [57–63]. The primary focus in these studies has laudably demonstrated that SERS spectra can be used with a finite set of organisms for rapid identification purposes once the fungi has been isolated from its growth medium or presenting body fluid. The 785 nm excited SERS spectra of some different fungi strains are shown in Fig. 16.8a. These organisms have been enriched from growth media and washed in water multiple times before being placed on Au SERS substrates. Again the barcode PLS-DA classification procedure demonstrates at least for the six fungi shown in Fig. 16.8a, these SERS signatures can be used for species identification (Fig. 16.8b). Although these SERS fungi vibrational bands have been assigned to

fungal cell membrane wall features in prior studies, the purine contributions to these 785 nm excited SERS spectra are readily recognized in these spectra. For example, the successful best-fit to the observed *C. albicans* 10231 SERS spectrum shows that these fungi spectra result from purine nucleotide degradation products as shown for bacteria excited at 785 nm. When fungi are similarly confronted with limitations of their carbon source in their environment during growth, they also exhibit a stringent or starvation response with accompanying transcription changes [64–66]. Thus, the SERS spectra of fungi similarly exhibit purine-based spectra from their starvation response as found for bacteria. Furthermore, it may be possible to rapidly determine fungicide susceptibilities via SERS in analogy to the bacterial response described above. For example in Fig. 16.8d, the intensity of *C. albicans* 11651 SERS spectra that have been incubated with the fungicides fluconazole and itraconazole, at 37 °C for 30 min, and an untreated *C. albicans* 11651 sample are compared. This fungal strain is known to be susceptible to fluconazole and resistant to itraconazole. Correspondingly, the SERS intensity is effectively unchanged for the *C. albicans* 11651 exposed to itraconazole but significantly reduced when this pathogen is incubated with fluconazole, consistent with the known susceptibilities of this strain for these two drugs. A transcriptional response to fungicides has been reported in fungi [67] and can thus account for these SERS susceptibility measures that are analogous to the more widely studied bacterial responses. In addition to providing early best care treatments for antifungal-resistant *Candida* and other fungal infections, reduction of unnecessary use of antifungals via antifungal stewardship is critical to limiting multidrug resistance proliferation. Thus, this rapid SERS antifungal testing procedure could potentially improve diagnostic outcomes critical to the successful management of patients with these infections.

## 16.4 SERS of Bacterial Spores (Au Vs. Ag)

As a reaction to concerns about the use of biological warfare agents in the wake of 9/11, considerable efforts were made to develop novel analytical techniques for this biosensing application. In particular, identification and detection of *bacillus anthracis* spores was a highly active area of research, and the sensitivity and specificity of SERS made it a natural analytical approach to try to develop for this purpose. Several groups examined procedures that could exploit SERS for the rapid detection and identification of bacterial spores [68–74]. However, as illustrated by the *B. subtilis* spore results in Fig. 16.9, SERS has had limited success for achieving this goal. In contrast to the bright SERS signals of vegetative bacterial cells, no species/strain-specific 785 nm SERS signature could be directly detected when bacterial spores are placed on the same Au or Ag SERS substrates. As shown in Fig. 16.9a, the SERS intensity of freshly water washed *B. subtilis* spores is very weak on both Au and Ag substrates excited at 785 nm. However, it was known that L-alanine induced the triggering of spore germination [75]. *Bacillus* spores are known to contain calcium dipicolinic acid (CaDPA) (5–10% of spore weight) in the spore core and that CaDPA

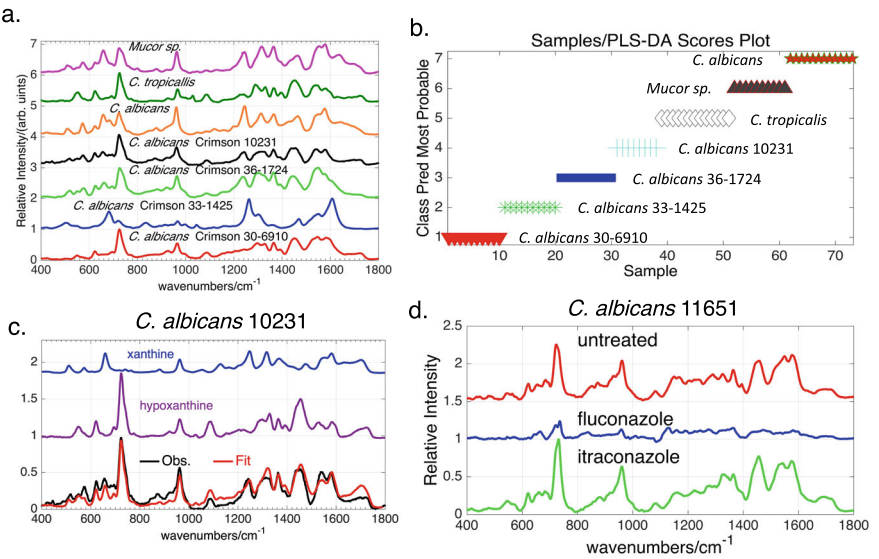



**Fig. 16.8** **a** 785 nm excited SERS spectra of six fungal strains on Au. **b** Within this limited set of 72 spectra, 100% sensitivity and specificity are achieved by a PLD-DA classification procedure. **c** Best-fit to the observed *C. albicans* 10231 SERS spectrum shows that the same purine components contribute to these SERS spectra as found for bacteria. d. The changes in relative SERS intensity observed for *C. albicans* 11651 after 30 min incubations with fungicides fluconazole and intraconazole, known to be susceptible and resistant, respectively, for this fungus is shown. SERS MIC determination of fungi should be possible given these preliminary results

is released upon germination. This phenomenon, resulting in the rapid release of DPA, was exploited in order to have a SERS-sensitive spore biomarker. The resulting SERS spectra of *B. subtilis* spores just a few minutes after being mixed with an L-alanine solution is shown in Fig. 16.9b. While this procedure provides a sensitive signature for bacterial spores, this signal is virtually identical for all the *Bacillus* species and thus is not very valuable as an instantaneous marker for species specificity. Distinguishing potentially lethal *bacillus anthracis* spores from other more benign, albeit pathogenic *bacillus* spores was a primary goal of this application. The other attribute curiously evident in Fig. 16.9b–d is that no CaDPA signal is observed on our Au substrates. This effect results from the very different interaction strengths between the resulting negatively charged, bi-dentate DPA anion in aqueous solution and the Au and Ag surfaces. The DPA carboxylate groups are much more strongly attracted to the Ag surface than the Au surface. In part, this biosensing example is included here to make the point that the choice of nanostructured metal can be crucial for the success of a given analytical SERS application due to chemical and physical-adsorption interaction effects. Other examples of such dramatic SERS metal dependence are discussed below.

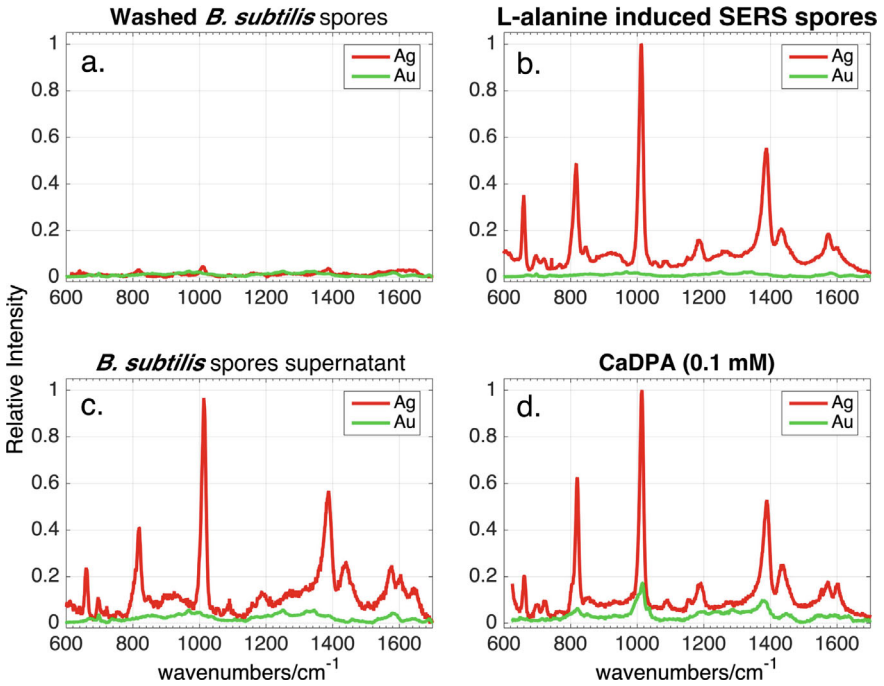



**Fig. 16.9** **a** 785 nm SERS spectra of *B. subtilis* spores immediately after water washing on Au and Ag substrates. **b** SERS spectra of *B. subtilis* spores a few minutes after mixing with an L-alanine solution on Au and Ag substrates. **c** SERS spectra of *B. subtilis* spores supernatant on Au and Ag substrates **d** SERS spectra of calcium dipicolinate acid (CaDPA) on Au and Ag substrates

## 16.5 SERS for Forensics Applications

Exploiting new and developing technologies can help ensure that the best and most accurate outcomes of a criminal investigation are achieved. Among the most important and common forensic evidence that can be collected at a crime scene are body fluids such as blood, semen, vaginal fluid, and saliva. The rapid detection and identification of these fluids helps identify the perpetrator and victim, and aids in understanding the events, including the timeline, of a crime. An ideal body fluid detection and identification platform is confirmatory, fast, portable for on-site capabilities, easy-to-use, highly sensitive, specific, and non-destructive.

With these considerations in mind, the development of a SERS-based platform for trace body fluid analysis could provide a highly valuable capability for forensic scientists. Raman, in general, offers many advantages for this purpose such as it provides unique molecular signatures of samples with extrinsic labeling, vibrational bands are narrow allowing multiplexing detection of complex biological mixtures, sample size can be small, data acquisition can be fast and easy-to-use, and it is non-destructive leaving sufficient amounts of trace evidence for other detection platforms.

Furthermore, while current forensic techniques are typically body fluid specific [76–78], Raman has the highly attractive feature of potentially being a single instrumental platform for the detection and identification of all relevant body fluids. When these Raman attributes are combined with the signal amplification, effective fluorescence suppression, resulting faster data acquisition times, and the ability to sample homogeneous solutions of dried body fluids that SERS can provide, new capabilities can result for forensic science investigations of human body fluids.

We have shown that SERS can be effectively used to detect and identify dried stains of different human body fluids [79]. As an example, good quality SERS spectra of 24 h dried stains of human blood, vaginal fluid, semen, saliva, and urine are shown in Fig. 16.10 (upper panel). These spectra are acquired by dropping 1 μL of a 50% acetic acid (HAc) solution (pH ~ 2) on the dried stain, and then, the resulting solution is pulled back into the pipet and placed on a Au SERS substrate. SERS spectra were obtained with an RM-2000 Renishaw Raman microscope employing a 50× objective. Incident 785 nm laser powers of typically ~ 0.4 mW and ~ 10 s of illumination time were used to obtain the displayed spectra which are averages of six to ten spectra per sample. These forensic SERS results illustrate how the choice of solvent can affect the outcomes of SERS analytical applications. Initial dried body fluid studies were carried out by the same procedure but with water as the extracting and transfer solvent [79], and resulted in less robust and reproducible results for all body fluids, most notably for the detection of blood on Au substrates [80]. Note that no fluorescence backgrounds are observed in these SERS spectra unlike the background emission reported in normal Raman studies of some dried body fluids [81–83].

In addition to the elimination of interfering emission backgrounds, SERS acquisition of human body fluids offers several other advantages relative to normal Raman including enormously increased sensitivity (vide infra), shorter signal acquisition times, and more homogeneous samples. The last property is due the liquid drop extraction procedure which results in the transfer of a homogeneous 1 μL solution to the SERS substrate when sampling a dried body fluid stain shown to be inhomogeneous on the dimensions of a focused laser beam. The resulting SERS spectra of body fluids are clearly distinguishable from each other and are interpretable in terms of constituent molecular components. The main spectral components for the key body fluids of most forensic interest are: blood; hemoglobin, vaginal fluid; hypoxanthine, adenine, and protein, semen; xanthine, hypoxanthine, and saliva; thiocyanate ($SCN^-$), protein, and urine. It is interesting to note that purines are prevalent in these 785 nm SERS body fluids spectra in addition to their dominance of the bacterial and fungal SERS spectra. This speaks to the ubiquitous role purines play in the metabolic activity of all cells and their favorable interaction with Au or Ag surfaces. These results, in addition to the bacterial results discussed above, also highlight another quality of SERS probably less explicitly addressed. Body fluids are highly complex mixtures of many biological components. Yet, due to the vastly wide range of SERS molecular susceptibilities which can effectively result in just a single or a few molecular spectral contributions to the SERS spectrum, the SERS spectra of such inherently complex, multicomponent biological samples can be remarkably simply.

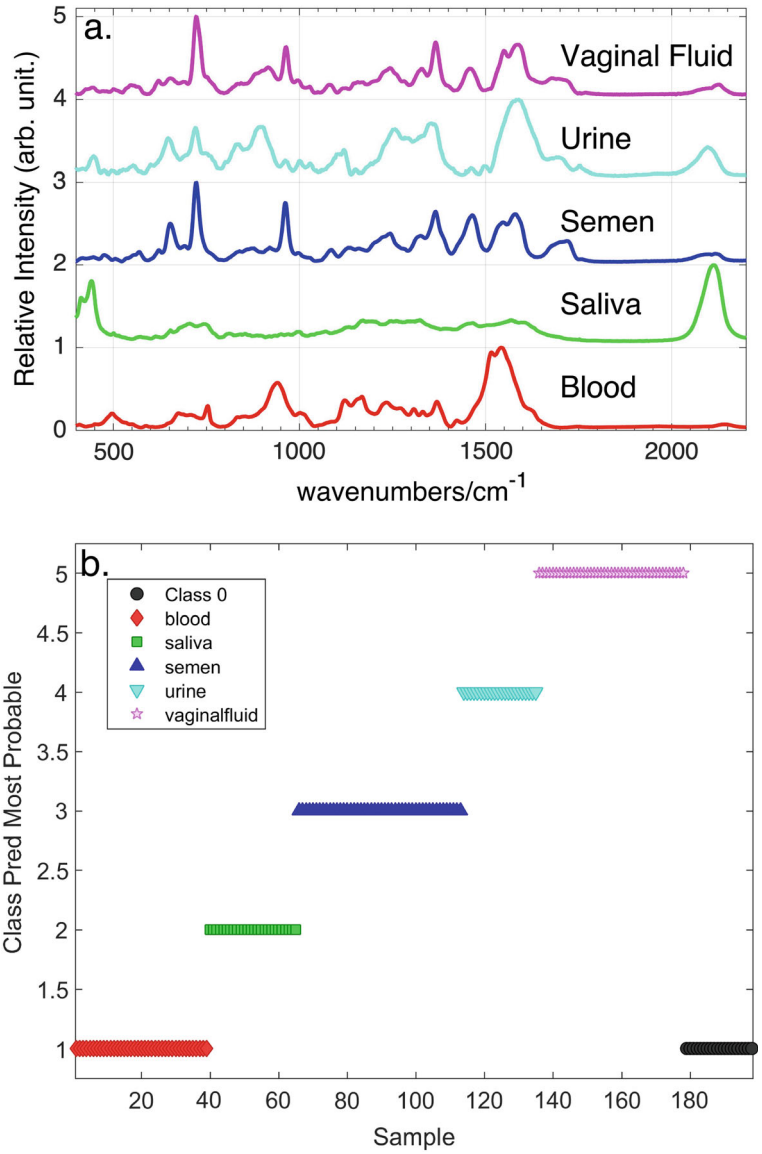



**Fig. 16.10** **a** SERS spectra of a dried bloodstain compared with dried stains due to vaginal fluid, urine, semen, and saliva on Au substrates extracted by the 1 μL 50% acetic acid procedure. SERS blood signature does not resemble the other body fluids. **b** Barcode PLS-DA body fluid classification comparison of blood (red), saliva (green), semen (blue), urine (cyan), vaginal fluid (magenta), and unknown body fluid class (gray). 100% sensitivity and 100% selectivity were achieved within this limited data set for identification of the "unknown" blood spectra. The horizontal red line represents the threshold for blood classification

These SERS spectra are very different and more distinct than their normal, non-SERS 785 nm excited Raman spectra [78, 81–86]. This last quality improves the specificity of these body fluid spectral signatures, and thus enhances their accuracy and precision for identification procedures. To more formally demonstrate the specificity of these SERS body fluid spectra, a barcode PLS-DA classification analysis was carried out and results are summarized in Fig. 16.10 (lower panel) [80]. All ~ 180 SERS spectra obtained by the HAc procedure on Au substrates of blood, semen, vaginal fluid, saliva, and urine result in 100% specificity and 100% sensitivity. When this model is challenged by 20 dried blood SERS spectra, unsurprisingly, all spectra are correctly identified (Fig. 16.10). The "unknown" spectra identified by this procedure are dried blood spectra of neat blood and blood diluted by various amounts of water. Thus, the SERS identification methodology does not misidentify blood, whether neat or diluted by water, as another body fluid.

## *16.5.1 SERS of Blood*

Given the common prevalence of blood at crime scenes, the very large role hemoglobin has played in the development of Raman spectroscopy and the inherent and dramatic fundamental surface-analyte effects that govern the SERS spectra of blood/hemoglobin, we will focus on this specific body fluid of strong forensic interest.

### 16.5.1.1 SERS Blood Sensitivity

As indicated above, the use of 50% acetic acid (HAc) resulted in enhanced robustness and reproducibility for these SERS spectra. It also resulted in greater sensitivity for blood samples. To quantify the analytical sensitivity for SERS detection of human blood, the SERS spectra of 24 h dried stains of water diluted blood are shown in Fig. 16.11. The normalized SERS spectra of diluted dried blood obtained by our 50% HAc procedure show the characteristic SERS signature of dried blood on Au substrates with excellent signal/noise in solutions diluted up to $10^5$ (v/v) in water. These fluorescence free spectra exhibit vibrational signatures that are the same as the neat dried blood spectrum. Dashed vertical lines in Fig. 16.11 highlight several of the characteristic vibrational bands that conclusively identify blood and will be discussed below but are all due to the hemoglobin component of blood [80, 87]. Due to the robustness of this spectrum, the identification of blood in these diluted samples and in body fluid mixtures can be made without the aid of additional classification analysis. It should be noted, that at dilutions $\geq 10^3$, the characteristic red color of blood vanishes. We estimate the absolute sensitivity limit achieved ($10^5$ dilution) with this current procedure is ~ 10 pL (~ 10 ng) of blood on Au substrates. This sensitivity limit compares favorably with that of the immunochromatographic detection strips, the hemoglobin HemDirect (20 pL) test, and HemaTrace (2 pL) tests and is higher than the RSID test (~ 20 nL) [88, 89]. Comparison of normal Raman and SERS intensities

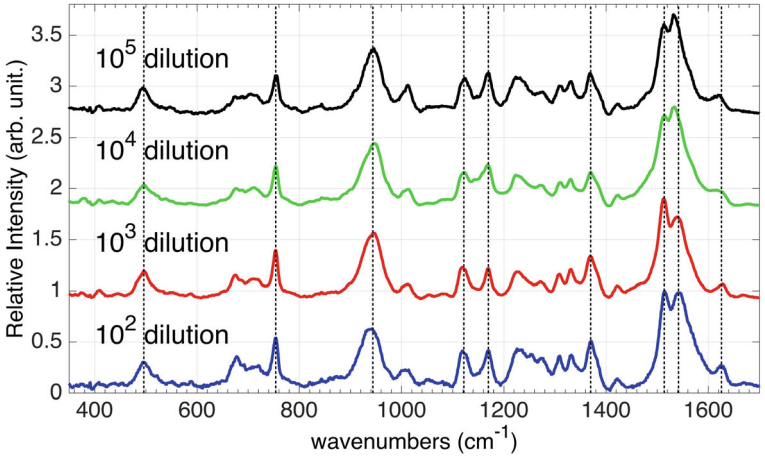



**Fig. 16.11** SERS spectra of dried bloodstains on Au substrates as a function of water dilution when extracted by the 50% HAc procedure. Each spectrum is an average of 5–10, 10 s scans at 0.3 mW of incident 785 nm power. Excellent signal/noise are observed for these spectra. Dashed vertical lines (496, 754, 944, 1122, 1170, 1370, 1514, 1543, 1626 $cm^{-1}$) show several of the robust vibrational bands that serve to identify and detect blood

results in a SERS enhancement factor estimate of $\geq 10^9$ for blood consistent with both a plasmonic ($\sim 10^7$) and chemical effect ($\geq 10^2$) contributing to the SERS intensities for dried blood at this excitation wavelength [80].

This efficiency highlights the value of SERS for trace blood detection at concentration levels where no red color may be visually evident. Additionally, another important consequence of this SERS methodology is that when a bloodstain is found on a household substrate such as cloth, carpet, word, and tiles, the SERS signal acquisition procedure is so sensitive and specific; no trace of contaminants from this background material is evident in the accompanying SERS spectrum of the dried bloodstain [80]. A swab-based SERS spectral acquisition procedure was developed to obtain spectra of these dried blood samples. A cotton swab was dipped in 50% acetic acid and lightly rubbed on the 24-h dried bloodstains. The swab was then just touched to an Au SERS chip and the characteristic dried blood spectrum signature on Au were immediately observed and acquired. This is an important attribute for the adoption of this methodology by forensic scientists. Background contamination was found to be a limitation in other spectroscopic identification techniques for forensic applications [90].

#### 16.5.1.2 Origin of SERS Signal of Blood on Au via 50% HAc

The 785 nm SERS spectrum of dried blood and a hematin (Fe(III) protoporphyrin IX OH) solution obtained by the 50% HAc procedure on Au substrates are compared

with the normal 785 nm spectrum of dried blood in Fig. 16.12. Although electronically off-resonant, the 785 nm normal Raman spectrum of blood is exclusively due to oxyhemoglobin and is dominated by vibrational modes from the Fe protoporphyrin IX (PPIX) moiety with a few bands arising from globin amino acid modes [91, 92]. As we have discussed previously, the SERS dried blood spectrum on Au bears relatively little resemblance to the normal dried blood spectrum but is nearly identical to that of hematin in terms of relative intensities and vibrational frequencies as seen in this figure [80, 93]. Such large differences between the 785 nm SERS and NR *relative* vibrational intensities indicate that there is a large chemical contribution and/or a very significant orientation dependence to the SERS enhancement mechanism giving rise to this dried blood SERS signature. Hematin (Fig. 16.13) is a high spin ferric PPIX compound, and thus, the observed dried blood SERS spectrum only exhibits bands due to the metalloporphyrin of hemoglobin and must have the same orientation and accessibility to the SERS active surface as globin-free, molecular hematin. This SERS signature is dominated by the contribution of denatured hemoglobin which allows a ferric heme moiety, that has partially escaped its native protein pocket, to get close to the nanostructured metal surface, here Au. The low pH (~ 2) and amphiphilic character of the 50% HAc solvent facilitates the hemoglobin protein denaturation, but leaves the $Fe^{+3}$ protoporphyrin heme moiety intact for physi-adsorption at the metal surface [80, 93]. We have shown that both solvation attributes, low pH and some low dielectric solvation character, are needed to maximize this 785 nm SERS signal on Au [87]. These 50% HAc solvation properties account for the robustness and sensitivity of this methodology for blood detection on Au substrates and contribute to the very significant difference between the normal Raman spectrum of dried blood and the SERS spectrum at the same excitation wavelength. Since the high specificity of this blood signature in 50% HAc on Au is due to the ferric PPIX moiety that has been freed from hemoglobin, we have found that a SERS detected human bloodstain can readily be distinguished from 35 other red-brown stains or stains of other foods that are potentially heme sources supporting its use for forensic applications [93].

#### 16.5.1.3 SERS of Animal Blood

Given the above mechanism for the success of the 50% HAc method giving rise to the SERS spectrum of blood, it is perhaps not surprising that this procedure is less than optimal for robustly distinguishing animal and human bloodstains. As described, this solvent denatures the hemoglobin and allows the resulting $Fe^{+3}$ PPIX moiety access to the Au surface. SERS spectra of dried blood from humans and different animals prepared by the 50% HAc SERS protocol are nearly identical and could not be consistently distinguished by barcode PLS-DA treatments [93]. However, when the solvent for extraction and transfer was changed to 0.1 M $NH_4Cl$ in 50% ethanol, thus allowing a larger range of molecular species to contribute to the SERS spectra of bloodstains, excellent animal blood differentiation was achieved as shown in Fig. 16.14a [93]. With this altered, high pH procedure, human blood could be distinguished from the bloods of household pets and food animals (Fig. 16.14b) and

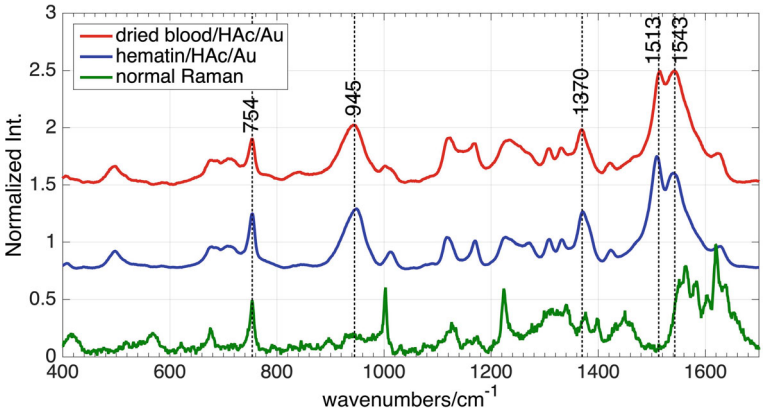
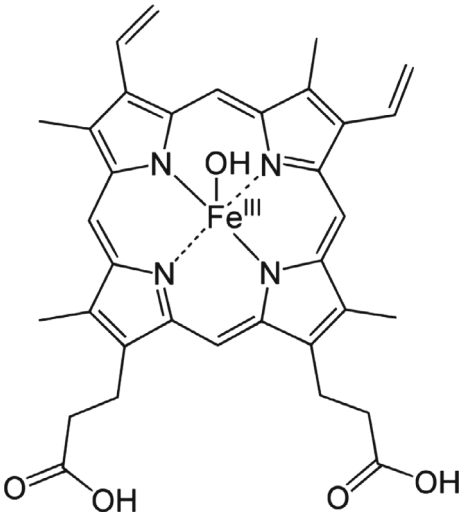



**Fig. 16.12** 785 nm excited SERS spectrum of dried blood extracted by the 1 μL 50% acetic acid procedure on Au substrates (red); the corresponding SERS spectrum of hematin in 50% acetic acid (blue); and the normal (non-SERS) 785 nm Raman spectrum of dried blood (green). Dashed vertical lines highlight the characteristic bands at 754, 945, 1370, 1513, and 1543 $cm^{-1}$ common to the dried blood and hematin SERS spectra on Au. The normal Raman and the SERS spectra share very few vibrational bands, and the relative intensity patterns are nearly completely different

**Fig. 16.13** Structure of hematin




more demandingly, from one another (Fig. 16.14c). The combination of the less acidic extraction solvent (pH ~ 5.2 vs. pH ~ 2), the mildly hydrophobic hydration offered by the alcohol component, and the organic solvating character of ammonium chloride in aqueous solution provided the solvation properties to enhance this SERS differentiation of animal bloods. This example again illustrates how solvation can be manipulated to achieve the desired analytical purpose via a SERS-based platform.

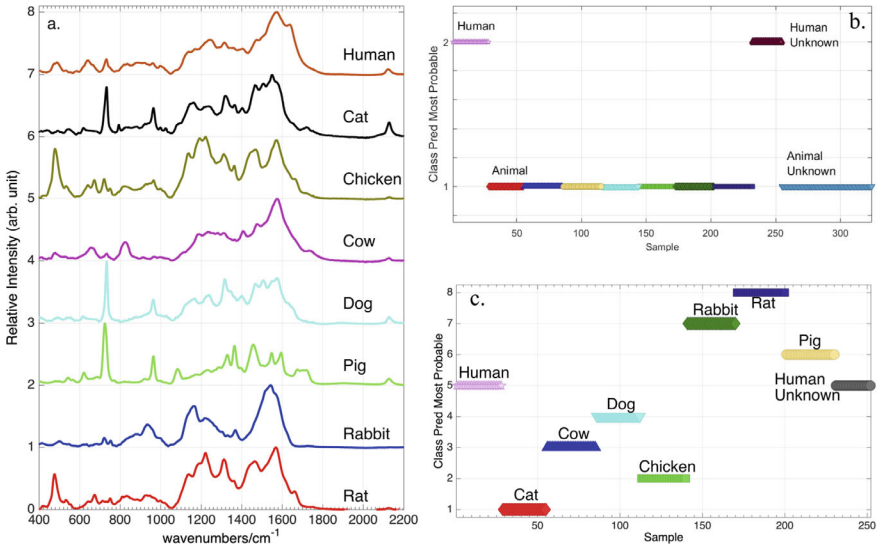



**Fig. 16.14** **a** SERS spectra (785 nm) of human and animal dried bloodstains extracted by 1 μL of 0.1 M $NH_4Cl$ in 50% ethanol acquired on Au substrates. Each displayed spectrum is an average of ten 10 s scans. **b** PLS-DA classification result for determining whether the SERS spectrum of a dried stain (20 μL) is from human or nonhuman blood. 100% specificity and sensitivity is achieved by the cross-validation results, and all human and nonhuman bloodstains are correctly identified by this procedure. **c** SERS animal blood spectra classify by species with 100% specificity and sensitivity, and correctly identify unknown bloodstain as a human bloodstain

#### 16.5.1.4 Peripheral Versus Menstrual Blood Identification via SERS

In a final example of how solvation can manipulate analytical SERS outcomes, the 785 nm SERS spectra of peripheral and menstrual bloodstains (PB/MB) on Au substrates are shown in Fig. 16.15. Distinguishing these two body fluids, which might be visually indistinguishable, can be an important piece of evidence when a violent crime is suspected. Water and 50% HAc extracted MB and PB dried stain SERS spectra on Au substrates are shown in Fig. 16.15. (Note the water extracted PB spectrum on Au only partially resembles the HAc bloodstain spectra due to the contributions of other molecular components such as proteins and uric acid.) The SERS spectra of menstrual blood via water extraction exhibits dominate spectral features due to hypoxanthine, with its strong characteristic band at ~ 724 $cm^{-1}$. This band is completely absent from the water extracted dried PB SERS spectrum [93]. In fact, this ~ 724 $cm^{-1}$ hypoxanthine band is also weakly evident in the menstrual blood spectrum extracted by the 50% solution. As given elsewhere [93], barcode PLS-DA procedures correctly distinguished PB from MB in all classification attempts when challenged by "unknown" blood spectra due to the presence of this hypoxanthine contribution. While both water and 50% HAc extracted sample were

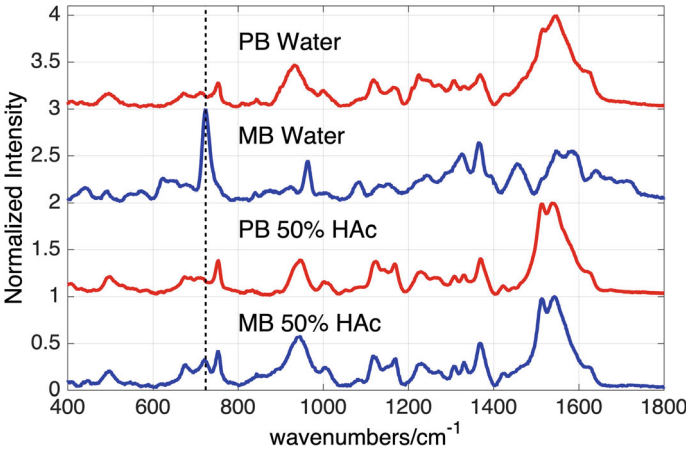



**Fig. 16.15** SERS spectra of dried peripheral bloodstains (PB) and menstrual bloodstains (MB) prepared by 50% acetic acid and water. The dashed vertical line indicates the SERS peak at 724 $cm^{-1}$ due to hypoxanthine present in the MB spectra

successfully classified via this approach, the spectra in Fig. 16.15 show the dramatic and potentially valuable role solvation can play in the exploitation of SERS for successful analytical results.

#### 16.5.1.5 SERS of Dried Bloodstains on Ag Versus Au

The choice of metal, Au or Ag, for SERS observations using visible/NIR radiation can have a significant effect on a given analytical application as already demonstrated above (Fig. 16.9). Aside from the need for the incident and scattered radiation to match the surface plasmon resonance (SPR) for a given nanostructured surface, surface-analyte interactions can play a measureable role in boosting SERS intensities beyond those due to the SPR alone as a result of newly created charge transfer electronic states for some analytes adsorbed on plasmonically active metal substrates [4, 94]. Although this well-known additional enhancement effect is generally weaker ($\sim 10^2$–$10^3$) than enhancement arising from plasmonic resonances, owing to the inherent smaller transition densities of the new surface-analyte complex, this chemical enhancement contribution can alter or control the observed relative SERS intensities. It is also well established that preferential orientation effects at the metal surface can also alter the pattern of relative SERS intensities owing to the anisotropy of the plasmonic enhancement effect at the nanostructured surface [95].

The 785 nm excited SERS spectra of dried blood extracted by the 50% HAc procedure on Au and Ag substrates are shown in Fig. 16.16 and exhibit a strong metal dependence. As evident in this figure and described previously [80, 87, 96, 97], the bloodstain spectrum on Ag exhibits a very different SERS vibrational signature than that on Au although their relative peak intensities are not very different. While

a few vibrational features are shared (e.g., 754, 1130, 1370 $cm^{-1}$), some bands in the SERS bloodstain spectrum on Au are completely missing in the Ag substrate spectrum and vice versa. For example, the most intense feature of the dried blood spectrum on Ag substrates is a 1254 $cm^{-1}$ band, and on Au, this feature is difficult to find. Similarly, one of the two most intense vibration transitions on Au at 1514 $cm^{-1}$ is completely absent in the dried blood on Ag substrate spectrum. In addition, the pattern of relative intensities in the 1450–1650 $cm^{-1}$ region is very different for dried blood on Au and Ag [96]. However, the dried blood SERS spectra on Au and Ag substrates both exhibit different relative intensities than the 785 nm normal Raman spectrum of dried blood (Fig. 16.16). This striking difference points to the importance of the chemical enhancement mechanism and/or orientational effects for the observed SERS intensity of this Fe PPIX moiety at 785 nm on these substrates. Analogous relative intensity patterns are found consistently for all protoporphyrin IX systems we have studied [98]. Ag and Au surfaces must interact very differently with the physi-adsorbed metalloporphyrin giving rise to these characteristic dried blood signatures.

This strong metal difference arises from two surface-analyte specific effects. First, the heme PPIX moiety (see Fig. 16.13) preferentially has different sites of attachment or physi-adsorption to the metal surface on Ag relative to Au surfaces. The heme moiety adsorbs predominantly through the PPIX propionic groups on Ag and through the PPIX ring $\pi$ electronic character on Au. Evidence supporting the strong

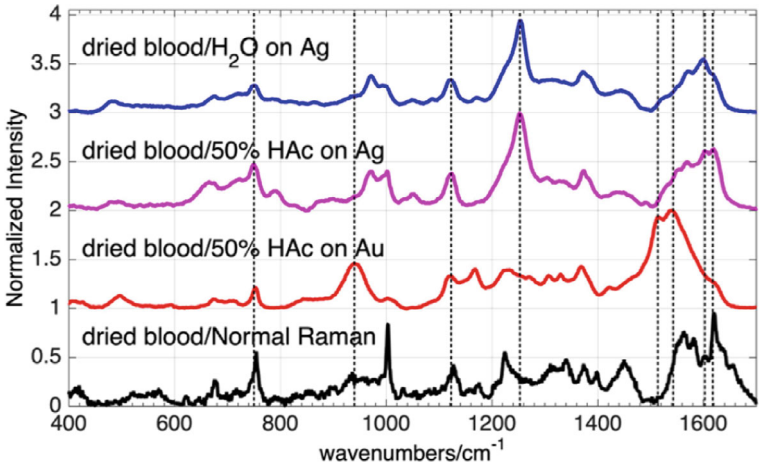



**Fig. 16.16** Normalized 785 nm excited SERS spectra of 24 h dried neat bloodstain extracted and transferred by 1 μL of 50% HAc (acetic acid) onto Au or Ag nanoparticle covered substrates compared with the SERS spectrum of dried blood extracted and transferred by 1 μL of water on Ag nanoparticle covered substrates. Dashed lines indicate strongest features on Au (1514–1543 $cm^{-1}$ doublet, 940 $cm^{-1}$) and Ag (1254, 1618, 1602 $cm^{-1}$). Some weaker characteristic vibrational features are common to both (e.g., 754/750 and 1121 $cm^{-1}$). Vibrational assignments are given in Ref. [80]. The 785 nm excited normal (non-SERS) Raman spectrum of dried blood is also shown here to contrast with the SERS on Au or Ag

preference for PPIX attachment via these organic acid groups on Ag is provided by several observations. First, computations find attachment of silver dimers to the propionic ligands of PPIX are energetically (solvation effects aside) more favorable than to the heme ring. Model porphyrin compounds lacking any propionic groups are 10–40 times weaker than say hemin, Fe(III)PPIXCl. The strongest band in the blood and all PPIX molecules in the 785 nm SERS spectrum on Ag is at ~ 1254 $cm^{-1}$ and corresponds to methyl motions in the propionic ligand and are the most strongly red-shifted modes in the SERS spectra on Ag substrates. Furthermore, SERS spectra of the simple model compound hydrocinnamic acid (phenyl ring attached to a single propionic group) also displays the strong 1254 $cm^{-1}$ band on Ag but not Au substrates. Finally, pH studies with model compounds on Au reveal that it is the deprotonated propionic groups that produce the "Ag type" spectrum.

In contrast, PPIX systems interact through the heme π structure allowing for weak Au ($\sigma$) → PPIX ($\pi$) charge transfer (CT) bands that are sufficiently close to the 785 nm excitation. As a result, Herzberg–Teller vibronic coupling due to these new CT bands is the dominant mechanism for determining the pattern of relative intensities at this nominally off-resonant excitation wavelength on Au substrates. A prior computational study supporting this conclusion in PPIX has already been given [96], and additional evidence of this so-called *B*-term effect [99, 100] in Raman vibronic theory will appear shortly [98].

Interestingly despite these two different orientations and enhancement mechanisms, the 785 nm SERS intensity of the PPIX systems is comparable on Au and Ag, although the spectra exhibit such vastly different patterns of relative intensities (Fig. 16.16). We attribute this to offsetting effects: the additional chemical enhancement effects on Au due to the newly formed Au → heme CT character contribute a factor of ~ $10^2$ in intensity. The more favorable near end on chem-adsorption due to the propionic groups that aligns the heme ring in a more perpendicular orientation with respect to the Ag plasmonic surface effectively matches this chemical enhancement effect for the more parallel orientated heme on Au.

## 16.6 SERS Detection of Dried Bloodstains on Ag Versus Au

Now that it is established the 785 nm SERS bloodstain spectrum results from the ferric PPIX moiety freed from denatured hemoglobin giving it access to the nanostructured Au or Ag surface, we compare the sensitivities of these two substrates for blood detection. It was noted above (Sect. 16.5.1.1) SERS results in the detection and identification of dried stains of blood that have been diluted by up to $10^5$ in water on Au when the 50% HAc extraction and transfer procedure was used. As described, low pH is needed to efficiently denature the hemoglobin protein. However, it was more recently found that a simple water only extraction and transfer procedure also results in reproducible 785 nm excited SERS spectra of 24 h dried bloodstains on Ag nanoparticle substrates and achieves the same $10^5$ dilution in water detection limit as shown in Fig. 16.17 [97]. The water/Ag methodology offers the advantage

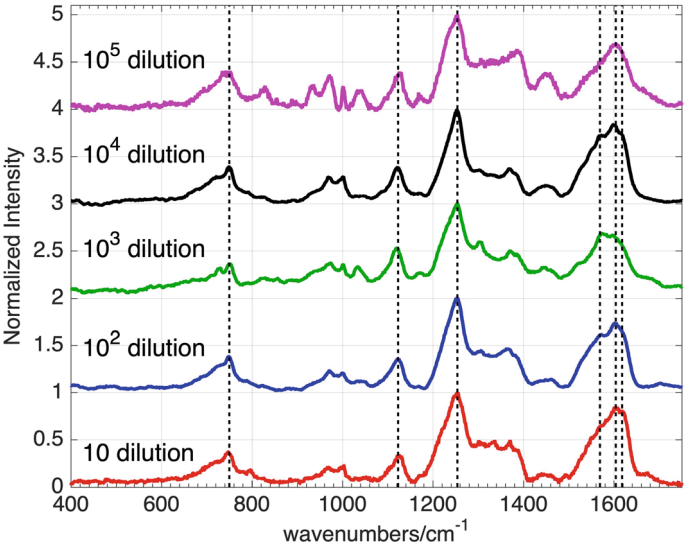



**Fig. 16.17** Normalized 785 nm SERS spectra of dried diluted blood on Ag substrates as a function of water dilution when extracted by 1 μL of water 50%. Each spectrum is an average of 5–10, 10 sec scans at 0.3 mW of incident power. Excellent signal/noise are observed for these spectra. Dashed vertical lines (750, 1122, 1252, 1569, 1602, 1618 $cm^{-1}$) show several of the vibrational bands that serve to identify blood

of avoiding any potential DNA damage when the sample size is extremely small ($\leq \sim 1$ μL) due to low pH exposure, an important attribute for forensic investigations. The water only procedure is not effective on Au SERS substrates however. This metal substrate difference results from the efficient red blood cell lysis and hemoglobin denaturation effects of the Ag nanoparticle surfaces as compare to that of Au nanoparticles. Consequently, the 50% acetic acid exposure is required for the acquisition of 785 nm SERS spectra of dried bloodstains on Au substrates.

## 16.7 Conclusion

Although some may argue that SERS has not delivered yet on its initial perceived potential for transforming analytical sensing, especially in the realm of biomedical related applications, we have endeavored to show the impact that can be anticipated on the development of ultra-rapid AST and in the field of forensic science. It is the intension of this review in particular to highlight the importance of understanding the molecular details and mechanisms of enhancement that is essential for maximizing the successful impact that this still promising discovery some fifty years ago can make for analytical applications generally. In this review, we have drawn mostly from past, recent, and ongoing work from our laboratory to illustrate these points.

Furthermore, more specifically, the examples cited here are intended to highlight maybe some less appreciated attributes of SERS. The molecular selectivity for some molecular species can be an added advantage when probing complex biological fluids, a judicious choice of metals can greatly benefit some applications due to orientational and chemical enhancement effects, and control of solvation properties can have large impact on SERS investigations of inherently multicomponent samples such as biological fluids. Thus, fifty years on SERS still appears to have a bright future.

**Acknowledgements** The support of the National Institute of Health (Grant # 1R01AI090815-01), the National Science Foundation I/UCRC Collaborative Research Award Grant # 1068070, Boston University Ignition Award and Boston University Clinical and Translational Science Institute Awards, and the Department of Justice, National Institute of Justice Grants # 2014-DN-BX-K021 and #2018-MU-MU-0013 are gratefully acknowledged.

## References

1. M. Fleischmann, P. J. Hendra and A. J. McQuillan, Raman spectra of pyridine adsorbed at a silver electrode, Chemical Physics Letters, **26**, 163–166 (1974)
2. D. L. Jeanmaire and R. P. Van Duyne, Surface Raman spectroelectrochemistry: Part I. Heterocyclic, aromatic, and aliphatic amines adsorbed on the anodized silver electrode, J. Electroanal. Chm., **84**, 1–20 (1977).
3. M. G. Albrecht and J. A. Creighton, Anomalously intense Raman spectra of pyridine at a silver electrode, Journal of the American Chemical Society, **99**, 5215–5217 (1977)
4. M. Moskovits, Surface-enhanced spectroscopy, Reviews of Modern Physics, **57**, 783–826 (1985)
5. J. Langer, D. Jimenez de Aberasturi, J. Aizpurua, R. A. Alvarez-Puebla, B. Auguié, J. J. Baumberg, G. C. Bazan, S. E. J. Bell, A. Boisen, A. G. Brolo, J. Choo, D. Cialla-May, V. Deckert, L. Fabris, K. Faulds, F. J. García de Abajo, R. Goodacre, D. Graham, A. J. Haes, C. L. Haynes, C. Huck, T. Itoh, M. Käll, J. Kneipp, N. A. Kotov, H. Kuang, E. C. Le Ru, H. K. Lee, J. F. Li, X. Y. Ling, S. A. Maier, T. Mayerhöfer, M. Moskovits, K. Murakoshi, J. M. Nam, S. Nie, Y. Ozaki, I. Pastoriza-Santos, J. Perez-Juste, J. Popp, A. Pucci, S. Reich, B. Ren, G. C. Schatz, T. Shegai, S. Schlücker, L. L. Tay, K. G. Thomas, Z. Q. Tian, R. P. Van Duyne, T. Vo-Dinh, Y. Wang, K. A. Willets, C. Xu, H. Xu, Y. Xu, Y. S. Yamamoto, B. Zhao and L. M. Liz-Marzán, Present and Future of Surface-Enhanced Raman Scattering, ACS nano, **14**, 28–117 (2020)
6. R. Pilot, R. Signorini, C. Durante, L. Orian, M. Bhamidipati and L. Fabris, A Review on Surface-Enhanced Raman Scattering, Biosensors, **9** (2019).
7. B. Sharma, R. R. Frontiera, A.-I. Henry, E. Ringe and R. P. Van Duyne, SERS: Materials, applications, and the future, Materials Today, **15**, 16–25 (2012)
8. J. P. Camden, J. A. Dieringer, J. Zhao and R. P. Van Duyne, Controlled plasmonic nanostructures for surface-enhanced spectroscopy and sensing, Acc Chem Res, **41**, 1653–1661 (2008)
9. Z. Q. Tian, Surface-enhanced Raman spectroscopy: advancements and applications, Journal of Raman Spectroscopy, **36**, 466–470 (2005)
10. A. J. Haes, C. L. Haynes, A. D. McFarland, G. C. Schatz, R. P. Van Duyne and S. Zou, Plasmonic Materials for Surface-Enhanced Sensing and Spectroscopy, MRS Bulletin, **30**, 368–375 (2005)

11. X. M. Qian and S. M. Nie, Single-molecule and single-nanoparticle SERS: from fundamental mechanisms to biomedical applications, Chemical Society Reviews, **37**, 912–920 (2008)
12. C. Deriu, S. Thakur, O. Tammaro and L. Fabris, Challenges and opportunities for SERS in the infrared: materials and methods, Nanoscale advances, **5**, 2132–2166 (2023)
13. J. Sitjar, J. D. Liao, H. Lee, H. P. Tsai, J. R. Wang and P. Y. Liu, Challenges of SERS technology as a non-nucleic acid or -antigen detection method for SARS-CoV-2 virus and its variants, Biosensors & bioelectronics, **181**, 113153 (2021)
14. C. Zong, M. Xu, L.-j. Xu, T. Wei, X. Ma, X.-S. Zheng, R. Hu and B. Ren, Surface-Enhanced Raman Spectroscopy for Bioanalysis: Reliability and Challenges, Chemical reviews, **118 10**, 4946–4980 (2018)
15. P. A. Mosier-Boss, Review on SERS of Bacteria, Biosensors, **7** (2017).
16. A. Colniță, N. E. Dina, N. Leopold, D. C. Vodnar, D. Bogdan, S. A. Porav and L. David, Characterization and Discrimination of Gram-Positive Bacteria Using Raman Spectroscopy with the Aid of Principal Component Analysis, Nanomaterials (Basel, Switzerland), **7** (2017).
17. R. Prucek, V. Ranc, L. Kvítek, A. Panáček, R. Zbořil and M. Kolář, Reproducible discrimination between Gram-positive and Gram-negative bacteria using surface enhanced Raman spectroscopy with infrared excitation, Analyst, **137**, 2866–2870 (2012)
18. R. M. Jarvis and R. Goodacre, Characterisation and identification of bacteria using SERS, Chemical Society Reviews, **37**, 931–936 (2008)
19. S. Efrima and L. Zeiri, Understanding SERS of bacteria, Journal of Raman Spectroscopy, **40**, 277–288 (2009)
20. H. Chu, Y. Huang and Y. Zhao, Silver nanorod arrays as a surface-enhanced Raman scattering substrate for foodborne pathogenic bacteria detection, Appl. Spectrosc., **62**, 922–931 (2008)
21. M. Culha, M. Kahraman, D. Cam, I. Sayin and K. Keseroglu, Rapid identification of bacteria and yeast using surface-enhanced Raman scattering, Surf. and Interface Anal., **42**, 462–465 (2010)
22. N. F. Fell Jr., A. G. B. Smith, M. Vellone and A. W. Fountain III, Optimization of substrates for surface enhanced Raman spectroscopy of bacteria, Proceed SPIE, **4577**, 174–181 (2002)
23. J. Guicheteau and S. D. Christesen, Principal component analysis of bacteria using surface-enhanced Raman spectroscopy, SPIE, **6218**, 62180G-62181–62180G-62188 (2006).
24. K. Hering, D. Cialla, K. Ackermann, T. Dörfer, R. Möller, H. Schneidewind, R. Mattheis, W. Fritzsche, P. Rösch and J. Popp, SERS: a versatile tool in chemical and biochemical diagnostics, Analytical and Bioanalytical Chemistry, **390**, 113–124 (2008)
25. M. Kahraman, M. M. Yazici, F. Sahin, O. F. Bayrak and M. Culha, Reproducible surface-enhanced Raman scattering spectra of bacteria on aggregated silver nanoparticles, Appl Spectrosc, **61**, 479–485 (2007)
26. T.-T. Liu, Y.-H. Lin, C.-H. Hung, T.-J. Liu, Y. Chen, Y.-C. Huang, T.-H. Tsai, H.-H. Wang, D.-W. Wang, J.-K. Wang, Y.-L. Wang and C.-H. Lin, A High Speed Detection Platform Based on Surface-Enhanced Raman Scattering for Monitoring Antibiotic-Induced Chemical Changes in Bacteria Cell Wall, PLoS ONE, **4**, e5470 (2009)
27. Y. Liu, Y.-R. Chen, X. Nou and K. Chao, Potential of surface-enhanced Raman spectroscopy for the rapid identification of Escherichia Coli and Listeria Monocytogenes cultures on silver colloidal nanoparticles, Appl. Spectrosc., **61**, 824–831 (2007)
28. A. Sengupta, M. Mujacic and E. J. Davis, Detection of bacteria by surface-enhanced Raman spectroscopy, Anal. Bioanal. Chem., **386**, 1379–1386 (2006)
29. K. E. Stephen, D. Homrighausen, G. DePalma, C. H. Nakatsu and J. Irudayaraj, Surface enhanced Raman spectroscopy (SERS) for the discrimination of Arthrobacter strains based on variations in cell surface composition, Analyst, **137**, 4280–4286 (2012)
30. M. Usman, J.-W. Tang, F. Li, J.-X. Lai, Q.-H. Liu, W. Liu and L. Wang, Recent advances in surface enhanced Raman spectroscopy for bacterial pathogen identifications, Journal of Advanced Research, **51**, 91–107 (2023)
31. X. Zhou, Z. Hu, D. Yang, S. Xie, Z. Jiang, R. Niessner, C. Haisch, H. Zhou and P. Sun, Bacteria Detection: From Powerful SERS to Its Advanced Compatible Techniques, Advanced Science, **7**, 2001739 (2020)

32. F. U. Ciloglu, A. Caliskan, A. M. Saridag, I. H. Kilic, M. Tokmakci, M. Kahraman and O. Aydin, Drug-resistant Staphylococcus aureus bacteria detection by combining surface-enhanced Raman spectroscopy (SERS) and deep learning techniques, Scientific Reports, **11**, 18444 (2021)
33. E. Witkowska, D. Korsak, A. Kowalska, A. Janeczek and A. Kamińska, Strain-level typing and identification of bacteria – a novel approach for SERS active plasmonic nanostructures, Analytical and Bioanalytical Chemistry, **410**, 5019–5031 (2018)
34. W. R. Premasiri, D. T. Moir, M. S. Klempner, N. Krieger, G. Jones II and L. D. Ziegler, Characterization of the Surface Enhanced Raman Scattering (SERS) of Bacteria, J. Phys. Chem. B, **109**, 312–320 (2005)
35. W. R. Premasiri, D. T. Moir, M. S. Klempner and L. D. Ziegler, Surface enhanced Raman scattering of microorganisms, in *New Approaches in Biomedical Spectroscopy*, Edited by K. Kneipp, R. Aroca, H. Kneipp and E. Wentrup-Byrne, (Oxford University Press, 2007), p. 164.
36. I. S. Patel, W. R. Premasiri, D. T. Moir and L. D. Ziegler, Barcoding bacterial cells: A SERS based methodology for pathogen identification, J Raman Spectrosc, **39**, 1660–1672 (2008)
37. W. R. Premasiri, Y. Chen, P. M. Williamson, D. C. Bandarage, C. Pyles and L. D. Ziegler, Rapid urinary tract infection diagnostics by surface-enhanced Raman spectroscopy (SERS): identification and antibiotic susceptibilities, Analytical and Bioanalytical Chemistry, **409**, 3043–3054 (2017)
38. W. R. Premasiri, J. C. Lee, A. Sauer-Budge, R. Théberge, C. E. Costello and L. D. Ziegler, The biochemical origins of the surface-enhanced Raman spectra of bacteria: a metabolomics profiling by SERS, Analytical and Bioanalytical Chemistry, **408**, 4631–4647 (2016)
39. Y. Chen, W. R. Premasiri and L. D. Ziegler, Surface enhanced Raman spectroscopy of Chlamydia trachomatis and Neisseria gonorrhoeae for diagnostics, and extra-cellular metabolomics and biochemical monitoring, Scientific Reports, **8**, 5163 (2018)
40. S. Kjelleberg (ed.), eds., *Starvation in Bacteria*, (Springer Science + Business Media, LLC, 1993).
41. J. Hochstadt-Ozer and E. R. Stadtman, The Regulation of Purine Utilization in Bacteria: II. Adenine phosphoribosyltransferase in isolated membrane preparations and its role in transport of adenine across the membrane, Journal of Biological Chemistry, **246**, 5304–5311 (1971)
42. A. Switzer, L. Burchell, J. McQuail and S. Wigneshweraraj, The Adaptive Response to Long-Term Nitrogen Starvation in Escherichia coli Requires the Breakdown of Allantoin, Journal of bacteriology, **202**, e00172-20 (2020).
43. S. Sivapragasam and A. Grove, The Link between Purine Metabolism and Production of Antibiotics in Streptomyces, Antibiotics (Basel, Switzerland), **8** (2019).
44. M. E. Ruppen and R. L. Switzer, Involvement of the stringent response in degradation of glutamine phosphoribosylpyrophosphate amidotransferase in Bacillus subtilis, Journal of bacteriology, **155**, 56-63 (1983)
45. M. P. Deutscher, Degradation of stable RNA in bacteria, The Journal of biological chemistry, **278**, 45041–45044 (2003)
46. J. Hochstadt-Ozer and E. R. Stadtman, The Regulation of Purine Utilization in Bacteria: III. The involvement of purine phosphoribosyltransferases in the uptake of adenine and other nucleic acid precursors by intact resting cells Journal of Biological Chemistry, **246**, 5312–5320 (1971)
47. R. D. Berlin and E. R. Stadtman, A Possible Role of Purine Nucleotide Pyrophosphorylases in the Regulation of Purine Uptake by Bacillus subtilis, Journal of Biological Chemistry, **241**, 2679–2686 (1966)
48. T. Smith-Palmer, C. Douglas and P. Fredericks, Rationalizing the SER spectra of bacteria, Vibrational Spectroscopy, **53**, 103–106 (2010)
49. A. K. Boardman, W. S. Wong, W. R. Premasiri, L. D. Ziegler, J. C. Lee, M. Miljkovic, C. M. Klapperich, A. Sharon and A. F. Sauer-Budge, Rapid Detection of Bacteria from Blood with Surface-Enhanced Raman Spectroscopy, Analytical Chemistry, **88**, 8026–8035 (2016)
50. D. M. Allen, G. G. Einarsson, M. M. Tunney and S. E. J. Bell, Characterization of Bacteria Using Surface-Enhanced Raman Spectroscopy (SERS): Influence of Microbiological Factors on the SERS Spectra, Analytical Chemistry, **94**, 9327–9335 (2022)

51. C.-Y. Liu, Y.-Y. Han, P.-H. Shih, W.-N. Lian, H.-H. Wang, C.-H. Lin, P.-R. Hsueh, J.-K. Wang and Y.-L. Wang, Rapid bacterial antibiotic susceptibility test based on simple surface-enhanced Raman spectroscopic biomarkers, Scientific Reports, **6**, 23375 (2016)
52. Y. Y. Han, Y. C. Lin, W. C. Cheng, Y. T. Lin, L. J. Teng, J. K. Wang and Y. L. Wang, Rapid antibiotic susceptibility testing of bacteria from patients' blood via assaying bacterial metabolic response with surface-enhanced Raman spectroscopy, Sci Rep, **10**, 12538 (2020)
53. M. A. Lobritz, P. Belenky, C. B. Porter, A. Gutierrez, J. H. Yang, E. G. Schwarz, D. J. Dwyer, A. S. Khalil and J. J. Collins, Antibiotic efficacy is linked to bacterial cellular respiration, Proceedings of the National Academy of Sciences of the United States of America, **112**, 8173–8180 (2015)
54. J. Berman and D. J. Krysan, Drug resistance and tolerance in fungi, Nature reviews. Microbiology, **18**, 319–331 (2020)
55. M. C. Arendrup and T. F. Patterson, Multidrug-Resistant Candida: Epidemiology, Molecular Mechanisms, and Treatment, The Journal of infectious diseases, **216**, S445–S451 (2017)
56. Stop neglecting fungi, Nature Microbiology, **2**, 17120 (2017)
57. J. Xia, W. Li, M. Sun and H. Wang, Application of SERS in the Detection of Fungi, Bacteria and Viruses, Nanomaterials (Basel, Switzerland), **12** (2022).
58. N. E. Dina, A. M. R. Gherman, V. Chiş, C. Sârbu, A. Wieser, D. Bauer and C. Haisch, Characterization of Clinically Relevant Fungi via SERS Fingerprinting Assisted by Novel Chemometric Models, Analytical Chemistry, **90**, 2484–2492 (2018)
59. F. Gu, S. Hu, Y. Wu, C. Wu, Y. Yang, B. Gu and H. Du, A SERS Platform for Rapid Detection of Drug Resistance of Non-Candida albicans Using Fe(3)O(4)@PEI and Triangular Silver Nanoplates, International journal of nanomedicine, **17**, 3531–3541 (2022)
60. E. Witkowska, T. Jagielski, A. Kamińska, A. Kowalska, A. Hryncewicz-Gwóźdź and J. Waluk, Detection and identification of human fungal pathogens using surface-enhanced Raman spectroscopy and principal component analysis, Analytical Methods, **8**, 8427–8434 (2016)
61. E. Witkowska, T. Jagielski and A. Kamińska, Genus- and species-level identification of dermatophyte fungi by surface-enhanced Raman spectroscopy, Spectrochimica Acta Part A: Molecular and Biomolecular Spectroscopy, **192**, 285–290 (2018)
62. I. Sayin, M. Kahraman, F. Sahin, D. Yurdakul and M. Culha, Characterization of Yeast Species Using Surface-Enhanced Raman Scattering, Appl. Spectrosc., **63**, 1276–1282 (2009)
63. M. Culha, M. Kahraman, D. Çam, I. Sayın and K. Keseroğlu, Rapid identification of bacteria and yeast using surface-enhanced Raman scattering, Surface and Interface Analysis, **42**, 462–465 (2010)
64. B. M. Nitsche, T. R. Jørgensen, M. Akeroyd, V. Meyer and A. F. Ram, The carbon starvation response of Aspergillus niger during submerged cultivation: insights from the transcriptome and secretome, BMC genomics, **13**, 380 (2012)
65. S. Amorim-Vaz, A. T. Coste, V. D. T. Tran, M. Pagni and D. Sanglard, Function Analysis of MBF1, a Factor Involved in the Response to Amino Acid Starvation and Virulence in Candida albicans, Frontiers in Fungal Biology, **2** (2021).
66. M. Ellström, F. Shah, T. Johansson, D. Ahrén, P. Persson and A. Tunlid, The carbon starvation response of the ectomycorrhizal fungus Paxillus involutus, FEMS microbiology ecology, **91** (2015).
67. V. Dumeaux, S. Massahi, V. Bettauer, A. Mottola, A. Dukovny, S. S. Khurdia, A. C. B. P. Costa, R. P. Omran, S. Simpson, J. L. Xie, M. Whiteway, J. Berman and M. T. Hallett, Candida albicans exhibits heterogeneous and adaptive cytoprotective responses to antifungal compounds, eLife, **12**, e81406 (2023).
68. M. Chisanga, H. Muhamadali, D. I. Ellis and R. Goodacre, Surface-Enhanced Raman Scattering (SERS) in Microbiology: Illumination and Enhancement of the Microbial World, Appl. Spectrosc., **72**, 987–1000 (2018)
69. S. Farquharson, A. D. Gift, P. Maksymiuk and F. E. Inscore, Rapid dipicolinic acid extraction from Bacillus spores detected by surface-enhanced Raman spectroscopy, Appl Spectrosc, **58**, 351–354 (2004)

70. J. K. Daniels, T. P. Caldwell, K. A. Christensen and G. Chumanov, Monitoring the kinetics of Bacillus subtillus endospore germination via surface enhanced Raman scattering spectroscopy, Anal Chem (2006).
71. X. Zhang, M. A. Young, O. Lyandres and R. P. Van Duyne, Rapid Detection of an Anthrax Biomarker by Surface-Enhanced Raman Spectroscopy, Journal of the American Chemical Society, **127**, 4484–4489 (2005)
72. D. D. Evanoff, Jr., J. Heckel, T. P. Caldwell, K. A. Christensen and G. Chumanov, Monitoring DPA release from a single germinating Bacillus subtilis endospore via surface-enhanced Raman scattering microscopy, Journal of the American Chemical Society, **128**, 12618–12619 (2006)
73. S. Farquharson, L. Grigely, V. Khitrov, W. Smith, J. F. Sperry and G. Fenerty, Detecting Bacillus cereus spores on a mail sorting system using Raman spectroscopy, J Raman Spectrosc, **35**, 82–86 (2004)
74. G. Jiang, W. Xu, X. Huang, Z. Dai, C. Zhou, P. Hong and C. Li, Detection of Bacillus cereus Spore Biomarkers Using SERS-Based Cuttlebone-Derived Organic Matrix/Silver Nanoparticles, ACS Sustainable Chemistry & Engineering, **11**, 4145–4154 (2023)
75. I. R. Scott and D. J. Ellar, Study of calcium dipicolinate release during bacterial spore germination by using a new, sensitive assay for dipicolinate, Journal of bacteriology, **135**, 133–137 (1978)
76. J. Gooch, A. V. Morillas and N. Frascione, Bioanalytical Advancements in the Reliable Visualization and Discrimination of Bodily Fluids, in *Emerging Technologies for the Analysis of Forensic Traces*, Edited by S. Francese, (Springer International Publishing, 2019), pp. 75–102.
77. R. Saferstein, eds., *Forensic Science Handbook*, 1st edn. (Prentice Hall, 1982).
78. K. Virkler and I. K. Lednev, Analysis of body fluids for forensic purposes: from laboratory testing to non-destructive rapid confirmatory identification at a crime scene, Forensic Sci Int, **188**, 1–17 (2009)
79. W. R. Premasiri, Y. Chen, J. Fore, A. Brodeur and L. D. Ziegler, SERS Biomedical Applications: Diagnostics, Forensics, and Metabolomics, in *Frontiers and Advances in Molecular Spectroscopy*, Edited by J. Laane, (Elsevier, 2018), pp. 327–367.
80. M. L. Shaine, W. R. Premasiri, H. M. Ingraham, R. Andino, P. Lemler, A. N. Brodeur and L. D. Ziegler, Surface enhanced Raman scattering for robust, sensitive detection and confirmatory identification of dried bloodstains, Analyst, **145**, 6097–6110 (2020)
81. V. Sikirzhytski, A. Sikirzhytskaya and I. K. Lednev, Multidimensional Raman spectroscopic signatures as a tool for forensic identification of body fluid traces: a review, Appl Spectrosc, **65**, 1223–1232 (2011)
82. K. Virkler and I. K. Lednev, Blood species identification for forensic purposes using Raman spectroscopy combined with advanced statistical analysis, Anal Chem, **81**, 7773–7777 (2009)
83. V. Sikirzhytski, K. Virkler and I. K. Lednev, in *Sensors*, 2010, vol. 10, pp. 2869–2884.
84. K. Virkler and I. K. Lednev, Raman spectroscopy offers great potential for the nondestructive confirmatory identification of body fluids, Forensic Sci Int, **181**, e1–5 (2008)
85. K. Virkler and I. K. Lednev, Raman spectroscopic signature of semen and its potential application to forensic body fluid identification, Forensic Sci Int, **193**, 56–62 (2009)
86. A. Sikirzhytskaya, V. Sikirzhytski and I. K. Lednev, Raman spectroscopic signature of vaginal fluid and its potential application in forensic body fluid identification, Forensic Sci Int, **216**, 44–48 (2012)
87. H. M. Ingraham, W. R. Premasiri and L. D. Ziegler, NIR surface enhanced Raman spectra of biological hemes: Solvation and plasmonic metal effects, Journal of Raman Spectroscopy, **52**, 2500–2515 (2021)
88. I. Horjan, L. Barbaric and G. Mrsic, Applicability of three commercially available kits for forensic identification of blood stains, Journal of Forensic and Legal Medicine, **38**, 101–105 (2016)
89. B. A. Schweers, J. Old, P. W. Boonlayangoor and K. A. Reich, Developmental validation of a novel lateral flow strip test for rapid identification of human blood (Rapid Stain Identification™-Blood), Forensic Science International: Genetics, **2**, 243–247 (2008)

90. G. McLaughlin, V. Sikirzhytski and I. K. Lednev, Circumventing substrate interference in the Raman spectroscopic identification of blood stains, Forensic Science International, **231**, 157–166 (2013)
91. W. R. Premasiri, J. C. Lee and L. D. Ziegler, Surface enhanced Raman spectroscopy study of whole human blood, blood plasma and red blood cells: New opportunities for bioanalytical sensing J. Phys. Chem. B, **116**, 9376–9386 (2012)
92. P. Lemler, W. R. Premasiri, A. DelMonaco and L. D. Ziegler, NIR Raman spectra of whole human blood: effects of laser-induced and in vitro hemoglobin denaturation, Analytical and bioanalytical chemistry, **406**, 193–200 (2014)
93. T. Reese, C. Suarez, W. R. Premasiri, M. L. Shaine, H. Ingraham, A. N. Brodeur and L. D. Ziegler, Surface enhanced Raman scattering specificity for detection and identification of dried bloodstains, Forensic Science International, **328**, 111000 (2021)
94. J. E. Moore, S. M. Morton and L. Jensen, Importance of Correctly Describing Charge-Transfer Excitations for Understanding the Chemical Effect in SERS, The Journal of Physical Chemistry Letters, **3**, 2470–2475 (2012)
95. I. D. G. Macdonald and W. E. Smith, Orientation of Cytochrome c Adsorbed on a Citrate-Reduced Silver Colloid Surface, Langmuir, **12**, 706–713 (1996)
96. J. McNeely, H. M. Ingraham, W. R. Premasiri and L. D. Ziegler, Chemical enhancement effects on protoporphyrin IX surface-enhanced Raman spectra: Metal substrate dependence and a vibronic theory analysis, Journal of Raman Spectroscopy, **52**, 323–338 (2021)
97. C. Suarez, W. R. Premasiri, H. Ingraham, A. N. Brodeur and L. D. Ziegler, Ultra-sensitive, rapid detection of dried bloodstains by surface enhanced Raman scattering on Ag substrates, Talanta, **259**, 124535 (2023)
98. H. Ingraham, J. McNeely and L. D. Ziegler, Herzberg-Teller vibronic couplingeffects on the SERS spectra of metallo-porphyrins (in preparation).
99. J. R. Lombardi, R. L. Birke, T. Lu and J. Xu, Charge-transfer theory of surface enhanced Raman spectroscopy: Herzberg–Teller contributions, The Journal of Chemical Physics, **84**, 4174–4180 (1986)
100. J. R. Lombardi and R. L. Birke, A Unified Approach to Surface-Enhanced Raman Spectroscopy, The Journal of Physical Chemistry C, **112**, 5605–5617 (2008)

# Chapter 17
# Surface-Enhanced Raman Spectroscopy in Clinical Point-of-Care Testing




**Tony Dib, Aradhana Dwivedi, Chen Liu, Edoardo Farnesi, Jürgen Popp, and Dana Cialla-May**

**Abstract** This chapter presents a comprehensive review of the progress and innovations over the last ten years in microdevices that are based on surface-enhanced Raman spectroscopy (SERS) for point-of-care testing. It highlights both the advantages and shortcomings of microfluidic devices, lateral flow immunoassay (LFIA) strips, and three-dimensional nanostructured plasmonic substrates as key platforms for SERS in clinical diagnostics. While the integration of microfluidics with SERS provides high-throughput homogeneous analyte detection, LFIA enhance sensitivity and quantification. Not to mention the essential role that reliable and consistent SERS nanotags and substrates play in this regard. We conclude by discussing the challenges and future directions for the clinical adoption of SERS-based technologies, including but not limited to the necessity of collaboration and establishing unified protocols.

**Keywords** Surface-enhanced Raman spectroscopy (SERS) · ppoint-of-care testing · Plasmonic substrates · Lateral flow immunoassay (LFIA) · Microfluidics, clinical diagnostics · SERS nanosensors

## 17.1 Introduction

Point-of-care testing (POCT) diagnostics can be defined by their ability to be performed at a single centre, in a time-bound manner, preferably within a single day, and then guide the physician to prescribe a treatment. They are designed for use at or near the location where a patient receives care, rather than in centralized laboratory facilities. These tests are typically rapid, user-friendly, and provide quick results, enabling prompt treatment decisions [1]. Normal physiological functions of

T. Dib · A. Dwivedi · C. Liu · E. Farnesi · J. Popp · D. Cialla-May (✉)
Department Spectroscopy and Imaging, Leibniz Institute of Photonic Technology, Member of Leibniz Health Technologies, Member of the Leibniz Centre for Photonics in Infection Research (LPI), Jena, Germany
e-mail: dana.cialla-may@leibniz-ipht.de

Institute of Physical Chemistry and Abbe Center of Photonics, Friedrich Schiller University Jena, Member of the Leibniz Centre for Photonics in Infection Research (LPI), Jena, Germany

© The Author(s), under exclusive license to Springer Nature Singapore Pte Ltd. 2024

M. Procházka et al. (eds.), *Surface- and Tip-Enhanced Raman Scattering Spectroscopy*,
https://doi.org/10.1007/978-981-97-5818-0_17

the human body involve the identification and detection of molecules and immunity. The World Health Organization (WHO) lays the criteria for POCT test in a level 1, i.e. low-resource settings as a test which is available to the intended population at a bearable cost (affordable), devoid of false negative (sensitive) and positives (specific), not having expertise as a perquisite (user-friendly), being able to withstand harsh environments (robust), be equipment free and deliverable, hence the acronym ASSURED [2], which was extended later to REASSURED to include real-time monitoring and environmental friendliness [3]. Usually, a POCT test employ a molecular recognition element (e.g. antibody or aptamer) to detect specific biomarkers (carbohydrate, protein, lipid, or a nucleic acid sequence) and a transducer (e.g. gold nanoparticles) that convert molecular recognition events into a detectable signal that may require reading by specific equipment [4]. The signal generated signal can be largely divided into optical (Fluorescence, surface plasmon resonance—SPR, surface-enhanced Raman spectroscopy—SERS, etc.), magnetic, and electrochemical which can then be translated into various sensing platforms like lateral flow strips and microfluidic chips [5, 6]. Nevertheless, it is difficult for all POCT devices to obtain all these criteria. For example, the classification of POCT devices based on setting (hospital or field) or budget (low or moderate) can show that some of the ASSURED criteria are not important in several specific cases [7]. In order to develop POCT devices, the question about what kinds of platforms or materials should be used is very important. Many commercially available POCT test kits, such as those for blood sugar, pregnancy, and COVID, do not require formal training for home usage [7–10].

Microbiological culture is a labour intensive and time-consuming process, and rapid tests like real-time PCR, ELISA, and electro-chemiluminescence techniques are impaired by their technical limitations, required expertise, and cost. Basically, the problem can be summarized in poor infrastructure (instruments and expertise) at level 1 facilities, and high cost and lengthy turn-around time [8]. In fluorescence-based bioassays, conventional organic dyes or inorganic quantum dots have been widely used as fluorescence labelling agents. However, fluorescence spectroscopy is limited by the broad emission bands which have large spectral overlap making the labels difficult to deconvolute [9–11]. Recently, several research groups have concluded that SERS-based detection methods have shown promise in overcoming the low sensitivity and multiplex detection challenges inherent to fluorescence [12–14]. Raman scattering peaks are much narrower than fluorescence or luminescence emission bands and SERS nanotags do not suffer from photobleaching unlike conventional fluorescence dyes [15–17]. Therefore, we will summarize the current status, challenges, and applications associated with SERS-based microdevices for clinical point-of-care testing. The integration of portable Raman spectroscopy with microdevices—namely microfluidic channels, lateral flow assay strips, and three-dimensional nanostructured substrates—provides an ideal platform for POCT using minimal sample volumes and at low analyte concentrations [16]. A significant number of studies on SERS assays have been performed recently to realize POCT diagnostics, especially under resource-limited conditions, where the portable SERS sensor is expected to be a next-generation POCT assay system [18, 19].

Incorporating SERS into POCT can address sensitivity limitations in these tests due to its high field enhancement and sensitivity [20, 21]. SERS-based POCT has been successfully employed in a variety of clinical scenarios [22–25]. Major challenges for SERS-based POCT include the feasibility of handheld or portable Raman system for on-site applications and integration with POCT platforms for rapid detection. Another issue that arises from the SERS substrate point of view is the stability and specificity of the substrate with the specific analyte under various measurement conditions [26, 27].

The continuous development of new SERS substrates with ultra-high sensitivity, selective capturing targets such as aptamers and antibodies, and integration with various technical elements and automation control has led to the potential application of SERS POCT that is comparable to large-scale testing equipment [28]. The advent of portable and handheld Raman instruments allows tests involving Raman processes to be conducted anytime, anywhere, with quick results. This has proven advantageous for on-site testing requirements, including integration with POCT devices, such as COVID-based breathalyser test kits and matchbox-sized Raman instruments that are already available in the market [29, 30]. Thus, SERS-based POCT holds promise for rapid and accurate disease detection in diverse settings and continues to evolve as a valuable tool in modern healthcare [21]. Within this book chapter, we will summarize the recent advances in the design of POCT platforms employing SERS as detection scheme as well as their application to various diseases in a clinical environment.

## 17.2 Advances in SERS-Based POCT Platform Designs

It is important to consider requirements such as the necessary sensitivity and speed of disease screening when designing SERS-based POCT platforms. Understanding the challenges and specific testing requirements can assist researchers in designing a POCT platform that is suitable for the budget and needs. Typically, SERS-based sensing platforms require a plasmonic-based SERS substrate, ranging from traditional silver and gold colloids to different shapes such as rods and stars, as well as solid substrates. Additionally, a functional probe molecule is needed to selectively capture the analyte of interest. Although SERS has high sensitivity and specificity, it suffers from low throughput and reproducibility. To standardize SERS-based POCT platforms, various efforts have been made, including integrating microfluidic-based devices, immunoassay strip-based designs, paper-based substrates, and wearable sensors. Each of these platforms has unique application qualities and can potentially be reliable for on-site detection. The following section briefly discusses some of these integrated SERS platforms.

### 17.2.1 Colloidal Nanoparticles

Noble metal nanoparticles, specifically those made of gold, silver, and copper, are commonly used in disease diagnostics due to their excellent plasmonic activities in the visible and NIR regions [31–34]. When the size of the nanoparticle is much smaller than the wavelength of the incident light, it gives rise to the oscillation of local charge in the nanoparticle. This, if in resonance with the incident electric field, generates surface plasmon resonance (SPR). The confinement of light at nanoscales significantly enhances scattering and absorption [35]. Metal nanoparticles are highly customizable in terms of shape, size, and aggregation to suit specific needs. These nanoparticles can be synthesized using various chemical routes, providing the freedom to adjust their geometry and functionalizability for different assays. The most used geometries for SERS substrates are nanospheres, nanocubes, nanostars, and nanorods due to their unique properties [36, 37]. These nanostructures primarily exhibit the localized surface plasmon resonance (LSPR) property for SERS enhancement. The major advantage of these substrates is the simplicity of the synthesis process and the low cost of materials required. The fabrication of nanostructures with high reproducibility, low cost, and stability is a major area of concern in SERS-based POCT platforms.

### 17.2.2 Solid SERS-Active Substrates

These systems consist of nanostructures grown on the substrate support material, which can be tuned by type of material, periodicity, area density, etc. These substrates are designed using galvanic replacement, lithography, etc. They are suitable for large-scale production and portability and are usable with smaller Raman systems [38, 39]. Silver and gold nanoparticles embedded into multilayer graphene have been designed with high detection limits and long-term stability, providing important insight into using 2D materials as SERS substrates [40–42]. A directed self-assembly mechanism transfers metal colloids on the solid surface to achieve dense and regular hot spots. Solid SERS substrates are also fabricated by depositing the metals over periodic templates such as silica. A melamine formaldehyde-silver-based periodic substrate was synthesized for sensitive detection of biomolecules such as haemoglobin, lysozyme, and dopamine [43]. In terms of practical usage, solid SERS substrates have better potential for commercialization or POCT platforms owing to their stability and reproducibility.

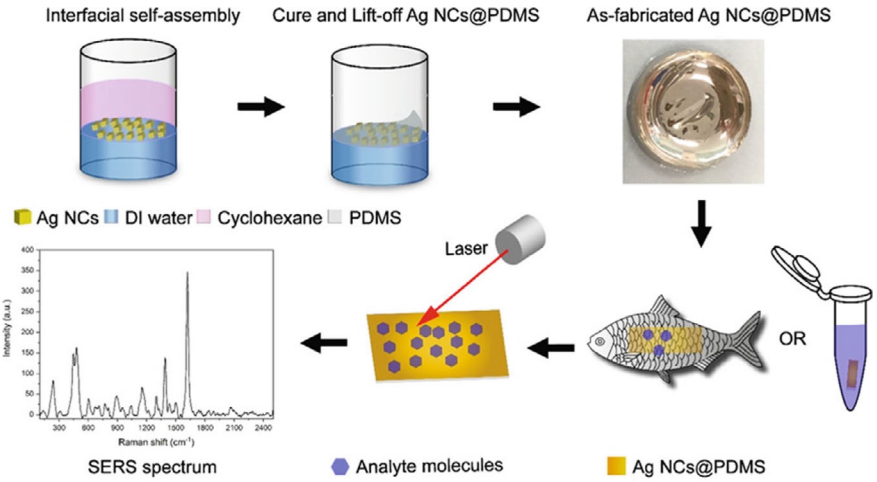



**Fig. 17.1** Fabrication and detection process of a Ag NCs@PDMS flexible SERS substrate [49]

### *17.2.3 Flexible SERS Substrates*

Flexible substrates can be attached directly to the surface of interest and provide non-invasive SERS detection compared to the solid and colloidal SERS substrates. These substrates can be used on non-planar and irregular surfaces and are reusable. These substrates typically involve a polymer such as polydimethylsiloxane (PDMS) and poly (vinylidene fluoride) (PVDF) and the addition of plasmonic nanoparticles over the polymers employing chemical reduction, physical deposition, or direct embedding [44–46]. A flexible substrate with gold nanostars embedded on PDMS enables conformal coverage on arbitrary surfaces, and their optical transparency allows the spatial detection of analytes [47]. A substrate based on plasma gold membrane combined with the flexible PDMS films is constructed for the early detection and in situ elimination of bacteria [48]. A silver nanocube@PDMS substrate is fabricated by the assembly of Ag NCs at the cyclohexane-water interface, followed by cyclohexane replacement by PDMS to make a flexible substrate as shown in Fig. 17.1 without the aid of rigid substrates (e.g. Si wafers or glass slides) [49]. The flexibility of SERS substrates is desirable, especially in POCT, owing to its non-invasiveness and reusability.

### *17.2.4 Paper-Based Devices*

POCT platforms require low cost yet high-quality SERS substrates. Due to biodegradability, porous structure and flexibility, paper is an excellent platform to

design SERS substrate for point of need applications. It is very similar to the polymer-based flexible substrates except being optically transparent [50]. With the commercial success of pH papers, paper-based materials became a great alternative due to cheap fabrication and large-scale commercialization for POCT platforms. These can be fabricated by *in situ* reduction of metal salts onto the paper or by immobilizing by techniques such as printing, dipping or vapour deposition [51]. Silver nanoparticles mixed with cellulose were spray-painted onto the filter paper to design the substrate. It could filter out macro particles such as interfering proteins from reaching to the hot spots making it desirable for on-site detection without sample pre-processing [52]. A plasmonic SERS Schirmer strip was fabricated by evaporating gold to form gold nano-islands on cellulose micro/nanofibre matrices for the direct detection of analytes in teardrops. The SEM image of the paper and SERS substrate after gold deposition are illustrated in Fig. 17.2, and the stripe can collect tears directly [53]. The paper-based SERS substrates are also fabricated by inkjet printing or pen writing techniques using gold and silver nanoparticles as ink. Large-scale sensing arrays are formed on cellulose paper by precisely writing with silver nanoparticles filled in the reservoir of a fountain pen [54]. The printing of plasmonic paper substrates could be done with a conventional inkjet printer to modify the plasmonic ink This method allows substrate patterning, which enables functions such as separation and preconcentration steps on the same sensor chip [55]. The degradation products of paper are carbohydrates, and the incineration products are carbon, both are environmentally safe.

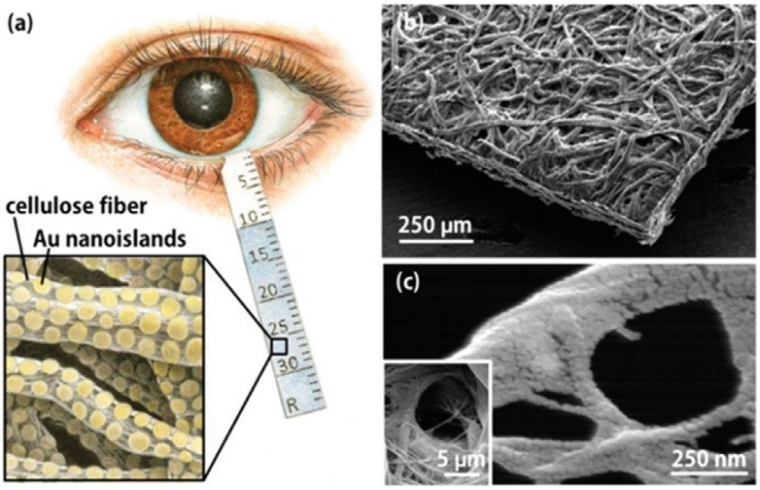



**Fig. 17.2** **a** Schematic diagram of a plasmonic Schirmer strip with the ability to collect tears directly and efficiently. **b**, **c** SEM images of plasmonic Schirmer strip [53]

### *17.2.5 Lateral Flow Assay Strips*

An inexpensive and simple platform that can provide POCT is the lateral flow immunoassay (LFIA) whereby a target forms a complex with a label and is trapped in the test zone. Spatially resolved multiplexed detection involves the placement of multiple test lines, or zones, on a single LFIA device. This allows the detection of multiple biomolecules simultaneously on one test strip. In some instances, the label for each biomolecule can be the same, in which case the spatial location differentiates the biomarker. This method has also been investigated using multiple labels that give a specific response depending on the analyte they are designed to detect [56–58]. Integration with SERS can significantly improve the sensitivity of LFIA tests, making it suitable for multiplex detection. To achieve this, the conjugate pad is modified with plasmonic nanoparticle labels [58]. Both isotropic and anisotropic nanostructures have been studied to modify the LFIA test strip for various POCT applications. Anisotropic nanoparticles are useful for detecting analytes in less complex solutions due to their distinct SERS signal, while isotropic nanoparticles offer good stability and reproducible detection performance for complex samples. In high-throughput clinical POCT testing, the multiplexity of SERS-based test strips has become increasingly important [1, 56, 59]. LFIA strips are most predominantly used for the POCT devices due to their durability, ease of fabrication, and user-friendliness.

Signal-resolved detection occurs when multiple labels are immobilized at a single test zone and can be identified through their specific signals. The key factor is that all signals are collected from the same region simultaneously, offering rapid analysis and short turn-around time without needing to deviate from the traditional device architecture [18, 56–58]. However, they suffer from low sensitivity since conventional LFIAs can only realize qualitative detection based on colorimetric signals, and therefore they lack multiplexing capabilities or are poor at providing POCT quantitative analysis and may requires further testing to eliminate false-negative results [60, 61]. An attractive method to overcome this is to use nanoparticles coated in Raman reporters as the labelled nanotags and to analyse test zone using SERS. Due to the wide variety of metal nanoparticles, Raman reporters and laser excitations that are available, SERS-based LFIA have been adapted to identify and quantify multiple targets at once. By transferring the analysis to portable Raman instruments, rapid and quantitative measurements can be taken on-site without any loss in sensitivity [62]. Portable or handheld SERS-LFIA platforms can therefore be used anywhere, from modern clinics to remote and resource-poor settings [18, 56–58]. The alternative to LFIA is vertical flow immunoassay (VFI), which offers faster analysis time and the absence of a false-negative inducing hook effect [63].

### *17.2.6 Microfluidic Devices*

Another effective solution is to incorporate SERS into a microfluidic platform to form "all-in-one" optofluidic devices, also called lab-on-chip (LOC), which can pretreat samples, transport liquid, and detect analytes in a single microchip. To enable POCT, optofluidic devices are desired to be miniaturized, portable, automated, non- or minimally invasive, can be readout by a handheld or a portable reader, and operated by a layperson with minimum to no training [6, 16, 62]. Microfluidic technology enables the integration of sample preparation, reaction and separation on a single micron-scale chip that can perform the entire biochemical analysis automatically. It greatly reduces analysis time and miniaturizes instrumentation. Introducing SERS substrates into the microchannels is of key importance to fabricate microfluidic SERS sensors. Substantial progress has been made in applying microfluidic technology in POCT [64]. Direct *in situ* synthesis of plasmonic substrates inside the microfluidic system can provide better clinical performance without any external force. The substrate is automatically formed in the channel by the guided chemical reactions between nanoparticles. A laser scribing method was utilized to integrate silver nanoparticles and graphene oxide into the chip where SERS-active patterns were directly scribed onto the microchannels to form the *in situ* substrate [65]. Microfluidic technology doesn't only shorten the analysis time and miniaturize the testing equipment, but also realizes large-scale and high-throughput biological detection due to the form of multi-channel fluid analysis. The scale of the microchannels has good biocompatibility with bacteria and other microorganisms, which provides an ideal platform for real-time sorting, cultivation and detection, and offers automated microfluidic SERS sensors for clinical application that benefit from portable smart detection [31, 66]. On-chip SERS detection with controlled flow yields more reproducible results, and problems like variable mixing times, variable scattering geometries, localized heating, and photo-dissociation could be effectively resolved. This provides more consistent geometries and heat dissipation properties for the detection of photosensitive or heat-sensitive analytes [16, 67, 68].

### *17.2.7 Wearable Sensors*

SERS is highly interesting for wearable sensors in POCT platform designs due to its sensitive and non-invasive medical diagnosis capabilities. The basic requirement for wearable SERS sensors is that it must fit perfectly at the biological interfaces such as epidermis, eyes, and teeth to assess human health conditions [69, 70]. Flexible and paper-based SERS substrates are most desirable in this type of sensor platforms [71–74]. A dual-functional smart contact lens sensor that combines peptide-modified gold nanobowls (AuNBs) with SERS substrates is shown as an example in Fig. 17.3.

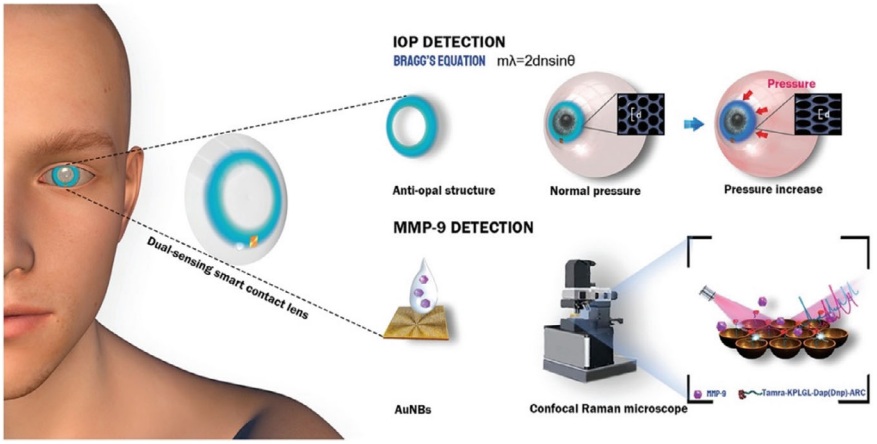



**Fig. 17.3** Dual-functional contact lens sensor composed of the antiopal structure for IOP monitoring and the peptide-functionalized AuNBs SERS substrate for MMP-9 detection [75]

This sensor allows for continuous monitoring of intraocular pressure for glaucoma diagnosis while avoiding potential damage to the eye from electronic components [75]. The wearable SERS sensors can bridge the gap between delayed diagnosis by fast and real-time tracking of relevant marker molecules inside the body.

Biosensors that employ SERS for POCT hold significant potential for further advancement. In the following, we will explore the utilization of SERS in POCT in several branches of medicine.

## 17.3 Clinical Applications

### *17.3.1 Infectology*

The simplest way to transfer SERS-LFIA analysis to POCT with no loss in sensitivity is to use a portable Raman spectrometer. In this setup, the laser can be focused onto the test zone using microscope with a 5 × or 20 × objective lens or using a fibre optic probe, and then, a number of scans can be taken to produce an average SERS response. The inclusion of a Raman microscope or fibre optic stand has a few disadvantages. These include reducing the portability as it may need to be set up in a central area near a POCT setting, for example in a lab at the hospital and the strips taken to the instrument, therefore increasing the time until results, whereas a handheld instrument allows the analysis to take place next to the patient. The microscope also increases the cost of the platform and makes it less user-friendly as training would be needed, whilst the open beam could also present a safety issue. The microscope can be removed

from the platform and the point and shoot feature of many portable Raman spectrometers can be exploited by holding the laser aperture directly above the test line of the LFIA strip and then taking a reading. Taking into account the focal distance of the laser, an inexpensive 3D printed adapter, which holds the strip in front of the laser at the correct focal distance, can be used to give reproducible results [56]. The adapter was first developed for the integration of SERS with paper-based microfluidics and colorimetric detection of miR-29a, a microRNA associated with myocardial infarction [76]. A photograph of the adapter and how it fits over the point and shoot lens of a handheld Raman spectrometer is shown in Fig. 17.4a. This platform has since been used in SERS-based LFIA by Hassanain et al. [77] who demonstrated the selective, sensitive, rapid, and cost-effective diagnosis of *clostridium difficile* infection, which is one of the most contagious diseases associated with high morbidity and mortality rates in hospitalized patients. Accurate diagnosis can slow its spread by determining the most effective treatment. They managed to carry out spatially resolved multiplex detection of two specific biomarkers on separate test lines, surface layer protein A (SlpA) and toxin B (ToxB), within 20 min. A schematic of the LFIA and point and shoot platform is shown in Fig. 17.4b. The use of a handheld Raman spectrometer to scan test lines allowed for the sensitive quantitative detection of both biomarkers with a lowest observable concentration of 0.01 pg $\mu L^{-1}$, and thus achieving cheap clinical evaluation of CDI at the point-of-care with minimal sample backlog.

Hwang et al. [13] introduced a SERS-based LFIA platform to detect staphylococcal enterotoxin (SEB) on an LFIA strip. Here, Raman reporter-labelled hollow gold nanospheres were used as detection labels instead of the AuNP labels in conventional naked-eye-based LFIA strips. This SERS-based LFIA platform enabled the rapid identification of SEB antigens through a colour change. A quantitative evaluation was possible by measuring the Raman signal of the test line as shown in Fig. 17.5. A limit of detection as low as 0.001 ng/mL of SEB was reported, making this approach approximately three orders of magnitude more sensitive than the ELISA-based assay method for SEB.

Sanchez-Purra et al. [78] developed a SERS-based duplex assay platform that could distinguish between Zika and dengue non-structural protein 1 (NS1) biomarkers. Zika and dengue viruses are mosquito-borne infectious diseases, both of which cause similar initial symptoms but possess different potential complications. Therefore, it has been of interest to develop a POCT assay capable of differentiating between the two viral diseases. It is known that NS1 is present at high levels (> 15 μg/mL) two days post infection for acute dengue, but the NS1 level of Zika virus is significantly lower. Thus, an increase in detection sensitivity is crucial for detecting Zika and would also be helpful in the early detection of both pathogens. In this study, the authors used SERS-encoded Au nanostars as nanotags that could distinguish between the different concentrations of NS1 for Zika and dengue viruses. They reported that the LODs were improved by 15-fold for Zika and 7.2-fold for dengue compared to LFIA strips.

Wang et al. [79] developed an automatic SERS-based digital microfluidic (DMF) device for quantitative detection of avian influenza virus H5N1 in human serum.

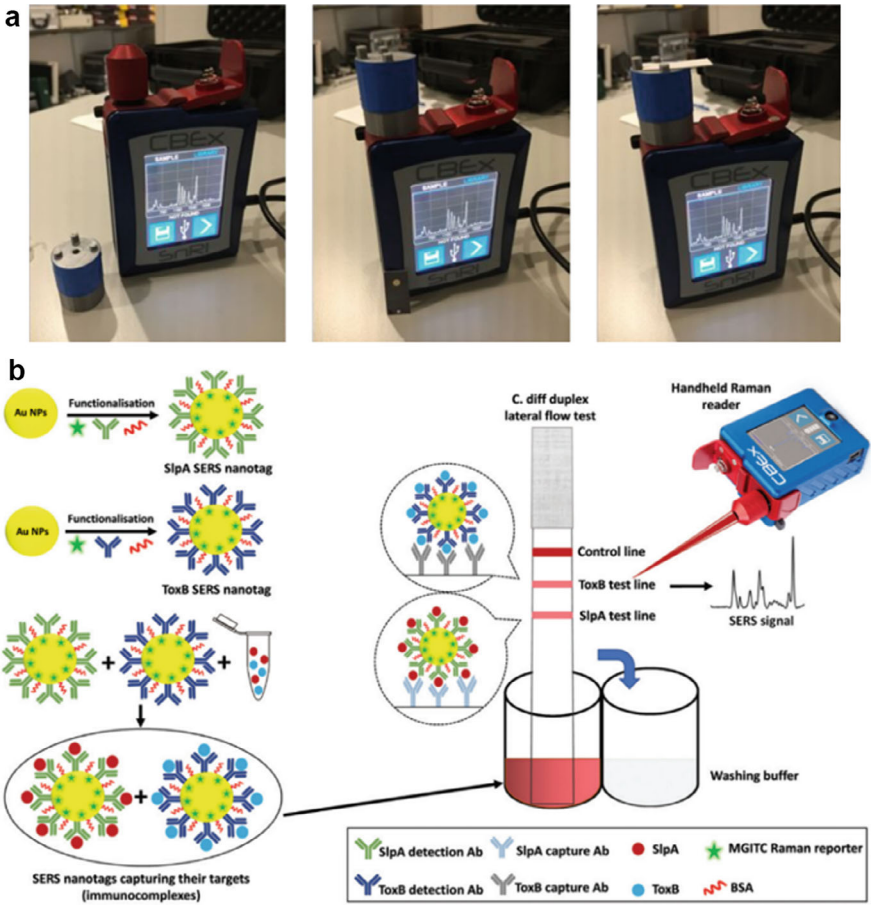



**Fig. 17.4** **a** The Raman aperture adaptor used for the analysis of the capture layer contained within the 3-D paper device. The adaptor was appropriately scaled to ensure that readouts were made at the optimal distance and centre of the spot. The images display how the adaptor fits over the point and shoot lens and how the capture layer is mounted to enable SERS analysis [76]. **b** Schematic representation for the duplex detection of SlpA and ToxB by SERS-based LFIA [77]

DMF can manipulate fluids as discrete droplets in a substrate. Droplets can be individually driven to transport, merge and dispense from original reservoirs by simply applying electric fields to an array of electrodes on the substrate. Capture antibody-immobilized magnetic beads (CA-M-Beads) and 4-mercaptobenzoic acid-labelled Ag core–shell nanoparticles were used as solid supports and detection probes, respectively. The automation capability of DMF can greatly simplify the assay procedure, cut down assay time, and reduce the risk of exposure to hazardous samples. First, reagents are introduced into reservoirs of the chip, then unit droplets of sample and detection antibody are dispensed from reservoirs to incubate with CA-M-Beads successively to form an immuno-complex. Efficient incubation and washing steps

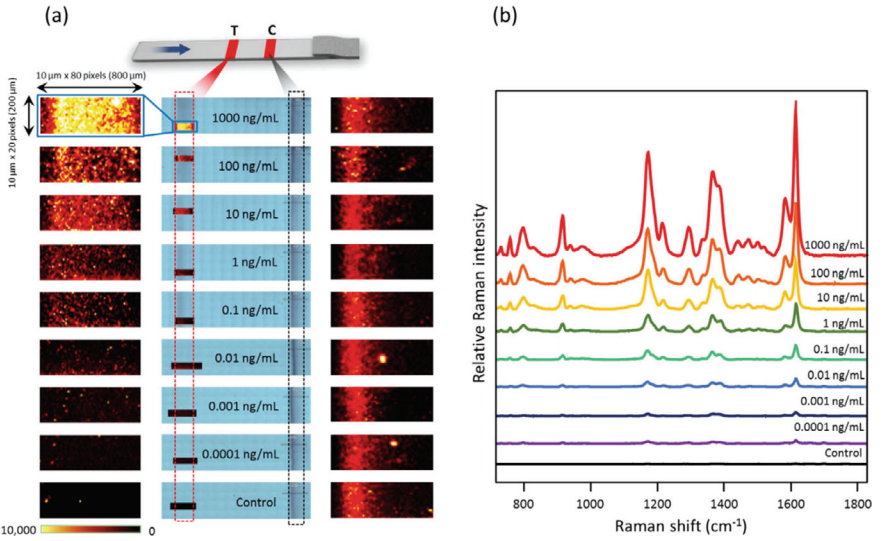



**Fig. 17.5** **a** SERS mapping images acquired using a peak intensity at 1650 $cm^{-1}$ for nine different SEB concentrations over a range of 0.1 pg $mL^{-1}$–1000 ng $mL^{-1}$; 80 × 20 pixels (1 pixel = 10 µm × 10 µm) were imaged for each concentration. The scale bar at the bottom displays the colour decoding scheme for different SERS intensities. **b** Average SERS spectra for the 1600-pixel points of the SERS mapping zones [13]

are realized automatically through DMF actuation. Afterward, sequential incubation with streptavidin and biotinylated SERS tags can functionalize the complex beads with SERS tags. After adequate washing, the SERS signal is read with a portable iRaman Plus. Quantitative analysis can be realized by measuring the Raman intensity of 4-MBA at the 1071 $cm^{-1}$ peak. The intensity is correlated with the amount of SERS tags, which is determined by the target concentration. They reported successful quantitative detection of influenza virus H5N1 in human serum within 1 h. The DMF also decreases the volume of sample and reagents down to 30 µL. Low reagent consumption decreases assay cost. Because of the excellent spatial resolution of SERS and parallel liquid processing capability of DMF, the DMF-SERS method can be easily extended to multiplex analysis.

Kamińska et al. [80] also used a SERS-based microfluidic device platform for the detection of Hepatitis B virus antigen (HBsAg) in human serum. The SERS-based sensor uses a GaN substrate covered with Au–Ag and a Raman label consisting of Au nanoflowers. This created a sandwich assay with HBV antigen (HBsAg) as the biomarker being detected. It is reported that this leads to larger enhancement factors as well as high stability and LODs comparable to clinically relevant concentrations of HBsAg. The acquisition of the SERS spectra was quick (10 min) but other sample preparations need to be taken into consideration, such as the extraction of blood plasma that requires 15 min.

In the microfluidic devices described above, various concentrations of the target reagent should be prepared prior to performing quantitative analysis. Therefore, manual dilution with repetitive pipetting is essential; however, this is a time-consuming process and may occasionally lead to experimental errors. To resolve this, Jeon et al. [81] developed a programmable and fully automatic SERS-based microfluidic gradient device that can automatically generate various concentrations of a target solution, as shown in Fig. 17.6. This allowed rapid and reproducible automatic SERS detection at multiple concentrations of a target solution through the generation of gradient microdroplets. This system provides several advantages over other microscale devices, including on-chip detection, high analytical throughput, facile automation, and reduced sample preparation requirements.

Lee et al. [82] developed a SERS-based LFIA strip for the sensitive diagnosis of scrub typhus. It is a mite-borne infectious disease that is caused by the gram-negative intracellular bacterium *Orientia tsutsugamushi*. Indirect immunofluorescence assay (IFA) is considered the gold standard serological method for detecting an increase in the titre concentration of *O. tsutsugamushi* IgG for the diagnosis of scrub typhus; however, this fluorescence image-based detection technique requires a high-cost fluorescence microscope and involves the subjective determination of endpoints. To address the problems associated with the methods currently in use for the diagnosis of scrub typhus, a rapid, accurate, and patient-friendly SERS-based

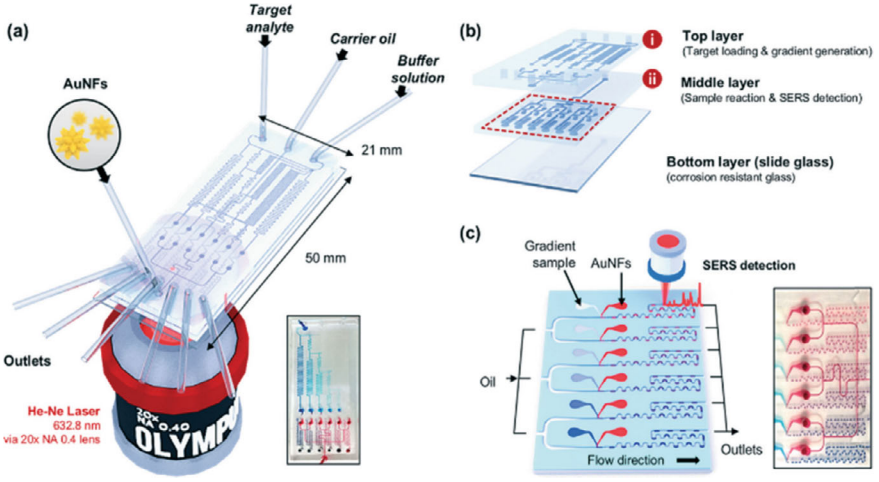



**Fig. 17.6** **a** Schematic design of a gradient droplet microfluidic chip for SERS-based high-throughput gradient analysis. Gold nanoflowers (AuNFs), target analyte to be diluted, buffer solution, and carrier oil were injected into the channel inlets, and the SERS signals were measured using a He–Ne laser for multiple droplets containing various concentrations of a target reagent. **b** The system consists of two parallel layers: (i) target loading and serial dilution occur in the top panel, (ii) nanoparticle distribution, droplet generation, and SERS detection occur in the middle panel. **c** Image (left) and photo (right) of the middle layer showing the droplet generation and SERS detection [81]

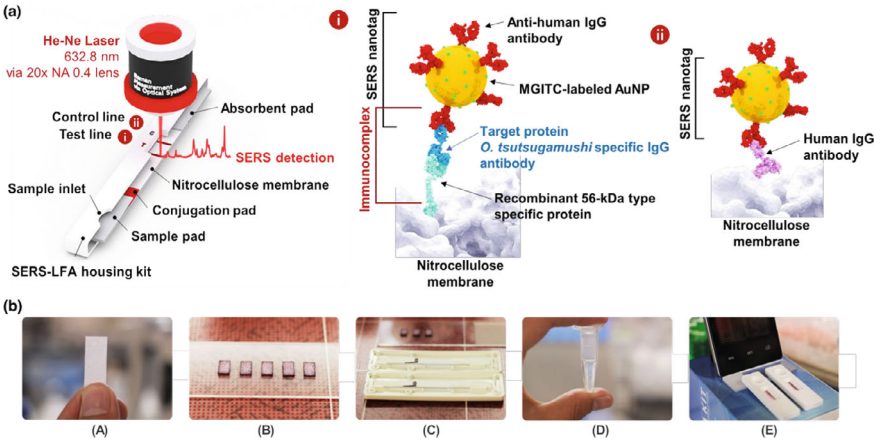



**Fig. 17.7** Schematic illustration for the SERS-LFIA process. **a** The 56-kDa recombinant proteins immobilized on the test line capture the *O. tsutsugamushi* specific IgG antibodies in the human serum. Sandwich immunocomplexes are formed when the anti-human IgG antibody-conjugated SERS nanotags bind with the target antibodies. Conversely, the human IgG antibodies are immobilized on the control line and directly bind with the antibody-conjugated SERS nanotags. **b** Fabrication procedure of the SERS-LFIA strips [82]

LFIA platform was developed. The results of the proposed method for 40 clinical samples exhibited an excellent linear relationship with those of IFA. Figure 17.7 shows a schematic illustration of the assay using a SERS-LFIA strip and its sequential fabrication process. Its advantages include the use of a smaller sample volume, fewer assay steps, shorter assay time, better quantitative analysis, and better storage condition and longer lifetime of the assay [82].

Although antibodies or antigens are the primary target agents in LFIA strips, other biomolecules such as DNA oligonucleotides were also employed. Fu et al. [83] developed a SERS-based LFIA strip for the highly sensitive detection of human immunodeficiency virus type-1 (HIV-1) DNA markers with high reproducibility. A linear relationship was established between the Raman intensity of the DNA-conjugated AuNPs and HIV-1 DNA concentration with a detection limit of 0.24 pg/ml, which was at least 1000 times more sensitive compared to colorimetric or fluorescent detection methods.

Conventional LFIA strips have a thermal stability issue when used in tropical regions as shown in Fig. 17.8. To resolve this problem, SERS-based LFIA strips using silica-encapsulated AuNPs were developed for use in locations high temperatures [84]. Wang et al. [85] reported a SERS-based LFIA strip for the simultaneous detection of two DNA oligonucleotides, one for Kaposi's sarcoma-associated herpesvirus (KSHV) and the other for bacillary angiomatosis (BA). This strip contained two test lines and one control line, and a 1:1 molar mixture of KSHV and BA DNA-immobilized SERS nanotags was stored in the conjugate pad. The LODs for KSHV and BA determined from the SERS-based LFIA strip were estimated to be 0.043 pM

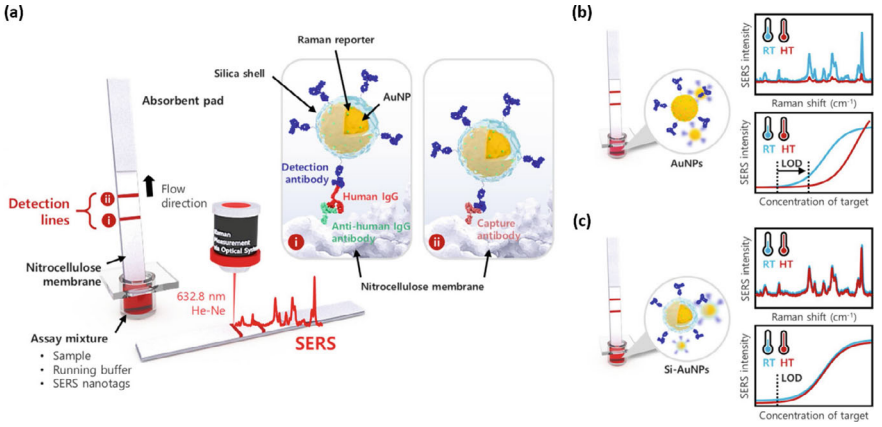



**Fig. 17.8** **a** Schematic illustration of the SERS-based LFIA for human IgG using thermally stable Si-AuNPs. Anti-human IgG antibodies on the test line capture the Si-AuNPs; the excess SERS nanoprobes were captured by capture antibodies on the control line. **b** SERS spectra of the AuNP-loaded LFIA strips and the corresponding calibration curves at 25 and 45 °C. **c** SERS spectra of the Si-AuNP-loaded LFIA strips and the corresponding calibration curves at 25 and 45 °C [84]

and 0.074 pM, respectively, which were approximated to be 10,000 times more sensitive than those achieved using the previously reported aggregation-based colorimetric method.

High throughput and ultrasensitive quantification of multiple nucleic acids is a challenge in a POCT device. Zhang et al. [86] developed a SERS-based LFIA strip that can simultaneously detect DNA oligonucleotides of 11 atypical pathogens implicated in respiratory tract infections (RTIs) that require the timely and accurate pathogen identification so that the individual treatment plan can be selected.

The primary limitation of utilizing SERS in LFIA is the time taken for a Raman microscope to scan the relatively large area of a test line. The test line consists of hundreds to thousands of pixels, and it takes 0.1 to a few seconds to read each pixel. Hence, it takes tens to hundreds of minutes to read the test line, which is impractical for a POCT rapid test [58]. To overcome this limitation, Tran et al. [30] developed a portable SERS reader for rapid LFIA strip scanning. Figure 17.9 shows that line illumination over the entire area of the test line was achieved using an optical fibre probe with a line focus. The pregnancy hormone human chorionic gonadotropin (hCG) was detectable in clinical samples within only 2–5 s down to approximately 1.6 mIU/mL. This line scanning detection method was faster by several orders of magnitude than conventional point-mapping acquisition schemes and 15 times more sensitive than a commercially available LFIA, making it suitable for POCT settings.

The noticeable drawback when using a complimentary DNA sequence in SERS-based LFIAs is that SERS spectra were affected when in the presence of a non-complimentary DNA sequence [87]. This may cause further problems with clinical samples in POCT settings. In clinically relevant samples such as serum, saliva, or semen, the presence of non-complimentary sequences is predominant, possibly

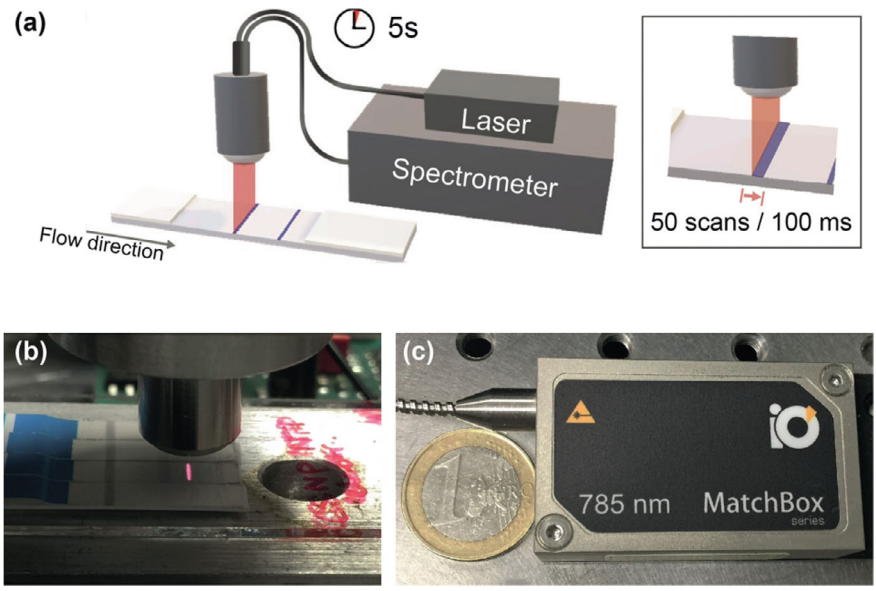



**Fig. 17.9** Portable Raman/SERS reader with a custom-designed optical fibre probe with laser line focus: **a** schematic representation of the setup: an averaged Raman spectrum from the entire TL (ca. 4 mm) is obtained within only 5 s by illuminating along the entire width of the TL with a line focus and then moving the test strip orthogonally to it using a motorized stage. **b** Photograph of the custom-designed optical fibre probe. **c** Photograph of the powerful (up to 450 mW) yet compact 785 nm diode laser [30]

causing further non-specific binding that may lead to inconclusive results. Instead of using DNA, Lee et al. used antibodies to capture HIV-1 virus-like particles (VLPs) on an indium tin oxide (ITO) substrate covered in Au nanodots [88]. The HIV-1 VLPs consisted of co-transfected HEK293 cells containing the Gag, Pol, and Env genes of the HIV-1 virus. Surface-bound antibodies were used to capture the VLPs, leading to concentrations in the range of 35 fg/mL–350 pg/mL being detected. Exploring new HIV-1 biomarkers may help improve specificity in HIV-1 SERS-based detection devices and create an applicable POCT device by eliminating complex sample preparation [89].

Viruses evolve rapidly and unpredictably, challenging the effectiveness of disease diagnostics. To help control outbreaks and understand their origins, the first step is often isolating viruses from infected samples for characterization. Yeh et al. [90] demonstrated that multiple emerging virus strains can be simultaneously enriched and optically detected in a few minutes without using any labels. They presented a portable microfluidic platform containing carbon nanotube arrays with herringbone patterns and decorated with gold nanoparticles. The CNT arrays have differential filtration porosity used to capture viruses based on their size for the rapid enrichment and optical identification. They called the platform "virus capture with rapid Raman spectroscopy detection and identification (VIRRION)". Different emerging strains

(or unknown viruses) can be enriched and identified in real time directly from clinical samples with 90% specificity. Furthermore, this viable enrichment process enables further culturing and characterization by electron microscopy and deep sequencing. Figure 17.10 shows a schematic illustration of that platform.

Haemorrhagic fever outbreaks such as Ebola are difficult to detect and control because of high costs, slow diagnostics and because initial clinical symptoms mimic other endemic diseases such as malaria. Current molecular diagnostic methods such as PCR require trained personnel and infrastructure that hinder diagnostics at the point-of-care. Although LFIAs can be broadly deployed, they are typically not well-suited for differentiating among multiple diseases presenting with similar symptoms. Early detection and control of Ebola outbreaks require simple, easy-to-use assays

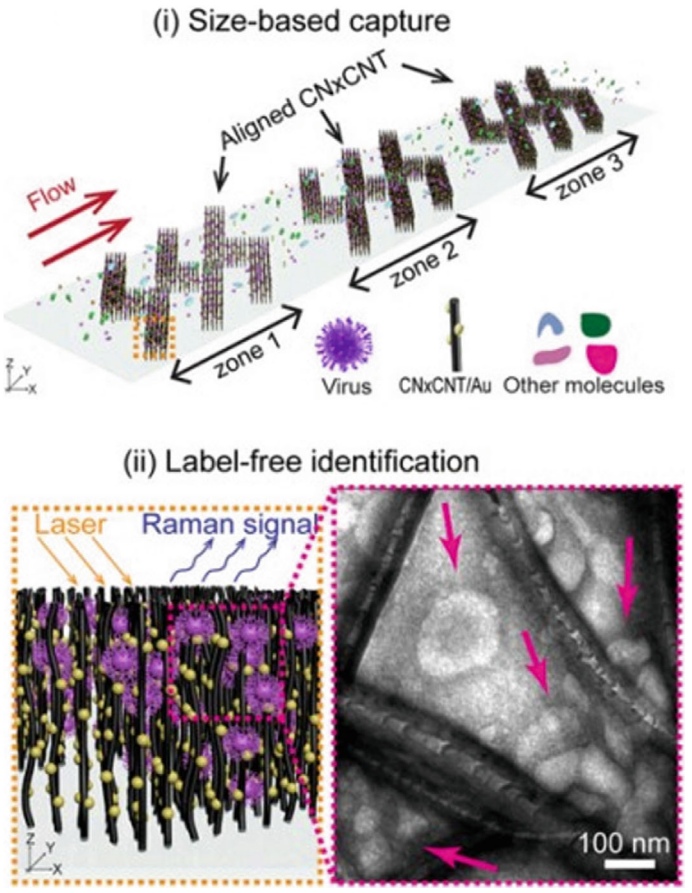



**Fig. 17.10** Design and working principle of VIRRION for effective virus capture and identification. Illustration of (i) size-based capture and (ii) in situ Raman spectroscopy for label-free optical virus identification. Images of electron microscopy showing captured avian influenza virus H5N2 by CN × CNT arrays [90]

that can detect and differentiate infection with Ebola virus from other more common febrile diseases. Sebba et al [91] developed and tested an immunoassay technology that uses SERS tags to simultaneously detect antigens of Ebola, Lassa, and malaria within a single blood sample. Rather than attempting to detect proteins directly by SERS signal, they instead created a stable optical signal by encapsulating the SERS-active Raman reporter between a 60-nm gold nanoparticle, which acts as the nanotag core, and a 20- to 30-nm silica shell (Fig. 17.11a). Different Raman reporters provide different SERS spectra (Fig. 17.11b), with each spectrum having a unique optical "fingerprint"; this enables each nanotag to be used to detect a different target. Sulfhydryl groups are incorporated into the outer surface of the silica to provide convenient functional groups for bioconjugation affinity. The silica shell stabilizes the optical signal in complex biological fluids such as blood, preventing desorption of the Raman reporter from the gold surface and blocking spurious SERS signals from the blood sample itself. The stable SERS signal from the SERS nanoparticle has several unique properties that make it well suited for multiplexed POCT. First, a single 785-nm excitation source can be used, regardless of the choice of Raman reporter, and the scattered SERS signal is read in the NIR (820–914 nm), where clinical samples such as blood have minimal absorbance. This enables the SERS signal to be read directly in a whole blood sample without sample manipulation such as washing or centrifugation. Second, because each Raman reporter provides a unique optical fingerprint, SERS tags with different Raman reporters can be readily differentiated from each other in complex mixtures, enabling multiplexed assays (where each SERS tag detects a different target) within a single assay tube. Results are provided in less than 30 min for individual or batched samples. They were able to detect Ebola with 90.0% sensitivity and 97.9% specificity and malaria with 100.0% sensitivity and 99.6% specificity. These results, along with corresponding live virus and non-human primate testing of an Ebola, Lassa, and malaria 3-plex assay, indicate the potential of the SERS in outbreak detection in low-resource settings.

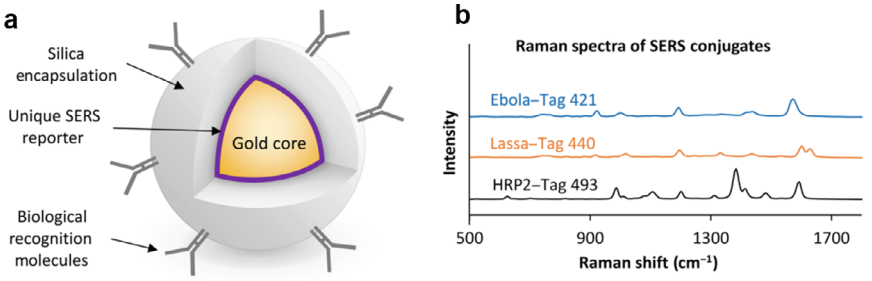



**Fig. 17.11** Schematic and representative spectra of Ebola, Lassa, and malaria detection using SERS nanotag technology. **a** Schematic of BD's SERS nanotag technology. **b** Representative spectra from three SERS nanotags used in a sandwich immunoassay to detect Ebola, Lassa, and malaria histidine-rich protein 2 (HRP2) antigen [91]

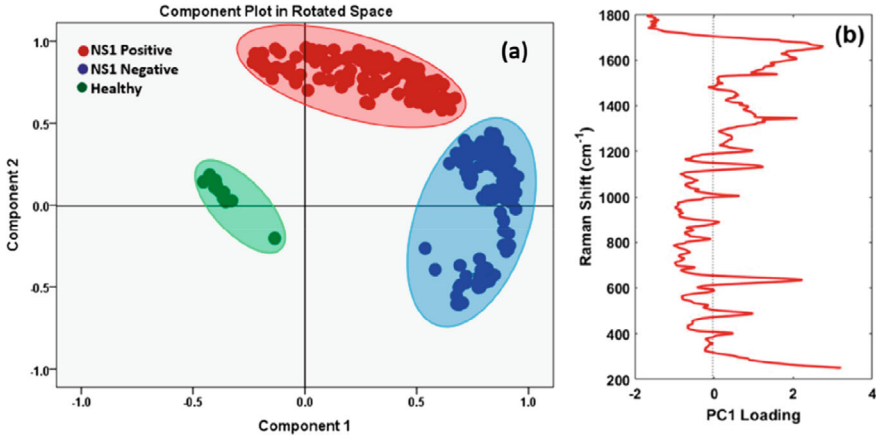



**Fig. 17.12** **a** Plot of principal component 1 versus principal component 2 for the three groups of samples, antigen NS1 positive, negative, and healthy. **b** Wavenumbers related to PC1 loading of plot (**a**) [92]

Another severe febrile illness is dengue, which is a serious global health concern especially in tropical and subtropical countries. Gahlaut et al. [92] carried out SERS-based diagnosis of dengue virus in clinical blood samples. All the samples were well characterized by conventional NS1 antigen and IgM antibody ELISA kits. A silver nanorods array was fabricated by glancing angle deposition technique and used as a substrate for the handheld SERS platform. A small amount of patient blood serum (5 μL) was taken for analysis and the report was prepared within a minute. SERS spectra of pure NS1 protein as well as spiked in serum was also recorded separately. Principal component analysis (PCA) was carried out to differentiate dengue positive, dengue negative, and healthy subjects based on their respective SERS spectra (Fig. 17.12). This rapid, portable, cost-effective technique renders early and on-site diagnosis of dengue with high sensitivity and reproducibility possible.

Luo et al. [93] reported an integrated active enrichment platform for direct hand-held detection of nucleic acid of COVID-19 in nanolitre samples without PCR. The platform consists of a capillary-assisted liquid-carrying system for sampling, integrated circuit system for ultrasound output, and cellphone-based SERS system. Functionalized gold nanorods can effectively capture and enrich biomarkers under ultrasonic aggregation. Such approach could actively assemble gold nanorods in 1 − 2 s and achieved highly sensitive ($6.15 \times 10^{-13}$ M) SERS detection of COVID-19 biomarkers in nanolitre samples within 5 min, making this a promising POCT tool.

Pang et al. developed a magnetic SERS biosensor using aptamer and antibiotic molecules for dual-recognition of bacterial cells at the point-of-care [94]. Aptamer-$Fe_3O_4$@Au magnetic nanoparticles were synthesized as magnetic and SERS-activ substrate for specific bacterial enrichment, while vancomycin-SERS tags were prepared for the sensitive quantification of the pathogenic bacteria (Fig. 17.13). The biosensor showed high specificity and sensitivity towards the target pathogenic

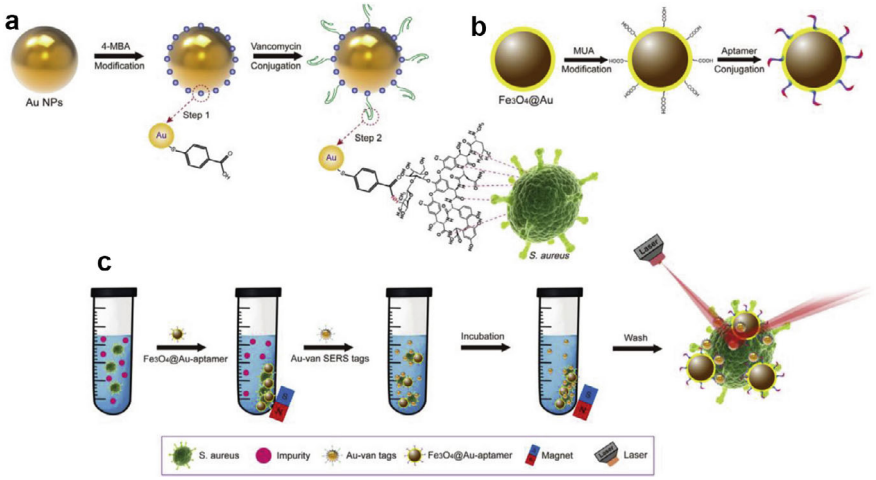



**Fig. 17.13** Schematic illustration of **a** the synthesis of Au-Van SERS tags, **b** the synthesis of aptamer-modified $Fe_3O_4$@Au MNPs, and **c** the operating procedure for *S. aureus* detection via the dual-recognition SERS biosensor [94]

bacteria with a low detection limit of 3 cells/mL and a wide dynamic linear range from 10 to $10^7$ cells/mL. Moreover, the whole process of the biosensor could be completed within 50 min and exhibited recoveries from 95.0% to 106.4% with relative standard derivation less than 5.3% in clinical samples.

Shi et al. designed a rapid SERS-based LFIA biosensor for the sensitive and quantitative POCT of *Escherichia coli O157:H7* in biological samples [95]. Firstly, novel gold-shell silica-core nanospheres ($SiO_2$/Au) with monodispersity, good stability, and excellent SERS activity were prepared as tags. The $SiO_2$/Au SERS tags were then modified with two layers of Raman reporter molecules and monoclonal antibodies for specifically and effectively binding with *E. coli O157:H7* and forming sandwich immune complexes on the test lines. *E. coli O157:H7* was quantitatively detected by measuring the Raman intensity at the test lines. Under optimal conditions, this biosensor showed a detection limit of 50 cells/mL in PBS solution and 100 cells/mL in real samples, which are 2000 times more sensitive than colloidal Au-based LFIA strips.

Krafft et al. [96] presented a disposable and low-cost lab-on-a-chip device utilizing a nanoporous membrane, which connects two stacked perpendicular microfluidic channels. The three-dimensional chip architecture together with the nanoporous membrane maintains two separate chemical environments for enrichment and detection of microorganisms within the same device. While one of the channels supplies the sample, the second one attracts it by potential-driven electrokinetic flow across the porous membrane, where bacteria, as well as AgNP clusters, are trapped, concentrated, and analysed by SERS. An illustrative image of the detection platform is

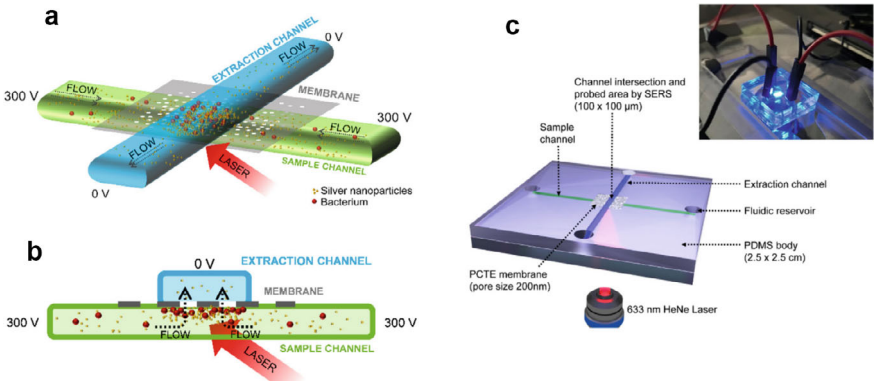



**Fig. 17.14** The working principle of the microfluidic device for bacteria enrichment and SERS analysis: **a** side view, **b** cross-section, **c** the overall appearance of the lab-on-a-chip device for the concentration of bacteria followed by SERS detection (inset shows a photo of the microfluidic chip with electrical connections during fluorescence measurement) [96]

provided in Fig. 17.14. Colloidal AgNPs (60–70 nm) were added to the sample to detect common pathogens (*Escherichia coli* DH5α and *Pseudomonas taiwanensis* VLB120) from spiked tap water via SERS. It has thus a high potential for rapid POCT of bacterial samples if combined with a portable Raman instrument. The results promise a disposable optical platform for reliable pathogen detection.

Smartphone-based Raman spectrometers equipped with a 5G cloud-based healthcare management system have also been applied for point and shoot analysis for the quick, on-site diagnosis of sepsis [97]. In this example, point scanning was carried out using a laser spot which could compromise the working efficiency as it only analyses a limited fraction of the test zone and leads to undersampling. A SERS-based LFIA strip was proposed for the simultaneous and quantitative detection of dual infection biomarkers, serum amyloid A (SAA), and C-reactive protein (CRP). In practice, mesoporous silica ($mSiO_2$)-coated gold nanoparticles (AuNPs) were used as the SERS substrate. Mercaptobenzoic acid (MBA) was embedded in the internal gap between the AuNPs and the $mSiO_2$ shell to prepare $Au^{MBA}@mSiO_2$ NPs, onto which SAA and CRP antibodies were modified to prepare two $Au^{MBA}@mSiO_2$ SERS nanotags. The Raman intensities of the test and control lines were simultaneously identified for the qualitative detection of SAA and CRP, with LODs as low as 0.1 and 0.05 ng/mL for SAA and CRP, respectively. Finally, aiming at POCT applications, they used a smartphone-based portable Raman spectrometer to quantitatively analyse the SERS-LFIA strips. The Raman signal could still be accurately detected when the concentration of SAA and CRP was 10 ng/mL, which is lower than the LOD required in clinical practice for most diseases. Therefore, taking into account its simple operation and short analysis time, using a portable Raman spectrometer equipped with a 5G cloud-based healthcare management system, could provide quick and on-site diagnosis of infectious diseases and guide their treatment in remote areas that lack

well-developed medical resources [97]. Orbital raster scans and multiple acquisitions along the test line can increase the reproducibility, as could line illumination [60].

A compact reader has been applied for the detection of SARS-CoV2-specific IgM and IgG antibodies [98]. The setup was slightly modified to rapidly scan both the test and control line using a mechanical sample holder. The compact reader was able to detect both antibodies when conventional naked eye detection showed no visible test line. Jia et al. have incorporated a motorized stage in their portable SERS-LFIA to automatically and randomly measure multiple points on the test zone in order to detect West Nile virus [99]. This reduced the detection error caused by unexperienced operators. However, there is also the issue of an open laser beam which is a major safety risk for POCT environments. To increase the likelihood of SERS-LFIA deployment in POCT, a compact, handheld all-in-one system is desirable. They used Au@Ag NPs labelled with double-layer Raman molecules as SERS tags to prepare WNV-specific SERS–LFIA strips. The WNV-specific antigen NS1 protein was quantitatively and sensitively detected with an LOD of 0.1 ng/mL, which was 100-fold more sensitive than visual signals and as sensitive as that of the fluorescence quantitative reverse transcription-polymerase chain reaction assay.

### *17.3.2 Oncology*

A proactive approach to early cancer detection can lead to more effective treatments with minimal side effects and better long-term patient survival. However, early detection of cancer is hindered by the existing limitations of conventional diagnostic methods. To enable early diagnosis and regular monitoring and improve automation, the development of integrated POCT and biosensors is needed. POCT-based techniques will help avoid complications that occur after invasive tissue biopsy, such as bleeding, infection, and pain [100]. The aim here is to provide a few examples of applying POCT SERS in oncology for the detection of biomarker proteins, miRNA, ctDNA, exosomes, and cancer cells with liquid biopsies.

Ning et al. [101] developed a SERS sensor for simultaneous detection of multiple cancer-related exosomes. The SERS detection probes were made of bimetallic SERS-active nanotags, gold–silver–silver core–shell–shell nanotrepangs (GSSNTs), which were composed of bumpy surface nanorod (gold nanotrepang, GNT) cores and bilayer silver shells, and decorated with linker DNAs, which were complementary to the aptamer targeting exosomes. Three kinds of SERS detection probes were designed via the adoption of different Raman reporter molecules and linker DNAs. The capture probes were prepared by modifying specific aptamers of the target exosomes on magnetic beads (MBs). In the absence of target exosomes, SERS detection probes were coupled with MBs via specific DNA hybridization for use as aptamer-based SERS sensors as illustrated in Fig. 17.15. In the presence of target exosomes, the aptamer specifically recognized and captured the exosomes, and GSSNTs were subsequently released into the supernatant. Thus, attenuated SERS signals were detected on the MBs, indicating the presence of target exosomes.

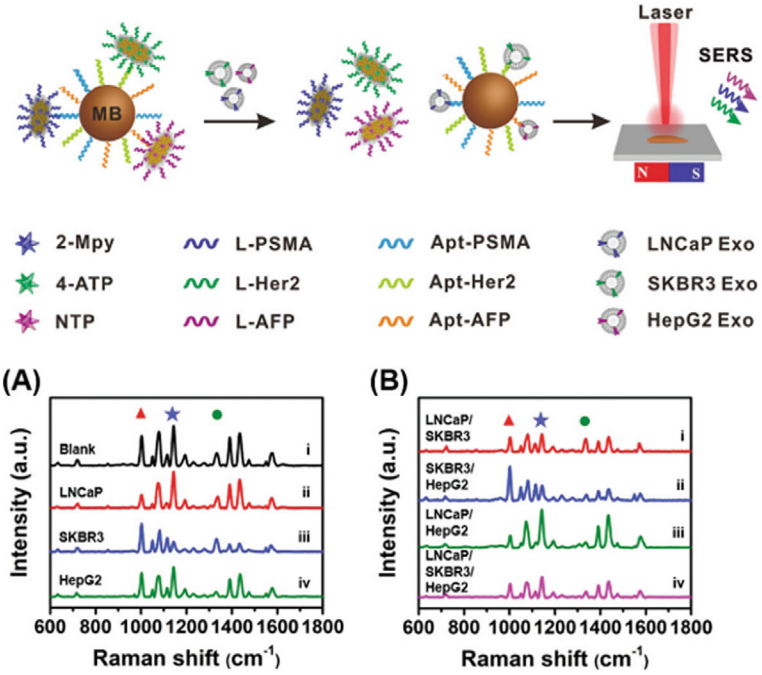



**Fig. 17.15** (top) Schematic illustration of the fabrication of the SERS sensor for multiplex exosome detection. Three kinds of SERS detection probes were prepared via the functionalization of linker DNAs on 2-Mpy, 4-ATP, and NTP-encoded GSSNTs. Multiplexed capture probes were constructed by co-modification of three types of aptamer DNAs. Each kind of GSSNT was captured by the corresponding aptamer DNA anchored on MBs, followed by the recognition between aptamers and target exosomes, leading to the released GSSNTs and attenuated SERS signals. (bottom) SERS spectra of the complexes obtained in the presence of **a** single and **b** multiple exosomes. SERS spectra (**a**-i), (**a**-ii), (**a**-iii), and (**a**-iv) were obtained for the detection of a blank control, LNCaP exosomes, SKBR3 exosomes and HepG2 exosomes, respectively. SERS spectra (**b**-i), (**b**-ii), (**b**-iii), and (**b**-iv) were obtained for the multiplex detection of a mixture of LNCaP/SKBR3 exosomes, SKBR3/HepG2 exosomes, LNCaP/HepG2 exosomes, and LNCaP/SKBR3/HepG2 exosomes, respectively [101]

SERS-based breath analysis has attracted increasing attention in cancer screening. Here, eight aldehydes and ketones in the human breath are reported as the volatile organic biomarker compounds for the non-invasive diagnosis of gastric cancer with a tubular SERS sensor. Huang et al. [102] equipped the tubular SERS sensor with a glass capillary loaded with ZIF-67-coated silver particles (Ag@ZIF-67), which offers Raman enhancement from the plasmonic nanoparticles and gas enrichment from the metal−organic framework (MOF) shells. The composite materials are modified with 4-aminothiophenol (4-ATP) to capture the aldehyde and ketone compounds, the SERS spectrum of which is altered upon interaction with the biomarker molecules. The tubular sensor serves as a gas flow channel and a detection chamber simultaneously, bringing higher gas capture efficiency than the planar SERS sensor. As

a proof-of-concept, the tubular SERS sensor has been successfully employed to screen gastric cancer patients with an accuracy of 89.83%. The detection scheme and representative results are illustrated in Fig. 17.16.

Furthermore, and because bladder cancer has the highest per patient cost of all cancer types, Moisoiu et al. [103] aimed to develop a non-invasive, POCT tool based on combined microRNA (miRNA) and SERS profiling of urine.

Keshavars et al. [104] described a novel concept of non-stoichiometric $TiO_2$ and the incorporation of oxygen vacancies as a strategy to significantly increase the SERS enhancement of self-assembled quantum scale structured (Q-structured) $TiO_x$. They found that reducing the $TiO_2$ particles to quantum scale can increase the EF by up to $3.5 \times 10^5$, while further enhancement can be achieved by inducing the oxygen vacancies to the Q-structured $TiO_x$, and demonstrated how this sensitive template

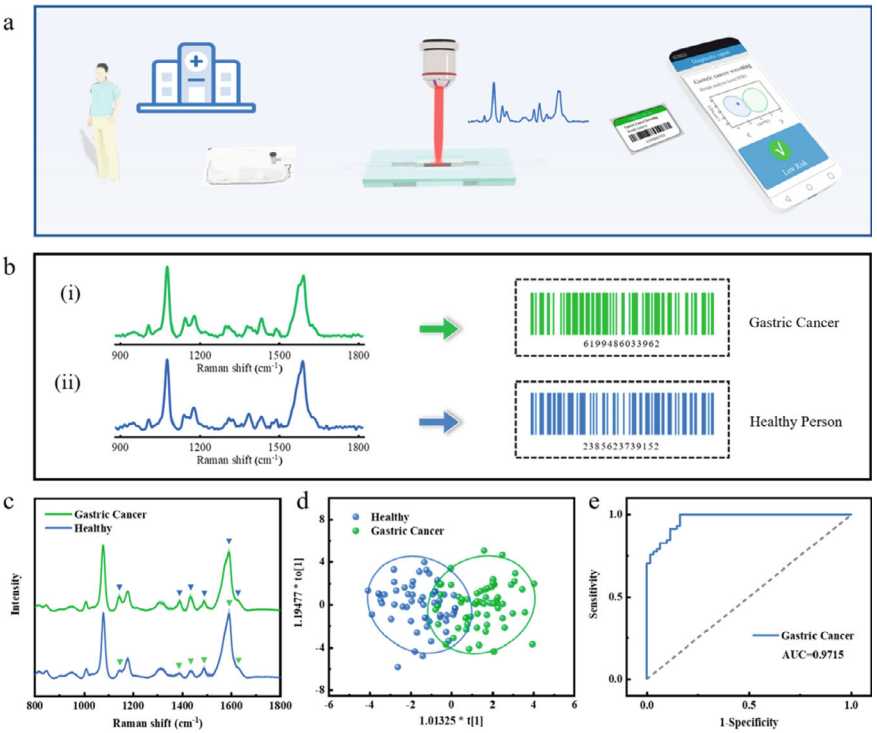



**Fig. 17.16** Breath analysis based on SERS sensor. **a** Schematic diagram of SERS sensor-based diagnostic workflow. **b** Typical SERS spectrum of breath sample obtained from (i) a gastric cancer patient and (ii) a healthy volunteer, and the barcodes were converted from the corresponding spectra. **c** Normalized average SERS spectra of breath samples from 57 GC patients and 61 healthy individuals based on the tubular sensors, respectively. The shaded areas represent the standard deviations. **d** OPLS-DA plot of SERS spectra of exhaled breath from GC patients and healthy individuals. Each data point represents the SERS spectrum of a breath sample measured by the gas sensor. **e** ROC curve based on the OPLS-DA model [102]

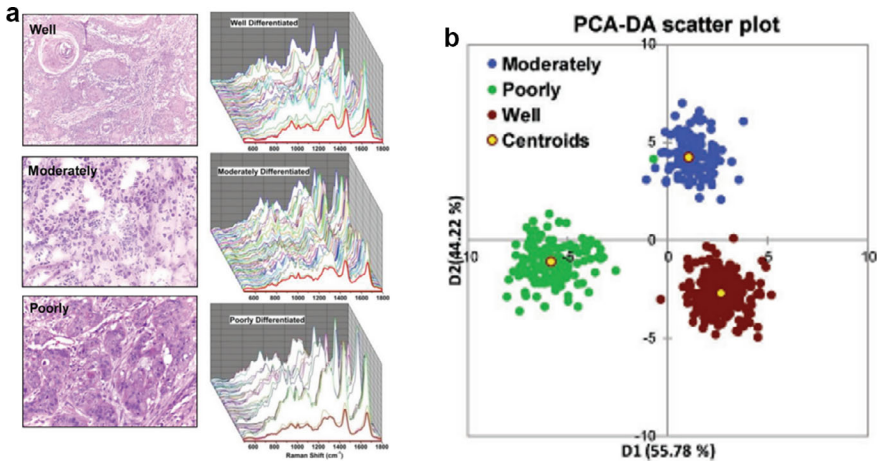



**Fig. 17.17** **a** H&E-stained images of well differentiated, moderately differentiated, and poorly differentiated OSCCs. SERS spectra acquired from these oral tissue grades (averaged group spectrum shown in red). **b** PCA-DA results: Scatter plot of discriminant function scores of individual grade specific spectrum showing good correlation within the groups and less correlation between grades [107]

intensifies the Raman signal of epidermal growth factor receptors (EGFR) to diagnose breast cancer. The reported detection limit was as low as 1 nM and the maximum EF was $3.4 \times 10^7$, which shows that the implementation of semiconductor materials as SERS templates would enormously widen the range of applications [105, 106].

Similarly, Chundayil Madathil et al. [107] reported the fabrication and testing of a novel nanostructured SERS catheter device for rapid detection, classification, and grading of normal, premalignant, and malignant tissues. The sensor part of the catheter is made up of leaf-like $TiO_2$ nanostructures decorated with 30 nm-sized Ag nanoparticles. The device is tested using a total of 37 patient samples wherein SERS signatures of oral tissues consisting of malignant oral squamous cell carcinoma (OSCC), verrucous carcinoma, premalignant leucoplakia, and disease-free conditions are detected and classified with an accuracy of 97.24% within a short turn-around time of nearly 25–30 min per patient. In Fig. 17.17, the grading-based spectral classification of OSCC is illustrated, including H&E staining, SERS spectra from related tissue samples as well as the scatter plot showing the good separation between oral tissue grades.

### *17.3.3 Pharmacology/Toxicology*

Diquat (DQ) is a quaternary ammonium herbicide, the exposure to which causes DQ poisoning, which results in neurological, respiratory, gastrointestinal, and miscellaneous health problems. Accuracy and speed are crucial requirements for detecting

patient poisoning. Li et al. [108] developed a fast, simple and practical strategy for the reliable identification and quantification of DQ in biological fluids. SERS POCT was realized under the acidic condition with gold nanoparticles as the substrate. Under optimal experimental conditions, the detection limits were 17.5 ppb and 1.99 ppm in human urine and gastric fluid, respectively (Fig. 17.18). High specificity and selectivity of the SERS strategy were demonstrated using common pesticides and coexisting biological substances. The method was also used to detect biofluids from 5 patients and urine samples from 10 healthy volunteers. The results were in high agreement with spectrophotometric and clinical liquid chromatography-mass spectrometry methods. The volume of urine samples required for this technique is merely 20 μL, and no sample preparation was required.

Bromadiolone is the most frequently detected anticoagulant rodenticide in human biofluids, resulting in increased cases of poisoning. Shang et al. [109] presented a portable kit that could realize rapid fingerprint detection of diquat in human biofluids based on SERS and salt-induced liquid–liquid phase separation (SILLPS) using

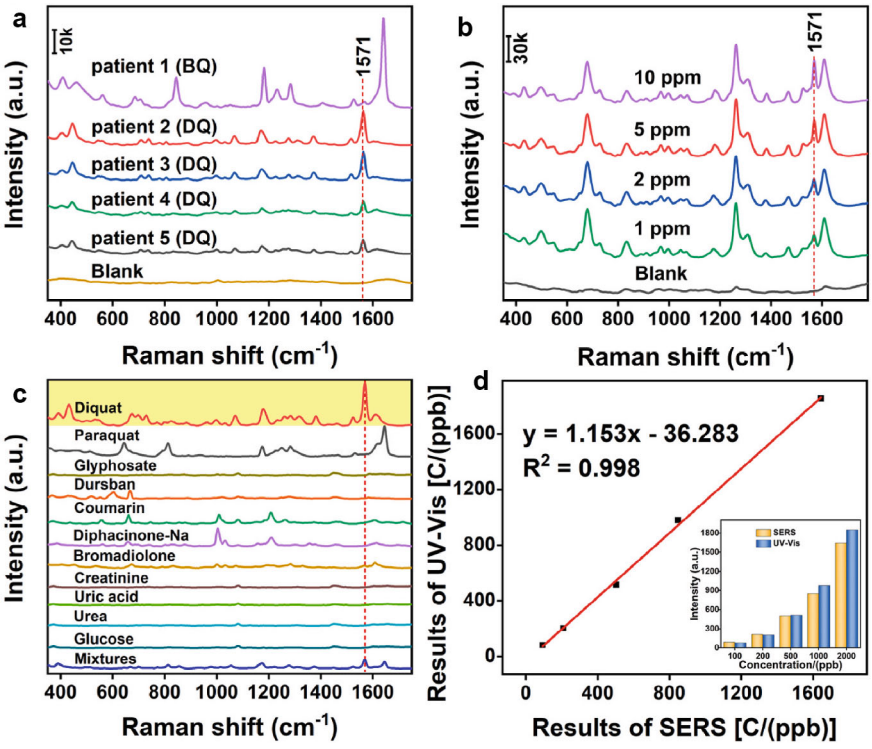



**Fig. 17.18** **a** SERS spectra of DQ and paraquat in urine samples of patients. **b** SERS spectra of DQ in human gastric juice. **c** Spectra of other pesticides and substances inherent to urine and a mixture obtained through the proposed method. **d** Linear correlation and comparison between the quantitative data of the SERS and UV–vis spectrophotometric methods [108]

a gold/silver core–shell nanoparticle (Au@Ag NPs) substrate. The kit included a portable Raman spectrometer and five tubes that contained Au@Ag NPs colloid, aqueous KI solution, aqueous highly concentrated NaCl solution, acetonitrile, and aqueous $Mg(NO_3)_2$ solution. This strategy did not require pre-treatment for urine samples. For blood samples, a 2-min SILLPS method was proposed with satisfactory recovery, providing unique insights into efficient pre-treatment of complex biomatrix. The detection limits for urine and blood were calculated to be 3.21 ppb and 6.86 ppb, respectively. A clear trend could be observed between signal intensity and concentration of bromadiolone with high reproducibility. Moreover, the SERS-based results were confirmed by applying the HPLC-based gold standard method. This simple-yet-practical "Pretreat & Detect" SERS kit may open new opportunities for point-of-care detection of toxins.

Zhang et al. [74] developed a wearable and flexible glove-based SERS sensor for on-site detection of the drugs tramadol and midazolam. The sensor was constructed by fixing the flexible adhesive tape substrate to the fingertip of a glove and then sticking to polystyrene sphere opal photonic crystal for secondary enhancement of Raman signal. The gold trisoctahedra (Au TOH) were assembled uniformly onto adhesive tape by interface self-assembly technique, which improved the signal reproducibility. Moreover, the prepared adhesive tape substrate exhibits good flexibility, which facilitates conformal contact with irregular surfaces and improves sampling efficiency (Fig. 17.19). Different degrees of bending and stretching did not affect the reproducibility of the glove-based SERS sensor with RSDs less than 6%. Given its advantages in efficient sample extraction and portable analysis, the proposed sensor enabled the trace detection of tramadol and midazolam in serum with LODs down to 69.19 $ng{\cdot}mL^{-1}$ and 35.03 $ng{\cdot}mL^{-1}$, respectively.

Monitoring the acetaminophen dosage is important to prevent adverse reactions such as liver failure and kidney damage. Since traditional approaches rely mainly on invasive blood collection, Xiao et al. [110] developed a non-invasive microfluidic-based wearable plasmonic sensor to achieve simultaneous sweat sampling and acetaminophen drug monitoring at the point-of-care. The fabricated sensor employs an Au nanosphere cone array as the key sensing component, which poses as substrate for SERS in order to noninvasively and sensitively detect the fingerprint of acetaminophen molecules. The sensor enabled the detection and quantification of acetaminophen at concentrations as low as 0.13 μM.

### *17.3.4 Immunology/Serology*

A portable SERS-based LFIA reader with multiplexed detection was developed by Xiao et al. [111] using an integrated LFIA reaction column. The proposed LFIA reader was designed to simultaneously detect multiple samples or samples with

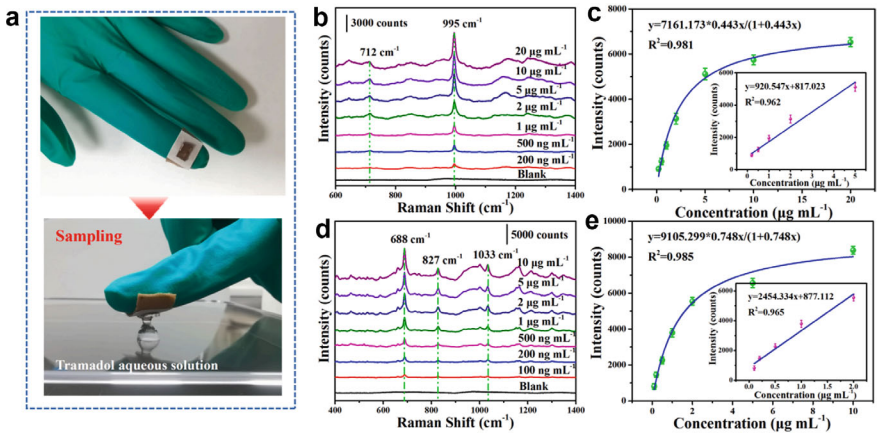



**Fig. 17.19** **a** Demonstration diagram of glove-based SERS sensor collecting liquid samples; **b** concentration-dependent SERS spectra of tramadol in serum; **c** function of the peak intensity at 995 $cm^{-1}$ with the spiked sample concentration; **d** concentration-dependent SERS spectra of midazolam in serum; **e** function of the peak intensity at 688 $cm^{-1}$ with the spiked sample concentration. Linear fitting was performed at low concentration regime [74]

multiple biomarkers. They managed to achieve the specific detection of alpha-fetoprotein (AFP), carcinoembryonic antigen (CEA), and prostate-specific antigen (PSA) with a detection limit of 0.01 ng/mL, which was three orders of magnitude lower than that of the visual signal. They also investigated the uniformity of channels based on an eight-channel integrated LFIA reaction column. The relative standard deviation values of the SERS intensity of the eight channels for measuring AFP, CEA, and PSA antigens at 1323 $cm^{-1}$ were 13%, 4.8%, and 5%, respectively. They reported the detection of 45 clinical serum samples of the three antigens using the proposed portable SERS-based LFIA reader to further confirm its applicability to clinical samples. The SERS signals of the positive sera were higher than those of the negative sera and their thrice standard deviation. An all-in-one enclosed handheld platform which allows the analysis of LFIA strips to take place directly next to the laser source, whilst maintaining safety measures, is vital if SERS-LFIA is ever to be recognized as a POCT analysis method. Their design and enclosure are shown in Fig. 17.20. They hypothesized that the major disadvantage of conventional SERS analysis is the expensive, large spectrometers which can only record the SERS spectrum at one position of the LFIA test strip at a time, and that multiple measurements require the strip to move on the *xy* translation stage repeatedly. Taking this into account, their proposed reader integrated a LFIA column which was mounted onto a step motor and moved up, down, back and forth by adjusting a two-axis translational stage allowing detection of both the test and control lines using a Raman probe with a laser spot of 200 μm. The automated SERS-based lateral flow system was housed in an enclosure with a handle to move the instrument, allowing the SERS-LFIA platform to be brought to the POCT.

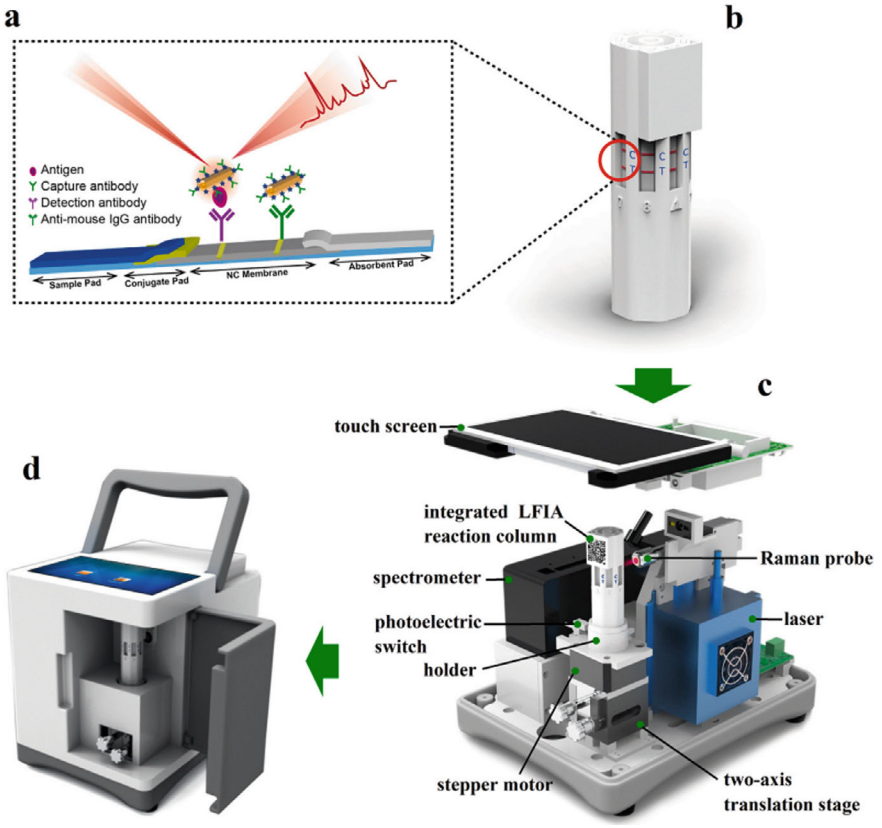



**Fig. 17.20** Schematic of portable SERS-based LFIA reader. **a** LFIA strip and **b** integrated reaction column. **c** Details of SERS-based LFIA reader and **d** the entire portable reader [111]

Similarly, triplex detection of three cardiac biomarkers (myoglobin, cardiac troponin I, and creatine kinase-MB isoenzymes) has been achieved using SERS-LFIA by Zhang et al. [112] on a single LFIA. The LFIA approach consists of three test lines with capture antibodies for each biomolecule and gold nanoparticles coated with the Raman reporter and the relevant detection antibodies. A multiplexed capture antibody test line is achieved via the application of three SERS tags coated with the relevant detection antibody and three different Raman reporters. The authors reported low detection limits, well within the clinical ranges of each biomarker. In another study, Sanchez-Purra et al. [113] demonstrated proof-of-concept study showing that a pentaplex SERS signal could be obtained from a single test region. A generic capture protein was immobilized on the test region of the LFIA device and the control line consisted of a second capture protein. Peaks from each of the individual SERS spectra were clearly visible in the pentaplex spectrum, therefore implying that signal-resolved pentaplex detection can be achieved using SERS, although quantification was not demonstrated.

The need for robust and low-cost tests is especially important in under-resourced and rural settings. Perhaps the greatest challenge is ensuring that an untrained individual is capable of operating and interpreting the test. Mabbott et al. [76] presented a paper-based diagnostic device capable of sensing miR-29a—a microRNA associated with myocardial infarction—using both colorimetric and SERS analysis. Rather than carry out the two types of analyses in tandem, they envisaged that the colorimetric output is easy enough to be interpreted by the untrained individual administering the test to provide them with qualitative feedback. If deemed positive, the test can be further validated using a handheld Raman spectrometer to provide a semiquantitative result. RGB analysis of the colorimetric output generated from samples containing miR-29a at different concentrations (18–360 pg/μL) showed differentiation from the control sample, but significant repeat variations indicated that it could not be used for quantifying miR-29a levels. However, the SERS analysis exhibited greater reproducibility at varying concentrations, achieving a LoD of 47 pg/μL. The union of the paper-based device and the two analysis methods resulted in the production of a sensitive, reproducible and facile, POCT.

### *17.3.5 Hepatology*

Bilirubin was first detected in blood in 1847 and since then has become one of the most widely used biomarkers for liver disease. Clinical routine bilirubin testing is performed at the hospital laboratory, and the gold standard colorimetric test is prone to interferences. The absence of a bedside test for bilirubin delays critical clinical decisions for patients with liver disease. This clinical care gap has motivated the development of a new generation of bioengineered point-of-care bilirubin assays [114].

Pan et al. [115] developed a paper-based SERS bilirubin sensor based on a filter paper, on which graphene oxide plasmonic gold nanostar (GOGNS) hybrids were deposited. When GOGNS hybrids were immersed in bilirubin-spiked buffer and serum for 20 min, bilirubin adsorbed to the GO nanosheets by electrostatic and $\pi-\pi$ interactions. After the incubation period, several bilirubin-indicating bands were identified in the SERS spectrum after ≈2 min. The sensor detected bilirubin in bilirubin-spiked fetal bovine serum in the range of 5 to 500 μmol $L^{-1}$ as illustrated in Fig. 17.21a, while Fig. 17.21b shows the ratio of the two marker bands and its relation to the concentration in the low ranges.

The concentration of bilirubin in serum is a key indicator for liver function, because excess bilirubin accumulation may lead to serious health problems like jaundice. It is known that in comparison with total bilirubin, the concentration of hydrophobic free bilirubin is more closely associated with jaundice because of its capability to cross the capillary walls and even blood–brain barrier. However, it is not easy to detect the low concentration of free bilirubin (~ nM) in the presence of large amount of protein-bound bilirubin (> 150 μM), and no POCT detection tool is available. Ouyang et al. [116] realized direct detection of free bilirubin by

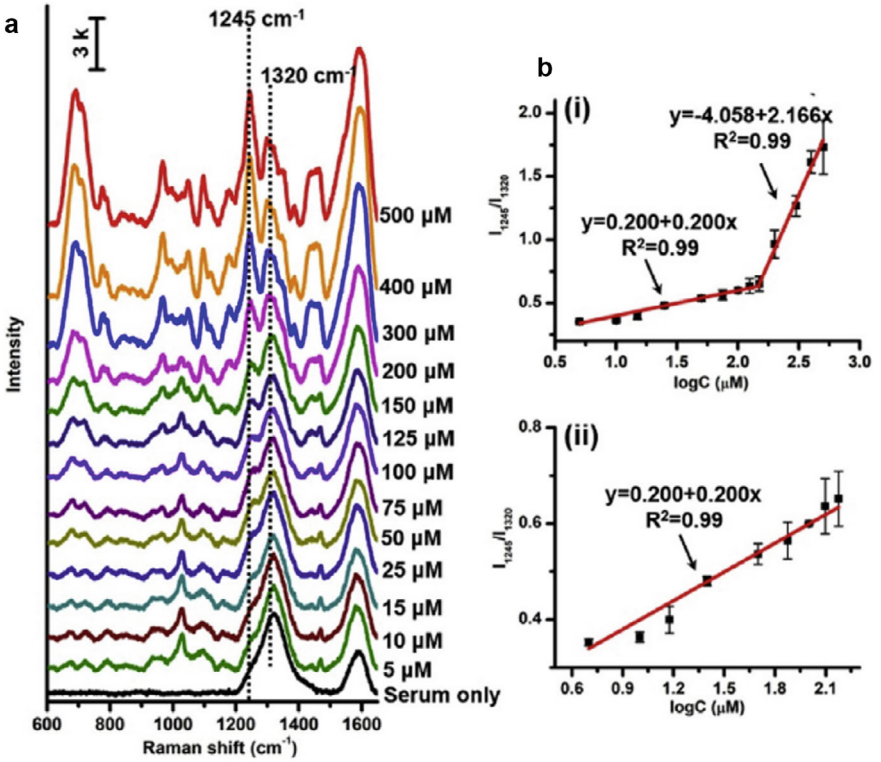



**Fig. 17.21** Label-free SERS detection of bilirubin in blood serum. **a** SERS spectra of the SERS-based biosensor upon addition of serum only and various concentrations of bilirubin in blood serum ranging from 5.0 to 500 μM. **b** (i) Plot of the $I_{1245}/I_{1320}$ ratio against the logarithmic concentration of bilirubin investigated, and (ii) the calibration curve of the $I_{1245}/I_{1320}$–log$C_{BR}$ curve at the low concentration region. The SERS measurements were conducted with the laser of 785 nm, laser power on the sample of 1.04 mW, exposure time of 1 s, and 10 accumulations [115]

using SERS. By mimicking the in vivo chemical interaction between glucuronic acid and bilirubin, glucose functionalized Au nanoparticles were synthesized for selective capture and detection of free bilirubin. By developing a convenient detection procedure of using robust Au array chip and internal standard calibration method, the sensitive detection of free bilirubin with detection limit down to 0.1 nM was achieved on a handhold Raman spectrometer. The clinical applicability was demonstrated by analysing spiked and real blood samples. As a proof-of-concept, the binding constant between bilirubin and human serum albumin (HSA) was determined with the present method. The influence of the binding capacity of the HSA for bilirubin in the presence of competing molecule salicylate sodium was also quantitatively measured, which demonstrated the importance of detection of free bilirubin instead of total bilirubin for warning the risk of bilirubin encephalopathy. In Fig. 17.22, the detection principle and the associated SERS spectra are plotted.

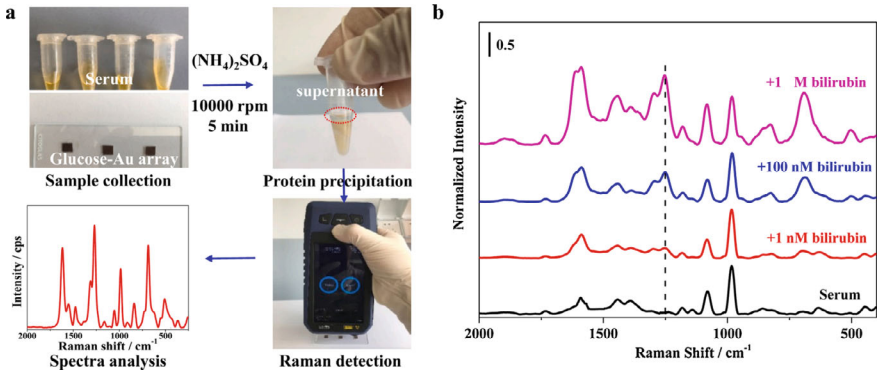



**Fig. 17.22** **a** Sample preparation and detection procedure for the detection of free bilirubin in serum. **b** SERS spectra of the serum supernatant without and with the addition of bilirubin standard (1–100 nM). The dotted line labelled the characteristic Raman peak of bilirubin at 1270 $cm^{-1}$ [116]

### *17.3.6 Cardiology*

Cardiovascular disease is a major global health issue. In particular, acute myocardial infarction (AMI) requires urgent attention and early diagnosis. The use of point-of-care diagnostics has improved the management of cardiovascular disease, but a major drawback is that the performance of POC devices does not rival that of central laboratory tests. SERS calibration-free methods have recently been explored to minimize the inconvenience and eliminate the limitations caused by the limited linear range and assay variations found in the calibration curves [25]. In addition, the incorporation of machine learning in SERS promotes multivariate analysis and enhances diagnostic accuracy, allowing the prediction of myocardial infarction within seconds [117].

Cardiac troponin I (cTnI) is a biomarker widely related to AMI. POCT of cTnI not only demands a short turn-around time for its detection but the highest accuracy levels for adequate clinical decisions [118]. Khlebtsov et al. [119] demonstrated a semiquantitative and sensitive detection of cTnI by developing a novel SERS-LFIA based on nonspherical gap-enhanced Raman tags (GERTs) with Raman molecules embedded in a 1-nm gap between Au nanorod core and Au shell. GERTs were conjugated with monoclonal antibodies and used for LFIA in the same way as ordinary functionalized colloidal gold. The presence of the target antigen, cTnI, was identified by Raman microscopy mapping of the test zone. The limit of cTnI detection was about 0.1 ng/mL, which is within the diagnostic range of cTnI in the blood serum of patients with heart infarction and is 30 times lower than that of the colorimetric LFIA test using the same antibodies and either GERTs or colloidal gold as labels (Fig. 17.23). Note that the Raman mapping data in the test zone of the strips can be calibrated by the conditional least-squares method to further eliminate the background interference of the nitrocellulose membrane and improve the LOD [120]. Considering

the current popularity of commercial LFIA strips, Khlebtsov et al. [121] have also reviewed the bright future of GERT-based POCT.

Cardiorenal syndrome (CRS) has posed tremendous challenges in patient management, and the detection of serum biomarkers may provide opportunities for early diagnosis and effective treatment. Su et al. [122] introduced a novel SERS-based sandwich immunoassay platform to simultaneously detect cTnI, N-terminal prohormone of brain natriuretic peptide (NT-ProBNP) and neutrophil gelatinase-associated lipoctalin (NGAL) for the early diagnosis of CRS. They used Ag-Au nanostars labelled with Raman reporters as nanotags and three-dimensional ordered macroporous Au–Ag–Au plasmonic array on ITO as substrate. The Ag-Au nanostars were

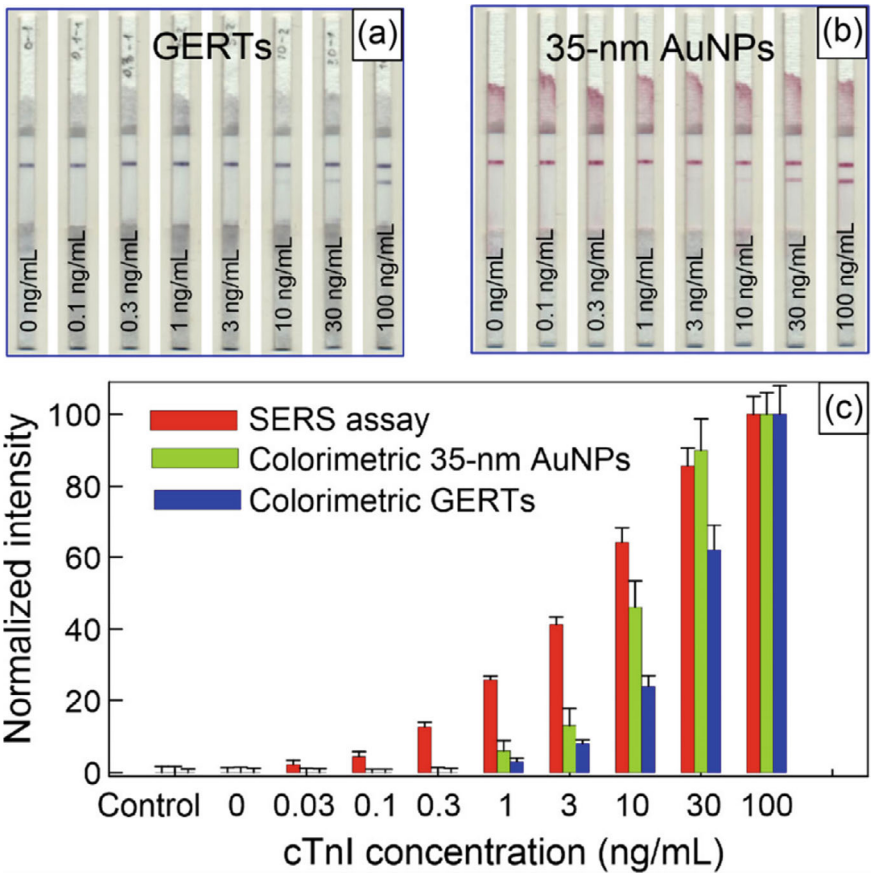



**Fig. 17.23** Photographic images of LFIA strips after application of different cTnI concentrations (0.1–100 ng/mL). **a** GERTs were used as labels. **b** 35-nm Au nanoparticles were used as labels. **c** Comparison of the assay results obtained with different cTnI concentrations in a GERT-based SERS assay and in colorimetric assays with GERTs and 35-nm Au nanoparticles. The error bars indicate standard deviations from three measurements [119]

prepared by galvanic replacement had a multi-branched structure, while the Au–Ag–Au array was fabricated through successive electrochemical deposition of Au and Ag on ITO slices modified with polystyrene nanospheres template. After that, the PS template was removed and followed by ion-beam sputtering deposition of Au. The multiplex detection was made under a sandwich immunoassay format; therefore, the developed substrate was modified with the monoclonal antibody of each evaluated antigen to obtain the capture substrate. Three SERS detection probes were used based on Ag−Au nanostars, each one modified with the polyclonal antibody and the Raman reporter molecule selected for each antigen. The simultaneous antigen detection was achieved by tracking one peak of each reporter molecule in the obtained spectrum. The proposed immunosensor proved to be stable after 4 weeks, it does not present significant cross-reactivity among the tested antigens, and the inter-assay reproducibility was good with a CV of 11.2% for cTnI. The limits of detection (LODs) were 0.76, 0.53, and 0.41 fg/mL for cTnI, NT-ProBNP, and NGAL, respectively, and the Raman images indicated the approximate concentration ranges of the detected proteins for visual analysis. Taking advantage of the ultrasensitivity and multiplexing capability of this approach, they further analysed clinical blood samples (Fig. 17.24) and concluded that the presented SERS immunoassay platform holds promise for POCT of CRS.

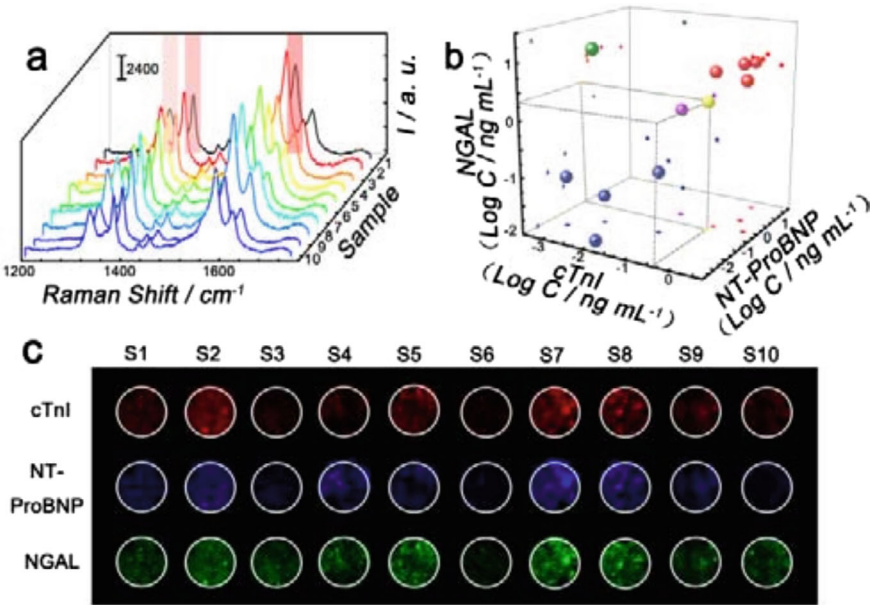



**Fig. 17.24** Clinical analysis of CRS biomarkers by the SERS immunoassay platform: **a** SERS spectra of 10 clinical serum samples. **b** Bubble chart of the diagnosis results of 10 clinical serum samples. **c** Optical barcodes of clinical serum samples using Raman mapping with the proposed method [122]

Just as the level of cTnI in human serum may significantly increase as the myocardial membrane ruptures, the creatine kinase-MB (CK-MB) is also associated with the AMI recurrence and infarct size. Liu et al. [123] proposed a single-track finger-pump microfluidic chip for simultaneous SERS detection of cTnI and CK-MB. The entire detection process takes only 5 min without the cumbersome syringe pump and enables multiple reagent addition and removal of the unbonded reactants. The microfluidic sensor employed "sandwich" immunoassays based on SERS nanoprobes, AMI biomarkers, and magnetic beads. It is possible to detect two cardiac biomarkers simultaneously in a single measurement, greatly simplifying the detection process and reducing the detection time. Magnetic beads with SERS nanoprobes were separated and captured in the microchamber by a round magnet integrated into the chip. Their results showed that the detection limits of cTnI and CK-MB could reach 0.01 ng $mL^{-1}$ and match the clinical threshold values for AMI biomarkers (Fig. 17.25).

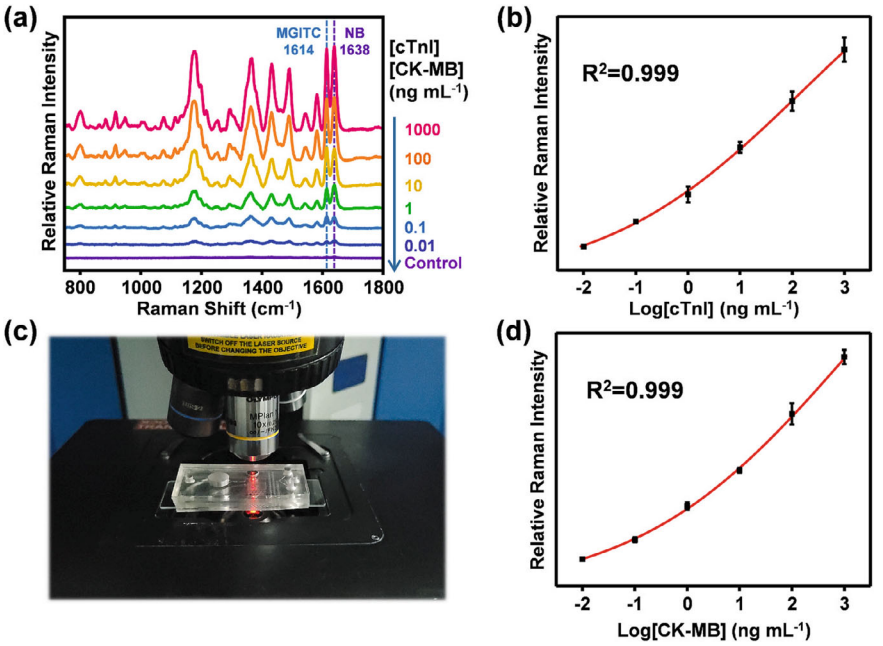



**Fig. 17.25** **a** The SERS spectra on the basis of cTnI and CK-MB concentrations on finger-pump microfluidic chip. The concentration ranges of cTnI and CK-MB were from 0.01 ng $mL^{-1}$ to 1000 ng $mL^{-1}$. Variations of SERS intensities of 1614 $cm^{-1}$ and 1638 $cm^{-1}$ peaks were utilized for cTnI and CK-MB quantitative analysis, respectively. **b**, **d** The calibration curves of dual AMI biomarkers. The standard deviations were from three measurements. **c** The photograph of microfluidic chip during SERS measurement [123]

### *17.3.7 Neurology*

The phosphorylation of tau protein at sites Ser(396, 404) (p-tau$^{396,404}$) and plasma p-tau$^{396,404}$ level appear to be a potentially promising biomarker of Alzheimer's disease (AD). The low abundance and easy degradation of p-tau in the plasma make the LFIA a suitable choice for POCT. Zhang et al. [124] developed a colorimetric and SERS dual-readout LFIA for the rapid, highly sensitive, and robust detection of plasma p-tau$^{396,404}$ levels. This LFIA realized a detection limit of 60 pg/mL by the naked eye or 3.8 pg/mL by SERS without cross-reacting with other tau species. More importantly, LFIA rapidly and accurately differentiated Alzheimer's patients from healthy controls, suggesting that it has the potential for clinical POCT in Alzheimer's diagnosis.

Electrochemical SERS (EC-SERS) is a promising technique for the diagnosis of trace amounts of neurotransmitters, and the miniaturization of EC-SERS devices is crucial for the early diagnosis of disease and POCT. Bai et al. [125] proposed a new type of EC-SERS sensor based on 3D microfluidic chips for the analysis of ascorbic acid in ultrasmall volumes. The microfluidic EC-SERS chip is fabricated by a ship-in-a-bottle technique based on hybrid laser processing. The working electrode is modified using silver/zinc oxide materials, enabling the formation of a unique "candy apple" structure. To assess the fabricated microfluidic EC-SERS chips, ascorbic acid is analysed to elucidate its redox reaction. Significantly, a sub-10 μL volume of analyte solution was sufficient for EC-SERS analysis, which is several orders smaller in volume than the requirements of current EC-SERS devices. Such EC-SERS chips could be used in portable and smart analysers for next-generation biomedicine. Figure 17.26 shows an overall view of the microfluidic EC-SERS chip. The size of the glass substrate was $10 \times 10 \times 2$ mm$^3$, on which three electrodes were embedded. The chip was connected to an EC workstation using copper conductive tape, as shown in Fig. 17.26c, and then the Raman signals were collected using a conventional Raman spectrometer. Figure 17.26d–f shows the results of ascorbic acid analysis and the schematic of its oxidation on the working electrode when applying a positive potential. $10^{-6}$ M ascorbic acid in a buffer solution with a total volume of 10 μL was injected into the microfluidic chip. Positive potentials were applied to the working electrode from the open circuit potential to + 1 V, and then SERS spectra were acquired at each potential as shown in Fig. 17.26d. With the increase in the potential to + 1 V, the Raman scattering intensity of ascorbic acid increased, which means that the ascorbic acid molecules in the solution moved towards the working electrode to gather on it. The increase in Raman scattering intensity with potential is also due to the charge transfer between the ascorbic acid and silver/zinc oxide nanostructures, since high potential facilitates charge transfer. In addition, since Ag–O bonds are induced by the oxidation of ascorbic acid on the silver surface, the ratio of $(Ag–O)_{vibration}/(C–C)_{ring\text{-}stretching}$ is more prominent than the ratio of $(C=O)_{stretching}/(C–C)_{ring\text{-}stretching}$.

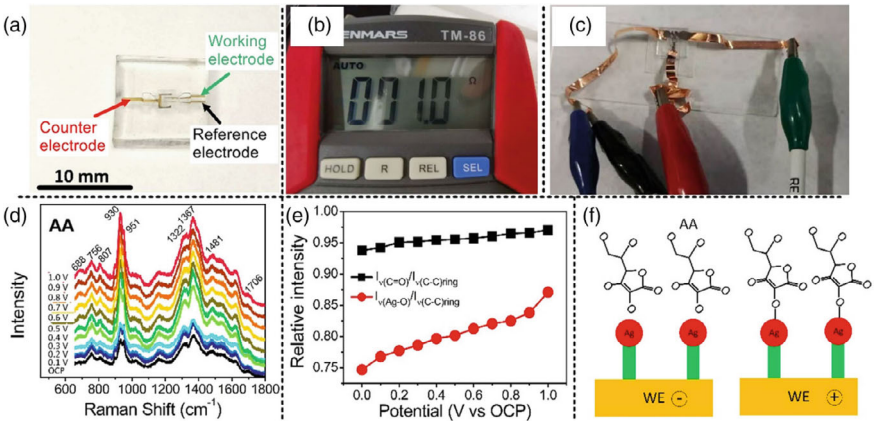



**Fig. 17.26** Analysis of neurotransmitters using microfluidic EC-SERS chips. **a** Overall view photograph of microfluidic EC-SERS chip with a three-electrode system. **b** The resistivity of the electrode measured by a multimetre. **c** EC-SERS analysis scheme using microfluidic EC-SERS chip. **d** SERS spectra of ascorbic acid at the concentration of $10^{-6}$ M with different potentials applied to the working electrode. **e** Variation of the intensity ratio of Raman vibrations at $(C{=}O)_{stretching}/(C–C)_{ring\ stretching}$ (blue line) and $(Ag–O)_{vibration}/(C–C)_{ring}$ (red line) with applied potential. f. Schematic of ascorbic acid oxidation on the working electrode [125]

Richard et al. [126] reported the development and testing of an optofluidic device for the rapid and label-free detection via SERS of picomolar concentrations of *N*-acetylasparate in finger-prick blood samples, which is released immediately from the central nervous system after traumatic brain injury (TBI). The SERS-active substrate of the device consists of electrohydrodynamically fabricated submicrometre pillars covered with a plasmon-active nanometric gold layer, integrated in an optofluidic chip. The simplicity, sensitivity, and robustness of SERS-integrated optofluidic technology might eventually help the triaging of TBI patients and assist clinical decision making at point-of-care settings.

Although SERS shows great promise for in vivo measurement of neurochemicals due to its excellent multiplexing ability to discriminate molecules with very similar chemical structures when utilized to detect secretion near living neurons, the toxicity of metallic nanoparticles required for SERS enhancement to the physiological environment remains an area of concern [127].

### *17.3.8 Molecular Biology*

SERS in translational medicine is usually combined with protein quantification, protein localization, PCR and other technologies, and utilized to detect exosomes, mitochondria, cell apoptosis, and cell differentiation [128]. ELISA, for example, has moderate sensitivity and relies on enzyme activity, which make it impossible to

reliably and inexpensively detect trace targets [129]. Instead of the traditional natural enzyme tags in an ELISA, SERS tags can be used as nanozymes to label the antibody [130].

One application of interest is the use of SERS in multiplexed optical readout following PCR. However, the reported PCR-SERS assays require endpoint mixing with a plasmonic nanoparticle solution for detection, thus adding manual steps and preventing real-time, quantitative PCR. Restaino et al. [131] detailed a real-time PCR-SERS thermoplastic microsystem that allows simultaneous nucleic acid amplification and product extraction and mixing with a SERS-active silver colloid for real-time detection (Fig. 17.27). Specifically, a laser cut thermoplastic fluidic chip has been devised to utilize a dialysis membrane capable of isolating a PCR reaction from the silver colloid. As the reaction progresses, a Raman-reporter-labelled DNA probe is degraded, liberating the reporter from the probe DNA, allowing to cross the size-restricting dialysis membrane into the SERS-active colloid, where the accumulating reporter can be measured in real time. They demonstrated that this system is capable of real-time and single-well multiplexed readout of a PCR reaction to simultaneously detect two biomarker genes for methicillin-resistant *S. aureus* (MRSA).

Wang et al. [132] reported a lateral flow microRNA-21 biosensing platform based on a portable SERS reader coupled with a catalytic hairpin assembly signal amplification strategy. Hairpin DNA probes were anchored on Au@Ag nanotags, and the presence of microRNA-21 triggered the formation of numerous double-stranded DNAs along with the exposure of biotin groups. By this means, the target was recycled, and signal amplification was achieved. The Au@Ag nanoprobes with exposed biotin can be captured on the test line via its interaction with streptavidin. By scanning the strip with a portable SERS reader, the sensitive quantification of microRNA-21

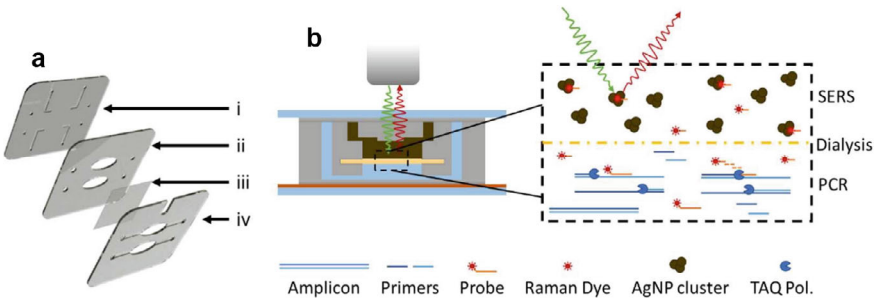



**Fig. 17.27** Illustration of dialysis driven PCR-SERS device. **a** Rendering of an exploded, 3-layer PCR-SERS device. The top layer (i) contains inlets and outlets as well as channels for the SERS well in the second layer (ii). A dialysis membrane (iii) is embedded between the middle and bottom layers (iv) to separate the SERS well from the PCR wells in the bottom layer. Holes passing through the top and middle layers enable fluid to enter channels engraved on the underside of the bottom layer. **b** Schematic of device function during a probe-based qPCR assay, in which hybridization of a dye labelled probe is degraded during extension of the PCR primer by Taq polymerase. Degradation of the probe liberates the dye, which can freely pass through membrane pores (20 kDa cutoff) to the AgNP colloid for SERS detection [131]

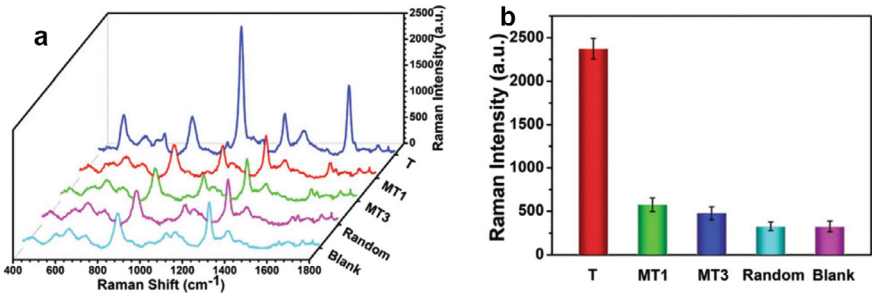



**Fig. 17.28** **a** SERS spectra with 0.1 nM microRNA-21 (T), 1 nM one-base mismatch sequence (MT1), 1 nM three-base mismatch sequence (MT3), 1 nM random sequence (random) or a blank. **b** SERS intensity at 1079 $cm^{-1}$ with 0.1 nM T, 1 nM MT1, 1 nM MT3, 1 nM Random and blank [132]

was realized with a detection limit as low as 84 fM. In Fig. 17.28, the selectivity investigation of the proposed biosensor is illustrated showing the capabilities in one-base mismatch specificity. The proposed strategy was employed to detect the target in a serum sample, demonstrating its great potential in amplified POCT biosensing for clinical diagnosis.

Preeclampsia is a condition that affects women during pregnancy. It is a leading cause of maternal and infant death worldwide and is typically detected in the second trimester or later. Predicting preeclampsia at an early stage is one of the most important goals of maternal–foetal medicine, ideally at the point-of-care. Since microRNA-20a shows an upregulation in the blood samples of the first trimester of preeclamptic pregnancies when compared to healthy mothers, Chaturvedi et al. [133] developed a dual capture probe sandwich assay sensitive to miR-20a that used SERS-active gold nanoparticles. The assay was translated to a lateral flow paper fluidic device, for potential low cost and ease of use in low-resource settings. Each paper layer has different pore sizes and features an array of buffers that store nanoparticle conjugates, guide flow, and reduce non-specific binding. Using a handheld Raman reader with a 638 nm excitation laser, reliable SERS detection of miR-20a was shown with resolutions down to 1 nM. Colorimetric detection of these concentrations using the RGB pixels from scanning the test line was carried out as well, showing multi-modal detection to potentially enhance specificity for this early epigenetic biomarker.

## 17.4 Conclusions and Prospects

Herein, we reviewed the development of SERS-based microdevices for point-of-care testing in the last decade. Three different types of SERS-based microdevice platforms, namely microfluidic devices, lateral flow immunoassay strips, and three-dimensional nanostructured substrates, have been introduced. Microfluidic devices provide several advantages, including reduced sample volumes, programmable sample handling, and automatic assay processes. Microfluidic platforms have been

coupled with SERS because of their ability to solve the heterogeneous binding problem of analytes to the surface by mixing the analyte homogeneously within the chambers or channels, thus enabling automatic high-throughput on-chip detection [6]. SERS-based LFIA strips can help address the limitation related to detection sensitivity and limit of quantification capability inherent to conventional LFIA strips [56]. To accelerate the clinical translation of SERS-based LFIAs to the area of in vitro diagnostics, however, more stable and reproducible SERS nanotags are crucial. For instance, high temperatures in tropical regions induce the desorption of Raman reporter molecules from the AuNP surface and impair their performance as SERS nanotags [59, 84]. 3D plasmonic nanostructured substrates with uniform nanogaps have been developed to circumvent irregularities in hot-spot formation in aggregates of nanoparticle colloids. For POCT in the medical field, a portable Raman system, which can be integrated with miniaturized microdevice platforms, is essential. Additionally, a close collaboration between researchers and clinical doctors is important for the fast translation from laboratory to bedside [59, 67].

Another issue that needs to be addressed when using SERS outside the confines of a controlled laboratory environment is the ability to accurately detect the concentration of a biomolecule in a complex biological sample without having to build a calibration model. For ideal POCT, the sample will be run on the LFIA, the strip analysed within minutes, and the intensity of the SERS signal as read will be directly related to the concentration. This requires a prior calibration model to be built that takes into account the sample component matrix and mitigate against any background interference from the sample matrix. Therefore, advanced data processing techniques, including neural networks and machine learning algorithms, are required for efficient, high-throughput analysis of clinical SERS data, which would relate the SERS signal to the concentration and produce an easily interpretable result for the end user [56, 134].

Although there are challenges that need to be overcome, it is expected that SERS-based assay platforms, composed of a miniaturized microdevice integrated with a portable Raman system, constitute a conceptually novel POCT tool in all fields of medicine.

**Acknowledgements** The Deutsche Forschungsgemeinschaft (DFG, German Research Foundation) supported this work under grant 465289819. We thank BMBF for financial support of the EU-LAK project ABSarbo (01DN23003). Funded by the Deutsche Forschungsgemeinschaft (DFG, German Research Foundation) under Germany´s Excellence Strategy—EXC 2051—Project-ID 390713860. The authors acknowledge financial support from the European Union's Horizon 2020 research and innovation programme under the Marie Sklodowska-Curie grant agreement No 860185 (PHAST = Photonics for Healthcare: multiscAle cancer diagnosiS and Therapy).

## References


1. L. Wang, X. Wang, L. Cheng, S. Ding, G. Wang, J. Choo and L. Chen, SERS-based test strips: Principles, designs and applications. Biosensors and Bioelectronics **189**, 113360 (2021)
2. P. K. Drain, E. P. Hyle, F. Noubary, K. A. Freedberg, D. Wilson, W. R. Bishai, W. Rodriguez and I. V. Bassett, Diagnostic point-of-care tests in resource-limited settings. The Lancet infectious diseases **14**, 239–249 (2014)
3. K. J. Land, D. I. Boeras, X.-S. Chen, A. R. Ramsay and R. W. Peeling, REASSURED diagnostics to inform disease control strategies, strengthen health systems and improve patient outcomes. Nature microbiology **4**, 46–54 (2019)
4. C. F. Markwalter, A. G. Kantor, C. P. Moore, K. A. Richardson and D. W. Wright, Inorganic complexes and metal-based nanomaterials for infectious disease diagnostics. Chemical reviews **119**, 1456–1518 (2018)
5. D. Quesada-González and A. Merkoçi, Nanomaterial-based devices for point-of-care diagnostic applications. Chemical Society Reviews **47**, 4697–4709 (2018)
6. H. Torul, E. Yıldırım and U. Tamer, Microfluidic platforms based on SERS imaging and their point-of-care applications. Current Opinion in Biomedical Engineering, 100510 (2023).
7. S. Nayak, N. R. Blumenfeld, T. Laksanasopin and S. K. Sia, Point-of-Care Diagnostics: Recent Developments in a Connected Age. Analytical Chemistry **89**, 102–123 (2017)
8. B. Chatterjee, N. Kalyani, S. Das, A. Anand and T. K. Sharma, Nano-realm for point-of-care (POC) bacterial diagnostics, in *Methods in Microbiology*, Edited by, (Elsevier, 2019), pp. 19–42.
9. T. Lee, M. Mohammadniaei, H. Zhang, J. Yoon, H. K. Choi, S. Guo, P. Guo and J. W. Choi, Single functionalized pRNA/gold nanoparticle for ultrasensitive microRNA detection using electrochemical surface-enhanced Raman spectroscopy. Advanced Science **7**, 1902477 (2020)
10. M. F. Cardinal, E. Vander Ende, R. A. Hackler, M. O. McAnally, P. C. Stair, G. C. Schatz and R. P. Van Duyne, Expanding applications of SERS through versatile nanomaterials engineering. Chemical Society Reviews **46**, 3886–3903 (2017).
11. Y. Wu, N. Choi, H. Chen, H. Dang, L. Chen and J. Choo, Performance evaluation of surface-enhanced Raman scattering–polymerase chain reaction sensors for future use in sensitive genetic assays. Analytical chemistry **92**, 2628–2634 (2020)
12. Y. L. Wong, W. C. M. Kang, M. Reyes, J. W. P. Teo and J. C. Y. Kah, Rapid detection of carbapenemase-producing enterobacteriacae based on surface-enhanced Raman spectroscopy with gold nanostars. ACS infectious diseases **6**, 947–953 (2020)
13. J. Hwang, S. Lee and J. Choo, Application of a SERS-based lateral flow immunoassay strip for the rapid and sensitive detection of staphylococcal enterotoxin B. Nanoscale **8**, 11418–11425 (2016)
14. J. Kelly, R. Patrick, S. Patrick and S. E. Bell, Surface-Enhanced Raman Spectroscopy for the Detection of a Metabolic Product in the Headspace Above Live Bacterial Cultures. Angewandte Chemie International Edition **57**, 15686–15690 (2018)
15. I. Bruzas, B. E. Brinson, Z. Gorunmez, W. Lum, E. Ringe and L. Sagle, Surface-enhanced Raman spectroscopy of fluid-supported lipid bilayers. ACS applied materials & interfaces **11**, 33442–33451 (2019)
16. Y. Hang, J. Boryczka and N. Wu, Visible-light and near-infrared fluorescence and surface-enhanced Raman scattering point-of-care sensing and bio-imaging: A review. Chemical Society Reviews **51**, 329–375 (2022)
17. S. Lin, Z. Cheng, Q. Li, R. Wang and F. Yu, Toward sensitive and reliable surface-enhanced Raman scattering imaging: From rational design to biomedical applications. ACS sensors **6**, 3912–3932 (2021)
18. M. E. Berry, H. Kearns, D. Graham and K. Faulds, Surface enhanced Raman scattering for the multiplexed detection of pathogenic microorganisms: towards point-of-use applications. Analyst **146**, 6084–6101 (2021)

19. A. J. Driscoll, M. H. Harpster and P. A. Johnson, The development of surface-enhanced Raman scattering as a detection modality for portable in vitro diagnostics: progress and challenges. Physical Chemistry Chemical Physics **15**, 20415–20433 (2013)
20. H. K. Lee, Y. H. Lee, C. S. L. Koh, G. C. Phan-Quang, X. Han, C. L. Lay, H. Y. F. Sim, Y.-C. Kao, Q. An and X. Y. Ling, Designing surface-enhanced Raman scattering (SERS) platforms beyond hotspot engineering: emerging opportunities in analyte manipulations and hybrid materials. Chemical Society Reviews **48**, 731–756 (2019)
21. J. Guo, Y. Liu, H. Ju and G. Lu, From lab to field: Surface-enhanced Raman scattering-based sensing strategies for on-site analysis. TrAC Trends in Analytical Chemistry **146**, 116488 (2022)
22. X. Zhang, S. Liu, X. Song, H. Wang, J. Wang, Y. Wang, J. Huang and J. Yu, Robust and universal SERS sensing platform for multiplexed detection of Alzheimer's disease core biomarkers using PAapt-AuNPs conjugates. Acs Sensors **4**, 2140–2149 (2019)
23. J. Cao, D. Zhao and Y. Qin, Novel strategy for fabrication of sensing layer on thiol-functionalized fiber-optic tapers and their application as SERS probes. Talanta **194**, 895–902 (2019)
24. D. Wu, Y. Chen, S. Hou, W. Fang and H. Duan, Intracellular and Cellular Detection by SERS-Active Plasmonic Nanostructures. ChemBioChem **20**, 2432–2441 (2019)
25. J. S. Y. Low, T. M. Thevarajah, S. W. Chang, B. T. Goh and S. M. Khor, Biosensing based on surface-enhanced Raman spectroscopy as an emerging/next-generation point-of-care approach for acute myocardial infarction diagnosis. Critical reviews in biotechnology **40**, 1191–1209 (2020)
26. B. Yang, S. Jin, Y. Wang, H. Bao, J. Sun, L. Chen, H. Chung and Y. M. Jung, Disease-related proteins determination based on surface-enhanced Raman spectroscopy. Applied Spectroscopy Reviews **54**, 856–872 (2019)
27. D. Lin, R. Dong, P. Li, S. Li, M. Ge, Y. Zhang, L. Yang and W. Xu, A novel SERS selective detection sensor for trace trinitrotoluene based on meisenheimer complex of monoethanolamine molecule. Talanta **218**, 121157 (2020)
28. J. Sun, L. Gong, W. Wang, Z. Gong, D. Wang and M. Fan, Surface-enhanced Raman spectroscopy for on-site analysis: a review of recent developments. Luminescence **35**, 808–820 (2020)
29. S. X. Leong, Y. X. Leong, E. X. Tan, H. Y. F. Sim, C. S. L. Koh, Y. H. Lee, C. Chong, L. S. Ng, J. R. T. Chen and D. W. C. Pang, Noninvasive and point-of-care surface-enhanced Raman scattering (SERS)-based breathalyzer for mass screening of coronavirus disease 2019 (COVID-19) under 5 min. ACS nano **16**, 2629–2639 (2022)
30. V. Tran, B. Walkenfort, M. König, M. Salehi and S. Schlücker, Rapid, quantitative, and ultrasensitive point-of-care testing: A portable SERS reader for lateral flow assays in clinical chemistry. Angewandte Chemie International Edition **58**, 442–446 (2019)
31. X. Liu, J. Guo, Y. Li, B. Wang, S. Yang, W. Chen, X. Wu, J. Guo and X. Ma, SERS substrate fabrication for biochemical sensing: Towards point-of-care diagnostics. Journal of Materials Chemistry B **9**, 8378–8388 (2021)
32. X. Meng, L. Qiu, G. Xi, X. Wang and L. Guo, Smart design of high-performance surface-enhanced Raman scattering substrates. SmartMat **2**, 466–487 (2021)
33. C. Li, Y. Huang, X. Li, Y. Zhang, Q. Chen, Z. Ye, Z. Alqarni, S. E. Bell and Y. Xu, Towards practical and sustainable SERS: A review of recent developments in the construction of multifunctional enhancing substrates. Journal of Materials Chemistry C **9**, 11517–11552 (2021)
34. X. Wang, E. Zhang, H. Shi, Y. Tao and X. Ren, Semiconductor-based surface enhanced Raman scattering (SERS): from active materials to performance improvement. Analyst **147**, 1257–1272 (2022)
35. H. Y. Lin, W. R. Chen, L. C. Lu, H. L. Chen, Y. H. Chen, M. Pan, C. c. Chen, C. Chen, T. H. Yen and D. Wan, Direct Thermal Growth of Gold Nanopearls on 3D Interweaved Hydrophobic Fibers as Ultrasensitive Portable SERS Substrates for Clinical Applications. Small, 2207404 (2023).

36. J. Perumal, Y. Wang, A. B. E. Attia, U. Dinish and M. Olivo, Towards a point-of-care SERS sensor for biomedical and agri-food analysis applications: A review of recent advancements. Nanoscale **13**, 553–580 (2021)
37. J. F. Betz, W. Y. Wei, Y. Cheng, I. M. White and G. W. Rubloff, Simple SERS substrates: powerful, portable, and full of potential. Physical Chemistry Chemical Physics **16**, 2224–2239 (2014)
38. K. Ge, Y. Hu and G. Li, Recent Progress on Solid Substrates for Surface-Enhanced Raman Spectroscopy Analysis. Biosensors **12**, 941 (2022)
39. Z. Ye, C. Li, Q. Chen, Y. Xu and S. E. Bell, Self-assembly of colloidal nanoparticles into 2D arrays at water–oil interfaces: rational construction of stable SERS substrates with accessible enhancing surfaces and tailored plasmonic response. Nanoscale **13**, 5937–5953 (2021)
40. Z. Cao, P. He, T. Huang, S. Yang, S. Han, X. Wang and G. Ding, Plasmonic coupling of AgNPs near graphene edges: A cross-section strategy for high-performance SERS sensing. Chemistry of Materials **32**, 3813–3822 (2020)
41. C. Serafinelli, A. Fantoni, E. C. Alegria and M. Vieira, Plasmonic metal nanoparticles hybridized with 2D nanomaterials for SERS detection: A review. Biosensors **12**, 225 (2022)
42. X. Liang, N. Li, R. Zhang, P. Yin, C. Zhang, N. Yang, K. Liang and B. Kong, Carbon-based SERS biosensor: From substrate design to sensing and bioapplication. NPG Asia Materials **13**, 8 (2021)
43. Z. Deng, P. Wen, N. Wang and B. Peng, Preparation of hierarchical superhydrophobic melamine-formaldehyde/Ag nanocomposite arrays as surface-enhanced Raman scattering substrates for ultrasensitive and reproducible detection of biomolecules. Sensors and Actuators B: Chemical **288**, 20–26 (2019)
44. R. Peng, T. Zhang, S. Yan, Y. Song, X. Liu and J. Wang, Recent Development and Applications of Stretchable SERS Substrates. Nanomaterials **13**, 2968 (2023)
45. H. Liu, Y. He and K. Cao, Flexible surface-enhanced Raman scattering substrates: A review on constructions, applications, and challenges. Advanced Materials Interfaces **8**, 2100982 (2021)
46. Z. Li, X. Huang and G. Lu, Recent developments of flexible and transparent SERS substrates. Journal of Materials Chemistry C **8**, 3956–3969 (2020)
47. S. Park, J. Lee and H. Ko, Transparent and flexible surface-enhanced Raman scattering (SERS) sensors based on gold nanostar arrays embedded in silicon rubber film. ACS applied materials & interfaces **9**, 44088–44095 (2017)
48. X. Gao, H. Wu, Z. Hao, X. Ji, X. Lin, S. Wang and Y. Liu, A multifunctional plasmonic chip for bacteria capture, imaging, detection, and in situ elimination for wound therapy. Nanoscale **12**, 6489–6497 (2020)
49. L. Li and W. S. Chin, Rapid fabrication of a flexible and transparent Ag nanocubes@ PDMS film as a SERS substrate with high performance. ACS applied materials & interfaces **12**, 37538–37548 (2020)
50. V. Eskandari, H. Sahbafar, L. Zeinalizad, R. Marashipour and A. Hadi, A review of paper-based substrates as surface-enhanced raman spectroscopy (SERS) biosensors and microfluidic paper-based SERS platforms. Journal of Computational Applied Mechanics **53**, 142–156 (2022)
51. M. L. Mekonnen, Y. A. Workie, W.-N. Su and B. J. Hwang, Plasmonic paper substrates for point-of-need applications: recent developments and fabrication methods. Sensors and Actuators B: Chemical **345**, 130401 (2021)
52. H. S. Siebe, Q. Chen, X. Li, Y. Xu, W. R. Browne and S. E. Bell, Filter paper based SERS substrate for the direct detection of analytes in complex matrices. Analyst **146**, 1281–1288 (2021)
53. M. Park, H. Jung, Y. Jeong and K.-H. Jeong, Plasmonic schirmer strip for human tear-based gouty arthritis diagnosis using surface-enhanced Raman scattering. ACS nano **11**, 438–443 (2017)
54. C. Han, Y. Li, Q. Jia, L. H. Bradley, Y. Gan, Y. Yao, L. Qu, H. Li and Y. Zhao, On-demand fabrication of surface-enhanced Raman scattering arrays by pen writing, and their application to the determination of melamine in milk. Microchimica Acta **184**, 2909–2917 (2017)

55. N. Godoy, D. García-Lojo, F. Sigoli, J. Pérez-Juste, I. Pastoriza-Santos and I. Mazali, Ultrasensitive inkjet-printed based SERS sensor combining a high-performance gold nanosphere ink and hydrophobic paper. Sensors and Actuators B: Chemical **320**, 128412 (2020)
56. S. Sloan-Dennison, E. O'Connor, J. W. Dear, D. Graham and K. Faulds, Towards quantitative point of care detection using SERS lateral flow immunoassays. Analytical and bioanalytical chemistry **414**, 4541–4549 (2022)
57. Y. Liu, L. Zhan, Z. Qin, J. Sackrison and J. C. Bischof, Ultrasensitive and highly specific lateral flow assays for point-of-care diagnosis. ACS nano **15**, 3593–3611 (2021)
58. J. H. Soh, H.-M. Chan and J. Y. Ying, Strategies for developing sensitive and specific nanoparticle-based lateral flow assays as point-of-care diagnostic device. Nano Today **30**, 100831 (2020)
59. K. Kim, L. Kashefi-Kheyrabadi, Y. Joung, K. Kim, H. Dang, S. G. Chavan, M.-H. Lee and J. Choo, Recent advances in sensitive surface-enhanced Raman scattering-based lateral flow assay platforms for point-of-care diagnostics of infectious diseases. Sensors and Actuators B: Chemical **329**, 129214 (2021)
60. H. Ye, Y. Liu, L. Zhan, Y. Liu and Z. Qin, Signal amplification and quantification on lateral flow assays by laser excitation of plasmonic nanomaterials. Theranostics **10**, 4359 (2020)
61. J. Guo, S. Chen, J. Guo and X. Ma, Nanomaterial labels in lateral flow immunoassays for point-of-care-testing. Journal of Materials Science & Technology **60**, 90–104 (2021)
62. A. Ali, E. E. Nettey-Oppong, E. Effah, C. Y. Yu, R. Muhammad, T. A. Soomro, K. M. Byun and S. H. Choi, Miniaturized Raman instruments for SERS-based point-of-care testing on respiratory viruses. Biosensors **12**, 590 (2022)
63. O. Clarke, B. Goodall, H. Hui, N. Vats and C. Brosseau, Development of a SERS-based rapid vertical flow assay for point-of-care diagnostics. Analytical chemistry **89**, 1405–1410 (2017)
64. S.-M. Yang, S. Lv, W. Zhang and Y. Cui, Microfluidic point-of-care (POC) devices in early diagnosis: A review of opportunities and challenges. Sensors **22**, 1620 (2022)
65. B. Han, Y.-L. Zhang, L. Zhu, X.-H. Chen, Z.-C. Ma, X.-L. Zhang, J.-N. Wang, W. Wang, Y.-Q. Liu and Q.-D. Chen, Direct laser scribing of AgNPs@ RGO biochip as a reusable SERS sensor for DNA detection. Sensors and Actuators B: Chemical **270**, 500–507 (2018)
66. M. Adampourezare, M. Hasanzadeh and F. Seidi, Microfluidic assisted recognition of miRNAs towards point-of-care diagnosis: Technical and analytical overview towards biosensing of short stranded single non-coding oligonucleotides. Biomedicine & Pharmacotherapy **153**, 113365 (2022)
67. H. Chen, A. Das, L. Bi, N. Choi, J.-I. Moon, Y. Wu, S. Park and J. Choo, Recent advances in surface-enhanced Raman scattering-based microdevices for point-of-care diagnosis of viruses and bacteria. Nanoscale **12**, 21560–21570 (2020)
68. K. Kant and S. Abalde-Cela, Surface-enhanced Raman scattering spectroscopy and microfluidics: Towards ultrasensitive label-free sensing. Biosensors **8**, 62 (2018)
69. G. Liu, Z. Mu, J. Guo, K. Shan, X. Shang, J. Yu and X. Liang, Surface-enhanced Raman scattering as a potential strategy for wearable flexible sensing and point-of-care testing non-invasive medical diagnosis. Frontiers in Chemistry **10**, 1060322 (2022)
70. L. Liu, P. Martinez Pancorbo, T. H. Xiao, S. Noguchi, M. Marumi, H. Segawa, S. Karhadkar, J. Gala de Pablo, K. Hiramatsu and Y. Kitahama, Highly scalable, wearable surface-enhanced Raman spectroscopy. Advanced Optical Materials **10**, 2200054 (2022).
71. K. Zhu, K. Yang, Y. Zhang, Z. Yang, Z. Qian, N. Li, L. Li, G. Jiang, T. Wang and S. Zong, Wearable SERS sensor based on omnidirectional plasmonic nanovoids array with ultra-high sensitivity and stability. Small **18**, 2201508 (2022)
72. W. Wang, Y. Chen, C. Xiao, S. Xiao, C. Wang, Q. Nie, P. Xu, J. Chen, R. You and G. Zhang, Flexible SERS wearable sensor based on nanocomposite hydrogel for detection of metabolites and pH in sweat. Chemical Engineering Journal **474**, 145953 (2023)
73. M. A. H. Chowdhury, N. Tasnim, M. Hossain and A. Habib, Flexible, stretchable, and single-molecule-sensitive SERS-active sensor for wearable biosensing applications. RSC advances **13**, 20787–20798 (2023)

74. M. Zhang, Y. Lu, L. Zhang, X. Xu, B. Li, X. Zhao, X. Yan, C. Wang, P. Sun and X. Liu, Flexible and wearable glove-based SERS sensor for rapid sampling and sensitive detection of controlled drugs. Sensors and Actuators B: Chemical **386**, 133738 (2023)
75. Y. Ye, Y. Ge, Q. Zhang, M. Yuan, Y. Cai, K. Li, Y. Li, R. Xie, C. Xu and D. Jiang, Smart contact lens with dual-sensing platform for monitoring intraocular pressure and matrix metalloproteinase-9. Advanced Science **9**, 2104738 (2022)
76. S. Mabbott, S. C. Fernandes, M. Schechinger, G. L. Cote, K. Faulds, C. R. Mace and D. Graham, Detection of cardiovascular disease associated miR-29a using paper-based microfluidics and surface enhanced Raman scattering. Analyst **145**, 983–991 (2020)
77. W. A. Hassanain, J. Spoors, C. L. Johnson, K. Faulds, N. Keegan and D. Graham, Rapid ultra-sensitive diagnosis of clostridium difficile infection using a SERS-based lateral flow assay. Analyst **146**, 4495–4505 (2021)
78. M. Sánchez-Purrà, M. Carré-Camps, H. de Puig, I. Bosch, L. Gehrke and K. Hamad-Schifferli, Surface-enhanced Raman spectroscopy-based sandwich immunoassays for multiplexed detection of Zika and Dengue viral biomarkers. ACS infectious diseases **3**, 767–776 (2017)
79. Y. Wang, Q. Ruan, Z.-C. Lei, S.-C. Lin, Z. Zhu, L. Zhou and C. Yang, Highly sensitive and automated surface enhanced Raman scattering-based immunoassay for H5N1 detection with digital microfluidics. Analytical chemistry **90**, 5224–5231 (2018)
80. A. Kamińska, E. Witkowska, K. Winkler, I. Dzięcielewski, J. L. Weyher and J. Waluk, Detection of Hepatitis B virus antigen from human blood: SERS immunoassay in a microfluidic system. Biosensors and bioelectronics **66**, 461–467 (2015)
81. J. Jeon, N. Choi, H. Chen, J.-I. Moon, L. Chen and J. Choo, SERS-based droplet microfluidics for high-throughput gradient analysis. Lab on a Chip **19**, 674–681 (2019)
82. S. H. Lee, J. Hwang, K. Kim, J. Jeon, S. Lee, J. Ko, J. Lee, M. Kang, D. R. Chung and J. Choo, Quantitative serodiagnosis of scrub typhus using surface-enhanced Raman scattering-based lateral flow assay platforms. Analytical chemistry **91**, 12275–12282 (2019)
83. X. Fu, Z. Cheng, J. Yu, P. Choo, L. Chen and J. Choo, A SERS-based lateral flow assay biosensor for highly sensitive detection of HIV-1 DNA. Biosensors and Bioelectronics **78**, 530–537 (2016)
84. J. Jeon, S. H. Lee, Y. Joung, K. Kim, N. Choi and J. Choo, Improvement of reproducibility and thermal stability of surface-enhanced Raman scattering-based lateral flow assay strips using silica-encapsulated gold nanoparticles. Sensors and Actuators B: Chemical **321**, 128521 (2020)
85. X. Wang, N. Choi, Z. Cheng, J. Ko, L. Chen and J. Choo, Simultaneous detection of dual nucleic acids using a SERS-based lateral flow assay biosensor. Analytical chemistry **89**, 1163–1169 (2017)
86. D. Zhang, L. Huang, B. Liu, Q. Ge, J. Dong and X. Zhao, Rapid and ultrasensitive quantification of multiplex respiratory tract infection pathogen via lateral flow microarray based on SERS nanotags. Theranostics **9**, 4849 (2019)
87. M. B. Wabuyele and T. Vo-Dinh, Detection of human immunodeficiency virus type 1 DNA sequence using plasmonics nanoprobes. Analytical chemistry **77**, 7810–7815 (2005)
88. J.-H. Lee, B.-C. Kim, O. Byeung-Keun and J.-W. Choi, Rapid and sensitive determination of HIV-1 virus based on surface enhanced Raman spectroscopy. Journal of biomedical nanotechnology **11**, 2223–2230 (2015)
89. S. Yadav, S. Senapati, D. Desai, S. Gahlaut, S. Kulkarni and J. P. Singh, Portable and sensitive Ag nanorods based SERS platform for rapid HIV-1 detection and tropism determination. Colloids and Surfaces B: Biointerfaces **198**, 111477 (2021)
90. Y.-T. Yeh, K. Gulino, Y. Zhang, A. Sabestien, T.-W. Chou, B. Zhou, Z. Lin, I. Albert, H. Lu and V. Swaminathan, A rapid and label-free platform for virus capture and identification from clinical samples. Proceedings of the National Academy of Sciences **117**, 895–901 (2020)
91. D. Sebba, A. G. Lastovich, M. Kuroda, E. Fallows, J. Johnson, A. Ahouidi, A. N. Honko, H. Fu, R. Nielson and E. Carruthers, A point-of-care diagnostic for differentiating Ebola from endemic febrile diseases. Science translational medicine **10**, eaat0944 (2018).

92. S. Gahlaut, D. Savargaonkar, C. Sharan, S. Yadav, P. Mishra and J. Singh, SERS platform for dengue diagnosis from clinical samples employing a hand held Raman spectrometer. Analytical chemistry **92**, 2527–2534 (2020)
93. Y. Luo, M. Zhou, C. Fan, Y. Song, L. Wang, T. Xu and X. Zhang, Active enrichment of nanoparticles for ultra-trace point-of-care COVID-19 detection. Analytical Chemistry **95**, 5316–5322 (2023)
94. Y. Pang, N. Wan, L. Shi, C. Wang, Z. Sun, R. Xiao and S. Wang, Dual-recognition surface-enhanced Raman scattering (SERS) biosensor for pathogenic bacteria detection by using vancomycin-SERS tags and aptamer-Fe3O4@ Au. Analytica Chimica Acta **1077**, 288–296 (2019)
95. L. Shi, L. Xu, R. Xiao, Z. Zhou, C. Wang, S. Wang and B. Gu, Rapid, quantitative, high-sensitive detection of Escherichia coli O157: H7 by gold-shell silica-core nanospheres-based surface-enhanced Raman scattering lateral flow immunoassay. Frontiers in Microbiology **11**, 596005 (2020)
96. B. Krafft, A. Tycova, R. D. Urban, C. Dusny and D. Belder, Microfluidic device for concentration and SERS-based detection of bacteria in drinking water. Electrophoresis **42**, 86–94 (2021)
97. Y. Li, X. Liu, J. Guo, Y. Zhang, J. Guo, X. Wu, B. Wang and X. Ma, Simultaneous detection of inflammatory biomarkers by SERS nanotag-based lateral flow assay with portable cloud Raman spectrometer. Nanomaterials **11**, 1496 (2021)
98. S. Srivastav, A. Dankov, M. Adanalic, R. Grzeschik, V. Tran, S. Pagel-Wieder, F. Gessler, I. Spreitzer, T. Scholz and B. Schnierle, Rapid and sensitive SERS-based lateral flow test for SARS-CoV2-specific IgM/IgG antibodies. Analytical Chemistry **93**, 12391–12399 (2021)
99. X. Jia, Z. Liu, Y. Peng, G. Hou, W. Chen and R. Xiao, Automatic and sensitive detection of West Nile virus non-structural protein 1 with a portable SERS–LFIA detector. Microchimica Acta **188**, 206 (2021)
100. S. Singh, P. S. Podder, M. Russo, C. Henry and S. Cinti, Tailored point-of-care biosensors for liquid biopsy in the field of oncology. Lab on a Chip **23**, 44–61 (2023)
101. C.-F. Ning, L. Wang, Y.-F. Tian, B.-C. Yin and B.-C. Ye, Multiple and sensitive SERS detection of cancer-related exosomes based on gold–silver bimetallic nanotrepangs. Analyst **145**, 2795–2804 (2020)
102. L. Huang, Y. Zhu, C. Xu, Y. Cai, Y. Yi, K. Li, X. Ren, D. Jiang, Y. Ge and X. Liu, Noninvasive diagnosis of gastric cancer based on breath analysis with a tubular surface-enhanced Raman scattering sensor. ACS sensors **7**, 1439–1450 (2022)
103. T. Moisoiu, M. P. Dragomir, S. D. Iancu, S. Schallenberg, G. Birolo, G. Ferrero, D. Burghelea, A. Stefancu, R. G. Cozan and E. Licarete, Combined miRNA and SERS urine liquid biopsy for the point-of-care diagnosis and molecular stratification of bladder cancer. Molecular Medicine **28**, 39 (2022)
104. M. Keshavarz, P. Kassanos, B. Tan and K. Venkatakrishnan, Metal-oxide surface-enhanced Raman biosensor template towards point-of-care EGFR detection and cancer diagnostics. Nanoscale Horizons **5**, 294–307 (2020)
105. J. Lin and A. Wu, Surface-Enhanced Raman Spectrum of TiO 2 Nanoparticle for Biosensing (TiO 2 Nanoparticle Served as SERS Sensing Substrate). TiO2 Nanoparticles: Applications in Nanobiotechnology and Nanomedicine, 133–152 (2020).
106. J. Lin and A. Wu, SERS methods based on nanomaterials as a diagnostic tool of cancer. Nanomaterials in Diagnostic Tools and Devices, 189–211 (2020).
107. G. Chundayil Madathil, S. Iyer, K. Thankappan, G. S. Gowd, S. Nair and M. Koyakutty, A novel surface enhanced Raman catheter for rapid detection, classification, and grading of oral cancer. Advanced healthcare materials **8**, 1801557 (2019).
108. W. Li, H. Wei, N. Li, S. Li, Y. Liu, R. Liu, W. Zou, P. Hu, Z. Zhang and C. Wang, Rapid identification and quantification of diquat in biological fluids within 30 s using a portable Raman spectrometer. Biosensors and Bioelectronics **225**, 115083 (2023)

109. M. Shang, H. Wei, G. Gao, N. Li, W. Zou, R. Liu, M. Zhang, X. Meng, W. Chen and Y. Sun, A portable kit for rapid detection of bromadiolone in human blood and urine via surface-enhanced raman scattering coupled with salt-induced liquid-liquid phase separation. Sensors and Actuators B: Chemical **374**, 132809 (2023)
110. J. Xiao, J. Wang, Y. Luo, T. Xu and X. Zhang, Wearable Plasmonic Sweat Biosensor for Acetaminophen Drug Monitoring. ACS sensors **8**, 1766–1773 (2023)
111. R. Xiao, L. Lu, Z. Rong, C. Wang, Y. Peng, F. Wang, J. Wang, M. Sun, J. Dong and D. Wang, Portable and multiplexed lateral flow immunoassay reader based on SERS for highly sensitive point-of-care testing. Biosensors and Bioelectronics **168**, 112524 (2020)
112. D. Zhang, L. Huang, B. Liu, H. Ni, L. Sun, E. Su, H. Chen, Z. Gu and X. Zhao, Quantitative and ultrasensitive detection of multiplex cardiac biomarkers in lateral flow assay with core-shell SERS nanotags. Biosensors and Bioelectronics **106**, 204–211 (2018)
113. M. Sánchez-Purrà, B. Roig-Solvas, C. Rodriguez-Quijada, B. M. Leonardo and K. Hamad-Schifferli, Reporter selection for nanotags in multiplexed surface enhanced Raman spectroscopy assays. ACS omega **3**, 10733–10742 (2018)
114. N. Guirguis, A. X. Bertrand, C. F. Rose and S. Matoori, 175 Years of Bilirubin Testing: Ready for Point-of-Care? Advanced Healthcare Materials, 2203380 (2023).
115. X. Pan, L. Li, H. Lin, J. Tan, H. Wang, M. Liao, C. Chen, B. Shan, Y. Chen and M. Li, A graphene oxide-gold nanostar hybrid based-paper biosensor for label-free SERS detection of serum bilirubin for diagnosis of jaundice. Biosensors and Bioelectronics **145**, 111713 (2019)
116. L. Ouyang, L. Yao, R. Tang, X. Yang and L. Zhu, Biomimetic point-of-care testing of trace free bilirubin in serum by using glucose selective capture and surface-enhanced Raman spectroscopy. Sensors and Actuators B: Chemical **340**, 129941 (2021)
117. Z. Liu, D. Meng, G. Su, P. Hu, B. Song, Y. Wang, J. Wei, H. Yang, T. Yuan and B. Chen, Ultrafast Early Warning of Heart Attacks through Plasmon-Enhanced Raman Spectroscopy using Collapsible Nanofingers and Machine Learning. Small **19**, 2204719 (2023)
118. A. I. Saviñon-Flores, F. Saviñon-Flores, G. Trejo, E. Méndez, Ş. Ţălu, M. A. González-Fuentes and A. Méndez-Albores, A review of cardiac troponin I detection by surface enhanced Raman spectroscopy: Under the spotlight of point-of-care testing. Frontiers in Chemistry **10**, 1017305 (2022)
119. B. N. Khlebtsov, D. N. Bratashov, N. A. Byzova, B. B. Dzantiev and N. G. Khlebtsov, SERS-based lateral flow immunoassay of troponin I by using gap-enhanced Raman tags. Nano Research **12**, 413–420 (2019)
120. Z. Tan, Y. Zhang, B. D. Thackray and J. Ye, Improvement of surface-enhanced Raman scattering detection and imaging by multivariate curve resolution methods. Journal of Applied Physics **125** (2019).
121. N. G. Khlebtsov, L. Lin, B. N. Khlebtsov and J. Ye, Gap-enhanced Raman tags: fabrication, optical properties, and theranostic applications. Theranostics **10**, 2067 (2020)
122. Y. Su, S. Xu, J. Zhang, X. Chen, L.-P. Jiang, T. Zheng and J.-J. Zhu, Plasmon near-field coupling of bimetallic nanostars and a hierarchical bimetallic SERS "hot field": toward ultrasensitive simultaneous detection of multiple cardiorenal syndrome biomarkers. Analytical chemistry **91**, 864–872 (2018)
123. Y. Liu, R. Gao, Y. Zhuo, Y. Wang, H. Jia, X. Chen, Y. Lu, D. Zhang and L. Yu, Rapid simultaneous SERS detection of dual myocardial biomarkers on single-track finger-pump microfluidic chip. Analytica Chimica Acta **1239**, 340673 (2023)
124. L. Zhang, Y. Su, X. Liang, K. Cao, Q. Luo and H. Luo, Ultrasensitive and point-of-care detection of plasma phosphorylated tau in Alzheimer's disease using colorimetric and surface-enhanced Raman scattering dual-readout lateral flow assay. Nano Research, 1–11 (2023).
125. S. Bai, Y. Ma, K. Obata and K. Sugioka, Ultraminiaturized Microfluidic Electrochemical Surface-Enhanced Raman Scattering Chip for Analysis of Neurotransmitters Fabricated by Ship-in-a-Bottle Integration. Small Science **3**, 2200093 (2023)
126. J. J. Rickard, V. Di-Pietro, D. J. Smith, D. J. Davies, A. Belli and P. G. Oppenheimer, Rapid optofluidic detection of biomarkers for traumatic brain injury via surface-enhanced Raman spectroscopy. Nature biomedical engineering **4**, 610–623 (2020)

127. T. D. Payne, A. S. Moody, A. L. Wood, P. A. Pimiento, J. C. Elliott and B. Sharma, Raman spectroscopy and neuroscience: from fundamental understanding to disease diagnostics and imaging. Analyst **145**, 3461–3480 (2020)
128. H. Liu, X. Liu, L. Mo, C. Chen, H. Zhong, Z. Guo and Z. Liu, Progress in the development and application of transitional technology of surface-enhanced Raman spectroscopy. Colloid and Interface Science Communications **43**, 100443 (2021)
129. Q. Zhao, D. Lu, G. Zhang, D. Zhang and X. Shi, Recent improvements in enzyme-linked immunosorbent assays based on nanomaterials. Talanta **223**, 121722 (2021)
130. Y. Su, D. Wu, J. Chen, G. Chen, N. Hu, H. Wang, P. Wang, H. Han, G. Li and Y. Wu, Ratiometric surface enhanced Raman scattering immunosorbent assay of allergenic proteins via covalent organic framework composite material based nanozyme tag triggered Raman signal "turn-on" and amplification. Analytical chemistry **91**, 11687–11695 (2019)
131. S. Restaino and I. White, Real-time multiplexed PCR using surface enhanced Raman spectroscopy in a thermoplastic chip. Lab on a Chip **18**, 832–839 (2018)
132. W. Wang, Y. Li, A. Nie, G.-C. Fan and H. Han, A portable SERS reader coupled with catalytic hairpin assembly for sensitive microRNA-21 lateral flow sensing. Analyst **146**, 848-854 (2021)
133. N. Chaturvedi, A. Kunkel, M. Schechinger, S. Mabbott, M. Choudhury and G. L. Coté, Optical Diagnostics and Sensing XXIII: Toward Point-of-Care Diagnostics, 2023.
134. F. Lussier, V. Thibault, B. Charron, G. Q. Wallace and J.-F. Masson, Deep learning and artificial intelligence methods for Raman and surface-enhanced Raman scattering. TrAC Trends in Analytical Chemistry **124**, 115796 (2020)

# Chapter 18
# Advanced Medical SERS Applications




**Chrysafis Andreou, Marios Stavrou, and Adrián Fernández-Lodeiro**

**Abstract** Surface enhanced Raman scattering (SERS) is a nanoscopic phenomenon through which the inelastic energy transfer between light and matter is greatly enhanced. It was first observed fifty years ago, and since then, it has been revealing molecules for multiple applications across many scientific disciplines. SERS has been employed in biomedical applications, especially in oncology—to date, in the preclinical setting. In this chapter, we present some of the most advanced medical applications of SERS. We begin with a brief history of SERS-based biomedical applications, for bioanalysis and medical imaging. Then, we present an overview of the nanoscopic phenomena that enable this technique, focusing on the design of different nanoparticles and Raman-active molecules. After that, we provide an overview of the recent advances in SERS-based Raman guided surgery, endoscopy, imaging of deep-seated lesions, as well as the combination of SERS nanoprobes with other established and upcoming medical imaging modalities. We end with a discussion of multiplexed molecular imaging and a brief discussion on the next steps for the technique.

**Keywords** Surface enhanced Raman scattering · Medical imaging · SERS nanoprobes · Raman-guided surgery · Endoscopy · SESORS · Multimodal imaging · Multiplexed imaging

## 18.1 History and Background

Surface Enhanced Raman Scattering (SERS) is a powerful optical spectroscopic technique with many emerging applications in chemical analysis, biological assays, medical imaging, and diagnostics [1]. The story of SERS begins when the phenomenon was first observed by Fleischmann and colleagues in 1974, who reported that the inelastic scattering of pyridine increased substantially in the vicinity of silver electrodes [2]. The observation was reproduced independently by the groups

C. Andreou (✉) · M. Stavrou · A. Fernández-Lodeiro
Department of Electrical and Computer Engineering, University of Cyprus, Nicosia, Cyprus
e-mail: andreou.chrysafis@ucy.ac.cy

© The Author(s), under exclusive license to Springer Nature Singapore Pte Ltd. 2024

M. Procházka et al. (eds.), *Surface- and Tip-Enhanced Raman Scattering Spectroscopy*,
https://doi.org/10.1007/978-981-97-5818-0_18

of Creighton and Van Duyne in 1977 and was identified as a phenomenon distinct from intrinsic Raman scattering; as the increase in scattering efficiency stemmed from rough metal surfaces, this new phenomenon was given the name SERS [3, 4]. The identification of surface plasmons as the main source of the enhancement was proposed shortly thereafter by Moskovits [5]. Briefly, when the electrons of the conduction band of the metal oscillate in resonance with the excitation light, they amplify the local electric field, mostly around sharp geometries such as nanoscale edges or low-order nanoparticle aggregates. We often refer to these areas of intense electric field as 'hotspots'; any molecules within these hotspots demonstrate massively enhanced Raman scattering cross section.

Initial studies, between the mid-1970s and early 1980s, used samples at concentrations in the high millimolar range, above the concentrations needed for biomedical analysis. The majority of studies involved small highly polarized molecules such as pyrimidine, benzoic acid, cyanide radical, and the anion of dithizone. In the mid-1980s, SERS returned to the spotlight as an analytical technique due to reports for the measurement of homocyclic and heterocyclic polyaromatic compounds at trace quantities on solid substrates coated with silver nanospheres [6].

In the 1990s, the first biomedical applications of SERS are reported. SERS was used for the detection of biomolecules based on the enhancement of their intrinsic Raman spectrum, their fingerprint, in what we now call label-free or direct detection. In the last three decades, SERS has been used for countless analytical and biomedical applications, from biomarker detection (DNA, miRNA, proteins) to the imaging of cells and bacteria, and in vivo preclinical imaging of cancer and other diseases. An early example of the method was demonstrated via the detection and identification of DNA bases as an alternative to using fluorescent or radioactive labels; specifically, adenine was detected using a silver colloid [7]. Similar applications demonstrated the detection of HIV-1 DNA [8], single base extension reaction [9], proteins such as hemoglobin [10], all using silver colloids aggregated to produce multiple hotspots. In the 2000s, SERS was demonstrated for more clinically-oriented applications, such as the first in vivo report for the detection and monitoring of glucose in a rat, via a surgically inserted nanopatterned silver film [11].

Around the turn of the millennium, the development of SERS nanoparticles with pre-encoded bright, bio-orthogonal signals, and targeting moieties, often called SERS tags or nanoprobes, enabled the indirect detection of biomolecules in the complex biological milieu, paving the way to SERS-based medical imaging, and ushering in the era of more advanced medical SERS applications. In 2008, SERS nanoprobes were reported for the first time for cancer detection in vivo using mouse models. Gold nanoparticles with an infrared Raman reporter (diethylthiatricarbocyanine—a cyanine dye) coated with polyethylene glycol (PEG) and single-chain variable fragment antibodies specific for epidermal growth factor receptor (EGFR) were shown to detect tumors [12]. Other groups demonstrated the potential of SERS for in vivo imaging using other model systems such as zebrafish embryos [13] and mice, highlighting the potential of multiplexed in vivo imaging [14], a feature that sets SERS apart from other imaging modalities.

In the 2010s, handheld spectroscopic devices were introduced for preclinical image-guided surgery, to detect breast cancer tumor margins in mice pre- and intraoperatively with high precision [15, 16]. SERS imaging and therapy were combined into nanorods used for the first time for SERS detection and photothermal therapy (PTT) [17]. Additionally, the combination of different imaging modalities using the same nanoconstruct was identified as a promising way to complement the limitations of Raman imaging, most importantly the limited penetration depth of light in tissue. In 2012, a triple-modality approach encoding magnetic resonance imaging (MRI), photoacoustic, and Raman contrast in the same nanoparticle was reported for delineating and excising brain tumors in a glioblastoma mouse model. The nanoparticles were detected with at least picomolar sensitivity by all three detection modalities, allowing precise brain tumor imaging and resection [18]. This strategy allowed imaging through the intact skull (with MRI), while Raman imaging accurately delineated the tumor margins. Imaging validation was performed via a comparison with histological analysis.

Endoscopes were enlisted as an alternative way to allow SERS-based imaging of internal structures, especially for the detection of tumors along the gastrointestinal tract. Endoscopic imaging was performed by combining Raman imaging with fluorescence and white light imaging, as well as by targeting multiple molecules of interest with different SERS nanoprobes [19–21]. Additionally, clever setups using different optical paths for excitation and signal collection were developed, allowing the detection of SERS signals from considerable depths within tissue. Deep Raman spectroscopy, based on spatially offset Raman spectroscopy (SORS), was used to visualize solid tumors through tissue in mouse models of cancer and tissue-mimicking phantoms, with up to 71 mm detection depth reported [22]. A related method, transmission Raman spectroscopy was used to identify in vivo deep lesions in rat lymph nodes [23] and was even capable of producing 3D ‘tomographic Raman’ images of tissue phantoms [24, 25].

In addition to the advances in optical hardware for SERS-based Raman imaging, considerable advancements have been reported for the nanoparticle contrast agents themselves. For example, SERS nanostars, with plasmonic excitation in the near infrared (NIR) combined with Raman reporter dyes with similar absorbances were shown to make highly effective SERS contrast agents, and used to visualize tumors, identifying their margins, invasion, localization, and microscopic residuals in mouse models of different cancer types, in a high precision manner [26]. New nanostructures and new Raman reporters are an active area of research, improving the already highly sensitive and specific imaging offered by SERS and enabling even more advanced medical applications.

## 18.2 SERS Nanoprobes for Biomedical Applications

Currently, SERS nanoprobes with bright, distinct signals and specific molecular targeting form the cornerstone of advanced medical applications of SERS. The design of an effective SERS nanoprobe relies on the Raman spectrum of a reporter molecule, plasmonically enhanced to bestow an intense and unique spectral signal, which remains stable in a complex molecular environment, such as the blood. It is thus necessary for the nanoparticle to include a metallic core, on which plasmons are excited upon laser illumination, a layer of molecules with a distinctive and high-intensity Raman spectrum to act as reporters, and a protective layer intended to maintain stability and biocompatibility, such as silica, PEG or a protein such as bovine serum albumin (BSA). Furthermore, this design enables postsynthesis functionalization with different targeting molecules, most often antibodies, which allows a highly specific design of the nanoprobe based on the desired application [27].

### *18.2.1 Raman Active Molecules*

SERS nanoprobes have been reported with a diverse set of molecules serving as Raman reporters, each featuring its distinct vibrational signature. These molecular fingerprints allow the simultaneous detection of different reporters via spectral unmixing of complex spectra with tens of constituents and enable multiplexed imaging. Additionally, employing a Raman reporter with electronic excitation energy levels close to that of the laser induces a resonance effect on the reporter molecule, which combined with the plasmonic enhancement leads to surface enhanced *resonance* Raman scattering (SERRS), which significantly boosts the total SERS enhancement. For imaging of biological tissues, laser excitation in the NIR region, commonly at 785 nm, is preferred. The spectral range in the far red and NIR is recognized as the ‘clear window’ for optical imaging due to the minimal electronic transitions in hemoglobin and water, leading to reduced light absorbance [12]. NIR lasers provide a notable advantage for imaging biological tissues, compared to visible wavelengths, as they provide greater penetration depths and exhibit negligible tissue autofluorescence, resulting in a lower background during Raman interrogation [27, 28]. Studies using SERS nanoprobes for biomedical imaging typically employ a 785 nm laser, and nanoprobes with both NIR resonant and nonresonant Raman reporters.

Typically, Raman reporters nonresonant with the NIR excitation laser are smaller molecules. These Raman reporters include aromatic thiols like 4-nitrobenzenethiol (NTP), 4-mercaptobenzoic acid (MBA), and thiophenols such as 4-aminothiophenol (ATP); these compounds possess relatively simple molecular structures contributing

simple features to their identifiable Raman patterns, facilitating accurate identification and analysis. Also, they can be readily attached on gold and other nanoparticle surfaces, broadening their applicability. However, as they do not exhibit resonance in the NIR they provide dimmer SERS signals compared to resonant reporters [29].

Raman reporters resonant in the NIR are bigger molecules with more complex spectra. Molecules with electronic transitions with energies close to the 785 nm laser are commonly members of the family of cyanine dyes, which includes 3,3′-diethylthiatricarbocyanine iodide (DTTC), hexa-dibenzo-indotricarbocyanine (HDITC), or cationic heptamethine cyanine NIR-resonant Raman dyes like Cy7, among others. Other infrared dyes, resonant when excited with 785 nm laser are IR775, IR780, or IR792. They all offer distinctive Raman signatures in the NIR spectral region, making them invaluable for labeling and visualization purposes [30]. Recently, chalcogenopyrylium dyes have emerged as a robust and versatile platform for SERRS in the NIR; these molecules show a high affinity for gold and silver surfaces, potentially simplifying their functionalization and encapsulation in nanoprobes [31]. One caveat of using resonant molecules, is that most of these molecules also exhibit fluorescence due to their electronic excitation, contributing an undesired fluorescent background to the SERRS signal [32].

Although tissue imaging benefits from excitation in the NIR, other lasers have been reported for SERRS-based detection. Dyes such as malachite green isothiocyanate (MGITC) or rhodamine-6G demonstrate resonant Raman scattering when exposed to 514 nm and 633 nm excitation wavelength, respectively, and have been used to produce SERRS nanoparticles resonant with visible wavelengths [32, 33].

### *18.2.2 Plasmonic Cores*

Gold, recognized for its exceptional plasmonic properties, is preferred among other metals due to its strong signal amplification capabilities in SERS. Gold's biocompatibility, inertness, and stability make it an excellent candidate for the metallic core of the nanoprobe, with clinical translation as the goal. Moreover, the unique optical properties of gold further contribute to its suitability, allowing for precise and reliable detection in various applications within the nanotechnology and biomedical research fields. These favorable attributes, including ease of synthesis and functionalization, render gold optimal for formulating efficient and versatile nanoprobe designs.

#### 18.2.2.1 Gold Nanospheres

Gold spheres are among the most prevalent shapes for plasmonic nanoparticle cores. Their uniformity in size and ease of functionalization make gold spheres an attractive choice for creating efficient and highly sensitive nanoprobe systems across various scientific and biomedical applications. Early in vivo SERS reports stated that the gold

nanoparticles ranging from 60 to 80 nm in core size demonstrate optimal enhancement when subjected to red (630–650 nm) and NIR (785 nm) excitations. Multiple studies employed diverse nanoprobes based on spherical gold nanoparticles with designs varying in size and functionalization, but a typical configuration is shown in Fig. 18.1a. For instance, 60 nm gold cores decorated with multiple Raman reporters and encapsulated in a silica layer enabled simultaneous imaging of multiple targets in living mice through the skin [14]. Electrostatically modified 60 nm gold nanoparticles with NIR dyes Cy7 and Cy7.5 derivatized with lipoic acid and encapsulated in BSA were used for the specific detection of tumors in living animals [34]. Other studies have employed gold nanoparticles functionalized with various Raman reporters like (trans-1,2-bis(4-pyridyl)ethylene (BPE)) and a silica shell to delineate liver tumors in mice [35], or with MGITC, Rh6G and Cy5 as Raman reporters, encapsulated in PEG and subsequently functionalized with different antibodies for imaging of a breast cancer model [33]. A SERS nanoprobe consisting of 60 nm gold spheres modified with NIR Raman molecule IR780, and a layer of ca. 15 nm of silica was coated with PEG to yield nanoparticles which were administered intravenously to mice to detect precursor lesions of gastrointestinal tract cancers in clinically relevant transgenic animal models [36].

Gold nanospheres have also been used to produce another type of SERS nanoprobe, reported as gap-enhanced Raman tags (GERTS). Starting with 50 nm diameter gold nanospheres covered with a thin layer of Raman reporter 1,4-benzenedithiol (BDT), an additional layer of gold was grown, with the process repeated up to three times, yielding nanoparticle assemblies with high SERS cross sections. A layer of mesoporous silica was then grown to stabilize the constructs, which were then used for high-contrast intraoperative sentinel lymph node Raman imaging in mice [41].

Gold nanospheres also form the basis for chemically responsive intracellular sensors. For example, the SERS signal of 4-aminothiophenol (ATP) changes based on its reactions with the chemical components in the tumor microenvironment; a smart SERS nanoprobe using ATP and calcium alginate was used to detect five major reactive oxygen species (ROS) in vivo [42]. In another example, spherical gold nanoparticles were functionalized with a pH-responsive material to induce aggregation at low pH values, forming highly SERS-active clusters. This was achieved by using citraconic anhydride to synthesize a pH-sensitive folic acid-targeted polyvinyl alcohol chain and the Raman reporter 4-MBA tethered onto 12 nm gold nanospheres. This strategy was reported to lead to effective tumor cell identification in mice [43]. Taking a somewhat similar approach, nanoparticles of two different sizes were used to form assemblies responsive to sialic acid. Gold spheres of 10 nm were decorated with 3,3-diethylthiatricarbocyanine iodide (DTTC) as the Raman reporter and 3-aminophenylboronic acid (APBA) as a linker for specific recognition of sialic acid. A second set of nanoparticles with a size of about 40 nm were modified with PEG covalently attached to sialic acid. The two nanoconstructs accumulated within the tumor region, where they bound to form gold conjugates yielding strong SERS signals [44].

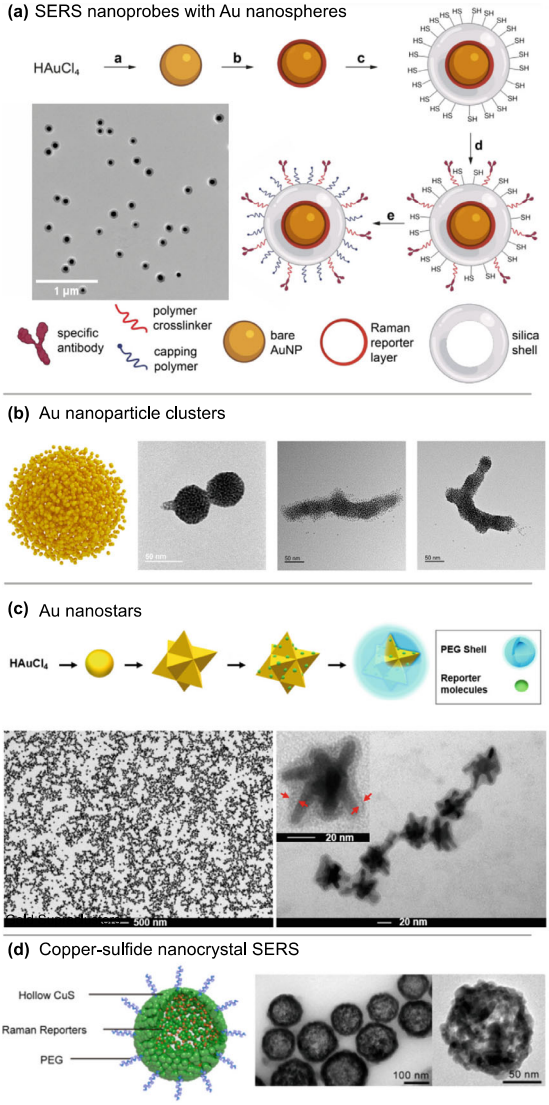



**Fig. 18.1 Typical SERS nanoprobes**. **a** Gold nanospheres decorated with a Raman reporter and encapsulated in a silica shell are a common configuration. They can be passivated with PEG or functionalized with targeting antibodies, adapted from [37]. **b** Clusters of small nanoparticles offer robust SERS enhancement and can be decomposed into their excretable subunits, adapted from [38]. **c** Nanostars offer an alternative to the spheres, with NIR absorbance and multiple SERS active hotspots, adapted from [39]. **d** Materials other than gold and silver can be used for SERS nanoprobes, such as CuS nanospheres, adapted from [40]

The inverse approach was also demonstrated, i.e., to generate SERS nanoprobes that can be broken down and expelled from the body, potentially alleviating any possible long-term toxicity effects. Gold nanoparticles with sizes less than 3 nm were assembled to form SERS-active nanoparticle clusters; these can eventually be decomposed into their constituents and eliminated from the body. Biodegradable and excretable gold "supraclusters" were reported with gold core diameters ranging from 1.3 to 2.7 nm, demonstrating active Raman signals for imaging subcutaneous tumors in mice. To produce the metallic supraclusters, glutathione (ester)-capped gold nanoclusters were reacted with bis(sulfosuccinimidyl) 2,2,4,4-glutarate (BS2G), yielding different sizes and shapes based on the starting nanocluster used, from spherical shapes to highly branched supraclusters, as seen in Fig. 18.1b. As a Raman reporter for the supraclusters, *N*-hydroxysuccinimide (NHS)-functionalized NIR resonant Raman dyes were added during the supracluster assembly to bind and be incorporated effectively within the structure. NIR-resonant nonfluorescent molecules were tested as Raman reporters, as they exhibit resonant Raman scattering while reducing the fluorescence background [38].

#### 18.2.2.2 Anisotropic Gold Nanoparticles

Considering that the modification of size and shape changes the optical properties of plasmonic nanomaterials, anisotropic gold nanoparticles have received marked interest for SERS applications. It has been established that nanoparticles with absorption maxima coinciding with incident light provided higher SERS enhancement, and geometric anisotropy offers the potential for plasmon tunability. Anisotropic nanomaterials thus allow precise control over their resonance to match the laser irradiation and also to expand their applicability to different multimodal theranostic strategies, such as photodynamic therapy or optoacoustic tomography, among others. For example, gold nanorods with a diameter of 50–100 nm were functionalized with Raman reporters tethered on DNA and coated in silica. The nanorods demonstrated NIR resonance, which resulted in a significant improvement in the SERS performance. The Raman signal from the nanoprobes with gold nanorods was reported to be more than 70 times higher than the Raman signal from spherical gold nanoparticles, allowing for more sensitive and accurate imaging of tumors [45].

In conventional bottom-up synthesis of gold nanorods, cytotoxic surfactants like cetyltrimethylammonium bromide (CTAB) are frequently used, compromising the biocompatibility of the resulting SERS nanoprobes. Hence, gold nanostars have emerged as a promising alternative due to their surfactant-free synthesis methodologies, as seen in Fig. 18.1c. Moreover, the star shape offers high plasmon tunability by varying the rays' length, and their unique morphology featuring multiple hotspots at the tips has the potential to significantly enhance the SERS signal due to the increased electromagnetic hotspots in these regions. Several studies showcase the diverse applications of gold nanostars for multimodal imaging and therapy approaches. Nanoprobes using PEG-coated gold nanostars (30 and 60 nm) with 4-MBA as a Raman reporter demonstrated multimodal theranostic capabilities, including SERS

detection and PTT in vivo [46]. Gold nanostars with a hydrodynamic diameter of 80 nm, functionalized with Cy7 and coated in PEG were successfully employed for in vivo SERS detection of tumors using a 785 nm handheld laser and an optical clearing agent [47]. Gold nanostars with 4-NTP and a silica shell were used to conduct imaging and biodistribution studies in tumor-bearing mice [48]. Another example of nanoprobes with gold nanostars as the core, coated with a silica layer embedding IR780 and functionalized with PEG, with median size of approximately 100 nm, was reported to combine SERRS with multispectral optoacoustic tomography (MSOT). Using a dual-modality approach (SERRS-MSOT), these nanoprobes serve as contrast agents in the NIR window and enabled noninvasive visualization of glioblastoma (GBM) with high signal sensitivity and specificity. The nanoprobes facilitate imaging at depths of several millimeters within the brains of mice [49]. Similar nanostar-based SERS nanoprobes were functionalized with a cyclic-RGDyK peptide for integrin-targeted GBM imaging in vivo in mice through the intact skull [50], and in a ratiometric approach with folate receptor targeting versus nontargeted PEG-terminated SERS nanoprobes for robust delineation of tumor deposits with microscopic precision in an ovarian cancer model [51]. Gold nanostars also served as the core for a multiplex imaging panel for immunotherapy [31].

Gold nanostars can also be tuned for resonance in the second infrared window. For example, 50 nm gold nanostars were modified with the addition of silver nanospheres to shift their plasmonic peak, and increase absorbance for a 1061 nm laser, inducing SERS and PTT with deep-tissue penetration and high-specificity tumor detection [52].

#### 18.2.2.3 Different Metals and Combinations

The combination of gold with other metals may give new functionalities and capabilities to the nanoprobe. For example, the design of a system based on multifunctional Au-Fe alloy nanoparticles, protected with PEG and functionalized with modified silicon 2,3-naphthalocyanine and sulforhodamine 101 was reported. The Au-Fe alloy NPs showed easy and versatile surface conjugation, MRI, and computed X-ray tomography (CT) signals, and intense SERS signals; high sensitivity and high-resolution intraoperative imaging were reported when tested in 4T1 tumors in mice [53].

Additionally, labelled nanoprobes to yield ultrabright SERRS nanoparticles with a suitable radiotracer would enable preoperative identification of regions of interest with whole body imaging that can be rapidly corroborated with a Raman imaging device or handheld Raman scanner in order to provide high precision guidance during surgical procedures. The spherical gold nanoparticles, in combination with IR-780 and silica, were labelled with $^{68}$Ga in order to produce the final nanoprobe. The positron emission tomography (PET)-SERRS NPs were evaluated in vivo by lymph node imaging near the periphery of an orthotopic 4T1 breast cancer tumor in mice [54].

Prussian blue (PB)-coated gold nanoparticles (AuNPs) and doped with $Gd^{3+}$ located in the lattice of PB enables the MRI ability with high relativity of the probe. Ovalbumin was functionalized on the surface of the nanoprobe as an antigen to activate dendritic cells. The SERS signal from the PB component enabled single-cell detection of colonized dendritic cells in the lymphatic system [55]. Nanoprobes comprising Au@CuS@polydopamine nanoparticles and DNA-conjugated tetrahedral nanostructures for a SERS-fluorescence dual-spectrum biosensor have been reported by covering a 15 nm gold core with plasmonic copper sulfide, encapsulated with polydopamine, and assembled with thiolated and Cy5 tagged hairpin DNA [56].

Recently, nanoprobes based on gold and carbon materials such as graphene oxide have gained attention. Graphene oxide presents several advantages such as good biocompatibility and low cytotoxicity or a large surface area that can be modified or functionalized to tailor its interaction with biological systems. Synthesis of gold-graphene hybrids tethered with folic acid-ligated chitosan-modified photosensitizer for targeted photothermal and photodynamic therapy has been reported. Their fabrication involved spiky gold nanostars on partially reduced graphene oxide, attached to NIR-emitting photosensitizer protoporphyrin IX, covalently conjugated with folic acid, ultimately tested in vivo for targeted theranostic ability in tumor-bearing mouse models, exhibiting fluorescence and SERS imaging capabilities [57]. The controlled assembly of hybrid graphene oxide/gold nanoparticles and subsequent nucleic acid conjugation was reported for cancer-specific multimodal imaging and combined therapeutics. These nanoprobes showed excellent SERS-mediated live-cell cancer detection and multimodal synergistic cancer therapy using photothermal, genetic, and chemotherapeutic strategies. Using gold nanospheres of about 40 nm and gold nanorods of 10 nm width and 40 nm length, a methodology was developed for the electrostatic self-assembly to controllably create different plasmonic metal-graphene oxide hybrid nanomaterials. These nanoconstructs enabled high contrast dark field imaging and the selective detection of an over-expressed cancer gene via SERS sensing in vivo [58].

Besides gold, the use of other nanoprobes based on silver or copper has also been reported. Silver nanoparticles offer some advantages such as a stronger SERS signal than gold due to a more significant enhancement factor. The plasmonic properties of silver and copper nanoparticles can be tuned differently compared to gold, allowing for optimization in different spectral ranges. Silver and copper are generally less expensive than gold, making them more cost-effective alternatives. However, despite these advantages, there are some limitations, such as potential toxicity concerns, stability issues, and the tendency for oxidation, which may affect their long-term performance or biological compatibility in vivo. Dual-mode NIR silver bumpy nanoprobes were reported for in vivo imaging and biomolecule detection using photoacoustic imaging and SERS. Silver SERS nanoprobes were synthesized on functionalized silica nanoparticles as a core, by growing Ag nanoparticles on the surface, functionalizing various Raman labels (4-fluorobenzenethiol, 4-bromobenzenethiol and 4-chlorothiophenol) and coated with a 15 nm silica layer and BSA for stability; they were successfully applied for in vivo sentinel lymph node detection [59].

A SERS probe consisting of hollow CuS nanoparticles, with a hollow interior encompassing a porous shell of 10–12 nm diameter formed by small CuS crystals has been reported, shown in Fig. 18.1d. The hollow CuS NPs were adsorbed with different Raman reporters as 3,3′-diethylthiatricarbocyanine iodide (DTTC), 3,3′-diethylthiadicarbocyanine iodide (DTDC), and 3,3′-diethylthiacarbocyanine iodide (DTC), resulting in significant amplification in Raman signature signals. The hollow CuS NPs can be disseminated into small clusters upon NIR light irradiation, thus facilitating their postimaging clearance from the tissues and avoiding potential long-term toxicity. They were tested in an orthotopic mouse model of prostate cancer to simulate tumor surgery in the clinic [40].

## 18.3 Raman Guided Surgery

SERS nanoparticles lend themselves to use as intraoperative contrast agents. During surgery, tumors in deep-seated locations and other tissues of interest can be exposed, providing an opportunity for direct optical imaging without the complication of light scattering and absorbance by tissues. Already, intraoperative fluorescence imaging is an established clinical technique, with a handful of approved fluorescent small molecule dyes, and many others in preclinical testing. It is pretty straightforward to imagine a scenario in which the surgeon has among her instruments a Raman spectrometer, the size of a pen, for the detection of SERS nanoparticles delineating a tumor, during a spectrally-guided resection.

The concept of a pen-like handheld probe for Raman spectroscopy geared for intraoperative applications was demonstrated in 2010 [15]. The system follows a configuration that is now standard in handheld systems, for biomedical applications or otherwise; it consists of the handheld probe and a tabletop Raman spectrometer, along with an excitation laser source (diode laser emitting at 785 nm). The handheld part, shown in Fig. 18.2a, contains an assembly of optical components. Primarily, it includes the ends of two bundles of fibers interfaced with optical frequency filters, a dichroic mirror, and an objective lens. The fiber bundles are each 5 m in length, providing flexibility and maneuverability for the user; the first brings the excitation light from the laser to the objective lens, illuminating the sample, while the second guides the collected light to the spectrometer for analysis. A bandpass filter, placed after the incoming fiber, removes undesired frequencies (such as harmonics) from the excitation light, while a long-pass filter between the objective and the returning fiber rejects Rayleigh-scattered photons, ensuring only Stokes-shifted photons reach the detector. The system detects Stokes-shifted photons produced via either Raman or fluorescence, so it can be used as a fluorescence detector for infrared fluorescent dyes, which enabled the demonstration of intraoperative detection of the fluorescent dye ICG in live tumor-bearing mice, while the detection of gold nanoparticles encoded with the Raman 3,3′-diethylthiatricarbocyanine iodide (DTTC) and stabilized with PEG was only demonstrated in tissue-mimicking phantoms.

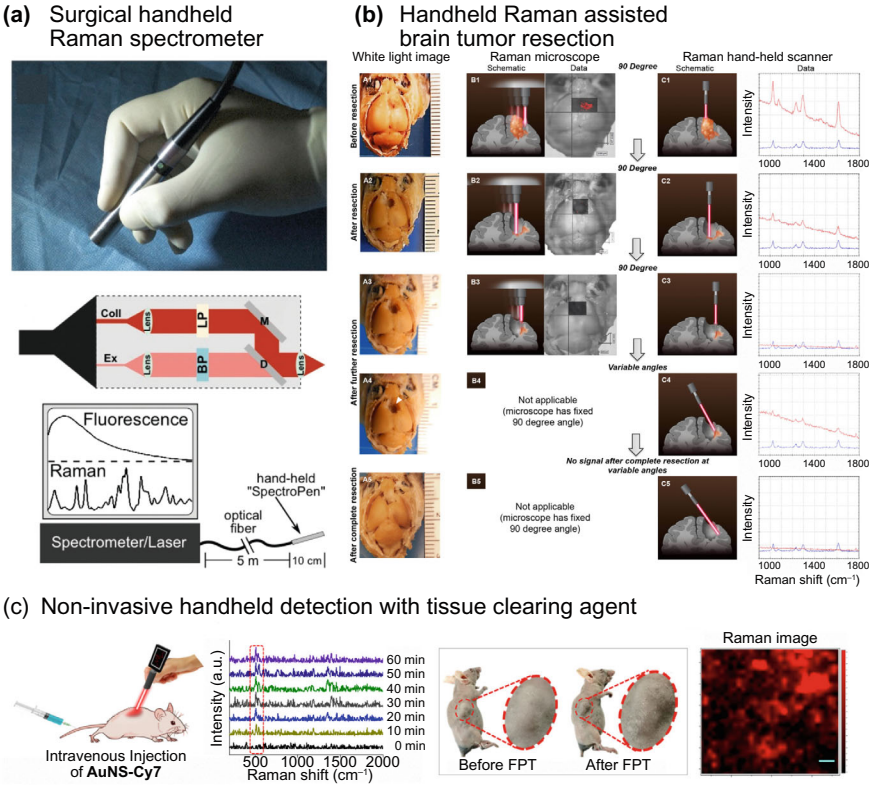



**Fig. 18.2 Handheld Raman spectrometers allow quick detection of SERS NPs in the body and are amenable to intraoperative use**. **a** The handheld system provides excitation and signal collection in a convenient and small assembly that can be manipulated by the surgeon. Fiberoptic bundles connect the handheld probe to the laser excitation source and to the spectrometer. Raman signals as well as fluorescence can be detected [15]. **b** Handheld systems provide versatility in detection, as they can be oriented at an angle, enabling the detection of lesions that are occult to scanning systems with vertical orientation. Adapted from [16]. **c** The combination of handheld probes and tissue-clearing agents allows noninvasive detection of tumors through the skin. Adapted from [39]

An application of a handheld Raman probe with SERS nanoparticles in a clinically relevant scenario was demonstrated by the group of Dr. Kircher. Specifically, a commercial handheld Raman system was used for the spectrally guided tumor resection in a mouse model of glioblastoma [16]. In this case, gold core silica shell SERS nanoparticles with the reporter molecule 4,4′-dipyridine were administered intravenously to the mice, and accumulated to the tumor via passive targeting. A surgical setting was emulated, where the surgeon excised the tumor with and without Raman guidance. Without guidance, histology of the tumor bed showed residual tumor foci. The handheld system was able to detect such residual lesions by detecting the SERS

signal emanating from the tumor-bound nanoparticles. When the SERS signal disappeared, the surgeon knew the true tumor margin had been reached. Additionally, the handheld system was compared to a confocal scanner with microscopic optics, as shown in Fig. 18.2b. Although the microspectrophotometer offers superior optics and higher magnification compared to the handheld probe, it is only able to image from a fixed angle. By adjusting the angle of the handheld probe, the surgeon was able to detect occult tumor residues, achieving a cleaner tumor bed.

Handheld Raman probes, similar to the ones mentioned above, have been used for the detection of tumors outside the intraoperative context. Such applications are of great interest as they can enable the noninvasive detection of lesions, bringing Raman imaging out of the surgical theater. However, the skin acts as not only a biological barrier but also an optical one, scattering and attenuating light, and complicating this task. One approach that has been presented is to make the skin transparent via the use of an optical tissue-clearing agent [39]. Tissue-clearing agents are typically used for ex vivo tissue analysis. They consist of chemicals that permeate biological tissues and adjust the local optical properties to facilitate light penetration. One such optical clearing agent, FPT (containing fructose, PEG, and thiazone) was used to clear the skin of mice around a tumor. In this way, detection of gold core silica shell nanoparticles with an infrared dye Raman reporter was improved. The handheld probe was used to measure the signal of SERS nanoparticles accumulated in the tumor before and after administration of the clearing agent. As shown in Fig. 18.2c, the Raman signal became apparent within 10 min after application of the optical clearing agent and remained strong for up to an hour.

The strength of using handheld Raman spectrometers during surgery or surgery planning lies in the quick interrogation of several points of interest. However, this approach requires the administration of not yet clinically approved SERS nanoparticles as a contrast agent, hindering the translation of the technique to the clinic. A different approach that leads to a similar result without the administration of nanoparticles involves the sampling of different areas in the patient, manually, via a water droplet suspended on a pipette, and the subsequent SERS interrogation of the collected samples. This approach has been demonstrated to detect the acidic pH associated with glioblastomas [60]. Instead of nanoparticles, plasmonic nanostructures on a 2D substrate are used to provide SERS signals. Although this approach is rather indirect, it shares similarities with the use of handheld Raman spectrometers for guided surgery and does not necessitate the administration of nanoparticles.

## 18.4 SERS Endoscopy

Another way to obtain Raman signals from tissues and malignancies within the body is via the use of an endoscope. Endoscopic Raman imaging and detection has been investigated preclinically as an approach to addressing the limited tissue penetration depth of light, without the need for surgery.

A strategy for endoscopic detection of SERS nanoparticles was formulated by the group of Professor Gambhir [61] and demonstrated soon afterward via the integration of a Raman spectrometer through a clinical endoscope [62]. Similar to the approach used for handheld probes, the Raman endoscope relies on long flexible bundles of optical fibers to guide the light from the excitation source to an insertable probe, and a second bundle to lead the collected Raman scattered light to the spectrometer. As shown in Fig. 18.3a, the probe contains a rotating mirror that enables Raman interrogation at variable angles, producing a 2D radial map, along the lumen where the endoscope is inserted. The Raman endoscope was tested in humans (without the administration of contrast) as well as in swine intestines and various phantoms [21]. The group demonstrated the ability of the endoscope to detect SERS nanoparticles with distinct spectra, toward multiplexed endoscopic imaging [21, 63].

A notable preclinical application of Raman endoscopy with SERS nanoparticles was demonstrated with the detection of malignancies along the gastrointestinal tract of rats and mice using nanoparticles for imaging contrast [36]. The nanoparticles employed demonstrated high Raman scattering intensity; the star-shaped gold core and the IR dye used as a Raman reporter, both resonant with the excitation laser, produced surface enhanced *resonance* Raman scattering (SERRS), with reported limit of detection in the low femtomolar range. Although the nanoparticles were not functionalized with any molecular targeting moieties, after intravenous administration they accumulated in tumors via nonspecific uptake mechanisms and were able to delineate them due to their intense and distinct Raman signal. A custom endoscope was developed, for use in rodents, shown in Fig. 18.3b, with smaller dimensions than the clinically oriented endoscopes used in other studies. The small size precluded the use of rotating optics; instead, a ring of constant illumination was produced, providing Raman signals in one dimension, along the lumen. The technique allowed the detection of even premalignant lesions in the esophagus, stomach, and intestine.

Endoscopic imaging in small animals was also demonstrated with topical administration of SERS nanoparticles in the esophagus of rats [64]. The endoscope, shown in Fig. 18.3c, was designed to provide illumination and signal collection from a single point on the side via a prism; a radial map was acquired by inducing the prism to rotate during endoscope retraction. Ratiometric image was performed, as shown in Fig. 18.3c. As different areas of the lumen retain nanoparticles variably, the detection of two distinct SERS nanoparticles allows the calculation of their ratio, through which the overabundance of one can be identified. Such a ratiometric strategy is deemed necessary for molecular imaging after topical administration of SERS nanoparticles, and it was used by the same group in a subsequent study [65]. SERS nanoparticles with three distinct spectra were used for the ratiometric imaging of two molecular targets (the biomarkers EGFR and HER2). A xenograft model was developed with the surgical implantation of three different human tumors with varying expression of the two biomarkers, in the esophagus of rats. Endoscopic imaging was able to identify the differential retention of the two targeted SERS nanoparticles in the tumors, by visualizing their ratio with the third (nontargeted) nanoparticle. A different group used a similar approach for imaging EGFR and VEGF expression in tumors in the mouse colon [20].

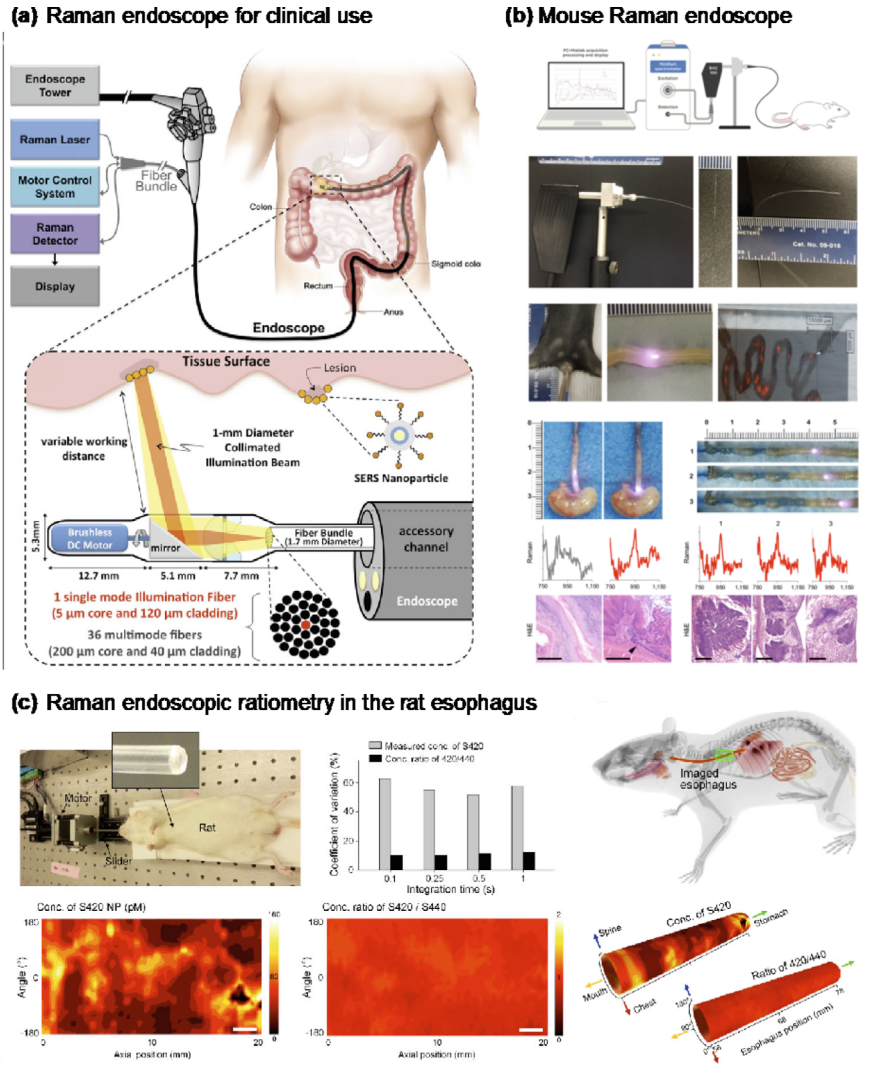



**Fig. 18.3 Raman endoscopes can be used for diagnostic procedures**. **a** A Raman spectrometer can be interfaced via the accessory channel of a clinical endoscope to provide the excitation light as well as collection optics. Locally administered SERS nanoprobes can potentially be used as contrast agents for molecular imaging, detecting multiple targets in a single scan. Adapted from [21]. **b** Preclinical endoscopy system was used for imaging the GI tract (upper and lower) of rodents after systemic administration of untargeted SERS nanoparticles. The endoscope images the GI tract in a lengthwise manner, illuminating in a ring pattern and acquiring a single spectrum per position along the imaged organ. Adapted from [36]. **c** A cylindrical image is acquired by rotating a Raman endoscope while moving along the esophagus of a rat. Ratiometric imaging was demonstrated by using SERS nanoparticles with two distinct spectra administered via oral gavage. Adapted from [64]

In addition to investigating the GI tract, Raman endoscopy has been used preclinically for detecting lung tumors via bronchoscopy [66]. SERS nanoparticles were embedded in microscopic drops of agarose gel which were inserted into an excised pig lung to emulate tumors.

Overall, Raman endoscopy with SERS nanoparticles as contrast agents is highly promising, as it allows the detection of microscopic lesions that are hard to identify by visual inspection alone. Endoscopy is still limited by the poor depth penetration of light in tissues but can be used to examine the GI lumen or other orifices, without surgery. As Raman endoscopes can be successfully interfaced with standard clinical endoscopes, their use for applications such as routine colonoscopy is straightforward, with the caveat that SERS nanoparticles are necessary to provide contrast. It may be possible to obtain approval for clinical use of these particles for topical administration, as this route does not appear to lead to the accumulation of nanoparticles in the patient.

## 18.5 Medical Imaging with SESORS

Raman imaging with confocal optics offers high resolution and low noise imaging for biomedical applications but suffers from poor penetration depth. This limitation is primarily due to the optical properties of biological tissues. Tissues absorb strongly in the visible frequencies and less so in the NIR, which is why excitation sources at 785 nm are preferred. Even then, the various microstructures and membranes in the tissue scatter photons in various directions, reducing the available signal that reaches the collection optics and limiting the depth of imaging possible. This limitation can be vastly improved via the use of a clever optical setup, where the excitation source and the collection path are decoupled and placed in different positions, allowing the detection of signals emanating from deep beneath the surface. With this technique, termed SORS the source of the Raman scattered signal can be computed, even if the photons take an indirect path to the collection optics. If a SERS agent is used, instead of an intrinsic Raman signal, the technique is termed SESORS [67]. This technique can be applied in a variety of optical configurations, often by retrofitting conventional handheld or confocal systems with additional excitation or collection optics.

A pioneering study presented by Stone et al. [68] built upon previous expertise in SORS, to detect the distinct spectra from 4 SERS nanoparticle types injected into excised porcine muscle tissue. The group demonstrated, for the first time, that SERS nanoparticles can be imaged even at depths greater than 40 mm. During the same time, Prof. Van Duyne's group used spatially offset optics to detect the SERS signal, not from encoded nanoprobes, but from glucose adsorbed onto a titanium/silver substrate in the abdominal area of a rat [69]. The versatility of SERS was yet again demonstrated, both as a biosensor and a contrast agent for bioimaging, especially when using highly intense SERRS nanoparticles, in a configuration termed SESORRS [70].

The combination of strong SERS signals and spatially offset optics in SESORS proved powerful enough to enable the detection of signals even through bone. The experimental setup, shown in Fig. 18.4a, used 785 nm illumination on the bone, to detect the SERS signals of nanotags injected on the other side [71]. Imaging through bone is particularly beneficial, as it allows minimally invasive intracranial imaging and sensing. For example, neurochemicals, such as melatonin, dopamine, and others may be monitored, as demonstrated using an ex vivo mouse model [72]. This approach may be used to diagnose and monitor neurological disorders, although the significant challenge of introducing a SERS substrate (nanoparticle or otherwise) into the skull needs to be addressed.

This challenge is more manageable when it comes to imaging brain cancer, as SERS nanoparticles were found to successfully infiltrate and delineate glioblastoma in mouse models using conventional (nonoffset) microscopic Raman optics [74, 75]. Nicolson et al. demonstrated the first in vivo application of SESORS imaging in a mouse model of glioblastoma [50] using SERS nanoparticles with a Raman reporter resonant in the infrared, and functionalized with an integrin-targeting peptide. The tumor locations within the skull were identified by spectrally unmixing the SORS signal of the skull (bone) and the SESORS signal from the nanoprobes and were found to match the MRI images. This application highlights the potential of SESORS for identification of deep-seated malignancies, which, combined with the molecular targeting and multiplexing capabilities of SERS nanoprobes can provide highly accurate information for cancer staging and presurgical planning. Although the technique was quite successful in mice, the challenges will be greater when applied to humans, due to the notable difference in skull size. The detection of signals from SERS nanoparticles embedded within a phantom enclosed in the skull of a macaque was demonstrated, with promises of clinical translation [76]. Although the macaque skull is thinner than its human counterpart, this study demonstrated that SESORS may be applicable for eventual use in patients. Toward this goal, different imaging phantoms have been developed, to further test and refine the technique [29, 77, 78].

The development of SESORS has enabled related theranostic and advanced imaging applications. For example, SESORS has been used in conjunction with a temperature-sensing technique to monitor the effects of nanoparticle-induced hyperthermia [79]. In this case, the plasmonic nanoparticles serve as a PTT agent, converting the incident laser power into heat, to yield localized thermal shock to the tumor, as a therapeutic strategy. At the same time, the Raman signal of the nanoparticles contains information about the local temperature, in the form of the anti-Stokes-to-Stokes Raman scattering ratio. In conventional PTT scenarios, only the surface temperature (at the skin level) can be monitored, instead of the actual temperature in the tumor. By using SESORS and thermal Raman sensing, it becomes possible to monitor the thermal effects where it really matters.

Additionally, the depth-related information acquired via SESORS can be used to perform Raman-tomographic imaging [80]. This incarnation of SESORS relies on the differential representation of signals from different depths in the acquired offset spectra. The imaging procedure involved a surface scan of porcine muscle tissue along a grid, with sample rotation for every point on the grid to obtain multiple

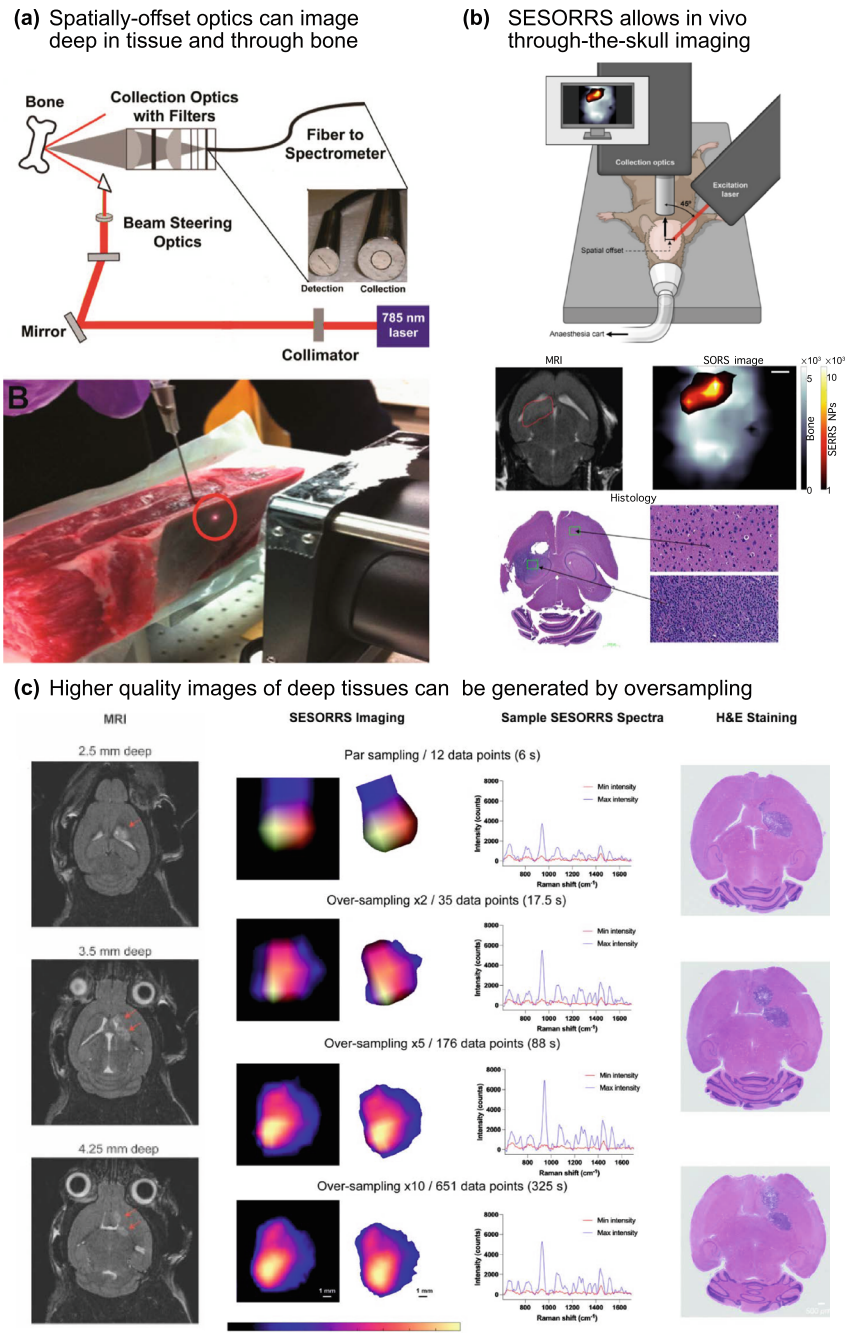



**Fig. 18.4 Spatially offset optics allow the acquisition of Raman spectra from deep within tissues**. **a** Early demonstration of the detection of SERS nanoparticles through bone. Adapted from [71]. **b** In vivo imaging of glioblastoma through the skull of a mouse after intravenous administration of integrin-targeting SERS nanoprobes. Adapted from [50]. **c** Oversampling with spatial offset can be used to image noninvasively with higher resolution. Adapted from [73]

offset readings for each point—the methodology could be streamlined by using ring-shaped collection optics. Once the SORS spectra were acquired on the grid, the three-dimensional position of the targets (SERS nanoparticles and silica powder) could be inferred, based on the ratio of their intensities versus the tissue Raman signal). This demonstration showed the importance of two parameters in image acquisition: symmetry, ring-shaped optics are necessary to reject imaging artifacts; and resolution, high-frequency spatial sampling allows clearer determination of the target's position. The benefit of imaging with small step sizes was also stressed by Dr. Nicolson's recent work [73] where they suggest that oversampling can achieve higher SESORS image quality, as shown in Fig. 18.4c.

Overall, SESORS is a very interesting development, as it addresses the main weakness of Raman imaging, namely its poor penetration depth. Additionally, SESORS relies primarily on acquisition optics, that can be applied to any Raman signal source, and as such, can be developed largely independently of new SERS nanoprobes. At the same time, this approach retains the main strengths of SERS imaging in general, such as its multiplexing and multimodality capabilities and could even be applied to endoscopic applications.

## 18.6 SERS with Multimodal Imaging and Therapy

Unlike small molecule contrast agents used in other biomedical imaging modalities, SERS-based contrast agents for Raman imaging are, by plasmonic necessity, nanoparticles. Nanoparticles are amenable to bulk modification and surface functionalization, and in this way, they can be engineered to offer multiple uses, such as offering contrast for multiple imaging modalities and also theranostic capabilities [81]. This multimodal approach can provide preoperative noninvasive imaging, intraoperative contrast, e.g., for tumor margin assessment, as well as potentially postoperative treatment.

For example, a quintuple modality nanoprobe was reported more than a decade ago, combining contrast for SERS, MRI, CT, and two-photon luminescence as well as PTT [82]. This nanoconstruct was demonstrated in phantoms and in cell cultures. The gold star-shaped core at the center of the nanoparticle bestows the plasmonic enhancement required for SERS, contrast for CT, as well as efficient absorbance of the incident light for PTT. The Raman reporter molecule provides the specific SERS signal. A silica shell protects the core, to provide stable SERS intensity, and also enables the attachment of chelators for gadolinium, for MRI contrast. In theory, such a nanoconstruct could provide an all-in-one theranostic platform, with even more imaging and treatment modalities combined.

A more straightforward multimodal approach is to combine SERS with fluorescence, as both techniques rely on optical signals and can be imaged via an optical microscope or endoscope. Typically, fluorescence imaging is much faster than Raman imaging but suffers from poor specificity due to high autofluorescence background

signals and overlapping emission spectra for many of the commonly used fluorophores. The combination of the two techniques allows for a quick fluorescence scan, e.g., to locate the tumor, and then a more thorough Raman scan to provide high-contrast imaging of the area of interest. The combination of SERS and fluorescence was demonstrated for 3D cell imaging over time, using fluorescent polymer scaffolds as a spatial reference and SERS nanoparticles NPs for cell labeling [83].

Other optical modalities can be integrated into the nanoconstruct. For example, folate-functionalized nanorods were used to produce signal for fluorescence, Raman, and photoacoustic imaging, as well as PTT, as shown in Fig. 18.5a [84]. Photoacoustic imaging is a hybrid technique, using light pulses for excitation and ultrasounds as the readout signal. This paradigm is popular because the effects that generate SERS, photoacoustic signal, and light conversion to heat rely on the same physical mechanism, namely, plasmon resonance. It has been demonstrated with several preclinical studies in mice, e.g., for the delineation of brain tumors [49] and for the intraoperative imaging and residual tumor eradication [48]. In a related application, a fluorescent-SERS nanoprobe was developed, with a pH dependent Raman signal, allowing the detection of NPs taken up into lysosomes [85].

Contrast for nonoptical modalities can be integrated into SERS nanoparticles as well, to provide even higher utility to the nanoconstruct. For example, silver nanoparticles were synthesized and embedded onto nitrogen microbubbles, enabling simultaneous contrast-enhanced ultrasound and SERS identification of small molecules [86]. However, a more popular imaging modality to combine with SERS, especially for preclinical oncological imaging, is PET. These two modalities strongly complement each other: PET is ideal for preoperative imaging, with high specificity but low spatial resolution, whereas Raman imaging with SERS has excellent sensitivity and spatial resolution and can be used during surgery. An early demonstration of this successful combination was provided by Prof. Gambhir's group, where a chelator was used to bind $^{64}$Cu onto the silica shell of the SERS nanoparticles [61]. A chelator-free approach was demonstrated for the imaging of liver cancer, shown in Fig. 18.5b, where $^{68}$Ga was incorporated directly into the mesoporous silica shell [54].

SERS nanoparticles can also incorporate contrast for MRI and CT. By combining iron oxide and gold in the same nanostructure, MRI and SERS were used together for preclinical imaging in mice [87], as well as with the addition of CT [53]. This triple-modality combination has been demonstrated again in more recent iterations [88]. Other triple-modality combinations have been demonstrated, highlighting the potential clinical applications of nanoparticle-based brain tumor resection [18].

New therapeutic modalities can also be incorporated into the nanoparticle, to combine multiple imaging contrasts and therapy in a single agent. For example, magnetic hyperthermia was demonstrated as a potential therapeutic approach for tumors, where SERS nanoparticles with MRI contrast (iron oxide) were heated up via an oscillating magnetic field [89]. This approach could complement PTT. The potential of photodynamic therapy together with SERS detection was demonstrated in a nanoconstruct that enabled the indirect detection of a target microRNA via SERS, and the production of ROS [90]. SERS was also used to monitor therapy delivery, for example, of cisplatin [91] and drugs targeting lipid metabolism [92].

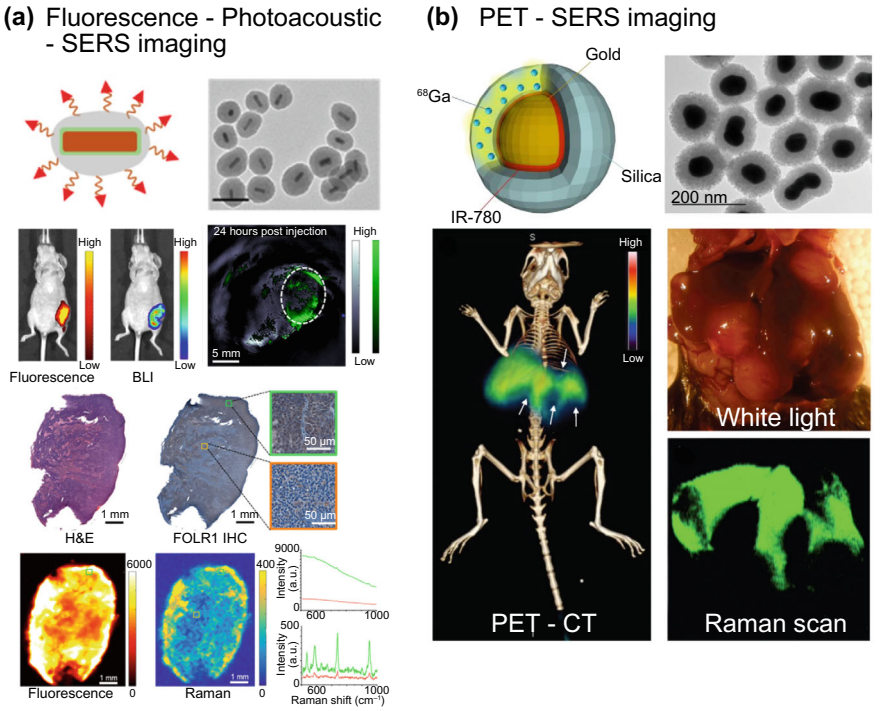



**Fig. 18.5 SERS nanoparticles allow the incorporation of other contrast agents for multimodal imaging. a** SERS nanorods provide contrast for photoacoustic, fluorescence, and Raman imaging. Functionalization of the silica shell with folate provides targeting specificity [84]. **b** A PET-SERS nanoparticle; Gallium-68 is incorporated into the mesoporous silica shell around the spherical gold core of a SERS nanoparticle to visualize the healthy liver parenchyma—the tumors appear hypointense for both modalities [54]

## 18.7 SERS Multiplexed Imaging

What makes Raman imaging with SERS nanoprobes stand out from other imaging techniques is its multiplexing capacity. Imaging multiple molecular targets in a single scan provides synergistically more diagnostic information, making multiplexed imaging a hot topic in biomedical research [93]. Unlike fluorescent contrast agents, SERS nanoparticles feature distinct spectra with sharp peaks specific to the Raman reporter incorporated during their synthesis, which can be identified from within the complex spectrum of a mixture. Other methods, such as mass spectrometry imaging or cyclic fluorescence, can image even more targets, but they cannot be readily implemented in vivo. SERS nanoparticles make a powerful platform for multiplexed imaging, as they have been used preclinically for molecularly targeted imaging, in living organisms as well as with excised samples.

The usefulness of SERS nanoprobes used for tagging biomolecules of interest has been employed for a variety of bioassays [94]. Typically, a gold or silver plasmonic nanostructure is decorated with a Raman reporter molecule, and functionalized against a specific target; when the reporter's spectrum is detected, the presence of the target is inferred. Many variations of this approach have been reported, using different nanostructure geometries and reporter molecule chemistries in the quest to produce bioanalysis panels for diagnostic purposes [94].

Raman imaging, as an optical technique, offers subcellular imaging resolution, and SERS nanoprobes can be used to tag cancer-related markers expressed on cell surfaces. By using two distinct SERS nanoprobes, functionalized with small molecules, it was possible to target the folate receptor and sialic acid on cancer cells; the ratio of the two markers was reported to be different for different types of cancer, as well as between cancer and healthy tissues [95]. Using a combination of three targeted SERS nanoprobes, it was possible to visualize markers expressed by breast cancer cells [96], as well as subcellular components and processes, in 3D and over time [97]. The same principles can be applied to imaging freshly excised tissues, by applying SERS nanoprobes functionalized with antibodies against 3 or 4 targets [98, 99].

However, great interest persists in multiplexed in vivo imaging, since the early demonstrations of the possibility by Prof. Zavaleta and her coworkers. These pioneering experiments used nontargeted SERS nanoprobes, injected at known locations under the skin of a mouse, and imaged noninvasively [14]. An example is shown in Fig. 18.6a, showing four distinct spectra, and corresponding spectrally unmixed images of the mouse flank. A step forward was the imaging of 3 distinct SERS nanoprobes targeted against cancer biomarkers following their intratumoral injection [33]. Nanoprobes with plasmon resonance in the IR were shown to be more readily detectable from deeper within tissues and demonstrated imaging with three different reporters injected subcutaneously [17, 100], while SERS nanoprobes with IR resonant reporters were used to show that in vivo targeted imaging for three markers is possible [34]. A different study utilized SERS to detect three different cancer biomarkers (EGFR, CD44, TGF-βRII) of breast cancer by injecting antibody-conjugated SERS nanotags and achieving maximum signal at 6 h [33]. Similar methodology was followed to detect three germ layers in teratoma formed from mouse embryonic stem cells (mESCs) in an animal xenograft model [101].

Advanced applications were developed based on the imaging of several distinct SERS nanoprobes in animal models and phantoms. For example, the detection of three distinct nanoparticles was achieved with spatially offset optics, using SESORRS [102]. Six-plex endoscopic imaging was performed in colon phantoms [21], whereas targeted triplex endoscopy was performed after topical application of nanoprobes in a rat model of esophageal cancer using a specialized small-animal endoscope [65]. Topical application of nanoprobes (instead of systemic administration) also yielded promising results. Surgical guidance with the application of up to 4 targeted nanoprobes on excised tissues was reported for lumpectomy [103, 104]. A ratiometric approach using topically applied resonant SERS nanoprobes was

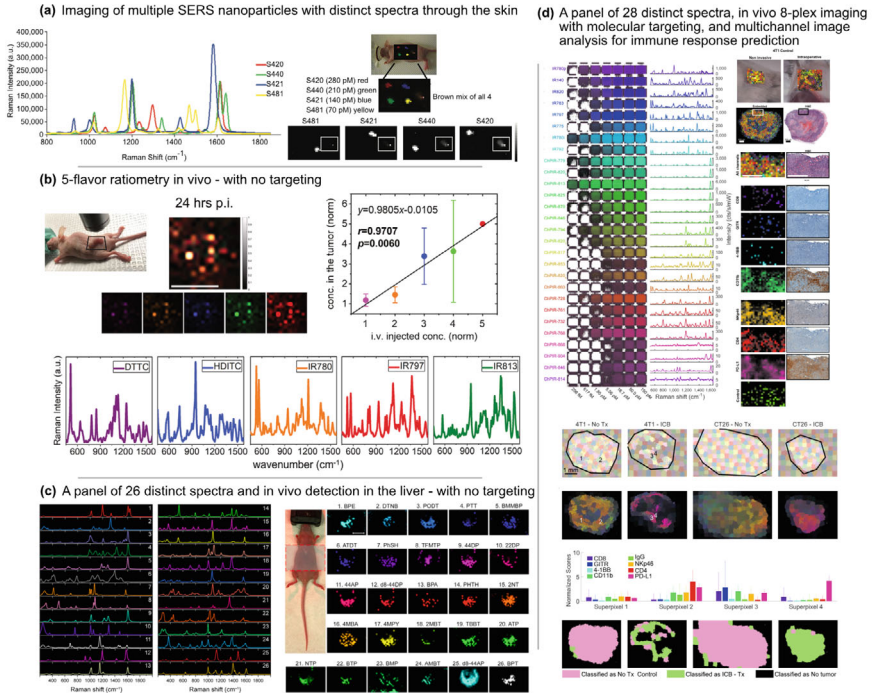



**Fig. 18.6 Multiplexed imaging is enabled by using SERS nanoparticles with distinct spectra.** **a** An early demonstration of imaging 4 distinct SERS nanoparticles injected locally under the skin of a mouse. Adapted from [14]. **b** Quantitative detection of a mixture of five SERS nanoparticles injected intravenously at different concentrations. The nanoparticles accumulate within a subcutaneous tumor. Adapted from [30]. **c** A panel of 26 distinct SERS nanoparticles was injected intravenously in a mouse. All flavors were detected in the animal's liver. Adapted from [37]. **d** A panel of 28 distinct SERS nanoparticles was developed, of which 8 were functionalized with antibodies against immune-related targets enabling in vivo of the animals and ex vivo imaging of the excised tumors. Multichannel image processing produced a machine-learning model revealing the tumor areas with active immune responses. Adapted from [31]

employed to map overexpression of the folate receptor compared to a nontargeted control, revealing microscopic residual tumors after debulking of ovarian cancer [51].

SERS multiplexed imaging has been used for applications other than oncologic imaging. For example, triplex imaging was performed for vascular inflammation in cell cultures and excised arteries from patients [105], and a molecular assay for detection of multiple biomarkers in sputum was demonstrated using enzymatically driven detection combining fluorescence and SERS signals [106].

### *18.7.1 More SERS Nanoprobes, More Applications*

Recently, more interest was demonstrated in high-performing applications of SERS multiplexing, advancing the state of the art in terms of multiplexing capacity, sensitivity, quantitation, and clinical utility. A five-color ratiometric panel was developed using IR resonant reporter molecules [30]. Shown in Fig. 18.6b, this panel demonstrated high sensitivity of detection and demonstrated superior quantitative analysis of the different signals. The five nanoparticles were injected intravenously into a tumor-bearing mouse and imaged. However, as the nanoparticles were not functionalized against any target, they all demonstrated similar tumor localization profiles, based on nonspecific uptake. A panel of 26 distinct nanoparticles was developed by the group of Prof. Zavaleta using small molecules as Raman reporters [37]. The group demonstrated nonspecific uptake of the nanoparticles in the liver of a mouse, seen in Fig. 18.6c, and targeted imaging in cell cultures using 5 distinct nanoprobes applied individually.

Multiplex SERS panels have been demonstrated for imaging the effects of immunotherapy. The effectiveness of immunotherapy relies on the complex interplay between tumor cells, the immune system, and other cells in the tumor microenvironment, and improving it requires imaging many of these actors at once. A panel of 32 SERS nanoparticles was developed, based on small molecule Raman reporters, of which 10 were functionalized and used for imaging 10 molecules (known immune checkpoints) in biopsies from 3 patients [107]. The acquired information was used to perform a network analysis, revealing correlations between the expression of the 10 targets. In a different study, spearheaded by the author, Dr. Andreou, a panel of 28 SERS nanoparticles was developed, of which 8 were used for the in vivo imaging of immune-related molecules in a mouse model of immunotherapy [31]. Imaging of 8 targets was performed in tumor-bearing mice receiving immune checkpoint blockade therapy, and sham-treatment as control. The tumors were excised and fixed, to allow high-resolution Raman imaging and validation via immunohistological imaging, as shown in Fig. 18.6d. Additionally, the study used quantitative analysis for the development of machine learning models that allowed the classification of tumor subareas as responsive to treatment or naïve.

## 18.8 Future Directions

The power and versatility of SERS have been demonstrated time and time again in the preclinical realm. The advanced medical applications of the technique have been discussed in the sections above, including notable recent advances in imaging systems and contrast agents. Yet, not a single example to date has made it to the clinic.

There are two possible paths to medical translation:

The hard path leads toward the in vivo administration of SERS nanoprobes to patients for diagnostic and theranostic purposes. This approach must pass through the Symplegades of clinical approval that have crashed most nanomedicine agents in the past [108, 109]. Toxicity studies are necessary to obviate concerns about the long-term effects of gold-based nanoparticles. Preclinical studies suggest that typical gold-core silica shell nanoparticles can be eliminated from the body [110], and more recent approaches aimed to improve this effect [38]. Effectiveness studies are also required, as nanoparticle-based agents have provided disappointing results in human trials, especially for tumor targeting [111]. Once these obstacles are cleared, then the utility of Raman endoscopes and similar apparatus will skyrocket.

The easier path leads towards the ex vivo use of SERS nanoprobes. SERS-based Raman imaging could provide a valuable alternative to histological assessment of excised tissues, specifically for tumor margin assessment [104]. This approach does not expose the patient to the SERS nanoparticles and could provide valuable information to the surgeon. The main obstacle to this application is the speed of signal acquisition; most studies to date have employed research-grade Raman imaging systems that only offer point-by-point acquisition. Faster imaging systems have been reported [112], but no commercial systems are available to date. The combination of faster scanning with brighter nanoparticles will benefit the clinical translation of the technique.

A third, alternative, path has become apparent in recent years, with the potential of acquiring patient-specific information from living tissues, without the need to expose the patient to nanoparticles. Namely, organ-on-chip technology has gained considerable momentum in various applications and has produced great interest in the field of nanomedicine [113]. These microsystems enable the recapitulation of tissues and tumors from a patient on a chip, where SERS nanoparticles could potentially be used to acquire patient-specific information, potentially related to predicting treatment response. These systems are cost-effective and fast, and once validated, they could produce a powerful companion platform to SERS-based Raman imaging, enabling novel clinical applications as well as revealing basic research mysteries.

**Acknowledgements** Partial funding support was received from the European Union's Horizon 2020 research and innovation program under the Marie Skłodowska-Curie grant agreement 101034403 ONISILOS, and the University of Cyprus Internal Funding program GutCY.

## References

1. J. Langer, D. Jimenez de Aberasturi, J. Aizpurua, R. A. Alvarez-Puebla, B. Auguie, J. J. Baumberg, G. C. Bazan, S. E. J. Bell, A. Boisen, A. G. Brolo, J. Choo, D. Cialla-May, V. Deckert, L. Fabris, K. Faulds, F. J. Garcia de Abajo, R. Goodacre, D. Graham, A. J. Haes, C. L. Haynes, C. Huck, T. Itoh, M. Kall, J. Kneipp, N. A. Kotov, H. Kuang, E. C. Le Ru, H. K. Lee, J. F. Li, X. Y. Ling, S. A. Maier, T. Mayerhofer, M. Moskovits, K. Murakoshi, J. M. Nam, S. Nie, Y. Ozaki, I. Pastoriza-Santos, J. Perez-Juste, J. Popp, A. Pucci, S. Reich, B. Ren,

G. C. Schatz, T. Shegai, S. Schlucker, L. L. Tay, K. G. Thomas, Z. Q. Tian, R. P. Van Duyne, T. Vo-Dinh, Y. Wang, K. A. Willets, C. Xu, H. Xu, Y. Xu, Y. S. Yamamoto, B. Zhao and L. M. Liz-Marzan, Present and Future of Surface-Enhanced Raman Scattering. ACS Nano **14**, 28–117 (2020)

2. M. Fleischmann, P. J. Hendra and A. J. Mcquillan, Raman-Spectra of Pyridine Adsorbed at a Silver Electrode. Chem Phys Lett **26**, 163–166 (1974)
3. M. G. Albrecht and J. A. Creighton, Anomalously Intense Raman-Spectra of Pyridine at a Silver Electrode. J Am Chem Soc **99**, 5215–5217 (1977)
4. D. L. Jeanmaire and R. P. Van Duyne, Surface Raman spectroelectrochemistry: Part I. Heterocyclic, aromatic, and aliphatic amines adsorbed on the anodized silver electrode. Journal of electroanalytical chemistry and interfacial electrochemistry **84**, 1–20 (1977)
5. M. Moskovits, Surface-Enhanced Spectroscopy. Rev Mod Phys **57**, 783–826 (1985)
6. T. Vo-Dinh, M. Y. K. Hiromoto, G. M. Begun and R. L. Moody, Surface-Enhanced Raman Spectrometry for Trace Organic-Analysis. Analytical Chemistry **56**, 1667–1670 (1984)
7. K. Kneipp, H. Kneipp, V. B. Kartha, R. Manoharan, G. Deinum, I. Itzkan, R. R. Dasari and M. S. Feld, Detection and identification of a single DNA base molecule using surface-enhanced Raman scattering (SERS). Phys Rev E **57**, R6281–R6284 (1998)
8. J. Hu, P. C. Zheng, J. H. Jiang, G. L. Shen, R. Q. Yu and G. K. Liu, Sub-attomolar HIV-1 DNA detection using surface-enhanced Raman spectroscopy. Analyst **135**, 1084–1089 (2010)
9. J. Hu and C. Y. Zhang, Single base extension reaction-based surface enhanced Raman spectroscopy for DNA methylation assay. Biosens Bioelectron **31**, 451–457 (2012)
10. H. X. Xu, E. J. Bjerneld, M. Käll and L. Börjesson, Spectroscopy of single hemoglobin molecules by surface enhanced Raman scattering. Phys Rev Lett **83**, 4357–4360 (1999)
11. D. A. Stuart, J. M. Yuen, N. S. O. Lyandres, C. R. Yonzon, M. R. Glucksberg, J. T. Walsh and R. P. Van Duyne, In vivo glucose measurement by surface-enhanced Raman spectroscopy. Analytical Chemistry **78**, 7211–7215 (2006)
12. X. Qian, X. H. Peng, D. O. Ansari, Q. Yin-Goen, G. Z. Chen, D. M. Shin, L. Yang, A. N. Young, M. D. Wang and S. Nie, In vivo tumor targeting and spectroscopic detection with surface-enhanced Raman nanoparticle tags. Nat Biotechnol **26**, 83–90 (2008)
13. Y. L. Wang, J. L. Seebald, D. P. Szeto and J. Irudayaraj, Biocompatibility and Biodistribution of Surface-Enhanced Raman Scattering Nanoprobes in Zebrafish Embryos: in vivo and Multiplex Imaging. Acs Nano **4**, 4039–4053 (2010)
14. C. L. Zavaleta, B. R. Smith, I. Walton, W. Doering, G. Davis, B. Shojaei, M. J. Natan and S. S. Gambhir, Multiplexed imaging of surface enhanced Raman scattering nanotags in living mice using noninvasive Raman spectroscopy. P Natl Acad Sci USA **106**, 13511–13516 (2009)
15. A. M. Mohs, M. C. Mancini, S. Singhal, J. M. Provenzale, B. Leyland-Jones, M. D. Wang and S. Nie, Hand-held spectroscopic device for in vivo and intraoperative tumor detection: contrast enhancement, detection sensitivity, and tissue penetration. Anal Chem **82**, 9058–9065 (2010)
16. H. Karabeber, R. Huang, P. Iacono, J. M. Samii, K. Pitter, E. C. Holland and M. F. Kircher, Guiding brain tumor resection using surface-enhanced Raman scattering nanoparticles and a hand-held Raman scanner. ACS Nano **8**, 9755–9766 (2014)
17. G. von Maltzahn, A. Centrone, J. H. Park, R. Ramanathan, M. J. Sailor, T. A. Hatton and S. N. Bhatia, SERS-Coded Gold Nanorods as a Multifunctional Platform for Densely Multiplexed Near-infrared Imaging and Photothermal Heating. Adv Mater **21**, 3175+ (2009)
18. M. F. Kircher, A. de la Zerda, J. V. Jokerst, C. L. Zavaleta, P. J. Kempen, E. Mittra, K. Pitter, R. M. Huang, C. Campos, F. Habte, R. Sinclair, C. W. Brennan, I. K. Mellinghoff, E. C. Holland and S. S. Gambhir, A brain tumor molecular imaging strategy using a new triple-modality MRI-photoacoustic-Raman nanoparticle. Nat Med **18**, 829–U235 (2012)
19. S. Jeong, Y. I. Kim, H. Kang, G. Kim, M. G. Cha, H. Chang, K. O. Jung, Y. H. Kim, B. H. Jun, D. W. Hwang, Y. S. Lee, H. Youn, Y. S. Lee, K. W. Kang, D. S. Lee and D. H. Jeong, Fluorescence-Raman dual modal endoscopic system for multiplexed molecular diagnostics. Sci Rep **5**, 9455 (2015)

20. Y. I. Kim, S. Jeong, K. O. Jung, M. G. Song, C. H. Lee, S. J. Chung, J. Y. Park, M. G. Cha, S. G. Lee, B. H. Jun, Y. S. Lee, D. W. Hwang, H. Youn, K. W. Kang, Y. S. Lee, D. H. Jeong and D. S. Lee, Simultaneous Detection of EGFR and VEGF in Colorectal Cancer using Fluorescence-Raman Endoscopy. Sci Rep-UK **7** (2017)
21. E. Garai, S. Sensarn, C. L. Zavaleta, N. O. Loewke, S. Rogalla, M. J. Mandella, S. A. Felt, S. Friedland, J. T. C. Liu, S. S. Gambhir and C. H. Contag, A Real-Time Clinical Endoscopic System for Intraluminal, Multiplexed Imaging of Surface-Enhanced Raman Scattering Nanoparticles. Plos One **10** (2015)
22. P. Dey, A. Vaideanu, S. Mosca, M. Salimi, B. Gardner, F. Palombo, I. Uchegbu, J. Baumberg, A. Schatzlein, P. Matousek and N. Stone, Surface enhanced deep Raman detection of cancer tumour through 71 mm of heterogeneous tissue. Nanotheranostics **6**, 337–349 (2022)
23. Z. Wu, B. Deng, Y. Zhou, H. Xie, Y. Zhang, L. Lin and J. Ye, Non-Invasive Detection, Precise Localization, and Perioperative Navigation of In Vivo Deep Lesions Using Transmission Raman Spectroscopy. Adv Sci (Weinh) **10**, e2301721 (2023)
24. Y. Zhang, R. Chen, F. Liu, P. Miao, L. Lin and J. Ye, In Vivo Surface-Enhanced Transmission Raman Spectroscopy under Maximum Permissible Exposure: Toward Photosafe Detection of Deep-Seated Tumors. Small Methods **7**, e2201334 (2023)
25. H. Q. Xie, Y. M. Zhang, Z. Y. Wu, Z. Z. Bao, L. Lin and J. Ye, Locating Three-Dimensional Position of Deep-Seated SERS Phantom Lesions in Thick Tissues Using Tomographic Transmission Raman Spectroscopy. Acs Appl Mater Inter **15**, 44665–44675 (2023)
26. S. Harmsen, R. Huang, M. A. Wall, H. Karabeber, J. M. Samii, M. Spaliviero, J. R. White, S. Monette, R. O'Connor, K. L. Pitter, S. A. Sastra, M. Saborowski, E. C. Holland, S. Singer, K. P. Olive, S. W. Lowe, R. G. Blasberg and M. F. Kircher, Surface-enhanced resonance Raman scattering nanostars for high-precision cancer imaging. Sci Transl Med **7**, 271ra277 (2015)
27. Kenry, F. Nicolson, L. Clark, S. R. Panikkanvalappil, B. Andreiuk and C. Andreou, Advances in Surface Enhanced Raman Spectroscopy for in Vivo Imaging in Oncology. Nanotheranostics **6**, 31–49 (2022)
28. C. Andreou, S. A. Kishore and M. F. Kircher, Surface-Enhanced Raman Spectroscopy: A New Modality for Cancer Imaging. J Nucl Med **56**, 1295–1299 (2015)
29. F. Nicolson, L. E. Jamieson, S. Mabbott, K. Plakas, N. C. Shand, M. R. Detty, D. Graham and K. Faulds, Surface enhanced resonance Raman spectroscopy (SERRS) for probing through plastic and tissue barriers using a handheld spectrometer. Analyst **143**, 5965–5973 (2018)
30. J. H. Yu, I. Steinberg, R. M. Davis, A. V. Malkovskiy, A. Zlitni, R. K. Radzyminski, K. O. Jung, D. T. Chung, L. D. Curet, A. L. D'Souza, E. Chang, J. Rosenberg, J. Campbell, H. Frostig, S. M. Park, G. Pratx, C. Levin and S. S. Gambhir, Noninvasive and Highly Multiplexed Five-Color Tumor Imaging of Multicore Near-Infrared Resonant Surface-Enhanced Raman Nanoparticles In Vivo. ACS Nano **15**, 19956–19969 (2021)
31. C. Andreou, K. Plakas, N. Berisha, M. Gigoux, L. E. Rosch, R. Mirsafavi, A. Oseledchyk, S. Pal, D. Zamarin, T. Merghoub, M. R. Detty and M. F. Kircher, Multiplexed molecular imaging with surface enhanced resonance Raman scattering nanoprobes reveals immunotherapy response in mice via multichannel image segmentation. Nanoscale Horiz **7**, 1540–1552 (2022)
32. O. E. Eremina, D. B. Eremin, A. Czaja and C. Zavaleta, Selecting Surface-Enhanced Raman Spectroscopy Flavors for Multiplexed Imaging Applications: Beyond the Experiment. J Phys Chem Lett **12**, 5564–5570 (2021)
33. U. S. Dinish, G. Balasundaram, Y. T. Chang and M. Olivo, Actively targeted in vivo multiplex detection of intrinsic cancer biomarkers using biocompatible SERS nanotags. Sci Rep **4**, 4075 (2014)
34. K. K. Maiti, U. S. Dinish, A. Samanta, M. Vendrell, K. S. Soh, S. J. Park, M. Olivo and Y. T. Chang, Multiplex targeted in vivo cancer detection using sensitive near-infrared SERS nanotags. Nano Today **7**, 85–93 (2012)
35. C. Andreou, V. Neuschmelting, D. F. Tschaharganeh, C. H. Huang, A. Oseledchyk, P. Iacono, H. Karabeber, R. R. Colen, L. Mannelli, S. W. Lowe and M. F. Kircher, Imaging of Liver Tumors Using Surface-Enhanced Raman Scattering Nanoparticles. Acs Nano **10**, 5015–5026 (2016)

36. S. Harmsen, S. Rogalla, R. M. Huang, M. Spaliviero, V. Neuschmelting, Y. Hayakawa, Y. Lee, Y. Tailor, R. Toledo-Crow, J. W. Kang, J. M. Samii, H. Karabeber, R. M. Davis, J. R. White, M. van de Rijn, S. S. Gambhir, C. H. Contag, T. C. Wang and M. F. Kircher, Detection of Premalignant Gastrointestinal Lesions Using Surface-Enhanced Resonance Raman Scattering-Nanoparticle Endoscopy. Acs Nano **13**, 1354–1364 (2019)
37. O. E. Eremina, A. T. Czaja, A. Fernando, A. Aron, D. B. Eremin and C. Zavaleta, Expanding the Multiplexing Capabilities of Raman Imaging to Reveal Highly Specific Molecular Expression and Enable Spatial Profiling. ACS Nano **16**, 10341–10353 (2022)
38. J. H. Yu, M. S. Jeong, E. O. Cruz, I. S. Alam, S. K. Tumbale, A. Zlitni, S. Y. Lee, Y. I. Park, K. Ferrara, S. H. Kwon, S. S. Gambhir and J. Rao, Highly Excretable Gold Supraclusters for Translatable in vivo Raman Imaging of Tumors. Acs Nano **17**, 2554–2567 (2023)
39. Y. Zhang, H. Liu, J. Tang, Z. Li, X. Zhou, R. Zhang, L. Chen, Y. Mao and C. Li, Noninvasively Imaging Subcutaneous Tumor Xenograft by a Handheld Raman Detector, with the Assistance of an Optical Clearing Agent. ACS Appl Mater Interfaces **9**, 17769–17776 (2017)
40. Y. Qiu, M. Lin, G. Chen, C. Fan, M. Li, X. Gu, S. Cong, Z. Zhao, L. Fu, X. Fang and Z. Xiao, Photodegradable CuS SERS Probes for Intraoperative Residual Tumor Detection, Ablation, and Self-Clearance. ACS Appl Mater Interfaces **11**, 23436–23444 (2019)
41. Z. Z. Bao, Y. Q. Zhang, Z. Y. Tan, X. Yin, W. Di and J. Ye, Gap-enhanced Raman tags for high-contrast sentinel lymph node imaging. Biomaterials **163**, 105–115 (2018)
42. K. Cui, C. C. Fan, G. X. Chen, Y. Y. Qiu, M. W. Li, M. Lin, J. B. Wan, C. S. Cai and Z. Y. Xiao, Aminothiophenol Radical Reaction-Functionalized Gold Nanoprobe for One-to-All Detection of Five Reactive Oxygen Species In Vivo. Analytical Chemistry **90**, 12137–12144 (2018)
43. X. Y. Niu, L. C. Yu, X. H. Wang, Z. J. Zhang, X. M. Li, X. Y. Feng, W. Wang and Z. Yuan, Acid-responsive aggregated SERS nanoparticles for improved tumor diagnosis. Mater Chem Front **6**, 644–651 (2022)
44. Y. R. Wang, Y. J. Yang, J. X. Guo, H. X. Ju and Y. L. Chen, Tumor Identification via in Vivo Portable Raman Detection of Sialic Acid with a Dual Gold Nanoprobe System. Chem Sci **14**, 923–927 (2023)
45. S. Pal, A. Ray, C. Andreou, Y. D. Zhou, T. Rakshit, M. Wlodarczyk, M. Maeda, R. Toledo-Crow, N. Berisha, J. Yang, H. T. Hsu, A. Oseledchyk, J. Mondal, S. L. Zou and M. F. Kircher, DNA-enabled rational design of fluorescence-Raman bimodal nanoprobes for cancer imaging and therapy. Nat Commun **10** (2019)
46. Y. Liu, J. R. Ashton, E. J. Moding, H. K. Yuan, J. K. Register, A. M. Fales, J. Choi, M. J. Whitley, X. G. Zhao, Y. Qi, Y. Ma, G. Vaidyanathan, M. R. Zalutsky, D. G. Kirsch, C. T. Badea and T. Vo-Dinh, A Plasmonic Gold Nanostar Theranostic Probe for in vivo Tumor Imaging and Photothermal Therapy. Theranostics **5**, 946–960 (2015)
47. Y. F. Zhan, H. R. Liu, J. L. Tang, Z. Y. Li, X. Y. Zhou, R. Zhang, L. Chen, Y. Mao and C. Li, Noninvasively Imaging Subcutaneous Tumor Xenograft by a Handheld Raman Detector, with the Assistance of an Optical Clearing Agent. Acs Appl Mater Inter **9**, 17769–17776 (2017)
48. Y. Wen, V. X. Truong and M. Li, Real-Time Intraoperative Surface-Enhanced Raman Spectroscopy-Guided Thermosurgical Eradication of Residual Microtumors in Orthotopic Breast Cancer. Nano Lett **21**, 3066–3074 (2021)
49. V. Neuschmelting, S. Harmsen, N. Beziere, H. Lockau, H. T. Hsu, R. M. Huang, D. Razansky, V. Ntziachristos and M. F. Kircher, Dual-Modality Surface-Enhanced Resonance Raman Scattering and Multispectral Optoacoustic Tomography Nanoparticle Approach for Brain Tumor Delineation. Small **14** (2018)
50. F. Nicolson, B. Andreiuk, C. Andreou, H. T. Hsu, S. Rudder and M. F. Kircher, Non-invasive In Vivo Imaging of Cancer Using Surface-Enhanced Spatially Offset Raman Spectroscopy (SESORS). Theranostics **9**, 5899–5913 (2019)
51. A. Oseledchyk, C. Andreou, M. A. Wall and M. F. Kircher, Folate-Targeted Surface-Enhanced Resonance Raman Scattering Nanoprobe Ratiometry for Detection of Microscopic Ovarian Cancer. Acs Nano **11**, 1488–1497 (2017)

52. J. He, S. Y. Hua, D. X. Zhang, K. Wang, X. Y. Chen and M. Zhou, SERS/NIR-II Optical Nanoprobes for Multidimensional Tumor Imaging from Living Subjects, Pathology, and Single Cells and Guided NIR-II Photothermal Therapy. Adv Funct Mater **32** (2022)
53. V. Amendola, S. Scaramuzza, L. Litti, M. Meneghetti, G. Zuccolotto, A. Rosato, E. Nicolato, P. Marzola, G. Fracasso, C. Anselmi, M. Pinto and M. Colombatti, Magneto-Plasmonic Au-Fe Alloy Nanoparticles Designed for Multimodal SERS-MRI-CT Imaging. Small **10**, 2476–2486 (2014)
54. M. A. Wall, T. M. Shaffer, S. Harmsen, D. F. Tschaharganeh, C. H. Huang, S. W. Lowe, C. M. Drain and M. F. Kircher, Chelator-Free Radiolabeling of SERRS Nanoparticles for Whole-Body PET and Intraoperative Raman Imaging. Theranostics **7**, 3068–3077 (2017)
55. C. Zhang, Z. W. Xu, H. X. Di, E. Z. Zeng, Y. Jiang and D. B. Liu, Gadolinium-doped Au@prussian blue nanoparticles as MR/SERS bimodal agents for dendritic cell activating and tracking. Theranostics **10**, 6061–6071 (2020)
56. P. He, W. H. Han, C. Bi, W. L. Song, S. Y. Niu, H. Zhou and X. R. Zhang, Many Birds, One Stone: A Smart Nanodevice for Ratiometric Dual-Spectrum Assay of Intracellular MicroRNA and Multimodal Synergetic Cancer Therapy. Acs Nano **15**, 6961–6976 (2021)
57. K. Jibin, J. S. Prasad, G. Saranya, S. Shenoy, K. K. Maiti and R. S. Jayasree, Optically controlled hybrid metamaterial of plasmonic spiky gold inbuilt graphene sheets for bimodal imaging guided multimodal therapy. Biomater Sci-UK **8**, 3381–3391 (2020)
58. L. Yang, T. H. Kim, H. Y. Cho, J. Luo, J. M. Lee, S. T. D. Chueng, Y. N. Hou, P. T. T. Yin, J. Y. Han, J. H. Kim, B. G. Chung, J. W. Choi and K. B. Lee, Hybrid Graphene-Gold Nanoparticle-Based Nucleic Acid Conjugates for Cancer-Specific Multimodal Imaging and Combined Therapeutics. Adv Funct Mater **31** (2021)
59. M. G. Cha, S. Lee, S. Park, H. Kang, S. G. Lee, C. Jeong, Y. S. Lee, C. Kim and D. H. Jeong, A dual modal silver bumpy nanoprobe for photoacoustic imaging and SERS multiplexed identification of in vivo lymph nodes. Nanoscale **9**, 12556–12564 (2017)
60. Z. Y. Jin, Q. Yue, W. J. Duan, A. Sui, B. T. Zhao, Y. H. Deng, Y. T. Zhai, Y. W. Zhang, T. Sun, G. P. Zhang, L. M. Han, Y. Mao, J. H. Yu, X. Y. Zhang and C. Li, Intelligent SERS Navigation System Guiding Brain Tumor Surgery by Intraoperatively Delineating the Metabolic Acidosis. Adv Sci **9** (2022)
61. C. L. Zavaleta, K. B. Hartman, Z. Miao, M. L. James, P. Kempen, A. S. Thakor, C. H. Nielsen, R. Sinclair, Z. Cheng and S. S. Gambhir, Preclinical Evaluation of Raman Nanoparticle Biodistribution for their Potential Use in Clinical Endoscopy Imaging. Small **7**, 2232–2240 (2011)
62. E. Garai, S. Sensarn, C. L. Zavaleta, D. Van de Sompel, N. O. Loewke, M. J. Mandella, S. S. Gambhir and C. H. Contag, High-sensitivity, real-time, ratiometric imaging of surface-enhanced Raman scattering nanoparticles with a clinically translatable Raman endoscope device. J Biomed Opt **18** (2013)
63. C. L. Zavaleta, E. Garai, J. T. C. Liu, S. Sensarn, M. J. Mandella, D. Van de Sompel, S. Friedland, J. Van Dam, C. H. Contag and S. S. Gambhir, A Raman-based endoscopic strategy for multiplexed molecular imaging. P Natl Acad Sci USA **110**, 10062–10063 (2013)
64. Y. Wang, A. Khan, S. Y. Leigh, D. N. Wang, Y. Chen, D. Meza and J. T. C. Liu, Comprehensive spectral endoscopy of topically applied SERS nanoparticles in the rat esophagus. Biomed Opt Express **5**, 2883–2895 (2014)
65. Y. W. Wang, S. Kang, A. Khan, P. Q. Bao and J. T. Liu, In vivo multiplexed molecular imaging of esophageal cancer via spectral endoscopy of topically applied SERS nanoparticles. Biomed Opt Express **6**, 3714–3723 (2015)
66. Z. Y. Wu, Z. W. Wang, H. Q. Xie, Y. M. Wang, H. Q. He, S. M. Nie, J. Ye and L. Lin, Raman-Guided Bronchoscopy: Feasibility and Detection Depth Studies Using Ex Vivo Lung Tissues and SERS Nanoparticle Tags. Photonics-Basel **9** (2022)
67. F. Nicolson, M. F. Kircher, N. Stone and P. Matousek, Spatially offset Raman spectroscopy for biomedical applications. Chem Soc Rev **50**, 556–568 (2021)
68. N. Stone, M. Kerssens, G. R. Lloyd, K. Faulds, D. Graham and P. Matousek, Surface enhanced spatially offset Raman spectroscopic (SESORS) imaging - the next dimension. Chem Sci **2**, 776–780 (2011)

69. J. M. Yuen, N. C. Shah, J. T. Walsh, M. R. Glucksberg and R. P. Van Duyne, Transcutaneous Glucose Sensing by Surface-Enhanced Spatially Offset Raman Spectroscopy in a Rat Model. Analytical Chemistry **82**, 8382–8385 (2010)
70. F. Nicolson, L. E. Jamieson, S. Mabbott, K. Plakas, N. C. Shand, M. R. Detty, D. Graham and K. Faulds, Through tissue imaging of a live breast cancer tumour model using handheld surface enhanced spatially offset resonance Raman spectroscopy (SESORRS). Chem Sci **9**, 3788–3792 (2018)
71. B. Sharma, K. Ma, M. R. Glucksberg and R. P. Van Duyne, Seeing through Bone with Surface-Enhanced Spatially Offset Raman Spectroscopy. J Am Chem Soc **135**, 17290–17293 (2013)
72. A. S. Moody, T. D. Payne, B. A. Barth and B. Sharma, Surface-enhanced spatially-offset Raman spectroscopy (SESORS) for detection of neurochemicals through the skull at physiologically relevant concentrations. Analyst **145**, 1885–1893 (2020)
73. F. Nicolson, B. Andreiuk, E. Lee, B. O'Donnell, A. Whitley, N. Riepl, and D. L. Burkhart, et al, In vivo Imaging using Surface Enhanced Spatially Offset Raman Spectroscopy (SESORS): Balancing Sampling Frequency to Improve Overall Image Acquisition. npj Imaging **2**(1), 7 (2024)
74. L. K. Rotter, N. Berisha, H. T. Hsu, K. H. Burns, C. Andreou and M. F. Kircher, Visualizing surface marker expression and intratumoral heterogeneity with SERRS-NPs imaging. Nanotheranostics **6**, 256–269 (2022)
75. R. Huang, S. Harmsen, J. M. Samii, H. Karabeber, K. L. Pitter, E. C. Holland and M. F. Kircher, High Precision Imaging of Microscopic Spread of Glioblastoma with a Targeted Ultrasensitive SERRS Molecular Imaging Probe. Theranostics **6**, 1075–1084 (2016)
76. R. A. Odion, P. Strobbia, B. M. Crawford and T. Vo-Dinh, Inverse surface-enhanced spatially offset Raman spectroscopy (SESORS) through a monkey skull. J Raman Spectrosc **49**, 1452–1460 (2018)
77. S. M. Asiala, N. C. Shand, K. Faulds and D. Graham, Surface-Enhanced, Spatially Offset Raman Spectroscopy (SESORS) in Tissue Analogues. Acs Appl Mater Inter **9**, 25488–25494 (2017)
78. M. Z. Vardaki and N. Kourkoumelis, Tissue Phantoms for Biomedical Applications in Raman Spectroscopy: A Review. Biomed Eng Comput Bi **11** (2020)
79. B. Gardner, P. Matousek and N. Stone, Direct monitoring of light mediated hyperthermia induced within mammalian tissues using surface enhanced spatially offset Raman spectroscopy (T-SESORS). Analyst **144**, 3552–3555 (2019)
80. M. E. Berry, S. M. McCabe, S. Sloan-Dennison, S. Laing, N. C. Shand, D. Graham and K. Faulds, Tomographic Imaging and Localization of Nanoparticles in Tissue Using Surface-Enhanced Spatially Offset Raman Spectroscopy. Acs Appl Mater Inter **14**, 31613–31624 (2022)
81. C. Andreou, S. Pal, L. Rotter, J. Yang and M. F. Kircher, Molecular Imaging in Nanotechnology and Theranostics. Mol Imaging Biol **19**, 363–372 (2017)
82. Y. Liu, Z. Chang, H. K. Yuan, A. M. Fales and T. Vo-Dinh, Quintuple-modality (SERS-MRI-CT-TPL-PTT) plasmonic nanoprobe for theranostics. Nanoscale **5**, 12126–12131 (2013)
83. E. Lenzi, D. J. de Aberasturi, M. Henriksen-Lacey, P. Piñeiro, A. J. Muniz, J. Lahann and L. M. Liz-Marzán, SERS and Fluorescence-Active Multimodal Tessellated Scaffolds for Three-Dimensional Bioimaging. Acs Appl Mater Inter **14**, 20708–20719 (2022)
84. S. Pal, J. K. Koneru, C. Andreou, T. Rakshit, V. K. Rajasekhar, M. Wlodarczyk, J. H. Healey, M. F. Kircher and J. Mondal, DNA-Functionalized Gold Nanorods for Perioperative Optical Imaging and Photothermal Therapy of Triple-Negative Breast Cancer. Acs Appl Nano Mater (2022)
85. C. C. Wen, H. Chen, X. L. Guo, Z. X. Lin, S. P. Zhang, X. C. Shen and H. Liang, Lysosome-Targeted Gold Nanotheranostics for in situ SERS Monitoring pH and Multimodal Imaging-Guided Phototherapy. Langmuir **37**, 569–577 (2021)
86. F. Yang, Q. Wang, Z. X. Gu, K. Fang, G. Marriott and N. Gu, Silver Nanoparticle-Embedded Microbubble as a Dual-Mode Ultrasound and Optical Imaging Probe. Acs Appl Mater Inter **5**, 9217–9223 (2013)

87. M. V. Yigit, L. Y. Zhu, M. A. Ifediba, Y. Zhang, K. Carr, A. Moore and Z. Medarova, Noninvasive MRI-SERS Imaging in Living Mice Using an Innately Bimodal Nanomaterial. Acs Nano **5**, 1056–1066 (2011)
88. B. W. Shi, B. Y. Zhang, Y. Q. Zhang, Y. Q. Gu, C. Zheng, J. Yan, W. B. Chen, F. H. Yan, J. Ye and H. Zhang, Multifunctional gap-enhanced Raman tags for preoperative and intraoperative cancer imaging. Acta Biomater **104**, 210–220 (2020)
89. Y. Han, S. L. Lei, J. H. Lu, Y. He, Z. W. Chen, L. Ren and X. Zhou, Potential use of SERS-assisted theranostic strategy based on $Fe_3O_4$/Au cluster/shell nanocomposites for bio-detection, MRI, and magnetic hyperthermia. Mat Sci Eng C-Mater **64**, 199–207 (2016)
90. J. Liu, T. T. Zheng and Y. Tian, Functionalized h-BN Nanosheets as a Theranostic Platform for SERS Real-Time Monitoring of MicroRNA and Photodynamic Therapy. Angew Chem Int Edit **58**, 7757–7761 (2019)
91. Y. W. He, Y. Q. Zhang, Y. C. Gong, Z. W. Zhang, T. C. Xu, L. Q. Tian, T. Pan, H. Yang, H. Pan, Q. M. Kou, H. Wang and G. L. Shao, Multimodal imaging of nano-assembled microspheres loaded with doxorubicin and Cisplatin for liver tumor therapy. Front Bioeng Biotech **10** (2022)
92. E. Sheikh, K. Agrawal, S. Roy, D. Burk, F. Donnarumma, Y. H. Ko, P. K. Guttula, N. C. Biswal, H. D. Shukla and M. R. Gartia, Multimodal Imaging of Pancreatic Cancer Microenvironment in Response to an Antiglycolytic Drug. Adv Healthc Mater (2023)
93. C. Andreou, R. Weissleder and M. F. Kircher, Multiplexed imaging in oncology. Nat Biomed Eng **6**, 527–540 (2022)
94. Y. Zeng, K. M. Koo, M. Trau, A. G. Shen and J. M. Hu, Watching SERS glow for multiplex biomolecular analysis in the clinic: A review. Appl Mater Today **15**, 431–444 (2019)
95. A. Verdin, C. Malherbe, W. H. Muller, V. Bertrand and G. Eppe, Multiplex micro-SERS imaging of cancer-related markers in cells and tissues using poly(allylamine)-coated Au@Ag nanoprobes. Anal Bioanal Chem **412**, 7739–7755 (2020)
96. M. Li, J. Wu, M. Ma, Z. Feng, Z. Mi, P. Rong and D. Liu, Alkyne- and Nitrile-Anchored Gold Nanoparticles for Multiplex SERS Imaging of Biomarkers in Cancer Cells and Tissues. Nanotheranostics **3**, 113–119 (2019)
97. Y. Chen, X. Bai, L. Su, Z. Du, A. Shen, A. Materny and J. Hu, Combined Labelled and Label-free SERS Probes for Triplex Three-dimensional Cellular Imaging. Sci Rep **6**, 19173 (2016)
98. S. Kang, Y. Wang, N. P. Reder and J. T. Liu, Multiplexed Molecular Imaging of Biomarker-Targeted SERS Nanoparticles on Fresh Tissue Specimens with Channel-Compressed Spectrometry. Plos One **11**, e0163473 (2016)
99. Y. W. Wang, J. D. Doerksen, S. Y. Kang, D. Walsh, Q. Yang, D. Hong and J. T. C. Liu, Multiplexed Molecular Imaging of Fresh Tissue Surfaces Enabled by Convection-Enhanced Topical Staining with SERS-Coded Nanoparticles. Small **12**, 5612–5621 (2016)
100. H. Kang, S. Jeong, Y. Park, J. Yim, B. H. Jun, S. Kyeong, J. K. Yang, G. Kim, S. Hong, L. P. Lee, J. H. Kim, H. Y. Lee, D. H. Jeong and Y. S. Lee, Near-Infrared SERS Nanoprobes with Plasmonic Au/Ag Hollow-Shell Assemblies for In Vivo Multiplex Detection. Adv Funct Mater **23**, 3719–3727 (2013)
101. A. Samanta, R. K. Das, S. J. Park, K. K. Maiti and Y. T. Chang, Multiplexing SERS nanotags for the imaging of differentiated mouse embryonic stem cells (mESC) and detection of teratoma in vivo. Am J Nucl Med Mol Imaging **4**, 114–124 (2014)
102. F. Nicolson, L. E. Jamieson, S. Mabbott, K. Plakas, N. C. Shand, M. R. Detty, D. Graham and K. Faulds, Multiplex imaging of live breast cancer tumour models through tissue using handheld surface enhanced spatially offset resonance Raman spectroscopy (SESORRS). Chem Commun **54**, 8530–8533 (2018)
103. Y. W. Wang, N. P. Reder, S. Kang, A. K. Glaser, Q. Yang, M. A. Wall, S. H. Javid, S. M. Dintzis and J. T. C. Liu, Raman-Encoded Molecular Imaging with Topically Applied SERS Nanoparticles for Intraoperative Guidance of Lumpectomy. Cancer Res **77**, 4506–4516 (2017)
104. Y. Wang, S. Y. Kang, J. D. Doerksen, A. K. Glaser and J. T. C. Liu, Surgical Guidance via Multiplexed Molecular Imaging of Fresh Tissues Labeled With SERS-Coded Nanoparticles. Ieee J Sel Top Quant **22** (2016)

105. J. Noonan, S. M. Asiala, G. Grassia, N. MacRitchie, K. Gracie, J. Carson, M. Moores, M. Girolami, A. C. Bradshaw, T. J. Guzik, G. R. Meehan, H. E. Scales, J. M. Brewer, I. B. McInnes, N. Sattar, K. Faulds, P. Garside, D. Graham and P. Maffia, In vivo multiplex molecular imaging of vascular inflammation using surface-enhanced Raman spectroscopy. Theranostics **8**, 6195–6209 (2018)
106. G. Saranya, M. M. Joseph, V. Karunakaran, J. B. Nair, V. N. Saritha, V. S. Veena, K. Sujathan, A. Ajayaghosh and K. K. Maiti, Enzyme-Driven Switchable Fluorescence-SERS Diagnostic Nanococktail for the Multiplex Detection of Lung Cancer Biomarkers. Acs Appl Mater Inter **10**, 38807–38818 (2018)
107. J. Li, F. Liu, X. Bi and J. Ye, Imaging immune checkpoint networks in cancer tissues with supermultiplexed SERS nanoprobes. Biomaterials **302**, 122327 (2023)
108. P. J. Gawne, M. Ferreira, M. Papaluca, J. Grimm and P. Decuzzi, New opportunities and old challenges in the clinical translation of nanotheranostics. Nat Rev Mater **8**, 783–798 (2023)
109. J. M. Metselaar and T. Lammers, Challenges in nanomedicine clinical translation. Drug Deliv Transl Re **10**, 721–725 (2020)
110. A. S. Thakor, R. Luong, R. Paulmurugan, F. I. Lin, P. Kempen, C. Zavaleta, P. Chu, T. F. Massoud, R. Sinclair and S. S. Gambhir, The fate and toxicity of Raman-active silica-gold nanoparticles in mice. Sci Transl Med **3**, 79ra33 (2011)
111. J. Park, Y. Choi, H. Chang, W. Um, J. H. Ryu and I. C. Kwon, Alliance with EPR Effect: Combined Strategies to Improve the EPR Effect in the Tumor Microenvironment. Theranostics **9**, 8073–8090 (2019)
112. S. E. Bohndiek, A. Wagadarikar, C. L. Zavaleta, D. Van de Sompel, E. Garai, J. V. Jokerst, S. Yazdanfar and S. S. Gambhir, A small animal Raman instrument for rapid, wide-area, spectroscopic imaging. Proc Natl Acad Sci U S A **110**, 12408–12413 (2013)
113. M. Stavrou, N. Phung, J. Grimm and C. Andreou, Organ-on-chip systems as a model for nanomedicine. Nanoscale **15**, 9927–9940 (2023)

# Chapter 19
# Analytical SERS for Liquid Biopsy Biomarkers Detection




**Anastasiia Tukova, Wei Zhang, Alison Rodger, and Yuling Wang**

**Abstract** Considerable research effort has been dedicated to devising analytical techniques for cancer diagnosis and monitoring of treatment progress and prognosis by tracking a range of cancer biomarkers including circulating tumour cells (CTCs), small extracellular vehicles (sEVs), circulating nucleic acids, RNA and DNA, and specific proteins, primarily in blood. These analyses are collectively referred to as liquid biopsies. Due to the low abundance of such biomarkers in the blood there is an urgent need to establish swift and dependable assays for gauging their presence and quantity within patient samples. Surface-enhanced Raman scattering (SERS) has garnered substantial attention for this purpose owing to its unique advantages of high sensitivity, specificity, multiplexing capability, and photostability. Therefore, SERS has been widely used in many applications, among which analytical SERS has been the focus in recent years. In this book chapter, we provide an overview of recent developments (within the last 5 years) in analytical SERS for liquid biopsy biomarkers detection. We also provide our insights into the forthcoming challenges in the realm of SERS applications for biomarkers detection towards cancer diagnosis.

**Keywords** SERS · Plasmonic nanostructure · Nanotags · Biosensing · Biomarker

## 19.1 Introduction

Traditional disease diagnostic methods, such as polymerase chain reaction (PCR), tissue biopsy, blood tests and imaging, are often time-consuming and invasive, requiring trained professionals and expensive equipment. This has limited their availability and leads to late diagnoses [1] as they generally detect biomarkers only when the disease is well-advanced [2–4]. Surface-enhanced Raman scattering

A. Tukova · W. Zhang · A. Rodger · Y. Wang (✉)
School of Natural Sciences, Faculty of Science and Engineering, Macquarie University, Sydney, NSW 2109, Australia
e-mail: yuling.wang@mq.edu.au

A. Rodger
Research School of Chemistry, Australian National University, Canberra, ACT 2601, Australia

© The Author(s), under exclusive license to Springer Nature Singapore Pte Ltd. 2024

M. Procházka et al. (eds.), *Surface- and Tip-Enhanced Raman Scattering Spectroscopy*,
https://doi.org/10.1007/978-981-97-5818-0_19

(SERS) stands out as an ultrasensitive analytical method that requires minimal sample amounts to even detect a single molecule under certain conditions [5, 6]. SERS is extensively used for detecting and distinguishing biomarkers in solution, providing unique spectral profiles or "molecular fingerprints" of the molecules on SERS substrates. Importantly, SERS-based detection using liquid samples is non-invasive, reducing patient risk and simplifying the analysis process [5, 7].

Briefly, SERS is a phenomenon whereby Raman signals of the molecules are greatly amplified when they are close to a nanoscale metal surface [7]. This effect involves two main mechanisms: electromagnetic enhancement and chemical enhancement. Electromagnetic enhancement arises from the generation of localized surface plasmons on nanoscale noble (usually silver and/or gold) metal substrates when illuminated by lasers. These plasmons create strong electromagnetic fields near the surface, enhancing Raman scattering significantly for analyte molecules close to the surface [5, 6]. This can boost Raman intensity by several orders of magnitude, enabling highly sensitive trace detection. Chemical enhancement is analyte-dependent and involves interactions between analyte molecules and the substrate, possibly through charge transfer, charge polarization, or resonant chemical interactions. This can further enhance Raman intensity of the molecules [7].

Analytical SERS employs two main detection concepts: label-based and label-free [7, 8]. In the label-based approach, SERS nanotags, which are nanoparticles with bound Raman-active molecules (refered to as reporter molecules), are used to detect the analyte indirectly by a change in the nanotag SERS signal [8]. SERS nanotags are often bio-conjugated with targeting ligands such as antibodies which allow specific target identification and quantification as only antibody-binding analytes affect the nanotag SERS signal. In contrast, label-free SERS detects the Raman spectrum of the analyte itself, revealing unique molecular signatures of molecules near the SERS substrate [9]. Label-free SERS is simpler to implement but can generate signals from various molecules in the vicinity, requiring statistical analysis to identify specific biomarkers. Label-free SERS also enables the discovery and identification of new biomarker. The successful implementation of analytical SERS, whether it is label-free or label-based, requires careful consideration of several key factors including choice of nanomaterial and assay design to ensure their effectiveness and reliability.

The selection of a specific analytical SERS assay is contingent on the nature of the biomarker and the essential information required for appropriate medical intervention. Biomarkers can take various forms, such as circulating tumour cells (CTCs), small extracellular vesicles (sEVs) with different molecular constituents depending on whether they originate from healthy and unhealthy cells, nucleic acids, and proteins including cytokines. Clinicians also need to consider the diagnostic questions they want to address with SERS analysis, which often includes determining the type of cancer or infection, the presence or absence of specific biomarkers, and the stage or severity of the disease. The range of SERS methods available (label-free or label-based, nanoparticle properties) allows clinicians to tailor their diagnostic tools to detect the specific biomarker for effective patient treatment and management.

In the following sections, we discuss the principles that underline the design of analytical SERS nanoparticles and SERS assays. Furthermore, the primary biomarkers that are currently identified by analytical SERS for diagnosis and clinical support are discussed. We will also provide our perspectives, and outline possible future directions of analytical SERS in biomarker detection.

## 19.2 Design of Analytical SERS Nanoparticles

The design of analytical SERS nanoparticles plays a pivotal role in enhancing the capabilities of this powerful technique. In this section, we delve into the critical aspects of SERS nanoparticle design, focusing on activity, stability, and multiplexing (Fig. 19.1). Achieving optimal detection sensitivity, ensuring stability under various conditions, and enabling multiplexed detection are central to harnessing the full potential of analytical SERS for a wide range of applications in cancer diagnostics.

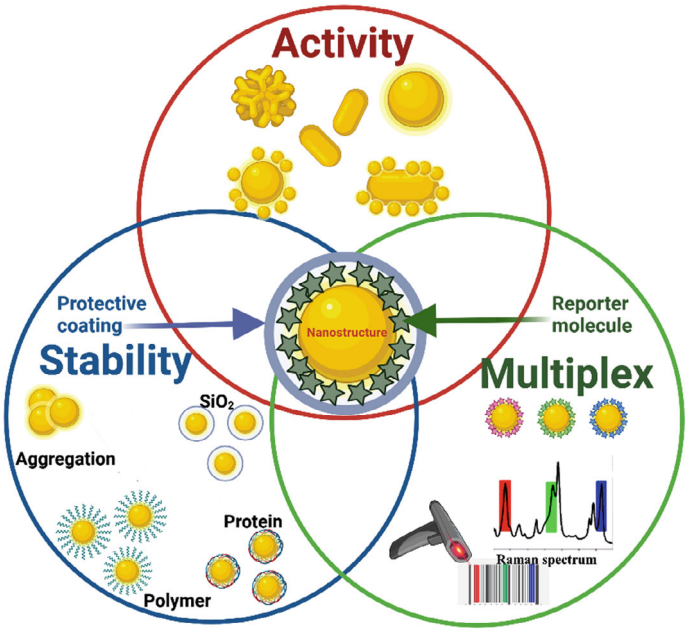



**Fig. 19.1** Schematic of optimization process for the rational design of SERS nanoparticles which involves integration of features that enhances sensitivity for detecting trace amounts of substances, ensures stability for reliable and enduring performance, and enables multiplexing capabilities to identify multiple analytes concurrently. Figure is created with BioRender.com

### 19.2.1 Activity

Common SERS substrates are plasmonic nanomaterials. Noble metals, particularly gold (Au) and silver (Ag), are widely used as SERS substrates due to their strong plasmonic properties, which are generated by light-matter interactions [10]. Spherical Au nanoparticles (AuNPs) exhibit strong plasmon resonance in the visible to near-infrared (NIR) region, typically around 520–550 nm [7, 8]. This makes gold ideal for applications that require excitation at visible wavelengths. AuNPs have high extinction efficiency, meaning they efficiently scatter and absorb light, leading to strong plasmonic effects. Au is also known for its excellent chemical stability, making it less prone to oxidation or degradation over time. Ag also exhibits plasmon resonance across a broad range from the visible to NIR region. Spherical Ag nanoparticles (AgNPs) under resonant wavelength have higher extinction efficiency than AuNPs, resulting in stronger plasmonic effects and higher enhancement factors in SERS [7, 8, 10]. However, Ag is more prone to oxidation compared to Au, which can lead to surface degradation over time, although surface modifications and protective coatings can help mitigate this issue [11]. Other materials such as copper, aluminium and as well as cobalt, magnesium, lead, and zinc also exhibit plasmon resonance in the visible to NIR region, similar to Au and Ag [7, 10, 12–15].

The morphology of the substrate also plays a critical role in SERS enhancement. The localized surface plasmon resonance (LSPR) wavelength of both gold and silver (and mixed metal) particles can be tuned by adjusting the nanoparticle size, shape, and dielectric environment of the nanoparticles [16, 17]. By tuning the nanoparticle, it is possible to adjust the LSPR wavelength over the range from UV to IR range to match excitation laser wavelengths, thus maximizing the SERS enhancement [16]. For instance, we found that gold nanostars produce 50% more SERS enhancement than gold nanospheres of a similar size under 785 nm laser excitation [16]. Moreover, substrates with high surface roughness or with higher surface area-to-volume ratios, such as nanorods, nanostars, or nanoflowers, provide larger contact areas for analyte molecules, usually leading to increased SERS enhancement. Specific nanoparticle shapes with high local curvature or nanogaps can create regions of enhanced electromagnetic fields, known as hot-spots, at specific locations on their surfaces. Branched or irregularly shaped nanoparticles tend to have more hot-spots, resulting in stronger SERS signals [16–19].

### 19.2.2 Multiplex Capability

Multiplexing is most simply achieved by introducing multiple SERS nanotags into a sample, with each nano tag designed to have a different molecular fishing hook and its specific Raman reporter. These tags can be designed to have different spectral characteristics, such as distinct Raman peak positions and intensities—"barcodes" [20, 21].

Since each tag has a unique Raman signature, their signals can be detected simultaneously and differentiated from one another [20, 22–24]. For instance, Nguyen et al. developed a barcoding system for analyzing Raman spectra of a mixture of SERS nanotags using gold nanostars (AuNSs) labelled with seven different Raman molecules, producing seven distinct SERS nanotags with unique Raman peaks [33]. The combination of these SERS nanotags provides 120 different spectra that can be analyzed using the barcoding system.

The choice of a probe molecule (Raman reporter) for a SERS tag is a crucial consideration as it directly influences spectral characteristics, and overall performance of the tag. The ideal Raman reporter molecule should possess certain key properties. (i) The molecule should exhibit strong Raman scattering signals with intense and well-resolved peaks in the desired spectral region [25, 26]. This ensures that the Raman reporter contributes significantly to the SERS signal and can be easily distinguished from background noise. (ii) The Raman reporter molecule should readily adsorb onto or interact with the SERS-active substrate or nanoparticles [8]. This interaction is essential for achieving the localized electromagnetic field enhancement required for SERS signal amplification. Most common Raman reporter molecules contain a thiol (–SH) functional group [7, 8]. Those types of molecules can be chemically attached to the surface of metal nanoparticles through strong covalent bonds between metal and sulphur. Additionally, thiol groups exhibit strong Raman scattering due to its highly polarizable sulphur atom. (iii) The reporter/nanoparticle attachment and the reporter itself must be chemically stable. (iv) The reporter must show a significant Stokes shift between the excitation wavelength and the Raman scattering.

There are various classes of Raman reporter molecules exhibiting the required properties for a SERS-labelled experiment.

1. Organic and fluorescent dyes: Some fluorescent dyes possess inherent Raman scattering capabilities, making them useful as Raman reporter molecules in SERS. These dyes exhibit both fluorescence and Raman scattering signals, allowing for dual-mode detection. Examples include Nile blue and various cyanine dyes and newly developed dyes [27, 28]. Examples of organic dyes are Rhodamine 6G, crystal violet, malachite green, and methylene blue [29, 30].
2. Small thiol molecules: Certain small organic molecules are known to exhibit intense Raman scattering, making them suitable as Raman reporter molecules. Examples include 4-mercaptobenzoic acid (4-MBA), p-aminothiophenol (p-ATP), 2,3,5,6-tetrafluoro-4-mercaptobenzoic acid (TFMBA), 5,5′-dithiobis-(2-nitrobenzoic acid) (DTNB), and others [31, 32].
3. Triple covalent bond: The utilization of relatively newly developed alkyne Raman reporters addresses challenges associated with conventional Raman reporters, such as oxidation, spectral crosstalk, and interference from complex backgrounds. Their Raman signals in the Raman-silent region (1800–2800 $cm^{-1}$) are completely interference-free from various backgrounds [33, 34].

Alternatively, as noted above, label-free SERS may have direct multiplex capability due to differences in analyte signatures. Usually such an approach is experimentally easier but requires more sophisticated data analysis.

### *19.2.3 Stability*

Ensuring the stability of SERS nanoparticles is crucial for reliable and reproducible measurements. Factors affecting (usually adversely) stability include surface modifications, protective coatings, and functionalization [7, 8, 25]. Nanoparticle aggregation is common and affects signal intensity and reproducibility. Aggregation can result from factors including high salt concentrations, pH changes, inadequate stabilization, protein fouling, or improper storage (light exposure, high temperature exposure, freezing) [35, 36]. Electrostatic or steric repulsion between nanoparticles inhibits aggregation, so nanoparticle surfaces are typically modified with stabilizing agents (e.g. thiol-based ligand, $SiO_2$, or polymer) or charged molecules such as ascorbic acid or spermine [37–40]. The term "gold nanoparticle", for example, seldom if ever means a naked gold particle. To select the optimal stabilizing agent for a given application, their properties and interaction with both the nanoparticles and analytes should be considered. For example, proteins are often used for surface blocking, as it can encapsulate nanoparticle and prevent aggregation, however, it will also reduce SERS analyte or reporter Raman signals, causing SERS signal decrease [16, 36]. For the label-free detection stabilizing agents are preferred to be molecules with low Raman signal that would not interfere with the analyte signal, such as ascorbic acid or spermine [39–41]. If targeting molecules, such as antibodies or aptamers are used, their interaction with the protective layer should also be assessed for proper functioning (such as targeting group orientation or even simple electrostatic repulsion) [8, 42].

The stability imparted by thiolate reporter ligands in label-based experiments is an effective means of preventing aggregation of nanoparticles, maintaining their colloidal stability, and preserving their unique properties. The thiol groups form self-assembled monolayers (SAMs) on the nanoparticle surface, creating a barrier that hinders particle–particle interactions [43, 44]. The length and structure of the ligands can influence the spacing and packing density of the ligand layer, impacting the stability and functionality of the nanoparticles [37, 38].

Polymers used to coat nanoparticles commonly have one end of molecule functionalized with a thiol for adsorption on the surface of the nanoparticle. The process of stabilizing nanoparticles through polymers operates through two fundamental mechanisms [45–47]. Electrostatic stabilization relies on the double-layer repulsion between particles, where the electric charges on the particles create a repulsive force, preventing aggregation. Alternatively, steric stabilization involves the covalent bonding or physical adsorption of macromolecules onto the surface of colloidal particles, creating a protective layer that hinders their close proximity and thereby maintains colloidal stability [47]. Polymers employed to shield AuNPs

include nonionic (poly(*N*-vinylpyrrolidone) (PVP), polyvinyl alcohol (PVA), polyacrylamide (PAAm), poly(*N*-isopropylacrylamide) (PNIPAm), poly(ethylene glycol) (PEG), anionic (poly(methacrylic acid) (PMAA)), poly(divinylbenzene-co-acrylic acid) (poly (DVB-co-AA)), poly(sodium 4-styrene sulfonate) (PSS)), and cationic (poly(ethyleneimine) (PEI), poly(*N*-isopropylacrylamide)-b-[poly(ethylacrylate)-g-poly(2-(diethylamino)ethyl meth-acrylate)] (PNIPAM-b-(PEA-g-PDEAEMA), and poly(styrene)-block-poly(4-vinylpyridine) (PSb-P4VPy)) characteristics [47]. The choice of polymer for coating should be based on factors such as the nature of the analyte, molecular mass of polymers, polymer/gold molar ratio, solvent nature, pH, and temperature as well as final use of protected nanostructure [47, 48].

"Silica" coating of gold nanoparticles usually employs the well-established Stöber method, utilizing tetraethyl orthosilicate (TEOS) to create a highly branched and mesoporous siloxane polymer on the gold surface. The process allows for precise control, enabling the tailoring of silica layer thickness by adjusting reaction time and reagent concentrations. The resulting siloxane polymer, referred to as silica, features hydroxyl (–OH) groups on its surface, serving as chemical handles for subsequent functionalization [49]. The advantages of silica coating on gold nanoparticles are manifold. Silica-coated gold nanorods, for instance, exhibit enhanced thermodynamic stability, particularly beneficial in applications involving pulsed lasers [49, 50]. In scenarios where gold nanorods with conventional coatings such as PEG, CTAB, or small polymers may experience shape changes under the influence of pulsed lasers, silica-coated counterparts resist such alterations [49, 50].

Any surface coating on a nanoparticle can change its properties. Therefore characterization of nanoparticles for the change of optical properties (the UV–vis spectroscopy absorption spectrum is probably sufficient) [51] is crucial to ensure reproducible and reliable SERS measurments [36, 52]. In addition, other measurements should be undertaken to check the status of a batch of nanoparticles. Dynamic light scattering (DLS) is the simplest method for determining the size distribution to ensure nanoparticles are of the desired size for optimal SERS enhancement. Surface charge (zeta-potential) [45, 51] is another important parameter [51] to be considered before any applications. Stability studies help ensure that the nanoparticles remain active and do not aggregate or degrade over time, which is crucial for the reliability of SERS measurements.

## 19.3 Design of SERS Assays

This section outlines various approaches adopted for SERS assays, highlighting their respective attributes and applications. These designs encompass both label-free and label-based SERS assays, as well as innovative concepts involving bead, microfluidic device, and lateral flow assay (LFA) (Fig. 19.2). Each approach offers unique benefits and is suited to different analytical challenges, making SERS a versatile tool in

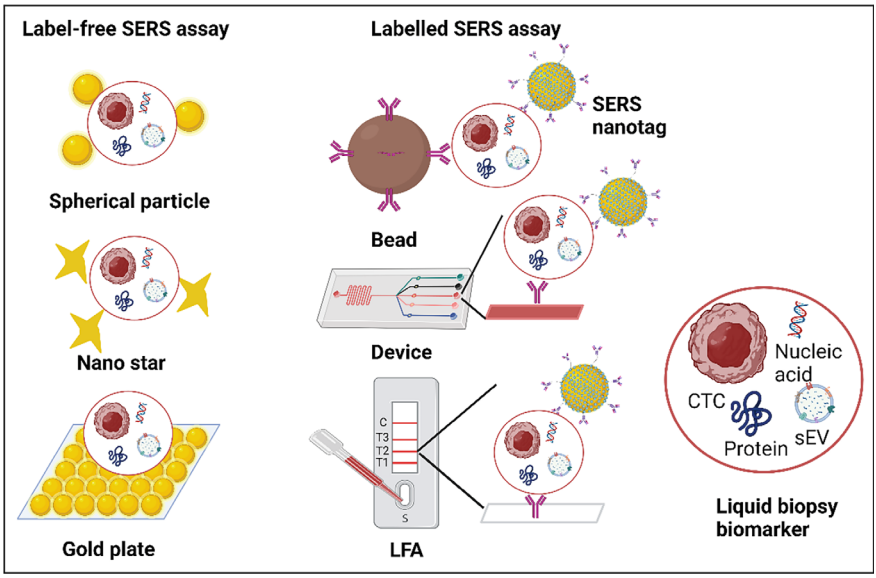



**Fig. 19.2** Schematic representation of SERS assays for liquid biopsy biomarker detection, incorporating both label-free (spherical particle, nano star and gold plate) and labelled SERS techniques (bead, device, and LFA). Figure is created with BioRender.com

fields ranging from biomedical diagnostics to environmental monitoring and beyond. This exploration of SERS assay design aims to provide insights into the growing capabilities of this technology and its potential for addressing complex analytical tasks. It emphasizes the adaptability of SERS, making it a promising avenue for further advancements in clinics.

### *19.3.1 Label-Free Assay*

Direct-SERS assays entail measuring the intrinsic Raman spectrum of the analyte adsorbed onto plasmonic nanoparticles. As noted above, it is commonly referred to as label-free SERS, mainly because it does not require labelling of particles with Raman reporter molecules [53]. This approach allows for the direct detection of molecular fingerprint signals from the biomarkers with high sensitivity and offers several distinct advantages [54]. Firstly, label-free SERS assays do not require the labelling of the reporter molecule, endowing label-free SERS the remarkable capability to scrutinize signal patterns emanating from a broad spectrum of analytes, including those that are undiscovered or non-target substances. Secondly, the Raman spectrum contains a wealth of valuable information about the analyzed targets. The Raman scattering bands, originating from biomarkers, offer insights into their chemical structure, thus providing essential information about the molecular composition of the targets.

Finally, label-free SERS assays are typically rapid and lower cost than label-based. In recent years, there has been a growing interest in the development of label-free SERS platforms for the detection of biomarkers with the aim of discriminating disease-associated biomarkers. In general, label-free SERS approaches involve two major distinct steps: detecting and analyzing the SERS signal.

SERS of disease-associated biomarkers may be analysed via particular Raman bands attributed to known vibrational modes, revealing differences in relative and absolute intensities, as well as changes in the Raman shift for different samples. Bioanalytes, such as proteins, nucleic acids, and lipids, are usually analyzed based on spectral fingerprint areas (between 800 and 1800 $cm^{-1}$) [55]. However, it is not always possible to identify clearly single peaks from different analytes for analysis. Therefore, signal analysis methods which use wide regions of the spectrum are required. Various methods which may be referred to as machine learning (ML, a subset of artificial intelligence (AI)) are used to analyze data. Methods widely used with Raman spectra include principal component analysis (PCA), support vector machine (SVM), convolutional neural network (CNN), distributed arithmetic (DA), quadratic discriminant analysis (QDA), linear discriminant analysis (LDA), partial least squares (PLS-DA), artificial neural network (ANN), and random forest (RF) [56]. The attraction of ML approaches lies in their ability to treat the information in the spectrum as whole dataset and, depending on the approach chosen, they can be nonlinear, unbounded, strongly adaptable, and/or fault tolerant. As a result, they extract more information from the complex SERS spectral datasets than the human mind can, generally leading to more accurate biomarker analysis [57].

### *19.3.2 Label-Based SERS Assay*

Label-free SERS detection of analytes with low concentrations or weak Raman scattering is challenging. However, SERS nanotags can be used to induce a strong SERS signal in such cases. The most common approach for designing label-based SERS assays is to form a "sandwich" structure with the target analyte between a capturing platform and SERS nanotags as the signal-generating unit [42]. This allows the target analyte to be detected through the Raman signals of SERS nanotags. Most common capturing platforms such as beads, devices (microfluidic chips), and lateral flow assays (LFAs) could be combined with SERS nanotags to achieve highly sensitive and specific detection of biomarkers.

#### 19.3.2.1 Beads-Based Assay

Bead-based SERS assays are a powerful analytical technique that combines the high sensitivity and specificity of SERS nanotags with the versatility and ease of use of tools such as magnetic beads [58]. In a beads-based SERS assay, the isolation of biomarkers is achieved by adsorbing them onto magnetic or polymer beads via

covalent bonds, followed by magnetic or centrifugal separation, allowing for more sensitive analyte detection. SERS nanotags functionalized with antibodies or other targeting molecules are then used to bind the biomarkers to form a sandwich complex, which can be detected by Raman spectrometer [59]. This method also allows for multiplex detection of biomarkers in a single reaction using various Raman reporters. Furthermore, bead-based SERS assays are generally faster than other SERS assays performed on 2D substrates due to easy and quick isolation via magnetic beads [60].

Magnetic bead is the most common bead for SERS assays. The design of magnetic bead for SERS assays is critical for achieving optimal performance for biomarker detection. These magnetic beads primarily comprise a magnetic core, a surface coating, and specific binding ligands on the surface [60]. Surface coating is essential to stabilize the magnetic beads and prevent them from aggregating. This is commonly achieved using non-polymeric stabilizers based on organic monomers such as alkane sulphonic and alkane phosphonic acids, or phosphonates [61]. Magnetic beads are then functionalized with a variety of molecules, including the carboxylic acid (–COOH) group, streptavidin, amino groups ($NH_2-$), aldehyde groups (CHO–), and epoxy groups [62]. These functional groups are used to bind a variety of molecules such as antibodies, aptamers, and DNAs for specific biomarker binding. Additionally, the size of magnetic beads may also affect the performance of SERS assay. For example, larger magnetic beads have a larger surface area, which allows them to capture more target molecules. However, they may be more difficult to disperse evenly in the sample, and they may also clog filters. In general, the optimal magnetic bead size for a particular application will depend on a number of factors, including the type of target molecule being isolated, the sample matrix, and the desired isolation efficiency. As the field of SERS continues to develop, bead-based SERS assays are expected to play an increasingly important role in a variety of analytical and diagnostic applications.

#### 19.3.2.2 Device-Based Assay

In bead-based SERS assays, the interaction between functionalized beads and target analytes primarily depends on Brownian motion. Recently, devices that consolidate numerous functional operations and methodologies onto a single chip have been introduced to speed up the biomarker detection process, enhancing diffusion kinetics and binding efficiencies [63]. Moreover, devices, such as microchips, have garnered substantial attention due to their capability for precise fluid manipulation, reduced sample and reagent consumption, and the streamline processing of samples [5]. Devices integrated with SERS assays have been increasingly used in biomarker detection due to their high sensitivity and short assay time, compared to most of other integrated devices such as enzyme-linked immunosorbent assays (ELISA), electrochemistry, and fluorescent assays [64].

The design of device-based SERS assays can be categorized into two main strategies: physical separation and molecular capturing techniques. Physical separation techniques are primarily size-based and are used to isolate target analytes based on

their size differences [64]. Molecular capturing techniques depend on the interaction between capturing antibodies and specific target analytes, including, but not limited to, antibodies or aptamers that bind to antigens, and ligand interactions with receptors [65]. Regardless of the surface chemistry between the capture molecules and target analytes, increasing the frequency of contact improves the capture efficiency of analytes and accelerates the analysis. A variety of micromixing designs for device-based SERS assays have been used for this purpose, including mixers with obstacles, dean flow with repeated turns, tesla structures, split and recombine mixers, and active methods such as electroosmotic mixing [66–68].

Device-based SERS assays have emerged as valuable tools for the multiplexed detection of specific biomarkers (e.g. proteins, nucleic acid). These assays facilitate the isolation of target analytes and analysis of them on a single chip. By employing this innovative approach, these devices enable enhanced sensitivity and precision for biomarker detection and hold great potential for clinic application.

#### 19.3.2.3 Lateral Flow Assay

LFAs are a platform for the rapid detection of a wide range of analytes. They are typically performed on a nitrocellulose, which is coated with antibodies or other capture molecules specific to the target analytes. The sample is applied to the strip with capillary action causing the molecules to move along the strip. If the target analyte is present, it will bind to the captured molecules. A detection reagent is added to the strip running pad, which contains coloured dye or nanoparticles. After passing though, they form a sandwich complex with the target analyte and the capture molecule on conjugation pad. If the target analyte is present, the detection reagent will produce a detectable signal (usually visible or perhaps UV) on the strip [69]. LFAs are simple to use and typically do not require any specialized equipment, making them ideal for point-of-care testing. LFAs are also relatively inexpensive and can be manufactured in large quantities.

LFA-based SERS assays are more sensitive than standard LFAs but require a means of measuring the SERS signal. LFA-based SERS assays are typically composed of four main compartments: sample pad, conjugation pad, nitrocellulose membrane, and absorption pad [69]. When the liquid sample is loaded onto the sample pad, the solution flows through the conjugation pad, where the target analyte can be specifically labelled by the SERS nanotags conjugated with detection molecules. The resultant complex of SERS nanotags and the target is then moved forward by capillary action and immobilized by the capture molecules located on the nitrocellulose membrane at the test line. The control line is designed to verify the assay has performed correctly and the test results are reliable. It typically contains a recognition moiety that can capture excess SERS nanotags, regardless of whether the target is present. The design of LFA-based SERS assays involves several critical aspects. One aspect is the immobilization of SERS nanotags on the LFA [70]. The SERS nanotags should be immobilized in a manner that allows them to interact with the target analyte and ensures their uniform distribution on the conjugation pad.

Different immobilization methods can be employed, such as physical adsorption and chemical bonding. Moreover, the design of the LFA itself is also crucial [71]. The LFA is designed by optimizing the sample flow rate, the conjugation pad pore size, and the test-control line distance. The biorecognition elements (e.g. antibodies or aptamers) should be specific for the target analytes and should be compatible with the SERS nanotags without affecting their SERS signal. LFA-based SERS assay is a powerful diagnostic tool that is simple to use, rapid, and sensitive, making them ideal for use in point-of-care settings.

## 19.4 Analytical SERS in Cancer Biomarker Detection

As discussed above, SERS is a versatile and powerful tool in biomarker detection, enabling early diagnosis, precise characterization, and comprehensive profiling of rare or complex biomarkers. Its exceptional sensitivity (up to femtomolar concentrations), multiplexing capabilities, and potential for quantitative detection make SERS a transformative technology with significant implications for healthcare and diagnostics. In the following sections we discuss the application of analytical SERS in detecting classes of biomarkers including CTCs, sEVs, nucleic acids, and proteins.

### *19.4.1 Circulating Tumour Cells*

Circulating tumour cells (CTCs) constitute neoplastic cells that have dissociated from the primary tumour and infiltrated the circulatory blood or lymphatic systems. They represent a pivotal facet of the metastatic cascade wherein malignant cells disseminate from their original site and migrate to distant anatomical locations. CTCs are discernible within the peripheral bloodstream and serve as a valuable biomarker with pertinence to cancer diagnosis, prognostication, and disease monitoring [72]. CTC detection via SERS is a rapidly developing research field.

SERS assays for CTC detection typically use label-free SERS and offer the potential to identify and characterize CTCs based on their intrinsic molecular composition [75, 76]. A common procedure implemented prior to label-free SERS measurements involves processing samples by isolating cells, employing gradient centrifugation, and then resuspending them in phosphate-buffered saline (PBS). Kamińska et al. created specialized membranes, which were designed to enhance the detection of CTCs (Fig. 19.3a) [73]. Their membranes were equipped with a thin layer of SERS-active metals deposited on a polymer mat, on which the SERS measurement was performed. The proof-of-concept study involved an analysis of SERS spectra obtained from various cell types, including prostate cancer cells (PC3), cervical carcinoma cells (HeLa), and healthy leucocytes, serving as an example of normal cells. They applied the traditional multivariate statistical technique, PCA to assess and quantify the differences in SERS data among the various cell types. By employing a

PCA algorithm, they were able to differentiate the studied cell types with high accuracy (95% in 2D PCA and 98% in 3D PCA) [73], which is an exceptional accuracy facilitated by a simple set up.

Label-based SERS assays for CTCs, on the other hand, provide less complex signals that make data processing easier. For example, Xue et al. reported a bead-assay to improve CTC detection sensitivity, specificity, and quantification [74]. As discussed above (in Sect. 3.2.2), magnetic bead/particles provide magnetic properties for CTC isolation and capture, which are usually attached via specific target molecules (biotin or antibodies) [77–79]. SERS nanotags with 4-MBA as the Raman reporter molecule and folic acid as the capture ligand ensured the specific detection of the folate receptor, which is often overexpressed on cancer cells (Fig. 19.3b). This approach allowed precise quantification of CTCs which is advantageous for disease monitoring. The technology's feasibility was demonstrated by measuring the concentrations of CTCs in the blood of a clinical patient, highlighting the potential clinical utility of the SERS-active magnetic nanoparticles [74].

As discussed above, device-based assays offer a promising solution to streamline labour-intensive sample preparation (separation, ultracentrifugation, and centrifugation). A range of SERS platforms, developed within the last 5 years, are summarized in Table 19.1. One instance of integrating an SERS platform with a microfluidic system is exemplified in the work by Gao et al. [75]. They achieved real-time detection of CTCs in whole blood samples. The approach involves mixing blood containing CTCs with SERS nanotags that have been tailored with aptamers for precise binding to cancerous cells. Subsequently, CTCs are captured based on size exclusion principles and can be analyzed using a Raman spectrometer (Fig. 19.3c). The design of this capture method and the characteristics of the SERS nanotags offer a two-fold validation for analyte-specific detection, considering both the size of the cells and the presence of biomarkers. In the published example, SERS nanotags were customized to target specific CTC biomarkers [75]. The microfluidic system incorporated 12 μm filters, which effectively separated CTCs from complex blood constituents due to disparities in size between CTCs and blood cells. This yielded capture rates of 87 ± 8% for SKBR3, 93 ± 6% for MCF7, and 87 ± 8% for MDA-MB-231 breast cancer cells. By synergistically utilizing multiplex SERS nanotags for CTCs labelling and a classification algorithm for discriminant analysis, this platform demonstrated remarkable proficiency in the precise categorization of cancer subpopulations [80].

### *19.4.2 Small Extracellular Vesicles*

Cancer-derived small extracellular vesicles (sEVs) of size range 30–200 nm are produced through the endosomal pathway from multivesicular bodies (MVBs) in cancer cells. MVBs may eventually fuse with plasma membrane to release sEVs into the extracellular milieu [88]. Structurally, cancer-derived sEVs have a lipid bilayer structure that encapsulates various biomolecules, such as nucleic acids, proteins, lipids, and glycans. These cancer-associated biomolecules can modulate signalling

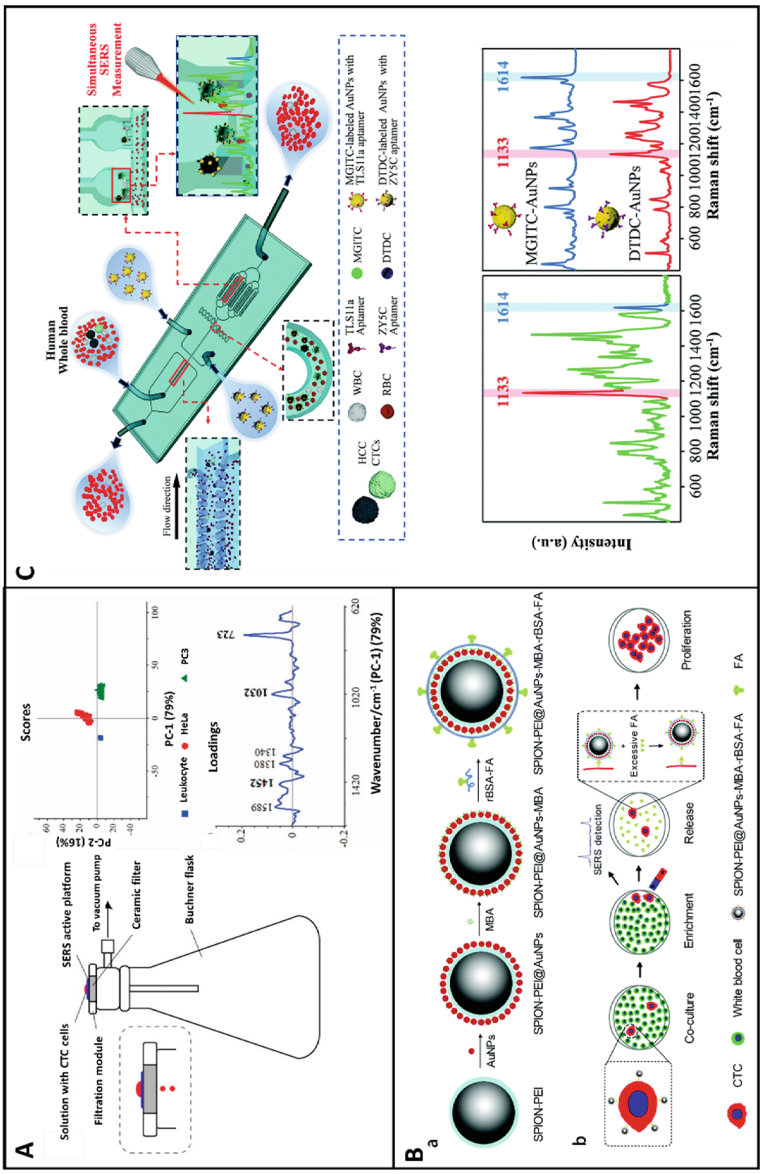



**Fig. 19.3** **a** Label-free detection of CTCs with SERS-active membrane that consists of plasmonic nanoparticles, reproduced with permission [73]. **b** Magnetic particles decorated with plasmonic nanoparticles (SPION-PEI@AuNPs-MBA-rBSA-FA) designed to capture CTCs and improve SERS assay sensitivity, reproduced with permission [74]. **c** Microfluidic device for real-time detection of CTCs in whole blood samples: CTCs are captured based on size exclusion principles and functionalized with targeting SERS nanotags, reproduced with permission [75]

**Table 19.1** SERS platforms for CTCs detection

| SERS substrate | Detection method | Surface marker | Sensitivity (LOD) | Multiplex capability | Sample type | Disease | References |
|---|---|---|---|---|---|---|---|
| Ag: Au semi-spheres on the mesh | Label-free (PCA) | N/A | Accuracy of 95% in 2D PCA to 98% in 3D PCA | N/A | Whole blood | Prostate cancer (PC3), cervical carcinoma (HeLa) | [73] |
| Ag nanoparticles on the film | Label-free (potentially PCA can be used) | Nucleic acid characteristic peaks | N/A | N/A | Whole blood | Lung cancer | [81] |
| Ag@$SiO_2$ shell-isolated nanoparticles (SHINs) | Label-free (PCA)/ microfluidic device | N/A | Accuracy of 89% | N/A | Whole blood | Renal cell carcinoma (Caki-1) and cervical carcinoma (HeLa) cells | [82] |
| p-MBA-labelled immuno-Ag@$Fe_2O_3$ | Microfluidic device/ magnetic nanoparticles | EpCAM | 1–100 cells/mL | Singleplex | Blood plasma | Lung cancer | [76] |
| AuNP SERS nanotags | Microfluidic device | TLS11a protein and vimentin | Capture efficiency of 84%, with up to 95% purity of collected CTC (SERS LOD not indicated) | Duplex | Whole blood | Hepatocellular carcinoma | [75] |

(continued)

**Table 19.1** (continued)

| SERS substrate | Detection method | Surface marker | Sensitivity (LOD) | Multiplex capability | Sample type | Disease | References |
|---|---|---|---|---|---|---|---|
| SPION-PEI@AuNPs-MBA-rBSA-FA | Magnetic beads | Folic acid receptors | 1 cell/mL | Singleplex | Pre-treated blood | Cervical cancer | [74] |
| $TiO_2$@Ag–R6G–rBSA–FA | SERS nanotag | Folic acid receptors | 1 cell/mL | Singleplex | Pre-treated blood | Liver cancer | [83] |
| SERS substrate (100 nm Ag layer) | Label-free/ microfluidic device | N/A | 20 cells/mL | N/A | Cell suspension in PBS | MCF-7 and MDA-MB-231 cells | [84] |
| Popcorn-shaped $Fe_2O_3-$Au core−shell NPs | Microfluidic device/ magnetic nanoparticles | pCAM,HER2, CD44, or IGF1R | 10 cells/μL (tested) | Fourplex | Spiked blood | SKBR-3, MDA-MB-231, or MCF-7 | [85] |
| Ag nanorods | Label-free/ magnetic beads | EpCAM | 2 cells/mL | N/A | Spiked PBS | MCF-7 cells | [86] |
| $Fe_3O_4$@Au SERS nanotag | Magnetic nanoparticles | Trop-2 | Detection sensitivity 90%, specificity 76% | Singleplex | Pre-treated blood | Triple negative breast cancer (TNBC) cells (HCC1806, MDA-MB-468 and MDA-MB-231) | [87] |

pathways and cellular functions of the recipient cells, regulating cancer growth and metastasis. Cancer-derived sEVs are abundant in patients' body fluids, including blood, urine, and saliva and can be easily enriched by methods such as ultracentrifugation and characterized using corresponsive techniques to provide the dynamic information about the tumour at the time of sampling [89]. Therefore, cancer-derived sEVs are potential biomarkers for cancer diagnosis/prognosis.

Label-free SERS has emerged as a powerful tool for the characterization of sEVs by providing their molecular signatures. For example, Liu et al. used positively charged gold-silver nanostars to explore the SERS profiles of sEVs from different origins, batches, and isolation approaches (Fig. 19.4a) [39]. The negatively charged sEVs were attracted to the positively charged gold-silver nanostar surfaces via electrostatic forces, resulting in SERS spectra that show characteristic vibrational modes of the different components of sEVs (i.e. proteins, lipids, and nucleic acids). SERS signatures of PANC1 sEVs down to $6.7 \times 10^8$ particles/mL could be analyzed by PCA, indicating the potential applications in clinics using this direct-SERS/PCA-LDA strategy [39].

Label-based SERS assays have also been widely used for sEV detection. To optimize a SERS assay for the detection of ovarian cancer-derived sEVs, Ngo et al. assessed the presence of ovarian cancer markers, such as EpCAM, on cancer cells and sEVs using flow cytometry and immunoblotting [92]. They found that cancer cells and their derived sEVs present EpCAM, and therefore, they used EpCAM to functionalize SERS nanotags for the comparison of sandwich immunocomplex assembling strategies [92]. They further compared three types of capturing probes: magnetic beads conjugated with anti-CD9, CD63, or CD81 antibodies for sEV detection. They found the strategy of pre-mixing sEVs with the SERS nanotags and the anti-CD9 capturing probe achieved the best performance, with a minimum detection of sEVs down to $1.5 \times 10^5$ particles/μL and high specificity in distinguishing sEVs from different ovarian cancer cell lines. They sensitively detected the surface protein biomarkers (EpCAM, CA125, and CD24) on ovarian cancer-derived sEVs in both PBS and plasma (sEVs spiked in healthy plasma) using the improved SERS assay.

Multiplex capability of SERS assays for sEV detection can be realized by SERS nanotags with different Raman molecules and detection molecules. Zhang et al. developed a sensitive and effective approach to simultaneously profile multiple protein biomarkers expressed on cancer-derived sEVs using surface-enhanced Raman spectroscopy SERS nanotags in a single test [42] by mixing multiple antibody-coated SERS nanotags, collected serum-free sEV medium, and captured antibody (CD63)-conjugated magnetic beads to form a sandwich immunoassay. As a proof-of-concept demonstration, they applied this approach to characterize pancreatic cancer-derived sEVs by simultaneously detecting three specific sEV surface receptors including Glypican-1, EpCAM, and CD44V6 (Fig. 19.4b). The sensitivity of this method was measured down to $2.3 \times 10^6$ particles/mL. To demonstrate the clinical application of this assay, Zhang et al. further profiled the phenotypes of plasma-derived sEVs for 13 healthy donors and 9 pancreatic ductal adenocarcinoma (PDAC) patients and evaluated the clinical sensitivity and specificity of the assay for simultaneous detection of multiple protein biomarkers on sEVs from plasma

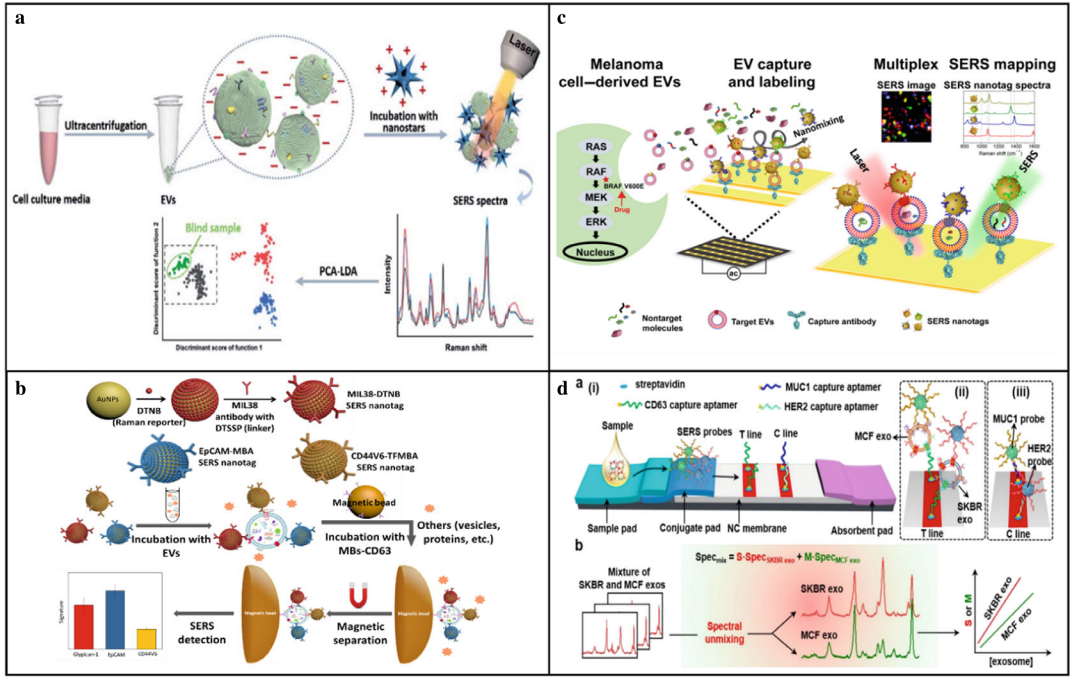



**Fig. 19.4** **a** Label-free SERS detection of the molecular features of cancer-derived sEVs with positively charged Au:Ag nanostars, reproduced with permission [39]. **b** Preparation of SERS nanotags, namely MIL38-DTNB, EpCAM-MBA, and CD44V6-TFMBA, for the molecular phenotype profiling of sEVs positive for CD63 and further capturing of sEVs via magnetic beads, reproduced with permission [59]. **c** Collected sEV sample is directly introduced into an EPAC (evanescent-field-activated capture) system, where the nanomixing fluid flow enhances collisions between sEVs, capture antibodies, and SERS nanotags. This process effectively removes non-target molecules such as protein aggregates and apoptotic bodies, as well as free SERS nanotags, reproduced with permission [90]. **d** Schematic of SERS-LFS biosensor (i) designed for the precise SERS detection of two distinct sEVs in a single test line (T line), along with depictions of the structures of (ii) complexes formed in the T line when both SKBR and MCF sEVs are present, and (iii) complexes formed in the control line (C line). And illustrative depiction of the dualplex detection of sEVs for cancer diagnostics using spectral unmixing assistance, reproduced with permission [91]

[93]. They found that the sEVs' phenotypic signature had sensitivity of 100% (95% confidential interval (CI): 66.4–100%), specificity of 100% (95% CI: 75.3–100%), and the area under the curve of 1.000 (95% CI: 84.6–100%) for PDAC diagnosis, indicating a strong correlation (accuracy of 88.9%) of sEV phenotypic signatures with cancer stages.

To enhance the sensitivity of SERS assays for sEV detection, Wang et al. proposed to profile plasma sEV phenotypes (relative expression of MCSP, MCAM, LNGFR and ErbB3) by a so-called sEV phenotype analyzer chip (EPAC) [90, 94]. This chip integrates a nanomixing-enhanced sEV microchip and a multiplex SERS signal readout system to enable a comprehensive investigation of tumour-specific sEVs in complex biological fluids, without the need for sEV purification (Fig. 19.4c). In the microfluidic chip, a tunable alternating current electrohydrodynamics (ac-EHD) creates electrical forces near the electrode surface (within the electrical layer). These forces generate precise, nanoscale fluid flows that selectively capture desired sEVs while minimizing unintended attachment of weaker molecules. The authors profiled melanoma patients' plasma sEV phenotypes with high sensitivity ($10^5$ particles/mL for MCSP). Furthermore, by tracking the sEV phenotypic changes, the researchers were able to monitor the treatment response in melanoma patients receiving molecular-targeted therapies, reflecting the potential of sEVs phenotyping for monitoring treatment responses.

A paper-based lateral flow strip (LFS) combined with multivariate spectral unmixing analysis (Fig. 19.4d) has been proposed by Su et al. for a quantitative SERS method to detect serum sEVs [91]. This SERS-LFS assay allows for the precise quantification of two distinct types of serum sEVs, achieving a remarkable limit of detection of approximately $10^6$ particles/mL. They also applied this technique to quantitatively detect serum sEVs in breast cancer patients. Their findings revealed that individuals with human epidermal growth factor receptor 2+ (HER2+) and luminal A breast cancer, who had not undergone surgery, exhibited an enrichment of serum sEVs derived from SKBR-3 cells and MCF-7 cells, respectively. Notably, surgical intervention led to a significant reduction in the presence of either SKBR or MCF sEVs in the serum. These results indicated the substantial potential of the SERS-LFS biosensor in combination with multivariate spectral unmixing for breast cancer subtyping and therapeutic monitoring. Several recent works, which are not explicitly referenced in the text but relate to this subject are summarized in Table 19.2.

SERS-based methods for the molecular characterization of sEVs have shown the potential for cancer diagnosis, prognosis, and treatment monitoring. To further promote their clinical application, efforts are needed to develop more efficient and reliable sEV isolation methods, highly sensitive SERS nanotags, and large clinical sample validation studies.

**Table 19.2** Summary of SERS assay for sEVs detection

| SERS substrate | Detection method | Surface marker | Sensitivity (LOD) | Multiplex capability | Sample type | Disease | References |
|---|---|---|---|---|---|---|---|
| Au–Ag nanostar | Label-free (PCA) | N/A | $6.7 \times 10^8$ particles/mL | N/A | Cell lines | Pancreatic cancer | [39] |
| AuNPs | Label-free | N/A | N/A | N/A | Cell lines, plasma | Osteosarcoma | [95] |
| Au nanohole | Label-free (logistic regression) | N/A | N/A | N/A | Cell lines | Ovarian cancer | [96] |
| Au pyramids | Label-free (PCA) | N/A | N/A | N/A | Cell lines, serum | Lung cancer | [97] |
| Au nanostar | Label-free artificial neutral network (ANN) | N/A | N/A | N/A | Cell lines, serum | Breast cancer | [98] |
| AgNPs | Label-free convolutional neural network (CNN) | N/A | N/A | N/A | Serum | Prostate cancer, renal cell cancer, bladder cancer | [99] |
| AuNP-coated plate | Label-free residual neural network (Resnet)-based deep learning model | N/A | N/A | N/A | Cell lines, plasma | Lung cancer | [100] |
| Au nanopyramid arrays | Label-free (LDA, SVM) | N/A | N/A | N/A | Tissue, blood, and saliva | Gastric cancer | [101] |
| $Fe_3O_4$/Au NPs | Label-free (PCA) | N/A | N/A | N/A | Cell lines, serum samples | Breast cancer | [102] |

(continued)

**Table 19.2** (continued)

| SERS substrate | Detection method | Surface marker | Sensitivity (LOD) | Multiplex capability | Sample type | Disease | References |
|---|---|---|---|---|---|---|---|
| AuNPs | Label-free (PC-DFA) | N/A | N/A | N/A | Cell lines, serum | Pancreatic cancer | [103] |
| 3D plasmonic AuNPs nanomembranes | Label-free (LDA) | N/A | N/A | N/A | Cell lines, serum | N/A | [104] |
| AuNP-aggregated array chip | Label-free (CNN) | N/A | N/A | N/A | Plasma | Lung, breast, colon, liver, pancreas, and stomach cancer | [105] |
| Au@Ag@MBA | Magnetic beads | PD-L1 | 1 particle/μL | Singleplex | Cell lines/ serum | Non-small cell lung cancer | [106] |
| AuNS@4-MBA@Au | Magnetic beads | N/A | 27 particles/μL | Singleplex | Cell lines/ serum | Liver cancer patient | [107] |
| Au nanostar substrate | SERS EpCAM-aptasensors | EpCAM | 2.4 particles/μL | Singleplex | Cell lines | Lung cancer | [108] |
| EpCAM-functionalized Raman beads | Magnetic beads/ microfluidics | EpCAM | $1.6 \times 10^2$ particles/mL | Singleplex | Cell lines/ serum | Prostate cancer | [109] |
| AuNPs | Magnetic beads | EpCAM, CA125, and CD24 | $1.5 \times 10^5$ particles/μL | Singleplex | Cell lines/ spiked plasma | Ovarian cancer | [92] |
| Antibody-reporter-Ag(shell)–Au(core) multilayer SERS nanotag | Modified glass slide | CD9, CD63, MIF and Glypican-1 | 1 particle/2 μL | Singleplex | Cell lines/ serum | Pancreatic cancer | [110] |

(continued)

**Table 19.2** (continued)

| SERS substrate | Detection method | Surface marker | Sensitivity (LOD) | Multiplex capability | Sample type | Disease | References |
|---|---|---|---|---|---|---|---|
| Au nanorods | Antibodies array | EpCAM, CD44, HER2, EGFR, IGH1R, CD9, CD63, CD81 | $2 \times 10^6$ particles/mL | Singleplex | Cell lines/ plasma | Breast cancer | [111] |
| Au nanorods | Vertical arrays with EpCAM aptamer | CD63, HER2 | $5.3 \times 10^3$ particles/mL | Duplex | Cell lines | Breast cancer | [112] |
| Au nanostar encapsulated with silica (nanotag) | LFA | HER2, MUC1 | 106 particles/ mL | Duplex | Cell lines/ serum | Breast cancer | [91] |
| AuNPs | Magnetic beads | HER2, PSMA, CEA | 32 particles/μL (SKBR3), 73 particles/μL (T84), 203 particles/μL (LNCaP) | Triplex | Cell lines | Breast cancer, prostate cancer cells, and colorectal cancer | [113] |
| AuNP | Magnetic beads | Glypican-1, EpCAM, and CD44V6 | $2.3 \times 10^6$ particles/mL | Triplex | Cell lines | Pancreatic cancer | [59] |
| AuNP | Microfluidics | CD63, VIM, EpCAM | $2 \times 10^3$ particles/mL | Triplex | Cell lines, plasma | Osteosarcoma | [114] |
| AuNP | Magnetic beads | Glypican-1, EpCAM, and CD44V6 | N/A | Triplex | Plasma | Pancreatic cancer | [93] |

(continued)

**Table 19.2** (continued)

| SERS substrate | Detection method | Surface marker | Sensitivity (LOD) | Multiplex capability | Sample type | Disease | References |
|---|---|---|---|---|---|---|---|
| AuNP | Microfluidics | MCSP, MCAM, LNGFR, ErbB3 | Anti-MCSP EPAC $10^5$ particles/mL | Fourplex | Cell lines, plasma | Melanoma | [90, 94] |
| AuNP | Microfluidics | MCSP, MCAM, LNGFR, ErbB3 | $10^3$ sEVs/mL | Fourplex | Cell lines, plasma | Melanoma, lung cancer, and breast cancer | [115] |
| Au–Ag alloy nanoboxes | Microfluidics | CD63, THSB2, VCAN, and TNC | 12 particles/μL | Fourplex | Cell lines, plasma | Lung adenocarcinoma | [116] |

### *19.4.3 Nucleic Acids*

Tumour-derived nucleic acids are DNA and RNA fragments shed by tumour cells representing one major component of any liquid biopsy [117]. Circulating tumour DNA (ctDNA) has a short half-life less than 2.5 h, making it a more real-time and dynamic biomarker for tumour progression than other biomarkers [118]. As abnormal changes in DNA can induce corresponding modifications in RNA during transcription, RNAs originating from tumours have also been recognized as valuable cancer biomarkers [117]. Therefore, tumour-derived nucleic acids are promising biomarkers for cancer diagnosis, prognosis, and treatment monitoring.

Label-free SERS has been used for nucleic acid detection. For example, Liu et al. and colleagues synthesized positively charged gold and silver nanostars for the label-free SERS detection of DNA (negative charged) mutations (Fig. 19.5a) [119]. They used statistical analysis methods (PCA − LDA) to successfully differentiate between wild-type (WT) and V600E mutant DNA, both from whole genome DNA lysed from cell lines and cell-free DNA from cell culture media.

SERS nanotags have been widely used to improve the sensitivity and specificity of SERS assays for nucleic acids detection in recent years. For example, Lyu et al. combined asymmetric PCR (Asy-PCR, use of unequal amounts of forward and

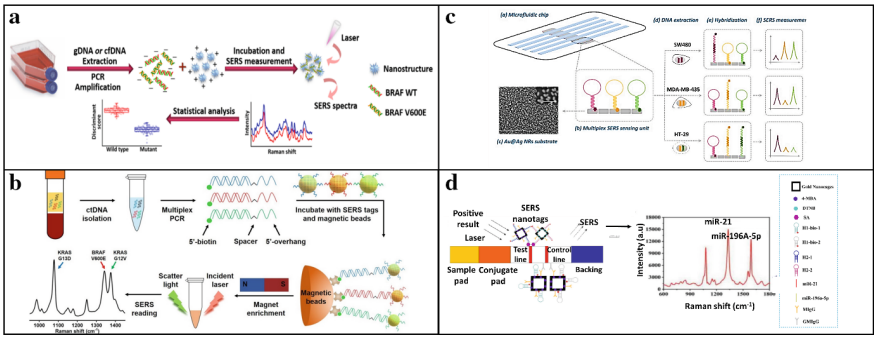



**Fig. 19.5** **a** Representation of a label-free SERS assay incorporating positively charged plasmonic nanostars in conjunction with statistical analysis through principal component analysis and linear discriminant analysis (PCA−LDA) for DNA mutations detection, reproduced with permission [119]. **b** Design of the multiplex PCR/SERS assay: amplicons were labelled using mutation-specific SERS nanotags and enriched with streptavidin magnetic beads for the capturing, reproduced with permission [22]. **c** Schematic representation of SERS biochip for ssDNA mutations analysis via Raman fingerprints, reproduced with permission [120]. **d** Design of SERS-LFA strip for miRNA-triggered catalytic hairpin assembly (CHA): the resulting double-stranded DNAs (H1eH2 complex) formed by the SERS nanotags and the corresponding hairpin-structured DNA sequence 2 ($H_2$), are immobilized on a single T line; this immobilization creates numerous "hot spots" due to the abundant formation of H1eH2 complexes, thereby facilitating enhanced SERS measurements. Reproduced with permission [121]

reverse primers) with magnetic bead-based SERS assay to achieve highly sensitive and specific detection of the KRAS G12V mutation, a common driver mutation in colorectal cancer (CRC) [22]. First, Asy-PCR was used to generate biotin-conjugated single-stranded DNA (ssDNA) which was then hybridized with SERS nanotags that were functionalized with oligonucleotides encoding the KRAS G12V mutant sequence. The labelled ssDNA was then captured via streptavidin-coated magnetic beads (Fig. 19.5b), resulting in increased assay sensitivity: as few as 0.1% mutant alleles of KRAS G12V mutation from CRC cell lines was detected. The authors also demonstrated that the Asy-PCR/SERS assay could distinguish between the same nucleotide location KRAS G12V (c.35G > T) and KRAS G12D (c.35G > A) mutations from patients' specimens.

SERS nanotags can also be integrated into a device to detect nucleic acids. For example, Wu et al. have developed an amplification-free device-based SERS assay that allows direct and simultaneous identification of multiple DNA mutations in tumour cells (Fig. 19.5c) [120]. This device integrates a SERS sensor (Au@Ag nanorods) into a microfluidic platform, enabling one-step multiplex analysis of DNA mutations in just 40 min. Three kinds of SERS nanotags were designed to specifically bind with KRAS G12V, BRAF V600E, and PIK3CA P449T mutations, respectively. When the target DNA hybridized with the nanotag, the hairpin nucleic acid nanotag underwent a structural change. This change caused the Raman reporter, which was labelled at the free end of the nanotag, to move away from the SERS substrate surface, resulting in a decrease in SERS intensity. They employed a combination of SERS spectral encoding and supervised learning algorithms classical least square-linear discriminant analysis (CLS-LDA) to distinguish various nucleotide mixtures based on their mutation profiles. This SERS device offers several advantages over traditional PCR-based methods: it achieves amplification-free detection of cellular mutations due to the ultrasensitivity of the substrate, requires only one SERS measurement for profiling multiple mutations, and can intelligently classify samples with different mutations using a supervised spectrum analysis based on the CLS-LDA algorithm.

A novel ultrasensitive LFA-based SERS assay has recently been developed for the simultaneous detection of miR-21 and miR-196a-5p in non-small-cell lung cancer (NSCLC) urine [121]. This strip utilizes catalytic hairpin assembly (CHA) as a signal amplification strategy. Raman molecules, either mercaptobenzoic acid (MBA) or 5,5′-dithiobis-2-nitrobenzoic acid (DTNA) were used as the label and two hairpin DNA sequences were modified on gold nanocages (GNCs) to serve as SERS nanotags (Fig. 19.5d). Upon target miRNA-triggered CHA, double-stranded DNAs (H1eH2 complexes) form and are immobilized on a single test line (T line) of the SERS-LFA strip, generating numerous "hot spots" for enhanced SERS measurements. The SERS-LFA strip exhibits high specificity and repeatability for miRNAs, with a short detection time of 30 min. Clinical feasibility was also demonstrated by testing urine samples from 30 NSCLC patients and 30 healthy subjects.

All the SERS technologies mentioned above have shown remarkable sensitivity and accuracy for nucleic acids detection. However, for SERS-based circulating nucleic acid detection to be clinically useful, it is crucial to thoroughly assess their

performance using a large number of patient samples for specific clinical applications, such as early cancer detection and treatment monitoring. Additionally, refining the assay workflows could enhance the practicality of SERS-based nucleic acid detection. In particular, simplifying the steps required for multiple target detection, which currently involves multiple labelling and detection steps, would be advantageous. Other related work is outlined in Table 19.3.

### *19.4.4 Proteins*

Peptides and proteins play important roles in the myriad of biological functions within living organisms. Given the fundamental significance of proteins in biology, they frequently serve as biomarkers for various diseases and health monitoring. As a result, the detection of proteins and measuring their levels have gained increasing attention, particularly in the context of early diagnosis and therapeutic interventions [134]. SERS has emerged as a novel and valuable approach for the detection, quantification, and characterization of proteins. Some advanced techniques incorporating SERS for protein detection are listed in Table 19.4. Others are discussed below.

Label-free SERS techniques have been applied in protein detection due to the simplicity of the measurement without the need for specific markers or labels. For example, extensive work has been conducted collecting SERS spectra of the blood serum samples obtained from cancer patients before and after surgical tumour removal [9]. Introduction of AgNPs into a serum sample triggered a complex interplay between proteins and molecular species, resulting in the formation of a molecular/ionic layer around the nanoparticles. This layer, akin to a protein corona, significantly influences the SERS spectrum, with the protein content and molecular crowding playing pivotal roles in shaping the spectral characteristics [36]. Additionally, changes in the orientation of molecules on the nanoparticle surface further contribute to the observed spectral variations. Researchers used PCA and PLS data analysis techniques and detected spectral patterns that can be utilized for the tumour progression monitoring [9]. Although there is a great potential in this approach, addressing the challenges related to how protein conformation and orientation on nanoparticles affects the spectral signatures is essential. Future research may explore techniques to stabilize proteins or mitigate conformational changes during detection.

It is important to note that label-free SERS is currently limited in its ability to analyze proteins, as it requires target proteins with high binding affinity to the surface of noble metal nanoparticles and strong signal intensities. The challenge of label-free SERS for proteins is exacerbated by the inherently weak Raman bands of proteins (even in SERS), resulting in relatively low sensitivity (signal to noise level or less than 100 counts at common reading modes) of the SERS substrate. This limitation becomes even more pronounced when target proteins are present in complex solutions, potentially overshadowed by other interfering protein signals. Furthermore, the recognition of protein signals can be particularly challenging due

**Table 19.3** Summary of SERS for nucleic acid detection

| SERS substrate | Detection method | Marker | Sensitivity (LOD) | Multiplex capability | Sample type | Disease | References |
|---|---|---|---|---|---|---|---|
| AgINPs | Label-free | miR-21 | 42 aM | N/A | Cell lines, serum | Cervical, lung, breast, liver cancer | [123] |
| Photo–etched GaN covered with the layer of Au | Label-free | BRAF V600E | 1 pg/μL | N/A | Tissue, plasma | Thyroid, melanoma | [124] |
| Au/Ag nanostars | Label-free | BRAF wild-type (WT) and V600E mutant genes | 100 copies | N/A | Cell lines, plasma | N/A | [119] |
| AgNPs | Label-free | ERG, PCA3, and KLK2 | 104 target copies | Singleplex | Cell lines, patient urine samples | Prostate cancer | [122] |
| Ag nanostructures in Au nanobowls | Molecular beacon configuration | miR-34a | 50 aM | Singleplex | Cell lines | Gastric cancer | [125] |
| AuNPs | PCR/SERS assay | KRAS G12V | 0.1% mutant alleles | Singleplex | Cell lines, blood and colorectal polyp biopsies | Colorectal cancer | [126] |
| AgNPs | Isothermal amplification | ERG, PCA3, and KLK2 RNA biomarkers | 100 target copies | Singleplex | Cell lines, patient urine samples | Prostate cancer | [6] |
| AgNPs | Catalytic hairpin assembly (CHA) amplification | miR-21 | 3.5 fM | Singleplex | Cell lines | Breast, cervical, lung cancer | [127] |
| Locked nucleicacid modified Au@DTNB | Magnetic beads | miRNA-10b | 0.21 fM | Singleplex | Cell lines, patient serum | Pancreatic ductal adenocarcinoma | [128] |

(continued)

**Table 19.3** (continued)

| SERS substrate | Detection method | Marker | Sensitivity (LOD) | Multiplex capability | Sample type | Disease | References |
|---|---|---|---|---|---|---|---|
| Au shell NP-based SERS tag | Magnetic beads | miR-122 | 8 fM | Singleplex | Mouse sera | Drug/ radiation-induced inflammation | [129] |
| Plasmonic Au nanopillar | Nanopillars | miR-21, miR-200 family | 1 aM | Singleplex | Cell lines, spiked serum | Breast cancer | [130] |
| AuNPs | Magnetic beads, PCR/SERS assay | mecA and femA | $10^4$ input copies | Duplex | Extracted genes and clinical samples | Methicillin-resistant Staphylococcus aureus | [131] |
| GNCs | LFA | miR-21 and miR-196a-5p | 2.08 Pm (PBS) and 3.31 pM (urine) for miR-21, 1.77 pM (PBS) 2.18 pM (urine) for miR-196a-5p | Duplex | Urine | Non-small cell lung cancer | [121] |
| AuNPs | Isothermal amplification | T1E4 T1E5 T1ETV1 RNA | 100 copies | Triplex | Cell lines | Prostate cancer | [132] |
| AuNPs | Magnetic beads, PCR/SERS assay | KRAS G12V, KRAS G13D, BRAF V600E | 0.1% mutant alleles | Triplex | Cell lines, plasma | Colorectal cancer | [22] |
| Au@Ag nanorods | Microfluidics | KRAS G12V, BRAF V600E, PIK3CA P449T | 10 fM | Triplex | Cell lines, tissue, plasma | Colorectal cancer | [120] |
| AuNPs | Microbead | miR-21 miR-122 miR-24 | 0.1 pM | Triplex | Cell lines | Liver cancer | [133] |

**Table 19.4** Summary of SERS for protein detection

| SERS substrate | Detection method | Marker | Sensitivity (LOD) | Multiplex capability | Sample type | Disease | References |
|---|---|---|---|---|---|---|---|
| AgNP | Label-free | HER2, MUC4, PSA, CA 15–3, and CA 27–29 | 5 μL of proteins (100 $\mu g/mL^{-1}$) | N/A | Protein solution | Cancer | [144] |
| Au-coated nanoplillars | Label-free | Recombinant and endogenous erythropoietin | 0.1 pM and 0.5 pM, respectively | Singleplex | Spiked blood plasma | Anaemia in cancer patients | [145] |
| AuNPs | Label-free/ microfluidics | Prostate-specific antigen | 10 pg/mL | Singleplex | Spiked bovine serum | Prostate cancer | [146] |
| $Fe_3O_4$@$SiO_2$@Ag | SERS-encoded magnetic beads | Carcinoembryonic antigen (CEA) and alpha-fetoprotein | 1 fg/mL | Triplex | Patients' serum | Cancer | [147] |
| AuNPs | SERS nanotags + magnetic beads | Thrombin | 20 pM | Singleplex | Human blood plasma from cancer and healthy patients | Cancer | [148] |
| Au film substrate@MBA | Microfluidics | Carcinoembryonic antigen (CEA) and vascular endothelial growth factor (VEGF) | 0.38 pg/mL for CEA and 0.82 pg/mL for VEGF | Duplex | 50 serum specimens (30 healthy subjects and 30 GC patients) | Gastric cancer | [149] |
| AgNP@4-MBN-VEGF-pAb | Microfluidic droplet-SERS | Vascular endothelial growth factor (VEGF) | Single-cell secreted within 10 min | N/A | Single-cell (MCF-7, SGC, and T24) | Cancer | [150] |

(continued)

**Table 19.4** (continued)

| SERS substrate | Detection method | Marker | Sensitivity (LOD) | Multiplex capability | Sample type | Disease | References |
|---|---|---|---|---|---|---|---|
| AuNPs | Label-free | Proteins | 89% sensitivity and 73% accuracy | N/A | Saliva (5 healthy and 6 patients subjects) | Squamous cell carcinoma (SCC) of oral cavity | [151] |
| AuNPs | Label-free | Antigen CA125 | 5 mM | N/A | Spiked PBS | Ovarian cancer | [152] |
| AgNPs | Label-free | Proteins | 94% specificity and 95.5% sensitivity | N/A | 84 blood serum samples: 64 patients with clinically detected oral cancer and 20 healthy | Oral cavity cancer | [153] |
| AgNP | SERS nanotags/ magnetic beads/ microfluidics | Extracellular vesicle-proteins (CD63, CD9, or FAK) | Single-cell | Triplex | Non-metastatic (MCF-7) and metastatic (MDA-MB-231) cells | Lung cancer | [154] |
| AgNPs | SERS nanotags | Thrombin | 100% specificity | Singleplex | 16 cancer patients and 8 healthy subjects | Cancer | [155] |

to them changing with proteins spectra being quiet similar to each other as well as changes in protein conformation and orientation [139, 140].

In response to these challenges Lin et al. developed a label-free platform coupled with cellulose acetate membrane to extract human serum proteins for breast cancer protein-fingerprints detection. The platform was tested on samples from 30 breast cancer patients and 45 healthy volunteers. Proteins extracted from blood serum samples via the membrane were mixed with silver nanoparticles for SERS measurement (Fig. 19.6a) [135]. Following data analysis via a partial least square-support vector machine algorithm, the study yielded high diagnostic accuracy of 94.67%.

Another approach to increase sensitivity and specificity of analytical SERS is to treat low Raman signals of proteins via increasing the concentration of the targeted analyte. Hu et al. designed a biosensor with two critical components: a SERS nanotag and a magnetic capture substrate (Fig. 19.6b) [136]. The SERS nanotag was composed of reporter-labelled gold nano-bridged nanogap particles (AuNNPs, reporter molecules' signal is amplified due to molecule being located in the hot-spot; hot-spot is created in the gap between nanoparticle core and metal outer layer), which enhance the Raman signals. The magnetic capture substrate was crafted from silver-coated iron oxide-gold nanoparticles (Ag-coated $Fe_3O_4$–Au NPs), providing magnetic properties for efficient capture. Researchers used C-reactive protein (CRP), a well-known biomarker for diagnosing various medical conditions, to assess the SERS biosensor's performance. Aptamers specific to CRP were linked on both the SERS tag and the magnetic capture substrate, creating a molecular sandwich assay: Au NNPs-CRP-Ag MNPs. This biosensor demonstrated remarkable sensitivity with a LOD for CRP of 10 fM (equivalent to 1.14 pg/mL). This LOD is significantly lower than had been achieved with previously reported analytical methods (~ 100 pM) [141, 142].

More advanced platforms, such as microfluidic devices, allow for more complex monitoring. Cao et al. reported an approach that combines Au nanobowl (AuNB) arrays and the hybridization chain reaction (HCR) in a microfluidic chip for the ultrasensitive and simultaneous detection of squamous cell carcinoma antigen (SCCA) and cytokeratin 19 fragment antigen 21-1 (CYFRA21-1) in the serum of cervical cancer patients (Fig. 19.6c) [137]. The method utilizes capture via antibody-oligonucleotide conjugation which initiates HCR by facilitating the hybridization between hairpin DNAs modified with Raman reporters and anchored onto Ag nanocubes. The hairpins ultimately formed nicked double-stranded DNAs on the AuNB arrays, which led to signal amplification in SERS via contact with plasmonic nanostructure. The developed chip achieved an impressive linear response range for SCCA and CYFRA21-1, spanning from $10^{-12}$ to $10^{-6}$ g/mL. Additionally, it attained an exceptionally low LOD for SCCA (0.08 pg/mL) and CYFRA21-1 (0.13 pg/mL). The results obtained from this novel approach align with those obtained using traditional ELISA and have potential in clinics.

Among devices for proteins, LFAs offer a range of advantages, including speed, simplicity, cost-effectiveness, versatility, and suitability for point-of-care testing. Integrating LFA with SERS for protein measurements represents a powerful approach that addresses the challenges of both techniques, resulting in improved sensitivity and

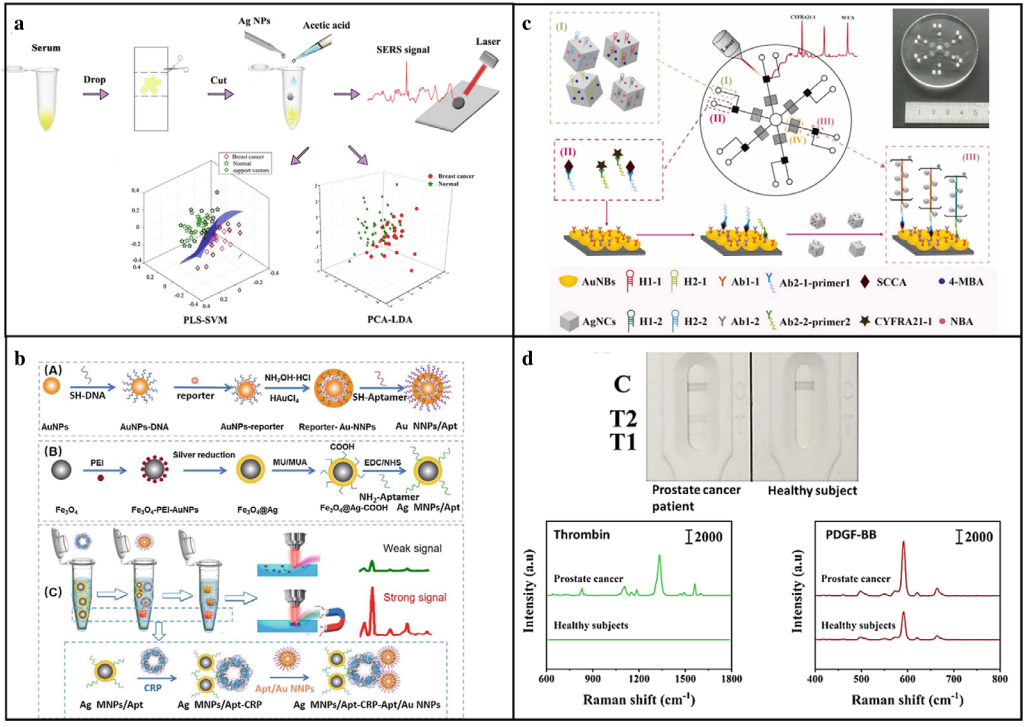



**Fig. 19.6** Various applications of SERS platforms for protein detection. **a** SERS detection of proteins purified on cellulose acetate membrane with further PCA-LDA and PLS-SVM analysis, reproduced with permission [135]. **b** Condensing protein sample via SERS-active magnetic beads (Ag-coated $Fe_3O_4$–Au NPs) from media for increased sensitivity, reproduced with permission [136]. **c** Microfluidic chip incorporating Au nanobowl arrays and hybridization chain reaction (HCR) for ultrasensitive and simultaneous detection of squamous cell carcinoma antigen (SCCA) and cytokeratin 19 fragment antigen 21-1 (CYFRA21-1) in cervical cancer patients' serum, reproduced with permission [137]. **d** SERS-LFA detection of thrombin and PDGF-BB in healthy and prostate cancer patients, reproduced with permission [138]

enhanced capturing capabilities [143]. Cao et al. utilized hollow Au–Ag nanoparticles functionalized with thiol-modified aptamers for simultaneous detection of thrombin and platelet-derived growth factor-BB (PDGF-BB) associated with prostate cancer from human plasma via LFA strip (Fig. 19.6d). The method was tested with 60 clinical samples composed of 30 healthy subjects and 30 prostate cancer patients. Reported LODs were 4.8 pg/ml and 3.8 pg/ml for thrombin and PDGF-BB, respectively [138].

The future of protein detection and measurement is poised to benefit from advancements in label-free SERS, analyte concentration techniques, microfluidic devices, and integrated approaches like LFA-SERS. These innovations will enhance sensitivity, specificity, and the practicality of protein diagnostics, ultimately improving early disease diagnosis and therapeutic interventions.

## 19.5 Conclusion and Perspective

To summarize, SERS has shown high potential to detect various biomarkers, including CTCs, sEVs, nucleic acids, proteins, and other analytes including organic and inorganic molecules and ions. SERS is playing a pivotal role in advancing the field of biomarker detection due to its unique capabilities including sensitivity and selectivity. In addition, SERS allows for multiplexed detection of multiple markers and provides high-resolution molecular information, enabling detailed characterization and early disease diagnosis. Improved capturing techniques for CTCs and sEVs, particularly through microfluidics, would enable its routine use in point-of-care diagnostics enhancing sensitivity and accuracy of biomarker detection. SERS also excels in sensitive detection of nucleic acids including DNA and RNA, thus it has potential in genetic testing and gene expression pattern analysis. SERS's high sensitivity in protein detection supports the identification of disease biomarkers, facilitating comprehensive biomarker profiling for early diagnosis and monitoring. The continued development of microfluidic devices is expected to enhance the precision and complexity of monitoring in these applications. EVs and individual proteins molecules are small enough to be ideal for LFA platform that provides both express and easy-to-process results.

Label-free SERS methods are growing in popularity and diversity of applications. They are particularly useful for identifying and characterizing analytes without the need for specific markers or labels and are being widely explored for the disease prognoses. The combination of the development of advanced AI data processing tools and SERS has the potential to transform healthcare by offering comprehensive and rapid diagnostics from just a small blood sample, a small instrument, and a mobile phone. This technology will enable early disease detection and decentralized healthcare as well as accelerating research, making it a promising and exciting prospect for the future of medical diagnostics and healthcare management.

Future efforts will involve optimizing platforms such as those discussed above to enable decentralized healthcare and remote diagnostics. Translating integrated microfluidic– and LFA–SERS systems into clinical practice is clearly gaining

momentum. The ongoing advances in Raman technology which mean that hand-held devices provide data of quality previously only achieved with large laboratory-based instruments open the possibility of SERS assays being used almost anywhere. Ensuring regulatory compliance and validating their accuracy in real-world clinical settings is essential.

**Acknowledgements** A.T. acknowledges funding support from the International Macquarie University Research Excellence Scholarship (iMQRES). A.R. and Y.W. acknowledge the funding support from the Australian Research Council (ARC) for the Discovery Project (DP220102086). Y.W. acknowledges funding support from ARC Future Fellowship (FT210100737). This work was supported by the Australian Research Council Industrial Transformation Training Centre for Facilitated Advancement of Australia's Bioactives (IC210100040).

## References

1. Tests and Procedures Used to Diagnose Cancer - NCI. https://www.cancer.gov/about-cancer/diagnosis-staging/diagnosis.
2. Pulumati, A., Pulumati, A., Dwarakanath, B. S., Verma, A. & Papineni, R. V. L. Technological advancements in cancer diagnostics: Improvements and limitations. *Cancer Rep* **6**, e1764 (2023).
3. Hussain, S. *et al.* Modern Diagnostic Imaging Technique Applications and Risk Factors in the Medical Field: A Review. *Biomed Res Int* **2022** (2022).
4. Kim, A., Nguyen, T. L. & Kim, D. H. Modern Methods of Diagnosis. *Diagnosis and Control of Diseases of Fish and Shellfish* 109–145 (2017).
5. Wang, J. *et al.* Engineering State-of-the-Art Plasmonic Nanomaterials for SERS-Based Clinical Liquid Biopsy Applications. *Advanced Science* **6**, 1900730 (2019).
6. Koo, K. M. *et al.* Design and Clinical Verification of Surface-Enhanced Raman Spectroscopy Diagnostic Technology for Individual Cancer Risk Prediction. *ACS Nano* **12**, 8362–8371 (2018).
7. Tavakkoli Yaraki, M., Tukova, A. & Wang, Y. Emerging SERS biosensors for the analysis of cells and extracellular vesicles. *Nanoscale* **14**, 15242–15268 (2022).
8. Lyu, N. & Wang, Y. SERS Nanotags. *World Scientific Series in Nanoscience and Nanotechnology* **22**, 215–243 (2022).
9. Avci, E. *et al.* Label-Free Surface Enhanced Raman Spectroscopy for Cancer Detection. *Cancers (Basel)* **14**, 5021 (2022).
10. Gutiérrez, Y., Brown, A. S., Moreno, F. & Losurdo, M. Plasmonics beyond noble metals: Exploiting phase and compositional changes for manipulating plasmonic performance. *J Appl Phys* **128** (2020).
11. Wang, J. *et al.* A high-resolution study of in situ surface-enhanced Raman scattering nanotag behavior in biological systems. *J Colloid Interface Sci* **537**, 536–546 (2019).
12. Wang, L. *et al.* Optical Properties and Applications of Plasmonic-Metal Nanoparticles. *Adv Funct Mater* **30**, 2005400 (2020).
13. Samriti, Rajput, V., Gupta, R. K. & Prakash, J. Engineering metal oxide semiconductor nanostructures for enhanced charge transfer: fundamentals and emerging SERS applications. *J Mater Chem C Mater* **10**, 73–95 (2021).
14. Er, E. *et al.* Metal nanoparticles/$MoS_2$ surface-enhanced Raman scattering-based sandwich immunoassay for α-fetoprotein detection. *ACS Appl Mater Interfaces* **13**, 8823–8831 (2021).
15. Kaushik, V., Kagdada, H. L., Singh, D. K. & Pathak, S. Enhancement of SERS effect in Graphene-Silver hybrids. *Appl Surf Sci* **574**, 151724 (2022).

16. Tukova, A., Kuschnerus, I. C., Garcia-Bennett, A., Wang, Y. & Rodger, A. Gold nanostars with reduced fouling facilitate small molecule detection in the presence of protein. *Nanomaterials* **11**, 2565 (2021).
17. Koya, A. N. *et al.* Nanoporous Metals: From Plasmonic Properties to Applications in Enhanced Spectroscopy and Photocatalysis. *ACS Nano* **15**, 6038–6060 (2021).
18. Wang, Y., Lee, K. & Irudayaraj, J. SERS aptasensor from nanorod–nanoparticle junction for protein detection. *Chemical Communications* **46**, 613–615 (2010).
19. Li, J. *et al.* Facile One-Pot Synthesis of Nanodot-Decorated Gold-Silver Alloy Nanoboxes for Single-Particle Surface-Enhanced Raman Scattering Activity. *ACS Appl Mater Interfaces* **10**, 32526–32535 (2018).
20. Li, J. *et al.* SERS Multiplex Profiling of Melanoma Circulating Tumor Cells for Predicting the Response to Immune Checkpoint Blockade Therapy. *Anal Chem* **94**, 14573–14582 (2022).
21. Nguyen, N. T. T., Tavakkoli Yaraki, M. & Wang, Y. Enabling spectral barcoding of SERS nanotags using gold nanostars. *Mol Syst Des Eng* **8**, 251–260 (2023).
22. Lyu, N. *et al.* Multiplex detection of ctDNA mutations in plasma of colorectal cancer patients by PCR/SERS assay. *Nanotheranostics* **4**, 224–232 (2020).
23. Lyu, N. *et al.* In situ synthesis of gold nanoparticles on layered double hydroxide nanoparticles for multiplexing molecular imaging of single cells. *Mater Today Chem* **33**, 101698 (2023).
24. Li, D. *et al.* Sensitive and Multiplexed SERS Nanotags for the Detection of Cytokines Secreted by Lymphoma. *ACS Sens* **4**, 2507–2514 (2019).
25. Wang, Y. & Schlücker, S. Rational design and synthesis of SERS labels. *Analyst* **138**, 2224–2238 (2013).
26. Sánchez-Purrà, M., Roig-Solvas, B., Rodriguez-Quijada, C., Leonardo, B. M. & Hamad-Schifferli, K. Reporter Selection for Nanotags in Multiplexed Surface Enhanced Raman Spectroscopy Assays. *ACS Omega* **3**, 10733–10742 (2018).
27. Shevchuk, A. I., Svinko, V. O., Smirnov, A. N. & Solovyeva, E. V. SERS study of cyanine dyes: Optimization of metal core and molecular label choice for plasmonic nanotags. *Dyes and Pigments* **216**, 111329 (2023).
28. Javaid, R. *et al.* Design and synthesis of boron complexes as new Raman reporter molecules for sensitive SERS nanotags. *Journal of Raman Spectroscopy* **51**, 2408–2415 (2020).
29. Seo, M. & Ha, J. W. Effective surface-enhanced Raman scattering of randomly branched gold nano-urchins with Rhodamine 6G as Raman reporters. *Microchemical Journal* **140**, 47–51 (2018).
30. Kim, S. *et al.* A facile, portable surface-enhanced Raman spectroscopy sensing platform for on-site chemometrics of toxic chemicals. *Sens Actuators B Chem* **343**, 130102 (2021).
31. Lai, Y., Sun, S., He, T., Schlücker, S. & Wang, Y. Raman-encoded microbeads for spectral multiplexing with SERS detection. *RSC Adv* **5**, 13762–13767 (2015).
32. Kearns, H., Shand, N. C., Smith, W. E., Faulds, K. & Graham, D. 1064 nm SERS of NIR active hollow gold nanotags. *Physical Chemistry Chemical Physics* **17**, 1980–1986 (2014).
33. Liang, D. *et al.* SERS Nanoprobes in Biologically Raman Silent Region for Tumor Cell Imaging and In Vivo Tumor Spectral Detection in Mice. *Adv Biosyst* **2**, 1800100 (2018).
34. Chen, Y. *et al.* Alkyne-Modulated Surface-Enhanced Raman Scattering-Palette for Optical Interference-Free and Multiplex Cellular Imaging. *Anal Chem* **88**, 6115–6119 (2016).
35. Chegel, V. *et al.* Gold nanoparticles aggregation: Drastic effect of cooperative functionalities in a single molecular conjugate. *Journal of Physical Chemistry C* **116**, 2683–2690 (2012).
36. Tukova, A. *et al.* Shape dependent protein-induced stabilization of gold nanoparticles: From a protein corona perspective. *Aggregate* **4**, e323 (2023).
37. Pedroso-Santana, S. & Fleitas-Salazar, N. The Use of Capping Agents in the Stabilization and Functionalization of Metallic Nanoparticles for Biomedical Applications. *Particle & Particle Systems Characterization* **40**, 2200146 (2023).
38. Wang, Y. *et al.* Enhanced dispersion stability of gold nanoparticles by the physisorption of cyclic poly(ethylene glycol). *Nature Communications 2020 11:1* **11**, 1–12 (2020).
39. Liu, Y. *et al.* Positively charged gold–silver nanostar enabled molecular characterization of cancer associated extracellular vesicles. *Analytical Methods* **12**, 5908–5915 (2020).

40. D'Souza, S. L., Pati, R. K. & Kailasa, S. K. Ascorbic acid functionalized gold nanoparticles as a probe for colorimetric and visual read-out determination of dichlorvos in environmental samples. *Analytical Methods* **6**, 9007–9014 (2014).
41. Garcia-Rico, E., Alvarez-Puebla, R. A. & Guerrini, L. Direct surface-enhanced Raman scattering (SERS) spectroscopy of nucleic acids: from fundamental studies to real-life applications. *Chem Soc Rev* **47**, 4909–4923 (2018).
42. Zhang, W., Jiang, L., Piper, J. A. & Wang, Y. SERS Nanotags and Their Applications in Biosensing and Bioimaging. *Journal of Analysis and Testing 2018 2:1* **2**, 26–44 (2018).
43. Zhou, W. *et al.* Thiol-Mediated Multidentate Phosphorylcholine as a Zwitterionic Ligand for Stabilizing Biocompatible Gold Nanoparticles. *Langmuir* **35**, 13031–13039 (2019).
44. Woehrle, G. H., Brown, L. O. & Hutchison, J. E. Thiol-functionalized, 1.5-nm gold nanoparticles through ligand exchange reactions: Scope and mechanism of ligand exchange. *J Am Chem Soc* **127**, 2172–2183 (2005).
45. Izadian, A., Gao, Y., McCall, B. & Hajrasouliha, A. R. The effect of Polymer Coating Gold Nanoparticles on Retinal Neovascularization and Electrophysiologic Function. *Invest Ophthalmol Vis Sci* **64**, 2828–2828 (2023).
46. Abdelkawi, A., Slim, A., Zinoune, Z. & Pathak, Y. Surface Modification of Metallic Nanoparticles for Targeting Drugs. *Coatings 2023, Vol. 13, Page 1660* **13**, 1660 (2023).
47. Baygazieva, E. K. *et al.* Polymer protected gold nanoparticles: synthesis, characterization and application in catalysis. (2014).
48. Schulz, F., Vossmeyer, T., Bastús, N. G. & Weller, H. Effect of the spacer structure on the stability of gold nanoparticles functionalized with monodentate thiolated poly(ethylene glycol) ligands. *Langmuir* **29**, 9897–9908 (2013).
49. Chen, Y. S. *et al.* Silica-coated gold nanorods as photoacoustic signal nanoamplifiers. *Nano Lett* **11**, 348–354 (2011).
50. Zijlstra, P., Chon, J. W. M. & Gu, M. Five-dimensional optical recording mediated by surface plasmons in gold nanorods. *Nature 2009 459:7245* **459**, 410–413 (2009).
51. Shnoudeh, A. J. *et al.* Synthesis, Characterization, and Applications of Metal Nanoparticles. *Biomaterials and Bionanotechnology* 527–612 (2019).
52. Borse, V. & Konwar, A. N. Synthesis and characterization of gold nanoparticles as a sensing tool for the lateral flow immunoassay development. *Sensors International* **1**, 100051 (2020).
53. Zheng, X. S., Jahn, I. J., Weber, K., Cialla-May, D. & Popp, J. Label-free SERS in biological and biomedical applications: Recent progress, current challenges and opportunities. *Spectrochim Acta A Mol Biomol Spectrosc* **197**, 56–77 (2018).
54. Xie, L. *et al.* State of the art in flexible SERS sensors toward label-free and onsite detection: from design to applications. *Nano Research 2022 15:5* **15**, 4374–4394 (2022).
55. Cai, L., Fang, G., Tang, J., Cheng, Q. & Han, X. Label-Free Surface-Enhanced Raman Spectroscopic Analysis of Proteins: Advances and Applications. *International Journal of Molecular Sciences 2022, Vol. 23, Page 13868* **23**, 13868 (2022).
56. Ding, Y. *et al.* SERS-Based Biosensors Combined with Machine Learning for Medical Application**. *ChemistryOpen* **12**, e202200192 (2023).
57. Qi, Y., Liu, Y. & Luo, J. Recent application of Raman spectroscopy in tumor diagnosis: from conventional methods to artificial intelligence fusion. *PhotoniX 2023 4:1* **4**, 1–42 (2023).
58. Muhammad, M. & Huang, Q. A review of aptamer-based SERS biosensors: Design strategies and applications. *Talanta* **227**, 122188 (2021).
59. Zhang, W. *et al.* Enabling Sensitive Phenotypic Profiling of Cancer-Derived Small Extracellular Vesicles Using Surface-Enhanced Raman Spectroscopy Nanotags. *ACS Sens* **5**, 764–771 (2020).
60. Modh, H., Scheper, T. & Walter, J. G. Aptamer-Modified Magnetic Beads in Biosensing. *Sensors 2018, Vol. 18, Page 1041* **18**, 1041 (2018).
61. Reddy, L. H., Arias, J. L., Nicolas, J. & Couvreur, P. Magnetic nanoparticles: Design and characterization, toxicity and biocompatibility, pharmaceutical and biomedical applications. *Chem Rev* **112**, 5818–5878 (2012).

62. He, J., Huang, M., Wang, D., Zhang, Z. & Li, G. Magnetic separation techniques in sample preparation for biological analysis: A review. *J Pharm Biomed Anal* **101**, 84–101 (2014).
63. Lin, B. *et al.* Microfluidic-Based Exosome Analysis for Liquid Biopsy. *Small Methods* **5**, 2001131 (2021).
64. Ngo, L. *et al.* Emerging integrated SERS-microfluidic devices for analysis of cancer-derived small extracellular vesicles. *Lab Chip* **23**, 2899–2921 (2023).
65. Shanmugasundaram, K. B., Li, J., Sina, A. I., Wuethrich, A. & Trau, M. Toward precision oncology: SERS microfluidic systems for multiplex biomarker analysis in liquid biopsy. *Mater Adv* **3**, 1459–1471 (2022).
66. Ebrahimi, S., Hasanzadeh-Barforoushi, A., Nejat, A. & Kowsary, F. Numerical study of mixing and heat transfer in mixed electroosmotic/pressure driven flow through T-shaped microchannels. *Int J Heat Mass Transf* **75**, 565–580 (2014).
67. Rafeie, M. *et al.* An easily fabricated three-dimensional threaded lemniscate-shaped micromixer for a wide range of flow rates. *Biomicrofluidics* **11** (2017).
68. Antognoli, M., Stoecklein, D., Galletti, C., Brunazzi, E. & Di Carlo, D. Optimized design of obstacle sequences for microfluidic mixing in an inertial regime. *Lab Chip* **21**, 3910–3923 (2021).
69. Wang, Z. *et al.* An Overview for the Nanoparticles-Based Quantitative Lateral Flow Assay. *Small Methods* **6**, 2101143 (2022).
70. Wang, L. *et al.* SERS-based test strips: Principles, designs and applications. *Biosens Bioelectron* **189**, 113360 (2021).
71. Dey, M. K., Iftesum, M., Devireddy, R. & Gartia, M. R. New technologies and reagents in lateral flow assay (LFA) designs for enhancing accuracy and sensitivity. *Analytical Methods* **15**, 4351–4376 (2023).
72. Lin, D. *et al.* Circulating tumor cells: biology and clinical significance. *Signal Transduction and Targeted Therapy 2021 6:1* **6**, 1–24 (2021).
73. Kamińska, A. *et al.* Detection of Circulating Tumor Cells Using Membrane-Based SERS Platform: A New Diagnostic Approach for 'Liquid Biopsy'. *Nanomaterials 2019, Vol. 9, Page 366* **9**, 366 (2019).
74. Xue, T. *et al.* Detection of circulating tumor cells based on improved SERS-active magnetic nanoparticles. *Analytical Methods* **11**, 2918–2928 (2019).
75. Gao, R. *et al.* Simultaneous single-cell phenotype analysis of hepatocellular carcinoma CTCs using a SERS-aptamer based microfluidic chip. *Lab Chip* **21**, 3888–3898 (2021).
76. Czaplicka, M. *et al.* Effect of Varying Expression of EpCAM on the Efficiency of CTCs Detection by SERS-Based Immunomagnetic Optofluidic Device. *Cancers 2020, Vol. 12, Page 3315* **12**, 3315 (2020).
77. Agarwal, A., Balic, M., El-Ashry, D. & Cote, R. J. Circulating Tumor Cells: Strategies for Capture, Analyses, and Propagation. *Cancer Journal (United States)* **24**, 70–77 (2018).
78. Lu, N. N. *et al.* Biotin-triggered decomposable immunomagnetic beads for capture and release of circulating tumor cells. *ACS Appl Mater Interfaces* **7**, 8817–8826 (2015).
79. Hu, Y. *et al.* Efficient capture of circulating tumor cells with low molecular weight folate receptor-specific ligands. *Scientific Reports 2022 12:1* **12**, 1–10 (2022).
80. Zhang, Y. *et al.* Combining Multiplex SERS Nanovectors and Multivariate Analysis for In Situ Profiling of Circulating Tumor Cell Phenotype Using a Microfluidic Chip. *Small* **14**, 1704433 (2018).
81. Zhang, Y. *et al.* Characterization and identification of lung cancer cells from blood cells with label-free surface-enhanced Raman scattering. *Laser Phys* **29**, 045602 (2019).
82. Niciński, K. *et al.* Detection of circulating tumor cells in blood by shell-isolated nanoparticle – enhanced Raman spectroscopy (SHINERS) in microfluidic device. *Scientific Reports 2019 9:1* **9**, 1–14 (2019).
83. Xu, Y. *et al.* Ultrahigh SERS activity of the $TiO_2$@Ag nanostructure leveraged for accurately detecting CTCs in peripheral blood. *Biomater Sci* **10**, 1812–1820 (2022).
84. Szymborski, T. R. *et al.* Dielectrophoresis-Based SERS Sensors for the Detection of Cancer Cells in Microfluidic Chips. *Biosensors (Basel)* **12**, 681 (2022).

85. Wilson, R. E. *et al.* Immunomagnetic Capture and Multiplexed Surface Marker Detection of Circulating Tumor Cells with Magnetic Multicolor Surface-Enhanced Raman Scattering Nanotags. *ACS Appl Mater Interfaces* **12**, 47220–47232 (2020).
86. Li, J. *et al.* Nondestructive separation/enrichment and rolling circle amplification-powered sensitive SERS enumeration of circulating tumor cells via aptamer recognition. *Biosens Bioelectron* **231**, 115273 (2023).
87. Zhang, D. *et al.* A novel dual-function SERS-based identification strategy for preliminary screening and accurate diagnosis of circulating tumor cells. *J Mater Chem B* **11**, 9666–9675 (2023).
88. Kalluri, R. & LeBleu, V. S. The biology, function, and biomedical applications of exosomes. *Science (1979)* **367** (2020).
89. Shao, H. L. *et al.* New Technologies for Analysis of Extracellular Vesicles. *Chem Rev* **118**, 1917–1950 (2018).
90. Wang, J. *et al.* Tracking extracellular vesicle phenotypic changes enables treatment monitoring in melanoma. *Sci Adv* **6**, eaax3223 (2020).
91. Su, X. *et al.* Absolute Quantification of Serum Exosomes in Patients with an SERS-Lateral Flow Strip Biosensor for Noninvasive Clinical Cancer Diagnosis. *ACS Appl Mater Interfaces* **15**, 37130–37142 (2023).
92. Ngo, L., Zhang, W., Hnit, S. S. T. & Wang, Y. Improving SERS biosensors for the analysis of ovarian cancer-derived small extracellular vesicles. *Analyst* **148**, 3074–3086 (2023).
93. Zhang, W. *et al.* Phenotypic profiling of pancreatic ductal adenocarcinoma plasma-derived small extracellular vesicles for cancer diagnosis and cancer stage prediction: a proof-of-concept study. *Anal Methods* **14**, 2255–2265 (2022).
94. Wang, J., Trau, M. & Wuethrich, A. A Microfluidic SERS Assay to Characterize the Phenotypic Heterogeneity in Cancer-Derived Small Extracellular Vesicles. in *Microfluidic Systems for Cancer Diagnosis* (eds. Garcia-Cordero, J. L. & Revzin, A.) 241–253 (Springer US, 2023).
95. Han, Z. *et al.* SERS and MALDI-TOF MS based plasma exosome profiling for rapid detection of osteosarcoma. *Analyst* **146**, 6496–6505 (2021).
96. Ćulum, N. M. *et al.* Characterization of ovarian cancer-derived extracellular vesicles by surface-enhanced Raman spectroscopy. *Analyst* **146**, 7194–7206 (2021).
97. Yan, Z. *et al.* A Label-Free Platform for Identification of Exosomes from Different Sources. *ACS Sens* **4**, 488–497 (2019).
98. Xie, Y., Su, X., Wen, Y., Zheng, C. & Li, M. Artificial Intelligent Label-Free SERS Profiling of Serum Exosomes for Breast Cancer Diagnosis and Postoperative Assessment. *Nano Lett* **22**, 7910–7918 (2022).
99. Qian, H. *et al.* Diagnosis of urogenital cancer combining deep learning algorithms and surface-enhanced Raman spectroscopy based on small extracellular vesicles. *Spectrochim Acta A Mol Biomol Spectrosc* **281**, 121603 (2022).
100. Shin, H. *et al.* Early-Stage Lung Cancer Diagnosis by Deep Learning-Based Spectroscopic Analysis of Circulating Exosomes. *ACS Nano* **14**, 5435–5444 (2020).
101. Liu, Z. *et al.* Gold Nanopyramid Arrays for Non-Invasive Surface-Enhanced Raman Spectroscopy-Based Gastric Cancer Detection via sEVs. *ACS Appl Nano Mater* **2022**, 12506–12517 (2022).
102. Han, L. *et al.* Integrated separation and detection of exosomes via a label-free magnetic SERS platform. *Chemical Communications* **59**, 7967–7970 (2023).
103. Carmicheal, J. *et al.* Label-free characterization of exosome via surface enhanced Raman spectroscopy for the early detection of pancreatic cancer. *Nanomedicine* **16**, 88–96 (2019).
104. Diao, X. *et al.* Machine Learning-Based Label-Free SERS Profiling of Exosomes for Accurate Fuzzy Diagnosis of Cancer and Dynamic Monitoring of Drug Therapeutic Processes. *Anal Chem* **95**, 7552–7559 (2023).
105. Shin, H. *et al.* Single test-based diagnosis of multiple cancer types using Exosome-SERS-AI for early stage cancers. *Nat Commun* **14**, 1644 (2023).
106. Pang, Y. *et al.* Personalized detection of circling exosomal PD-L1 based on $Fe_3O_4$@$TiO_2$ isolation and SERS immunoassay. *Biosens Bioelectron* **148**, 111800 (2020).

107. Tian, Y.-F., Ning, C.-F., He, F., Yin, B.-C. & Ye, B.-C. Highly sensitive detection of exosomes by SERS using gold nanostar@Raman reporter@nanoshell structures modified with a bivalent cholesterol-labeled DNA anchor. *Analyst* **143**, 4915–4922 (2018).
108. Fan, C. *et al.* Ultrasensitive Exosome Detection by Modularized SERS Labeling for Postoperative Recurrence Surveillance. *ACS Sens* **6**, 3234–3241 (2021).
109. Wang, Y. *et al.* Microfluidic Raman biochip detection of exosomes: a promising tool for prostate cancer diagnosis. *Lab Chip* **20**, 4632–4637 (2020).
110. Li, T.-D. *et al.* An ultrasensitive polydopamine bi-functionalized SERS immunoassay for exosome-based diagnosis and classification of pancreatic cancer. *Chem Sci* **9**, 5372–5382 (2018).
111. Kwizera, E. A. *et al.* Molecular Detection and Analysis of Exosomes Using Surface-Enhanced Raman Scattering Gold Nanorods and a Miniaturized Device. *Theranostics* **8**, 2722–2738 (2018).
112. Wang, J., Xie, H. & Ding, C. Designed Co-DNA-Locker and Ratiometric SERS Sensing for Accurate Detection of Exosomes Based on Gold Nanorod Arrays. *ACS Appl Mater Interfaces* **13**, 32837–32844 (2021).
113. Wang, Z. *et al.* Screening and multiple detection of cancer exosomes using an SERS-based method. *Nanoscale* **10**, 9053–9062 (2018).
114. Han, Z. *et al.* Integrated microfluidic-SERS for exosome biomarker profiling and osteosarcoma diagnosis. *Biosens Bioelectron* **217**, 114709 (2022).
115. Wang, J. *et al.* Characterizing the Heterogeneity of Small Extracellular Vesicle Populations in Multiple Cancer Types via an Ultrasensitive Chip. *ACS Sens* **6**, 3182–3194 (2021).
116. Li, J. *et al.* Digital Decoding of Single Extracellular Vesicle Phenotype Differentiates Early Malignant and Benign Lung Lesions. *Advanced Science* **10**, 2204207 (2023).
117. Stejskal, P. *et al.* Circulating tumor nucleic acids: biology, release mechanisms, and clinical relevance. *Mol Cancer* **22**, 15 (2023).
118. Wan, J. C. M. *et al.* Liquid biopsies come of age: towards implementation of circulating tumour DNA. *Nat Rev Cancer* **17**, 223–238 (2017).
119. Liu, Y. *et al.* Sensitive and Direct DNA Mutation Detection by Surface-Enhanced Raman Spectroscopy Using Rational Designed and Tunable Plasmonic Nanostructures. *Anal Chem* **92**, 5708–5716 (2020).
120. Wu, L. *et al.* Profiling DNA mutation patterns by SERS fingerprinting for supervised cancer classification. *Biosens Bioelectron* **165**, 112392 (2020).
121. Mao, Y., Sun, Y., Xue, J., Lu, W. & Cao, X. Ultra-sensitive and high efficiency detection of multiple non-small cell lung cancer-related miRNAs on a single test line in catalytic hairpin assembly-based SERS-LFA strip. *Anal Chim Acta* **1178**, 338800 (2021).
122. Wang, J., Koo, K. M., Wang, Y. & Trau, M. "Mix-to-Go" Silver Colloidal Strategy for Prostate Cancer Molecular Profiling and Risk Prediction. *Anal Chem* **90**, 12698–12705 (2018).
123. Yao, Y. *et al.* Iodide-modified Ag nanoparticles coupled with DSN-Assisted cycling amplification for label-free and ultrasensitive SERS detection of MicroRNA-21. *Talanta* **235**, 122728 (2021).
124. Kowalczyk, A. *et al.* New strategy for the gene mutation identification using surface enhanced Raman spectroscopy (SERS). *Biosens Bioelectron* **132**, 326–332 (2019).
125. Lee, T. *et al.* Highly robust, uniform and ultra-sensitive surface-enhanced Raman scattering substrates for microRNA detection fabricated by using silver nanostructures grown in gold nanobowls. *Nanoscale* **10**, 3680–3687 (2018).
126. Lyu, N. *et al.* Highly specific detection of KRAS single nucleotide polymorphism by asymmetric PCR/SERS assay. *Analyst* **146**, 5714–5721 (2021).
127. Chen, J. *et al.* Ratiometric SERS biosensor for sensitive and reproducible detection of microRNA based on mismatched catalytic hairpin assembly. *Biosens Bioelectron* **143**, 111619 (2019).
128. Jiang, S. *et al.* In Situ Exosomal MicroRNA Determination by Target-Triggered SERS and $Fe_3O_4$@$TiO_2$-Based Exosome Accumulation. *ACS Sens* **6**, 852–862 (2021).

129. Muhammad, M., Shao, C.-S., Liu, C. & Huang, Q. Highly Sensitive Detection of Elevated Exosomal miR-122 Levels in Radiation Injury and Hepatic Inflammation Using an Aptamer-Functionalized SERS-Sandwich Assay. *ACS Appl Bio Mater* **4**, 8386–8395 (2021).
130. Lee, J. U., Kim, W. H., Lee, H. S., Park, K. H. & Sim, S. J. Quantitative and Specific Detection of Exosomal miRNAs for Accurate Diagnosis of Breast Cancer Using a Surface-Enhanced Raman Scattering Sensor Based on Plasmonic Head-Flocked Gold Nanopillars. *Small* **15**, 1804968 (2019).
131. Potluri, P. R., Rajendran, V. K., Sunna, A. & Wang, Y. Rapid and specific duplex detection of methicillin-resistant Staphylococcus aureus genes by surface-enhanced Raman spectroscopy. *Analyst* **145**, 2789–2794 (2020).
132. Zeng, Y., Koo, K. M., Shen, A.-G., Hu, J.-M. & Trau, M. Nucleic Acid Hybridization-Based Noise Suppression for Ultraselective Multiplexed Amplification of Mutant Variants. *Small* **17**, 2006370 (2021).
133. Lu, X. *et al.* Amplification-Free and Mix-and-Read Analysis of Multiplexed MicroRNAs on a Single Plasmonic Microbead. *Nano Lett* **21**, 6718–6724 (2021).
134. Chen, Y. *et al.* Application of SERS in In-Vitro Biomedical Detection. *Chem Asian J* **18**, e202201194 (2023).
135. Lin, Y. *et al.* Label-free diagnosis of breast cancer based on serum protein purification assisted surface-enhanced Raman spectroscopy. *Spectrochim Acta A Mol Biomol Spectrosc* **263**, 120234 (2021).
136. Hu, Z. *et al.* Aptamer-based novel Ag-coated magnetic recognition and SERS nanotags with interior nanogap biosensor for ultrasensitive detection of protein biomarker. *Sens Actuators B Chem* **334**, 129640 (2021).
137. Cao, X. *et al.* A SERS microfluidic chip for ultrasensitive and simultaneous detection of SCCA and CYFRA21-1 in serum based on Au nanobowl arrays and hybridization chain reaction. *Sens Actuators B Chem* **375**, 132894 (2023).
138. Rahim Ruslinda, A. *et al.* A SERS-LFA biosensor combined with aptamer recognition for simultaneous detection of thrombin and PDGF-BB in prostate cancer plasma. *Nanotechnology* **32**, 445101 (2021).
139. Szekeres, G. P. & Kneipp, J. SERS probing of proteins in gold nanoparticle agglomerates. *Front Chem* **7**, 434849 (2019).
140. Ma, H. *et al.* Surface-enhanced Raman scattering for direct protein function investigation: Controlled immobilization and orientation. *Anal Chem* **91**, 8767–8771 (2021).
141. Kim, H. *et al.* Label-free C-reactive protein SERS detection with silver nanoparticle aggregates. *RSC Adv* **5**, 34720–34729 (2015).
142. CRP ELISA Kits. https://www.thermofisher.com/immunoassays/elisa/target/CRP/filter/species/Human?gclid=CjwKCAiAhJWsBhAaEiwAmrNyqy-gv1qmg1PurZNV0vz6oA0ZjveZTRWxFLuAtlmH0ojG6vXeYfc7GRoCnR8QAvD_BwE&ef_id=CjwKCAiAhJWsBhAaEiwAmrNyqy-gv1qmg1PurZNV0vz6oA0ZjveZTRWxFLuAtlmH0ojG6vXeYfc7GRoCnR8QAvD_BwE:G:s&s_kwcid=AL!3652!3!5194311119613!e!!g!!human%20crp%20elisa!352133802!69314251624&cid=bid_pca_iel_r01_co_cp1359_pjt0000_bid00000_0se_gaw_nt_pur_con&gad_source=1.
143. Rey Gomez, L. M., Hirani, R., Care, A., Inglis, D. W. & Wang, Y. Emerging Microfluidic Devices for Sample Preparation of Undiluted Whole Blood to Enable the Detection of Biomarkers. *ACS Sens* **8**, 1404–1421 (2023).
144. Saridag, A. M. & Kahraman, M. Layer-by-layer coating of natural diatomite with silver nanoparticles for identification of circulating cancer protein biomarkers using SERS. *Nanoscale* **15**, 13770–13783 (2023).
145. Hassanain, W. A., Theiss, F. L. & Izake, E. L. Label-free identification of Erythropoietin isoforms by surface enhanced Raman spectroscopy. *Talanta* **236**, 122879 (2022).
146. Lai, C., Zeng, C., Wen, J. & Jiang, X. Label-free long-range detection of prostate cancer biomarkers based on surface-enhanced Raman scattering. *Meas Sci Technol* **34**, 125503 (2023).

147. Zou, B., Lou, S., Wang, J., Zhou, S. & Wang, Y. Periodic Surface-Enhanced Raman Scattering-Encoded Magnetic Beads for Reliable Quantitative Surface-Enhanced Raman Scattering-Based Multiplex Bioassay. *Anal Chem* **94**, 11557–11563 (2022).
148. Liao, L. *et al.* Highly stable surface-enhanced Raman spectroscopy assay on abnormal thrombin levels in the blood plasma of cancer patients. *Analytical Methods* **13**, 4328–4333 (2021).
149. Huang, Y. *et al.* Ultrasensitive detection of gastric cancer biomarkers via a frequency shift-based SERS microfluidic chip. *Analyst* **148**, 3295–3305 (2023).
150. Cong, L. *et al.* Microfluidic Droplet-SERS Platform for Single-Cell Cytokine Analysis via a Cell Surface Bioconjugation Strategy. *Anal Chem* **94**, 10375–10383 (2022).
151. Fălămaş, A., Rotaru, H. & Hedeşiu, M. Surface-enhanced Raman spectroscopy (SERS) investigations of saliva for oral cancer diagnosis. *Lasers Med Sci* **35**, 1393–1401 (2020).
152. TunÇ, İ. & Susapto, H. H. Label-Free Detection of Ovarian Cancer Antigen CA125 by Surface Enhanced Raman Scattering. *J Nanosci Nanotechnol* **20**, 1358–1365 (2019).
153. Amber, A., Nawaz, H., Bhatti, H. N. & Mushtaq, Z. Surface-enhanced Raman spectroscopy for the characterization of different anatomical subtypes of oral cavity cancer. *Photodiagnosis Photodyn Ther* **42**, 103607 (2023).
154. Wang, J., Cong, L., Shi, W., Xu, W. & Xu, S. Single-Cell Analysis and Classification according to Multiplexed Proteins via Microdroplet-Based Self-Driven Magnetic Surface-Enhanced Raman Spectroscopy Platforms Assisted with Machine Learning Algorithms. *Anal Chem* **95**, 11019–11027 (2023).
155. Su, M. *et al.* Intrinsic SERS Fingerprints of Aptamer-Peptide Conjugates for Direct High-Specific Profiling Abnormal Protein Levels in Cancer Patients. *Anal Chem* **95**, 12398–12405 (2023).

# Chapter 20
# SORS and SESORS Biomedical Applications




**Priyanka Dey**

**Abstract** Spatially offset Raman spectroscopy (SORS) and surface-enhanced spatially offset Raman spectroscopy (SESORS) represent an exciting evolution in the realm of analytical chemistry and molecular spectroscopy. Its ability to probe subsurface layers in both SORS and SESORS, while also enhancing Raman signals using plasmonic SERS nanostructures in SESORS, makes them a versatile tool. As researchers address the challenges and refine the technique, both techniques are poised to contribute significantly to our understanding of complex materials, environmental monitoring, and advancements in healthcare technology. They enable non-invasive depth profiling in biological tissues which has found immense importance for investigating skin, bone, and organ tissues, aiding in disease diagnosis, drug delivery studies, and tissue characterization. Till date, SORS and SESORS have made enormous progress in achieving cancer margin analysis, bone health determination, proof-of-concept studies into monitoring of neurotransmitters, and exploring non-invasive SESORS cancer diagnosis by tracking the SERS agents through more than 7 cm of protein-rich tissue. Advances in optics, nanostructures, and instrumentation are driving vital breakthroughs and innovation in SORS and SESORS biomedical applications. This chapter delves into the discovery, classification, and biomedical applications of SORS and SESORS, discussing their limitations and future potential in biomedical research.

**Keywords** Deep Raman · Transmission Raman · Offset Raman · Nano-structures · Nano-assemblies · Disease diagnosis

P. Dey (✉)
School of Medicine, Pharmacy and Biomedical Sciences, University of Portsmouth, Portsmouth PO1 2UP, UK
e-mail: priyanka.dey@port.ac.uk

© The Author(s), under exclusive license to Springer Nature Singapore Pte Ltd. 2024

M. Procházka et al. (eds.), *Surface- and Tip-Enhanced Raman Scattering Spectroscopy*,
https://doi.org/10.1007/978-981-97-5818-0_20

## 20.1 Introduction

Surface-enhanced Raman spectroscopy (SERS) [1] and spatially offset Raman spectroscopy (SORS) [2] are both powerful tools in the field of analytical chemistry. The SERS phenomenon enhances Raman signals by exploiting plasmonic nanoparticles, while the SORS instrumentation allows for subsurface Raman analysis. Surface-enhanced spatially offset Raman spectroscopy (SESORS) [3] is a remarkable synergy of these two techniques, offering the ability to probe subsurface layers of complex samples while enhancing the Raman signals obtained. SESORS has garnered significant attention in recent years, representing a cutting-edge analytical tool with the potential to transform various scientific and industrial applications. In this comprehensive exploration of SORS and SESORS, we will delve into its principles, historical development, applications particularly in the medical field, and future prospects.

Both SORS and SESORS have found diverse applications across multiple fields, offering unique analytical capabilities and depth-resolved insights. SESORS is valuable in biomedical applications, enabling non-invasive depth profiling in biological tissues. It has been used to investigate skin, bone, and organ tissues, aiding in disease diagnosis, drug delivery studies, and tissue characterization. It has also been employed in pharmaceutical research to assess drug formulations, identify active pharmaceutical ingredients, and monitor the distribution of components within pharmaceutical tablets and capsules. In cultural heritage preservation, SORS can provide non-destructive analysis of historical artefacts, paintings, and manuscripts. It assists in identifying pigments, dyes, and degradation products. SORS and SESORS both play a vital role in detection and quantification of environmental pollutants, heavy metals, and contaminants in environmental samples, which is crucial for environmental protection and remediation efforts. It is used to investigate complex materials such as polymers, composites, and coatings. It helps researchers gain insights into material composition, quality control, and the development of advanced materials. Furthermore, SORS and SESORS have the potential for in-field use in security applications, where it can identify concealed substances or explosives, through opaque or turbid materials. Such instruments and analysis are often found at the airport security screening. In forensics, it aids in the analysis of trace evidence. These make both the SORS and SESORS techniques very promising for multiple sensing applications. This chapter will focus on the development of SORS and SESORS for biomedical applications.

## 20.2 Conventional Raman for In Vivo Biomedical Use

Traditional Raman spectroscopy (RS) has historically been employed for the identification and characterization of known and unknown molecules by deciphering their chemical structures. One of the early scoping studies for Raman spectroscopy for in vivo studies was reported by Qian and co-workers [4] in 2008. They employed

a tumour-targeted gold nanoparticle functionalized with Raman tags (also referred to as, labels or reporters) as the surface-enhanced Raman (SERS) agent and demonstrated detection of the SERS agent signal using a conventional Raman microspectrometer from whole mice. Although this was a groundbreaking research direction, the depth-restricted Raman signal collection particularly in highly scattering and fluorescence matrix like the tissue was soon recognized as the bottleneck for Raman in vivo biomedical applications.

In the realm of biomedical optical detection, Raman spectroscopy has also gained prominence due to the ability in detecting inherent disparities in the composition of fluids, cells, and tissue components. These variations encompass proteins, lipids, nucleic acids, carbohydrates, water, and other constituents, each exhibiting distinct ratios in healthy and cancerous tissues [5, 6]. Raman techniques have been extensively integrated into clinical research, applied to biopsy tissue sections and the surface analysis of organs that are affected by cancers, including epithelial, breast, head and neck, lung, and esophageal cancers [7]. This widespread use highlights its efficacy as a diagnostic tool. Moreover, Raman spectroscopy, when combined with multivariate statistical analysis or machine learning algorithms [8], has proven effective in identifying primary and secondary cancers in lymph nodes, particularly in the head and neck and axillary breast nodes during surgical procedures. Recent investigations have delved into the use of calcium hydroxyapatite in breast cancer tissues, specifically as a component of type II microcalcifications. These studies encompass large surgically resected breast tissue specimens and biopsies, by leveraging specialized Raman instrumentation as discussed in subsequent sections. While standard spontaneous Raman mapping offers comprehensive insights into the spatial distribution and intracellular compositional alterations, the time required for image acquisition, even for small tissue areas (e.g. $2 \times 2$ mm$^2$), can extend to many hours. To expedite this process, compressive sensing of spontaneous Raman scattering and coherent Raman imaging have gained traction [9, 10] These techniques aim to accelerate image acquisition to a pace suitable for pathologists while delivering detailed structural images of cells or tissue sections, often ranging from a few tens to hundreds of micrometers in thickness. In the realm of in vivo Raman spectroscopy-based medical applications, endogenous tissue contrast has been successfully demonstrated in clinical trials. However, it typically necessitates access to either the skin's surface or the lining of hollow organs through optical fibres. Examples include endoscopic probes [11, 12] for Raman laser illumination and collection within the body, as seen in cases of esophageal and brain cancer with Raman-based detection approaches. More recently, needle probes have been developed to investigate disease-specific molecular changes in solid organs. Ideally, non-invasive methods for sampling Raman signals are desired.

In vivo medical applications often demand the ability to track signals of agents, inherent biomolecules, or cellular processes that inform about health conditions. While Raman spectroscopy allows chemical fingerprinting of molecules making it suitable for identification, it is a surface measurement technique limited in its detection depth capability to about 100–200 microns [2]. There is therefore a need

for detecting Raman signal from tissue depths if in vivo Raman-based medical applications are to be made clinically-useable.

## 20.3 SORS—Seeing Deeper with Raman

### *20.3.1 Discovery of SORS*

For biomedical applications, the challenge of detecting signals from within tissues is compounded by the diffuse scattering characteristics of the tissue itself, alongside the strong lateral spread of photons within the tissues due to multiple scattering events. This results in dominant Raman signals from surface tissues that can mask the subtler Raman information emanating from deeper layers, thereby complicating the detection of signals from within. Moreover, the additional background noise, primarily from melanin in the skin, can cause significant fluorescence emission, which tends to overshadow the weaker Raman signals from the tissue's deeper regions.

However, advanced Raman techniques that employ spatial gating (separation) have emerged, distinguishing Raman signals based on their depth of origin within the sample. Spatially offset Raman spectroscopy (SORS) is the most prevalent deep Raman technique. The capture of Raman photons emanating from beneath the surface is achieved by separating the points of laser excitation and signal collection spatially, unlike in confocal systems where they align. Hence, standard backscattered Raman spectroscopy can be viewed as a SORS configuration with zero offset. The first report of SORS was by Matousek and colleagues [13], where they used a spatial separation between the point of laser excitation and the signal collection of about a few millimetres. The spatial offset is often referred to as '$\Delta s$' or '$\Delta x$' and often within 1-15 mm. The offset distance plays a crucial role in suppressing the detection of signals from the surface against those from beneath. As the photons scattering from deeper within the tissue have a broader distribution upon reaching the surface, this lateral separation in the collection point provides a significant reduction in intensity loss from surface fluorescence and the lateral dispersion of photons, enhancing the detection of deeper signals. This has been pictorially depicted in Fig. 20.1, where the offset denoted as $\Delta x$ is directly related to the depth d (indicated by a star), where the maximal signal information is garnered for the given set-up. The figure also shows that a larger offset leads to the retrieval of signals from deeper within the tissue.

Since its introduction, a variety of configurations within the deep Raman detection have been developed to delve deeper into materials and improve the signal contrast between subsurface layers and the outer surface. Innovations have also been made in the adaptability of SORS instruments. For instance, incorporation of a mechanisms to either vary the spatial offset by moving the backscattered point-like signal collection away from the point-like laser excitation, or the use of an axicon lens to transform the point excitation into a ring, with the backscattered collection at the ring's centre (known as inverse SORS, where $\Delta s$ or $\Delta x$ equals the ring's radius), or

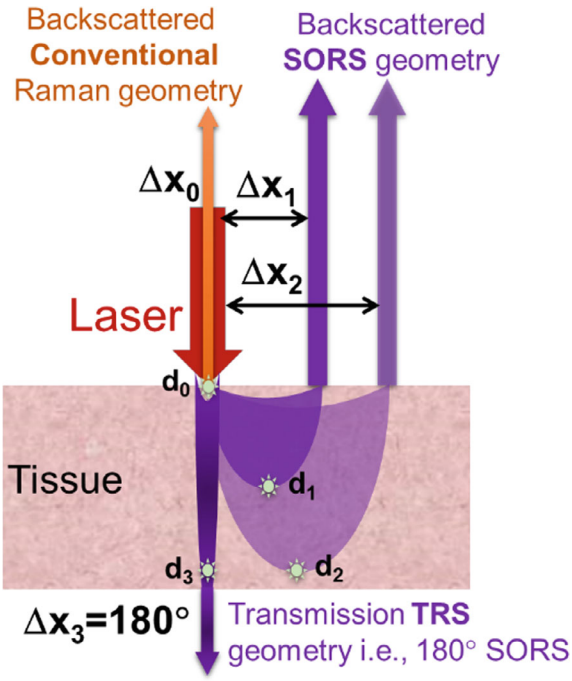
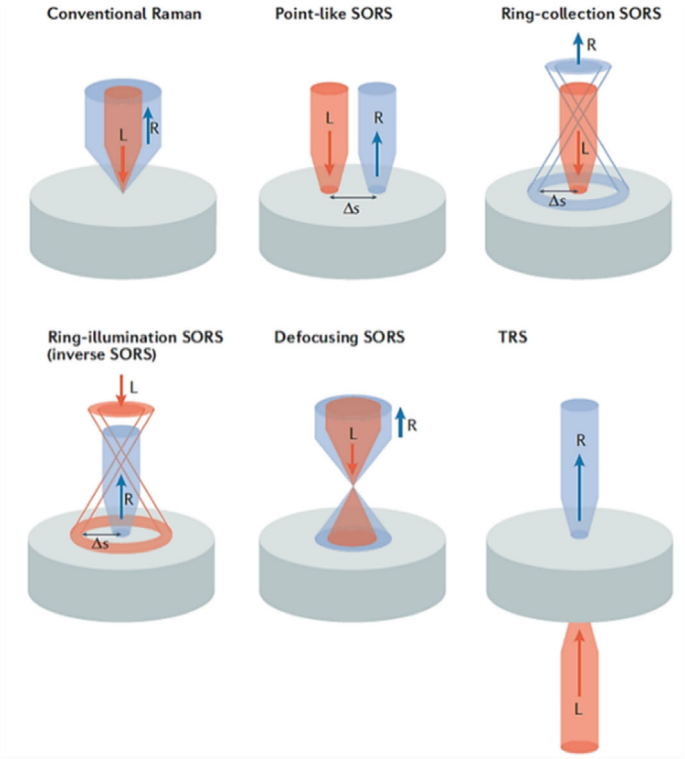



**Fig. 20.1** Extracting chemical information from embedded layers with deep Raman i.e., SORS (offset RS) and TRS (Transmission RS). Reproduced from [14] under CC BY 4.0 DEED

the employment of the point-like excitation and collection in a transmission set-up, referred to as transmission Raman spectroscopy (TRS). This has been elaborated in Sect. 20.3.2 and Fig. 20.2.




| SORS modality | Advantages | Disadvantages |
|---|---|---|
| Point-like SORS | Simple to implement | High illumination intensities at all spatial offsets |
| Ring-collection SORS | Effective collection of available Raman signals at the sample surface | High illumination intensities at all spatial offsets |
| Ring-illumination SORS (inverse SORS) | Enables greater laser powers to be used with larger spatial offsets | Complexity of implementation; moving optical components |
| Defocusing SORS | Simple to implement | Low layer contrast |
| TRS | Volumetric averaging; suited to overall compositional studies | Does not separate individual layers |
| SESORS | Exceptional sensitivity, high accessible depth and chemical specificity | Requires nanoparticles or SERS substrate inside sample |
| Micro-SORS | High spatial resolution; ideal for thin layers such as paints and coatings | Added complexity as requires a Raman microscope |

**Fig. 20.2** Types of SORS. *SERS* Surface-enhanced Raman spectroscopy; *SESORS* Surface-enhanced spatially offset Raman spectroscopy; *SORS* Spatially offset Raman spectroscopy; *TRS* Transmission Raman spectroscopy. Reproduced from [2] with permission from Nature Research

In addition to the detection from depth, the SORS technique leverages the higher penetration capabilities of the near-infrared NIR photons. These advancements have unlocked new potential in various applications, particularly in biomedical domain such as non-invasive diagnosis of bone diseases, identification of calculi in urology, and the detection of cancers in several organs. The below sections will delve into the advancements in biomedical applications that have happened as a ripple effect of the discovery of SORS or deep Raman.

## *20.3.2 Types of Offset Raman*

### 20.3.2.1 Spatial Offset Micro-SORS

Spatially offset Raman spectroscopy (SORS) with microscopy or micro-SORS has been successfully demonstrated for investigating chemical information underneath very thin layers on a scale ranging from micrometres to sub-millimetres. The microscopic Raman system is utilized where the point illumination is defocused to enable a larger illumination spot with the collection at the confocal centre of the illumination spot. This allows a variation of micron-level spatial offset allowing detection of chemical signatures from micrometre to sub-millimetre depths. This technique has found extensive utility, particularly in the analysis of historical paint in cultural heritage artefacts, agricultural produce, and in the study of small animal models. Micro-SORS may find use for investigating skin barriers and skin-related diseases in dermatology at depths which allows investigation of stratum corneum, epidermis, and possibly dermis at thinner skin regions. In medical applications, micro-SORS demonstrates significant promise for integration with endoscopy, allowing non-invasive detection within the body and effectively overcoming the limitations of traditional methods. Research and commercial entities have developed efficient fibre optic probes of various designs enabling the above. This surpasses the capabilities of traditional confocal Raman microscopy.

### Backscattered SORS

Traditionally, SORS has been the backscattered SORS where the scattered photons are reflected back towards the excitation source the collection, and both the illumination and collection are physically on the same side of the sample but separated by few millimetres. The spatial distance typically used is 0–10 mm. Backscattered SORS is valuable in applications where scattering is a significant challenge, such as the analysis of powders and suspensions. The most important contribution of SORS is in allowing Raman signal extraction from turbid biological tissues at depths of few millimetres to centimetres recently. Backscattered SORS finds applications in the analysis of thin films, coatings, and transparent materials. It is commonly used in pharmaceutical research for tablet and capsule analysis. This variant is also useful for subsurface analysis of transparent or semi-transparent biological tissues.

**Direct backscattered SORS**: Direct SORS is the most common and straightforward implementation of SORS. In direct SORS, the laser excitation and Raman signal collection occur on the same side of the sample where the offset is a spatial distance between an illumination and the collection. Often a round or elliptical point-like illumination spot and a point-like or ring-like collection is utilized.

**Inverse backscattered SORS**: Inverse SORS is a variant of SORS where the laser excitation and Raman signal collection both occur on the same side of the sample like direct SORS, while the illumination presumes the shape of a ring and the collection is a spot at the centre of that ring. The radius of this ring offers a spatial offset. As the laser power per illumination area is reduced in an indirect SORS, typically a higher laser power could be employed as opposed to the direct SORS. A higher laser power is expected to convert into a higher Raman signal intensity.

Figure 20.2 elaborately captures the common types of SORS, the placements of the excitation and collection, along with their advantages and disadvantages.

#### 20.3.2.2 Angular Offset or Transmission SORS

Transmission SORS is a subtype of SORS, where the laser excitation area and Raman collection area are located on opposing sides of the sample, can also be considered an extreme case of SORS or an angular 180°. It is popularly known as TRS and is employed in applications involving the analysis of transparent films, polymers, and biological tissues, where access to both sides of the sample is available and the sample itself is not majorly scattering the Raman signals. Matousek and Parker [13] have explored the benefits of backscattered and transmission SORS. They report that with increase in depth, the signal intensity for a backscattered set-up dropped by 5 orders of magnitude compared to the transmitted set-up. More importantly, this suggests that below an optimum depth (in this case, 2 mm) the backscattered set-up is beneficial, while beyond that depth the transmitted set-up offers higher possibility of signal detection.

#### 20.3.2.3 Time-Offset and Frequency-Offset Raman

The time and frequency-offset (or gated) Raman gained importance due to its ability in suppressing fluorescence by blocking off part of the fluorescence signal while retaining the Raman signal. Often time-gating in nanoseconds have been used. Time-gated detectors like multi-channel plates (MCPs), photo-multiplier tubes (PMTs), MCP-MPTs, intensified gated charge-coupled devices (ICCDs), and complementary metal oxide semiconductor single-photon avalanche diodes (CMOS SPADs) have aided its application, but definitely overall requires more complicated instrumentation than the SORS system.

**Time-offset**. Time-gated diffuse Raman (TGDR) combines time-gating technology with Raman spectroscopy to enhance the depth-resolved capabilities of SORS. By

selecting specific time intervals for signal collection, TGDR can selectively probe subsurface layers. It is particularly useful in applications involving biological tissues and materials with complex structures. It allows for precise subsurface analysis, reducing the interference from superficial layers and improving the signal-to-noise ratio. A combination of time-gated along with spatial offset has been reported by Petterson et al. [15] to be beneficial in extracting signals at depth.

**Frequency offset**. This is typically achieved by changing the excitation frequency or laser wavelength. (FORS) measurements can be conducted by using multiple excitation wavelengths for Raman measurements, tailored to the varying optical properties (absorption coefficient $\mu_a$ and reduced scattering coefficient $\mu_s'$ ) of the medium being studied. This necessitates the use of a variable laser excitation system along with suitable optical filters for the efficient collection of the corresponding Raman signals. Sekar et al. [16] have reported a hybrid FORS-SORS to enable better discrimination of sub-surface composition than either of them individually.

All the above allow detection form depths while they all might not use a spatial offset to achieve it. Therefore, recently the term ***deep Raman spectroscopy*** *or* ***DRS*** has found better suitability in the field.

### *20.3.3 SORS Biomedical Applications*

The benefit of SORS in biomedical applications has been many-fold from detecting adulterations in medical supplies through bottles towards in vivo detection of disease markers. Specific applications include analysing the quality of blood in blood-storage bags over time [17], in COVID vaccine discrimination [18] between original (or genuine) and adulterated (or falsified) as shown in Fig. 20.3 (top panel). Mahadevan-Jansen's research group has worked extensively in developing clinic-friendly Raman techniques where they employ a modified SORS probe featuring a single laser excitation and simultaneous collection of Raman signal from multiple spots in a linear and multiple concentric circle setting. This has allowed them to investigate breast cancer margin [19], as well as, assess bone-related health conditions [20].

***Cancer Margin analysis***. For cancer margin analysis, the current clinical approaches of visual examination and frozen section pathology are able to achieve sensitivity of 50–60% and specificity of 72–85%. The current researched methods include optical coherence tomography (OCT) which has been reported with 100% sensitivity and 100% specificity [21] for in vivo oral cancer margin analysis. But the major limitation of the OCT is its inability to interrogate tissue over 2 mm depth, as suggested in the above study. In contrast, the biggest challenge for the SORS handheld probes, especially compared with the above techniques, is adapting the probe and other system components to interrogate larger areas of tissue in a shorter time. This can be where SORS could be used in conjunction with OCT.

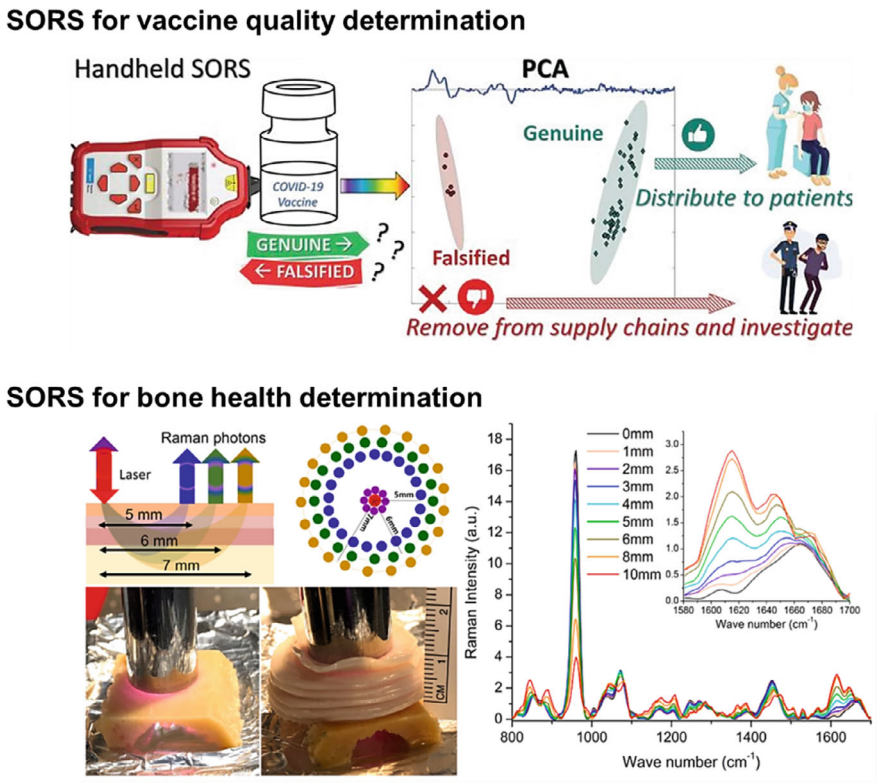



**Fig. 20.3** SORS biomedical applications (top panel). Discriminating original or genuine and adulterated (or falsified) COVID vaccine through the bottle. Reproduced from [18] under CC BY 4.0 DEED (bottom panel). Bone quality assessment. Reproduced from [20] with permission from Elsevier

***Bone Quality analysis***. Besides tissue investigation, bone assessment using SORS has been intriguing as it could lead to non-invasive diagnosis of bone-related diseases like osteoarthritis, rheumatoid arthritis, and bone cancer among others. Figure 20.3 (bottom panel) depicts a study employing a handheld SORS probe in laboratory bone fracture resistance analysis based on the hydroxyapatite crystal and collagen structures. Matousek and co-workers [22] have employed SORS probes for in vivo analysis of finger bone from human subjects. They were able to obtain a pure bone Raman spectrum, supressing any surface (skin tissue, etc.) signal. These signatures were indicators of bone collagen quality and obtained by scaled spectral subtraction of the offset spectra from the non-offset spectra.

***Cancer diagnosis***. SORS for measurement of inherent signals from depth for medical use. In particular, the detection of micro-calcifications in breast tumour has been suggestive of the presence of breast cancer. Nevertheless, signals acquired in this manner tend to be weak and could benefit from robust disease-specific distinctive

biochemical markers. Such an example is the detection of hydroxyapatite which is observed at around 960 $cm^{-1}$ indicative of micro-calcifications in breast cancer progression. SORS has been utilized to probe such native biochemical signals from depths of up to 4 cm [23]. Lately, to assist in breast cancer diagnosis by identifying micro-calcification Raman signatures in the fingerprint region and water associated Raman peaks in the high wavenumber region. Stone and his group are spearheading this work with in vivo clinical trials. In their preliminary report [24], TRS was employed to assess specimens suspected of harbouring either invasive or in-situ diseases pre-operatively. The tissue was measured under Raman before formaldehyde treatment. Interestingly, the collected data ($n = 135$) revealed that high-quality spectra could be acquired in just 3 s from tissues with thicknesses ranging from 1 to 4 cm. Despite the presence of patent blue V dye (used in sentinel node localization), the samples that showed a high level of calcification on X-rays also exhibited corresponding indicative Raman signals. This confirms the importance of the development of SORS as a biomedical tool.

### *20.3.4 SORS Limitations and Experimental Considerations*

The efficacy of SORS is contingent on a combination of instrumental factors and sample-specific characteristics. Below we discuss the challenges in each domain and ways to mitigate it while being aware of the limitations and artefacts it can generate.

#### 20.3.4.1 Improving the Excitation Light Delivery to Depth

***Sample absorption***. The ability of SORS to probe depth is notably influenced by a sample's absorption characteristics, especially crucial in biomedical contexts. Consequently, SORS typically uses near-infrared (NIR) lasers (e.g.. 785 nm, 808 nm, or 830 nm) [14], which align with the tissue's NIR optical window, minimizing the absorption of both the laser and Raman photons and thereby enhancing SORS's effectiveness in such applications.

***Sample scattering***. In most biological tissues excited with NIR wavelength, light absorption is minimal compared to scattering. Scattering, the deviation of light from its initial path, is considered 'elastic' when the photon's energy remains constant. This phenomenon largely occurs due to the refractive index variations in tissues, which are more pronounced than in materials like glass due to the heterogeneous mix of molecules and structures in cells. Scattering is measured by the 'mean free path' ($l_s$), indicating the average distance photons travel between scattering events. The probability and pattern of scattering vary with the refractive index differences, the size of objects relative to the wavelength, and the wavelength itself. For tiny objects like isolated atoms, scattering is almost uniform and highly dependent on wavelength ($\propto \lambda^{-4}$, known as 'Rayleigh scattering'). In larger objects, like cells,

which are comparable to the wavelength of light, scattering predominantly happens in the forward direction. This is quantifiable by the anisotropy parameter ($g$) or the 'transport mean free path' ($l_t = l_s/(1 - g)$)[25], which indicates the distance at which the original direction of light is essentially lost. For instance, measurements in brain grey matter showed a mean free path of 50–100 μm at 630 nm and about 200 μm at 800 nm.

***Sample fluorescence***. The effectiveness of SORS can be affected by factors such as fluorescence interference, particularly in darker tissues like the liver or melanin-rich skin. Additionally, dark hair or white hair on a sample can pose challenges, although shaving the area can alleviate this issue. Spatial offsets in SORS are instrumental in reducing fluorescence interference from surface melanin, especially when examining deeper layers. This technique not only diminishes surface Raman signals but also effectively lowers surface fluorescence compared to deeper signals. Time-gated fluorescence suppression methods are also viable alternatives to manage such interference.

#### 20.3.4.2 Boosting the Raman Signal from Depth

Determining the most effective spatial offsets is crucial, considering the sample's geometry and optical properties. Methods such as theoretical simulations and experimental trials are used to find the optimal offset. Generally, the depth probed increases with the spatial offset. Numerical methods, like photon propagation simulations, help predict the signal-to-noise ($S/N$) ratio for specific offsets, although this approach demands an in-depth understanding of the sample's optical characteristics and is less common. Maher and Berger [26] have explored optimal spatial offsets, highlighting the need for longer acquisition times at larger offsets to maximize $S/N$ ratios.

However, there is a trade-off, as larger spatial offsets can weaken the Raman signal. Balancing these aspects is key to achieving optimal conditions for specific tissue depths. Achieving the best $S/N$ ratio often involves empirical methods, adjusting variables such as laser power and acquisition time through trial and error.

Therefore, estimating the optimal offset (discussed above), along with the use of medically approved laser power, use of spectrographs with high quantum efficiency in the near-infrared (NIR) region and choosing the correct configuration of SORS for Raman signal collection at depth (discussed later in Sect. 20.4.4.2) needs to be considered.

## 20.4 SESORS or SEDRS

### *20.4.1 SESORS Discovery and Its Benefits*

With the discovery and biomedical implementations of SORS, it became apparent that detecting the inherent or indigenous spectral signatures from depth may not always be feasible or informative. This led to the exploration of tracking diagnostic and therapeutic agents in vivo using SORS. Achieving this necessitates an innovative Raman instrumentation strategy of SORS with a more compact instrumentation and capitalizes on the advantages of gold nanostructure-based SERS biomedical agents. With appropriate targeting ligands, these exogenous agents can specifically reach certain cancer types, facilitating diagnosis. This approach becomes feasible when employing suitable pairs of targeting ligands and Raman tags on gold nanostructure contrast agents.

With four decades of SERS and about half a decade of SORS gathered expertise, in 2011 combining these two unique approaches was attempted. The union of the above approaches would help deliver a tool capable of discriminating enhanced signals embedded in depth. This has popularly been referred to as *SESORS* or *surface-enhanced spatially offset Raman spectroscopy*. The first report in SESORS was published in 2011 [3]. As discussed above, with the advent of multiple offset Raman beyond the traditional spatial offset, DRS when combined with SERS has been referred to as *surface-enhanced deep Raman spectroscopy or SEDRS* [27].

Table 20.1 briefly summarizes the features, benefits, and limitations of SESORS compared to confocal Raman, SERS, and SORS. To demonstrate the importance further, in Fig. 20.4 the comparison of the ratio of top-layer, i.e. tissue to the SERS-tagged nanoparticle (NP) buried at depth is performed both with conventional confocal Raman and deep Raman or SESORS [27]. It is evident that the contribution of both the tissue signal depicted by a red bar and that of NP depicted by a blue bar is observed in both scenarios, while the signal contribution of NP to that of the tissue is significantly higher in deep Raman SESORS (NP: Tissue $\cong$ 1:1) than confocal conventional (NP: Tissue $\cong$ 1:2), demonstrating the experimental benefit of SESORS. Over the years, SESORS has undergone refinement and adaptation to different application areas. Researchers have explored various nanoparticle materials, geometries, and excitation wavelengths to optimize SESORS performance. As a result, SESORS has become a versatile tool with applications ranging from biomedical research to environmental monitoring.

**Table 20.1** Summary of comparison among various Raman techniques leading to SESORS

| | Features | Benefits | Limitations |
|---|---|---|---|
| Confocal Raman spectroscopy | Confocal illumination and collection, often microscopic set-up available commercially | High sensitivity, informative | It is a surface technique. It cannot detect chemical signatures from beyond few microns of depth from the surface<br>Comparatively costly instrumentation |
| Surface-enhanced Raman spectroscopy (SERS) | Trace molecules were adsorbed on the surface of Ag, Au, and other metals and electrodes. The signal enhancement was $10^4$–$10^{10}$ times of the inherent Raman | High sensitivity and resolution, high molecule specificity | Often non-uniform signal enhancement of all Raman peaks.<br>Reproducibility still an issue |
| Spatially offset Raman spectroscopy (SORS) | The point of illumination and point of collection are spatially offset and not confocal | Eliminate fluorescence, high sensitivity, noncontact inspection, remote computing<br>Recent reports have suggested detection > 4 cm (dramatically improved from few microns in conventional Raman) | Different instrumentation required to enable detection at depth.<br>Spatial offset determines at what depths the detection is possible and hence limited on instrument using traditionally fixed offsets<br>Depth like MRI is still not feasible |
| SESORS | Combines benefits of SERS and SORS | Recent reports suggest a maximum detection depth achievable at > 7 cm | Use of SERS nanostructures limits the in vivo use. But is key in boosting the detection and tracking diseases |

## *20.4.2 SESORS Types and Benefits*

### 20.4.2.1 Types of SESORS

Researchers have exploited various forms or modalities of SESORS each tailored to specific biomedical challenges and applications.

**Micro-SESORS**. Similar to micro-SORS in combination with SERS nanoparticles, micro-SESORS finds significantly less usefulness in biomedical applications due to its micron-scale depth analysis capabilities—which is often not deep enough for

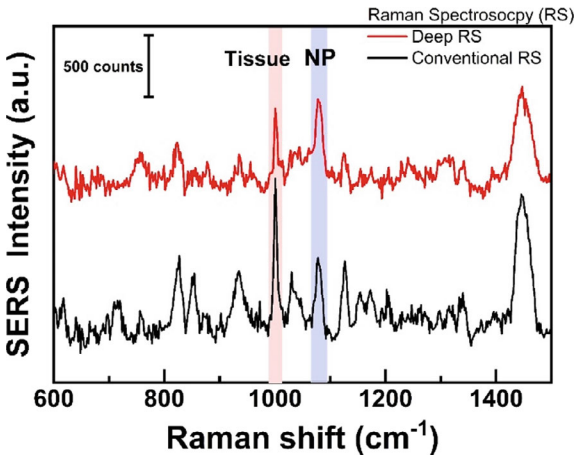



**Fig. 20.4** Conventional non-SORS and deep Raman SORS detection of SERS NPs. Raman spectroscopy is denoted as RS. Reproduced from [27] under CC BY 4.0 DEED

disease scoping. Additionally, the use of microscopic objectives restricts the clinic-friendliness of the instrument.

***Backscattered SESORS***. Similar to the backscattered SORS set-up, this configuration employs both excitation and collection optics on the same side of the sample. This is particularly useful for investigating opaque or highly scattering materials and is employed in various industrial and environmental analyses. Backscattered SESORS could be either of direct SESORS or indirect SESORS variety depending on how the offset is created (identical concept of direct and inverse SORS). An additional benefit of using an indirect ring illumination is the ability to use higher total laser power on the surface in contrast to a point illumination in a direct SESORS set-up. Both variants of SESORS offer valuable depth-resolved capabilities, and the selection of the appropriate method depends on the specific biomedical requirements and sample characteristics.

***Transmission SESORS***. This variant of SESORS involves illuminating the sample from one side and collecting Raman signals on the opposite side, enabling the analysis of subsurface layers. It finds applications in the study of thick biological tissues and pharmaceutical formulations.

***Resonance SESORS***. This subtype involves using plasmonic nanoparticles and/or Raman tags that are in resonance with the incident laser wavelength. The resonant enhancement of Raman signals in SESORS can greatly improve sensitivity and has been applied in the study for SESO(R)RS where (R) stands for the resonance effect.

From the above discussion, it is clear that all the above modalities may not comfortably be collated under the umbrella of SORS or SESORS, and hence, it has often been interchangeably referred to as deep Raman spectroscopy (DRS) and SEDRS where DRS is combined with SERS nanostructures.

As there has been various SESORS or SEDRS modalities proposed for deep Raman diagnosis, there have been some efforts to compare these modalities. Such

an evaluation would offer valuable insights and assist end-users in selecting the most suitable modality tailored to their specific requirements. For instance, Mustafa et al. [28] explored the distinctions between diffuse and inverse SORS. Matousek and colleagues [13] utilized both experimental methods and Monte Carlo simulations to show that, in transmission geometry detection efficiency remained constant regardless of the thickness of the sample. Conversely, in a backscattered geometry, the intensity diminished dramatically—by a factor of ten thousand—when analysing at a depth of 3 mm within a tablet that was 4 mm thick. Dey et al. [27] interrogates the depth of transmission and inverse SESORS and further compared them to conventional Raman, i.e. backscattering point-modality Raman. They have reported that the sub-surface to surface signal discrimination was higher for transmission modality, but it was impacted by the sample orientation and tumour positioning inside the tissue layers (i.e. depended if the tumour containing the SERS nanostructures was closer to the excitation side or signal collection side or nearer to the middle, etc.). Hence, it could be concluded that each modality demonstrates strengths and weaknesses and should be chosen based on specific end-use and sample type. Invariably, if a combination of modalities could be employed, it could provide the synergistic benefits of the individual modalities, helping to strengthen the scope of SEDRS diagnosis.

## *20.4.3 SERS Nanostructures for SESORS*

### 20.4.3.1 SERS Single Nanostructures

SERS-labelled spherical nanoparticles used typically include 60 and 100 nm diameter gold nanoparticles. Specifically made Oxonica/Cabot nanoparticles (Nanoplex Biotags) had also gained importance (when they were available in the market) for SESORS studies. They were commercial silica-coated SERS labelled gold nanoparticles often single nanoparticles and sometimes 2–3 NPs encapsulated within a silica coating. The Oxonica gold core/silica shell NPs were reported to consist primarily of monomers (59%), with 17% dimers and 11% trimers [29]. The highest yet reported detection depth of 7 cm [27] in mice have employed spherical gold nanoparticles of 60 nm diameter labelled with biphenyl thiol (BPT). Due to the comparative ease of synthesizing single gold nanospheres and a comparative better understanding of SERS label functionalization and SERS signal enhancement, spherical nanostructures have played a vital role in the SESORS biomedical applications.

The SERS signal is not the strongest for single spherical nanostructures, and hence to detect low concentration disease markers and achieve detection from higher depths, researchers have experimented with silver nanostructures and shaped gold nanostructures. Among them, van Duyne's group explored the use of silver films over silica nanospheres substrates or AgFONs [30, 31], whereas Fauld's group [32, 33] exploited colloidal gold nanostars. Unlike the nanospheres and nanostar colloids, the AgFONs act as SERS solid substrates and are not injectable. The developed AgFON surfaces were hence functionalized with self-assembled monolayers and implanted

subcutaneously to monitor blood glucose in rats. On the other hand, to maximize SERS signal intensities at biomedical NIR (785–830 nm) laser excitation, colloidal gold nanostars of approximately 100 nm dimensions with a localized resonance of around 600–700 nm, further functionalized with a resonant SERS label, i.e. SERRS has been used in multiple studies.

#### 20.4.3.2 SERS Nano-assemblies

There has been very limited study in the use of controlled gold nano-assemblies in SESORS or SEDRS. The only report in 2013 by Dey and co-workers [34] strategically combines SERS gold nano-assemblies with direct SORS to investigate the benefit of replacing single SERS nanostructures with SERS nano-assemblies. They employed a SORS probe with a 2–3 mm offset, utilizing a configuration where the laser excites a point, and the scattered light is collected via a fibre optic ring probe. With 785 nm laser illumination, they achieved SORS detection from within animal tissues at depths up to 8 mm. This significant research was the first of its kind to use sub-100 nm gold nanostructures, which were clusters of nanoparticles bonded together with polymer linkers to form a stable colloidal structure and tagged with a 2-quinolinethiol SERS label. This report demonstrates the significant improvement in detection depths achieved through animal tissue when employing SERS assemblies in contrast to single SERS nanoparticles, confirming the added advantage of SERS-active nano-assemblies for deep Raman applications.

#### 20.4.3.3 SERS Non-resonant and Resonant Labels

Researchers have been investigating ways to boost SERS signals, not just through nanostructure design and SORS configurations, but also by using specific Raman labels (also referred to as, tags or reporters) for further boosting SERS signal with an expectation of detecting through larger depths, see Fig. 20.5. Although most of the below studies typically involved the detection of SERS nanoparticle colloids either in cuvettes buried within tissues or injected directly at various depths within the ex vivo animal tissue, it provides a critical initial understanding for exploring clinical biomedical applications. A recent review by Dey discusses the parameters, particularly Raman labels, for maximizing SERS signal [35].

Raman labels like trans-1,2-bis(4-pyridyl)-ethylene (BPE), 5-(4-pyridyl)-1,3,4-oxadiazole-2-thiol (POT), as well as near-infrared (NIR) resonant dyes like IR792 and IR830. For instance, van Duyne's team demonstrated that nanostructures with a concentration of $10^{12}$–$10^{13}$ nanoparticles, coated with a potent SERS label like BPE can enable detection through 8 mm of porcine bone. This was achieved using a 785 nm laser and a 2–3 mm backscattered SORS offset. Faulds and colleagues have also made significant progress, designing and applying NIR-absorbing SERS labels [36–38] for resonant SESORS using 830 nm laser excitation. Their work includes PCA-distinctive detection at 48 mm depth in porcine tissue with an 8 mm offset in

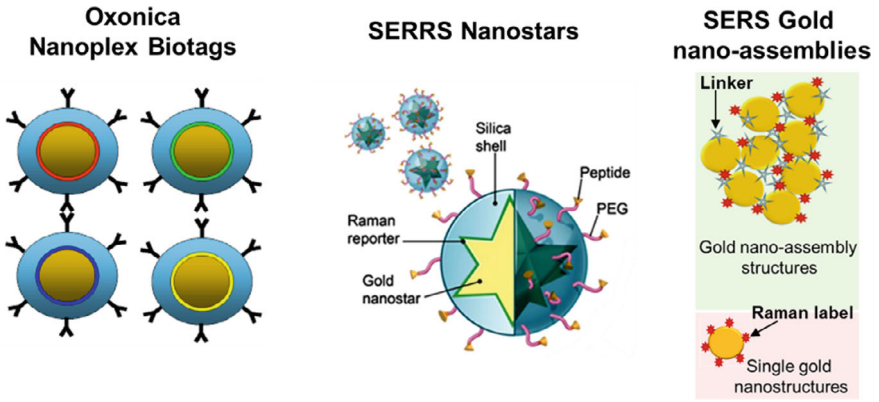



**Fig. 20.5** SERS agents that are employed extensively in SEDRS biomedical applications. Reproduced from [41] under CC BY 4.0 DEED. Reproduced from [40] with permission from Royal Society of Chemistry. Reproduced from [34] with permission from JOHN/WILEY & SONS LTD

a standard SORS set-up. Notably, they found that the NIR label 'dye 823' yields a signal approximately 40 times stronger than BPE [39]. Stone and colleagues [40] have successfully detected non-resonant Oxonica/Cabot nanoparticles (100 nm gold spherical NPs functionalized with the SERS label 5-(4-pyridyl)-1,3,4-oxadiazole-2-thiol, or POT, encapsulated in silica) from within 50 mm of porcine tissue using a transmission Raman spectroscopy (TRS) approach. This detection was achieved with $3 \times 10^{10}$ NPs and a 300-s accumulation time, employing an 830 nm laser with a power of 210 mW directed at the sample surface. So selection of strong Raman labels should be key in maximizing Raman signal.

## *20.4.4 SESORS Biomedical Applications*

### 20.4.4.1 Biomarker and Bioprocess Detection In Vivo

***Glucose sensing***. Ma et al. [30, 31], in 2011, have utilized the backscattered SESORS system for detecting blood glucose level in a rat model by placing the silver films in a pocket made in the rat skin. Keren et al. [41] achieved a depth of 5.5 mm from within phantom tissue by employing a backscattered SESORS system for deep tissue detection of SERS-barcoded monomeric Oxonica NPs.

***Towards cancer cell bioprocess analysis***. It has been established that the pH of cancer cells is acidic, which if utilized appropriately could aid in pH-responsive drug delivery specific to cancer cells. Cancer cell death by exposing to higher temperatures, with or without drugs, have also been exploited as an alternative means of cancer therapy or hyperthermia. This necessitates the need of estimating the pH and temperature

of the cancer cells locally. Stone and Matousek have reported the use of SESORS to experimentally measure the local pH, i.e. pH-SESORS [42] when utilizing a pH-sensitive SERS label MBA functionalized onto gold nanoparticles and the local temperature of the nanoparticles as T-SESORS [43] by exploiting the anti-Stokes to Stokes ratio of SERS signals at depth.

***Neurotransmitters***. The detection of neurotransmitters in brain through the skull bone has been explored by Sharma and co-workers [44–46] in a proof-of-concept study by attempting SESORS detection of labelled gold nanostructures through few millimetres of animal bone. In various studies, they have reported the detection using a SERS nanostructure concentration of $10^{12}$ NPs and about 0.1 mM concentration of neurotransmitters like serotonin through approximately 3 mm of bone [45]. The SESORS detection was achieved when employing a 785 nm laser and 3 mm SORS offset (i.e. point illumination and ring collection).

### 20.4.4.2 Improving Detection Depths

Scientists working within the realm of surface-enhanced deep Raman spectroscopy (SEDRS) encounter constraints due to the relatively diminutive size of the prevailing animal models suitable for in vivo investigations. Consequently, most deep Raman studies conducted so far have been showcased using ex vivo animal tissues or simulated models (phantoms) to fully harness the depth-detection potential offered by SEDRS. Initial studies have explored the use of SERS agents filled in quartz cuvettes and embedded at known depths within store-bought animal tissues, like chicken and porcine tissues, for probing SEDRS or SESORS detection. Some studies from the groups of Stone and Matousek, Faulds, and Sharma have implemented this approach for proof-of-concept studies. Critical to mention here were the studies by Stone et al. in 2011[40] where they reported the detection of SERS agents from 50 mm of porcine tissue depth in transmission set-up. Recently in 2022, Berry et al. [39] reported the detection of SERS labels from randomly aggregated gold nanospheres in a backscattered SESORS set-up at 48 mm detection depths. As the SERS labels, gold nanostructures and set-ups were different for these studies, a direct comparison was difficult.

A few studies further explored the strategy of injecting the SERS agents at certain depths in store-bought animal tissues for studying the detection depths possible. Although it was deemed a more realistic approach, experimentally it was faced with leaking of the SERS agents from the location of injection. Such studies were later followed by the demonstration of an in vivo SESORS study by Nicolsan and co-workers [47]. They employed resonant SERS label 'IR792' functionalized onto gold nanostars injected intravenously to reach the brain tumour. SESORRS detection was performed by detecting the signal of SERRS label IR792 through a mouse skull (shaved mouse head) using a 785 nm laser excitation and 2.5 mm SORS offset. Figure 20.6 summarizes the milestone publications in driving the field of SESORS towards biomedical tracking applications.

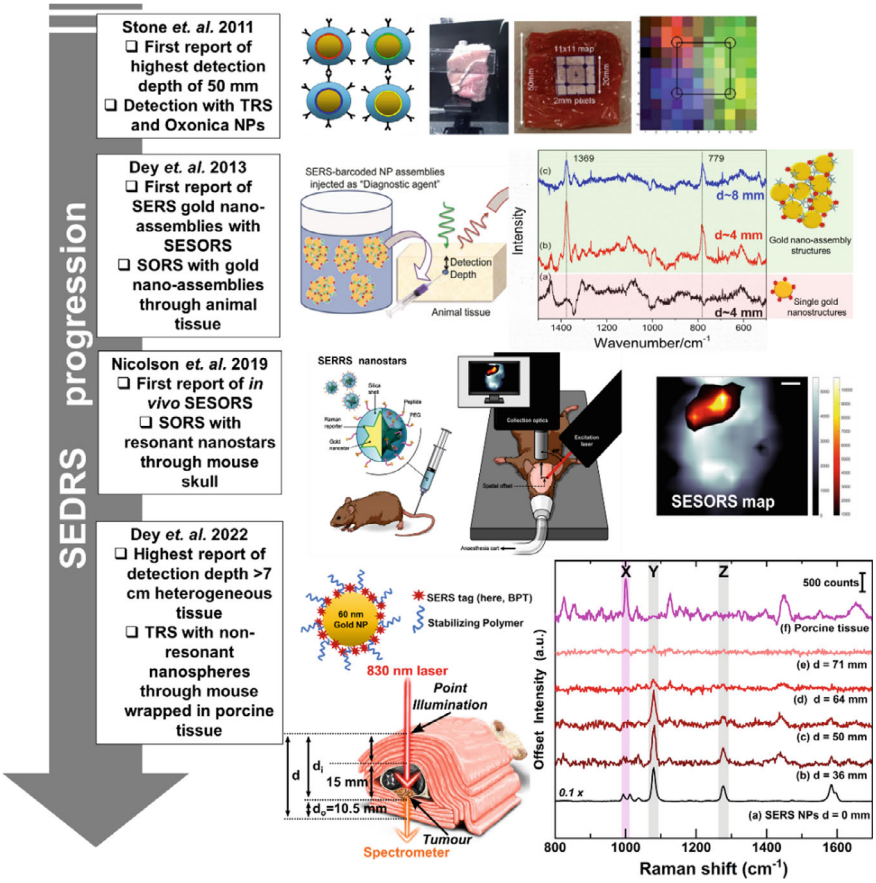



**Fig. 20.6** SEDRS advancement through the years. Reproduced from [40] with permission from Royal Society of Chemistry. Reproduced from [34] with permission from JOHN/WILEY & SONS LTD. Reproduced from [41] under CC BY 4.0 DEED. Reproduced from [27] under CC BY 4.0 DEED

In vivo mouse models were restricted to few millimetres of skull bone thickness and a maximum of about 15 mm of whole-body thickness, which were not ideal for demonstrating the SEDRS capabilities. In an endeavour to bridge the gap between in vivo and ex vivo animal models that are conventionally explored, Dey and co-workers [27] designed a study to illustrate the depth capabilities of SEDRS in a scenario that not only showcases its potential but also served as an initial demonstration towards a scenario more closely resembling the conditions relevant to human applications. This investigation employed SERS gold nanospheres injected subcutaneously near the tumour site in vivo mouse model. The mouse skin was shaved near the tumour, and it was externally wrapped with store-bought porcine tissue slices.

The SEDRS detection was performed utilizing both a transmission and backscattered set-up with a inverse SORS where the illumination ring and point detection provided an offset of about 5 mm and a laser of 830 nm. The study provided the highest detection depth achieved till date of 71 mm in transmission set-up [27]. Such a significant detection depth has been attributed to the fact that 90% of the detected Raman photons originate from a significantly greater depth than that of the median [48]. Importantly the detection was (a) blind as the tumour was not visible to the eye, (b) was through a heterogeneous media of different component including tissue, bone, and blood, as well as (c) provided a comparison of the transmission SEDRS and backscattered SESORS or SEDRS capabilities.

## 20.5 Challenges and Prospects of SORS and SESORS Biomedical Applications

With about two decades of SORS and a decade of SESORS discovery and continued research efforts, its importance and contribution in biomedical applications is ever rising. The advent of optical component engineering in lasers, optical filters, compact and efficient spectrometers, and the interest in developing clinic-friendly deep Raman set-ups has been very encouraging. The commercially available Agilent offset Raman handheld system, although has limited applications in biomedical applications, it has become a well-accepted analytical tool in manufacturing and pharmaceutical-like industries to determine quality through opaque containers and bags. In the biomedical arena of SORS, clinical trials of deep Raman in transmission set-up for breast cancer microcalcification diagnosis are underway in the UK. Fibre optic SORS probes and endoscopes are being trialled for cancer margin analysis in the USA. This suggests that SORS by itself has made a strong footing in biomedical applications. For SEDRS, although the SERS agents are truly beneficial for tracking diseases where inherent disease signatures are not prominent (unlike microcalcifications), the additional clinical implications of injected nanomaterials are definitely a hurdle in clinical translation of SEDRS.

The progress made in SORS and SESORS or SEDRS, particularly, detection from beyond 7 cm (equivalent to the thickest muscles in leg, wrist and bicep width, etc., in humans) of heterogeneous tissue, in vivo SESORS demonstration, boost in SERS signal using a combination of tailormade nanostructures and SERS labels, along with the research of handheld SESORS set-ups for detection can be considered a significant achievement within a decade of its discovery. Few questions that still need focused discussions include what depth would a clinical application need, and how in vivo compatibility and detection would be trialled for SEDRS.

The future of SESORS holds great promise as researchers continue to explore its potential in various fields. However, there are several challenges that must be addressed for SESORS or SEDRS to reach its full potential. This includes: (i) Instrumentation development where advanced SESORS instrumentation is needed to make

the technique more accessible and user-friendly for a broader range of applications. Development and commercial availability of high-power lasers, flexibility in the offset system, i.e. variable offset or change between SORS and TRS, fibre optic combined probe that is sterilizable, plug-and-play devices, portability, and cost-effectiveness of the instrument are key aspects. (ii) The lack of standardized procedures and protocols for SESORS can hinder its adoption in some fields. Developing standards is essential for reproducibility and data comparison across research labs for efficient comparison of the progress in the field. (iii) Medical applications require the use of permissible laser exposure limits on skin, as well as, a better understanding of the long-term effects of nanomaterial injection and its excretion. (iv) Tailoring SERS nanoparticles need to be engineered for specific applications, and optimizing their properties is an ongoing challenge. Researchers must continue to explore novel nanoparticle designs. (v) In biomedical and pharmaceutical applications, ensuring the biocompatibility of nanoparticles used in SESORS is crucial for safety. (vi) Complex data analysis and interpretation are often required in SESORS. Developing user-friendly software for data processing is essential. And last but not the least, (vii) To fully unlock the potential of SESORS, interdisciplinary collaboration between scientists, engineers, and industry experts is essential.

Nevertheless, the advancements in micro-SORS and SORS for developing fibre optic endoscopes for disease diagnosis, handheld or clinic-friendly SORS or deep Raman instrumentation for exploring in vivo trials, and in vivo compatible SERS nanostructures are crucial in allowing the research translation of Raman spectroscopy-based biomedical applications from the lab to the clinic.

## References

1. J. Langer, D. J. de Aberasturi, J. Aizpurua, R. A. Alvarez-Puebla, B. Auguié, J. J. Baumberg, G. C. Bazan, S. E. J. Bell, A. Boisen, A. G. Brolo, J. Choo, D. Cialla-May, V. Deckert, L. Fabris, K. Faulds, F. J. G. de Abajo, R. Goodacre, D. Graham, A. J. Haes, C. L. Haynes, C. Huck, T. Itoh, M. Käll, J. Kneipp, N. A. Kotov, H. Kuang, E. C. Le Ru, H. K. Lee, J. F. Li, X. Y. Ling, S. A. Maier, T. Mayerhöfer, M. Moskovits, K. Murakoshi, J. M. Nam, S. Nie, Y. Ozaki, I. Pastoriza-Santos, J. Perez-Juste, J. Popp, A. Pucci, S. Reich, B. Ren, G. C. Schatz, T. Shegai, S. Schlücker, L. L. Tay, K. G. Thomas, Z. Q. Tian, R. P. van Duyne, T. Vo-Dinh, Y. Wang, K. A. Willets, C. Xu, H. Xu, Y. Xu, Y. S. Yamamoto, B. Zhao, and L. M. Liz-Marzán, Present and future of surface-enhanced Raman scattering. ACS Nano **14**, 28 (2020).
2. S. Mosca, C. Conti, N. Stone, and P. Matousek, Spatially offset Raman spectroscopy. Nat. Rev. Methods Primers **1**, 1 (2021).
3. N. Stone, K. Faulds, D. Graham, and P. Matousek, Prospects of deep Raman spectroscopy for noninvasive detection of conjugated surface enhanced resonance Raman scattering nanoparticles buried within 25 mm of mammalian tissue. Anal. Chem. **82**, 3969 (2010).
4. X. Qian, X. H. Peng, D. O. Ansari, Q. Yin-goen, G. Z. Chen, D. M. Shin, L. Yang, A. N. Young, M. D. Wang, S. Nie, Q. Y. Goen, G. Z. Chen, D. M. Shin, L. Yang, A. N. Young, M. D. Wang, and S. Nie, In vivo tumor targeting and spectroscopic detection with surface-enhanced Raman nanoparticle tags. Nat. Biotechnol. **26**, 83 (2008).
5. H. Abramczyk and B. Brozek-Pluska, Raman imaging in biochemical and biomedical applications. Diagnosis and treatment of breast cancer. Chem. Rev. **113**, 5766 (2013).

6. X. Liu, X. Liu, P. Rong, and D. Liu, Recent advances in background-free Raman scattering for bioanalysis. Trends Anal. Chem. **123**, 115765 (2020).
7. G. W. Auner, S. K. Koya, C. Huang, B. Broadbent, M. Trexler, Z. Auner, A. Elias, K. C. Mehne, and M. A. Brusatori, Applications of Raman spectroscopy in cancer diagnosis. Cancer Metastasis Rev. **37**, 691 (2018).
8. D. P. dos Santos, M. M. Sena, M. R. Almeida, I. O. Mazali, A. C. Olivieri, and J. E. L. Villa, Unraveling surface-enhanced Raman spectroscopy results through chemometrics and machine learning: principles, progress, and trends. Anal. Bioanal. Chem. **145**, 3945 (2023).
9. C. Scotté, H. B. De Aguiar, D. Marguet, E. M. Green, P. Bouzy, S. Vergnole, C. P. Winlove, N. Stone, and H. Rigneault, Assessment of Compressive Raman versus Hyperspectral Raman for Microcalcification Chemical Imaging. Anal. Chem. **90**, 7197 (2018).
10. C. H. Camp, Y. J. Lee, J. M. Heddleston, C. M. Hartshorn, A. R. H. Walker, J. N. Rich, J. D. Lathia, and M. T. Cicerone, High-speed coherent Raman fingerprint imaging of biological tissues. Nat. Photonics **8**, 627 (2014).
11. L. M. Almond, J. Hutchings, G. Lloyd, H. Barr, N. Shepherd, J. Day, O. Stevens, S. Sanders, M. Wadley, N. Stone, and C. Kendall, Endoscopic Raman spectroscopy enables objective diagnosis of dysplasia in Barrett's esophagus. Gastrointest. Endosc. **79**, 37 (2014).
12. E. Garai, S. Sensarn, C. L. Zavaleta, N. O. Loewke, S. Rogalla, M. J. Mandella, S. A. Felt, S. Friedland, J. T. C. Liu, S. S. Gambhir, and C. H. Contag, A real-time clinical endoscopic system for intraluminal, multiplexed imaging of surface-enhanced Raman scattering nanoparticles. PLoS One **10**, 1 (2015).
13. P. Matousek and A. W. Parker, Bulk Raman analysis of pharmaceutical tablets. Appl. Spectrosc. **60**, 1353 (2006).
14. P. Dey, I. Blakey, and N. Stone, Diagnostic prospects and preclinical development of optical technologies using gold nanostructure contrast agents to boost endogenous tissue contrast. Chem. Sci. **11**, 8671 (2020).
15. I. E. Iping Petterson, P. Dvoák, J. B. Buijs, C. Gooijer, and F. Ariese, Time-resolved spatially offset Raman spectroscopy for depth analysis of diffusely scattering layers. Analyst **135**, 3255 (2010).
16. S. K. V. Sekar, S. Mosca, A. Farina, F. Martelli, P. Taroni, G. Valentini, R. Cubeddu, and A. Pifferi, Frequency offset Raman spectroscopy (FORS) for depth probing of diffusive media. Opt. Express **25**, 4585 (2017).
17. M. Z. Vardaki, C. G. Atkins, H. G. Schulze, D. V. Devine, K. Serrano, M. W. Blades, and R. F. B. Turner, Raman spectroscopy of stored red blood cell concentrate within sealed transfusion blood bags. Analyst **143**, 6006 (2018).
18. S. Mosca, Q. Lin, R. Stokes, T. Bharucha, B. Gangadharan, R. Clarke, L. G. Fernandez, M. Deats, J. Walsby-Tickle, B. Y. Arman, S. R. Chunekar, K. D. Patil, S. Gairola, K. Van Assche, S. Dunachie, H. A. Merchant, R. Kuwana, A. Maes, J. McCullagh, C. Caillet, N. Zitzmann, P. N. Newton, and P. Matousek, Innovative method for rapid detection of falsified COVID-19 vaccines through unopened vials using handheld Spatially Offset Raman Spectroscopy (SORS). Vaccine **41**, 6960 (2023).
19. M. D. Keller, E. Vargis, N. de Matos Granja, R. H. Wilson, M.-A. Mycek, M. C. Kelley, and A. Mahadevan-Jansen, Development of a spatially offset Raman spectroscopy probe for breast tumor surgical margin evaluation. J. Biomed. Opt. **16**, 077006 (2011).
20. R. Gautam, R. Ahmed, E. Haugen, M. Unal, S. Fitzgerald, S. Uppuganti, A. Mahadevan-Jansen, and J. S. Nyman, Assessment of spatially offset Raman spectroscopy to detect differences in bone matrix quality. Spectrochim. Acta A: Mol. Biomol. Spectrosc. **303**, 123240 (2023).
21. S. P. Sunny, S. Agarwal, B. L. James, E. Heidari, A. Muralidharan, V. Yadav, V. Pillai, V. Shetty, Z. Chen, N. Hedne, P. Wilder-Smith, A. Suresh, and M. A. Kuriakose, Intra-operative point-of-procedure delineation of oral cancer margins using optical coherence tomography. Oral Oncol. **92**, 12 (2019).
22. P. Matousek, E. R. C. Draper, A. E. Goodship, I. P. Clark, K. L. Ronayne, A. W. Parker, and A. W. P. Royal, Noninvasive Raman Spectroscopy of Human Tissue In Vivo. Appl. Spectrosc. **60**, 758 (2006).

23. A. Ghita, P. Matousek, and N. Stone, High sensitivity non-invasive detection of calcifications deep inside biological tissue using Transmission Raman Spectroscopy. J. Biophotonics **11**, 1 (2018).
24. B. Gardner, J. Haskell, A. Ghita, P. Matousek, C. Ives, D. Ferguson, and N. Stone P123: Preliminary evaluation of Raman spectroscopy to detect calcifications in excised breast tissue: A prelude to the first in vivo whole breast study. Eur. J. Surg. Oncol. **46**, e43 (2020).
25. F. Helmchen and W. Denk, Deep tissue two-photon microscopy. Nat. Methods **2**, 932 (2005).
26. J. R. Maher and A. J. Berger, Determination of Ideal Offset for Spatially Offset Raman Spectroscopy. Appl. Spectrosc. **64**, 61 (2010).
27. P. Dey, A. Vaideanu, S. Mosca, M. Salimi, B. Gardner, F. Palombo, I. Uchegbu, J. Baumberg, A. Schatzlein, P. Matousek, and N. Stone, Surface enhanced deep Raman detection of cancer tumour through 71 mm of heterogeneous tissue. Nanotheranostics **6**, 337 (2022).
28. H. A. B. Mustafa and O. Akkus, Comparison of diffuse versus inverse spatially-offset Raman spectroscopy modalities for analyte detection through barriers. Vib. Spectrosc. **113**, 103228 (2021).
29. T. P. Tyler, A. I. Henry, R. P. Van Duyne, and M. C. Hersam, Improved monodispersity of plasmonic nanoantennas via centrifugal processing. J. Phys. Chem. Lett. **2**, 218 (2011).
30. K. Ma, J. M. Yuen, N. C. Shah, J. T. Walsh, M. R. Glucksberg, and R. P. Van Duyne, In vivo, transcutaneous glucose sensing using surface-enhanced spatially offset Raman spectroscopy: Multiple rats, improved hypoglycemic accuracy, low incident power, and continuous monitoring for greater than 17 days. Anal. Chem. **83**, 9146 (2011).
31. J. M. Yuen, N. C. Shah, J. T. Walsh, M. R. Glucksberg, and R. P. Van Duyne, Transcutaneous glucose sensing by surface-enhanced spatially offset Raman spectroscopy in a rat model. Anal. Chem. **82**, 8382 (2010).
32. S. Sloan-Dennison, S. Laing, D. Graham, and K. Faulds, From Raman to SESORRS: Moving deeper into cancer detection and treatment monitoring. Chem. Commun. **57**, 12436 (2021).
33. F. Nicolson, L. E. Jamieson, S. Mabbott, K. Plakas, N. C. Shand, M. R. Detty, D. Graham, and K. Faulds, Through tissue imaging of a live breast cancer tumour model using handheld surface enhanced spatially offset resonance Raman spectroscopy (SESORRS). Chem. Sci. **9**, 3788 (2018).
34. P. Dey, W. Olds, I. Blakey, K. J. Thurecht, E. L. Izake, and P. M. Fredericks, SERS-based detection of barcoded gold nanoparticle assemblies from within animal tissue. J. Raman Spectrosc. **44**, 1659 (2013).
35. P. Dey, Aiming for Maximized and Reproducible Enhancements in the Obstacle Race of SERS. ACS Meas. Sci. Au **3**, 434 (2023).
36. G. McNay, D. Eustace, W. E. Smith, K. Faulds, and D. Graham, Surface-enhanced Raman scattering (SERS) and surface-enhanced resonance Raman scattering (SERRS): A review of applications. Appl. Spectrosc. **65**, 825 (2011).
37. K. Faulds, R. Jarvis, W. E. Smith, D. Graham, and R. Goodacre, Multiplexed detection of six labelled oligonucleotides using surface enhanced resonance Raman scattering (SERRS). Analyst **133**, 1505 (2008).
38. M. A. Bedics, H. Kearns, J. M. Cox, S. Mabbott, F. Ali, N. C. Shand, K. Faulds, J. B. Benedict, D. Graham, and M. R. Detty, Extreme red shifted SERS nanotags. Chem. Sci. **6**, 2302 (2015).
39. M. E. Berry, S. M. McCabe, N. C. Shand, D. Graham, and K. Faulds, Depth prediction of nanotags in tissue using surface enhanced spatially offset Raman scattering (SESORS). Chem. Commun. **58**, 1756 (2022).
40. N. Stone, M. Kerssens, G. R. Lloyd, K. Faulds, D. Graham, and P. Matousek, Surface enhanced spatially offset Raman spectroscopic (SESORS) imaging - the next dimension. Chem. Sci. **2**, 776 (2011).
41. S. Keren, C. Zavaleta, Z. Cheng, A. De La Zerda, O. Gheysens, and S. S. Gambhir, Noninvasive molecular imaging of small living subjects using Raman spectroscopy. Proc. Natl. Acad. Sci. U S A **105**, 5844 (2008).
42. B. Gardner, P. Matousek, and N. Stone, Subsurface Chemically Specific Measurement of pH Levels in Biological Tissues Using Combined Surface-Enhanced and Deep Raman. Anal. Chem. **91**, 10984 (2019).

43. B. Gardner, P. Matousek, and N. Stone, Direct monitoring of light mediated hyperthermia induced within mammalian tissues using surface enhanced spatially offset Raman spectroscopy (T-SESORS). Analyst **144**, 3552 (2019).
44. A. S. Moody, T. D. Payne, B. A. Barth, and B. Sharma, Surface-enhanced spatially-offset Raman spectroscopy (SESORS) for detection of neurochemicals through the skull at physiologically relevant concentrations. Analyst **145**, 1885 (2020).
45. B. Sharma, K. Ma, M. R. Glucksberg, and R. P. Van Duyne, Seeing through bone with surface-enhanced spatially offset Raman spectroscopy. J. Am. Chem. Soc. **135**, 17290 (2013).
46. A. S. Moody, P. C. Baghernejad, K. R. Webb, and B. Sharma, Surface Enhanced Spatially Offset Raman Spectroscopy Detection of Neurochemicals Through the Skull. Anal. Chem. **89**, 5688 (2017).
47. F. Nicolson, B. Andreiuk, C. Andreou, H. T. Hsu, S. Rudder, and M. F. Kircher, Non-invasive in vivo imaging of cancer using Surface-Enhanced spatially offset Raman spectroscopy (SESORS). Theranostics **9**, 5899 (2019).
48. S. Mosca, P. Dey, M. Salimi, B. Gardner, F. Palombo, N. Stone, and P. Matousek, Spatially Offset Raman Spectroscopy - How Deep? Anal. Chem. **93**, 6755 (2021).

# Chapter 21
# Recent Advances in SERS-based Biomedical Diagnostics of Covid-19

**Sungwoon Lee, Sang-Woo Joo, and Jaebum Choo**

**Abstract** Airborne viruses such as COVID-19 spread rapidly through the air, making them highly contagious. Therefore, there is an urgent need to develop a point-of-care diagnostic method that can perform quick and accurate on-site diagnosis. The reverse transcription polymerase chain reaction method, which involves the extraction and amplification of viral RNA and detection using fluorescence analysis, is the standard diagnostic method adopted worldwide. However, this method has a limitation in that it requires 3–4 h from preprocessing to detection, which makes on-site diagnosis challenging. By contrast, for immunological analysis, lateral flow assay kits that can be used individually for on-site self-testing have been commercialized. However, they have the disadvantage of low sensitivity, leading to false-negative results in early stage patients or asymptomatic carriers with low viral concentrations. Various on-site diagnostic technologies for COVID-19 have been developed to address these issues using SERS detection and microdevice technologies. SERS detection has a higher sensitivity than that of fluorescence detection, and can overcome the false-negative problem. Further, miniaturization technologies using various microdevices enable the accurate and rapid on-site diagnosis of COVID-19. This paper reviews the on-site diagnostic technologies that integrate SERS-based microdevices and portable Raman readers developed during the COVID-19 pandemic. Additionally, several machine learning techniques designed to enhance the accuracy of SERS-based detection results for COVID-19 are presented. The SERS-based microdevices and machine learning technologies introduced in this paper are evaluated as new diagnostic technologies that can respond to infectious diseases that may recur in the future.

**Keywords** Surface-enhanced Raman scattering · Diagnostics · Point-of-care · Infectious diseases · COVID-19 · SARS-CoV-2

S. Lee · J. Choo (✉)
Department of Chemistry, Chung-Ang University, Seoul 06974, South Korea
e-mail: jbchoo@cau.ac.kr

S.-W. Joo
Department of Chemistry, Soongsil University, Seoul 06978, South Korea
e-mail: sjoo@ssu.ac.kr

© The Author(s), under exclusive license to Springer Nature Singapore Pte Ltd. 2024

M. Procházka et al. (eds.), *Surface- and Tip-Enhanced Raman Scattering Spectroscopy*,
https://doi.org/10.1007/978-981-97-5818-0_21

## 21.1 Introduction

Optical detection technologies such as fluorescence and chemiluminescence have been widely used in infectious disease diagnostics [1, 2]. However, these two methods have limitations in terms of sensitivity and multiplex detection capabilities, making it challenging to simultaneously detect multiple samples with high sensitivity. Recently, surface-enhanced Raman scattering (SERS) has been demonstrated to overcome the limitations of traditional detection methods [3–5]. When light interacts with the nanostructures of metals such as Au or Ag, it induces the oscillation of free electrons on the metal surface, known as the localized surface plasmon resonance (LSPR) effect. This LSPR phenomenon significantly enhances the Raman scattering signal of molecules in the nanogaps, enabling highly sensitive assays for biomolecules. Furthermore, the narrow widths of Raman peaks enhance their potential for multiplex detection [6, 7]. In recent years, microdevices capable of effectively handling various clinical samples have been developed, and portable Raman readers that miniaturize desktop-level Raman spectrophotometers have become commercially available. Consequently, researchers have developed SERS-based on-site diagnostic technologies by combining these microdevices with mobile Raman readers [8, 9]. In this chapter, we explore SERS-based diagnostic platform technology recently developed for the accurate on-site diagnosis of infectious diseases such as Coronavirus Disease 2019 (COVID-19).

In 2019, COVID-19, caused by the Severe Acute Respiratory Syndrome Coronavirus 2 (SARS-CoV-2), developed into a global pandemic and continues to pose a critical threat to healthcare systems worldwide. Infectious respiratory diseases such as COVID-19 can spread through airborne transmission, making it crucial to diagnose confirmed cases and isolate individuals quickly and accurately [10, 11]. The gold standard for diagnosing SARS-CoV-2 worldwide is reverse transcription polymerase chain reaction (RT-PCR), which detects ribonucleic acid (RNA) markers within the virus [12, 13]. Although this method has the advantage of high sensitivity and selectivity, it requires 3–4 h from the pretreatment of clinical samples to PCR amplification and detection, making on-site diagnosis difficult. Suspected patient samples are collected at screening centers and sent to clinical laboratories for analysis. This process is disadvantageous in managing the surge in infected patients when highly infectious viruses, such as Omicron, spread rapidly. Lateral flow assay (LFA) strips that detect target antigens by utilizing antigen–antibody binding can allow infected individuals to determine their infection status within 10 min [14, 15]. However, it has a low sensitivity, which increases the false-negative diagnostic rate. Commercial LFA strips may result in false-negative diagnoses of initial or asymptomatic infections with very low viral loads, leading to increased viral spread.

Therefore, during the COVID-19 pandemic, researchers made substantial efforts to develop faster and more sensitive SARS-CoV-2 on-site diagnostic technologies [16–20]. Particularly, several technologies have been studied to enhance the diagnostic sensitivity of SARS-CoV-2 biomarkers, and diagnostic technologies utilizing SERS detection based on the localized surface plasmon effects of nanostructures

have been developed [21–25]. Several biomarkers, clinical specimens, and diagnostic methods that for diagnosing multiple viruses, and recent research results on graphene-based biosensors and SERS-based LFA strips have been reported. Sitjar et al. [26] summarized the substrate design, laser conditions, and detection mechanisms required for optimal SERS detection of viruses. The Vikesland group [27] introduced various sensing platforms for the viruses present in drinking water and wastewater systems, whereas the Ray group [28] introduced various bioconjugated nanomaterials for the targeted diagnosis of SARS-CoV-2. Liu et al. [29] presented the recent research trends in aptamer-based biosensors for viral protein detection. However, several issues need to be addressed to clinically utilize SERS techniques for on-site diagnosis of infectious diseases such as SARS-CoV-2. This paper discusses the recent advances in SERS-based detection technology for contagious diseases. Particularly, we examine current research examples that have improved the sensitivity of immunoassay technologies, such as enzyme-linked immunosorbent assay (ELISA) and LFA using SERS detection technology, and examples of recent research integrating machine learning (ML) with SERS to improve diagnostic accuracy [30–33]. Finally, we examine the problems that need to be solved and prospects to replace existing infectious disease on-site diagnosis techniques with SERS-based diagnosis techniques.

## 21.2 Development of New SERS Nanotags

Several SERS nanotags have been developed to enhance the diagnostic sensitivity for SARS-CoV-2. An ELISA plate is the immunoassay platform most commonly used by biological scientists and medical doctors. However, in the SERS-ELISA platform, Au nanoparticles (NPs), which are most frequently used as SERS nanotags, cannot form sufficient hot spots because of the irregular distance distribution of the particles when sandwich immunocomplexes are formed in the well plate, making it difficult to obtain strong localized surface plasmon effects. To solve this problem, Yu et al. [24] developed new SERS nanotags in the form of silica-encapsulated core-satellite (CS) NPs (Fig. 21.1). These CS NPs comprise multiple 32-nm AuNPs assembled on a 75-nm core AuNP, forming nanogaps inside individual CS NPs, which allowed for strong signal enhancement. Furthermore, CS NPs were encapsulated in silica ($CS@SiO_2$) to enhance particle stability and facilitate antibody anchoring. Using $CS@SiO_2$, they achieved good sensitivity with a limit of detection (LoD) of 8.8 PFU/mL in a 1536-well plate SARS-CoV-2 assay and obtained 87% sensitivity and 100% specificity for samples with threshold cycle (Ct) < 30 when testing 30 clinical samples.

Ray et al. [28] developed aptamer-conjugated Au nanostar tags for SARS-CoV-2 assays. In this study, we used spike-protein-specific aptamer-attached Au nanostars as SERS nanotags. By utilizing the phenomenon in which Au nanostars quench fluorescence dyes attached to the DNA aptamer terminal and are then restored when binding with a spike protein, they could detect target proteins down to 100 fg/mL. Leong et al.

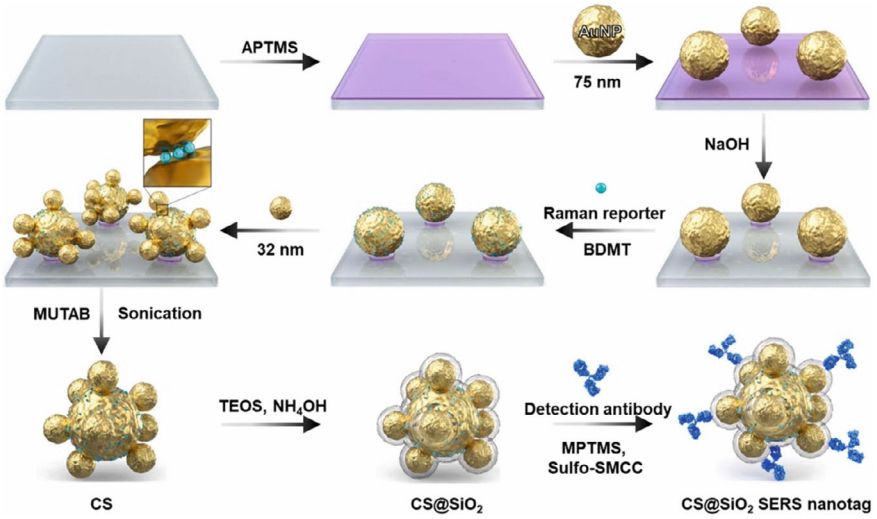



**Fig. 21.1** Assembly method for the synthesis of antibody-conjugated CS@$SiO_2$ SERS nanotags. Raman reporter BDMT was attached to the surface of the 75-nm AuNPs through an Au–S bond. Then, the 32-nm AuNPs were bound to the 75-nm AuNP through an Au–S bond. CS particles were separated from the glass substrate via sonication and encapsulated with $SiO_2$. Finally, the N-protein antibodies were immobilized on CS@$SiO_2$ using sulfo-SMCC linker [24]

[34] developed a SERS-based breathalyzer to observe COVID-19-infected individuals within 5 min. The authors used Ag nanocubes with attached molecular receptors as SERS tags to detect breath-volatile organic compounds. Statistical analysis of the Raman spectral data for positive and negative discrimination was performed using partial least-squares discriminant analysis. A study involving 501 patients showed 96.2% sensitivity and 99.9% specificity. Research has been conducted to improve SERS nanotags for effective SARS-CoV-2 SERS-based assays by developing plasmonic enhancements of individual particles, generating multiple hot spots, and developing stability-increasing techniques using $SiO_2$ or PEG. In addition, bioconjugation techniques have been developed to stably immobilize receptors, such as antibodies and DNA aptamers, on the surface of SERS tags.

## 21.3 SERS Detection Devices for SARS-CoV-2 Diagnosis

Another critical issue in SARS-CoV-2 diagnosis using SERS technology is the detection platform for target biomarkers. Various SERS-based immunoassay platforms have been developed, including magnetic beads, lateral flow assay strips, microfluidic channels, and gold-patterned microarrays. This review examines recently published studies on point-of-care (POC) test platforms for SARS-CoV-2 detection using SERS-based detection techniques.

### 21.3.1 Magnetic Bead-Based SERS Assays

Currently, most clinical laboratories use automated equipment based on chemiluminescence technology produced by specialized companies such as Roche, Abbott, and Siemens for the immunological analysis of blood. Three diagnostic reagents were used for chemiluminescent analysis of specific biomarkers. The first is an antibody set that selectively binds to specific protein biomarkers in blood. The second is the use of magnetic beads to immobilize the bound sandwich immunocomplexes. The last reagent comprises a luminescent agent, such as luminol, which can activate immobilized immunocomplexes without radiation. In magnetic bead-based SERS immunoassays, the same method is used for the chemiluminescence platforms in clinical laboratories. Magnetic beads were used as capture templates and SERS nanotags were used as detection labels for the assay.

Guan et al. [35] developed an assay platform using high-binding-affinity aptamers for the spike protein as receptors that can detect SARS-CoV-2 and several variants with high sensitivity. Magnetic beads and AuNPs were used as capture support materials and detection probes, respectively, and the LoD was 20 fM for the three SARS-CoV-2 variants. Furthermore, testing of 20 positive/negative clinical samples yielded 95% sensitivity and 100% specificity. Mohammadi et al. [36] successfully detected SARS-CoV-2 spike protein in saliva with high sensitivity (LoD = 4.7 fg/mL) using gold-coated magnetic NPs and single-chain variable fragment (scFv) receptors. Antoine et al. [37] successfully detected three siemens protein variants using the same scFv receptor and a magnetic bead-based sandwich immunoassay platform. They obtained an LoD of 257 fg/mL for the spike protein. Cha et al. [38] performed a SARS-CoV-2 immunoassay using a monoclonal antibody set for the nucleocapsid protein, magnetic beads, and hollow Au SERS nanotags (Fig. 21.2). They obtained LoDs of 2.56 fg/mL for nucleocapsid protein and 3.4 PFU/mL for SARS-CoV-2. Magnetic bead-based assay methods are widely used in clinical laboratories for immunoassays using chemiluminescence detection, and are also used in SERS-based immunoassay platforms. However, to apply SERS detection to POC testing, the development of microdevices such as LFA strips or microfluidic chips that can miniaturize the assay system and a compact Raman spectrophotometer is required.

### 21.3.2 SERS-Based LFA Strips

The LFA strip can quickly diagnose the presence or absence of a specific biomarker found in blood, urine, nasal mucus, and other bodily fluids at the POC. Antibody-conjugated AuNPs are widely used in colorimetric LFA strips, and the phenomenon of localized surface plasmon effects of AuNPs changing color from colorless to red is leveraged when AuNPs accumulate on the test line of the strip owing to antibody-antigen interactions [39–41]. Although colorimetric LFA strips have been

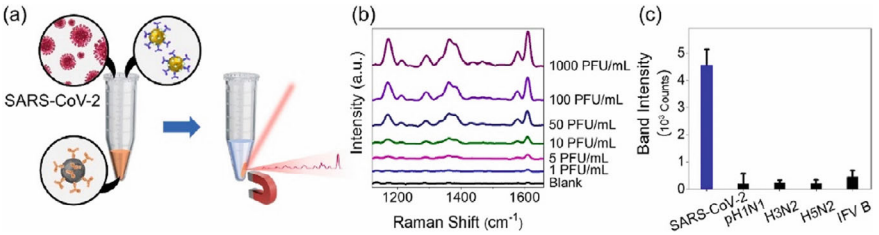



**Fig. 21.2** **a** Schematic of the magnetically assisted SERS immunoassay for SARS-CoV-2. **b** SERS spectra of MGITC measured using hollow Au NP-assembled magnetic beads after detection of SARS-CoV-2 (0–1000 PFU/mL). **c** A plot of 1170 $cm^{-1}$ band intensity as a function of the virus. Data represent average ± standard deviation from ten measurements [38]

successfully used for the on-site diagnosis of COVID-19, they have the problem of increasing false-negative diagnostic rates when considering low viral concentrations, such as in initial or asymptomatic infections, where the sensitivity drops to below 50%. According to the analysis results of the US Food and Drug Administration, the false-negative rate increases by 13% for every ten-fold increase in the LoD [15, 42, 43]. Therefore, to prevent the spread of SARS-CoV-2, it is critical to significantly improve the sensitivity of immunodiagnostics, and several researchers have focused on improving the sensitivity of colorimetric LFA strips. Technologies have been developed that use various optical strip readers and detection labels to enhance the detection sensitivity of analytes, and not just to observe color changes in the test line due to AuNP accumulation with the naked eye, as in colorimetric LFA strips. The most extensively used method involves the use of portable fluorescence readers to measure the optical signal of LFA strips using fluorescence dyes, microspheres, or quantum dots [44, 45]. However, this fluorescence measurement method has limitations in terms of significantly improving the detection sensitivity of colorimetric LFA.

SERS has attracted attention as a highly sensitive detection technology that can overcome the low detection sensitivity limit of a specific biomarker in immunoassays. When SERS nanotags are exposed to a laser beam, the incident electromagnetic field is substantially enhanced at active sites called “hot spots” due to localized surface plasmon effects. This electromagnetic enhancement can solve the inherent low sensitivity problem of colorimetric and fluorescence detection [46, 47]. Recently, the SERS-LFA platform has been widely used to diagnose infectious diseases. In addition, SERS-LFA strips have the advantage of being identifiable with the naked eye, unlike fluorescent LFA, because they use the same AuNPs. Thus, high-virus samples can be identified with the naked eye, and low-virus samples can be detected with high sensitivity by monitoring the characteristic Raman peak intensity of the SERS tags. Moreover, various portable Raman systems have recently been developed, and combining them with SERS-LFA strips makes it possible to implement SERS-based LFA technology for highly sensitive on-site diagnosis of SARS-CoV-2 [48, 49].

In 2022, Joung et al. [8] developed a highly sensitive SARS-CoV-2 detection system to address the problem of high false-negative diagnostics caused by the low sensitivity of existing commercial colorimetric LFA strips (Fig. 21.3). They combined a SERS-LFA strip with a home-built portable Raman reader. Figure 21.3a shows the structure of the SERS-LFA strip designed for high-sensitivity detection of the target antigen marker, the nucleocapsid protein of SARS-CoV-2. Figure 21.3b shows the portable Raman reader capable of automatically measuring Raman signals from the test and control lines. This technology enables the detection of relatively low viral concentrations with a Ct value higher than 25, which is not achievable using colorimetric LFA strips. Using the SERS-LFA strip, the authors measured concentrations of the SARS-CoV-2 virus as low as 3.5 PFU/mL. When tested with 54 COVID-19 clinical samples of various viral concentrations, the commercial colorimetric LFA strip showed a sensitivity of 57%, whereas the SERS-based LFA strip exhibited remarkable sensitivity enhancement, reaching 96%.

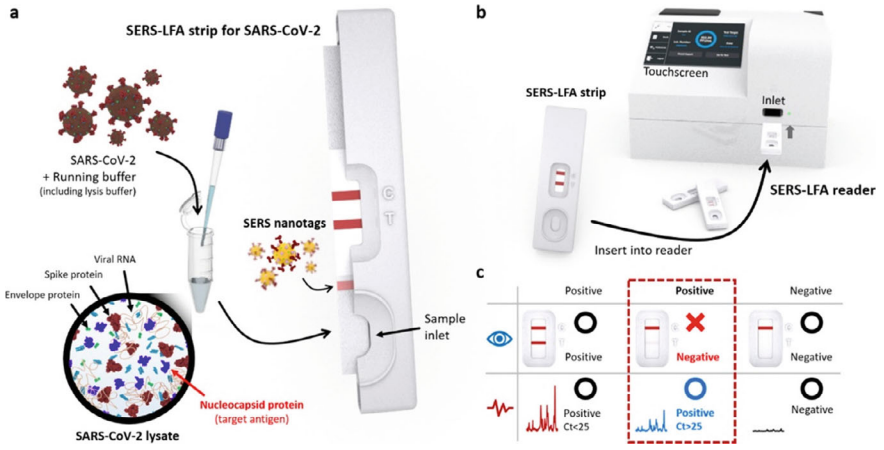



**Fig. 21.3** Illustration of the SERS-LFA system for on-site diagnosis of SARS-CoV-2. **a** Schematic of the SERS-LFA strip for the SARS-CoV-2 antigen test. SARS-CoV-2 is added to the lysis buffer to decompose the virus. After mixing the SARS-CoV-2 lysate with the running buffer, the solution was loaded into the inlet of the SERS-LFA strip. When this SARS-CoV-2 lysate reaches the conjugate pad, target NC proteins and NC antibody-conjugated SERS nanotags form immunocomplexes through antibody—antigen interactions. The running buffer, including the NC protein-SERS nanotag complexes, moved toward the test and control lines. **b** After the running buffer reaches the absorption pad through the test and control lines, the SERS-LFA strip is inserted into the portable Raman reader. **c** Advantage of the SERS-LFA system over the commercial LFA strip. Both LFA and SERS-LFA indicate negative tests for SARS-CoV-2 negative patients. Both methods are positive for clinical samples with high-virus concentrations (Ct < 25 in RT-PCR). Most LFA assays indicate false negatives in clinical samples with a relatively low-virus concentration (25 < Ct in RT-PCR); however, the SERS-LFAs show true positives owing to their high sensitivity [8]

### *21.3.3 SERS-Based Microfluidics*

In cases where bioassays are conducted using the SERS-based method with magnetic beads or LFA strips, issues regarding the automation of the sample pretreatment process and the reproducibility of the detection signal persist. Recently, researchers have developed SERS-based microfluidics that integrate microfluidic devices with SERS detection to address these challenges [50–52]. The SERS detection method offers a highly sensitive detection capability, and microfluidic technology allows for automatic sampling processes and enables signal collection for average ensembles, thereby significantly enhancing the reproducibility [53, 54]. Therefore, researchers have developed SERS-based microfluidic systems to leverage the advantages of recent developments in microfluidic devices and SERS detection platforms.

In microfluidic technology, chemical or biological processes occur within microchannels instead of in flasks or tubes, allowing reagents to be manipulated in very small volumes. In addition, the reagents driving the reactions can be manipulated using pressure, electric or acoustic fields, or centrifugal force. Several microfluidic devices capable of handling minute samples within microfluidic channels have been developed to diagnose infectious diseases such as COVID-19. However, in cases where extremely small volumes of reagents (ranging from nanoliters to femtoliters) react within the microfluidic channels, it is crucial to employ a detection technique that can focus on a small beam, such as a laser, within the channel for highly sensitive on-chip detection [55, 56].

Fluorescence-on-chip detection technology, which involves the quantitative analysis of the binding of fluorescent dyes to target biomarkers within microfluidic channels, has been widely used in the early stages of microfluidic development. However, because of the sensitivity limits of the fluorescence signal intensity arising from the small focal volume in this approach, there is a growing need for on-chip detection technologies that can achieve higher sensitivity. In response to this limitation, the development of an on-chip detection technology using SERS nanotags to measure the localized surface plasmon signals of biomarkers within the chip has gained prominence [3]. This SERS-based on-chip technology allows high-sensitivity detection, even when measuring optical signals in small focal volumes [57]. Consequently, various infectious disease diagnostic technologies that utilize this approach have been developed [58].

Park et al. [59] developed a SERS-based microfluidic sensor capable of automatically performing SARS-CoV-2 immune analysis (Fig. 21.4). This microfluidic chip includes three inlets into which SARS-CoV-2 lysates, captured antibody-conjugated magnetic beads, and detected antibody-conjugated SERS nanotags can be injected. Three aqueous laminar flows form microdroplets using carrier oil (i), and as they pass through a winding channel, sandwich immunocomplexes are formed through the antibody-antigen reaction (ii). When these mother droplets passed through the splitting channels with embedded magnetic bars, the magnetic immunocomplexes moved through the narrow channels below. By contrast, the remaining supernatant solution passes through the wide channel above (iii). By monitoring the characteristic

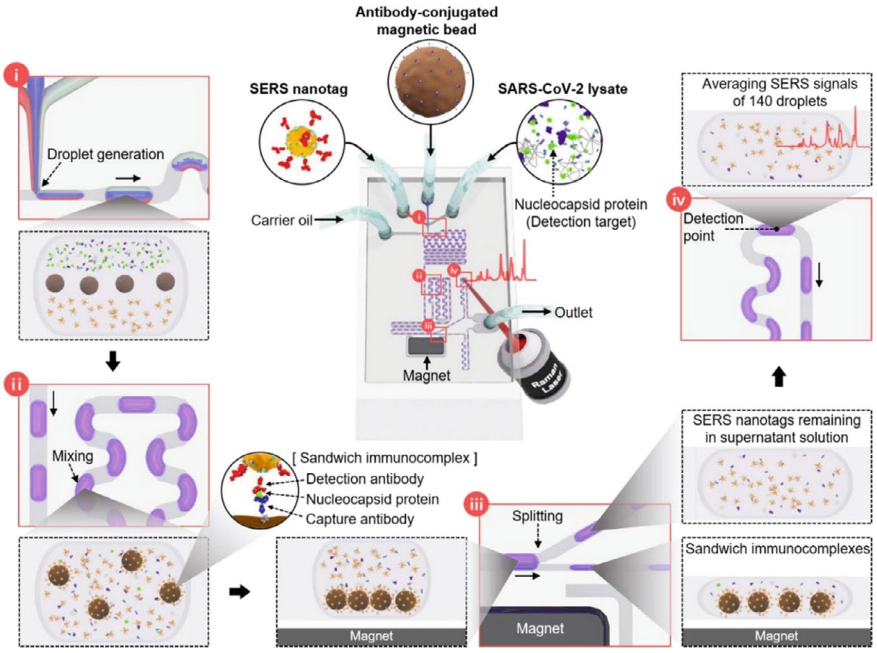



**Fig. 21.4** Schematic of the microdroplet channel used to detect severe acute respiratory syndrome coronavirus 2 (SARS-CoV-2). This microfluidic channel comprises four compartments for **i** droplet generation, **ii** droplet mixing, **iii** droplet splitting, and **iv** optical signal measurements [59]

Raman signal intensity of the remaining SERS nanotags in the supernatant solution (iv), the concentration of the SARS-CoV-2 antigen could be determined. Utilizing SERS-based microfluidic technology allows the averaging of Raman signals from 140 droplets passing through a fixed laser beam for 15 s, ensuring superior reproducibility compared to other SERS-based assay methods. When applying this method to the immune analysis of SARS-CoV-2, an LoD of 0.22 PFU/mL was achieved, and the average coefficient of variation value was also exceptionally low at 1.79%, indicating excellent reproducibility.

### *21.3.4 SERS-Based Microarrays*

Choo et al. fabricated a three-dimensional (3D) nanopopcorn substrate to implement an accurate and reproducible SARS-CoV-2 lysate assay [60, 61]. This 3D nanopopcorn substrate was fabricated using the surface energy difference between a perfluorodecanethiol spacer and Au layer. This energy difference induced uniform self-assembly of the Au nanoparticles, forming multiple hot spots. The localized surface plasmon effects generated by these hotspots significantly increased the incident field intensity. Using a DNA aptamer that selectively binds to the spike protein

expressed on the surface of SARS-CoV-2 and this 3D nanopopcorn substrate, SARS-CoV-2 was detected within 15 min with an LoD of 10 PFU/mL, as shown in Fig. 21.5 [62]. In addition, a SERS-based dual-mode DNA aptasensor that can rapidly distinguish between SARS-CoV-2 and influenza A infections was developed using the same method [63]. Studies on label-free SERS detection of SARS-CoV-2 lysates directly using this 3D nanopopcorn substrate have also been introduced [64–66]. To detect the SARS-CoV-2 spike (S) and nucleocapsid (N) proteins with high sensitivity, Luo et al. [25] fabricated bowtie nanoaperture arrays based on long-range surface plasmon resonance (LRSPR), which can achieve stronger electromagnetic enhancement than that in conventional surface plasmon resonance. Controlling the polarization of the incident light using this LRSPR-based SERS substrate makes it possible to detect target biomarkers with high sensitivity. LoDs of 9.2 and 11.3 pg/mL were obtained for S and N proteins, respectively. Huang et al. [67] developed a fishing-mode device that can detect low concentrations of SARS-CoV-2 receptor-binding domain (RBD) in different detection environments. They used a substrate with 55-nm AuNPs attached to the surface of an Ag acupuncture needle as an RBD detection platform and a DNA aptamer that selectively bound to the RBD as a receptor. RBD could be detected up to 0.625 ng/mL using this fishing-mode device within 15 min. Zhang et al. [68] fabricated a Au film substrate by self-assembling AuNPs at oil/water/oil three-phase liquid–liquid interfaces to implement an accurate and reproducible SARS-CoV-2 assay. Spike antibodies conjugated with AgNPs were used as SERS nanotags. This SERS-based biosensor detected spike protein up to 0.77 fg/mL (in PBS buffer) and 6.07 fg/mL (in saliva). Choi et al. [69] successfully demonstrated the amplification-free detection of SARS-CoV-2 DNA markers using a graphene oxide/triangle nanoflower array, ss-DNA-conjugated AuNP SERS nanotags, and a CRISPR/Cas-2a system. This study demonstrated the possibility of detecting a target gene without amplification using thermocycling steps by complementing the ultra-sensitive SERS assay platform with CRISPR/C as technology, similar to RT-PCR. Payne et al. [70] demonstrated that it is possible to detect the selective binding of a peptide to the SARS-CoV-2 spike protein on an Au substrate surface instead of using a receptor such as an antibody or DNA aptamer. When a technology for rapidly finding a specific virus-capture peptide using phage display is developed, it is expected to be helpful in developing receptors for viruses that may emerge in the future. The development of SERS substrates to detect SARS-CoV-2 has mainly focused on simultaneously improving the diagnostic sensitivity and reproducibility of the substrate, while immobilizing receptors with high selectivity for the target biomarkers of the virus.

## 21.4 Application of Artificial Intelligence Technology

Various ML techniques have been developed to enhance the accuracy of SERS-based on-site diagnosis of SARS-CoV-2. Figure 21.6 shows the SERS detection of infectious diseases using ML. The concepts, benefits, and constraints of integrating SERS

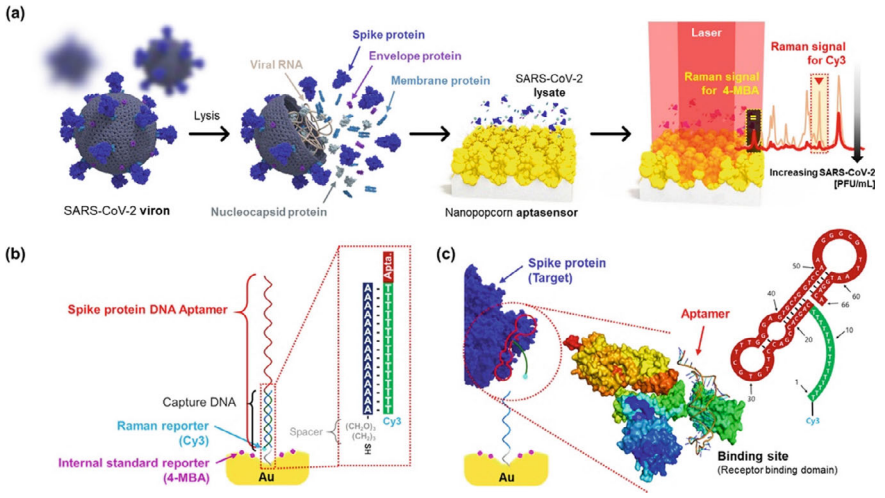



**Fig. 21.5** Schematic of the quantitative evaluation of SARS-CoV-2 using the SERS-based aptasensor. **a** After SARS-CoV-2 lysates release the target spike proteins, they are recognized by the aptamer DNAs on the Au nanopopcorn surfaces. The spike protein-bound aptamers move away from the Au nanopopcorn surfaces, leading to a decreased Raman peak intensity of Cy3 reporters. **b** Cy3-tagged aptamer DNAs are hybridized with capture DNAs on the Au nanopopcorn substrate. The internal standard 4-MBAs are immobilized along with aptamer DNAs on the Au nanopopcorn substrate. **c** Recognition of the spike protein of SARS-CoV-2 induces a conformational change of aptamer DNAs, enabling the aptamer DNAs to bind with the receptor-binding domain (RBD) on the spike protein [62]

with chemometrics and ML were recently examined to boost qualitative selectiveness and quantitative sensitivity, along with emerging patterns in data analysis tools [71]. The development status was reviewed for ongoing challenges and prospects of artificial intelligence-based SERS sensors crafted to detect body signals, monitor infectious diseases in close proximity, diagnose diseases, and support clinical decision-making [72]. ML and SERS/SEIRA were integrated to explore the advantages of the algorithms with a focus on molecular diagnostics and preliminary examination through synergy. An outlook is provided for the future progression and integration of ML with SEIRA/SERS [21]. The development of existing and upcoming forms of SARS-CoV-2 biosensors was assessed to identify variants/biomarkers using nanophotonic-based medical testing [73]. Label-free SERS and chemometrics have been utilized to swiftly examine the time-dependent changes in metabolic profiles in samples collected over time from non-hospitalized patients with mild infections ($n = 22$) at both 4 and 16 weeks following a PCR-positive diagnosis, comparing the results with those of negative controls ($n = 8$) [74].

Genetic algorithms have been used to computationally screen a metasurface platform with gold nanopatterning in a design space comprising 2100 permutations to achieve significantly intensified virus interactions and utilize this to detect and measure SARS-CoV-2 [75]. A new and improved substrate was introduced to identify

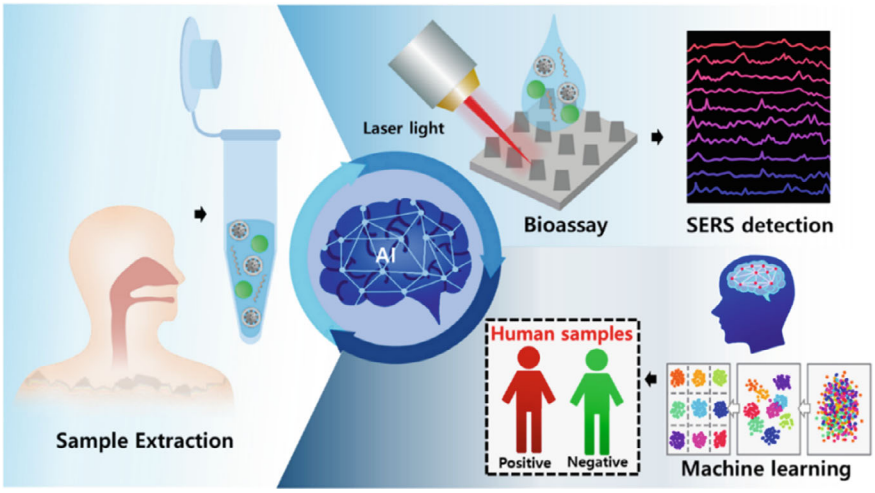



**Fig. 21.6** Scheme for SERS detection of infectious diseases using machine learning (ML). The extracted human samples were subjected to SERS bioassays. ML methods have been introduced to interpret and determine the prevalence of infectious diseases

respiratory viruses without labeling using SERS. Well-established linear correlations have been observed in the spectral patterns and concentration-dependent profiles of respiratory viruses such as SARS-CoV-2, human adenovirus type 7, and H1N1 virus [76]. A straightforward screening method was presented that relies on label-free SERS to examine alterations in saliva samples attributed to SARS-CoV-2-mediated among individuals classified as healthy at the molecular scale, individuals diagnosed with COVID-19, and those who have successfully overcome COVID-19. LF-SERS technology has been used to distinguish three types of coronavirus spike proteins originating from SARS-CoV-2, SARS-CoV, and MERS-CoV [77]. To address the challenges of bacterial identification technology, it has been suggested that a deep neural network can recognize bacteria that have antibiotic resistance through SERS [78]. A predictive diagnostic ML method was investigated using SERS to identify COVID-19 infection in biological samples. Gaussian process categorization was performed using a likelihood-driven ML technique to accurately anticipate the categorization of samples as either unfavorable or favorable based on low-dimensional spatial variables [79].

Figure 21.7 illustrates basic properties associated with the optical recognition of the SARS-CoV-2 spike protein's RBD were studied for a crucial element in viral invasion [80]. There was a study demonstrating human angiotensin-converting enzyme 2 (ACE2)-functionalized gold "virus trap" nanostructures as ultrasensitive SERS biosensors for selective capture and rapid detection of S protein-expressing coronaviruses, such as SARS-CoV-2 [81]. Additionally, one study reported a large-scale testing platform without labeling by combining SERS and MI to rapidly and accurately detect SARS-CoV-2 [82]. SERS sensors with deep learning algorithms

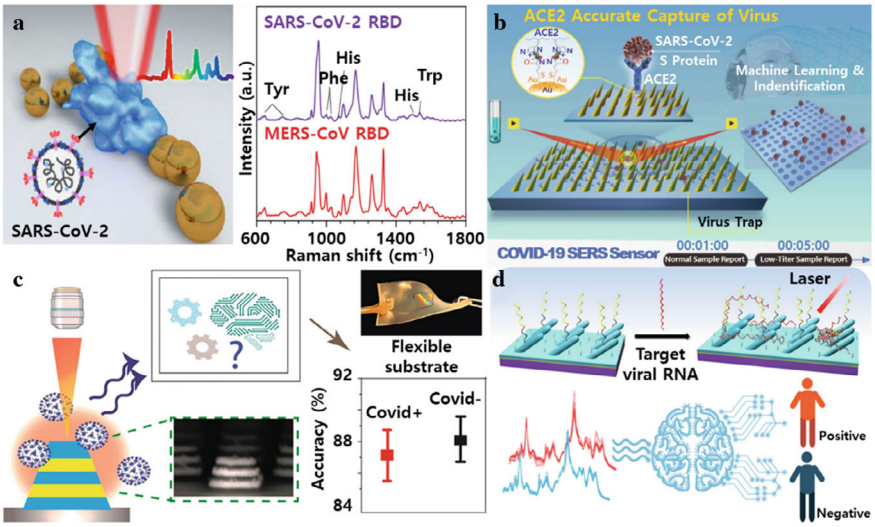



**Fig. 21.7** **a** Raman modes of the SARS-CoV-2 RBD and Raman spectra of RBDs from SARS-CoV-2 and MERS-CoV [80]. **b** Human Angiotensin-converting-enzyme 2 (ACE2)-functionalized gold "virus traps" structure at a nanoscale [81]. **c** An extensive testing without the need for a labeling system integrating surface-enhanced Raman spectroscopy and machine learning for the swift and precise identification of SARS-CoV-2 [82]. **d** A sensor employing surface-enhanced Raman spectroscopy (SERS) alongside a deep learning algorithm [83]

have been found to swiftly identify SARS-CoV-2 RNA in specimens from human nasopharyngeal swabs [83].

As shown in Fig. 21.8, the correlation between the Raman signals and purine metabolites of pathogenic Vibrio microorganisms was analyzed using label-free SERS technology [84]. Although SERS has recently become a potent method for identifying numerous microorganisms, its broad application has faced challenges due to constant signals from the surrounding medium, which require bacterial isolation steps. SERS analysis with a recently suggested deep learning framework called the dual-branch wide kernel network (DualWKNet) provided a straightforward, quicker, and more efficient way of categorizing two prevalent bacteria, *E. coli*, and *S. epidermidis*, along with the inherent signals of the bacteria [85]. After combining SERS and MI without labels, a diagnostic platform was developed to swiftly and accurately identify 13 respiratory viruses, including SARS-CoV-2, typical human coronaviruses, and influenza viruses [30]. Acoustic bioprinters have been developed to convert samples into a myriad of droplets containing several cells using SERS and ML [86].

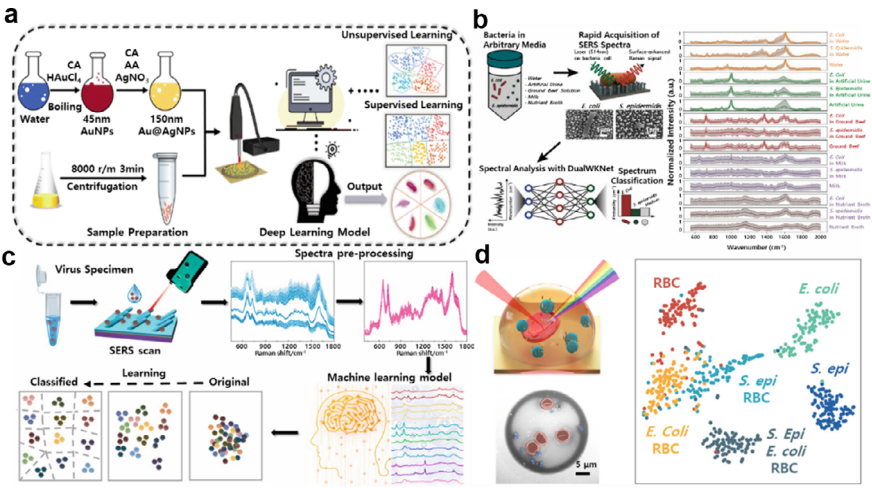



**Fig. 21.8** **a** Swift identification and detection of six pathogenic Vibrio species responsible for pollution of seafood utilizing mobile Raman in conjunction with ML [84]. **b** Common experimental process with analyte images and recorded Raman spectra [85]. **c** Diagrammatic representation of virus differentiation using machine learning [30]. **d** An acoustic bioprinter designed to convert samples into myriad droplets, each housing a small number of cells identified through the combination of SERS and ML [86]

**Acknowledgements** This study was supported by the National Research Foundation of Korea (grant numbers 2020R1A5A1018052 and RS-2024-00352256).

## References

1. G. F. Blackburn, H. P. Shah, J. H. Kenten, J. Leland, R. A. Kamin, J. Link, J. Peterman, M. J. Powell, A. Shah and D. B. Talley, Electrochemiluminescence detection for development of immunoassays and DNA probe assays for clinical diagnostics. Clin. Chem. **37**, 1534–1539 (1991)
2. W. Miao, Electrogenerated chemiluminescence and its biorelated applications. Chem. Rev. **108**, 2506–2553 (2008)
3. H. Chen, A. Das, L. Bi, N. Choi, J.-I. Moon, Y. Wu, S. Park and J. Choo, Recent advances in surface-enhanced Raman scattering-based microdevices for point-of-care diagnosis of viruses and bacteria. Nanoscale **12**, 21560–21570 (2020)
4. K. Kim, L. Kashefi-Kheyrabadi, Y. Joung, K. Kim, H. Dang, S. G. Chavan, M.-H. Lee and J. Choo, Recent advances in sensitive surface-enhanced Raman scattering-based lateral flow assay platforms for point-of-care diagnostics of infectious diseases. Sens. Actuators B: Chem. **329**, 129214 (2021)
5. H. Chon, S. Lee, S. W. Son, C. H. Oh and J. Choo, Highly sensitive immunoassay of lung cancer marker carcinoembryonic antigen using surface-enhanced Raman scattering of hollow gold nanospheres. Anal. Chem. **81**, 3029–3034 (2009)

6. R. Zhang, Y. Zhang, Z. C. Dong, S. Jiang, C. Zhang, L. G. Chen, L. Zhang, Y. Liao, J. Aizpurua, Y. Luo, J. L. Yang and J. G. Hou, Chemical mapping of a single molecule by plasmon-enhanced Raman scattering. Nature **498**, 82–86 (2013)
7. S.-Y. Ding, E.-M. You, Z.-Q. Tian and M. Moskovits, Electromagnetic theories of surface-enhanced Raman spectroscopy. Chem. Soc. Rev. **46**, 4042–4076 (2017)
8. Y. Joung, K. Kim, S. Lee, B.-S. Chun, S. Lee, J. Hwang, S. Choi, T. Kang, M.-K. Lee, L. Chen and J. Choo, Rapid and accurate on-site immunodiagnostics of highly contagious severe acute respiratory syndrome coronavirus 2 using portable surface-enhanced Raman scattering-lateral flow assay reader. ACS Sens. **7**, 3470–3480 (2022)
9. V. Tran, B. Walkenfort, M. Koenig, M. Salehi and S. Schluecker, Rapid, quantitative, and ultrasensitive point-of-care testing: A portable SERS reader for lateral flow assays in clinical chemistry. Angew. Chem., Int. Ed. **58**, 442–446 (2019)
10. X. He, E. H. Y. Lau, P. Wu, X. Deng, J. Wang, X. Hao, Y. C. Lau, J. Y. Wong, Y. Guan, X. Tan, X. Mo, Y. Chen, B. Liao, W. Chen, F. Hu, Q. Zhang, M. Zhong, Y. Wu, L. Zhao, F. Zhang, B. J. Cowling, F. Li and G. M. Leung, Temporal dynamics in viral shedding and transmissibility of COVID-19. Nat. Med. **26**, 672–675 (2020)
11. L. Scott, N.-y. Hsiao, S. Moyo, L. Singh, H. Tegally, G. Dor, P. Maes, O. G. Pybus, M. U. G. Kraemer, E. Semenova, S. Bhatt, S. Flaxman, N. R. Faria and T. de Oliveira, Track Omicron's spread with molecular data. Science **374**, 1454–1455 (2021)
12. V. M. Corman, O. Landt, M. Kaiser, R. Molenkamp, A. Meijer, D. K. W. Chu, T. Bleicker, S. Brünink, J. Schneider, M. L. Schmidt, D. G. J. C. Mulders, B. L. Haagmans, B. v. d. Veer, S. v. d. Brink, L. Wijsman, G. Goderski, J.-L. Romette, J. Ellis, M. Zambon, M. Peiris, H. Goossens, C. Reusken, M. P. G. Koopmans and C. Drosten, Detection of 2019 novel coronavirus (2019-nCoV) by real-time RT-PCR. Euro Surveill. **25**, 2000045 (2020)
13. M. Shen, Y. Zhou, J. Ye, A. A. Abdullah Al-maskri, Y. Kang, S. Zeng and S. Cai, Recent advances and perspectives of nucleic acid detection for coronavirus. J. Pharm. Anal. **10**, 97–101 (2020)
14. D. Wang, S. He, X. Wang, Y. Yan, J. Liu, S. Wu, S. Liu, Y. Lei, M. Chen, L. Li, J. Zhang, L. Zhang, X. Hu, X. Zheng, J. Bai, Y. Zhang, Y. Zhang, M. Song and Y. Tang, Rapid lateral flow immunoassay for the fluorescence detection of SARS-CoV-2 RNA. Nat. Biomed. Eng. **4**, 1150-1158 (2020)
15. Y. Zhou, Y. Wu, L. Ding, X. Huang and Y. Xiong, Point-of-care COVID-19 diagnostics powered by lateral flow assay. TrAC, Trends Anal. Chem. **145**, 116452 (2021)
16. J. Budd, B. S. Miller, N. E. Weckman, D. Cherkaoui, D. Huang, A. T. Decruz, N. Fongwen, G.-R. Han, M. Broto, C. S. Estcourt, J. Gibbs, D. Pillay, P. Sonnenberg, R. Meurant, M. R. Thomas, N. Keegan, M. M. Stevens, E. Nastouli, E. J. Topol, A. M. Johnson, M. Shahmanesh, A. Ozcan, J. J. Collins, M. Fernandez Suarez, B. Rodriguez, R. W. Peeling and R. A. McKendry, Lateral flow test engineering and lessons learned from COVID-19. Nat. Rev. Bioeng. **1**, 13–31 (2023)
17. R. G. Mannino, E. J. Nehl, S. Farmer, A. F. Peagler, M. C. Parsell, V. Claveria, D. Ku, D. S. Gottfried, H. Chen, W. A. Lam and O. Brand, The critical role of engineering in the rapid development of COVID-19 diagnostics: Lessons from the RADx Tech Test Verification Core. Sci. Adv. **9**, eade4962 (2023)
18. B. Wang, Y. Li, M. Zhou, Y. Han, M. Zhang, Z. Gao, Z. Liu, P. Chen, W. Du, X. Zhang, X. Feng and B.-F. Liu, Smartphone-based platforms implementing microfluidic detection with image-based artificial intelligence. Nat. Commun. **14**, 1341 (2023)
19. M. Alafeef and D. Pan, Diagnostic approaches for COVID-19: Lessons learned and the path forward. ACS Nano **16**, 11545–11576 (2022)
20. G. Rong, Y. Zheng, X. Li, M. Guo, Y. Su, S. Bian, B. Dang, Y. Chen, Y. Zhang, L. Shen, H. Jin, R. Yan, L. Wen, P. Zhu and M. Sawan, A high-throughput fully automatic biosensing platform for efficient COVID-19 detection. Biosens. Bioelectron. **220**, 114861 (2023)
21. H. Zhou, L. Xu, Z. Ren, J. Zhu and C. Lee, Machine learning-augmented surface-enhanced spectroscopy toward next-generation molecular diagnostics. Nanoscale Adv. **5**, 538–570 (2023)

22. E. Vermisoglou, D. Panáček, K. Jayaramulu, M. Pykal, I. Frébort, M. Kolář, M. Hajdúch, R. Zbořil and M. Otyepka, Human virus detection with graphene-based materials. Biosens. Bioelectron. **166**, 112436 (2020)
23. F. Cui and H. S. Zhou, Diagnostic methods and potential portable biosensors for coronavirus disease 2019. Biosens. Bioelectron. **165**, 112349 (2020)
24. Q. Yu, H. D. Trinh, Y. Lee, T. Kang, L. Chen, S. Yoon and J. Choo, SERS-ELISA using silica-encapsulated Au core-satellite nanotags for sensitive detection of SARS-CoV-2. Sens. Actuators B: Chem. **382**, 133521 (2023)
25. X. Luo, W. Yue, S. Zhang, H. Liu, Z. Chen, L. Qiao, C. Wu, P. Li and Y. He, SARS-CoV-2 proteins monitored by long-range surface plasmon field-enhanced Raman scattering with hybrid bowtie nanoaperture arrays and nanocavities. Lab Chip **23**, 388–399 (2023)
26. J. Sitjar, J.-D. Liao, H. Lee, H.-P. Tsai, J.-R. Wang and P.-Y. Liu, Challenges of SERS technology as a non-nucleic acid or -antigen detection method for SARS-CoV-2 virus and its variants. Biosens. Bioelectron. **181**, 113153 (2021)
27. A. Rahman, S. Kang, W. Wang, A. Garg, A. Maile-Moskowitz and P. J. Vikesland, Nanobiotechnology enabled approaches for wastewater based epidemiology. TrAC, Trends Anal. Chem. **143**, 116400 (2021)
28. A. Pramanik, Y. Gao, S. Patibandla, K. Gates and P. C. Ray, Bioconjugated nanomaterial for targeted diagnosis of SARS-CoV-2. Acc. Mater. Res. **3**, 134–148 (2022)
29. B. Lou, Y. Liu, M. Shi, J. Chen, K. Li, Y. Tan, L. Chen, Y. Wu, T. Wang, X. Liu, T. Jiang, D. Peng and Z. Liu, Aptamer-based biosensors for virus protein detection. TrAC, Trends Anal. Chem. **157**, 116738 (2022)
30. Y. Yang, B. Xu, J. Murray, J. Haverstick, X. Chen, R. A. Tripp and Y. Zhao, Rapid and quantitative detection of respiratory viruses using surface-enhanced Raman spectroscopy and machine learning. Biosens. Bioelectron. **217**, 114721 (2022)
31. J. Lukose, A. K. Barik, N. Mithun, M. Sanoop Pavithran, S. D. George, V. M. Murukeshan and S. Chidangil, Raman spectroscopy for viral diagnostics. Biophys. Rev. **15**, 199–221 (2023)
32. J. Yang, S. Lu, B. Chen, F. Hu, C. Li and C. Guo, Machine learning-assisted optical nano-sensor arrays in microorganism analysis. TrAC, Trends Anal. Chem. **159**, 116945 (2023)
33. C. Spedalieri and J. Kneipp, Surface enhanced Raman scattering for probing cellular biochemistry. Nanoscale **14**, 5314–5328 (2022)
34. S. X. Leong, Y. X. Leong, E. X. Tan, H. Y. F. Sim, C. S. L. Koh, Y. H. Lee, C. Chong, L. S. Ng, J. R. T. Chen, D. W. C. Pang, L. B. T. Nguyen, S. K. Boong, X. Han, Y.-C. Kao, Y. H. Chua, G. C. Phan-Quang, I. Y. Phang, H. K. Lee, M. Y. Abdad, N. S. Tan and X. Y. Ling, Noninvasive and point-of-care surface-enhanced Raman scattering (SERS)-based breathalyzer for mass screening of coronavirus disease 2019 (COVID-19) under 5 min. ACS Nano **16**, 2629–2639 (2022)
35. P.-C. Guan, H. Zhang, Z.-Y. Li, S.-S. Xu, M. Sun, X.-M. Tian, Z. Ma, J.-S. Lin, M.-M. Gu, H. Wen, F.-L. Zhang, Y.-J. Zhang, G.-J. Yu, C. Yang, Z.-X. Wang, Y. Song and J.-F. Li, Rapid point-of-care assay by SERS detection of SARS-CoV-2 virus and its variants. Anal. Chem. **94**, 17795–17802 (2022)
36. M. Mohammadi, D. Antoine, M. Vitt, J. M. Dickie, S. Sultana Jyoti, J. G. Wall, P. A. Johnson and K. E. Wawrousek, A fast, ultrasensitive SERS immunoassay to detect SARS-CoV-2 in saliva. Anal. Chim. Acta **1229**, 340290 (2022)
37. D. Antoine, M. Mohammadi, M. Vitt, J. M. Dickie, S. S. Jyoti, M. A. Tilbury, P. A. Johnson, K. E. Wawrousek and J. G. Wall, Rapid, point-of-care scFv-SERS assay for femtogram level detection of SARS-CoV-2. ACS Sens. **7**, 866–873 (2022)
38. H. Cha, H. Kim, Y. Joung, H. Kang, J. Moon, H. Jang, S. Park, H.-J. Kwon, I.-C. Lee, S. Kim, D. Yong, S.-W. Yoon, S.-G. Park, K. Guk, E.-K. Lim, H. G. Park, J. Choo, J. Jung and T. Kang, Surface-enhanced Raman scattering-based immunoassay for severe acute respiratory syndrome coronavirus 2. Biosens. Bioelectron. **202**, 114008 (2022)
39. V.-T. Nguyen, S. Song, S. Park and C. Joo, Recent advances in high-sensitivity detection methods for paper-based lateral-flow assay. Biosens. Bioelectron. **152**, 112015 (2020)

40. F. Li, M. You, S. Li, J. Hu, C. Liu, Y. Gong, H. Yang and F. Xu, Paper-based point-of-care immunoassays: Recent advances and emerging trends. Biotechnol. Adv. **39**, 107442 (2020)
41. Q. H. Nguyen and M. I. Kim, Nanomaterial-mediated paper-based biosensors for colorimetric pathogen detection. TrAC, Trends Anal. Chem. **132**, 116038 (2020)
42. A. N. Baker, G. W. Hawker-Bond, P. G. Georgiou, S. Dedola, R. A. Field and M. I. Gibson, Glycosylated gold nanoparticles in point of care diagnostics: from aggregation to lateral flow. Chem. Soc. Rev. **51**, 7238–7259 (2022)
43. K. Dighe, P. Moitra, M. Alafeef, N. Gunaseelan and D. Pan, A rapid RNA extraction-free lateral flow assay for molecular point-of-care detection of SARS-CoV-2 augmented by chemical probes. Biosens. Bioelectron. **200**, 113900 (2022)
44. N. Higashi-Kuwata, K. Tsuji, H. Hayashi, H. Bulut, M. Kiso, M. Imai, H. Ogata-Aoki, T. Ishii, T. Kobayakawa, K. Nakano, N. Takamune, N. Kishimoto, S.-i. Hattori, D. Das, Y. Uemura, Y. Shimizu, M. Aoki, K. Hasegawa, S. Suzuki, A. Nishiyama, J. Saruwatari, Y. Shimizu, Y. Sukenaga, Y. Takamatsu, K. Tsuchiya, K. Maeda, K. Yoshimura, S. Iida, S. Ozono, T. Suzuki, T. Okamura, S. Misumi, Y. Kawaoka, H. Tamamura and H. Mitsuya, Identification of SARS-CoV-2 Mpro inhibitors containing P1' 4-fluorobenzothiazole moiety highly active against SARS-CoV-2. Nat. Commun. **14**, 1076 (2023)
45. R. Mothes, A. Pascual-Reguant, R. Koehler, J. Liebeskind, A. Liebheit, S. Bauherr, L. Philipsen, C. Dittmayer, M. Laue, R. von Manitius, S. Elezkurtaj, P. Durek, F. Heinrich, G. A. Heinz, G. M. Guerra, B. Obermayer, J. Meinhardt, J. Ihlow, J. Radke, F. L. Heppner, P. Enghard, H. Stockmann, T. Aschman, J. Schneider, V. M. Corman, L. E. Sander, M.-F. Mashreghi, T. Conrad, A. C. Hocke, R. A. Niesner, H. Radbruch and A. E. Hauser, Distinct tissue niches direct lung immunopathology via CCL18 and CCL21 in severe COVID-19. Nat. Commun. **14**, 791 (2023)
46. K. Jibin, J. S. Prasad, G. Saranya, S. J. Shenoy, K. K. Maiti and R. S. Jayasree, Optically controlled hybrid metamaterial of plasmonic spiky gold inbuilt graphene sheets for bimodal imaging guided multimodal therapy. Biomater. Sci. **8**, 3381–3391 (2020)
47. Z. Li, L. Leustean, F. Inci, M. Zheng, U. Demirci and S. Wang, Plasmonic-based platforms for diagnosis of infectious diseases at the point-of-care. Biotechnol. Adv. **37**, 107440 (2019)
48. Z. Huang, S. Siddhanta, G. Zheng, T. Kickler and I. Barman, Rapid, label-free optical spectroscopy platform for diagnosis of heparin-Induced thrombocytopenia. Angew. Chem., Int. Ed. **59**, 5972–5978 (2020)
49. S. Kim, T. G. Kim, S. H. Lee, W. Kim, A. Bang, S. W. Moon, J. Song, J.-H. Shin, J. S. Yu and S. Choi, Label-free surface-enhanced Raman spectroscopy biosensor for on-site breast cancer detection using human tears. ACS Appl. Mater. Interfaces **12**, 7897–7904 (2020)
50. M. M. Gong and D. Sinton, Turning the page: Advancing paper-based microfluidics for broad diagnostic application. Chem. Rev. **117**, 8447–8480 (2017)
51. C. Wang, M. Liu, Z. Wang, S. Li, Y. Deng and N. He, Point-of-care diagnostics for infectious diseases: From methods to devices. Nano Today **37**, 101092 (2021)
52. H.-K. Huang, H.-W. Cheng, C.-C. Liao, S.-J. Lin, Y.-Z. Chen, J.-K. Wang, Y.-L. Wang and N.-T. Huang, Bacteria encapsulation and rapid antibiotic susceptibility test using a microfluidic microwell device integrating surface-enhanced Raman scattering. Lab Chip **20**, 2520–2528 (2020)
53. J. Jeon, N. Choi, H. Chen, J.-I. Moon, L. Chen and J. Choo, SERS-based droplet microfluidics for high-throughput gradient analysis. Lab Chip **19**, 674–681 (2019)
54. R. Gao, Z. Cheng, X. Wang, L. Yu, Z. Guo, G. Zhao and J. Choo, Simultaneous immunoassays of dual prostate cancer markers using a SERS-based microdroplet channel. Biosens. Bioelectron. **119**, 126–133 (2018)
55. R. Gao, Z. Cheng, A. J. deMello and J. Choo, Wash-free magnetic immunoassay of the PSA cancer marker using SERS and droplet microfluidics. Lab Chip **16**, 1022–1029 (2016)
56. Y. Joung, S. Park, B. Kang and J. Choo, Toward rapid and sensitive point-of-care diagnosis with surface-enhanced Raman scattering-based optofluidic systems. Bull. Korean Chem. Soc. **44**, 718–727 (2023)

57. N. Choi, J. Lee, J. Ko, J. H. Jeon, G.-e. Rhie, A. J. deMello and J. Choo, Integrated SERS-based microdroplet platform for the automated immunoassay of F1 antigens in Yersinia pestis. Anal. Chem. **89**, 8413–8420 (2017)
58. S. Lee, L. Bi, H. Chen, D. Lin, R. Mei, Y. Wu, L. Chen, S.-W. Joo and J. Choo, Recent advances in point-of-care testing of COVID-19. Chem. Soc. Rev. **52**, 8500–8530 (2023)
59. S. Park, C. Su Jeon, N. Choi, J.-I. Moon, K. Min Lee, S. Hyun Pyun, T. Kang and J. Choo, Sensitive and reproducible detection of SARS-CoV-2 using SERS-based microdroplet sensor. Chem. Eng. J. **446**, 137085 (2022)
60. X. Wang, S.-G. Park, J. Ko, X. Xiao, V. Giannini, S. A. Maier, D.-H. Kim and J. Choo, Sensitive and reproducible immunoassay of multiple mycotoxins using surface-enhanced Raman scattering mapping on 3D plasmonic nanopillar arrays. Small **14**, 1801623 (2018)
61. A. Das, K. Kim, S.-G. Park, N. Choi and J. Choo, SERS-based serodiagnosis of acute febrile diseases using plasmonic nanopopcorn microarray platforms. Biosens. Bioelectron. **192**, 113525 (2021)
62. H. Chen, S.-G. Park, N. Choi, H.-J. Kwon, T. Kang, M.-K. Lee and J. Choo, Sensitive detection of SARS-CoV-2 using a SERS-based aptasensor. ACS Sens. **6**, 2378–2385 (2021)
63. H. Chen, S.-G. Park, N. Choi, J.-I. Moon, H. Dang, A. Das, S. Lee, D.-G. Kim, L. Chen and J. Choo, SERS imaging-based aptasensor for ultrasensitive and reproducible detection of influenza virus A. Biosens. Bioelectron. **167**, 112496 (2020)
64. S.-G. Park, C. Mun, X. Xiao, A. Braun, S. Kim, V. Giannini, S. A. Maier and D.-H. Kim, Surface energy-controlled SERS substrates for molecular concentration at plasmonic nanogaps. Adv. Funct. Mater. **27**, 1703376 (2017)
65. S.-G. Park, X. Xiao, J. Min, C. Mun, H. S. Jung, V. Giannini, R. Weissleder, S. A. Maier, H. Im and D.-H. Kim, Self-assembly of nanoparticle-spiked pillar arrays for plasmonic biosensing. Adv. Funct. Mater. **29**, 1904257 (2019)
66. H. Dang, Y. Joung, C. Jeong, C. S. Jeon, S. H. Pyun, S.-G. Park and J. Choo, Nanoplasmonic assay platforms for reproducible SERS detection of Alzheimer's disease biomarker. Bull. Korean Chem. Soc. **44**, 441–448 (2023)
67. G. Huang, H. Zhao, P. Li, J. Liu, S. Chen, M. Ge, M. Qin, G. Zhou, Y. Wang, S. Li, Y. Cheng, Q. Huang, J. Wang, H. Wang and L. Yang, Construction of optimal SERS hotspots based on capturing the spike receptor-binding domain (RBD) of SARS-CoV-2 for highly sensitive and specific detection by a Fish model. Anal. Chem. **93**, 16086–16095 (2021)
68. M. Zhang, X. Li, J. Pan, Y. Zhang, L. Zhang, C. Wang, X. Yan, X. Liu and G. Lu, Ultrasensitive detection of SARS-CoV-2 spike protein in untreated saliva using SERS-based biosensor. Biosens. Bioelectron. **190**, 113421 (2021)
69. J.-H. Choi, M. Shin, L. Yang, B. Conley, J. Yoon, S.-N. Lee, K.-B. Lee and J.-W. Choi, Clustered regularly interspaced short palindromic repeats-mediated amplification-free detection of viral DNAs using surface-enhanced Raman spectroscopy-active nanoarray. ACS Nano **15**, 13475–13485 (2021)
70. T. D. Payne, S. J. Klawa, T. Jian, S. H. Kim, M. J. Papanikolas, R. Freeman and Z. D. Schultz, Catching COVID: Engineering peptide-modified surface-enhanced Raman spectroscopy sensors for SARS-CoV-2. ACS Sens. **6**, 3436–3444 (2021)
71. D. P. dos Santos, M. M. Sena, M. R. Almeida, I. O. Mazali, A. C. Olivieri and J. E. L. Villa, Unraveling surface-enhanced Raman spectroscopy results through chemometrics and machine learning: principles, progress, and trends. Anal. Bioanal. Chem. **415**, 3945–3966 (2023)
72. M. Chen, D. Cui, H. Haick and N. Tang, Artificial intelligence-based medical sensors for healthcare system. Adv. Sens. Res. **3**, 2300009 (2023)
73. B. A. Taha, Y. Al Mashhadany, Q. Al-Jubouri, A. R. B. A. Rashid, Y. Luo, Z. Chen, S. Rustagi, V. Chaudhary and N. Arsad, Next-generation nanophotonic-enabled biosensors for intelligent diagnosis of SARS-CoV-2 variants. Sci. Total Environ. **880**, 163333 (2023)
74. M. Chisanga, H. Williams, D. Boudreau, J. N. Pelletier, S. Trottier and J.-F. Masson, Label-free SERS for rapid differentiation of SARS-CoV-2-induced serum metabolic profiles in non-hospitalized adults. Anal. Chem. **95**, 3638–3646 (2023)

75. H. Torun, B. Bilgin, M. Ilgu, N. Batur, M. Ozturk, T. Barlas, G. Guney-Esken, C. Yanik, S. Celik, O. Dogan, O. Ergonul, F. Can, I. Solaroglu and M. C. Onbasli, Rapid nanoplasmonic-enhanced detection of SARS-CoV-2 and variants on DNA aptamer metasurfaces. Adv. Devices Instrum. **4**, 0008 (2023)
76. Z. Zhang, S. Jiang, X. Wang, T. Dong, Y. Wang, D. Li, X. Gao, Z. Qu and Y. Li, A novel enhanced substrate for label-free detection of SARS-CoV-2 based on surface-enhanced Raman scattering. Sens. Actuators B: Chem. **359**, 131568 (2022)
77. V. Karunakaran, M. M. Joseph, I. Yadev, H. Sharma, K. Shamna, S. Saurav, R. P. Sreejith, V. Anand, R. Beegum, S. Regi David, T. Iype, K. L. Sarada Devi, A. Nizarudheen, M. S. Sharmad, R. Sharma, R. Mukhiya, E. Thouti, K. Yoosaf, J. Joseph, P. Sujatha Devi, S. Savithri, A. Agarwal, S. Singh and K. K. Maiti, A non-invasive ultrasensitive diagnostic approach for COVID-19 infection using salivary label-free SERS fingerprinting and artificial intelligence. J. Photochem. Photobiol., B **234**, 112545 (2022)
78. F. U. Ciloglu, A. Caliskan, A. M. Saridag, I. H. Kilic, M. Tokmakci, M. Kahraman and O. Aydin, Drug-resistant Staphylococcus aureus bacteria detection by combining surface-enhanced Raman spectroscopy (SERS) and deep learning techniques. Sci. Rep. **11**, 18444 (2021)
79. E. Ikponmwoba, O. Ukorigho, P. Moitra, D. Pan, M. R. Gartia and O. Owoyele, A machine learning framework for detecting COVID-19 infection using surface-enhanced Raman scattering. Biosensors **12**, 589 (2022)
80. K. Zhang, Z. Wang, H. Liu, N. Perea-López, J. C. Ranasinghe, G. Bepete, A. M. Minns, R. M. Rossi, S. E. Lindner, S. X. Huang, M. Terrones and S. Huang, Understanding the excitation wavelength dependence and thermal stability of the SARS-CoV-2 receptor-binding domain using surface-enhanced Raman scattering and machine learning. ACS Photonics **9**, 2963-2972 (2022)
81. Y. Yang, Y. Peng, C. Lin, L. Long, J. Hu, J. He, H. Zeng, Z. Huang, Z.-Y. Li, M. Tanemura, J. Shi, J. R. Lombardi and X. Luo, Human ACE2-functionalized gold "virus-trap" nanostructures for accurate capture of SARS-CoV-2 and single-virus SERS detection. Nano-Micro Lett. **13**, 109 (2021)
82. D. Paria, K. S. Kwok, P. Raj, P. Zheng, D. H. Gracias and I. Barman, Label-free spectroscopic SARS-CoV-2 detection on versatile nanoimprinted substrates. Nano Lett. **22**, 3620–3627 (2022)
83. Y. Yang, H. Li, L. Jones, J. Murray, J. Haverstick, H. K. Naikare, Y.-Y. C. Mosley, R. A. Tripp, B. Ai and Y. Zhao, Rapid detection of SARS-CoV-2 RNA in human nasopharyngeal specimens using surface-enhanced Raman spectroscopy and deep learning algorithms. ACS Sens. **8**, 297–307 (2023)
84. H. Yu, Z. Yang, S. Fu, Y. Zhang, R. Panneerselvamc, B. Li, L. Zhang, Z. Chen, X. Wang and J. Li, Intelligent convolution neural network-assisted SERS to realize highly accurate identification of six pathogenic Vibrio. Chem. Commun. **59**, 5779–5782 (2023)
85. E. Rho, M. Kim, S. H. Cho, B. Choi, H. Park, H. Jang, Y. S. Jung and S. Jo, Separation-free bacterial identification in arbitrary media via deep neural network-based SERS analysis. Biosens. Bioelectron. **202**, 113991 (2022)
86. F. Safir, N. Vu, L. F. Tadesse, K. Firouzi, N. Banaei, S. S. Jeffrey, A. A. E. Saleh, B. T. Khuri-Yakub and J. A. Dionne, Combining acoustic bioprinting with AI-assisted Raman spectroscopy for high-throughput identification of bacteria in blood. Nano Lett. **23**, 2065–2073 (2023)

# Part IV
# TERS Studies

# Chapter 22
# Ångström-Resolved Tip-Enhanced Raman Spectroscopy




**Yao Zhang and Zhen-Chao Dong**

**Abstract** This chapter describes the principle and application of Ångström-resolved tip-enhanced Raman spectroscopy (TERS). The theoretical background for TERS, particularly regarding the origin of ultrahigh spatial resolution, is briefly introduced from several different aspects, namely from plasmonic nanocavity to picocavity, from single molecules to single chemical bonds, and from electromagnetic to chemical enhancement. Then we describe the experimental setups for single-molecule TERS measurements, including the technical details of sample preparation and optic measurements as well as the fabrication and judgement of TERS-active tips. This is followed by a detailed account on recent advances in single-molecule TERS, mainly from three aspects: (1) imaging a single molecule with subnanometer resolution; (2) resolving single chemical bonds and their making and breaking processes, including chemical structure reconstruction through scanning Raman picoscopy, tracking bond making and breaking processes in surface reactions, and anti-Stokes Raman thermometry in a single molecule; and (3) applications in 2D materials. The conclusion and future outlook of the Ångström-resolved TERS technique are briefly described at the end of this chapter.

**Keywords** Tip-enhanced Raman spectroscopy · Single molecule · Single chemical bond · Ångström resolution · Raman thermometry

## 22.1 Introduction of Theoretical Background

Different from the surface-enhanced Raman spectroscopy (SERS), the invention of tip-enhanced Raman spectroscopy (TERS) by introducing a probing tip above the sample provides an additional dimension to control plasmonic hot-spot properties and

Y. Zhang · Z.-C. Dong (✉)
Hefei National Research Center for Physical Sciences at the Microscale, University of Science and Technology of China, Hefei, China
e-mail: zcdong@ustc.edu.cn

Hefei National Laboratory, University of Science and Technology of China, Hefei, China

© The Author(s), under exclusive license to Springer Nature Singapore Pte Ltd. 2024

M. Procházka et al. (eds.), *Surface- and Tip-Enhanced Raman Scattering Spectroscopy*,
https://doi.org/10.1007/978-981-97-5818-0_22

interactions with single molecules [1–5]. In this combined technique of a scanning probe microscope (SPM) with a Raman spectrometer, both the vertical field enhancement and the lateral position of the hot spot can be precisely controlled by directly tuning the nano-gap distances and tip positions [2, 3]. Although the concept of TERS was first proposed in 1985 [6], the first experimental demonstrations of TERS were achieved independently in 2000 by the groups of Zenobi, Kawata, Anderson, and Pettinger [7–10]. After two decades of development, TERS has become a powerful technique that can offer both exceptional sensitivity for chemical specificity and high spatial resolution at the subnanometer sub-molecular scale [11, 12]. Recent advancements in TERS have even pushed the spatial resolution down to the Angström level, enabling to probe the intramolecular structure at the single-chemical-bond limit [13–17]. In this section, we shall briefly introduce the basic concepts and principles underlying ultrahigh-resolution TERS studies.

### *22.1.1 From Plasmonic Nanocavity to Picocavity*

Thanks to the strongly confined and enhanced local plasmonic field at the apex of a metallic probing tip in the near-field region, the Abbe diffraction limit [18] in the far-field measurement is no longer valid, and the spatial resolution of TERS is only limited by the nano-gap morphologies and materials [19], which can even go down to the atomistic scale through the use of atomistic protrusions at the tip apex [20, 21]. As shown in Fig. 22.1, the far-field incident light is first scattered by the shaft of the tip to convert the light into the near-field surface plasmon propagating along the tip surface toward the tip apex. Then the tip apex plays a role as a local scatter to convert the propagating surface plasmon to the highly confined local plasmon, known as the nanocavity plasmon (NCP) mode [1–3]. The localized NCPs are further enhanced and concentrated by the atomic-scale protrusion due to the "atomistic lightning rod effect" [22], successively focusing the free-space light into the picocavity at the atomistic scale.

Based on the classical electromagnetic theory, the spatial resolution of TERS can be roughly estimated from the spatial confinement of the local field [2, 23–30]. For an individual metal tip with the permittivity $\varepsilon_m$, the local-field enhancement can be obtained from the tip radius ($R$) and the distance of the sample to the tip apex ($z$) as $|\mathbf{E}_{loc}|/|\mathbf{E}_{inc}| \propto (\varepsilon_m - 1)/(\varepsilon_m + 2)\left[R/(R+z)\right]^3$, and the local-field confinement ($w$) can be estimated via $w \propto R+z$ [31]. Therefore, the spatial resolution of TERS can be improved by decreasing the curvature radius of the tip. However, a smaller radius of the tip would also result in the decreasing in the local-field enhancement, making it as a dilemma for achieving both the strong enhancement and the high confinement in TERS. By further introducing a metal substrate with a tip-substrate gap distance $d$ to generate the gap-plasmon mode, the local electric field can be enhanced following

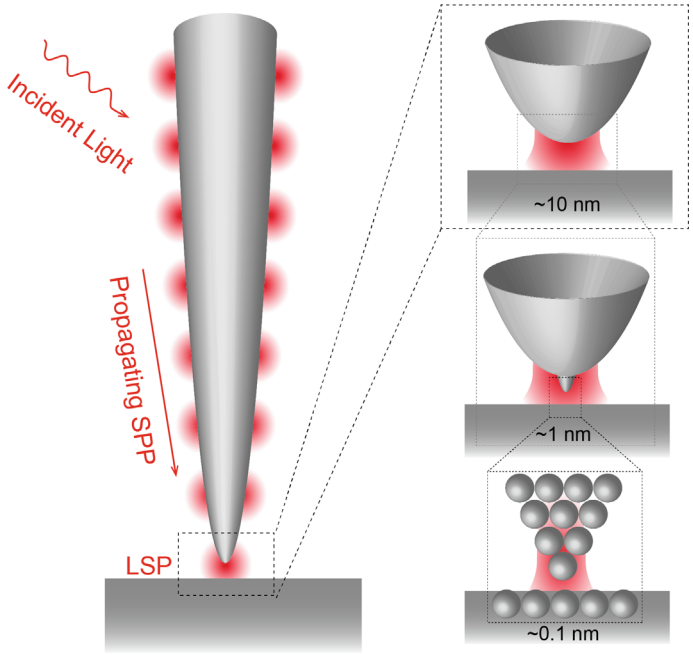



**Fig. 22.1** Schematic of local plasmonic field confinement from an isolated tip to a nanocavity and further to an atomistic picocavity. Reproduced from Ref. [1] with permission

the relation $|\mathbf{E}_{\text{loc}}|/|\mathbf{E}_{\text{inc}}| \propto \left[(2R+d)/d\right]^3$, and the field confinement ($w$) can be estimated by $w \propto \sqrt{Rd}$ [31]. Therefore, reducing the gap distance alone can also dramatically improve both the signal enhancement and spatial resolution of TERS even when the tip apex is not sharp enough.

Further improvement in the local-field confinement can be achieved via the localization of electromagnetic fields in close proximity to the atomistic structures within the nanocavities [22, 32–34]. As shown in Fig. 22.2, the initially enhanced local plasmonic field serves as a background, and in analogy to the classical macroscopic "lightning rod effect" in which the field can be enhanced due to the large curvature of a metallic interface, the atomistic protrusion would produce an additional enhancement of the local electric field over the background through the "atomic-scale lightning rod effect" [22]. Therefore, the enhanced local plasmonic fields would be very sensitive to the single-atom placement, especially in the subnanometer region [32, 35]. Based on the simulations from both the classical and quantum theories, the induced plasmonic fields are localized in an effective mode volume less than a cubic nanometer [36], thus providing high spatial resolution in TERS studies at the submolecular or even Ångström scale. Such an atomic sensitivity of the picocavity has been demonstrated experimentally through the activation of surface atoms to become mobile and protrude out of the metal surface by shining an intense laser power to the plasmonic nanocavities, resulting the fluctuations in TERS signals [32]. The

controlled gentle indentations between the metal tip and substrate can also generate an atomistic protrusion at the tip apex, and the picocavity thus formed can be stabilized once the system is cooled down to cryogenic temperatures and the incident laser power is kept low to avoid thermal diffusions [1, 13, 14, 20, 37]. The cascaded enhancement mentioned above implies that the formation of an effective picocavity for high-resolution spectromicroscopy demands not only the formation of appropriate atomistic protrusions at the tip apex, but also effective coupling between the protrusion and gap modes induced by the tip shaft [22]. Although the nonresonant "lightning rod effect" alone, without the plasmonic substrate, could also account for the main functionality of the picocavity, it was reported that when the incident photon is resonant with the hybridized protrusion modes, the field intensity and spatial confinement are greatly enhanced due to the resonant accumulation of conduction electrons around the atomistic protrusion [21, 38, 39].

However, the spatial resolution is unlikely to be improved down to the sub-Ångström level because of the quantum effects involved. Within a local electromagnetic response model, the induced electron charges are assumed to distribute on a layer of infinitesimal thickness on the metal surface. However, in real metals, the electron densities would smear outside the ideal metal surface slightly. Such an electron spill-out effect would restrict the further improvement of spatial resolution [40, 41]. Due to such a plasmonic nonlocal effect, the spatial resolution is said to be limited by a Thomas–Fermi screening length of approximately 0.1 nm [42, 43]. On the other hand, the quantum tunneling effect in the subnanometer gap could significantly change the optical response and even quench the electric field enhancements [41]. Moreover, when the size of a nanoparticle becomes small, the electron scattering at the surface could reduce the surface plasmon mean free path, thus increasing the decay of plasmons into electron–hole pairs, a process known as the Landau damping [44–47]. Owing to the extremely small size of an atomistic protrusion, Landau damping could be a significant factor that may quench the optical fields around the protrusion and thus limit the field intensity in the picocavities [46, 48, 49]. Fortunately, a recent theoretical work by Li et al. has shown that the coupling of the protrusion modes to the host modes will accelerate the radiation rate of the former so that it can compete with the intrinsic Landau damping [38].

### *22.1.2 From Single Molecules to Single Chemical Bonds*

For a molecule under the illumination of an incident light, the optical response of the molecule can be described as a polarized dipole moment $\mathbf{p}^{\mathrm{mol}} = \alpha^{\mathrm{mol}}\mathbf{E}_{\mathrm{loc}}\left(\mathbf{r}^{\mathrm{mol}}\right)$, where $\alpha^{\mathrm{mol}}$ is the polarizability of the molecule, and $\mathbf{E}_{\mathrm{loc}}$ is the local electric field at the molecular position $\mathbf{r}^{\mathrm{mol}}$. If the size of the molecule is quite small when compared with the local-field distributions, it is reasonable to assume the single molecule as a point dipole and to describe the responses of the molecule by the polarizability. However, for the local electric fields inside a nanocavity that are extremely confined, the size of the local-field distribution is comparable to or even smaller than the molecular

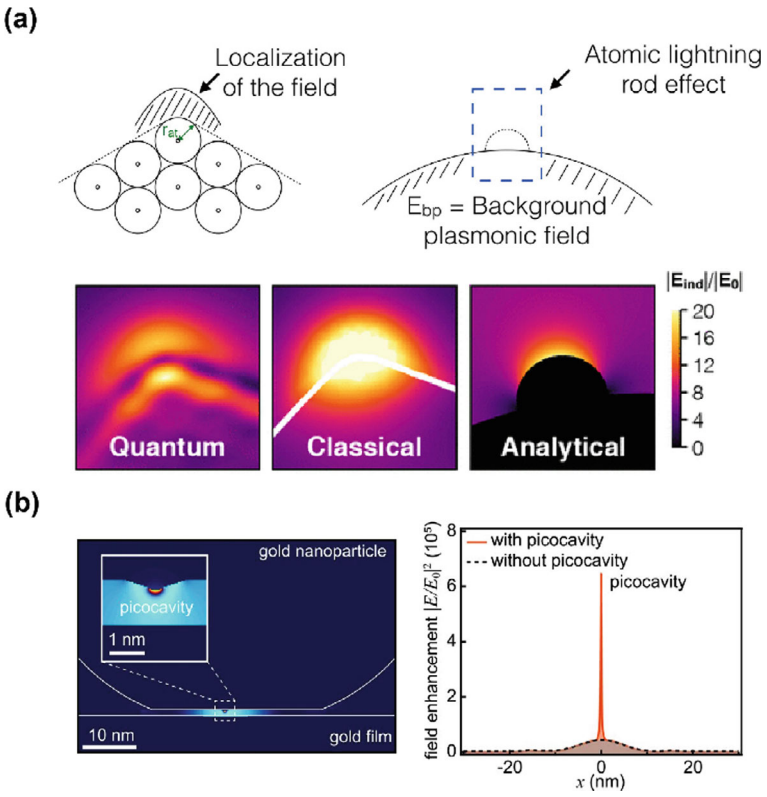



**Fig. 22.2 Local electric field distributions in plasmonic picocavities**. **a** Sketch showing one apex out of an icosahedral atomistic nanoparticle (circles represent atoms) and an atomistic protrusion on a spherical nanoparticle that produces an atomic lightning rod effect, enhancing the background plasmonic field given by the spherical nanoparticle. Comparisons between the quantum, classical, and analytical simulation results of local electric fields are also shown in the lower sub-panels, exhibiting a similar feature in both field intensities and spatial distributions. Reproduced from Ref. [22] with permission. **b** Simulated local electric field distribution in the picocavity with an atomistic protrusion, providing high spatial resolution for the optical studies at the sub-molecular or even Ångström scale. Reproduced from Ref. [32] with permission

size, even down to the atomistic level for picocavities. In this situation, the point-dipole approximation would not be valid, and different atoms inside a molecule may experience different polarizations induced by the extremely localized and highly inhomogeneous near field. Thus, the spatial distribution of the local electric field $\mathbf{E}_{\mathrm{loc}}(\mathbf{r})$ should be taken into account when considering the polarized molecular dipole moment as follows [14, 16, 50, 51]

$$\mathbf{p}^{\mathrm{mol}} = \frac{1}{\hbar}\sum_{r\neq i,f}\left\{\frac{\langle\Psi_f|\hat{\mathbf{p}}|\Psi_r\rangle\langle\Psi_r|\hat{\mathbf{p}}\cdot\mathbf{E}_{\mathrm{loc}}(\mathbf{r})|\Psi_i\rangle}{\omega_{ri}-\omega} + \frac{\langle\Psi_f|\hat{\mathbf{p}}\cdot\mathbf{E}_{\mathrm{loc}}(\mathbf{r})|\Psi_r\rangle\langle\Psi_r|\hat{\mathbf{p}}|\Psi_i\rangle}{\omega_{ri}+\omega}\right\}, \tag{22.1}$$

where $\hbar$ is Planck's constant, $\Psi_{i(r,f)}$ is the molecular wavefunction of the initial (intermediate, final) state, $\omega_{ri}(rf)$ is the transition energy between state $r$ and state $i(f)$, and $\omega$ is the frequency of the incident light. Under the point-dipole approximation, the molecule can be assumed in a homogeneous field, and the molecular polarizability $\alpha^{\mathrm{mol}}_{\rho\sigma}$ can be generally defined as [52]

$$\alpha^{\mathrm{mol}}_{\rho\sigma} = \frac{1}{\hbar}\sum_{r\neq i,f}\left\{\frac{\langle\Psi_f|\hat{p}_\rho|\Psi_r\rangle\langle\Psi_r|\hat{p}_\sigma|\Psi_i\rangle}{\omega_{ri}-\omega} + \frac{\langle\Psi_f|\hat{p}_\sigma|\Psi_r\rangle\langle\Psi_r|\hat{p}_\rho|\Psi_i\rangle}{\omega_{ri}+\omega}\right\}, \tag{22.2}$$

where $\rho(\sigma)$ refers to the $x$-, $y$-, or $z$-component of transition dipole moment operator $\hat{\mathbf{p}}$. For the Raman scattering process, the contributions from molecular vibrations enter through the series expansion of the above integral term as

$$\langle\Psi_r|\cdots|\Psi_i\rangle = \langle\psi_r|\cdots|\psi_i\rangle\langle v'_r|v_i\rangle + \sum_k\left(\frac{\partial\langle\psi_r|\cdots|\psi_i\rangle}{\partial Q_k}\right)_0\langle v'_r|\hat{Q}_k|v_i\rangle. \tag{22.3}$$

Here, $|\psi_{i(r)}\rangle$ is the molecular electronic wavefunction of the initial (or intermediate) state, $|v_i(v'_r)\rangle$ is the molecular vibrational wavefunction of the initial (or intermediate) state, and $Q_k$ is the normal coordinate of the $k$-th vibrational mode. By substituting Eq. (22.3) into Eq. (22.1) and transforming the coordinates from the normal-mode coordinates ($Q_k$) to the atomic Cartesian coordinates ($\xi^{(n)}$), we can attribute the polarized molecular dipole moment associated with the $k$-th vibrational mode to the contributions from individual atoms within the molecule, with the assumption that only the local electronic wavefunctions near the vibrating atoms play a dominant role [14, 51],

$$\mathbf{p}_k = \sqrt{\frac{\hbar}{2\mu_k\omega_k}}\sum_n\phi_k^{(n)}\left(\frac{\partial\alpha}{\partial\xi^{(n)}}\right)_0\mathbf{E}_{\mathrm{loc}}(\mathbf{r}_n) \equiv \sum_n\mathbf{p}_{n,k}, \tag{22.4}$$

where $\mathbf{E}^{\mathrm{loc}}(\mathbf{r}_n)$ is the local electric field at the position of atom $n$. The final TERS intensity can be obtained through the emission of such a polarized molecular dipole that is further scattered by the nanocavity acting as a nano-antenna through the Green's function $\overleftrightarrow{\mathbf{G}}_k(\mathbf{r}_\infty, \mathbf{r}_n)$. As a result, the Raman scattering cross section can be expressed as the contribution from each atomic polarized dipole $\mathbf{p}_{n,k}$ as follows [52]

$$\frac{d\sigma_k}{d\Omega} \propto \left|\sum\overleftrightarrow{\mathbf{G}}_k(\mathbf{r}_\infty, \mathbf{r}_n)\mathbf{p}_{n,k}\right|^2. \tag{22.5}$$

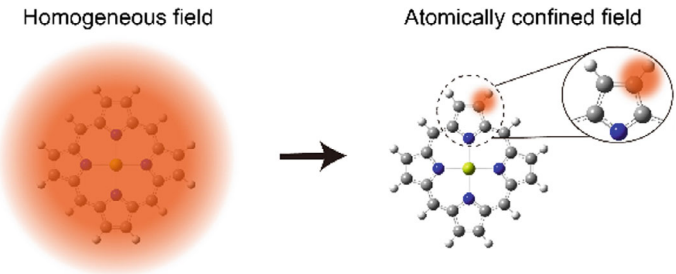



**Fig. 22.3** Schematic of different situations of a single molecule from a homogeneous field to an atomically localized field. Reproduced from Ref. [52] with permission

In other words, only the atomic vibrations within the local-field region would contribute dominantly to the TERS signals from a single molecule. Considering the relation between the dipole moment $\mathbf{p}$ and the electronic density $\rho$ as $\mathbf{p} = -\int \rho \mathbf{r} d\mathbf{r}$, if there is only one single bond located in the near-field region, as exemplified in Fig. 22.3 for the stretching vibration of a C–H bond in a porphyrin molecule, the compression of the bond length would result in the increase of the local electronic density ($\rho$), while the stretching would result in a decrease in $\rho$, thus the polarizability derivatives can be obtained as [52]

$$\frac{\partial \alpha}{\partial \xi^{(n)}} = \frac{\partial^2 \mathbf{p}}{\partial \mathbf{E} \partial \xi^{(n)}} = -\int \frac{\partial}{\partial \mathbf{E}} \left[ \frac{\partial \rho}{\partial \xi^{(n)}} \right] \mathbf{r} d\mathbf{r}. \tag{22.6}$$

Therefore, the real-space perturbation of different chemical-bond vibrations (including amplitudes and phases) on the electronic densities can interfere with each other, resulting in different TERS signal intensities and spatial mapping images for different vibrational modes. For example, for the symmetric stretching mode of two adjacent C–H bonds in a "boat-like" configuration, the vibrational contributions from the two bonds will sum up and generate a constructive interference, while for the anti-symmetric stretching mode, the contributions from the two bonds will cancel out each other, resulting in a destructive TERS signal [14, 52]. Therefore, by confining the electric field at the atomic scale, the Raman signals from single chemical bonds and even the phase relations between the vibrations of neighboring bonds can be directly visualized by TERS mapping in real space.

### *22.1.3 From Electromagnetic Enhancement to Chemical Enhancement*

In the above discussion, only the electromagnetic enhancement mechanism of TERS signals due to the excitation of localized surface plasmonic fields is considered for the Raman signal enhancement. Such an electromagnetic enhancement, also often

called as the physical enhancement, usually plays a dominant role in the TERS signal enhancement and has been understood thoroughly [53–62]. Briefly speaking, as discussed in Sects. 22.1.1 and 22.1.2, the total electromagnetic Raman enhancement is contributed from two processes: One is the excitation enhancement ($M_{\mathrm{exc}}$) by converting the incident plane wave ($\mathbf{E}_{\mathrm{inc}}$) into the localized plasmonic field ($\mathbf{E}_{\mathrm{loc}}$) inside the nanocavity, the other is the emission enhancement ($M_{\mathrm{em}}$) from the polarized molecule due to the modulation of photon emission behaviors through the optical antenna effect [63]. Thus, the total electromagnetic Raman enhancement factor can be expressed as

$$M_{EM}(Q_k) = M_{\mathrm{exc}}(\omega_{\mathrm{exc}})M_{\mathrm{em}}(\omega_{\mathrm{em}}) = \left|\frac{\mathbf{E}_{\mathrm{loc}}(\omega_{\mathrm{exc}})}{\mathbf{E}_{\mathrm{inc}}(\omega_{\mathrm{exc}})}\right|^2 \times \left|\frac{\mathbf{E}_{\mathrm{loc}}(\omega_{\mathrm{em}})}{\mathbf{E}_{\mathrm{inc}}(\omega_{\mathrm{em}})}\right|^2. \tag{22.7}$$

If ignoring the enhancement difference caused by different frequencies between the excitation and emission processes, one can obtain the so-called $|E|^4$ rule as an approximation of the enhancement factor for TERS and SERS, where $|E|$ is the local electric field strength at the molecular position [63, 64].

However, it is well known that, apart from the physical enhancement described above, TERS/SERS usually also contains contributions from the chemical effects, often called as the chemical enhancement. The chemical mechanism is caused by the molecule–substrate interaction, which often involves charge-transfer (CT) processes. Although the electromagnetic mechanism usually makes dominant contributions to SERS/TERS enhancement, the chemical mechanism can often add additional enhancement and even change the spectral features considerably, including the peak positions and their relative intensities. Despite nearly half a century of extensive researches [58, 65–77], the exact mechanism of chemical effects on Raman signals is still inconclusive due to the complexities in chemical contributions that depend on many factors such as chemical properties of the molecule and substrate under study, molecular adsorption configurations as well as the molecule–substrate hybridization strength, apart from the excitation wavelength. The situation gets even more difficult since the chemical and electromagnetic mechanisms usually coexist and the chemical enhancement often contributes only a relatively small fraction to the total enhancement, making it challenging to clearly separate out the chemical enhancement. Since conventional SERS techniques are difficult to precisely control and characterize the local interactions around a single molecule, well-defined single-molecule TERS could provide an effective platform to this end, allowing to unravel the chemical enhancement mechanisms in TERS/SERS.

In 2023, Dong's group utilized the single-molecule TERS technique at ultrahigh-vacuum and cryogenic conditions to investigate the influence mechanism of chemical effects through the changes in the Raman response of a single zinc-phthalocyanine (ZnPc) molecule under different contact environments [78]. As shown in Fig. 22.4, by elaborately designing and constructing four different well-defined single-molecule contact environments, they find that both chemical enhancement and quenching phenomena can be observed in TERS spectra depending on the contact nature around

a single molecule. For example, the "weak" face contact between the planar ZnPc molecule and NaCl substrate (Configuration 1 in Fig. 22.4a) keeps the molecule in a nearly unperturbed state, showing very similar spectral fingerprints with those of a powder sample. On the other hand, the tip–molecule point contact (Configuration 2 in Fig. 22.4a) for the electronically decoupled molecule can significantly enhance TERS intensities while preserving most of intrinsic molecule-specific features. On the other hand, the "strong" molecule–substrate face contact (Configuration 3 in Fig. 22.4b) between the chemisorbed ZnPc molecule and Ag substrate is found to strongly quench TERS signals, particularly for in-plane vibrational modes. They attribute the additional enhancement upon making a weak tip–molecule point contact to a combined physico-chemical effect, namely the generation of a ground-state charge-transfer (GSCT)-induced vertical Raman polarizability that is further enhanced by the strong vertical plasmonic field. Specifically, the TERS intensity can be approximated as $|E|^4 \times |\partial\alpha/\partial Q_k|^2$, and the enhancement factor due to the tip–molecule point contact can be expressed as [78]

$$M_{\mathrm{CT}}(Q_k) = \frac{I_{\mathrm{tip-mol}}(Q_k)}{I_{\mathrm{mol}}(Q_k)} \approx \frac{|E_\perp|^4}{|E_\parallel|^4} \times \frac{\left|\partial\tilde{\alpha}_\perp / \partial Q_k\right|^2}{\left|\partial\tilde{\alpha}_\parallel / \partial Q_k\right|^2} \tag{22.8}$$

Equation (22.8) suggests that the TERS enhancement induced by the tip–molecule point contact is a combined effect of both electromagnetic contribution (from the difference between the vertical and horizontal electric fields) and chemical contribution (from the different influence on the vertical and horizontal polarizabilities). Such an enhancement mechanism, evidently not a purely chemical effect, is also different

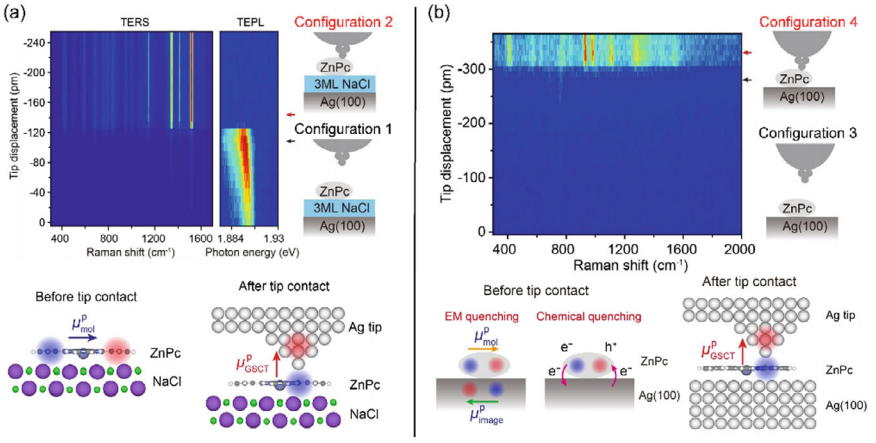



**Fig. 22.4 TERS studies of the chemical effect of a single ZnPc molecule on either the dielectric NaCl and or Ag(100) surface with four different configurations**. **a** TERS enhancement with the tip-molecule point contact for a single ZnPc molecule on NaCl due to the GSCT effect. **b** Quenching of TERS signals induced by the face contact with a metal substrate due to IDCT effect. Reproduced from Ref. [78] with permission

from the prevailing belief that a resonance charge-transfer (RCT) mechanism is dominant in the chemical enhancement process. In the RCT mechanism, the wavelength of the excitation laser is resonant with the molecule–metal charge-transfer transition, while in GSCT, the charge-transfer-induced interaction is not associated with any excitation of the molecule–metal complex.

On the other hand, the quenching effect upon making "strong" molecule–substrate face contacts is mainly attributed to the Raman polarizability screening effect induced by interfacial dynamic charge transfer (IDCT). Moreover, the quenched signals can be "rescued" by an additional tip–molecule point contact, as shown in Configuration 4 in Fig. 22.4b, due to the combined effect of the GSCT-induced physicochemical mechanism described above. It is worth noting that the tip–molecule point contact under the off-resonance scheme is found to offer an exceptionally large CT enhancement over 300 in addition to the plasmonic enhancement, which provides an attractive approach to chemically identify surface species with high sensitivity, particularly useful for off-resonance Raman studies or for molecules whose intrinsic Raman signals are weak.

## 22.2 Experimental Setups

Having introduced the basic concepts and principles underlying ultrahigh-resolution TERS studies, we now describe typical experimental setups for single-molecule TERS typically adopted in our laboratory. These include technical details of both single-molecule sample preparation and optic measurements. The fabrication and justification of TERS-active tips are also discussed in detail since the tip quality is the key to successful TERS experiments, particularly for those with spatial resolution down to subnanometer scale.

### *22.2.1 Technical Details in Single-Molecule TERS Measurements*

Typical experimental setups for single-molecule TERS measurements in our laboratory are shown in Fig. 22.5, containing a low-temperature ultrahigh vacuum (UHV) scanning tunneling microscope (STM) and a photon collection and detection system for the Raman spectral measurements in a confocal-type side illumination configuration [11, 14]. The low-temperature and ultrahigh vacuum is quite crucial for the single-molecule TERS measurements. Under UHV conditions, both the tip and sample surface can be maintained clean to avoid serious contamination in ambient conditions, thus enhancing the stability of the tip–sample junction. In addition, clean molecular samples can be prepared via vacuum deposition onto surfaces with a controlled coverage, which is particularly important for well-defined single-molecule

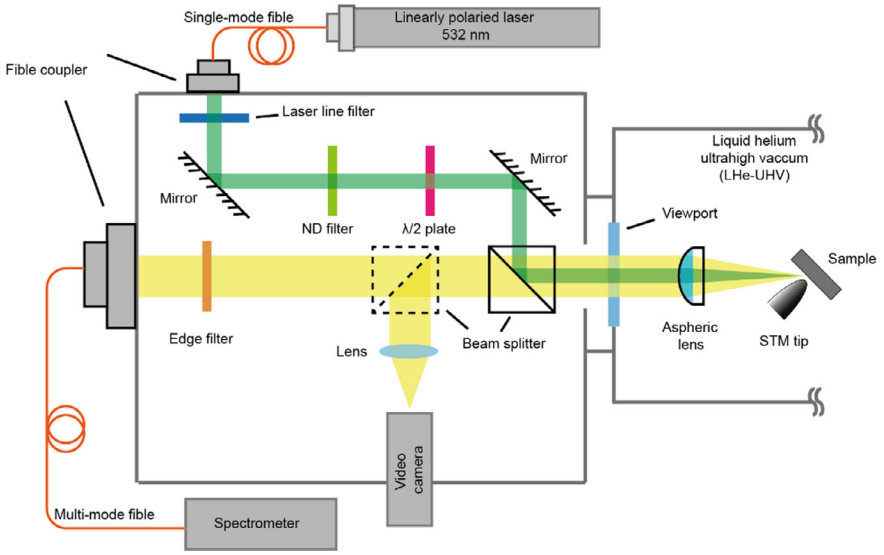



**Fig. 22.5** Schematic of the typical TERS setup with combined LT-UHV STM and optical system for Raman spectral measurements. Reproduced from Ref. [14] with permission

TERS studies. On the other hand, cooling the substrate down to cryogenic temperature is also very helpful for stabilizing single molecules on a surface, thus suppressing the diffusion and desorption problem. The thermal drift can be suppressed at low temperature even under light illumination, thus allowing molecules to be measured with longer time and repeatedly.

Single molecules were generally thermally evaporated onto the metal surface that was previously cleaned by cycles of argon ion sputtering and annealing. Silver (Ag) is usually used as the tip and substrate material because the nano-gap defined by the Ag tip and Ag substrate can offer very strong plasmonic resonance [79]. The details of fabrication and judgement of the TERS-active tips can be found in the next section. The photon collection and detection systems usually contain the following parts [11, 14]: A single-longitude-mode diode-pumped laser at 532 nm is used to provide a linearly polarized laser beam (degree of polarization: > 300:1) for Raman excitation. The beam is fiber-coupled to a dark-box via a single-mode polarization-maintaining fiber with a collimated output beam of ∼1.0 mm. A round continuously variable metallic neutral density filter is used to adjust the laser output power. Two reflective mirrors are used to provide freedoms for optical alignment. A half-wave plate is used to achieve desired *p*-polarization for incident laser. The laser beam is introduced into the UHV chamber via a quartz viewport after reflected by a 30:70 (R:T) beam splitter. Another beam splitter, which is removed during Raman measurements, is positioned in the optical collection path to help monitor the focusing of the laser beam into the tunnel junction with a video camera. The collimated beam is refocused by an aspheric lens (e.g., $f = 12.4$ mm, NA = 0.46)

into the tip–substrate junction at an angle of 60° from the surface normal. The TERS signals are collected through the same lens, filtered to remove the residual incident laser light, and then fiber-coupled to a spectrometer using a slit size of 100 μm. The Raman photons are dispersed by a grating and detected by a liquid-nitrogen cooled charge-coupled device (CCD). The laser power used in typical TERS experiments is $\sim 0.8$ mW or lower, corresponding to a photon flux of less than $10^2$ W/cm$^2$. The STM operation is controlled by Nanonis-SPECS electronics. The Raman spectral mapping is carried out through a synchronization function between the STM controller and CCD camera, acquiring a spectrum at each pixel during scanning [11, 14].

### *22.2.2 Fabrication and Judgement of TERS-Active Tips*

Up to date, ultrahigh-resolution TERS studies at the subnanometer scale are mainly achieved via using STM-based TERS setups, in which the tip is usually prepared by electrochemical etching. To obtain sharp tips, electrical voltage and current are used as a feedback to achieve quick circuit cutoff and avoid over-etching problems [79–85], which includes the use of pulsed electrochemical etching [86] and two-step etching processes [87]. Further tip sharpening strategies have also been proposed and elegantly demonstrated, such as via the field-directed sputter sharpening technique under the vacuum condition [88, 89]. Along with the development of tip fabrication techniques, the spatial resolution of single-molecule TERS imaging has been further driven to the Ångström level, even enabling the imaging of single chemical bonds in a molecule [4, 13, 14]. The presence of an atomistic protrusion at the tip apex is believed to be responsible for such Ångström-resolved TERS experiments based on recent experimental and theoretical studies that demonstrated the extreme sensitivity of the local-field enhancement and confinement to the atomic-scale structures at the tip apex [3, 17, 21, 22, 32, 51, 90, 91]. Dong's group recently developed a practical method that can quickly fabricate an atomic-scale protrusion at the tip apex and in-situ judge the TERS activity of the tips thus fabricated [37], as detailed below.

The flowchart of a TERS tip fabrication procedure is shown in Fig. 22.6. The tip is first prepared by direct-current electrochemical etching with a homemade electrochemical cell and electronic control circuit [79], with the electrolyte solution composed of perchloric acid and ethanol in a 3:8 ratio. The diameter of the Ag wire used for tip fabrication is 0.3 mm, with an initial etching voltage of about 1 V. Based on the scanning electron microscope (SEM) measurement of the as-prepared Ag tip, the typical radius of the tip apex is generally less than 100 nm [37]. After the electrochemical etching, the Ag tip is loaded into the vacuum chamber, cleaned via argon ion sputtering ($1.5 \times 10^{-5}$ Torr, 1500 V) for 15 min, and then annealed by electron bombarding (electron beam current: 0.4 mA, high voltage: 1200 V) for more than 10 h to get a smooth tip apex. Then, further atomic-scale modifications of the tip apex are performed to tune the tip status into TERS-active, specifically through cycles of

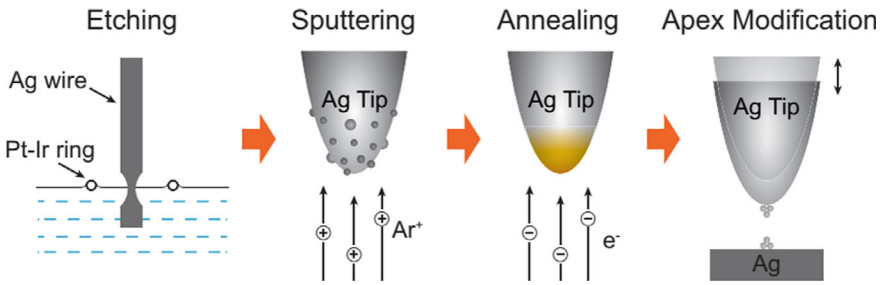



**Fig. 22.6** Flowchart of Ag tip fabrication for TERS experiments. Reproduced from Ref. [37] with permission

controlled gentle tip indentations to the Ag substrate at a relatively high bias voltage such as + 3.8 V [20, 37]. After these treatments, the TERS-active tips can produce TERS spectra with both large signal enhancement and high spatial resolution.

When accounting for the observation of Raman signals during the TERS measurement, there are generally two issues that need to be considered: one is the coupling from the far-field incident laser to the near-field plasmon, and the other is the coupling from the near-field polarization to the far-field emission. As shown in Fig. 22.7, for the first issue on the far-field to the near-field conversion, the coupling efficiency can be directly estimated through the change of the Stark-shifted peak position for the first image potential state (IPS) under laser illumination [92–94]. In STM, the distance–voltage ($Z$–$V$) curve or its $dZ/dV$ differential spectrum at a constant current can reveal the resonant tunneling feature of IPS [95], and more importantly, the IPS peak positions may change under laser illumination, depending on the tip plasmonic property [92]. As regards the second issue on the coupling from the near-field to the far-field emission, the Raman scattering signal from the tip apex itself can be used to judge whether the scanning tip can act as an effective antenna to enhance the far-field emission of TERS signals. For the TERS-active tip, one or more sharp scattering peaks can be always observed below 200 $cm^{-1}$, which is likely to associate with the presence of an atomistic protrusion at the tip apex.

In other words, two criteria are proposed to in-situ judge a tip's TERS activity: One is based on the downshift of the first IPS peak position under laser illumination by an amount of the incident laser energy, and the other is based on the appearance of sharp low-wavenumber Raman scattering peaks that are associated with an atomistic protrusion at the tip apex itself. These criteria can provide a quick judgement on the tip's TERS activity before real TERS measurements on target molecules or other materials. It is worth noting that, during TERS experiments, the "same" tip can exhibit quite different TERS activities once the tip apex is modified even at an atomic scale [37]. Moreover, the tip status and the related plasmonic properties can be directly monitored in situ by the STM-induced luminescence, allowing to achieve exquisite tuning between the nanocavity plasmon resonance and molecular vibronic transitions. Especially, the spectral matching of the nanocavity plasmon resonance

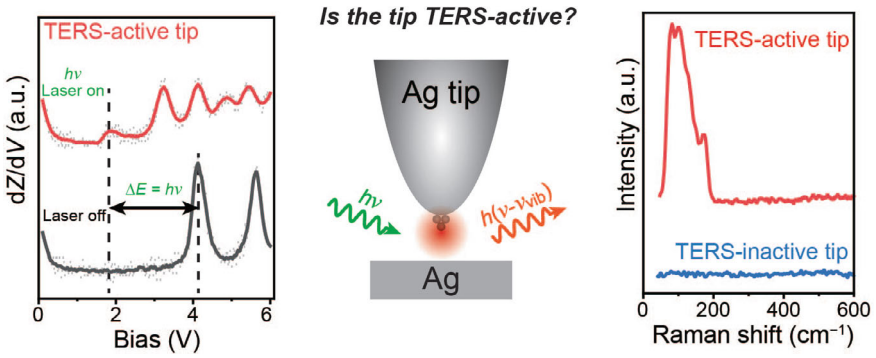



**Fig. 22.7** Two criteria to in-situ judge the tip's TERS activity for tip-enhanced Raman measurements: One criterion (left panel) is based on the downshift of the first IPS to monitor the coupling between the far-field incident laser and near-field plasmon; the other (right panel) is based on the appearance of the low-wavenumber Raman peaks associated with an atomistic protrusion at the tip apex to judge the coupling efficiency of emissions from the near field to the far field. Reproduced from Ref. [37] with permission

to the downward transitions associated with the emission of Raman photons is found to be crucial for enhancing and stabilizing the inelastic scattering signals [11].

## 22.3 Recent Advances in Single-Molecule TERS

Soon after the first experimental demonstration of TERS in 2000 by four independent groups [7–10], the spatial resolution of TERS imaging surpassed the Abbe's diffraction limit and was improved down to tens of nanometers [96–98]. In 2005, the TERS measurement on a single-walled carbon nanotube by Anderson et al. demonstrated a spatial resolution down to ~ 15 nm [97]. In 2008, the same resolution was also reported by Steidtner et al. using a TERS-based microscopy on single dye molecules [98]. Since then, many efforts have been made to improve the spatial resolution of TERS from a few nanometers to subnanometer scale, making the TERS technique a versatile tool to either investigate the molecular structures or induce surface reactions at the single-molecule level [11, 13, 14, 99].

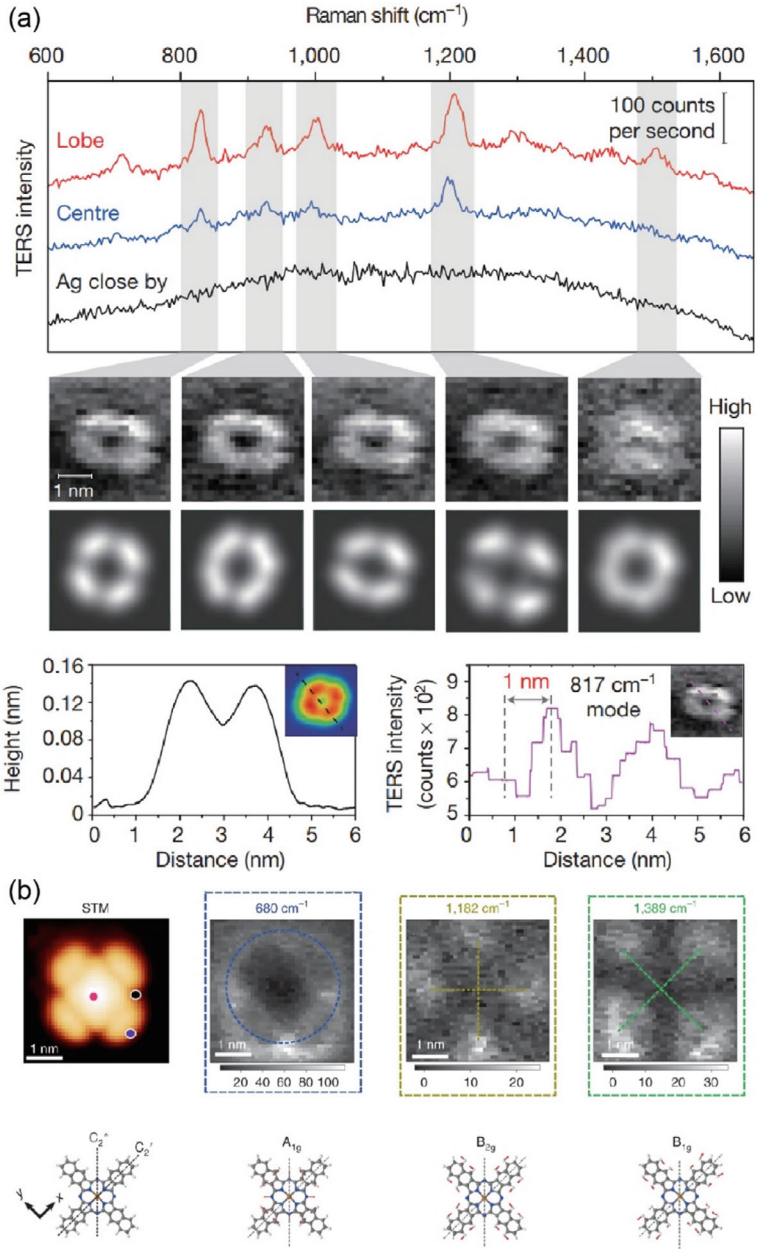
### *22.3.1 Imaging a Single Molecule by TERS with Subnanometer Resolution*

Despite early TERS efforts to chemically map single molecules [10, 97, 98, 100–106], well-defined single-molecule TERS measurements become feasible only after combining Raman spectroscopy with low-temperature UHV-STM systems [11]. In

2013, Dong's group first pushed the spatial resolution of TERS mapping down to the subnanometer scale (~ 0.5 nm) by using an STM-based LT-UHV TERS setup at ~ 80 K [11]. As shown in Fig. 22.8a, for the model system of an isolated single *meso*-tetrakis(3,5-di-tertiarybutylphenyl)-porphyrin ($H_2$TBPP) molecule deposited on the Ag(111) surface, the TERS spectra acquired on the molecular lobe are stronger than those on the center, whereas the nearby Ag gives a broad continuum, highlighting the highly localized nature of the TERS signals. Such contrast is best illustrated in the panoramic TERS mapping images for five selected Raman peaks.

The spectral mapping images for individual modes (represented by their respective gray zones) exhibit the characteristic four-lobe features of $H_2$TBPP molecule, showing good agreement with the theoretical simulations. The subnanometer lateral resolution can be clearly demonstrated from the spectral mapping image of the representative 817 $cm^{-1}$ mode, showing a remarkable spatial resolution of TERS mapping for a single molecule down to ~ 0.5 nm. In 2020, Kim's group reported the single-molecule resonance Raman effect of an isolated copper naphthalocyanine (CuNc) molecule on a three-monolayer-thick NaCl film supported by the Ag(111) substrate [12], and the corresponding TERS mapping images present different patterns depending on the symmetries of different vibrational modes, as shown in Fig. 22.8b. Since the CuNc molecule belongs to the $D_{4h}$ point group, the vibrational modes with $A_{1g}$, $B_{2g}$, and $B_{1g}$ symmetries are Raman active, which possess different matrix elements in Raman tensors and are directly related to the circle, plus, and cross patterns categorized in the experimental TERS maps, respectively.

The ultrahigh spatial resolution at the subnanometer scale also allows to distinguish different molecular species and surface structures at the single-molecular level. In 2015, Jiang et al. utilized the LT-UHV TERS to investigate the capability of distinguishing two adjacent $H_2$TBPP and ZnTPP (zinc-5,10,15,20-tetraphenyl porphyrin) molecules with similar structural skeletons [107]. As shown in Fig. 22.9 (a), when two molecular islands were packed closely together within van der Waals contact (approximately 0.3 nm), the variations in TERS spectral features along the line trace allowed to determine that the edge molecule on the top island is ZnTPP, while the edge molecule on the bottom island is $H_2$TBPP. Weak mixed TERS signals from both molecules were observed at the contact interface. Moreover, for these two molecules adsorbed at the step edge forming a mixed molecular chain (Fig. 22.9b), both the chemical identity and spatial distribution of different molecular species can be obtained by combining subnanometer TERS imaging with the multivariate analysis method [108]. Even for two adjacent small molecules, taking the single DNA base molecules as an example, the single-molecule TERS technique can also distinguish individual bases even when they are compactly assembled in a network [109]. As shown in Fig. 22.9c, the line-trace TERS measurements across the boundary show distinct TERS spectral features between the adenine (A) and thymine (T) molecules in spite of the similarity in their topographic features. It is worth noting that, besides the lateral spatial resolution at the subnanometer scale, the chemical resolving ability of TERS in the vertical direction is also capable of distinguishing two different molecules in the vertical hetero-molecular structures. Figure 22.9d shows the TERS measurements on a single fullerene ($C_{60}$) molecule when using a


(a)
Raman shift (cm−1)
600
800
1,000
1,200
1,400
1,600
TERS intensity
Lobe
Centre
Ag close by
100 counts per second
1 nm
High
Low
Height (nm)
0.16
0.12
0.08
0.04
0
Distance (nm)
TERS intensity (counts × 10²)
1 nm
817 cm−1 mode
(b)
STM
680 cm−1
1,182 cm−1
1,389 cm−1
20 40 60 80 100
0 10 20
0 10 20 30
C2
C2′
A1g
B3g
B1g

◀**Fig. 22.8 Subnanometer-resolved TERS imaging of a single molecule**. **a** Representative TERS spectra (top panel) obtained from the lobe, center, and Ag substrate, as well as experimental and simulated TERS mapping (middle panels) for various Raman peaks with each spectral image processed from the individual TERS spectra acquired at each pixel, corresponding to a single $H_2$TBPP molecule deposited on Ag(111) surface. The profile analyzes (bottom panel) for a line-trace extracted from the inset STM topography and the TERS intensity mapping at 817 $cm^{-1}$ indicate a subnanometer resolution of single-molecule TERS imaging. Reproduced from Ref. [11] with permission. **b** TERS mappings of a single CuNc molecule adsorbed on the NaCl surface schematics showing the symmetry of the corresponding vibrational modes. Reproduced from Ref. [12] with permission

modified Ag tip with a copper phthalocyanine (CuPc) molecule attached to the tip apex in a flat-lying configuration [110]. A mixed feature of both molecules in the TERS spectra can be clearly resolved even when the CuPc-tip is retracted a bit away from the $C_{60}$ molecule, showing an detection depth as large as ~ 580 pm associated with a hot-spot transfer effect [111].

In addition to chemical identification of molecular species, different configurations and molecular orientations, even for a same type of molecules, can also be distinguished through the changes of Raman spectral features due to the TERS selection rule. Figure 22.10a shows two representative TERS spectra acquired from the same molecules but with different adsorption configurations [11]. Although the TERS spectrum of a flat-lying $H_2$TBPP molecule adsorbed on the terrace of Ag(111) shows vibrational fingerprints similar to the spectrum of a tilted molecule adsorbed at the step edge, there are noticeable differences in the relative intensities of Raman peaks, which is consistent with the theoretical simulations when the tilting angle of the molecule is altered. In 2019, Zhang et al. demonstrated another example to show the influence of molecular adsorption configurations on the Raman spectral features [112]. As shown in Fig. 22.10b, for single small 4,4′-bipyridine (44BPY) molecules adsorbed at the step edge of Ag(111), their corresponding Raman spectra exhibit notable differences in the relative intensities of different vibrational peaks, which can be assigned to three different molecular orientations, each featuring a specific fingerprint pattern based on the TERS selection rule. In 2020, Jiang's group reported multiple configurations of rubrene molecules on the Ag(100) surface, which can be directly characterized by STM and TERS in combination with TDDFT simulations [113]. Figure 22.10c indicates a more tilted orientation for the molecules at the step edges, with larger tilting angles compared to the molecules on the flat terraces. Variations in adsorption configuration, particularly with different twisting angles of the phenyl ring are also suggested by the simulations, resulting in variations in the relative intensities of the corresponding Raman peaks. Such sensitivity in single-molecule configurations from the TERS signals can be even achieved by using a silver tip on a non-plasmonic nonmetal substrate, indicating the vital rule of the tip in inducing strong and highly localized electric fields. In 2022, Wang et al. demonstrated single-molecule TERS measurements on an isolated bis(phthalocyaninato) terbium(III) ($TbPc_2$) molecule adsorbed on the Si(111) substrate [114]. Even though the single-molecular TERS signal on Si(111) is relatively weak compared to that adsorbed on the silver metal substrates, the spatial resolution can still reach the

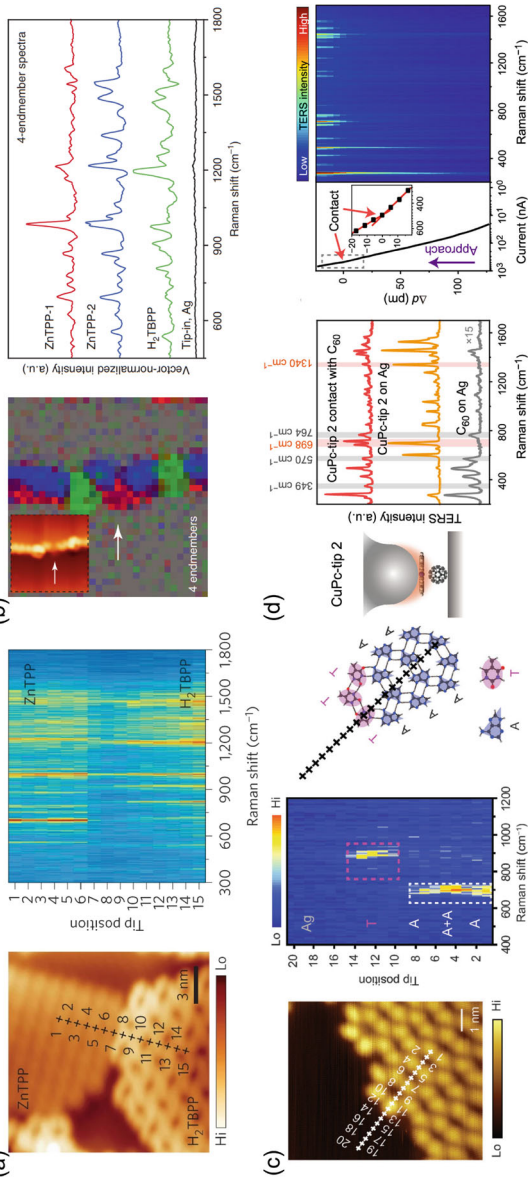



**Fig. 22.9 Recognition ability of TERS for different types of molecules. a** Sequential TERS spectra (right panel) measured along the line trace indicated in the STM topograph (left panel) of two adjacent molecular islands of ZnTPP and $H_2$TBPP. Reproduced from Ref. [107] with permission. **b** Left: TERS-VCA image for a mixed molecular chain of ZnTPP and $H_2$TBPP adsorbed at the silver step edge, acquired over the area shown in the inset STM topograph. Right: corresponding endmember spectra for four endmembers. Reproduced from Ref. [108] with permission. **c** Left: STM topograph for a molecular island containing mixed A and T molecules. Middle: sequential TERS spectra acquired along the line-trace marked in the left panel. Right: proposed molecular arrangement along the line-trace in the left panel. Reproduced from Ref. [109] with permission. **d** Left: schematic of TERS measurements using a CuPc-terminated tip over the $C_{60}$ molecule. Middle: comparisons of TERS spectra measured under different conditions. The red curve is measured when the CuPc-tip contacts $C_{60}$, showing mixed signals of the two molecules. The shadows in different colors are used to indicate the different features of CuPc (red) and $C_{60}$ (gray), respectively. The yellow curve is collected on the bare Ag surface for comparison. Right: dependence of tunneling currents and TERS spectra on the separation between the CuPc and C60 molecules ($\Delta d$), measured as the CuPc-tip approaches $C_{60}$. Reproduced from Ref. [110] with permission

subnanometer scale of ~ 0.6 nm. Notably, the TERS spectral features of $TbPc_2$ are very sensitive to the adsorption configuration of the molecule on Si(111), as shown in Fig. 22.10d.

Furthermore, TERS can even go beyond identifying different molecular orientations and also recognize the local position and configuration of different functional groups within a single molecule. For example, in the above-mentioned TERS images

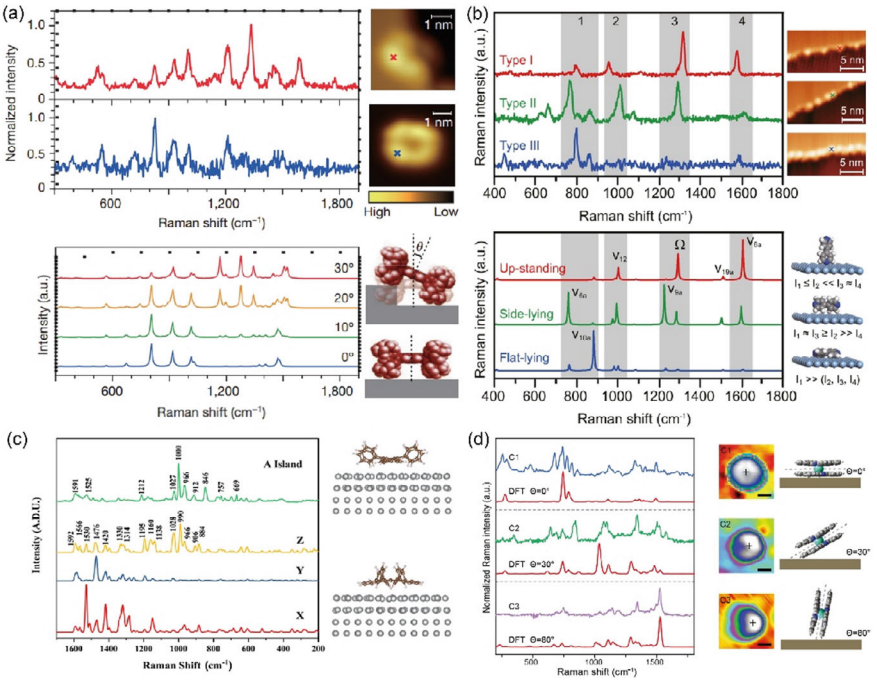



**Fig. 22.10 Dependency of single-molecule TERS spectra on molecular orientations**. **a** Top: experimental TERS spectra for an isolated $H_2TBPP$ molecule adsorbed at the step edge or on the terrace of Ag(111), acquired on the molecular lobe marked with a cross in the STM images shown on the right. Bottom: simulated TERS spectra for different tilt angles. Reproduced from Ref. [11] with permission. **b** Top: experimental TERS spectra for three types of 44BPY molecules adsorbed at the step edge with the corresponding STM images shown on the right. Bottom: simulated Raman spectra for single 44BPY molecules with three different orientations: upstanding, side-lying, and flat-lying. Reproduced from Ref. [112] with permission. **c** Left: experimental TERS spectra of self-assembled rubrene on Ag(100), together with simulated Raman spectra separated into X, Y, and Z components in Cartesian coordinates. Right: side view from y- and x-direction of the planar binding configuration of rubrene for the Raman spectrum calculation. Reproduced from Ref. [113] with permission. **d** Left: TERS spectra of single $TbPc_2$ molecules for different adsorption configurations on Si(111) and corresponding simulated Raman spectra for three different tilting angles. Middle: STM images for three isolated $TbPc_2$ molecules in different adsorption configurations, C1, C2, and C3, respectively. TERS spectra were acquired at the positions marked by "+". Right: Schematics for the corresponding $TbPc_2$ molecular adsorption configurations with different tilting angles (Θ), which are defined by the tilt angle between the molecular plane and the surface plane. Reproduced from Ref. [114] with permission

of $H_2$TBPP shown in Fig. 22.8, the features of four lobes of the molecule are still relatively blurry without any detailed patterns of the functional groups. However, by developing single-molecule TERS techniques that can operate at cryogenic temperature down to ~ 7 K, not only the molecular stability but also the spatial resolution of TERS can be improved. In this way, Dong's group demonstrated more detailed patterns from the TERS imaging of a single $H_2$TBPP molecule on Ag(100) [115]. As shown in Fig. 22.11a, the spatial distribution of the observed TERS image associated with the representative vibrational mode at 817 $cm^{-1}$ still exhibits an approximate four-fold symmetry, but the intensity distribution is quite inhomogeneous with a clear eight-dot pattern. The outer four dots are likely to be contributed by the C–H bonds from the molecular lobes, while the inner four dots are believed to come from the C–H bonds in the pyrroles of the molecular core. Of particular interest is the TERS mapping for the 1500 $cm^{-1}$ mode, which reveals a vertically aligned "two-dot" pattern with a separation distance of about 0.4 nm. This mode is likely to associate with the rocking motions of the N–H bonds around the molecular center. The separation between the two dots agrees very well with the distance of ~ 0.4 nm estimated between two nitrogen atoms from the theoretically optimized geometry of a $H_2$TBPP molecule. Therefore, the observation of such a two-dot pattern appears to suggest the absence of tautomerization process within a porphyrin ring of the $H_2$TBPP molecule at ~ 7 K even under light illumination. In 2020, Li et al. also applied the TERS technique to investigate the spatial orientation of single phenyl groups within a nano-hoop composed of a single [12]cycloparaphenylene ([12]CPP) molecule [116]. As shown in Fig. 22.11b, the STM image of [12]CPP shows a parallelogram-like pattern and the TERS spectra exhibit paired similarities at the symmetric positions over the hoop. Based on the further analysis and comparison of both topographic and spectral features, the adsorption configuration of [12]CPP on Ag(110) is considered to be deformed, forming a "Möbius-like" strip pattern. Further TERS imaging provides a panoramic view on the local structural deformations caused by different tilting of the benzene units in real space, which offers insights into the subtle changes in the aromatic properties over the deformed hoop owing to inhomogeneous molecule–substrate interactions. In 2023, they further applied TERS to investigate the photocatalytic dimerization reaction of *p*-nitrothiophenol (PNTP) to *p*,*p*′- dimercaptoazobenzene (DMAB) on the Ag substrates [117]. As shown in Fig. 22.11c, the PNTP molecules are always found to pair into two bright dots, and TERS measurements indicate that the PNTP molecules have undergone an on-surface deoxydimerization reaction to form dimerized DMAB molecules on the Ag substrate. This is because at the center of a two-dot pair, the TERS spectrum indeed shows strong Raman peaks that are associated with the N=N stretching vibration, consistent with the molecular structure of DMAB. Further careful analyses for the TERS spectra acquired over the highly ordered assembly suggest that the hexagonal pattern around each dark center is formed by six equilateral triangular structures, with each triangle composed of three end-to-end DMAB molecules.

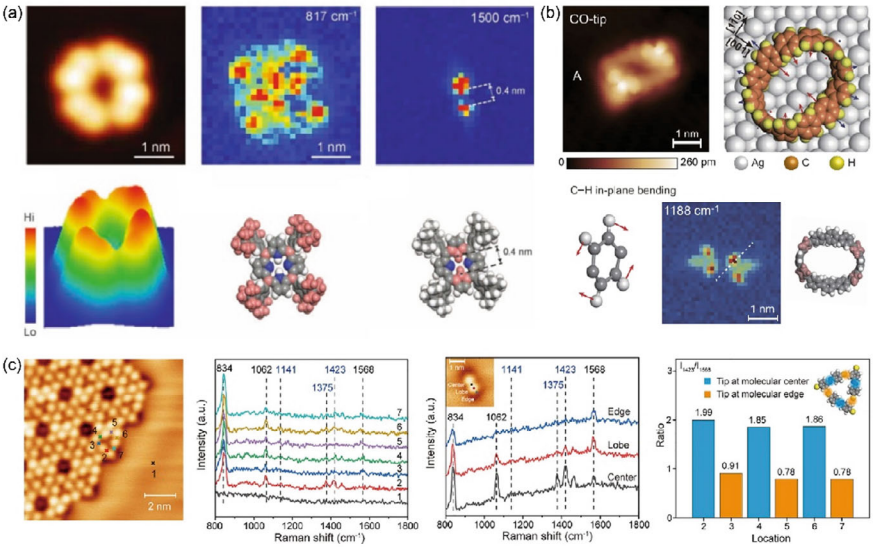



**Fig. 22.11 Identification of different functional groups within a single molecule**. **a** 2D and 3D STM topography (two left panels) of a single $H_2$TBPP molecule as well as TERS images (two top-right panels) for two representative Raman modes. Also shown in the two bottom-right panels are the molecular structures with pink-colored atoms highlighting the main contribution for corresponding vibrational modes. Reproduced from Ref. [115] with permission. **b** STM images (top-left panel) and schematic structure (top-right panel) of a [12]CPP molecule on Ag(110). The TERS mapping image for the exemplified 1188 $cm^{-1}$ mode is shown in the bottom-middle panel, while the molecular structure shown in the bottom right highlights the atoms involved in the vibrational motion in pink, and the schematic shown in the bottom left highlights the benzene units that are involved in this vibration. Reproduced from Ref. [116] with permission. **c** From left to right panels: STM image of the PNTP molecules on Ag(111); typical Raman spectra acquired at the corresponding positions labeled by "×" in the left panel; Site-dependent TERS spectra of a single DMAB molecule on Ag (111) with the inset showing the corresponding STM image; histogram plot of the $I_{1423}/I_{1568}$ ratio at six positions labeled in the left panel, with the inset illustrating the schematic of the assembly model to show different measuring positions, where the orange sites represent the intermolecular gap, and the blue sites represent the molecular center. Reproduced from Ref. [117] with permission

### 22.3.2 *Resolving Single Chemical Bonds and Their Making and Breaking Processes*

As the spatial resolution of TERS has been improved from tens of nanometers to the subnanometer level after years of developments [11, 13, 14, 96–98, 104], it naturally raises a fundamental question: *What is the ultimate limit in the spatial resolution of TERS?* As we have discussed theoretically in Sect. 22.1, in principle there is no fundamental limit preventing such confinement down to atomic scales [25]. The only requirement is from the experimental side that how to obtain an exquisite control over the tip structure and stability, especially at the atomistic level to control the tip apex to form a picocavity for the local-field confinement at the subnanometer scale. By

employing the UHV and cryogenic (liquid nitrogen or liquid helium) conditions, as well as the delicate fabrication of the tip discussed in Sect. 22.2.2, a TERS-active tip with the apex decorated by an atomistic protrusion can be prepared and remain stable for long-time TERS measurements (e.g., spatial mapping) with Ångström resolution. Such a capability enables to directly resolve single chemical bonds within a molecule and even to explore the bond breaking and making processes.

#### 22.3.2.1 Scanning Raman Picoscopy: Imaging of Individual Vibrational Modes at Single-Bond Limit and Molecular Structure Reconstruction

Using all the strategies described above, the vibrations of single chemical bonds can be clearly resolved through the TERS measurements. In 2019, Apkarian's group [13] first demonstrated the mode-resolved spatial mapping of a single Co(II)-tetraphenyl porphyrin (CoTPP) molecule on Cu(100) with a spatial resolution down to ~ 1.67 Å, as shown in Fig. 22.12a. The TERS signal intensity for the phenyl stretch at ~ 3000 $cm^{-1}$ falls below the detection limit when the tip is retracted from 2 to 3 Å, showing a vertical confinement also at the Ångström level. The lateral confinement is illustrated by the spatial mapping of the C–H stretching mode at ~ 2982 $cm^{-1}$, showing a Gaussian fitted full-width at half-maximum (FWHM) of 1.67 Å, enabling to distinguish the individual C–H bond in the phenyl ring. Moreover, the TERS mapping image shows a feature with three bright spots, corresponding to three related C–H bonds with two in-phase C–H stretches and one out-of-phase C–H stretch on alternating carbon atoms of the phenyl ring. While for the total symmetric C–H stretching mode, a horseshoe-shaped intensity peaked on the five carbon atoms of the phenyl ring is observed. In the same year, Dong's group also reported a similar spatial resolution of ~ 1.5 Å for another molecular system, a single Mg-porphine (MgP) molecule on Ag(100) [14]. As shown in Fig. 22.12b, since the highly localized C–H stretching vibration at 3072 $cm^{-1}$ can be identified as the anti-symmetric stretching mode of the $sp^2$ C–H bonds, the out-of-phase destructive interference associated with two neighboring C–H bonds would result in a pattern with eight bright spots, with each corresponding to an individual C–H bond. On the contrary, if two neighboring C–H bonds are stretching with the same phase for the symmetrical vibrational mode at 3092 $cm^{-1}$, the constructive interference would result in a four-lobe feature, with the brightest spot close to the center of two connected C–H bonds. Even for an upstanding molecule on a surface, e.g., a single melamine molecule chemically adsorbed on the Cu(100) surface [5], the location of two N–H bonds at the top of the melamine molecule as well as their vibrational phases can be clearly resolved through the TERS measurement for the symmetric and anti-symmetric N–H stretching vibrational modes, as shown in Fig. 22.12c.

As we have theoretically discussed in Sect. 22.1.2, different spatial features in the TERS mapping images are originated from the interferences between different chemical bonds, and thus, different vibrational phases would result in different patterns. Therefore, the more chemical bonds or groups are involved in the vibrations, and

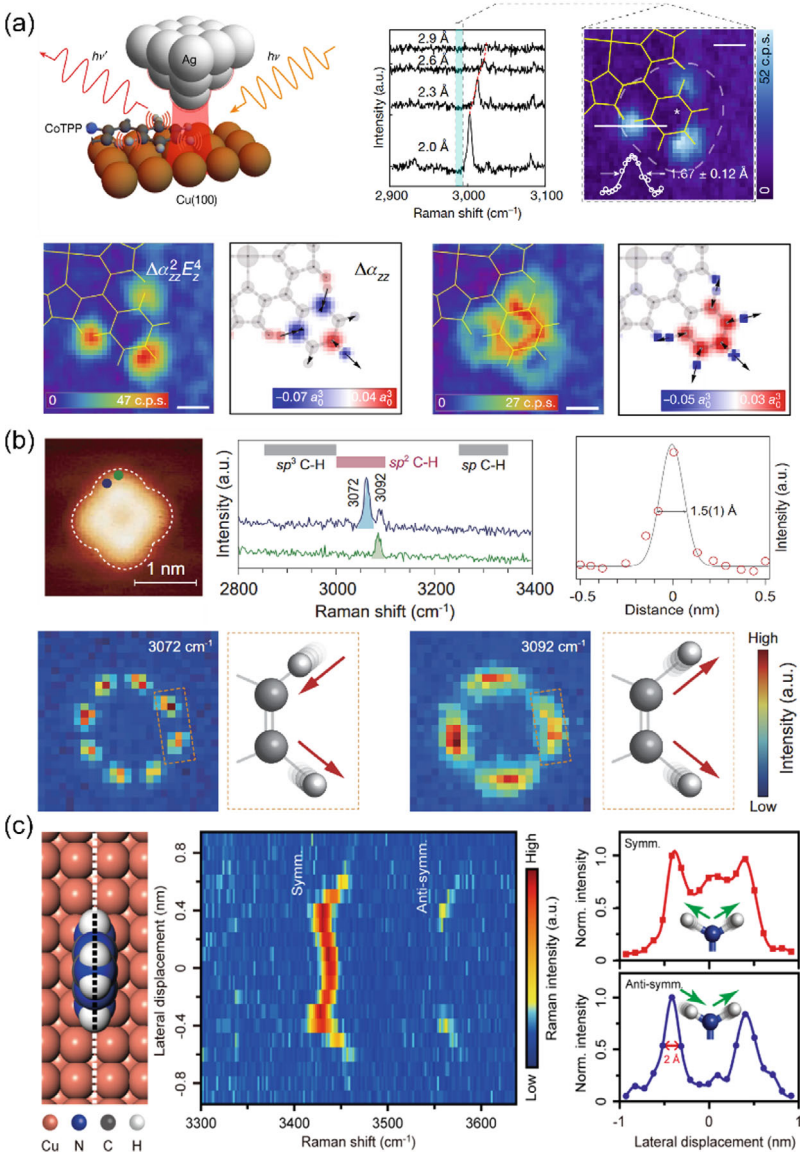



**Fig. 22.12** Spatial resolution of TERS down to the level of single chemical bonds. **a** TERS mapping images for representative vibrational normal modes of CoTPP on Cu(100), achieving spatial resolution down to ~1.67 Å. Reproduced from Ref. [13] with permission. **b** Spatial resolution at the single chemical-bond level (1.5 Å), attained for Mg-porphine on TERS. Reproduced from Ref. [14] with permission. **c** Line-trace TERS plot enabling the discrimination of individual chemical bond patterns of a single upright melamine molecule chemisorbed on Cu(100). Reproduced from Ref. [5] with permission

the more complicated the mapping images are obtained. As shown in Fig. 22.13a and b, the characteristic TERS mapping images corresponding to different vibrational modes represent their own characteristics with rich details distributed over different parts in the single molecule due to different contributions and their phase relations from different chemical groups or bonds. In this sense, a new methodology called scanning Raman picoscopy (SRP) [14] was proposed for visually constructing the chemical structure of a single molecule through a "Lego-like" building process. As shown in Fig. 22.13c, if one pretends that the chemical structure of the MgP molecule is unknown in advance, the assembling process can be realized stepwise by identifying different "Lego" components with the help of high spatial resolution TERS spectra and the associated TERS mapping images. As discussed above, the C–H stretching vibration at 3072 $cm^{-1}$ is identified as the $sp^2$ C–H stretching mode, pinpointing the spatial positions of eight $sp^2$ C–H bonds and their connections. Similarly, the Raman peaks at 1463 $cm^{-1}$, 841 $cm^{-1}$, and 211 $cm^{-1}$ correspond to TERS mapping images revealing the structures and positions of pyrrole rings, bridging C–H bonds, and a central Mg atom, respectively. Through this sequential process of recognition and assembly of structural and chemical bond components, the chemical structure of the MgP molecule is unequivocally confirmed in real space.

Since the central metal atoms in the CoTPP and MgP molecules can be clearly resolved from the TERS mapping images, such atomic resolving ability can be further implemented to achieve the atomic-level resolution on a substrate by using molecular modified tips [15]. As shown in Fig. 22.14a, by manipulating a CoTPP molecule adsorbed on $Cu_2N$ substrate to the apex of the silver tip, the N atom sites can be clearly resolved from the TERS intensity imaging of the $Cu_2N$ surface with a spatial resolution of ~ 1.5 Å, which is constant with the STM topography at − 1 V. Since the same electron density is implicated in both STM and TERS, the atomic-resolved contrast would be associated with the inhomogeneity of the nitride dielectric property at the atomic scale. The larger electron density on the N-sites and resultant larger polarizability would lead to a greater confinement of the local field and would explain the observed TERS intensity contrast. From the peak-shift TERS map of the 388 $cm^{-1}$ mode, the N and Cu sites as well as the fourfold hollow sites can be also clearly resolved [15]. In 2022, Jiang's group also demonstrated an example in which single oxygen adatoms on a boron monolayer (i.e., borophene) can be identified and mapped via the UHV-TERS with ~ 4.8 Å spatial resolution and single B–O bond sensitivity [118]. As shown in Fig. 22.14b, a TERS line scan conducted across the interface of an oxygen adatom on borophene reveals two characteristic modes at 205 $cm^{-1}$ and 189 $cm^{-1}$, corresponding to the vibrational modes of pristine and O-adsorbed $v_{1/6}$ borophene, respectively. The TERS intensity profiles (in green) and the corresponding height profile (in black) of the oxygen atom demonstrate that the individual oxygen atom can be clearly resolved from the TERS measurements.

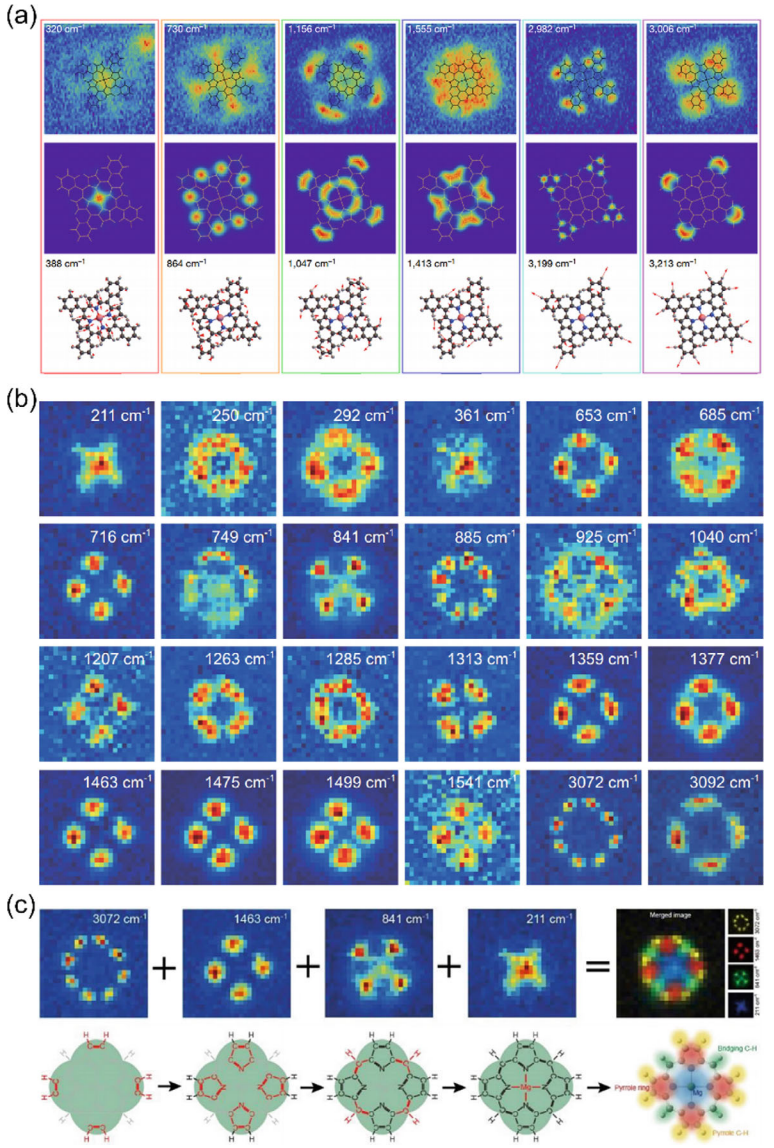



**Fig. 22.13 Reconstruction of molecular structure from TERS mapping**. **a** Visualizing vibrational normal modes of a single CoTPP molecule by TERS. Reproduced from Ref. [13] with permission. **b** Spatial mapping images for various Raman peaks of a single MgP molecule on Ag(100). Reproduced from Ref. [14] with permission. **c** Reconstruction of the full molecular structure from the TERS mapping images of representative vibrational modes by assembling constituent chemical units together, including pyrrole C–H bonds, pyrrole rings, bridging C–H bonds, and a central Mg atom. Reproduced from Ref. [14] with permission

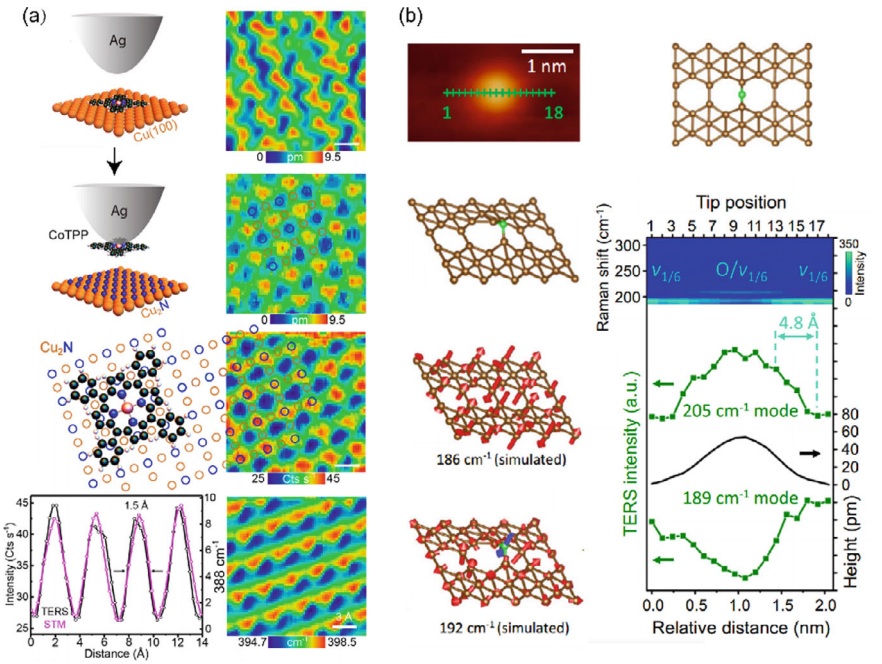



**Fig. 22.14 Atomic-level resolution of TERS**. **a** From top to bottom: Utilizing a molecule-terminated tip to achieve TERS intensity mapping of the $Cu_2N$ substrate, with a spatial resolution of ~ 1.5 Å that follows the STM topographic contrast. Reproduced from Ref. [15] with permission. **b** Angstrom-scale chemical identification of single oxygen adatoms on borophene via UHV-TERS. Reproduced from Ref. [118] with permission

### 22.3.2.2 Resolving Bond Making and Breaking in Surface Reactions

In the above discussions, TERS is generally applied to investigate the single molecules or surfaces with the single-chemical-bond or even atomistic resolution for the static structures. However, when the molecules or surfaces undergo chemical reactions, the chemical bonds might break or form, resulting in the chemical structural changes that can be also captured through the TERS measurements. In 2017, Ren's group employed phenyl isocyanide (PIC) as a probe molecule adsorbed on different metal surfaces to study the bimetallic Pd/Au(111) model catalyst [119]. As shown in Fig. 22.15a, the N≡C bond of the adsorbed PIC molecule is found to be weakened at the Pd step edge, indicating enhanced reactivity when compared with that at the Pd terrace. On the other hand, the TERS intensities are always enhanced at the step edges, which is related to the stronger electromagnetic fields at the step edge. In 2020, Li's group and Zenobi's group together studied the catalytic sites during a hydrogenation reaction on the same Pd/Au(111) bimetallic catalyst [120]. As shown in Fig. 22.15b, since the hydrogenation reaction from chloronitrobenzenethiol (CNBT) to chloroaminobenzenethiol (CABT) occurs selectively on the

well-defined bimetallic Pd/Au(111) surface, the TERS imaging of the surface after catalytic hydrogenation confirms that the reaction occurs beyond the location of Pd sites. In 2023, Dong's group investigated the photocatalytic dimerization reaction of p-nitrothiophenol (PNTP) molecules [117]. When PNTP coverage reaches a full monolayer on Ag(100), the molecules are not favorable for dimerization due to steric hindrance effects or isolation from the metal substrate. However, when the coverage is less than a full monolayer, as shown in Fig. 22.15c, PNTP molecules are found to be easily catalyzed by the Ag substrate, undergoing an on-surface dimerization to form the DMAB molecules. Such structure changes from PNTP to DMAB can be directly captured through TERS, especially from the appearance of 1355 $cm^{-1}$ and 1407 $cm^{-1}$ peaks related with the N=N stretching vibrations.

Considering the capability of TERS in resolving the single chemical bonds within a single molecule, not only the structural differences between the reactant and product molecules can be identified, the intricacies of intramolecular single chemical bonds including the bond breaking and making processes can also be disentangled by using the Ångström-resolved TERS. In 2021, Xu et al. combined three techniques, i.e., STM, noncontact atomic force microscopy (AFM), and TERS together to study the structural and chemical heterogeneities of three pentacene-derivative species through specific C–H bond breaking process [4]. As shown in Fig. 22.16a, characterizations through TERS measurements reveal three pentacene derivatives (α, β, γ) on the Ag(110) surface, in which the C–H bonds at the central benzene ring sequentially break from α to γ. Simultaneously, the pentacene skeleton undergoes deformation with atomic rearrangements at the core. The TERS mapping images for the C–H stretching mode in the wavenumber range of 2800–2900 $cm^{-1}$ distinctly show the breaking of two C–H bonds at the center, which is consistent with the skeletal features evident in the AFM images. Moreover, even the complexities of intramolecular isotope effects in pentacene and its fully deuterated analogue can be clearly studied [121], underscored the capability of TERS as a non-destructive, highly sensitive, and chemically-bond-resolved methodology for isotope detection and recognition. For the upstanding adsorbed molecules, e.g., the melamine molecule on Cu(100), as we discussed in Fig. 22.12c, the bond breaking and making processes can also be examined through TERS. As shown in Fig. 22.16b, the breaking of top N–H bonds and the transformation to its tautomer during photon-induced hydrogen transfer reactions can be clearly specified, indicating the chemical and structural sensitivity of TERS for single-bond recognition beyond flat-lying planar molecules.

It should be noted that during the TERS measurements, the tip is not only a probe to characterize the inherent properties of molecules, and the interactions between the tip and the adsorbed molecule can also significantly influence the chemical structure of molecules and even induce the chemical bond breaking processes [122]. As shown in Fig. 22.16c for the model system of an individual carbon monoxide (CO) molecule adsorbed on the Cu(100) surface, the vibration frequency of the C–O stretching mode consistently exhibits a redshift when the tip approaches to the molecule. Such a redshift indicates that the C–O bond is weakened due to the interaction between the tip and the molecule. A more in-depth exploration of the vibrational Stark effect and TERS imaging patterns reveals the presence of a tilting phenomenon in the

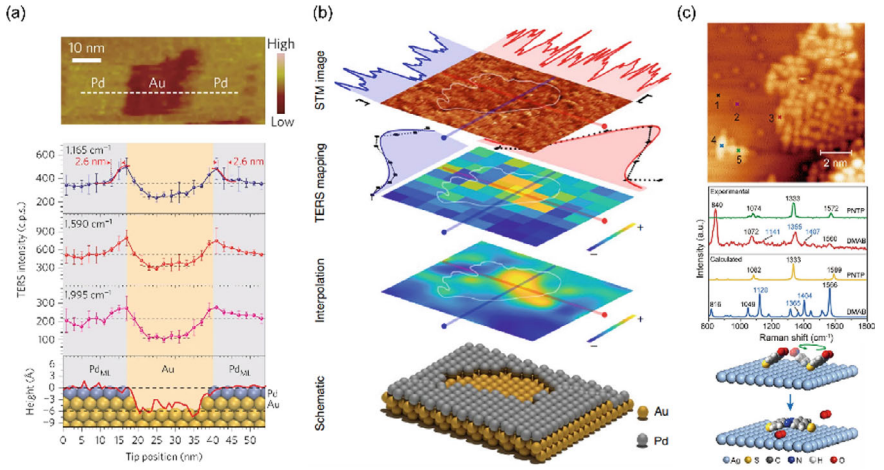



**Fig. 22.15 Detection of molecular structural changes through TERS**. **a** Characterization of multiple metal surfaces on a Pd/Au(111) bimetallic model catalyst using phenyl isocyanide as a probe molecule. Reproduced from Ref. [119] with permission. **b** Investigation of catalytic hydrogenation of CNBT molecules on the same catalyst, revealing surface characterization through molecular structural changes. Reproduced from Ref. [120] with permission. **c** Exploration of the photocatalytic dimerization reaction of p-nitrothiophenol (PNTP) to p,p′-dimercaptoazobenzene (DMAB) on Ag(100), unveiling coverage-dependent adsorption configurations and on-surface dimerization of PNTP molecules. Reproduced from Ref. [117] with permission

CO molecule upon tip approaching, ultimately leading to the lateral hopping of the molecules. Moreover, an analysis of the Raman shift during two successive jumps confirms that the hopping event is more likely to occur via the bridge site, moving toward the nearest Cu neighbor along the [100] or [010] direction.

### 22.3.2.3 Anti-Stokes Raman Thermometry in a Single Molecule

Chemical reactions are always accompanied by thermal effects that are manifested through an increase or decrease in temperatures, and the measurements of such temperature variations are quite crucial for the understanding of reaction processes. Considering the quantum nature of a single molecule, the thermal effect at subnanometer scale is generally under nonequilibrium conditions, resulting in an inhomogeneous spatial distribution of temperatures [123]. Raman spectroscopy has been used as non-invasive methods to obtain the value of the thermal energy and thus the value of temperature based on the analysis of temperature-dependent peak widths, positions, or intensities of various vibrational modes [124–127]. For example, in 2018, Ren's group found that molecules like phenyl isocyanide, when modified on the surface of Au nanoparticles, exhibit both a temperature-sensitive shift in vibrational frequencies and broadening in the Stokes Raman peaks [124], as shown in Fig. 22.17a. Especially, the sensitive shift of stretching vibration of

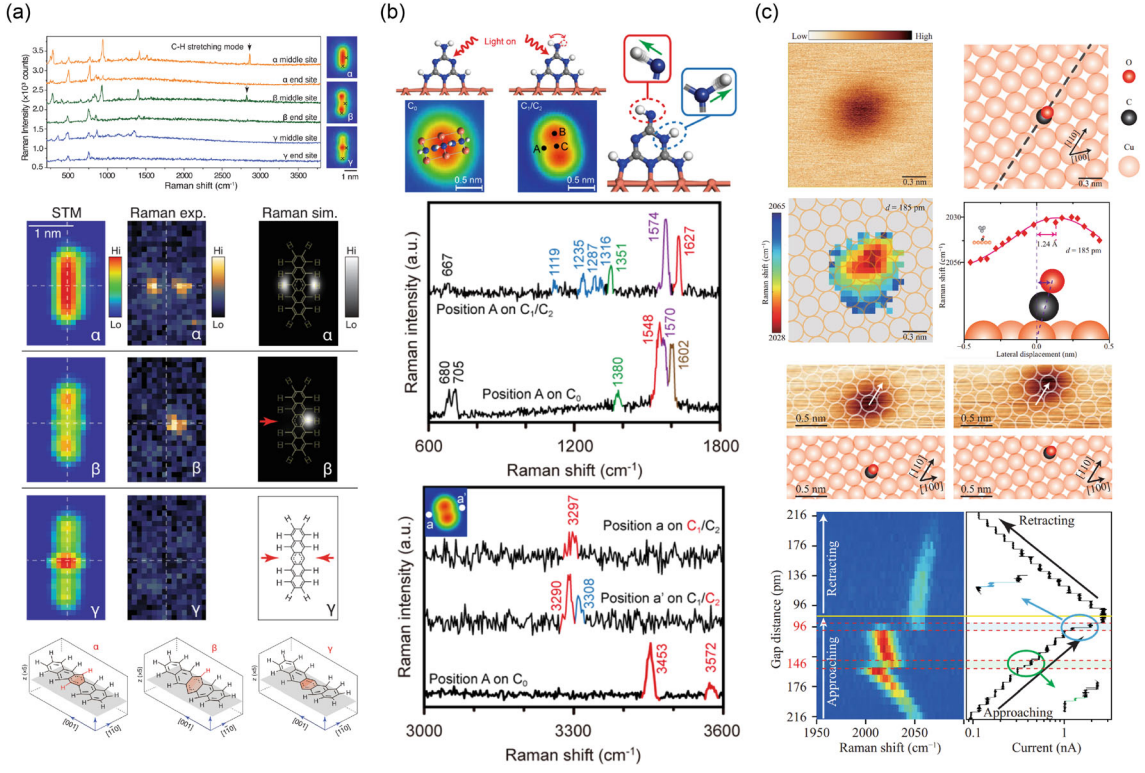



**Fig. 22.16 Exploring the making and breaking processes of chemical bonds using TERS. a** Monitoring the bond breaking and transformation of pentacene molecules through a joint STM-AFM-TERS strategy. Reproduced from Ref. [4] with permission. **b** Raman detection of bond breaking and making of a chemisorbed upstanding single melamine molecule. Reproduced from Ref. [5] with permission. **c** Tracking tip-induced bond weakening, tilting, and hopping of a single CO molecule on Cu(100). Reproduced from Ref. [122] with permission

phenyl isocyanide molecule at ~ 2200 $cm^{-1}$ can be utilized to facilitate the surface temperature measurement of plasmonic nanostructures.

On the other hand, it is noteworthy that apart from the Stokes Raman signals that always show up in Raman experiments, the anti-Stokes Raman signals can also be measured occasionally, though somewhat depending on the material system under study and the measurement condition. Notably, the anti-Stokes-to-Stokes ratio for a vibrational mode can be directly related to the vibrational population through the relation

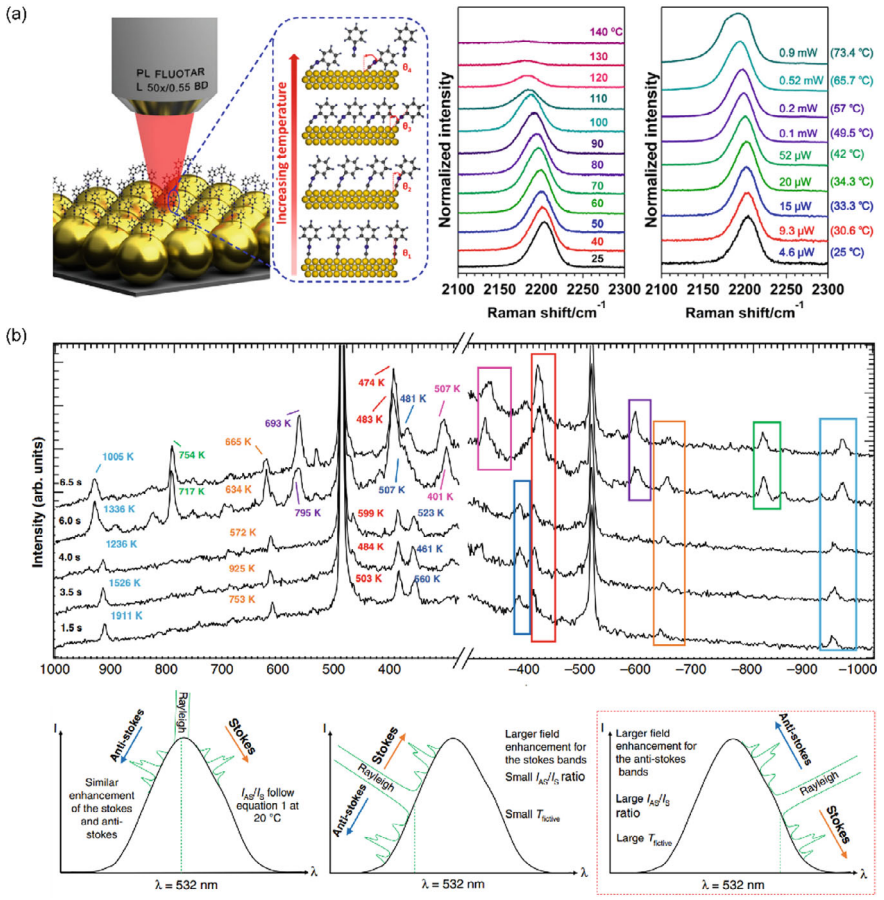



**Fig. 22.17 Temperature measurements via Raman spectroscopy**. **a** Sensing temperature variations through frequency shifts in Raman spectra of PIC molecules adsorbed on an Au nanoparticle surface. Reproduced from Ref. [124] with permission. **b** Inconsistent temperature values obtained from the experimental Raman spectra when directly utilizing the anti-Stokes/Stokes intensity ratio for individual vibrational modes. This underscores the importance of the ratio calibration by different electromagnetic enhancement conditions. Reproduced from Ref. [128] with permission

$$\frac{I_{\mathrm{AS}}}{I_{\mathrm{S}}} = \frac{M_k^{\mathrm{AS}}}{M_k^{\mathrm{S}}} \left( \frac{\omega_L + \omega_k}{\omega_L - \omega_k} \right)^4 \frac{n_k}{n_k + 1}, \tag{22.9}$$

where $\omega_L$ is the frequency of incident laser, $\omega_k$ is the frequency of the $k$-th vibrational mode, $M_k{}^{\mathrm{AS(S)}}$ is the enhancement factor of anti-Stokes (Stokes) signals of the vibrational mode due to the plasmonic enhancement, and $n_k$ is the vibrational population of the $k$-th vibrational mode. Under thermal equilibrium, $n_k$ generally follows a Bose–Einstein distribution statistically via

$$n_k = \left[ \exp\left( \frac{\hbar \omega_k}{k_B T_k} \right) - 1 \right]^{-1}, \tag{22.10}$$

where $k_B$ is the Boltzmann constant, and $T_k$ is the mode temperature for the $k$-th vibrational mode. Therefore, one can measure the temperature of a system based on the anti-Stokes to Stokes intensity ratios through the vibrational population. In 2020, Deckert's group tried to measure the near-field temperature from the Stokes and anti-Stokes spectral intensities using TERS, but found pronounced discrepancies in the temperature values measured [128]. As shown in Fig. 22.17b, inconsistent temperature values are obtained by directly utilizing the anti-Stokes to Stokes intensity ratio for each vibrational mode, which clearly does not make any physical sense since a molecular system, if under thermal equilibrium, should have the same temperature value for all vibrational modes. They attributed such a discrepancy to the different electromagnetic enhancement factors experienced by different modes. By incorporating a Lorentzian description to rectify such variations in the electromagnetic enhancement, they extracted the near-field temperature at the hot spot using the anti-Stokes and Stokes TERS signals.

For a single molecule under local heating by electrons or photons at the subnanometer scale, how to measure the local thermal effect still remains a great challenge since the molecule is believed to be under a nonequilibrium condition. In 2024, Dong's group proposed a method to characterize the local thermal properties of a single $C_{60}$ molecule during current-induced heating processes through tip-enhanced anti-Stokes Raman spectroscopy [129]. As shown in Fig. 22.18, by analyzing the tip-enhanced Stokes and anti-Stokes Raman spectra, they were able to estimate the local thermal effect of a single molecule within the tunnel junction. Even after the calibrations of the anti-Stokes to Stokes ratios by different enhancement factors, they find that the mode temperatures for different vibrational modes of the single molecule are still significantly different, up to several hundreds, and all these mode temperatures are much higher than the ambient temperature. Such a phenomenon is a clear indication that the molecule is in a nonequilibrium state. However, strikingly, they also find that the measured vibron populations always follow a Bose–Einstein distribution statistically, allowing to define an "effective temperature ($T^{\mathrm{eff}}$)" for describing the local-equilibrium state of the whole single molecule, i.e., a steady state within itself but out of equilibrium with the environment, as shown in Fig. 22.18 and Eq. (22.11).

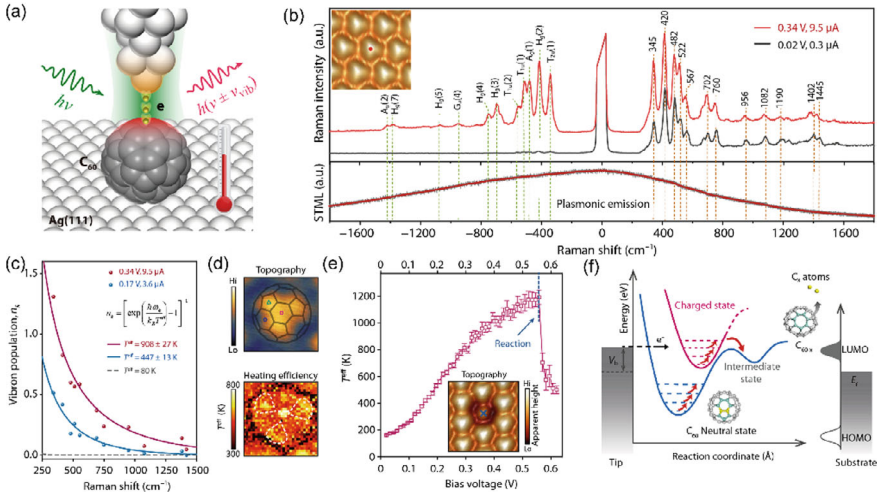



**Fig. 22.18 Local heating and Raman thermometry in a single $C_{60}$ molecule**. **a** Schematic of the TERS measurement for a single $C_{60}$ molecule on Ag(111). **b** Representative Raman spectra of a single $C_{60}$ molecule under different tunneling conditions. **c** Mode-dependent vibron populations under two different tunneling conditions at a constant tip height above the molecular center. **d** Spatial distribution of effective temperatures reflecting local heating efficiencies, with the upper inset showing an STM image and lower inset displaying a mapping image of $T^{\text{eff}}$ associated with the local heating efficiencies. **e** Effective temperatures as a function of increasing bias voltages. **f** Schematic showing electron-induced $C_{60}$ decomposition mechanism. Reproduced from Ref. [129] with permission

$$n_k = \left[\exp\left(\frac{\hbar\omega_k}{k_B T^{\text{eff}}}\right) - 1\right]^{-1}. \tag{22.11}$$

The local effective temperature of a heated $C_{60}$ is found to rise with increasing tunneling currents, and the maximum $T^{\text{eff}}$ temperature that the heated $C_{60}$ can stand is about 1150 K, beyond which the $C_{60}$ cage decomposes. Surprisingly, such a local effective temperature is found similar to the decomposition temperature of $C_{60}$ molecules reported in conventional ensemble experiments, thus justifying to some extent the validity of the thus-defined effective temperature to serve as a measure for the local thermal effect of a single molecule upon heating. By using $T^{\text{eff}}$ as an indicator of the local heating effect, even the differences in heating efficiencies over a single molecule can be specified, showing a higher effective temperature when heated at the molecular center. This method offers a practical approach not only for noninvasively detecting the local heating effect inside a single molecule under nonequilibrium conditions, but also for tracking the change of local temperatures during single-molecule reactions.

### 22.3.3 Applications in 2D Materials

The high-resolution TERS technique can not only be applied in the studies of molecular systems with the single-bond sensitivity, but can also serve as a transformative technique for the studies of two-dimensional (2D) materials. Owing to its nanoscale spatial resolution and surface sensitivity, TERS has been utilized in surface science for studying localized surface phenomena, including surface structures, surface interactions, surface catalysis, and dynamic surface processes. Such comprehensive characterization capability makes TERS a powerful versatile technique for studying the intricate properties of atomically thin materials such as graphene and transition metal dichalcogenides (TMDs).

In 2017, Wu's group first achieved a $10^9$ TERS enhancement and a 0.5 nm spatial resolution using monolayer silicene on Ag(111) as a prototypical 2D material system [130]. Since the vertical vibrational modes are selectively enhanced in TERS, the characteristic Raman modes in silicene are evidently observed, identified as $A^1$, $A^2$, and $E$ modes shown in Fig. 22.19a. Their work also identified the vibrational properties of distinct silicene phases, along with the characterization of defects and domain boundaries in silicone. In 2021, Jiang's group investigated the interfacial interaction within the tetraphenyldibenzoperiflanthene (DBP) and borophene vertical heterostructure using Ångström-resolved TERS [131]. As shown in Fig. 22.19b, the subtle ripples and compressive strains of the borophene lattice underneath the molecular layer can be clearly resolved from the TERS measurements, and the induced interfacial strain is found to extend in borophene by ~ 1 nm beyond the molecular region through the analysis of frequency shift of the $B_{3g}^2$ ($\nu_{1/6}$) mode of borophene at ~ 190 $cm^{-1}$. In 2019, Ren's group demonstrated the edge-related vibrational properties of $MoS_2$ on an Au film using TERS [132]. As shown in Fig. 22.19c, an edge-induced Raman peak at 396 $cm^{-1}$ is observed due to the double resonance Raman scattering process, revealing the electron–phonon interactions at the edges. They also directly visualized the defect-induced band-bending region and the electronic transition region at the edge in real space. Even the types of different zigzag and armchair edges can be clearly distinguished from the peak shifts in the TERS spectra due to the different influences of local strains at different edges. In 2021, Jorio's group achieved the TERS imaging of the reconstructed twisted bilayer graphene by using a specially fabricated pyramid tip [133]. As shown in Fig. 22.19d, the presence of strain solitons and topological points can be detected from the spectral variations, which is highly related to the vibrational and electronic properties of the twisted structures, particularly for small twist angles.

High-resolution TERS has shown remarkable abilities in the investigation of local optical properties, strain distributions, defects, and electronic structures within the local domains of 2D materials. For example, it has played a pivotal role in exploring the phonon dispersion [134], strain-induced effects [135], and variations of local

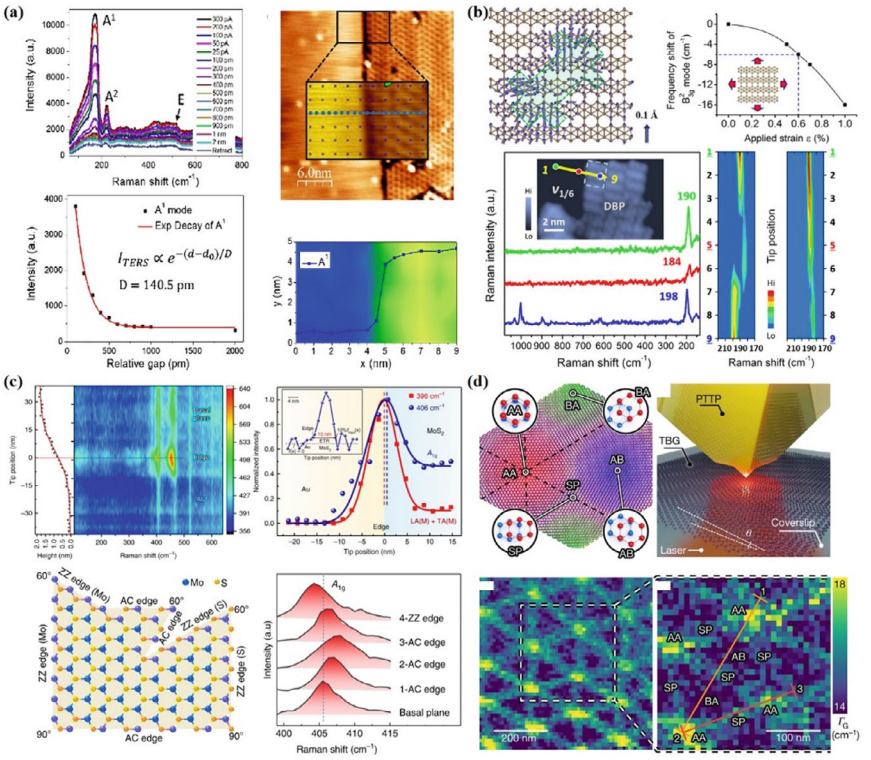



**Fig. 22.19 Applications of TERS for the characterization of two-dimensional materials**. **a** Investigation of TERS enhancement factor and spatial resolution through gap-distance dependent spectra and intensity mapping of the $A^1$ mode on silicene $\sqrt{13} \times \sqrt{13}$ phase on Ag(111), with corresponding STM topography showing the surface structure and the line-trace for the TERS measurements. Reproduced from Ref. [130] with permission. **b** Evolution of TERS spectra and spectral measurements along a yellow line-trace on $\nu_{1/6}$ borophene with DBP adsorption, illustrating spectral changes upon removal of DBP molecules as well as correlation between lattice strain and frequency shift of the $B_{3g}^2$ mode. Reproduced from Ref. [131] with permission. **c** TERS imaging and spectral analysis of the edge structure of the bilayer $MoS_2$, including topographic height profiles, normalized intensities of TERS peaks, illustration of edge structures, and TERS spectra of different edge types. Reproduced from Ref. [132] with permission. **d** Schematics of AB- and BA-stacked domains, strain solitons (SP), topological points (AA), plasmon-tunable tip pyramid (PTTP) nanoantenna, and crystallographic hyperspectral imaging of rotated twisted bilayer graphene (rTBG) based on G′-band nano-Raman intensity. Reproduced from Ref. [133] with permission

doping behaviors [136] in graphene studies, also providing crucial insights into excitonic effects [137] and valley polarization phenomena [138]. All these studies will improve the understanding of the electronic and optical behaviors in 2D materials at the subnanometer scale. Therefore, the capability of TERS to discern and characterize these intricate features has notably contributed to the exploration and elucidation of

the unique properties of 2D materials, offering valuable insights for both fundamental research and their potential technological applications in diverse fields.

## 22.4 Conclusion and Outlook

In this chapter, we have overviewed the basic concepts and recent advances in the field of the Ångström-resolved tip-enhanced Raman spectromicroscopy. Although the Ångström-resolved TERS has been developed as a powerful tool to unravel the chemical structures and chemical bond changes in various systems with subnanometer resolution, there are still many challenges remaining, which might be suggested as the potential directions in the future developments of the Ångström-resolved TERS in both technical and application aspects:

1. **Time-resolved TERS**: Due to the relatively long collection time of TERS measurements, the temporal resolution of Ångström-resolved TERS is very limited. This is why TERS is usually applied for the studies of static processes. Even for the applications in chemical reactions, only the spectral differences between the reactants and the products can be captured, while the signals from the dynamic processes and intermediate states are very difficult to obtain. Therefore, further combination with ultrafast spectroscopic techniques may enable the Ångström-resolved TERS to possess both ultrahigh spatial and ultrafast temporal resolution simultaneously. With such a powerful ability, it will help to unravel the dynamic mechanism at the nanoscale, shedding light on transient phenomena, reaction kinetics, and real-time surface dynamics.
2. **TERS studies of complex molecular systems**: So far, Ångström-resolved TERS has shown its unrivaled ability in resolving single chemical bonds or even single atoms in simple model systems. However, in the more practical applications, the molecular systems are no longer simple and planar structures, but can be more complex molecules including three-dimensional structures and twisted biomolecules (such as DNA/RNA helix chains and folded protein structures). For these complex systems, both the lateral and vertical resolving ability of TERS are required in order to obtain the full stereo structures through a tomographic-like procedure with the aid of artificial intelligence (AI) techniques. The AI-assisted TERS could also improve the data qualities of spectra and mapping images from the complex and noisy environment.
3. **Multi-modal imaging**: Since the TERS measurements only reveal the information related with the vibrational states and chemical structures, it is usually difficult to investigate the electronic and other properties directly by only using TERS. Moreover, the molecules would also interact with the external electric, magnetic, light, and force fields, resulting in different responses characterized by different techniques. Therefore, how to realize a comprehensive study of the heterogeneous properties of a single molecule at the Ångström scale is still a great challenge. For example, how to utilize only one same tip to fulfill the functions

of different scanning probe microscopes (e.g., probing electronic states using STM and molecular skeletons using AFM simultaneously together with TERS measurements) as many as possible would be the potential directions in the future development of Ångström-resolved TERS.

## References


1. Itoh, T. *et al.*, Toward a new era of SERS and TERS at the nanometer scale: from fundamentals to innovative applications, Chem. Rev. **123**, 1552–1634 (2023).
2. Aizpurua, J., Apell, S. P. & Berndt, R., Role of tip shape in light emission from the scanning tunneling microscope, Phys. Rev. B **62**, 2065–2073 (2000).
3. Dong, Z. C. *et al.*, Generation of molecular hot electroluminescence by resonant nanocavity plasmons, Nat. Photonics **4**, 50–54 (2009).
4. Xu, J. *et al.*, Determining structural and chemical heterogeneities of surface species at the single-bond limit, Science **371**, 818–822 (2021).
5. Wang, R. P. *et al.*, Raman detection of bond breaking and making of a chemisorbed up-standing single molecule at single-bond level, J. Phys. Chem. Lett. **12**, 1961–1968 (2021).
6. Wessel, J., Surface-enhanced optical microscopy, J. Opt. Soc. Am. B. **2**, 1538–1541 (1985).
7. Stöckle, R. M., Suh, Y. D., Deckert, V. & Zenobi, R., Nanoscale chemical analysis by tip-enhanced Raman spectroscopy, Chem. Phys. Lett. **318**, 131–136 (2000).
8. Anderson, M. S., Locally enhanced Raman spectroscopy with an atomic force microscope, Appl. Phys. Lett. **76**, 3130–3132 (2000).
9. Hayazawa, N., Inouye, Y., Sekkat, Z. & Kawata, S., Metallized tip amplification of near-field Raman scattering, Opt. Commun. **183**, 333–336 (2000).
10. Pettinger, B., Picardi, G., Schuster, R. & Ertl, G., Surface enhanced Raman spectroscopy: towards single molecule spectroscopy, Electrochem. **68**, 942–949 (2000).
11. Zhang, R. *et al.*, Chemical mapping of a single molecule by plasmon-enhanced Raman scattering, Nature **498**, 82–86 (2013).
12. Jaculbia, R. B. *et al.*, Single-molecule resonance Raman effect in a plasmonic nanocavity, Nat. Nanotechnol. **15**, 105–110 (2020).
13. Lee, J., Crampton, K. T., Tallarida, N. & Apkarian, V. A., Visualizing vibrational normal modes of a single molecule with atomically confined light, Nature **568**, 78–82 (2019).
14. Zhang, Y. *et al.*, Visually constructing the chemical structure of a single molecule by scanning Raman picoscopy, Natl. Sci. Rev. **6**, 1169–1175 (2019).
15. Crampton, K. T., Lee, J. & Apkarian, V. A., Ion-selective, atom-resolved imaging of a 2D $Cu_2N$ insulator: field and current driven tip-enhanced Raman spectromicroscopy using a molecule-terminated tip, ACS Nano **13**, 6363–6371 (2019).
16. Duan, S. *et al.*, Theoretical modeling of plasmon-enhanced Raman images of a single molecule with subnanometer resolution, J. Am. Chem. Soc. **137**, 9515–9518 (2015).
17. Liu, P., Chulhai, D. V. & Jensen, L., Single-molecule imaging using atomistic near-field tip-enhanced Raman spectroscopy, ACS Nano **11**, 5094–5102 (2017).
18. Abbe, E., Beiträge zur theorie des mikroskops und der mikroskopischen wahrnehmung, Arch. Mikroskop. Anatom. **9**, 413–468 (1873).
19. Betzig, E., Proposed method for molecular optical imaging, Opt. Lett. **20**, 237–239 (1995).
20. Yang, B. *et al.*, Sub-nanometre resolution in single-molecule photoluminescence imaging, Nat. Photonics **14**, 693–699 (2020).
21. Zhu, J. Z., Chen, G., Ijaz, T., Li, X. G. & Dong, Z. C., Influence of an atomistic protrusion at the tip apex on enhancing molecular emission in tunnel junctions: a theoretical study, J. Chem. Phys. **154**, 214706 (2021).

22. Urbieta, M. *et al.*, Atomic-scale lightning rod effect in plasmonic picocavities: a classical view to a quantum effect, ACS Nano **12**, 585–595 (2018).
23. García de Abajo, F. J. & Aizpurua, J., Numerical simulation of electron energy loss near inhomogeneous dielectrics, Phys. Rev. B **56**, 15873–15884 (1997).
24. Huber, C., Trugler, A., Hohenester, U., Prior, Y. & Kautek, W., Optical near-field excitation at commercial scanning probe microscopy tips: a theoretical and experimental investigation, Phys. Chem. Chem. Phys. **16**, 2289–2296 (2014).
25. Kern, J. *et al.*, Atomic-scale confinement of resonant optical fields, Nano Lett. **12**, 5504–5509 (2012).
26. Micic, M., Klymyshyn, N., Suh, Y. D. & Lu, H. P., Finite element method simulation of the field distribution for AFM tip-enhanced surface-enhanced Raman scanning microscopy, J. Phys. Chem. B **107**, 1574–1584 (2003).
27. Oubre, C. & Nordlander, P., Optical properties of metallodielectric nanostructures calculated using the finite difference time domain method, J. Phys. Chem. B **108**, 17740–17747 (2004).
28. Rahaman, M. *et al.*, The role of a plasmonic substrate on the enhancement and spatial resolution of tip-enhanced Raman scattering, Faraday Discuss. **214**, 309–323 (2019).
29. Yang, M. *et al.*, Tip-enhanced Raman excitation spectroscopy (TERES): direct spectral characterization of the gap-mode plasmon, Nano Lett. **19**, 7309–7316 (2019).
30. Yang, Z. L. *et al.*, FDTD for plasmonics: applications in enhanced Raman spectroscopy, Chin. Sci. Bull. **55**, 2635–2642 (2010).
31. Richard-Lacroix, M., Zhang, Y., Dong, Z. C. & Deckert, V., Mastering high resolution tip-enhanced Raman spectroscopy: towards a shift of perception, Chem. Soc. Rev. **46**, 3922–3944 (2017).
32. Benz, F. *et al.*, Single-molecule optomechanics in "picocavities", Science **354**, 726–729 (2016).
33. Baumberg, J. J., Aizpurua, J., Mikkelsen, M. H. & Smith, D. R., Extreme nanophotonics from ultrathin metallic gaps, Nat. Mater. **18**, 668–678 (2019).
34. Shin, H. H. *et al.*, Frequency-domain proof of the existence of atomic-scale SERS hot-spots, Nano Lett. **18**, 262–271 (2018).
35. Marchesin, F., Koval, P., Barbry, M., Aizpurua, J. & Sánchez-Portal, D., Plasmonic response of metallic nanojunctions driven by single atom motion: quantum transport revealed in optics, ACS Photonics **3**, 269–277 (2016).
36. Barbry, M. *et al.*, Atomistic near-field nanoplasmonics: reaching atomic-scale resolution in nanooptics, Nano Lett. **15**, 3410–3419 (2015).
37. Zhang, X. B. *et al.*, Fast fabrication and judgement of tip-enhanced Raman spectroscopy-active tips, Chin. J. Chem. Phys. **35**, 713–719 (2022).
38. Li, W., Zhou, Q., Zhang, P. & Chen, X. W., Bright optical eigenmode of 1 $nm^3$ mode volume, Phys. Rev. Lett. **126**, 257401 (2021).
39. Zhu, J. Z., Chen, G. & Dong, Z. C., Influence of atomistic protrusion on the substrate on molecular luminescence in tunnel junctions, Chin. J. Chem. Phys. **36**, 1–8 (2023).
40. Savage, K. J. *et al.*, Revealing the quantum regime in tunnelling plasmonics, Nature **491**, 574–577 (2012).
41. Zhu, W. *et al.*, Quantum mechanical effects in plasmonic structures with subnanometre gaps, Nat. Commun. **7**, 11495 (2016).
42. Atkin, J. M. & Raschke, M. B., Techniques: Optical spectroscopy goes intramolecular, Nature **498**, 44–45 (2013).
43. Luo, Y., Fernandez-Dominguez, A. I., Wiener, A., Maier, S. A. & Pendry, J. B., Surface plasmons and nonlocality: a simple model, Phys. Rev. Lett. **111**, 093901 (2013).
44. Goncalves, P. A. D. *et al.*, Plasmon-emitter interactions at the nanoscale, Nat. Commun. **11**, 366 (2020).
45. Kale, M. J. & Christopher, P., Plasmons at the interface, Science **349**, 587–588 (2015).
46. Khurgin, J., Tsai, W. Y., Tsai, D. P. & Sun, G., Landau damping and limit to field confinement and enhancement in plasmonic dimers, ACS Photonics **4**, 2871–2880 (2017).

47. Li, X. G., Xiao, D. & Zhang, Z. Y., Landau damping of quantum plasmons in metal nanostructures, New J. Phys. **15**, 023011 (2013).
48. Alcaraz Iranzo, D. *et al.*, Probing the ultimate plasmon confinement limits with a van der Waals heterostructure, Science **360**, 291–295 (2018).
49. Tserkezis, C., Mortensen, N. A. & Wubs, M., How nonlocal damping reduces plasmon-enhanced fluorescence in ultranarrow gaps, Phys. Rev. B **96**, 085413 (2017).
50. Duan, S., Tian, G. & Luo, Y., Theory for modeling of high resolution resonant and nonresonant Raman images, J. Chem. Theory Comput. **12**, 4986–4995 (2016).
51. Zhang, Y., Dong, Z. C. & Aizpurua, J., Theoretical treatment of single-molecule scanning Raman picoscopy in strongly inhomogeneous near fields, J. Raman Spectrosc. **52**, 296–309 (2021).
52. Zhang, Y., Zhang, Y. & Dong, Z. C., Scanning Raman picoscopy: Ångstrom-resolved tip-enhanced Raman spectromicroscopy, Chin. J. Chem. Phys. **34**, 1–14 (2021).
53. Pozzi, E. A. *et al.*, Ultrahigh-vacuum tip-enhanced Raman spectroscopy, Chem. Rev. **117**, 4961–4982 (2017).
54. Wang, X., Huang, S. C., Hu, S., Yan, S. & Ren, B., Fundamental understanding and applications of plasmon-enhanced Raman spectroscopy, Nat. Rev. Phys. **2**, 253–271 (2020).
55. Sun, M., Fang, Y., Yang, Z. & Xu, H., Chemical and electromagnetic mechanisms of tip-enhanced Raman scattering, Phys. Chem. Chem. Phys. **11**, 9412–9419 (2009).
56. Jeanmaire, D. L. & Van Duyne, R. P., Surface Raman spectroelectrochemistry, J. Electroanal. Chem. Interfacial Electrochem. **84**, 1–20 (1977).
57. Albrecht, M. G. & Creighton, J. A., Anomalously intense Raman spectra of pyridine at a silver electrode, J. Am. Chem. Soc. **99**, 5215–5217 (1977).
58. Moskovits, M., Surface-enhanced spectroscopy, Rev. Mod. Phys. **57**, 783–826 (1985).
59. Nie, S. & Emory, S. R., Probing single molecules and single nanoparticles by surface-enhanced Raman scattering, Science **275**, 1102–1106 (1997).
60. Kneipp, K. *et al.*, Single molecule detection using surface-enhanced Raman scattering (SERS), Phys. Rev. Lett. **78**, 1667–1670 (1997).
61. Jensen, L., Aikens, C. M. & Schatz, G. C., Electronic structure methods for studying surface-enhanced Raman scattering, Chem. Soc. Rev. **37**, 1061–1073 (2008).
62. Cong, S., Liu, X., Jiang, Y., Zhang, W. & Zhao, Z., Surface enhanced Raman scattering revealed by interfacial charge-transfer transitions, Innovation. **1**, 100051 (2020).
63. Novotny, L. & Hecht, B., *Principles of Nano-Optics.* (Cambridge university press, 2012).
64. Le Ru, E. & Etchegoin, P., *Principles of Surface-Enhanced Raman Spectroscopy: and Related Plasmonic Effects.* (Elsevier, 2008).
65. Otto, A., Mrozek, I., Grabhorn, H. & Akemann, W., Surface-enhanced Raman-scattering, J. Phys.-Condens. Matter **4**, 1143–1212 (1992).
66. Campion, A., Ivanecky, J. E., Child, C. M. & Foster, M., On the mechanism of chemical enhancement in surface-enhanced Raman-scattering, J. Am. Chem. Soc. **117**, 11807–11808 (1995).
67. Zhao, L. L., Jensen, L. & Schatz, G. C., Surface-enhanced raman scattering of pyrazine at the junction between two $Ag_{20}$ nanoclusters, Nano Lett. **6**, 1229–1234 (2006).
68. Fromm, D. P. *et al.*, Exploring the chemical enhancement for surface-enhanced Raman scattering with Au bowtie nanoantennas, J. Chem. Phys. **124**, 61101 (2006).
69. Morton, S. M. & Jensen, L., Understanding the molecule-surface chemical coupling in SERS, J. Am. Chem. Soc. **131**, 4090–4098 (2009).
70. Oren, M., Galperin, M. & Nitzan, A., Raman scattering from molecular conduction junctions: charge transfer mechanism, Phys. Rev. B **85**, 115435 (2012).
71. Le Ru, E. C. & Etchegoin, P. G., Quantifying SERS enhancements, MRS Bull. **38**, 631–640 (2013).
72. Valley, N., Greeneltch, N., Van Duyne, R. P. & Schatz, G. C., A look at the origin and magnitude of the chemical contribution to the enhancement mechanism of surface-enhanced Raman spectroscopy (SERS): theory and experiment, J. Phys. Chem. Lett. **4**, 2599–2604 (2013).

73. Birke, R. L., Lombardi, J. R., Saidi, W. A. & Norman, P., Surface-enhanced Raman scattering due to charge-transfer resonances: a time-dependent density functional theory study of $Ag_{13}$-4-Mercaptopyridine, J. Phys. Chem. C **120**, 20721–20735 (2016).
74. Yilmaz, M. *et al.*, Nanostructured organic semiconductor films for molecular detection with surface-enhanced Raman spectroscopy, Nat. Mater. **16**, 918–924 (2017).
75. Zhan, C. *et al.*, From plasmon-enhanced molecular spectroscopy to plasmon-mediated chemical reactions, Nat. Rev. Chem. **2**, 216–230 (2018).
76. Langer, J. *et al.*, Present and future of surface-enhanced Raman scattering, ACS Nano **14**, 28–117 (2020).
77. Chen, R. & Jensen, L., Interpreting chemical enhancements of surface-enhanced Raman scattering, Chem. Phys. Rev. **4**, 021305 (2023).
78. Yang, B. *et al.*, Chemical enhancement and quenching in single-molecule tip-enhanced Raman spectroscopy, Angew. Chem. Int. Ed. **62**, e202218799 (2023).
79. Zhang, C. *et al.*, Fabrication of silver tips for scanning tunneling microscope induced luminescence, Rev. Sci. Instrum. **82**, 083101 (2011).
80. Iwami, M., Uehara, Y. & Ushioda, S., Preparation of silver tips for scanning tunneling microscopy imaging, Rev. Sci. Instrum. **69**, 4010–4011 (1998).
81. Ren, B., Picardi, G. & Pettinger, B., Preparation of gold tips suitable for tip-enhanced Raman spectroscopy and light emission by electrochemical etching, Rev. Sci. Instrum. **75**, 837–841 (2004).
82. Lloyd, J. S., Williams, A., Rickman, R. H., McCowen, A. & Dunstan, P. R., Reproducible electrochemical etching of silver probes with a radius of curvature of 20 nm for tip-enhanced Raman applications, Appl. Phys. Lett. **99**, 143108 (2011).
83. Xu, G. *et al.*, Constant current etching of gold tips suitable for tip-enhanced Raman spectroscopy, Rev. Sci. Instrum. **83**, 103708 (2012).
84. Kharintsev, S. S., Rogov, A. M. & Kazarian, S. G., Nanopatterning and tuning of optical taper antenna apex for tip-enhanced Raman scattering performance, Rev. Sci. Instrum. **84**, 093106 (2013).
85. Li, M. H. *et al.*, Electrochemical fabrication of silver tips for tip-enhanced Raman spectroscopy assisted by a machine vision system, J. Raman Spectrosc. **47**, 808–812 (2016).
86. Plathier, J., Pignolet, A. & Ruediger, A., Note: controlling the length of plasmonic tips obtained by pulsed electrochemical etching, Rev. Sci. Instrum. **89**, 096107 (2018).
87. Sasaki, S. S. *et al.*, Note: automated electrochemical etching and polishing of silver scanning tunneling microscope tips, Rev. Sci. Instrum. **84**, 096109 (2013).
88. Pitters, J. L., Urban, R., Vesa, C. & Wolkow, R. A., Tip apex shaping of gas field ion sources, Ultramicroscopy **131**, 56–60 (2013).
89. Tallarida, N., Lee, J. & Apkarian, V. A., Tip-enhanced Raman spectromicroscopy on the angstrom scale: bare and co-terminated Ag tips, ACS Nano **11**, 11393–11401 (2017).
90. Trautmann, S. *et al.*, A classical description of subnanometer resolution by atomic features in metallic structures, Nanoscale **9**, 391–401 (2017).
91. Yang, B. *et al.*, Sub-nanometre resolution in single-molecule photoluminescence imaging, Nat. Photonics **14**, 693+ (2020).
92. Liu, S., Wolf, M. & Kumagai, T., Plasmon-assisted resonant electron tunneling in a scanning tunneling microscope junction, Phys. Rev. Lett. **121**, 226802 (2018).
93. Binnig, G. *et al.*, Tunneling spectroscopy and inverse photoemission: image and field states, Phys. Rev. Lett. **55**, 991–994 (1985).
94. Schouteden, K. & Van Haesendonck, C., Lateral quantization of two-dimensional electron states by embedded Ag nanocrystals, Phys. Rev. Lett. **108**, 076806 (2012).
95. Dougherty, D. B. *et al.*, Tunneling spectroscopy of Stark-shifted image potential states on Cu and Au surfaces, Phys. Rev. B **76**, 125428 (2007).
96. Hartschuh, A., Sanchez, E. J., Xie, X. S. & Novotny, L., High-resolution near-field Raman microscopy of single-walled carbon nanotubes, Phys. Rev. Lett. **90**, 095503 (2003).
97. Anderson, N., Hartschuh, A., Cronin, S. & Novotny, L., Nanoscale vibrational analysis of single-walled carbon nanotubes, J. Am. Chem. Soc. **127**, 2533–2537 (2005).

98. Steidtner, J. & Pettinger, B., Tip-enhanced Raman spectroscopy and microscopy on single dye molecules with 15 nm resolution, Phys. Rev. Lett. **100**, 236101 (2008).
99. Chiang, N. *et al.*, Conformational contrast of surface-mediated molecular switches yields angstrom-scale spatial resolution in ultrahigh vacuum tip-enhanced Raman spectroscopy, Nano Lett. **16**, 7774–7778 (2016).
100. Pettinger, B., Schambach, P., Villagomez, C. J. & Scott, N., Tip-enhanced Raman spectroscopy: near-fields acting on a few molecules, Annu. Rev. Phys. Chem. **63**, 379–399 (2012).
101. Jiang, N. *et al.*, Observation of multiple vibrational modes in ultrahigh vacuum tip-enhanced Raman spectroscopy combined with molecular-resolution scanning tunneling microscopy, Nano Lett. **12**, 5061–5067 (2012).
102. Sonntag, M. D. *et al.*, Single-molecule tip-enhanced Raman spectroscopy, J. Phys. Chem. C **116**, 478–483 (2011).
103. Liu, Z. *et al.*, Revealing the molecular structure of single-molecule junctions in different conductance states by fishing-mode tip-enhanced Raman spectroscopy, Nat. Commun. **2**, 305 (2011).
104. Yano, T., Verma, P., Saito, Y., Ichimura, T. & Kawata, S., Pressure-assisted tip-enhanced Raman imaging at a resolution of a few nanometres, Nat. Photonics **3**, 473–477 (2009).
105. Neacsu, C. C., Dreyer, J., Behr, N. & Raschke, M. B., Scanning-probe Raman spectroscopy with single-molecule sensitivity, Phys. Rev. B **73**, 193406 (2006).
106. Xu, H., Aizpurua, J., Kall, M. & Apell, P., Electromagnetic contributions to single-molecule sensitivity in surface-enhanced raman scattering, Phys. Rev. E **62**, 4318–4324 (2000).
107. Jiang, S. *et al.*, Distinguishing adjacent molecules on a surface using plasmon-enhanced Raman scattering, Nat. Nanotechnol. **10**, 865–869 (2015).
108. Jiang, S. *et al.*, Subnanometer-resolved chemical imaging via multivariate analysis of tip-enhanced Raman maps, Light Sci. Appl. **6**, e17098 (2017).
109. Zhang, R. *et al.*, Distinguishing individual DNA bases in a network by non-resonant tip-enhanced Raman scattering, Angew. Chem. Int. Ed. **56**, 5561–5564 (2017).
110. Zhang, J. X. *et al.*, Probing the vertical resolving ability of tip-enhanced Raman spectroscopy, ACS Photonics **10**, 3682–3690 (2023).
111. Wan, M. *et al.*, Dielectric-loading approach for extra electric field enhancement and spatially transferring plasmonic hot-spots, Nanotechnology **32**, 035205 (2021).
112. Zhang, Y., Zhang, R., Jiang, S., Zhang, Y. & Dong, Z. C., Probing adsorption configurations of small molecules on surfaces by single-molecule tip-enhanced Raman spectroscopy, ChemPhysChem **20**, 37–41 (2019).
113. Schultz, J. F. *et al.*, Defining multiple configurations of rubrene on a Ag(100) surface with 5 Å spatial resolution via ultrahigh vacuum tip-enhanced Raman spectroscopy, J. Phys. Chem. C **124**, 2420–2426 (2020).
114. Wang, R. P. *et al.*, Sub-nanometer resolved tip-enhanced Raman spectroscopy of a single molecule on the Si(111) substrate, J. Phys. Chem. C **126**, 12121–12128 (2022).
115. Ghafoor, A. *et al.*, Site-dependent TERS study of a porphyrin molecule on Ag(100) at 7 K, Chin. J. Chem. Phys. **32**, 287–291 (2019).
116. Li, H. *et al.*, Probing the deformation of [12]cycloparaphenylene molecular nanohoops adsorbed on metal surfaces by tip-enhanced Raman spectroscopy, J. Chem. Phys. **153**, 244201 (2020).
117. Li, H. *et al.*, Probing coverage-dependent adsorption configuration and on-surface dimerization by single-molecule tip-enhanced Raman spectroscopy, Appl. Phys. A **129**, 3 (2022).
118. Li, L. *et al.*, Chemically identifying single adatoms with single-bond sensitivity during oxidation reactions of borophene, Nat. Commun. **13**, 1796 (2022).
119. Zhong, J. H. *et al.*, Probing the electronic and catalytic properties of a bimetallic surface with 3 nm resolution, Nat. Nanotechnol. **12**, 132–136 (2017).
120. Yin, H. *et al.*, Nanometre-scale spectroscopic visualization of catalytic sites during a hydrogenation reaction on a Pd/Au bimetallic catalyst, Nat. Catal. **3**, 834–842 (2020).

121. Zhu, X. *et al.*, Revealing intramolecular isotope effects with chemical-bond precision, J. Am. Chem. Soc. **145**, 13839–13845 (2023).
122. Dong, X. R. *et al.*, Tip-induced bond weakening, tilting, and hopping of a single CO molecule on Cu(100), Light Adv Manuf. **3**, 729–738 (2022).
123. Zhang, D. C., Zheng, X. & Di Ventra, M., Local temperatures out of equilibrium, Phys. Rep. **830**, 1–66 (2019).
124. Hu, S. *et al.*, Quantifying surface temperature of thermoplasmonic nanostructures, J. Am. Chem. Soc. **140**, 13680–13686 (2018).
125. Pop, E. *et al.*, Electronic, thermal, and unconventional applications of 2D materials, 2017 IEEE 17th International Conference on Nanotechnology (IEEE-NANO), IEEE, 916–917 (2017).
126. Yoon, D., Son, Y. W. & Cheong, H., Negative thermal expansion coefficient of graphene measured by Raman spectroscopy, Nano Lett. **11**, 3227–3231 (2011).
127. Calizo, I., Balandin, A. A., Bao, W., Miao, F. & Lau, C. N., Temperature dependence of the Raman spectra of graphene and graphene multilayers, Nano Lett. **7**, 2645–2649 (2007).
128. Richard-Lacroix, M. & Deckert, V., Direct molecular-level near-field plasmon and temperature assessment in a single plasmonic hotspot, Light Sci. Appl. **9**, 35 (2020).
129. Meng, Q. S. *et al.*, Local heating and Raman thermometry in a single molecule, Sci. Adv. **10**, eadl1015 (2024).
130. Sheng, S. *et al.*, Vibrational properties of a monolayer silicene sheet studied by tip-enhanced Raman spectroscopy, Phys. Rev. Lett. **119**, 196803 (2017).
131. Li, L. *et al.*, Angstrom-scale spectroscopic visualization of interfacial interactions in an organic/borophene vertical heterostructure, J. Am. Chem. Soc. **143**, 15624–15634 (2021).
132. Huang, T. X. *et al.*, Probing the edge-related properties of atomically thin MoS(2) at nanoscale, Nat. Commun. **10**, 5544 (2019).
133. Gadelha, A. C. *et al.*, Localization of lattice dynamics in low-angle twisted bilayer graphene, Nature **590**, 405–409 (2021).
134. Balois, M. V. *et al.*, Visualization of subnanometric phonon modes in a plasmonic nano-cavity via ambient tip-enhanced Raman spectroscopy, npj 2D Mater. Appl. **3**, 38 (2019).
135. Beams, R., Cancado, L. G., Jorio, A., Vamivakas, A. N. & Novotny, L., Tip-enhanced Raman mapping of local strain in graphene, Nanotechnology **26**, 175702 (2015).
136. Iwasaki, T. *et al.*, Local hole doping concentration modulation on graphene probed by tip-enhanced Raman spectroscopy, Carbon **111**, 67–73 (2017).
137. Park, K. D. *et al.*, Hybrid tip-enhanced nanospectroscopy and nanoimaging of monolayer $WSe_2$ with local strain control, Nano Lett. **16**, 2621–2627 (2016).
138. Kim, Y. & Kim, J., Near-field optical imaging and spectroscopy of 2D-TMDs, Nanophotonics **10**, 3397–3415 (2021).

# Chapter 23
# Nanoscale Imaging of Photocatalytic Processes Using Tip-Enhanced Raman Spectroscopy

**Dmitry Kurouski**

**Abstract** Tip-enhanced Raman spectroscopy (TERS) is a modern analytical technique that has single molecule sensitivity and sub-nanometer spatial resolution. These unique properties of TERS are based on localized surface plasmon resonances (LSPRs) that are generated at the apex of the metallized scanning probes. Decaying, LSPRs produce hot carriers, highly energetic species that can trigger chemical reactions. Consequently, the scanning probe in TERS can be used to monitor and trigger chemical reactions on the sample of interest. This chapter summarizes the most recent advances in nanoscale imaging of plasmon-driven reactions on mono- and bimetallic nanostructures. It also critically discusses advantages and disadvantages of TERS in plasmon-driven catalysis.

**keywords** TERS · 4-NBT · DMAB · Plasmons · Hot carriers · LSPR · Catalysis

## 23.1 TERS Instrumentation

Tip-enhanced Raman spectroscopy (TERS) is a modern analytical technique that shares advantages of both scanning probe microscopy (SPM) and surface-enhanced Raman spectroscopy (SERS) [1–3]. The atomic force microscope (AFM) variant of SPM is capable of providing nanoscale spatial resolution of sample's topography [4–7], whereas scanning tunneling microscopy (STM) can be used to image analyzed specimens with sub-nanometer spatial resolution [8–13]. Spatial resolution of STM

D. Kurouski (✉)
Department of Biochemistry and Biophysics, Texas A&M University, College Station, Texas 77843, USA
e-mail: dkurouski@tamu.edu

Department of Biomedical Engineering, Texas A&M University, College Station, Texas 77843, USA

Institute for Advancing Health Through Agriculture, College Station, Texas 77843, USA

© The Author(s), under exclusive license to Springer Nature Singapore Pte Ltd. 2024

M. Procházka et al. (eds.), *Surface- and Tip-Enhanced Raman Scattering Spectroscopy*,
https://doi.org/10.1007/978-981-97-5818-0_23

imaging performance can be further enhanced by ultra-high vacuum (UHV) chambers [10, 12, 13]. Such chambers primarily minimize thermal drift, as well as help to minimize oxidation and contamination of both samples and scanning probes.

Scanning probes used in both AFM and STM have to be modified for TERS. Thermal evaporation is typically utilized to deposit 40–80 nm of gold (Au) or silver (Ag) on commercially available silicon or silicon nitride AFM probes [14–22]. In some cases, a thin 2–3 nm thick layer of titanium (Ti) can be deposited on such tips prior to Au- or Ag-coating to enable better adhesion of plasmonic metal to the silicon or silicon nitride surface of the scanning probes. Once fabricated, Au-coated tips can retain their plasmonic activity for weeks, whereas Ag-coated probes pretty quickly oxidize under ambient environment. Their storage under nitrogen or argon atmosphere only slightly decelerates oxidation rather than prevents it. Sokolov group proposed that this problem can be solved by subsequent deposition of a thin 2–3 nm layer of aluminum (Al) on the surface of plasmonic metal [23]. Oxidation of Al results in the formation of highly hard aluminum oxide ($Al_2O_3$) that protects soft plasmonic metals from both oxidation and mechanic deformation upon TERS imaging. Although broadly known and tested in several laboratories, this idea did not reach broad implications.

STM probes used in TERS are fragments of Au or Ag wires that are electrochemically etched [9, 10, 24, 25]. Precision of electrochemical etching has a direct correlation with the yield of plasmonically active scanning probes. Therefore, potentials are commonly used to enhance the precision of Au or Ag wire etching [9, 24]. Under UHV conditions, etched wires can have relatively long-life span that ranges from weeks to months. However, under ambient conditions both Au and Ag wires very quickly lose their plasmonic performance. This can happen as a result of contaminations or mechanical deformations upon TERS imaging or both. Overall, highly probable contamination of both AFM and STM probes make their fabrication required on-site in any TERS laboratory [26–28]. This largely dimmed the popularity of TERS in the spectroscopy field simultaneously making this technique inaccessible to biological laboratories that do not possess required equipment for the fabrication of scanning probes. Recently, several companies commercialized metal-coated probes that can be used for TERS. However, their cost remains relatively high for the vast majority of academic laboratories [29].

By a rough approximation, each plasmonic probe has a plasmonic nanoparticle at its apex [30, 31]. The size of such nanoparticle will determine its plasmonic performance. A rule of the thumb is that with an increase in the size of the nanoparticle, its absorption will shift to the red part of the electromagnetic spectrum [32–34]. Thus, varying thickness of deposited metal, one can change the size of nanostructure located at the apex of AFM-based scanning probes and, consequently, optimize their performance for the particular laser used in such in AFM-TERS system. A similar strategy can be used to fabricate STM-based probes with the desired plasmonic performance [35]. In addition to the size, chemical nature of metal plays an important role in the plasmonic performance of the scanning probes [36, 37]. Au and Au-coated probes are typically utilized for TERS performed with red ($\lambda = 633$ or

671 nm) excitation laser wavelengths, whereas Ag and Ag-coated probes are mostly employed if the system has green ($\lambda = 532$ nm) excitation wavelength.

In TERS, laser light can be brought to the scanning probe either from the side (side-TERS) or from the bottom (bottom-TERS) using objectives with high numerical apertures (NAs) [38–41]. Bottom illumination can be performed with an oil-immersed objectives that enable highly efficient light collection [42–45]. However, such configurations are limited to transparent and translucent samples. Side-TERS can be used to analyze all kinds of samples [5, 17–22, 46–49]. In addition to these traditional configurations, TERS with top-illumination of the scanning probe and parabolic mirror-based TERS were reported [50–52]. In the first case, more exotic angled scanning probes are required to enable light access to the tip apex. Parabolic mirrors, although show outstanding light collection efficiency, are very difficult to align. This, in light of highly probably tip contamination during TERS imaging and other issues related to the plasmonic performance of the scanning probes that were discussed above, drastically limited popularity of such optical configurations in TERS community [36, 53, 54].

## 23.2 Fundamental Physical Principles of Plasmon Chemistry

If illuminated by a laser light that matches their absorption, Ag or Au nanostructures generate collective oscillations of conductive electrons on their surfaces. These collective oscillations of conductive electrons are also known as localized surface plasmon resonances (LSPRs) [32, 34, 55–58]. LSPRs enable $10^6$–$10^8$-fold enhancement of the electric field in the vicinity of metallic nanostructures [59–62]. This physical phenomenon determines single-molecule sensitivity of TERS [33, 34, 63–65]. Furthermore, the probe can be positioned at the point of interest or rastered above the sample's surface. In the former case, chemical information about a particular surface location can be obtained. The latter case TERS provides a chemical map of the sample of interest [13, 66].

LSPRs can decay either by radiative and non-radiative processes [67, 68]. The radiative decay is typical expected for large metallic objects. In this case, the LSPR energy dissipates producing heat. In the case of non-radiative decay, also known as Landau damping, LSPRs produce hot carriers [68–70]. These highly energetic species persist over a few tens of femtoseconds and further decay via electron–electron or electron–phonon scattering [71, 72]. Alternatively, hot carriers can be directly or indirectly injected into molecular orbitals of a molecules present in the close proximity to the metal surfaces. This triggers chemical transformations in the molecular species [73, 74].

Jain group demonstrated that hot electrons and holes exhibit unequal rates of dissipation on the metallic surfaces [75, 76]. This asymmetry leads to the accumulation of hot carriers with "slower" dissipation rates. By other means, light generates a "steady-state charge" or an "electrostatic potential" which can be considered as a driving force of chemical reactions [75, 76]. Li and co-workers demonstrated that electrostatic potential at different surface sites of mono- and bimetallic nanostructures could be quantified by TERS [47]. Using benzonitrile as a molecular probe, the researchers investigated light-induced changes in the steady-state potential on the surface of gold (AuNPs), gold–palladium (Au@PdNPs), and gold-platinum (Au@PtNPs). It was found that intensity of the steady-state potential was substantially greater around the perimeter of the nanostructures compared to their central parts. This information can be used to explain distinctly different catalytic reactivity exhibited by these surface locations. Li and co-workers also found that Au@PdNPs and Au@PtNPs exhibited much greater intensities of the steady-state potential on their surfaces compared to AuNPs at the same light intensity [47]. Specifically, 70–80 MV $cm^{-1}$ electric field was observed on Au@PdNPs and Au@PtNPs at 140 μW of 633 nm light, whereas only ~ 25 MV $cm^{-1}$ was observed on AuNPs. These results indicate that bimetallic nanostructures would likely have much greater catalytic reactivity compared to monometallic AuNPs. Expanding upon this, Li and Kurouski demonstrated that TERS could be also used to quantify light-induced changes in the reactivity on AuNPs and Au@PdNPs [20, 22, 48]. Using several molecular probes, the researchers demonstrated that with an increase in the light intensity, the reactivity of both mono and bimetallic nanostructures increased. Furthermore, the reactivity of bimetallic nanostructures was always greater than the reactivity of monometallic nanostructures at the same light intensity. These results further probed that (i) reactivity of hot-carrier driven reactions directly depends on the intensity of the incident light and (ii) there is a direct relationship between the metallic composition of nanostructures and their reactivity [77, 78]. At the same time, El-Khoury group reported the absence of a direct correlation between the magnitude of the light intensity and plasmon-driven reactivity of AuMPs [79]. Specifically, Bhattarai and El-Koury found that plasmon-drive dimerization of 4-NBT was not evident on the surfaces of AuMPs even at high intensity of incident light. Furthermore, the researchers observed that in solution, dimerization of 4-NBT is reversible and both *trans* and *cis* forms of DMAB could be observed [79].

It is important to note that LSPR decay is also linked to the radiative decay, which causes plasmonic heating [80, 81]. Consequently, these is an ongoing debate about the role of temperature effect in the chemical processes observed in the tip-sample junction [82, 83]. To answer this question, Li and co-workers used finite density time domain (FDTD) simulations [83]. It was found that only a small (~ 40 K) increase in temperature in the tip-sample junction could be expected if 20–500 μW of 671 nm light was used. Results of these computational simulations are in a good agreement with experimental findings that were reported by Richard-Lacroix and Deckert [16]. The researchers measured intensities of vibrational bands of 16-mercaptohexadodecanoic acid Stokes and anti-Stokes in the collected TERS spectra at different intensities of 532 nm light. It was found that at 100 uW, the temperature

in the tip-sample junction reaches only ~ 80 ºC [16]. Similar findings were found by Frontiera group in SERS experiments [82]. Keller and Frontiera found only a very small, on the order of tens of Kelvin, increases in temperature in the junction between two nanostructures even for extremely high photoexcitation values [82]. These pieces of experimental evidence demonstrate that plasmonic heating plays very little if any role in the light-driven chemistry observed in both TERS and SERS experiments.

## 23.3 Nanoscale Imaging of Plasmon-Driven Processes on Mono- and Bimetallic Nanostructures

The first evidence of plasmon-driven processes in the tip-sample junction was reported by Van Schrojenstein Lantman and co-workers [84]. The researchers decorated the surface of gold microplates (AuMPs) with 4-nitrobenzenethiol (4-NBT), placed Ag-coated tip on the surface and illuminated by 532 nm light. This resulted in nearly instantaneous dimerization of 4-NBT into *p,p′*-dimercaptoazobisbenzene (DMAB), which could be witnessed by the appearance of two vibrational bands originated from N=N vibration around ~ 1400 $cm^{-1}$ [84]. It was also shown that substantially slower dimerization processes of 4-NBT into DMAB was observed at 633 nm laser excitation, Fig. 23.1 [84]. These results indicated that nature of the plasmonic metal plays an important role in the efficiency of plasmon-driven processes.

Expanding upon this, Li and Kurouski used TERS to examine the nanoscale photocatalytic reactivity of AuNPs and AuMPs [17]. It was been found that edges and corners of these monometallic nanostructures exhibited much greater yield of DMAB compared to their central parts, Fig. 23.2a–d [17]. Similar conclusions were

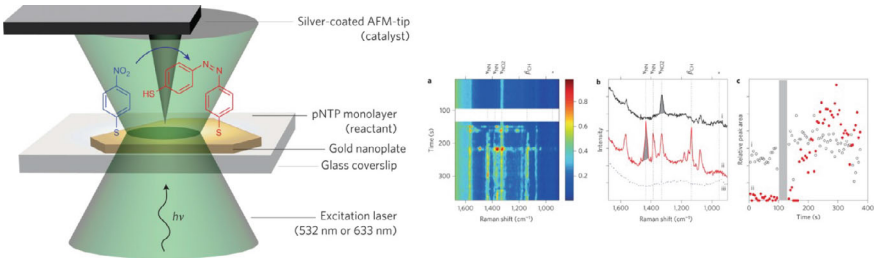



**Fig. 23.1** **Top**: Schematic illustration of the TERS experiment used to monitor the photocatalytic conversion of 4-NBT (blue) into DMAB (red) on AuNPs. Bottom: **a** Waterfall of TERS spectra collected with 633 nm excitation before (top) and after (below white band) illumination. **b** TERS spectra that correspond to 4-NBT (black) and DMAB (red). Spectrum (iii) is the reference spectrum taken after the time-dependent spectra. **c** Peak areas as a function of time for the 4-NTP band at 1335 $cm^{-1}$ (i) and for the band at 1440 $cm^{-1}$ (ii), belonging to DMAB. The period of green illumination between 100 and 130 s is indicated by the shaded band. Reprinted with permission from Ref. [57]. Copyright (2012) Nature Springer [84]

independently reported by El-Khoury group. Using TERS, the researchers investigated plasmonic and photocatalytic properties of Ag nanoparticles (AgNPs) and Ag nanowires (AgNWs) [4, 85]. It was found that edges and corners of such nanostructures exhibited greater reactivity compared to their flat terraces [86, 87]. These results are in a good agreement with the discussed above differences in the intensities of the steady-state potential on edges and corners of monometallic nanostructures compared to their central parts.

Several research groups found that orientation of molecular analytes, which is determined by crystal facets could play an important role in the efficiency of plasmon-driven reactions [5, 88]. Using 3D-TERS, Wang and Kurouski investigated the relationship between metal crystal facets and catalytic activity of AuMPs [89]. In 3D-TERS probes, plasmonic nanostructures are localized not only the tip apex, but also on the shaft of the scanning probes. Consequently, shaft-localized plasmonic nanostructures can be used to probe the chemical reactivity of both sides and top surfaces of analyzed nanostructures. Wang and Kurouski showed that Au (111) present on the top of AuMPs exhibited much higher rates of 4-NBT reduction by $NaBH_4$ comparing to Au (100) and Au (110) facets located on the AuMPs sides, Fig. 23.3 [89]. Expanding

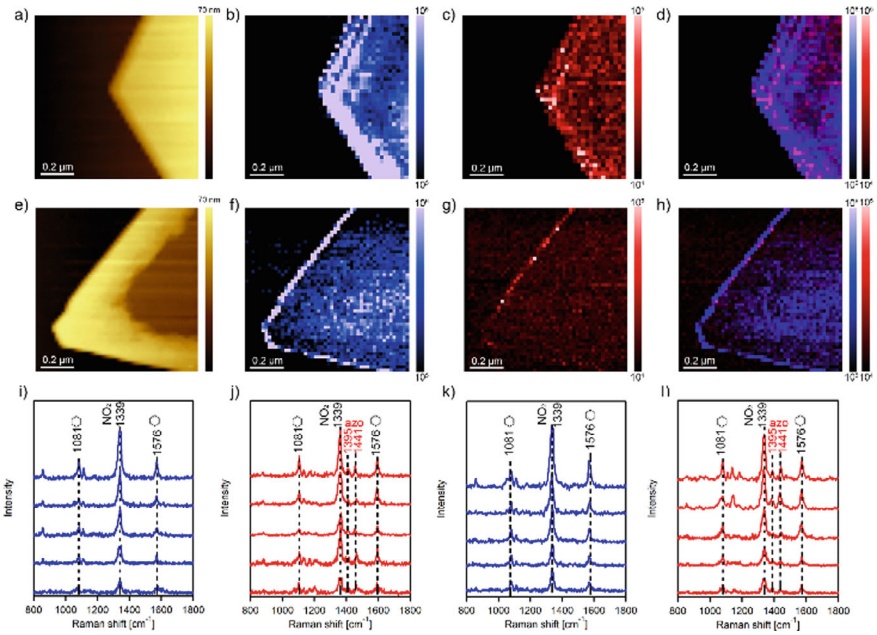



**Fig. 23.2** **a** AFM images of AuMPs and **e** WAuMPs. TERS images of **b**, **c**, **d** AuMPs and **f**, **g**, **h** WAuMPs (20 nm per pixel). Intensity of 1339 $cm^{-1}$ band ($NO_2$) of 4-NBT is shown in blue, intensities of 1397 and 1441 $cm^{-1}$ (azo) of DMAB is shown in red. (i-l) Typical TERS spectra extracted from chemical maps on **b**, **f** showing presence of 4-NBT (blue). Randomly picked TERS spectra from chemical maps shown in **c**, **g** demonstrate presence of DMAB (red). Reprinted with permission from Ref. [67]. Copyright (2021) Royal Society of Chemistry [5]

upon this, Li and co-workers discovered that deformation of (111) crystal facets, which was taken place upon thermal exposition of AuMPs to 400 °C for 30–120 min, drastically lowered the yield of DMAB. Such thermal heating resulted in the formation of walls around the perimeter of nanostructures [90]. The wall formation was caused by a migration of Au atoms from the edges of AuMPs toward their centers. At the same time, WAuMPs exhibited higher reactivity in the electrocatalytic conversion of methanol compared to AuMPs at lower formal potential [90].

Independently, Rossi and co-authors found that lower-coordinated surface sites, such as corners and edges, as well as (100) facets could provide higher reactivity in plasmon-driven reactions compared to the higher-coordinated surface sites such as (111) facets [91]. Thus, one can expect that more stable (111) facets exhibited greater reactivity in chemical, whereas (100) and (110) in light-driven catalytic reactions.

Zenobi group reported that lower packed areas of 4-NBT on AuNPs exhibited greater reactivity in DMAB formation rather than thermodynamically stable ordered clusters of 4-NBT [88]. Thus, orientation of molecular analytes on the surfaces of plasmonic materials should be strongly considered in plasmon-driven photocatalysis. These conclusions are further supported by Ren group. Specifically, the researchers showed that rough Ag, AgNPs and AuNPs, had dissimilar orientation

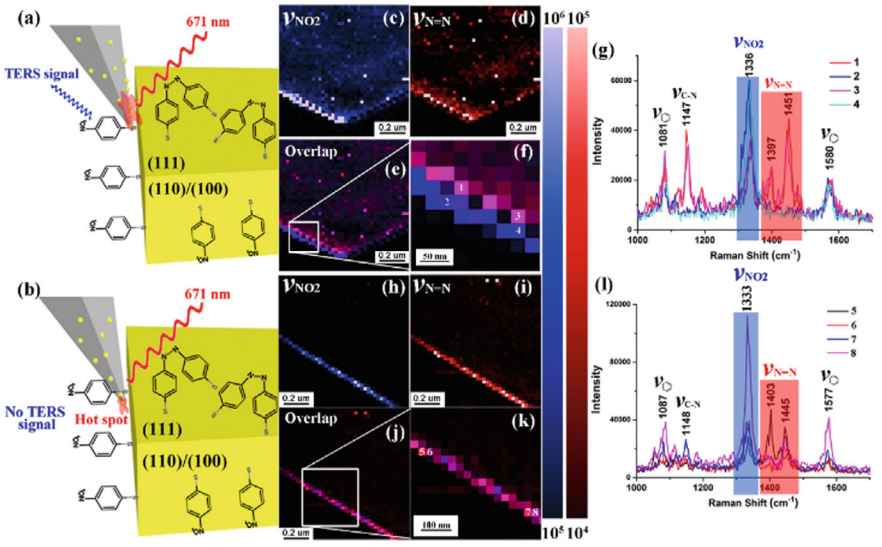



**Fig. 23.3** TERS imaging of the facet-dependent reduction of 4-NTP catalyzed by AuMPs. **a**, **b** Proposed schemes showing the hot-spot located at both the shaft and apex (**a**) and only at the apex (**b**) of the TERS probe. **c**, **d**, **h**, **i** High resolution TERS images of the distribution of $-NO_2$ (**c**, **h**) and N=N groups (**d**, **i**) obtained with 3D TERS active and inactive probes, respectively. **e**, **j** Corresponding overlap of $NO_2$ and N=N images (**c**, **d** for **e**; **h**, **i** for **j**). **f**, **k** Zoomed-in TERS images of the white rectangle position in **e**, **j**, respectively. **g**, **l** Typical TERS spectra extracted from the marked position in **f**, **k**. Reprinted with permission from Ref. [69]. Copyright (2018) American Chemical Society [89]

of 4-aminothiophenol (4-ATP) [92]. This molecular orientation determined plays an important role in plasmon-driven dimerization of 4-ATP into DMAB. However, strongly vertical orientation of this molecular analyte on Ag (111) prevented plasmon-driven dimerization of 4-ATP. The researchers attributed stability 4-ATP on Ag(111) to the $\pi$-stacking of aromatic moieties of these molecules [92].

Our group also showed that TERS could be used to quantify not only the yield but also rates of plasmon-driven reactions. Using TERRS, Li and Kurouski determined rates of 4-NBT to DMAB conversion on AuNPs at different intensities of the external electric field [48]. It has been found that with an increase in the electric field, the increase in the reaction rates was observed ($k_{30\,\mu w} = 0.126\ s^{-1}$, $k_{90\,\mu w} = 0.343\ s^{-1}$, and $k_{150\,\mu w} = 0.819\ s^{-1}$). TERS was also used to determine rates of redox conversion of 4-mercapto-phenyl-methanol (4-MPM) to 4-mercaptobenzoic acid (4-MBA) and vice versa [20]. These experimental findings revealed the direct relationship between an intensity of the external electric field and the rates of plasmon-driven reactions on mono and bimetallic nanostructures.

As was mentioned above, bimetallic nanostructures possess much greater intensities of the steady-state potential on their surfaces compared to their monometallic analogs at the same intensities of the incident light [17, 19, 20, 46]. The question to ask is whether the presence of catalytic metals offers any other advantages in the plasmon chemistry of such nanostructures [93].

Kurouski group used TERS to analyze the nanoscale photocatalytic properties of Au@PtNPs [17]. It was found that Au@PtNPs were capable of oxidizing 4-ATP directly to 4-NBT. At the same time, under the same experimental conditions only partial oxidation of 4-ATP was observed on AuNPs that yielded DMAB [7, 17, 89]. TERS revealed that edges and corners of Au@PtNPs had substantially greater catalytic reactivity compared to flat terraces. TERS analysis of Au@PdMPs revealed that 4-NBT could be reduced to both 4-ATP and DMAB. Furthermore, both products were primarily observed around the perimeter of nano-Pd clusters formed on the surface of AuMPs [48]. It should be noted that monometallic AuMPs were capable of reducing 4-NBT only to DMAB. These results demonstrate that the presence of the catalytic metal on the surface of a plasmonic antenna allows for broadening the chemical properties of the nanostructures. These findings also showed that Pd provides much stronger photo-reduction properties enabling complete proto-reduction of 4-NBT to 4-ATP, whereas the presence of Pt resulted in the complete photo-oxidation of 4-ATP to 4-NBT. At the same time, the absence of these catalytic metals drastically lower redox potential of the nanostructures, which results in only "half-way" oxidation and reduction. In this case, redox reactions of both 4-NBT and 4-ATP stop on DMAB.

Li and co-workers also found that rages of 4-NBT to DMAB reduction on the surface of Au@PdMPs could be altered by different intensities of the external electric field [48]. They observed an increase in the reaction rate of 4-NBT to DMAB conversion with an increase in the intensity of incident light [48]. These results showed that light intensity could be used to control reaction rates on both mono- and bimetallic nanostructures.

Li and Kurouski also examined the selectivity of Pd- and Pt-driven such redox reactions on two molecular systems, 4-MPM to 4-MBA [20]. It was found that Au@PtNPs could be used only to oxidize 4-MPM to 4-MBA, whereas the reversed reaction was not possible. Au@PdNPs, on the other hand, enabled exclusively the reversed reduction of 4-MBA to 4-MPM, Fig. 23.4. It was also shown that none of these chemical transformations was possible on AuNPs. In such cases both 4-MBA and 4-MPM were decarboxylated producing only thiophenol. These findings demonstrated that Pt determines unique oxidation, whereas Pd unique reduction properties of bimetallic nanostructures.

Ren group utilized TERS and phenyl isocyanide (PIC) as a molecular reporter to probe changes in the nanoscale reactivity of sub-monolayer of Pd on Au surface [94]. The researchers found that spectra collected from edges of Pd islands exhibited 60 $cm^{-1}$ red-shift of C≡N vibration compared to the spectra collected from Pd terraces, Fig. 23.5a–c. This shift was explained by the back donation from the d-band of the metal to the antibonding $\pi^*$ orbital of PIC. Thus, molecules located at Pd edges had higher reactivity compared to Pd atoms present in terraces. Similar approach was utilized by Ren group to examine electronic properties of Pt nanoisland on Au surfaces [95]. The researchers found a blue-shift of C≡N vibration of 4-chlorophenyl isocyanide, a similar to PIC molecular reporter, in the spectra collected from lower-coordinated Pt sites in which higher d-band center was expected, Fig. 23.5d–g. These results indicated a drastic difference in the electronic structures between Pt and Pd, which in turn, could be used to explain differences in molecule–metal interaction that are taken place in the case of these two catalytic metals.

Using TERS, Li and co-workers also evaluated the photocatalytic properties of alloy-type and "sandwich-like" bimetallic nanostructures [5]. Specifically, the researchers measured the yield of DMAB produced from 4-NBT on "sandwich-like" Au@PdNPs and their alloy analogs, walled-Au@PdNPs (WAu@PdNPs). It should be noted that thermal reshaping of "sandwich-like" Au@PdNPs fully erases the borders between plasmonic and catalytic metals forging both metals into alloy. Au@PdNPs and WAu@PdNPs yielded both DMAB and 4-ATP. Au@PdNPs yielded ~ 65% of DMAB with only ~ 6% of 4-ATP, whereas the yield of these products on WAu@PdNPs was ~ 47 and ~ 17% [5]. Thus, alloy-type bimetallic nanostructures could be used to produce large amount of 4-ATP than their "sandwich-like" analogs. These studies demonstrated that fine tuning of the interplay between catalytic and plasmonic metals can be used to alter the yield of plasmon-driven reactions.

## 23.4 TERS of Novel Material and Novel Chemistry at the Nanoscale

Ren and Zenobi reported TERS imaging of catalytic hydrogenation of chloronitrobenzenethiol on Pd sub-monolayer present on Au (111) surface [96]. There researchers found that catalytic hydrogenation occurred beyond the location of Pd

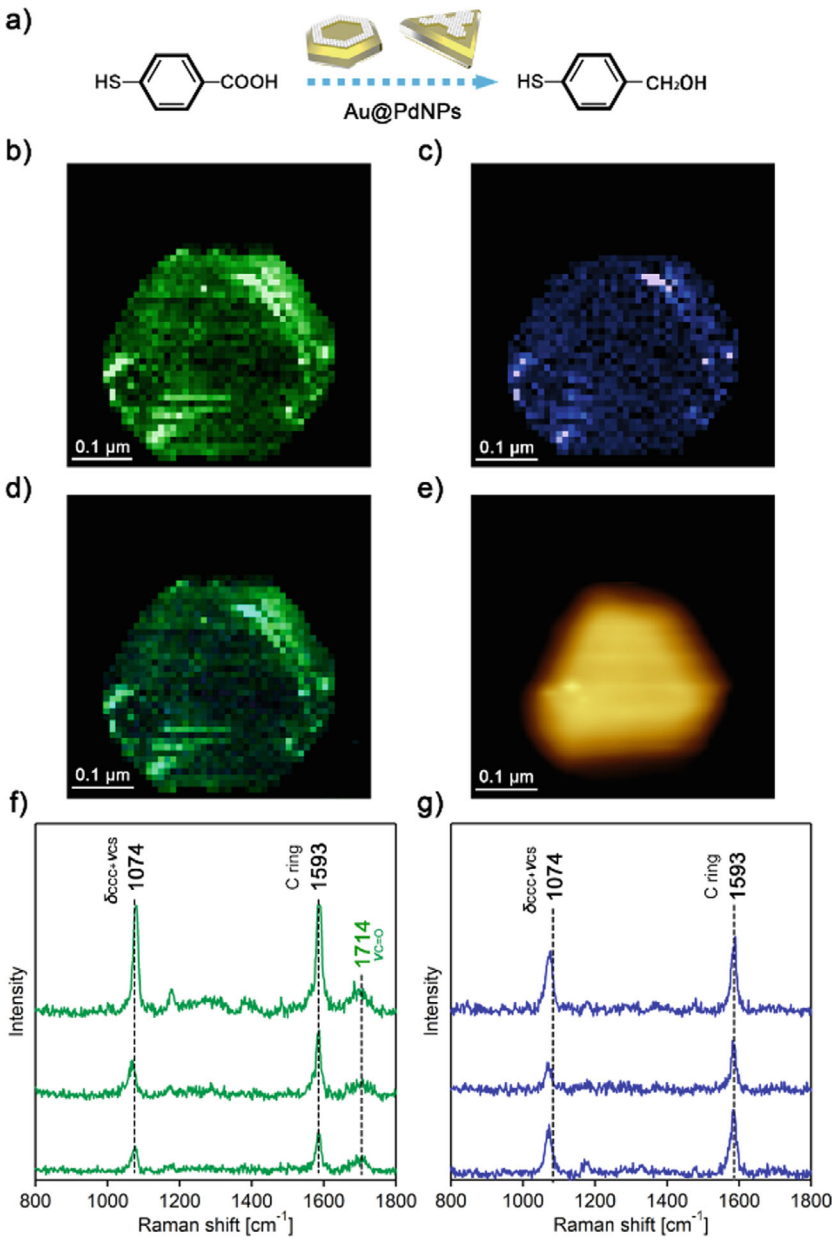



**Fig. 23.4** Plasmon-driven reduction of 4-MBA to 4-MPM on Au@PdNPs. **a** Schematic illustration of MBA reduction to MPM by Au@PdNPs; **b–c** TERS images of Au@PdNPs (10 nm per pixel). Intensity of intensities of 1570–1750 $cm^{-1}$ containing C ring vibration and C=O vibration of 4-MBA is shown in green; 1593 $cm^{-1}$ band (C ring vibration) of MPM without showing C=O vibration band (1714 $cm^{-1}$) is shown in blue. **d** Overlapping TERS image of 4-MPM and 4-MBA. **e** In-situ AFM image of Au@PdNPs during TERS imaging. **f–g** Typical TERS spectra extracted from chemical maps on Au@PdNPs **a**, **b** showing presence of 4-MPM (blue), 4-MBA (green). Reprinted with permission from Ref. [73]. Copyright (2021) American Chemical Society [20]

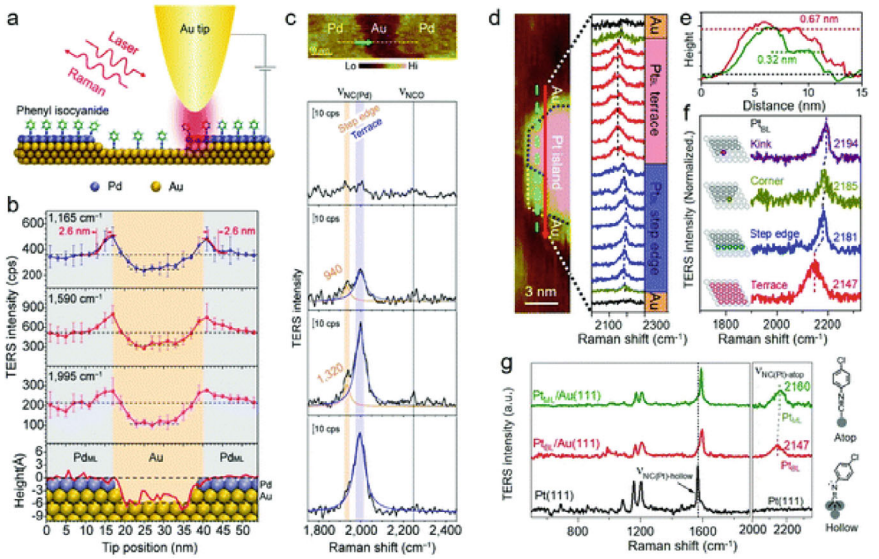



**Fig. 23.5** **a** A sketch of TERS experiments used to probe reactivity of Pd@Au(111) surfaces. **b** Intensity of TERS spectra collected from Pd step edge with 3 nm spatial resolution. **c** STM image (top panel) and line-trace TERS spectra (bottom panel) along the green arrow in the STM image, showing a unique red-shifted νNC at the Pd step edge. Reproduced with permission from Ref. [75]. Copyright (2017) Nature Springer. **d** The STM image of the Pt/Au(111) bimetallic surface (left panel) and line-trace TERS spectra (right panel) along the red arrow in the STM image. **e** Height profiles along the green and red lines in **d**. **f** Site-specific νNC peaks at Pt sites. **g** Bimetallic effects on PtML/Au(111), PtBL/Au(111), and Pt(111). Reproduced with permission from Ref. [76]. Copyright 2018 John Wiley & Sons, Inc

sites and was observed as far as 20 nm from the bimetallic Pd/Au boundary. These findings suggested that the interplay between plasmonic and catalytic metals at the nanoscale was far more complex than it was previously expected. Recently reported findings by Kurouski group showed that TERS could be used to probe molecular reactivity of aromatic halides in Suzuki–Miyaura coupling reaction [21]. Specifically, the researchers were able to determine the reactivity of 4-bromo-, 4-chloro- and 4-fluoro-thiophenols (4-BTP, 4-CTP and 4-FTP) in the Suzuki–Miyaura coupling reaction with 4-mercaptophenylboronic acid (4-MPBA), Fig. 23.6.

Expanding upon this, Patil and Kurouski investigated the extent to which Ni-based bimetallic nanostructures could be used to perform dimerization of aromatic halides [97]. They fabricated Ni@AuNPs that were able to dimerize molecular analytes forming BPDT. Using TERS, the researchers demonstrated that the highest yield of BPDT was observed on Ni nano lands on the surface of these bimetallic nanostructures. Spectroscopic analysis of reaction products also helped to determine mechanisms of this plasmon-driven reaction. It was shown that thiophenol, which was formed upon dehalogenation of aromatic halides interacted with another molecule

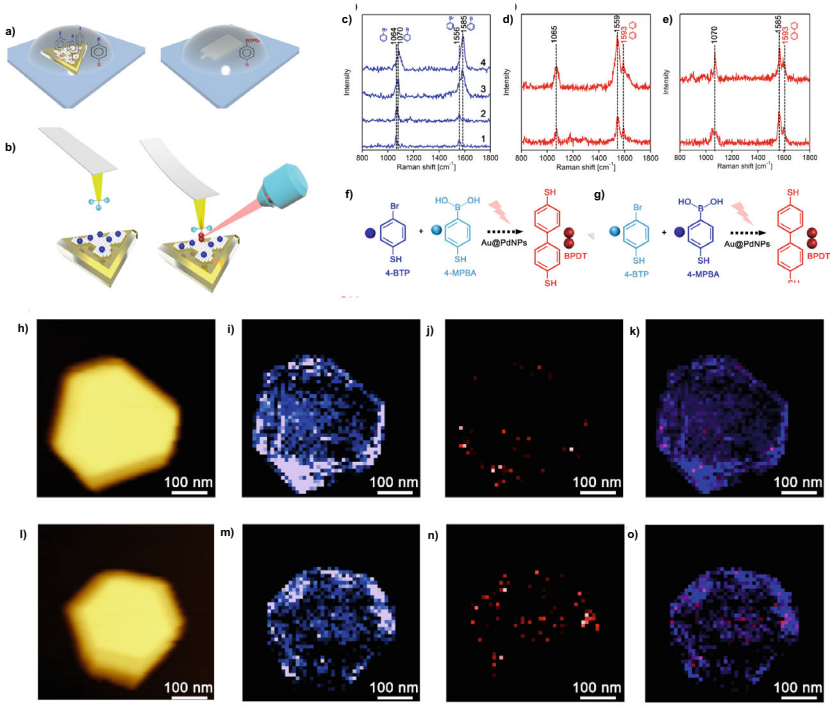



**Fig. 23.6** **a** A scheme of chemical modification of Au@PdNPs with 4-BTP and Au-coated scanning probes with 4-MPBA; **b** Plasmon-driven Suzuki–Miyaura coupling of 4-MPBA and 4-BTP on the surface of Au@PdNPs that yields biphenyl-4,4-dithiol (BPDT). **c** Representative TERS spectra of 4-BTP (1,2) and 4-MPBA (3,4) on the surface of Au@PdNPs; **d** SERS of 4-MPBA (5,6) and 4-BTP (7,8) on an Au-coated probe. **e** TERS spectra of BPDT on Au@PdNPs. **f** The schematic representation of the Suzuki–Miyaura coupling reaction between 4-BTP-modified Au@PdNPs and the 4-MPBA-modified Au-coated probe. **g** The schematic representation of the Suzuki–Miyaura coupling reaction between the 4-BTP-modified Au-coated probe and 4-MPBA-modified Au@PdNPs. **h** AFM and the corresponding **i** TERS image of 4-BTP-modified Au@PdNPs before the Suzuki–Miyaura coupling reaction and **j** after demonstrating the formation of BPDT (red pixels). **k** An overlay TERS image of 4-BTP (blue) and BPDT (red) signals on Au@PdNPs. **l** AFM and the corresponding; **m** TERS image of 4-MPBA-modified Au@PdNPs before the Suzuki–Miyaura coupling reaction and **n** after demonstrating the formation of BPDT (red pixels). **o** An overlay TERS image of 4-MPBA (blue) and BPDT (red) signals on Au@PdNPs. The scale bar in each image is 100 nm. Reprinted with permission from Ref. [79]. Copyright (2021) Royal Society of Chemistry [21]

of aromatic halide forming C–C bond. Next, this molecular analyte was oxidized by the electron-deficient Ni and deprotonated to give BPDT, Fig. 23.7. [97]

TERS also revealed a novel class of plasmon-driven chemical reactions. Kurouski group showed that 4-NBT could be ionized into 4-nitrobenzothiolate (4-NBT$^-$) on the surface of AuNPs [7]. This conclusion was made by an observation of the shift of 1335 cm$^{-1}$ vibration of 4-NBT to 1305 cm$^{-1}$ of 4-NBT$^-$ [7]. It was also demonstrated that such a shift could not be caused by a Stark effect or by changes in the

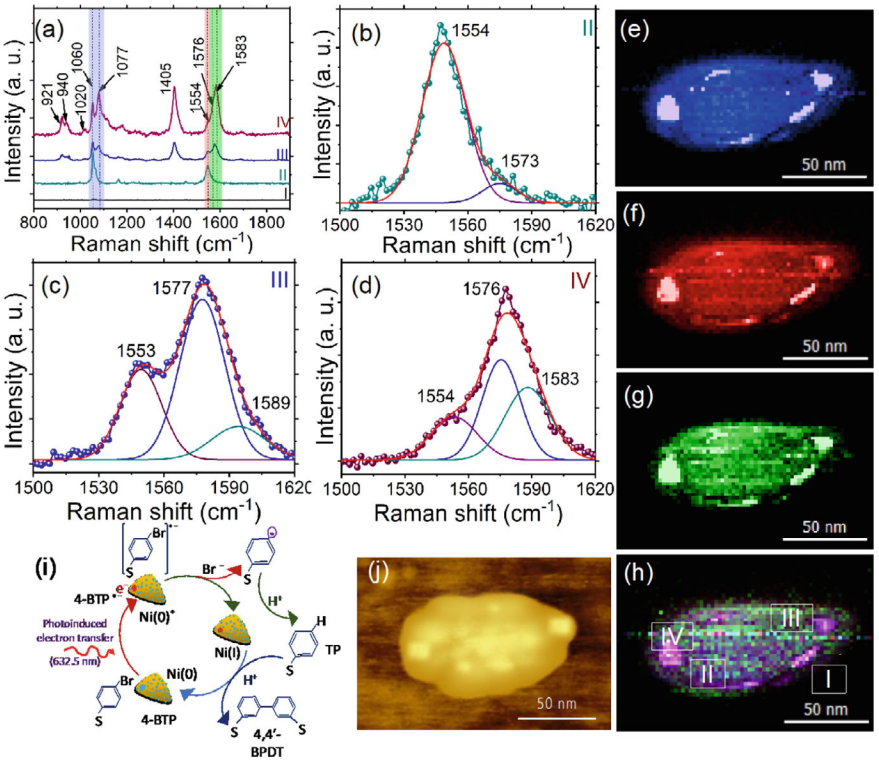



**Fig. 23.7** Plasmon-driven formation of 4,4′-BPDT and TP on Ni@AuNPs. **a** Selected TER spectra acquired from Ni@AuNPs at different areas outlined in **h** and the corresponding AFM image shown in (**j**). The deconvoluted TER spectrum in the region of 1500–1620 $cm^{-1}$ confirms the presence of intact 4-BTP (1554 $cm^{-1}$ ($\nu$C-$C_{(ring)}$)) (**b**), and in addition the formation of TP (1575 $cm^{-1}$ ($\nu$C-$C_{(ring)}$)), and 4,4′-BPDT (1583 $cm^{-1}$) (**c**, **d**) on Ni@AuNPs. TERS maps for the distribution of 4-BTP (1060 $cm^{-1}$ ($\nu$C-Br), 1077 $cm^{-1}$ ($\nu$CS)) (**e**), and 1554 $cm^{-1}$ (**f**), TP (1575 $cm^{-1}$) and 4,4′-BPDT (1583 $cm^{-1}$) (**g**). An overlay TERS maps of (**e**, **f**, **g**) in (**h**). **i** Schematic representation of a TERS study on the interfacial transmission of hot electrons using photocatalytic dehalogenation of 4-BTP

molecule orientation on the metal surfaces. Following on this study, El-Khoury group found that nearly 100% ionization of 4-NBT on Ag nanoparticles [6]. Thus, the yield of plasmon-driven ionization directly depends on the nature of the plasmonic metal [98]. Recently reported results showed that TERS could be used to improve the understanding about the physics of novel metallic and semiconductor 2D and 3D materials. Kurouski group reported that TERS could be used to probe plasmonic and photocatalytic properties of copper nanocubes and nanowires (CuNCs and CuNWs, respectively) [22]. Li and Kurouski found that both CuNCs and CuNWs reduced 4-NBT to DMAB, as well as oxidized 4-MPM to 4-MBA. However, the reversed reduction of 4-MBA to 4-MPM was not evident on Cu nanomaterials due to strong interactions of the carboxylic group of 4-MBA with Cu, which prevents its reduction.

Using TERS, Patil and co-workers investigated plasmonic and photocatalytic properties of magnesium nanoplates (MgNPs), as well as their bimetallic analogs [99]. It was found that MgNPs had very weak photocatalytic properties due to the thick oxide layer on their surfaces. However, this limitation can be overcome by decoration of MgNPs by 2–5 nm Au nanoparticles. Such tiny nanoparticles are not plasmonic themselves. However, the resulted Mg@AuNPs exhibited an outstandingly strong photocatalytic properties enabling reduction of 4-NBT to DMAB, Fig. 23.8 [99]. Gogotsi group utilized TERS to analyze single-layer and few-layer flakes of $Ti_3C_2T_x$ MXene deposited on a gold substrate [100]. The researchers found that intensity of TERS responses from the single- and few-layer flakes of $Ti_3C_2T_x$ could be used to track early stages of degradation, well before significant morphological changes appear.

Using UHV-TERS, Hou and Jiang groups were able to probe weak molecule–substrate interactions and conformations of molecular analytes on metallic surfaces [10, 11, 101–103]. Xu and co-workers found that an electric field of scanning probe could be utilized to trigger conformational changes in pentacene adsorbed on Ag(110) [102]. The researchers reported α to γ conformational changes in the central benzene ring of pentacene. These changes were triggered by the ring expansion along the long molecular axis. Using TERS, the researchers demonstrated that α to γ conformational changes were caused by C−H bond breaking at the central benzene ring of pentacene followed by the skeleton deformation of this molecule. Recently, Jiang group reported that a scanning probe could be used to trigger a dissociation of specific molecular site (C–Si bond) in individual 5,10,15,20-(tetra-trimethylsilylethynyl) porphyrin molecules adsorbed on a Cu(100) surface, Fig. 23.9 [11]. To enable such bond scissoring, the scanning probe had to be positioned precisely at the chemical bond atop the molecule. These findings confirmed the discussed above property of the scanning probes used in TERS to trigger photochemical transformation in the molecular analytes present on metallic surfaces.

Jeong group utilized TERS to investigate defects in α- and β-domains and edges of single-crystalline $WS_2$ nanosheets [104, 105]. The researchers observed shifting of A1g and D modes on the W- and S-edges of α-domains, respectively. In the case of the β-domain, a blue-shift of A1g modes was accompanied by a red-shift of D modes. It was shown that this happened because VW-d defects were dominated in β-domains. Furthermore, the researchers showed that the β-domain exhibited a relatively higher D mode intensity than the α-domain. Similar conclusions were reported by Verma group for micrometer-size WS2 samples [106].

## 23.5 Conclusions

Experimental results summarized and critically reviewed in this chapter describe the most recent findings on TERS-based imaging of plasmon-driven catalysis on mono and bimetallic nanostructures. These studies demonstrate that TERS can be used to (i) study mechanism plasmon-driven transformations in molecules present

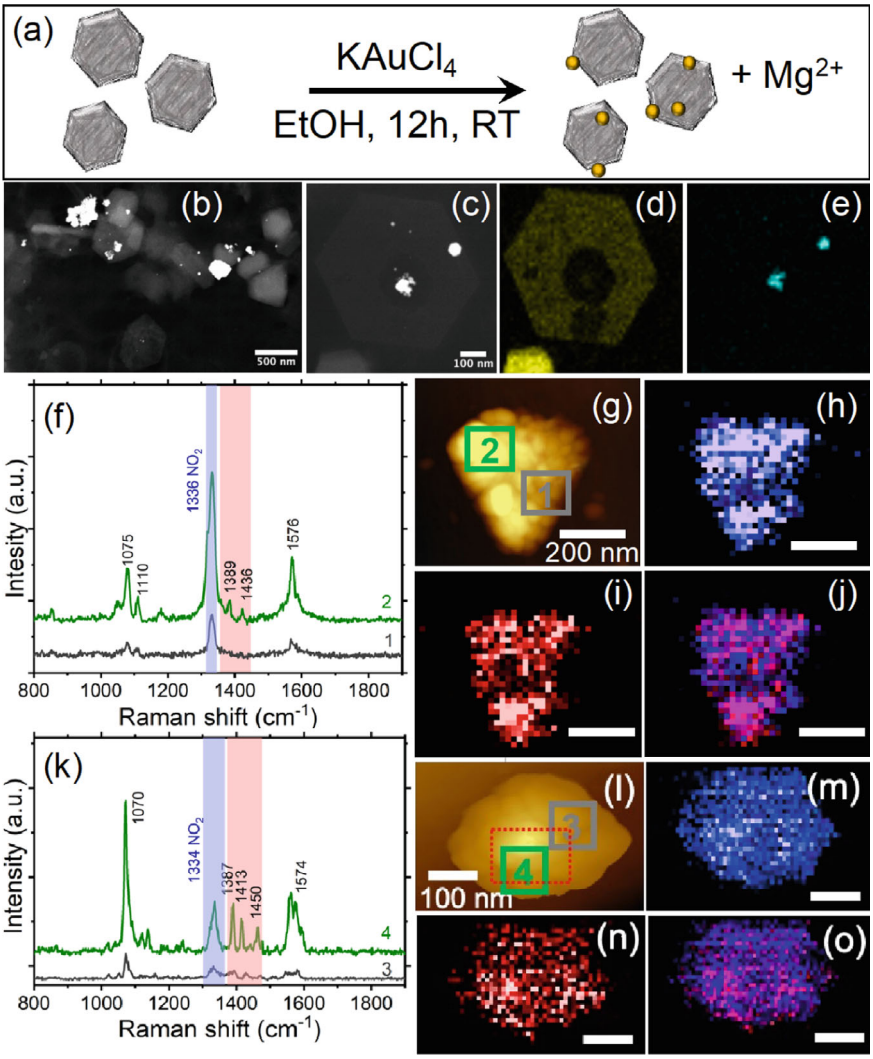



**Fig. 23.8** Conversion of 4-NBT to DMAB is observed across the entire structure for Au-decorated MgNPs. **a** Schematic of the partial galvanic replacement synthesis of Au-decorated MgNPs, **b**–**c** representative HAADF-STEM images of Au-decorated MgNPs (additional images in the SI), STEM-EDS maps of **d** Mg K $\alpha$ and **e** Au M lines, **f** TER spectra from the areas outlined and color-coded ("1" and "2") in **g** the AFM image of an Au-decorated MgNPs, **h** map of the 4-NBT band at 1336 $cm^{-1}$, **i** map of the 1389, and 1436 $cm^{-1}$ region including bands from DMAB, and **j** overlay of the maps in (**h**) and (**i**) (scalebar 200 nm). **k** TER spectrum of Au-decorated MgNPs at different areas outlined and color-coded ("1" and "2") in the **l** AFM image of Au-decorated MgNPs, **m** map of the 4-NBT band at 1334 $cm^{-1}$, **n** map of the 1387, 1413 and 1450 $cm^{-1}$ region including bands from DMAB, and **o** overlay of the maps in **m** and **n** (scalebar 100 nm). **p** AFM image from the outlined region in **l**, **q** map of the 4-NBT band at 1334 $cm^{-1}$, **r** map of the 1387, 1413 and 1450 $cm^{-1}$ region including bands from DMAB, and **s** overlay of the maps in **q** and **r** (scalebar 50 nm)

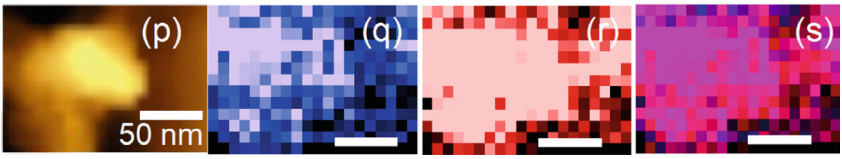



**Fig. 23.8** (continued)

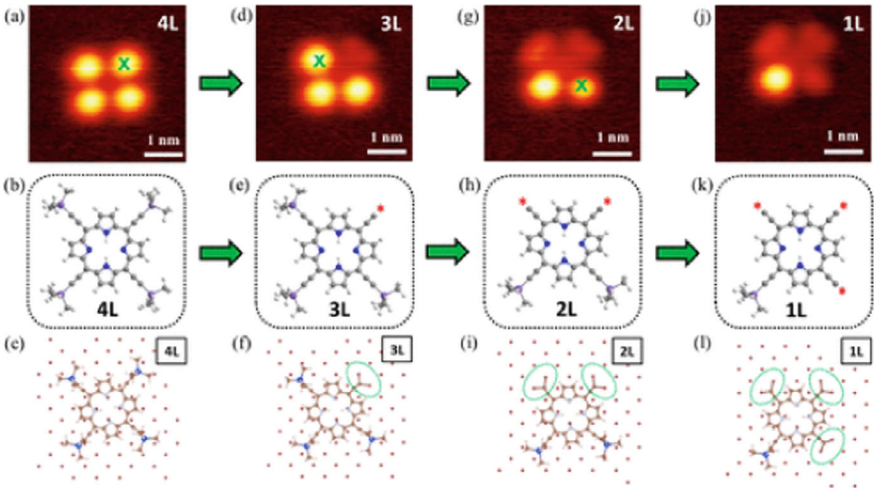



**Fig. 23.9** Consecutive C–Si bond dissociations in individual 5,10,15,20-(tetra-trimethylsilylethynyl) porphyrin molecule. STM image, ball-and-stick model, and calculated adsorption geometry (top view) for 4L (**a**, **b**, **c**), 3L (**d**, **e**, **f**), 2L (**g**, **h**, **i**), and 1L (**j**, **k**, **l**), respectively. Reprinted with permission from Ref. [84]. Copyright (2022) American Chemical Society [11]

on metallic surfaces, as well as (ii) investigate rates and yields of photochemical reactions at different surface sites, including edges and corners of the nanostructures. Thus, TERS can be used for highly accurate analysis of reactivity of molecular analytes, determine kinetics and thermodynamics of novel reactions, as well as examine plasmonic and photocatalytic properties of novel materials. This knowledge will be utilized to tailor synthetic approaches and fabricate novel nanostructures with desired optical, plasmonic, and photocatalytic properties.

## References


1. Stöckle, R. M.; Suh, Y. D.; Deckert, V.; Zenobi, R. Nanoscale chemical analysis by tip-enhanced Raman spectroscopy. *Chem. Phys. Lett.* **2000**, *318* (1–3), 131–136.
2. Hayazawa, N.; Inouye, Y.; Sekkat, Z.; Kawata, S. Metallized tip amplification of near-field Raman scattering. *Opt. Commun.* **2000**, *183* (1–4), 333–336.
3. Anderson, M. S. Locally Enchanced Raman Spectroscopy with an Atomic Force Microscope *Appl. Phys. Lett.* **2000**, *76* (21), 3130–3132.
4. Bhattarai, A.; Novikova, I. V.; El-Khoury, P. Z. Tip-Enhanced Raman Nanographs of Plasmonic Silver Nanoparticles. *J. Phys. Chem. C* **2019**, *123*, 27765–27769.
5. Li, Z.; El-Khoury, P.; Kurouski, D. Tip-Enhanced Raman Imaging of Photocatalytic Reactions on Thermally-Reshaped Gold and Gold-Palladium Microplates. *Chem. Commun.* **2021**.
6. Wang, C. F.; O'Callahan, B. T.; Kurouski, D.; Krayev, A.; El-Khoury, P. Z. The Prevalence of Anions at Plasmonic Nanojunctions: A Closer Look at p-Nitrothiophenol. *J Phys Chem Lett* **2020**, *11* (10), 3809–3814.
7. Wang, R.; Li, J.; Rigor, J.; Large, N.; El-Khoury, P.; Yu., R. A.; Kurouski, D. Direct Experimental Evidence of Hot-Carrier-Driven Chemical Processes in Tip-Enhanced Raman Spectroscopy (TERS). *J. Phys. Chem. C* **2020**, *124*, 2238–2244.
8. Chen, C.; Hayazawa, N.; Kawata, S. A 1.7 nm resolution chemical analysis of carbon nanotubes by tip-enhanced Raman imaging in the ambient. *Nat. Commun.* **2014**, *5*, 3312.
9. Jiang, N.; Foley, E. T.; Klingsporn, J. M.; Sonntag, M. D.; Valley, N. A.; Dieringer, J. A.; Seideman, T.; Schatz, G. C.; Hersam, M. C.; Van Duyne, R. P. Observation of multiple vibrational modes in ultrahigh vacuum tip-enhanced Raman spectroscopy combined with molecular-resolution scanning tunneling microscopy. *Nano Lett* **2012**, *12* (10), 5061–5067.
10. Mahapatra, S.; Ning, Y.; Schultz, J. F.; Li, L.; Zhang, J. L.; Jiang, N. Angstrom Scale Chemical Analysis of Metal Supported Trans- and Cis-Regioisomers by Ultrahigh Vacuum Tip-Enhanced Raman Mapping. *Nano Lett.* **2019**, *19* (5), 3267–3272.
11. Mahapatra, S.; Schultz, J. F.; Li, L.; Zhang, X.; Jiang, N. Controlling Localized Plasmons via an Atomistic Approach: Attainment of Site-Selective Activation inside a Single Molecule. *J Am Chem Soc* **2022**, *144* (5), 2051–2055.
12. Zhang, R.; Zhang, X.; Wang, H.; Zhang, Y.; Jiang, S.; Hu, C.; Zhang, Y.; Luo, Y.; Dong, Z. Distinguishing Individual DNA Bases in a Network by Non-Resonant Tip-Enhanced Raman Scattering. *Angew. Chem. Int. Ed. Engl.* **2017**, *56* (20), 5561–5564.
13. Zhang, R.; Zhang, Y.; Dong, Z. C.; Jiang, S.; Zhang, C.; Chen, L. G.; Zhang, L.; Liao, Y.; Aizpurua, J.; Luo, Y.; et al. Chemical mapping of a single molecule by plasmon-enhanced Raman scattering. *Nature* **2013**, *498* (7452), 82–86.
14. Kurouski, D.; Deckert-Gaudig, T.; Deckert, V.; Lednev, I. K. Structure and composition of insulin fibril surfaces probed by TERS. *J. Am. Chem. Soc.* **2012**, *134* (32), 13323–13329.
15. Kurouski, D.; Deckert-Gaudig, T.; Deckert, V.; Lednev, I. K. Surface characterization of insulin protofilaments and fibril polymorphs using tip-enhanced Raman spectroscopy (TERS). *Biophys. J.* **2014**, *106* (1), 263–271.
16. Richard-Lacroix, M.; Deckert, V. Direct molecular-level near-field plasmon and temperature assessment in a single plasmonic hotspot. *Light Sci Appl* **2020**, *9*, 35.
17. Li, Z.; Kurouski, D. Elucidation of Photo-Catalytic Properties of Goldplatinum Bimetallic Nanoplates Using Tip-Enhanced Raman Spectroscopy. *J. Phys. Chem. C* **2020**, *124* (12850–12854).
18. Li, Z.; Kurouski, D. Plasmon-Driven Chemistry on Mono- and Bimetallic Nanostructures. *Acc Chem Res* **2021**, *54* (10), 2477–2487.
19. Li, Z.; Kurouski, D. Nanoscale structural characterization of plasmon-driven reactions. *Nanophotonics* **2021**, *10*, 1657–1673.
20. Li, Z.; Kurouski, D. Probing the Redox Selectivity on Au@Pd and Au@Pt Bimetallic Nanoplates by Tip-Enhanced Raman Spectroscopy. *Acs Photonics* **2021**, *8* (7), 2112–2119.
21. Li, Z.; Kurouski, D. Probing the plasmon-driven Suzuki-Miyaura coupling reactions with cargo-TERS towards tailored catalysis. *Nanoscale* **2021**, *13* (27), 11793–11799.

22. Li, Z.; Kurouski, D. Tip-Enhanced Raman Analysis of Plasmonic and Photocatalytic Properties of Copper Nanomaterials. *J Phys Chem Lett* **2021**, *12* (34), 8335–8340.
23. Agapov, R. L.; Sokolov, A. P.; Foster, M. D. Protecting TERS probes from degradation: extending mechanical and chemical stability. *J. Raman Spectrosc.* **2013**, *44* (5), 710-716.
24. Klingsporn, J. M.; Jiang, N.; Pozzi, E. A.; Sonntag, M. D.; Chulhai, D.; Seideman, T.; Jensen, L.; Hersam, M. C.; Van Duyne, R. P. Intramolecular insight into adsorbate-substrate interactions via low-temperature, ultrahigh-vacuum tip-enhanced Raman spectroscopy. *J. Am. Chem. Soc.* **2014**, *136* (10), 3881–3887.
25. Chiang, N.; Chen, X.; Goubert, G.; Chulhai, D. V.; Chen, X.; Pozzi, E. A.; Jiang, N.; Hersam, M. C.; Seideman, T.; Jensen, L.; et al. Conformational Contrast of Surface-Mediated Molecular Switches Yields Angstrom-Scale Spatial Resolution in Ultrahigh Vacuum Tip-Enhanced Raman Spectroscopy. *Nano Lett.* **2016**, *16* (12), 7774–7778.
26. Shao, F.; Zenobi, R. Tip-enhanced Raman spectroscopy: principles, practice, and applications to nanospectroscopic imaging of 2D materials. *Anal. Bioanal. Chem.* **2018**, 1–25.
27. De Angelis, F.; Das, G.; Candeloro, P.; Patrini, M.; Galli, M.; Bek, A.; Lazzarino, M.; Maksymov, I.; Liberale, C.; Andreani, L. C.; et al. Nanoscale chemical mapping using three-dimensional adiabatic compression of surface plasmon polaritons. *Nat. Nanotechnol.* **2010**, *5* (1), 67–72.
28. Bek, A.; De Angelis, F.; Das, G.; Di Fabrizio, E.; Lazzarino, M. Tip enhanced Raman scattering with adiabatic plasmon focusing tips. *Micron* **2011**, *42* (4), 313–317.
29. Huang, T. X.; Huang, S. C.; Li, M. H.; Zeng, Z. C.; Wang, X.; Ren, B. Tip-enhanced Raman spectroscopy: tip-related issues. *Anal Bioanal Chem* **2015**, *407* (27), 8177-8195.
30. Becker, S. F.; Esmann, M.; Yoo, K.; Gross, P.; Vogelgesang, R.; Park, N.; Lienau, C. Gap-Plasmon-Enhanced Nanofocusing Near-Field Microscopy. *ACS Photonics* **2016**, *3*, 223–232.
31. Zhang, Y.; Voronine, D. V.; Qiu, S.; Sinyukov, A. M.; Hamilton, M.; Liege, Z.; Sokolov, A. V.; Zhang, Z.; Scully, M. O. Improving resolution in quantum subnanometre-gap tip-enhanced Raman nanoimaging. *Sci Rep* **2016**, *6*, 25788.
32. Kleinman, S. L.; Frontiera, R. R.; Henry, A. I.; Dieringer, J. A.; Van Duyne, R. P. Creating, characterizing, and controlling chemistry with SERS hot spots. *Phys Chem Chem Phys* **2013**, *15* (1), 21–36.
33. Sharma, B.; Frontiera, R. R.; Henry, A. I.; Ringe, E.; Van Duyne, R. P. SERS: Materials, applications, and the future. *Materials Today* **2012**, *15* (1–2), 16–25.
34. Brown, R. J.; Milton, M. J. T. Nanostructures and nanostructured substrates for surface-enhanced Raman scattering (SERS). *J. Raman. Spectr.* **2008**, *39*, 1313–1326.
35. Gao, L.; Zhao, H.; Li, Y.; Li, T.; Chen, D.; Liu, B. Controllable Fabrication of Au-Coated AFM Probes via a Wet-Chemistry Procedure. *Nanoscale Res Lett* **2018**, *13* (1), 366.
36. Sharma, B.; Frontiera, R. R.; Henry, A. I.; Ringe, E.; Van Duyne, R. P. SERS: Materials, applications, and the future. *Mater. Today* **2012**, *15* (1–2), 16–25.
37. Stiles, P. L.; Dieringer, J. A.; Shah, N. C.; Van Duyne, R. P. Surface-enhanced Raman spectroscopy. *Annu Rev Anal Chem (Palo Alto Calif)* **2008**, *1*, 601–626.
38. Shao, F.; Dai, W.; Zhang, Y.; Zhang, W.; Schlüter, A. D.; Zenobi, R. Chemical Mapping of Nanodefects within 2D Covalent Monolayers by Tip-Enhanced Raman Spectroscopy. *ACS nano* **2018**, *12* (5), 5021–5029.
39. Yeo, B.-S.; Amstad, E.; Schmid, T.; Stadler, J.; Zenobi, R. Nanoscale Probing of a Polymer-Blend Thin Film with Tip-Enhanced Raman Spectroscopy. *Small* **2009**, *5* (8), 952–960.
40. Zeng, Z. C.; Huang, S. C.; Wu, D. Y.; Meng, L. Y.; Li, M. H.; Huang, T. X.; Zhong, J. H.; Wang, X.; Yang, Z. L.; Ren, B. Electrochemical Tip-Enhanced Raman Spectroscopy. *J. Am. Chem. Soc.* **2015**, *137* (37), 11928–11931.
41. Zhong, J. H.; Jin, X.; Meng, L.; Wang, X.; Su, H. S.; Yang, Z. L.; Williams, C. T.; Ren, B. Probing the electronic and catalytic properties of a bimetallic surface with 3 nm resolution. *Nat. Nanotechnol.* **2017**, *12* (2), 132–136.
42. Böhme, R.; Mkandawire, M.; Krause-Buchholz, U.; Rösch, P.; Rödel, G.; Popp, J.; Deckert, V. Characterizing cytochrome c states – TERS studies of whole mitochondria. *Chemical Communications* **2011**, *47* (41), 11453–11455.

43. Deckert-Gaudig, T.; Kämmer, E.; Deckert, V. Tracking of nanoscale structural variations on a single amyloid fibril tip-enhanced Raman scattering. *J. Biophotonics* **2012**, *5*, 215–219.
44. Deckert-Gaudig, T.; Kurouski, D.; Hedegaard, M. A.; Singh, P.; Lednev, I. K.; Deckert, V. Spatially resolved spectroscopic differentiation of hydrophilic and hydrophobic domains on individual insulin amyloid fibrils. *Sci. Rep.* **2016**, *6*, 33575.
45. Krasnoslobodtsev, A. V.; Deckert-Gaudig, T.; Zhang, Y.; Deckert, V.; Lyubchenko, Y. L. Polymorphism of amyloid fibrils formed by a peptide from the yeast prion protein Sup35: AFM and Tip-Enhanced Raman Scattering studies. *Ultramicroscopy* **2016**, *165*, 26–33.
46. Li, Z.; Kurouski, D. Can Light Alter the Yield of Plasmon-Driven Reactions on Gold and Gold-Palladium Nanoplates? *Nano Lett* **2022**, *22* (18), 7484–7491.
47. Li, Z.; Rigor, J.; Large, N.; El-Khoury, P.; Kurouski, D. Underlying Mechanisms of Hot Carrier-Driven Reactivity on Bimetallic Nanostructures. *J. Phys. Chem. C* **2021**, *in press*.
48. Li, Z.; Wang, R.; Kurouski, D. Nanoscale Photocatalytic Activity of Gold and Gold-Palladium Nanostructures Revealed by Tip-Enhanced Raman Spectroscopy. *J. Phys. Chem. Lett.* **2020**, *11*, 5531–5537.
49. Hartschuh, A.; Sánchez, E. J.; Xie, X. S.; Novotny, L. High-resolution near-field Raman microscopy of single-walled carbon nanotubes. *Physical Review Letters* **2003**, *90* (9), 095503.
50. Touzalin, T.; Dauphin, A. L.; Joiret, S.; Lucas, I. T.; Maisonhaute, E. Tip enhanced Raman spectroscopy imaging of opaque samples in organic liquid. *Phys. Chem. Chem. Phys.* **2016**, *18*, 15510–15513.
51. Touzalin, T.; Joiret, S.; Lucas, I. T.; Maisonhaute, E. Electrochemical tip-enhanced Raman spectroscopy imaging with 8 nm lateral resolution. *Electrochem. Commun.* **2019**, *108*, 106557.
52. Zhang, D.; Wang, X.; Braun, K.; Egelhaaf, H.-J.; Fleischer, M.; Hennemann, L.; Hintz, H.; Stanicu, C.; Brabec, C. J.; Kern, D. P.; et al. Parabolic mirror-assisted tip-enhanced spectroscopic imaging for non-transparent materials. *J. Raman Spectrosc.* **2009**, *40* (10), 1371–1376.
53. Kleinman, S. L.; Frontiera, R. R.; Henry, A. I.; Dieringer, J. A.; Van Duyne, R. P. Creating, characterizing, and controlling chemistry with SERS hot spots. *Phys. Chem. Chem. Phys.* **2013**, *15* (1), 21–36.
54. Kurouski, D.; Lee, H.; Roschangar, F.; Senanayake, C. Surface-Enhanced Raman Spectroscopy: From Concept to Practical Application. *Scpectroscopy* **2017**, *32*, 36–44.
55. Moskovits, M. Surface roughness and the enhanced intensity of Raman scattering by molecules adsorbed on metals *J. Chem. Phys.* **1978**, *69*, 4159–4161.
56. Gersten, J.; Nitzan, A. Electromagnetic Theory of Enhanced Raman-Scattering by Molecules Adsorbed on Rough Surfaces. *J. Chem. Phys.* **1980**, *73*, 3023–3037.
57. Kerker, M.; Wang, D. S.; Chew, H. Surface enhanced Raman scattering (SERS) by molecules adsorbed at spherical particles. *Applied optics* **1980**, *19* (19), 3373–3388.
58. King, F. W.; Van Duyne, R. P.; Schatz, G. C. Theory of Raman scattering by molecules adsorbed on electrode surfaces. *J. Chem. Phys.* **1978**, *69* (10), 4472–4481.
59. Kelly, K. L.; Coronado, E.; Zhao, L. L.; Schatz, G. C. The Optical Properties of Metal Nanoparticles: The Influence of Size, Shape, and Dielectric Environment. *J. Phys. Chem. B* **2003**, *107* (3), 668–677.
60. Wustholz, K. L.; Henry, A. I.; McMahon, J. M.; Freeman, R. G.; Valley, N.; Piotti, M. E.; Natan, M. J.; Schatz, G. C.; Van Duyne, R. P. Structure-activity relationships in gold nanoparticle dimers and trimers for surface-enhanced Raman spectroscopy. *Journal of the American Chemical Society* **2011**, *132* (31), 10903–10910.
61. Haes, A. J.; Haynes, C. L.; McFarland, A. D.; Schatz, G. C.; Van Duyne, R. P.; Zou, S. Plasmonic Materials for Surface-Enhanced Sensing and Spectroscopy. *MRS Bulletin* **2005**, *30*, 368–375.
62. Ringe, E.; McMahon, J. M.; Sohn, K.; Cobley, C.; Xia, Y.; Huang, J.; Schatz, G. C.; Marks, L. D.; Van Duyne, R. P. Unraveling the Effects of Size, Composition, and Substrate on the Localized Surface Plasmon Resonance Frequencies of Gold and Silver Nanocubes: A Systematic Single-Particle Approach. *J. Phys. Chem. C* **2010**, *114*, 12511–12516.

63. Kurouski, D.; Large, N.; Chiang, N.; Greeneltch, N.; Carron, K. T.; Seideman, T.; Schatz, G. C.; Van Duyne, R. P. Unraveling near-field and far-field relationships for 3D SERS substrates–a combined experimental and theoretical analysis. *Analyst* **2016**, *141* (5), 1779-1788.
64. Henry, A. I.; Sharma, B.; Cardinal, M. F.; Kurouski, D.; Van Duyne, R. P. Surface-Enhanced Raman Spectroscopy Biosensing: In Vivo Diagnostics and Multimodal Imaging. *Anal Chem* **2016**, *88* (13), 6638–6647.
65. Kleinman, S. L.; Frontiera, R. R.; Henry, A. I.; Dieringer, J. A.; Van Duyne, R. P. Creating, characterizing, and controlling chemistry with SERS hot spots. *Phys Chem Chem Phys 15* (1), 21–36.
66. Lee, J.; Crampton, K. T.; Tallarida, N.; Apkarian, V. A. Visualizing vibrational normal modes of a single molecule with atomically confined light. *Nature* **2019**, *568* (7750), 78–+.
67. Liu, J. G.; Zhang, H.; Link, S.; Nordlander, P. Relaxation of Plasmon-Induced Hot Carriers. *ACS Photonics* **2018**, *5* (7), 2584–2595.
68. Manjavacas, A.; Liu, J. G.; Kulkarni, V.; Nordlander, P. Plasmon-induced hot carriers in metallic nanoparticles. *ACS nano* **2014**, *8* (8), 7630–7638.
69. Khurgin, J. B. How to deal with the loss in plasmonics and metamaterials. *Nat. Nanotechnol.* **2015**, *10* (1), 2–6.
70. Narang, P.; Sundararaman, R.; Atwater, H. A. Plasmonic hot carrier dynamics in solid-state and chemical systems for energy conversion. *Nanophotonics* **2016**, *5* (1), 96–111.
71. Brown, A. M.; Sundararaman, R.; Narang, P.; Goddard III, W. A.; Atwater, H. A. Nonradiative plasmon decay and hot carrier dynamics: effects of phonons, surfaces, and geometry. *ACS nano* **2015**, *10* (1), 957–966.
72. Hartland, G. V. Optical studies of dynamics in noble metal nanostructures. *Chem. Rev.* **2011**, *111* (6), 3858–3887.
73. Ma, J.; Wang, Z.; Wang, L.-W. Interplay between plasmon and single-particle excitations in a metal nanocluster. *Nat. Commun.* **2015**, *6*, 10107.
74. Cortés, E.; Xie, W.; Cambiasso, J.; Jermyn, A. S.; Sundararaman, R.; Narang, P.; Schlücker, S.; Maier, S. A. Plasmonic hot electron transport drives nano-localized chemistry. *Nat. Commun.* **2017**, *8*, 14880.
75. Wilson, A. J.; Jain, P. K. Light-Induced Voltages in Catalysis by Plasmonic Nanostructures. *Acc Chem Res* **2020**, *53*, 1773–1781.
76. Yu, S.; Jain, P. K. The Chemical Potential of Plasmonic Excitations. *Angew. Chem., Int. Ed.* **2020**, *59*, 2085–2088.
77. Marr, J. M.; Schultz, Z. D. Imaging Electric Fields in SERS and TERS Using the Vibrational Stark Effect. *J Phys Chem Lett* **2013**, *4* (19).
78. Kwasnieski, D. T.; Wang, H.; Schultz, Z. D. Alkyl-Nitrile Adlayers as Probes of Plasmonically Induced Electric Fields. *Chem Sci* **2015**, *6* (8), 4484–4494.
79. Bhattarai, A.; El-Khoury, P. Z. Nanoscale Chemical Reaction Imaging at the Solid-Liquid Interface via TERS. *J Phys Chem Lett* **2019**, *10* (11), 2817–2822.
80. Brongersma, M. L.; Halas, N. J.; Nordlander, P. Plasmon-induced hot carrier science and technology. *Nat. Nanotech.* **2015**, *10* (1), 25–34.
81. Lauchner, A.; Schlather, A. E.; Manjavacas, A.; Cui, Y.; McClain, M. J.; Stec, G. J.; Garcia de Abajo, F. J.; Nordlander, P.; Halas, N. J. Molecular Plasmonics. *Nano Lett* **2015**, *15* (9), 6208–6214.
82. Keller, E. L.; Frontiera, R. R. Ultrafast Nanoscale Raman Thermometry Proves Heating Is Not a Primary Mechanism for Plasmon-Driven Photocatalysis. *ACS nano* **2018**, *12* (6), 5848–5855.
83. Wang, R.; Li, J.; Rigor, J.; Large, N.; El-Khoury, P.; Yu., R. A.; Kurouski, D. Direct Experimental Evidence of Hot-Carrier-Driven Chemical Processes in Tip-Enhanced Raman Spectroscopy (TERS). *J. Phys. Chem. C* **2020**, *124* (3), 2238–2244.
84. van Schrojenstein Lantman, E. M.; Deckert-Gaudig, T.; Mank, A. J.; Deckert, V.; Weckhuysen, B. M. Catalytic processes monitored at the nanoscale with tip-enhanced Raman spectroscopy. *Nat. Nanotechnol.* **2012**, *7* (9), 583–586.
85. Bhattarai, A.; Crampton, K. T.; Joly, A. G.; Kovarik, L.; Hess, W. P.; El-Khoury, P. Z. Imaging the Optical Fields of Functionalized Silver Nanowires through Molecular TERS. *J Phys Chem Lett* **2018**, *9* (24), 7105–7109.

86. Mayevsky, A. D.; Funston, A. M. Control of Electric Field Localization by Three-Dimensional Bowtie Nanoantennae. *J. Phys. Chem. C.* **2018**, *122*, 18012–18020.
87. Yang, H.; Owiti, E. O.; Jiang, X.; Li, S.; Liu, P.; Sun, X. Localized Surface Plasmon Resonance Dependence on Misaligned Truncated Ag Nanoprism Dimer. *Nanoscale Res Lett* **2017**, *12* (1), 430.
88. Cai, Z. F.; Merino, J. P.; Fang, W.; Kumar, N.; Richardson, J. O.; De Feyter, S.; Zenobi, R. Molecular-Level Insights on Reactive Arrangement in On-Surface Photocatalytic Coupling Reactions Using Tip-Enhanced Raman Spectroscopy. *J Am Chem Soc* **2022**, *144* (1), 538–546.
89. Wang, R.; Kurouski, D. Elucidation of Tip-Broadening Effect in Tip-Enhanced Raman Spectroscopy (TERS): A Cause of Artifacts or Potential for 3D TERS. *J. Phys. Chem. C* **2018**, *122*, 24334–24340.
90. Wang, R.; Kurouski, D. Thermal Reshaping of Gold Microplates: Three Possible Routes and Their Transformation Mechanisms. *ACS Appl Mater Interfaces* **2019**, *11* (44), 41813–41820.
91. Rossi, T. P.; Erhart, P.; Kuisma, M. Hot-Carrier Generation in Plasmonic Nanoparticles: The Importance of Atomic Structure. *ACS nano* **2020**, *14* (8), 9963–9971.
92. Sun, J.-J.; Su, H.-S.; Yue, H.-L.; Huang, S.-C.; Huang, T.-X.; Hu, S.; Sartin, M. M.; Cheng, J.; Ren, B. Role of adsorption orientation in surface plasmon-driven coupling reactions studied by tip-enhanced Raman spectroscopy. *J. Phys. Chem. Lett.* **2019**, *10* (10), 2306–2312.
93. Sytwu, K.; Vadai, M.; Dionne, J. A. Bimetallic nanostructures: combining plasmonic and catalytic metals for photocatalysis. *Advances in Physics: X* **2019**, *4* (1), 394–418.
94. Zhong, J. H.; Jin, X.; Meng, L.; Wang, X.; Su, H. S.; Yang, Z. L.; Williams, C. T.; Ren, B. Probing the electronic and catalytic properties of a bimetallic surface with 3 nm resolution. *Nature nanotechnology* **2017**, *12* (2), 132–136.
95. Su, H. S.; Zhang, X. G.; Sun, J. J.; Jin, X.; Wu, D. Y.; Lian, X. B.; Zhong, J. H.; Ren, B. Real-Space Observation of Atomic Site-Specific Electronic Properties of a Pt Nanoisland/Au(111) Bimetallic Surface by Tip-Enhanced Raman Spectroscopy. *Angew Chem Int Ed Engl* **2018**, *57* (40), 13177–13181.
96. Yin, H.; Zheng, L.; Fang, W.; Lai, H. L.; Porenta, N.; Goubert, G.; Zhang, H.; Su, H. S.; Ren, B.; Richardson, J. O.; et al. Nanometre-scale spectroscopic visualization of catalytic sites during a hydrogenation reaction on a Pd/Au bimetallic catalyst. *Nat. Catal.* **2020**, *3*, 834–842.
97. Patil, S. J.; Kurouski, D. Tip-enhanced Raman imaging of plasmon-driven dimerization of 4-bromothiophenol on nickel-decorated gold nanoplate bimetallic nanostructures. *Chem Commun (Camb)* **2023**, *59* (73), 10976–10979. From NLM PubMed-not-MEDLINE.
98. O'Callahan, B. T.; El-Khoury, P. Z. A Closer Look at Tip-Enhanced Raman Chemical Reaction Nanoimages. *J Phys Chem Lett* **2022**, *13* (17), 3886–3889.
99. Patil, S. J.; Lomonosov, V.; Ringe, E.; Kurouski, D. Tip-Enhanced Raman Imaging of Plasmon-Driven Coupling of 4-Nitrobenzenethiol on Au-Decorated Magnesium Nanostructures. *J Phys Chem C Nanomater Interfaces* **2023**, *127* (16), 7702–7706. From NLM PubMed-not-MEDLINE.
100. Sarycheva, A.; Shanmugasundaram, M.; Krayev, A.; Gogotsi, Y. Tip-Enhanced Raman Scattering Imaging of Single- to Few-Layer $Ti_3C_2T_x$ MXene. *ACS nano* **2022**.
101. Mahapatra, S.; Schultz, J. F.; Ning, Y.; Zhang, J. L.; Jiang, N. Probing surface mediated configurations of nonplanar regioisomeric adsorbates using ultrahigh vacuum tip-enhanced Raman spectroscopy. *Nanoscale* **2019**, *11* (42), 19877–19883.
102. Xu, J.; Zhu, X.; Tan, S.; Zhang, Y.; Li, B.; Tian, Y.; Shan, H.; Cui, X.; Zhao, A.; Dong, Z.; et al. Determining structural and chemical heterogeneities of surface species at the single-bond limit. *Science* **2021**, *371* (6531), 818–822.
103. Zhang, Y.; Yang, B.; Ghafoor, A.; Zhang, Y.; Zhang, Y. F.; Wang, R. P.; Yang, J. L.; Luo, Y.; Dong, Z. C.; Hou, J. G. Visually constructing the chemical structure of a single molecule by scanning Raman picoscopy. *Natl Sci Rev* **2019**, *6* (6), 1169–1175.
104. Lee, C.; Jeong, B. G.; Kim, S. H.; Kim, D.-H.; Yun, S. J.; Choi, W.; An, S.-J.; Lee, D.; Kim, Y.-M.; KIm, K. K.; et al. Investigating heterogeneous defects in single-crystalline WS2 via tip-enhanced Raman spectroscopy. *npj 2D Materials and Applications* **2022**, *6*, 67.

105. Lee, C.; Jeong, B. G.; Yun, S. J.; Lee, Y. H.; Lee, S. M.; Jeong, M. S. Unveiling Defect-Related Raman Mode of Monolayer WS(2) via Tip-Enhanced Resonance Raman Scattering. *ACS nano* **2018**, *12* (10), 9982–9990. From NLM PubMed-not-MEDLINE.
106. Kato, R.; Moriyama, T.; Umakoshi, T.; Yano, T. A.; Verma, P. Ultrastable tip-enhanced hyperspectral optical nanoimaging for defect analysis of large-sized WS(2) layers. *Sci Adv* **2022**, *8* (28), eabo4021. From NLM PubMed-not-MEDLINE.

# Chapter 24
# Tip-Enhanced Raman Microscopy: Theory, Practice, and Applications for Nanomaterials Visualization and Characterization




**Atsushi Taguchi**

**Abstract** Tip-enhanced Raman scattering (TERS) microscopy enables high-resolution optical visualization and analysis of materials at the nanoscale. Although TERS shares similarities with surface-enhanced Raman scattering (SERS), it offers unique advantages, particularly through the utilization of plasmonic TERS tips. This chapter provides an overview of TERS techniques, focusing on the physics of TERS tips as optical antennas and their fabrication techniques. Special emphasis is placed on the theoretical aspects of plasmonic tip behavior, including surface plasmon resonances and localized modes of plasmon resonances on nanostructures. Practical considerations in the fabrication of multi-grain TERS probes, such as optimizing the arrangement of nanoparticles and the effects of deposition parameters, are discussed. Experimental results on the enhancement and resolution of multi-grain TERS probes are presented through comparisons with other probe morphologies, along with TERS imaging of carbon nanotubes (CNTs). Applications of TERS microscopy in characterizing nano-materials such as CNTs, graphene, semiconductor crystals, and twisted bilayer graphene (TBG) are showcased. Additionally, the utilization of deep ultraviolet (DUV) TERS, which extends the capabilities of TERS microscopy to analyze materials with wide-bandgap properties or specific molecular vibrations, is discussed. DUV plasmon resonance in metal nanostructures, such as aluminum and indium, is explored theoretically and experimentally. This comprehensive discourse underscores the potential of TERS microscopy for nanoscale molecular identification and imaging applications.

**Keywords** Surface plasmon polaritons · Multi-grain antennas · DUV plasmons · Atomic-force correlated TERS · Twisted bilayer graphene · carbon nanotubes

A. Taguchi (✉)
Research Institute for Electronic Science, Hokkaido University,
N20W10, Kita-Ward, Sapporo 001-0020, Japan
e-mail: taguchi@es.hokudai.ac.jp

© The Author(s), under exclusive license to Springer Nature Singapore Pte Ltd. 2024

M. Procházka et al. (eds.), *Surface- and Tip-Enhanced Raman Scattering Spectroscopy*,
https://doi.org/10.1007/978-981-97-5818-0_24

## 24.1 Introduction

Tip-enhanced Raman scattering (TERS) microscopy enables the optical visualization, identification, and analysis of materials with nanoscale spatial resolution. The principle of TERS shares some similarities with surface-enhanced Raman scattering (SERS), where surface plasmon polaritons and associated localized electromagnetic fields play a crucial role in locally enhancing Raman scattering of the sample. However, a distinction between SERS and TERS arises when considering plasmonic TERS tips and their resulting applications.

In this chapter, the author discusses the theory and application of TERS techniques, with special emphasis on the physics of TERS tips, which act as optical antennas—the physical interface between the near and far-field. Practical fabrication techniques for TERS probes are then discussed, and applications of TERS are exemplified. Additionally, the emerging technique of TERS in the deep ultraviolet (DUV) region is also discussed.

## 24.2 Theoretical Aspect of Plasmonic Tip

### *24.2.1 Surface Plasmon Resonances*

When electromagnetic waves hit a metal, they are mostly reflected but do not deeply penetrate the subsurface. However, they do enter the thin surface layer of the metal structure, a phenomenon known as the skin effect. These penetrating electromagnetic waves interact with the free electrons in the metal's surface layer, causing them to oscillate collectively. This collective oscillation of free electrons interacting with the surface electromagnetic waves is referred to as a surface plasmon polariton (Fig. 24.1a).

The dispersion relation of surface plasmons at the interface between a metal and a dielectric (e.g., vacuum or glass) can be expressed by the following equation [1]:

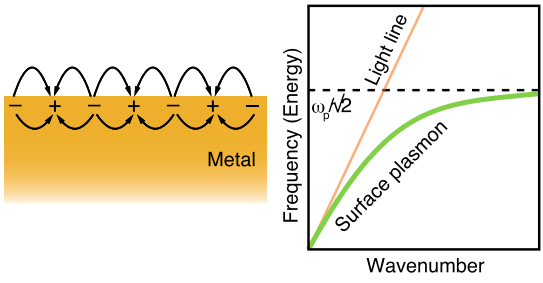



**Fig. 24.1** **a** Schematic of charge and electric field of surface plasmon polaritons, and **b** its dispersion relation

$$k_x = \frac{\omega}{c}\left(\frac{\epsilon_1\epsilon_2}{\epsilon_1+\epsilon_2}\right)^{1/2} \tag{24.1}$$

Here, $k_x$ represents the wave number within the interface, $\omega$ is the frequency, $\epsilon_1$ and $\epsilon_2$ are the dielectric constants of the metal and the dielectric, respectively, and $c$ is the speed of light. The dispersion relation is illustrated in Fig. 24.1b. The dispersion curve of surface plasmons always lies to the right of the dispersion of light propagating in free space, $k = \omega/c$ (the light line). This indicates that the wave number of surface plasmons $k = 2\pi/\lambda$ is larger than that of propagating light, corresponding to the fact that the wavelength of surface plasmons is always shorter compared to propagating light. At the same time, the non-crossing relation between the dispersion curves of surface plasmons and the propagating light implies that the surface plasmons become a non-radiative, localized mode at the surface as an evanescent wave.

The denominator of Eq. 24.1 approaches zero as $\epsilon_1 \to -\epsilon_2$, leading to an increase in the wave number $k_x$. Assuming air ($\epsilon_2 = 1$) as the surrounding dielectric and a lossless Drude metal for the dielectric function $\epsilon_1$:

$$\epsilon_1 = 1 - \frac{\omega_p^2}{\omega^2} \tag{24.2}$$

where $\omega_p$ is the plasma frequency of the metal, the condition $\epsilon_1 = -\epsilon_2 = -1$ yields the resonance frequency $\omega = \omega_{sp} = \omega_p/\sqrt{2}$. At this frequency, the slope of the dispersion curve, corresponding to the group velocity of surface plasmon waves, becomes zero, as indicated by the dashed line in Fig. 24.1b. This represents the surface plasmon resonance state, where the surface waves oscillate and remain localized at the same place. At the resonance frequency $\omega_{sp}$ of surface plasmons, the wave number diverges to infinity. The increase in the wave number $k_x = 2\pi/\lambda$ corresponds to a decrease in wavelength, leading to an improvement in spatial resolution when used as a microscope. Metallic probes in tip-enhanced Raman scattering (TERS) microscopy utilize this phenomenon to read and write molecular information at nanoscale spatial resolutions beyond the wavelength of light.

The resonance frequency of the surface plasmon, given by $\omega_{sp} = \omega_p/\sqrt{2}$, is determined by a material-specific value $\omega_p$. As seen in Fig. 24.1b, the region where surface plasmons exist lies on the lower energy (longer wavelength) side of this resonance frequency $\omega_{sp}$. Therefore, knowing the value of $\omega_{sp}$ for specific materials is important to predict the plasmon region of the material used. Figure 24.2 plots the plasmon dispersion relations for gold (Au), silver (Ag), and aluminum (Al), using the experimentally measured values of the dielectric functions [2]. For commonly used plasmonic metals such as Au and Ag, $\omega_p$ is around 500 nm and 360 nm, respectively. This explains why Au and Ag are used as plasmonic metals in the visible to near-infrared wavelength range. On the other hand, it is understood that Au or Ag do not provide the plasmons in the ultraviolet (UV) range, where the photon energy exceeds the material's $\omega_p$. A straightforward way to achieve the surface plasmons in the UV region is to find a material having a higher $\omega_p$. In addition, chemical stability and

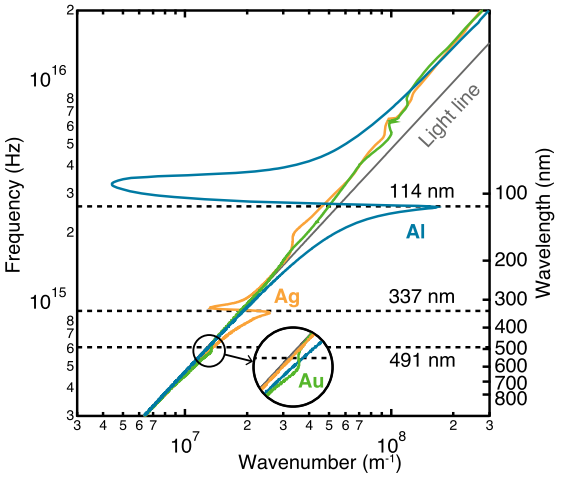



**Fig. 24.2** Surface plasmon dispersion relations for gold (Au), silver (Ag), and aluminum (Al). Dashed lines represent the resonance frequency of surface plasmons, $\omega_{sp}$

material abundance would also be considerations. Exploring metallic materials under such conditions, Al [3, 4] and indium [5] appear promising. As shown in Fig. 24.2, the plasmon region of Al lies between 114 and about 300 nm.

The Drude dispersion given by Eq. 24.1 ignores the losses in the metal's dielectric function (the imaginary part of the dielectric function), resulting in the finite wavenumber observed in Fig. 24.1b. Considering that the losses in metals fold back at finite wave numbers to the left of the light line, as seen in Fig. 24.2b. The curved portion to the left of the light line corresponds to the Brewster angle. Unlike surface plasmon, which is non-radiative, the Brewster state is radiative.

### *24.2.2 Localized Modes of Plasmon Resonances on Nanostructures*

Surface plasmon waves, generated at the metal-dielectric interface, facilitate the formation of localized resonance modes depending upon the shape and dimensions of the nanostructure. For instance, in metal nanorods, as depicted in Fig. 24.3, eigenmodes emerge depending on the rod's length, at which the surface plasmon waves resonate with the structure. This phenomenon bears a resemblance to radio antennas, where the antenna length typically corresponds to an integer multiple of the electromagnetic wave's half-wavelength. However, due to the increased wave numbers, surface plasmons possess effective wavelengths smaller than those of propagating light. Consequently, resonant structures are typically nano-sized, smaller than the wavelength of propagating light. This constitutes a primary mechanism for effectively localizing light within nano-sized regions using metal nanostructures. In Fig. 24.3, odd-order modes exhibit dipoles with opposite charges at both ends, while even-order modes

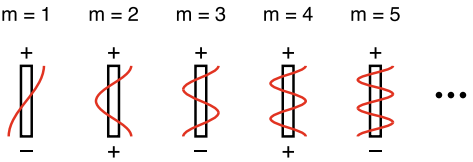



**Fig. 24.3** Eigenmodes and charge distribution of metal nanorods

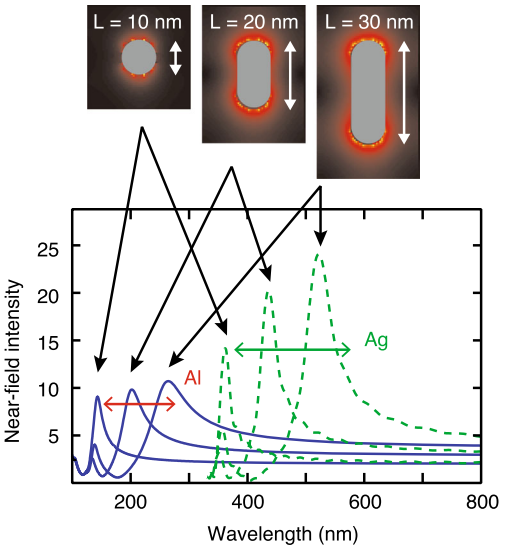



**Fig. 24.4** Near-field enhancement spectra at the tips of metal nanorods obtained from FDTD calculations. The rod lengths are 10, 20, and 30 nm, with a width of 10 nm. The materials are Al and Ag. The top panels illustrate the near-field distributions at the cross-section of the rod at the resonance wavelength. Reproduced with permission from Ref. [6]. Copyright 2015 Springer Nature

have the same polarity at both ends and do not form dipoles. Modes forming dipoles are radiative and can couple with propagating light, thereby enabling the excitation of plasmon resonances in nanostructures by propagating light.

By adjusting the length of the rod, one can alter the energy of the resonance states, similar to how the pitch of a piano string is determined by its length. Figure 24.4 presents the computed results of the near-field enhancement at the tips of rods with varying lengths, using finite-difference time-domain (FDTD) simulation [6]. Calculations were conducted for nanorods with widths of 10 nm and lengths of 10, 20, and 30 nm, using Al and Ag materials. In both metals, the near-field enhancement increases at the plasmon resonance wavelength. Furthermore, the plasmon resonance wavelength shifts toward longer wavelengths as the rod length increases. Additionally, for rods of the same length, Al exhibits resonance in the deep ultraviolet (DUV) wavelength region, while Ag resonates in the visible wavelength region. Based on these simulation results, it is anticipated that Al can achieve plasmon resonance in the DUV wavelength region.

### *24.2.3 Multi-grain Tip Structure*

TERS is a spectroscopic technique that enhances Raman scattering of molecules exposed under the enhanced field provided by a plasmonic tip [7, 8]. By scanning the probe over the sample in two dimensions, Raman images can be obtained with nanoscale spatial resolution, offering highly sensitive molecular identification and visualization with high spatial resolution. In TERS microscopy, it is crucial to create a hotspot at the very end of the nanoprobes' tips in a reproducible manner. However, metal nanoparticles produced by vacuum deposition, one of the techniques widely used for tip fabrication, are not necessarily uniform in size and shape, leading to non-uniform probe-by-probe enhancement characteristics. Additionally, as the probe is sharpened, the Raman scattering cross-section decreases with the sixth power of the particle size at the tip. This results in a weak Raman scattering signal, making it difficult to detect Raman scattering signals from molecules with a small detection volume. This trade-off presents a challenge in increasing Raman enhancement while localizing the near-field at the tip. Therefore, developing metal probes with both high enhancement and reproducibility has been a long-standing challenge for TERS researchers and engineers [9].

To address the aforementioned dilemma, Fig. 24.5 numerically examines the Raman scattering intensity by varying the number of grains at the probe tip [10]. The simulation model is depicted in Fig. 24.5a. The Ag nanoparticles, each having a diameter of 40 nm, are discretely arranged on a silicon dioxide ($SiO_2$) cone. The tip was excited with a radially polarized beam focusing on the tip apex at a wavelength of 532 nm. First, the near-field spectrum at the tip was calculated. Next, the far-field scattering spectrum of a molecule placed at the tip of the probe was calculated. Multiplying these two spectra provides a reasonable evaluation of the Raman enhancement spectrum of the probe-molecule system.

The results, as shown in Fig. 24.5b, revealed that the scattering intensity increases as the number of particles increases from one to four compared to when there is a single particle. Furthermore, with the addition of more particles, although the peak intensity decreases, it remains stronger than that of a single particle. This suggests that the particle ensemble behind the sensing particle at the tip enhances the Raman scattering intensity. By placing additional particles behind the sensing particle, the localization at the tip is maintained. Utilizing such an ensemble of nanoparticles should effectively enhance Raman scattering. The existence of an optimal number of particles is explained by the fact that, as depicted in Fig. 24.5c, when the number of particles becomes too large, the metal absorption during propagation due to plasmonic coupling between particles increases. It is important to emphasize that the scattering spectrum in Fig. 24.5b evaluates a two-step process of excitation and scattering intermediated by the molecules, not the simple scattering of a nanoparticle assembly without molecules.

The arrangement of particles, whether discrete or interconnected, also significantly influences the enhancement characteristics of metal probes. Figure 24.6 presents the results of calculating the near-field spectra at the tip for the probes mod-

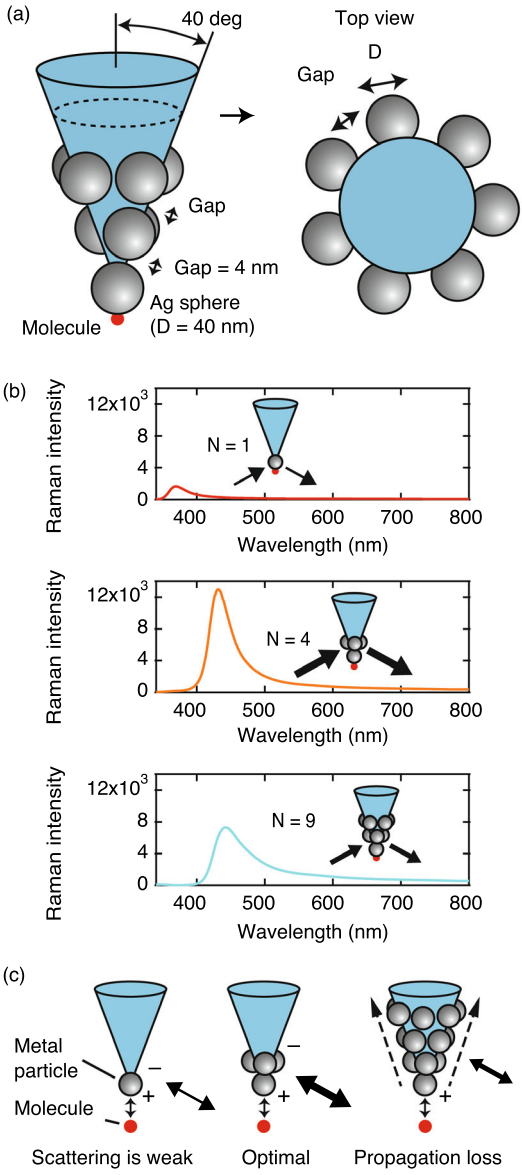



**Fig. 24.5** **a** FDTD computational model of a Ag probe. Ag nanoparticles with a diameter of 40 nm are discretely arranged with a 4 nm gap. **b** Computational results of Raman enhancement spectra of probes with different numbers of particles. Reproduced with permission from Ref. [10]. Copyright 2015 RCS Publication. **c** Explanation of the optimal number of particles

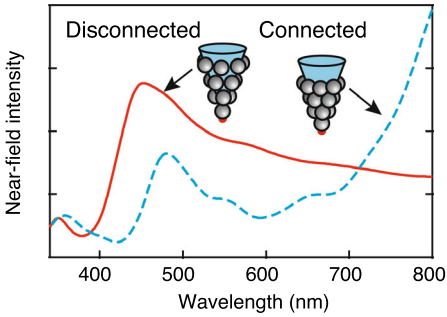



**Fig. 24.6** Comparison of near-field spectra for Ag grain probes calculated by FDTD, with discrete and interconnected particle arrangements. Reproduced with permission from Ref. [10]. Copyright 2015 RCS Publication

eled with particles arranged discretely or connected. Figure 24.6 shows the results of calculating the near-field spectra at the tip for the probes modeled with particles arranged discretely or connected. When the particles are discrete, the spectrum exhibits a single broad peak shape, while when the particles are connected, multiple peaks appear and the spectrum becomes sharper. This corresponds to the excitation of higher-order plasmon modes in the rod-like system illustrated in Fig. 24.3, resulting in the appearance of multimodal plasmon peaks. The resonance wavelength in the multimodal state is sensitive to the length of the rod, so even a slight change in the rod length can lead to a significant shift in the spectrum. Therefore, precise control of the metal shape at the tip is required, making it more challenging as a probe fabrication technique.

Raman scattering measures wavelength shifts. To detect Raman bands across a wide range, from the fingerprint region to low wavenumbers, a broad enhancement spectrum is necessary. The discrete arrangement of metal nanoparticles provides a broader bandwidth for the enhancement spectrum, making it a desirable characteristic for Raman spectroscopy. A similar concept of using discrete stacking of metal nanorods is also employed in near-field magnification devices, where a broader near-field transfer bandwidth enables color image formation [11].

## 24.3 Fabrication of Multi-grain Ag Tips

In this section, we present the fabrication techniques for Ag TERS probes, with an emphasis on achieving discretely arranged grains. Ag is chosen for its superior enhancement effect compared to other noble plasmonic metals (e.g., Au). We discuss the oxidation of silicon (Si) probes as a technique to maximize the plasmonic activity of the metal on TERS probes. The results of Ag vacuum deposition are investigated under various evaporation conditions.

### *24.3.1 Oxidization*

A commonly used technique to prepare Ag TERS probes is to coat Ag onto Si probes using thermal evaporation [12]. Before Ag deposition on the tip, a Si cantilever is oxidized to form a layer of $SiO_2$. This step is crucial because the plasmon resonance wavelength of an Ag-coated probe depends on the refractive index of the underlying material [3, 13]. Si has a high refractive index of $n = 4.4$, causing the resonance wavelength of localized plasmons of the Ag tip to significantly redshift to longer wavelengths, even in the near-infrared, which makes Raman scattering inefficient [3]. Moreover, the inherent light absorption by Si reduces the field enhancement provided by the plasmon resonance. To address this issue, a technique was proposed to transfer a superficial part of the Si cone into $SiO_2$ through oxidation [3]. $SiO_2$ has a much smaller refractive index ($n = 1.5$) than Si ($n = 4.4$). Depending on the thickness of the $SiO_2$ layer, the plasmon resonance wavelength varies within the visible region [3]. The oxidation process involves thermally oxidizing the base material of a Si tip [14]. Figure 24.7a shows the results of the oxidation of a Si tip [3]. Transmission electron micrographs depict a layer of amorphous $SiO_2$ on the outer surface of Si probes, with the thickness increasing with oxidation time. The cantilever tip can be practically fully converted into $SiO_2$ at a controlled temperature and oxidation time. The tip radius and shape remain unchanged after oxidation. Figure 24.7b compares the dark-field scattering spectra of Ag tips made on oxidized and non-oxidized Si tips. As shown in the figure, the resonance of an Ag tip on $SiO_2$ is blue-shifted compared to that on a Si tip, indicating better resonance for wavelengths in the visible range. Moreover, the scattering intensity is increased by oxidation. The resonance peak wavelength can be controlled by adjusting the thickness of the $SiO_2$ layer [3].

There are two types of oxidation furnaces available: one uses water vapor to oxidize Si (known as wet oxidation), and the other uses dry oxygen (dry oxidation). Wet oxidation is efficient for producing a thick oxide layer within a short period. The thickness of the oxidation layer quickly reaches hundreds of nanometers within 20 min of oxidation at 1100 °C [3]. In contrast, dry oxidation is slower in growing the thickness of the oxidation layer. Figure 24.7c shows the thickness of $SiO_2$ on a Si wafer relative to the oxidation time using a dry oxidation furnace at one atmosphere. The oxidation layer grows almost linearly with oxidation time. The slower process of dry oxidation compared to wet oxidation allows for more precise control of thickness. The deviation between the measured thickness (blue open circles) and the fitted line (red solid line) is less than 10 nm. This demonstrates the ability to control $SiO_2$ thickness by oxidation time with a precision of a few nanometers. Wet oxidation environments are prone to contamination. Dry oxidation is preferable for maintaining the cleanliness of the tip surface.

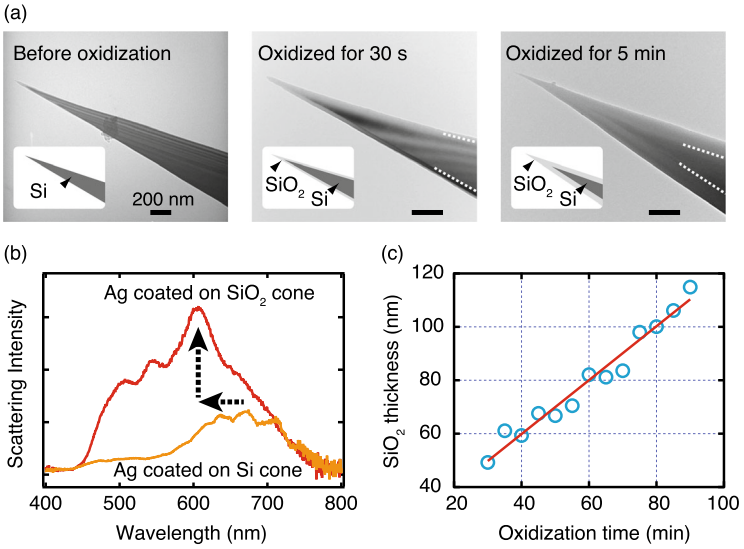



**Fig. 24.7** **a** Transmission electron microscope (TEM) images of the Si probes before oxidization (left panel) and after oxidization for 30 s (middle panel) and 5 min (right panel). Material compositions are schematically explained in the inset in each image. Dotted lines are guides to indicate the material boundary. Reproduced with permission from Ref. [15]. Copyright 2009 Optical Society of America. **b** Dark-field scattering spectra of Ag-coated oxidized Si probe and Ag-coated non-oxidized Si probe. Reproduced with permission from Ref. [15]. Copyright 2009 Optical Society of America. **c** $SiO_2$ thickness on planer Si wafer with respect to oxidization time at 950 °C. The blue open circles show the thickness of $SiO_2$ measured by an ellipsometer (Elli-SE-OW, Ellipse Technology Co., Ltd.). The red line represents the least-square fitting. Reproduced with permission from Ref. [16]. Copyright 2019 Elsevier

### *24.3.2 Evaporation*

After the oxidation of the Si probe, the $SiO_2$ cone is metalized by coating it with a thin layer of Ag. This coating can be conveniently achieved through thermal evaporation, which is a well-established technique for depositing one material over another. To maintain the purity of the material during the deposition process, especially for easily oxidized materials like Ag, a high vacuum level is preferable for the evaporation chamber [17]. The vacuum level is typically $10^{-5}$–$10^{-7}$ Pa. Another factor to consider is the uniformity of deposition on the probe surface, which helps reduce tip-to-tip variation. Since the material source is located at the bottom of the chamber and the probes are fixed at the top, the vapor path of the material follows a random scattering trajectory as it flows upwards. This randomness can lead to non-uniform coating on the conical shape of the probe. To minimize this non-uniformity, a rotor that imposes rotation on the probe is installed in the chamber.

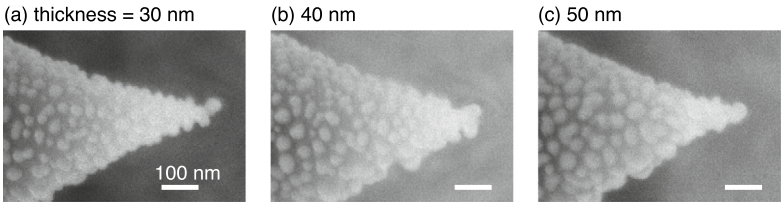



**Fig. 24.8** Vacuum-deposited Ag nanoparticles on $SiO_2$ cone formed at nominal deposition thicknesses of **a** 30 nm, **b** 40 nm, and **c** 50 nm. Deposition rate was 0.2 Å/s. Reproduced with permission from Ref. [16]. Copyright 2019 Elsevier

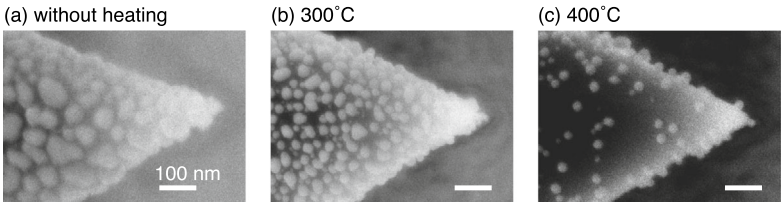



**Fig. 24.9** Vacuum-deposited Ag nanoparticles on $SiO_2$ cone formed with **a** no heating and **b** with heating at a temperature of 300 °C and **c** 400 °C. Deposition rate was 0.2 Å/s; deposition thickness, 40 nm. Reproduced with permission from Ref. [16]. Copyright 2019 Elsevier

In practice, three deposition parameters, namely deposition thickness, rate, and probe temperature, are controlled. The effect of changing deposition thickness on the morphologies of the formed Ag nanoparticles is examined. Figure 24.8 illustrates a series of scanning electron microscopy (SEM) images showing different average sizes of Ag nanoparticles formed on the probe tip, each deposited at different thicknesses. The results indicate that a larger thickness yields larger nanoparticles, demonstrating that the size of the nanoparticles on the surface of the probe can be controlled by deposition thickness.

The deposition rate is another factor to control. In our experience, changing the deposition rate results in no apparent difference in the morphologies of the formed nanoparticles. However, some researchers have reported that a high deposition rate is preferable to reduce the chance of chemical reactions (such as oxidation) inside the chamber [17].

We also examine the effect of heating up the probe during evaporation. Figure 24.9 shows a series of SEM images resulting from different temperatures of the $SiO_2$ cone onto which Ag is deposited. The results show that a higher heating temperature yields a smaller number of nanoparticles formed on the probe surface and makes the nanoparticles smaller. This is because increasing the temperature on the surface reduces the chance of vapor atoms to condense and makes it more inclined to re-evaporate. By using probe heating, the nanoparticle density can be controlled.

Finally, shown in Fig. 24.10 is the effect of changing the deposition thickness of Ag nanoparticles at an elevated probe temperature of 340 °C. The results demonstrate variations in both the size and density of nanoparticles. By combining the probe

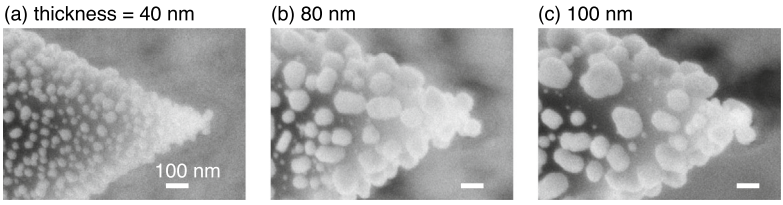



**Fig. 24.10** Vacuum-deposited Ag nanoparticles on $SiO_2$ cone formed at nominal deposition thicknesses of **a** 40 nm, **b** 80 nm, and **c** 100 nm with the probes heated up at a temperature of 340 °C. Deposition rate was 0.2 Å/s. Reproduced with permission from Ref. [16]. Copyright 2019 Elsevier

heating technique, large-sized nanoparticles can be obtained without being connected to each other to form a film-like surface morphology, which has been shown to be less effective for TERS enhancement (see Fig. 24.6).

## 24.4 Enhancement and Resolution of Multi-grain Probe: Experimental Verification

TERS enhancements of TERS probes with different morphologies were compared using monolayer graphene as a sample. Three types of probes were fabricated: probes with discrete Ag particles, probes with connected Ag particles, and probes with smooth Ag surfaces. The results are shown in Fig. 24.11 [10]. In the case of probes with a discrete arrangement of Ag particles, the Raman enhancement intensity reaches 5500-fold (Fig. 24.11a), whereas in probes with connected particles (Fig. 24.11b), the enhancement was 800-fold. These results demonstrate the significant enhancement effect of discrete particle probes. The probes with smooth surfaces exhibited the lowest enhancement intensity. This is attributed to the lack of surface roughness, which prevents the formation of dipoles needed for efficient coupling with the incident field and radiation into the far-field.

Figure 24.12 shows the TERS image of carbon nanotubes (CNTs) obtained using the discretely arranged multi-grain probe (Fig. 24.12a), along with the simultaneously acquired topography image (Fig. 24.12b) [18]. The CNT is visualized in the TERS image. Judging from the height of the A–B cross-sectional profile in the topography, the region A–B corresponds to a single CNT. The spatial resolution, evaluated from the TERS image, is 16 nm based on the half-width of the cross-sectional profile. These results demonstrate that discrete particle probes are effective in TERS imaging.

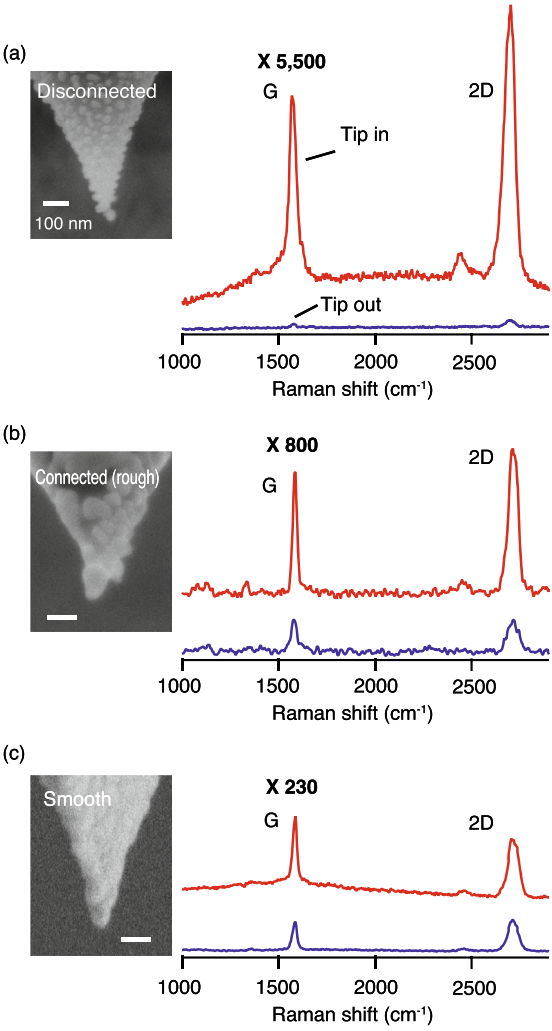



**Fig. 24.11** TERS spectra of monolayer graphene measured with Ag probes of various tip morpholoties. **a** Discrete particle probe. **b** Connected particle probe. **c** Smooth surface probe. SEM images of the probes are shown on the left. Excitation wavelength is 488 nm. Reproduced with permission from Ref. [10]. Copyright 2015 RCS Publication

## 24.5 Applications

TERS microscopy has been applied to visualize and characterize various nanomaterials, including CNTs [12, 19], $C_{60}$ [8, 20], graphene [21, 22], and related two-dimensional materials such as $MoS_2$ [23], as well as semiconductor crystals including patterned substrates [24] and nanostructures [25–27]. Here, we introduce three typical applications of TERS microscopy: nano-resolution Raman intensity mapping, frequency shift mapping, and chemical mapping.

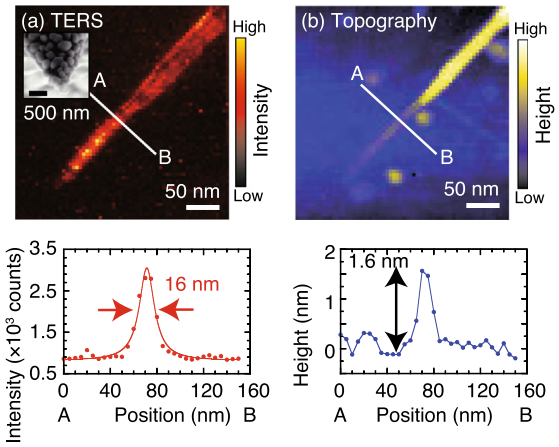



**Fig. 24.12** TERS intensity image at G-band of CNT measured with a discrete particle probe **a** and **b** simultaneously obtained AFM topography. The inset in **a** shows the SEM image of the probe, showing the discreetly arranged Ag particles. The bottom image shows the cross-sectional profile along line A–B. Excitation wavelength is 488 nm. Reproduced with permission from Ref. [18]. Copyright 2019 AIP Publishing

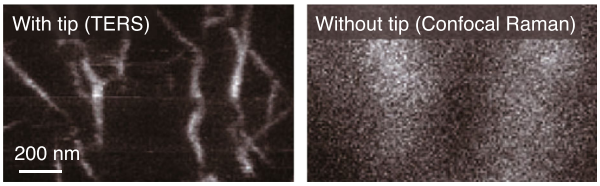



**Fig. 24.13** Raman intensity image of single-walled CNTs at *G*-band measured with Ag tip (left) and without the tip (right). Reproduced with permission from Ref. [28]. Copyright 2012 John Wiley and Sons

### *24.5.1 Intensity Mapping with Nanoscale Spatial Resolution*

The left panel in Fig. 24.13 displays a Raman intensity image of CNTs, which was acquired using an Ag tip [28]. The distribution of CNTs on a substrate is visualized with a spatial resolution of approximately 20 nm. In contrast, the right panel in Fig. 24.13 images the same sample position as the left panel, but with the metal tip retracted from the sample surface. In the right image, the fine structure observed in the left panel is absent, leaving only the low-resolution far-field signal. Recent reports on TERS experiments have demonstrated spatial resolutions typically ranging from 10 to 20 nm [10, 19]. Furthermore, resolutions as fine as several nanometers to sub-nanometers have been achieved in the STM gap-mode configuration, where the sample is positioned between a metal tip and a metal substrate [29, 30]. However, it is worth noting that samples must be exceptionally thin to accommodate the STM feedback scheme.

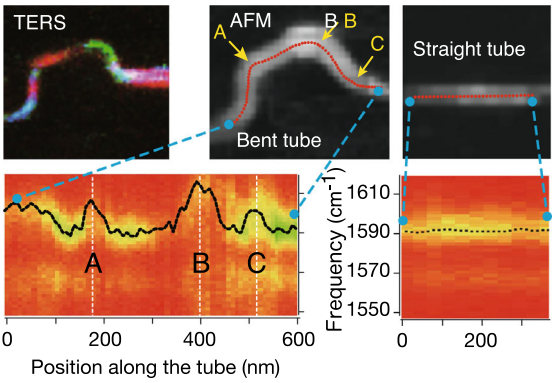



**Fig. 24.14** Frequency shift image of a CNT. (Upper left) TERS image colored with three frequencies of 1590 $cm^{-1}$ (red), 1600 $cm^{-1}$ (blue) and 1610 $cm^{-1}$ (green). Frequency-shifted components (blue and green) are dominantly seen at the bent corners. (Middle and right) AFM images of bent and straight CNT (upper) and corresponding G-band spectra along the CNT (red line in the AFM image) (lower panel). High-frequency shifts were found at the bent corners, indicating the nanotube structure was distorted by an internal force. Reproduced with permission from Ref. [31]. Copyright 2013 Springer Nature

### *24.5.2 Frequency Shift Mapping*

Figure 24.14 shows a TERS image of a CNT that maps out the shift in Raman peak rather than intensity [31]. The amount of Raman peak shift correlates with the local strain in the deformed CNT. In the lower panel of Fig. 24.14, the *G*-band spectrum of the CNT is presented against its axial position. The *G*-band peak exhibits a notable shift to higher frequencies at the highly deformed corner, as indicated by the yellow arrows in the upper middle panel, whereas peak shift is negligible at the straight section, as shown in the upper right panel. This analysis of local strains via TERS spectral shift is also valuable in characterizing strained silicon substrates [24]. The presence of local strain in silicon is crucial in semiconductor industry applications, as it influences the mobility of electrons and holes, thereby enhancing the speed of electronic devices and reducing power consumption [32].

### *24.5.3 Chemical Mapping*

Figure 24.15 shows a TERS image of a single-layer graphene reconstructed from various vibrational modes, including 2*D*, *G*, and *D*-bands, as well as CH stretching vibration [22]. In the *D*-band image, highly localized defects on the graphene are visible. The 2*D* and CH images display complementary distributions, indicating spatial variations in the local structure of the single-layer graphene.

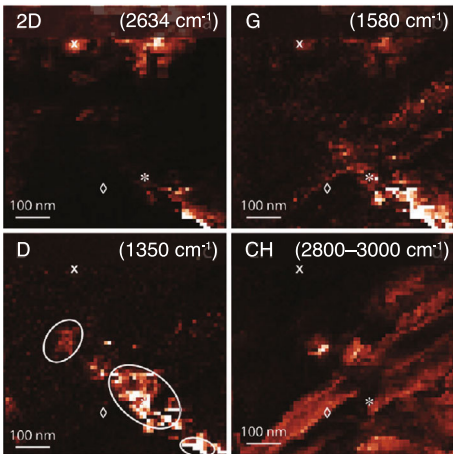



**Fig. 24.15** TERS images of a single-layer graphene at different Raman modes of $2D$, $G$, and $D$-band and CH stretching mode. Reproduced with permission from Ref. [22]. Copyright 2011 American Chemical Society

TERS microscopy has also been extensively employed to study the local chemical properties of CNTs [19, 33, 34]. By visualizing the distribution of localized defects along a single CNT through the intensity ratio of $D$ to $G$ bands, spatial resolutions of 15 nm or less have been achieved [34]. Additionally, simultaneous TERS and near-field photoluminescence measurements of CNTs have been conducted, suggesting variations in chirality along the nanotube [35].

The aforementioned three functions of TERS microscopy are combined to characterize a specific sample of interest. In the following section, we introduce an application of TERS microscopy to imaging and analysis of twisted bilayer graphene.

## 24.6 Twisted Bilayer Graphene

Twisted bilayer graphene (TBG) refers to a configuration where two layers of graphene are stacked on top of each other with a rotational mismatch. As observed in Fig. 24.16a, when these two hexagonal lattices overlap at an angle $\theta$, they create a distinct Moiré pattern [36–38]. TBG exhibits a unique electrostatic potential resulting from the interaction between the misaligned layers. This potential enables the transfer of momentum to photo-excited electrons, giving rise to a symmetry-selective double-resonance Raman scattering process, characterized by a distinctive $R'$ Raman signature. Unlike the disorder-induced $D'$ and $D$ bands, the frequency of $R'$ remains non-dispersive and fixed for a specific rotational angle $\theta$ [37].

To characterize TBG using TERS microscopy, first, the distribution of bilayer graphene, monolayer graphene, and multilayer graphene within a TBG sample is identified. This can be performed by quantifying $2D/G$ peak ratio [39]. Figure 24.16b presents a $2D/G$ ratio image captured by a TERS microscope (TERSsense, Nanophoton). Distributions of the three types of graphene—monolayer, bilayer, and

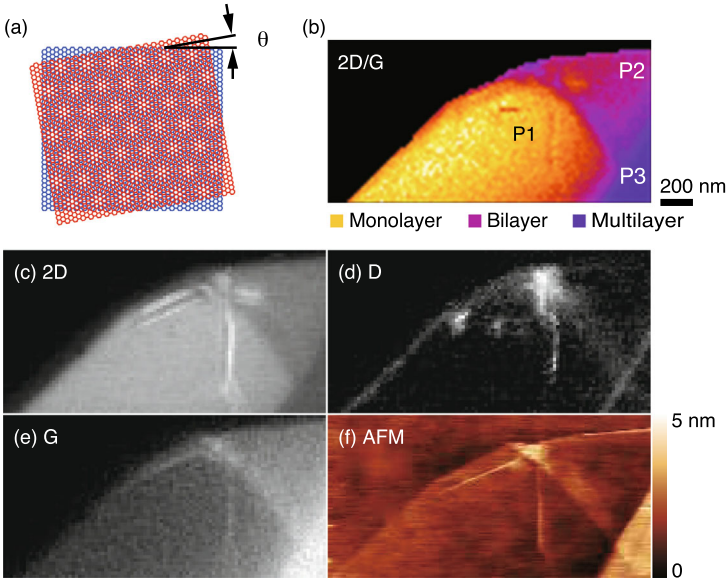



**Fig. 24.16** Twisted bilayer graphene (TBG). **a** Bilayer graphene stacked in a rotational arrangement, with the red layer positioned on top of the blue layer, featuring a mismatched angle of $\theta$. **b–e** TERS images of twisted bilayer graphene, displaying **b** $2D/G$, **c** $2D$, **d** $D$, and **e** $G$ bands. **f** Simultaneously obtained AFM image showing the topography of the TBG sample. Excitation laser wavelength, 488 nm; objective, 100 × N.A. = 1.4; scan area, 99 × 50 pixels with 20 nm step/pixel; exposure time; 0.3 s/pixel. The data was acquired using TERSsense by Nanophoton Corporation. Reproduced with permission from Ref. [16]. Copyright 2019 Elsevier

multilayer—were identified based on the different colors representing the $2D/G$ ratio. Additionally, TERS images of graphene at the $2D$, $D$, and $G$ bands are included in Fig. 24.16c–e, respectively. For comparison, an AFM image is provided in Fig. 24.16f, displaying only the edges and ridges of the graphene.

Upon close examination of the TERS spectra of graphene taken at positions corresponding to monolayer and bilayer regions, their differences are evident, as illustrated in Fig. 24.17. In Fig. 24.17a, a notable peak shift of the $2D$ band to a higher frequency is observed in bilayer graphene compared to monolayer graphene. Additionally, the peak width of bilayer graphene appears to be larger than that of monolayer graphene.

Figure 24.17b displays a slight peak shift of the $G$ band and the emergence of a new characteristic Raman band, denoted as $R'$. This $R'$ peak is distinctive of bilayer graphene and originates from the interaction between the two misoriented layers. Its presence serves as strong evidence that the bilayer graphene is twisted relative to each other.

The characteristic Raman peak $R'$, observed in bilayer graphene, was utilized to map the distribution of TBG, as shown in Fig. 24.18a. The spatial distribution of the $R'$-band signature correlates well with the bilayer region depicted in the $2D/G$

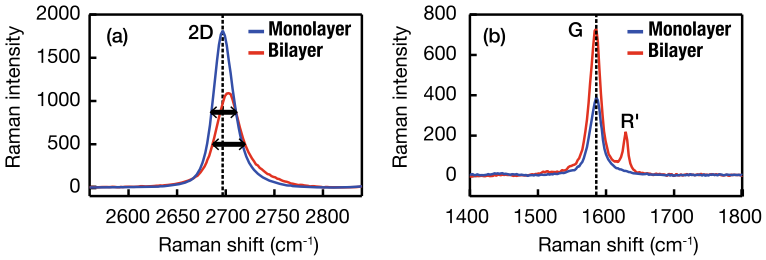



**Fig. 24.17** TERS spectra from monolayer and bilayer graphene shown in Fig. 24.16. **a** $2D$-band. **b** $G$-band and $R'$-peak that is a characteristic signature of TBG. Reproduced with permission from Ref. [16]. Copyright 2019 Elsevier

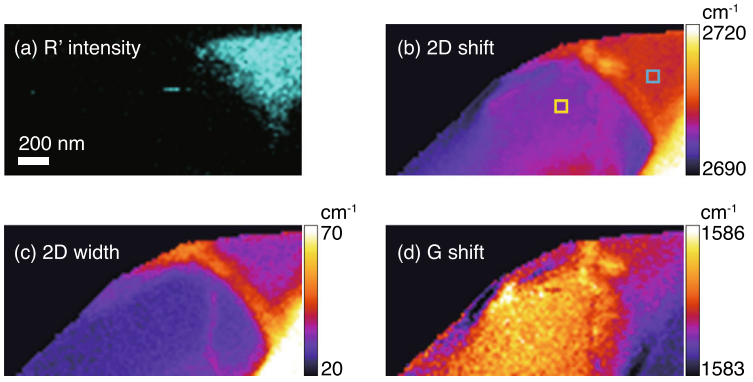



**Fig. 24.18** TERS images of twisted bilayer graphene. **a** Intensity distribution of the $R'$-band. **b** Peak shift image of the $2D$-band. **c** Peak width image of the $2D$-band. **d** Peak shift image of the $G$-band. Reproduced with permission from Ref. [16]. Copyright 2019 Elsevier

ratio image shown in Fig. 24.16. Moreover, the absence of the $D$ peak in the TERS spectrum suggests a low defect density in this region, further confirming the origin of the observed $R'$ peak as being attributed to twisted bilayer graphene.

Other spectral features, such as the peak shift and width of the $2D$-band, and the peak shift of the $G$-band, as observed in Fig. 24.17, are also mapped in Fig. 24.18b–d, respectively.

In the TBG region, a clear peak shift of the $2D$-band is observed in contrast to the monolayer region. Additionally, the $2D$ peak width (full-width at half-maximum) appears larger in the TBG region compared to the monolayer region. Furthermore, a slight shift of the $G$ peak is also evident.

The spatial resolution achieved in these TERS images is approximately 40 nm. This resolution is significantly higher than that of confocal Raman images, which typically range from 300 to 400 nm. TERS imaging enables the visualization of distinct details within nano-sized TBG domains, as well as graphene edges and local

strains on the nanoscale. Such high resolution is unachievable with confocal Raman microscopy due to its limited spatial resolution.

## 24.7 Force-Correlated TERS Spectroscopy

A unique application of TERS is to measure tip-sample force or mechanical properties of a sample by AFM while simultaneously recording Raman spectra. This correlated spectroscopy between force and Raman at the nanoscale cannot be achieved by surface-enhanced Raman spectroscopy (SERS), but only by TERS. For example, CNTs were pushed and deformed using a TERS tip operated in contact mode AFM, and a significant peak shift of the $G$-band was observed due to the local lattice perturbation [40].

Unlike contact- or tapping-mode AFM-based TERS microscopes, where only the repulsive force can be measured, non-contact mode AFM (nc-AFM) is capable of measuring force in both attractive and repulsive force regions. The nc-AFM has been integrated into a TERS microscopy system using a quartz tuning fork (QTF) sensor, as illustrated in Fig. 24.19a [18]. By monitoring the mechanical resonance frequency of the QTF interacting with the sample, the attractive force is measured as a negative shift of the resonance frequency, while the repulsive force manifests itself as a shift to the positive side. With an Ag tip mounted on the QTF probe, the force curve and TERS spectra were simultaneously measured on a bundle of semiconductor CNTs, as shown in Fig. 24.19b, c. Figure 24.19b plots the peak intensities of $G^+$- and $G^-$-band, and radial breathing mode (RBM)-band, as a function of tip height $z$, with the origin of $z$ defined at the point where the tip was brought closest to the sample. The graph shows exponential decay functions with the decay lengths of about $L_{G+} = 1.4$ nm, $L_{G-} = 2.9$ nm, and $L_{\mathrm{RBM}} = 1.7$ nm, for $G^+$, $G^-$, and RBM peaks, respectively. The values of the decay length (hatched region in Fig. 24.19b) are significantly smaller compared to the excitation laser wavelength ($\lambda = 488$ nm), demonstrating the highly localized near-field enhancement effect.

The force curve, displayed in Fig. 24.19c, demonstrates a typical behavior that transitions from attractive to repulsive force as the tip approaches the sample. The hatched region in Fig. 24.19c represents the tip-sample distance where repulsive force is exerted. As observed in Fig. 24.19b, c, the decay length $L$ is situated within the repulsive force region. In the region where attractive force is present, the near-field enhancement mostly diminishes. This observation indicates that TERS enhancement is achieved at the tip-sample distance where repulsive force is active, i.e., when the tip and sample are in contact or in close proximity.

TERS microscopy has been utilized for visualizing nanoscale strain distribution in a strained silicon substrate [24, 41] and a bent CNT [31]. The aforementioned observations suggest that, in such applications, tip-sample force is a crucial parameter to control when assessing the strain of the intact sample. Understanding the tip-sample force during TERS experiments and its impact on TERS spectra is essen-

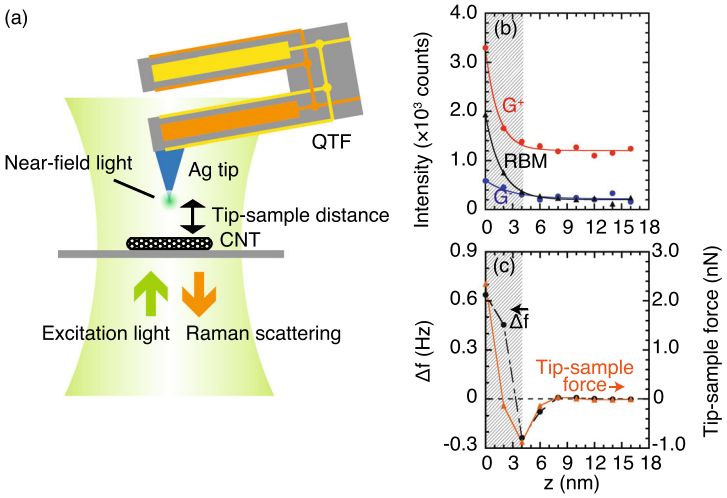



**Fig. 24.19** **a** Force-correlated TERS spectroscopy. A force curve and TERS spectra are measured simultaneously on a CNT sample using an Ag tip mounted on a quartz tuning fork (QTF). **b** Peak intensities of $G^+$-band, $G^-$-band, and radial breathing mode (RBM)-band as a function of the tip-sample distance $z$. The solid curves represent exponentially decaying fits to the measured data, indicating decay lengths of $L_{G+} = 1.4$ nm, $L_{G-} = 2.9$ nm, and $L_{\mathrm{RBM}} = 1.7$ nm, for $G^+$, $G^-$, and RBM peaks, respectively. **c** Simultaneously measured resonance frequency shift of QTF, $\Delta f$, and the corresponding calculated tip-sample force derived from $\Delta f$. The hatched region represents the repulsive force region. Reproduced with permission from Ref. [18]. Copyright 2019 AIP Publishing

tial for analyzing TERS spectra confidently, and force-correlated TERS offers valuable insights in this regard.

## 24.8 DUV-TERS

In this section, we explore TERS in the DUV region, where DUV refers to light with wavelengths ranging from 200 to 300 nm. With DUV excitation, Raman scattering of molecules such as benzene, amino acids, and nucleic acids is enhanced primarily due to resonance Raman effects arising from resonance with $\pi$ electrons within the molecules. The enhancement of resonance Raman scattering intensity can be as high as $10^8$ [42]. Resonance Raman scattering is effective for analyzing low-concentration samples and specific molecular vibrations, and it is utilized in the structural analysis of proteins. DUV resonance Raman spectroscopy is also useful for the analysis of wide-gap semiconductors, and there is a high demand for nanoscale analytical methods for developing nanodevices using such wide-bandgap materials. Therefore, combining resonance Raman scattering with TERS enhancement using a metallic tip

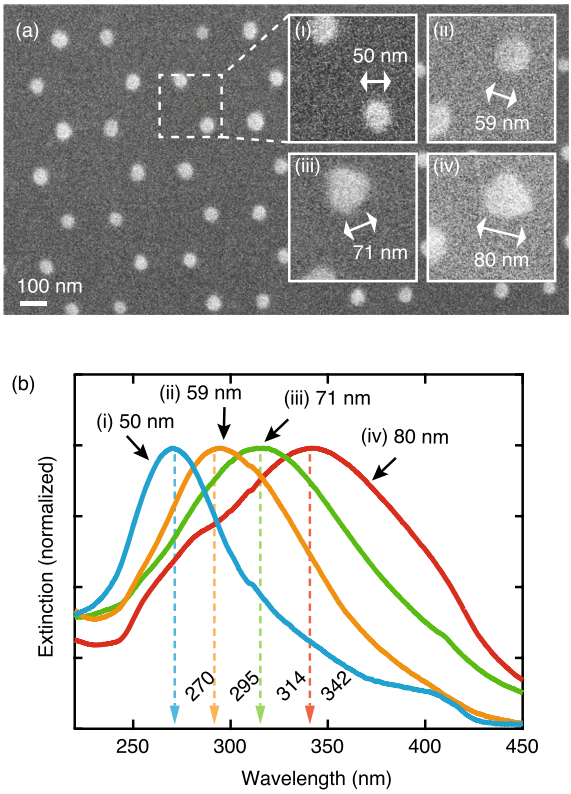



**Fig. 24.20** Localized surface plasmon spectroscopy of Al nanoparticles. **a** Scanning electron microscopy (SEM) image of Al nanoparticles fabricated using vacuum deposition and nanosphere lithography techniques. **b** Extinction spectrum of the Al nanoparticle array. Reproduced with permission from Ref. [4]. Copyright 2012 AIP Publishing

offers a unique opportunity for nanoscale spectroscopic analysis of materials such as wide-bandgap materials and biological molecules.

### *24.8.1 DUV Plasmon Resonance in Metal Nanostructures*

As discussed in Sect. 24.2.1, Al shows promise as a DUV plasmonic metal. Experimental validation of Al's plasmon resonance in the DUV wavelength range has been achieved. Figure 24.20 illustrates the measurement results of plasmon resonance in Al nanoparticles of various sizes [4]. The extinction spectra peaks of Al nanoparticles were observed at wavelengths ranging from 270 to 342 nm, depending on the particle size (Fig. 24.20b). These peaks are reproduced by electromagnetic field simulations based on Al nanoparticles of similar sizes, confirming that they are plasmon resonance peaks [4].

The Al nanoparticles shown in Fig. 24.20a are fabricated using a technique known as nanosphere lithography. In this method, polystyrene spheres are self-assembled into a hexagonally close-packed monolayer on a quartz substrate, forming a lithog-

raphy mask. Al is then vacuum-deposited onto the substrate through this mask. Consequently, the pattern of the nano-sized gaps between adjacent spheres is transferred onto the substrate as Al nanostructures. Additionally, prior to deposition, the self-assembled structure of polystyrene spheres is immersed in ethanol and heated in a microwave oven, resulting in the expansion of the nanospheres and narrowing of the gaps. This phenomenon is exploited to adjust the size of the Al nanoparticles [4]. Unlike Ag and Au, Al has a negative redox potential, making it difficult to chemically synthesize Al nanoparticles through ion reduction in aqueous solution. Therefore, physical vapor deposition is commonly used for fabricating Al nanostructures. Liquid-phase synthesis of Al single crystals has also been reported [43].

### *24.8.2 DUV Tip-Enhancement of Resonant Raman Scattering*

Figure 24.21a shows a scanning electron microscopy (SEM) image of a Si cantilever probe coated with Al by vacuum evaporation [3]. It can be observed that Al is deposited on the tip of the probe, forming nanoparticles with a diameter of approximately 20 nm. Figure 24.21b shows the result of measuring DUV resonance Raman

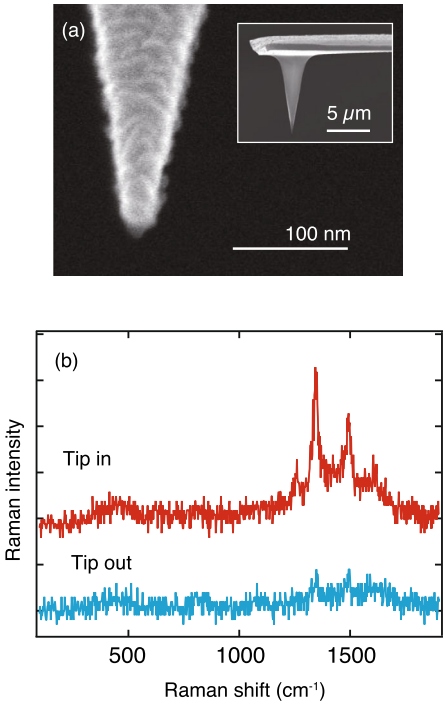



**Fig. 24.21** **a** SEM image of a Si probe coated with Al. **b** DUV resonance Raman spectrum of adenine nanocrystals measured with and without the Al probe. Excitation wavelength was 266 nm. Reproduced with permission from Ref. [3]. Copyright 2009 John Wiley and Sons

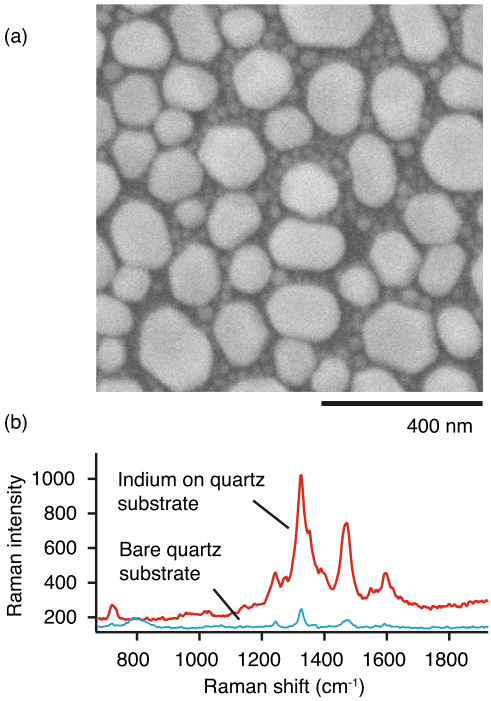



**Fig. 24.22** **a** SEM image of an indium-deposited substrate. The average film thickness during deposition is 25 nm. **b** Deep ultraviolet Raman spectra of adenine thin films formed on indium-deposited substrates and quartz substrates. The excitation wavelength is 266 nm. Reproduced with permission from Ref. [5]. Copyright 2014 American Chemical Society

scattering by bringing this probe close to adenine nanocrystals. The excitation wavelength used for Raman scattering was 266 nm, overlapping with the absorption of adenine. The intensity of Raman scattering when the Al probe is brought close to the sample is significantly stronger compared to when the Al probe is removed. The Raman enhancement under these conditions is approximately 1300 times [3].

DUV resonance Raman scattering enhancement has also been observed with indium. Figure 24.22a displays a SEM image of the structure where indium is deposited on a quartz substrate [5]. Indium forms crystalline grains when it is deposited on a quartz substrate, as depicted in this figure. Figure 24.22b illustrates the DUV Raman spectra of adenine films coated on the indium substrate and a quartz substrate [5]. The excitation wavelength is 266 nm. As observed in the figure, resonance Raman scattering of adenine is significantly enhanced in the case of indium. The Raman enhancement in this case is estimated to be 100 [5].

**Acknowledgements** I am grateful to S. Kawata, K. Saitoh, and J. Yu for their collaboration at Osaka University when the main results of this article were obtained.

## References


1. H. Raether, *Surface-Plasmons on Smooth and Rough Surfaces and on Gratings*, *Springer-Verlag*, vol. 111 (Springer-Verlag, 1988)
2. E.D. Palik, *Handbook of Optical Constants of Solids*. Academic Press (Academic Press, 1997)
3. A. Taguchi, N. Hayazawa, K. Furusawa, H. Ishitobi, S. Kawata, Journal of Raman Spectroscopy **40**(9), 1324 (2009).
4. A. Taguchi, Y. Saito, K. Watanabe, S. Yijian, S. Kawata, Applied Physics Letters **101**(8), 081110 (2012).
5. Y. Kumamoto, A. Taguchi, M. Honda, K. Watanabe, Y. Saito, S. Kawata, ACS Photonics **1**(7), 598 (2014).
6. Y. Ozaki, S. Kawata (eds.), *Far- and Deep-Ultraviolet Spectroscopy* (Springer, 2015)
7. N. Hayazawa, Y. Inouye, Z. Sekkat, S. Kawata, Optics Communications **183**(1–4), 333 (2000).
8. R.M. Stöckle, Y.D. Suh, V. Deckert, R. Zenobi, Chemical Physics Letters **318**(1–3), 131 (2000).
9. C. Blum, L. Opilik, J.M. Atkin, K. Braun, S.B. Kämmer, V. Kravtsov, N. Kumar, S. Lemeshko, J. Li, K. Luszcz, T. Maleki, A.J. Meixner, S. Minne, M.B. Raschke, B. Ren, J. Rogalski, D. Roy, B. Stephanidis, X. Wang, D. Zhang, J. Zhong, R. Zenobi, Journal of Raman Spectroscopy **45**(1), 22 (2014).
10. A. Taguchi, J. Yu, P. Verma, S. Kawata, Nanoscale **7**(41), 17424 (2015).
11. S. Kawata, A. Ono, P. Verma, Nature Photonics **2**(7), 438 (2008).
12. N. Hayazawa, T. Yano, H. Watanabe, Y. Inouye, S. Kawata, Chemical Physics Letters **376**(1–2), 174 (2003).
13. B.S. Yeo, T. Schmid, W. Zhang, R. Zenobi, Analytical and Bioanalytical Chemistry **387**(8), 2655 (2007).
14. A. Ono, K. Masui, Y. Saito, Y. Saito, T. Sakata, A. Taguchi, M. Motohashi, T. Ichimura, H. Ishitobi, A. Tarun, N. Hayazawa, P. Verma, Y. Inouye, S. Kawata, Chemistry Letters **37**(1), 122 (2008).
15. A. Taguchi, N. Hayazawa, Y. Saito, H. Ishitobi, A. Tarun, S. Kawata, Optics Express **17**(8), 6509 (2009).
16. A. Taguchi, J. Yu, K. Saitoh, in *Comprehensive Nanoscience and Nanotechnology*, vol. 4, ed. by D.L. Andrews, R.H. Lipson, T. Nann (Elsevier, 2019), pp. 13–32.
17. K.M. McPeak, S.V. Jayanti, S.J.P. Kress, S. Meyer, S. Iotti, A. Rossinelli, D.J. Norris, ACS Photonics **2**(3), 326 (2015).
18. K. Saitoh, A. Taguchi, S. Kawata, APL Photonics **4**(2), 021301 (2019).
19. A. Bouhelier, M. Beversluis, A. Hartschuh, L. Novotny, Physical Review Letters **90**(1), 013903 (2003).
20. Y. Saito, K. Yanagi, N. Hayazawa, H. Ishitobi, A. Ono, H. Kataura, S. Kawata, Japanese Journal of Applied Physics Part 1-Regular Papers Brief Communications & Review Papers **45**(12), 9286 (2006).
21. Y. Saito, Y. Saito, M. Motohashi, N. Hayazawa, M. Iyoki, S. Kawata, Applied Physics Letters **88**(14), 143109 (2006).
22. J. Stadler, T. Schmid, R. Zenobi, ACS Nano **5**(10), 8442 (2011).
23. Y. Zhang, D.V. Voronine, S. Qiu, A.M. Sinyukov, M. Hamilton, Z. Liege, A.V. Sokolov, Z. Zhang, M.O. Scully, Scientific Reports **6**(1), 25788 (2016).
24. N. Hayazawa, M. Motohashi, Y. Saito, H. Ishitobi, A. Ono, T. Ichimura, P. Verma, S. Kawata, Journal of Raman Spectroscopy **38**(6), 684 (2007).
25. E. Poliani, M.R. Wagner, J.S. Reparaz, M. Mandl, M. Strassburg, X. Kong, A. Trampert, C.M.S. Torres, A. Hoffmann, J. Maultzsch, Nano Letters **13**(7), 3205 (2013).
26. M. Böhmler, Z. Wang, A. Myalitsin, A. Mews, A. Hartschuh, Angewandte Chemie International Edition **50**(48), 11536 (2011).
27. N. Marquestaut, D. Talaga, L. Servant, P. Yang, P. Pauzauskie, F. Lagugné-Labarthet, Journal of Raman Spectroscopy **40**(10), 1441 (2009).
28. N. Hayazawa, T. Yano, S. Kawata, Journal of Raman Spectroscopy **43**, 1177 (2012).

29. R. Zhang, Y. Zhang, Z.C. Dong, S. Jiang, C. Zhang, L.G. Chen, L. Zhang, Y. Liao, J. Aizpurua, Y. Luo, J.L. Yang, J.G. Hou, Nature **498**(7452), 82 (2013).
30. C. Chen, N. Hayazawa, S. Kawata, Nature Communications **5**, 3312 (2014).
31. T. Yano, T. Ichimura, S. Kuwahara, F. H'Dhili, K. Uetsuki, Y. Okuno, P. Verma, S. Kawata, Nature Communications **4**(1), 2592 (2013).
32. A. Tarun, N. Hayazawa, S. Kawata, Analytical and Bioanalytical Chemistry **394**(7), 1775 (2009).
33. A. Hartschuh, Angewandte Chemie International Edition **47**(43), 8178 (2008).
34. C. Georgi, A. Hartschuh, Applied Physics Letters **97**(14), 143117 (2010).
35. A. Hartschuh, H.H. Qian, A.J. Meixner, N. Anderson, N. Anderson, L. Novotny, Nano Letters **5**(11), 2310 (2005).
36. K. Kim, S. Coh, L.Z. Tan, W. Regan, J.M. Yuk, E. Chatterjee, M.F. Crommie, M.L. Cohen, S.G. Louie, A. Zettl, Physical Review Letters **108**(24), 246103 (2012).
37. V. Carozo, C.M. Almeida, E.H.M. Ferreira, L.G. Cançado, C.A. Achete, A. Jorio, Nano Letters **11**(11), 4527 (2011).
38. R.W. Havener, H. Zhuang, L. Brown, R.G. Hennig, J. Park, Nano Letters **12**(6), 3162 (2012).
39. D. Graf, F. Molitor, K. Ensslin, C. Stampfer, A. Jungen, C. Hierold, L. Wirtz, Nano Letters **7**(2), 238 (2007).
40. T. Yano, P. Verma, Y. Saito, T. Ichimura, S. Kawata, Nature Photonics **3**(8), 473 (2009).
41. A. Tarun, N. Hayazawa, M. Motohashi, S. Kawata, Review of Scientific Instruments **79**(1), 013706 (2008).
42. S.A. Asher, R.W. Bormett, X.G. Chen, D.H. Lemmon, N. Cho, P. Peterson, M. Arrigoni, L. Spinelli, J. Cannon, Applied Spectroscopy **47**(5), 628 (1992).
43. M.J. McClain, A.E. Schlather, E. Ringe, N.S. King, L. Liu, A. Manjavacas, M.W. Knight, I. Kumar, K.H. Whitmire, H.O. Everitt, P. Nordlander, N.J. Halas, Nano Letters **15**(4), 2751 (2015).